Northeastern University

DEPARTMENT OF CIVIL AND ENVIRONMENTAL ENGINEERING REPORTS

Deconstructable Systems for Sustainable Design of Steel and Composite Structures

June 2020

Lizhong Wang
Northeastern University

Mark D. Webster
Simpson Gumpertz &Heger, Inc.

Jerome F. Hajjar
Northeastern University

Report No. NEU-CEE-2020-01

Recommended Citation

Wang, Lizhong; Webster, Mark D.; and Hajjar, Jerome F., "Deconstructable Systems for Sustainable Design of Steel and Composite Structures" (2020). *Department of Civil and Environmental Engineering Reports.* Report No. NEU-CEE-2020-01. Department of Civil and Environmental Engineering, Northeastern University, Boston, Massachusetts.

This report is available open access, hosted by Northeastern University.

Northeastern University was founded in 1898, as a private research university. Northeastern University is a leader in worldwide experiential learning, urban engagement, and interdisciplinary research that meets global and societal needs. Department of Civil and Environmental Engineering has over 100 years of history and tradition in research, teaching and service to the community, making important contributions to the development of our civil infrastructure and the environment, both nationally and internationally.

Contact:
Department of Civil & Environmental Engineering
400 Snell Engineering Center
Northeastern University
360 Huntington Avenue
Boston, MA 02115
(617) 373-2444
(617) 373-4419 (fax)

The authors would like to thank former graduate student Clayton Brown for working on the life cycle assessment part of this research, Prof. Matthew Eckelman for reviewing this part and providing constructive recommendations, and graduate student Luke Troup for continuing and finishing the work. The authors also would like to thank Kyle Coleman, Michael McNeil, Kurt Braun, Corinne Bowers, Edward Myers, Majed Alnaji, Madeline Augustine, Ian Carver, Morgan Foster, Michael Bangert-Drowns, Kara Peterman, Angelina Jay, Justin Kordas, David Padilla-Llano, and Yujie Yan for their assistance with the experiments. The authors acknowledge Prof. Gian A. Rassati and graduate student Andrew Roenker from the University of Cincinnati for performing ancillary shear and tension testing for bolts and rods. The authors also appreciate the communication with and advice from Dan Costello of Costello Dismantling Co., Inc.

This material is based upon work supported by the National Science Foundation under Grant No. CMMI-1200820 and Grant No. IIS-1328816, the American Institute of Steel Construction, Northeastern University, and Simpson Gumpertz and Heger. Computational analyses in this work used the Extreme Science and Engineering Discovery Environment (XSEDE), which is supported by National Science Foundation grant number ACI-1548562. In-kind support is provided by Benevento Companies, Capone Iron Corporation, Fastenal, Halfen, Lehigh Cement Company, Lindapter, Meadow Burke, S&F Concrete, and Souza Concrete. This support is gratefully acknowledged. Any opinions, findings, and conclusions expressed in this material are those of the authors and do not necessarily reflect the views of the National Science Foundation or other sponsors.

ABSTRACT

According to the U.S. Energy Information Administration, construction and use of buildings consumed almost half of the total energy used in the United States in 2012. Design for Deconstruction (DfD) of buildings was proposed to minimize the environmental impacts and reduce the pollution and waste produced during the construction and demolition of buildings by reclaiming the materials at the end of the service life of buildings. Traditional steel-concrete composite flooring system makes the most efficient use of the two materials, with steel being subjected to tension and concrete resisting compression. However, in this system the concrete slabs are poured integrally with the supporting steel framing systems, inhibiting the separation and reuse of the structural components.

The objectives of the proposed research are to develop new structural system concepts for deconstructable steel and steel-concrete composite construction to facilitate DfD coupled with the use of recycled materials in sustainably optimized construction. The proposed system not only maintains the benefits offered by composite construction but also enables disassembly and reuse of the structural components.

This report first describes the deconstructable composite floor system utilizing clamping connectors. This floor system is anticipated to be used along with all-bolted construction for the remainder of the structure to facilitate deconstruction. The environmental benefits of utilizing DfD in the design of buildings is demonstrated with the life cycle assessment results of prototype structures. The experimental program for investigating the performance of the system is then introduced. Pushout tests are conducted to quantify the strength and ductility of the clamping connectors and evaluate the influences of the parameters. It is indicated that the strength of the ductile clamping connectors is comparable to that of steel headed stud anchors. In addition, the behavior of the clamping connectors is further validated through full-scale beam tests in which the flexural behavior of the deconstructable composite beams is investigated comprehensively. Combining experimental and finite element analysis results, strength design equations and resistance factors are proposed for calculating the shear strength of the clamping connectors and the flexural strength of the associated composite beams. This report culminates with conclusions and future work.

TABLE OF CONTENTS

ABSTRACT ii
LIST OF FIGURES xii
LIST OF TABLES xxi
1. INTRODUCTION 1
  1.1 Deconstructable composite prototype system 3
  1.2 Research scope and organization 5
2. LITERATURE REVIEW 8
  2.1 Design for Deconstruction 8
  2.2 Prefabricated structural systems 10
  2.3 Steel headed stud anchors 12
    2.3.1 Pushout tests and beam tests 12
    2.3.2 Deconstructable shear connectors 20
    2.3.3 Analytical and computational analysis of steel headed stud anchors and composite beams 23
  2.4 Seismic design of diaphragms 24
    2.4.1 Seismic demand on diaphragms 25
    2.4.2 Seismic behavior of diaphragms 26
    2.4.3 Diaphragm analysis 26
    2.4.4 Diaphragm component design 27
      2.4.4.1 Composite diaphragm strength 27
      2.4.4.2 Steel members 28
      2.4.4.3 Shear connectors 29
    2.4.5 Diaphragm seismic design methodology 29
3. PROTOTYPE STRUCTURES 32
  3.1 Selection and design of prototype structures 32
  3.2 Loads 35
    3.2.1 Gravity load 35

3.2.2 Live load reduction 36
3.2.3 Earthquake load 36
3.2.4 Wind and snow load 39
3.2.5 Load combinations for strength design 41
3.3 Design criteria 41
3.3.1 Gravity system 41
3.3.2 Lateral force resistance system 43
3.3.3 Member requirements 44
3.3.4 Story drift determination 45
3.4 Final design 48
3.5 Results from life cycle assessment 51
3.6 Communication with dismantler 54
4. PUSHOUT TESTS 57
4.1 Test matrix 57
4.2 Test specimen design 60
4.3 Material properties 66
4.4 Pretension tests 75
4.4.1 Test setup and instrumentation 75
4.4.2 Specimen performance 77
4.4.3 Behavior of bolts and channel lips 79
4.5 Pushout tests 82
4.5.1 Test setup 83
4.5.2 Instrumentation 93
4.5.3 Loading protocol 100
4.5.4 Specimen performance 101
4.5.4.1 Monotonic specimens 101
4.5.4.2 Cyclic specimens 111
4.5.4.3 Comparison with steel headed stud anchors 134
4.5.5 Formation of cracks on concrete surfaces 136
4.5.6 Influences of different parameters 141
4.5.7 Behavior of bolts and channel lips 144
4.5.8 Force distribution in the system 153
4.5.9 Response of channel anchors and reinforcement 158

4.6 Finite element analysis 161
  4.6.1 Finite element model and mesh 161
  4.6.2 Boundary conditions, load applications and contact 162
  4.6.3 Material model for concrete 163
  4.6.4 Material models for steel beams, reinforcement, channels and bolts 165
  4.6.5 Finite element analysis results 166
4.7 Design recommendations 171
4.8 Conclusions 179
5. BEAM TESTS 184
5.1 Test matrix 185
5.2 Test specimen design and test setup 187
  5.2.1 Test specimen design 187
  5.2.2 Test setup 189
  5.2.3 Pretension tests on fully threaded rods 194
5.3 Material properties 198
5.4 Instrumentation 209
5.5 Loading protocol 217
5.6 Assessment of deconstructable composite beams 218
  5.6.1 Gaps between concrete planks 219
  5.6.2 Behavior of composite beam specimens 223
    5.6.2.1 Specimen 1-M24-2C-RH 224
    5.6.2.2 Specimen 2-M24-1C-RL 230
    5.6.2.3 Specimen 3-M20-3C-RL 237
    5.6.2.4 Specimen 4-M20-1C-RL 244
    5.6.2.5 Strength and stiffness comparison 255
    5.6.2.6 Ductility 259
    5.6.2.7 Camber 267
    5.6.2.8 Effect of friction produced by actuator loading and self-weight of specimen 268
  5.6.3 Slip of clamps 269
  5.6.4 Beam section strain 273
    5.6.4.1 Strain distribution along the depth of the section 273
    5.6.4.2 Location of neutral axis in steel beam 283

5.6.4.3 Load versus steel section strain 286
5.6.4.4 Verification of strain gage readings 289
5.6.5 Bolt tension 291
5.6.6 Rod tension 297
5.6.7 Response of channel anchors and reinforcement 300
5.6.8 Effective width 303
5.6.9 Behavior of clamping connectors in pushout tests and beam tests 309
5.7 Finite element analysis 312
5.7.1 Finite element model and mesh 312
5.7.2 Boundary conditions, load applications and contact 313
5.7.3 Material model for concrete 314
5.7.4 Material models for steel beam, reinforcement, channels and bolts 315
5.7.5 Finite element analysis results 316
5.8 Design recommendations 320
5.9 Conclusions 322
6. RELIABILITY ASSESSMENT OF COMPOSITE BEAMS 327
6.1 Shear strength of clamping connectors 333
6.2 Flexural strength of composite beams 336
7. CONCLUSIONS AND FUTURE WORK 340
7.1 Summary of pushout tests 340
7.2 Conclusions from composite beam tests 345
7.3 Recommendations 350
7.3.1 Design 350
7.3.1.1 Clamping connectors 351
7.3.1.2 Deconstructable composite beams 351
7.3.2 Future research 352
REFERENCES 354
APPENDIX 366
Appendix A PROTOTYPE STRUCTURE DESIGN SUMMARY 367
Appendix B PRECAST CONCRETE PLANK DESIGN 374
B.1 Flexural reinforcement and shear reinforcement design 374
B.2 Shear key design 394
Appendix C SPECIMEN DRAWINGS 397

C.1 Pushout tests 398
C.1.1 Steel specimen shop drawings 398
C.1.2 Concrete specimen design drawings 407
C.1.3 Cast-in channel drawing 411
C.2 Beam tests 412
C.2.1 Steel specimen shop drawings 412
C.2.2 Concrete specimen design drawings 436
C.2.3 Cast-in channel drawing 443
Appendix D MILL CERTIFICATIONS 444
D.1 Pushout tests 445
D.1.1 Steel frame 445
D.1.2 Halfen channels and bolts 447
D.1.3 Lindapter clamps and washers 451
D.1.4 Reinforcement 459
D.1.5 Concrete 461
D.2 Beam tests 462
D.2.1 Steel frame 462
D.2.2 Fully threaded rods 464
D.2.3 Halfen channels and bolts 468
D.2.4 Lindapter clamps and washers 472
D.2.5 Reinforcement 478
D.2.6 Concrete 481
Appendix E EXPERIMENTAL RAW DATA 484
E.1 Pushout test specimens 485
E.1.1 Pretension tests 485
E.1.2 Pushout tests 486
E.1.2.1 Actuator forces, actuator displacements and slips 486
E.1.2.2 Beam strain gages 491
E.1.2.3 Bolt strain gages 493
E.1.2.4 Channel lip strain gages 494
E.1.2.5 Channel anchor strain gages 497
E.1.2.6 Reinforcement strain gages 498
E.2 Beam test specimens 498

E.2.1 Actuator forces and actuator displacements 499
E.2.2 Beam deformation 500
E.2.3 Beam rotation 502
E.2.4 Slip of clamps 504
E.2.5 Rod tension 504
E.2.6 Steel section strain gages 506
E.2.7 Concrete plank strain 508
E.2.8 Bolt strain gages 511
E.2.9 Channel lip strain gages 514
E.2.10 Channel anchor strain gages 516
E.2.11 Reinforcement strain gages 517
Appendix F DATA REDUCTION 518
F.1 Pushout tests 518
F.1.1 Load distribution among clamps 519
F.1.2 Bolt pretention force variation 523
F.1.2.1 Pretension test 526
F.1.2.2 Pushout test 527
F.1.3 Forces acting on channel anchors 528
F.2 Beam tests 533
F.2.1 Error in vertical and horizontal deflection measurements 534
F.2.2 Beam end rotation calculation 538
F.2.3 Beam 3 center deflection extrapolation 539
F.2.4 Effective width calculation 540
F.2.5 Bolt tension variation 542
F.2.6 Axial force and bending moment at a cross section 545
F.2.7 Location of neutral axis in steel beam 556
F.2.8 Forces acting on channel anchors 558
Appendix G SELECTION OF REACTION ANGLES IN PUSHOUT TESTS 560
Appendix H SHEAR FORCE TRANSFER FOR COMPOSITE DIAPHRAGMS, LIFTING INSERTS, AND FULLY THREADED RODS DESIGN 562
H.1 Shear force transfer for composite diaphragms 562
H.2 Lifting points on concrete planks 569
H.3 Selection of fully threaded rods 572

Appendix I MOMENT OF INERTIA OF A COMPOSITE BEAM SECTION..................... 574

Appendix J COMPOSITE BEAM STRENGTH AND STIFFNESS CALCULATION........ 578

Appendix K DIAPHRAGM BEHAVIOR OF DECONSTRUCTABLE COMPOSITE FLOOR SYSTEMS 592

K.1 Finite element model and mesh 592

K.1.1 Boundary conditions, load applications and contact....................................... 593

K.1.2 Material models 594

K.2 Analysis results 597

LIST OF FIGURES

Figure 1.1 Deconstructable composite beam prototype 4
Figure 1.2 Precast concrete plank connections 4
Figure 1.3 Precast concrete plank cross section (units: inches) 5
Figure 1.4 Typical floor plan for deconstructable composite floor system (units: feet) 5
Figure 2.1 Diaphragm components 25
Figure 2.2 Loading pattern for diaphragms at different levels 26
Figure 3.1 Building layout for three-story buildings 33
Figure 3.2 Relative LCA results comparing Traditional and DfD building designs assuming 0-3 reuses; disaggregated by life cycle stage; Traditional building = 100% 52
Figure 3.3 Absolute LCA results for Global Warming (ton CO2e) comparing building configurations; disaggregated by life cycle stage 53
Figure 3.4 Results of Monte Carlo simulation for uncertainty analysis; Traditional and DfD building designs assuming 0-3 reuses; disaggregated by life cycle stage; Traditional building mean = 100%; 95% confidence intervals 54
Figure 4.1 Different use of shims 59
Figure 4.2 Tensile load transfer in different applications 62
Figure 4.3 Different reinforcement patterns for pushout test specimens 64
Figure 4.4 Supplementary reinforcement and surface reinforcement arrangement 65
Figure 4.5 Pushout test tensile coupon dimensions (units: inches) 68
Figure 4.6 T-bolt tensile testing fixture 70
Figure 4.7 Tensile load versus axial elongation 71
Figure 4.8 Failed M24 and M20 bolts under tension 71
Figure 4.9 T-bolt shear testing fixture 72
Figure 4.10 Shear load versus shear deformation 72
Figure 4.11 Failed M24 and M20 bolts under shear 72
Figure 4.12 Bolt pretension test setup 76
Figure 4.13 Strain gage layout in bolt pretension tests 77
Figure 4.14 Photographs of bolt pretension tests 79
Figure 4.15 Bolt tension variation in pretension tests 82
Figure 4.16 Pushout test loading frame 85
Figure 4.17 Isometric view of pushout test setup 86
Figure 4.18 Different views of pushout test specimen 87
Figure 4.19 Clamping connector loading scenario comparison 92
Figure 4.20 Displacement measurements in pushout tests 94

Figure 4.21 Strain gages attached on the bolts, channel lips and beams in pushout test specimens 97
Figure 4.22 Strain gages attached on the reinforcement and channel anchors in pushout test specimens 99
Figure 4.23 Cyclic slip history and loading rates for pushout test specimens 101
Figure 4.24 Load–slip curve of Specimen 2-M24-2C-RH-LM 103
Figure 4.25 Observations in Specimen 2-M24-2C-RH-LM 103
Figure 4.26 Load–slip curve of Specimen 4-M24-2C-RH-LM-S 105
Figure 4.27 Observations in Specimen 4-M24-2C-RH-LM-S 105
Figure 4.28 Load-slip curve of Specimen 7-M24-3C-RH-LM 107
Figure 4.29 Observations in Specimen 7-M24-3C-RH-LM 107
Figure 4.30 Load-slip curve of Specimen 9-M20-2C-RH-LM 109
Figure 4.31 Observations in Specimen 9-M20-2C-RH-LM 109
Figure 4.32 Load-slip curve of Specimen 3-M24-2C-RL-LC 113
Figure 4.33 Observations in Specimen 3-M24-2C-RL-LC 114
Figure 4.34 Load-slip curve of Specimen 5-M24-2C-RH-LC 115
Figure 4.35 Observations in Specimen 5-M24-2C-RH-LC 116
Figure 4.36 Load-slip curve of Specimen 6-M24-2C-RH-LC-S 118
Figure 4.37 Observation in Specimen 6-M24-2C-RH-LC-S 119
Figure 4.38 Load-slip curve of Specimen 8-M24-3C-RH-LC 120
Figure 4.39 Observations in Test 8-M24-3C-RH-LC 121
Figure 4.40 Load-slip curve of Specimen 10-M20-2C-RH-LC 123
Figure 4.41 Observations in Specimen 10-M20-2C-RH-LC 124
Figure 4.42 Relationship between cyclic strength reduction and slip in pushout tests 129
Figure 4.43 Illustration of ductility index, energy dissipation and stiffness 132
Figure 4.44 Clamp teeth damage 134
Figure 4.45 Different black stripe patterns in pushout test specimens 138
Figure 4.46 Schematic presentation of flange profiles 138
Figure 4.47 Channel anchor and bolt positions in a pushout test specimen 139
Figure 4.48 Illustration of the strut-and-tie model 140
Figure 4.49 Distributed area for frictional force 140
Figure 4.50 Load-slip curve comparison between specimens with different rebar patterns 142
Figure 4.51 Cracks at the steel/concrete interface in beam specimens 143
Figure 4.52 Boundary conditions for bolts 145
Figure 4.53 Bolt tension versus slip curves for pushout specimens 152
Figure 4.54 Effect of clamping force on the load-displacement curve [after (Frank et al. 1981)] 153
Figure 4.55 Section axial force-slip curves for pushout test specimens 158
Figure 4.56 Channel anchor stresses in pushout specimens 160
Figure 4.57 Test setup assembly and boundary conditions 163
Figure 4.58 Concrete compressive and tensile damage variable 165
Figure 4.59 Loading and unloading behavior of concrete in compression and tension 165
Figure 4.60 Load-slip curve comparison 167
Figure 4.61 Rotation of clamps in finite element model (plan view) 168

Figure 4.62 Maximum equivalent plastic strain in bolt 168
Figure 4.63 Stress-strain curves of bolt material in beam tests 169
Figure 4.64 Bolt tension-slip relationship 170
Figure 4.65 Normal force at clamp teeth to bolt tension ratio 170
Figure 4.66 Free body diagram of steel beam and clamp 172
Figure 4.67 Impressions on steel flange in pretension test for M24 bolts 173
Figure 4.68 Damage of steel flange in 173
Figure 4.69 Typical clamping connections [after (Lindapter 2011)] 177
Figure 5.1 Different views of a composite beam specimen 192
Figure 5.2 Composite beam test setup 193
Figure 5.3 Photographs of threaded rod pretension tests 196
Figure 5.4 Rod tension variation in pretension tests 197
Figure 5.5 Mill tolerances on a W-shape cross section [after (AISC 303-16)] 199
Figure 5.6 Fully threaded rod coupon dimension (units: inches) 200
Figure 5.7 Tensile load versus axial elongation 202
Figure 5.8 Shear load versus Shear deformation 203
Figure 5.9 Failed specimens under tension 204
Figure 5.10 Failed specimens under shear 204
Figure 5.11 Location of instrumentation on beams 212
Figure 5.12 Steel beam and concrete plank sensor layout 213
Figure 5.13 Channel lip and bolt gage layout 214
Figure 5.14 Channel anchor gage layout 215
Figure 5.15 Longitudinal and transverse reinforcement gage layout 216
Figure 5.16 Location of instrumented threaded rods 217
Figure 5.17 Localized concrete crushing after pretensioning fully threaded rods 219
Figure 5.18 Solid or insulated flat structural wall panel tolerance [after PCI MNL-135-00 (2000)] 220
Figure 5.19 Measured gap widths for the composite beams (units: inches) 222
Figure 5.20 Total load vs beam midspan deflection curve for Specimen 1-M24-2C-RH 227
Figure 5.21 Center section moment vs beam end rotation curve for Specimen 1-M24-2C-RH .. 227
Figure 5.22 Actuator force variation in Specimen 1-M24-2C-RH 228
Figure 5.23 Observations in Specimen 1-M24-2C-RH 230
Figure 5.24 Total load vs beam midspan deflection curve for Specimen 2-M24-1C-RL 232
Figure 5.25 Center section moment vs beam end rotation curve for Specimen 2-M24-1C-RL .. 232
Figure 5.26 Actuator force variation in Specimen 2-M24-1C-RL 233
Figure 5.27 Gaps and contact at steel/concrete interface during beam construction 234
Figure 5.28 Observations in Specimen 2-M24-1C-RL (after terminating the test) 235
Figure 5.29 Relative deformation between planks at inner loading point section 236
Figure 5.30 Normal force at lateral brace 236
Figure 5.31 Total load vs beam midspan deflection curve for Specimen 3-M20-3C-RL 239
Figure 5.32 Center section moment vs beam end rotation curve for Specimen 3-M20-3C-RL .. 239
Figure 5.33 Actuator force variation in Specimen 3-M20-3C-RL 240
Figure 5.34 Unsupported steel flange in different scenarios 242
Figure 5.35 Bending of steel flange after bolt pretension 243

Figure 5.36 Concrete crushing at center section of Specimen 3-M20-3C-RL............................ 244
Figure 5.37 Total load vs beam midspan deflection curve for Specimen 4-M20-1C-RL 246
Figure 5.38 Center section moment vs beam end rotation curve for Specimen 4-M20-1C-RL .. 246
Figure 5.39 Actuator force variation in Specimen 4-M20-1C-RL.. 247
Figure 5.40 Observations after deconstructing composite beams... 250
Figure 5.41 Top flange local buckling in conventional composite beams [after (Grant 1973)] .. 251
Figure 5.42 Composite beam stiffness definition 253
Figure 5.43 Effect of end restraint on beam deflections [after (Leon 1990)] 253
Figure 5.44 Plastic stress distribution for positive moment in composite beams 256
Figure 5.45 Experimental-to-predicted beam strength versus percentage of composite action .. 258
Figure 5.46 Concrete crushing in different composite beam specimens 259
Figure 5.47 M/M_u versus center deflection for composite beams [after (Toprac 1965)] 260
Figure 5.48 Definition of rotation capacity [after (AISC 360-16)].. 261
Figure 5.49 Yield deformation and ultimate deformation of a composite beam 262
Figure 5.50 Load-deflection curve comparison 265
Figure 5.51 Composite beam test setups [after (Grant 1973) and (Rambo-Roddenberry 2002)] 266
Figure 5.52 Camber stress in a symmetric steel section 268
Figure 5.53 Axial interface force in a composite beam 269
Figure 5.54 Slip in a composite beam [after (Oehlers et al. 1995)] 270
Figure 5.55 Applied load-slip response of composite beam specimens 271
Figure 5.56 Slip of clamping connectors along the beams at various load levels 273
Figure 5.57 Stress and strain diagrams for full and partial shear connection 274
Figure 5.58 Strain distribution at instrumented sections 283
Figure 5.59 Applied load versus neutral axis location in steel beam in Test 1-M24-2C-RH 284
Figure 5.60 Applied load versus neutral axis location in steel beam in Test 2-M24-1C-RL 284
Figure 5.61 Applied load versus neutral axis location in steel beam in Test 3-M20-3C-RL 285
Figure 5.62 Applied load versus neutral axis location in steel beam in Test 4-M20-1C-RL 285
Figure 5.63 Applied load-steel section strain curves for beam specimens 288
Figure 5.64 Actual moment versus calculated moment in Test 1-M24-2C-RH 290
Figure 5.65 Actual moment versus calculated moment in Test 2-M24-1C-RL.......................... 290
Figure 5.66 Actual moment versus calculated moment in Test 3-M20-3C-RL.......................... 291
Figure 5.67 Actual moment versus calculated moment in Test 4-M20-1C-RL.......................... 291
Figure 5.68 Force and stress distribution in bolt shank 293
Figure 5.69 Applied load versus bolt tension response for the beam specimens......................... 296
Figure 5.70 Bolt tension versus slip response for the beam specimens...................................... 297
Figure 5.71 Applied load versus rod tension 300
Figure 5.72 Deformation of fully threaded rod in Test 1-M24-2C-RH 300
Figure 5.73 Channel anchor and bolt positions in a beam test specimen 301
Figure 5.74 Channel anchor stress in beam 2-M24-1C-RL 302
Figure 5.75 Concrete compressive strain comparison 303
Figure 5.76 Effective width of a composite beam 304
Figure 5.77 Longitudinal strain distribution on the top surfaces of center concrete planks 305
Figure 5.78 Applied load versus effective width for all the specimens...................................... 307
Figure 5.79 Effects of slab width on the strength and stiffness of composite beams 308

Figure 5.80 Average shear resistance and average slip calculation 310
Figure 5.81 Applied load versus shear resistance per connector 310
Figure 5.82 Load-slip curve comparison between pushout tests and beam tests 312
Figure 5.83 Finite element model of composite beam test specimen 314
Figure 5.84 Concrete stress-strain curves for beam 1 315
Figure 5.85 Concrete damage variables 315
Figure 5.86 Material stress-strain curves 316
Figure 5.87 Load-deflection curve comparison 317
Figure 5.88 Load-slip curve comparison 318
Figure 5.89 Crushing between concrete planks at inner loading point sections at peak strength 319
Figure B.1 Shell model of DfD floor system 378
Figure B.2 Pattern uniform live loading for DfD floor system 379
Figure B.3 Pattern concentrated live loading for DfD floor system 380
Figure B.4 Required strengths of DfD planks under concentrated live loading 382
Figure B.5 Concrete plank bending stresses in different loading scenarios (units: kips/ft.^{2}) 385
Figure B.6 Strain compatibility under positive bending 387
Figure B.7 Strain compatibility under negative bending 388
Figure B.8 Reinforcement configurations 393
Figure B.9 Preliminary configuration of shear keys 395
Figure C.1 Steel Section WT5x30 398
Figure C.2 Steel Section WT4x15.5 399
Figure C.3 Stiffened W6x25 Beam Assembly 400
Figure C.4 Stability Frame for WT5x30 401
Figure C.5 Stability Frame for WT4x15.5 402
Figure C.6 Stiffened Channel C15x50 403
Figure C.7 Reaction Angle 404
Figure C.8 Shim between Reaction Angle and Stiffened Channel for WT4x15.5 405
Figure C.9 Shim between WT4x15.5 and Clamp Tooth 406
Figure C.10 Light Reinforcement Pattern 407
Figure C.11 Heavy Reinforcement Pattern for Two-Channel Specimens 408
Figure C.12 Heavy Reinforcement Pattern for Three-Channel Specimens 409
Figure C.13 Reinforcement Details 410
Figure C.14 Cast-in channel details 411
Figure C.15 Steel Section W14x38 412
Figure C.16 Steel Section W14x26 413
Figure C.17 Steel Section W18x46 414
Figure C.18 Top Spreader Beam W14x132 415
Figure C.19 Bottom Spreader Beam W8x58 416
Figure C.20 Brace Section W18x86 417
Figure C.21 Brace Section W10x49 418
Figure C.22 Flange Tab for Column Base 419
Figure C.23 Web Tab for Column Base 420
Figure C.24 Cross Beam Adapter 421
Figure C.25 Beam Roller Support 422

Figure C.26 Beam Pin Support 423
Figure C.27 Plate under Bottom Spreader Beam 424
Figure C.28 6’’ Roller 425
Figure C.29 Clamp Plate for Braces 426
Figure C.30 Clamp Plate for Column Ends 427
Figure C.31 Brace Section WT4x17.5 428
Figure C.32 Clamp Plate for Braces 429
Figure C.33 Column End Shim 1 430
Figure C.34 Column End Shim 2 431
Figure C.35 Stub Beam W12x72 432
Figure C.36 Coupon Section W14x38 433
Figure C.37 Coupon Section W18x46 434
Figure C.38 Coupon Section W14x38 435
Figure C.39 One-Channel Specimen 436
Figure C.40 One-Channel Specimen Reinforcement 437
Figure C.41 Two-Channel Specimen 438
Figure C.42 Two-Channel Specimen Reinforcement 439
Figure C.43 Three-Channel Specimen 440
Figure C.44 Three-Channel Specimen Reinforcement 441
Figure C.45 Reinforcement Details 442
Figure C.46 Cast-in channel details 443
Figure E.1 Strain gage readings in bolt pretension tests 485
Figure E.2 Actuator forces, actuator displacements and slips in Test 2-M24-2C-RH-LM 486
Figure E.3 Actuator forces, actuator displacements and slips in Test 3-M24-2C-RL-LC 487
Figure E.4 Actuator forces, actuator displacements and slips in Test 4-M24-2C-RH-LM-S 487
Figure E.5 Actuator forces, actuator displacements and slips in Test 5-M24-2C-RH-LC 488
Figure E.6 Actuator forces, actuator displacements and slips in Test 6-M24-2C-RH-LC-S 488
Figure E.7 Actuator forces, actuator displacements and slips in Test 7-M24-3C-RH-LM 489
Figure E.8 Actuator forces, actuator displacements and slips in Test 8-M24-3C-RH-LC 489
Figure E.9 Actuator forces, actuator displacements and slips in Test 9-M20-2C-RH-LM 490
Figure E.10 Actuator forces, actuator displacements and slips in Test 10-M20-2C-RH-LC 490
Figure E.11 Beam strain gage readings in Test 3-M24-2C-RL-LC 491
Figure E.12 Beam strain gage readings in Test 5-M24-2C-RH-LC 491
Figure E.13 Beam strain gage readings in Test 8-M24-3C-RH-LC 492
Figure E.14 Beam strain gage readings in Test 10-M20-2C-RH-LC 492
Figure E.15 Bolt strain gage readings in pushout tests 493
Figure E.16 Channel lip strain gage readings in Test 3-M24-2C-RL-LC 495
Figure E.17 Channel lip strain gage readings in Test 5-M24-2C-RH-LC 495
Figure E.18 Channel lip strain gage readings in Test 8-M24-3C-RH-LC 496
Figure E.19 Channel lip strain gage readings in Test 10-M20-2C-RH-LC 497
Figure E.20 Channel anchor strain gage readings in Test 3-M24-2C-RL-LC 497
Figure E.21 Channel anchor strain gage readings in Test 5-M24-2C-RH-LC 498
Figure E.22 Channel anchor strain gage readings in Test 8-M24-3C-RH-LC 498
Figure E.23 Reinforcement strain gage readings in pushout tests 498

Figure E.24 Actuator forces and actuator displacements in Test 1-M24-2C-RH 499
Figure E.25 Actuator forces and actuator displacements in Test 2-M24-1C-RL 499
Figure E.26 Actuator forces and actuator displacements in Test 3-M20-3C-RL 500
Figure E.27 Actuator forces and actuator displacements in Test 4-M20-1C-RL 500
Figure E.28 Beam deformation in Test 1-M24-2C-RH 501
Figure E.29 Beam deformation in Test 2-M24-1C-RL 501
Figure E.30 Beam deformation in Test 3-M20-3C-RL 501
Figure E.31 Beam deformation in Test 4-M20-1C-RL 502
Figure E.32 Loading structure rotation in beam tests 503
Figure E.33 Slip measurements in beam tests 504
Figure E.34 Rod tension variation in beam tests 505
Figure E.35 Steel beam strain readings in Test 1-M24-2C-RH 506
Figure E.36 Steel beam strain readings in Test 2-M24-1C-RL 506
Figure E.37 Steel beam strain readings in Test 3-M20-3C-RL 507
Figure E.38 Steel beam strain readings in Test 4-M20-1C-RL 507
Figure E.39 Concrete plank strain Test 1-M24-2C-RH 509
Figure E.40 Concrete plank strain Test 2-M24-1C-RL 509
Figure E.41 Concrete plank strain in Test 3-M20-3C-RL 510
Figure E.42 Concrete plank strain in Test 4-M20-1C-RL 510
Figure E.43 Bolt strain readings in Test 1-M24-2C-RH 512
Figure E.44 Bolt strain readings in Test 2-M24-1C-RL 512
Figure E.45 Bolt strain readings in Test 3-M20-3C-RL 513
Figure E.46 Bolt strain readings in Test 4-M20-1C-RL 513
Figure E.47 Channel lip strain readings in beam tests 515
Figure E.48 Channel anchor strain readings in beam tests 516
Figure E.49 Reinforcement strain readings in beam tests 517
Figure F.1 Strain gage locations and numbering for WT sections 521
Figure F.2 Axial force variation for cross sections in WT beam in Test 3-M24-2C-RL-LC 521
Figure F.3 Axial force variation for cross sections in WT beam in Test 5-M24-2C-RH-LC 521
Figure F.4 Axial force variation for cross sections in WT beam in Test 8-M24-3C-RH-LC 522
Figure F.5 Axial force variation for cross sections in WT beam in Test 10-M20-2C-RH-LC 522
Figure F.6 Stress analysis model 524
Figure F.7 Pushout test bolt stress-strain curves 525
Figure F.8 Bolt material loading and unloading behavior in pretension tests 526
Figure F.9 Bolt axial force variation in pushout tests 527
Figure F.10 Bolt material loading and unloading behavior in pushout tests 528
Figure F.11 Strain transformation between different coordinates 529
Figure F.12 Rosette strain gage orientation and defined coordinate system 529
Figure F.13 Anchor strain and stress variation in Test 3-M24-2C-RL-LC 531
Figure F.14 Anchor strain and stress variation in Test 5-M24-2C-RH-LC 532
Figure F.15 Anchor strain and stress variation in Test 8-M24-3C-RH-LC 532
Figure F.16 Measurement error calculation 535
Figure F.17 Measured displacements and modified displacements 536
Figure F.18 Relative vertical deflection measurement errors 537

Figure F.19 Beam end rotation calculation 538
Figure F.20 End rotation variation of beam specimens 539
Figure F.21 Other vertical deflections versus center deflection 540
Figure F.22 Extrapolated center deflection 540
Figure F.23 Center concrete plank compressive strain and stress variation in Test 1-M24-2C-RH 541
Figure F.24 Center concrete plank compressive strain and stress variation in Test 2-M24-1C-RL 541
Figure F.25 Center concrete plank compressive strain and stress variation in Test 3-M20-3C-RL 541
Figure F.26 Center concrete plank compressive strain and stress variation in Test 4-M20-1C-RL 542
Figure F.27 Beam test bolt stress-strain curves 543
Figure F.28 Bolt tension variation in beam tests 544
Figure F.29 Bolt material loading and unloading behavior in beam tests 545
Figure F.30 Internal force calculation for a composite beam section 547
Figure F.31 Actual moment versus calculated moment in Test 1-M24-2C-RH 552
Figure F.32 Actual moment versus calculated moment in Test 2-M24-1C-RL 552
Figure F.33 Actual moment versus calculated moment in Test 3-M20-3C-RL 554
Figure F.34 Actual moment versus calculated moment in Test 4-M20-1C-RL 554
Figure F.35 Calculated axial forces at the instrumented steel sections 555
Figure F.36 Shear resistance variation of clamp in different regions (per connector) 556
Figure F.37 Locations of neutral axes in steel sections in Test 1-M24-2C-RH 557
Figure F.38 Locations of neutral axes in steel sections in Test 2-M24-1C-RL 557
Figure F.39 Locations of neutral axes in steel sections in Test 3-M20-3C-RL 558
Figure F.40 Locations of neutral axes in steel sections in Test 4-M20-1C-RL 558
Figure F.41 Anchor strain and stress variation in beam test 559
Figure G.1 Two scenarios in a composite beam 560
Figure G.2 Finite element models developed for bearing stiffness comparison 561
Figure H.1 Prototype structure floor plan 563
Figure H.2 Member sizes for the exterior girders and collector beams 569
Figure H.3 Moment diagram of a concrete plank under gravity loading (units: lb-ft) 570
Figure H.4 Section with the smallest moment of inertia (units: inches) 571
Figure I.1 Lower bound moment of inertia (reproduced from AISC 2016a) 576
Figure J.1 Moment diagram for Beam 2 580
Figure J.2 Bending moment at center and inner loading point sections due to actuator loading 580
Figure J.3 Bending moment at center and inner loading point sections due to actuator loading 584
Figure J.4 Bending moment at center and inner loading point sections due to actuator loading 587
Figure J.5 Idealized W-shape steel section (reproduced from AISC 2016a) 589
Figure J.6 Composite beam flexural strength calculation (Neutral axis in steel web) 590
Figure K.1 Deconstructable composite diaphragm finite element model 593
Figure K.2 Displacement loading history for computational models 594
Figure K.3 Material stress-strain curves 596
Figure K.4 Load-displacement curves 598

Figure K.5 Limit states of deconstructable composite diaphragm models 598
Figure K.6 Steel moment to concrete moment ratio 599

LIST OF TABLES

Table 2.1 Summary of key pushout tests and beam tests 17
Table 3.1 Prototype structure matrix 34
Table 3.2 Breakdown of dead load 35
Table 3.3 Reduced design live load for different members 37
Table 3.4 Seismic load and wind load for the prototype structures 40
Table 3.5 Limiting width-to-thickness ratios 45
Table 3.6 Stability coefficients for the prototype structures 47
Table 3.7 Member sizes for the conventional composite flooring system with solid slabs 49
Table 3.8 Member sizes for the deconstructable composite flooring systema 50
Table 4.1 Pushout test matrix 59
Table 4.2 Limit states for anchor channels 60
Table 4.3 Pushout test steel coupon testing results 69
Table 4.4 Pushout test concrete cylinder testing results (units: psi) 74
Table 4.5 Summary of monotonic pushout test results 110
Table 4.6 Summary of cyclic pushout test results 125
Table 4.7 Peak strength reduction in cyclic pushout specimens 130
Table 4.8 Ductility and energy dissipation of clamps in pushout specimens (per connector) 131
Table 4.9 Channel true stress and true plastic strain 166
Table 4.10 Mean Slip Coefficient in pushout specimens 174
Table 4.11 Tested strength to predicted strength ratio 175
Table 4.12 Peak strength reduction in cyclic pushout specimens 175
Table 4.13 Slip coefficients between different contact surfaces 179
Table 4.14 Clamp shear strength comparison 179
Table 5.1 Composite beam test matrix 186
Table 5.2 Measured dimensions of steel beams and stubs 199
Table 5.3 Beam test steel coupon testing results 201
Table 5.4 Direct tension and shear testing results 205
Table 5.5 Beam test concrete cylinder testing results (units: psi) 208
Table 5.6 Beam test concrete plank pour sequence 209
Table 5.7 Self-weight of all the components in a composite beam specimen 224
Table 5.8 Tilt of Specimen 3-M20-3C-RL flanges 240
Table 5.9 Tilt of Specimen 4-M20-1C-RL flanges 247
Table 5.10 Composite beam test results 253
Table 5.11 Strength comparison between concrete, steel and clamps (units: kips) 254
Table 5.12 Composite beam strength and stiffness comparison 257

Table 5.13 Ductility of composite beam specimens 265
Table 5.14 Effect of additional friction produced by self-weight and actuator loading 269
Table 5.15 Composite beam strength and stiffness comparison 320
Table 6.1 Material properties reported by Galambos and Ravindra (1978) 331
Table 6.2 Material properties reported by Dexter et al. (2000) 331
Table 6.3 Tested-to-predicted strength ratio of monotonic pushout specimens 335
Table 6.4 Parameters for resistance factor calculation 336
Table 6.5 Tested-to-predicted strength ratio of composite beam specimens 337
Table A.1 Member sizes for the deconstructable composite floor system 368
Table A.2 Member sizes for the conventional composite floor system with solid slabs 368
Table A.3 Member sizes of lateral-force resisting systems 369
Table A.4 Member sizes of gravity columns 372
Table B.1 Required strengths for concrete slab and plank design 381
Table F.1 Pushout test bolt stress and strain 525
Table F.2 Residual horizontal movements at various locations of beam specimens (units: inches) 536
Table F.3 Beam test bolt stress and strain 543
Table I.1 Moment of inertia calculation 577
Table J.1 Breakdown of bending moment (units: ft.-kips) 580
Table J.2 Breakdown of bending moment (units: ft.-kips) 584
Table J.3 Breakdown of bending moment (units: ft.-kips) 588
Table K.1 Analytical model parameters 597

1. INTRODUCTION

According to the U.S. Energy Information Administration, buildings consumed almost half of the total energy used in the United States in 2012, while the transportation sector and the industrial sector accounted for 28% and 23%, respectively. As the leading contributor to CO_2 emission, the building sector was also responsible for 45% of all CO_2 emissions (Energy Information Administration 2012). Although the embodied energy only amounts to 10-20% of the total energy use of buildings (Ramesh et al. 2010), it will hold a larger proportion in the future, as technologies are developed to increase the efficiencies of the heating, ventilating and lighting systems. In addition to depleting nonrenewable resources and aggravating climate change, waste related to building construction and deconstruction is a major concern. Construction and demolition (C&D) waste totals nearly 160 million tons per year, including debris generated during demolition (48 percent), renovation (44 percent) and new construction (8 percent) (U.S. Environmental Protection Agency 2008). Recycling and reusing C&D waste conserves landfill, cuts down the expenses for purchasing new materials, and reduces the environmental impacts.

Hot-rolled structural steel used in the construction of engineered steel building structures and infrastructure components currently is produced in the U.S. from nearly 100% recycled materials. A variety of sustainable concrete mixes (e.g., measured by a lowering of the required carbon footprint to manufacture the concrete) are also being developed worldwide. However, the manufacture of new building materials, even based on the use of recycled materials, still currently consumes significant energy derived from non-renewable fossil fuels. Achieving comprehensive sustainability in the built environment requires significant reduction in and eventual elimination of the use of most nonrenewable resources, both for construction materials and for energy consumption.

The need to reduce the energy consumption and material waste related to the construction industry motivates the exploration of Design for Deconstruction (DfD) of buildings. DfD of buildings, first proposed in the 1990s (Kibert 2003), aims at resolving these issues by reclaiming and repurposing the materials at the end of their service life. Contrary to the conventional linear material flow, which starts with the extraction of raw materials and ends with the disposal of debris in landfills, DfD could help close this loop by reducing the cost of recovering and reusing resources.

The benefits of deconstruction could be more rapidly realized if the building service life is much shorter. Although buildings are commonly designed for a 50-year or more service life, the actual life of many buildings is much less. A survey conducted by O'Conner (2004) revealed that demolition of buildings was rarely due to damage in structural systems and materials, but mainly because of the lack of maintenance for non-structural components, changing land values and inability to meet current owners' needs.

Structural steel framing systems are particularly conducive to deconstruction at the end of the service life of a structure, so long as they have not been subjected to extensive permanent damage from an extreme hazardous event or deteriorated due to environmental or other factors. When structural members are protected from the environment within a building envelope, as with this system, little deterioration occurs. Composite construction makes efficient use of the two materials, with concrete being subjected to compression and steel resisting tension. In conventional composite construction, steel frames are erected in place, with corrugated metal deck often laid atop the steel beams and girders, shear connectors shot onto the top flanges of the steel members, reinforcement laid in place, and a monolithic concrete floor slab cast in place. However, composite steel-concrete floor systems, by far the most ubiquitous type of structural steel framing for commercial and institutional buildings, are not reusable at end-of-life. The integration of steel beams and concrete slabs via shear connectors inhibits the separation of the two materials, making impossible the deconstruction of the composite flooring systems and reuse of the structural components. Steel beams and shear studs can be recycled after being extracted from demolition debris, while concrete slabs can be crushed for fill or making aggregates for new concrete. Conventional composite floor systems are therefore not the best choice for reducing the long-term environmental impacts of building materials.

The aim of this research is to establish fundamental strategies for predicting the behavior of and designing sustainable steel structures through combining sustainably optimized prefabrication strategies with DfD, achieving nearly 100% reusability for composite floor framing systems within the context of reusable bolted steel framing. This research combines an experimental testing program and finite element analysis to characterize the behavior of the new composite floor system under gravity loading and lateral loading, including seismic loading.

1.1 Deconstructable composite prototype system

A new deconstructable composite floor system is proposed in this project. This system is designed to maintain the benefits of steel-concrete composite construction, such as enhanced flexural strength and stiffness, reduced steel beam size and weight, and ease of construction, and enable sustainable design of composite floor systems in steel building structures, components disassembly and reuse of the structural components. The deconstructable composite prototype is illustrated in Figure 1.1; this concept was first introduced in Webster et al. (2007). The system consists of precast concrete planks and steel beams connected using clamping connectors. Frictional forces are generated at the steel-concrete interface to resist required shear flow and achieve composite action. Cast-in channels are embedded in concrete to provide flexibility for where the beam intersects the plank and allow for different beam widths. Tongue-and-groove joints at the concrete plank edge ensure vertical load transfer between adjacent planks, and offer a level and well-matched surface. By untightening the bolts, the clamping connectors enable the precast concrete planks and steel beams to be easily disassembled and reconfigured in future projects.

Mechanical connectors are usually used in conventional precast concrete construction to transfer in-plane diaphragm forces. In order to achieve deconstructablity of the system, grouting the planks and placing a cast-in place concrete topping, which help to tie all the planks together, are not possible. In the proposed deconstructable system, the precast concrete planks are connected using unbonded threaded rods before being attached to the steel beams, as shown in Figure 1.2, with a pattern of connections aligned at 4 ft. on center and the planks staggered to help facilitate transfer of forces across the diaphragm. Friction, developed by pretensioning the rods, provides the resistance against joint sliding due to diaphragm shear and joint opening due to diaphragm flexure.

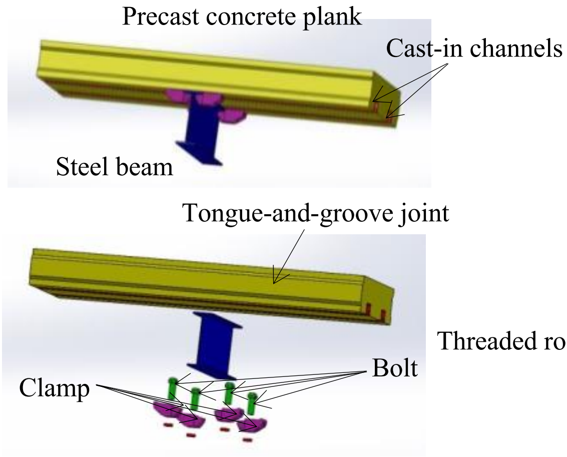

Figure 1.1 Deconstructable composite beam prototype

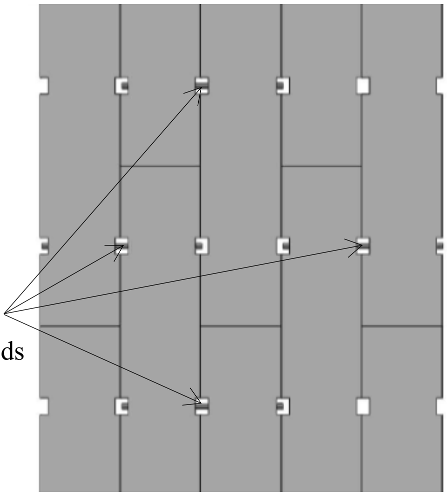

Figure 1.2 Precast concrete plank connections

Preliminary plank dimensions, presented in Figure 1.3, are 20 ft. x 2 ft. x 6 in. This size is believed to be small enough to facilitate transportation and handling, and promote reconfiguration in future structures, but large enough to have structural integrity and reduce labor for construction and deconstruction. Ideally, the planks are stocked in different sizes and concrete strengths for ready use, comparable to how steel is currently stocked at supply centers. A typical plan layout for a prototype office building using this system with a staggered plank configuration, as seen in Figure 1.2, is shown in Figure 1.4.

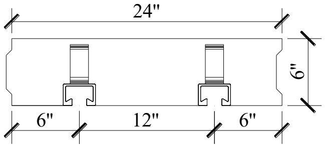

a) Plank perpendicular to steel beam

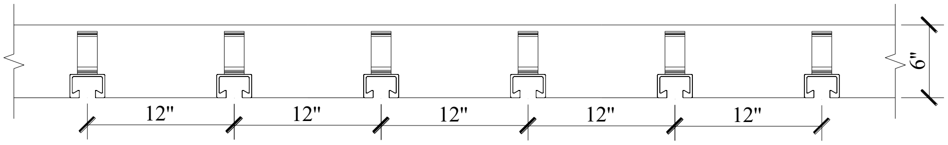

b) Plank parallel to steel girder

Figure 1.3 Precast concrete plank cross section (units: inches)

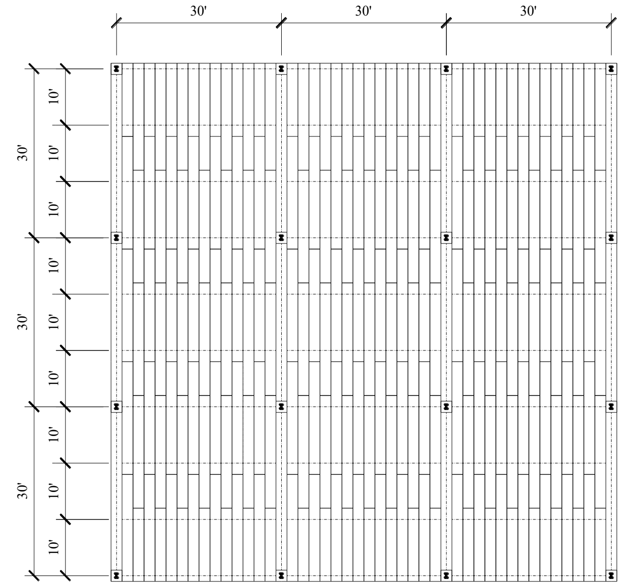

Note:
1. The dashed lines show the steel framing. The beams are perpendicular to the precast concrete planks, while the girders are parallel to the planks.
2. Other precast plank patterns are also possible for the DfD system.

Figure 1.4 Typical floor plan for deconstructable composite floor system (units: feet)

1.2 Research scope and organization

This research investigates the use of Design for Deconstruction for steel building structures, including buildings having a range of gravity loading (offices, warehouses, etc.,) and lateral loading that includes both wind loading and seismic loading. A review of previous research on several subjects is presented in Chapter 2, including DfD, prefabricated structural systems, steel headed stud anchors and seismic design of diaphragms. Chapter 3 covers the design of several prototype structures that can be used to explore the applicability of the proposed system in an entire class of buildings. Life cycle assessment results are also presented to demonstrate the environmental benefits of adopting DfD in the design of buildings. From a dismantler's perspective, challenges and opportunities for dismantling current steel structures and the flow of the demolished materials are also indicated.

In Chapter 4, results from the pushout tests are presented to demonstrate the strength and ductility of the clamping connectors, influences of different parameters, load distribution among the clamps, behavior of the bolts and channel lips, formation of cracks, responses of the channel anchors and reinforcement, etc. Finite element models are developed to study the inherent indeterminacy of the system, such as the bolt tension variation and bolt tension transfer. Combining experimental results and finite element analysis results, design equations are proposed to calculate the shear strengths of the clamping connectors. To evaluate the clamping connector behavior in a realistic manner and validate the findings from the pushout tests, beam tests are performed, and the findings are presented in Chapter 5, including the strength and stiffness of the composite beam specimens, slip between the steel beams and concrete planks, strain distribution along the depth of the beam sections, location and migration of the neutral axes in the steel beams and concrete planks, behavior of the bolts and rods, effective widths, etc. Finite element models are also developed which predict the overall behavior of the beam specimens well. In Chapter 6, resistance factors are derived for the proposed equations that estimate the shear strengths of the clamping connectors and the AISC model that predicts the positive flexural strength of composite beams assuming a plastic stress distribution. This report finishes with conclusions and future work.

In the appendices, Appendix A summarizes the design results of the prototype structures illustrated in Chapter 3 and reports the sizes of the steel beams, girders, braces and columns. The precast concrete planks are designed in Appendix B, including the selection of the flexural and shear reinforcement and the design of the shear keys. Appendix C contains drawings for the load frame steel components, specimen steel parts, and precast concrete planks, all of which comprise the experimental setups for the pushout tests and composite beam tests. The associated mill certifications are documented in Appendix D.

Raw data for all the tests is provided in Appendix E, and data reduction calculations are shown in Appendix F. Appendix G indicates the selection of the reaction angles in the pushout tests. The grade and dimension of the rods, which are utilized to connect the precast concrete planks in the floor system and resist in-plane diaphragm forces, are determined in Appendix H. An effective moment of inertia and a lower bound moment of inertia are calculated and compared for the composite beam specimens in Appendix I. Using three beam specimens as examples, the calculations of the flexural strength and bending stiffness of the deconstructable composite beams are demonstrated in Appendix J. Appendix K presents the diaphragm behavior of the deconstructable composite floor system.

2. LITERATURE REVIEW

This section highlights the key studies and developments on the subjects related to this research, including Design for Deconstruction (DfD), prefabricated structural systems, steel headed stud anchors and seismic design of diaphragms.

2.1 **Design for Deconstruction**

DfD is believed to be beneficial environmentally and economically. Reuse of components is usually favored compared to recycling of materials, as less production is needed. In DfD, salvaged materials from old buildings are repurposed in new projects, thus eliminating the costs of waste disposal and material manufacturing. However, the ability to reclaim materials from retired buildings depends on how the materials are integrated during building construction. The lack of practice and research on how to design with reclaimed materials also makes it difficult to implement for now.

Kibert (2003) believed that deconstruction reserves the embodied energy of the used materials and reduces the energy input required for reprocessing and remanufacturing the materials. Of the 1.9 billion metric tons of raw materials in 1996, 1.6 billion metric tonnes was related to the building sector. The huge material flow in the building sector necessitates DfD to reduce the material extraction and demolition waste. Although the design life of buildings is usually 50 to 100 years, the actual service life is unpredictable due to the degradation of the shorter-life components, rendering buildings in disuse and disrepair. DfD, properly implemented, could mitigate these issues to facilitate material recycling and reuse.

Kilbert (2003) indicated that numerous challenges remained for DfD, such as the lack of tools for deconstructing buildings, the low disposal cost for demolition waste, the need for building codes addressing how to design with reused materials, and the inadequacy in establishing the environmental and economic benefits. Principles of DfD were suggested to address these challenges. Kilbert (2003) also indicated that the government could play a bigger role in promoting deconstruction. Increasing the disposal costs and providing tax advantages for recovered materials would encourage the owners, contractors, architects and engineers to consider and incorporate DfD into the design of new structures. This work stressed that time is a significant factor for deconstruction and should be provided in the overall project scheduling.

Durmisevic et al. (2002) argued that traditional design of buildings focused on the short-term performance, such as the optimization of functions, costs and construction schedules. Likewise, previous research on sustainable buildings concentrated on designing energy efficient buildings and using environmental-friendly materials. Because buildings are constantly changing to cater to the needs of the owners, Durmisevic (2002) indicated they could be dynamic and flexible structures with parts that could be disassembled, replaced, recycled or reused.

The authors defined three levels of building composition: building level, system level and component level. Elements and materials are first assembled to achieve component functions. The components are then integrated to carry system functions, such as finishing, distributing and insulation. In the end, the systems are clustered to perform building functions, for example, load-bearing, enclosure, partitioning and servicing. Building composition, therefore, should be considered at each level at the beginning of the design stage to enable building disassembly. When buildings are disassembled, disassembly at the building level could offer reuse of the systems, spatial adaptation and functional adaptation of the buildings. The authors thus indicated that disassembly at the system level provides reuse of the components and functional adaptation of the systems. Disassembly at the component level enables reuse of elements and materials as well as functional adaptation of the components. In order to design decomposable structures, the main characteristics are summarized, including modular parts dry assembled on site, independence of various systems, application of parallel instead of sequential assembly/disassembly, use of mechanical connections, etc.

Two case studies were examined by Gorgolewski (2008) to highlight the challenges inherent in DfD. Gorgolewski (2008) indicated that reuse of the components is more favorable than using recycled materials in terms of environmental impacts, but designing with reclaimed materials could add complexity to the design process. Recycled materials, which are manufactured with the used materials, have almost the same properties as the virgin materials. However, reusing deconstructed components in a new project requires the establishment of their structural characteristics. Coordinating demand with supply is also important. It is common that the materials are not available at the right time, in the right amount and dimension. Unlike the traditional design approach in which the components sizes are specified before design, reused components are identified on the demolition site. The designers usually have to redesign and choose the components available. It iss beneficial for the design engineers and architects to communicate and develop working relationships with the demolition and salvage contractors to obtain an inventory of available components and purchase the needed components to prevent the contractors from selling them. Gorgolewski (2008) also indicated that additional fees and costs related to identifying, testing and restoring the purchased materials are also inevitable.

2.2 Prefabricated structural systems

In prefabrication, structural components are manufactured in factories, and then transported to the construction site for assembly. Prefabrication and modularization have received increasing attention due to reduced construction time and labor cost, controlled manufacturing process, fewer restraints by adverse weather, and standardization and customization of the products. All of these benefits are conducive to DfD.

A survey conducted by McGraw-Hill Construction (2011) indicated the following related to prefabrication and modular construction: 66% reported a decreased project schedule, with 35% reporting a decrease of four weeks or more; 65% indicated a decreased project budget, with 41% indicating a decrease of 6% or more; 77% described decreased construction waste, with 44% describing a decrease of 5% or more. All these improvements in productivity are the driving factors for contractors, engineers and architects to adopt prefabricated/modular construction. The report highlighted that a main reason for not using prefabricated/modular construction is because the architect does not design it into the project.

As an alternative to traditional bolting and welding connections between steel components, Lindapter clamping connections are designed to eliminate on-site drilling and welding, retain the integrity of the steel pieces and suit any steel beam size. The Lindapter connection can be designed for tensile, combined, frictional, compression and shear loading. More importantly, the connection can be deconstructed and reused several times (Lindapter 2013).

Sandwich plate system (SPS) is a composite material comprising two steel plates bonded with a polyurethane elastomer core. The core increases the distance between the steel plates, thus increasing the flexural strength and stiffness. In addition, the presence of the core suppresses the buckling of the steel plates. SPS delivers a high strength to weight ratio, making it an excellent alternative to both reinforced concrete and stiffened steel. SPS also promotes a sustainable built environment. SPS panels can be unbolted from the supporting steel frames and relocated to a new building. The two components of SPS panels are fully recyclable (Intelligent Engineering 2011).

A proprietary steel framing system has been developed by ConXtech (Renz 2005). ConXtech moment-resisting frames are intended for high seismic zones and eliminate the need for braced frames and shear walls. Lowering and locking connections aid both construction and deconstruction on site, enabling structural steel reuse. The moment frames employ reduced beam sections to dissipate energy during earthquakes. The absence of interior obstacles makes the structures more adaptable for future use. ConXtech utilizes robotic welding to reduce construction time and labor while increasing quality control.

2.3 **Steel headed stud anchors**

Extensive research has been conducted to establish the behavior of steel headed stud anchors since their introduction after World War II. Full-scale beam tests demonstrate the realistic behavior of steel headed stud anchors; however, the shear connectors are loaded indirectly from bending of the beams and unevenly along the beam length. Because the forces acting on a stud depend on the relative stiffness of all the structural components, it is difficult to establish the behavior of the steel headed stud anchors from beam tests. As an alternative, pushout tests have been widely used to study the behavior of shear connectors. However, the pushout tests cannot represent the actual loading scenario of the shear connectors in composite beams and may lead to estimated strengths and failure modes that are inaccurate if they are not properly designed. This section summarizes several key studies related to the use of steel headed stud anchors in steel connections.

2.3.1 Pushout tests and beam tests

Chinn (1965) tested ten pushout specimens and two composite beam specimens using lightweight concrete. The parameter of the pushout tests was stud diameter. In the pushout tests, the flanges were greased before casting the concrete slabs to prevent bond and reduce the effects of friction at the steel/concrete interface. A quantity, which was termed as the useful capacity, was defined to represent the beginning of considerable inelastic behavior of the specimens. The two beam specimens differed in terms of the compressive strength of the slabs. The limit state of the beams was yielding of the steel beam which was followed by concrete crushing. The strengths of the beams were very close to the predicted values.

Goble (1968) explored a pull-out failure of shear studs from thin steel flanges. Based on the results obtained from 41 specimens, the failure mode shifted from stud failure to flange pull-out at a stud diameter to flange thickness ratio of 2.7. Near this limit, the specimens did not exhibit significant strength and ductility reduction, but the limit state of flange pull-out should probably be avoided in design. An equation was proposed to predict the strength of studs that might fail in this manner. This research leads to the restriction in AISC 360-16 (2016) which requires that the steel flange be thicker than the stud diameter divided by 2.5 unless the stud is welded directly over the web.

Hawkins et al. (1984) compared ten pushout specimens under reversed cyclic loading with thirteen specimens tested monotonically. The variables were type of loading, presence of ribbed metal deck, geometry of metal deck and orientation of metal deck. When the controlling failure mode was stud shearing, ductile responses were observed, and the hysteresis loops exhibited large energy dissipating capacities, although the cyclic shear strength was about 83% of the monotonic shear strength. In contrast, when the limit state was concrete pull-out failure, brittle behavior was seen, resulting in poor hysteresis responses. The cyclic shear strength was about 29% lower than the monotonic shear strength. S-shaped hysteresis loops and little energy absorption were common characteristics in cyclic specimens failing due to rib shearing.

Oehlers et al. (1986) derived the shear stiffness of stud connectors based on the results from 116 pushout tests. It was shown that a large permanent set occurs even if the applied loading is small, since the weld collars embeds into the concrete. The studs embedded in stronger concrete are stiffer than those in weaker concrete. The slip at failure is about one-third of the stud diameter. The authors also concluded that the slip at lower loads is affected by voids, dense aggregates, and the roughness of weld collar, while the slip is dependent on the concrete strength at higher loads.

Oehlers et al. (1987) utilized the results from 110 pushout specimens which included 8 specimens in which the axial forces applied to the shear studs were known, and derived a shear strength equation that could account for the number and position of the shear connectors in the slabs. It was also concluded that the strength of shear studs with zero axial load was 81% of the strength predicted using the proposed equation.

Jayas et al. (1988) conducted 18 full-size push-out tests and 4 pull-out tests to study the behavior of shear studs in composite beams with corrugated metal decks perpendicular and parallel to the steel beams. The main test parameters were the longitudinal spacing of the shear studs and the geometry of the metal decks. When the studs are spaced sufficiently apart in solid slabs and in composite slabs with parallel metal decks, the shear strength of the studs is adequately predicted by the Canadian provisions. If the longitudinal stud spacing is less than 6 times the stud diameter, concrete-related failures need to be checked. When the metal deck is perpendicular to the steel beam, the controlling limit state is stud pull-out, and two empirical equations were proposed for specimens with 38 mm and 76 mm metal deck.

Jayas et al. (1989) tested four full-scale composite beams with different deck profiles and stud layouts, along with two pushoff specimens, to verify previously reported results. The parameters included the longitudinal spacing of studs and the number of studs per rib. Concrete pull-out was the main failure mechanism. It was shown that the shear stud strength equations proposed by the authors accurately predicted the ultimate flexural strengths of the beams in the program.

Gattesco et al. (1996) designed a direct shear test which was capable of simulating the actual boundary conditions of shear studs close to the ends of a simple beam. The direct shear test setup was validated by the monotonic test results that were very similar to the results from previous research, and then employed to study the behavior of shear studs under cyclic loading which subjected the specimens to various blocks of cycles between two load values. It was shown that the stud slip increased at each cycle and the increment was almost constant after a few cycles, indicating a progressive accumulation of damage and no shakedown. During the load cycles including load reversal, the slip increment increased at every cycle. After the cyclic tests, the specimens were loaded monotonically to failure, and the accumulated damage reduced the monotonic strength and ultimate slip of the shear studs by 10% and 30%, respectively.

Lyons et al. (1996) performed 87 pushout tests using composite slabs. The variables were stud position, metal deck height, stud height, and deck gage. Various failure modes were briefly described, including stud shearing, stud rupture, concrete pull-out, rib punching, rib cracking, and slab splitting. The comparison between the test results and predicted strengths indicated that the AISC stud strength equations were unconservative, and three factors that were not included in the AISC formulas contributed to the discrepancy, namely, the number of studs in a rib, the embedment length above the top of the steel deck, and the weak/strong position difference.

Johnson et al. (1998) developed strength equations based on theoretical models for seven failure modes. Results from 269 existing pushout tests and 34 new tests were used to calibrate these equations. When the metal deck is perpendicular to the beam, five limit states were studied, including shank shearing, concrete pull-out failure, rib punching, combined concrete pull-out failure and rib punching. When the metal deck is parallel to the beam, two limit states were investigated, including splitting of concrete and concrete pull-out failure. Compared to the current design provisions, the new equations required more parameters, but led to consistent results with low scatter and covered a wide scope.

Bursi et al. (1999) tested two series of pushout specimens with different boundary conditions under monotonic, variable and constant equi-amplitude displacements. It was shown that symmetric boundary conditions improved the shear strength and displacement ductility. Relevant codes overestimated the strength of shear studs under reversed displacement.

Civjan et al. (2003) performed a series of experimental and analytical tests on modified composite push-out specimens and bare steel shear studs to investigate the behavior of shear studs subjected to fully reversed low-cycle fatigue load. In the modified pushout tests, the variables were monotonic loading versus cyclic loading, concrete strength, weld quality, and weld methods. In the bare stud tests, the parameters were monotonic loading versus cyclic loading and shear to moment ratio. Boundary conditions and dominant stresses were evaluated in finite element simulation.

In the modified pushout tests, when subjected to fully reversed cyclic loading, the shear stud capacity could decrease as much as 40%. This observation could be attributed to low-cycle fatigue of the stud/weld materials as well as concrete degradation. Increasing the weld area at the base of studs increased the overall stud capacity. Initial bending of studs did not affect the shear stud load capacity. Failure of studs was typically reported at a slip of 0.02 in. In the bare stud tests, the stud strength reduction under cyclic loading was less than that in the push-out specimens. Studs subjected to predominately shear load exhibited a smoother fracture surface, while a tension fracture failure was observed when the bending moment was dominant, as was typical in the modified push-out specimens. Based on the computational results from four elastic finite element models, it was concluded that bending stress was critical, while tension stress became negligible when friction at the steel/concrete interface and bearing between concrete and steel were accounted for.

Hicks (2007) presented the experimental results from two full-scale composite beam tests and the companion pushout tests. The performance of the beam with a single stud in each trough was satisfactory; however, the strength of the beam with pairs of studs in favorable positions was lower than anticipated. The author pointed out that any brittle behavior exhibited by shear studs in pushout tests is because of the deficiencies in the pushout specimen, rather than shear connections. A standard pushout test configuration was proposed for shear studs embedded in composite slabs that use metal decks.

Pallarés et al. (2009) reviewed 391 monotonic and cyclic tests on shear studs using solid slabs and proposed design equations and resistance factors for the limit states of steel failure and concrete failure of headed stud anchors subjected to shear force. The ratio of the overall stud height to the shank diameter was also discussed to avoid concrete pryout failure. These recommendations are summarized in the “User Note” in Section I 8.3 in AISC 360-16 (2016). It was also suggested to use 75% of the monotonic shear strength as the design strength of studs under seismic loading.

Ranzi et al. (2009) tested two full-scale composite beams utilizing deep trapezoidal metal deck and welded shear studs. The two beams, which had low degrees of shear connection, were intended to provide benchmark data to calibrate theoretical models and design recommendations. The test results showed that the beams behaved in a ductile manner, and the tested ultimate flexural strengths were greater than those predicted by Eurocode 4.

Table 2.1 summarizes the pushout tests and beam tests whose results and conclusions lay the foundation for the design of steel headed stud anchors and composite beams in the AISC Specification (2016a).

Table 2.1 Summary of key pushout tests and beam tests

Reference	Test	Key parameters	Major findings
Ollgarrd et al. (1971)	Pushout tests with solid slabs	Concrete strength; stud diameter; type of aggregate; number of connectors per slab	1. A design equation is proposed for the shear strength of shear studs embedded in solid concrete slabs. 2. An empirical load-slip formula is proposed for monotonically loaded specimens.
Grant et al. (1977)	Beam tests with composite slabs	Yield strength of the steel beam; deck geometry; degree of shear connection	1. A revised shear strength model is proposed for shear studs embedded in composite slabs. 2. Modified models are proposed for calculating effective moment of inertia and effective section modulus.
Easterling et al. (1993)	Pushout tests and beam tests with composite slabs	Stud position	1. The design equation of shear studs embedded in composite slabs is unconservative and unable to account for different stud positions.
Rambo-Roddenberry (2002)	Pushout tests with solid slabs and composite slabs; beam tests with composite slabs	Pushout tests: flange thickness; steel/concrete surface; normal force; stud diameter; concrete strength; deck height; friction at the deck/steel beam surface; tension in the stud shank Beam tests: stud position	1. The design equation for the shear strength of shear studs embedded in solid concrete slabs is acceptable. 2. Different coefficients are proposed for the shear strength model of shear studs embedded in composite slabs to account for stud positions.

Ollgarrd et al. (1971) tested 48 solid slab specimens. The parameters included concrete compressive strength, concrete split tensile strength, modulus of elasticity, density, stud diameter, type of aggregate and number of connectors per slab. The test results showed that when the connectors were embedded in lightweight concrete, the strengths decreased

15% to 25% compared to the strengths of connectors in normal weight concrete. As a result of greater restraint, larger curvature was observed for the stud embedded in normal weight concrete, while the stud was seen to be nearly straight in lightweight concrete. Different crack patterns were observed for the upper and lower connectors. For the upper connectors, the crack was almost vertical to the free end, while the crack at the lower stud propagated toward the steel beam surface at about a 45° angle. A regression analysis was employed to obtain an equation for the stud strength. An empirical expression for the load-slip relationship was also determined.

Grant et al. (1977) reported test results of 17 composite beams. The variables were the yield strength of the steel beam, the deck geometry, and the degree of shear connection. The test results of 58 beam tests conducted by other researchers were also evaluated. The parameters were weight and strength of concrete, diameter and height of shear connectors, slab reinforcements and type of loading. All tested beams were ductile, as demonstrated by the large deflections of the beams and the plastic hinges occurring near the midspan. The predominant failure mode was rib punch-through failure for the shear connectors in beams with wider slabs, while horizontal rib cracking first occurred in narrower slabs since the full development of the failure surface was truncated. A revised model for shear connector strength was provided to include the effects of rib height and embedment of the connector. Modified models for calculating effective moment of inertia and section modulus were also proposed for deflection estimation and allowable stress design of composite beams.

Strong and weak position issues in composite beams were explored through four beam tests by Easterling et al. (1993). The authors indicated that the best approach for evaluating shear connector strength was to use pushout tests to investigate the influences of the parameters and formulate design equations and then validate the equations in beam tests. The only nominal parameter was the stud positions. All the beams were ductile, but the behavior was different for strong position and weak position studs. The strong position studs exhibited higher strength than the weak positon studs, which was attributed to more concrete between the studs and the metal deck. The strong position studs failed by developing concrete shear cones or shearing off in the shank, and punching through the deck rib was the limit state for the weak position studs. Test results revealed that the shear stud strength used in the AISC Specification (1986) was unconservative in many cases and needed further modification.

Extensive research conducted by Rambo-Roddenberry (2002) laid the basis for the steel headed stud anchor strength expression in AISC (2016a). Twenty-four solid slab pushout test specimens were tested, and the variables were flange thickness, steel/concrete surface and normal force. The results showed (1) flange thickness did not affect the stud strength significantly; (2) sheet metal between steel beam and concrete slab reduced the frictional component of the stud strength; (3) applying normal force on the concrete slabs increased the stud strength. The equation developed by Ollgarrd et al. (1971), which was employed in the AISC Specification (1993), was slightly unconservative when normal force was not applied to the specimens.

Ninety-three composite slab pushout tests were also performed. The following parameters were studied: stud diameter, concrete strength, deck height, friction at the deck/steel beam surface, and tension in the stud shank. The main conclusions were (1) strong position studs exhibited stud shearing failure, and weak position studs exhibited rib punching through failure; (2) the limit state was rib shearing for deep deck tests; (3) 7/8’’ studs had much less strength than 3/4’’ studs because of limited welding abilities at the lab. The AISC strength equation for shear connectors in composite slabs was also based on the formula developed by Ollgarrd et al. (1971), but a strength reduction factor, SRF, was included to account for the presence of the metal deck. The tested shear connector strengths were significantly less than the AISC predictions. New strength prediction models were concluded from the pushout test results, which were proved to be adequate comparing to the test results elsewhere.

Three partially composite beams were designed to confirm the validity of the new equation. The main differences were the stud position and the number of studs per rib. The test results correlated well with the expected flexural strength using the AISC flexural model. Based on all composite beam test results reported, a resistance factor for composite beam flexural strength was calculated through reliability analysis.

2.3.2 Deconstructable shear connectors

Lam et al. (2013) conducted both experimental and analytical research on demountable shear connectors. The connector with a 16 mm threaded end was fabricated from the standard 19 mm diameter T. W. Nelson headed stud connector. An M16 Gr 8.8 nut was used to fasten the connector to the steel beam. Eight specimens were tested, and the parameters were the concrete compressive strength and the headed/stud collar size. Two types of failure modes were observed: fracture of the shear connectors close to the threaded end or failure by concrete crushing and splitting. For specimens failed by concrete crushing, the slabs could be easily disassembled from the steel beam and the threaded portion of the shear connectors was not damaged. By comparing the load-slip curves for welded headed studs and demountable connectors, Lam et al. (2013) found that when the concrete strength and the failure mode are similar, the demountable connectors achieve similar strength but with higher ductility than the welded connectors. A nonlinear finite element model was developed to investigate the capacity of these shear connectors embedded in a solid slab. The analytical model proved to give a good prediction of the connector capacity and load-slip behavior. This research was extended to investigate the performance of the same type of demountable shear connectors designed with composite slabs, and very similar conclusions were obtained (Rehman et al. 2016). The beam test results showed that the behavior of the beam with the demountable shear connectors was comparable to that of the specimen with welded shear studs (Lam et al. 2017).

Lee et al. (2013) considered the deconstructability and sustainability of bolted shear connectors in composite beams. Precast geopolymer concrete (GPC) slabs replaced ordinary Portland concrete (OPC) slabs, as GPC was believed to mitigate the excessive CO_2 emissions associated with OPC. Four pushout tests were designed according to the

Eurocode 4 Specifications. Two tests were designed using M20 8.8 single nut bolts embedded in concrete slabs, and the others were designed using M20 8.8 bolts through 24 mm precast holes. Three distinct stages were discovered in the load-slip curves for the pretensioned bolted shear connectors: viz. a region of “full interaction”, a region of “zero interaction” and a region of “partial interaction”. These were delineated by the frictional force at the steel-concrete interface, by the size of the clearance hole relative to the diameter of the bolt, and by the shear flow force as a result of bolts bearing against concrete. For the first two tests, only two stages were observed because the bolts were embedded in the concrete panels during the pre-casting process, and therefore there were no hole clearances between the bolts and the surrounding GPC concrete.

As the second phase of the research conducted by Lee et al. (2013), composite beam tests were performed by Ataei (2016). Among the four beam specimens, three specimens consisted of steel beams, precast geopolymer slabs and post-tensioned friction-grip bolted shear connectors, while the fourth specimen was a control specimen that used single-nut embedded shear connectors and a cast-in-place geopolymer slab. The control specimen was a fully composite beam, and the other three beams had a degree of shear connection of more than 100%, 97% and 55%. The ultimate flexural strength and initial stiffness of the control specimen were shown to be greater than those of the counterpart beam. The authors attributed the lower stiffness of the counterpart specimen with precast panels and bolted shear connectors to the discontinuity of the precast panel system and the rotation of the panels. The disparity in the ultimate flexural strengths was due to different failure modes of the specimens. The monolithic concrete slab was crushed in the control specimen, while localized concrete crushing and longitudinal splitting of the panels were observed in the other beam. The post-tensioned friction-grip bolts induced friction at the steel-concrete interface. At the early loading stages, the friction resisted the required shear flow without generating any interface slip. Therefore, the stiffness of the partially composite beams was close to that of the corresponding fully composite beams.

Moynihan et al. (2014) tested three composite beams, of 2 m, 10 m and 5 m long, constructed utilizing M20 bolts as demountable shear connectors. The first two beams were loaded to service loading, unloaded, deconstructed and reassembled, and all three beams were loaded to failure. The test results showed that the flexural strengths of the three beams were all larger than the predicted strengths in accordance with Eurocode 4. The behavior of the 10 m specimen was similar to that of a previously published composite beam designed with welded shear studs.

Pathirana et al. (2015) tested the static flexural strength of seven composite beams. Three composite beams respectively adopted three different connector types, including welded shear studs and two types of bolted connectors. Another three beams were non-composite and respectively retrofitted using these three types of connectors. The last beam was a non-composite beam and used as a reference beam. The load-slip behavior of these connectors in normal and retrofitted conditions was compared in the companion pushout tests. Finite element models were developed for the beam specimens, and the calibrated models were utilized to parametrically study the effects of the concrete and grout strength, grout-hole size and shear connection ratio on the flexural behavior of retrofitted beams.

Compared to the welded shear studs, the bolted connectors achieved much higher shear capacity in both conditions. The shear strength of the bolted connectors were not sensitive to the test conditions, whereas the shear studs exhibited much higher shear strength in normal conditions than in retrofitted conditions. By comparing the load-slip behavior, it was concluded that the majority of the stud slip occurred after yielding, while the bolted connectors slipped as a result of shear transformation without yielding. The retrofitted beams utilizing bolted connectors demonstrated similar strength and ductility behavior to the normal beams with the same connectors. For the welded stud connectors, the flexural strength of the retrofitted beams was not as large as that of the normal beams. Hence, it was feasible to retrofit existing composite beams utilizing these bolted connections. The parametric study conducted using calibrated finite element models indicated that the flexural strength of the retrofitted beams was affected by the concrete strength, not by the grout strength and grout hole sizes.

2.3.3 Analytical and computational analysis of steel headed stud anchors and composite beams

Closed form solutions for calculating the shear connector force and slip and the beam deflection were first derived by Newmark et al. (1951). The derivation was based on the assumption of equal curvature and no separation between the steel and concrete elements.

The uplift effects in composite beams were studied by Naraine (1984). A sixth order differential equation was derived which included both the slip and uplift at the steel/concrete interface, whereas Newmark's theory only considered the slip and involved a second order differential equation. Different loading scenarios were investigated. When a beam is under uniform loading, such as a secondary beam in a building, approximately uniform compressive force exists between the steel beam and concrete slab, except for the supports where the compressive force is much greater. This implies that there is normally no separation at the steel/concrete interface, and the shear connectors are not under tensile axial loading. When a concentrated force acts on the bottom steel flange, separation between the steel beam and concrete slab may occur, and the shear connectors are subjected to tension as well as shear.

An equation was derived by Oehlers et al. (1995) to predict the maximum slip demand on the shear connectors in composite beams, thereby avoiding stud fracture in composite beams with a low composite action. It was assumed that the steel beams and concrete slabs are elastic along the beam length. When the plastic moment or fracture moment of the composite beam is reached, all the shear connectors placed between the beam end and the maximum moment section are inelastic. This work was expanded in Burnet et al. (2001) which imposed additional slip requirements to account for cracking of the concrete slab, yielding of the steel beam, and plastic rotation at the plastic hinge region if the composite beam is ductile.

A numerical procedure was proposed by Gattesco (1999) accounting for the nonlinear behavior of concrete slabs, steel beams and shear connectors. The beam was discretized into several elements with four degrees of freedom at each end: vertical displacement, rotation, horizontal displacement at the centroid of concrete and horizontal displacement at the centroid of steel section. Stiffness matrices were formed for each segment and then assembled to generate equilibrium equation for the system, which could be solved to obtain the displacements at the nodes and the internal forces.

Qureshi et al. (2011) investigated the influences of spacing and layout on the shear connector capacity parametrically. Three-dimensional nonlinear finite element models, which take into account material nonlinearity and geometric nonlinearity, were verified against the experimental test results. Three-dimensional eight-node brick and six-node wedge reduced integration elements were used for the concrete slab, shear studs and steel beam flange. The steel metal deck was modelled with four-node shell reduced integration elements, and the wire mesh was modelled by three-dimensional two-node truss elements. Surface to surface contact was defined between the top of the metal deck and the bottom of the concrete slab. Contact was also assigned between the shear studs and the surrounding concrete. The frictional coefficient was assumed to be 0.5 in both cases. The concrete damaged plasticity model, provided in ABAQUS (2011), was chosen to simulate concrete cracking under tension and concrete crushing under compression. An elastic-perfectly-plastic material was utilized for the steel components. The quasi-static solution was obtained using ABAQUS/Explicit by applying the loads sufficiently slowly to render the dynamic effects negligible. Subsequently, the validated models were employed to study the effects of transverse spacing and stud position on the strength of shear studs.

2.4 Seismic design of diaphragms

Diaphragms serve multiple functions in a building. Diaphragms are responsible for transferring the inertia forces within the floor systems to the seismic force-resisting systems, and also provide supports to the vertical elements to prevent buckling and reduce the additional forces associated with P-delta effects (Moehle et al. 2010). For modelling and design, diaphragms are usually simplified as deep beams consisting of the following components: diaphragm slab, tension and compression chords, collectors, and the connections to the seismic force-resisting system; see Figure 2.1.

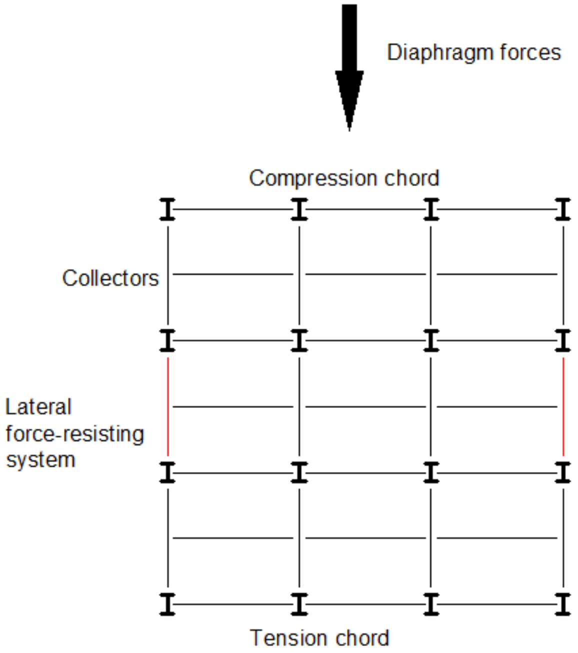
Diaphragm forces
Compression chord
Collectors
Lateral force-resisting system
Tension chord

Figure 2.1 Diaphragm components

2.4.1 Seismic demand on diaphragms

Seismic demand on diaphragms is given in ASCE 7-10 Section 12.10.1.1. Design forces for vertical elements and diaphragms are different. The reason is that the maximum seismic demands on diaphragms at various levels occur at different times; therefore, using the diaphragm force to design the vertical elements would be overly conservative. Figure 2.2 presents the appropriate load patterns for evaluating the diaphragm at different levels (Sabelli et al. 2011). It should be noted that collectors are to be designed using load combinations with overstrength factors.

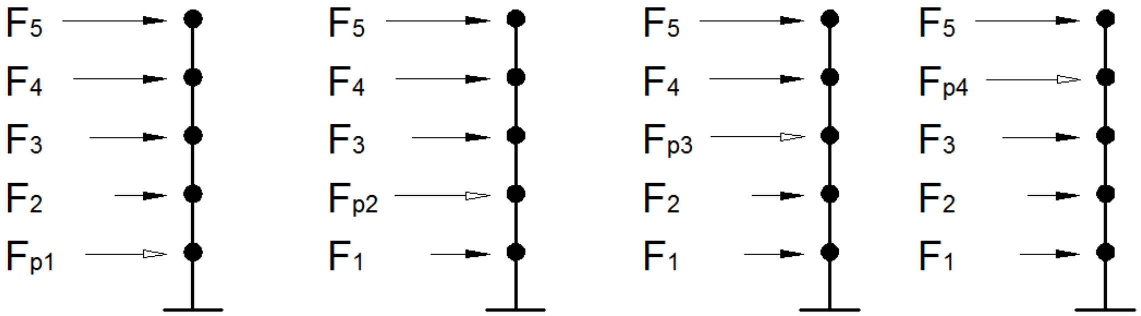

Figure 2.2 Loading pattern for diaphragms at different levels

2.4.2 Seismic behavior of diaphragms

Traditionally, diaphragms are designed to remain elastic because of their importance in maintaining building integrity. There have been few cases of observed damage in diaphragms after earthquakes (Moehle et al. 2010).

Based on the relative rigidity of the diaphragms and the seismic force-resisting systems, diaphragms can be classified as rigid, flexible and semi-rigid per ASCE 7-10 Section 12.3.1. Examples of rigid diaphragms are concrete slabs and composite slabs with span-to-depth ratio of 3 or less. For structures with rigid diaphragms, the distribution of the lateral forces depends on the relative stiffness of the vertical elements in the seismic force-resisting systems. The seismic force distribution among the vertical elements in structures with flexible diaphragms, however, depends on the tributary area supported by the vertical element. It is permitted to idealize the diaphragm as flexible if the maximum in-plane deflection of the diaphragm is more than twice the average story drift. Examples include metal deck and wood panels spanning braced frames or concrete shear walls.

2.4.3 Diaphragm analysis

Simplified models, such as an equivalent beam model, equivalent beam-on-spring model and corrected equivalent beam model, are usually adequate for modeling of diaphragms in regular buildings. Complicated models such as finite element models and strut-and-tie models are necessary for buildings with irregularities (Moehle et al. 2010). No specific provision for deciding forces in individual components is available. The required strength should be calculated in accordance with the assumed distributions, and adequate ductility is provided to ensure force redistribution. For example, when shear is uniformly distributed along the depth of the diaphragm, it is reasonable to infer that chord forces are concentrated at the diaphragm boundaries. In this case, shear ductility is required for the metal deck when the axial deformation is significant for a long collector (Sabelli et al. 2011).

2.4.4 Diaphragm component design

2.4.4.1 *Composite diaphragm strength*

Easterling et al. (1994) summarized the test results on composite diaphragms where the strength, stiffness and limit states were reported. Parameters for the specimens were steel-deck type, steel-deck thickness, connector types, number of connectors, slab aspect ratio, edge member size, and concrete thickness. No primary or secondary reinforcement was used. All diaphragms displayed brittle behavior, but the author believed that the ductility of some specimens could be improved by adding reinforcement in the slabs. Governing limit states were identified and described. Concrete diagonal cracking or cracking parallel to and above the deck flange might occur when the concrete above the deck was thin. Deck-concrete shear transfer failure appeared in welded composite diaphragms, but this limit state was unlikely for diaphragms connected with steel headed stud anchors because shear studs restrained the relatively slip between the steel deck and the concrete slab effectively. It was also concluded that load transfer from the edge member to the composite slab took place in the edge zone, a small region along the diaphragm edge. This was shown during tests when the separation between the metal deck and the concrete slab was significant at the corners, and the interior region remained composite. Equation (2.1) was proposed to estimate the concrete shear strength. Steel Deck Institute Diaphragm Design Manual (SDI DDM03) uses a different design equation that incorporates the contributions from both the concrete slab and the deck-to-steel framing connectors.

$$V_n = 3.2 t_e b \sqrt{f_c'} \tag{2.1}$$

Where

V_n = shear strength of the diaphragm

t_e = effective thickness of the composite slab including a construction from the steel deck using a transformed section approach

b = depth of the diaphragm (inches)

f_c' = concrete compressive strength (psi)

2.4.4.2 *Steel members*

Steel members include chords, collectors as well as members that are part of the lateral resisting system. The design procedure for all these members is not outlined in detail in design guides or specifications. Simplified design approaches are provided in the AISC 360-16 commentary (2016).

Steel girders that are part of a moment frame or braced frame are often designed as non-composite sections. This is because the moments on the girders in moment frames are both positive and negative, and the axial forces in moment frame or braced frame girders could be tension or compression depending on the direction of the external loading. Designing composite sections for the negative moment region may not be economical for using extra reinforcement in the slab. In addition, the shear connectors necessary for shear transfer in this region can only be placed in a very small length, making construction difficult.

Steel collectors can be designed for combined loading of axial force due to shear transfer between the concrete slab and the steel beam as well as flexural force resulting from gravity loading and lateral loading. It is recommended in the commentary that non-composite axial strength and composite flexural strength are used in the interaction equation in Chapter H in AISC (2016a) for strength check of steel chords. Even though designed as noncomposite members, all collector beams should consider the slip capacity of the shear connectors. The reason is that although the anchors are properly detailed for diaphragm force transfer, they are also subjected to gravity loading even if the sections are designed as bare steel.

The design of beam-to-column connections and columns needs to account for combined loads due to diaphragm behavior, for example, collector axial force that is collected through shear studs transferring the force into columns in the seismic resisting system.

2.4.4.3 *Shear connectors*

Typically, the flexural design of composite beams determines the detailing of shear connectors. However, while the in-plane diaphragm forces may make additional shear connectors necessary, typically they are not needed. Guidance on this issue is also provided in the AISC Commentary (AISC 2016a). The commentary states that it is not required to superimpose the horizontal shear due to bending of the beams and the horizontal shear resulting from diaphragm behavior for two reasons. First, it is recognized that reduced live load is used in load combinations with lateral loads in ASCE 7. This reduced live load decreases the demand on the shear connectors, and the “residual” strength provides certain capacity for diaphragm force transfer. Secondly, the shear flows on the shear connectors are not additive for gravity and lateral loading. Lateral loads overload the shear connectors on half of the beam and underload those on the other half, which is deemed to be acceptable since steel headed stud anchors are ductile.

2.4.5 Diaphragm seismic design methodology

A new seismic design methodology for precast concrete diaphragms was developed by Fleischman et al. (2014). Unlike the conventional design approach for diaphragms where all the structural components are designed to be elastic or sustain minor damage during earthquakes, the new performance-based design approach utilizes prequalified precast connectors as the main energy-dissipating mechanism in the diaphragms.

Depending on the geometry of the diaphragm and the seismic design category, three seismic demand levels are defined: low, moderate and high. Three design options are also available to achieve the anticipated performance: elastic design option (EDO), basic design option (BDO) and reduced design option (RDO).

1. EDO: the diaphragm is designed to remain elastic not only for the design basis earthquake (DBE), but also for the maximum considered earthquake (MCE). The ductility requirement on the precast connectors is relatively low.

2. BDO: this approach targets elastic diaphragm under the DBE, and permits inelastic behavior in the MCE. Precast connectors with moderate ductility are required to prevent brittle failure in the MCE.

3. RDO: diaphragm yielding under the DBE is allowed for this design method. In exchange for the lower design forces, the precast connectors need to be highly ductile.

The primary improvements over the traditional design methodology are summarized as follows:

1. New equations with different coefficients were proposed for calculating the seismic demand in a precast concrete diaphragm, because the current design equations in ASCE 7-10 underestimated the required seismic forces, and could not take advantage of different design options.

2. The axial, shear and flexural strength of a precast concrete diaphragm were derived by taking into consideration the contribution from all the reinforcement at a diaphragm joint. An interaction equation could be applied to check the adequacy of reinforcement at the joint.

3. Effective flexural and shear modulus were also obtained by accounting for all the reinforcement at a joint. The effective diaphragm stiffness could be used to perform a drift check for the gravity columns and thus ensure the connections and non-structural components were detailed for this drift.

3. PROTOTYPE STRUCTURES

The behavior and design of a new structural system can be studied through the use of prototype structures. Prototype structures are developed to establish typical member sizes, expand the knowledge of this system and investigate its applicability to an entire class of buildings. This section summarizes the prototype structures detailed in this research to help explore a range of design issues arising in the DfD system. Life cycle assessment results are also briefly presented to demonstrate the environmental benefits of adopting DfD in the design of buildings. From a dismantler's perspective, challenges and opportunities for dismantling current steel structures and the flow of the demolished materials are discussed. In addition, Appendix A summarizes the member sizes of all the frames designed in this chapter. The selection of the flexural and shear reinforcement for the precast concrete planks, along with the design of the shear keys, is given in Appendix B.

The prototype structures in this work are designed in accordance with the following codes: *Minimum Design Loads for Buildings and Other Structures* (ASCE 2010), the AISC *Specification for Structural Steel Buildings* (AISC 2016a) and the AISC *Seismic Provisions for Structural Steel Buildings* (AISC 2016b).

3.1 Selection and design of prototype structures

The prototype buildings in this work all are designed to have the same plan layout: 3 bays by 3 bays with bay widths of either 20 ft. or 30 ft. (Figure 3.1a). The buildings are 3 or 9 stories tall with a story height of 13 ft. Simple connections are assumed for beam-to-beam and beam-to-column connections within the gravity system. Concentrically braced frames are utilized to resist lateral loads, including wind loads and seismic loads. Since the buildings are assumed to be located in Los Angeles, the steel systems are detailed for seismic resistance, and special concentrically braced frames (SCBF) are chosen (Figure 3.1b), with a focus on ensuring all bolted construction in the field to maximize the potential for deconstruction. The lateral loads are investigated in this system especially to highlight issues related to using deconstructable flooring systems as diaphragm systems within buildings to help transfer lateral loads to the lateral-force resistance system.

A composite floor framing system is used for all configurations, and composite beams are designed accordingly. Either headed stud anchors or girder clamps (Lindapter 2011) connect the concrete slabs with the steel beams in the conventional composite system and the deconstructable composite system, respectively. Solid slabs are chosen for the prototype structures, since it is assumed that the limit states of composite beams with solid slabs are more comparable to the proposed system using clamping connections. As opposed to composite slabs that are cast on corrugated metal deck, solid slabs refer to slabs formed with flat soffits.

Two levels of live loads are selected: high gravity, which corresponds to storage warehouse live load (250 psf) and low gravity, which corresponds to office live load and partition allowance (80 psf). In this work, it is assumed that the 3-story buildings are used as storage warehouses, while the 9-story structures are office buildings.

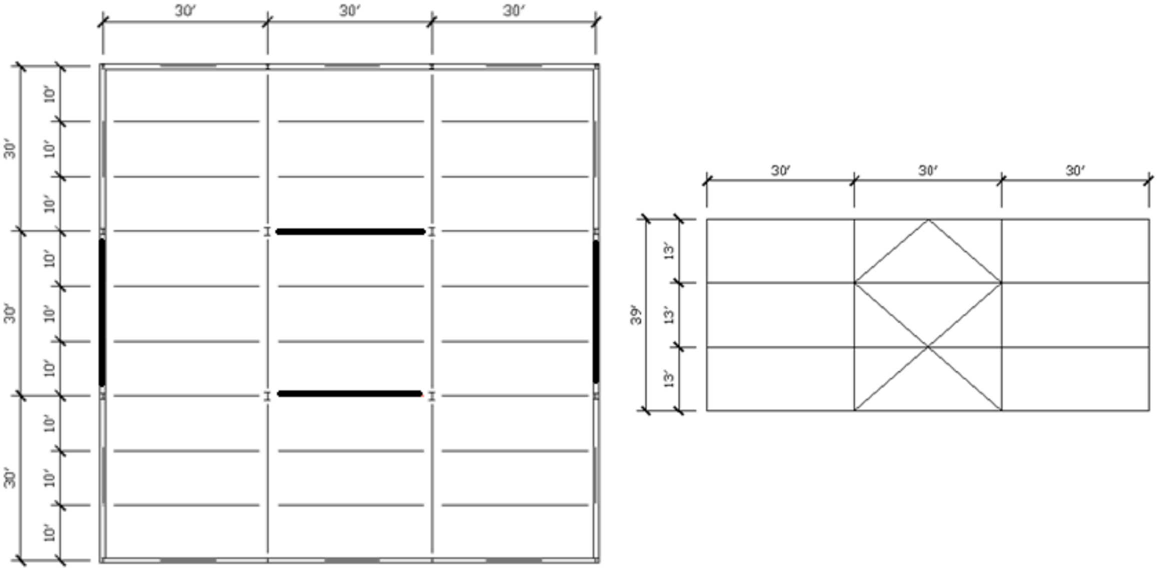

Thick solid lines represent lateral braces.

a) Plan view b) Elevation view

Figure 3.1 Building layout for three-story buildings

Sixteen framing systems are designed with variations of bay width, number of stories, concrete slab thickness, and shear connection between concrete slabs and steel beams. The frames are also named in this order with “ss” and “gc” representing steel headed stud anchor connections in solid slabs and girder clamp connections, respectively. The prototype structure matrix is summarized in Table 3.1.

In the prototype structures, all the headed stud shear connectors are 3/4 in. diameter, Type B shear studs which have a minimum tensile strength of 65 ksi. All the clamps used in the deconstructable composite floor system are 1 in. diameter. Since the shear strength of the clamp connections was unknown during the design which was performed prior to conducting the experiments, a nominal shear strength of 15.74 kips was assumed for the clamps, according to the manufacturer’s catalog (Lindapter 2011). As shown in Chapter 4, the tested shear strength of the 1 in. diameter clamps is 22.1 kips, greater than 15.74 kips. With the exception of the HSS braces that use A500 Grade B steel, A992 Grade 50 steel is used for all the shapes. The strength of the cast-in-place concrete slabs and precast concrete planks is assumed to be 4 ksi. All designs use the LRFD design method in AISC 360-16 (2016).

Table 3.1 Prototype structure matrix

Frame Number	Name	Bay width (ft.)	Number of stories	Concrete slab/plank thickness (in.)	Live load (psf)	Connections between concrete and steel
1	20-3-6-ss	20	3	6	250	Studs in solid slabs
2	20-3-8-ss	20	3	8	250	Studs in solid slabs
3	20-9-6-ss	20	9	6	80	Studs in solid slabs
4	20-9-8-ss	20	9	8	80	Studs in solid slabs
5	30-3-6-ss	30	3	6	250	Studs in solid slabs
6	30-3-8-ss	30	3	8	250	Studs in solid slabs
7	30-9-6-ss	30	9	6	80	Studs in solid slabs
8	30-9-8-ss	30	9	8	80	Studs in solid slabs
9	20-3-6-gc	20	3	6	250	Girder clamps
10	20-3-8-gc	20	3	8	250	Girder clamps
11	20-9-6-gc	20	9	6	80	Girder clamps
12	20-9-8-gc	20	9	8	80	Girder clamps
13	30-3-6-gc	30	3	6	250	Girder clamps
14	30-3-8-gc	30	3	8	250	Girder clamps
15	30-9-6-gc	30	9	6	80	Girder clamps
16	30-9-8-gc	30	9	8	80	Girder clamps

3.2 Loads

Loading on the prototype structures includes gravity load (dead load and live load), seismic load and wind load.

3.2.1 Gravity load

The composite flooring and roofing systems are comprised of a normal weight concrete slab, mechanical/electrical/plumbing, roof deck, rigid insulation, roofing (five-ply felt and gravel), ceiling system (acoustical tile and mechanical system allowance) and steel framing (beams, girders and columns). Minimum design dead load for these components can be found in Table C3-1 of ASCE (2010).The dead load on the roof and 6 in. thick floor system of the prototype structures is described in Table 3.2. The weight of exterior wall systems, which is assumed to be 15 psf, is transferred to the foundation directly.

Table 3.2 Breakdown of dead load

Description	Roof (psf)	Floor (psf)
Concrete slab	N/A	72.5
Mech./elec./piping	10	10
Roof deck	3	N/A
Rigid insulation	3	N/A
Roofing	6	N/A
Ceiling system	N/A	5
Steel framing	5	5
Total	27	92.5

The live load is provided in Table 4-1 of ASCE (2010). Low live load is supposed to be 70 psf (50 psf + 20 psf for partitions). However, corridor loading above the first floor is given as 80 psf. Therefore, an envelope of 80 psf, rather than 70 psf, is used conservatively throughout the layout. The roof live load is assumed to be 20 psf for all configurations.

3.2.2 Live load reduction

Live load is reduced in accordance with the provisions in Section 4.7 of ASCE (2010). In the prototype structures, the beams and columns for which a value of $K_{LL}A_T$ is 400 ft^2 or more are designed for a reduced live load in accordance with the following formula:

$$L = L_0(0.25 + \frac{15}{\sqrt{K_{LL}A_T}}) \tag{3.1}$$

Where

L = reduced design live load per ft^2 of area supported by the member

L_0 = unreduced design live load per ft^2 of area supported by the member

K_{LL} = live load element factor

A_T = tributary area in ft^2

L is no less than $0.5L_0$ for members supporting one floor and L is no less than $0.4L_0$ for members supporting two or more floors. Live loads that equal to or exceed 100 lb/ft^2 are not reduced.

Table **3.3** shows the reduced live load used for the design of the members in the prototype structures.

3.2.3 Earthquake load

Three types of analytical procedures for calculating seismic load are permitted in ASCE (2010); in this work, the equivalent lateral force method is adopted for all the buildings.

Table 3.3 Reduced design live load for different members

Name	Unreduced design live load (psf)	Reduced design live load (psf)						
		Members						
		Columns			Beams		Girders	
		Level	Corner	Edge	Interior	Exterior	Interior	Exterior
20-3-6	250	All	250					
20-3-8								
30-3-6								
30-3-8								
20-9-6	80	9	80	69	80	80	62	80
		8	80	55				
		7	69	48				
		6	62	44				
20-9-8		5	58	42				
		4	55	40				
		3	52	39				
		2	50	37				
30-9-6	80	9	77	53	69	80	48	76
		8	60	43				
		7	53	39				
		6	48	36				
30-9-8		5	45	35				
		4	43	33				
		3	41	32				
		2	40	32				

Seismic base shear

The seismic base shear, V, in a given direction is determined in accordance with the following equations:

$$V = C_s W \tag{3.2}$$

$$C_s = \frac{S_{DS}}{\left(\frac{R}{I_e}\right)} \leq \begin{cases} \dfrac{S_{D1}}{T\left(\frac{R}{I_e}\right)} & for\ \ T \leq T_L \\ \dfrac{S_{D1} T_L}{T^2\left(\frac{R}{I_e}\right)} & for\ \ T > T_L \end{cases} \tag{3.3}$$

C_s is no less than

$$C_s = 0.044 S_{DS} I_e \geq 0.01 \tag{3.4}$$

Where

C_s = the seismic response coefficient

W = the effective seismic weight

S_{DS} = the design spectral response acceleration parameter in the short period range (Section 11.4.4 or 11.4.7 (ASCE 2010))

S_{D1} = the design spectral response acceleration parameter at a period of 1.0 s (Section 11.4.4 or 11.4.7 (ASCE 2010))

T = the fundamental period of the structure

T_L = long-period transition period (Section 11.4.5 (ASCE 2010))

R = the response modification factor (Table 12.2-1 (ASCE 2010))

I_e = the importance factor (Section 11.5.1(ASCE 2010))

Effective seismic weight

The effective seismic weight of a structure is determined as per Section 12.7.2 in ASCE (2010). The effective seismic weight, W, is the sum of the following:

- 100% of the dead load
- 25% of the floor live load for 3 story buildings used for storage
- 100% of the partition allowance and exterior wall systems

Period determination

The fundamental period of the structure, T, in the direction under consideration is established using the structural properties and deformational characteristics of the resisting elements in a properly substantiated analysis. As an alternative to performing an analysis to determine the fundamental period, T, the approximate building period, T_a, is used directly.

$$T_a = C_t h_n^x \tag{3.5}$$

Where

h_n = the structural height

C_t *and* x =coefficients based on the structural types chosen (Table 12.8.2 (ASCE 2010))

Vertical distribution of seismic forces

The lateral seismic force, F_x, induced at any level is determined from the following equations:

$$F_x = C_{vx}V \tag{3.6}$$

$$C_{vx} = \frac{w_x h_x^k}{\sum_{i=1}^{n} w_i h_i^k} \tag{3.7}$$

Where

C_{vx} = vertical distribution factor

V = total design lateral force or shear at the base of the structure (Equation 3.2)

w_i and w_x = the portion of the total seismic weight (W) of the structure located or assigned to Level i or x

h_i and h_x = the height from base to Level i or x

k = an exponent related to the structure period

$$k = \begin{cases} 1 & T \le 0.5 \\ 1 + 0.5(T - 0.5) & 0.5 < T < 2.5 \\ 2 & T \ge 2.5 \end{cases} \tag{3.8}$$

3.2.4 Wind and snow load

Wind loads on the main wind-force resisting system (MWFRS) are determined using the directional procedure in accordance with Chapter 27 of ASCE (2010). Table 3.4 shows the seismic load and wind load used for the design of the lateral force-resisting systems (LFRS) in the prototype structures. Because the prototype structures are located in Los Angeles, seismic loads, rather than wind loads, dominate the design of the lateral resisting system.

Snow loads are assumed to be zero.

Table 3.4 Seismic load and wind load for the prototype structures

Name	Level	Lateral force (kips)	
		Seismic load	Wind load
20-3-6	Roof	56.6	10.0
	3	189.7	18.6
	2	94.9	17.1
20-3-8	Roof	57.1	10.0
	3	214.0	18.6
	2	107.0	17.1
30-3-6	Roof	119.8	15.0
	3	404.1	28.0
	2	202.0	25.6
30-3-8	Roof	120.8	15.0
	3	461.4	28.0
	2	230.7	25.6
20-9-6	Roof	22.8	13.7
	9	68.4	26.9
	8	59.3	26.3
	7	50.2	25.6
	6	41.0	24.8
	5	31.9	24.0
	4	23.2	22.9
	3	14.9	21.5
	2	7.1	19.9
20-9-8	Roof	26.8	13.7
	9	95.3	26.9
	8	82.6	26.3
	7	69.9	25.6
	6	57.2	24.8
	5	44.5	24.0
	4	32.3	22.9
	3	20.8	21.5
	2	9.8	19.9
30-9-6	Roof	105.2	20.6
	9	324.5	40.4
	8	280.1	39.4
	7	236.5	38.4
	6	193.5	37.2
	5	151.4	35.9
	4	110.3	34.3
	3	70.6	32.3
	2	32.9	29.9
30-9-8	Roof	123.7	20.6
	9	381.6	40.4
	8	328.6	39.4
	7	277.4	38.4
	6	227.9	37.2
	5	178.4	35.9
	4	129.0	34.3
	3	83.0	32.3
	2	38.9	29.9

3.2.5 Load combinations for strength design

Basic load combinations are provided in Section 2.3.2 in ASCE (2010).

1. $1.4D$
2. $1.2D+1.6L+0.5(L_r \text{ or } S \text{ or } R)$
3. $1.2D+1.6(L_r \text{ or } S \text{ or } R)+(L \text{ or } 0.5W)$
4. $1.2D+1.0W+L+0.5(L_r \text{ or } S \text{ or } R)$
5. $1.2D+1.0E+L+0.2S$
6. $0.9D+1.0W$
7. $0.9D+1.0E$

The load factor on L in combinations 3, 4, and 5 equals 0.5 for all occupancies in which L_0 is less than or equal to 100 psf, and is 1.0 otherwise. As such, 0.5 is used as the load factor on L in combinations 3, 4, and 5 for office buildings, and 1.0 is used for warehouse storage.

3.3 Design criteria

The available strength for each member is computed in accordance with the AISC Specifications (AISC 2016a, 2016b). A tolerance of 5% is allowed so that small overstresses are acceptable.

3.3.1 Gravity system

Elastic analysis is required to obtain the required strength for beams, girders and columns, which comprise the gravity system. Shored construction and unshored construction are assumed for the conventional composite floor system and deconstructable composite floor system, respectively. For the conventional composite floor system, the available flexural strengths of the composite beams should be greater than the required strengths. In the deconstructable composite floor system, once the planks are placed on and clamped to the steel beams, the concrete planks and steel sections act compositely. Lateral-torsional buckling is thus not considered as a limit state. In this design, the bare steel sections are conservatively chosen to support the weight of the steel beams and concrete planks and other construction dead loads and live loads. Otherwise, as the planks are attached to the steel beams, it is necessary to ensure that the available flexural strengths exceed the required flexural strengths over the full lengths of the beams. Depending on the level of live loads, either the bare steel section or composite section needs to be selected first. After the most economical steel section is chosen, shear connectors are determined such that the available strength is slightly larger than the required strength.

A minimum of 50% composite action is recommended by the AISC Specification and is targeted in these designs to prevent early departure from elastic behavior in both the beams and the studs. A lower amount of shear connection also requires large rotation to reach the available flexural strength of the member.

Since the method of designing composite beams using girder clamps is not available at the time of design, rigid plastic analysis developed for composite beams using shear studs is utilized.

Deflection limitation

Deflections at two phases need to be checked for the conventional composite floor systems, while the deflections of the deconstructable composite beams are only checked in the second phase.

Before the concrete hardens, dead load from the weight of the wet concrete and the steel beam and live load from the construction workers and equipment are taken by the steel beam alone. The deflection limit is $L/240$, and the steel beams can be cambered to reduce ponding effects if the limit is violated.

After the concrete hardens, all the loads are supported by the composite sections. Traditionally, the live load deflection is restricted to a maximum of $L/360$. The lower-bound moment of inertia, I_{LB}, provided in Equation (C-I3-1) in the AISC 360-16 Commentary (2016) or transformed section properties, I_{tr}, can be used to compute live load deflection.

3.3.2 Lateral force resistance system

Due to the symmetry of the frames, the structure can be decomposed into two lateral-resisting frames when the lateral loads are applied in a certain direction.

The direct analysis method is selected to compute the required strength of the frames. A factor of 0.80 is applied to all stiffness in the structure for second-order analysis. To account for imperfections, a notional load equal to 0.002 times the gravity load at each floor level is applied. An additional 0.001 times the gravity load at each floor level is also used so that τ_b can be taken as unity. As an alternative to a rigorous second-order analysis, the approximate second-order analysis method (also known as the B_1-B_2 method) in Appendix 8 of the AISC Specification (AISC 2016a) is applied.

Braced frame design

An elastic analysis is used to proportion the braces. Rectangular HSS and W shape sections are selected for the braces. A redundancy factor, ρ, is be assigned to the seismic force-resisting system to account for less redundancy in the structures. The value of this factor is either 1.0 or 1.3. A value of 1.3 is chosen for the prototype structures.

SCBFs designed in accordance with these provisions are expected to provide significant inelastic deformation capacity primarily through brace buckling and yielding of the brace in tension. Therefore, a capacity design method is used for beams, girders and columns to avoid failing prior to the braces.

The required strength of the columns, beams and connections in the SCBF is based on the load combinations in the applicable building code that include the amplified seismic load. In determining the amplified seismic load, the effect of horizontal forces, including overstrength, E_{mh}, is taken as the larger force determined from the following two analyses:

1. An analysis in which all braces are assumed to resist forces corresponding to their expected strength in compression or in tension
2. An analysis in which all braces in tension are assumed to resist forces corresponding to their expected strength and all braces in compression are assumed to resist their expected post-buckling strength

A vertical seismic load effect is considered in designing the beams, girders and columns that are part of the lateral resisting system:

$$E_v = 0.2S_{DS}D \tag{3.9}$$

Where

S_{DS} = design spectral response acceleration parameter at short periods (Section 11.4.4 or 11.4.7 (ASCE 2010))

D = effect of dead load

HSS braces are used when their strength is adequate; otherwise, W shape braces are used.

3.3.3 Member requirements

According to AISC (2016b), columns and braces in SCBFs satisfy the requirements for highly ductile members, and beams satisfy the requirements for moderately ductile members. The width-to-thickness ratios of compression members do not exceed the limiting ratios (Table 3.5) to achieve these requirements. It is assumed that the beams are provided with sufficient lateral bracing to achieve their full plastic moment strength.

Table 3.5 Limiting width-to-thickness ratios

Member	Section requirements	*b/t*	*h/t* or *h/t*$_w$
W shape beams	Moderately ductile	$0.38\sqrt{E/F_y}$	$0.64\sqrt{E/F_y}$
W shape columns	Highly ductile	$0.30\sqrt{E/F_y}$	For $C_a \leq 0.125$ $2.45\sqrt{E/F_y}\,(1-0.93C_a)$ For $C_a > 0.125$ $0.77\sqrt{E/F_y}\,(1-0.93C_a) \geq 1.49\sqrt{E/F_y}$ Where $C_a = \frac{P_u}{\emptyset_c P_y}$ P_u = required axial strength using LRFD load combination P_y= nominal axial yield strength of a member, equal to $F_y A_g$ $\emptyset_c$= resistance factor for compression
Rectangular HSS braces	Highly ductile	$0.55\sqrt{E/F_y}$	$0.55\sqrt{E/F_y}$
W shape braces	Highly ductile	$0.30\sqrt{E/F_y}$	$1.49\sqrt{E/F_y}$

3.3.4 Story drift determination

The deflection at level x (δ_u) used to compute the design story drift, Δ, is determined in accordance with the following equation:

$$\delta_u = \frac{C_d \delta_{xe}}{I_e} \tag{3.10}$$

Where

C_d = the deflection amplification factor (Table 12.2-1 (ASCE 2010))

δ_{xe} = the deflection at the location required by this section determined by an elastic analysis

I_e = the importance factor (Section 11.5.1(ASCE 2010))

The allowable story drift can be found in Table 12.12-1 of ASCE (2010).

P-Delta effect

P-delta effects on story shears and moments, the resulting member forces and moments, and the story drifts induced by these effects are considered where the stability coefficient (θ) as determined by the following equation is equal to or less than 0.10:

$$\theta = \frac{P_x \Delta I_e}{V_x h_{sx} C_d} \tag{3.11}$$

Where

P_x = the total vertical design load at and above Level x; where computing P_x, no individual load factor need exceed 1.0

Δ = the design story drift occurring simultaneously with V_x

I_e = the importance factor (Section 11.5.1(ASCE 2010))

V_x = the seismic shear force acting between Level x and x-1

h_{sx} = the story height below Level x

C_d =the deflection amplification factor (Table 12.2-1 (ASCE 2010))

When the stability coefficient (θ) is greater than 0.10 but less than or equal to θ_{max}, the displacements and member forces are multiplied by $1.0/(1-\theta)$. When θ is greater than θ_{max}, the structure is potentially unstable and is redesigned.

The stability coefficients are calculated and shown in Table 3.6 for all the structures. Since all the buildings are braced frames which are inherently stiff structures, the stability coefficients are much smaller than 0.10.

Table 3.6 Stability coefficients for the prototype structures

Name	Level	Stability coefficients
20-3-6	3	0.005
	2	0.014
	1	0.013
20-3-8	3	0.005
	2	0.014
	1	0.013
30-3-6	3	0.006
	2	0.015
	1	0.017
30-3-8	3	0.006
	2	0.015
	1	0.017
20-9-6	9	0.009
	8	0.009
	7	0.011
	6	0.013
	5	0.015
	4	0.016
	3	0.016
	2	0.015
	1	0.015
20-9-8	9	0.009
	8	0.009
	7	0.011
	6	0.013
	5	0.015
	4	0.016
	3	0.016
	2	0.015
	1	0.015
30-9-6	9	0.009
	8	0.007
	7	0.009
	6	0.011
	5	0.013
	4	0.014
	3	0.015
	2	0.015
	1	0.017
30-9-8	9	0.009
	8	0.007
	7	0.010
	6	0.012
	5	0.012
	4	0.014
	3	0.015
	2	0.016
	1	0.017

3.4 Final design

The following tables describe the design results for the composite flooring systems of the prototype structures. It is seen that the steel weight per sqft is higher in the deconstructable composite floor system than in the conventional composite floor system. The difference could be attributed to the following: first, since the shear strength of the clamps is underestimated in the design, the selected steel sections for the deconstructable composite beams and girders may be oversized, and the required number of clamps may be overestimated; second, because unshored construction is presumed for the deconstructable composite beams, the steel sizes may be bumped up to support the weight of the concrete planks and steel beams as well as the live load during construction, especially for buildings supporting low gravity loading; third, the precast concrete panels in the prototype structures are assumed to be two-channel planks, and there is an upper bound for the number of clamps used in the deconstructable beams and girders. If the maximum shear resistance provided by the clamps is inadequate, the weight and sizes of the steel sections are increased. As such, more efficient designs may be possible based on the results of this research. Design results of the gravity columns and members that belong to the lateral-force resisting system are given in Appendix A.

Table 3.7 Member sizes for the conventional composite flooring system with solid slabs

Name	Floor interior beam			Floor exterior beam			Floor interior girder			Floor exterior girder			Weight per sqft (lbs)
	Member size	# of shear studs	% of composite action	Member size	# of shear studs	% of composite action	Member size	# of shear studs	% of composite action	Member size	# of shear studs	% of composite action	
30-3-8-ss	W18x35	48	100%	W14x22	24	79.5%	W27x84	88	69.5%	W21x44	68	100%	52.73
30-3-6-ss	W18x40	48	87.6%	W14x26	36	100%	W27x84	88	69.5%	W21x50	68	87.9%	58.00
20-3-8-ss	W12x19	30	100%	W10x15	12	58.5%	W18x35	30	62.7%	W12x19	30	100%	31.15
20-3-6-ss	W12x22	20	66.3%	W10x15	12	58.5%	W18x35	48	100%	W14x22	24	79.5%	33.70
30-9-8-ss	W12x19	30	100%	W10x15	12	58.6%	W21x44	52	79.5%	W16x26	36	89.8%	29.20
30-9-6-ss	W12x19	30	100%	W10x15	12	58.6%	W21x44	52	79.5%	W16x26	44	100%	29.20
20-9-8-ss	W10x15	12	58.6%	W10x15	12	58.6%	W12x19	30	100%	W10x15	12	58.6%	22.95
20-9-6-ss	W10x15	12	58.6%	W10x15	12	58.6%	W12x19	30	100%	W10x15	12	58.6%	22.95

Table 3.8 Member sizes for the deconstructable composite flooring system[a]

Name	Floor interior beam			Floor exterior beam			Floor interior girder			Floor exterior girder			Weight per sqft (lbs)
	Member size	# of bolts	% of composite action	Member size	# of bolts	% of composite action	Member size	# of bolts	% of composite action	Member size	# of bolts	% of composite action	
30-3-8-gc	W18×35	60	91.7%	W14×22	32	77.6%	W30×90	40	23.9%	W21×55	40	38.9%	55.40
30-3-6-gc	W18×40	60	80.0%	W14×26	32	65.5%	W30×99	40	21.7%	W21×55	40	38.9%	61.67
20-3-8-gc	W10×19	40	100%	W10x15	24	85.7%	W18×35	40	61.1%	W12×19	32	90.4%	31.15
20-3-6-gc	W12×22	40	97.2%	W10x15	24	85.7%	W18×40	40	53.4%	W14×26	24	49.1%	36.00
30-9-8-gc	W16x31	32	55.1%	W12x22	32`	77.7%	W21x62	40	34.4%	W16x40	40	53.3%	44.87
30-9-6-gc	W14x30	32	56.9%	W12x19	32	90.4%	W21x55	40	38.9%	W18x35	40	61.1%	41.47
20-9-8-gc	W12x19	24	67.8%	W10x15	24	85.7%	W14x30	24	42.7%	W12x19	24	67.8%	29.65
20-9-6-gc	W12x16	24	80.2%	W10x15	24	85.7%	W14x26	24	49.1%	W12x16	24	80.2%	25.90

[a] The final design results may change depending on the design strategies concluded from the composite beam tests .

3.5 Results from life cycle assessment

A separate study was conducted that used life cycle assessment (LCA) to compare the environmental impacts of the prototype structures with the deconstructable composite floor systems to those of the buildings with conventional composite floors. The aim of the study was to demonstrate whether DfD leads to environmental benefits, and, if so, how much. Materials and processes that are significant contributors to the environmental impacts were also identified. Four environmental impact categories were included, namely, fossil fuel depletion, global warming, respiratory effects, and smog. With the assumed probability distributions, parameter uncertainties were evaluated using a Monte Carlo analysis. More details of the LCA are given in Brown et al. (2014). Key results from the study are shown below.

Figure 3.2 compares the LCA results of the conventional and deconstructable buildings for the 20-3-6 building geometry. In all the categories, the DfD building has higher impacts than the traditional building for production and transportation of components and labor. This is reflective of the greater mass of materials and longer assembly time required for the DfD building. This is due to the fact that the DfD building uses solid concrete planks, rather than composite slabs cast on corrugated metal deck of the traditional building. This corrugation allows the traditional building to use 20-25% less concrete than the DfD building, which in turn reduces the weight of the steel structure required to resist the loads of the building. If the DfD building components are not reused at all, they are recycled or landfilled in the same way as those in the traditional building design, and again due to their larger mass, incur larger impacts across all the categories. Overall, assuming no reuses, the DfD building has between 5-30% higher impacts than the traditional building. However, as noted above, based on several assumptions used in the prototype design, these prototype structures may be modestly overdesigned in comparison to a design that would use the results from this research more integrally.

For DfD buildings, if the components are reused once and substitute for primary raw materials, their production and disposal impacts are now distributed across two buildings.

With each successive reuse, the impacts associated with these life cycle stages decreases proportionally. The decreases are partially offset by the increases in material and worker transportation, as reuse requires additional labor for deconstruction and the DfD components must be transported to a central storage location. However, transportation impacts are minor compared to those of production and disposal; worker transportation is essentially insignificant. For the scenario where components are used to a maximum of 3 times, the environmental impacts of the average DfD building are 60-70% lower than those of the traditional building.

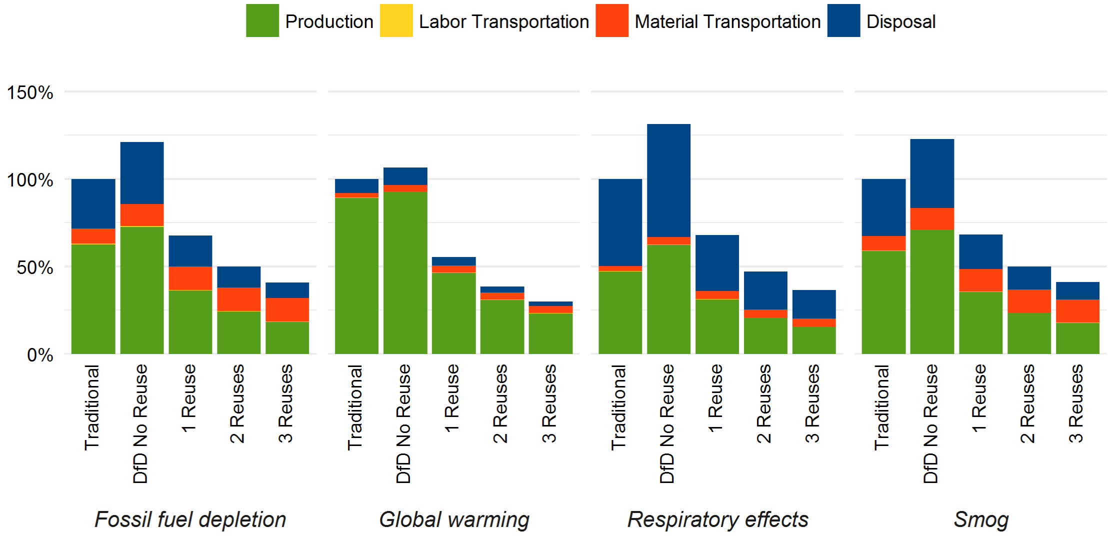

Figure 3.2 Relative LCA results comparing Traditional and DfD building designs assuming 0-3 reuses; disaggregated by life cycle stage; Traditional building = 100%

Figure 3.3 shows the LCA results for global warming between buildings with varying bay size, number of stories, and floor thickness. The baseline 20-3-6 configuration has the smallest dimensions and thus requires the fewest materials and associated transportation and disposal activities. The 20-3-8 configuration raises the DfD plank thickness to 8 in., which increases the amount of concrete required by approximately a third. This design change increases the production-phase GHG emissions from 120 to 155 ton CO_2e, or +29%, or nearly in proportion to the change in the concrete mass. The 20-9-6 configuration considers nine stories instead of three, requiring a different steel structural design and sizing of members. On a per story basis, the global warming impacts increase from 40 ton CO_2e for a 3-story structure up to 44 ton CO_2e for a 9-story structure, reflecting the larger members and more extensive connections required. Increasing the bay size also changes the structural design, with longer spans and a less dense geometry. The 30-3-6 configuration has 2.25 times the floorspace of the baseline 20-3-6 configuration and 2.27 times the absolute GHG emissions, with the small extra proportion attributable to the larger members required for longer spans.

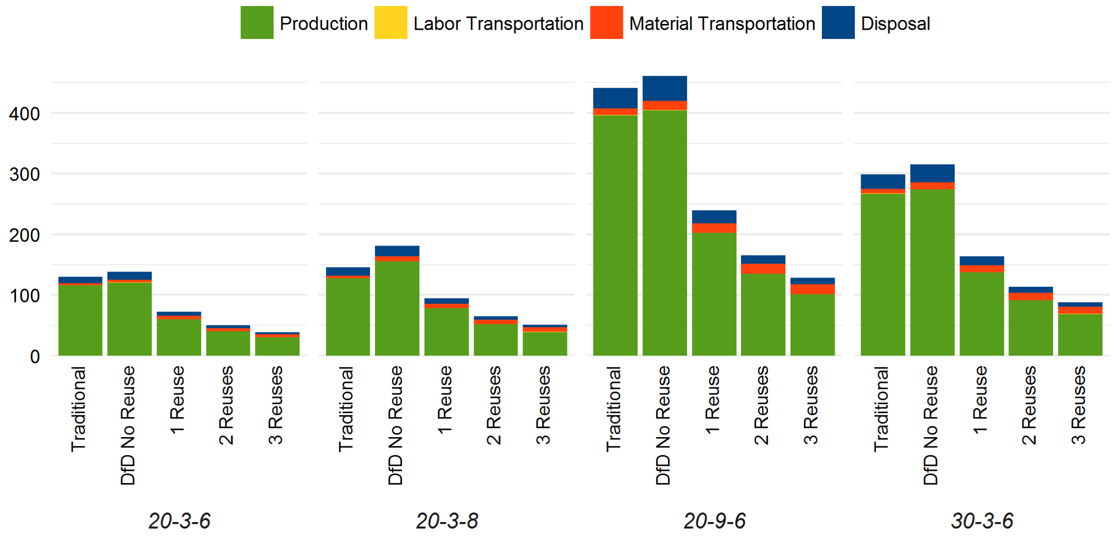

Figure 3.3 Absolute LCA results for Global Warming (ton CO2e) comparing building configurations; disaggregated by life cycle stage

Figure 3.4 illustrates the Monte Carlo simulation results for traditional versus DfD building designs for the baseline 20-3-6 configuration, analogous to Figure 3.2. There is significant overlap between 95% confidence intervals for the traditional and no-reuse DfD designs, indicating little statistical difference between the two. However, there is no overlap between the traditional and 1-3 reuse DfD designs (with the exception of a small overlap for respiratory effects and smog formation in the single reuse scenario), indicating that the DfD designs have statistically lower environmental impacts over their life cycles than the traditional designs, assuming at least one reuse as intended. Simulation ranges are narrowest for global warming, as emissions are commonly reported and there is little uncertainty in the characterization (global warming potential) factors.

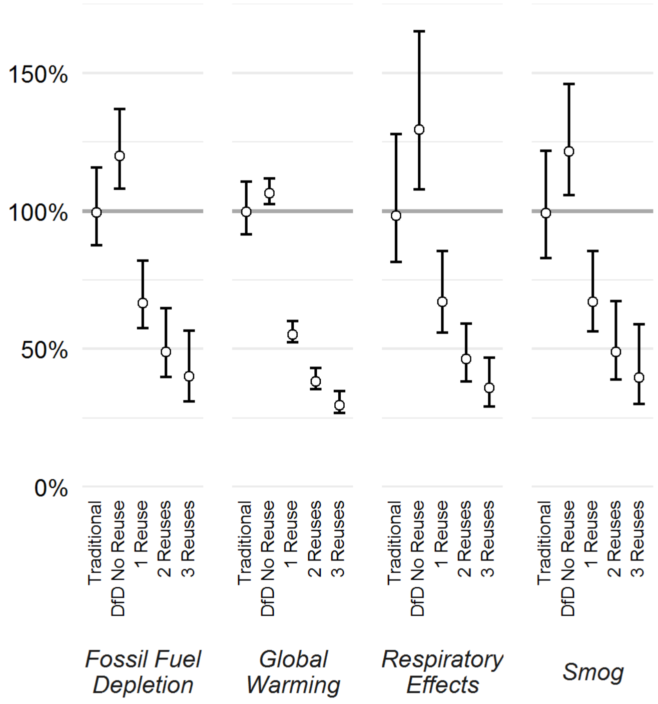

Figure 3.4 Results of Monte Carlo simulation for uncertainty analysis; Traditional and DfD building designs assuming 0-3 reuses; disaggregated by life cycle stage; Traditional building mean = 100%; 95% confidence intervals

3.6 Communication with dismantler

In parallel with comparing the environmental impacts of the traditional buildings with the DfD buildings, this research also included extensive discussions with a demolition contractor, including observing a building undergoing dismantling to ascertain the challenges for dismantling current steel structures and the flow of the disassembled materials. Main conclusions are summarized below:

- An extensive environmental survey (checking for asbestos, lead paint, PCBs, etc.) is necessary before dismantling to ensure that there is nothing harmful for the health of the workers and also to determine which materials may be reused or recycled depending on whether there are harmful materials involved (painted bricks, asbestos in caulk attached to steel framing, etc.). Usually a dismantler will isolate several samples of each material for testing. After the environmental survey is completed, they cut and cap utilities. The dismantler will first remove partition walls, suspended ceiling systems and mechanical systems, and then remove the structural system. Typically, the dismantler will also determine which materials can be reused, recycled, or sent to a landfill. After locating buyers and identifying the value of each of the materials, the dismantler decides whether reusing, recycling, or sending the materials to a landfill is most cost-effective.

- Bricks or concrete blocks are often crushed and used as aggregates. The dismantler also tries to salvage bricks or blocks where possible, as reclaimed bricks have enough value if the mortar is easily removable, and if any paint can be removed safely. Mortar is typically removed manually. Monolithic concrete is typically recycled (downcycled to aggregate) or disposed of in a landfill. Steel members and joists are in some cases salvaged for reuse (e.g., by removing bolts) or more typically recycled (in which case they often torch, saw, or tear with machines during dismantling). Aluminum, copper, and metals are generally recycled. There is no determination made for whether the steel was ever overloaded during its life in the building. The architectural finishes are mostly mixed and crushed and sent off site to a sorting facility.

- The values of steel scrap vary, with top quality being for beams, plate, and other structural steel, followed by bar joists, then sheet metal/light iron, which is voluminous, and must be shredded.

- It is more expensive to sort items if a soft demolition of finish materials cannot be conducted prior to the major structural dismantling.

- Materials that go to landfill only account for 10% of all the materials for this specific demolition project.

- The dismantlers may use strong magnets and eddy currents to separate ferrous and nonferrous metals from mixed debris, like reinforced concrete rubble.

- The dismantler felt that, in the future, use of robotics will enhance options for deconstruction.

4. PUSHOUT TESTS

The pushout experimental program includes two series of tests to characterize the basic behavior of the clamping systems. In the pretension tests, the number of turns of the nut is first determined to ensure adequate and reliable axial force generated in the bolts. Pushout tests are then performed to study the strength and ductility of the clamping connectors and explore the influences of the testing parameters. This research focuses on hot-rolled channels HTA-CE 72/48 with shortened anchors, HS 72/48 Grade 8.8 M24 and M20 bolts, and Type AFW clamps with short tails (Halfen 2011; Lindapter 2011).

In this chapter, a general description of the testing program is first given, including the test matrix, test setup, instrumentation plan and loading protocol. The global and local performance of the test specimens is then presented, including the load-slip responses, formation of cracks, bolt tension variation, force distribution in the system, and behavior of the channel anchors and reinforcement. Finite element models are also developed to investigate the indeterminacy of the system and predict the load-slip relationship of the clamps. Combining the experimental results with the finite element analysis results, design equations are proposed to estimate the slip strength and peak strength of similar clamping connectors.

More information regarding the pushout experimental program is provided in the appendices, with Appendix C illustrating the drawings for the load frame steel, specimen steel and concrete planks, Appendix D documenting the mill certifications for the components, Appendix E reporting the experimental raw data, and Appendix F demonstrating the useful quantities extracted from the experimental raw data. Some design issues are given in Appendix G and Appendix H.

4.1 Test matrix

Parameters for the pushout tests include bolt diameter, number of channels, reinforcement configuration, loading protocol, and use of shims, as given in Table 4.1.

The naming convention of the specimens is explained using Test 4-M24-2C-RH-LM-S, with 4 describing the cast sequence of the specimen during the concrete pour, M24 describing M24 bolts, 2C describing two channels embedded in the concrete plank, RH describing heavy reinforcement pattern, LM describing monotonic loading, and S describing shims.

Two-channel planks are considered as standard specimens in this research; nonetheless, long span beams with heavy gravity loading may necessitate three-channel planks to obtain larger flexural strength than the two-channel planks. Loading on a shear connector in a composite beam under gravity loading is usually unidirectional, but the load could change sign when the composite floor system is under seismic loading and shear connectors are employed to connect the composite diaphragm with the collector beams in a lateral force-resisting system. Typically, cyclic loading decreases the ultimate strength of steel headed stud anchors (in design, a 25% reduction in shear strength is typical; see AISC 2016b). Its influence on the clamping connectors is also investigated in the pushout tests. Shims are common in bolted steel connections to make up differences in plate thicknesses. Clamped connections may also incorporate steel shims to expand the range of applicability of a given clamp size for use when the steel shape flange thickness is less than the clamp's specified range (see Figure 4.1a). In Tests 4-M24-2C-RH-LM-S and 6-M24-2C-RH-LC-S, 5 in. x 2 in. x 1/8 in. A36 steel shims are inserted between the thin steel flanges and clamp teeth. Figure 4.1b illustrates another shim application if the steel flange is thicker than the clamp's specified range. This type of use of shims is similar to that recommended by the clamp manufacturer, but this idea is not investigated in this research. Two reinforcement patterns are designed for the concrete specimens. Premature concrete failure modes are anticipated to be suppressed or restrained in the specimens designed with the heavy reinforcement pattern, and the desired limit state of these specimens is slip of the clamps. In contrast, premature concrete failure is expected to be the limit state of the specimen with less reinforcement. The reinforcement configuration is further discussed in Section 4.2.

Table 4.1 Pushout test matrix

Name	Test parameters									
	Bolt diameter		Number of channels		Reinforcement configuration		Loading		Shim	
	M24	M20	2	3	Light	Heavy	Monotonic	Cyclic	Yes	No
1-pretension test	✓	✓	N/A			✓	N/A			✓
2-M24-2C-RH-LM	✓		✓			✓	✓			✓
3-M24-2C-RL-LC	✓		✓		✓			✓		✓
4-M24-2C-RH-LM-S	✓		✓			✓	✓		✓	
5-M24-2C-RH-LC	✓		✓			✓		✓		✓
6-M24-2C-RH-LC-S	✓		✓			✓		✓	✓	
7-M24-3C-RH-LM	✓			✓		✓	✓			✓
8-M24-3C-RH-LC	✓			✓		✓		✓		✓
9-M20-2C-RH-LM		✓	✓			✓	✓			✓
10-M20-2C-RH-LC		✓	✓			✓		✓		✓

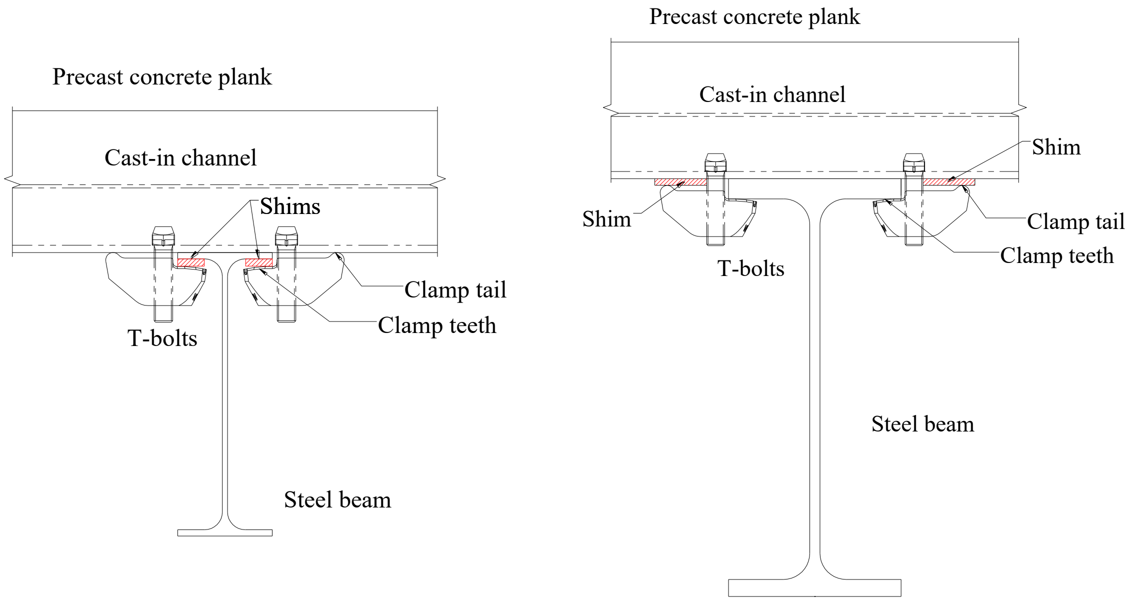
Precast concrete plank
Cast-in channel
Shims
Clamp tail
Clamp teeth
T-bolts
Steel beam
Precast concrete plank
Cast-in channel
Shim
Shim
Clamp tail
Clamp teeth
T-bolts
Steel beam

a) Thin steel flange b) Thick steel flange

Figure 4.1 Different use of shims

4.2 Test specimen design

Cast-in channels

Design guidelines for anchor channels are not provided in ACI 318-11 Appendix D, whereas Eurocode 2 (CEN 2009) has a specific document for the design of anchor channels embedded in concrete. All the limit states for anchor channels under tension and shear are summarized in Table 4.2. Some terminologies used in the Eurocode are modified so that they are specific to the current application and consistent with the nomenclatures adopted in ACI 318-11.

Table 4.2 Limit states for anchor channels

Loading	Failure modes			Channel	Most unfavorable anchor or bolt
Tension	Steel failure	Anchor			×
		Weld between anchor and channel			×
		Local deformation of channel lips		×	
		Bolt			×
		Flexural of channel		×	
	Pullout failure				×
	Concrete breakout				×
	Concrete splitting failure				×
	Side-face blowout				×
	Steel failure of anchor reinforcement				×
	Anchorage failure of anchor reinforcement				×
Shear	Steel failure	Shear force without lever arm	Bolt		×
			Local flexure of channel lips	×	
		Shear force with lever arm	Bolt		×
	Concrete pry-out failure				×
	Concrete edge failure				×
	Steel failure of anchor reinforcement				×
	Anchorage failure of anchor reinforcement				×

Although the channels and T-bolts are commercially available components, they are not designed to work together in the proposed configuration. Between the conventional applications and the current application, the load transfer is similar when the bolts are under shear perpendicular to the axis of the channel, but the mechanism is significantly different when the bolts are under tension.

As shown in Figure 4.2a, in the conventional application, when the bolt is subjected to tension, the load is transferred to the anchors, and a linear force distribution with the influence length l_i is assumed (CEN 2009). After the anchor forces are determined, the resistance of the channel anchors against all the failure modes in Table 4.2 can be checked. The same method could also be utilized to calculate the shear force acting on the anchors when the shear is perpendicular to the axis of the channel, but this approach is conservative and does not reflect the actual loading scenario where the shear loading is mainly directly transferred into concrete by bearing at the channel/concrete interface. When subjected to combined shear and tension loading, interaction equations are utilized to verify the strength of the bolts, channel lips, channel anchors and concrete.

In contrast, in the clamping system, when the bolt is pretensioned, the majority of the load is counteracted by the reactions at the clamp tail and the steel beam, rather than transferred to the anchors. Apparently, the linear distribution assumed in the Eurocode (see Figure 4.2a) is overly conservative when calculating the anchor forces. In addition, the resistance of the anchors could be enhanced by the reactions which do not exist in the conventional application. For example, as shown in Figure 4.2b, the formation of the concrete breakout cone of the center anchor is inhibited by the reaction at the edge of the steel flange. Hence, the required forces and available strengths of the anchors cannot be readily determined in the clamping system.

A preliminary finite element model, which is similar to that presented in Section 4.6, was utilized to estimate the forces the anchors would be subjected to during the pushout tests. In this model, nominal material properties were used. A frictional coefficient of 0.3 was assumed for all the contact surfaces. The pretension of the M24 bolts was approximately 46.1 kips (205 kN), which is the minimum bolt pretension for Group A M24 bolts in Table J3.1M in the AISC Specification (AISC 2016a). According to the FE analysis results, among all the anchors, the center anchor has the largest tensile force, which is 3.84 kips (17.1 kN), and the shear force acting on the anchors is minimal. The tensile capacity of the anchor is conservatively taken as 14.6 kips (65 kN) (Halfen 2013), if the beneficial effect of F_2 in Figure 4.2b in preventing the formation of the concrete failure cones is ignored. Therefore, the FE simulation results indicated that no anchor-related concrete failure modes would occur in the pushout tests.

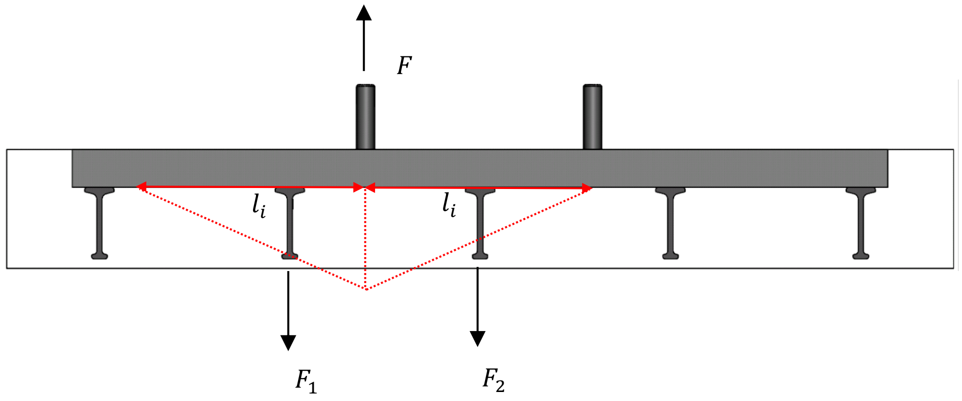

Note: The read lines indicate the linear force distribution assumed in Eurocode 2; F is the external force acting on the bolt; F_1 and F_2 are anchor forces.

a) Conventional configuration

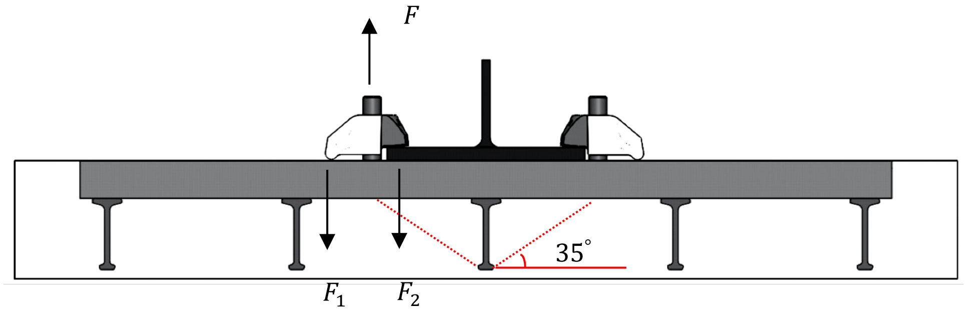

Elevation view

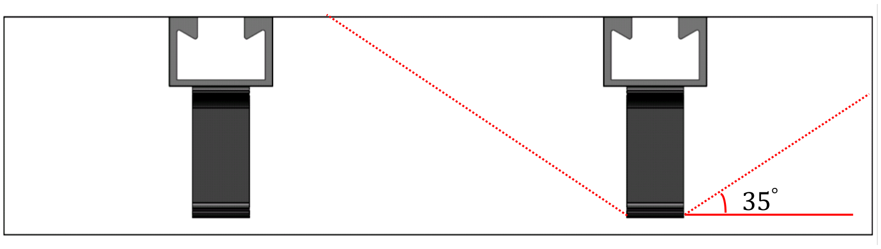

Side view

Note: The read lines denote potential concrete break-out cones; F is the external force acting on the bolt; F_1 and F_2 are forces transferred to the clamp tail and clamp teeth, respectively.

b) Current configuration

Figure 4.2 Tensile load transfer in different applications

The standard HTA-CE 72/48 channel configuration is slightly modified by shortening the channel anchors, which gives a concrete cover thickness of 1/2 in. above the top of the anchors. This concrete cover thickness is the same as that required for steel headed stud anchors in AISC 360-16 (2016). The shop drawing for the channel is given in Figure C.14 in Appendix C.

Precast concrete plank

The precast concrete specimens have the same width and thickness as the planks designed in the prototype structures in Chapter 3. When testing stud shear connectors, the length of the concrete slabs is a nontrivial parameter for two reasons: (1) the compressive stress due to shear connectors bearing against concrete is distributed over the length of the slabs; (2) a smaller length makes possible longitudinal splitting of the concrete slabs. These justifications may also hold for the clamp connectors. Considering the geometry of the test rig illustrated in Figure 4.16 in Section 4.5.1, the length of the plank specimens is taken as 4 ft. As shown in Figure 4.2b, the plank is sufficiently long so that the behavior of the clamp system is not affected by the boundaries of the plank in the pushout tests.

Reinforcement

Two reinforcement patterns for the precast concrete planks were designed for the pushout test specimens, as shown in Figure 4.3 and specimen drawings in Appendix C.1.2 in Appendix C. The heavy reinforcement pattern includes supplementary reinforcement that was placed to bridge all potential concrete failure planes to restrain the opening and propagation of the cracks. The red lines in Figure 4.4 indicate possible concrete failure cones under different forces. Because this reinforcement was not designed to take the entire load, they were considered as supplementary reinforcement, not anchor reinforcement. Considering the splitting force, surface reinforcement was also added to resist the force arising from the strut-and-tie model (CEN 2009). Even though the preliminary FE analysis results showed that the limit states of the pushout specimens would not be anchor failure modes, the heavy reinforcement configuration was conservatively employed for most of the concrete planks to ensure that the governing limit state would be slip of the clamps, rather than concrete failure.

The light reinforcement pattern, which only retains the bars designed for gravity loading and eliminates some of the shear reinforcement, was used for specimens where premature concrete failure was anticipated to explore this limit state. The spacing of the channel anchors is 9.65 in. (245 mm), which is equal to the distance between the transverse reinforcement in the light reinforcement pattern. In the heavy reinforcement pattern, the reinforcement spacing decreased close to the clamping connectors to provide extra protection against concrete breakout.

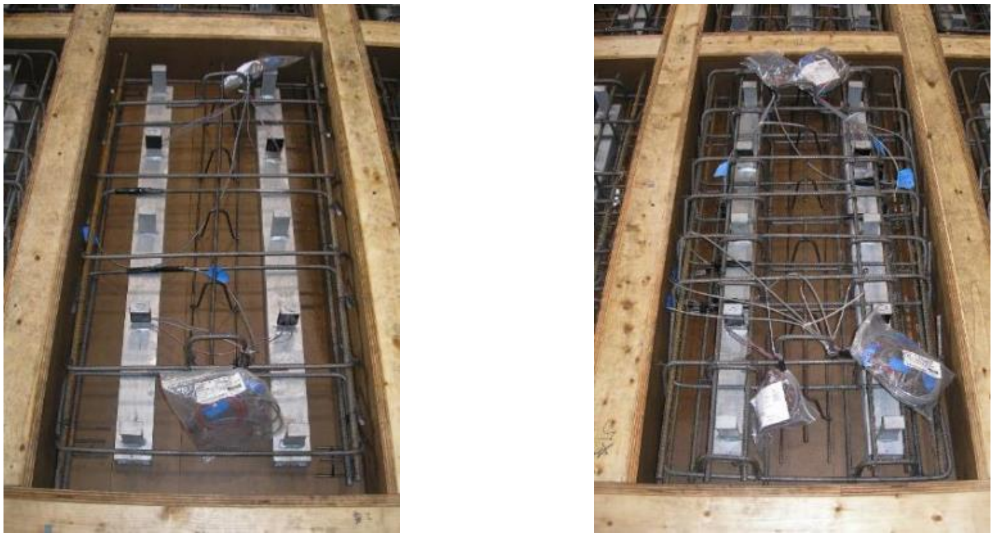
a) Light reinforcement pattern b) Heavy reinforcement pattern

Figure 4.3 Different reinforcement patterns for pushout test specimens

All the reinforcement conformed to the detailing requirements in ACI 318-11, as drawn in Figure C.13 in Appendix C. The hooks for the transverse bars were regarded as standard hooks, and the bend diameter and the end extension were $6D_b$ and $12D_b$, respectively. The transverse bars were rotated to fit into the thickness of the planks. The waveform bars were considered as stirrups, and the bend diameter and the end extension were $4D_b$ and $6D_b$, respectively. ACI Section 12.13.2.1 stipulates that the ends of waveform bars can be anchored using a standard hook around longitudinal reinforcement. However, straight anchorage is not allowed because it is difficult to hold the stirrup in the right position when pouring concrete and the development of the stirrup is ineffective. A706 reinforcement with a minimum yield stress of 60,000 psi was selected. No.4 bars were used as longitudinal reinforcement, and No.3 bars were chosen as the transverse and waveform reinforcement. Reinforcement drawings are provided in Appendix C.1.2.

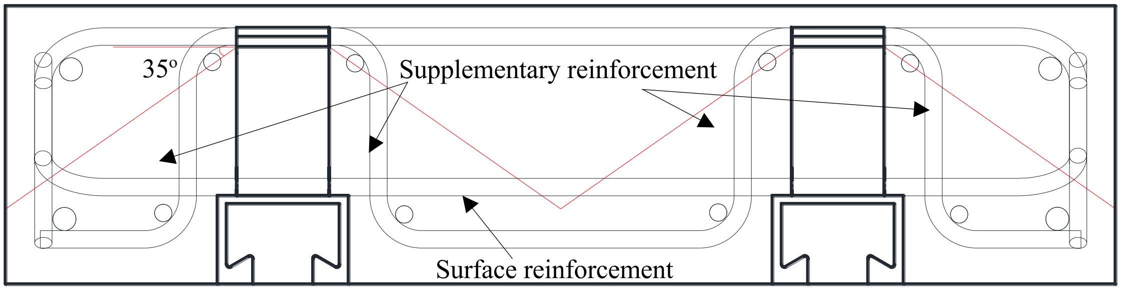
35°
Supplementary reinforcement
Surface reinforcement

a) Anchor tensile force

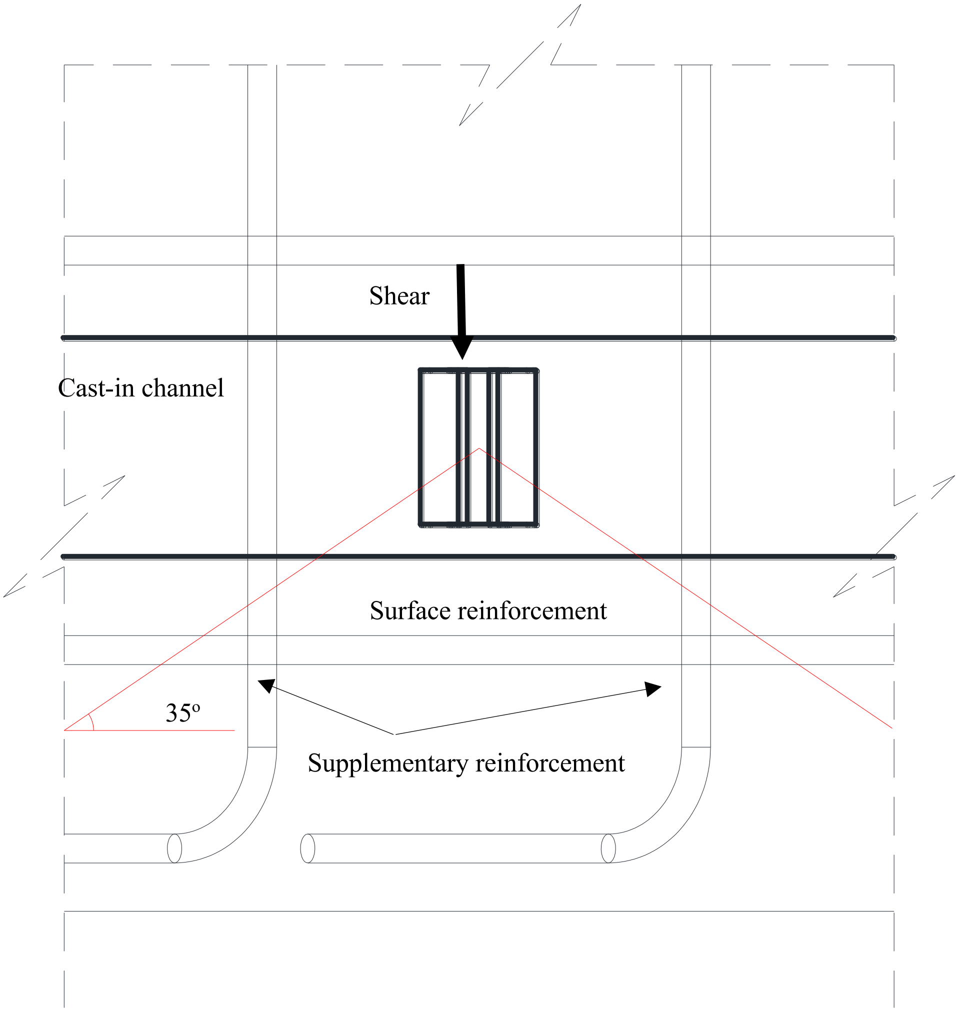
Shear
Cast-in channel
Surface reinforcement
35°
Supplementary reinforcement

b) Anchor shear force

Figure 4.4 Supplementary reinforcement and surface reinforcement arrangement

Steel beam

Since the shear at the steel-concrete interface is anticipated to flow mainly through the beam flange, WT sections are chosen over W sections. WT5x30 and WT4x15.5 are chosen for two reasons. First, the M24 clamps are designed for sections with flange thicknesses ranging from 1/2 in. to 11/16 in., whereas the M20 clamps are designed for flanges with thicknesses from 3/8 in. to 7/16 in. The selected beams fit within the range of use of the two types of clamps, with the flanges of the WT5×30 and WT4×15.5 sections being 0.68 in. and 0.435 in. thick, respectively. Second, clamp slip is the desired limit state; steel sections are sized to avoid other limit states, such as yielding, buckling, and local buckling of the steel sections. In the pushout tests, WT4x15.5 were also used with M24 clamps in two specimens, with 5 in. x 2 in. x 1/8 in. A36 steel shims inserted between the clamp teeth and the WT flange.

4.3 Material properties

This section covers the ancillary testing for both pretension tests and pushout tests. In these tests, all materials of the same size were from the same heat or batch. Mill certifications for the steel components are attached in Appendix D, including steel specimens, cast-in channels, T-bolts, reinforcement, and clamps. Material testing is conducted to measure and compare the material properties of the specimen components to those documented in the mill certifications.

Round coupon specimens were machined from the T-bolts and tested to obtain the stress-strain curve of the bolt material, which is crucial for deciding the nut rotation for pretensioning and tracking the bolt pretension variation during pushout tests and beam tests based on the strain gage measurements. Dogbone-shaped coupons were machined for the other steel parts. ASTM A370-14 and ASTM E8/E8M-13a dictate the dimensions of these coupons. All the tested reinforcement specimens were bars with full sections. The compressive strength and splitting tensile strength of cylindrical concrete specimens were determined according to ASTM C496/C496M-11 and ASTM C39/C39M-14a. Testing details and results are provided in the following sections.

Steel properties

Two coupons were machined for the bolts from each diameter. Although the bolt coupons all had the same diameter for the reduced section, the other dimensions were slightly different between the two diameters because the shank lengths were 6 in. and 4 in. for the M24 and M20 bolts, respectively. The dimensions had to be adjusted to ensure that the grip length was adequate, and the minimum length and radius required by the ASTM standard were satisfied. Among the six coupons cut for each WT section, three were from the flange, and the other three were from the web. These coupons were away from the edges and flange-to-web joint of the section to minimize the influence of residual stresses. Similarly, coupons were cut from the flange and web of the channels. Dimensions of all the coupons are depicted in Figure 4.5. Three bars were tested for each type of reinforcement.

According to ASTM E8/E8M-13a, the gage length for the bolt coupons should be 2 in.; however, the limited height between the loading heads of the testing machine prevented a 2 in. extensometer from being installed. Hence, a 1 in. extensometer was used to measure the strain of the coupons. The gage length for the cast-in channel coupons was 2 in., while all the other dogbone-shaped specimens and reinforcement used a gage length of 8 in.

The loading process was based on the Technical Memorandum of Structural Stability Research Council (SSRC), which summarizes the methods for determining static yield stress (Ziemian 2010). In this process, several pauses were needed to establish the yield stress at zero strain rate, i.e., the static yield stress. For the coupons with a gage length of 2 in., the loading rate started at 0.025 in. /min, and increased to 0.125 in. /min after the first pause. These rates were adjusted to 0.10 in. /min and 0.50 in. /min for the specimens with a gage length of 8 in.

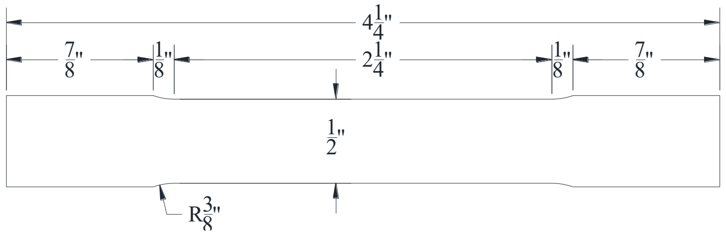

M20 bolt coupon

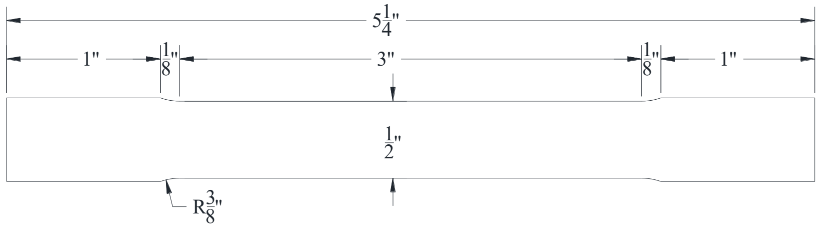

M24 bolt coupon

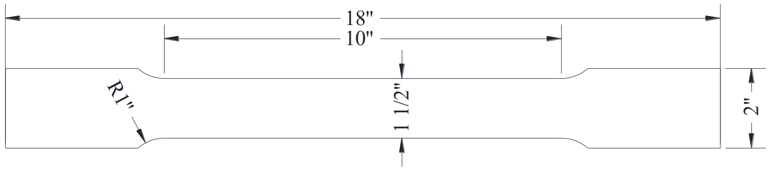

WT section coupon

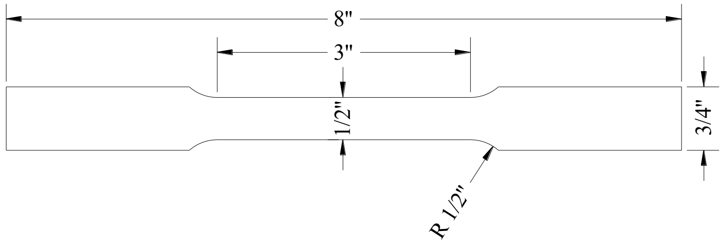

Cast-in channel coupon

Figure 4.5 Pushout test tensile coupon dimensions (units: inches)

For the coupons exhibiting a plateau region in the stress-strain curve, the material properties reported are: elastic modulus E_s, strain hardening modulus E_{sh}, static yield stress F_{ys}, dynamic yield stress F_{yd}, ultimate tensile stress F_u, and strain at the initiation of strain hardening ε_{sh}. The static yield stress is taken as the average of the three low values at the pauses. When a plateau region is not seen in the stress-strain curve, the material properties documented include: elastic modulus E_s, static yield stress F_{ys}, dynamic yield stress F_{yd}, and ultimate tensile stress F_u. A line is plotted through the low points of the pauses, and the static yield stress is determined by the 0.2% offset intercept. In Table 4.3, because the testing was paused at large strains for the first M24 bolt coupon, its dynamic yield stress was lower than the static yield stress. Hence, the pauses were moved earlier for the other coupons to avoid this issue. All the bolt coupons failed outside of the 1 in. gage length, but within the 2 in. gage length. Fracture of all the other coupons occurred within the gage length.

Table 4.3 Pushout test steel coupon testing results

Type		E_s (ksi)	E_{sh} (ksi)	F_{ys} (ksi)	F_{yd} (ksi)	F_u (ksi)	ε_{sh} (με)
WT5x30	Flange 1	30800	330	51.0	55.0	73.4	21900
	Flange 2	30700	360	51.8	55.3	-	20800
	Flange 3	30200	350	50.8	54.6	-	21300
	Web 1	29800	320	54.3	58.1	74.5	26100
	Web 2	29700	300	54.4	58.7	74.3	29700
	Web 3	29500	300	54.2	58.3	74.1	26700
WT4x15.5	Flange 1	30100	320	50.4	54.3	69.1	25400
	Flange 2	30200	290	50.7	54.4	69.4	25100
	Flange 3	30000	280	50.7	54.2	69.2	27300
	Web 1	28500	210	56.0	59.6	69.5	30000
	Web 2	29100	220	57.0	60.5	70.7	30500
	Web 3	28800	210	56.1	59.3	69.8	30000
Cast-in channel	Flange 1	27900	130	63.5	67.5	72.3	26000
	Flange 2	27400	120	65.1	68.3	73.5	24700
	Flange 3	28700	80	62.5	65.9	70.7	29500
	Web 1	26500	100	56.7	60.2	65.0	37000
	Web 2	28500	40	58.5	63.2	67.4	39000
	Web 3	28500	80	58.5	62.6	67.5	34000
No.4 longitudinal reinforcement	1	24100	600	62.0	65.9	89.8	15200
	2	27200	600	63.9	68.0	91.7	15300
	3	25100	510	62.8	66.9	90.4	15500
No.3 longitudinal reinforcement	1	29000	520	61.2	65.0	91.8	14500
	2	28800	510	61.3	64.2	90.8	14400
	3	27400	580	61.2	65.2	91.7	15100
No.3 transverse reinforcement	1	29500	N/A	67.5	73.0	102.0	N/A
	2	29200	N/A	65.2	70.5	99.7	N/A
	3	26900	N/A	64.7	70.4	101.7	N/A
M24 bolt	1	31800	N/A	122.4	121.6	138.2	N/A
	2	30200	N/A	110.1	117.7	134.6	N/A
M20 bolt	1	29800	N/A	107.9	116.6	133.0	N/A
	2	31900	N/A	108.9	117.1	132.5	N/A

Bolt tension and shear testing

In addition to tensile coupon testing, tension testing was conducted on the T-bolts in accordance with ASTM F606/F606M-14a using the testing fixture at the University of Cincinnati shown in Figure 4.6. Details regarding this test rig can be found in Moore et al. (2008). The relationship between the bolt axial load and axial elongation is shown in Figure 4.7. The fractured specimens are shown in Figure 4.8. Different failure modes were found for the M24 and M20 bolts. The M24 bolts fractured at the bolt heads, whereas the M20 bolts fractured at the bolt shanks. The average ultimate tensile strength was 68.8 kips and 49.7 kips for the M24 and M20 bolts, respectively. Using Equation (4.1) given in Kulak et al. (1987), the stress area of the M24 and M20 bolts is 0.55 in^2 and 0.38 in^2, respectively. The ultimate tensile strength of the bolt materials is thus determined to be 131 ksi and more than 125 ksi for the M20 bolt and M24 bolts, respectively.

$$stress\ area = 0.785\,(D - \frac{0.9743}{n})^2 \tag{4.1}$$

Where

D = nominal bolt diameter (in.)

n = number of threads per inch

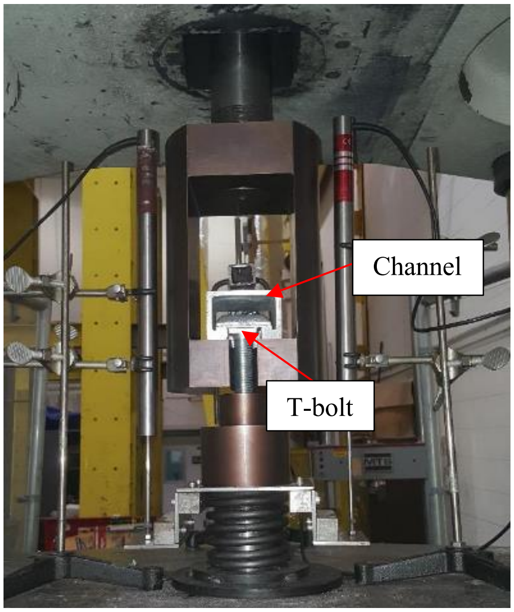

Figure 4.6 T-bolt tensile testing fixture

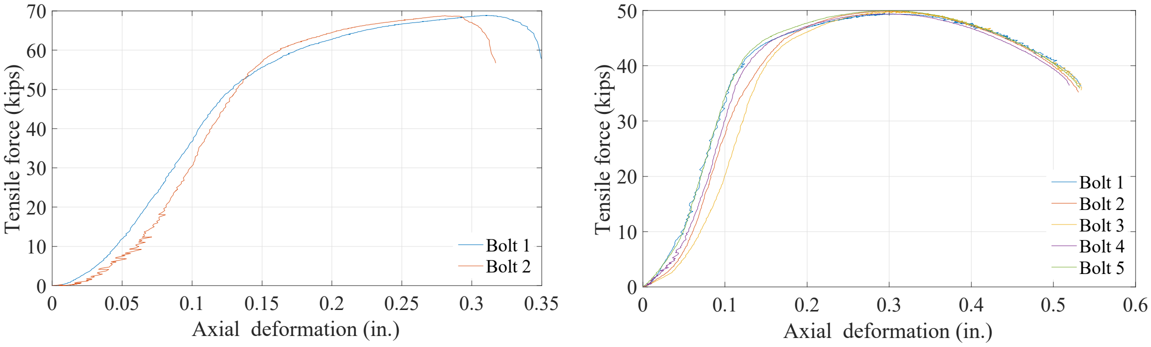

a) M24 bolts b) M20 bolts

Figure 4.7 Tensile load versus axial elongation

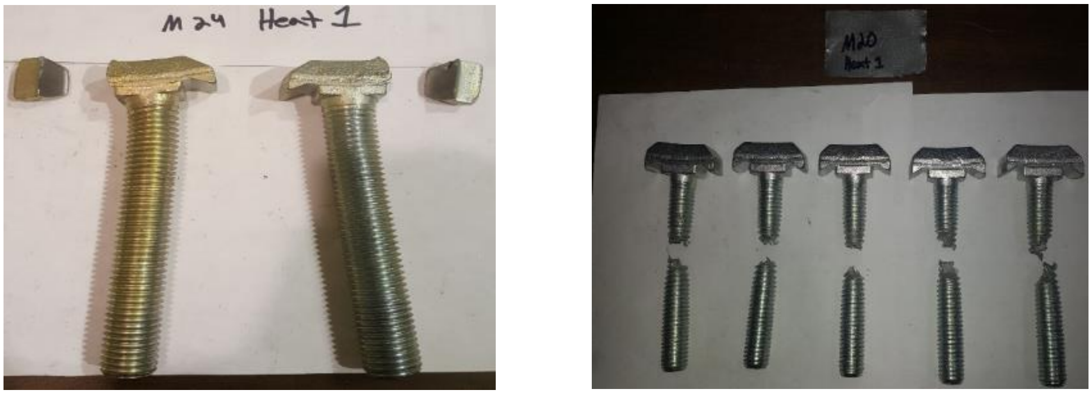

a) M24 bolts b) M20 bolts

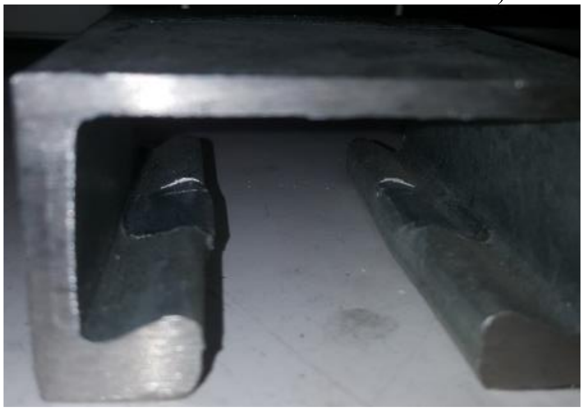

c) Impression on the channel lips

Figure 4.8 Failed M24 and M20 bolts under tension

Shear testing was also performed on the T-bolts in accordance with ASTM F606/F606M-14a with the testing fixture at the University of Cincinnati shown in Figure 4.9. Details regarding this test rig can be found in Moore et al. (2008). The relationship between the bolt shear force and shear deformation is plotted in Figure 4.10. The average peak shear strength was 47.7 kips and 32.1 kips for the M24 and M20 bolts, respectively. Based on the stress area of the bolts and a shear/tension ratio of 0.625 (AISC 2016a), the ultimate tensile strength is determined to be 139.5 ksi and 135.2 ksi for the M24 and M20 bolts, respectively. The fractured specimens are shown in Figure 4.11.

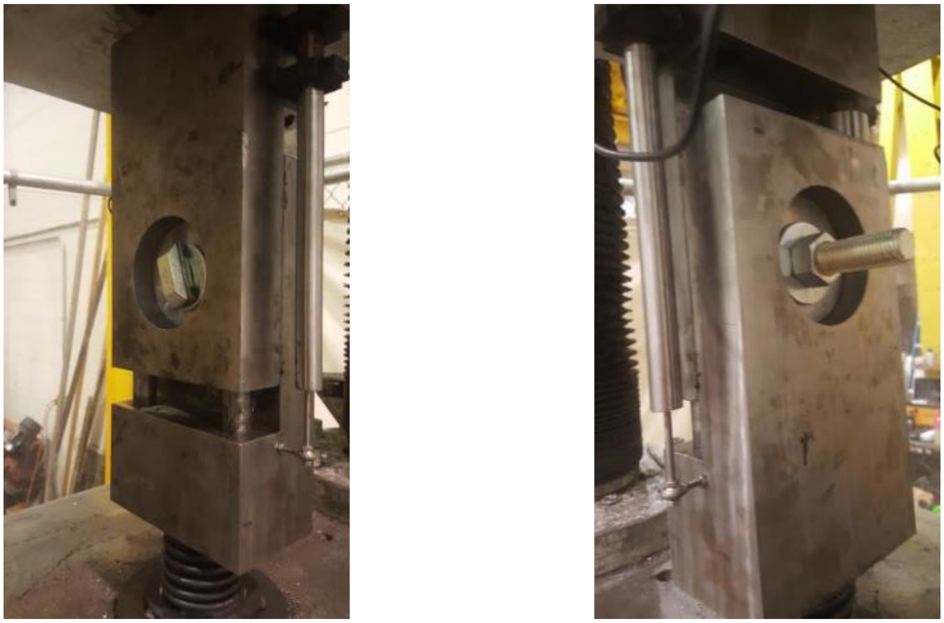

Figure 4.9 T-bolt shear testing fixture

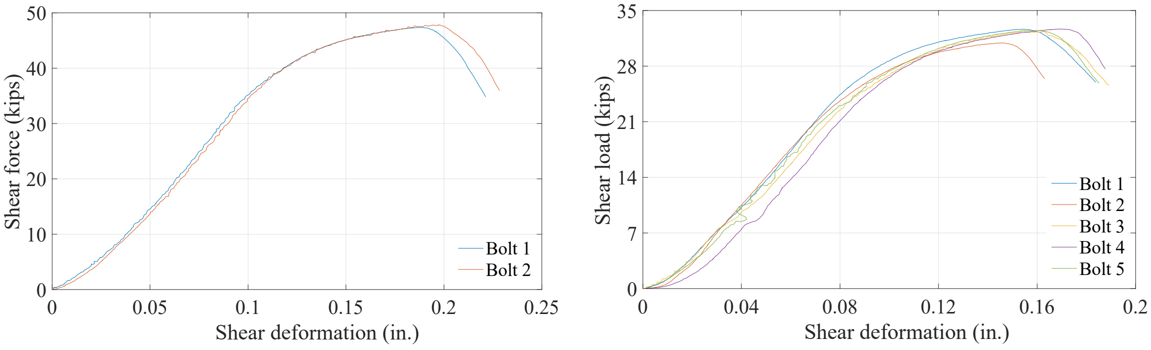

a) M24 bolts b) M20 bolts

Figure 4.10 Shear load versus shear deformation

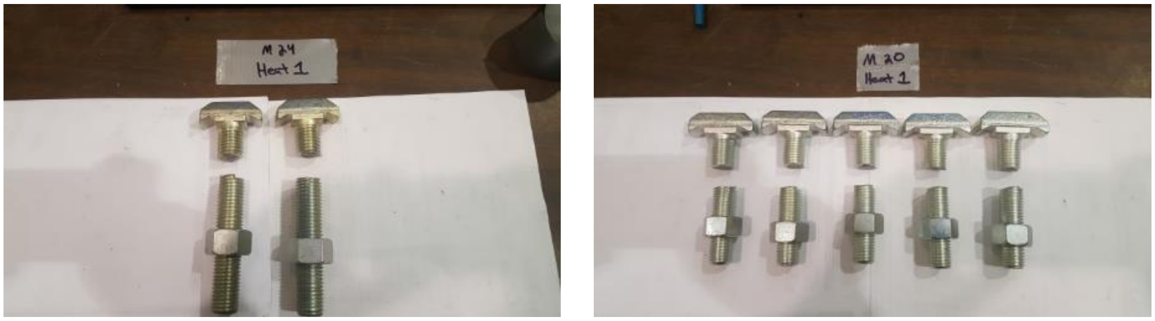

a) M24 bolts b) M20 bolts

Figure 4.11 Failed M24 and M20 bolts under shear

It can be seen that the ultimate strength, calculated from the direct tension and shear test results, is close to that obtained from tensile bolt coupon testing.

Concrete properties

In the proposed deconstructable composite floor system, precast concrete planks are favorable over cast-in-place slabs to achieve maximum efficiency and facilitate reuse. However, in this research, due to cost, the concrete planks utilized in the pushout tests and beam tests were all cast in place. The pushout specimens were cast with single-use plywood formwork, while the formwork for the beam specimens was reused twice. The performance of the pushout specimens did not appear to be affected by the quality of the planks. In the beam tests, some local behavior of the specimens might have been affected due to the construction tolerances of the concrete specimens, but the overall performance of the beams was not influenced. This will be further discussed in Chapter 5.

A "green" concrete mix was designed to decrease the embodied energy of concrete. In the mix, a certain amount of cement was substituted with fly ash or slag to reduce the environmental impacts as well as maintain high performance. Type III cement, an accelerating admixture, was added to the mix to help concrete gain high early strength since fly ash or slag slows strength gain. Nonetheless, the concrete supplier preferred to provide one of its own pre-designed standard mixes. Considering material strength is more important than sustainability in terms of structural testing, a standard mix provided by the concrete supplier was used.

The initially measured slump in the concrete plant was 3.0 in.; however, the desired slump was from 6.0 in. to 8.0 in. Hence, 6.0 gallons of water was added before the pour to adjust slump and increase workability, which increased the water/cement ratio and decreased the concrete strength.

Thirty-three cylinders were divided into three groups, with each group consisting of eleven 6 in. by 12 in. cylinders. Along with concrete cylinder group A, Specimens 1 through 3 were first poured and vibrated. Specimens 4 through 6 and concrete cylinder group B were then poured and vibrated. Three slump tests were conducted consecutively, and the measured slumps were 6.25 in., 5.25 in., and 4.50 in., respectively. Cylinder group C was cast between Specimen 8 and Specimen 9. These three groups of cylinders represent concrete at different stages (i.e., beginning, middle, and end) during the pour.

Concrete specimens were left to air-dry for a couple of hours until they started to harden. After about 8 hours, specimens were sprayed and covered with wet burlaps. A plastic sheet was put over the burlaps to prevent loss of moisture. Forms for the specimens and cylinders were stripped on the next day to simulate the scenario that forms are usually stripped within 24 hours to facilitate reuse in the precast concrete industry. Approximately half of the cylinders in each group were placed close to the specimens and dry cured in the same manner as the specimens, while the other cylinders were put into a water bath to mimic moisture-cured conditions. All specimens were cured for 28 days. Table 4.4 provides the curing condition, testing date and purpose of the testing for the cylinders.

Table 4.4 Pushout test concrete cylinder testing results (units: psi)

Curing condition	Test type	Testing date	Cylinder A	Cylinder B	Cylinder C	Average
Moist-cured	Compressive strength (psi)	3 days	2,802	3,117	2,796	2,905
		7 days	3,835	3,810	3,393	3,679
		21 days	4,450	4,309	4,200	4,320
		28 days	4,079	4,373	4,158	4,203
	Splitting tensile strength (psi)	28 days	373	356	419	383
Same as the specimen	Compressive strength (psi)	3 days	2,832	3,148	2,669	2,883
		7 days	3,715	3,661	3,252	3,542
		28 days	4,651	4,659	4,122	4,477
		Test day for specimens 1-3 (approximately 153 days)	6,319	6,232	6,543	6,365
		Test day for specimens 4-6 (approximately 197 days)	6,587	6,347	6,403	6,446
		Test day for specimens 7-10 (approximately 300 days)	5,933	5,883	5,833	5,883

4.4 **Pretension tests**

Bolts can be pretensioned by either the turn-of-nut method or using a calibrated wrench. The turn-of-nut method is based on displacement control; therefore, the pretension depends on the material properties of the bolts. For regular bolts, the nut rotation needed to develop the minimum bolt pretension from a snug-tight position can be found in Table 8.2 in the RCSC Specification (RCSC 2014), provided the joint is properly compacted and the bolt head (or nut) is held when the nut (or bolt head) is turned. The calibrated wrench method is a torque-controlled method which is affected by various factors, such as the finish and tolerance on the bolt and nut threads, the uniformity, degree and condition of lubrication, and the friction between the nut and washer and between the nut and bolt threads. Equations and tables that correlate torque to tension cannot be used without verification. Calibration should be performed at least daily, and each time when the joint assembly is changed, the surface conditions of the bolts, nuts, and washers are different or major changes are made for the wrench (RCSC 2014). The turn-of-nut method is preferred in the field due to its ease and consistency, and thus selected as the method for pretensioning the T-bolts.

Unlike regular bolts, the T-bolts are inserted in cast-in channels which can deform when the bolts are pretensioned. As a result, more turns of the nut than in standard bolted connections are needed to enable the bolts to deform into the inelastic range and meet the minimum pretension requirements in the AISC Specifications (2016a). Three M24 and M20 bolts were tested under torqued tension until fracture to develop the relationship between the number of turns of the nut and the bolt axial force.

4.4.1 Test setup and instrumentation

A 4 ft. by 2 ft. by 6 in. heavily reinforced concrete slab was placed on a flat surface with the channels facing up, and the steel beam was then attached to the slab with the clamps. WT5x30 and WT4x15.5 were chosen for testing M24 and M20 bolts, respectively.

While torque was applied to a bolt, the other three bolts were at snug-tight positions to ensure the beam was stationary, as shown in Figure 4.12. No additional restraint is needed, as the system is self-reacting when the nut is being turned. Before testing, the bolt and nut threads and the washers were all lubricated, and the required nut rotation is not affected by the lubrication condition in the turn-of-nut method, which is a strain-controlled method. The tested bolt was first turned to a hand-tight position, and then to a snug-tight position using an 18 in. long spud wrench. The nut and clamp were marked to facilitate recording their relative rotation when a hydraulic wrench was used to rotate the nut from the snug-tight position until fracture. The nut was turned at an increment about 15 degrees, and the total rotation was recorded at each turn. When testing a new bolt, undeformed cast-in channel portions and intact steel flange segments were required, since the channel lips were deformed, and impressions were generated on the steel flange during the test, as shown in Figure 4.14 in Section 4.4.2.

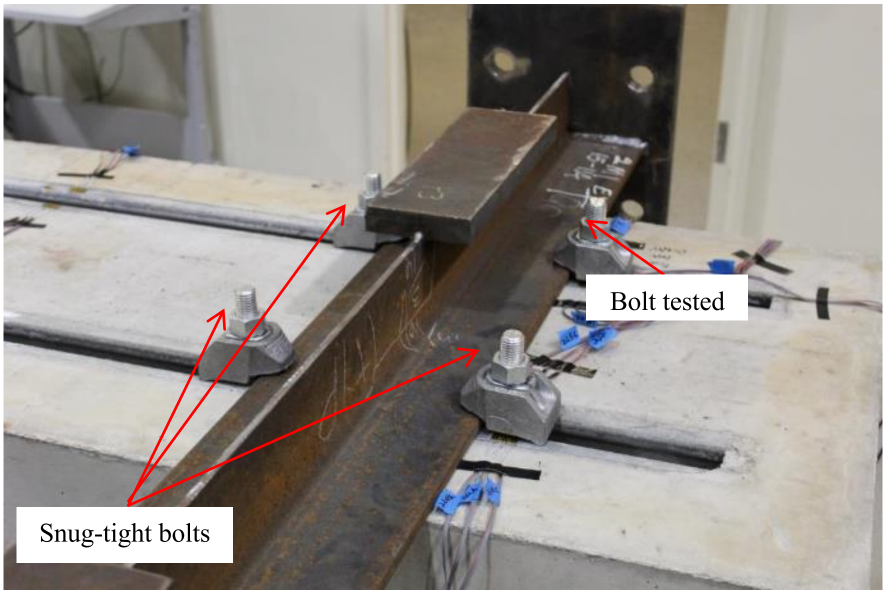

Figure 4.12 Bolt pretension test setup

The configuration of the clamping connections enables strain gages to be attached to the bolt shanks after the threads are removed locally. The strain gage locations are shown in Figure 4.13. Channel lips were instrumented with rosette strain gages to study their behavior.

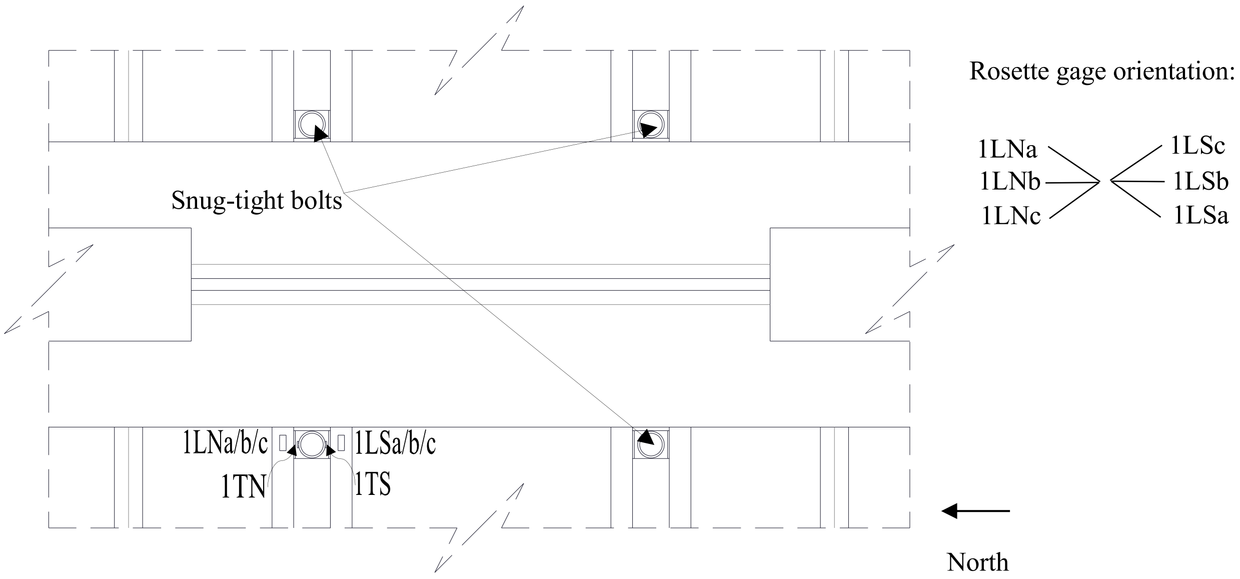
Rosette gage orientation:
1LNa
1LNb
1LNc
1LSc
1LSb
1LSa
Snug-tight bolts
1LNa/b/c
1LSa/b/c
1TN
1TS
North

a) Plan view

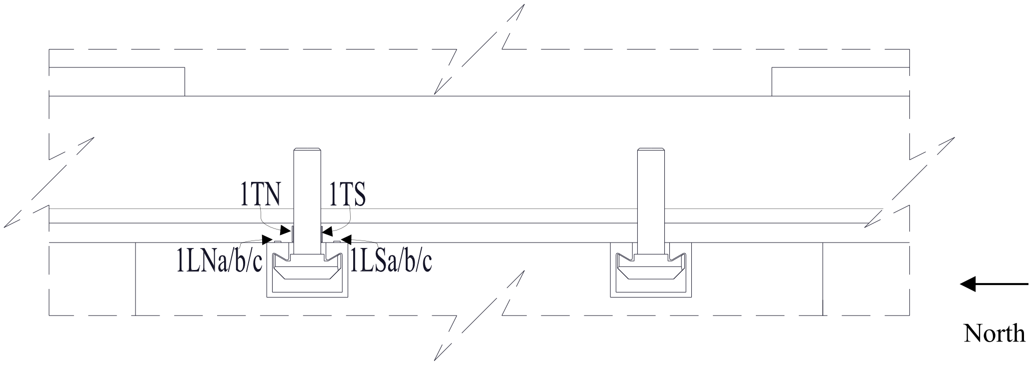
1TN
1TS
1LNa/b/c
1LSa/b/c
North

b) Side view

Note: 1TN and 1TS are uniaxial strain gages attached on the bolt shank; 1LNa/b/c and 1LSa/b/c are rosette strain gages attached on the channel lips.

Figure 4.13 Strain gage layout in bolt pretension tests

4.4.2 Specimen performance

M24 bolts

After some rotations, minor concrete spalling was observed due to the deformed channel lips bearing against the surrounding concrete. When the clamping connections were disassembled after the tests, plastic deformation of the lips, as well as impressions on the beam flanges under the clamp teeth, were found. The failure modes, nonetheless, were different for the three bolts. Fracture occurred at the heads of the first bolt, with the north head fracturing at 4.29 turns and the south head fracturing at 5.83 turns. Twist of the shank was insignificant during the test. For Bolts 2 and 3, the shanks were twisted off at 5.44 and 4.79 turns respectively, and 90° twists of the shanks were observed when the fracture was approached. Cracking at the bolt head was also detected for the second bolt after the test, as seen in Figure 4.14a.

M20 bolts

The channel lip deformation was imperceptible because the pretension force of the M20 bolts was much less than that generated in the M24 bolts. All three bolts fractured due to twisting of the shanks under the applied torque, as shown in Figure 4.14b. Bolts 1 and 2 both fractured at 5.16 turns, while Bolt 3 fractured at 5.33 turns.

The necking and fracture of the unthreaded portion of the bolts indicate a torqued tension failure mode. Since the reduced sections are prone to fracture prematurely, removing threads may have altered the ultimate failure modes of the bolt specimens, and the total rotations prior to fracture could also be underestimated for the bolts.

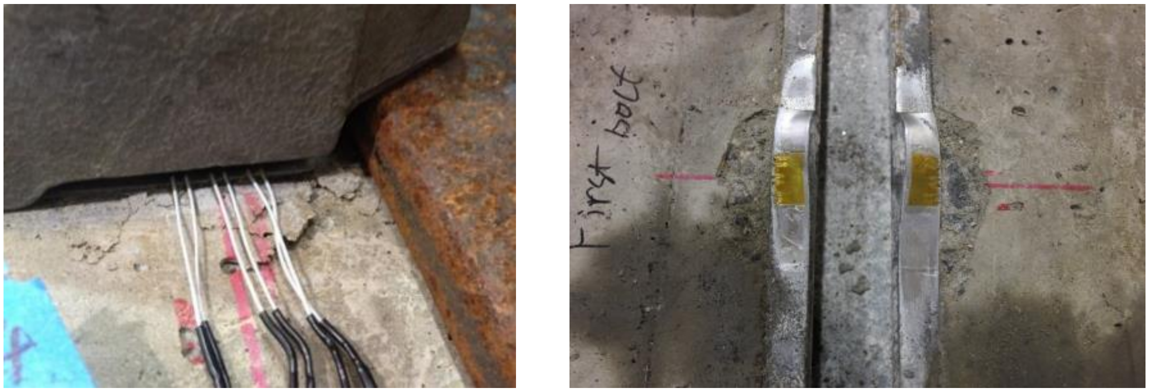

(1) During testing (2) After testing

Concrete spalling and channel lip deformation

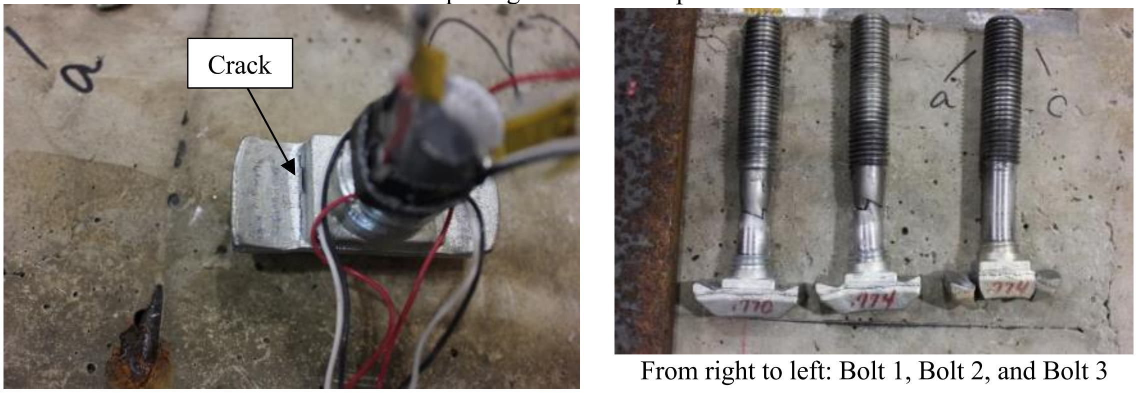

From right to left: Bolt 1, Bolt 2, and Bolt 3

(3) Cracking in the bolt head (4) Fracture of bolts

a) M24 bolts

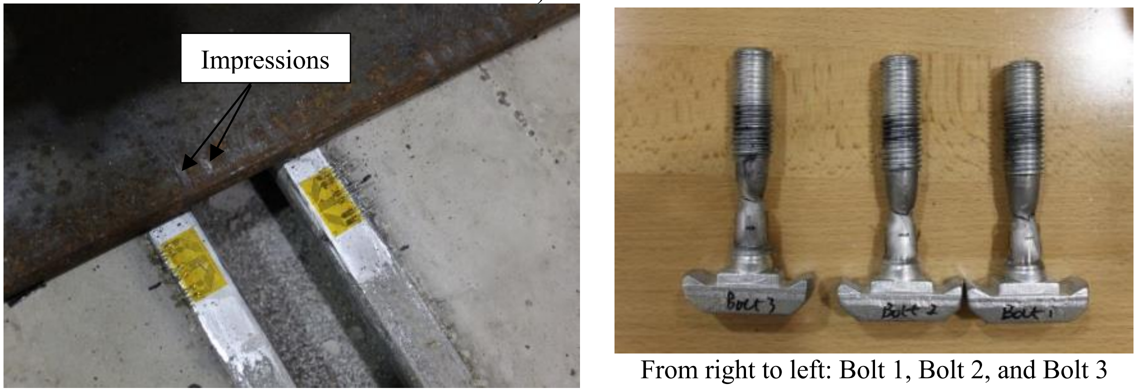

From right to left: Bolt 1, Bolt 2, and Bolt 3

(1) Channel lip deformation (2) Fracture of bolts

b) M20 bolts

Figure 4.14 Photographs of bolt pretension tests

4.4.3 Behavior of bolts and channel lips

The uniaxial strain gage readings in the pretension tests are plotted in Figure E.1 in Appendix E. After each turn, the readings dropped and then stabilized because the test was paused to record the nut rotation and the general behavior of the specimens, and the bolt pretension relaxed. During the tests, numerous gages debonded at large strains as a result of combined axial and torsional deformation of the bolt shanks.

A number of mechanical models have been developed that specify how steel behaves under cyclic loading, ranging from simple ones, such as the elastic-perfectly-plastic model and Prager model (Prager 1949), to complex ones, such as Shen steel model (Shen et al. 1995) and Chaboche model (Chaboche et al. 1986). Most models use the Von Mises yield function to determine the yield condition and the associated flow rule to prescribe the direction of the plastic flow, but they differ in terms of strain hardening rules that stipulate the post-yielding material behavior.

Since bolts are not supposed to be the main energy dissipating components in a structural system, the cyclic behavior of the bolt material under shear or tension has not been studied by researchers. In the material property testing, since the bolt coupons were not loaded in compression, the test data is insufficient to calibrate the isotropic hardening rule. Therefore, the Chaboche model without isotropic hardening, which is incorporated in ABAQUS (2011), is employed to calculate the stress variation based on the strain history. This model is believed to be capable of interpreting the bolt behavior, because the axial stress in the bolt cannot be compressive no matter how the strain varies in the pretension tests and pushout tests, and material yielding in the compressive direction is not of a concern. Appendix F contains the details regarding how to implement the material model in ABAQUS to track the bolt axial stress variation under torqued tension. It should be pointed out that once the bolt material is yielded, the axial stress or force could be underestimated or overestimated by the current model that neglects the shear stress due to torsion and shear.

In Figure 4.15, the bolt tension variation, which is calculated using the average axial strain measurement, is depicted until strain gage debonding happens because the actual behavior of the bolt cannot be captured thereafter, and the recorded data is meaningless. The loading and unloading behavior of the bolt material during the tests is plotted in Appendix F.

The plots in Figure 4.15 show that the bolt tension increase becomes less for the same amount of nut rotation, indicating that the bolts have yielded, and any variation in the strain or elongation in the bolts leads to a small change in the pretension force. Two turns and 1.5 turns are selected for pretensioning the M24 and M20 bolts, respectively. After these rotations, the tension of the M24 bolts, calculated by multiplying the stress converted from the measured strain by the area of the reduced section, is 59.9 kips, 56.7 kips, and 57.3 kips, respectively, and the tension of the M20 bolts is 41.7 kips, 42.2 kips, and 41.6 kips, respectively. The tension in both bolts meets the minimum pretension requirements, which are 46.1 kips (205 kN) and 31.9 kips (142 kN) for Group A M24 and M20 bolts, respectively, in Table J3.1M in the AISC Specification (AISC 2016a). The ratios of the mean measured bolt tension to the minimum bolt pretension are 1.26 and 1.31 for the M24 and M20 bolts, respectively. For both diameters, the number of turns of the nut required for twist-off in the shank or fracture at the bolt head is at least 2 times the recommended turns of the nut for establishing pretension.

Initially, three full turns was utilized for the M24 bolts in Tests 2-M24-2C-RH-LM and 4-M24-2C-RH-LM-S. However, the bolt head of one of the four bolts fractured during Test 4. Subsequently, it was decided that two full turns be used for the remaining M24 tests. Table 4.5 in Section 4.5.4.1 indicates that three full turns does not yield higher pretension force than two full turns, which is demonstrated by the negligible difference of the slip load and the peak strength per clamp between Test 2-M24-2C-RH-LM and Test 7-M24-3C-RH-LM.

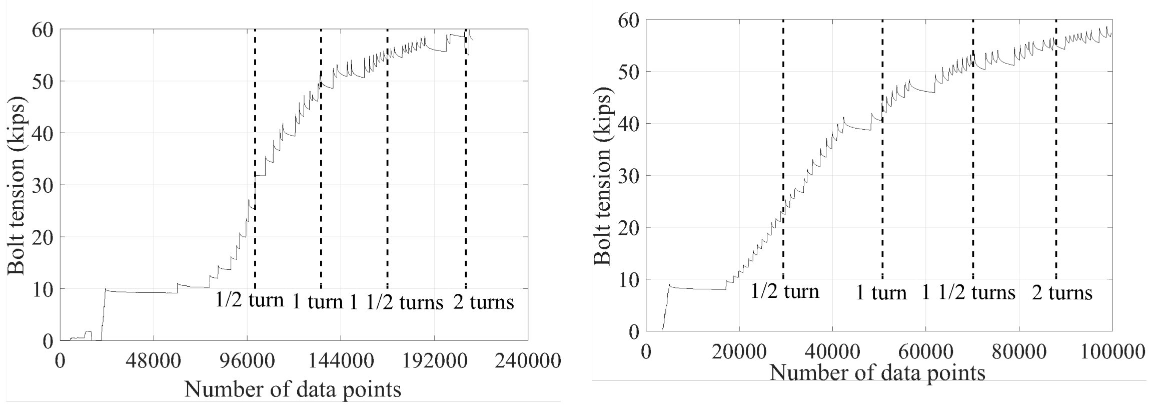

M24 bolt 1 M24 bolt 2

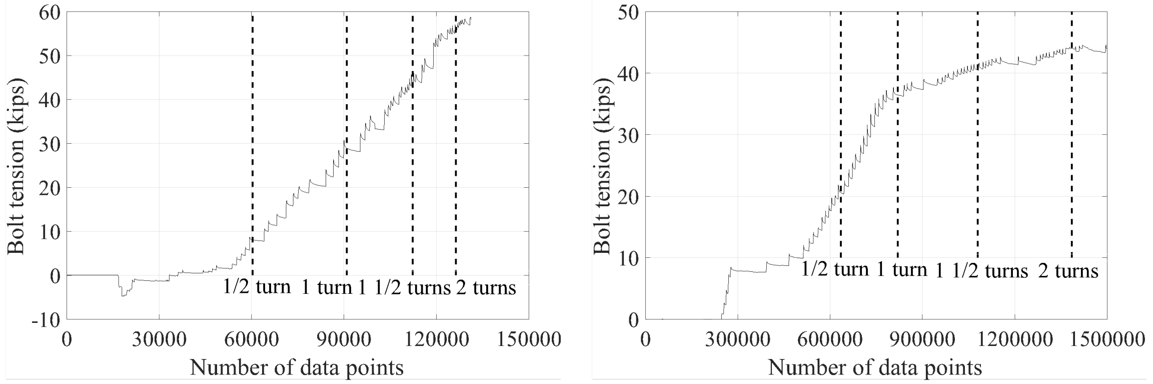

M24 bolt 3 M20 bolt 1

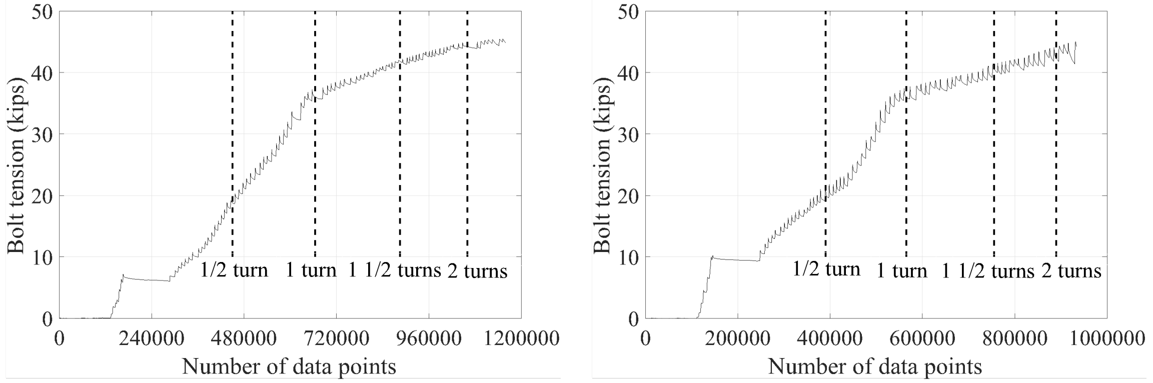

M20 bolt 2 M20 bolt 3

Figure 4.15 Bolt tension variation in pretension tests

4.5 Pushout tests

The strength of steel headed stud anchors in both solid slabs and composite slabs has been well studied and established in the relevant design provisions. Shear connectors in composite beams should be strong to transfer the shear force between concrete slabs and steel beams; otherwise, the two materials would behave individually, and no composite action exists. The ductility requirements on shear connectors are as important as the strength requirements, and slip capacity checks are now required by the AISC Specification (AISC 2016a). In composite beams with a low amount of composite action, shear connectors undergo large shear deformation as well as some bending and axial deformation, resulting in possible fracture in the connector shanks and loss of load-carrying capacity. Adequate ductility ensures that the shear force can redistribute from the weaker connectors to the stronger connectors at large slips, and the composite beams retain their flexural strengths at large deflections. In addition, shear connectors are responsible for transferring in-plane inertia forces in composite diaphragms to lateral force-resisting systems under earthquakes. When shear connectors are the governing components, their strength and ductility under cyclic loading determine the behavior of the diaphragm during earthquakes. Therefore, the strength and ductility of shear connectors should be treated equally.

4.5.1 Test setup

Numerous pushout test setups have been developed in the past to study the behavior of steel headed stud anchors, see Gattesco et al. (1996), Anderson et al. (2000), Saari et al. (2004) and Lam et al. (2005). The behavior of shear studs can vary considerably depending on the test setup. An extensive discussion on the influences of various parameters is reported by Ernst (2006). These parameters include width of the concrete specimen, number of connectors in one slab, the reinforcing of the specimen, recess in concrete slabs, specimen preparation, horizontal restraints, normal forces, stress regime in concrete, etc. Eurocode 4 (CEN 2004) specifies a standard test specimen for shear studs embedded in solid slabs, and it is permitted to modify the standard test specimen to conform to the beam to which the pushout test is related. However, no comment is provided on how to modify the test when metal deck is employed. Generally, it is believed that pushout tests yield conservative strength estimation for shear connectors due to the following reasons: (1) normal forces existing in a composite floor system will induce compression between concrete slabs and steel beams, suppressing concrete crushing and fracture of steel anchors; (2) compressive stress due to shear connectors bearing against concrete is distributed over a smaller width in pushout tests; (3) the smaller width also makes possible longitudinal splitting of concrete slabs.

The pushout test setup utilizing a self-reacting frame is illustrated in Figure 4.16. An isometric view of the test setup is given in Figure 4.17. This test setup can be used for both monotonic and cyclic loading tests. The test specimen consists of a precast concrete plank attached to a WT section using clamping connectors. The size of the precast concrete plank is 4 ft. × 2 ft. × 6 in.

The stem of the WT at the end of the member that attached to the actuators was coped to ensure that the actuator load was applied primarily to the flange to reduce eccentricity of the force application in the WT. The coping is indicated by the 1/2 in. gap between the end plate and the web of the WT section in the left side of Figure 4.18. A stiffened C15x50 connected the test specimen to the self-reacting frame. L8x4x1 was chosen as the reaction angle to react against the concrete plank and provide bearing stiffness and compressive stress distribution within the concrete comparable to those in a composite beam (see Appendix G). The whole test setup was restrained vertically by stiffened W6x25 assemblies, as separation between concrete slabs and steel beams is rarely seen in composite beams. Plates welded on the WT stems distributed the reaction generated due to the overturning of the specimen and provided support against web local buckling. Steel guides were designed to ensure that the WT section moved only along its axial direction. Detailed dimensions of the test setup are given in Figure 4.18. ASTM A992 steel was used for the WT sections, while A36 steel was selected for the reaction angle sections and the plates that constituted the remainder of the load frame. Gaps between the concrete plank specimen and the reaction angles were eliminated by placing thin steel shims to minimize the rigid body motion of the concrete plank during the test.

All connections were designed as slip-critical to reduce as much slip as possible. Since the reuse of A325 bolts is allowed, they were selected for connections where tightening and untightening bolts were frequent due to switching new concrete specimens and steel beams. A490 bolts, however, were used for connections that remained intact during the testing. Teflon sheeting was attached at the interface between the WT section and the steel guides to minimize friction effects on the tested strengths of the specimens.

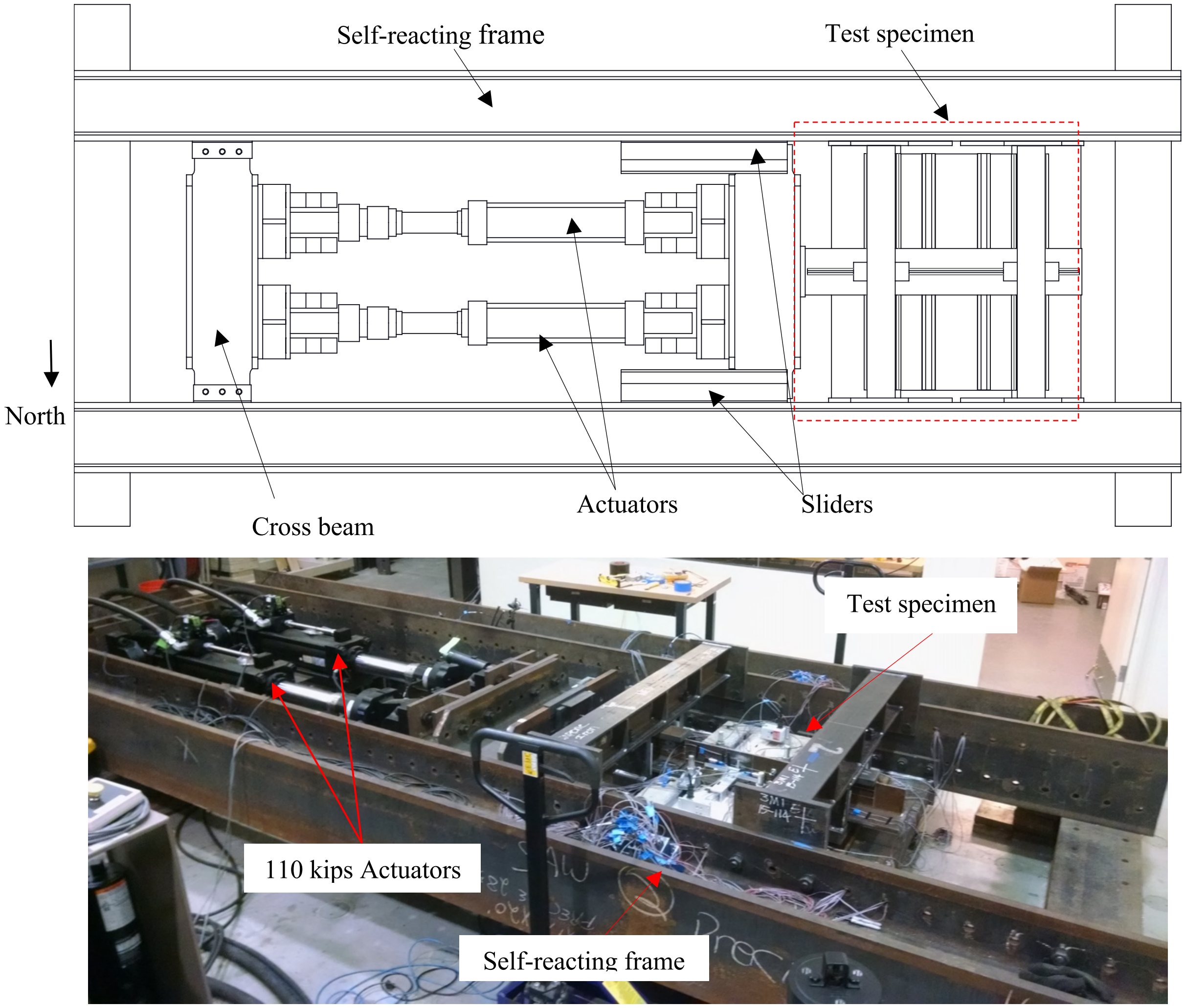
Self-reacting frame
Test specimen
North
Cross beam
Actuators
Sliders
Test specimen
110 kips Actuators
Self-reacting frame

Figure 4.16 Pushout test loading frame

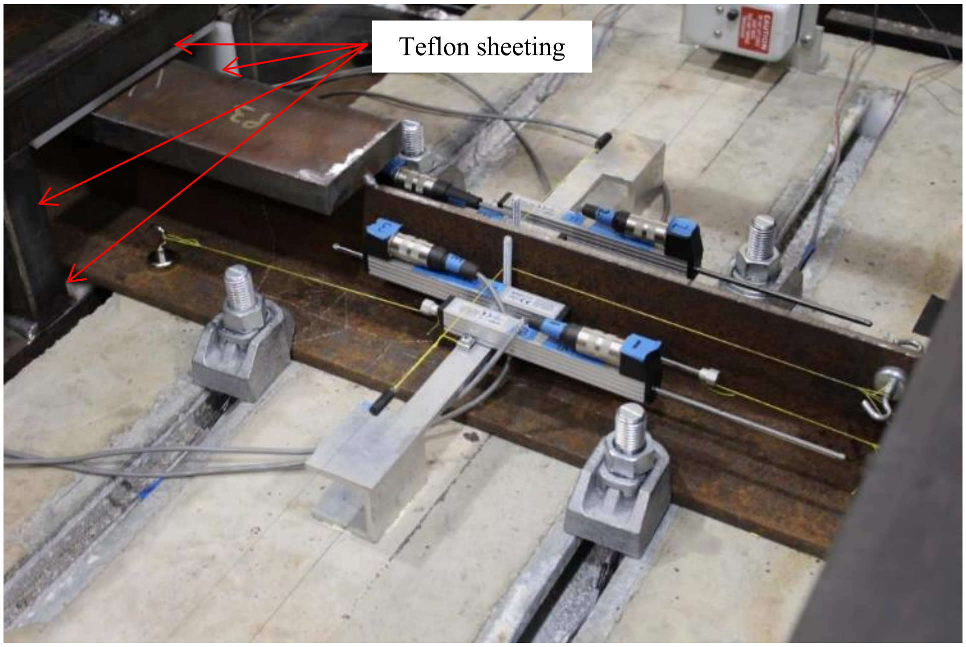
Teflon sheeting
P3

Figure 4.17 Isometric view of pushout test setup

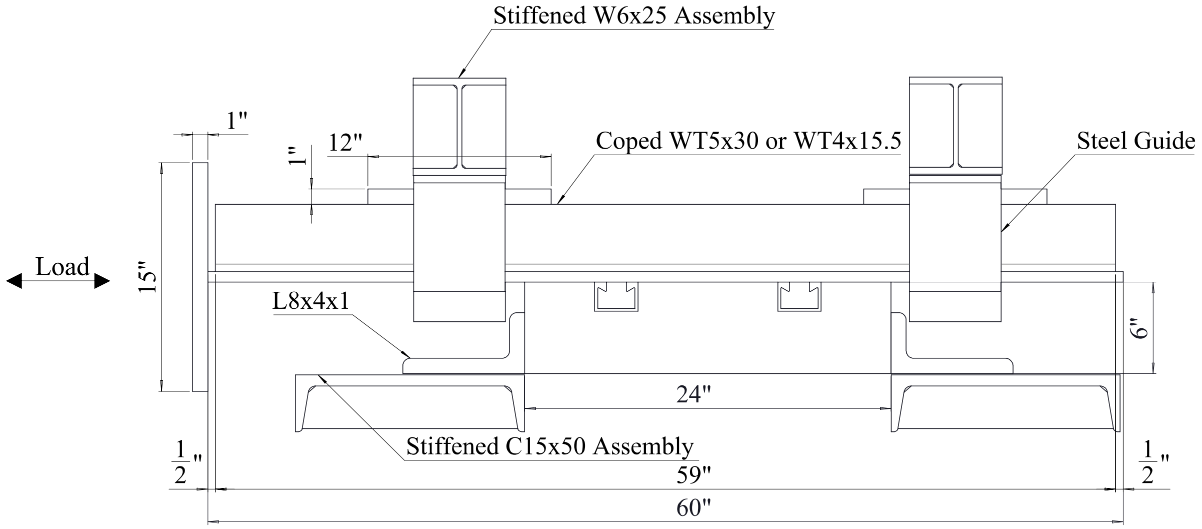
Stiffened W6x25 Assembly
1"
1"
12"
Coped WT5x30 or WT4x15.5
Steel Guide
Load
15"
L8x4x1
6"
24"
Stiffened C15x50 Assembly
1/2"
59"
1/2"
60"

a) Elevation view

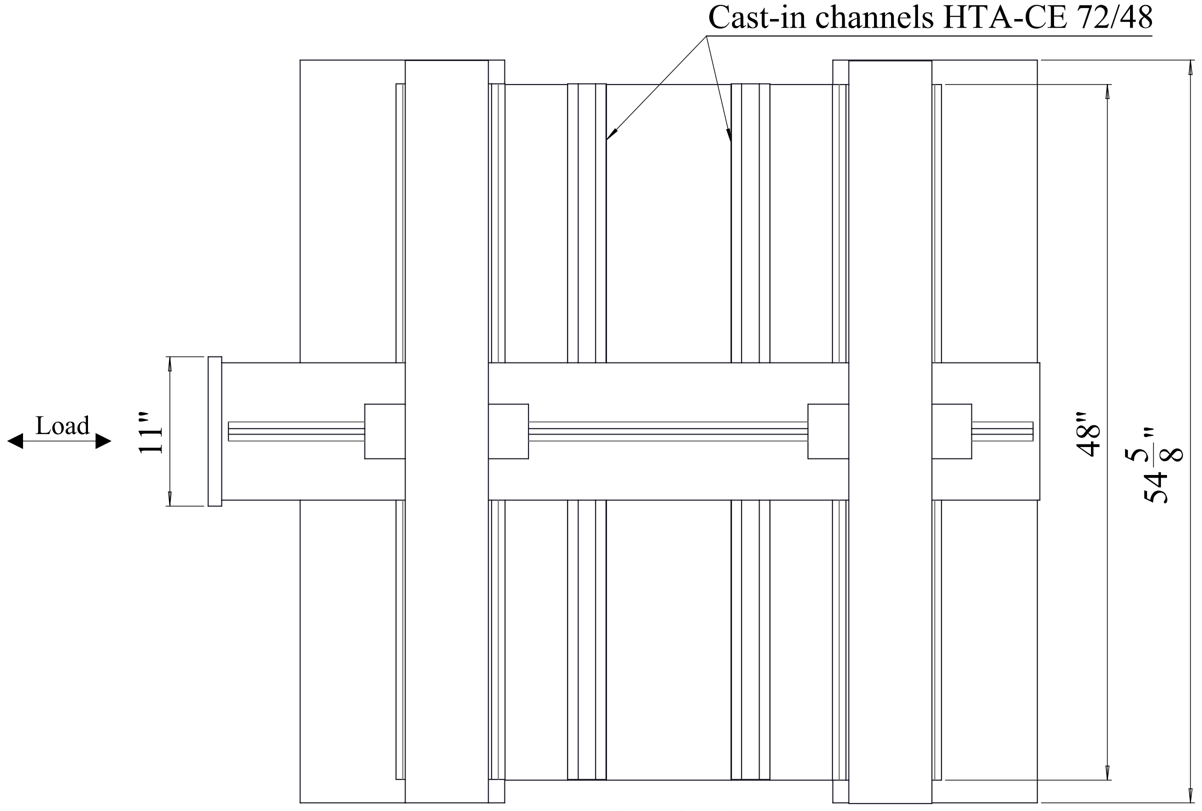
Cast-in channels HTA-CE 72/48
Load
11"
48"
54 5/8"

b) Plan view

Figure 4.18 Different views of pushout test specimen

Although pushout tests cannot precisely replicate the actual loading scenario of shear connectors in composite beams, they should be designed properly to imitate the forces induced in the shear connectors and eliminate limit states that never happen in composite beams. A comparison of the forces acting on the shear connectors in a composite beam and in the pushout test setup is illustrated in Figure 4.19. The slab uniform loading applied in a composite beam is missing in the pushout test setup. However, compared to shear studs, the absence of the uniform loading has minimal impacts on the tested shear strength of the clamps for two reasons: first, as demonstrated in Table 5.14 in Chapter 5, the friction generated at the steel/concrete interface due to the applied loading on the concrete slab contributes to less than 5% of the total shear resistance in the composite beam specimens; second, the consequences of ignoring the uniform loading could be different for shear studs and clamps. In a composite beam, under uniform loading applied to the concrete slab, the axial force between the steel beam and the concrete slab is compressive, and no uplift exists. Hence, the axial forces acting on the shear connectors are compressive. In the proposed pushout test configuration, it is shown in Figure 4.19b that the overturning of the concrete specimen leads to additional tension applied to one pair of shear connectors and additional compression applied at the steel/concrete interface (not necessarily to the other pair of shear connectors). The effects of tensile force on the shear strength of shear studs are not entirely clear, as Teraszkiewicz (1965) reported that the tensile force induced in the stud shank reduced the shear strength up to a third, while Oehlers and Johnson (1987) concluded that the detrimental effect of axial tension could be offset by the beneficial effect of axial compression. In a regular slip-critical bolted connection, tensile loading acting on the connection results in the release of the normal force at the component interface, and the bolt tension varies slightly. Similarly, for the clamping connections, the additional tension and compression increases and decreases the normal force at the steel/concrete interface, respectively, and thus the resultant frictional resistance of the system may not be affected.

In the pushout test setup, compared to the bolt pretension force and applied actuator loading, the self-weight of the concrete plank and steel beam is negligible, as the magnitude of the dead load is only approximately 820 lbs (600 lbs for the concrete plank and 220 lbs for the steel beam). Therefore, to simply the derivation, the dead load of the specimens is ignored in the following equations.

If the actuator force is not large enough, there is no contact between the steel beam and the steel guides, and the behavior of the system can be interpreted using Equation (4.2). The shear connectors are still under pure shear.

Steel beam free body diagram:

$$F_{shear} = F_{act} \tag{4.2}$$

Where

F_{shear} = shear force acting on the shear connectors

F_{act} = horizontal actuator force exerted on the steel beam

Equations (4.3) through (4.10) present the behavior of the system when the actuator force is large enough to cause the steel beam to bear against the steel guides.

Concrete free body diagram:

$$F_{shear} = F_{reac2} - F_{reac1} \tag{4.3}$$

$$F_{fric1} = \mu F_{reac1} \tag{4.4}$$

$$F_{fric2} = \mu F_{reac2} \tag{4.5}$$

Steel beam free body diagram:

$$F_{act} = F_{shear} + f_1 + f_2 \tag{4.6}$$

$$f_1 = \mu' P_{reac1} \tag{4.7}$$

$$f_2 = \mu' P_{reac2} \tag{4.8}$$

Pushout specimen free body diagram:

$$P_{reac1} + F_{fric1} = P_{reac2} + F_{fric2} + V_{act} \tag{4.9}$$

Take moment of all the external forces applied to the pushout specimen with respect to point O, which is the intersection of F_{act} and V_{act}:

$$\begin{aligned} &P_{reac1}D_1 + f_1d_1 + F_{reac1}H_1 + F_{fric1}h_1 + M_{act} \\ &\qquad = P_{reac2}D_2 + f_2d_2 + F_{reac2}H_2 + F_{fric2}h_2 \end{aligned} \tag{4.10}$$

Where

F_{reac1} and F_{reac2} = resultant horizontal reaction forces from the angles

F_{fric1} and F_{fric2} = friction generated at the concrete and reaction angle interfaces

F_{norm1} and F_{norm2} = idealized normal forces induced at the steel-concrete interface

P_{reac1} and P_{reac2} = vertical reaction forces from the steel guides

f_1 and f_2 = friction generated at the steel beam and steel guides interfaces

D_1 = distance between P_{reac1} and point O, which is equal to 49 in.

D_2 = distance between P_{reac2} and point O, which is equal to 16.5 in.

d_1 = distance between f_1 and point O, which is equal to section depth minus half flange thickness

d_2 = distance between f_2 and point O, which is equal to half flange thickness

H_1 = distance between F_{reac1} and point O

H_2 = distance between F_{reac2} and point O

h_1 = distance between F_{fric1} and point O, which is equal to 44.75 in.

h_2 = distance between F_{fric2} and point O, which is equal to 20.75 in.

μ = frictional coefficient between concrete plank and steel reaction angle

μ' = frictional coefficient between Teflon sheets and steel beam

As the system is indeterminate, it is not possible to solve Equations (4.3) through (4.10) to find the relationship between F_{act} and F_{shear}. Therefore, some assumptions are made to simplify the derivation. Since the shear force, V_{act}, and bending moment, M_{act}, from the actuators resist the rotation and movement of the steel beam, these forces are ignored. In addition, when the concrete plank bears against one reaction angle and rotates, the reaction force (F_{reac1}) from the other angle as well as the friction at the steel angle/concrete plank interface (F_{fric1}) are insignificant, since the gap between the angles is always larger than the width of the plank specimen to facilitate construction. It can also be concluded that the normal force at the steel-concrete interface now becomes uneven, with the normal forces increasing on one side and decreasing on the other side.

Combining Equations (4.3) through (4.10) results in the following:

$$\frac{F_{act}}{F_{shear}} = 1 + \mu\mu' + 2\mu' \frac{H_2 + \mu h_2 - \mu D_1 - \mu\mu' d_1}{D_1 + \mu' d_1 - D_2 - \mu' d_2} \tag{4.11}$$

It is seen from the above equation that F_{shear} becomes F_{act} when $\mu' = 0$. During the tests, the directions of the forces were the same as those depicted in Figure 4.19; therefore, the last term in Equation (4.11), which represents the ratio of P_{reac2} to F_{shear}, has to be greater than 0. A relationship is determined between μ and μ'.

$$\frac{H_2 + \mu h_2 - \mu D_1 - \mu\mu' d_1}{D_1 + \mu' d_1 - D_2 - \mu' d_2} > 0 \tag{4.12}$$

$$\mu < \frac{H_2}{D_1 + \mu' d_1 - h_2} \tag{4.13}$$

Conservatively assuming that $H_2 = 6\ in.$, and $\mu' = 0.2$,
For Section WT5x30:

$$\mu < \frac{H_2}{D_1 + \mu' d_1 - h_2} = \frac{6}{49 + 0.2 \times (5.11 - 0.34) - 20.75} = 0.205 \tag{4.14}$$

$$\begin{aligned}\frac{F_{act}}{F_{shear}} &= 1 + 2 \times 0.2 \times \frac{6}{49 + 0.2 \times (5.11 - 0.34) - 16.5 - 0.2 \times 0.34} \\ &= 1.072\end{aligned} \tag{4.15}$$

For Section WT4x15.5:

$$\mu < \frac{H_2}{D_1 + \mu' d_1 - h_2} = \frac{6}{49 + 0.2 \times (4 - 0.22) - 20.75} = 0.207 \tag{4.16}$$

$$\frac{F_{act}}{F_{shear}} = 1 + 2 \times 0.2 \times \frac{6}{49 + 0.2 \times (4 - 0.22) - 16.5 - 0.2 \times 0.22} = 1.072 \tag{4.17}$$

The above calculations indicate that the majority of the actuator force is taken by the shear connectors after the steel guides are involved, and the friction generated at the WT and steel guides interfaces is negligible.

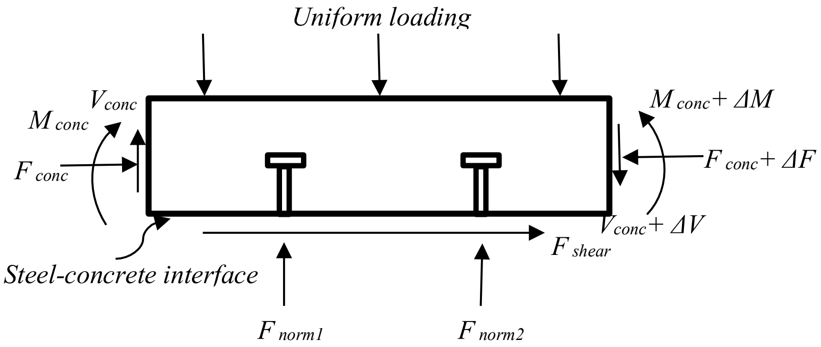
Uniform loading
V_{conc}
M_{conc}
F_{conc}
$M_{conc}+ \Delta M$
$F_{conc}+ \Delta F$
$V_{conc}+ \Delta V$
F_{shear}
Steel-concrete interface
F_{norm1}
F_{norm2}

a) Concrete slab in a composite beam

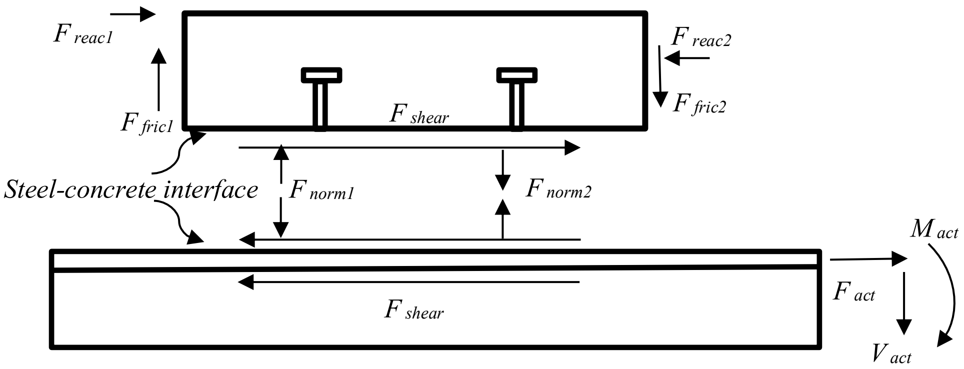
F_{reac1}
F_{fric1}
F_{reac2}
F_{fric2}
F_{shear}
Steel-concrete interface
F_{norm1}
F_{norm2}
M_{act}
F_{act}
V_{act}
F_{shear}

(1) Before steel guides are engaged

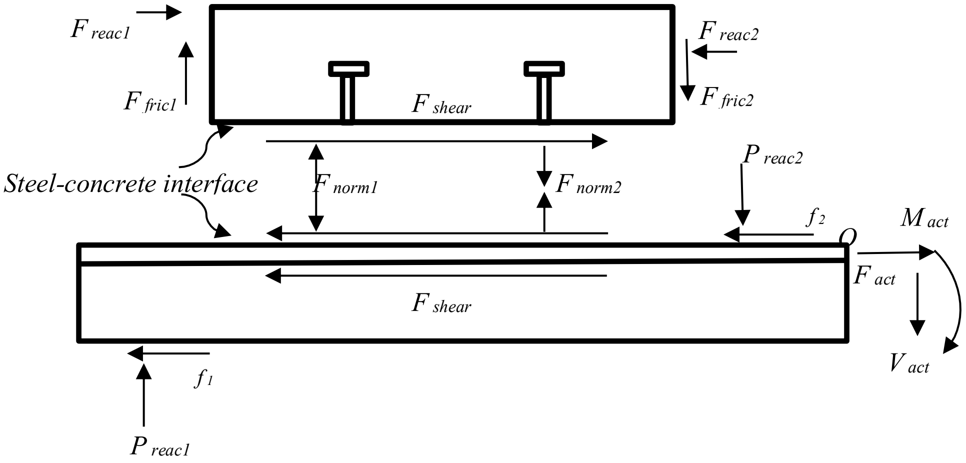
F_{reac1}
F_{fric1}
F_{reac2}
F_{fric2}
F_{shear}
Steel-concrete interface
F_{norm1}
F_{norm2}
P_{reac2}
f_2
O
M_{act}
F_{act}
V_{act}
F_{shear}
f_1
P_{reac1}

(2) After steel guides are engaged

b) Concrete plank and steel beam in the pushout test setup

Figure 4.19 Clamping connector loading scenario comparison

4.5.2 Instrumentation

Displacement measurements

Four linear potentiometers with a stroke length of 4 in. were placed to record the relative displacement between the steel beam and the concrete slab at each clamp, i.e., slip of the clamps. Two string pots were also utilized which are capable of measuring up to 15 in. displacement. During testing, the pauses needed for adjusting loading rates were based on the readings from the linear potentiometers since they have a better resolution for smaller slips than the string pots. After the linear potentiometers reached their capacity and were disabled, the string pots became the only sensors for slip measurements.

In addition, relative deflection of the cantilever legs of the reaction angles with respect to the channels C15x50 was measured with four linear potentiometers with a stroke length of 1 in., as shown in Figure 4.20. Dial gages were installed to monitor the vertical deflection of the steel guides which were designed to be sufficiently stiff to restrain the overturning of the system. The horizontal deflection of the steel guides reflects the out-of-plane movement of the beam. The load and displacement measurements were recorded for all the specimens with the data acquisition system.

Strain measurements

Strains were measured only for Specimens 3-M24-2C-RL-LC, 5-M24-2C-RH-LC, 8-M24-3C-RH-LC and 10-M20-2C-RH-LC. Specimen 3-M24-2C-RL-LC is chosen because premature concrete failure is anticipated only in this specimen. Using shims for steel beams with thin flanges is not considered to be common. Hence, Specimen 5-M24-2C-RH-LC is preferred to Specimen 6-M24-2C-RH-LC-S. Compared to Specimen 7-M24-3C-RH-LM, Specimen 8-M24-3C-RH-LC is under cyclic loading, and more data is available for interpreting the behavior. Between the two specimens using M20 bolts, Specimen 10-M20-2C-RH-LC is chosen over Specimen 9-M20-2C-RH-LM. In Tests 6-

M24-2C-RH-LC-S and 9-M20-2C-RH-LM, the bolts were instrumented to track the change of the pretension force.

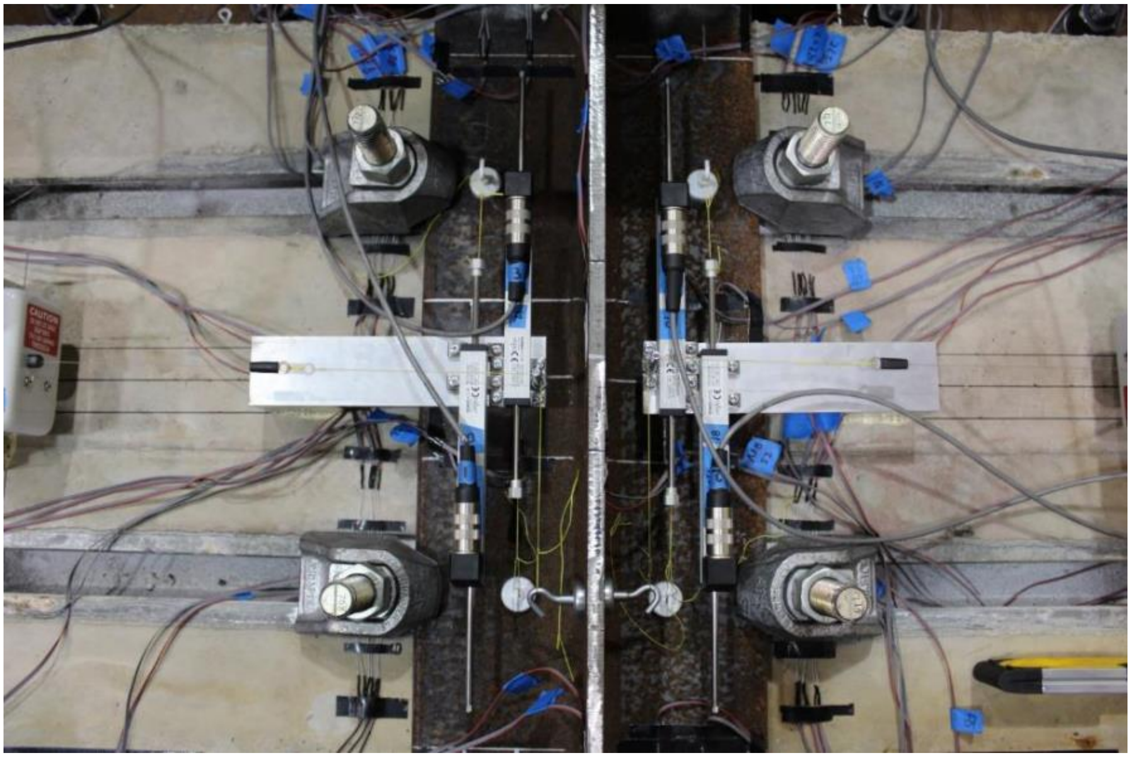

Slip measurements

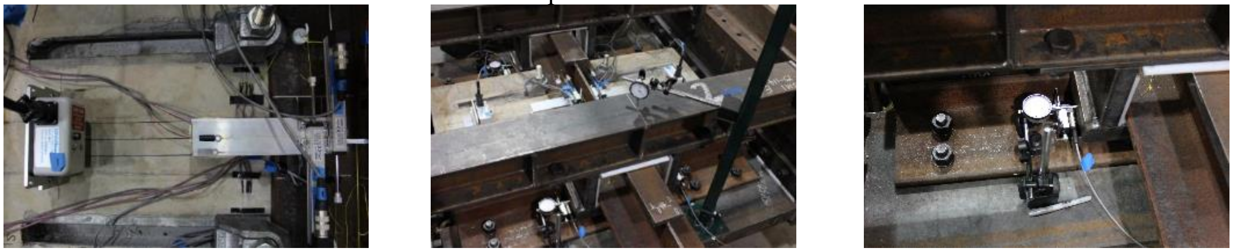

North string pot Dial gages linear potentiometer at northwestern corner

Figure 4.20 Displacement measurements in pushout tests

The force distribution among these clamps is calculated based on the axial strain measurements at several sections of the WT beams. These sections are far from the clamps since the clamping force acting on the flanges could make the stress vary along the flange thickness. The gaged locations are the third points of the webs and flanges. Meanwhile, uniaxial strain gages were attached on the bolt shanks to study the variation of the bolt pretension. Bolt gages in the pushout tests were placed at right angles to those used in the pretension tests to avoid being crushed when the bolts bore against the clamps under shear. Channel lips were instrumented with rosette strain gages to capture their three-dimensional behavior. The layout of the strain gages on the beams, channel lips and bolts is depicted in Figure 4.21.

The rosette strain gages are identified with the convention below: the first number describes the number of the gaged channel lip; the second letter indicates the member (i.e., channel lips); the third letter demonstrates the channel lip location using cardinal directions; the last letter implies one of the legs in the gage. The uniaxial strain gages attached on the bolt shanks employ a very similar method, with the first number describing the number of the gaged bolt, the second letter indicating the member (i.e., bolts), and the third letter demonstrating the gage location using cardinal directions.

The following nomenclature is employed for the uniaxial strain gages on the beams: the first letter indicates the instrumented section using cardinal directions; the second letter represents the gaged member; the third letter implies the gage location using cardinal directions; the last letter shows whether the gage is close to or further way from the flange and web joint.

The following strain gages were placed inside the concrete specimen before pouring concrete. Rosette strain gages were attached to the channel anchors to measure the strain variations in three directions (0°-45°-90°), and these measurements can be used to estimate the axial force and shear force acting on the anchors. On each channel, two strain gages were installed on the same side of the two selected anchors, which were deemed to take large forces and have small resistance against concrete failure. All the strain gages were placed along the anchor centerline and as close to the welds as possible. Uniaxial strain gages were utilized to monitor the axial strain variation in the transverse and vertical reinforcement. Using preliminary finite element analysis results, the bar gages were placed at the maximum tensile stress locations.

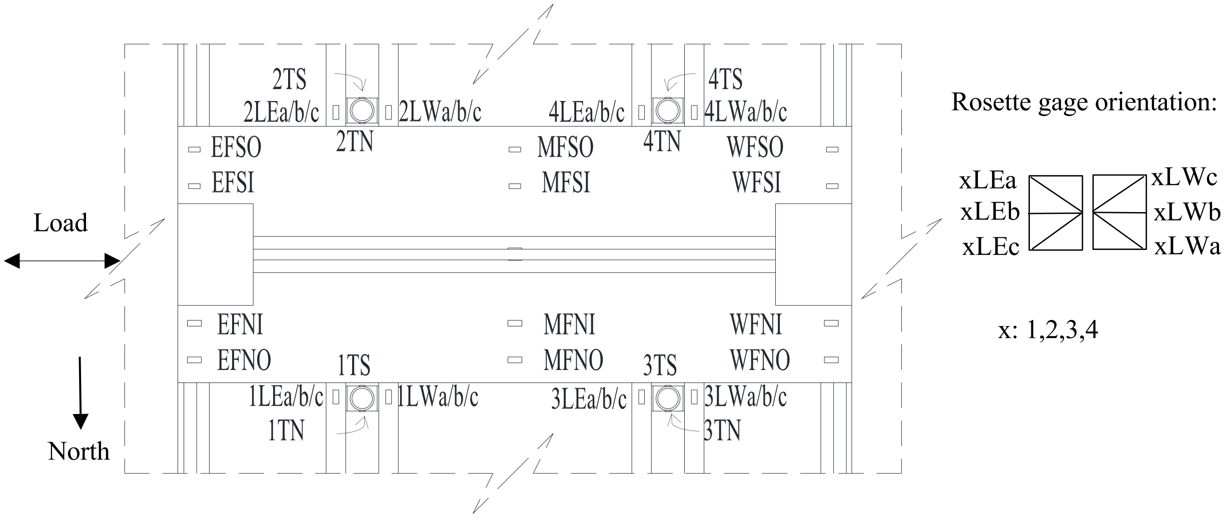
2TS
2LEa/b/c
2LWa/b/c
2TN
4LEa/b/c
4TS
4LWa/b/c
4TN
EFSO
EFSI
MFSO
MFSI
WFSO
WFSI
Load
EFNI
EFNO
MFNI
MFNO
WFNI
WFNO
1TS
1LEa/b/c
1LWa/b/c
1TN
3TS
3LEa/b/c
3LWa/b/c
3TN
North
Rosette gage orientation:
xLEa
xLEb
xLEc
xLWc
xLWb
xLWa
x: 1,2,3,4

a) Plan view of two-channel test specimen instrumentation

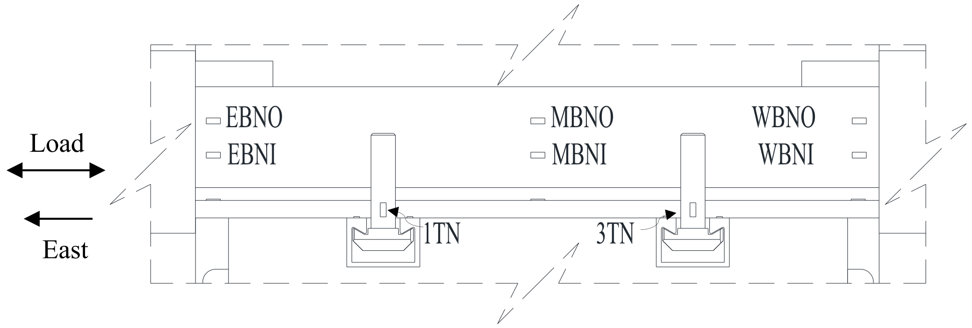
EBNO
EBNI
MBNO
MBNI
WBNO
WBNI
Load
East
1TN
3TN

b) Side view of two-channel specimen instrumentation

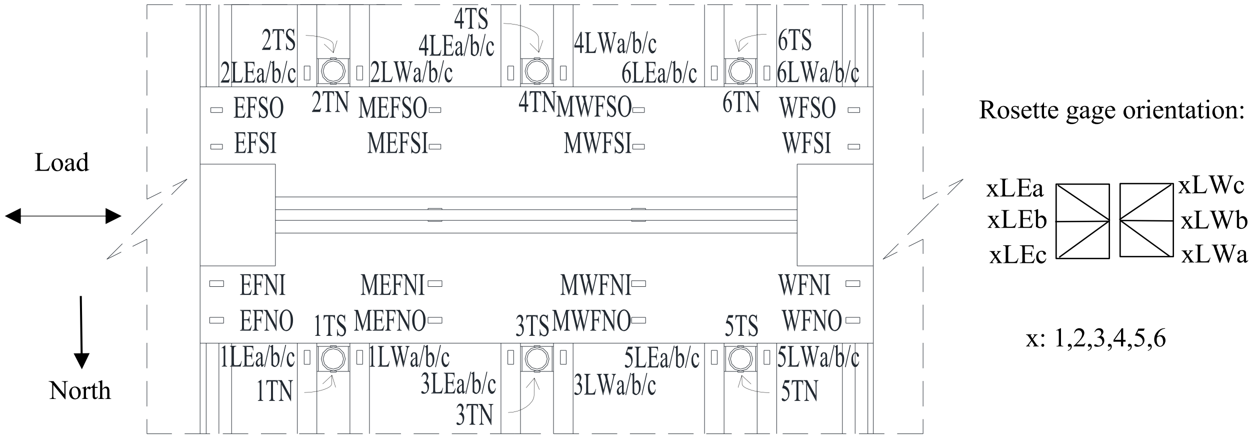
2TS
2LEa/b/c
2LWa/b/c
2TN
4TS
4LEa/b/c
4LWa/b/c
4TN
6LEa/b/c
6TS
6LWa/b/c
6TN
EFSO
EFSI
MEFSO
MEFSI
MWFSO
MWFSI
WFSO
WFSI
Load
EFNI
EFNO
MEFNI
MEFNO
MWFNI
MWFNO
WFNI
WFNO
1TS
1LEa/b/c
1LWa/b/c
1TN
3TS
3LEa/b/c
3LWa/b/c
3TN
5TS
5LEa/b/c
5LWa/b/c
5TN
North
Rosette gage orientation:
xLEa
xLEb
xLEc
xLWc
xLWb
xLWa
x: 1,2,3,4,5,6

c) Plan view of three-channel specimen instrumentation

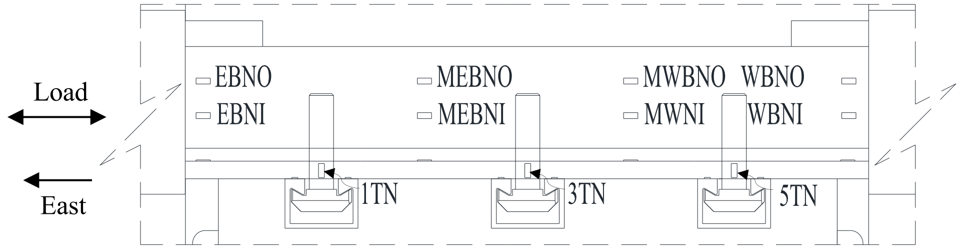
EBNO
EBNI
MEBNO
MEBNI
MWBNO
MWNI
WBNO
WBNI
Load
East
1TN
3TN
5TN

d) Side view of three-channel specimen instrumentation

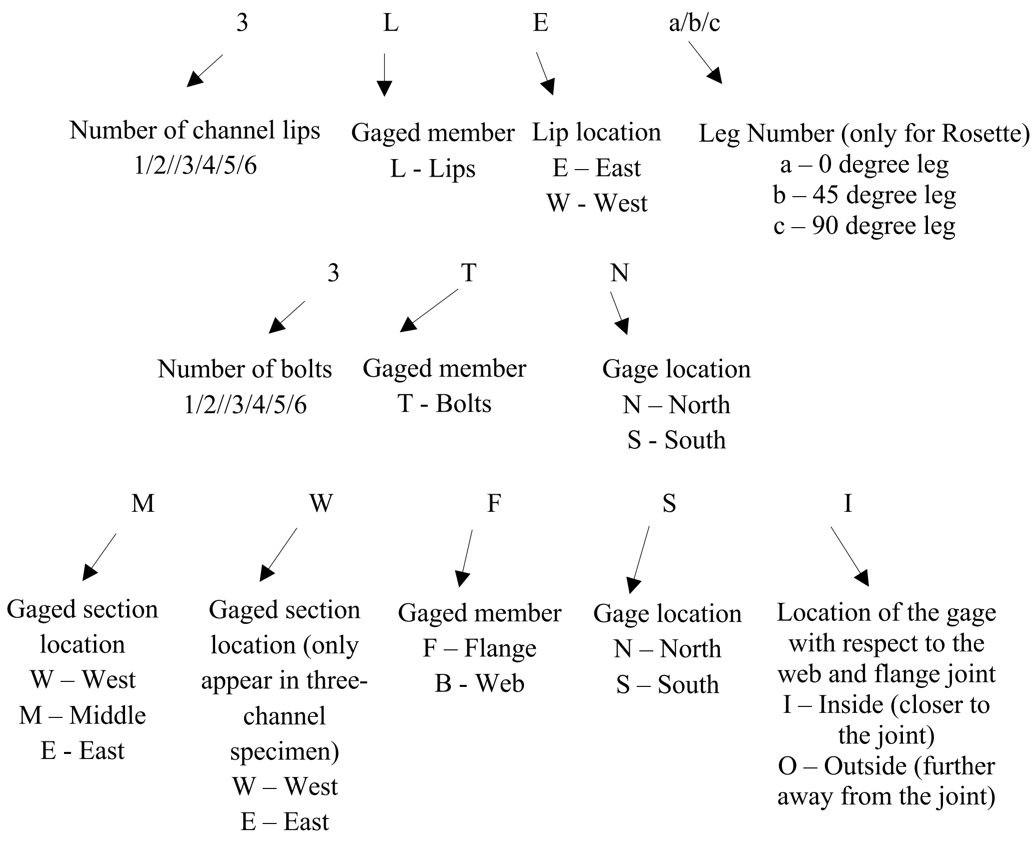
3
L
E
a/b/c
Number of channel lips
1/2//3/4/5/6
Gaged member
L - Lips
Lip location
E – East
W - West
Leg Number (only for Rosette)
a – 0 degree leg
b – 45 degree leg
c – 90 degree leg
3
T
N
Number of bolts
1/2//3/4/5/6
Gaged member
T - Bolts
Gage location
N – North
S - South
M
W
F
S
I
Gaged section location
W – West
M – Middle
E - East
Gaged section location (only appear in three-channel specimen)
W – West
E – East
Gaged member
F – Flange
B - Web
Gage location
N – North
S – South
Location of the gage with respect to the web and flange joint
I – Inside (closer to the joint)
O – Outside (further away from the joint)

Figure 4.21 Strain gages attached on the bolts, channel lips and beams in pushout test specimens

The rosette strain gages are named in the following manner: the first number indicates the anchor being instrumented; the second letter defines the measuring grid in the rosette gage. The nomenclature for the uniaxial strain gages adopts another approach: the first letter represents the type of reinforcement; the second letter indicates the location of the gage with respect to the centerline of the specimen; and the last number indicates whether the gage is closer to or further away from the centerline. Reinforcement cages and instrumentations before pouring concrete are shown in Figure 4.22.

All the strain gages are capable of measuring 50,000 microstrains in the positive direction (tensile strain) and the negative direction (compressive strain).

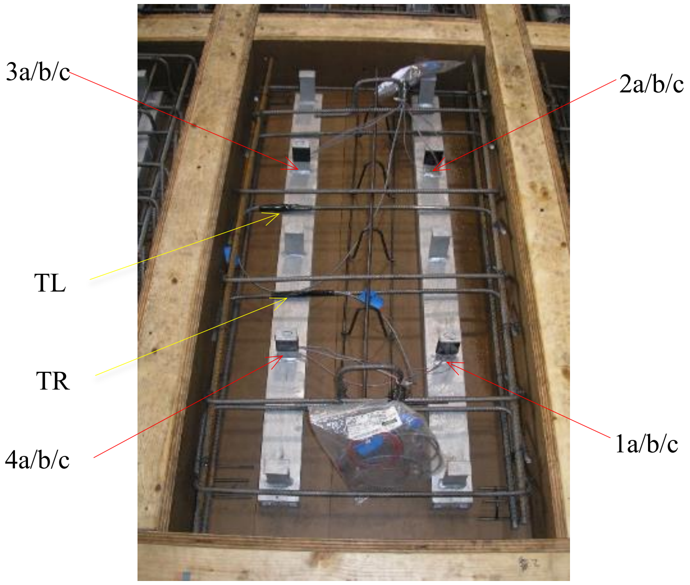
3a/b/c
2a/b/c
TL
TR
4a/b/c
1a/b/c

a) Light reinforcement pattern with two channels

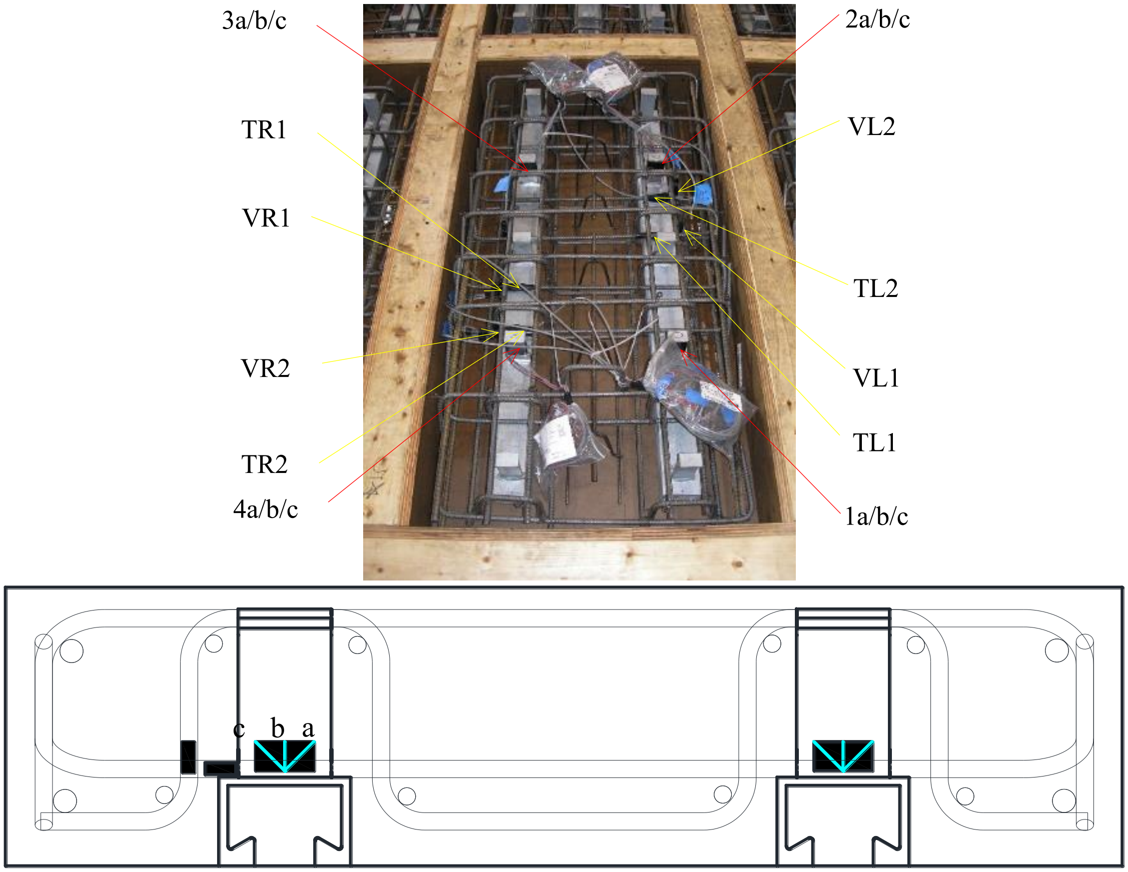
3a/b/c
2a/b/c
TR1
VL2
VR1
TL2
VR2
VL1
TL1
TR2
4a/b/c
1a/b/c
c
b
a

b) Heavy reinforcement pattern with two channels

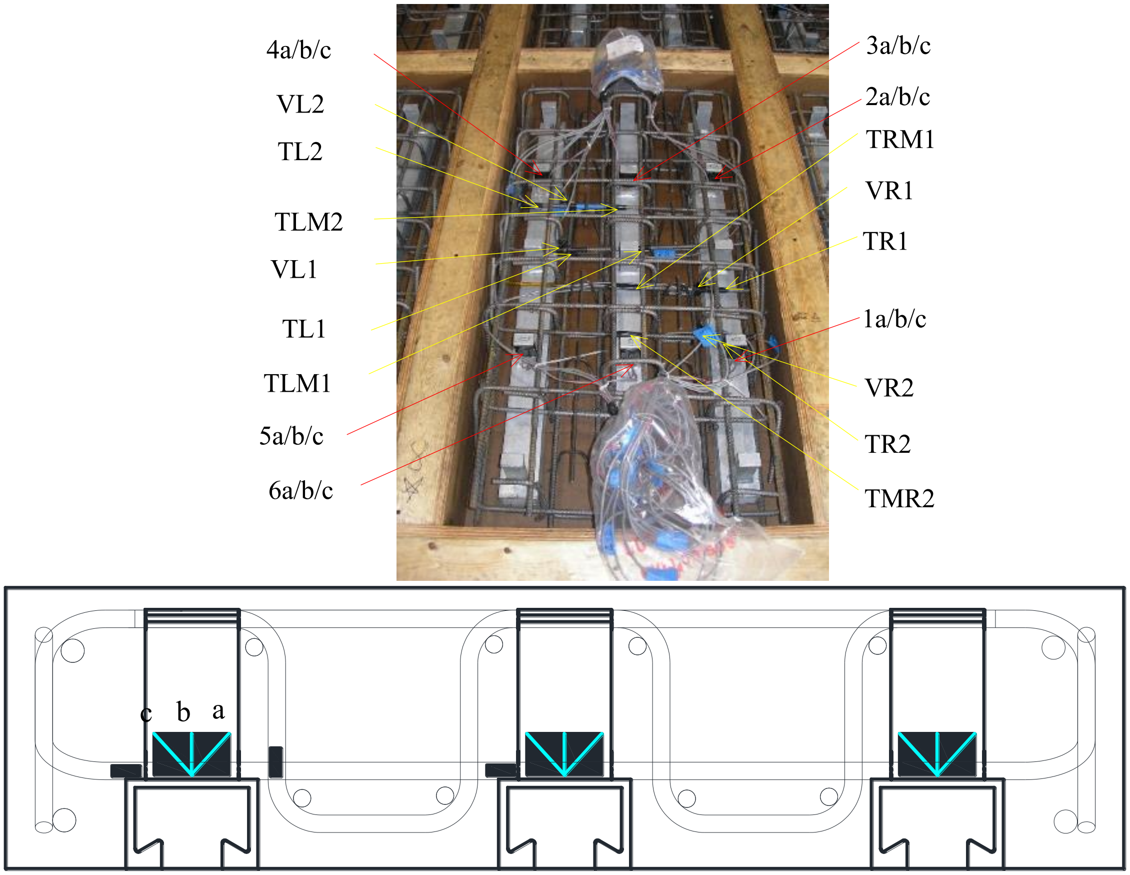
4a/b/c
VL2
TL2
TLM2
VL1
TL1
TLM1
5a/b/c
6a/b/c
3a/b/c
2a/b/c
TRM1
VR1
TR1
1a/b/c
VR2
TR2
TMR2
c
b
a

c) Heavy reinforcement pattern with three channels

3 a/b/c

3 – Location of the gage: the numbering is in a counter-clockwise direction; the 1st gage is at the lower right corner 1/2/3/4/5/6

a/b/c – Leg Number (only for Rosette)
a – 0 degree leg
b – 45 degree leg
c – 90 degree leg

T L M 2

T – Reinforcement type
T - Transverse
V – Vertical

L – Location of the reinforcement with respect to the specimen centerline
L- Left
R- Right

M – Gage at the middle of the transverse reinforcement M/Not Applicable

2 – Location of the reinforcement with respect to the specimen centerline
1 – closer to the centerline
2 – further away from the centerline

Figure 4.22 Strain gages attached on the reinforcement and channel anchors in pushout test specimens

4.5.3 Loading protocol

The loading for all the pushout specimens is displacement-controlled. In the first monotonic test, i.e., Test 2-M24-2C-RH-LM, the actuator displacement rate was chosen to be 0.0025 in. per minute before the slip reached 0.02 in. However, the actual slip rate was seen to be much smaller than the rate of movement of the actuator at the beginning of the test. Therefore, for the remaining monotonic tests, a rate of 0.0075 in. per minute movement of the actuators was first adopted until slips between the concrete plank and steel beam were detected, which means gaps between the components, such as the gap between the concrete plank and reaction angles, were closed and contact was established. Subsequently, the variation of the actuator displacement started to match the change of the slips. The actuator displacement rate was switched to 0.0025 in. per minute until a slip of 0.02 in. was attained. The subsequent loading rates were the same as those used in the cyclic tests at the same slip, as illustrated in Figure 4.23. In the monotonic tests, the specimens were loaded in the east direction or the tensile direction. Although pushout tests are different from slip tests, which are performed to quantify the slip coefficients for coatings in accordance with Appendix A of the RCSC Specification (RCSC 2014), the load corresponding to a slip of 0.02 in. is similarly defined as the slip load, since the monotonic load-slip curves show gradual changes in response.

The AISC loading protocol for beam-to-column moment connections is used as a guide for establishing the cyclic slip history depicted in Figure 4.23 for the clamping connections (AISC 2016b). Because the slips at the first three levels are less than 0.004 in., which is approximately the resolution of the 4 in. stroke displacement sensors, 37.5%, 50% and 75% of the slip load, which is obtained from the corresponding monotonic test, were used as the respective targets for these three levels. Slip displacements were then used as the targets for the other cycles. During each loading cycle, the specimen was first loaded in the east direction or the tensile direction, then unloaded, then loaded in the west direction or the compressive direction, and then unloaded. In the first cyclic test, i.e., Test 5-M24-2C-RH-LC, the actuator displacement rate was 0.0075 in. per minute for the first load level. However, this rate was found to be slow, and this test was then completed using the rates shown in Figure 4.23.

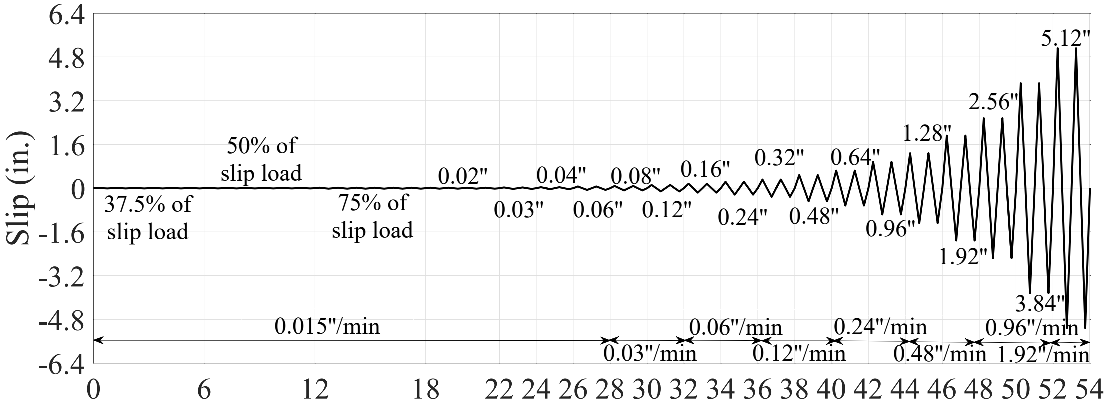

Figure 4.23 Cyclic slip history and loading rates for pushout test specimens

4.5.4 Specimen performance

Although the concrete plank and steel beam that were used for the pretension tests may have been damaged during the tests, a shakedown test was performed using these specimens to verify the adequacy of the data acquisition system, the control system, the test frame, etc.

4.5.4.1 *Monotonic specimens*

In this section, the overall load-slip behavior of the M24 and M20 clamps in the monotonically loaded pushout specimens is presented; however, their performance at slips comparable to the magnitude seen in actual composite beams is of particular interest, if the clamps are utilized as shear connectors in composite beams. For a composite beam, its performance at three levels of loading is important, namely, service load, design load, and ultimate state. Based on the composite beam test results shown in Chapter 5, the slip at full service loading varies from nearly zero to 0.02 in. among the specimens. At design load, the slip is between 0.019 in. and 0.062 in. The maximum slip measured at approximately 15 in. deflections ranges from 0.018 in. to 0.35 in. The behavior of the pushout specimens is primarily assessed at these three slip levels.

At the service slip level, the initial and very stiff portions of the load-slip curves probably indicate the behavior of the clamps. It is seen that the strengths of the M24 and M20 clamps have not degraded even at the ultimate slip level. The excellent behavior of the clamps must have contributed to the ductile behavior of the beams demonstrated in Chapter 5. The clamp system is very stiff at the service slip level, which could reduce the deflection of the composite beams at serviceability. As the slip increases, the stiffness of the clamp system reduces.

Test 2-M24-2C-RH-LM

This specimen is regarded as the baseline specimen. The load-slip curve for Specimen 2-M24-2C-RH-LM is shown in Figure 4.24 using the slip measurement from the north string pot. The system starts to deviate from being elastic when the force and slip are approximately 53 kips and 0.003 in. Defined at 0.02 in. slip, the slip load is about 60.8 kips. The peak load, which occurs at a slip of 1.12 in., is around 88.5 kips.

Rotation of clamps was not found prior to reaching a slip of 0.64 in., which is approximately twice the ultimate slip level. Figure 4.25a shows the clamp rotation at 1.28 in. slip. When the slip was approximately 2.15 in., the load started to drop gradually, which could be caused by the loss of pretension force in Clamp 3 because of the large rotation of the clamp. As the specimen was further loaded to the next level (5.12 in. slip), the south string pot was found to be malfunctioning due to some configuration issues. Due to safety concern for the test rig, the test was terminated when the slip was about 10 in. As illustrated in Figure 4.25b, cracks, similar to those discovered in the pretension tests, were detected at the heads of some bolts after disassembling the specimen, which probably indicates that the rotation was excessive because the bolts in this test were pretensioned with three full turns from a snug-tight condition.

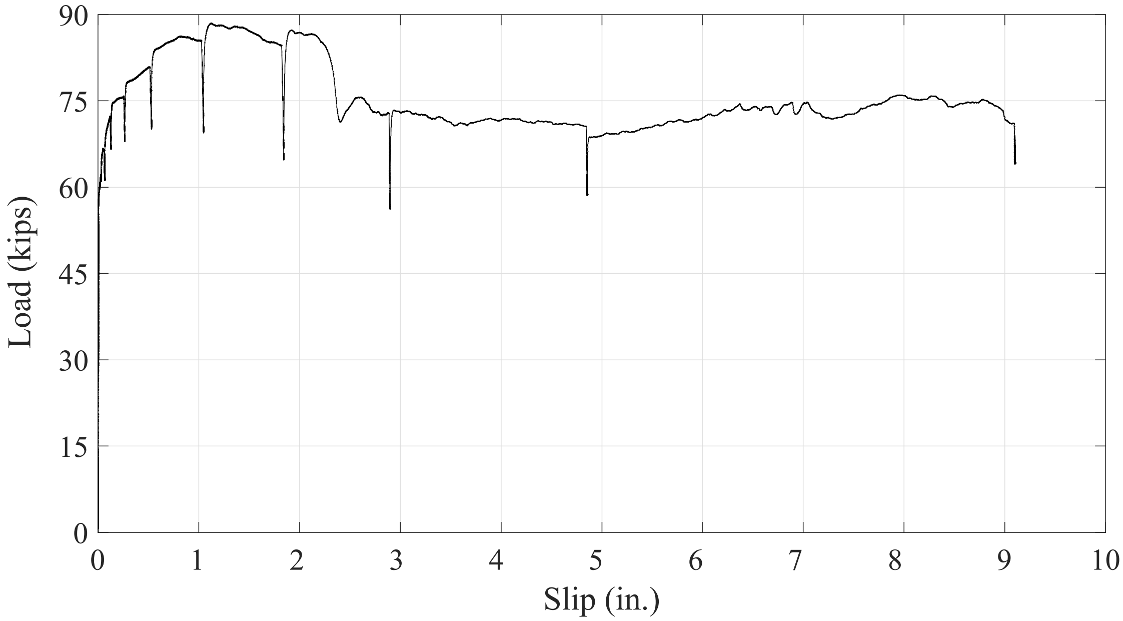

Figure 4.24 Load–slip curve of Specimen 2-M24-2C-RH-LM

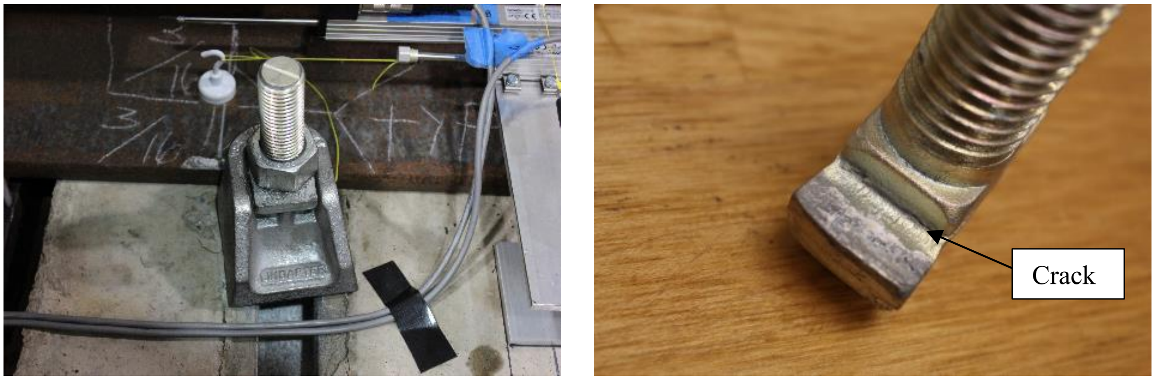

a) Rotation of Clamp 1 at 1.28 in. slip

b) Crack in bolt head

Figure 4.25 Observations in Specimen 2-M24-2C-RH-LM

Test 4-M24-2C-RH-LM-S

Compared to Specimen 2, shims were inserted between the clamp teeth and steel flange in this specimen. The load-slip curve for Specimen 4-M24-2C-RH-LM-S is shown in Figure 4.26 using the average slip measurement from the string pots. The slip load is about 56.5 kips. Occurring at a slip of 0.55 in., the peak load is around 87.9 kips.

As illustrated in Figure 4.27a, bolt head fracture occurred in one of the four bolts, which is signified by the dramatic load drop slightly under 1 in. The strength rebounded to 66 kips quickly, only 75% of the peak load. This ratio may indicate that the pretension was fully released in the fractured bolt. Subsequently, the load began to oscillate, which could be caused by a stick-slip mechanism, exacerbated by the shims. The alternation happens along with a change of the friction force for the difference between the static frictional coefficient and the kinetic frictional coefficient. This phenomenon was also observed in prior research by Grigorian and Popov (1994) on the energy dissipation of slotted bolted connections by means of friction between sliding surfaces. It is also shown in the same research that stable hysteretic load-deformation behavior could be achieved with brass shims and degreased clean mill scale steel surface. However, it should be noted that the shims have minimal impacts on the behavior of the system at slips that are comparable to those seen in composite beams, such as less than 0.5 in.

Linear potentiometer 4 in this test did not work properly before 0.08 in. slip, but it functioned successfully thereafter. The hook for linear potentiometer 2 fell off during the test, as indicated in the slip plot. No movement of the clamps and shims was seen at the service slip level. At a slip of 0.16 in., the clamps started to rotate. Figure 4.27b illustrates the rotation of Clamp 4 at 0.32 in. slip, which is approximately the ultimate slip level. Slip of the shim is also indicated in this figure because the shim was initially symmetric with respect to the longitudinal axis of the channel. When the beam was loaded to a slip of 1.28 in., a loud sound was heard, which was later found to be bolt head fracture in one of the four bolts after disassembling the test setup. Along with frequent noises caused by slips, oscillation in the loading started to appear and became significant. In order to eliminate the oscillation, the loading rate was slowed down from 0.96 to 0.12 in. per minute in the last step; however, the fluctuation still existed. The test was terminated at a slip of 5.12 in. because the Teflon sheet attached to the west guide was severely torn off (see Figure 4.27c). As shown in Figure 4.27d, the concentrated clamping force crushed the A36 steel plate shims and caused deep impressions. Hence, hardened steel plates may be worth considering.

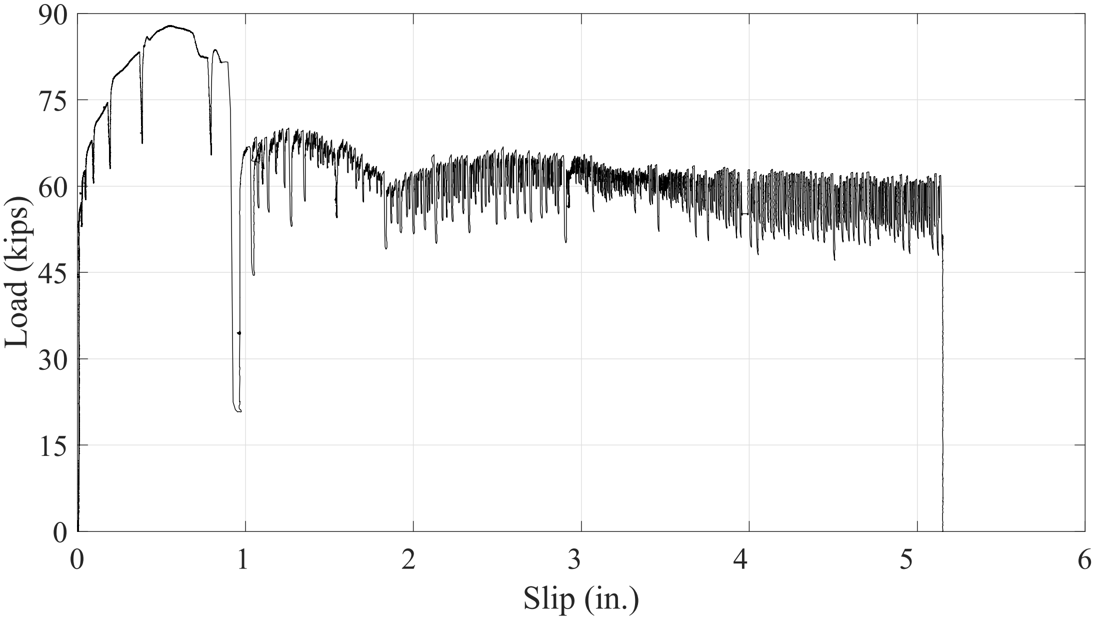

Figure 4.26 Load–slip curve of Specimen 4-M24-2C-RH-LM-S

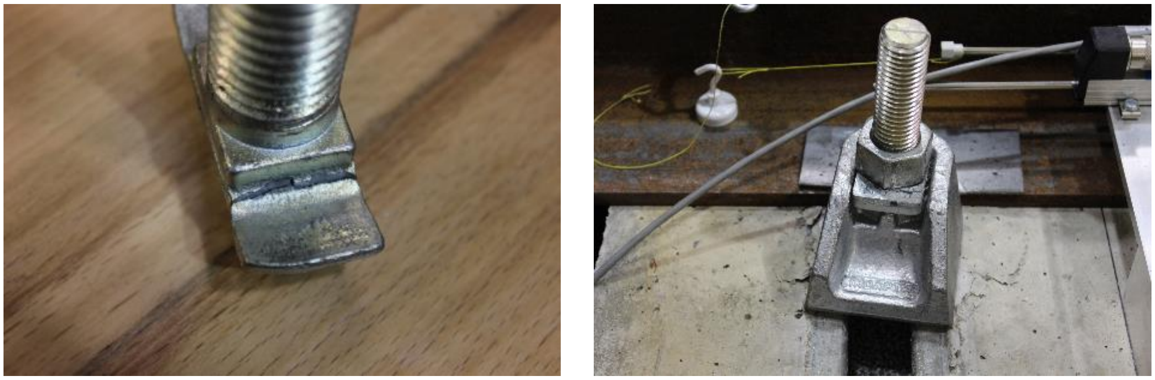

a) Head fracture in Bolt 4

b) Rotation of Clamp 4 at 0.32 in. slip

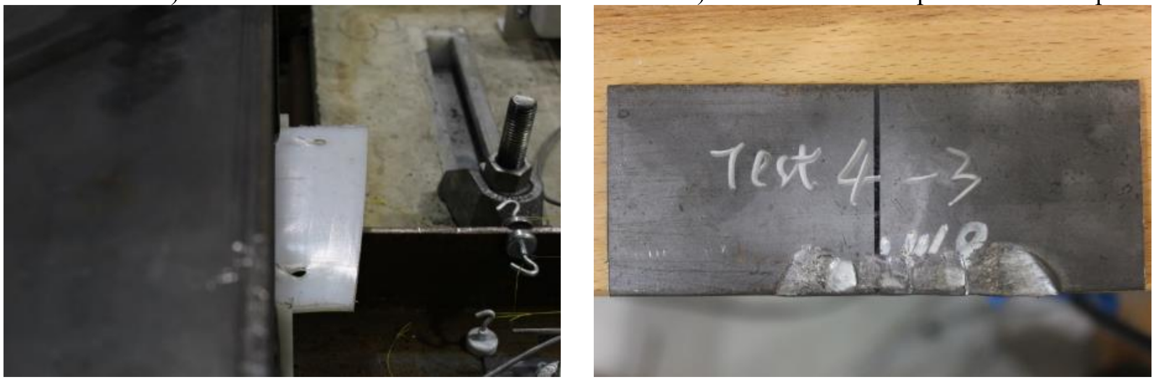

c) Teflon torn off

d) Shim crushed

Figure 4.27 Observations in Specimen 4-M24-2C-RH-LM-S

Test 7-M24-3C-RH-LM

Compared to Specimen 2, three channels, rather than two channels, were embedded in the concrete plank. The load-slip curve for Specimen 7-M24-3C-RH-LM is shown in Figure 4.28 using the average slip measurement from the string pots. Based on this curve, the slip load defined at 0.02 in. slip is about 113.2 kips. However, the slip load is only 87.0 kips when the readout from linear potentiometer 1 and 2 is 0.02 in. The peak load, which occurs at a slip of 0.30 in., is 130.1 kips. The system can still retain about 80% of the peak load even at a slip of 5 in.

Linear potentiometers 1 and 2 first detected slip of the clamps, but the remaining linear potentiometers and string pots did not read slip until sensors 1 and 2 displayed a slip of 0.04 in. and 0.08 in., respectively. During the test, concrete cracks emerged behind Clamps 1 and 3 at a slip of 0.32 in., and the cracks became wider as the slip increased. At approximately the same slip, rotation was first found for the clamps on the north side, and the south clamps remained still, as depicted in Figure 4.29a. Hence, at the service slip level and design slip level, rotation of the clamps and cracking in the concrete plank are not anticipated. As the test continued, the south clamps started to rotate, but the rotation was always less than that of the north clamps. Similar to Test 4, due to the frictional force induced by the steel beam bearing against the west guide, the Teflon sheet was torn off, and the test was terminated at 5.12 in. slip. After dismantling the specimen, cracks, which were deeper and wider than those found in other tests, were discovered behind the rear clamps (i.e., Clamps 5 and 6) and underneath the steel beam. The dismantled concrete specimen also revealed that the lip of the rear channel was significantly bent due to friction, which is a unique observation among all the tests (see Figure 4.29b).

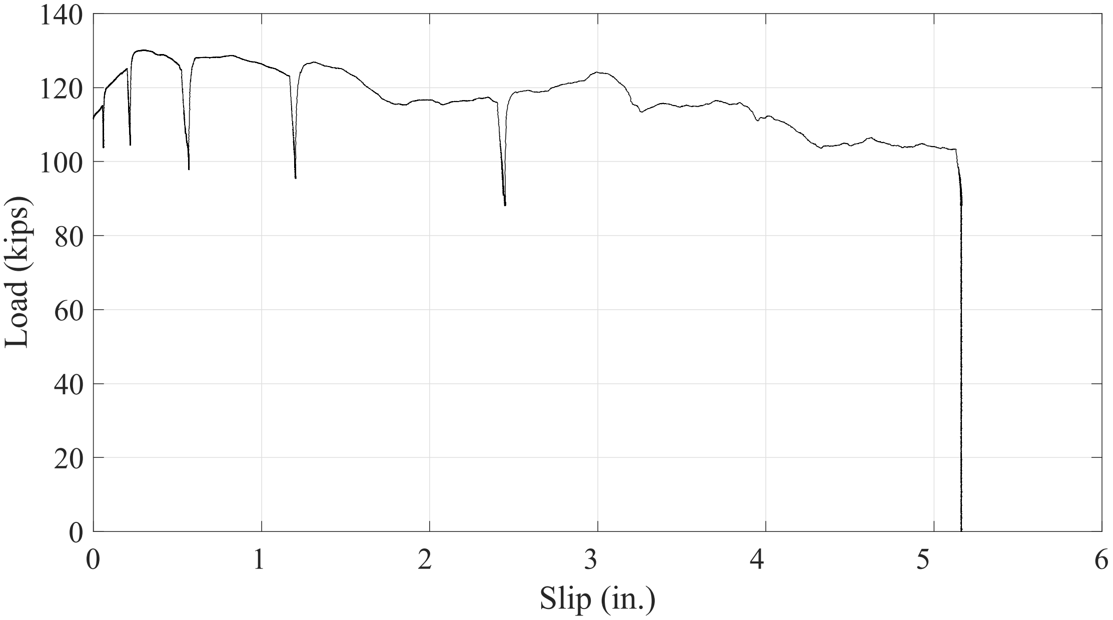

Figure 4.28 Load-slip curve of Specimen 7-M24-3C-RH-LM

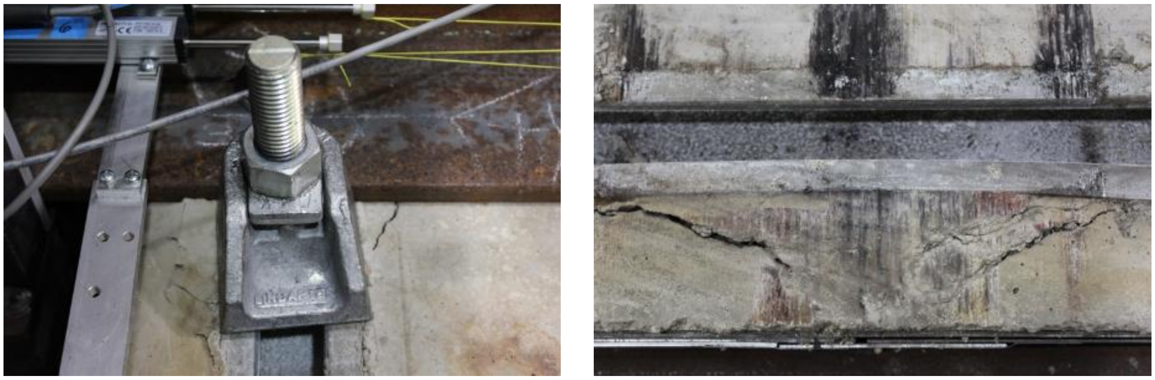

a) Concrete crack and rotation of Clamp 1 at 0.32 in. slip

b) Concrete crack and bent channel lip adjacent to rear clamps

Figure 4.29 Observations in Specimen 7-M24-3C-RH-LM

Test 9-M20-2C-RH-LM

Compared to Specimen 2, M20 bolts and clamps were tested in this specimen. The load-slip curve for Specimen 9-M20-2C-RH-LM is shown in Figure 4.30 using the average slip measurement from the string pots. The slip load defined at 0.02 in. slip is about 36.5 kips. The peak load, which occurs at a slip of 0.54 in., is around 55.3 kips. Unlike the M24 bolts which retained most of their strength at large slips, the load started to drop after 0.68 in. slip until the end of the test. At the same slip level, the M20 clamps in Test

9-M20-2C-RH-LM rotated more than the M24 clamps in Test 2-M24-2C-RH-LM. This is due to the channel lips (which are the same size for all tests) not being adequately large to support the M20 clamps as fully as the M24 clamps are supported, or due to the contact of the clamp teeth with the steel flange having too small an area compared to the M24 clamp. It could be deduced that this motion of the clamps have reduced the bolt tension, thus resulting in the reduction in the clamping strength of the specimen. Redesigning the M20 clamps and utilizing appropriately sized channels may mitigate the strength degradation of the smaller clamps at large slips. However, if used in composite beams, the descending branch illustrated in Figure 4.30 is not a concern, as the slip at which the load starts to drop is much larger than the ultimate slip normally seen in composite beams.

Cracks, shown in Figure 4.31a, appeared behind all four clamps when the slip was 0.02 in., and they became wider as the beam moved. This indicates that cracks could initiate even at the service slip level. As illustrated in Figure 4.31b, rotation of clamps was noticeable at a slip of 0.16 in., which occurred much earlier than the M24 bolt tests. The rotation of clamps at 0.32 in. slip is shown in Figure 4.31c. Because of their relatively small sizes, the M20 clamps could not hold their positions as stably as the M24 clamps. As depicted in Figure 4.31d, clamp 3 was first disengaged when the slip was close to 2.56 in., followed by Clamps 1 and 4 before reaching a slip of 5.12 in. Only Clamp 2 maintained its position during the whole test. Due to safety concern for the test rig, the test was terminated when the slip was about 10 in.

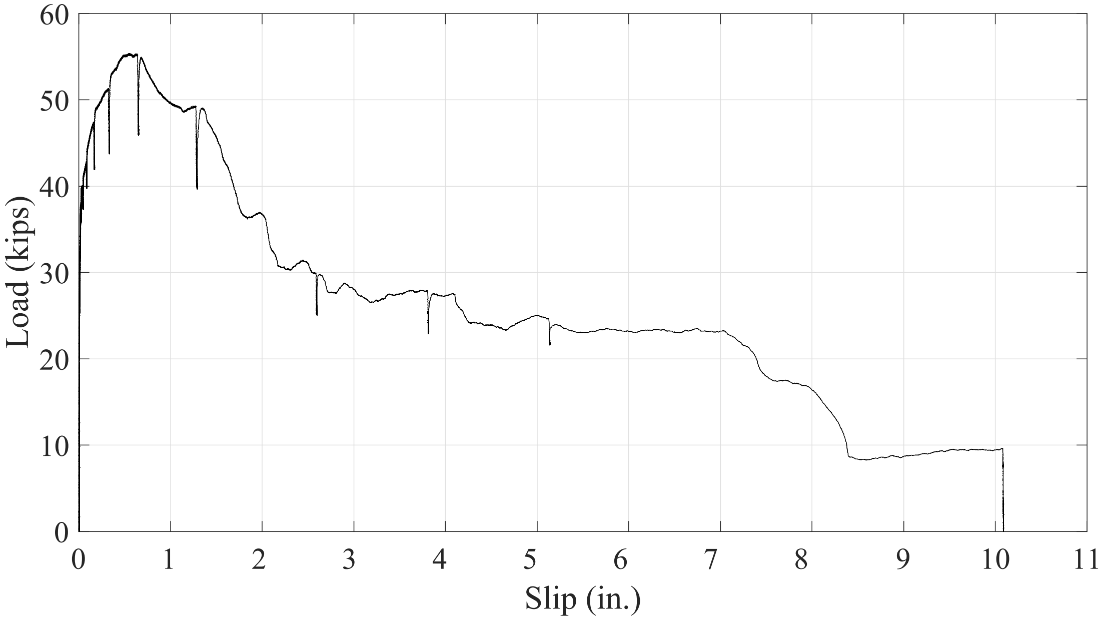

Figure 4.30 Load-slip curve of Specimen 9-M20-2C-RH-LM

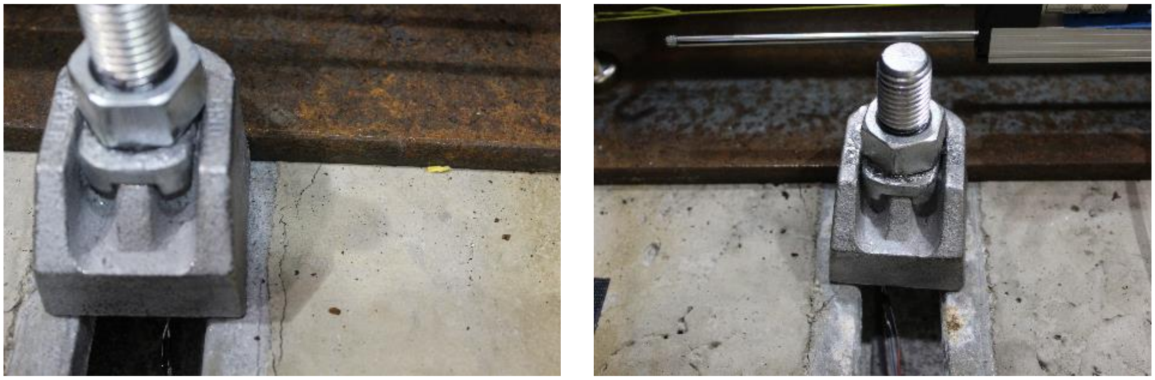

a) Crack at Clamp 3 at 0.02 in. slip

b) Rotation of Clamp 4 at 0.16 in. slip

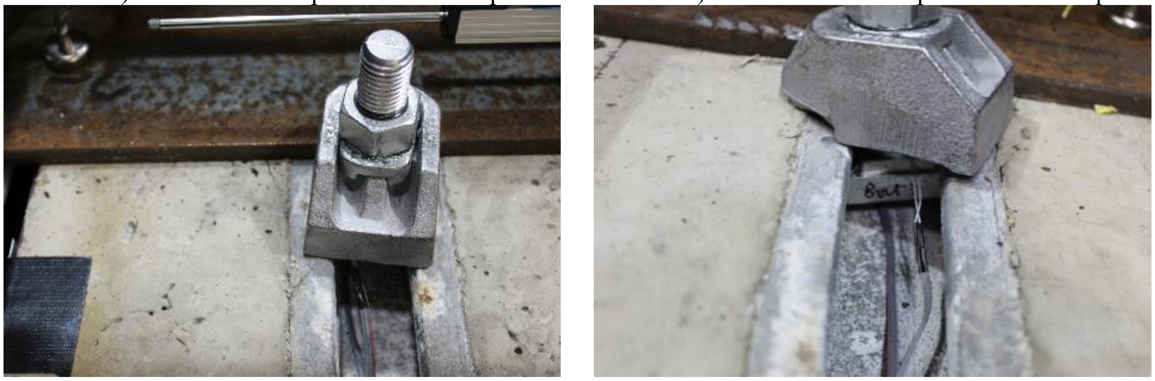

c) Rotation of Clamp 4 at 0.32 in. slip

d) Complete disengagement of Clamp 3 at 2.56 in. slip

Figure 4.31 Observations in Specimen 9-M20-2C-RH-LM

The monotonic test results are summarized in Table 4.5. Elastic stiffness is defined as the secant stiffness at the slip load. For each test, the slip load and peak load are both normalized relative to Test 2-M24-2C-RH-LM, which is regarded as the baseline specimen. The selected steel shims do not exhibit desirable behavior at large slips due to a stick-slip mechanism; however, the use of the shims neither reduces the slip load or peak load of the specimen nor affects the behavior of the system at slips comparable to those normally seen in composite beams. The slip strength and peak strength of Test 7-M24-3C-RH-LM in which three channels are used are approximately 50% higher than those of Test 2-M24-2C-RH-LM, which uses two channels, implying that the shear force can be distributed among the clamps. Although wide cracks are seen in Test 7-M24-3C-RH-LM, they do not reduce the specimen strength. In Test 9-M20-2C-RH-LM, M20 bolts are tested, and the strength is about 60% of the standard M24 bolt specimen (i.e., Test 2-M24-2C-RH-LM). The M20 bolts cannot maintain their strength as well as the M24 bolts, as is indicated by the load decrease at larger slips. Nonetheless, the strength degradation starts at a slip that is much larger than the maximum slip measured in the composite beam tests presented in Chapter 5.

Table 4.5 Summary of monotonic pushout test results

Monotonic test	Initial stiffness (kips/in.)	Slip load (kips)		Peak load (kips)			Peak load/ Slip load	Load at 5 in. slip (kips)	
		Absolute	Normalized	Absolute	Normalized	Slip (in.)		Absolute	Percentage of peak load
2-M24-2C-RH-LM	3040	60.8	1.00	88.5	1.00	1.12	1.46	68.9	78%
4-M24-2C-RH-LM-S	2825	56.5	0.93	87.9	0.99	0.55	1.56	55.1	63%
7-M24-3C-RH-LM	4350	87.0	1.43	130.1	1.47	0.30	1.50	104.0	80%
9-M20-2C-RH-LM	1825	36.5	0.60	55.3	0.62	0.54	1.52	24.9	45%

4.5.4.2 *Cyclic specimens*

The following sign convention is defined for the slip and load measurements: the load is positive when the beam is under compression; the slip is positive when the beam moves west.

If the clamps are intended to transfer in-plane diaphragm force to lateral load-resisting systems, the slip demand on the clamps needs to be determined and the behavior of the clamps could be evaluated accordingly. This is similar to the assessment of the monotonically loaded pushout specimens at slip levels that are correlated to composite beams. The slips used to evaluate the behavior of the cyclically loaded pushout specimens should be obtained from dynamic analysis or shake table testing of composite diaphragms designed with clamps, which are beyond the scope of this research. Meanwhile, research concerning the slip demand on steel headed stud anchors in conventional composite diaphragms is also absent. As a result, the three slip levels are unknown, namely, the service load slip, design load slip and ultimate slip. Therefore, the performance of the cyclic specimens is conservatively assessed at slips less than 1 in., much greater than the slip capacity of 3/4 in. shear studs, which is approximately 0.29 in., as discussed in Section 4.5.4.3.

In current design practice, after calculating the seismic demand on a diaphragm, the shear connectors are designed to transfer the inertia forces from the diaphragm to the LFRS. In Appendix H.1, two prototype structures are used as examples to show that the clamps designed for the gravity loading are sufficient to transfer the inertia forces to the perimeter frames. Because the shear force demand on the clamps due to the diaphragm forces is much smaller than the capacity of the clamps, the slip of the clamps could be tiny at design earthquakes.

For each specimen, the overall load-slip curve is plotted which is followed by a second graph focusing on a slip within 1 in. As shown in the second graph for each specimen, the behavior of the clamping system is excellent for peak slips that are likely to be typical demand ranges for steel headed stud anchors commonly used in traditional composite diaphragms, such as within 1 in. of slip.

Test 3-M24-2C-RL-LC

The load-slip curve for Specimen 3-M24-2C-RL-LC is shown in Figure 4.32 using the average slip measurement from the string pots. The plateau load at the second cycle of each slip level decreased compared to that of the first cycle, particularly at larger slips. As more and more cycles were completed, the teeth of the clamps and the steel flanges began to wear down, possibly reducing the coefficient of friction and the normal force and shear resistance between the components after extensive slip had occurred. At each cycle, the load first stabilized, and then increased considerably at the maximum slip because the clamp teeth engaged with a portion of the steel beam flange that had not been damaged in earlier cycles.

This is the only specimen designed with the light reinforcement pattern, and premature concrete failure was anticipated. The slip load, which is necessary to define the first three load magnitudes in the cyclic loading protocol, adopted that obtained from Test 2-M24-2C-RH-LM, since no corresponding monotonic specimen exists for Specimen 3. Starting at a slip of 0.06 in., diagonal concrete cracking adjacent to clamps 2 and 4 was discovered. The cracks opened when the beam was loaded in the compressive or west direction, and closed when the beam was loaded in the tensile or east direction. At a slip of 0.64 in., the clamps rotated slightly, as shown in Figure 4.33a. Illustrated in Figure 4.33b, clamp 1 was almost disengaged at the end of the test, while the others seemed to maintain their positions well. The test was terminated at a slip of 5.12 in., which is the maximum slip that could be measured by the string pots was reached.

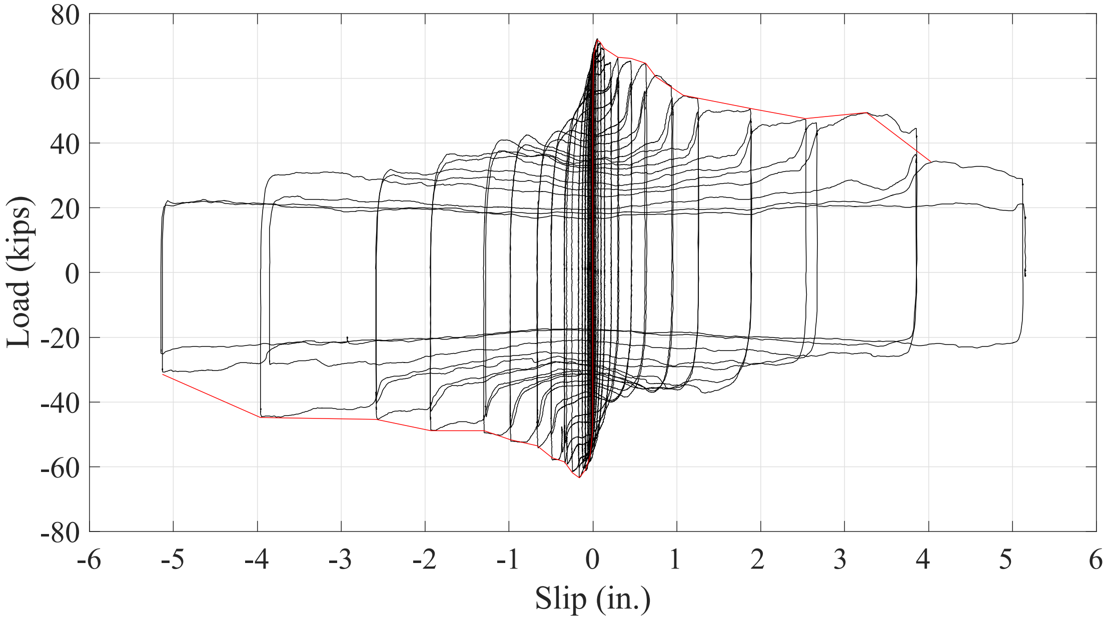

a) Overall behavior

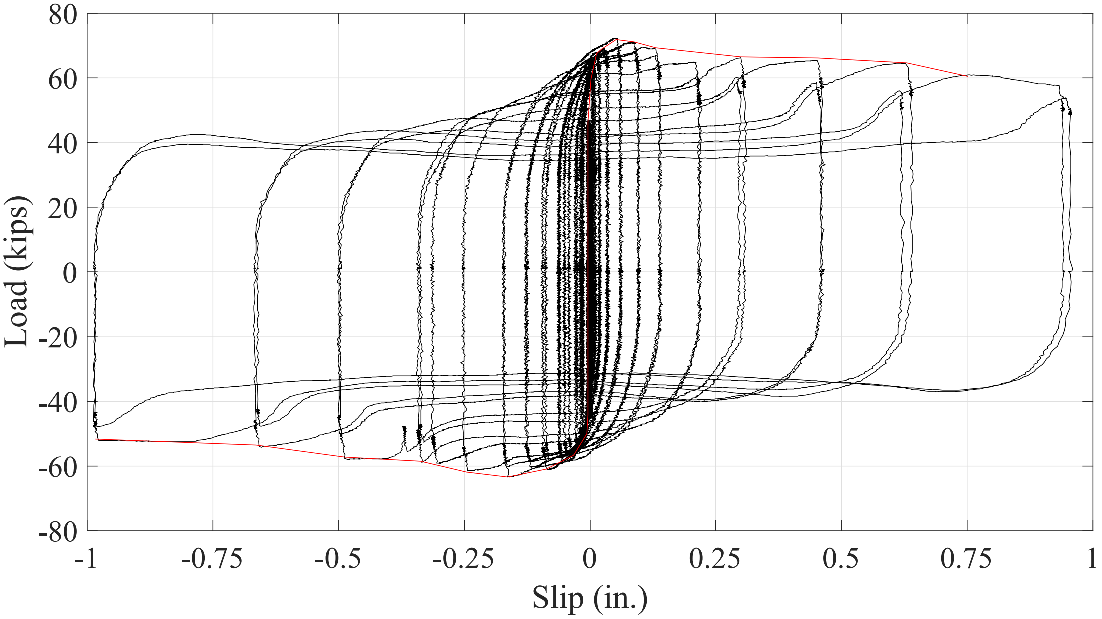

b) Behavior within 1 in. slip

Figure 4.32 Load-slip curve of Specimen 3-M24-2C-RL-LC

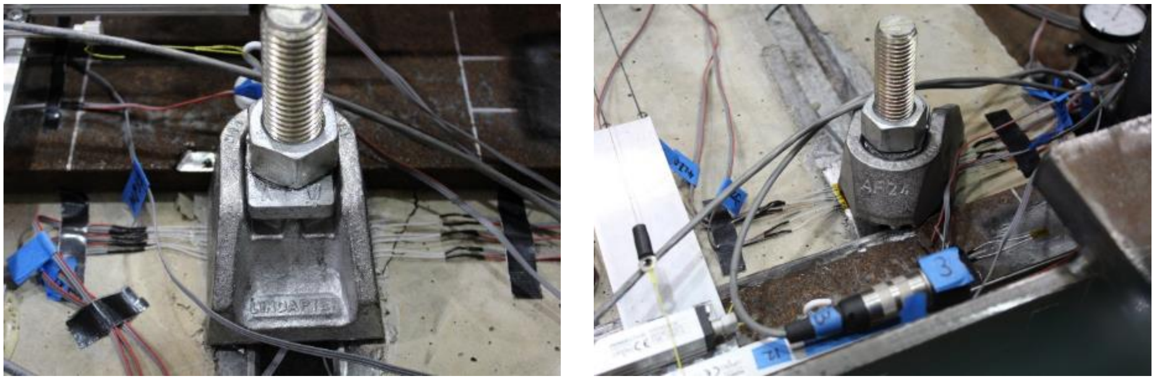

a) Rotation of Clamp 2 at 0.64 in. slip b) Clamp 1 almost disengaged at 5.12 in. slip

Figure 4.33 Observations in Specimen 3-M24-2C-RL-LC

Test 5-M24-2C-RH-LC

This specimen is the corresponding cyclic specimen for Specimen 2-M24-2C-RH-LM which is the baseline specimen. The load-slip curve for Specimen 5-M24-2C-RH-LC is shown in Figure 4.34 using the average slip measurement from the string pots. The load-slip plot of this specimen is very similar to that of Specimen 3-M24-2C-RL-LC.

This specimen behaved in a similar manner as Test 3-M24-2C-RL-LC. As shown in Figure 4.35a, rotation of the clamps was discerned at a slip of 0.48 in. Figure 4.35b illustrates the rotation at a slip of 1.28 in. Wearing off of the flange was observed as the beam moves further. It is noted that clamps 2 and 4 occasionally rotated in opposite directions because the rotation of the clamps did not synchronize with the displacement of the beam, especially at larger slips. At a slip of 1.92 in., clamps 3 and 4 started to lose contact, and clamp 4 was completely disengaged in the very last cycle (5.12 in. slip). The test was terminated at a slip of 5.12 in., which is the maximum slip that could be measured by the string pots was reached.

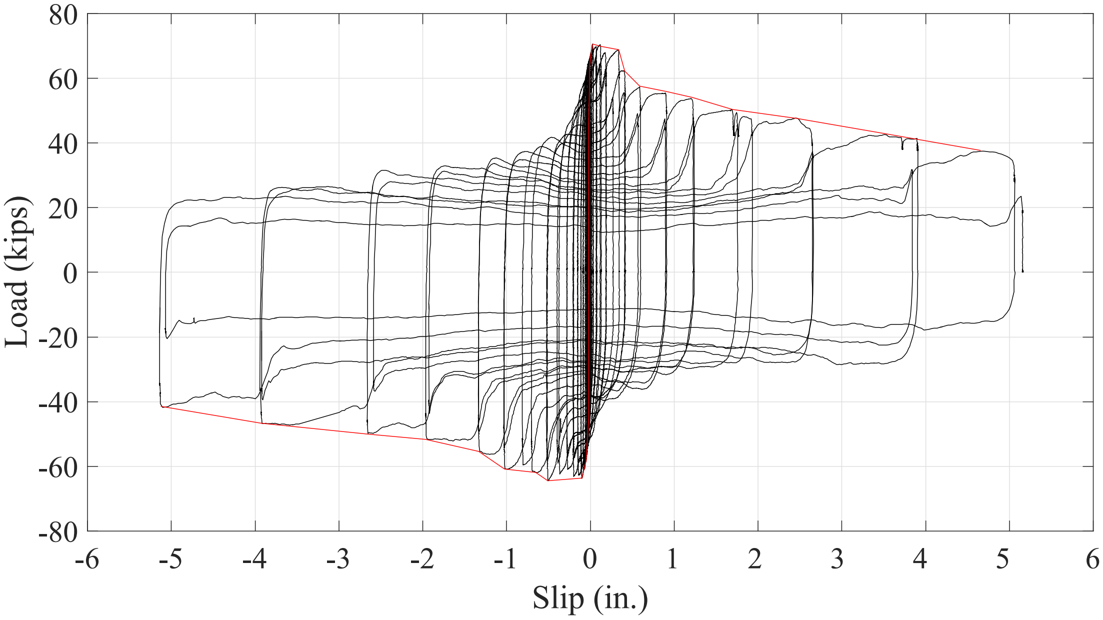

a) Overall behavior

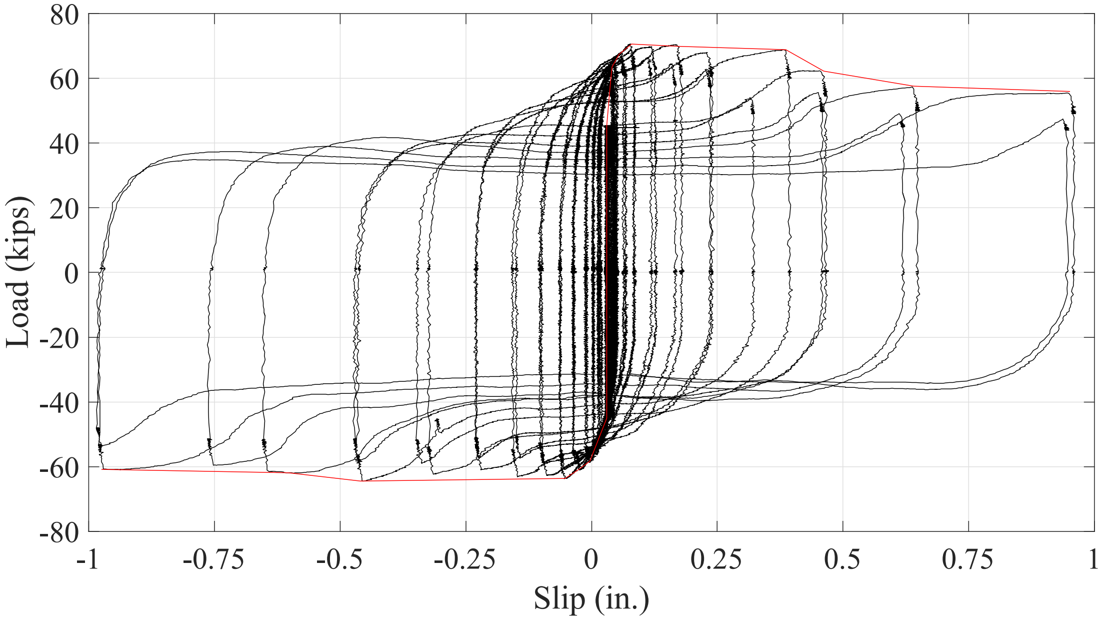

b) Behavior within 1 in. slip

Figure 4.34 Load-slip curve of Specimen 5-M24-2C-RH-LC

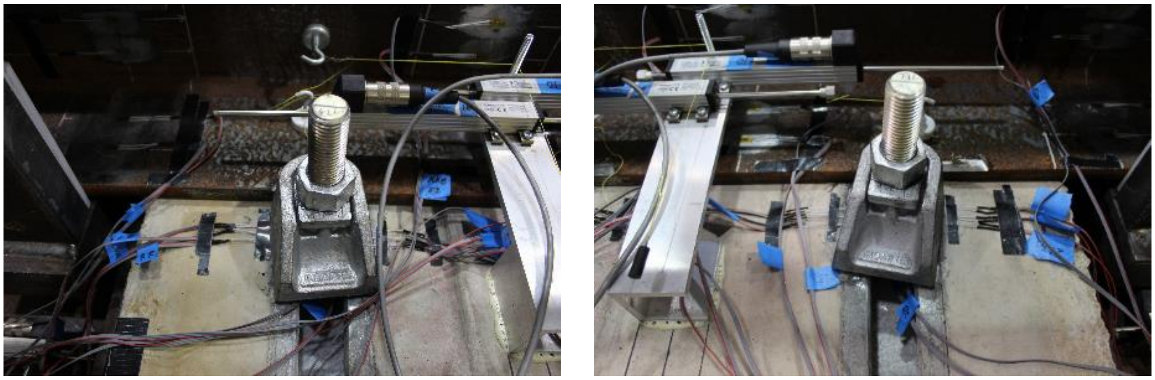

a) Rotation of Clamp 4 at 0.32 in. slip b) Rotation of Clamp 2 at 1.28 in. slip

Figure 4.35 Observations in Specimen 5-M24-2C-RH-LC

Test 6-M24-2C-RH-LC-S

This specimen is the corresponding cyclic specimen for Specimen 4-M24-2C-RH-LM-S. Shims were used in these tests. The load-slip curve for Specimen 6-M24-2C-RH-LC-S is shown in Figure 4.36 using the average slip measurement from the string pots. The readouts from the string pots are asymmetric, and the plot is shifted towards the negative slip direction. On the whole, this curve has a similar shape as the other cyclic specimens, but distinct differences can be seen. As indicated by the sudden load drop and slip measurement change in the load-slip plot, the stick-slip phenomenon persisted, similar to what occurred in Test 4-M24-2C-RH-LM-S, and load oscillation usually ensued. The load reduced dramatically once the shims started to separate from the clamps consecutively, and ultimately the capacity approached zero after all the shims were detached.

Since one bolt head fractured in Test 4-M24-2C-RH-LM-S, the corresponding monotonic test, bolts were instrumented in Test 6. The strains in bolt 4 reached about 0.04 after one and two-thirds turns, and pretensioning of this bolt was stopped due to concern of bolt fracture. The strains were reasonable for the other bolts after two full turns. During the test, the specimen rotated because of the eccentricity between the actuator force and the reaction from the reaction angle. The specimen jerked when it was unloaded from 42.4 kips (75% of the slip load) to approximately 10 kips in compression. The reason is that the rotated specimen could not return to a level position smoothly. Hence, the sliders shown in Figure 4.16 were reinforced to minimize the vertical movement of the cross beam, which connects the actuators and the test specimen, as well as the overturning of the system during loading.

Concrete cracking first occurred at 0.02 in. slip. When the specimen was loaded to a slip of 0.48 in., a loud noise was heard, followed by a considerable load drop and continuous noise from slip. This signified the initiation of the stick-slip behavior. The strength rebounded shortly, and the load started to oscillate. The subsequent loud noises were always accompanied by sudden changes in the slip measurements. This phenomenon occurred in every following cycle. Shims detached from the clamps one after another at large slips. The sequence and the slip levels are: shim 1 at 1.92 in.; shim 3 at 2.56 in.; shim 4 at 3.84 in.; shim 2 at 3.84 in. Accordingly, the test was terminated. The shims, which were made of A36 steel, were heavily scraped in the test, as indicated in Figure 4.37. As such, hardened steel plates may be recommended for future study.

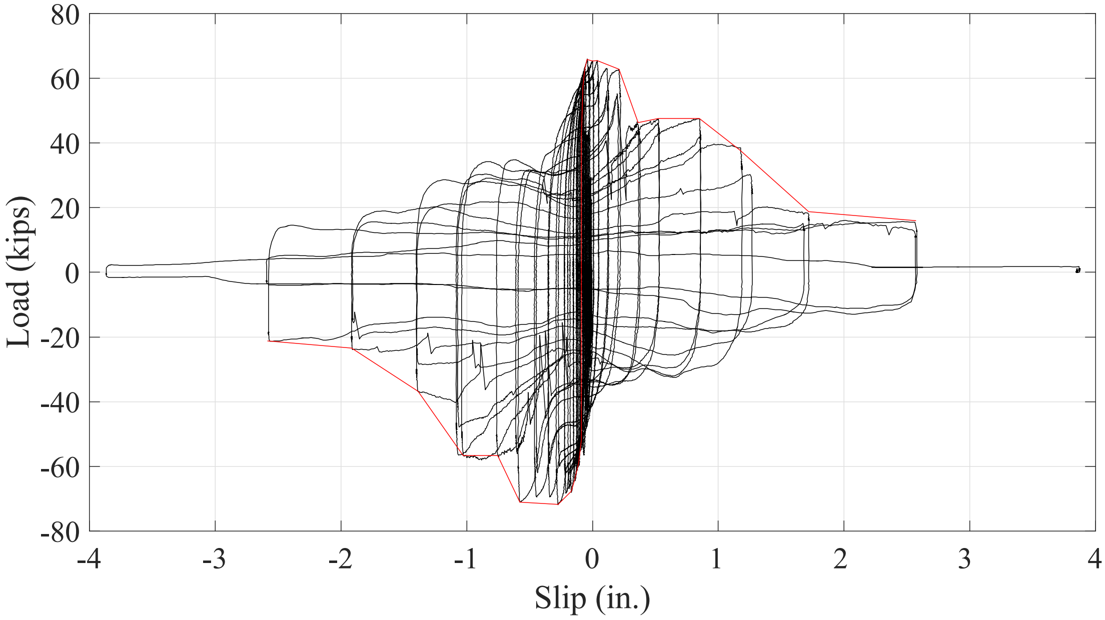

a) Overall behavior

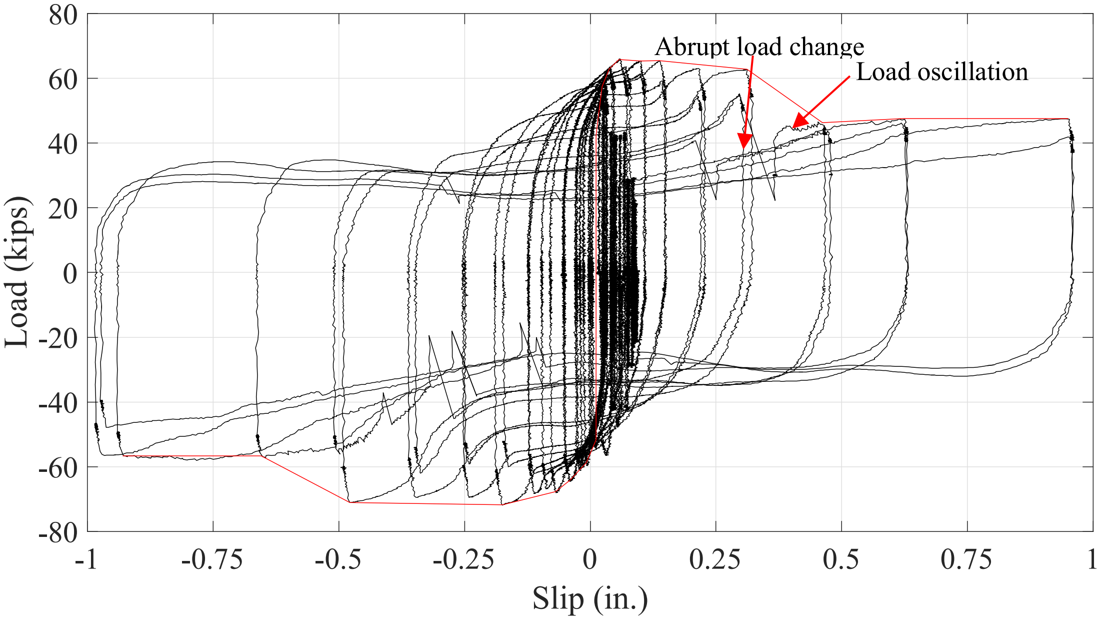

b) Behavior within 1 in. slip

Figure 4.36 Load-slip curve of Specimen 6-M24-2C-RH-LC-S

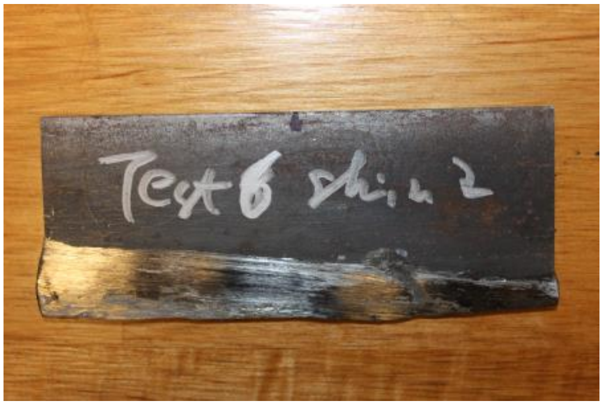

Scraped steel shim

Figure 4.37 Observation in Specimen 6-M24-2C-RH-LC-S

Test 8-M24-3C-RH-LC

This specimen is the corresponding cyclic specimen for Specimen 7-M24-3C-RH-LM. Three channels were embedded in the concrete planks. The load-slip curve for Specimen 8-M24-3C-RH-LC is shown in Figure 4.38 using the average slip measurement from the string pots. Except for the strength, the load-slip curve of this specimen is very similar to those of Specimens 3-M24-2C-RL-LC and 5-M24-2C-RH-LC.

When the slip was 0.03 in., concrete cracks were found at clamps 1 and 2, as illustrated in Figure 4.39a. At 0.06 in. slip, another crack was seen in the neighborhood of clamp 6. At a slip of 0.96 in., rotations of clamps 1, 3, and 6 were observed, as shown in Figure 4.39b. The test was terminated when the maximum slip that could be measured by the string pots was reached.

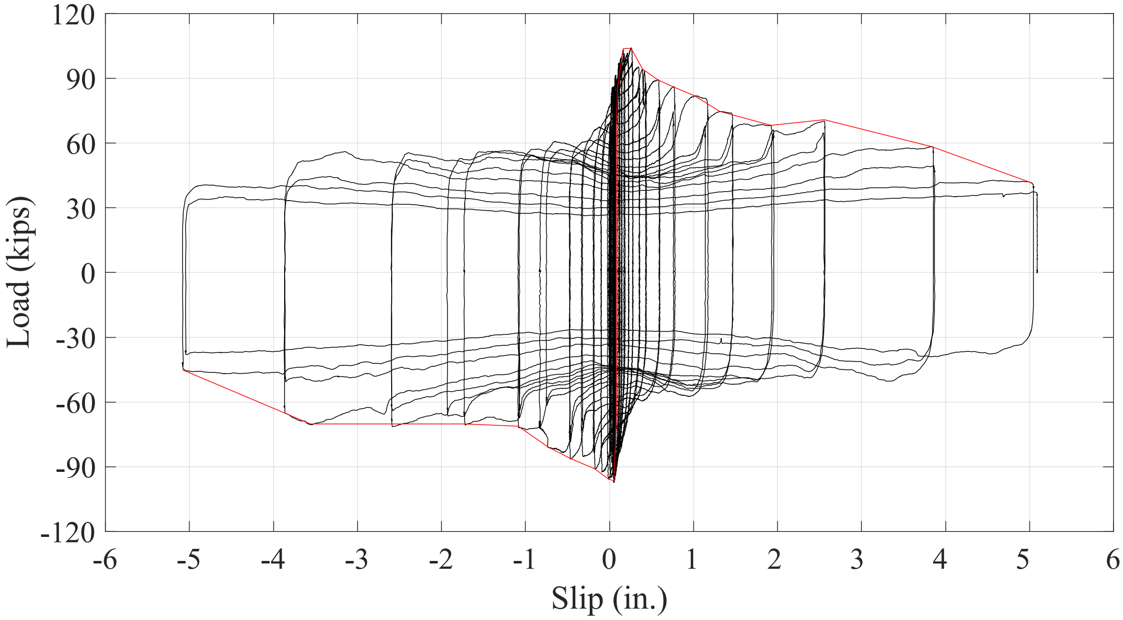

a) Overall behavior

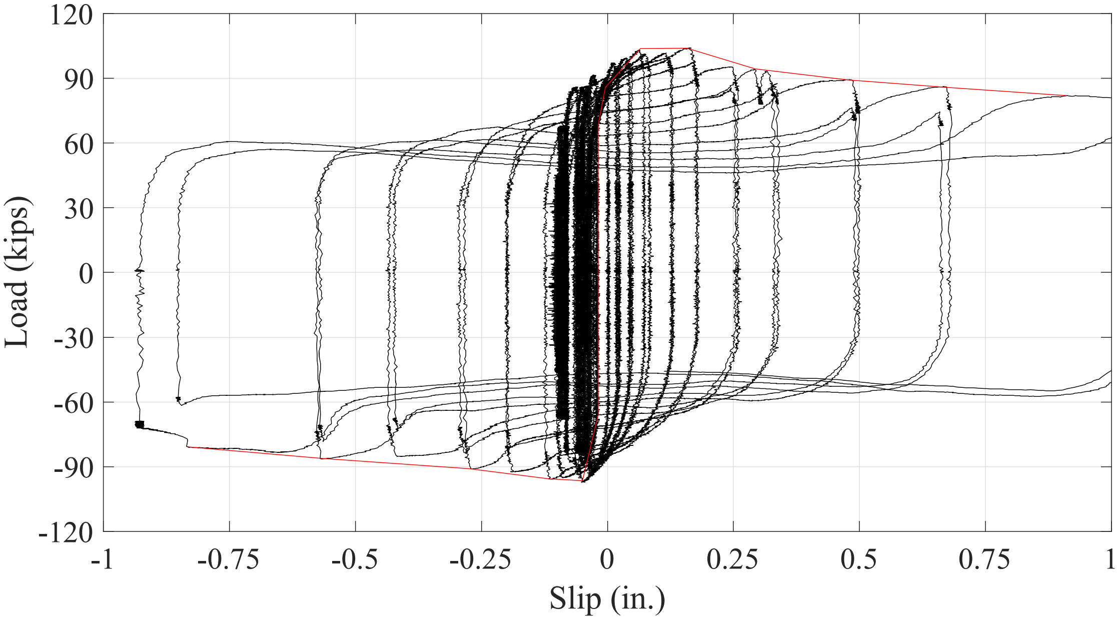

b) Behavior within 1 in. slip

Figure 4.38 Load-slip curve of Specimen 8-M24-3C-RH-LC

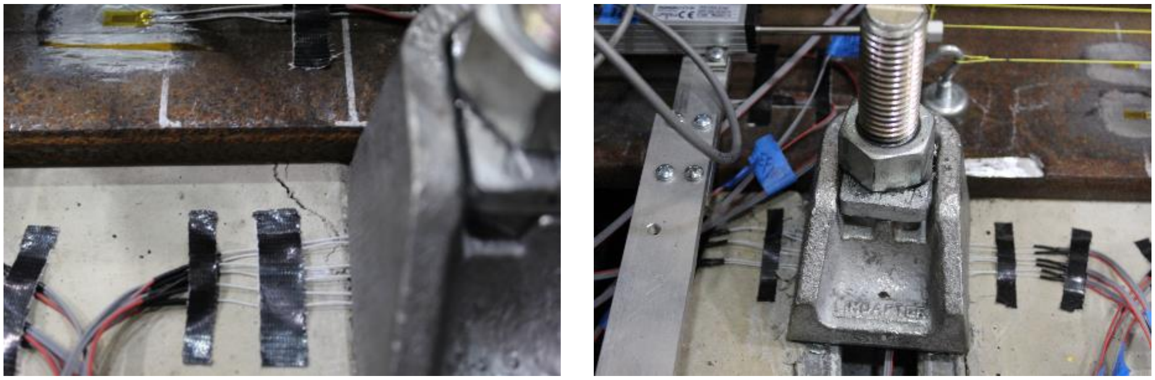
a) Concrete crack adjacent to Clamp 2 b) Rotation of clamp 1 at 0.96 in. slip

Figure 4.39 Observations in Test 8-M24-3C-RH-LC

Test 10-M20-2C-RH-LC

This specimen is the corresponding cyclic specimen for Specimen 9-M20-2C-RH-LM. M20 bolts were tested in these specimens. It was believed that the loss of contact between the clamp teeth and steel beam flange and between the clamp tail and channel lips led to the undesirable strength degradation at large slips in the corresponding monotonic test. Hence, it was decided that steel blocks be inserted into the channels to improve the clamp performance under cyclic loading by supporting the clamp tails once they fell into the channels (see Figure 4.41a). These blocks were finely machined such that they were flush with the channel lips and fitted tightly inside the channels. One and a half turns were still utilized for pretensioning the M20 bolts.

The load-slip curve for Specimen 10-M20-2C-RH-LC is shown in Figure 4.40 using the average slip measurement from the string pots. In this test, the decrease of peak load and plateau load at each cycle was more than that in the M24 bolt testing. Compared to the corresponding monotonic test, Test 9-M20-2C-RH-LM, considerable strength reduction occurred at much larger slips in this test, implying that the inserted steel blocks deferred the pretension loss of the bolts. After all the clamps lost contact with the steel beam, the strength of the system approached zero at 5.12 in. slip.

Hairline cracks first emerged in the concrete specimen at 27.38 kips (75% of slip load), and as the slip increased, existing cracks became wider and additional cracks appeared.

As shown in Figure 4.41b, the clamps began to rotate when the slip was 0.16 in. As a result of the large rotation, the corner of clamp 4 fell into the gap between the channel lips at a slip of 0.96 in., as illustrated in Figure 4.41c. However, the majority of the tail still bore against the block inside the channels, which may defer the decrease of the loading. As the test proceeded, all clamps started to lose contact, and all four clamps were disengaged ultimately, and the concrete slab was no longer clamped to the steel beam (see Figure 4.41d).

The cyclic test results are summarized in Table 4.6. For the two cycles of the same slip level, the strength generally degrades less in the first cycle than the second cycle. In each test, the peak load and plateau load of a cycle in a loading direction are normalized relative to the peak load of the overall load-slip curve in that loading direction as well as the peak strength of the corresponding monotonic specimen. Figure 4.42 depicts the strength reduction variation with slip. The peak load decreases roughly linearly, while the plateau load declines approximately exponentially.

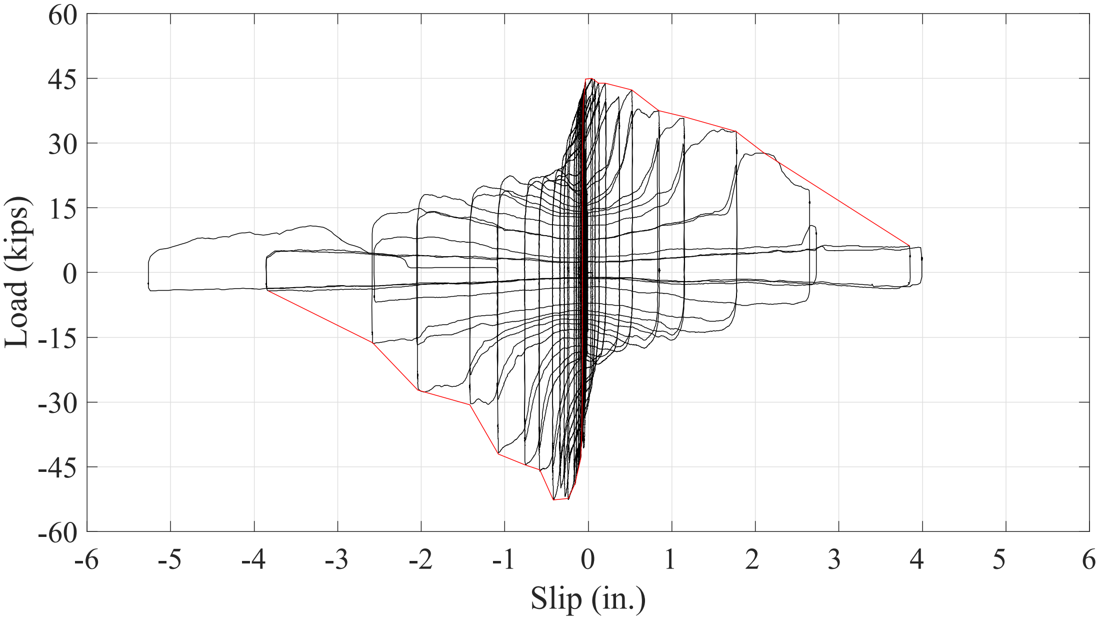

a) Overall behavior

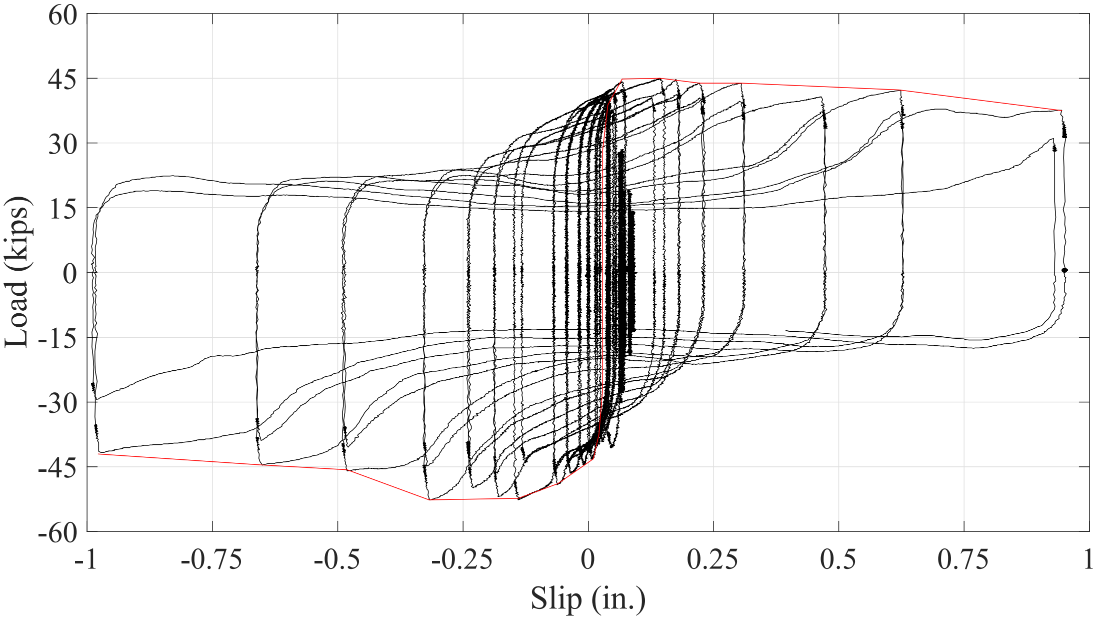

b) Behavior within 1 in. slip

Figure 4.40 Load-slip curve of Specimen 10-M20-2C-RH-LC

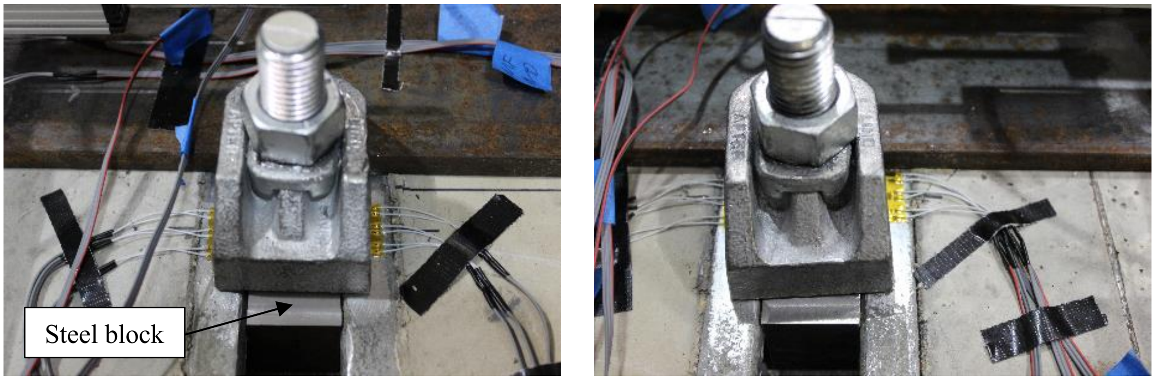

a) Steel block inserted into channel b) Rotation of clamp 4 at 0.16 in. slip

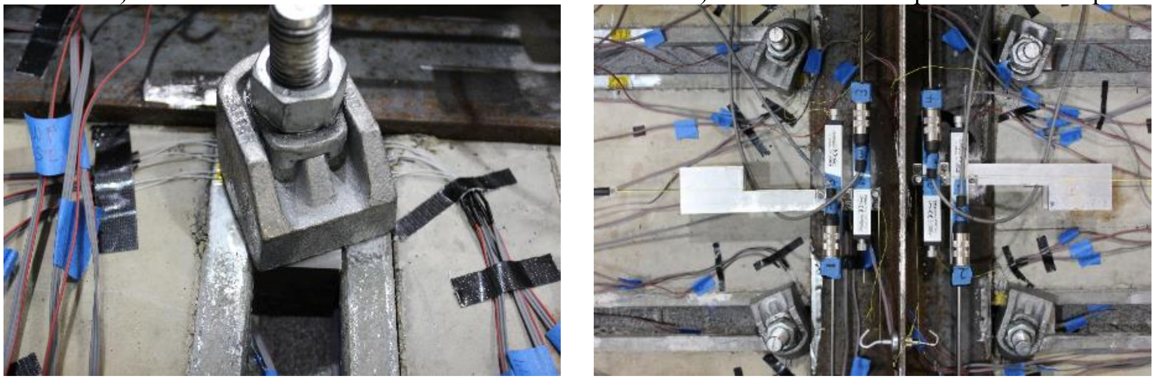

c) Rotation of clamp 4 at 0.96 in. slip d) Complete detachment of clamps with beam

Figure 4.41 Observations in Specimen 10-M20-2C-RH-LC

Table 4.6 Summary of cyclic pushout test results

Cyclic test	Slip (in.)	Peak load (kips)								Plateau load (kips)							
		Positive slip				Negative slip				Positive slip				Negative slip			
		Cycle 1	Cycle 2	Ratio 1	Ratio 2	Cycle 1	Cycle 2	Ratio 1	Ratio 2	Cycle 1	Cycle 2	Ratio 1	Ratio 2	Cycle 1	Cycle 2	Ratio 1	Ratio 2
3-M24-2C-RL-LC	0.08	72.2	69.6	1.00	0.96	-58.4	-61.2	0.92	0.97	65.3	63.3	0.90	0.88	-53.0	-53.8	0.84	0.85
				0.82	0.79			0.66	0.69			0.74	0.72			0.60	0.61
	0.12	70.9	68.2	0.98	0.94	-60.2	-58.5	0.95	0.92	64.3	62.5	0.89	0.87	-54.2	-54.3	0.86	0.86
				0.80	0.77			0.68	0.66			0.73	0.71			0.61	0.61
	0.16	69.4	66.9	0.96	0.93	-63.3	-60.2	1.00	0.95	64.0	61.5	0.89	0.85	-57.7	-55.8	0.91	0.88
				0.78	0.76			0.72	0.68			0.72	0.69			0.65	0.63
	0.24	64.9	60.0	0.90	0.83	-61.4	-59.1	0.97	0.93	60.6	55.2	0.84	0.76	-54.6	-52.5	0.86	0.83
				0.73	0.68			0.69	0.67			0.68	0.62			0.62	0.59
	0.32	66.3	59.8	0.92	0.83	-58.7	-52.6	0.93	0.83	55.0	50.7	0.76	0.70	-48.1	-45.0	0.76	0.71
				0.75	0.68			0.66	0.59			0.62	0.57			0.54	0.51
	0.48	65.3	58.5	0.90	0.81	-57.9	-50.0	0.91	0.79	46.9	42.4	0.65	0.59	-40.9	-37.7	0.65	0.60
				0.74	0.66			0.65	0.56			0.53	0.48			0.46	0.43
	0.64	64.5	55.6	0.89	0.77	-54.0	-47.8	0.85	0.76	41.7	39.3	0.58	0.54	-35.9	-34.3	0.57	0.54
				0.73	0.63			0.61	0.54			0.47	0.44			0.41	0.39
	0.96	60.9	53.6	0.84	0.74	-52.4	-47.9	0.83	0.76	36.9	34.7	0.51	0.48	-32.7	-31.5	0.52	0.50
				0.69	0.61			0.59	0.54			0.42	0.39			0.37	0.36
	1.28	54.5	49.3	0.75	0.68	-50.2	-44.2	0.79	0.70	35.0	33.1	0.48	0.46	-30.9	-31.4	0.49	0.50
				0.62	0.56			0.57	0.50			0.40	0.37			0.35	0.35
	1.92	50.6	47.4	0.70	0.66	-48.7	-42.5	0.77	0.67	32.2	31.2	0.45	0.43	-30.5	-28.8	0.48	0.45
				0.57	0.54			0.55	0.48			0.36	0.35			0.34	0.33
	2.56	47.5	46.1	0.66	0.64	-45.1	-39.6	0.71	0.63	27.9	25.8	0.39	0.36	-28.1	-26.2	0.44	0.41
				0.54	0.52			0.51	0.45			0.32	0.29			0.32	0.30
	3.84	49.4	35.9	0.68	0.50	-44.7	-28.8	0.71	0.45	23.6	19.7	0.33	0.27	-23.2	-19.6	0.37	0.31
				0.56	0.41			0.51	0.33			0.27	0.22			0.26	0.22
	5.12	34.4	21.3	0.48	0.30	-30.8	-24.9	0.49	0.39	18.4	16.8	0.25	0.23	-17.8	-17.5	0.28	0.28
				0.39	0.24			0.35	0.28			0.21	0.19			0.20	0.20
5-M24-2C-RH-LC	0.08	70.6	68.7	1.00	0.97	-63.6	-60.8	0.99	0.94	62.7	61.5	0.89	0.87	-52.8	-54.1	0.82	0.84
				0.80	0.78			0.72	0.69			0.71	0.69			0.60	0.61
	0.12	69.7	66.3	0.99	0.94	-62.5	-58.7	0.97	0.91	62.0	59.2	0.88	0.84	-54.2	-53.5	0.84	0.83
				0.79	0.75			0.71	0.66			0.70	0.67			0.61	0.60
	0.16	70.4	64.4	1.00	0.91	-63.0	-57.3	0.98	0.89	60.3	56.6	0.85	0.80	-54.6	-52.1	0.85	0.81
				0.80	0.73			0.71	0.65			0.68	0.64			0.62	0.59
	0.24	67.9	62.8	0.96	0.89	-60.9	-57.2	0.95	0.89	55.2	52.7	0.78	0.75	-50.7	-48.4	0.79	0.75
				0.77	0.71			0.69	0.65			0.62	0.60			0.57	0.55

	0.32	68.8	54.1	0.97	0.77	-62.3	-58.9	0.97	0.91	52.9	45.2	0.75	0.64	-47.4	-44.1	0.74	0.68
				0.78	0.61			0.70	0.67			0.60	0.51			0.54	0.50
	0.48	62.3	55.6	0.88	0.79	-64.4	-58.2	1.00	0.90	42.3	39.1	0.60	0.55	-41.1	-38.3	0.64	0.59
				0.70	0.63			0.73	0.66			0.48	0.44			0.46	0.43
	0.64	57.2	48.6	0.81	0.69	-62.0	-59.5	0.96	0.92	37.2	35.1	0.53	0.50	-38.0	-36.4	0.59	0.57
				0.65	0.55			0.70	0.67			0.42	0.40			0.43	0.41
	0.96	55.4	47.3	0.78	0.67	-60.9	-53.6	0.95	0.83	32.6	30.1	0.46	0.43	-33.3	-31.3	0.52	0.49
				0.63	0.53			0.69	0.61			0.37	0.34			0.38	0.35
	1.28	53.7	46.8	0.76	0.66	-56.3	-49.0	0.87	0.76	28.4	26.9	0.40	0.38	-30.1	-29.3	0.47	0.45
				0.61	0.53			0.64	0.55			0.32	0.30			0.34	0.33
	1.92	50.4	48.2	0.71	0.68	-52.2	-43.1	0.81	0.67	25.7	25.3	0.36	0.36	-28.7	-27.8	0.45	0.43
				0.57	0.54			0.59	0.49			0.29	0.29			0.32	0.31
	2.56	47.6	36.7	0.67	0.52	-49.7	-36.4	0.77	0.57	23.7	22.6	0.34	0.32	-26.5	-23.5	0.41	0.36
				0.54	0.41			0.56	0.41			0.27	0.26			0.30	0.27
	3.84	42.6	31.6	0.60	0.45	-47.2	-38.8	0.73	0.60	20.0	20.5	0.28	0.29	-21.1	-18.7	0.33	0.29
				0.48	0.36			0.53	0.44			0.23	0.23			0.24	0.21
	5.12	37.4	23.1	0.53	0.33	-41.9	-19.8	0.65	0.31	17.5	13.2	0.25	0.19	-14.0	-11.4	0.22	0.18
				0.42	0.26			0.47	0.22			0.20	0.15			0.16	0.13
6-M24-2C-RH-LC-S	0.12	65.4	61.3	0.99	0.93	-68.2	-62.0	0.95	0.86	56.7	54.9	0.86	0.83	-59.6	-54.9	0.83	0.76
				0.74	0.70			0.78	0.71			0.65	0.62			0.68	0.62
	0.16	65.5	59.2	1.00	0.90	-71.8	-60.0	1.00	0.84	56.5	53.4	0.86	0.81	-57.0	-53.8	0.79	0.75
				0.75	0.67			0.82	0.68			0.64	0.61			0.65	0.61
	0.24	63.0	54.6	0.96	0.83	-69.4	-59.1	0.97	0.82	50.8	44.4	0.77	0.67	-51.8	-46.7	0.72	0.65
				0.72	0.62			0.79	0.67			0.58	0.51			0.59	0.53
	0.32	62.6	55.0	0.95	0.84	-69.5	-61.8	0.97	0.86	41.7	35.9	0.63	0.55	-46.0	-38.5	0.64	0.54
				0.71	0.63			0.79	0.70			0.47	0.41			0.52	0.44
	0.48	55.0	43.9	0.84	0.67	-71.1	-54.8	0.99	0.76	33.1	32.6	0.50	0.50	-33.9	-33.5	0.47	0.47
				0.63	0.50			0.81	0.62			0.38	0.37			0.39	0.38
	0.64	47.7	45.8	0.72	0.70	-56.6	-57.9	0.79	0.81	31.3	27.4	0.48	0.42	-34.6	-32.9	0.48	0.46
				0.54	0.52			0.64	0.66			0.36	0.31			0.39	0.37
	0.96	47.6	41.9	0.72	0.64	-56.5	-47.8	0.79	0.67	24.3	23.8	0.37	0.36	-28.4	-25.6	0.40	0.36
				0.54	0.48			0.64	0.54			0.28	0.27			0.32	0.29
	1.28	39.6	30.3	0.60	0.46	-40.1	-29.8	0.56	0.42	21.4	18.2	0.33	0.28	-23.8	-20.5	0.33	0.29
				0.45	0.34			0.46	0.34			0.24	0.21			0.27	0.23
	1.92	20.2	15.0	0.31	0.23	-24.7	-20.1	0.34	0.28	13.2	11.3	0.20	0.17	-16.9	-14.5	0.24	0.20
				0.23	0.17			0.28	0.23			0.15	0.13			0.19	0.16
	2.56	15.9	15.7	0.24	0.24	-21.4	-5.4	0.30	0.08	11.1	9.8	0.17	0.15	-9.2	-5.2	0.13	0.07
				0.18	0.18			0.24	0.06			0.13	0.11			0.10	0.06

	3.84	6.7		0.10		-5.8		0.08		5.9		0.09		-5.2		0.07	
				0.08				0.07				0.07				0.06	
8-M24-3C-RH-LC	0.16	104.0	97.4	1.00	0.94	-95.6	-84.4	0.99	0.87	92.8	85.4	0.89	0.82	-79.6	-78.0	0.82	0.80
				0.80	0.75			0.73	0.65			0.71	0.66			0.61	0.60
	0.24	95.4	85.2	0.92	0.82	-92.4	-81.0	0.95	0.84	82.4	75.2	0.79	0.72	-69.8	-70.8	0.72	0.73
				0.73	0.65			0.71	0.62			0.63	0.58			0.54	0.54
	0.32	94.2	87.4	0.91	0.84	-91.2	-96.4	0.94	0.99	75.4	68.8	0.73	0.66	-65.2	-61.8	0.67	0.64
				0.72	0.67			0.70	0.74			0.58	0.53			0.50	0.48
	0.48	89.4	76.4	0.86	0.73	-85.2	-72.8	0.88	0.75	64.2	59.6	0.62	0.57	-59.4	-57.4	0.61	0.59
				0.69	0.59			0.65	0.56			0.49	0.46			0.46	0.44
	0.64	86.2	73.4	0.83	0.71	-86.4	-77.4	0.89	0.80	55.6	52.8	0.53	0.51	-53.2	-51.6	0.55	0.53
				0.66	0.56			0.66	0.59			0.43	0.41			0.41	0.40
	0.96	81.8	67.8	0.79	0.65	-83.4	-61.0	0.86	0.63	49.0	47.0	0.47	0.45	-46.6	-45.8	0.48	0.47
				0.63	0.52			0.64	0.47			0.38	0.36			0.36	0.35
	1.28	74.8	67.8	0.72	0.65	-72.8	-66.4	0.75	0.68	44.4	45.2	0.43	0.43	-44.8	-44.4	0.46	0.46
				0.57	0.52			0.56	0.51			0.34	0.35			0.34	0.34
	1.92	68.8	66.0	0.66	0.63	-70.4	-66.8	0.73	0.69	45.2	45.2	0.43	0.43	-44.6	-44.2	0.46	0.46
				0.53	0.51			0.54	0.51			0.35	0.35			0.34	0.34
	2.56	70.2	63.6	0.68	0.61	-70.8	-63.8	0.73	0.66	43.0	41.2	0.41	0.40	-43.6	-41.2	0.45	0.42
				0.54	0.49			0.54	0.49			0.33	0.32			0.34	0.32
	3.84	58.2	49.2	0.56	0.47	-70.4	-50.4	0.73	0.52	38.2	33.4	0.37	0.32	-36.0	-31.8	0.37	0.33
				0.45	0.38			0.54	0.39			0.29	0.26			0.28	0.24
	5.12	42.6	37.4	0.41	0.36	-47.2	-37.8	0.49	0.39	30.0	26.8	0.29	0.26	-28.6	-26.4	0.29	0.27
				0.33	0.29			0.36	0.29			0.23	0.21			0.22	0.20
10-M20-2C-RH-LC	0.12	44.9	44.9	1.00	1.00	-52.5	-44.0	1.00	0.84	39.9	35.0	0.89	0.78	-41.0	-36.0	0.78	0.69
				0.81	0.81			0.95	0.80			0.72	0.63			0.74	0.65
	0.16	44.6	41.3	0.99	0.92	-51.8	-46.4	0.99	0.88	36.1	33.1	0.80	0.74	-35.2	-32.9	0.67	0.63
				0.81	0.75			0.94	0.84			0.65	0.60			0.64	0.59
	0.24	43.9	40.5	0.98	0.90	-49.9	-44.8	0.95	0.85	32.5	29.1	0.72	0.65	-30.4	-28.0	0.58	0.53
				0.79	0.73			0.90	0.81			0.59	0.53			0.55	0.51
	0.32	43.8	39.7	0.98	0.88	-52.7	-44.8	1.00	0.85	28.0	22.9	0.62	0.51	-27.0	-22.8	0.51	0.43
				0.79	0.72			0.95	0.81			0.51	0.41			0.49	0.41
	0.48	40.6	37.2	0.90	0.83	-46.0	-40.3	0.88	0.77	21.0	19.0	0.47	0.42	-20.1	-19.8	0.38	0.38
				0.73	0.67			0.83	0.73			0.38	0.34			0.36	0.36
	0.64	42.3	37.4	0.94	0.83	-44.5	-38.9	0.85	0.74	18.1	16.1	0.40	0.36	-18.5	-17.0	0.35	0.32
				0.76	0.68			0.80	0.70			0.33	0.29			0.33	0.31
	0.96	37.9	30.7	0.84	0.68	-41.7	-29.3	0.79	0.56	15.4	14.2	0.34	0.32	-15.3	-13.2	0.29	0.25
				0.69	0.56			0.75	0.53			0.28	0.26			0.28	0.24

	1.28	35.7	29.8	0.80	0.66	-30.6	-23.6	0.58	0.45	13.6	12.9	0.30	0.29	-11.9	-10.9	0.23	0.21
				0.65	0.54			0.55	0.43			0.25	0.23			0.22	0.20
	1.92	33.2	24.2	0.74	0.54	-27.7	-16.7	0.53	0.32	10.8	7.9	0.24	0.18	-9.8	-8.8	0.19	0.17
				0.60	0.44			0.50	0.30			0.20	0.14			0.18	0.16
	2.56	27.7	11.0	0.62	0.24	-16.5	-6.8	0.31	0.13	7.8	3.5	0.17	0.08	-7.1	-3.4	0.14	0.06
				0.50	0.20			0.30	0.12			0.14	0.06			0.13	0.06
	3.84	6.3	6.1	0.14	0.14	-4.3	-3.7	0.08	0.07	2.4	2.6	0.05	0.06	-1.3	-1.2	0.02	0.02
				0.11	0.11			0.08	0.07			0.04	0.05			0.02	0.02

Note: Two ratios are given for each strength. The upper value is determined as the ratio of the strength to the peak load in the same loading direction, while the lower value is calculated as the ratio of the strength to the peak strength of the corresponding monotonic specimen.

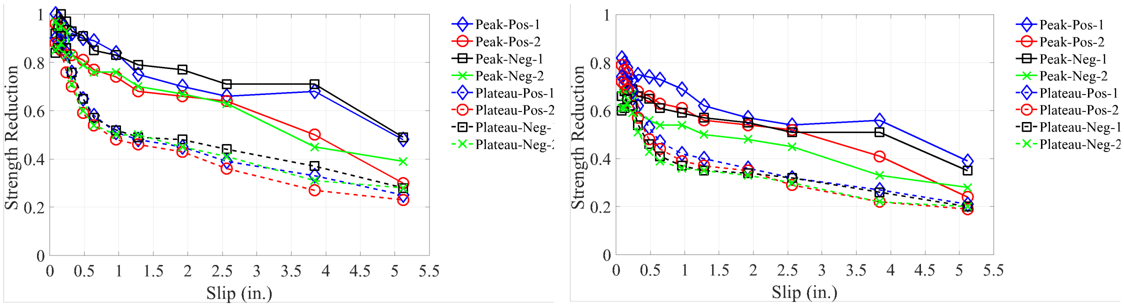

Test 3-M24-2C-RL-LC

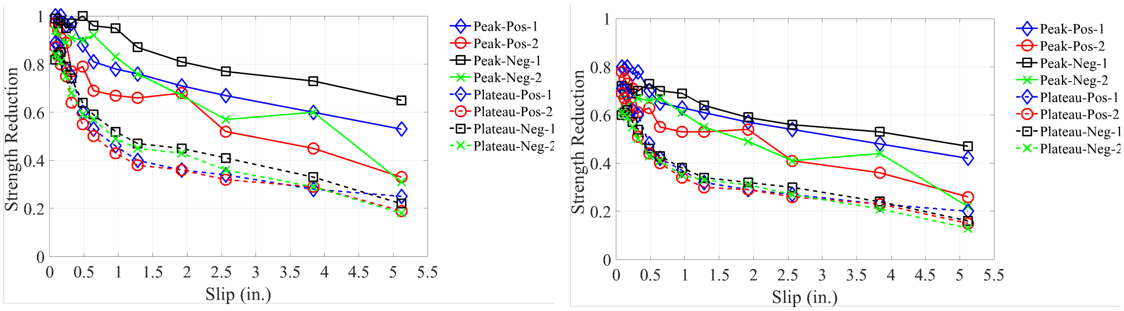

Test 5-M24-2C-RH-LC

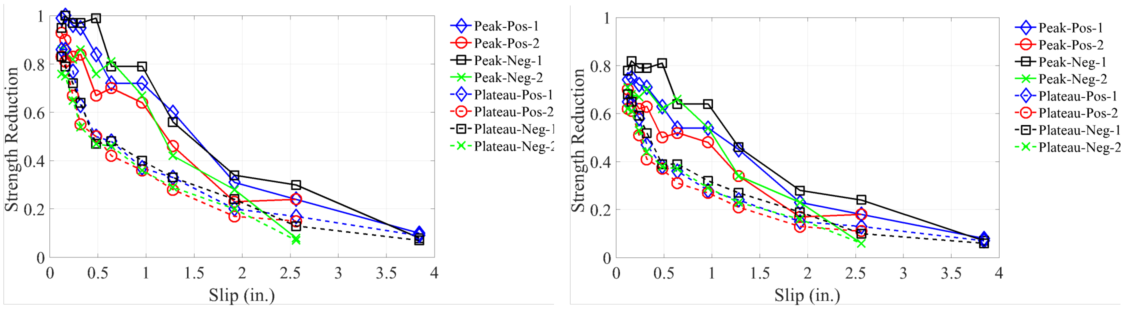

Test 6-M24-2C-RH-LC-S

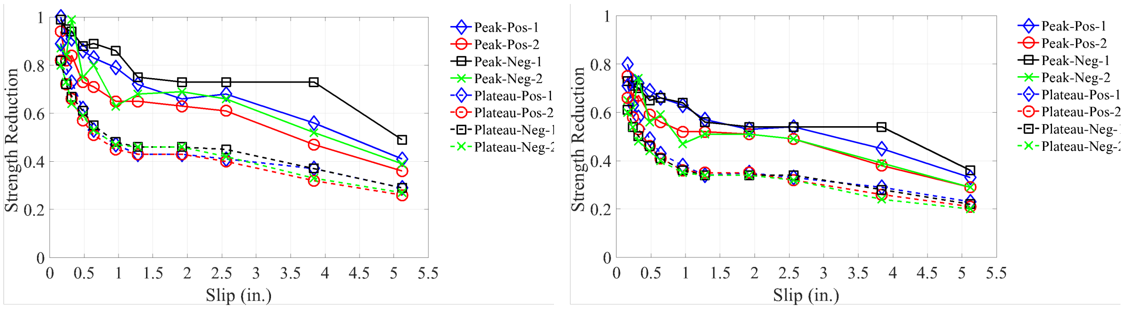

Test 8-M24-3C-RH-LC

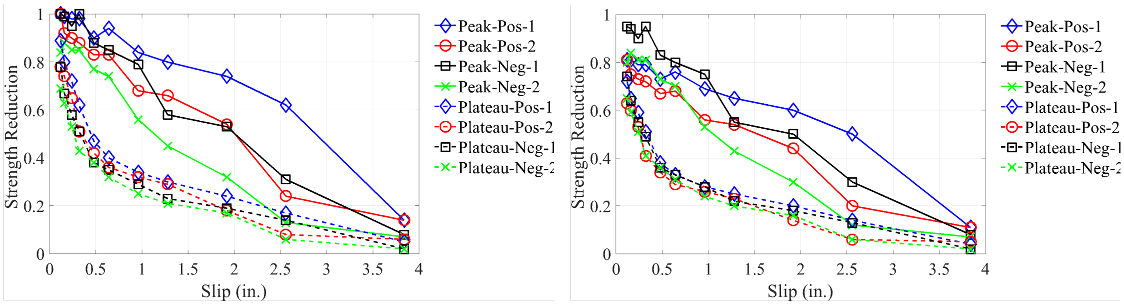

Test 10-M20-2C-RH-LC

Figure 4.42 Relationship between cyclic strength reduction and slip in pushout tests

Compared to the monotonic pushout specimens, the peak strength reduction of the cyclically loaded pushout specimens is indicated in Table 4.7. For the five cyclic pushout specimens, the average peak strength reduction is 21%. Hence, it could be suggested to use 80% of the monotonic shear strength of clamps as their cyclic shear strength.

Table 4.7 Peak strength reduction in cyclic pushout specimens

Specimen	Cyclic tests (kips)		Monotonic tests (kips)	Ratio	
	Positive	Negative		Positive	Negative
3-M24-2C-RL-LC	72.2	63.3	88.5	0.82	0.72
5-M24-2C-RH-LC	70.6	64.4	88.5	0.80	0.73
6-M24-2C-RH-LC-S	65.5	71.8	87.9	0.75	0.82
8-M24-3C-RH-LC	104.0	97.0	130.1	0.80	0.75
10-M20-2C-RH-LC	44.9	52.5	55.3	0.81	0.95
			Average	0.79	0.79

In addition to strength, the ductility and energy dissipation of the clamps are also presented in Table 4.8. The ductility index of the cyclic specimens is computed with the cyclic backbone curves and reported in both loading directions. The ductility of a shear stud can be calculated as: $\mu = \Delta_u/\Delta_y$, where Δ_y and Δ_u are defined as slips at which the strength of the stud increases or reduces to 95 % of its peak strength, respectively (Burnet et al. 2001). The ductility indexes of the clamps are calculated similarly. Two load levels are employed for the clamps to determine Δ_y and Δ_u: one at 95% of the peak strength; the other one at 80% of the peak strength. The former strength level enables a direct comparison between the clamps and shear studs in terms of yield slip, ultimate slip and ductility. Unlike shear studs which normally fracture when their strengths decline to 95% of the peak strengths, the clamps possess further deformation capacity without significant strength degradation, and the latter strength level is thus used to investigate these larger deformations. Comparing the monotonic load-slip curves to the cyclic backbone curves, it is noted that the peak strengths of the cyclic specimens are achieved at smaller slips than the corresponding monotonic specimens, which may result from the abrasion between the components in the cyclic specimens. Since the yield slips of the cyclic specimens are small, the calculated ductility indexes are occasionally very large.

In a monotonic pushout test specimen, the energy dissipation of the clamp is equivalent to the area below the load-slip curve, whereas the energy dissipation of the clamp subjected to cyclic loading is calculated as the summation of the area of all the loops. All the parameters are illustrated in Figure 4.43. As presented in Table 4.8, the dissipated energy per connector in Specimen 6-M24-2C-RH-LC-S is only half that of the same size clamp in other specimens because the clamps disengaged from the steel beam earlier. Likewise, the energy dissipation is reduced in Test 10-M20-2C-RH-LC due to the lower strength of the M20 clamps and the earlier detachment from the steel beam. As a result of their excellent energy dissipating capacity, if clamping connectors are utilized to connect the concrete slab to the collectors in a lateral force-resisting system, they could be designed as ductile components and the induced friction at the slip planes could be used as an energy dissipating mechanism in a diaphragm.

Table 4.8 Ductility and energy dissipation of clamps in pushout specimens (per connector)

Specimen	Yield slip (in.)				Ultimate slip (in.)				Ductility index				Energy dissipation (kips-in.)
	80%[a]		95%		80%		95%		80%		95%		
	Pos	Neg	Pos	Neg	Pos	Neg	Pos	Neg	Pos	Neg	Pos	Neg	
2-M24-2C-RH-LM	0.097		0.59		9.10		2.27		93.9		3.85		171
4-M24-2C-RH-LM-S	0.104		0.37		5.15		0.71		49.6		1.92		82
7-M24-3C-RH-LM	0.054		0.17		5.13		1.16		95.1		6.82		100
9-M20-2C-RH-LM	0.092		0.34		1.55		0.78		16.9		2.29		65
3-M24-2C-RL-LC	0.0048	0.0052	0.024	0.072	0.92	1.08	0.18	0.29	193.7	207.7	7.50	4.03	967
5-M24-2C-RH-LC	0.0064	0.017	0.023	0.052	0.82	1.99	0.38	1.03	130.6	120.2	16.5	19.8	1042
6-M24-2C-RH-LC-S	0.0084	0.016	0.026	0.053	0.39	0.62	0.30	0.57	46.8	39.1	11.5	10.8	438
8-M24-3C-RH-LC	0.012	0.012	0.065	0.027	0.86	0.95	0.25	0.22	70.9	81.4	3.85	8.15	1073
10-M20-2C-RH-LC	0.0074	0.017	0.025	0.11	1.23	0.99	0.61	0.41	167.7	58.1	24.4	3.73	324

[a] *Errors may exist in these tiny slip measurements.*

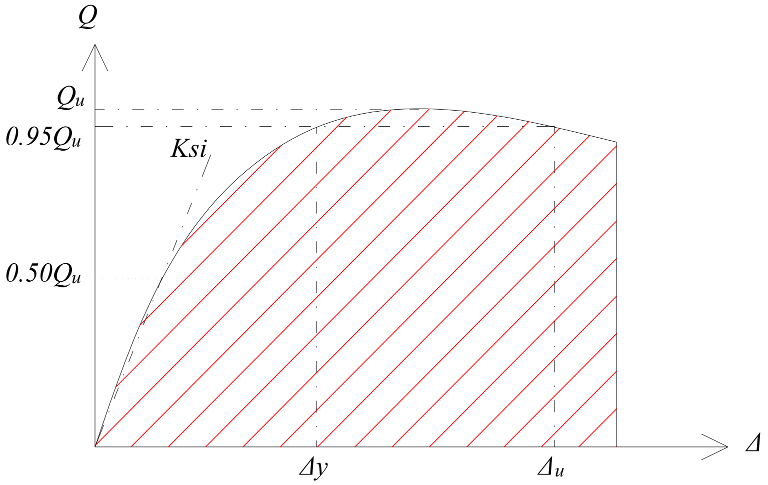

Q
Qu
0.95Qu
Ksi
0.50Qu
Δy
Δu
Δ

Figure 4.43 Illustration of ductility index, energy dissipation and stiffness

As presented in Figure 4.44, a trilinear or quadrilinear relationship, which could be used for nonlinear analysis, is derived for each monotonic test. The slip at Point A is 0.02 in. Point B represents the peak strength of the clamping connector. The shear strength decreases to 80% of the peak strength at Point C and remains the same until Point D. All the values are shown in Table 4.9.

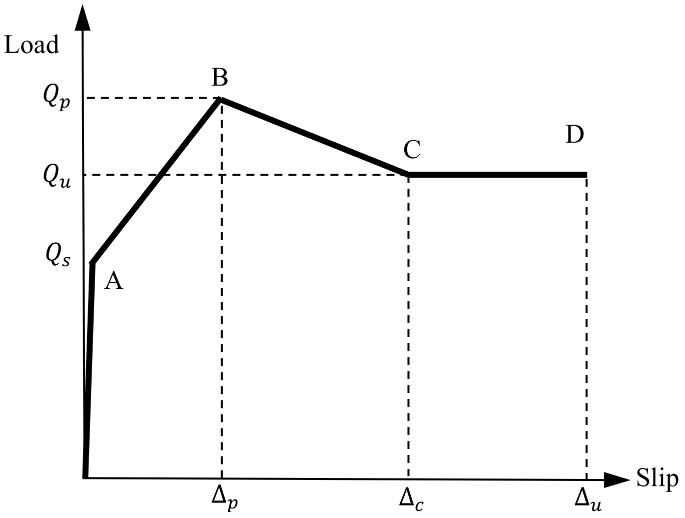

Load
Q_p
Q_u
Q_s
A
B
C
D
Δ_p
Δ_c
Δ_u
Slip

Figure 4.44 Trilinear or quadrilinear representation of experimental load-slip curve

Table 4.9 Points on Idealized Trilinear or Quadrilinear Load-slip Curves

Specimen	Point A	Point B		Point C and D		
	Q_s (kips)	Q_p (kips)	Δ_p (in.)	Q_e (kips)	Δ_c (in.)	Δ_u (in.)
2-M24-2C-RH-LM	15.2	22.1	1.12	17.7	5.54	9.1
4-M24-2C-RH-LM-S	14.1	22.0	0.55	17.6	5.15[a]	-
7-M24-3C-RH-LM	14.5	21.7	0.32	17.4	4.30	5.13
9-M20-2C-RH-LM	9.1	13.8	0.54	11.0	1.55	-

[a] *Error may exist in the slip measurement due to the load drop after bolt head fracture.*

Typical clamp teeth damage is illustrated in Figure 4.45. For the M24 clamps, the damage of the clamp teeth is similar between the monotonically and cyclically loaded pushout specimens. The clamp tested in the beam test has the least damage, which is probably due to the relatively small ultimate slip (less than 0.35 in.) experienced by the clamp. In contrast, the teeth of the M20 clamps that experienced monotonic loading are not severely damaged, but the teeth of the clamp tested in the cyclic pushout specimen are seriously abraded. As a result, the frictional coefficient between the steel flange and clamp teeth varied, and the bolt tension was also affected.

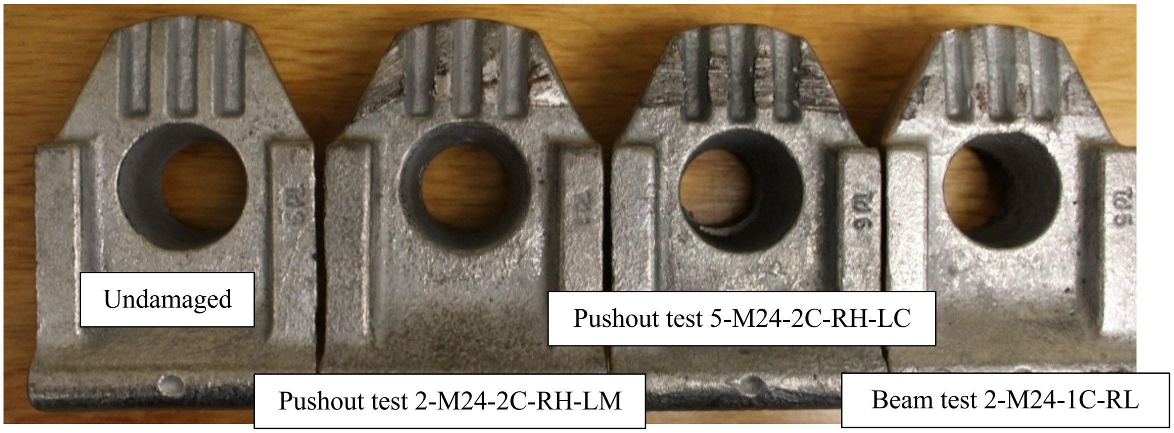
Undamaged
Pushout test 5-M24-2C-RH-LC
Pushout test 2-M24-2C-RH-LM
Beam test 2-M24-1C-RL

a) M24 clamps

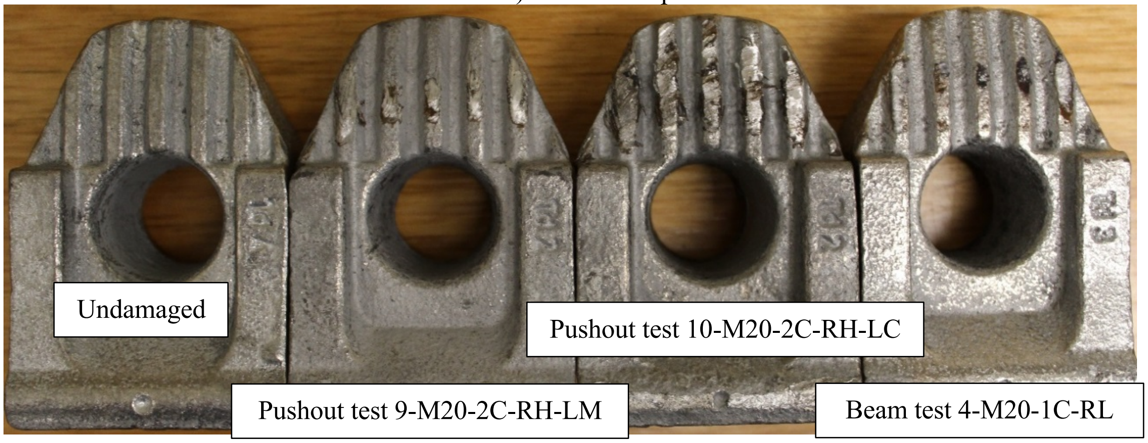
Undamaged
Pushout test 10-M20-2C-RH-LC
Pushout test 9-M20-2C-RH-LM
Beam test 4-M20-1C-RL

b) M20 clamps

Figure 4.45 Clamp teeth damage

4.5.4.3 *Comparison with steel headed stud anchors*

The strength of the shear connectors is a limiting factor in the design of a composite beam. Ductile shear connectors ensure that the shear force can redistribute from weaker connectors to stronger connectors in a composite beam without premature fracture and that the plastic design method is applicable.

Provided the governing limit state is stud fracture, the shear strength of a steel headed stud anchor embedded in a solid concrete slab used in a composite beam is given in the AISC Specification (AISC 2016a).

$$Q_n = 0.75 A_{sa} F_u \tag{4.18}$$

Where A_{sa} is the cross-sectional area (in.^{2}) and F_u is the specified minimum yield strength of a steel headed stud anchor (ksi). No resistance factor is added to this strength; a resistance factor is used when calculating the design flexural strength of the composite beam.

Oehlers et al. (1986) conducted a statistical analysis of load and slip characteristics of 116 pushout tests in which concrete slabs did not failure prematurely, and recommended Equations (4.19) and (4.20) to estimate the mean initial tangent stiffness K_{si}, which was assumed to be the stiffness at $0.5Q_n$, and ultimate slip Δ_u, at which shear studs fracture at about 95% of their shear strength, of steel headed stud anchors embedded in solid concrete slabs. The parameters are shown in Figure 4.43.

$$K_{si} = \frac{Q_n}{d(0.16 - 0.0017f_c')} \tag{4.19}$$

$$\Delta_u = (0.45 - 0.0021f_c')d \tag{4.20}$$

Where f_c' is the compressive cylinder strength of concrete (MPa), and d is the diameter of the shank of a steel head stud anchor (mm).

Using the above equations, a 3/4 in. diameter shear stud embedded in a 4 ksi solid concrete slab has an ultimate strength of 21.5 kips, an initial tangent stiffness of 256 kips/in., and an ultimate slip of 0.29 in. Using Test 2-M24-2C-RH-LM as the baseline specimen, the peak shear strength and initial stiffness of an M24 clamp are 22.1 kips and 760 kips/in., respectively. For an M20 clamp, based on Test 9-M20-2C-RH-LM, these characteristics are 13.8 kips and 455 kips/in., respectively. When defined at 95% of the peak strengths, the ultimate slips of the M24 and M20 clamps are 57.7 mm (2.27 in.) and 19.8 mm (0.78 in.), respectively. If defined at 80% of the peak strengths, the ultimate slips are 231.0 mm (9.10 in.) and 39.4 mm (1.55 in.) for the M24 and M20 clamps, respectively.

Apparently, the higher initial stiffness of the clamps could reduce the slip at the steel-concrete interface at serviceability and enhance the stiffness of the composite beams.

Because of the limited slip capacity of shear studs, design provisions, such as AISC 360-16 (2016), recommend that the ductility of composite beams be evaluated unless one of the following conditions is met:

(1) Beams with span not exceeding 30 ft.;
(2) Beams with a degree of composite actin of at least 50%;
(3) Beams with an average nominal shear connector capacity of at least 16 kips per ft. along their shear span, corresponding to a 3/4 in. steel headed stud anchor placed at 12-in. spacing on average.

However, even if the foregoing criteria is not met, it is probable that ductility is not a concern for composite beams utilizing clamps which exhibit excellent slip capacity.

Since the dissipated energy of shear connectors under cyclic loading is directly related to the loading protocol, the energy dissipation capacity is only compared between shear studs and clamping connectors under monotonic loading. An empirical load-slip relationship is given for shear studs in Ollgaard et al. (1971), as shown in Equation (4.21).

$$Q = Q_n(1 - e^{-18\Delta})^{0.4} \tag{4.21}$$

Where Δ is the slip of the shear stud (in.)

Using the ultimate capacity and slip of a 3/4 in. diameter shear stud calculated above, the integration of Equation (4.21) with respect to Δ is the dissipated energy of the stud under monotonic loading, which equals 5.6 kips-in. Civjan et al. (2003) also reported similar values, with the energy being 4.9 kips-in and 6.9 kips-in for a shear stud attached to a steel flange using standard stud gun welding and shielded metal arc welding, respectively. Compared to the values shown in Table 4.8, the clamping connectors demonstrate a much larger energy dissipation capacity because of the excellent slip capacity.

4.5.5 Formation of cracks on concrete surfaces

Concrete cracks observed during testing mostly initiated and remained localized in the vicinity of the bolts. Through observations of the test specimens, it was seen that initial visible cracking tended to occur at approximately the time that noticeable slip (~0.02 in.) initiated. The slip load of different specimens could differ greatly, for example, between Test 7-M24-3C-RH-LM and Test 9-M20-2C-RH-LM. Hence, the initiation of concrete cracking could be correlated to other factors, in addition to the magnitude of loading. As discussed earlier, under service loads, since the maximum slip observed in the deconstructable composite beam specimens ranges from almost zero to 0.05 in., cracking may occur in the concrete planks at serviceability, particularly for those at the ends of the beams. After disassembling the test setup, cracks, mainly located in the middle of the plank, were found at the steel-concrete interface in some specimens. Most of the cracks are less than 1/16 in. wide, and the widest crack, which penetrated through the concrete cover, has a width of 1/2 in. in the three-channel monotonic specimen (i.e., Test 7-M24-3C-RH-LM).

As shown in Figure 4.46, two black stripes were always found on the concrete specimen surfaces at the contact surfaces between the concrete planks and the edges of the steel beam flanges. Hence, it is likely that the frictional forces were mainly transferred along the edges of the flange (i.e., at the locations of the direct clamp force). An additional stripe was also seen in the middle of the plank in the tests using the larger steel section. A preliminary inspection has revealed that the flanges of the WT5x30 and WT4x15.5 sections had outlines schematically shown in Figure 4.47. The profiles of the flanges explain why the additional stripe appeared in the tests where WT5x30 was used.

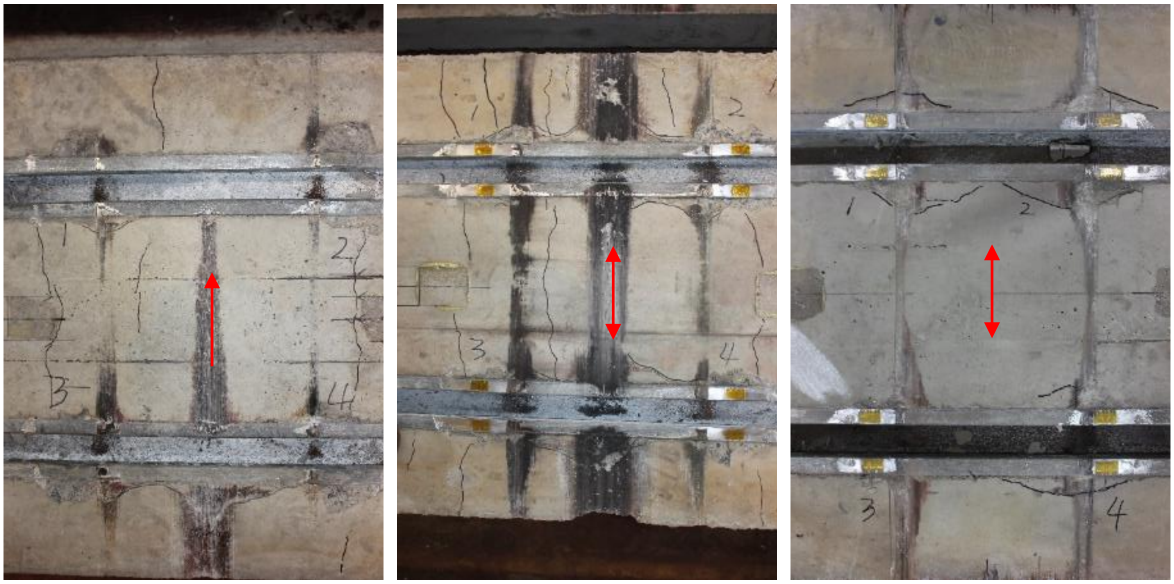

a) Test 2 b) Test 5 c) Test 10

Note: Arrows in the figures show the loading direction.

Figure 4.46 Different black stripe patterns in pushout test specimens

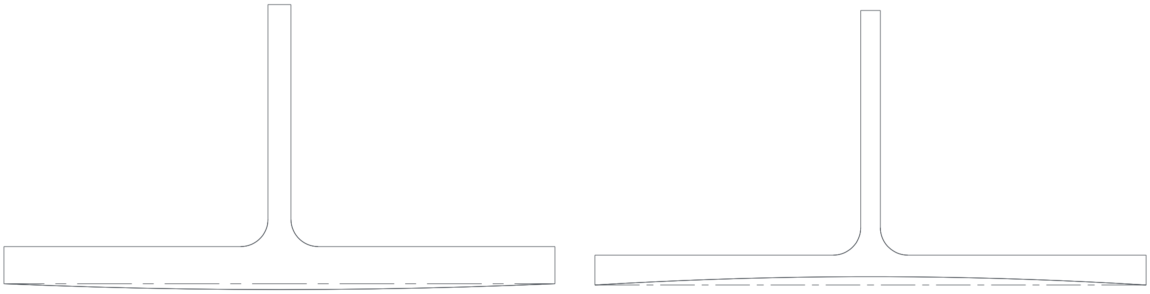

a) WT5x 30 b) WT4x15.5

Note: Dashed lines are the theoretical profiles of the flanges; solid lines are the actual profiles of the flanges.

Figure 4.47 Schematic presentation of flange profiles

Concrete pry-out failure under shear is not likely to be the main cause of the cracks, in that the locations of the cracks did not always match the positions of the channel anchors, especially for the cracks in the vicinity of the bolts, i.e., no anchors were located right below those cracks, as shown in Figure 4.48. The peak strengths of the tests using shims (i.e., Tests 4-M24-2C-RH-LM-S and 6-M24-2C-RH-LC-S) were close to those of the tests without shims (i.e., Tests 2-M24-2C-RH-LM and 5-M24-2C-RH-LC); therefore, the shear force the middle channel anchor was subjected to should be almost identical for both types of tests. Nonetheless, no cracks formed in the middle of the planks in Tests 4-M24-2C-RH-LM-S and 6-M24-2C-RH-LC-S. In addition, Eurocode 2 (CEN 2009) states that the majority of the shear force acting on the anchor channels is transferred to concrete directly through channel bearing. Only a small fraction flows into the anchors via bending of the anchors.

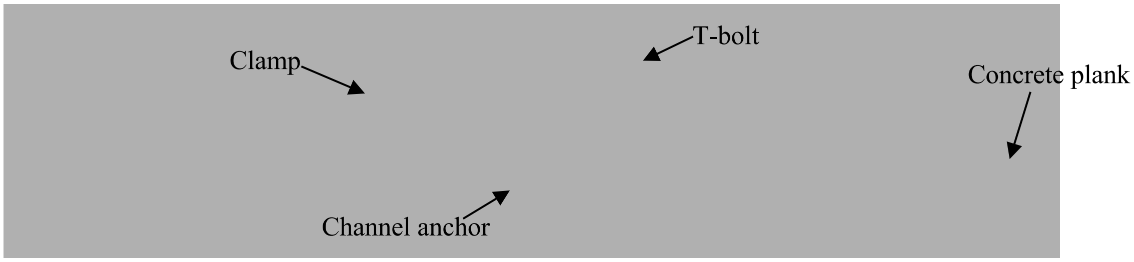

Figure 4.48 Channel anchor and bolt positions in a pushout test specimen

As shown in Figure 4.49, diagonal cracks were observed at the steel-concrete interface in Test 7-M24-3C-RH-LM. These cracks were approximately 25° from a line parallel to the channel longitudinal axis. The cracks spanned from the region of the primary frictional force acting on the surface of the concrete plank to the areas around the bolts where reactions from the bolts were occurring. Cracks initiated once the principal tensile stress in the concrete exceeded the tensile strength of the concrete plank. The force flow can be idealized using a strut-and-tie model, with inclined struts transferring the compressive force and the channel serving as the tie. The cracks in the neighborhood of the bolts can also be interpreted with this model.

As discussed in Section 4.5.1, the normal force between the concrete plank and steel beam becomes uneven after the steel guides are involved. Consequently, the friction is not uniformly distributed across the concrete surface. As the beam is loaded in the west (or east) direction, more friction is generated at the east (or west) side of concrete. This speculation can be verified by the tapered stripe in Figure 4.46a, because the stripe is wider at the end where the friction is larger and narrower at the end where the friction is smaller. Likewise, in Figure 4.46b, as a result of the unevenly distributed friction on the concrete surface, the stripe is light in the middle and dark at both ends.

In the three-channel specimen, the outside channel was closer to the concrete edge, and therefore the frictional force was distributed over a smaller area than the two-channel specimen, as illustrated in Figure 4.50, increasing the tensile stress in concrete and leading to wider and deeper cracks.

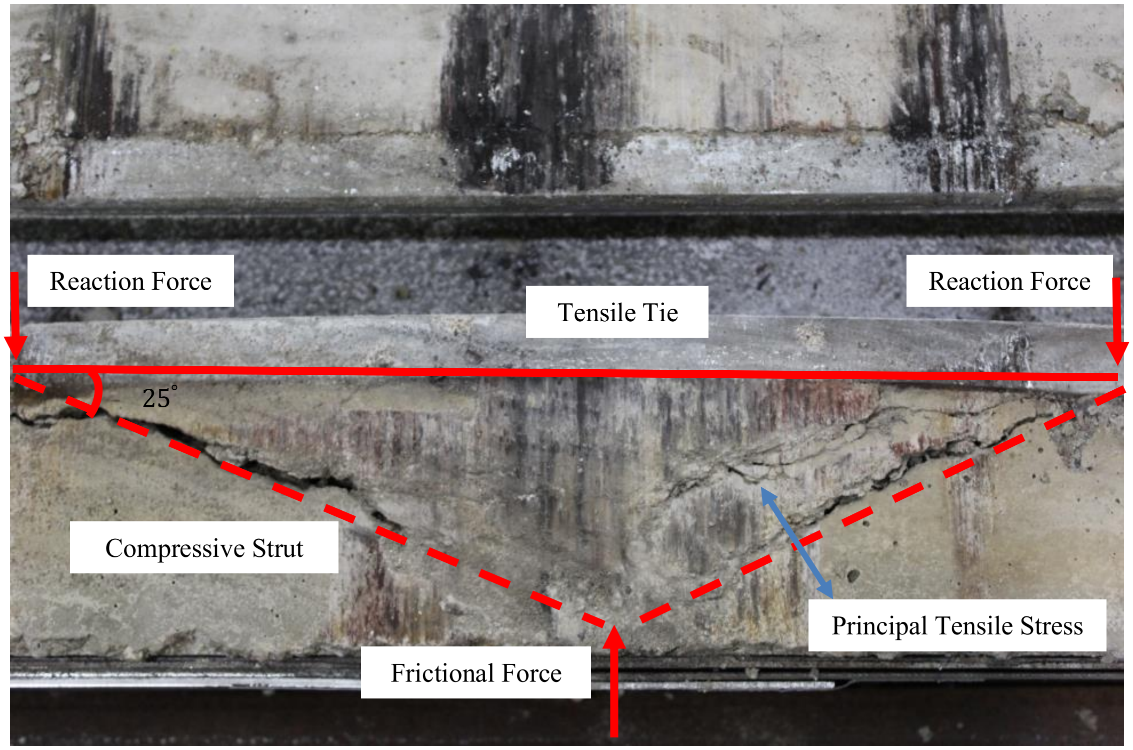
Reaction Force
Reaction Force
Tensile Tie
25°
Compressive Strut
Principal Tensile Stress
Frictional Force

Figure 4.49 Illustration of the strut-and-tie model

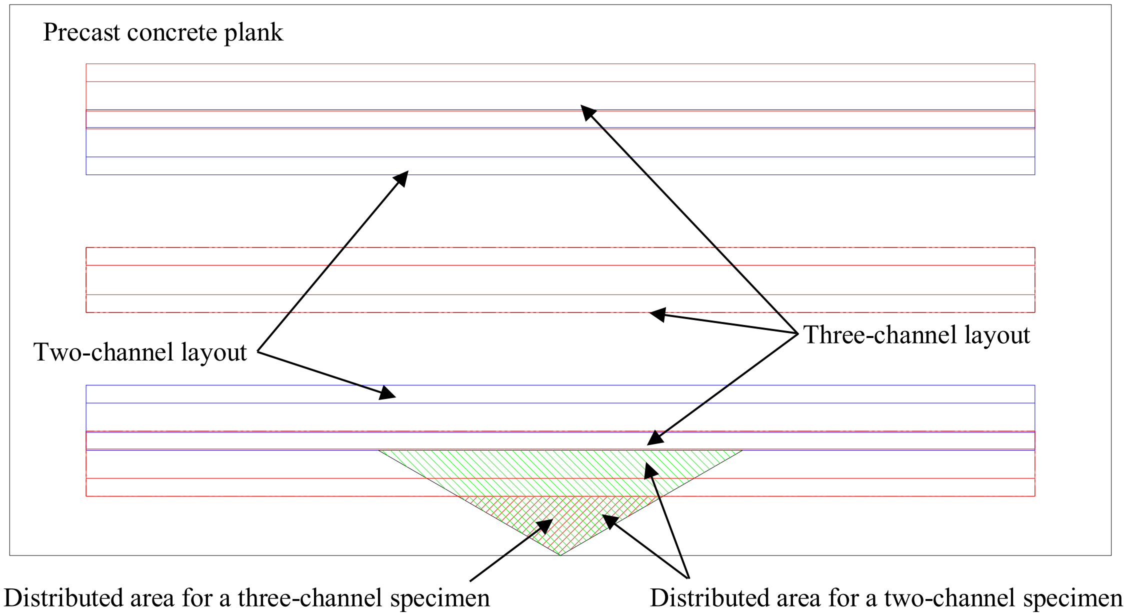
Precast concrete plank
Two-channel layout
Three-channel layout
Distributed area for a three-channel specimen
Distributed area for a two-channel specimen

Figure 4.50 Distributed area for frictional force

4.5.6 Influences of different parameters

Bolt Size

In the monotonic tests, the strength of the specimen using M20 bolts declines more quickly at large slips, while the specimens using M24 bolts maintain most of their strengths. The reason is that the smaller M20 clamps are prone to rotate and could not hold their positions as stably as the M24 clamps starting at a slip of 0.68 in., which is approximately twice the maximum slip demand on the clamps in the deconstructable composite beam specimens (see Table 5.10 in Chapter 5). If needed for withstanding large slip values, this could be addressed by increasing the contact area between the clamp teeth and steel beam and between the clamp tail and concrete plank or developing an interlocking design where the channel lips restrain the rotation of the clamps. In these cases, it is anticipated that the behavior of the M20 clamps will be comparable to the M24 clamps in this work at larger slip levels.

Reinforcement Configuration

The comparison presented in Figure 4.51 does not demonstrate significant disparities between the load-slip curves of the two specimens with different reinforcement configurations (i.e., Test 3-M24-2C-RL-LC and Test 5-M24-2C-RH-LC), indicating that the elimination of the additional supplementary reinforcement does not induce a premature concrete failure mode and strength reduction. Moreover, the wide cracks do not affect the load-slip curve or the overall behavior of Specimen 7. Concrete cracking is thus not regarded as a key limit state in the pushout tests. However, new limit states, which are different from those observed in the pushout tests, may occur in specimens with low strength concrete and/or a low amount of reinforcement. In addition, the initiation of cracking in concrete is related to the tensile strength of the concrete plank, and the width and propagation of these cracks may affect the reusability and refabrication of the planks.

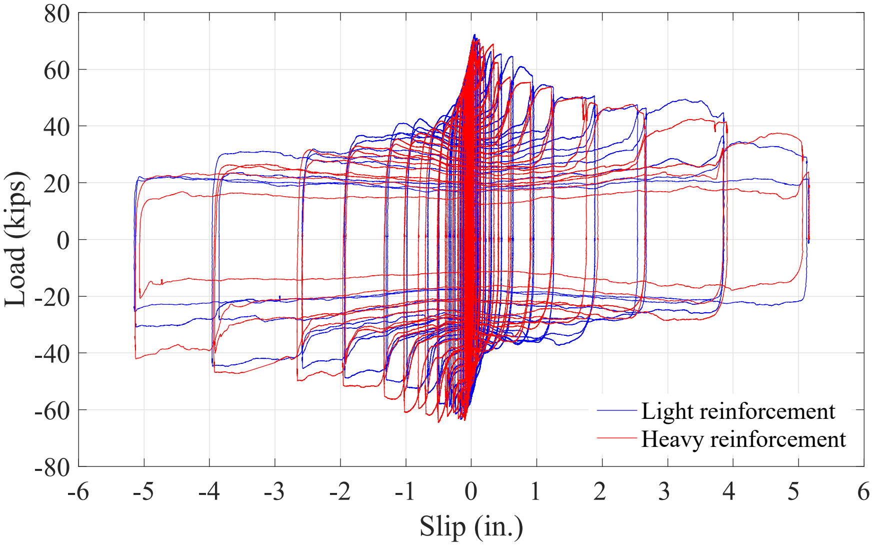

Figure 4.51 Load-slip curve comparison between specimens with different rebar patterns

Number of Channels

The pushout test program focuses on two-channel specimens and three-channel specimens used with M24 clamps. In the composite beam tests presented in Chapter 5, the concrete specimens incorporate one-channel planks and three-channel planks designed with M20 clamps. Since no more than 3 channels can be embedded in a plank, the influences of the spacing between adjacent clamping connectors and channels on the initiation of cracking are demonstrated thoroughly in the pushout tests and composite beam tests. Typical cracks at the steel-concrete interface in the beam specimens are shown in Figure 4.52. The location and pattern of these cracks are similar to those seen in the pushout specimens. These cracks do not affect the shear strength per connector in the pushout specimens or the flexural strength of the beam specimens.

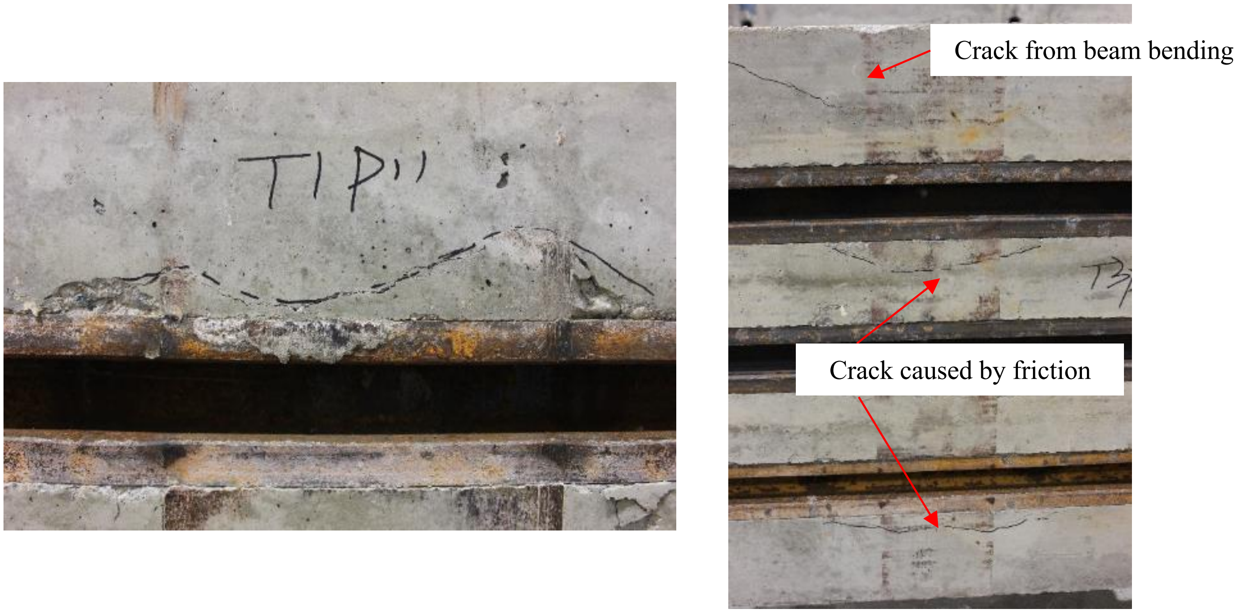

a) Two-channel specimen with M24 clamps

b) Three-channel specimen with M20 clamps

Figure 4.52 Cracks at the steel/concrete interface in beam specimens

Monotonic vs. Cyclic Loading

Similar to the strength reduction seen in steel headed stud anchors under cyclic loading (Pallarés et al 2009), the strengths of the cyclic specimens are lower than the strengths of the corresponding monotonic specimens, and the average peak strength reduction is approximately 20%, as indicated in Table 4.7. For steel headed stud anchors, the cyclic strength reduction is attributed to low-cycle fatigue of the stud and weld materials as well as concrete degradation (Civjan et al. 2003), whereas the strength reduction of clamps is due to the abrasion between the steel flange and clamp teeth and between the steel flange and concrete slab, which reduces the frictional coefficients and releases the bolt pretension force.

Furthermore, the monotonic pushout specimens generally exhibit very ductile behavior, with the exception of the specimen that uses M20 clamps. In contrast, the cyclic specimens all reach their peak strengths at relatively small slips, and strength degradation ensues. However, the load-slip behavior of the cyclically loaded pushout specimens is excellent within 1 in. slip which is conservatively assumed to be a typical slip range for clamps used in composite diaphragms.

Use of Shims

Although little loss in the slip load and peak strength was seen, load oscillation caused by a stick-slip mechanism was observed in Tests 4-M24-2C-RH-LM-S and 6-M24-2C-RH-LC-S in which shims were used. The use of the selected shims may therefore be limited to applications where the slip is small, such as in composite beams that are part of the gravity system; further testing is recommended to explore different types of shims between the clamps and steel flange to eliminate load oscillation.

4.5.7 Behavior of bolts and channel lips

In order to estimate the bolt tension variation, bolt axial strains were measured in the pushout tests. As shown in Figure E.15 in Appendix E, after pretensioning, the strain measurements from the two gages attached on the same bolt showed substantial differences, which could result from the bending of the bolt shank. Figure 4.53 illustrates different boundary conditions for the bolt. Depending on the thickness of the steel flange, the clamp may tilt forward or backward slightly during pretensioning, bending the bolt and causing different strain measurements from the two strain gages. However, the axial deformation, rather than the bending deformation, was dominant for the bolts after the required nut rotation was applied, because the axial strains measured by both gages were greater than the yield strain of the bolt material. During the tests, although the shear deformation of the bolt shanks could not be directly captured by the uniaxial strain gages, their influences on the bolt axial force were demonstrated by the measured bolt strains which gradually decreased. In the pretension tests, the bolt gages were placed at right angles to those used in the pushout tests. Since the boundary conditions were the same for the bolt in the pretension tests, the strain results from the two gages on the same bolt were very similar, as seen in Figure E.1.

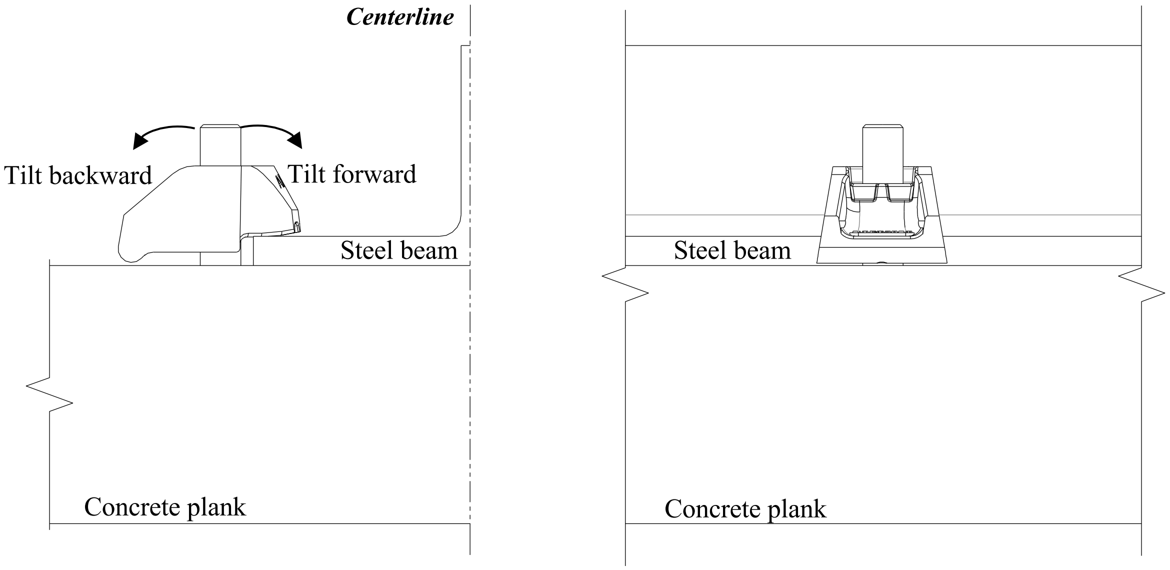

Pushout test (Elevation view) Pretension test (Side view)

Figure 4.53 **Boundary conditions for bolts**

The model described in Appendix F is utilized to convert the strain readings to stress values. As discussed in Section 4.4.3, once the bolt material is yielded, the axial stress or force could be underestimated or overestimated by the current model that neglects the shear stress due to torsion and shear.

Figure 4.54 illustrates the bolt tension-slip relationship. The slip in these plots uses the average measurement from the two string pots. The left graphs in the figure show the overall relationship throughout the tests, and those in the right side focus on the behavior of the bolts within 1 in. slip which is likely to be a typical demand range for steel headed stud anchors commonly used in traditional composite diaphragms. Because the readings from the string pots are not necessarily the same in the positive and negative directions, the bolt tension-slip curves in the right graphs are offset such that the plots are symmetric about the zero slip positions on the whole. Consequently, the initial slips of these curves may be non-zero. Calculated with the average axial strain measurements, the bolt tension variations throughout the tests are plotted in Appendix F. The loading and unloading behavior of the bolt material during the tests is also given.

During the cyclic tests, the bolt tension appeared to gradually decrease along with increasing slip. The initial loss of pretension could be primarily attributed to the increasing shear force which will be discussed in Section 4.7. Since the Von Mises yield criterion is presumed when converting axial strain measurements to axial stresses, the axial stress may decline as the shear stress increases to not breach the yield criterion. After several cycles, the bolt tension might be released mainly because of the damage to the clamp teeth and beam flange. The damage removed materials, reducing the clamping force and shear resistance at the steel-concrete interface.

In some of the later cycles, the bolt tension reached its maximum value at the maximum slip of the cycle, because it was at those slips that the clamps engaged with a portion of the steel beam flange that had not been rubbed in earlier cycles. Similarly, the minimum bolt tension occurred at the zero slip where the damage of the steel flange was the most. Because of the accumulating damage to the steel flange, the bolt tension reduced less in the first cycle than in the second cycle of the same slip level. These observations are consistent with the overall load-slip curves of the cyclic specimens. However, the tension of some bolts decreased at small slips and then increased at large slips, which may contradict the continuously declining strength of the cyclic pushout specimens. In the monotonic test, the bolt tension maintained, and then decreased as the slip increased.

In Figure 4.54, the axial force of some bolts is negative at larger slips, which is unrealistic since these bolts were not likely to be under compression. This could be due to the shifting of the zero signals of the strain gages at very high strains, i.e., yielding of the strain gage material. The strains measured by the rosette strain gages attached on the channel lips are shown in Appendix E.

It should be noted that the strengths of the pushout specimens are dependent upon the normal force and frictional coefficients at the slip surfaces. The former is generated due to the bolt tension which was tracked using strain gage measurements in several tests, while the latter could be difficult to quantify, particularly in the cyclic tests, since the frictional coefficients are related to the damage of the steel flange and clamp teeth which results from the relative movement between the components. Therefore, the bolt tension variation cannot fully reflect the strength variation of the specimens.

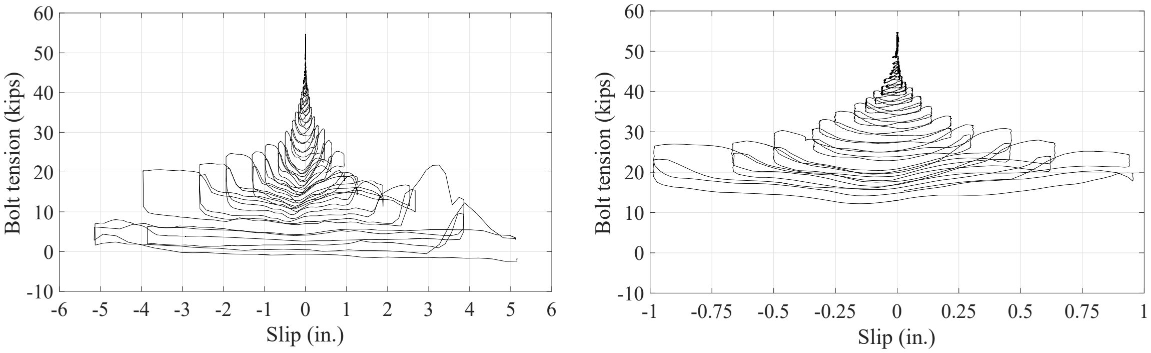

Bolt 1

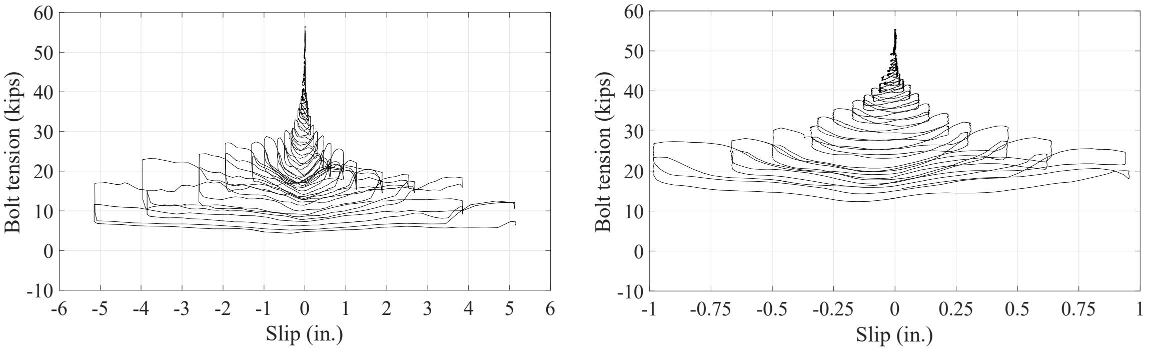

Bolt 2

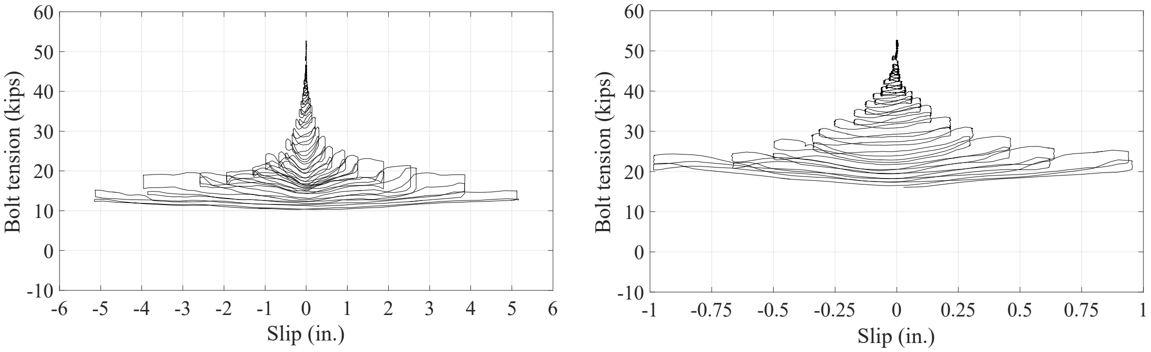

Bolt 3

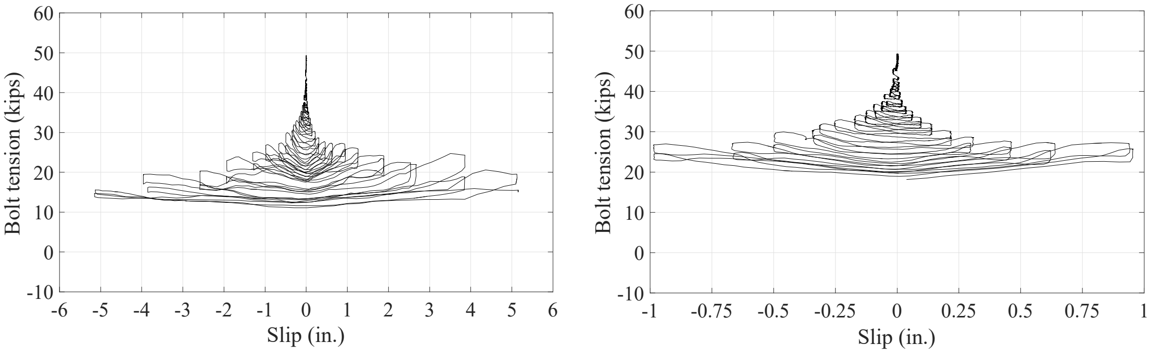

Bolt 4
Test 3-M24-2C-RL-LC

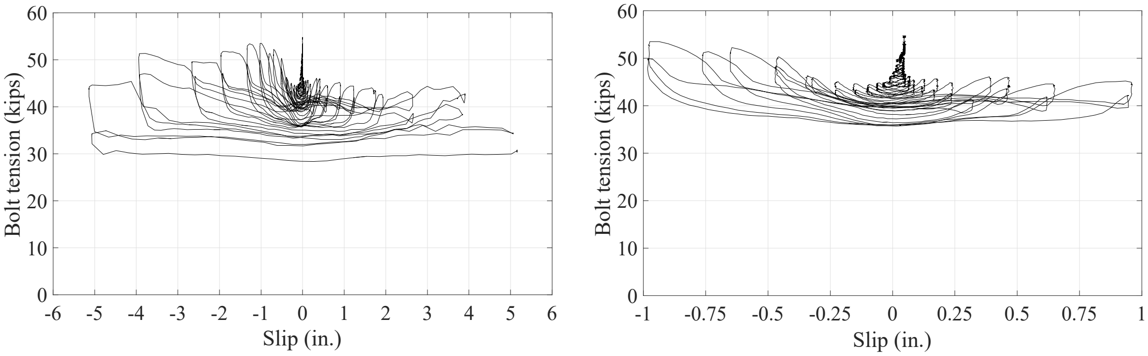

Bolt 1

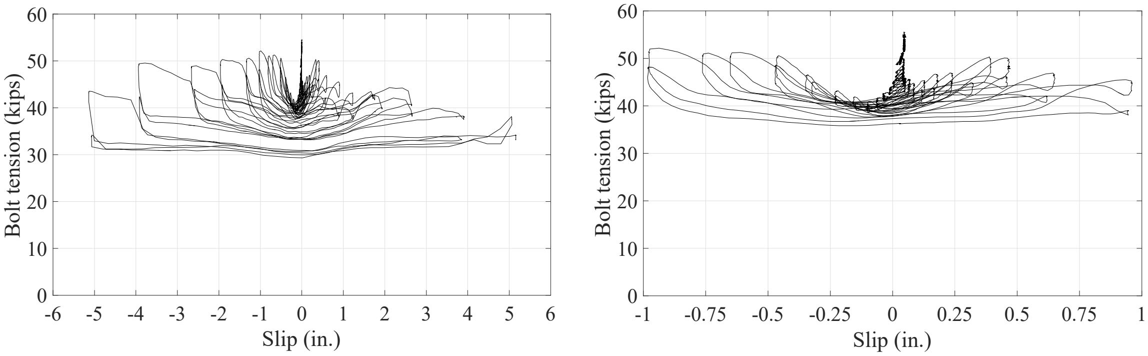

Bolt 2

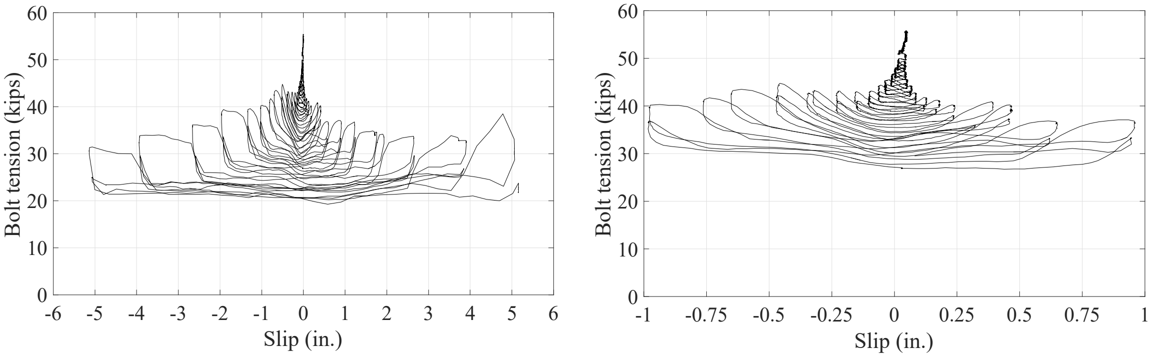

Bolt 3

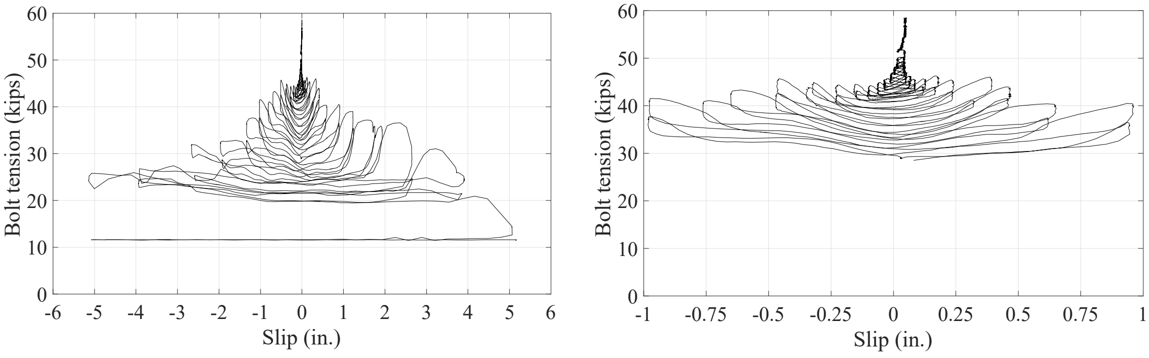

Bolt 4

Test 5-M24-2C-RH-LC

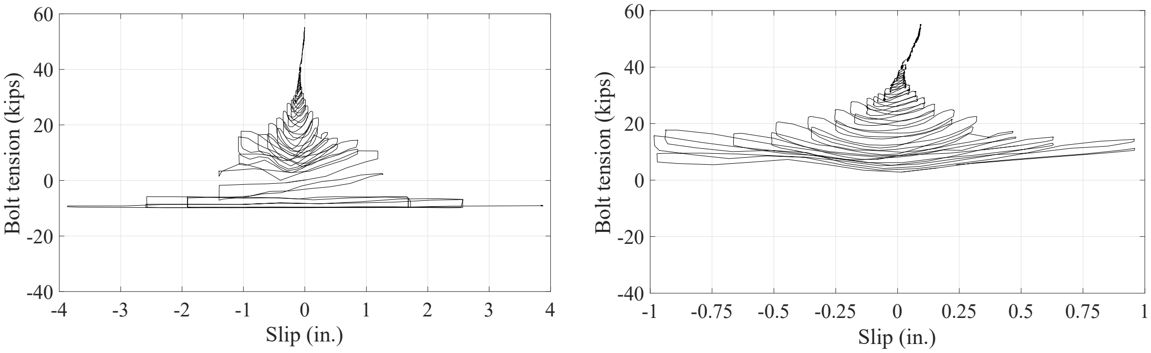

Bolt 1

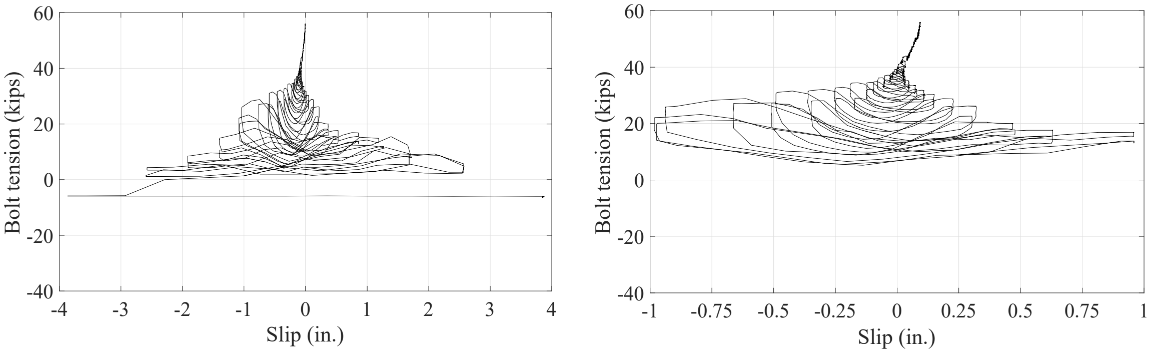

Bolt 2

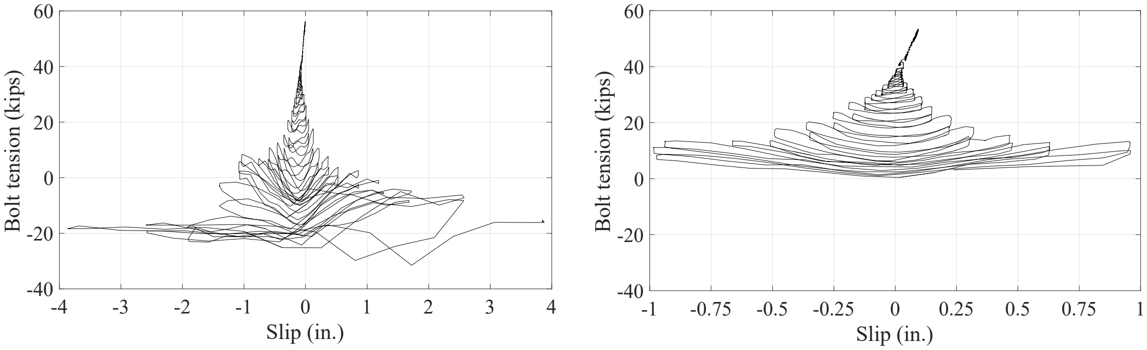

Bolt 3

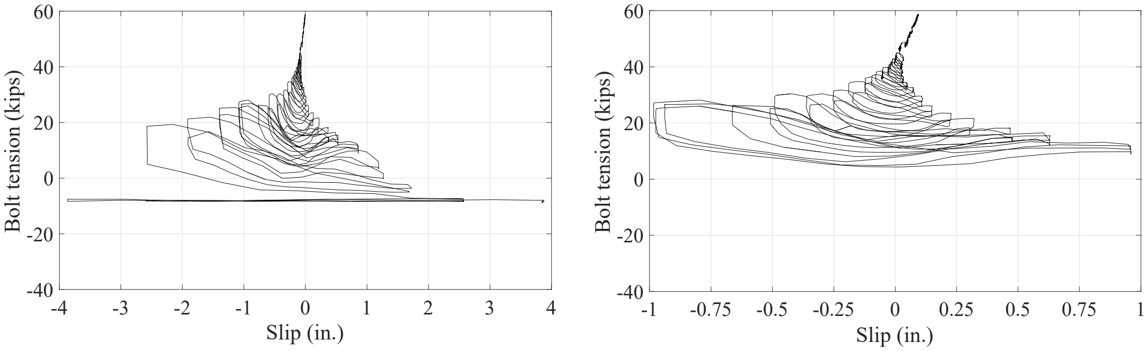

Bolt 4

Test 6-M24-2C-RH-LC-S

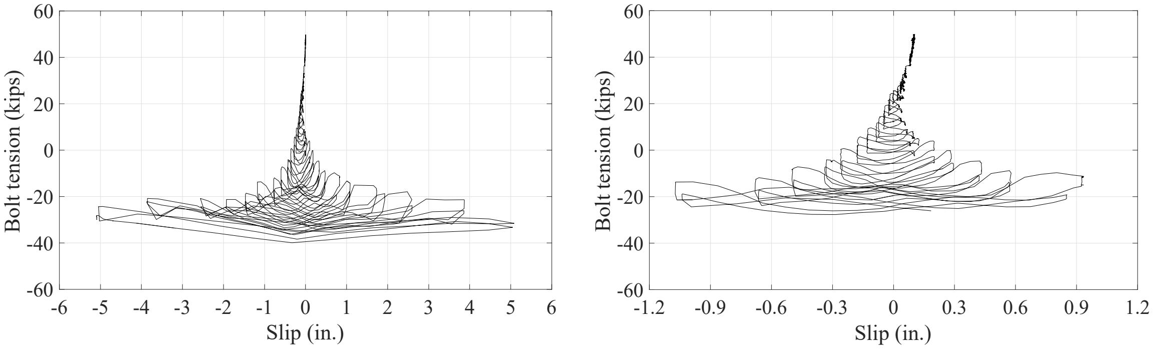

Bolt 1

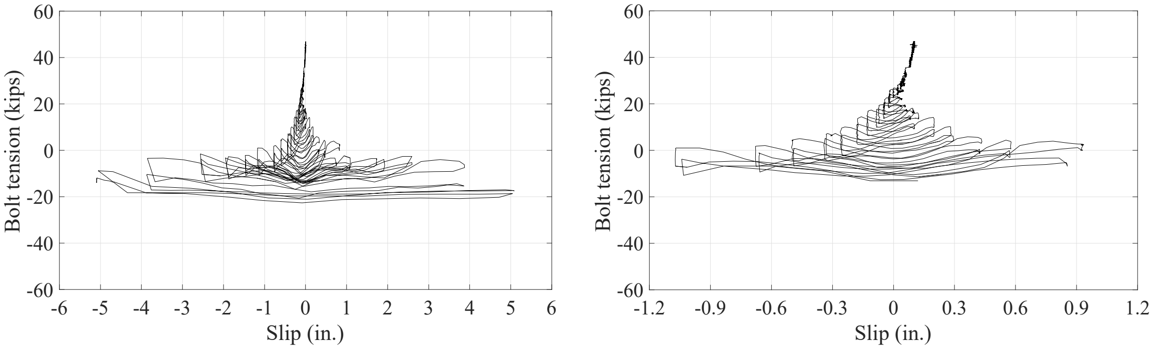

Bolt 2

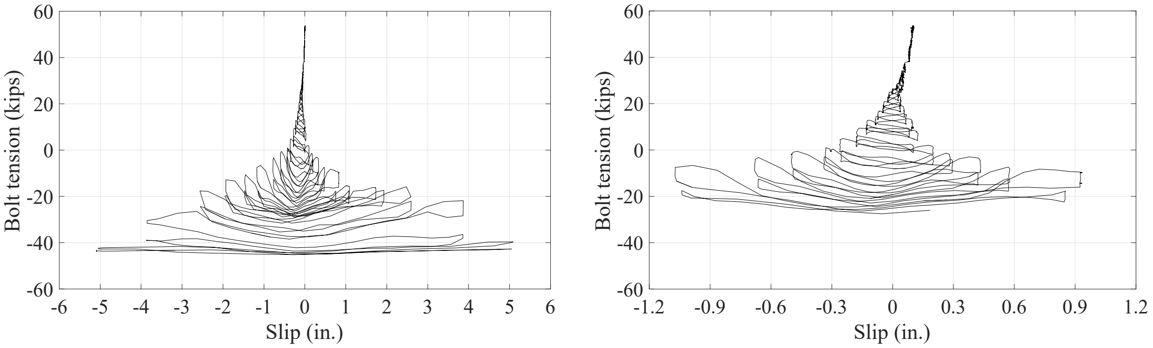

Bolt 3

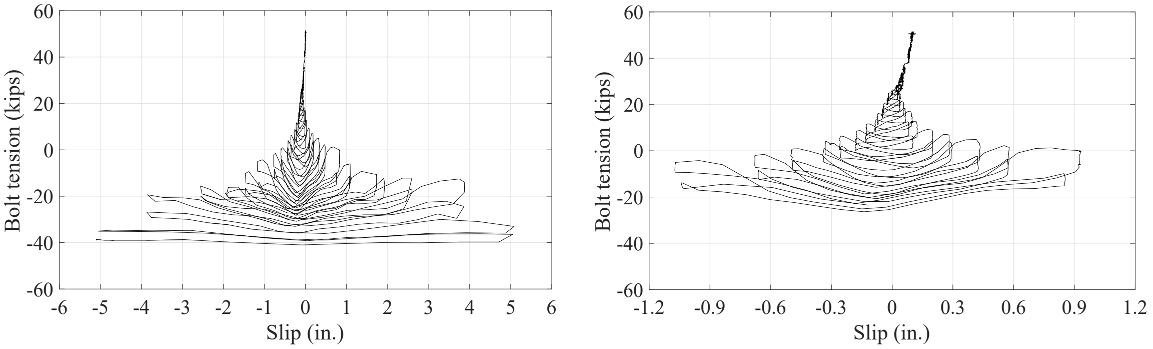

Bolt 4

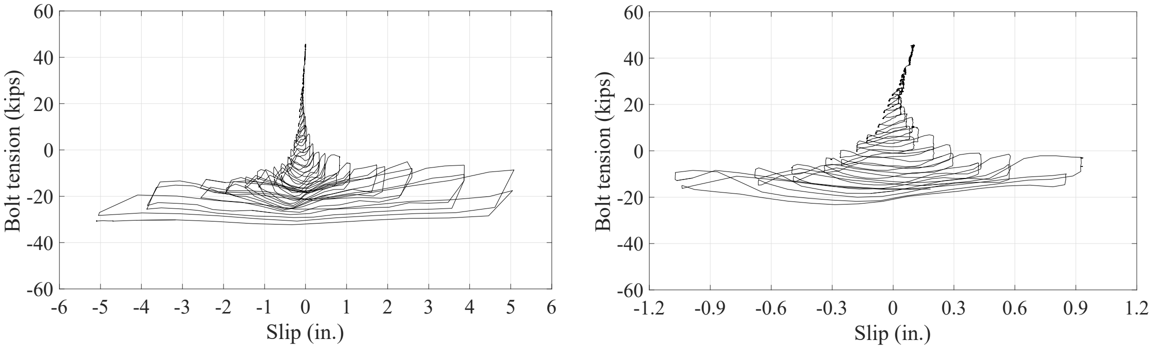

Bolt 5

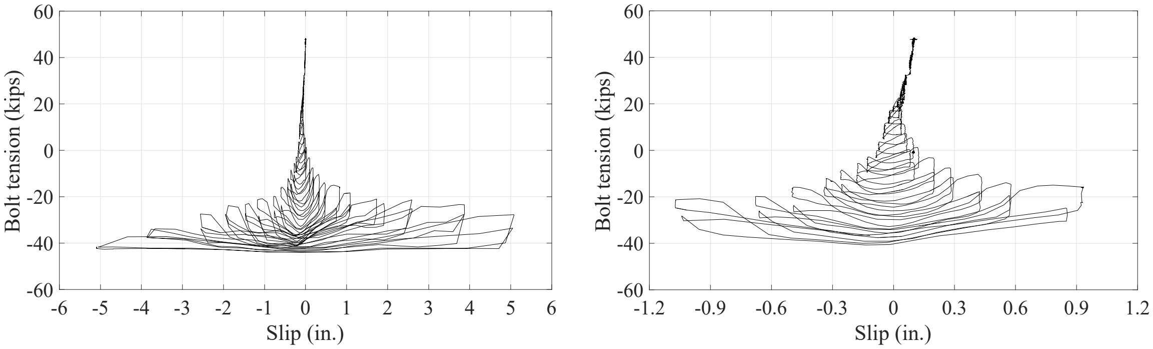

Bolt 6

Test 8-M24-3C-RH-LC

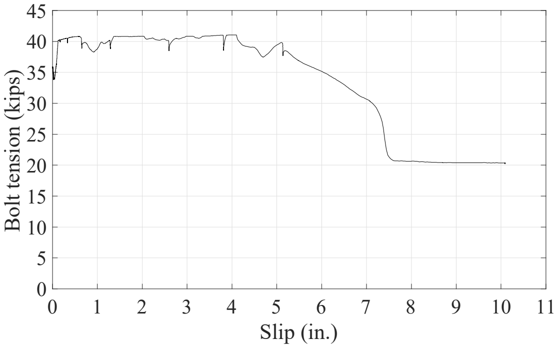

Bolt 1

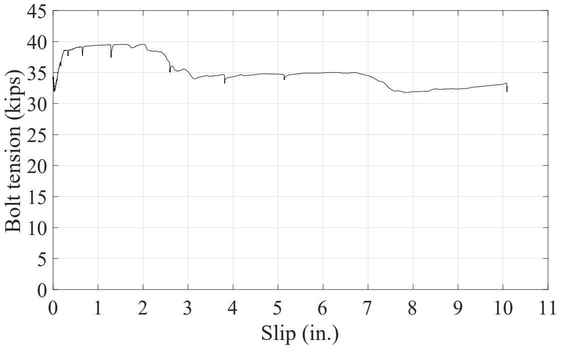

Bolt 2

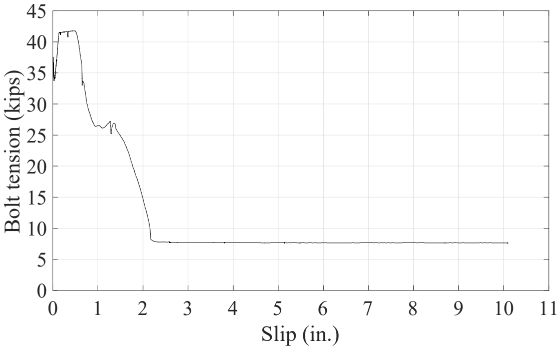

Bolt 3

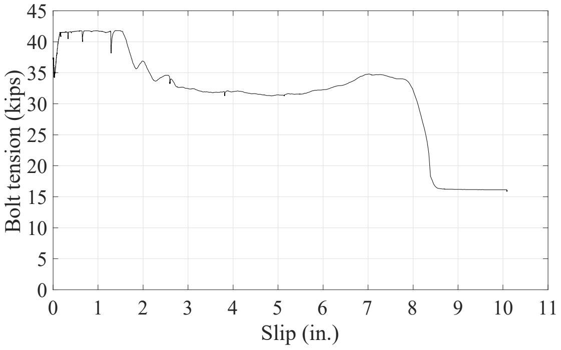

Bolt 4

Test 9-M20-2C-RH-LM

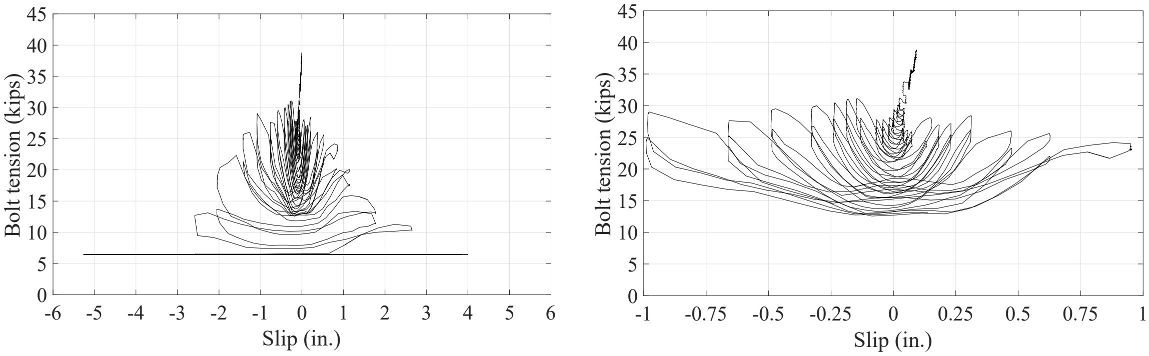

Bolt 1

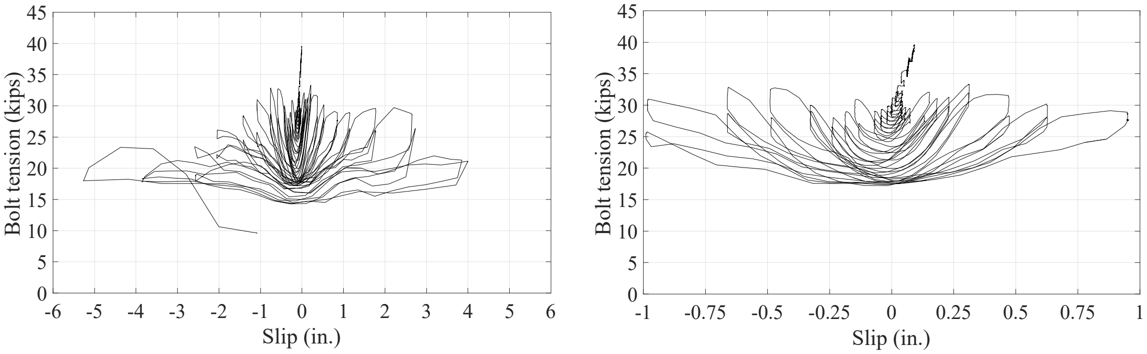

Bolt 2

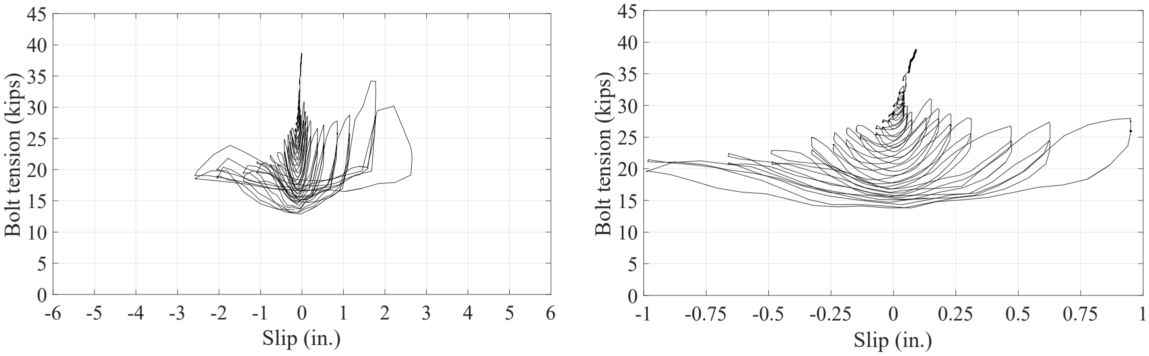

Bolt 3

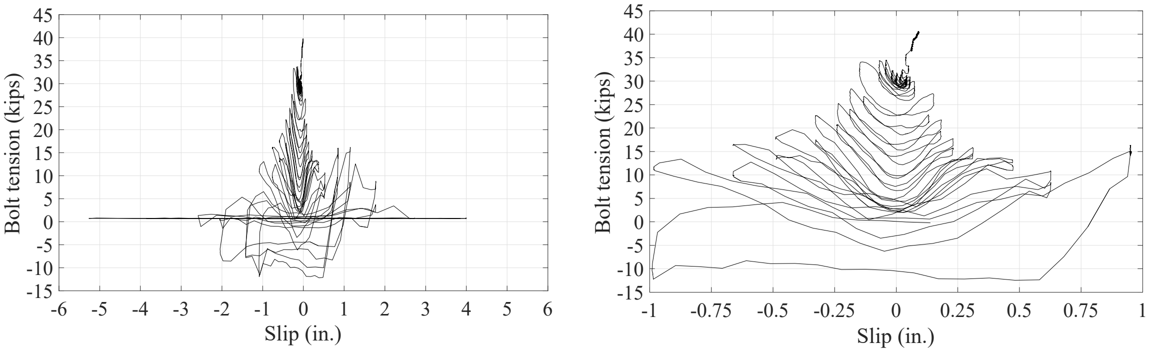

Bolt 4

Test 10-M20-2C-RH-LC

Figure 4.54 Bolt tension versus slip curves for pushout specimens

The pretension loss of bolts under shear force was also demonstrated in regular slip-critical bolted joints. Frank and Yura (1981) tested symmetric butt splice specimens and demonstrated that the initial bolt clamping force only affected the initial stiffness of the load-displacement curves, as illustrated in Figure 4.55. The difference between the two curves gradually diminished because the initial bolt pretension in the torqued bolts released as the bolts deformed inelastically in shear. Ultimately, the axial deformation of the pretensioned bolts, as well as the frictional resistance of the connection, completely dissipated. The slip-critical joint eventually behaved like the bearing-type connection.

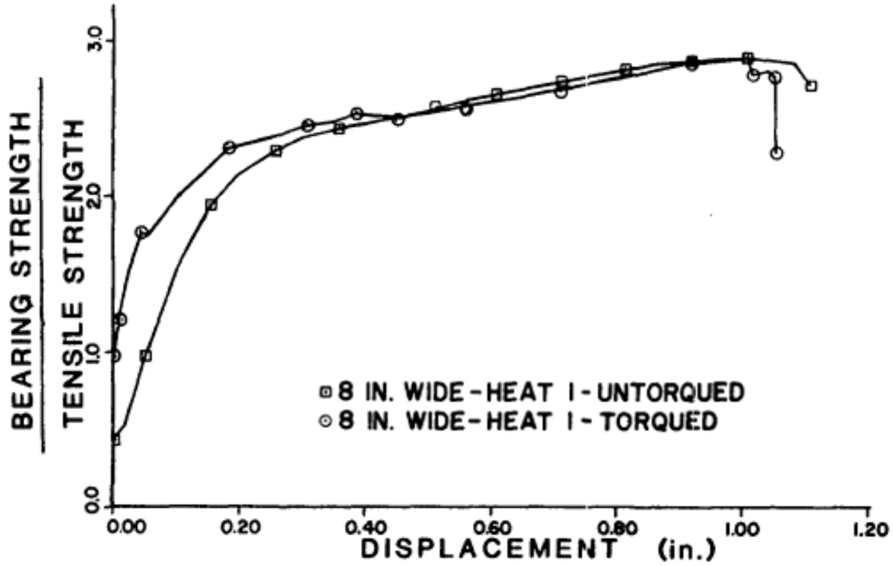

Figure 4.55 Effect of clamping force on the load-displacement curve [after (Frank et al. 1981)]

4.5.8 Force distribution in the system

The load-slip curves show ductile behavior of the clamping connectors. Hence, it is predicted that the applied shear is distributed among the connectors. This prediction is validated with the strain gages on the WT sections. Strain measurements at different sections of the beams are shown in Appendix E. It is seen that all the strains are smaller than the yield strain of the steel beams, indicating that the instrumented locations were elastic during testing.

Figure 4.56 compares the axial forces calculated with the strain gage readings to the theoretical values, provided that the shear force is evenly distributed among the clamps. The left graphs in the figure show the overall comparison throughout the tests, and those in the right side focus on the comparison within 1 in. slip which is likely to be a typical demand range for steel headed stud anchors commonly used in traditional composite diaphragms. It should be pointed out that the calculated axial forces were not negligible at the instrumented sections after pretensioning the bolts, which is contrary to the belief that these forces were trivial before shear was applied. Hence, the axial forces are offset such that the axial force-slip plots start from the origin. Common features are distinguished from the plots. As the beam moved west, the axial force at the west section did not vary much, coinciding with the fact that the west end is free. With the beam loaded east, the axial force at the east section matched the applied actuator forces. When the strain gages approached the clamps, compressive strains were measured at numerous spots on the selected sections, and compressive axial forces were thus obtained.

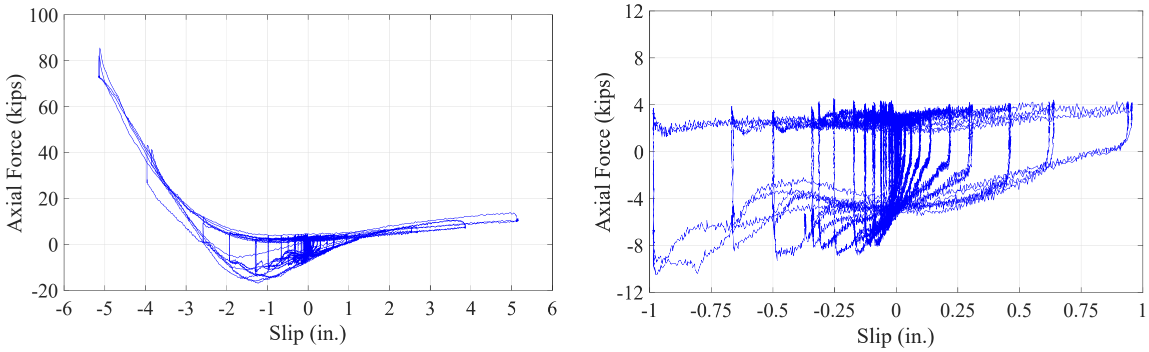

West section

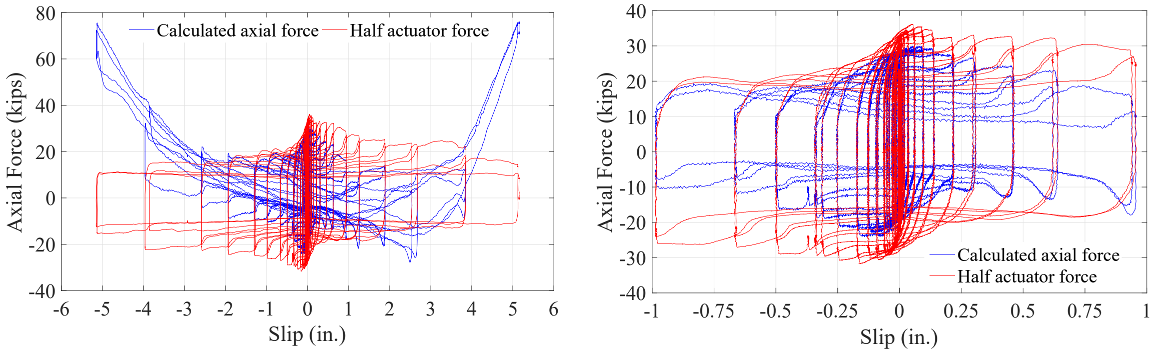

Middle section

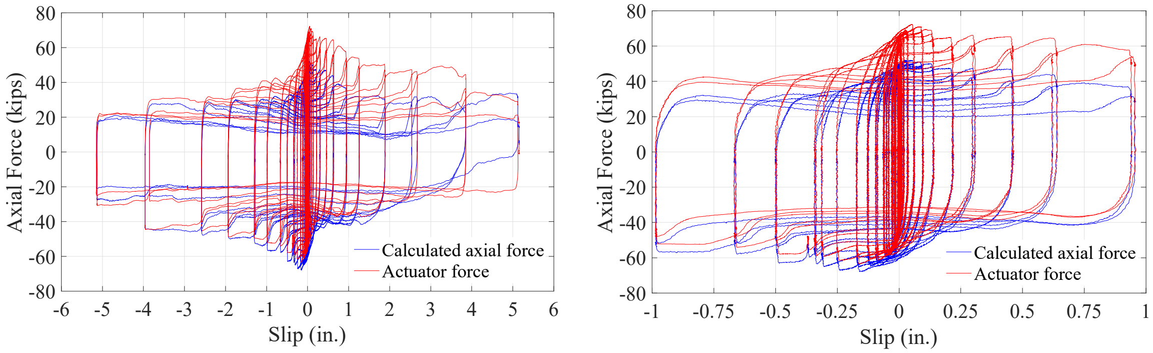

East section

a) Test 3-M24-2C-RL-LC

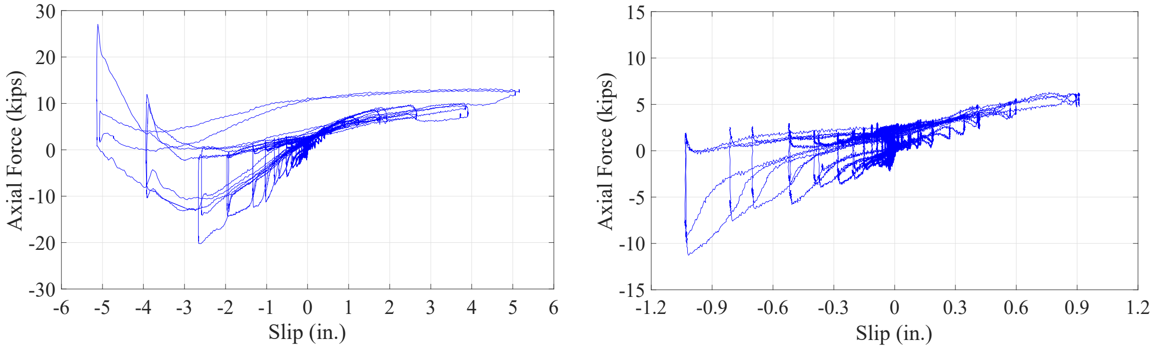

West section

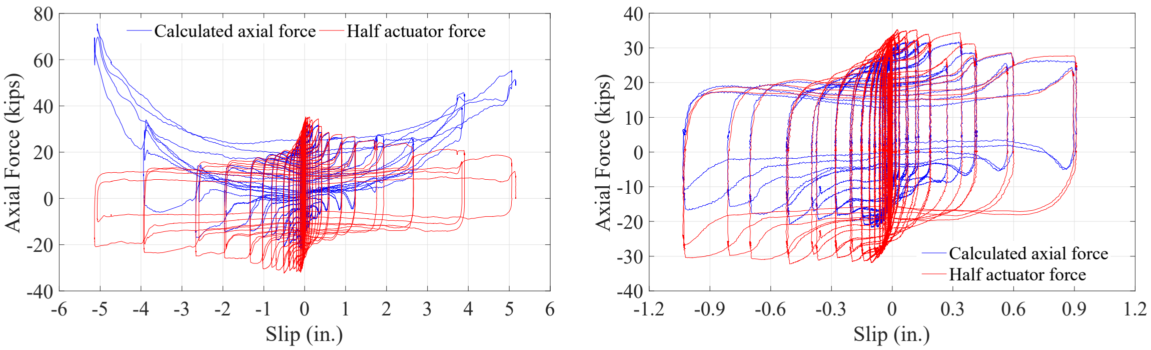

Middle section

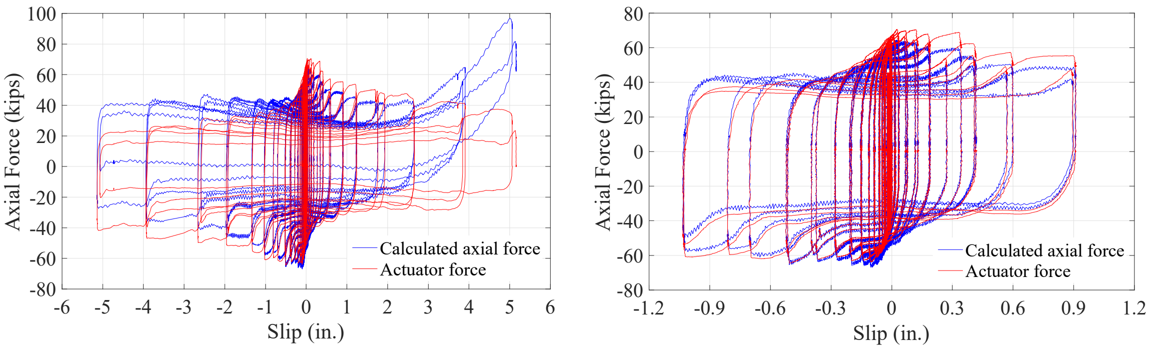

East section

b) Test 5-M24-2C-RH-LC

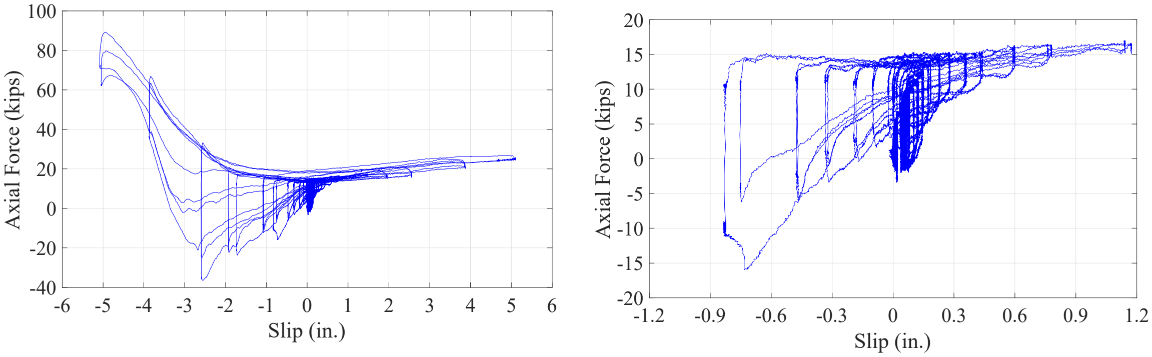

West section

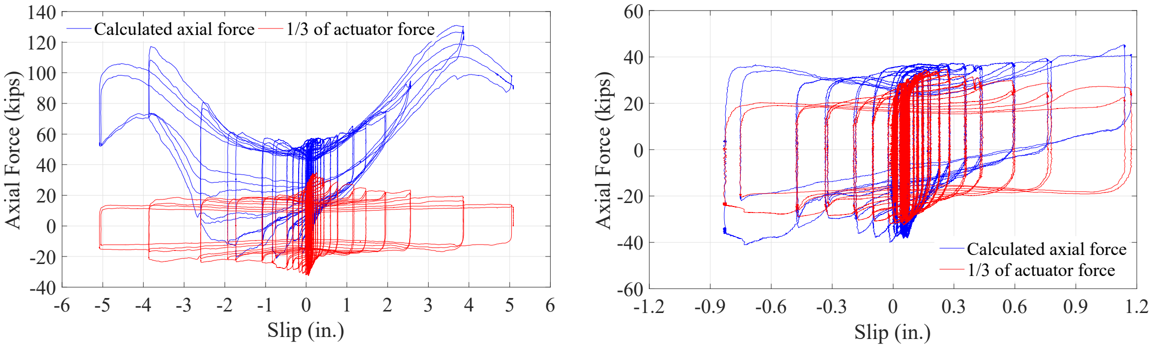

Middle west section

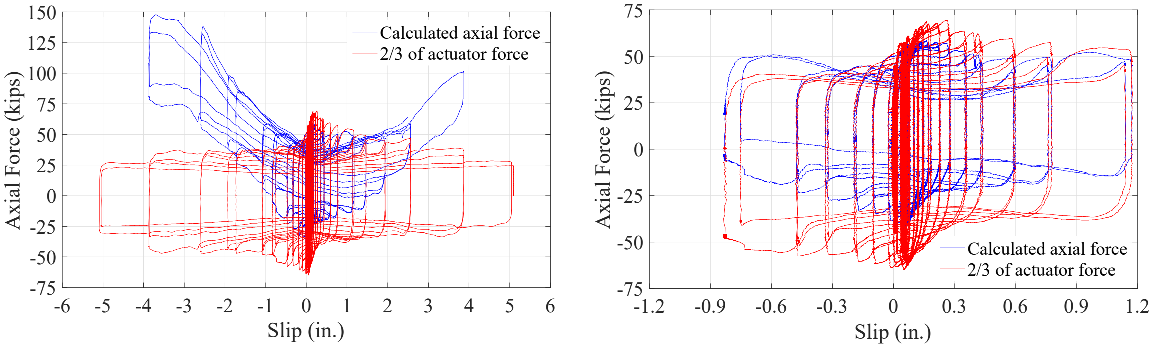

Middle east section

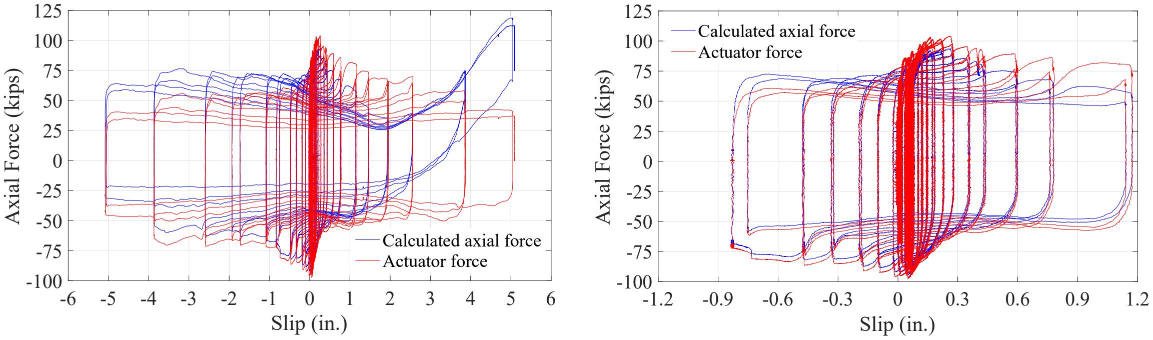

East section

c) Test 8-M24-3C-RH-LC

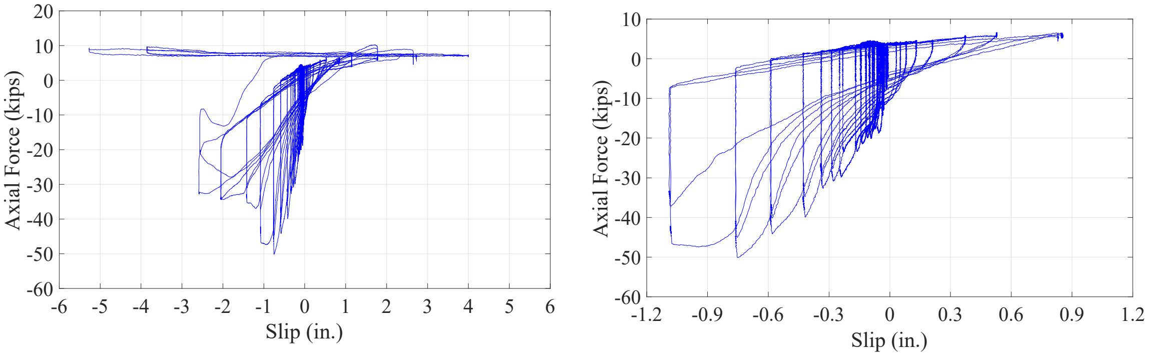

West section

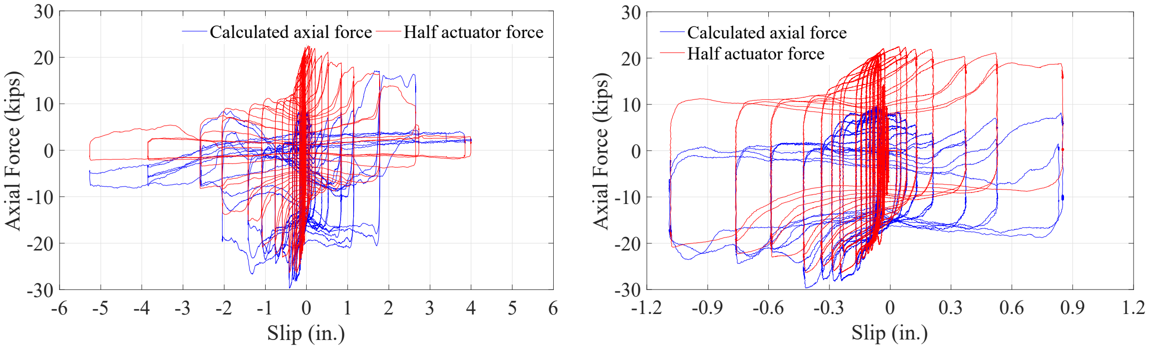

Middle section

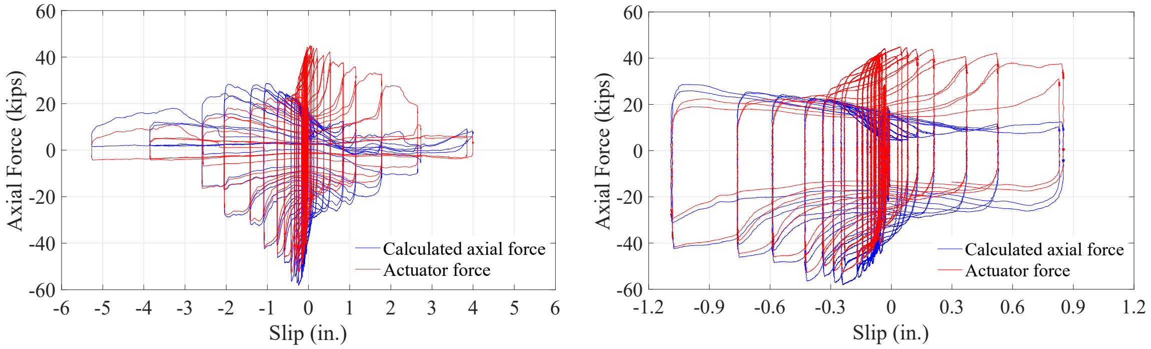

East section

d) Test 10-M20-2C-RH-LC

Note: Positive values represent compressive forces; negative values represent tensile forces.

Figure 4.56 Section axial force-slip curves for pushout test specimens

4.5.9 Response of channel anchors and reinforcement

Channel Anchors

In the pushout tests, none of the limit states listed in Table 4.2 was observed, except for local deformation of channel lips.

Rosette strain gages were attached to the channel anchors to estimate the tensile force and in-plane shear force the anchors were subjected to. The out-of-plane forces acting on the anchors were assumed to be negligible, and thus the anchors were assumed to be in a two-dimensional plane stress state. Using the procedures prescribed in Appendix F.1.3, the tensile stress and shear stress were recovered from the strain gage data and are illustrated in Figure 4.57. In addition, the Von Mises stress is calculated to ascertain whether the anchor behaved elastically because the process described in Appendix F.1.3 is no longer applicable when the material yields. The forces the anchors were subjected to are then calculated by multiplying the stresses with the cross-sectional area of the anchors, which equals to 0.372 in.^{2}.

In the beam tests, as shown in Figure F.41, the tensile stresses in the anchors are relatively consistent, whereas the tensile stresses in the anchors instrumented in the pushout tests range from 75 ksi (tension) to -20 ksi (compression). This could be attributed to the out-of-plane deformation of the channel anchors, which invalidates the plane stress assumption. Since only one strain gage was attached on one side of a channel anchor, the measured axial strain included the normal strain induced by tension in the anchor and in-plane and out-of-plane bending of the anchor. Since the strain gage was placed at the centerline of the anchor, the strain caused by in-plane bending could be small. However, the out-of-plane deformation, if any, cannot be eliminated from the total strain measurements. Therefore, the anchor tensile forces cannot be obtained from the axial stresses calculated in Figure 4.57.

The shear stresses illustrated in Figure 4.57 were calculated based on the assumption that the shear strain is constant along the thickness of the channel anchor. It is shown that the shear stresses in the anchors were generated during bolt pretension. In contrast, in the beam tests, the shear stresses in the anchors were negligible throughout the whole test, as depicted in Figure 5.74 in Chapter 5. The difference between the shear stress variations in the two experiments could result from the out-of-plane force that appeared to be nontrivial in the pushout tests. The fluctuation of the shear stress could be attributed to the varying cyclic shear force applied to the beam.

To eliminate the influences of the out-of-plane deformation of the channel anchors, two strain gages, which are attached on both sides of the channel anchors, could be recommended in future investigation.

Reinforcement

Uniaxial strain gages were attached on the reinforcement to ascertain whether the reinforcement functioned to control the crack propagation in the specimens.

As shown in Figure E.23 in Appendix E, the maximum measured axial strain in the reinforcement is approximately 600 microstrains. The tensile stresses in the reinforcement are calculated to be no more than 18 ksi.

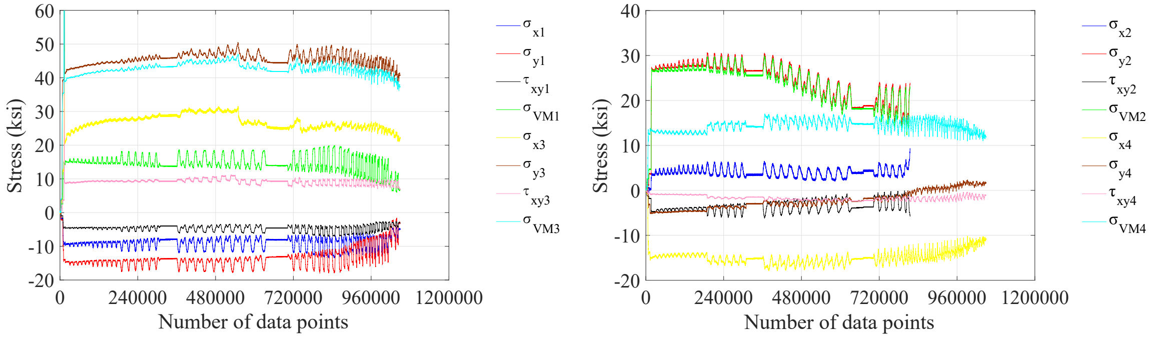

Anchors 1 and 3 Anchors 2 and 4

Test 3-M24-2C-RL-LC

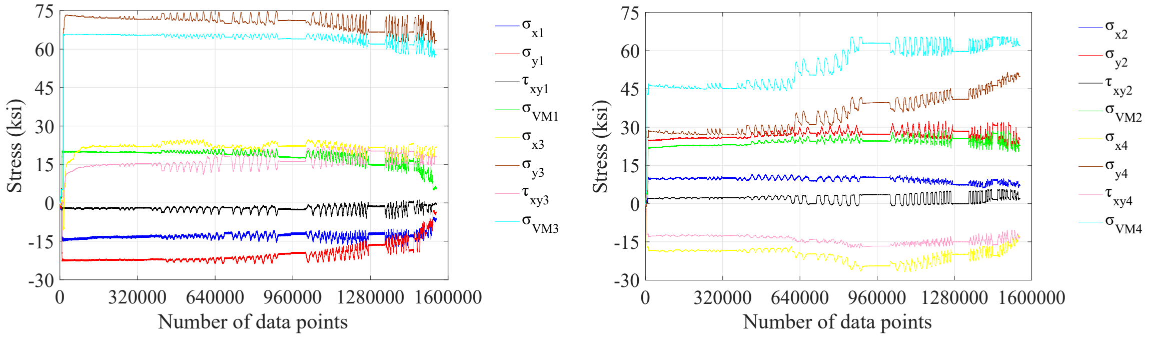

Anchors 1 and 3 Anchors 2 and 4

Test 5-M24-2C-RH-LC

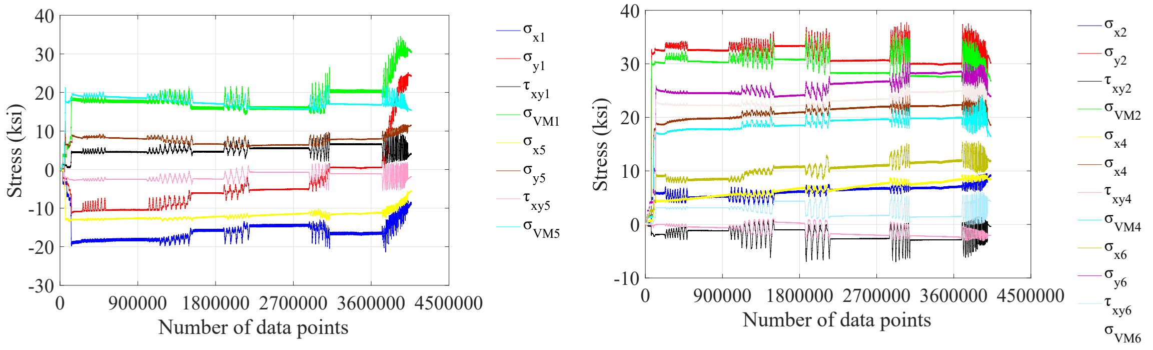

Anchors 1, 3 and 5 Anchors 2, 4 and 6

Test 8-M24-3C-RH-LC

Note: σ_y *describes the normal stress along the axial direction of the anchor;* σ_x *indicates the normal stress perpendicular to the axial direction of the anchor;* τ_{xy} *represents the shear stress acting on the anchor.*

Figure 4.57 Channel anchor stresses in pushout specimens

Assuming the reinforcement and concrete plank were bonded throughout the tests, the concrete strains at the strain gage locations were the same as the reinforcement strains. Since the tensile cracking strain of concrete is normally around 100 microstrains, the strain measurements indicate that internal concrete cracks may exist. This cracking was primarily generated during bolt pretensioning. During the pushout tests, the reinforcement strains fluctuated. Similar to those cracks generated on the concrete plank surface, these potential internal cracks did not appear to affect the behavior of the specimens.

4.6 **Finite element analysis**

Finite element models were developed for the pushout specimens in ABAQUS/CAE (ABAQUS 2011) and analyzed using a central difference algorithm within ABAQUS/Explicit, which is effective for simulations containing material failure and contact. This procedure can be used for quasi-static problems if the loads are applied sufficiently slowly.

4.6.1 Finite element model and mesh

Cast-in channels and T-bolts were meshed with both eight-node reduced integration brick elements (C3D8R) and six-node linear triangular prism elements (C3D6). Steel beams and concrete planks were meshed with C3D8R only. Reinforcement was modelled using two-node three-dimensional truss elements (T3D2). All these components are deformable, except for the clamps that are regarded as rigid parts, as minimal deformation is expected and the computational time can be greatly reduced.

As a result of shear locking, the displacement is usually underpredicted in an analysis where the load mainly produces bending in the model, and fully integration linear solid elements are used for the mesh. Shear locking can be eliminated by using reduced integration elements which have fewer integration points than the full integration elements and are computationally more efficient. The reduced integration elements lose the resistance to certain types of deformation, and therefore ABAQUS automatically adds a small amount of artificial “hourglass stiffness” to avoid the propagation of the spurious modes. In this analysis, enhanced hourglass stiffness was used to avoid excessive element distortion.

4.6.2 Boundary conditions, load applications and contact

The boundary conditions for the models are shown in Figure 4.58. A symmetric boundary condition was defined such that nodes on these surfaces are prevented from translating in the Z direction and rotating in the X and Y directions.

The loading process was divided into two steps. Pretension was first applied by assigning a thermal expansion coefficient and temperature change to the bolt shanks, creating thermal shrinkage and generating tensile forces in the bolt shanks because of the constraints at the bolt ends. The steel beam flange was then loaded in the X direction using displacement control. In order to obtain a quasi-static solution, it is essential to apply the loading slowly and smoothly to minimize dynamic effects.

Tie constraints were defined for surface pairs where the surfaces are attached using slip-critical connections, making all the active DOFs equal for the surface pair. The interaction between the concrete plank and the reinforcement was simulated using an embedded constraint. The translational DOFs of the embedded reinforcement were constrained to those of the corresponding points in the plank. The contact behavior between surfaces was defined in both the normal direction and the tangential direction. “Hard contact”, the default normal behavior in ABAQUS, puts no limit on the magnitude of the contact pressure when the contact restraint is activated once the surface clearance is zero. The contact restraint is removed when the surfaces separate, and the contact pressure becomes zero or negative. A penalty formulation was used to characterize the behavior along the interface. In this formulation, no limit is placed on the shear stress, and an elastic slip is used that generates a small amount of relative movement between the surfaces when they are still sticking. The frictional coefficient was taken as 0.35 for all the surfaces, except for the contact between the steel beam and the steel guides where the frictional coefficient was 0.1. General contact, rather than the contact pair algorithm, was selected to automatically select potential contact surfaces.

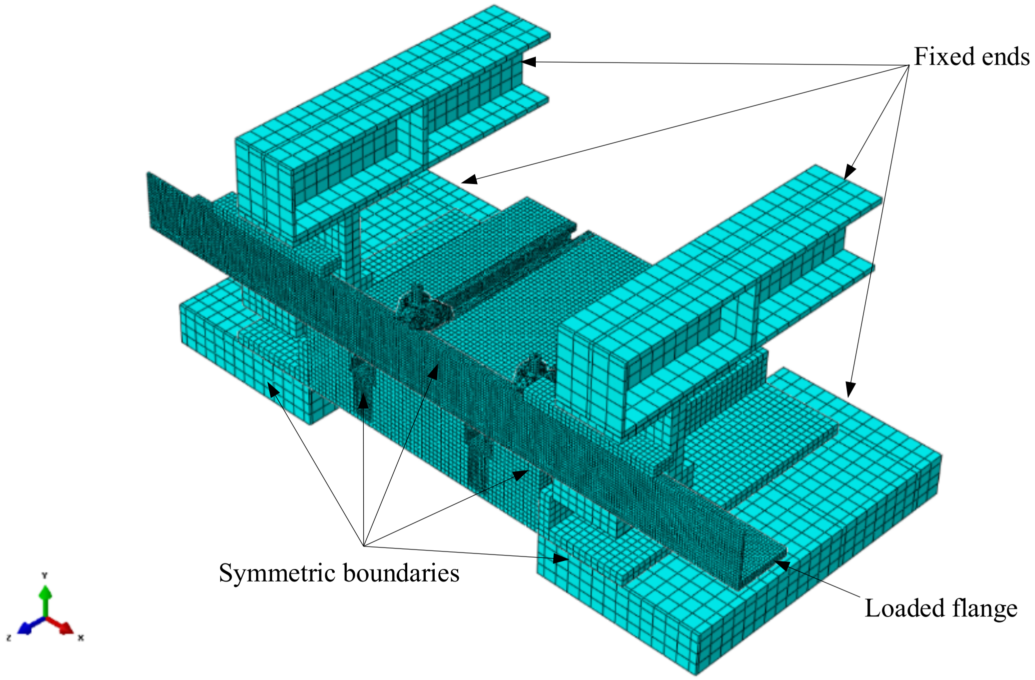

Figure 4.58 Test setup assembly and boundary conditions

4.6.3 Material model for concrete

A concrete damaged plasticity model was used to model the concrete planks. The concrete model assumes a nonassociated flow rule, and the plastic potential function and yield function are different. The Drucker-Prager hyperbolic function is used to define the direction of the plastic flow, while the yield function is based on the model proposed by Lublinear et al. (1989) and modified by Lee and Fenves (1998). The compressive stress-strain curve proposed by Popovics (1973) was employed for this analysis, as shown in Equation (4.22). The elastic modulus was calculated using Equation (4.23). The Poission's ratio was taken as 0.15.

$$f_c = f_c' \frac{\varepsilon_c}{\varepsilon_c'} \frac{n}{n - 1 + (\frac{\varepsilon_c}{\varepsilon_c'})^n} \tag{4.22}$$

$$E_c = 57{,}000\sqrt{f_c'} \tag{4.23}$$

Where

f_c = concrete compressive stress

f_c' = concrete peak compressive stress

ε_c = concrete compressive strain
ε_c' = concrete compressive strain at peak stress
n = normalized modulus of elasticity = $0.4 \times 10^{-3} f_c' + 1$

The default parameters specified in ABAQUS for the concrete damaged plasticity model were used to characterize the plastic behavior under general stress and stress states. The parameters include: dilation angle = 38°, signifying the volumetric change of concrete under inelastic stress states, eccentricity = 0.1, implying the dilation angle does not vary much as the confining stresses change. K_c , the ratio of the second invariant of the stress deviator on the tensile meridian to that on the compressive meridian at initial yield at a given first invariant of stress such that the maximum principal stress is negative, is equal to 0.67. The ratio of biaxial compressive yield stress to uniaxial compressive yield stress σ_{bo}/σ_{co} is taken as 1.16.

Mesh dependency, meaning that mesh refinement does not lead to a converged solution for the problem, exists for concrete with no or little reinforcement. As the mesh size becomes smaller, the structure can withstand more loading. Concrete also exhibits size effect, in the sense that the cracking stress depends on the specimen size (Bazant 1984). To eliminate mesh dependency in the analysis, a postfailure stress-strain relationship was defined which assumes the ultimate strain at nearly zero stress to be 10 times the cracking strain.

Concrete damage variables characterize stiffness degradation when the specimen is unloaded from any point on the softening branch. The damage variables range from zero for an undamaged model to one, exhibiting complete loss of strength and stiffness. Concrete compressive damage D_c and tensile damage D_t are derived using the following expressions:

$$D_c = 1 - \sigma_c/f_c \tag{4.24}$$

$$D_t = 1 - \sigma_t/f_t \tag{4.25}$$

The damage evolution of concrete under compression and tension is shown in Figure 4.59. Considering the degraded unloading stiffness due to damage, the concrete compressive and tensile loading/unloading responses are plotted in Figure 4.60. When defining material properties, the compressive strength of the concrete planks used the cylinder strength tested on the test day. No concrete cylinders were tested for the splitting tensile strength of the concrete planks on the test day; therefore, the tensile strength of the concrete planks was taken as 1/10 of their compressive strength (Arıoglu et al. 2006).

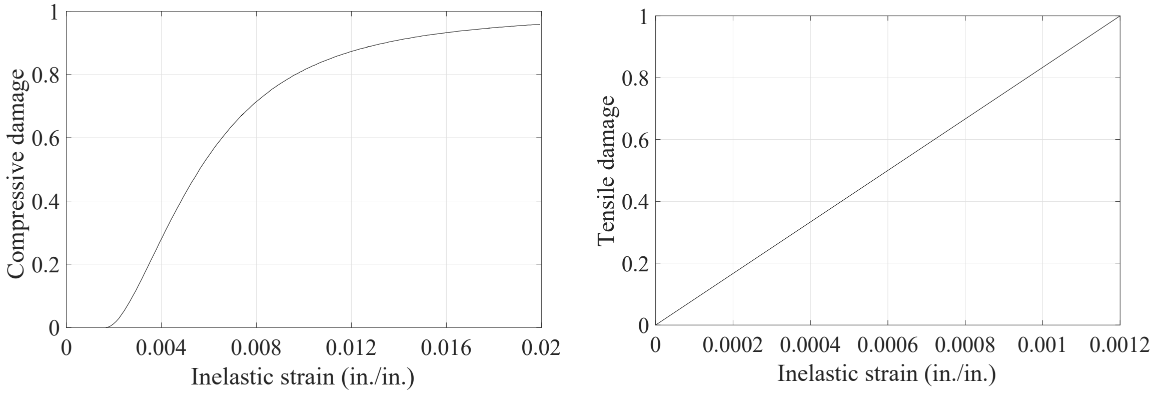

a) Compression b) Tension

Figure 4.59 Concrete compressive and tensile damage variable

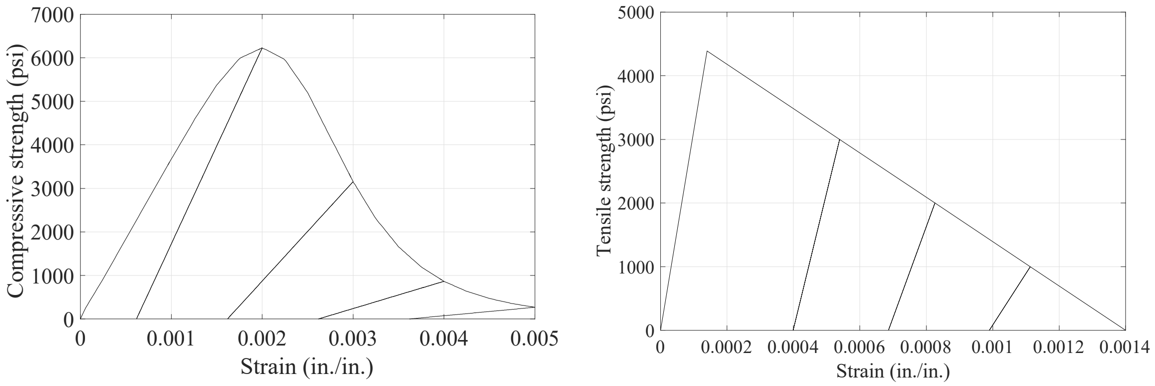

a) Compression b) Tension

Figure 4.60 Loading and unloading behavior of concrete in compression and tension

4.6.4 Material models for steel beams, reinforcement, channels and bolts

The steel beam, reinforcement, channels and bolts were simulated using a metal model which uses a Von Mises yield function and an associated flow rule.

Except for localized regions that may yield under the clamping force, the steel section remained elastic during the tests. An elastic-perfectly-plastic material model was defined for the steel beam and reinforcement. The yield stress was taken as 51.2 ksi, 50.6 ksi, and 63.3 ksi for the WT5x30 section, WT4x15.5 section, and reinforcement, respectively. The elastic modulus was taken as 30600 ksi, 30100 ksi, and 27500 ksi for the WT5x30 section, WT4x15.5 section, and reinforcement, respectively. The mechanical behavior was assumed to be the same in both tension and compression. A bilinear relationship was assumed for the channels, as shown in Table 4.10. The elastic modulus was 28000 ksi. The bolt stress-strain curve used for the FE analysis is given in Figure F.7.

Table 4.10 Channel true stress and true plastic strain

True stress (ksi)	True plastic strain
65.3	0.000
71.8	0.029

4.6.5 Finite element analysis results

In Figure 4.61, the monotonic load-slip curves of Tests 2-M24-2C-RH-LM and 9-M20-2C-RH-LM are compared to those obtained from the finite element analysis. As shown in the plot, the peak strength of the finite element model of Specimen 2-M24-2C-RH-LM is very close to that of the test specimen, while the finite element model slightly overestimates the peak strength of Specimen 9-M20-2C-RH-LM, which could indicate that the actual frictional coefficient between the components was a little smaller than 0.35 in this specimen. In addition, the monotonic shear strength of the M20 clamps was obtained from Specimen 9-M20-2C-RH-LM only, and the variability of the result is unknown. In contrast, even though the parameters were varied, the monotonic behavior of the M24 clamps was studied in Specimens 2-M24-2C-RH-LM, 4-M24-2C-RH-LM-S and 7-M24-3C-RH-LM, which exhibited consistent slip strength and peak strength.

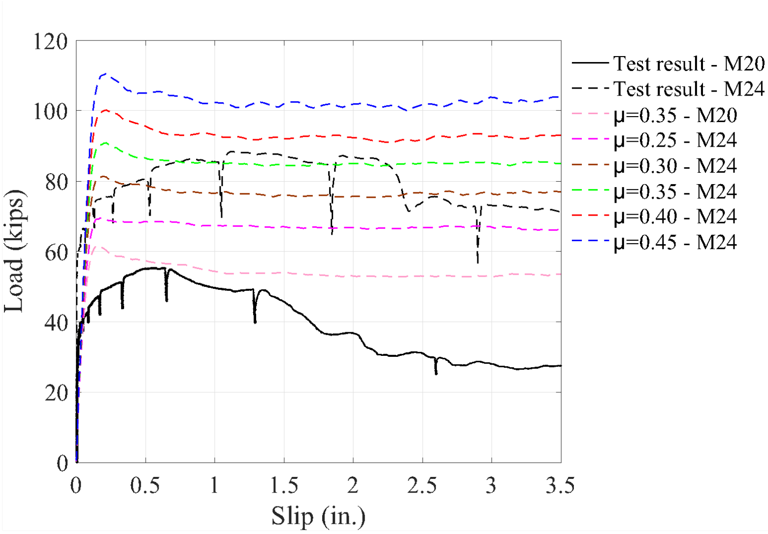

Figure 4.61 Load-slip curve comparison

It is noted that the slip at which the peak strength occurs is different between the computational and experimental load-slip curves. In the specimens, if the frictional resistance between two sticking contact surfaces is not overcome, the actual slip is negligible. However, the friction simulation in general contact in ABAQUS automatically chooses a penalty stiffness to ensure that an elastic slip, which is a very small fraction of the characteristic element length, is present when the contact surfaces are still sticking. That is why the peak strengths of the computational load-slip curves do not occur at approximately zero slip. The experimental load-slip curve is discussed in Section 4.7.

In the finite element models, due to the frictional force between the clamp teeth and steel flange, both clamps rotate along with the moving steel beam. After reaching the maximum rotation, the clamps maintain their positions while the beam continues moving. However, as observed in the experiments, some clamps remained nearly still throughout the whole test, and some rotated until they fully detached from the steel beam. These differences may explain why the computational load-slip curves show little strength degradation, while the post-peak strength reduction appears to be greater in the tested load-slip curves, especially for Specimen 9-M20-2C-RH-LM.

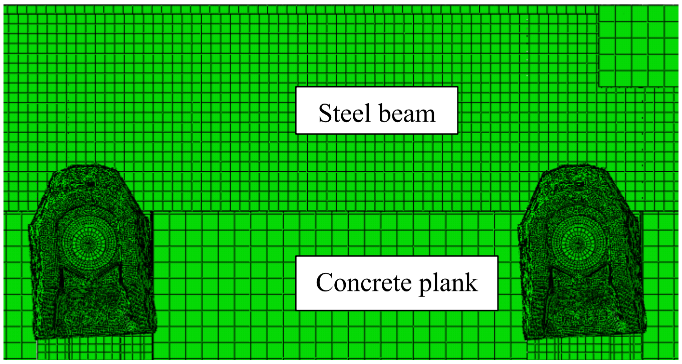
Steel beam
Concrete plank

M24 clamps and μ = 0.35

Figure 4.62 Rotation of clamps in finite element model (plan view)

Using the finite element model of Specimen 2-M24-2C-RH-LM, a parametric study was performed by varying the frictional coefficients from 0.25 to 0.45. Although a higher frictional coefficient is desirable to achieve higher shear strength, the maximum equivalent plastic strain (PEEQ) in the bolts is also larger. When the frictional coefficient is 0.45, the maximum PEEQ of the bolts is approximately 0.097, as illustrated in Figure 4.63.

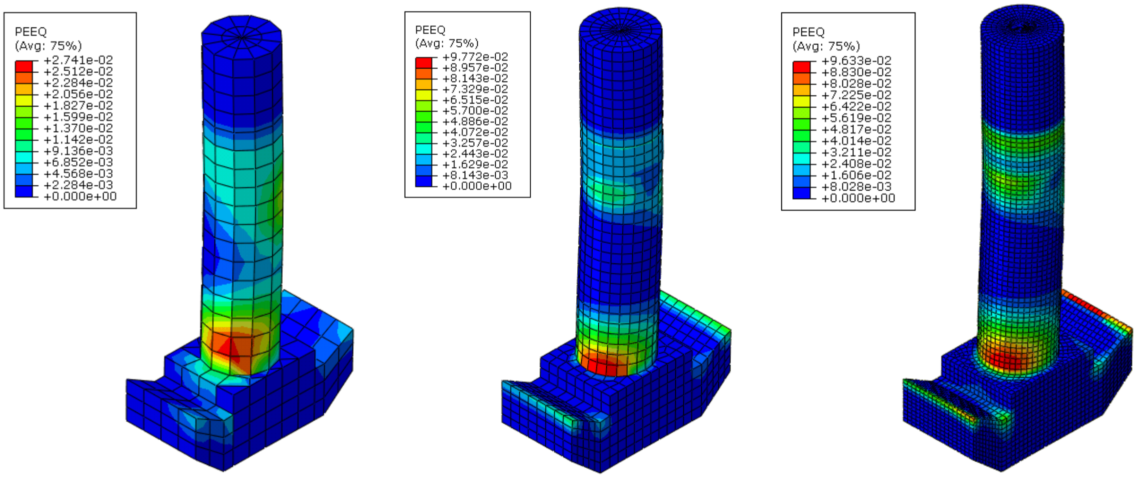
PEEQ
(Avg: 75%)
+2.741e-02
+2.512e-02
+2.284e-02
+2.056e-02
+1.827e-02
+1.599e-02
+1.370e-02
+1.142e-02
+9.136e-03
+6.852e-03
+4.568e-03
+2.284e-03
+0.000e+00
PEEQ
(Avg: 75%)
+9.772e-02
+8.957e-02
+8.143e-02
+7.329e-02
+6.515e-02
+5.700e-02
+4.886e-02
+4.072e-02
+3.257e-02
+2.443e-02
+1.629e-02
+8.143e-03
+0.000e+00
PEEQ
(Avg: 75%)
+9.633e-02
+8.830e-02
+8.028e-02
+7.225e-02
+6.422e-02
+5.619e-02
+4.817e-02
+4.014e-02
+3.211e-02
+2.408e-02
+1.606e-02
+8.028e-03
+0.000e+00

Bolt mesh size = 6 mm Bolt mesh size = 3 mm Bolt mesh size = 1.5 mm

Figure 4.63 Maximum equivalent plastic strain in bolt

As discussed in Section 4.3, the bolt coupons fractured outside of the 1 in. gage length; therefore, a complete stress-strain curve of the bolts utilized in the pushout tests cannot be obtained from material testing. Two complete stress-strain curves of the bolts utilized in the beam tests are provided for reference. It could be deduced from Figure 4.64 that necking may initiate when PEEQ is 0.07, which could be undesirable since bolt fracture is imminent. Future testing is required to demonstrate whether the bolts would neck or fracture when the frictional coefficient is equal to or greater than 0.45.

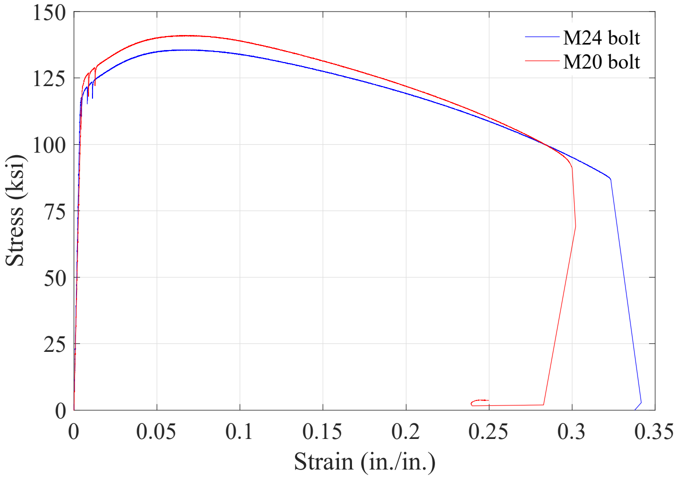

Figure 4.64 Stress-strain curves of bolt material in beam tests

From the finite element analysis results, the relationship between the bolt tension and slip is provided in Figure 4.65. As illustrated in Figure 4.65a, after pretensioning, the axial tension of the M24 and M20 bolts reaches approximately 55 kips and 40 kips, respectively, which are close to the measured bolt tension given in the pretension tests (see Section 4.4.3). As the slip increases, the bolt tension first decreases and then levels off. The bolt tension reduction is shown to be related to the magnitude of the frictional coefficient. Since the bolts are yielded after pretensioning, a higher frictional coefficient leads to larger shear force acting on the bolts as well as greater bolt tension reduction. The tension of the bolts is normalized in Figure 4.65b relative to their initial values. The finite element analysis results also indicate that the slip corresponding to the peak load ranges from 0.148 in. to 0.214 in. At this slip level, the bolt tension reduction is shown to be similar among all the models, and the percentage of reduction varies from 20% to 25%.

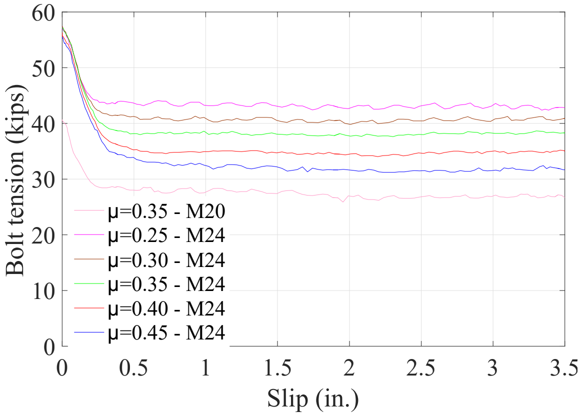

a) Bolt tension vs slip

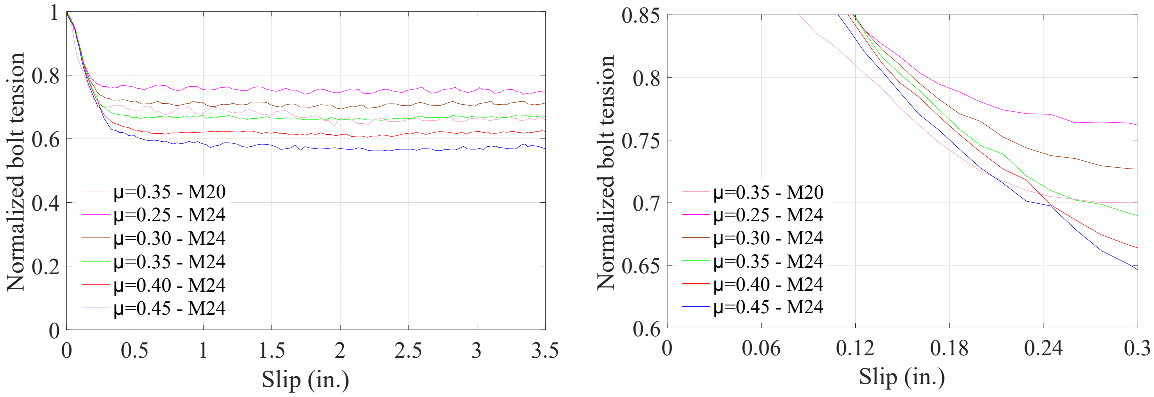

b) Normalized bolt tension vs slip

Figure 4.65 Bolt tension-slip relationship

When a bolt is pretensioned, the bolt force is distributed between the clamp teeth and clamp tail. Only the force transferred to the clamp teeth contributes to the shear resistance of the system. Figure 4.66 shows the ratio of the force at the clamp teeth to the total bolt tension, which varies from 0.68 to 0.74.

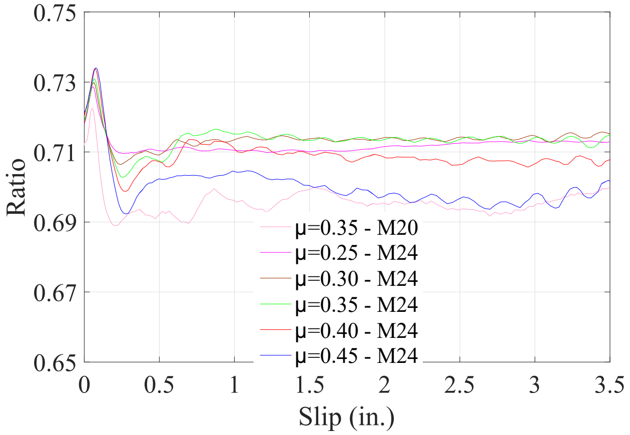

Figure 4.66 Normal force at clamp teeth to bolt tension ratio

4.7 Design recommendations

Since the shear strength of a clamp relies on friction, it is critical to quantify the normal forces and the frictional coefficients at the two slip planes, with one slip plane between the clamp teeth and steel flange and the other one between the steel flange and concrete plank. When the rotation of the clamps is insignificant, free body diagrams for a steel beam segment and two clamps in a pushout specimen are illustrated in Figure 4.67. During the tests, it was observed that the clamps started to rotate as the slip increased, indicating the rotational resistance at the clamp tail (M_1) and teeth (M_2) was insufficient to restrain the movement of the clamps. After the tests, it was also found that the bolt shanks were bent due to the shear force (f) transferred from the clamps. Although it is very difficult to determine the magnitude of the forces illustrated in Figure 4.67, an analysis is sufficient so long as the bolt tension variation can be estimated.

In the pushout tests, before slip occurs, the resistance of the clamps primarily relies on static friction. After slip occurs, the strength increase mainly stems from the bearing effect at the clamp teeth. As shown in Figure 4.68, impressions on the steel flanges in the pretension tests results from the normal force applied by the clamp teeth. Therefore, the clamp teeth have to overcome the resistance from the surrounding steel flange material to slip. The bearing effect is also evidenced by the scraped steel flange seen in the pushout tests, as shown Figure 4.69. For the finite element model, the bearing effect is simplified and simulated with a frictional coefficient of 0.35 which is validated by the similar peak strengths of the computational and tested load-slip curves. The single frictional coefficient explains why the load-slip curve obtained from finite element analysis only contains two segments, with the first and second segments demonstrating the behavior of the clamps before and after slip, respectively. The first segment of the curve is not as stiff as that seen in the tested load-slip curves due to the elastic slip stiffness automatically assigned by ABAQUS.

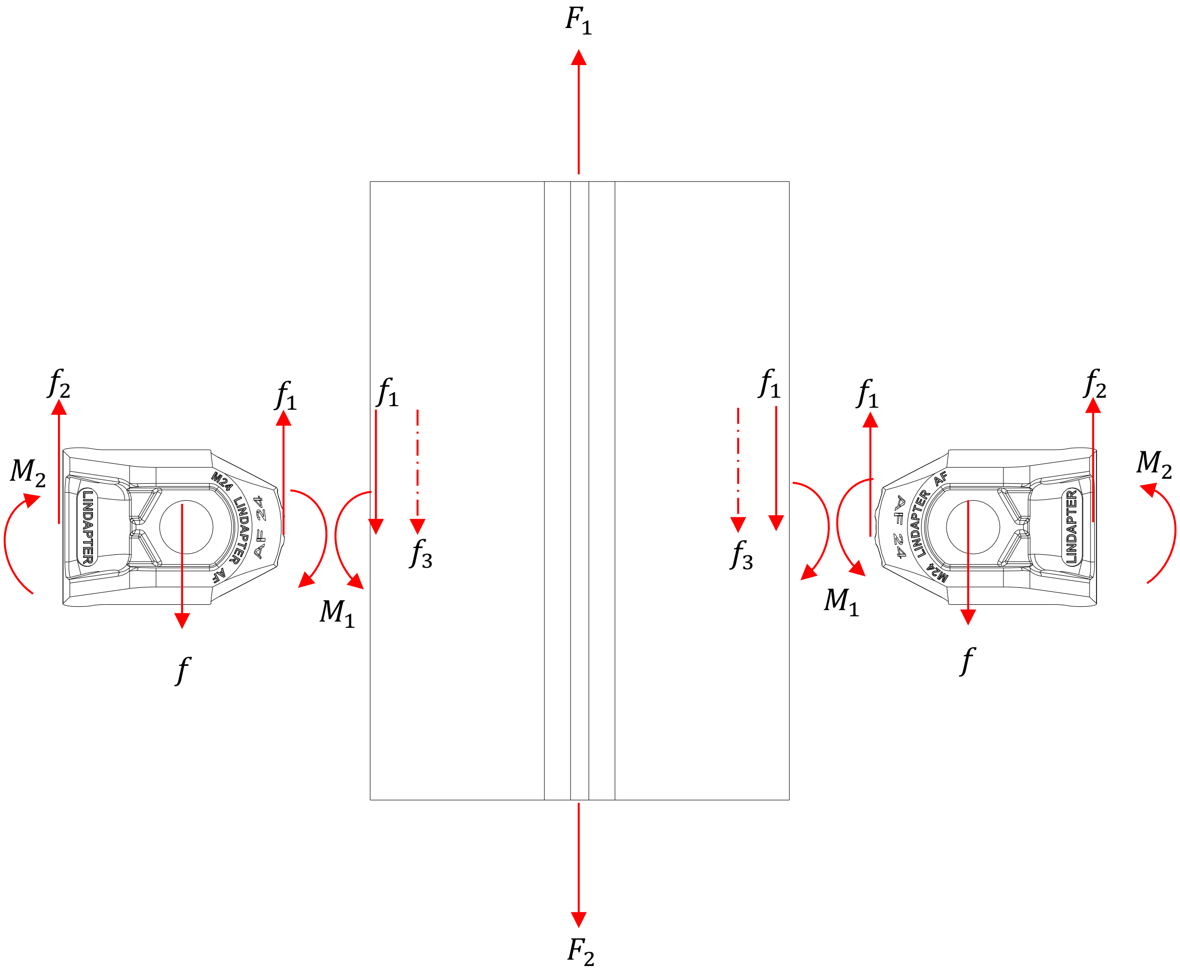
F_1
f_2
f_1
f_1
f_1
f_1
f_2
M_2
M_2
M24 LINDAPTER AF 24
LINDAPTER
f_3
f_3
M_1
M_1
f
f
F_2

F_1 and F_2 : forces at the ends of the steel beam segment

f : shear force acting the bolt

f_1 : friction between the clamp teeth and steel beam flange

f_2 : friction between the clamp tail and concrete plank

f_3 : friction between the steel beam flange and conrete plank

M_1 : rotational resistance at the clamp teeth

M_2 : rotational resistance at the clamp tail

Figure 4.67 Free body diagram of steel beam and clamp

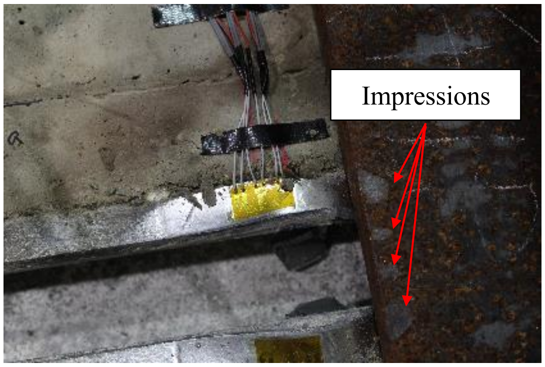

Figure 4.68 Impressions on steel flange in pretension test for M24 bolts

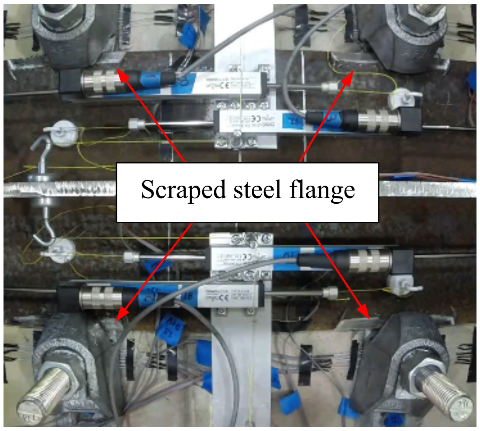

Figure 4.69 Damage of steel flange in Test 5-M24-2C-RH-LC at 1.28 in. slip

According to the finite element analysis results, the ratio of the normal force distributed to the clamp teeth to the bolt tension is plotted in Figure 4.66. It is seen that this ratio oscillates around 0.7 throughout the analysis. In the pushout tests, since the bolts are yielded after pretensioning, the bolt shear shown in Figure 4.67 releases the initial axial deformation, and the bolt tension gradually decreases until the bolt shear stabilizes. The bolt tension versus slip relationship is given in Figure 4.65. The reduction of bolt tension at 0.02 in. slip is insignificant, but the reduction at peak load is about 1/4, which is appreciable. It is seen that the detrimental effect of bolt tension reduction is offset by the beneficial effect of overcoming the bearing of the clamp teeth against the steel flange. Hence, these two coefficients are essential for the proposed design equations: a coefficient of 0.7 to describe the normal force at the clamp teeth and a coefficient of 0.75 (or 3/4) to account for the actual bolt tension when the peak strength of the clamps is reached.

Slip tests are not conducted in accordance with Appendix A of the RCSC Specification (2014), but the mean slip coefficient, given in Table 4.11, is still determined as the ratio of the slip load, which corresponds to a slip of 0.02 in., to the effective normal force at the clamp teeth, which is 70% of the bolt tension. Based on the measured bolt tension in the pretension tests shown in Section 4.4.3, the actual bolt force is assumed to be 1.3 times the minimum bolt pretension in Table J3.1M in AISC 360-16 (2016). The slip coefficient between the unroughened galvanized clamp teeth and as-received mill scale steel flange surface could vary between 0.2 and 0.3, which are the mean slip coefficients for unroughened galvanized surfaces and clean mill scale surfaces, respectively (Grondin et al. 2007). Meanwhile, it is shown in BS 5975:2008 that the frictional coefficient between the cast surface of hardened concrete and plain unrusted steel could be as low as 0.1. Hence, the mean slip coefficients calculated in Table 4.11 are reasonable.

Table 4.11 Mean Slip Coefficient in pushout specimens

Specimen	Slip load (kips)	Bolt tension (kips)	Mean slip coefficient
2-M24-2C-RH-LM	60.8	239.6	0.181
4-M24-2C-RH-LM-S	56.5	239.6	0.168
7-M24-3C-RH-LM	87.0	239.6	0.173
9-M20-2C-RH-LM	36.5	166.0	0.157
		Mean	0.170
		C.O.V.	0.051

Equations (4.26) and (4.27), which are similar to the design equation for a slip-critical bolted connection provided in AISC 360-16 (2016), are thus proposed to predict the slip strength Q_s and peak strength Q_p of a clamp under monotonic loading.

$$Q_s = k_d \mu_s D_u T_b n_s \tag{4.26}$$

$$Q_p = k_d k_r \mu_p D_u T_b n_s \tag{4.27}$$

Where

k_d and k_r = coefficients accounting for the portion of bolt tension transferred to the clamp teeth and the bolt tension reduction at peak strength, which are 0.70 and 0.75, respectively

μ_s = mean slip coefficient, which is 0.17 in the pushout tests series

μ_p = idealized frictional coefficient at peak strength, which is 0.35 in the pushout test series

D_u =1.13, a multiplier representing the ratio of the mean installed bolt pretension to the specified minimum bolt tension

T_b = minimum fastener tension given in Table J3.1M in AISC 360-16

n_s = number of slip planes, which is 2

Although the turn-of-nut method is investigated in this research, the calibrated wrench method is also acceptable for pretensioning the T-bolts. As the method of pretensioning is unknown, D_u is conservatively taken as 1.13, which is established for regular bolted connections pretensioned using the calibrated wrench method (Kulak et al. 1987).

Table 4.12 shows the tested strength to predicted strength ratios for both M24 and M20 clamps. The proposed design equations provide conservative predictions of the slip strength and peak strength of a M24 clamp. The difference comes from D_u which is approximately 1.3 for the bolts in the pushout specimens. For the M20 clamps, the predicted strengths are close to the tested strengths.

Table 4.12 Tested strength to predicted strength ratio

Specimen	Tested strength (kips)		Predicted strength (kips)		Ratio	
	Q_s	Q_p	Q_s	Q_p	Slip	Peak
2-M24-2C-RH-LM	60.8	88.5	49.6	76.6	1.23	1.16
4-M24-2C-RH-LM-S	56.5	87.9	49.6	76.6	1.14	1.15
7-M24-3C-RH-LM	87.0	130.1	74.4	114.9	1.17	1.13
9-M20-2C-RH-LM	36.5	55.3	34.3	53.0	1.06	1.04
				Mean	1.15	1.12
				SD	0.0612	0.0474
				COV	0.0533	0.0424

A reduction factor could be used with Equation (4.26) to account for the lower shear strength of clamps under cyclic loading. For the five cyclic pushout specimens, the average peak strength reduction is 21%, as shown in Table 4.13. Hence, it is suggested to use 80% of the predicted monotonic shear strength of clamps as their cyclic shear strength.

Table 4.13 Peak strength reduction in cyclic pushout specimens

Specimen	Cyclic tests (kips)		Monotonic tests (kips)	Ratio	
	Positive	Negative		Positive	Negative
3-M24-2C-RL-LC	72.2	63.3	88.5	0.82	0.72
5-M24-2C-RH-LC	70.6	64.4	88.5	0.80	0.73
6-M24-2C-RH-LC-S	65.5	71.8	87.9	0.75	0.82
8-M24-3C-RH-LC	104.0	97.0	130.1	0.80	0.75
10-M20-2C-RH-LC	44.9	52.5	55.3	0.81	0.95
			Average	0.79	0.79

The clamp manufacturer conducted tests and proposed design strength values for the clamps, but their recommended design shear strengths cannot be used as references for the clamps used in composite beams. Although the details regarding the manufacturer's tests are not entirely clear, the known differences between the manufacturer's tests and the pushout tests are given below.

- Materials and surface conditions: Conventional applications of clamps normally focus on connections between steel sections. An example is given in Figure 4.70. Two slip planes exist which include the surface between the clamp teeth and the steel section and the surface between the steel section and the location plate. The steel section can be painted or galvanized, while the clamps and the location plate are in hot dip galvanized finishes (Lindapter 2011). However, no experiments have been conducted by the manufacturer to measure the actual frictional coefficients at these slip surfaces. In the pushout tests, there are also two slip planes, which are the surface between the clamp teeth and the steel section and the surface between the steel section and the cast surface of the concrete plank. The steel sections in the pushout tests have as-received mill scale surface conditions. At these slip surfaces, neither the frictional coefficients nor their variations are thoroughly investigated in the pushout tests.

- Bolt pretension: In the pushout tests, the turn-of-nut method is employed to generate adequate and reliable pretension in the bolts. The bolts are expected to yield after pretensioning. The manufacturer, on the other hand, recommends minimum torque values for tightening the bolts. Since the bolts are tightened with a calibrated wrench in the manufacturer's tests, the lubrication condition affects the bolt tension. However, the lubrication for the bolts and nuts is vaguely mentioned in the manufacturer's tests. Therefore, the pretension in the bolts could vary considerably after the minimum required torque is applied.

- Strength definition: The manufacturer defined the design shear strength of clamps as the load at a slip of 0.004 in. with a safety factor of 2 (Lindapter 2011).

However, this slip is too small for clamps used in composite beams (the service slip is 0.04 in. based on the beam test results presented in Chapter 5). Therefore, in this research, the nominal shear strength of clamps is defined as the peak strength predicted with Equation (4.27) or the peak strength obtained from pushout tests.

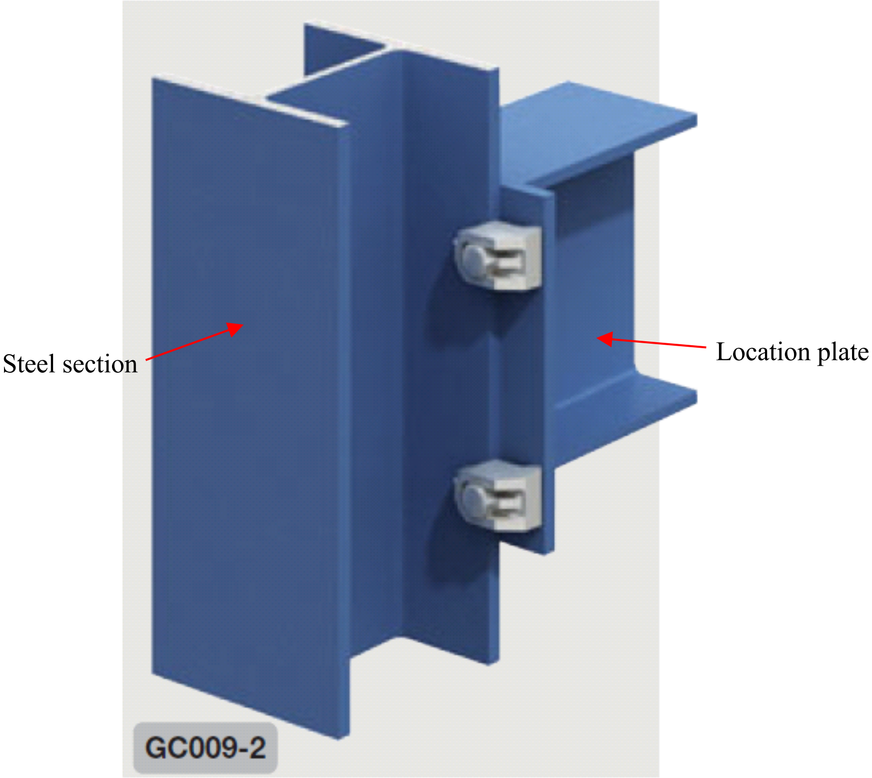

Figure 4.70 Typical clamping connections [after (Lindapter 2011)]

In the manufacturer's tests, the M24 and M20 bolts are pretensioned with a torque of 800 N-m and 470 N-m, respectively (Lindapter 2011). Equations (4.28) and (4.29) could be used to estimate the bolt tension after the torque is applied. In these equations, the frictional coefficient is a key parameter, but the exact value is unknown.

M24 bolt tension:

$$T = 12\tau/(KD) = 12 \times 590/(0.2 \times 0.945) \times 4.448/1000 = 167 \text{ kN} \qquad (4.28)$$

M20 bolt tension:

$$T = 12\tau/(KD) = 12 \times 347/(0.2 \times 0.787) \times 4.448/1000 = 118\,\mathrm{kN} \qquad (4.29)$$

Where

τ = torque applied to a bolt (ft-lbs)

K = frictional coefficient; 0.2 is used for plain steel threads

D = diameter of a bolt (in.)

Provided in the manufacturer's catalog (Lindapter 2011), the design tensile strengths of the M24 and M20 clamping connections using Group A bolts are 40.0 kN and 26.3 kN per bolt, respectively. The nominal tensile strengths of the clamping connections could be calculated by multiplying the design tensile strengths with the factor of safety of 5. Therefore, the nominal tensile strengths are 200.0 kN and 131.5 kN for the M24 and M20 clamping connections using Group A bolts, respectively. However, it is unclear whether the nominal tensile strengths represent the average tensile strengths of the connections. . The nominal tensile strengths are larger than the calculated tension in Equations (4.28) and (4.29), but smaller than 205 kN and 142 kN, the minimum bolt pretension for Group A M24 and M20 bolts given in Table J3.1M in AISC 360-16, respectively. Therefore, the bolts are probably elastic after the recommended torque is applied.

In the manufacturer's tests, when the slip is 0.004 in., the bolt tension may not reduce if the bolt is elastic after applying the recommended torque or may reduce slightly if the bolt is inelastic after pretensioning. The slip coefficients between different contact surfaces are given in Table 4.14. 0.35, 0.3 and 0.2 are the slip coefficients for roughened hot-dip galvanized surfaces, shot blast and painted surfaces, and unroughened hot-dip galvanized surfaces, respectively (Grondin et al. 2007; RCSC 2014). Since the clamps are hot galvanized, but not roughened, the slip coefficient between the steel beam and the clamp teeth is averaged. The values listed in the last column of the table are the mean slip coefficients of the two slip planes.

Table 4.14 Slip coefficients between different contact surfaces

Coating	Steel beam/location plate	Steel beam/clamp teeth	Mean
Painted	0.3	(0.2+0.3)/2	0.275
Galvanized	0.35	(0.2+0.35)/2	0.31

The shear strengths of the clamps are predicted using Equation (4.26). The calculation in Equation (4.30) assumes galvanized surfaces and M24 clamps. The other shear strengths are determined accordingly, and all the results are summarized in Table 4.15.

$$Q_s = k_d \mu T n_s = 0.7 \times 0.31 \times 167 \times 2 = 72.5 \text{ kN} \tag{4.30}$$

Where

k_d = coefficient accounting for the portion of bolt tension transferred to the clamp teeth, which is 0.70

μ = mean slip coefficient, which is 0.31

T = estimated bolt tension

n_s = number of slip planes, which is 2

Table 4.15 Clamp shear strength comparison

Diameter	Nominal strength (kips)				Predicted/Reported	
	Reported		Predicted			
	Painted	Galvanized	Painted	Galvanized	Painted	Galvanized
M20	2.92	3.60	10.2	11.5	3.49	3.19
M24	5.40	6.77	14.5	16.3	2.69	2.41

4.8 Conclusions

Two series of experiments were conducted in the pushout test program. The number of turns of the nut was first determined in the pretension tests to ensure that adequate and reliable axial force would be generated in the bolts. In these tests, three M24 and M20 bolts were tested under torqued tension until fracture to develop the relationship between the number of turns of the nut and the bolt axial force. Pushout tests were then performed to study the strength and ductility of the clamping connectors and explore the influences of the testing parameters. In these tests, the pushout specimens consisted of 4 ft. × 2 ft. × 6 in. precast concrete planks attached to WT5x30 or WT4x15.5 sections using the clamping connectors. The steel beams were pulled or pushed by the actuators, while the concrete planks were restrained from translation. The specimens were tested under monotonic loading or cyclic loading until the slip was excessive. All the monotonic specimens exhibit ductile behavior, with the exception of the specimen that uses M20 clamps. Despite the strength degradation at large slips, the behavior of the cyclic specimens is excellent within 1 in. slip which is conservatively assumed to be a typical demand range for clamps used in deconstructable composite diaphragms. Finite element models were developed to study the inherent indeterminacy of the system, such as the bolt tension variation and bolt tension transfer. Combining experimental results and finite element analysis results, design equations were proposed to predict the slip strength and peak strength of clamps under shear force.

Based on the experimental and analysis results presented in this chapter, the following conclusions can be reached:

(1) Except for the bolt that fractured at the bolt heads, all the bolts in the pretension tests ultimately fractured due to combined torsional and tensile deformation. Two turns and 1.5 turns after a snug-tight condition are selected for pretensioning the M24 and M20 bolts, respectively. It is also noted that in the M24 bolt tests, moderate plastic deformation occurred in the channel lips, while the inelastic deformation of the channel lips was minor when the M20 bolts were pretensioned. Channels with higher yielding strength could be studied to minimize the inelastic deformation of lips and withstand bolts with higher pretension force.

(2) The load-slip curve of Test 2-M24-2C-RH-LM, which is a baseline specimen, indicates that the behavior of the M24 clamps is ductile under monotonic loading. Compared to shear studs which normally fracture at a much smaller slip, the M24 clamping connectors can retain almost 80% of the peak strength even at 5 in. slip.

(3) Shims were used for specimens using M24 clamps and thin flange sections, and undesirable load oscillation was observed due to a stick-slip mechanism, although

the peak strength was not affected. Usage of the selected shims between the clamp and the flange may be limited to applications where the slip of the clamps is small, such as in composite beams that are part of gravity systems. Different types of shims, such as brass shims, could be further investigated to eliminate load oscillation.

(4) Compared to the monotonic specimens, the peak strengths of the cyclic specimens are approximately 20% lower, which is comparable to the strength decrease seen in steel headed stud anchors when subjected to cyclic loading. After undergoing a couple of cycles, the strengths of the cyclic specimens begin to degrade, which could be attributed to the reduction of the bolt pretension and the lowering of frictional coefficient as a result of the abrasion between the clamp teeth and steel flange and between the concrete plank and steel beam. However, the load-slip behavior of the cyclically loaded pushout specimens is excellent within 1 in. slip which is conservatively assumed to be a typical slip range for clamps used in composite diaphragms. The hysteresis load-slip loops show excellent energy dissipating capacity of the clamping connectors, and thus they may perform well if used as connectors between composite diaphragms and steel collectors in lateral force-resisting systems.

(5) A considerable load drop was seen after 0.68 in. slip in the load-slip curve of the monotonic specimen using M20 bolts. Large rotation and complete disengagement of clamps were noted. If the M20 clamps are utilized in composite beams where the slip demand is normally much less than 0.68 in., the strength degradation is not a concern. If they are needed to withstand large slip, the performance of the M20 clamps could be improved by increasing the contact area between the clamp teeth and steel beam and between the clamp tail and concrete plank to delay rotation or developing an interlocking design where the channel lips fully restrain the rotation of the clamps. With the steel blocks inserted into the channels to support the clamp tails, the cyclically loaded specimen performed better than the corresponding monotonic specimen, even though all the clamps ultimately lost contact with the beam flanges.

(6) In terms of strength and state of cracks, the cyclic pushout specimen with light reinforcement did not perform worse than the specimen with heavy reinforcement. This implies that the additional reinforcement was not engaged which was designed to bridge potential cracking planes due to channel anchor forces. This is further proved by the low stress in the reinforcement. For the channel configuration investigated in this research, the bolt pretension force is primarily resisted by the reactions at the clamp tail and the steel beam flange, rather than transferring to the channel anchors. Therefore, the limit states for anchor channels in common applications, such as concrete cone failure under tension, are negligible, and the supplementary reinforcement has minimal effects on the behavior of the specimens.

(7) A strut-and-tie model is used to explain the formation of the cracks which were induced by the friction acting on the concrete surface, rather than concrete pryout failure. Since the frictional force at the steel-concrete interface distributes in a non-uniform manner, the damage concentrates on one side of the concrete plank when it is loaded monotonically.

(8) According to the bolt axial strains measured in the cyclic tests, the bolt tension gradually decreases. When the slip is small, the tension decrease is primarily attributed to the shear force acting on the bolt. At large slips, the damage to the steel flange and clamp teeth caused by abrasion could release the bolt tension.

(9) Because of the ductile behavior of the clamps, the shear force applied to the steel beams is distributed among the clamps, demonstrating the potential of using clamps as shear connectors in composite beams. With the strain gages attached on the steel beams, the force distribution in the system is validated by the axial force plots that show the force variation at different sections along the beam length.

(10) The strength and stiffness of the clamping connectors are compared to those of steel headed stud anchors. A single M24 clamp has a similar shear capacity to a

single conventional 3/4 in. diameter shear stud. Since friction is the mechanism of resisting the shear flow, the initial stiffness of the clamps is larger than that of shear studs. The ultimate slip of both M24 and M20 clamps is also greater than that of the 3/4 in. diameter shear studs.

(11) Finite element models were developed which takes into account material nonlinearity, geometric nonlinearity and contact between different components. Assuming a frictional coefficient of 0.35, the finite element models predicts the peak strength of the baseline test specimens well, although the slip at which the peak strength occurs is shifted because of the friction simulation in ABAQUS which assumes an elastic slip while the two contact surfaces are still sticking. Based on the finite element models and test results, design equations, similar to that used for calculating the resistance of slip-critical bolted joints, are recommended for estimating the slip strength and peak shear strength of the clamping connectors under monotonic loading. It is seen that the equations predict the slip strength and peak strength of the clamps very well. A coefficient of 0.8 could be used with the monotonic shear strength as the cyclic shear strength of the clamps.

5. BEAM TESTS

Full-scale beam tests are essential in evaluating the realistic behavior of shear connectors. As discussed in Section 2.3, deducing the ultimate shear strength of shear connectors from beam test results is problematic. Hence, beam tests are usually used as confirmatory tests where the proposed design strength equations or the load-slip curves obtained from pushout tests are validated. In prior research, various configurations have been used for composite beam tests. For example, most composite beams are loaded on the concrete slabs, but the loading is applied directly to the top flange of the steel beam through a concrete pocket in the tests conducted by Ernst et al. (2006). Alternatively, the loading could be applied across the whole concrete slab (Grant et al. 1977; Ranzi et al. 2009) or only the region above the steel flange (Easterling et al. 1993). Ductile behavior is generally observed for composite beams with steel headed stud anchors connecting concrete and steel, and the predicted ultimate flexural strengths based on the rigid plastic assumption match the test results very well (Ranzi et al. 2009). The same types of bolts, channels and clamps studied in the pushout tests are investigated in the beam tests.

In this chapter, a general description of the testing program is first given, including the test matrix, test specimen design, test setup, instrumentation plan and loading protocol. The global and local performance of the test specimens is then presented, including the load-deflection relationships, behavior of the clamps, beam section strain distribution, bolt tension variation, rod tension variation, responses of the channel anchor and reinforcement, effective width of the deconstructable beam specimens, and correlation between the pushout tests and beam tests. Three-dimensional nonlinear finite element models are also developed for the beam specimens to predict their overall performance.

More information regarding the composite beam tests is provided in the appendices, with Appendix C illustrating the drawings for the load frame steel, specimen steel and concrete planks, Appendix D documenting the mill certifications for the components, Appendix E reporting the experimental raw data, and Appendix F demonstrating the useful quantities extracted from the experimental raw data. Other design issues are detailed in Appendix H, Appendix I, and Appendix J.

5.1 Test matrix

A total of four specimens were designed and tested to document the progression of damage in deconstructable composite beams utilizing clamping connectors, as given in Table 5.1. The naming convention of the specimens is explained using Test 2-M24-1C-RL, with 2 describing the test sequence of the beam, M24 describing M24 bolts, 1C describing single-channel specimens, RL describing light reinforcement pattern. The key parameter in the test matrix is the percentage of composite action listed in the last column of Table 5.1, since it directly affects the behavior and limit states of the composite beams. This parameter is related to other parameters, including bolt diameter, number of channels per plank, and steel beam section. Two reinforcement configurations, similar to those designed in the pushout tests, are used to explore whether anchor-related concrete failure modes could occur in the beam tests.

Generally, only partially composite beams are tested, since the behavior of the shear connectors governs the strength and stiffness of the beams. However, a fully composite beam was also designed and tested in this research to verify the design methodology and obtain a comprehensive understanding of the deconstructable composite floor system under gravity loading. In Table 5.1, the amount of composite action is varied such that composite beams with a wide range of composite action can be investigated. Normally, the percentage of composite action of a composite beam is defined for the maximum moment location. Depending on the type of loading, the maximum moment location could be at the mid-section of the beam if the loading is uniform or at one of the loading points when the beam is subjected to concentrated forces. For the test setup illustrated in Figure 5.1 and Figure 5.2, the maximum moment occurs at one of the two inner loading points. The degree of shear connection is specified as the ratio of the total shear strength of the clamps placed between the zero moment section, which is the end section of the beam, and the maximum moment section, which is located at one of the two inner loading points, to the lesser of the tensile strength of the steel beam and the compressive strength of the concrete slab (the tensile strength of the steel beam controls in this test series). The shear strengths of the M24 and M20 clamping connectors respectively utilize the peak strengths obtained from Tests 2-M24-2C-RH-LM and 9-M20-2C-RH-LM, which are considered as baseline specimens in Table 4.5 in Chapter 4. The yield strength of the steel beam is calculated using the nominal cross-sectional area and the nominal and tested static yield stress of the section. All the steel sections have a nominal yield strength of 50 ksi, while the tested material properties of the beams are documented in Table 5.3 in Section 5.3. The "nominal" composite action calculated with nominal material properties as well as predicted clamp strengths is usually referred to in design practice, while the "actual" composite action determined using tested material properties as well as tested clamp strengths is more important when exploring the behavior of a composite beam. It is shown in Table 5.1 that the difference between the "nominal" and "actual" composite action is not significant. In a composite beam specimen, since the clamps in the constant moment region between the two inner loading points contribute little to the flexural strength of the beam, the number of clamps used in this region could be reduced for efficiency, especially for Test 3-M20-3C-RL. Nonetheless, in order to study the performance of a certain type of plank at different locations of a beam, the planks used in each test were all the same. The number of clamps in the constant moment regions of the specimens was not decreased.

Table 5.1 Composite beam test matrix

Composite beam #	Bolt size	# of channels per plank	Steel beam section	Reinforcement configuration	Number of bolts (clamps)	Percentage of composite action	
						Nominal	Actual
1-M24-2C-RH	M24	2	W14x38	Heavy	56	75.2%	82.7%
2-M24-1C-RL	M24	1	W14x38	Light	30	41.0%	45.1%
3-M20-3C-RL	M20	3	W14x26	Light	90	124.1%	137.8%
4-M20-1C-RL	M20	1	W14x26	Light	30	41.4%	43.8%

Design guidelines in the U.S. normally limit the percentage of composite action to a minimum of 25%. However, it is not advised that less than 50% composite action be designed for composite beams utilizing shear studs for two reasons. First, large slips of shear studs are required to reach the ultimate strengths of the beams, resulting in limited ductility of the beams. Second, the steel beams and shear studs may deform inelastically at serviceability. Nonetheless, Beams 2 and 4 in the test matrix were designed to explore the behavior of deconstructable composite beams with composite action below 50%.

5.2 Test specimen design and test setup

5.2.1 Test specimen design

Steel beam

W14x38 and W14x26 were selected as the steel beam specimens. The M24 clamps are designed for sections with flange thicknesses ranging from 1/2 in. to 11/16 in., whereas the M20 clamps are designed for flanges with thicknesses from 3/8 in. to 7/16 in. Both steel sections fit within the range of use of the two types of clamps, with the flanges of the W14x38 and W14×26 sections being 0.515 in. and 0.42 in. thick, respectively. In Table 5.1, beam 1 and beam 4 are also potential members in the prototype structures that have a bay width of 30 ft. and a slab thickness of 6 in., as indicated in Chapter 3, with the former and latter being capable of supporting high and low gravity loading, respectively. To compare to the behavior of these two beams, the same steel sizes were adopted for the other two beams, but the percentage of composite action was varied.

The steel sections all have as-received mill scale surfaces, and the frictional coefficient is believed to be similar to that of the steel beams tested in the pushout specimens. It is critical to ensure that the frictional coefficients at the contact surfaces are close between the pushout tests and beam tests; otherwise, the behavior of the clamps in the pushout tests cannot relate to that of the clamps in the beam tests.

Precast concrete plank

The planks used in the beam specimens are 8 ft. long, which provides a sufficient composite slab width to prevent premature concrete failure in a narrow slab (Grant et al. 1977). This composite slab width is also close to 7.5 ft., a quarter of the beam span, which is the effective width determined in accordance with the AISC Specification (AISC 2016a). To simplify specimen construction, tongue-and-groove joints in the planks shown in Figure 1.1 in Chapter 1 were eliminated. These connections can assist vertical load transfer between planks, but they are not believed to affect the overall beam strength. since the joint forces due to composite beam behavior are primarily compressive rather than shear.

Calculations are required to ensure that the precast concrete components have sufficient strength to resist permanent loading as well as temporary loading during form removal, transportation, erection, etc. The concrete panels were lifted at the outer fifth points of both ends using embedded lifting lugs to reduce the maximum tensile stress induced by self-weight when stripping off the formwork and pulling planks from the formwork. Calculations are included in Appendix H.2 to show that the concrete planks were intact during handling. Design for stresses induced by additional transportation and handling is not critical for the short planks used in the beam tests, but they may be important when the planks are long.

All the planks are connected to the beam flanges using clamps in the current design. In the future, it might be valuable to study the effect of not attaching certain planks to the beams. It should be pointed out that 56, rather than 60, clamps were used in Test 1-M24-2C-RH, because the very end bolts conflicted with the bearing stiffeners at the ends of the beam.

Cast-in channels and reinforcement

Since no anchor-related concrete failure modes were observed in the pushout tests, the same type of cast-in channels was selected for the concrete plank specimens used in the beam tests. The only difference is that the length of the channels was varied to match the length of the planks.

Two reinforcement patterns were designed for the specimens. The bars that comprise the light reinforcement configuration were designed for all the tests. Planks in Test 1 used the heavy reinforcement configuration in which additional waveform bars were utilized to bridge potential cracking planes induced by channel anchor forces. In addition to supporting gravity loading, the longitudinal reinforcement was designed to resist negative bending of the planks, because the actuator loading was spread across the slab width during the tests. Two types of U bars were placed around the cutouts. The longer type reinforces the cutout corners that are vulnerable to handling, while the shorter type could restrain the propagation of potential bursting cracks caused by post-tensioning forces of the rods (ACI 2011). The reinforcement selections enable testing of two extremes: a heavily reinforced, partially composite beam with high composite action in which concrete breakout failures are less likely; and a lightly reinforced, partially composite beam with low composite action in which concrete breakout failures are more likely. Since the lightly reinforced specimen did not fail prematurely in the pushout test, this pattern was used for three out of the four beam tests.

All the reinforcement met the detailing requirements in ACI 318-11, as shown in Figure C.45 in Appendix C. The U bars and the waveform reinforcement were regarded as stirrups, and the bend diameter and the end extension were $4D_b$ and $6D_b$, respectively. The transverse loops, which replaced the inclined transverse bars in the pushout specimens, had standard hooks, and the bend diameter and the end extension were $6D_b$ and $12D_b$, respectively. Legs of the transverse loops were spliced with a splice length of 8.5 in. The longitudinal reinforcement used No.4 bars, and No.3 bars were chosen for the other reinforcement.

5.2.2 Test setup

The full-scale composite beam test setup is provided in Figure 5.1 and Figure 5.2. The test specimens consist of 30-foot long W-shape beams, each with fifteen 2-ft.-wide by 8-ft.-long planks attached using clamping connectors. The composite beam span is 30 ft., but the total beam length is 32 ft. due to having a 1 ft. extension of the steel beam at each end to facilitate out-of-plane support and accommodate the deflection of the beam. Because of the vertical reactions at the beam supports, stiffeners were welded at the ends of the beam to suppress limit states such as web local crippling and web local yielding. The actuator force was applied across the concrete slab and spread using spreader beams to approximately simulate uniform loading acting on a secondary beam. A thin layer of grout was cast between the concrete planks and the bearing plates placed under the spreader systems to achieve a flat and level loading surface. Stiffeners were welded on the spreader beams to increase their torsional resistance and eliminate instability during testing. The bolted connections between the top spreader beams and the bottom spreader beams not only enhanced the stability of the spreader system but also facilitated test setup assembly. Braces at both sides of the slab are engaged if the slab torques or displaces laterally due to uneven loading. Potential twisting of the steel beam was inhibited by the guides at the ends of the section. A pin support at one end and a roller support at the other were used to simulate the actual boundary conditions of a simple beam. Teflon sheeting was attached to surfaces where frictional forces were undesirable, such as the interface between the steel beam and end guides and between the concrete slab and side braces. Figure 5.1 shows the components in the composite beam specimen.

ASTM A992 steel was used for all the W shapes and WT shapes, and A500 Grade B steel was used for the HSS sections. ASTM A36 steel was selected for the remainder of the load frame. A325 bolts were selected for all the connections which were designed as slip-critical to reduce as much slip as possible. All the concrete planks had a nominal compressive strength of 5 ksi. All the beams were shored during construction and instrumentation installation. Shop drawings for the composite beam test setup can be found in Appendix C.

The steel reaction frame without diagonal braces was connected to the other reaction frame using WT sections as lateral braces to enhance its stiffness when resisting lateral loading. The cross beams in both frames are W24x335 sections, which are very stocky to minimize the actuator movement at the ends that attach to the reaction frames. The flexibility of the reaction frames affects the displacement of the actuators, but the actuator forces and measured deflections of the beams are not influenced.

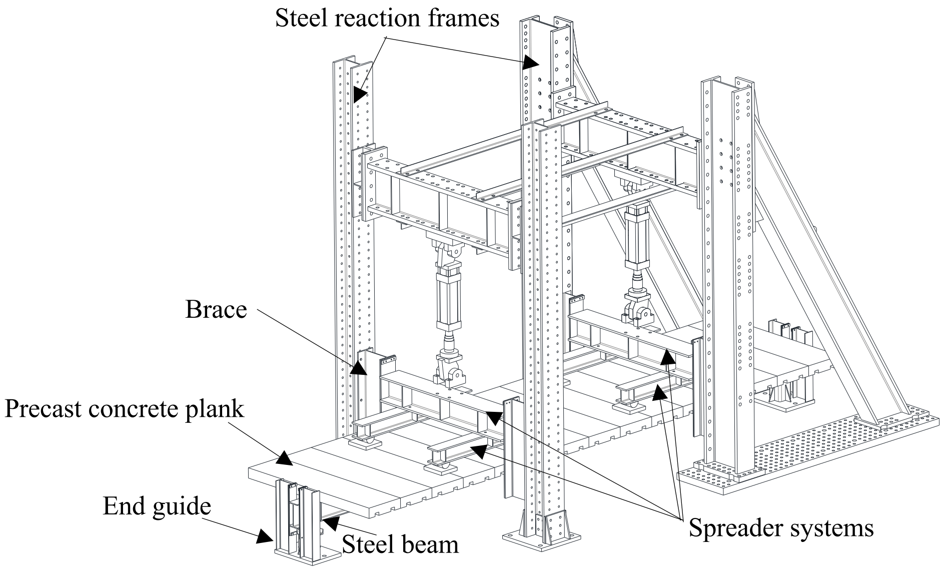
Steel reaction frames
Brace
Precast concrete plank
End guide
Steel beam
Spreader systems

a) Three-dimensional view

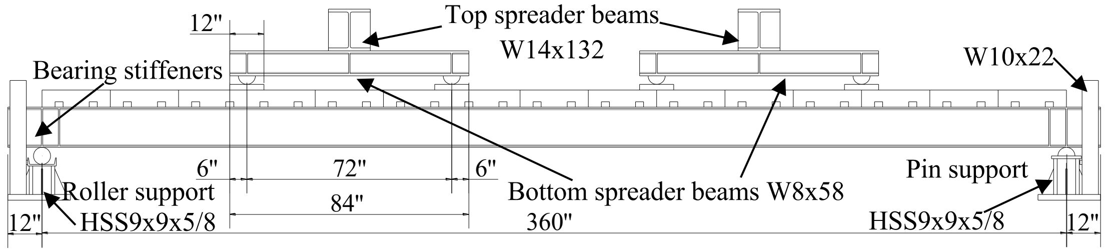
12"
Top spreader beams
W14x132
Bearing stiffeners
W10x22
6"
72"
6"
Pin support
Roller support
84"
Bottom spreader beams W8x58
12"
HSS9x9x5/8
360"
HSS9x9x5/8
12"

b) Elevation view

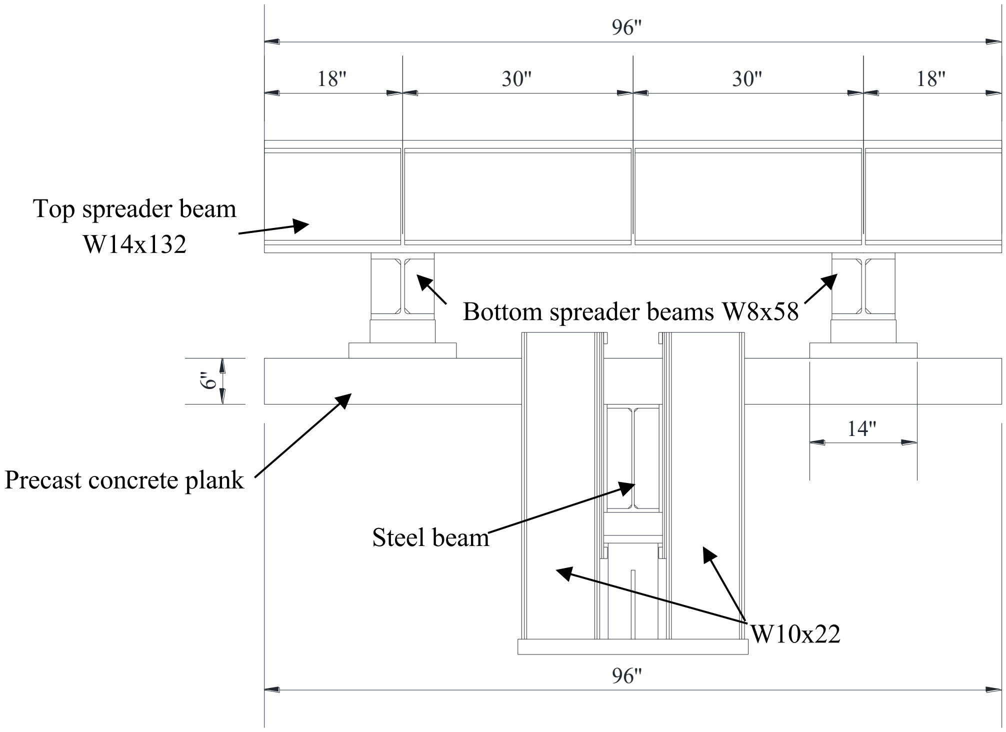
96"
18"
30"
30"
18"
Top spreader beam
W14x132
Bottom spreader beams W8x58
6"
14"
Precast concrete plank
Steel beam
W10x22
96"

c) Side view

Figure 5.1 Different views of a composite beam specimen

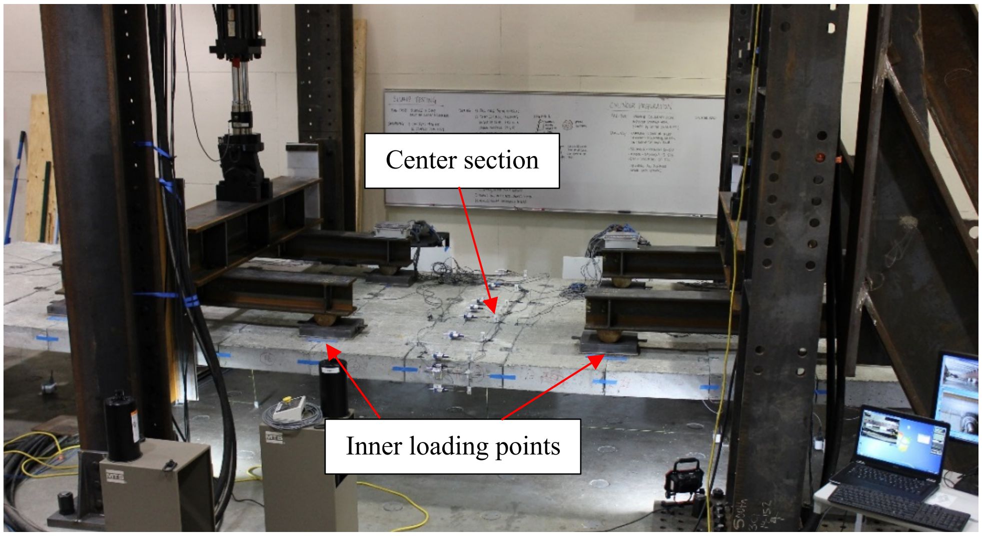
Center section
Inner loading points

Overall view of beam specimen

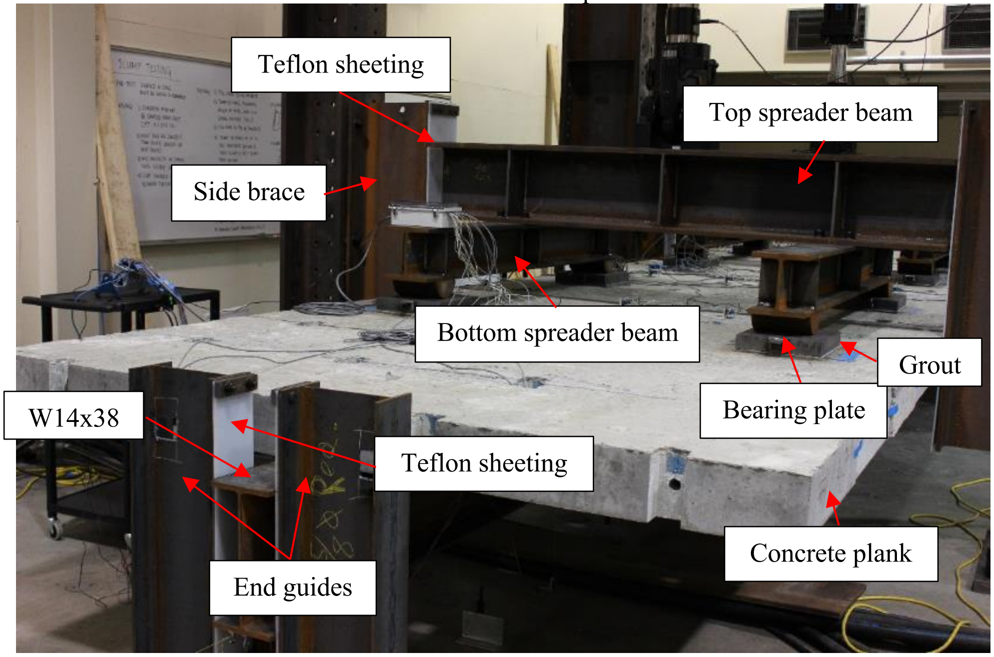
Teflon sheeting
Top spreader beam
Side brace
Bottom spreader beam
Grout
Bearing plate
W14x38
Teflon sheeting
Concrete plank
End guides

Beam specimen components

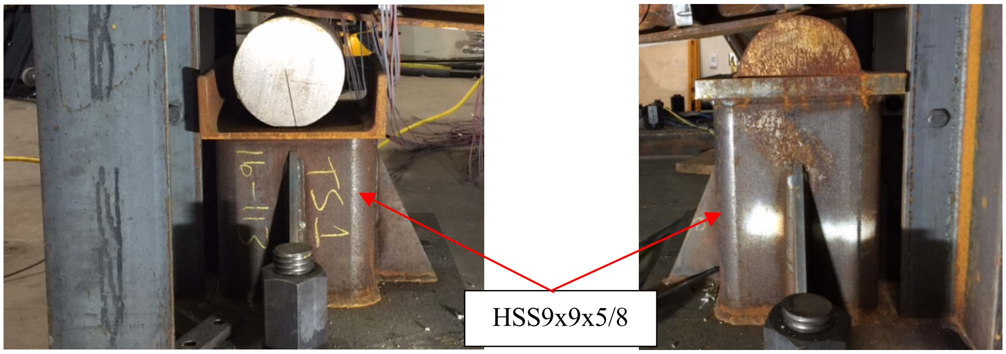

Roller support

Pin support

Figure 5.2 Composite beam test setup

5.2.3 Pretension tests on fully threaded rods

As indicated in Section 1.1 in Chapter 1, fully threaded rods are proposed to connect adjacent concrete planks, which is essential to generate frictional force at the concrete-concrete interface and avoid relative sliding between the planks under diaphragm forces. The in-plane connections between the concrete planks may not be necessary for supporting gravity loading, but they are required to ensure the integrity of the structural system under seismic loading.

ASTM A36-14/A529-05 Grade 50, 5/8 in. threaded rods were chosen for connecting adjacent planks in the beam tests. The calculations in Appendix H.3 justify the selection of these rods. Spaced at a distance of 24 in., 3 in. by 2 ½ in. cutouts were needed for the threaded rod connections. The cutouts should be small enough to preserve the strength of the planks, but large enough to facilitate the installation of the rods. Schedule 40, 3/4 in. inside diameter PVC pipes were placed in the formwork to be integrated into the planks as the ducts for the threaded rods. To reduce the tension variation in the rods, it was decided that they be loaded into the inelastic range. For such long rods, the RCSC Specification (RCSC 2014) requires testing that mimics the actual application of the rods to determine the required nut rotation for yielding the rods from a snug-tight position.

The fully threaded rods employed in the pretension tests and beam tests were from three different heats. Rods that were 46.5 in. long and used in Test 1-M24-2C-RH were used in the pretension tests, and the required nut rotation was thus determined directly for this material. In Test 1-M24-2C-RH, both 45 in. and 46.5 in. long rods were utilized. Since the percentage of length difference was small (≈3.3%) and the material properties were similar, as shown in Table 5.3, the same nut rotation is believed to be valid for the shorter rods. In the remaining beam tests, 46.5 in. long rods, which were from a different heat, were also used. As they had similar material properties as those used in the pretension tests, the same nut rotation was employed. The plots in Figure E.34 in Appendix E indicate that all the rods were inelastic after turning the nuts the same rotation.

To give some flexibility to address plank-to-plank alignment, all the PVCs embedded in the concrete planks were removed before the pretension tests. Since the composite beam specimens were shored during construction by supporting the ends of the concrete planks to avoid lateral-torsional buckling of the steel beams under the self-weight of the planks and steel beams, the planks were also propped in the pretension tests in a similar manner. The pretension test setup is shown in Figure 5.3a. Plank 1 was clamped to the steel beam and not allowed to move during the test. As the rod was twisted, plank 2, which seated on the beam freely, started to move towards and bore against plank 1. A load cell was placed on one side of the rod to monitor the tension variation, while the nut on the other side was turned. On the load side, a square washer was placed next to the concrete plank to distribute the compressive load. The 1/4 in. thick square washer had a dimension of 2 in. by 2 in., with a 5/8 in. diameter hole at the center. A regular thin round washer was between the nut and the square washer to ensure the deformation of the washers was minimized, and the hole in the concrete plank was found to be intact after testing. On the other side, the load cell was between the square washer and the nut. Along with the load cell, two hardened washers were also supplied which were employed as force introduction components for the load cells, as seen in Figure 5.3b and Figure 5.3c. Before testing, the washers and nut threads on the load side were lubricated. A snug-tight condition was first achieved with the full effort of a worker using a torque wrench with a 12 in. lever arm. A multiplier was then used with the torque wrench to reduce the effort to turn the nut. As the worker turned the nut, the rod tension was recorded. Two rods were tested, and both fractured as a result of torqued tension, as shown in Figure 5.3d. Necking of the rods was not observed.

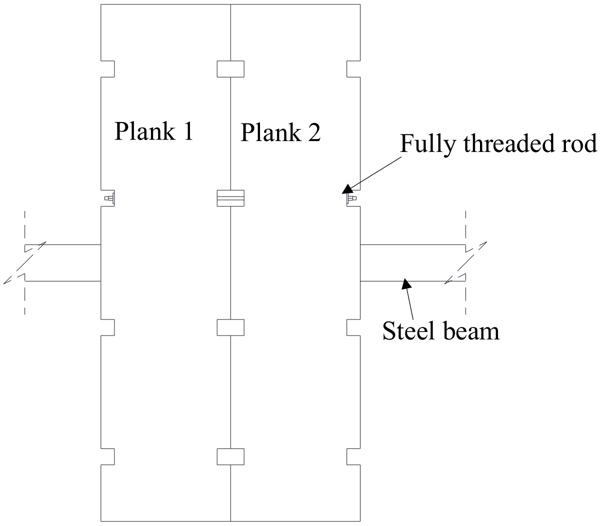
Plank 1
Plank 2
Fully threaded rod
Steel beam

a) Test setup

Before testing:

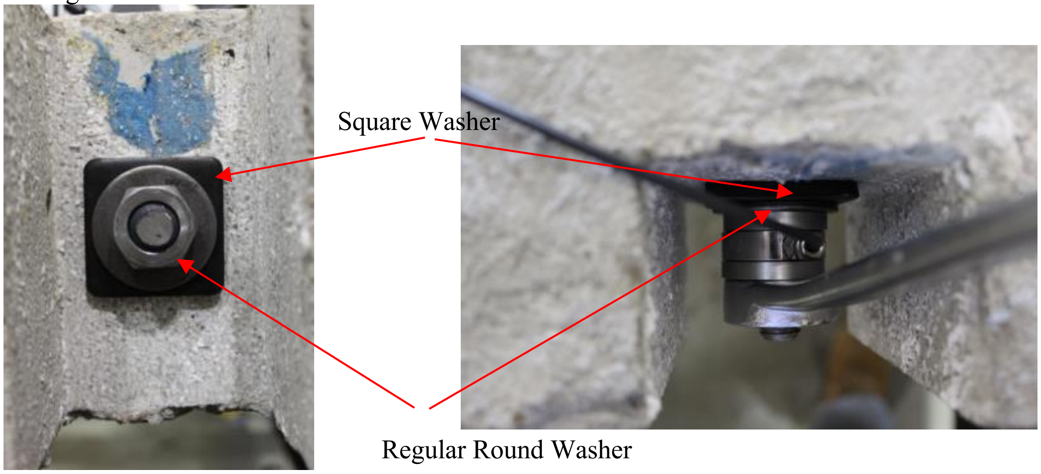
Square Washer
Regular Round Washer

b) Load side

c) Load cell side

After testing:

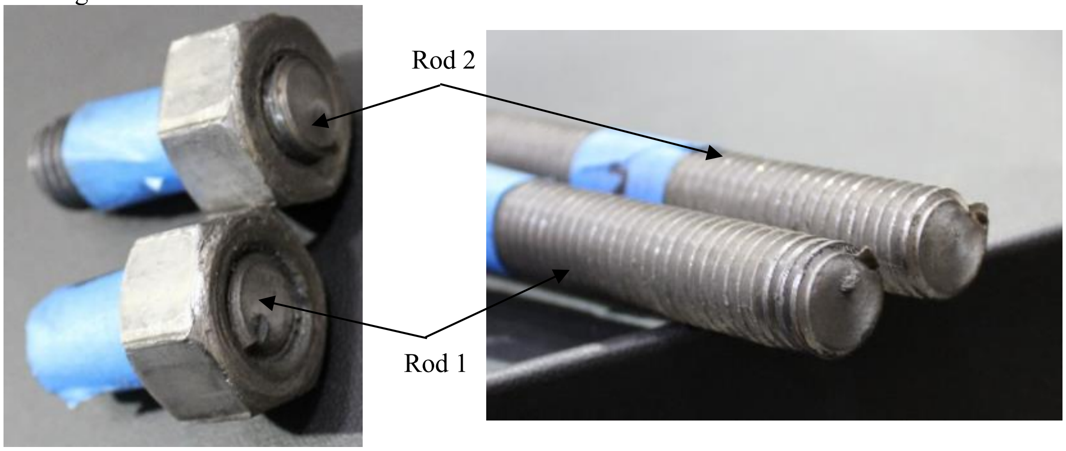

d) Fractured specimens

Figure 5.3 Photographs of threaded rod pretension tests

The rod tension variation is plotted in Figure 5.4. Each dashed line indicates a complete turn of the nut (360 degrees). The force decrease is caused by excessive torsional deformation, which releases the tensile strain in the rod. Based on these plots, it is decided that 1 turn is adequate to ensure yielding of the rods. For both rods, the number of turns of the nut required for twist-off fracture in the rods is at least 22 times the recommended turns of the nut for establishing pretension.

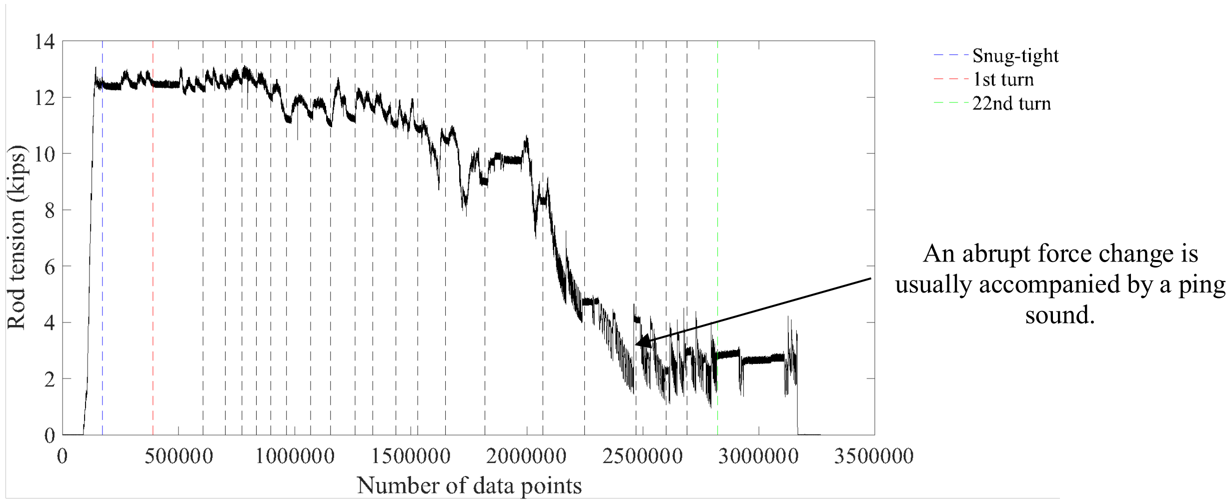

a) Rod 1

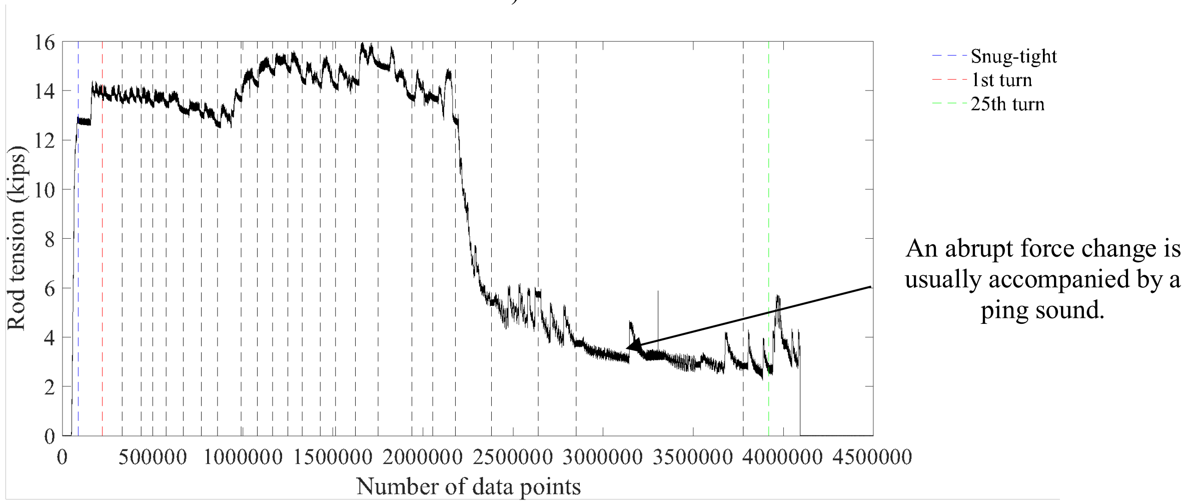

b) Rod 2

Figure 5.4 Rod tension variation in pretension tests

When testing rod 1, a ping was first heard at the 8th complete turn of the nut after a snug-tight position. Starting from the 12th complete turn of the nut, the ping noise became frequent. As the rod was elongated, it was more difficult to achieve the engagement between the nut threads and rod threads. When new rod threads were again engaged, an abrupt force change was seen, and a ping sound was also heard. At the 17th complete turn of the nut, the ratchet of the wrench stopped clicking, and it became very difficult to turn the nut. Rod 1 fractured after 22 complete turns of the nut. For rod 2, the first ping was heard at the 8th complete turn of the nut, and the ping noise became frequent after the 16th turn of the nut. At the 18th turn of the nut, a squeak was heard. Starting from the 20th turn of the nut, it was very hard to turn the nut. A loud noise was heard at the 23rd turn of the nut, and turning the nut was slightly easier. The rod ultimately fractured after 25 complete turns of the nut. Because the square washers showed no deformation, the holes in the concrete planks were intact after both tests.

5.3 Material properties

Steel properties

In the beam tests, steel beams of the same size had been requested to be from the same heat. When the steel beams were delivered, the flange width of one of the W14x26 beams was noticeably narrower than that of the other W14x26 beams. The major dimensions of all the beams were thus measured, as shown in Table 5.2. Beams 1 through 4 correspond to the steel sections used in Tests 1-M24-2C-RH through 4-M20-2C-RL. Steel stubs where the coupons were cut are designated as Beams 5 and 6.

After comparing the measured dimensions to the tolerances given in Figure 5.5, the flange widths of Beams 4 and 6 were found to be larger than the maximum allowable width, which is equal to 5.28 in. Except for the marking on Beam 4, which was too blurry to identify the designated beam size, those on steel Beams 1, 2 and 3 indicate the sizes are as requested. No markings were found on Beams 5 and 6 since they are too short. Yet, the measured dimensions of Beams 4 and 6 are closest to the nominal dimensions of a W14x26 section, and the coupons from Beam 6 are used to represent the material properties from Beam 4.

Because all the W14x38 sections had similar dimensions, they were assumed to be from the same heat, and coupons cut from Beam 5 are representative. Because it was not as clear whether Beam 3 was from the same heat as Beams 4 and 6, the material properties of Beam 3 were obtained by testing coupons cut from the low stress regions of the beam after completing the beam test. As discussed in Section 5.6.2.3, since the top flange of Beam 3 was deformed, all the flange coupons were cut from the bottom flange. From Table 5.3, it is seen that the yield strength of the flange coupons cut directly from Beam 3 is slightly less than the yield strength of the flange coupons machined from Beam 6.

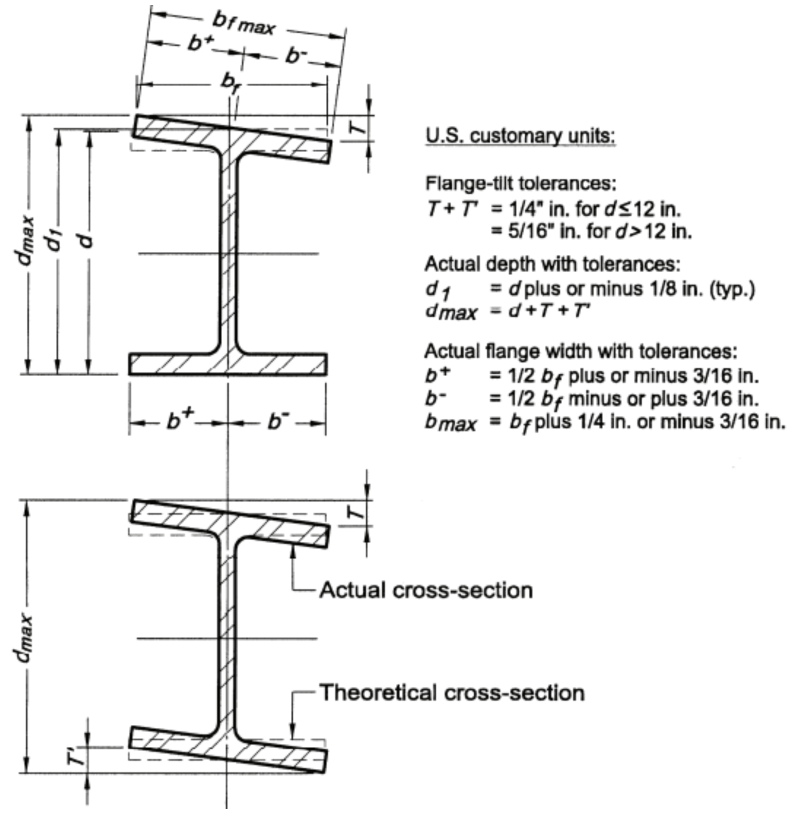
$b_{f\,max}$
b^+
b^-
b_f
T
d_{max}
d_1
d
U.S. customary units:
Flange-tilt tolerances:
T + T' = 1/4" in. for d≤12 in.
= 5/16" in. for d>12 in.
Actual depth with tolerances:
d_1 = d plus or minus 1/8 in. (typ.)
d_{max} = d + T + T'
Actual flange width with tolerances:
b^+ = 1/2 b_f plus or minus 3/16 in.
b^- = 1/2 b_f minus or plus 3/16 in.
b_{max} = b_f plus 1/4 in. or minus 3/16 in.
b^+
b^-
T
Actual cross-section
d_{max}
Theoretical cross-section
T'

Figure 5.5 Mill tolerances on a W-shape cross section [after (AISC 303-16)]

Table 5.2 Measured dimensions of steel beams and stubs

Beam #	Section	Length (ft)	d (in.)	t_w (in.)	b_f (in.)	t_f (in.)
1	W14x38	32.0	14-1/8	0.310	6-3/4	0.527
2	W14x38	32.0	14-1/4	0.349	6-3/4	0.460
3	W14x26	32.0	14	0.270	4-7/8	0.419
4	W14x26	32.0	13-7/8	0.270	5-3/8	0.378
5	W14x38	3.5	14-1/4	0.323	6-3/4	0.531
6	W14x26	3.5	13-7/8	0.282	5-1/2	0.358

Tension testing was conducted on the steel coupons to document their material properties. Refer to Section 4.3 in Chapter 4 for the dimensions and procurement of the steel coupons from the beams, channels, reinforcement and bolts. In addition, coupons were machined from the fully threaded rods, and the dimensions are given in Figure 5.6. The testing procedures described in Section 4.3 were utilized, and the test results are given in Table 5.3.

In accordance with ASTM E8/E8M-13a, the gage lengths for the bolt coupons and rod coupons are 2 in. and 1.4 in., respectively, but a 1 in. extensometer was chosen to measure the strain of these coupons. The gage lengths stipulated by the ASTM standard were used for all the other coupons. Some of the bolt coupons and rod coupons failed outside of the 1 in. gage length, but within the 2 in. and 1.4 in. gage lengths. Fracture of all the other coupons occurred within the gage length.

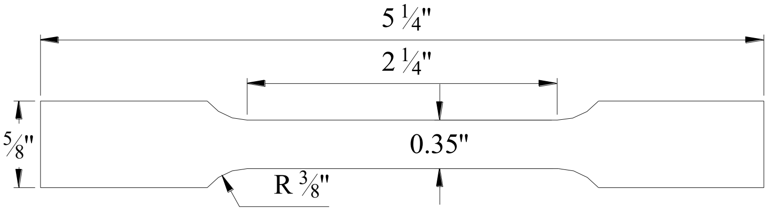

Figure 5.6 Fully threaded rod coupon dimension (units: inches)

Table 5.3 Beam test steel coupon testing results

Type		E_s (ksi)	E_{sh} (ksi)	F_{ys} (ksi)	F_{yd} (ksi)	F_u (ksi)	ε_{sh} (με)
W14x38	Flange 1	30300	340	50.9	54.9	70.5	27000
	Flange 2	30100	300	49.0	53.0	69.5	22500
	Flange 3	30800	280	50.3	54.0	70.4	24300
	Web 1	28700	250	58.1	62.1	73.9	37500
	Web 2	28600	270	55.0	59.7	72.0	41000
	Web 3	28700	250	56.8	61.3	72.4	37500
W14x26 cut from steel stub (Beam 6)	Flange 1	29800	260	48.4	51.7	65.4	22400
	Flange 2	29800	260	48.5	51.6	65.6	22900
	Flange 3	29400	260	48.2	51.6	65.5	23000
	Web 1	29700	220	49.7	53.4	64.6	36300
	Web 2	29600	230	49.7	53.7	64.7	37200
	Web 3	28100	250	50.7	54.2	65.2	36600
W14x26 cut from Beam 3	Flange 1	30100	250	46.4	50.9	65.8	25300
	Flange 2	30100	270	45.0	49.7	64.5	27200
	Flange 3	30200	260	45.3	49.1	65.0	20800
	Web 1	29500	260	48.6	53.0	65.9	40060
	Web 2	29900	240	49.5	53.6	66.5	41000
	Web 3	30300	240	47.2	51.5	64.5	38400
Cast-in channel	Flange 1	28800	N/A	58.0	60.3	67.5	N/A
	Flange 2	28500	N/A	58.1	60.2	68.0	N/A
	Flange 3	28500	N/A	58.7	60.2	68.5	N/A
	Web 1	27200	N/A	-	59.5	66.4	N/A
	Web 2	28400	N/A	56.5	59.2	66.8	N/A
	Web 3	27700	N/A	55.8	58.5	65.4	N/A
No.4 longitudinal reinforcement	1	27500	660	60.0	63.3	97.0	12200
	2	26400	650	60.2	63.2	97.0	12200
	3	26700	680	59.6	63.3	96.4	11800
No.3 transverse reinforcement	1	28200	N/A	68.3	74.1	105.2	N/A
	2	28100	N/A	65.6	71.7	103.0	N/A
	3	28900	N/A	63.5	69.7	101.6	N/A
M24 bolt	1	31200	N/A	112.0	119.5	135.7	N/A
	2	31600	N/A	115.1	122.9	139.4	N/A
	3	32500	N/A	117.3	125.5	141.4	N/A
M20 bolt	1	29800	N/A	113.8	122.0	138.1	N/A
	2	31900	N/A	117.4	126.0	142.3	N/A
	3	26900	N/A	-	124.9	141.1	N/A
45 in. rod for beam specimen 1	1	30200	130	53.5	57.9	77.1	21400
	2	33100	150	56.2	60.6	79.9	23700
	3	33600	130	55.7	60.5	79.2	20900
46.5 in. rod for beam specimen 1	1	33100	125	58.0	61.7	82.4	24200
	2	33300	130	55.8	60.1	80.0	21400
	3	29300	135	53.6	58.0	77.8	21600
46.5 in. rod for beam specimen 2-4	1	30600	170	-	60.8	83.2	14700
	2	32500	150	54.6	59.0	80.2	18800
	3	33000	155	57.6	61.5	83.2	14300

Direct tension and shear testing

Similar to the procedures used for the T-bolts used in the pushout tests, tension and shear testing was also conducted on the T-bolts as well as the fully threaded rods in the beam tests. The rod specimens were 10 in. long. More details of the testing methodology can be found in Section 4.3 in Chapter 4. The load-deformation curves and failure of the specimens are shown in Figure 5.7 through Figure 5.10. The rods were bent in the tension test because wedge tension testing was performed in accordance with ASTM F606/F606M-14a. The average ultimate tensile and shear strengths of the specimens are given in Table 5.4, and the ultimate tensile strengths of the materials are also estimated. The tensile strength of the M24 bolt material cannot be determined since the fracture occurred in the bolt head, rather than the shank.

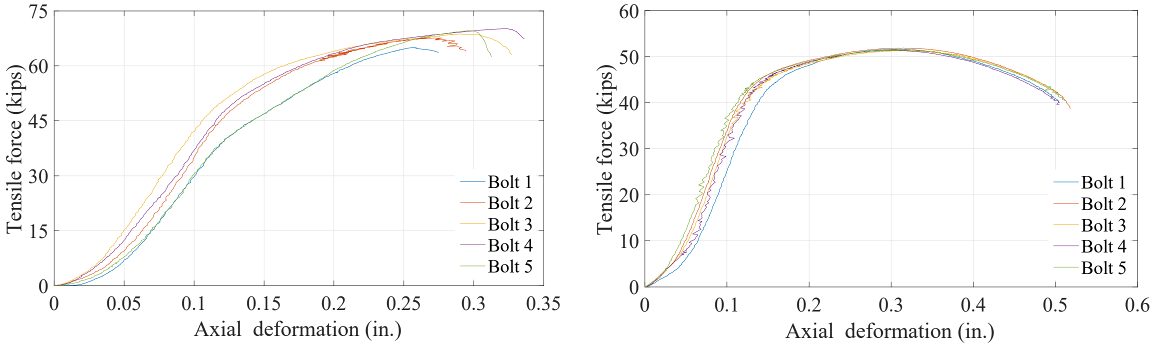

a) M24 bolts b) M20 bolts

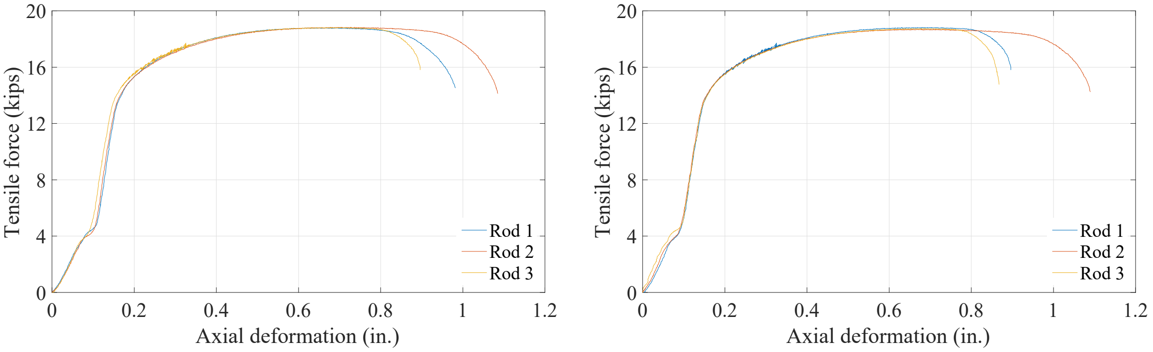

c) 46.5 in. rods in beam test 1 d) 46.5 in. rods for remaining beam tests

Figure 5.7 Tensile load versus axial elongation

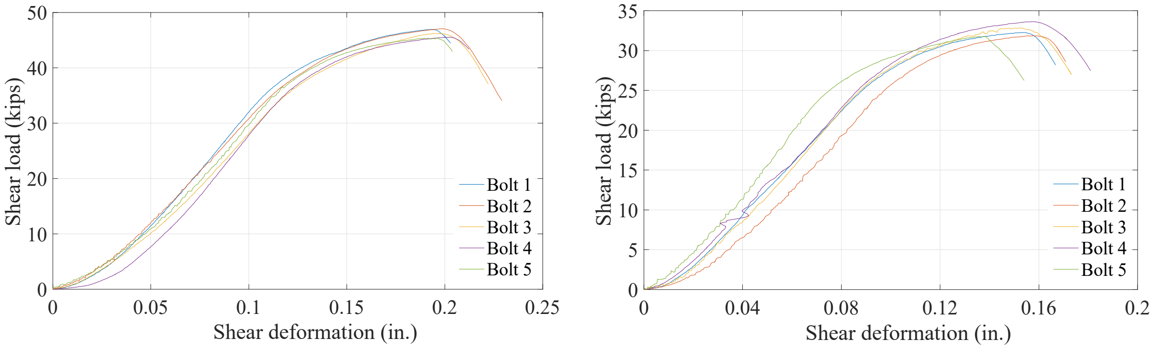

a) M24 bolts

b) M20 bolts

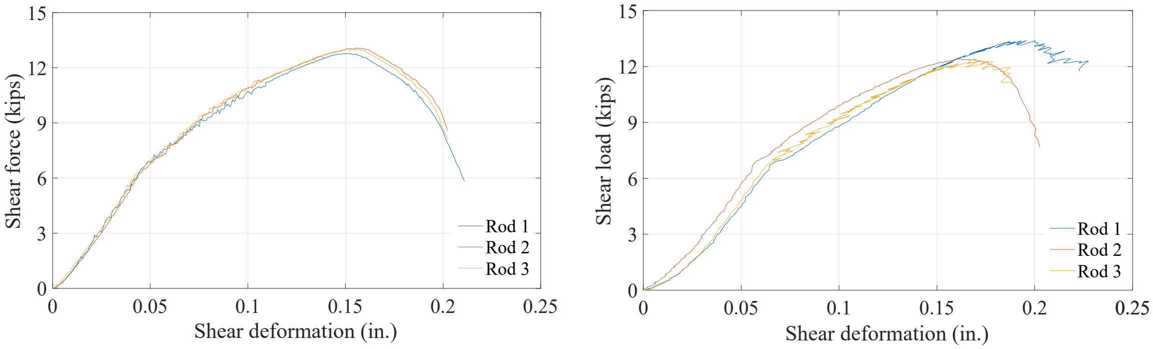

c) 45 in. rods in beam test 1

d) 46.5 in. rods in beam test 1

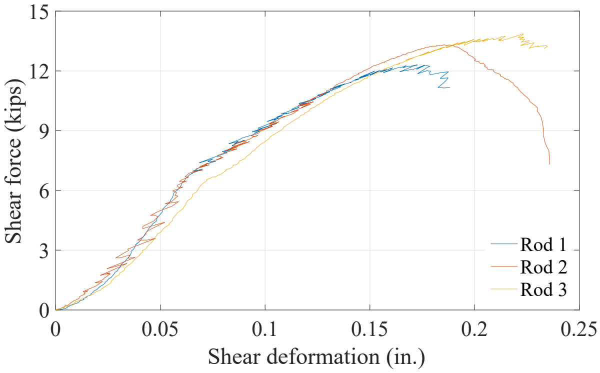

e) 46.5 in. rods for remaining beam tests

Figure 5.8 Shear load versus Shear deformation

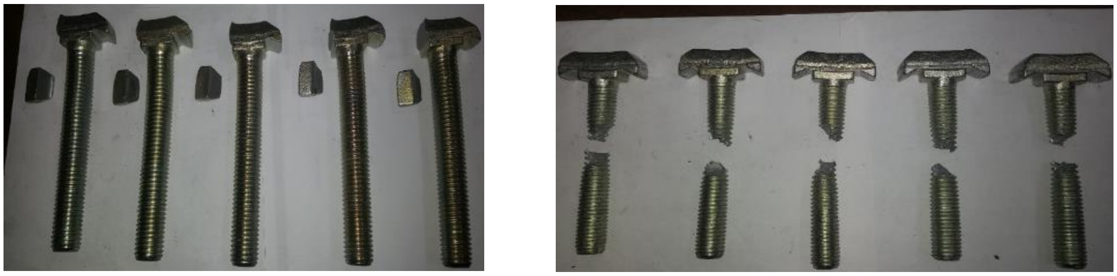

a) M24 bolts b) M20 bolts

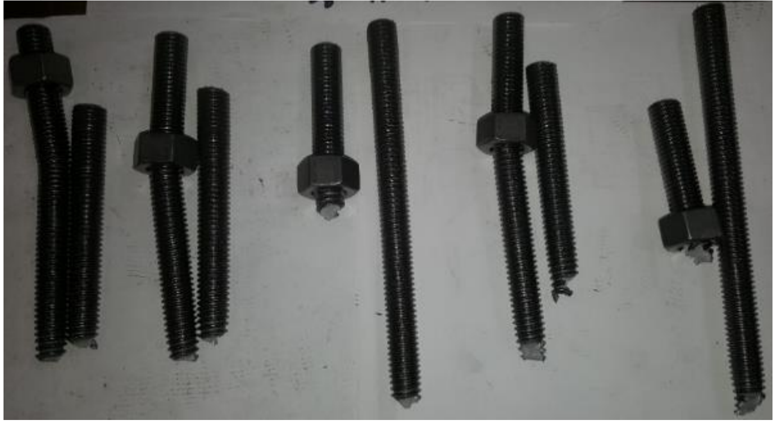

c) Rods

Figure 5.9 Failed specimens under tension

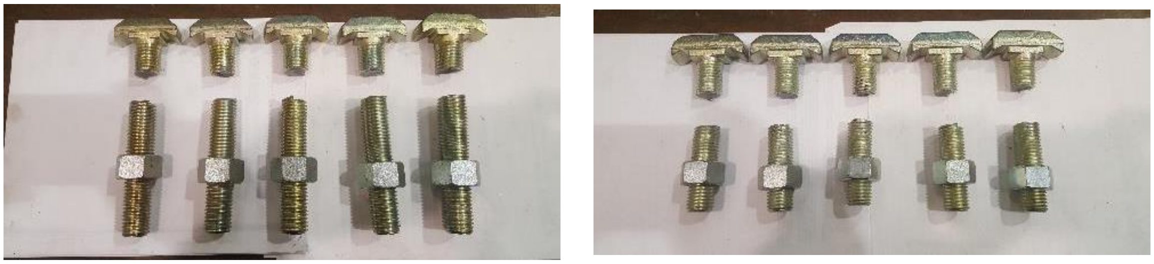

a) M24 bolts b) M20 bolts

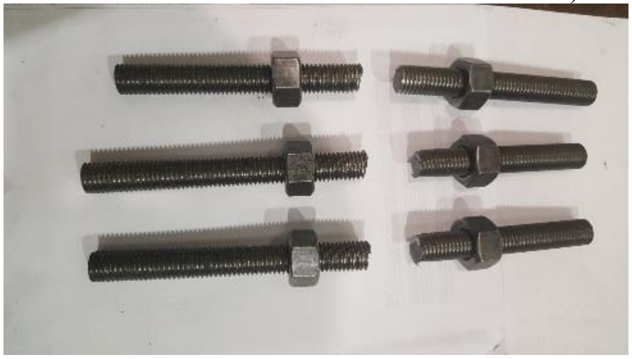

c) Rods

Figure 5.10 Failed specimens under shear

Table 5.4 Direct tension and shear testing results

Specimen	Ultimate strength (kips)		Ultimate tensile stress (ksi)	
	Tension	Shear	Tension testing	Shear testing
M24 bolts	68.2	46.2	> 124.0	135.2
M20 bolts	51.6	32.4	135.8	136.5
45 in. rods in beam test 1	-	12.9	-	91.3
46.5 in. rods in beam test 1	18.8	12.6	83.3	89.3
46.5 in. rods in beam tests 2,3 and 4	18.7	13.1	82.9	93.1

From Table 5.4, it is seen that the ultimate tensile stresses calculated using the direct tension and shear testing results are very close to those given in Table 5.3, except for the tensile stress of the fully thread rods, which is about 11% ~ 16% larger than that obtained from tensile coupon testing.

Concrete properties

The precast concrete planks were completed in three pours, with 20 planks cast in each pour. Planks from each of the first three beam tests were from the same pour. Test 4-M20-1C-RL, however, had planks from all three pours, which could mimic the situation where planks of different strength reclaimed from different projects are reused in a new project. For each pour, thirty-nine cylinders were cast and divided into three groups, with each group consisting of thirteen 6 in. by 12 in. cylinders. These three groups of cylinders represent concrete at different stages (i.e., beginning, middle and end) during the pour. The batch sheets and the delivery tickets for all the pours are included in Appendix D.2.6. It should be noted that the mix designs are not the same among the pours.

An overview is given for each pour.

- Pour 1: An initial slump of 5.0 in. was measured before pouring the specimens and cylinders. Specimens 1 through 5 were first poured and vibrated. While cylinder group A was cast and vibrated, another slump test was conducted, and the measured slump was 6 in. Specimens 6 through 10 were poured and vibrated, followed by cylinder group B. Two slump tests were conducted consecutively, and the measured slumps were both 3.0 in. Because the slump decreased substantially, two gallons of water was added to the truck mixer after pouring slab 10. Specimens 11 through 15 were then poured and vibrated. The concrete for cylinder group C was sampled before pouring the remaining planks, except for cylinders 2C, 4C, 7C and 11C, half volume of which was cast using concrete concurrent with the remaining planks. Meanwhile, another test showed the slump was 4.25 in. The last 5 specimens, which were all single-channel slabs, were poured. After the pour ended, the measured slump was 3 in.

- Pour 2: An initial slump of 6.0 in. was measured before pouring the specimens and cylinders. Specimens 1 through 5 were first poured and vibrated. While cylinder group A was cast and vibrated, another slump test was conducted, and the measured slump was 5-3/8 in. Specimens 6 through 10 were poured and vibrated, followed by cylinder group B and a slump test that displayed a slump of 4.5 in. Five gallons of water was added to the truck mixer after casting the cylinders. Specimens 11 through 15 were then poured and vibrated. The concrete for cylinder group C was sampled before pouring the remaining 5 planks; another test showed the slump is 5 in. After the pour ended, the measured slump was 3 in.

- Pour 3: When the concrete truck mixer arrived, the slump was estimated to be 3.5 in., and 10 gallons of water was thus added to increase workability of the concrete. An initial slump of 4.5 in. was measured after water was added. Specimens 1 through 5 were first poured and vibrated. While cylinder group A was cast and vibrated, another slump test was conducted, and the measured slump was 3.75 in. Specimens 6 through 10 were poured and vibrated, followed by cylinder group B and a slump test that showed a slump of 1.5 in. Due to the low slump, per ASTM C31/C31M-12, the vibration of most cylinders in group B was prolonged to 8s. 7B, 8B, 10B, and 11B were vibrated for 10 seconds. In addition, the outside of the cylinder forms was usually tapped 12 times for each layer, but it was increased to 20 times each layer as a result of the poor workability of the concrete. After adding 15 gallons of water to the remaining concrete, Specimens 11 through 15 were then poured and vibrated. The concrete for cylinder group C was sampled

> before pouring the last 5 planks; another test showed the slump was 5-3/4 in. After the pour ended, the measured slump was 3-7/8 in. It was noticed that the 15 gallons of water, which were added before pouring specimens 11 through 15, might be excessive, as was indicated by the lower concrete strength shown in Table 5.5.

When the concrete specimens started to harden, the specimens were sprayed and covered with wet burlaps. A plastic sheet was put over the burlaps to prevent loss of moisture. Except for the plywood underneath the concrete planks, all the other formwork for the specimens and cylinders was stripped on the next day. Some of the cylinders in each group were placed close to the specimens and dry cured in the same manner as the specimens, while the other cylinders were put into a water bath to mimic moisture-cured conditions. All the specimens were left in place for 7 days, and then moved into the lab. Curing of specimens continued until 28 days. Table 5.5 includes the concrete compressive and splitting tensile strength under different curing conditions at various testing dates.

Planks in the composite beams are numbered, with the very west plank numbered as 1 and the very east plank numbered as 15, as seen in Figure 5.11 in Section 5.4. The correspondence between the plank numbering and the plank pour sequence is given in Table 5.6.

Table 5.5 Beam test concrete cylinder testing results (units: psi)

Pour #	Curing Condition	Test type	Testing date	Cylinder A	Cylinder B	Cylinder C	Average
1	Moist-cured	Compressive test	3 days	3,625	3,380	3,360	3,455
			7 days	4,160	4,210	3,850	4,073
			21 days	4,870	5,210	5,195	5,092
			28 days	5,131	5,521	5,493	5,382
		Splitting tensile strength	28 days	481	493	438	470
	Same as the specimen	Compressive test	3 days	4,115	3,895	3,545	3,852
			7 days	4,560	4,390	4,175	4,375
			21 days	5,135	5,315	5,080	5,177
			28 days	5,450	5,761	5,513	5,575
			Test day for specimen 1 (168 days)	5,828	5,836	5,676	5,780
			Test day for specimen 4 (277 days)	6,341	6,472	6,617	6,477
		Splitting tensile strength	Test day for specimen 1 (168 days)	505	541	514	520
			Test day for specimen 4 (277 days)	560	536	569	555
2	Moist-cured	Compressive test	3 days	3,382	3,273	3,164	3,273
			7 days	4,117	4,262	4,247	4,209
			21 days	5,318	5,532	5,516	5,456
			28 days	5,667	6,245	5,918	5,943
		Splitting tensile strength	28 days	449	477	436	454
	Same as the specimen	Compressive test	3 days	3,713	3,750	3,377	3,613
			7 days	4,597	4,590	4,590	4,592
			21 days	5,886	6,034	5,941	5,953
			28 days	5,734	6,076	5,545	5,785
			Test day for specimen 2 (198 days)	6,653	6,768	6,475	6,632
			Test day for specimen 4 (251 days)	7,237	7,063	6,799	7,033
		Splitting tensile strength	Test day for specimen 2 (198 days)	583	564	572	573
			Test day for specimen 4 (251 days)	572	617	589	593
3	Moist-cured	Compressive test	3 days	3,404	3,421	2,464	3,096
			7 days	3,733	3,974	3,243	3,650
			21 days	4,931	4,571	3,936	4,479
			28 days	5,225	5,340	4,193	4,919
		Splitting tensile strength	28 days	459	481	358	433
	Same as the specimen	Compressive test	3 days	3,331	3,510	2,597	3,146
			7 days	4,534	4,629	3,525	4,228
			21 days	5,779	5,805	4,511	5,365
			28 days	5,674	5,929	4,932	5,511
			Test day for specimen 3 (214 days)	6,969	6,731	5,419	6,373

			Test day for specimen 4 (235 days)	6,862	6,756	5,630	6,416
		Splitting tensile strength	Test day for specimen 3 (214 days)	544	533	421	500
			Test day for specimen 4 (235 days)	545	573	471	530

Table 5.6 Beam test concrete plank pour sequence

Test #	Plank #	Pour sequence	Pour #	Test #	Plank #	Pour sequence	Pour #
1	1	19	1	2	1	3	2
	2	17			2	12	
	3	11			3	16	
	4	16			4	13	
	5	20			5	5	
	6	12			6	15	
	7	9			7	1	
	8	18			8	2	
	9	14			9	17	
	10	15			10	11	
	11	7			11	8	
	12	10			12	9	
	13	8			13	7	
	14	13			14	6	
	15	6			15	4	
3	1	9	3	4	1	5	3
	2	10			2	5	1
	3	7			3	19	2
	4	11			4	4	1
	5	20			5	3	3
	6	14			6	3	1
	7	18			7	2	1
	8	19			8	1	3
	9	15			9	1	1
	10	8			10	18	2
	11	6			11	2	3
	12	17			12	10	2
	13	16			13	20	2
	14	13			14	14	2
	15	12			15	4	3

5.4 Instrumentation

The following sections describe the instrumentation plan adopted for the composite beam specimens. Slight changes were made among different tests.

Displacement measurements

Composite beam deflections, which are utilized to estimate the stiffness of the beam specimens, were measured at different locations along the beam length. Those locations are named as V0 through V6 in Figure 5.11. Linear potentiometers with a stroke length of 4 in. were employed to measure deflections at V0 and V6, while string pots capable of measuring displacement up to 15 in. were used for the other deflections. The ductility of the composite beam specimens can also be computed based on the load-displacement curves. Slips between the steel beams and concrete planks were measured at locations from S1 through S10. S1 through S5 and S6 through S10 were placed at the south and north sides of the beams, respectively. 1 in. stroke linear potentiometers were utilized for S4 through S7, while 2 in. stroke linear potentiometers measured slips at the other locations. These sensors were positioned along the length of the beams. The maximum slip provides the slip demand on the deconstructable connectors in the tested beams. The horizontal deflections were also measured using linear potentiometers with a stroke length of 4 in. at the two ends of the beams. In addition, after completing Test 1, inclinometers were placed on the top flanges of the top spreader beams in the other specimens to measure the rotations resulting from the bending of the specimens and tilting of the concrete slab.

Strain measurements

Several cross sections were instrumented along the length of each beam. As shown in Figure 5.12, at section SS3 eight strain gages were attached on the steel cross section: two at the bottom of the top flange; four at the third points of the web; two at the bottom of the bottom flange. Sections SS2 and SS4 were instrumented with six strain gages. Since sections SS1 and SS5 were expected to be elastic during the test, only the flange strains were measured. All the strain gages were placed at locations where the residual stresses are minimal, except for those attached at the mid-height of the web at sections SS2 and SS4. The directions of the uniaxial gages align with the longitudinal axes of the beams. In order to evaluate the effective width of the deconstructable composite beams, the strain variation in the direction of the longitudinal axis of the beam was measured at the locations shown in Figure 5.12. Because concrete is an inhomogeneous material, it is commonly recommended to choose strain gages with longer measuring grids to avoid localized strains. In this test, the concrete strains were calculated by tracking the length change of an 8 in. gage length with linear potentiometers. For the mid-section where the bending moment is maximum, linear potentiometers with a stroke length of 1 in. were selected, while linear potentiometers with a stroke length of 0.5 in. were utilized at the other sections. The recorded concrete and steel strain profiles are used to track the migration of the neutral axes in concrete and steel.

According to the pushout test results, different reinforcement patterns and the number of channels in a plank do not affect the strains of the channel lips and channel anchors. It was thus decided to instrument a limited number of channel lips, specifically the channel lips in Test 2-M24-1C-RL and Test 4-M20-1C-RL, to investigate their behavior under different amount of pretension. In each test, only the channel lips of two end planks (Planks 1 and 15 in Figure 5.11) and one middle plank (Plank 8 in Figure 5.11) were gaged. The two end planks are at regions where the shear is maximum, and the moment is zero, while the moment is maximum, and the shear is zero for the middle plank. In Test 2-M24-1C-RL, strain gages were also attached to the middle two channel anchors in these three planks, since the anchor axial and shear forces were anticipated to be the largest among all the tests. Bolts at the ends and middle of all the beams were instrumented to track the bolt tension variation during the tests, as these were considered as the most important components. The strains of the very end bolts were measured with rosette strain gages from which both the axial strain and shear strain were obtained. Uniaxial strain gages were attached on the other bolts, and the directions of the gages align with the axes of the shanks. In Test 1-M24-2C-RH and Test 4-M20-1C-RL, transverse and longitudinal reinforcement were gaged. The strains in the transverse reinforcement were extrapolated to obtain the strains at the top surface of the concrete planks, which were compared to the calculated concrete strains from the linear potentiometers. The layout of all these gages and the directions of the rosette gages are illustrated in Figure 5.13 through Figure 5.15.

Rod tension measurements

Load cells were utilized to track the tension variation of four rods that are spread along half of the beam. Figure 5.16 shows the locations of the rods.

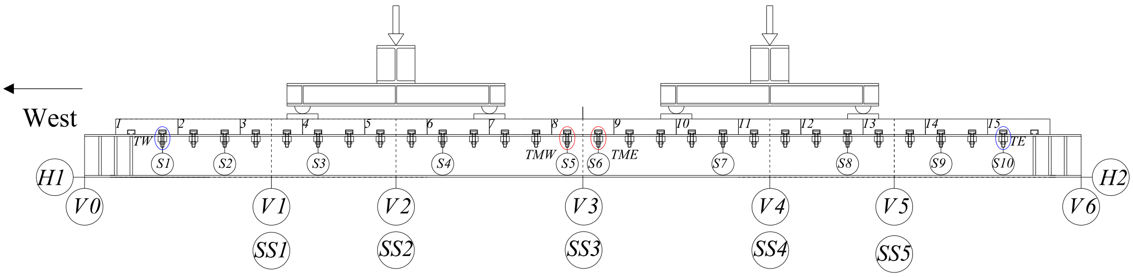
West
1
2
3
4
5
6
7
8
9
10
11
12
13
14
15
TW
TMW
TME
TE
S1
S2
S3
S4
S5
S6
S7
S8
S9
S10
H1
H2
V0
V1
V2
V3
V4
V5
V6
SS1
SS2
SS3
SS4
SS5

Beam 1

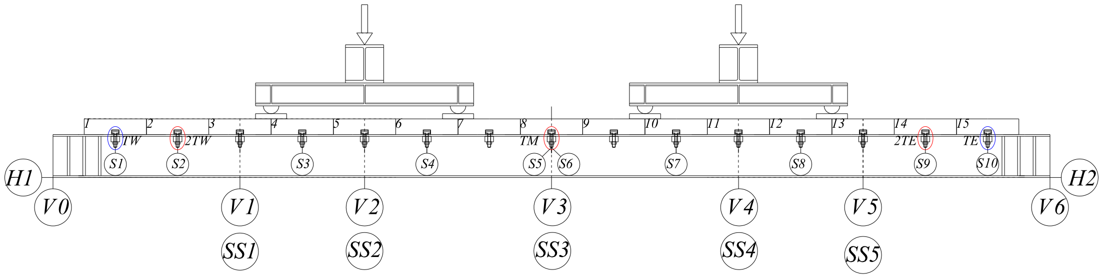
1
2
3
4
5
6
7
8
9
10
11
12
13
14
15
TW
2TW
TM
2TE
TE
S1
S2
S3
S4
S5
S6
S7
S8
S9
S10
H1
H2
V0
V1
V2
V3
V4
V5
V6
SS1
SS2
SS3
SS4
SS5

Beams 2 and 4

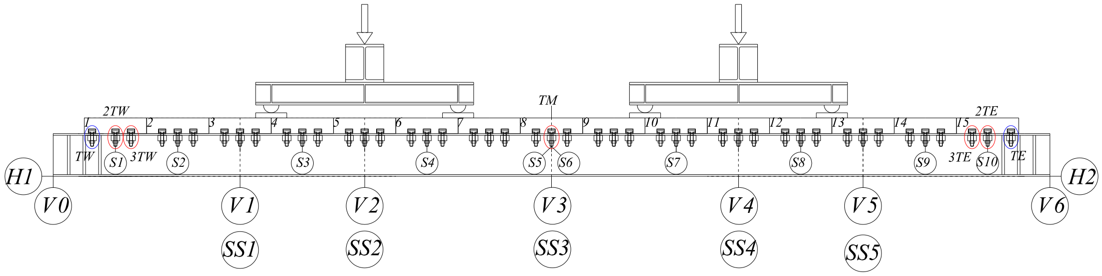
2TW
TM
2TE
1
2
3
4
5
6
7
8
9
10
11
12
13
14
15
TW
3TW
3TE
TE
S1
S2
S3
S4
S5
S6
S7
S8
S9
S10
H1
H2
V0
V1
V2
V3
V4
V5
V6
SS1
SS2
SS3
SS4
SS5

Beam 3

S1-S10 : slip of clamps

V0-V6: vertical deflection

H1-H2: horizontal movement

SS1-SS5: strain gaged sections

Note: Bolts attached with uniaxial strain gages are circled in red; bolts attached with rosette strain gages are circled in blue.

Figure 5.11 Location of instrumentation on beams

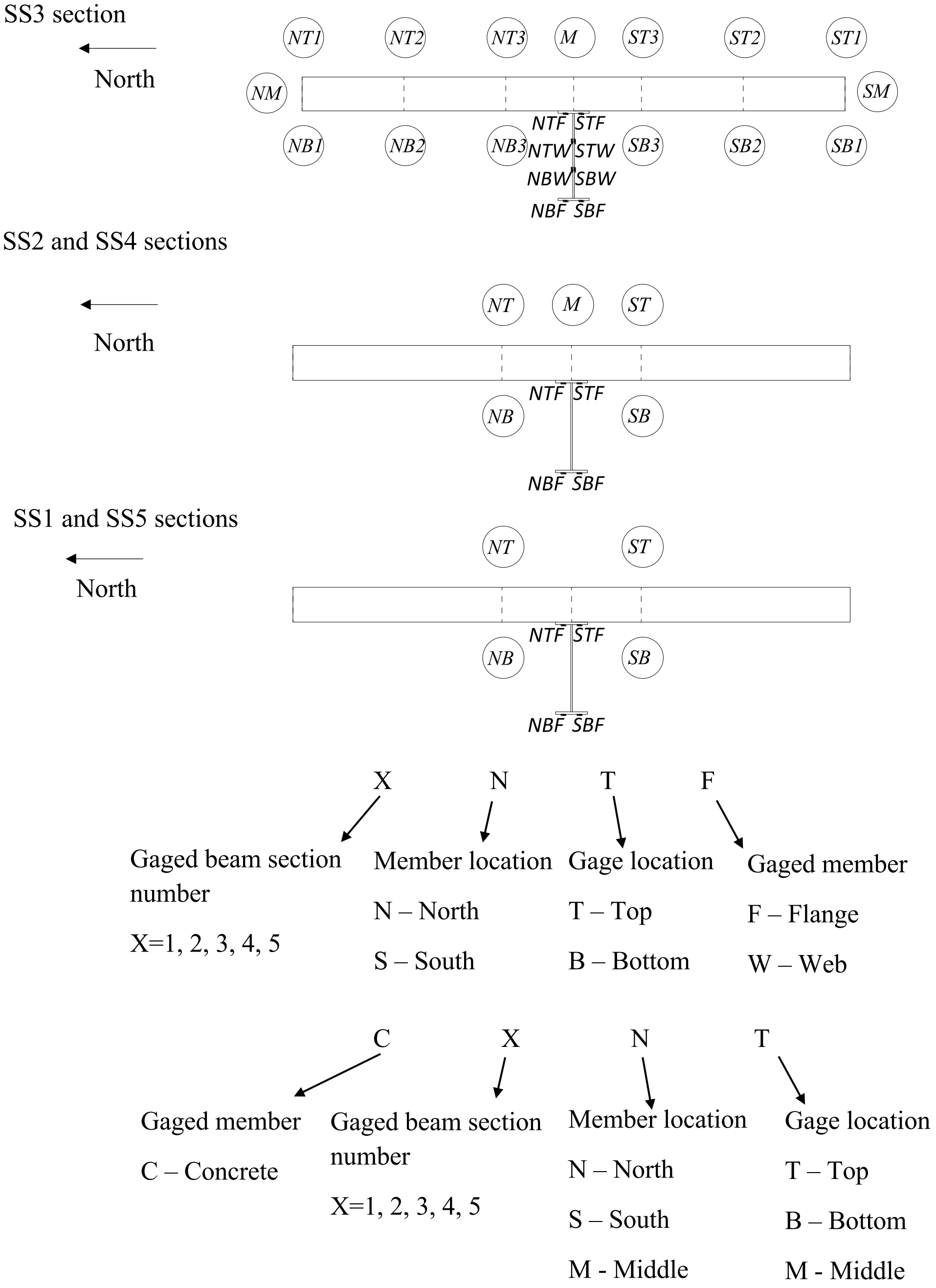
SS3 section
North
NT1
NT2
NT3
M
ST3
ST2
ST1
NM
SM
NTF STF
NB1
NB2
NB3
NTW STW
SB3
SB2
SB1
NBW SBW
NBF SBF
SS2 and SS4 sections
North
NT
M
ST
NTF STF
NB
SB
NBF SBF
SS1 and SS5 sections
North
NT
ST
NTF STF
NB
SB
NBF SBF
X
N
T
F
Gaged beam section number
X=1, 2, 3, 4, 5
Member location
N – North
S – South
Gage location
T – Top
B – Bottom
Gaged member
F – Flange
W – Web
C
X
N
T
Gaged member
C – Concrete
Gaged beam section number
X=1, 2, 3, 4, 5
Member location
N – North
S – South
M - Middle
Gage location
T – Top
B – Bottom
M - Middle

Figure 5.12 Steel beam and concrete plank sensor layout

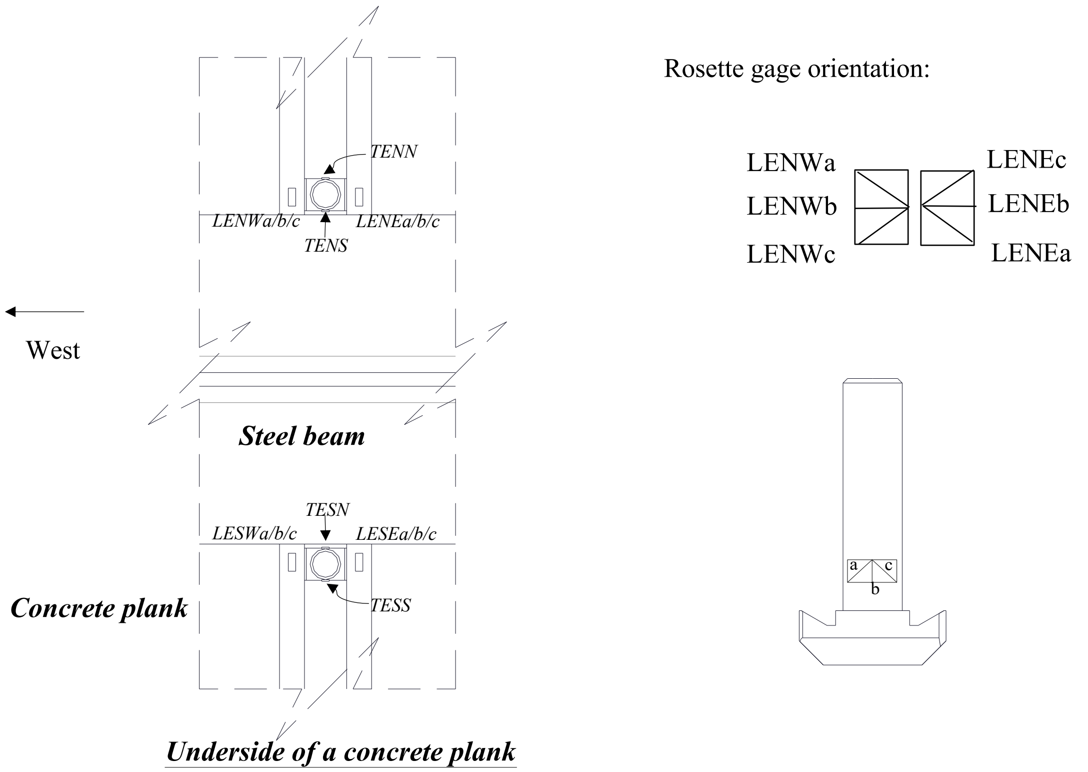
Rosette gage orientation:
LENWa
LENWb
LENWc
LENEc
LENEb
LENEa
TENN
LENWa/b/c
LENEa/b/c
TENS
West
Steel beam
TESN
LESWa/b/c
LESEa/b/c
TESS
Concrete plank
a
c
b
Underside of a concrete plank

L	E	NW	a/b/c
Gaged member	Plank position	Gage location	Leg number (only for rosette)
L – Channel lips	E – East	NW – Northwest	a – 0 degree leg
	M – Middle	NE – Northeast	b – 45 degree leg
	W – West	SW – Southwest	c – 90 degree leg
		SE – Southeast	

T	E	N	N	a/b/c
Gaged member	Plank position	Bolt location	Gage location	Leg number (only for rosette)
T - Bolts	E – East	N – North	N – North	a – 0 degree leg
	M – Middle	S – South	N – South	b – 45 degree leg
	W – West			c – 90 degree leg

Figure 5.13 Channel lip and bolt gage layout

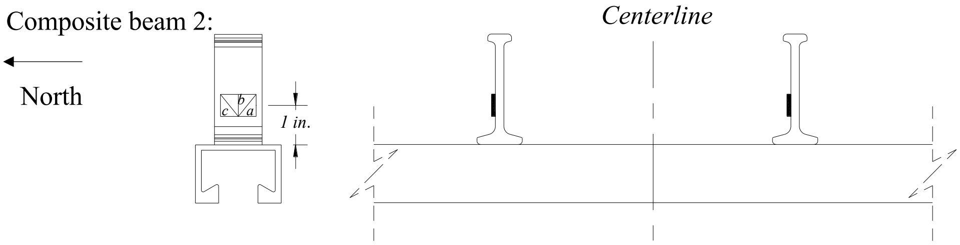
Composite beam 2:
North
Centerline
b
c
a
1 in.

A E N a/b/c

Gaged member	Plank position	Member location	Leg number (only for Rosette)
A – Channel anchors	E – East	N – North	a – 0 degree leg
	M – Middle	S – South	b – 45 degree leg
	W – West		c – 90 degree leg

Figure 5.14 Channel anchor gage layout

Composite beam 1:

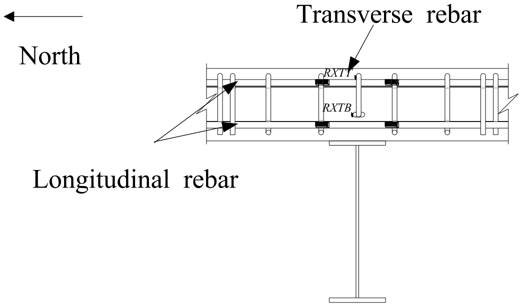
North
Transverse rebar
RXTT
RXTB
Longitudinal rebar

Elevation view

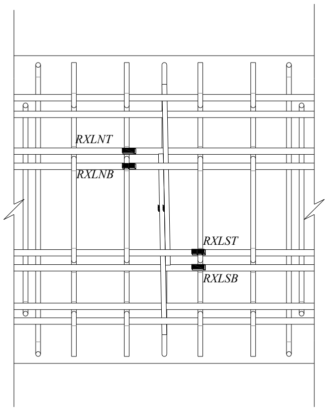
RXLNT
RXLNB
RXLST
RXLSB

Plan view

Composite beam 4:

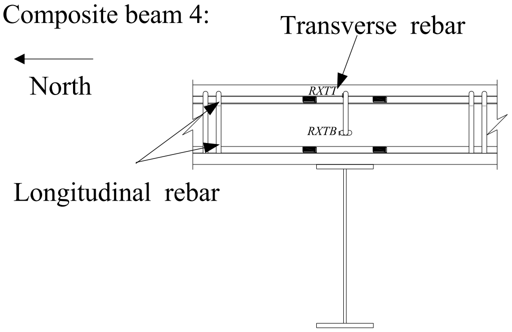
North
Transverse rebar
RXTT
RXTB
Longitudinal rebar

Elevation view

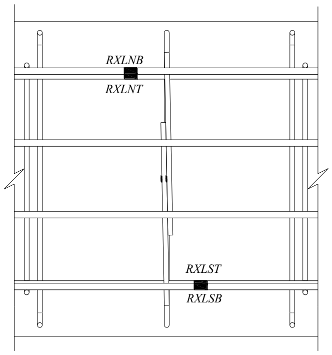
RXLNB
RXLNT
RXLST
RXLSB

Plan view

Longitudinal reinforcement:

R	X	L	NT
Gaged member	Plank number	Longitudinal rebar	Gage location
R - Rebar	X=1, 5, 8, 11, 15		NT – North and top
			ST – South and top
			NB – North and bottom
			SB – South and bottom

Transverse reinforcement:

R	X	T	T
Gaged member	Plank number	Transverse rebar	Gage location
R - Rebar	X=1, 5, 8, 11, 15		T – Top
			B – Bottom

Figure 5.15 Longitudinal and transverse reinforcement gage layout

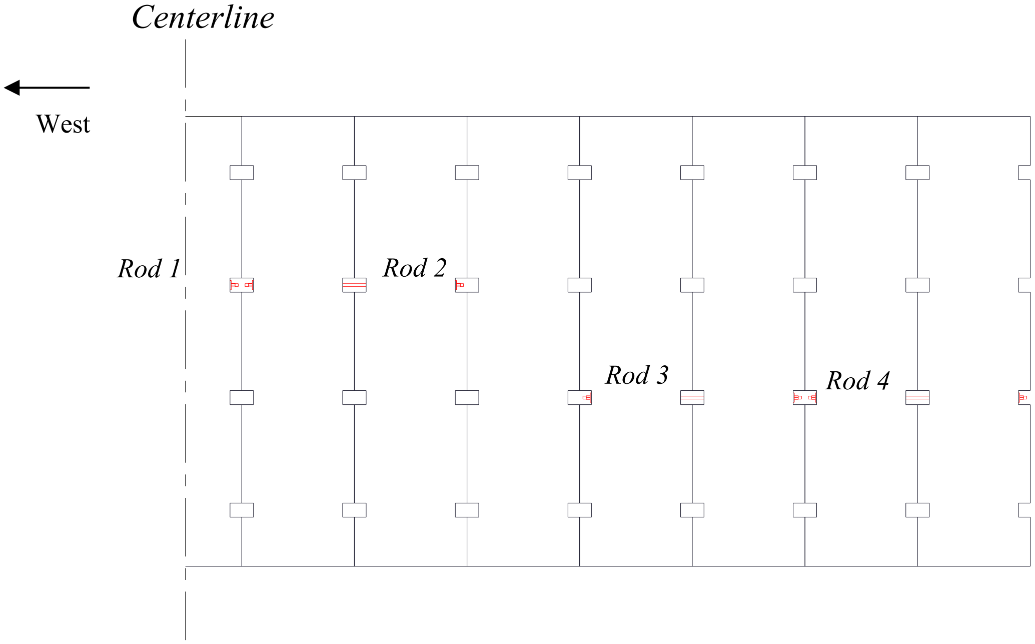

Figure 5.16 Location of instrumented threaded rods

5.5 Loading protocol

Both actuators used in the composite beam tests were displacement-controlled. The specimens were loaded to 40% of their expected flexural strengths and then reloaded three times. Two more cycles were then undertaken, with one cycle at 60% and another one at 80% of the estimated flexural strengths. In the pushout tests, it has been exhibited that the behavior of the clamping connectors is affected by the loading protocol, i.e., monotonic loading vs. cyclic loading. These loading/unloading cycles, which were intended to mimic serviceability conditions, were included to consider whether the loading protocols might affect the shear strengths of the clamping connectors as well as the flexural strengths of the beams. After completing the cycles, the beams were then loaded until the deflections were excessive. The actuator displacement rate was 1.57 in. /h (40 mm/h) throughout the tests (Ataei et al. 2016).

When testing Specimen 1-M24-2C-RH, which is the first specimen in the experimental program, the estimated flexural strength of this beam was based on the preliminary finite element analysis results, which indicated that the ultimate flexural strength of this beam was approximately 90% of that predicted by AISC design Equations (C-I3-6) through (C-I3-10) in the AISC 360-16 commentary (2016). Nominal material properties were used in the preliminary FE model, but tested material properties were used in the AISC equations. More importantly, in the preliminary finite element model, a frictional coefficient of 0.3 was assumed for all the contact, whereas the test result of specimen 1-M24-2C-RH suggested that the actual frictional coefficient was approximately 0.35 (see Section 5.7). This coefficient of friction is the same as that in the companion pushout tests (see Section 4.6), indicating that the behavior of the clamps obtained from the pushout tests can be related to that of the clamps in the beam tests. The tested ultimate flexural strength of this specimen also closely matched that predicted by the AISC provisions using tested material properties. As a result, for the other specimens, the expected flexural strengths were assumed to be those calculated using the AISC equations using nominal material properties, as well as using tested clamp strengths from the appropriate pushout tests.

5.6 Assessment of deconstructable composite beams

When constructing the beam specimens, mild concrete crushing occasionally happened while pretensioning the fully threaded rods, as seen in Figure 5.17. As a result of the deformation of the plywood formwork during the concrete pour, the side surfaces of the planks were slightly slanted. As adjacent planks were compressed, the rod tension was only transferred to regions where contact was established. Compared to planks with accurate dimensions, the localized compressive stress between adjacent concrete specimens might have led to premature concrete crushing that was observed in the beam tests.

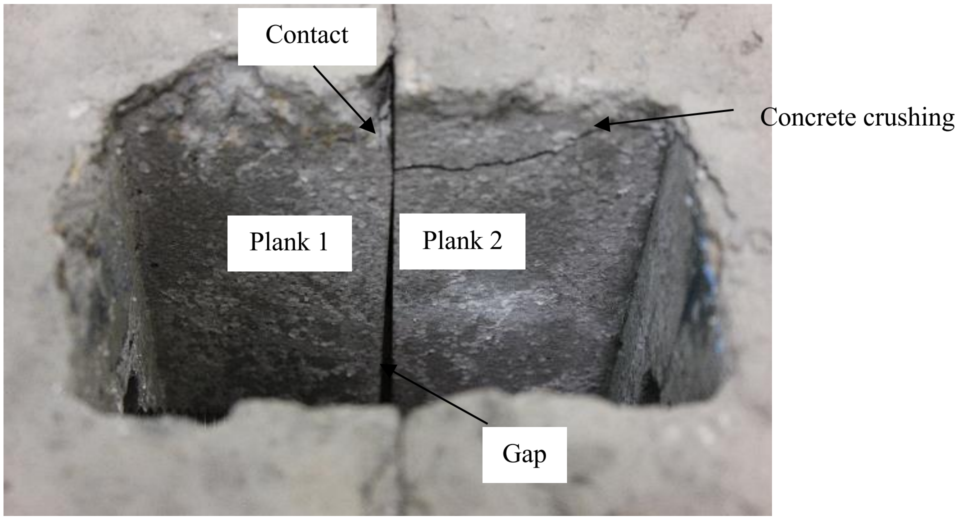

Figure 5.17 Localized concrete crushing after pretensioning fully threaded rods

5.6.1 Gaps between concrete planks

Since grouting planks and placing a cast-in place concrete topping are avoided to simplify disassembly and improve reuse potential, the gaps between the concrete planks might affect the behavior of the deconstructable composite beams. Figure 10.2.1 in PCI MNL-135-00 (2000) shows the maximum allowable horizontal misalignment or sweep, which results from both formwork and component width tolerance. For solid flat structural wall panels, the maximum sweep is ± 3 mm per 6 m, with ± 10 mm being maximum, which is represented by the variable f in Figure 5.18.

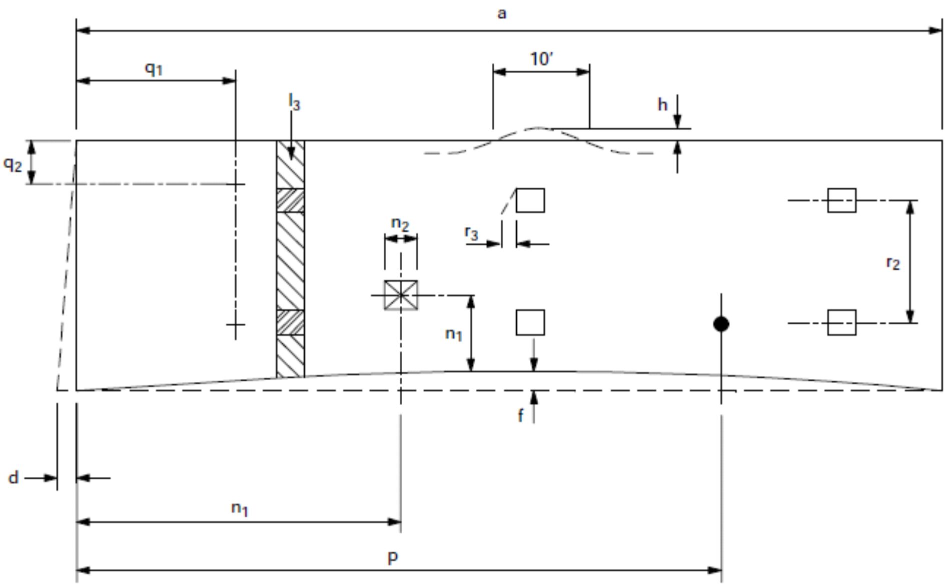

Figure 5.18 Solid or insulated flat structural wall panel tolerance [after PCI MNL-135-00 (2000)]

The gaps between adjacent concrete planks were measured at several locations on the top surface of the concrete slab, as shown in Figure 5.19. The widths of some gaps, especially those at the ends of the planks, exceeded the tolerance of 0.096 in. for the 8 ft. long planks used in the beam tests. The distribution of the gaps may indicate that some of the planks were slightly convex along their long edges. After testing, as a result of the deflection of the beam, adjacent concrete planks contacted at the top and separated at the bottom. Therefore, almost all the gaps on the top surface of the concrete slab were closed, except for some of those at the very ends of the planks.

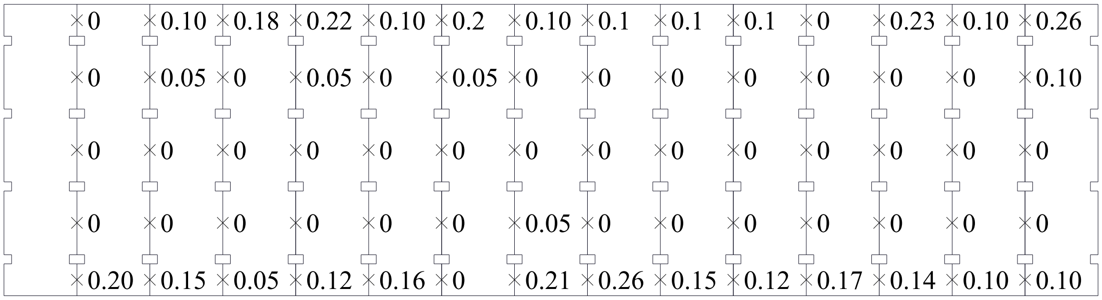

0	0.10	0.18	0.22	0.10	0.2	0.10	0.1	0.1	0.1	0	0.23	0.10	0.26
0	0.05	0	0.05	0	0.05	0	0	0	0	0	0	0	0.10
0	0	0	0	0	0	0	0	0	0	0	0	0	0
0	0	0	0	0	0	0.05	0	0	0	0	0	0	0
0.20	0.15	0.05	0.12	0.16	0	0.21	0.26	0.15	0.12	0.17	0.14	0.10	0.10

Before test

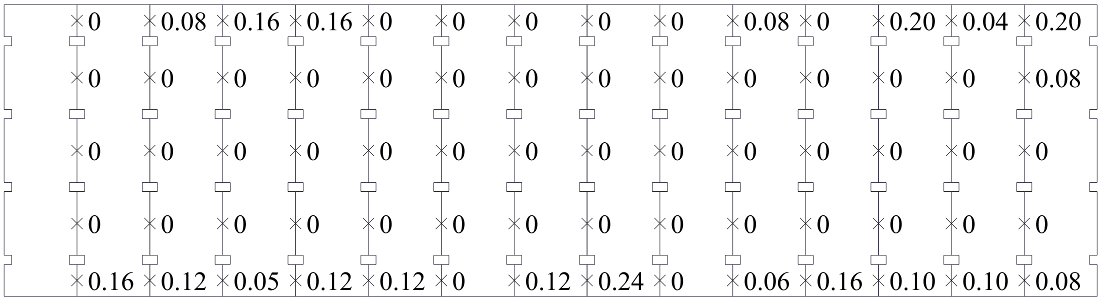

0	0.08	0.16	0.16	0	0	0	0	0	0.08	0	0.20	0.04	0.20
0	0	0	0	0	0	0	0	0	0	0	0	0	0.08
0	0	0	0	0	0	0	0	0	0	0	0	0	0
0	0	0	0	0	0	0	0	0	0	0	0	0	0
0.16	0.12	0.05	0.12	0.12	0	0.12	0.24	0	0.06	0.16	0.10	0.10	0.08

After test

a) Beam 1-M24-2C-RH

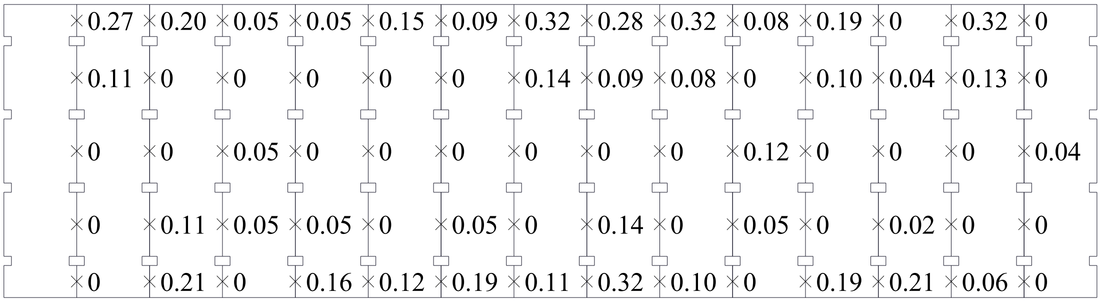

0.27	0.20	0.05	0.05	0.15	0.09	0.32	0.28	0.32	0.08	0.19	0	0.32	0
0.11	0	0	0	0	0	0.14	0.09	0.08	0	0.10	0.04	0.13	0
0	0	0.05	0	0	0	0	0	0	0.12	0	0	0	0.04
0	0.11	0.05	0.05	0	0.05	0	0.14	0	0.05	0	0.02	0	0
0	0.21	0	0.16	0.12	0.19	0.11	0.32	0.10	0	0.19	0.21	0.06	0

Before test

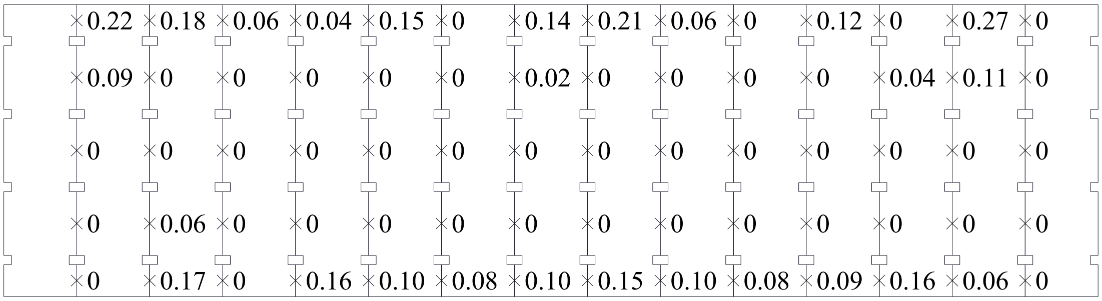

0.22	0.18	0.06	0.04	0.15	0	0.14	0.21	0.06	0	0.12	0	0.27	0
0.09	0	0	0	0	0	0.02	0	0	0	0	0.04	0.11	0
0	0	0	0	0	0	0	0	0	0	0	0	0	0
0	0.06	0	0	0	0	0	0	0	0	0	0	0	0
0	0.17	0	0.16	0.10	0.08	0.10	0.15	0.10	0.08	0.09	0.16	0.06	0

After test

b) Beam 2-M24-1C-RL

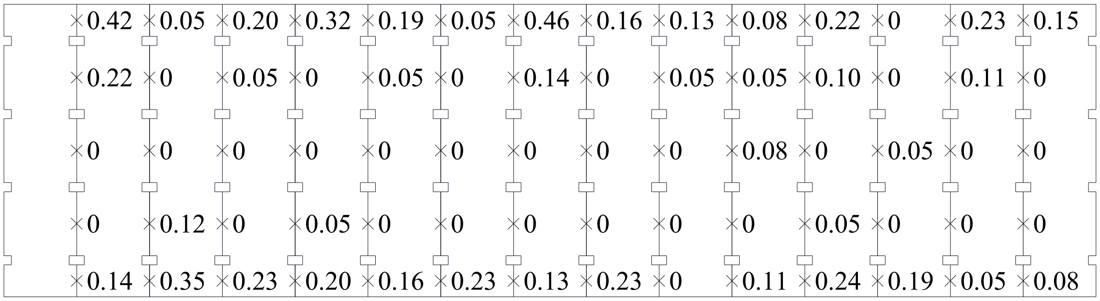

0.42	0.05	0.20	0.32	0.19	0.05	0.46	0.16	0.13	0.08	0.22	0	0.23	0.15
0.22	0	0.05	0	0.05	0	0.14	0	0.05	0.05	0.10	0	0.11	0
0	0	0	0	0	0	0	0	0	0.08	0	0.05	0	0
0	0.12	0	0.05	0	0	0	0	0	0	0.05	0	0	0
0.14	0.35	0.23	0.20	0.16	0.23	0.13	0.23	0	0.11	0.24	0.19	0.05	0.08

Before test

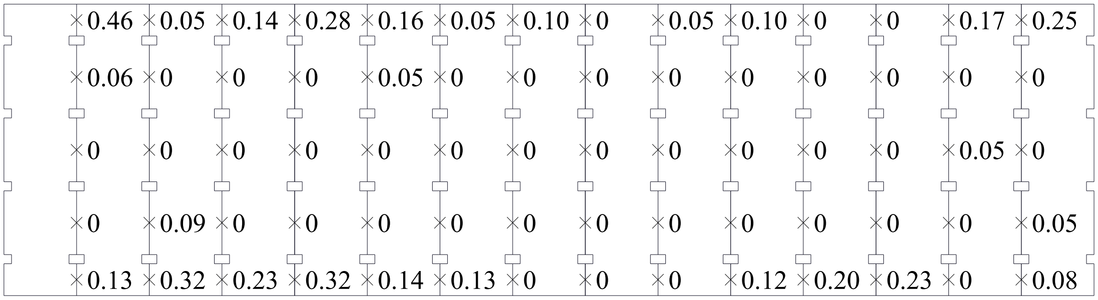

0.46	0.05	0.14	0.28	0.16	0.05	0.10	0	0.05	0.10	0	0	0.17	0.25
0.06	0	0	0	0.05	0	0	0	0	0	0	0	0	0
0	0	0	0	0	0	0	0	0	0	0	0	0.05	0
0	0.09	0	0	0	0	0	0	0	0	0	0	0	0.05
0.13	0.32	0.23	0.32	0.14	0.13	0	0	0	0.12	0.20	0.23	0	0.08

After test

c) Beam 3-M20-3C-RL

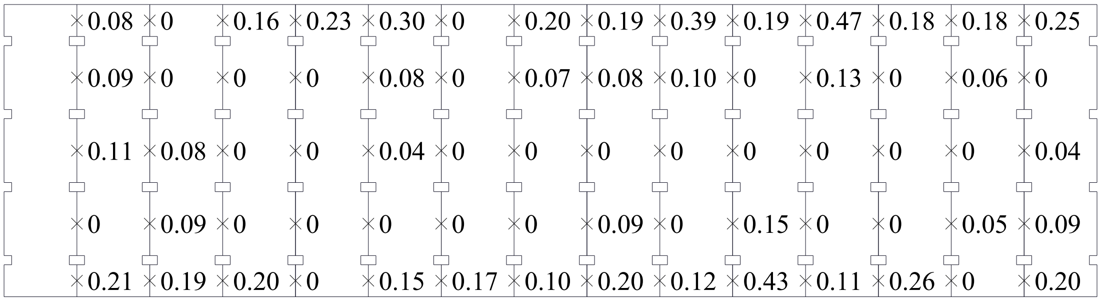

0.08	0	0.16	0.23	0.30	0	0.20	0.19	0.39	0.19	0.47	0.18	0.18	0.25
0.09	0	0	0	0.08	0	0.07	0.08	0.10	0	0.13	0	0.06	0
0.11	0.08	0	0	0.04	0	0	0	0	0	0	0	0	0.04
0	0.09	0	0	0	0	0	0.09	0	0.15	0	0	0.05	0.09
0.21	0.19	0.20	0	0.15	0.17	0.10	0.20	0.12	0.43	0.11	0.26	0	0.20

Before test

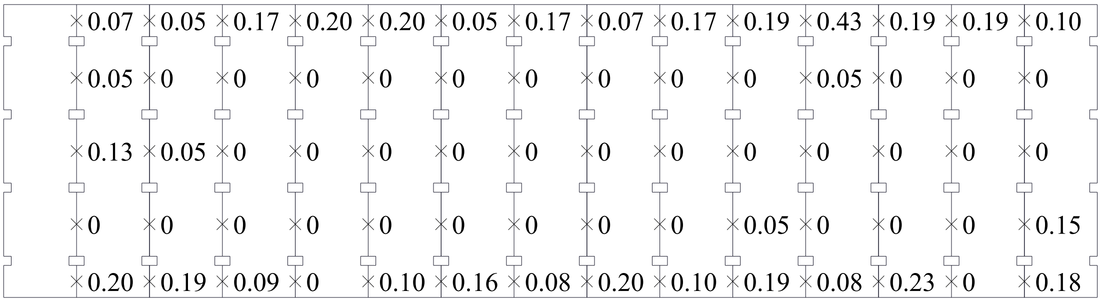

0.07	0.05	0.17	0.20	0.20	0.05	0.17	0.07	0.17	0.19	0.43	0.19	0.19	0.10
0.05	0	0	0	0	0	0	0	0	0	0.05	0	0	0
0.13	0.05	0	0	0	0	0	0	0	0	0	0	0	0
0	0	0	0	0	0	0	0	0	0.05	0	0	0	0.15
0.20	0.19	0.09	0	0.10	0.16	0.08	0.20	0.10	0.19	0.08	0.23	0	0.18

After test

d) Beam 4-M20-1C-RL

× : Locations where the gap widths are measured.

All the drawings use left as the west direction.

Figure 5.19 Measured gap widths for the composite beams (units: inches)

As shown in Table 5.12 in Section 5.6.2.6, because the tested beam strength and stiffness are very close to or greater than the predicted values, the width and distribution of the cracks between the planks may not adversely affect the performance of the beams.

5.6.2 Behavior of composite beam specimens

Load and Resistance Factor Design (LRFD) is the most common approach to design a composite beam. In this method, the available flexural strength of the beam needs to exceed the required flexural strength generated by factored loads, as shown in Equation (5.1). Although the deflection of the beam may be checked at serviceability, it is not clear whether the beam behaves elastically under service loading. Therefore, it is important to understand the performance of the beam under unfactored loads by estimating the ratio of the required flexural strength at serviceability to the ultimate flexural strength of the beam.

$$\emptyset_b M_n \geq M_u \tag{5.1}$$

Assuming a beam is designed to support both dead load D and live load L, the service load acting on the beam may be taken as $D + L$. If the design of the beam is controlled by strength, the required flexural strength under the factored loads $1.2D + 1.6L$ is approximately 90% of the ultimate flexural strength of the beam (assuming a resistance factor = 0.9). The ratio of applied service load to applied ultimate load may thus be calculated as:

$$k = \frac{D + L}{(1.2D + 1.6L)/0.9} \tag{5.2}$$

This ratio varies from 0.56 to 0.75. The former is calculated by neglecting the dead load, while the latter is obtained if the live load is ignored.

The total loading acting on a beam includes the weight of the concrete planks, steel beam, spreader beams, and plates, as well as the applied actuator loads. The weight of the clamps and bolts is very small and not accounted for. The weight of the concrete planks and steel beam is treated as a uniform loading, while the weight of the spreader beams and plates, along with the applied actuator forces, is regarded as concentrated point loading. It should be noted that as the concentrated forces are transferred to the steel beam, the loads spread and the actual loading scenario for the beam is between uniform loading and concentrated loading. Since the actual weight of the steel components and concrete planks cannot be measured, the nominal weight is utilized for weight and bending moment calculation. The densities of concrete and steel are taken as 150 $lb/ft.^3$ and 0.284 $lb/in.^3$, respectively. The self-weight of all the components is given in Table 5.7. For simplicity, the total self-weight is thus estimated to be 25,000 lbs for all the composite beam specimens. For each specimen, the weight of the concrete planks and steel beam is about 20,000 lbs, and the resulting bending moment is 75 ft.-kips at the center sections of the composite beams. Similarly, the spreader beams and plates approximately weigh 5,000 lbs, leading to a moment of 22.5 ft.-kips at the same locations. Hence, at the mid-sections of the beams, the total bending moment under the self-weight equals 97.5 ft.-kips.

Table 5.7 Self-weight of all the components in a composite beam specimen

Component	Quantities	Weight per piece (lbs)
Top spreader beam	2	1123
Bottom spreader beam	4	498
Plate under bottom spreader beam	8	95
Concrete plank	15	1254
Steel beam section	1	1289 (W14x38) or 891 (W14x26)
Total		25278 or 24709 lbs (843 or 824 lbs/ft.)

5.6.2.1 *Specimen 1-M24-2C-RH*

The load-deflection curve of composite beam specimen 1-M24-2C-RH is shown in Figure 5.20. The curve is shifted from the origin to account for the bending moment and deflection under the self-weight of the composite beam and loading structures. Before applying any actuator load, the beam deflected about 0.38 in. under its self-weight after removing the wood supports used for shoring the beam during construction. This is equivalent to a bending moment of 97.5 ft.-kips at the center section of the beam. In Figure 5.20, the curve starts from 21.67 kips, which is calculated to be the equivalent concentrated loading to generate the same amount of bending moment at the center section as the total self-weight of 25,000 lbs obtained from the prior section. Such conversion enables all the loading (i.e., the self-weight and the actuator loads) to be treated as concentrated loading. As an alternative, the behavior of the specimen is demonstrated by the relationship illustrated in Figure 5.21 between the center section moment and calculated beam end rotation that is taken as the average of the rotations at both ends of the beam. The initial stiffness of the moment-rotation curve is very close to those of the reloading curves of the 60% cycle and 80% cycle. The method of calculation to obtain the beam end rotations is shown in Appendix F.2.2. The range of load and moment that correspond to full service loading is indicated in the load-deflection curve and moment-rotation curve.

Using the measured beam center deflection under its self-weight, the initial stiffness of the beam is calculated as: 25/0.38 = 65.8 kips/in. This stiffness may not be directly compared to the values given in Table 5.10 for three reasons. First, the beam might not have been "fully" shored during construction, and as such the composite beam might still be resisting a small amount of its self-weight. Consequently, the deflection may be underestimated. Second, the stiffness of a beam is dependent on the type of loading acting. The value given in Table 5.10 indicates the stiffness of the beam under concentrated forces, whereas after removing the shoring, the beam deflects under both uniform loading, which includes the weight of the concrete planks and steel beam, and concentrated loading, which includes the weight of the spreader beams and bearing plates. Third, it is unclear whether settling of the beam also contributes to the deflection.

Major events are identified on the load-deflection curve, including initiation of steel beam yielding, initiation of slip of the clamps, registering of the first loud noise to be heard (first bang), and initial signs of concrete crushing. Steel beam yielding is defined based on the average tensile strain measurement at the bottom flange of the center section. However, material yielding may first occur at one of the two inner loading point sections that are under combined shear force and bending moment. In addition, in a hot-rolled steel section, the residual stress is tensile at the intersection region of the flange and web and compressive at the tips of the flanges. The residual stress in the bottom flange may cause the intersection region to yield earlier than the tips. Slip of clamps is identified when the maximum measured slip is approximately 0.02 in., which is the slip level used to determine the slip load of a slip test in accordance with the Appendix A of the RCSC Specification (2014). These definitions apply to the other beam specimens as well.

During the first loading cycle at 40% of the expected flexural strength, the beam settled because a residual deflection of 0.101 in. was present when the load was removed. The load-deflection curves of the other two cycles at 40% of the expected flexural strength overlapped, indicating the beam was seated and behaved elastically at this load level. Nonlinear behavior was seen when the beam was loaded to 60% of its predicted flexural strength, as the slope of the load-deflection curve was reduced, and the strains at the bottom flange of the middle steel section exceeded the yield strain.

Slip of the clamps was commonly accompanied by a noticeable bang which caused the beam to vibrate, and the actuator loads thus slightly decreased abruptly and oscillated, but the loads rebounded and stabilized quickly. This phenomenon, which could be due to a stick-slip mechanism, occurred frequently during the test. The stick-slip mechanism is also believed to result in the load oscillation and sudden slip measurement changes in the pushout specimens designed with shims. However, such events were not observed in the other pushout specimens. In the pushout tests, the clamps were subjected to direct shear, whereas the clamps in the beam specimens were loaded indirectly by bending of the beams. Only four clamps were tested in a two-channel pushout specimen, while all the clamps placed between the zero moment section and maximum moment section resisted the shear flow at the steel/concrete interface in a beam specimen. These differences between the two series of experiments may lead to the stick-slip behavior of the clamps in the beam specimens that use no shims. The post-peak strength of the specimen declined gradually, and this could be attributed to the localized concrete crushing at the inner loading point sections, which may reduce the stiffness of the sections and lower the positions of the resultant compressive forces in concrete.

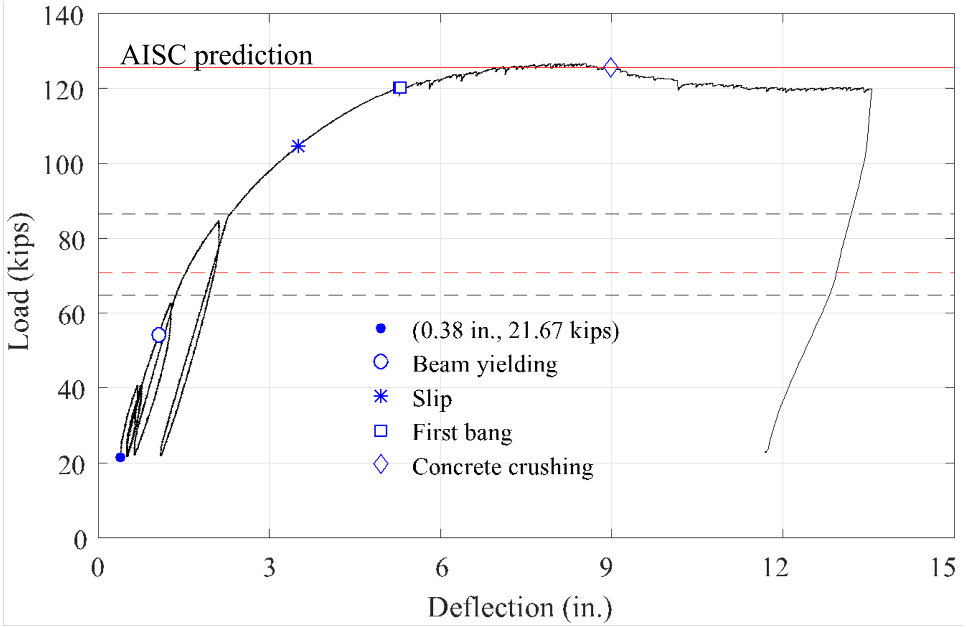

Note: If the beam is strength-controlled and efficiently designed, the two black dashed lines illustrate the range of the full service loading, and the red dashed line indicates the full service loading when the dead load is 92.5 psf, as is used in the prototype structrues in Chapter 3.The red solid line indicates the strength predicted by the AISC design equations.

Figure 5.20 Total load vs beam midspan deflection curve for Specimen 1-M24-2C-RH

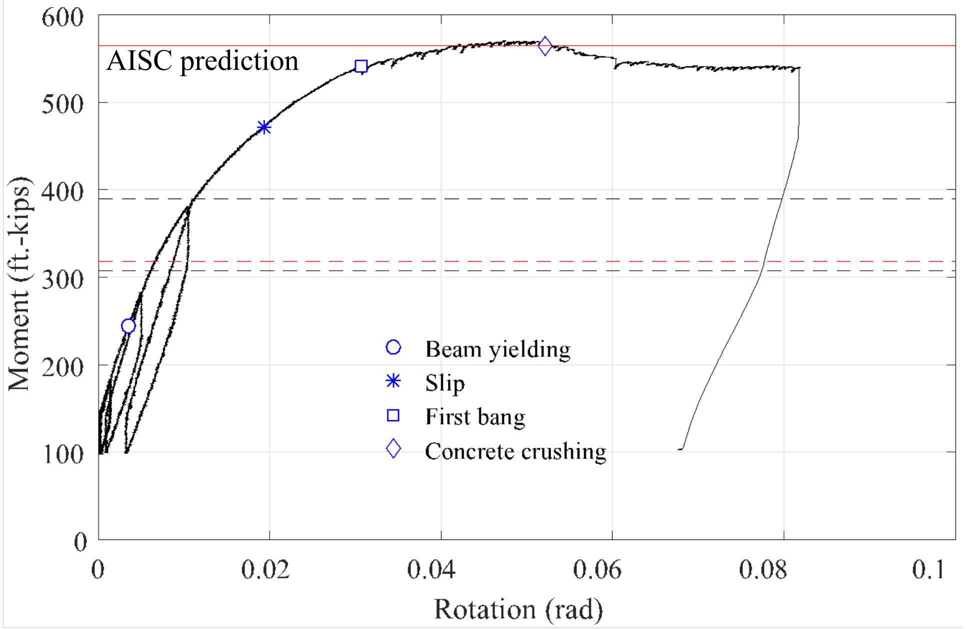

Note: If the beam is strength-controlled and efficiently designed, the two black dashed lines illustrate the range of the full service loading, and the red dashed line indicates the full service loading when the dead load is 92.5 psf, as is used in the prototype structrues in Chapter 3.The red solid line indicates the strength predicted by the AISC design equations.

Figure 5.21 Center section moment vs beam end rotation curve for Specimen 1-M24-2C-RH

The actuator force variation is plotted in Figure 5.22. During the elastic cycles, due to the asymmetry of the beam, the forces in the two actuators were not identical, and the load of the east actuator was always larger than that of the west actuator, showing that the east half of the beam was stiffer than the west half. The difference was within 3 kips when the load target for both actuators was about 20.5 kips. When the west actuator force surpassed that of the east actuator, both actuator forces experienced sudden force changes. This coincided with the bang heard during the test, and slip of the east side clamps was also demonstrated in the slip measurements. The behavior of the actuators indicates that slip of the clamps probably reduced the stiffness of the east half of the beam. As a result of the larger applied load after the slip on the east side, major concrete crushing first happened at the west side of the beam, which altered the relative stiffness of the two halves of the beam again. In the inelastic range, the load applied to the west side of the beam was generally greater than that exerted on the east side, and more severe concrete crushing was also seen at the west side.

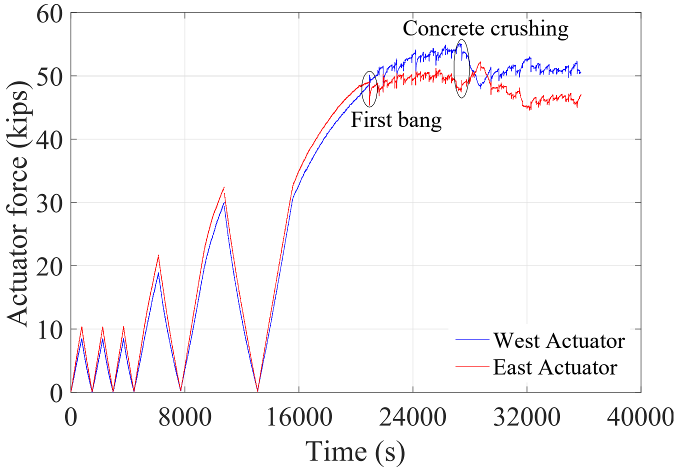

Figure 5.22 Actuator force variation in Specimen 1-M24-2C-RH

At a deflection of 4.5 in., tilting of the concrete slab became visible, possibly due to the uneven stiffness of the concrete slab at the north side and south side, as shown in Figure 5.23a. When the beam deflected about 5.25 in., a bang was heard and abrupt changes were seen in the slip measurements of the clamps at the east side of the beam. Subsequently, loud bangs were heard as the beam deflected, signifying slipping of more clamps. Figure 5.23b illustrates the composite beam at a deflection of 9.0 in. As shown in Figure 5.23c, major concrete crushing occurred along the top edges of the concrete planks at the inner loading point sections at a deflection of 9.0 in., and the crushing was more severe at the west side than at the east side. Minor and localized concrete crushing was also found between planks 10 and 11. When the deflection of the beam approached 12.0 in., the in-plane rotation of the beam was measured at the outer bearing plates that support the spreader beams, with the rotational angles being 4.64 and 4.86 degrees at the west side and east side, respectively. As the beam deflected, only the vertical components of the actuator loads contributed to the flexure of the beam, but as a result of the small rotation, the total actuator forces were used for bending moment calculation.

Longitudinal cracks parallel to the steel beam were too narrow to discern during the test, even at the peak strength of the beam, but hairline cracks were found after inspecting the planks closely after the test. During the test, the strains of the longitudinal reinforcement embedded inside the concrete planks (i.e., reinforcement running in the long direction of the planks and thus perpendicular to the longitudinal axis of the beam) also indicated concrete cracking along the length of the beam. Transverse cracking (i.e., cracks transverse to the longitudinal axis of the beam, running in the long direction of the planks) was not seen throughout the test. Since the deconstructable composite beams are composed of concrete planks that are connected using threaded rods, the gaps between the planks are the weakest "link" in the system. When the concrete slab is under tension along its bottom edge, the gaps open and thus transverse cracking is not expected.

When the beam center deflected approximately 13.6 in., the actuators were accidentally shut off due to some control issues, and the unloading of the specimen was thus completed in a very short period of time. Since the deflection of the beam was excessive, the specimen was not reloaded, and the test was thus terminated. Even though tilting of the concrete planks appeared to be significant, the lateral braces were not engaged during the test.

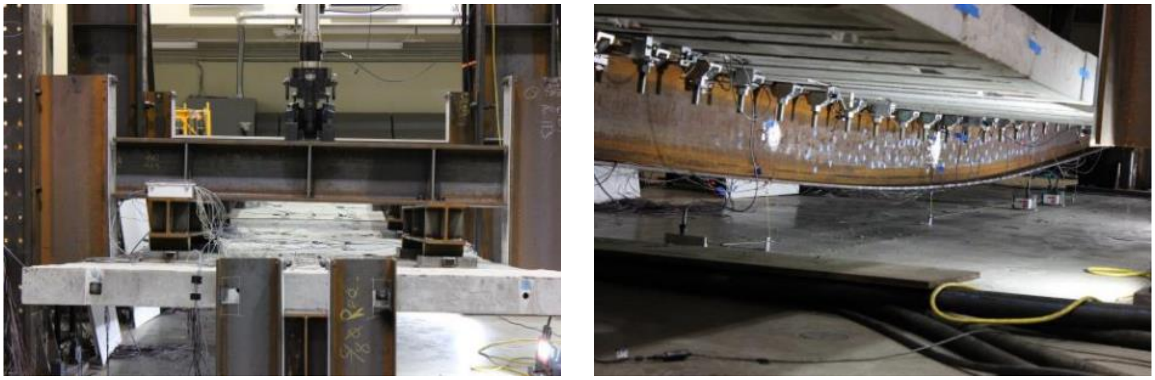

a) Tilting of concrete slab at 4.5 in. deflection b) Deflected steel beam at 9.0 in. deflection

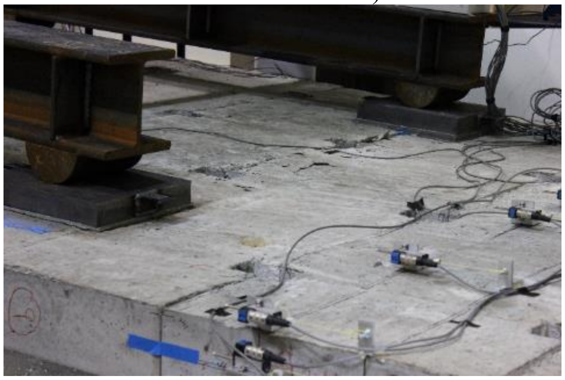

c) Concrete crushing at the west inner loading point at 9.0 in. deflection

Figure 5.23 Observations in Specimen 1-M24-2C-RH

5.6.2.2 *Specimen 2-M24-1C-RL*

The load-deflection curve of composite beam specimen 2-M24-1C-RL is shown in Figure 5.24. Before applying any actuator load, the beam deflected about 0.48 in. under its self-weight after removing the wood supports used for shoring the beam during construction. This is equivalent to a bending moment of 97.5 ft.-kips at the center section of the beam. The initial stiffness of the beam is estimated as: 25/0.48 = 52.1 kips/in. As an alternative, the behavior of the specimen is demonstrated by the relationship illustrated in Figure 5.25 between the center section moment and calculated beam end rotation that is taken as the average of the rotations at both ends of the beam. The initial stiffness of the moment-rotation curve is smaller than those of the reloading curves of the 60% cycle and 80% cycle. The range of load and moment that correspond to full service loading is indicated in the load-deflection curve and moment-rotation curve.

During the first three elastic cycles (i.e., 40% of the expected flexural strength), the beam settled. After the first cycle, a residual displacement of 0.162 in. was present. A residual displacement of 0.008 in. still existed after the last elastic cycle, which was probably due to the unrecoverable slip of the clamps after removing the loads.

Similar to Beam 1-M24-2C-RH, load oscillation was seen when the clamps slipped, accompanied by noticeable bangs. The loads rebounded and stabilized quickly. Although the slip of the clamps in Test 2-M24-1C-RL was larger than the clamp slip in Test 1-M24-2C-RH, the occurrence of bangs and load oscillation was not as frequent as Test 1-M24-2C-RH. Unlike Beam 1-M24-2C-RH, the strength degradation of Beam 2-M24-1C-RL after severe concrete crushing was insignificant. The concrete crushing and whitewash flaking demonstrated that plastic hinges formed at the inner loading point sections. Localized concrete crushing at these two sections resulted in the decrease of the actuator forces, and the compression in the concrete could be distributed to a wider region. Since the sections had further bending capacity, the actuator forces gradually increased and then plateaued along with increasing beam deflection.

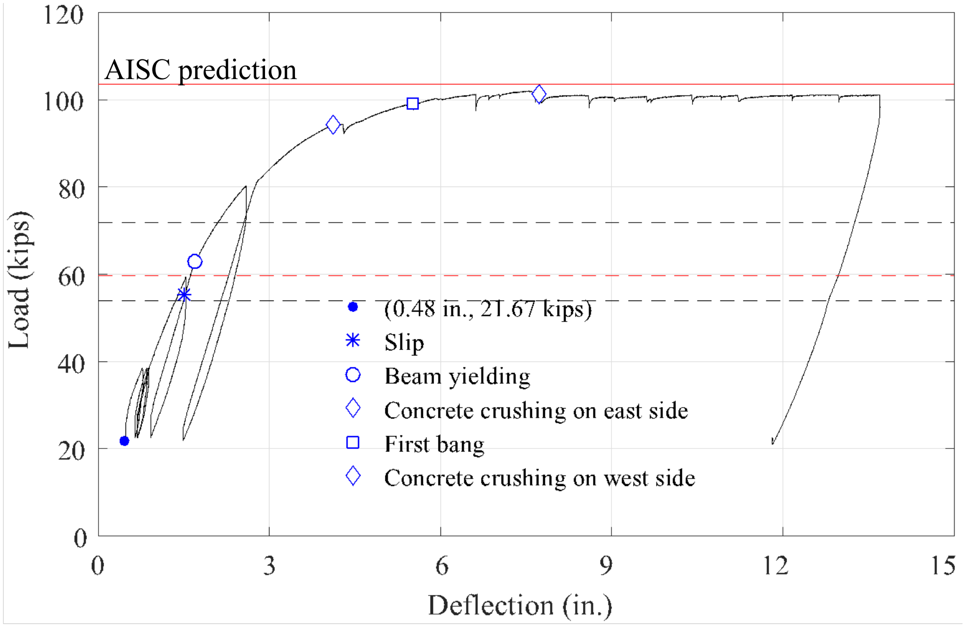

Note: If the beam is strength-controlled and efficiently designed, the two black dashed lines illustrate the range of the full service loading, and the red dashed line indicates the full service loading when the dead load is 92.5 psf, as is used in the prototype structrues in Chapter 3.The red solid line indicates the strength predicted by the AISC design equations.

Figure 5.24 Total load vs beam midspan deflection curve for Specimen 2-M24-1C-RL

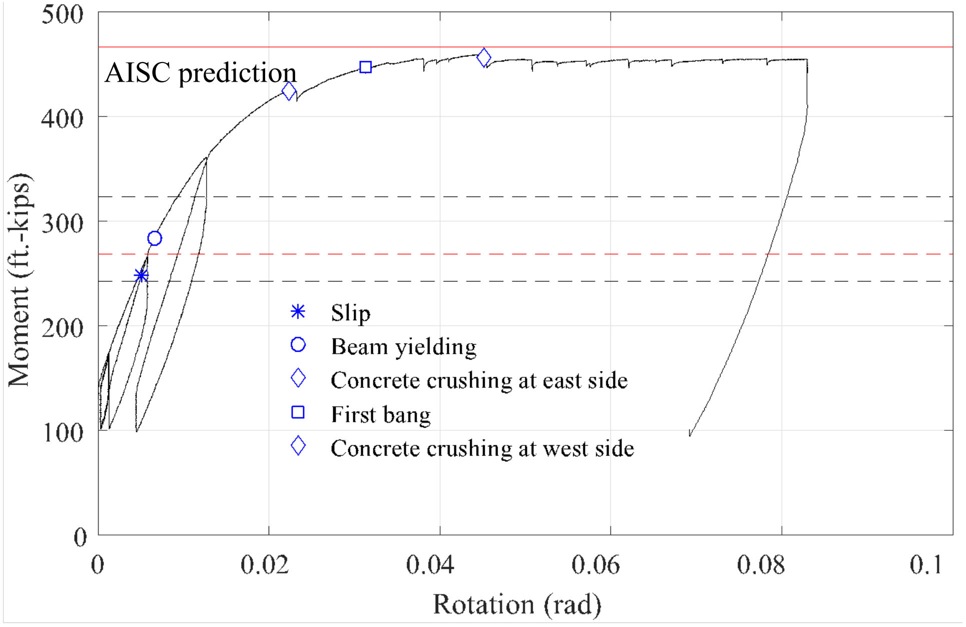

Note: If the beam is strength-controlled and efficiently designed, the two black dashed lines illustrate the range of the full service loading, and the red dashed line indicates the full service loading when the dead load is 92.5 psf, as is used in the prototype structrues in Chapter 3.The red solid line indicates the strength predicted by the AISC design equations.

Figure 5.25 Center section moment vs beam end rotation curve for Specimen 2-M24-1C-RL

Figure 5.26 shows the actuator force variation throughout the test. During the elastic cycles, the actuator loads were very close. At the 80% cycle, the concrete planks started to crush at the east inner loading point section. The crushing was probably accompanied by a stiffness change of the beam, because the west actuator force gradually surpassed the east actuator force. As the beam deflected, significant concrete crushing was first found at the east inner loading point section, causing the force of the east actuator to decrease substantially and the west actuator load to increase. Subsequently, a bang was heard which indicated slip of the clamps, with load oscillation observed in both actuators. The abrupt load changes on the curves represent the several bangs heard during the test. The actuators responded similarly when the concrete crushed at the west inner loading point section.

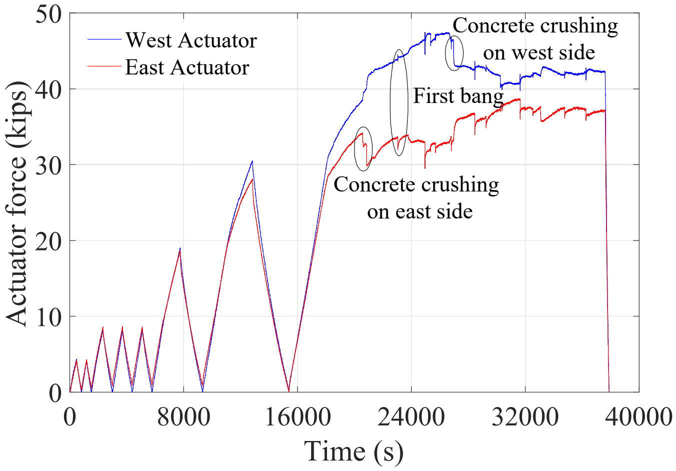

Figure 5.26 Actuator force variation in Specimen 2-M24-1C-RL

Unlike Specimen 1-M24-2C-RH that appears to have flat flanges, the profile of the W14x38 section in this specimen is similar to the lower sketch in Figure 5.5, and the worst tilt of the flanges is about 0.329 in., slightly larger than the tolerance of 5/16 in. (0.3125 in.) for sections deeper than 12 in. (AISC 303-16). For Specimens 3-M20-3C-RL and 4-M20-1C-RL, the tilt of the flanges is documented more comprehensively by measuring the flange tilt at the sections attached with strain gages (see Figure 5.11).

When assembling the structural components, the concrete planks were shored such that they stayed flat during the construction. Therefore, gaps existed before the bolts were tightened. As the bolts were pretensioned, the firmest contact was established in the vicinity of the bolts, and gaps were commonly seen between the steel flange and the sides of the concrete planks, as shown in the sketches in Figure 5.27. After the construction was complete and the wood supports were removed, tilting of the system was imperceptible. However, the planks tilted shortly after the actuator loads were applied and the beam settled. During the first three 40% cycles, tilting of the system was significant enough to engage the southeastern lateral brace to prevent further lateral deformation of the system. When the load was removed, the loading structure still bore against the lateral brace as a result of the settlement of the beam. Contact between the loading structure and the southeastern lateral brace persisted for the remaining of the test. When the beam was loaded to 60% of the predicted ultimate strength, a squeak was heard, and the axial load of rod 2 reduced considerably, which was probably caused by the localized and moderate concrete crushing at the east inner loading point section. No sudden force change was demonstrated by the east actuator. As discussed earlier, the slanted slide surfaces of the planks might lead to localized compressive stress between adjacent concrete planks, and thus the concrete crushing could be premature.

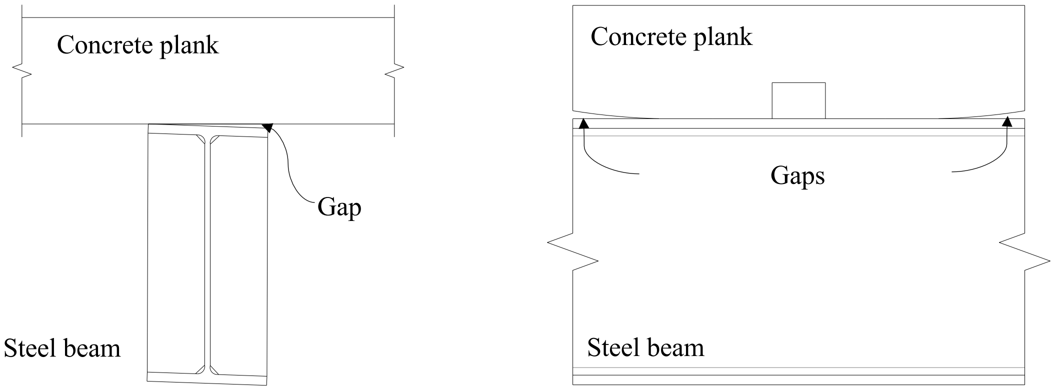

Figure 5.27 Gaps and contact at steel/concrete interface during beam construction

At a center deflection of 3.4 in., significant concrete crushing first occurred at the east inner loading point section, and as a result, the load of the east actuator dropped. At the east side of the beam, the whitewash on the web started to flake off at a deflection of 5.2 in. When the beam deflected to 7.5 in., concrete crushing occurred at the west side of the beam, and the west actuator load consequently decreased. Crushing was also observed between planks 8 and 9 at a deflection of 11.2 in. Longitudinal cracking parallel to the steel beam was discovered during the test. These cracks usually appeared close to the center of the planks that were under direct loading, and they were wider than those observed in Test 1-M24-2C-RH. Major observations from Test 2-M24-1C-RL are shown in Figure 5.28.

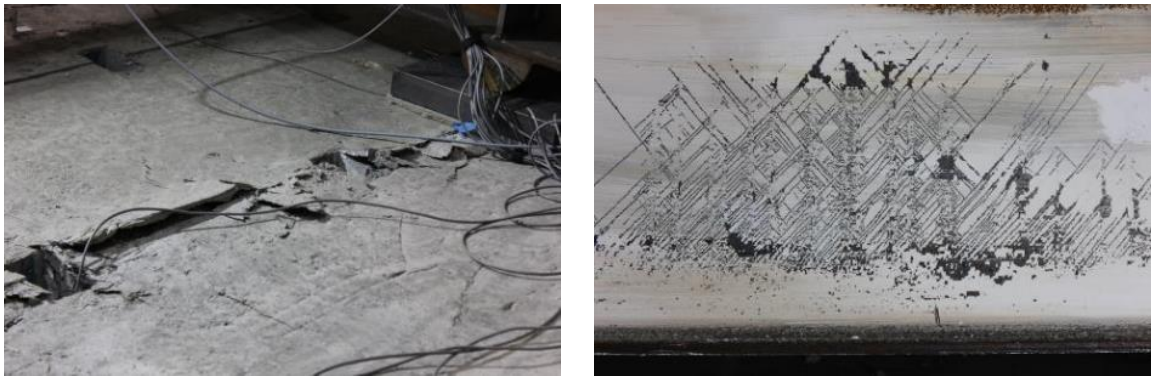

a) Concrete crushing at west inner loading point

b) Whitewash chipping at east inner loading point

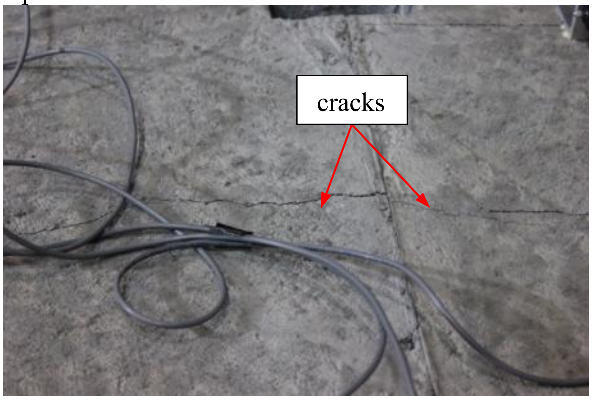

c) Longitudinal cracking in planks 10 and 11

Figure 5.28 Observations in Specimen 2-M24-1C-RL (after terminating the test)

Relative vertical movement was normally seen between a plank under the loading plates and its neighbor plank that was not loaded directly. This phenomenon was not pronounced in Specimen 1-M24-2C-RH, but was also observed in the other two specimens. For such planks, contact was achieved in the middle region, but gaps were usually present at the ends. Hence, the planks deformed together at the center, but individually at the ends. At the inner loading point sections, although both planks were under direct loading, relative vertical movement was still seen, as shown in Figure 5.29. If constructed with tongue-and-groove joints and better quality control, adjacent planks would deform together due to bearing between the tongue and the groove.

Since the lateral brace was involved during the test, the actuator force was required to resist bending of the beam as well as the small amount of friction that may have occurred between the test specimen and the lateral brace, which was faced with Teflon sheeting. The horizontal reaction from the lateral brace can be assumed to be the horizontal component of the actuator force. As shown in Figure 5.30, the angle of the actuator cylinder with respect to the vertical axis is calculated as: $\theta = \Delta_x/L$, where Δ_x is the horizontal movement of the free end of the actuator, and L is the length of the actuator. Because the top spreader beam can move horizontally no more than 1/2 in. before contacting the lateral brace and the shortest length of the actuator is 72 in., the angle is conservatively calculated as 1/144. If the frictional coefficient between the top spreader beam and the Teflon sheeting is assumed to be 0.15, the friction between the specimen and the lateral brace is less than 1/1000 of the actuator force and considered negligible.

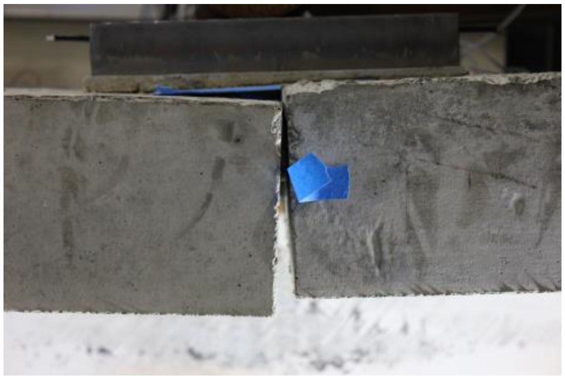

Figure 5.29 Relative deformation between planks at inner loading point section

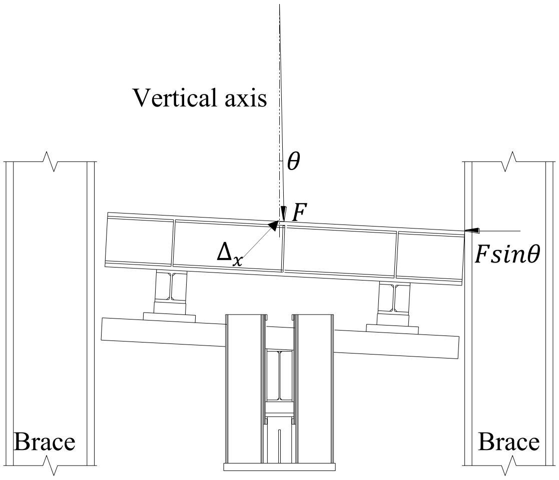

Figure 5.30 Normal force at lateral brace

Right before terminating the test, the actuator rotations resulting from the deflection of the beam and the lateral deformation of the concrete slab (i.e., tilting of the concrete slab) were measured. For the west actuator, the rotations were 1.78 and 0.36 degrees, respectively, and the rotations of the east actuator were 2.60 and 0.34 degrees, respectively. Since these angles were very small, the resultant actuator forces, rather than the vertical force components, were used for bending moment calculation. The testing was terminated at a beam center deflection of 13.7 in.

5.6.2.3 *Specimen 3-M20-3C-RL*

The load-deflection curve of composite beam specimen 3-M20-3C-RL is shown in Figure 5.31. By the time the full stroke of the center string pot, which measures the center deflection of the beam, was reached, the load-deflection curve still ascended slowly. It was thus decided to continue deflecting the beam until the beam almost touched the concrete strong floor or the load plateaued. Although the center deflection was not measured after the string pot was disabled, it may be extrapolated using the displacement measurements from the other sensors, as shown in Appendix F.2.3. Therefore, both the direct vertical deflection measurement from the center string pot and the indirect vertical deflection measurement extrapolated from the other sensors are used in Figure 5.31.

Before applying any actuator load, the beam deflected about 0.79 in. under its self-weight after removing the wood supports used for shoring the beam during construction. This is equivalent to a bending moment of 97.5 ft.-kips at the center section of the beam. The initial stiffness of the beam is estimated as: 25/0.79 = 31.6 kips/in. As an alternative, the behavior of the specimen is demonstrated by the relationship illustrated in Figure 5.32 between the center section moment and calculated beam end rotation that is taken as the average of the rotations at both ends of the beam. The initial stiffness of the moment-rotation curve is smaller than those of the reloading curves of the 60% cycle and 80% cycle. The range of load and moment that correspond to full service loading is indicated in the load-deflection curve and moment-rotation curve.

During the first three elastic cycles (i.e., 40% of the expected flexural strength), the beam settled. After the first cycle, a large residual displacement of 0.264 in. was seen. A residual displacement of 0.037 in. still existed after the last elastic cycle. As the slip of the clamps is tiny, settling of the beam is believed to be the main cause of the permanent deflection. The slope of the reloading curve of the 40% cycle is also smaller than that of the reloading curve of the 60% cycle, implying that the settling of the beam was not accomplished after the three elastic cycles. While the loading in this fully composite beam test never decreased, the ultimate strength of the beam was likely close to the maximum that was achieved in the test, as the load-deflection curve exhibits a plateau region when the beam center deflected 16 in. Unlike the first two tests, load oscillation was not seen while the clamps slipped, which could be due to the very small magnitude of the slips.

Based on the whitewash flaking pattern and concrete crushing locations, it can be inferred that a plastic hinge formed at the center section of the beam. The behavior of the center section influenced the actuator responses. After concrete crushing occurred, the compressive force in the center concrete plank redistributed and the location of the resultant force in the concrete might descend. The strain measurements on the steel section indicate that the strains continuously increased throughout the test. In addition, comparing the maximum strain measurements at the bottom flange of the center steel section (~31770 με) to the strain at the initiation of strain hardening obtained from tensile coupon testing results (~22767 με), it is seen that the bottom flange material has deformed into the strain hardening region. Hence, the load-deflection curve shows that the ultimate flexural strength of the beam did not decrease, although the resultant compression in the center concrete plank descended due to concrete crushing.

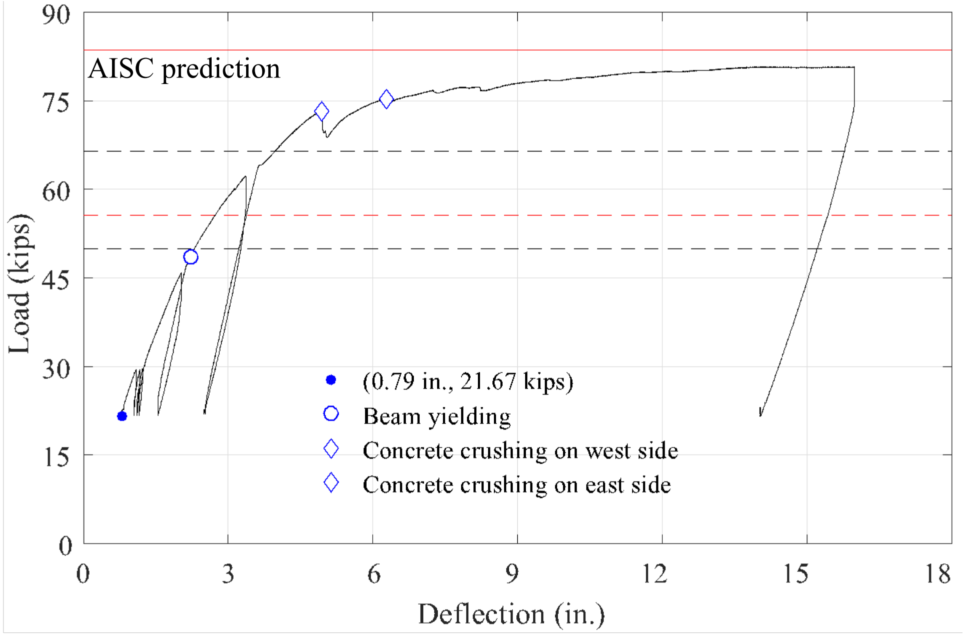

Note: If the beam is strength-controlled and efficiently designed, the two black dashed lines illustrate the range of the full service loading, and the red dashed line indicates the full service loading when the dead load is 92.5 psf, as is used in the prototype structrues in Chapter 3.The red solid line indicates the strength predicted by the AISC design equations.

Figure 5.31 Total load vs beam midspan deflection curve for Specimen 3-M20-3C-RL

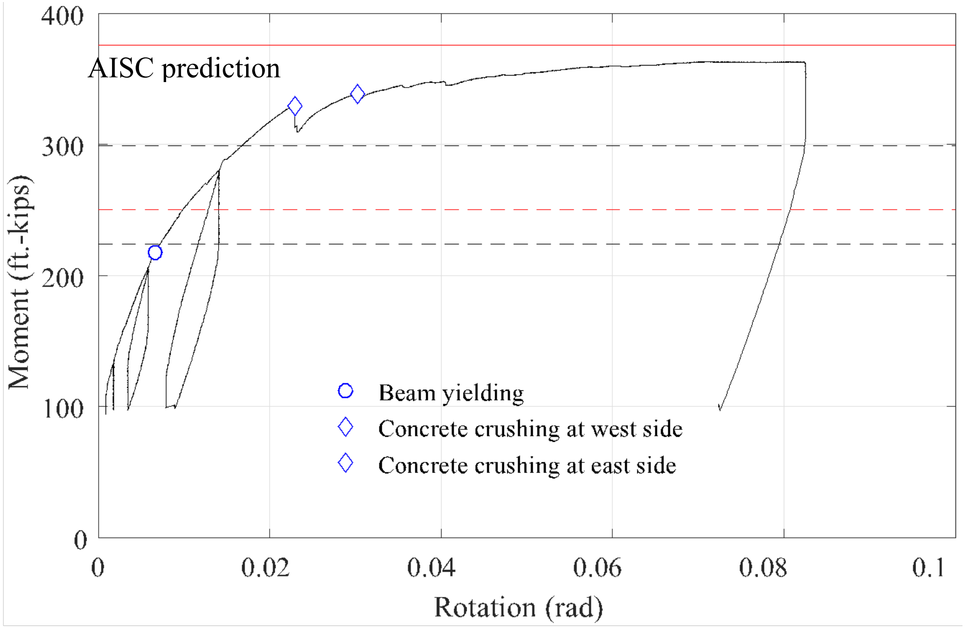

Note: If the beam is strength-controlled and efficiently designed, the two black dashed lines illustrate the range of the full service loading, and the red dashed line indicates the full service loading when the dead load is 92.5 psf, as is used in the prototype structrues in Chapter 3.The red solid line indicates the strength predicted by the AISC design equations.

Figure 5.32 Center section moment vs beam end rotation curve for Specimen 3-M20-3C-RL

The variation of the actuator forces is illustrated in Figure 5.33. During the elastic cycles, the load of the west actuator was about 40% larger than that of the east actuator, indicating that the west half of the beam was much stiffer than the east half. When the beam was loaded to 80% of its estimated flexural strength, minor concrete crushing occurred between planks 7 and 8. Consequently, the west actuator load dropped slightly. Major concrete crushing first occurred between planks 8 and 9, and as a result, the load in the east actuator decreased, while the west actuator load increased. The actuators responded in a similar manner when major concrete crushing was seen between planks 7 and 8, with the loading of the west actuator increasing and the loading of the east actuator decreasing. At the end of the test, the loads in both actuators were very close.

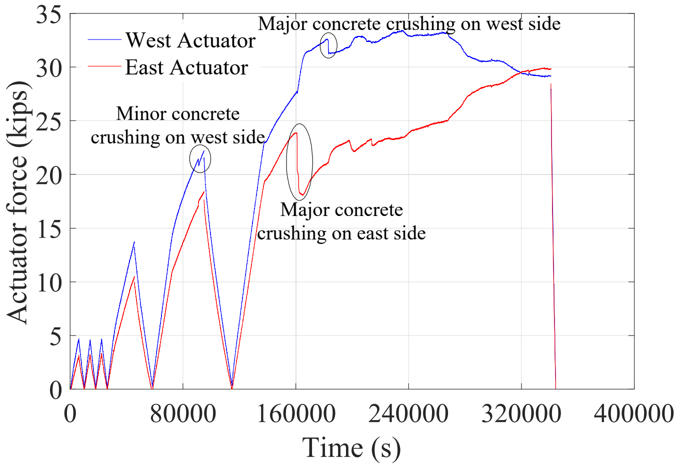

Figure 5.33 Actuator force variation in Specimen 3-M20-3C-RL

After the bare steel section was placed on the roller and pin supports, the tilt of the flanges was measured at the sections attached with strain gages (see Figure 5.11) and shown in Table 5.8. It is seen that the worst tilt of the flanges is about 0.188 in., smaller than the tolerance of 5/16 in. (0.3125 in.) for sections deeper than 12 in. (AISC 303-16).

Table 5.8 Tilt of Specimen 3-M20-3C-RL flanges

Section	$T\ (in.)$	$T'\ (in.)$	$T+T'\ (in.)$
1	0.075	0.034	0.109
2	0.060	0.048	0.108
3	0.070	0.034	0.104
4	0.102	0.068	0.188
5	0.088	0.037	0.125

As will be discussed in Section 5.6.5, according to the bolt axial strain measurements, some M20 bolts remained elastic after rotating the nut one and a half turns, which is the required nut rotation for yielding the M20 bolts after a snug-tight condition. The abnormal behavior of these M20 bolts can be correlated to the observations during bolt pretensioning.

Assuming that a plank has a shape similar to the sketch shown in Figure 5.27, firm contact can be readily achieved between the plank and the steel beam after pretensioning the middle pair of bolts. The consequences of installing the other two pairs of bolts depend on the flexural stiffness of the steel flanges. For example, provided that the steel flanges are very stiff, no bending deformation is generated, and bolt yielding happens. If the steel flanges are flexible, the flanges deform until they bear against the concrete plank, as is the case for this specimen. In addition, the lips of the cast-in channels were supposed to be flush with the bottom surfaces of the concrete planks. However, all of the planks used in this test came from the same pour, and they shared the same issue that the concrete bottom surfaces were 1~2 mm higher than the channel lips. Hence, the steel flanges were also bent to contact the channel lips. It is noted that the planks tested in the first two experiments did not have the same problem.

As illustrated in Figure 5.34, if the channel lips are flush with the bottom surface of the concrete plank, the length of the unbraced steel flange segment equals to the gap between the lips, l_{ub}. The unbraced length increases to the width of the channel, L_{ub} , when the channel lips are not flush with the bottom surface of the concrete plank. To minimize the deformation of steel flanges under the compression transferred from the clamp teeth, further investigation is needed to ascertain the behavior of flanges of different thickness used with different channel and clamp sizes.

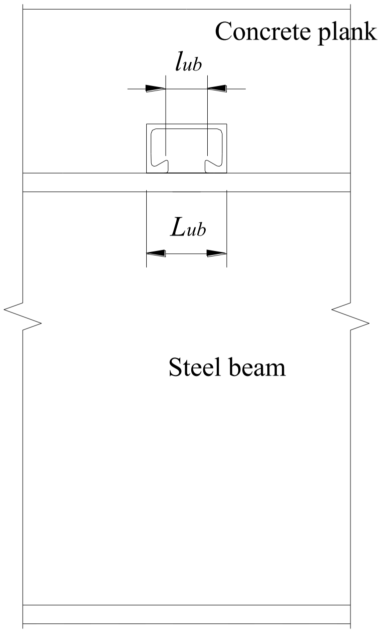

Figure 5.34 Unsupported steel flange in different scenarios

After snug-tightening the bolts, the gaps between the planks and the steel flanges may not vanish, and the steel flanges may not bear against the channel lips. When a hydraulic wrench was utilized to rotate the nut one and a half turns, the bolts were further stretched only after closing the gaps and bending the flanges. As shown in Figure 5.35, bending of the steel beam flanges was observed after the bolt was pretensioned. Therefore, the actual elongations of the bolt shanks were less than that intended, and the bolts could still be elastic.

RCSC Specification (2014) defines snug tight as “the condition that exists when all of the plies in a connection have been pulled into firm contact by the bolts in the joint and all of the bolts in the joint have been tightened sufficiently to prevent the removal of the nuts without the use of a wrench”. In this test, since the contact between the steel flanges and channel lips and between the steel flanges and concrete planks might not be firm, the connections were in fact not in a snug-tightened condition after applying the full effort of a worker on an ordinary spud wrench. In practice, it is advised that the channel lips be flush with the concrete surfaces to avoid bending of the steel flanges. For a composite beam utilizing three channel planks, if wide gaps are present between the plank and the beam after pretensioning the first pair of bolts, the installation of the other bolts could be affected by the gaps.

Based on the discussion in Section 5.6.5, since the tension in some bolts may not meet the minimum bolt pretension requirements in Table J3.1M in AISC 360-16, the actual percentage of composite action of the beam could be less than the ratio presented in Table 5.1. However, the specimen could still behave as a fully composite beam, since the specimen was designed with a percentage of composite action much larger than 100%. This is further validated by the tiny slip of the clamps. As a result, the available flexural strength of the beam could still be governed by the tensile strength of the steel section, rather than the shear strength of the clamps. This is substantiated by the comparison between the tested beam strength and the predicted beam strength shown in Table 5.12.

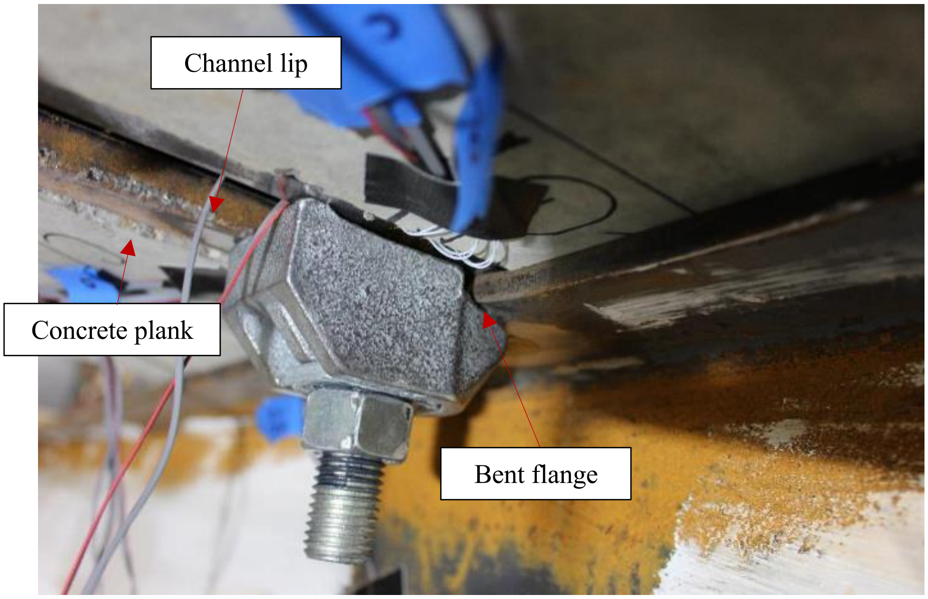

Figure 5.35 Bending of steel flange after bolt pretension

When the beam midspan deflection was around 1.8 in., minor concrete spalling occurred on the top surface of plank 8, and the southwestern brace was engaged because of tilting of the concrete slab. As the beam was loaded to 80% of its predicted flexural strength, the involvement of the southeastern brace prevented further lateral movement of the slab. At a beam center deflection of 3.2 in., moderate concrete crushing was found between planks 7 and 8. Severe concrete crushing was seen between planks 8 and 9 at 4.9 in.

center deflection, and the west actuator force experienced two consecutive drops. When the beam center deflected 5.9 in., the whitewash on the web of the center section started to chip off. At a beam center deflection of 11.5 in., minor concrete crushing was also found between planks 5 and 6 and between planks 6 and 7. In the first two tests, slip of the clamps was usually accompanied by loud noises; however, such noises were not heard in this test. Concrete crushing at the center section is shown in Figure 5.36.

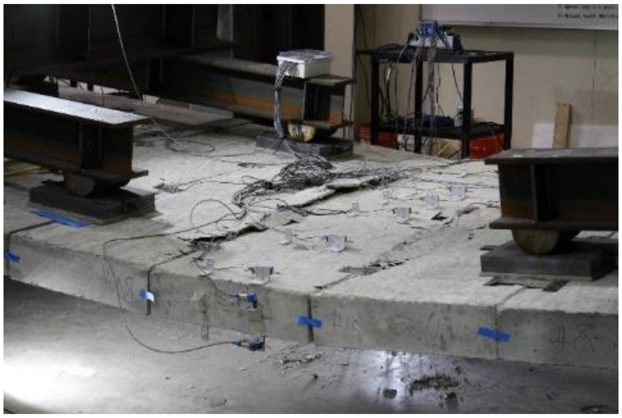

Figure 5.36 Concrete crushing at center section of Specimen 3-M20-3C-RL (after terminating the test)

Right before terminating the test at a beam center deflection of 16.0 in., the actuator rotations resulting from the deflection of the beam and the lateral deformation of the concrete slab were measured. For the west actuator, the rotations were 2.22 and 0.20 degrees, respectively, and the rotations of the east actuator were 3.16 and 0.40 degrees, respectively. Because of the small angles, the total actuator forces were used for moment calculation.

5.6.2.4 *Specimen 4-M20-1C-RL*

The load-deflection curve of composite beam specimen 4-M20-1C-RL is shown in Figure 5.37. After removing the wood supports used for shoring the beam during construction, the beam deflects about 0.89 in. under its self-weight. This is equivalent to a bending moment of 97.5 ft.-kips at the center section of the beam. The initial stiffness of the beam is estimated as: 25/0.89 = 28.1 kips/in. As an alternative, the behavior of the specimen is demonstrated by the relationship illustrated in Figure 5.38 between the center section moment and calculated beam end rotation that is taken as the average of the rotations at both ends of the beam. The initial stiffness of the moment-rotation curve is smaller than those of the reloading curves of the 60% cycle and 80% cycle. The range of load and moment that correspond to full service loading is indicated in the load-deflection curve and moment-rotation curve.

Similar to the other beams, settling of the beam is the main cause of the permanent displacement after the first 40% cycle. For the other 40% cycles, the residual deflection could result from the settling of the beam as well as the unrecoverable slip of the clamps after unloading the specimen.

During the test, bangs were heard which were accompanied with load oscillation and sudden changes in the slip measurements. Because the slip was tiny, bangs were not heard in Test 3-M20-3C-R. Since the M20 clamps were tested in this specimen, the size of the clamps and the pretension of the bolts are smaller than the M24 clamps and bolts, and the noises were thus not as loud as those heard in Tests 1-M24-2C-RH and 2-M24-1C-RL which utilize M24 clamps.

According to the flaking of the whitewash on the beam, the first plastic hinge formed at the east inner loading point section. The plastic hinge at the west inner loading point section formed earlier than that at the center section. Ultimately, among the three sections, the most significant plastification occurred at the east plastic hinge, while the west plastic hinge had the least significant plastification. As a result of the severe plastification, the stiffness of the east inner loading point section was greatly reduced, and the east actuator force was much smaller than the west actuator force. Figure 5.39 illustrates the actuator force variation throughout the test.

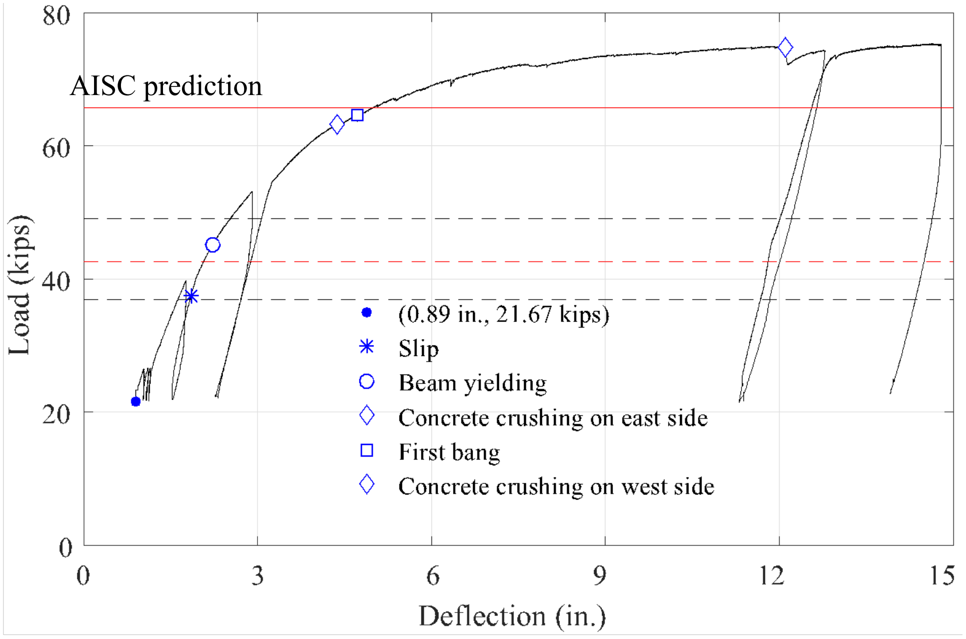

Note: If the beam is strength-controlled and efficiently designed, the two black dashed lines illustrate the range of the full service loading, and the red dashed line indicates the full service loading when the dead load is 92.5 psf, as is used in the prototype structrues in Chapter 3.The red solid line indicates the strength predicted by the AISC design equations.

Figure 5.37 Total load vs beam midspan deflection curve for Specimen 4-M20-1C-RL

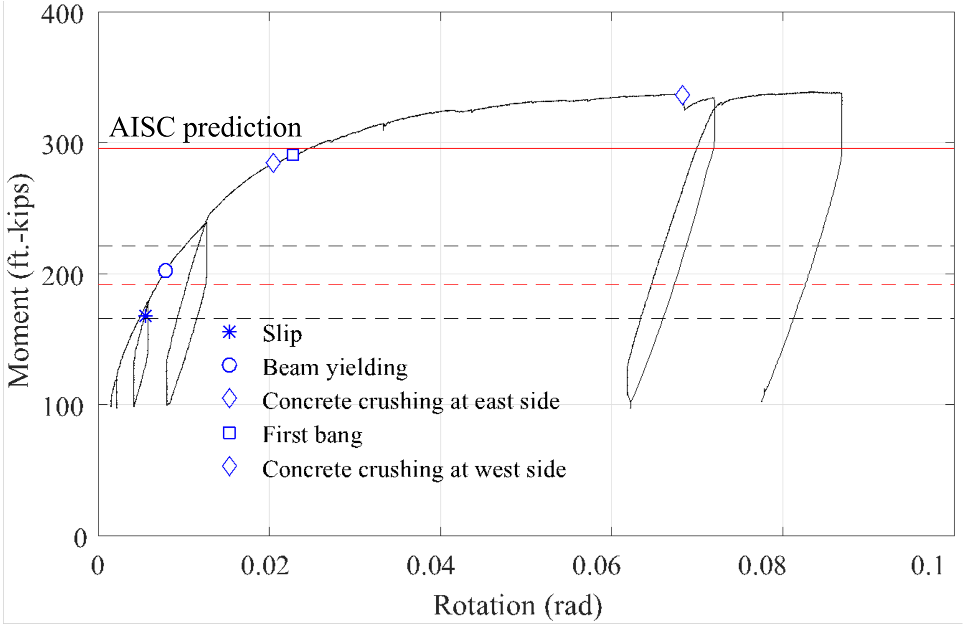

Note: If the beam is strength-controlled and efficiently designed, the two black dashed lines illustrate the range of the full service loading, and the red dashed line indicates the full service loading when the dead load is 92.5 psf, as is used in the prototype structrues in Chapter 3.The red solid line indicates the strength predicted by the AISC design equations.

Figure 5.38 Center section moment vs beam end rotation curve for Specimen 4-M20-1C-RL

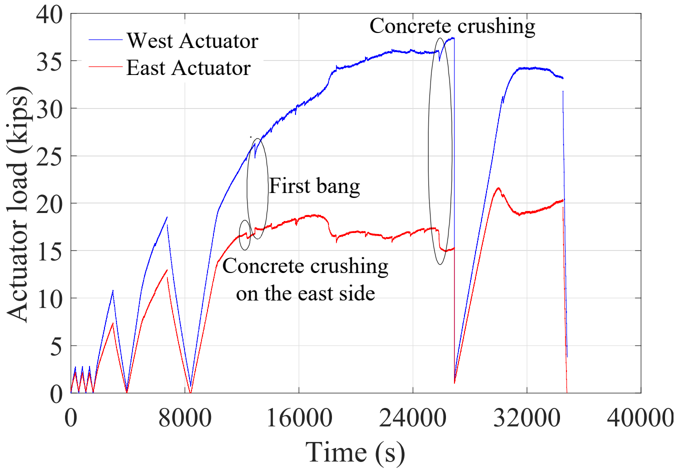

Figure 5.39 Actuator force variation in Specimen 4-M20-1C-RL

Beam 4-M20-1C-RL consists of 15 concrete planks, with 5 planks cast in each of the three pours. The 5 planks cast in the third pour shared the same issue with the planks tested in Specimen 3-M20-3C-RL in that the bottom surfaces of the concrete planks were not flush with the channel lips. Therefore, the bolts that connected these 5 planks with the steel beam could be insufficiently elongated and remained elastic. This speculation is proved by the measured bolt axial strains that were below or barely above the yield strain of the bolt material. However, as shown in Table 5.12, the tested strength of this beam is greater than the predicted strength, indicating that the behavior of the beam may not have been affected by the bolts with inadequate pretension.

Similar to Specimen 3-M20-3C-RL, the tilt of the flanges was measured at the gaged sections and shown in Table 5.9 after the bare steel section was placed on the roller and pin supports. It is seen that the worst tilt of the flanges is about 0.413 in., much larger than the tolerance of 5/16 in. (0.3125 in.) for sections deeper than 12 in. (AISC 303-16).

Table 5.9 Tilt of Specimen 4-M20-1C-RL flanges

Section	$T\ (in.)$	$T'\ (in.)$	$T + T'\ (in.)$
1	0.090	0.062	0.152
2	0.015	0.235	0.250
3	0.146	0.165	0.311
4	0.178	0.156	0.334
5	0.188	0.225	0.413

The west end of the beam started to engage the end steel guides during the loading of the 60% cycle. Tilting of the specimen caused the concrete planks to contact the southwest brace in the 80% cycle. When the beam center deflected 3.8 in., concrete crushing occurred between planks 10 and 11 and between planks 11 and 12. A load bang was heard from the west side of the beam at a beam center defection of 4.4 in., and as a result, sudden changes were seen in the slip measurements. As a response, the west actuator force decreased, whereas the east actuator force increased. Later in the test, several bangs were heard, indicating slips of the clamps. At a center deflection of 4.9 in., the whitewash on the north side of the beam web began to chip off. More severe concrete crushing happened when the beam deflected 5.4 in. and 6.2 in. Both actuator forces decreased at a beam deflection of 12.1 in., which may imply the occurrence of concrete crushing, but the crushing was unnoticeable. Flaking of the whitewash was more severe on the north side than the south side of the beam. When the beam deflected 12.8 in., the actuators were accidently shut off. After restarting the actuators, the beam was further deflected until it almost touched the concrete strong floor.

The actuator rotations resulting from the deflection of the beam and the lateral deformation of the concrete slab were measured before the test was terminated at a beam center deflection of 14.8 in. For the west actuator, the rotations were 1.94 and 0.32 degrees, respectively, and the rotations of the east actuator were 2.88 and 0.26 degrees, respectively. As with the other specimens, the bending moment calculation still used the total actuator forces due to the small angles.

The strength of the concrete planks in specimen 4-M20-1C-RL ranged from 6480 psi to 7030 psi, but the specimen was not purposely designed to trigger failure at specific locations, and the plastic hinges still formed at the inner loading points, similar to the other specimens. In testing, a composite beam with varied concrete strengths may fail at the section where the concrete strength is the lowest, rather than at the maximum moment location. In design, use of concrete planks with different strengths may require that the available strength be compared to the required strength at all sections and that the former envelope the latter along the whole length of the beam. Further investigation may be warranted to explore the behavior and design of composite beams with varied concrete strengths.

After the tests, the composite beams were deconstructed by loosening the bolts, clamps, and rods. A typical deconstructed steel beam is shown in Figure 5.40. Impressions resulting from the normal force at the clamp teeth were seen on the beam flanges. In Beam 4-M20-1C-RL, the rotation of the clamps was not negligible, while the clamps in the other beams rotated slightly, which validates the observation from the pushout tests that the M20 clamps are more prone to rotate than the M24 clamps, and that clamps of adequate sizes should be used in this structural system to ensure little or no rotation at extreme loads. The steel flanges were bent where the planks from the third concrete pour were attached. Cracks in the vicinity of the bolts were found at the bottom surfaces of some planks. This cracking pattern is the same as that observed in the pushout tests, and the initiation of these cracks is discussed in Section 4.5.5 in Chapter 4.

In conventional composite beams utilizing shear studs, despite the support from the composite slabs, top steel flange local buckling was reported in prior research (Toprac 1965; Grant 1973), as shown in Figure 5.41. However, due to sufficient bracing of the clamps, this limit state was suppressed in all of the deconstructable composite beam specimens.

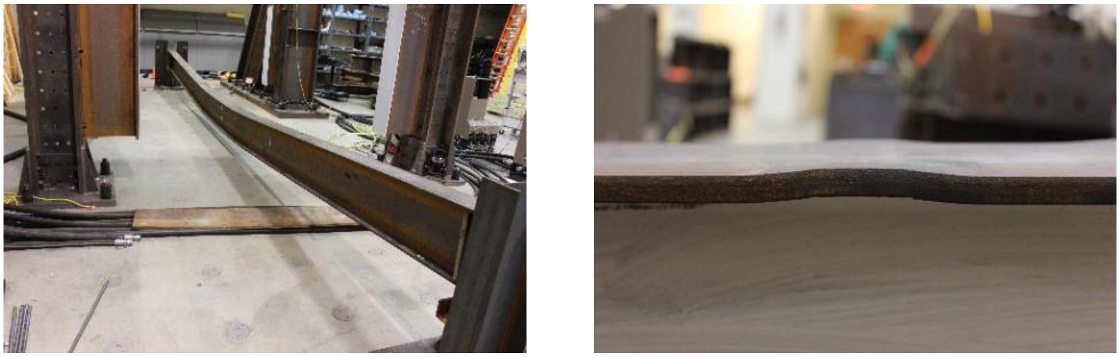

Deconstructed steel beam 1-M24-2C-RH Bent steel flange in beam 3-M20-3C-RL

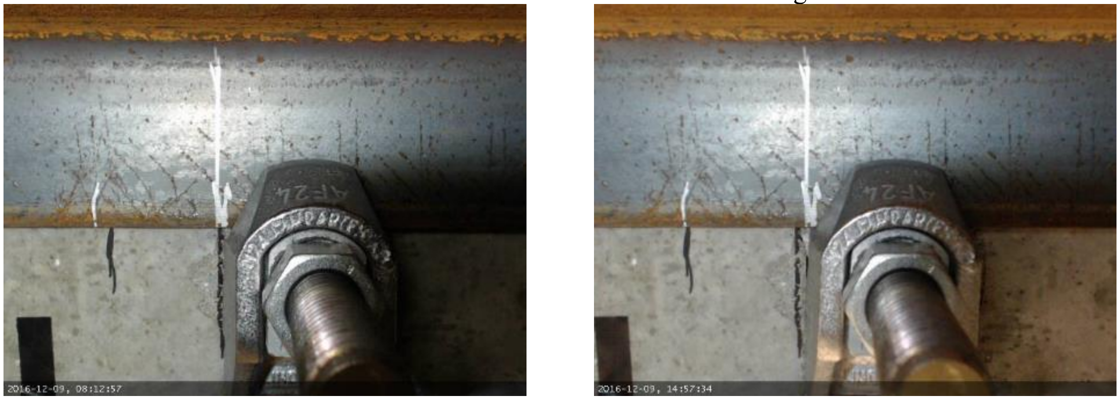
2016-12-09, 08:12:57
2016-12-09, 14:57:34

Before test After test

Rotation of northwestern clamp in beam 2-M24-1C-RL

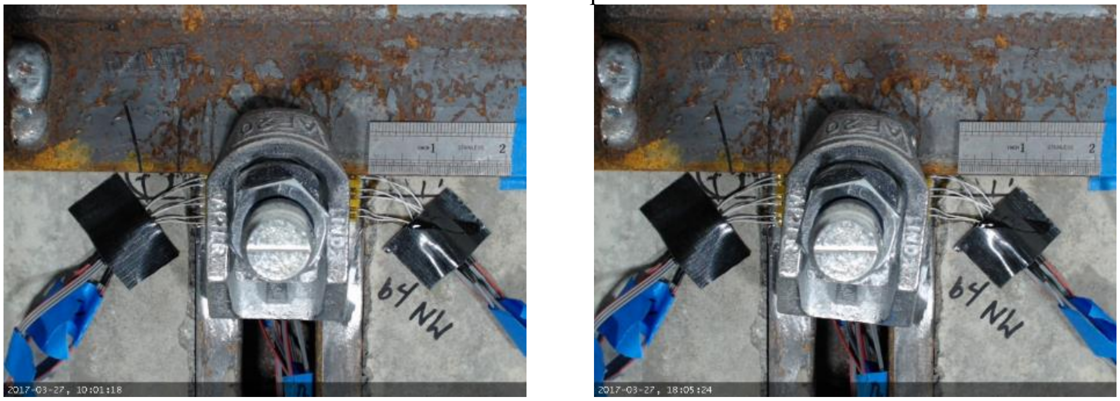
2017-03-27, 10:01:18
2017-03-27, 18:05:24

Before test After test

Rotation of northwestern clamp in beam 4-M20-1C-RL

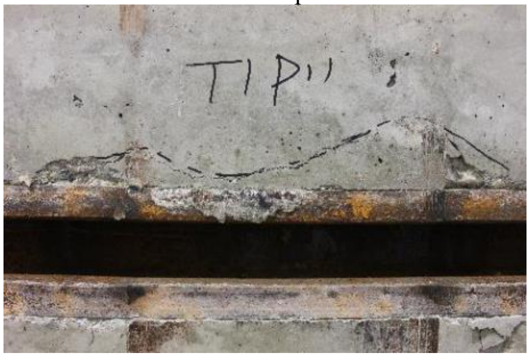

Cracking at the bottom surface of plank 11 in beam 1-M24-2C-RH

Figure 5.40 Observations after deconstructing composite beams

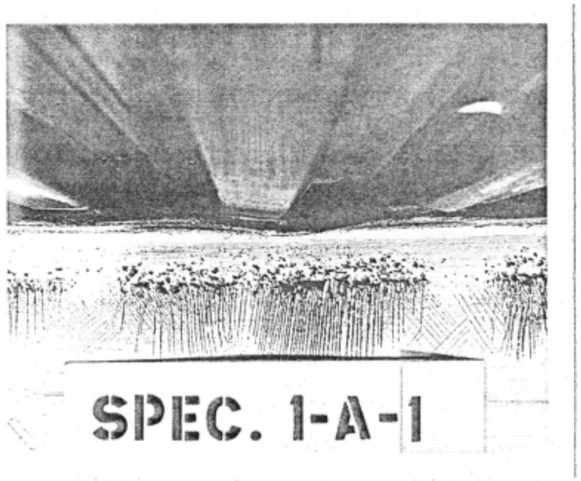

Figure 5.41 Top flange local buckling in conventional composite beams [after (Grant 1973)]

Table 5.10 summarizes the key results of the four composite beam tests. In this table, the ultimate strength is the summation of the applied actuator loads and the self-weight of the specimen. The maximum deflection also accounts for the deflection resulting from the self-weight of the specimen. The elastic stiffness is defined as the tangential stiffness of two curves: the reloading curve of the 60% cycle and the reloading curve of the 80% cycle. The two curves are illustrated in Figure 5.42 using Test 2-M24-1C-RL as an example. Prior to reaching 60% of the predicted beam flexural strength, yielding of the beam or slip of the clamps may have occurred (Grant 1973; Rambo-Rodenberry 2002), whereas the behavior of the beam is elastic when it is unloaded or reloaded along the two curves.

The stiffness comparison between the first two specimens indicates that the degree of shear connection affects the stiffness of the beams, but the other two specimens, which are designed with significantly different levels of composite action, have similar stiffness. Hence, further investigation is needed to determine the relationship between the degree of shear connection and the stiffness of the deconstructable beams. The stiffness in Table 5.10 shows the stiffness of the tested composite beam specimens. Nonetheless, composite beams in structures are often framed into girders or columns. Leon (1990) showed that the rigidity of the end connections significantly affected the deflection of a composite beam, as illustrated in Figure 5.43.

It should be emphasized that the degree of shear connection and the degree of interaction are not interchangeable. The degree of shear connection indicates whether the shear connectors control the design of a composite beam, while the degree of interaction depends on the stiffness of the shear connectors. However, these two terms are directly related, as more shear connectors decrease the maximum slip and increase the degree of interaction of the beam.

According to the load-deflection curves and moment-rotation curves shown in Section 5.6.2.1 through Section 5.6.2.4, the behavior of the beams is nonlinear at full service loading which approximately corresponds to 56% ~75% of the ultimate strengths of the beams. In reality, when a beam experiences the maximum loading (for example, 60% of the ultimate strength) during its service life, yielding of the steel beam and slip of the clamps may occur, both of which are indications of nonlinear behavior. However, when the maximum loading is removed, the beam is unloaded elastically, and during the loading/unloading cycles in the future, the behavior of the beam always follows the elastic loading/unloading curve until the maximum bending moment the beam saw in the past is exceeded. Similarly, due to yielding of the steel beam and slip of the clamps, the beam deflection may be large when the beam experiences the maximum loading during its service life. In the future, if the maximum loading is not exceeded, due to its elastic behavior during loading/unloading, the deflection of the beam is approximately determined as the external loading divided by the elastic stiffness of the beam.

To investigate this behavior further, in this work we assume the specimens are secondary beams in a structure, which are spaced at a distance of 10 ft., subjected to uniform loading and designed using AISC 360-16. If the dead load for all the beam specimens is presumed to be 92.5 psf, which is the same as that used in the prototype structures designed in Chapter 3, the live load the specimens are designed to support is 190.1 psf, 146.1 psf, 130.1 psf, and 78.1 psf, respectively, which are calculated based on the design flexural strengths of the beams (i.e., M_n in Table 5.12). It is normally assumed that secondary beams in structures are subjected to uniform loading. Hence, the design flexural stiffness, which is k_n given in Table 5.12, should be adjusted because the beam specimens are subjected to six-point bending. Based on statics, a beam under uniform loading is 21% stiffer than a beam under six-point bending. Using the adjusted beam stiffness, which are 54.7 kips/in., 43.8 kips/in., 40.5 kips/in., and 29.2 kips/in. for the four specimens, respectively, the live load deflection is determined as 1.04 in., 1.00 in., 0.96 in., and 0.80 in., respectively. All the live load deflections are very close to or less than 1 in. (L/360), which indicates that the design of the beams is strength controlled.

Table 5.10 Composite beam test results

Specimen #	Elastic stiffness (kips/in.)		Peak strength (kips)	Strength at maximum deflection (kips)	Maximum deflection (in.)	Maximum slip (in.)		Limit state
	k_1	k_2				West	East	
1-M24-2C-RH	53.0	52.5	127.0	120.0	13.6	0.234	0.253	CC and ED
2-M24-1C-RL	44.5	44.0	102.3	101.1	13.7	0.322	0.254	CC and ED
3-M20-3C-RL	37.5	36.2	80.8	80.7	16.0	0.018	0.009	CC and ED
4-M20-1C-RL	35.0	34.4	75.4	75.3	14.8	0.346	0.318	CC and ED

Note: CC = Concrete Crushing; ED = Excessive Deflection

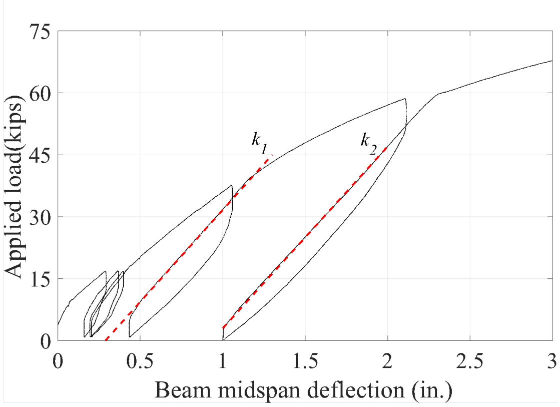

Figure 5.42 Composite beam stiffness definition

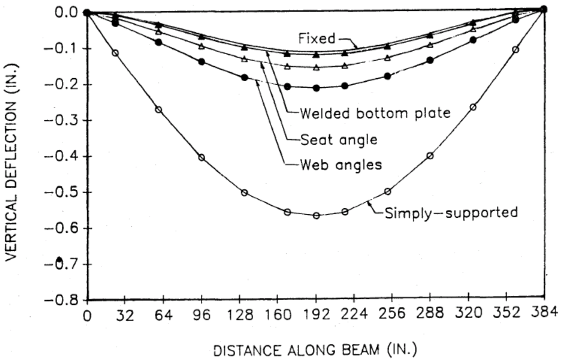

Figure 5.43 Effect of end restraint on beam deflections [after (Leon 1990)]

As shown in Table 5.11, in all the composite beam specimens, the compressive strength of the concrete slab ($0.85f_c'A_c$) is at least 5 times larger than the tensile strength of the steel beam ($F_y A_s$) or the shear strength of the clamps ($\sum Q_n$). The concrete crushing that was seen in the specimens occurred along the top edges of adjacent concrete planks. For conventional composite beams using monolithic concrete slabs, concrete crushing is uncommon if the strength of the concrete slab does not govern the design. Therefore, the discontinuity in the concrete plank system is a main cause of concrete crushing in the deconstructable composite beam specimens. However, at service and design load levels and deflections, concrete crushing was not significant in any of the specimens. Moreover, because of the construction tolerances discussed in Section 5.6.1, the contact between adjacent planks cannot be established through the whole depth and width of the planks. Gaps between the concrete planks prevent continuous flow of compressive forces along the whole width of the concrete slab. In addition, as shown in Figure 5.17, after pretensioning the rods, compressive stresses may concentrate and lead to early concrete crushing during the test. Nonetheless, as demonstrated in Table 5.12 in Section 5.6.2.6, the ultimate flexural strengths of the specimens do not appear to be affected by localized crushing of the concrete planks and gaps between the planks, which may be due to redistribution of the compressive force in the concrete slab and overdesign of the concrete slab.

Table 5.11 Strength comparison between concrete, steel and clamps (units: kips)

Specimen #	Concrete plank ($0.85 f_c' A_c$)	Steel beam ($F_y A_s$)	Clamp ($\sum Q_n$)	($0.85 f_c' A_c$) /smaller of ($F_y A_s, \sum Q_n$)
1-M24-2C-RH	2653	588.5	486.2	5.46
2-M24-1C-RL	3044	588.5	265.2	11.48
3-M20-3C-RL	2488	360.3	496.8	6.91
4-M20-1C-RL	3062	377.7	165.6	18.49

In the test specimens, tongue-and-groove joints were eliminated that could facilitate vertical load transfer between adjacent planks. It may be inferred that if tongue-and-groove joints were cast and the quality of the planks were better controlled, concrete crushing could be deferred in the tests and the discontinuity in the concrete plank system could be minimized, improving the overall performance of the specimens.

5.6.2.5 *Reusability of deconstructable composite beams*

As shown in Sections 5.6.2.1 through 5.6.2.4, prior to their full service loading, slight slip of the clamps occurred in Specimens 2-M24-1C-RL and 4-M20-1C-RL. The inelastic slip at the steel-concrete interface resulted in permanent deflections after the load was removed. However, the steel beams and concrete planks in these two beams remained nearly elastic at their full service loading. In contrast, Specimens 1-M24-2C-RH and 3-M20-3C-RL exhibited slight yielding of the steel beams prior to their full service loading. According to AISC 360-16 (2016), composite beams are not required to remain elastic under service loading. As such, conventional composite beams may yield slightly at service loading. In addition, many composite beams are cambered during fabrication, introducing mild amounts of nonlinearity into the steel beams. It is likely that if these steel beams are reused, they may be restraightened or recambered. The maximum loading applied to a composite beam during its life may also be smaller than the full service loading, and structural members are generally somewhat stronger than their design strengths. For all these reasons, the deconstructed steel beam and concrete planks in the deconstructable composite beam are believed to be reusable with minor or no concern about any possible yielding that, in relatively rare cases, may occur at full service loading.

5.6.2.6 *Strength and stiffness comparison*

The maximum bending moment the composite beam specimens are subjected to can be computed and compared to the available strength obtained using a rigid plastic analysis method, as shown in Equation (C-I3-10) given in the AISC 360-16 commentary (2016). The parameters needed in the strength design equation are illustrated in Figure 5.44. For the composite beam specimen, since the maximum bending moment occurs at one of the two inner loading point sections, the available flexural strength of the beam is predicted using the shear connectors between the inner loading point where the moment is the maximum and the near support. In the calculation, the effective width is assumed to be 90 in., which is a quarter of the beam span. As indicated in Section 5.6.8, the influence of different effective widths on the strength and stiffness calculation of a composite beam is minimal. The elastic stiffness of the test specimen is defined in Figure 5.42, while the stiffness of the specimen can be predicted using either an effective moment of inertia or a lower bound moment of inertia. The calculation of the two types of moment of inertia is detailed in Appendix I. The beam stiffness is computed using a lower bound moment of inertia and assuming four concentrated forces applied at the fifth points of the beam.

Equation (C-I3-10) $$M = C(d_1 + d_2) + P_y(d_3 - d_2) \quad (5.3)$$

where

C = smallest of the yield strength of the steel section, $F_y A_s$, the compressive strength of the concrete slab, $0.85 f_c' A_c$, and the strength of the shear connectors, $\sum Q_n$, kips (N)

P_y = tensile strength of the steel section; $P_y = F_y A_s$, kips (N)

d_1 = distance from the centroid of the compression force, C, in the concrete to the top of the steel section, in. (mm)

d_2 = distance from the centroid of the compression force in the steel section to the top of the steel section, in. (mm). For the case of no compression in the steel section, d_2 = 0.

d_3 = distance from P_y to the top of the steel section, in. (mm)

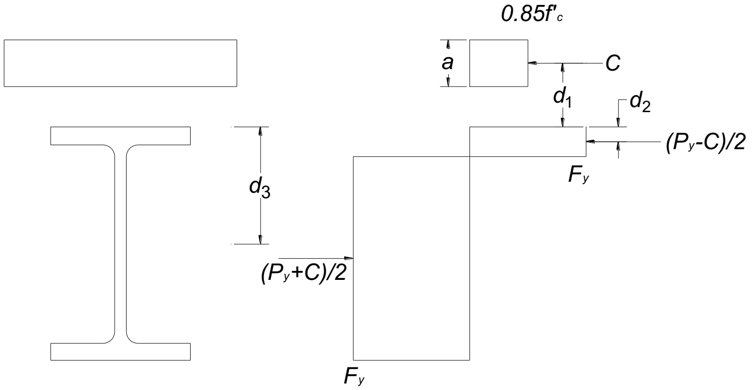

Figure 5.44 Plastic stress distribution for positive moment in composite beams (reproduced from AISC 2016a)

The strength and stiffness comparison is given in Table 5.12. In this table, M_n and k_n are calculated using nominal material properties, and the clamp strengths employ the strengths predicted with Equation (4.27) in Chapter 4. In contrast, M_t and k_t are calculated using tested material properties, and the clamp strengths use the strengths obtained from the pushout tests presented in Chapter 4. The predicted shear strengths of the M24 and M20 clamps are 19.15 kips and 13.25 kips, respectively, while the tested shear strengths of the M24 and M20 clamps are 22.13 kips and 13.83 kips, respectively. It is shown that the strength and stiffness of the beam specimens calculated using nominal material properties are very close to those calculated using tested material properties, indicating that the conservatively predicted clamp strengths do not result in overly conservative estimations of the beam strength and stiffness.

Using the parameters of Beams 2-M24-1C-RL, 3-M20-3C-RL and 4-M20-1C-RL, examples are given in Appendix J to demonstrate the calculation of the predicted ultimate flexural strength and elastic stiffness of these three beams, which represent a partially composite beam with a neutral axis lying in the steel flange, a fully composite beam, and a partially composite beam with a neutral axis lying in the steel web, respectively.

Table 5.12 Composite beam strength and stiffness comparison

Test #	Strength (ft.-kips)					Stiffness (kips/in.)				
	M_e	M_n	M_t	M_e/M_n	M_e/M_t	k_e	k_n	k_t	k_e/k_n	k_e/k_t
1	571	519	565	1.10	1.01	52.8	45.2	49.5	1.17	1.07
2	469	431	466	1.09	1.01	44.3	36.2	38.9	1.22	1.14
3	364	399	376	0.91	0.97	36.9	33.5	34.8	1.10	1.06
4	351	295	296	1.19	1.19	34.7	24.2	25.3	1.43	1.37
Mean				1.073	1.045	Mean			1.230	1.165
Standard deviation				0.1016	0.0853	Standard deviation			0.1231	0.1213
COV				0.0947	0.0816	COV			0.1000	0.1042

Note:

M_e = *Experimental flexural strength;* M_n = *Calculated flexural strength using nominal steel and concrete strength as well as predicted clamp strength;* M_t = *Calculated flexural strength using tested steel and concrete strength as well as tested clamp strength;*

k_e = *Experimental beam stiffness;* k_n = *Calculated beam stiffness using nominal steel and concrete strength as well as predicted clamp strength;* k_t = *Calculated beam stiffness using tested steel and concrete strength as well as tested clamp strength.*

Rambo-Roddenberry (2002) summarized the experimental-to-predicted flexural strength of 64 composite beams using steel headed stud anchors, as shown in Figure 5.45. It was calculated that the average ratio was 1.017, and the standard deviation was 0.089. The strength comparison in Table 5.12 shows that the AISC design equations provide very good estimations for the flexural strengths of the partially composite beams utilizing M24 clamps and the fully composite beam utilizing M20 clamps. Although the capacity of Beam 4, a partially composite beam using M20 clamps, is underestimated by the AISC provisions, the ratio of 1.19 is still reasonable, given the scatter of the test-to-prediction ratios in Figure 5.45.

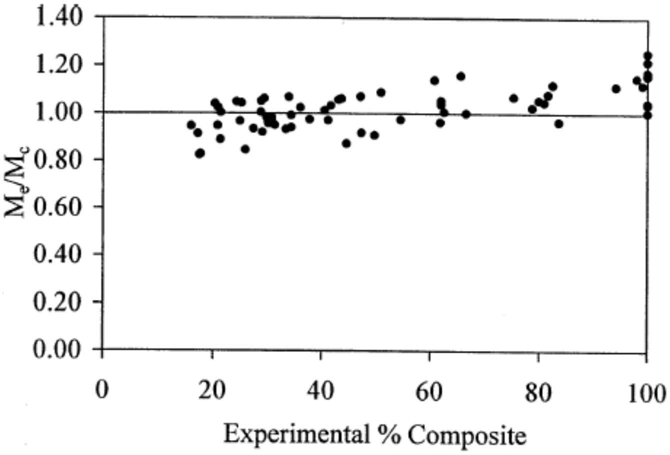

Figure 5.45 Experimental-to-predicted beam strength versus percentage of composite action [after (Rambo-Roddenberry 2002)]

The elastic stiffness of a conventional composite beam utilizing shear studs is proportional to the percentage of composite action of the beam. In a partially composite beam, the slip at the steel/concrete interface is larger than that in a fully composite beam in which the shear studs are not fully loaded and the deformation of the studs is not as significant. The deconstructable composite beams are slightly stiffer than the conventional composite beams, which could be due to different mechanisms of achieving composite action for the two types of shear connectors, with clamping connectors relying on the friction between the structural components and shear studs bearing against concrete slabs. The stiffness comparison given in Section 4.5.4.3 in Chapter 4 shows that clamps exhibit much larger initial stiffness than shear studs. The influence of the degree of shear connection on the stiffness of the beams is not decisive, since the stiffness of the first two specimens appears to be affected by the amount of composite action, whereas the other two specimens have similar stiffness.

Ataei et al. (2016) recently tested four beam specimens utilizing deconstructable bolted shear connectors. The bolted shear connectors were embedded in the monolithic concrete slab in CB1, which was designed as a fully composite beam. CB2 was similar to CB1, except that the bolts were post-installed and numerous concrete panels replaced the monolithic concrete slab. The difference between CB2 and CB3 and CB4 was the percentage of composite action. The experimental results show that the stiffness of CB1 was 32% higher than that of CB2, and the authors believed that it was attributed to the monolithic slab in CB1 and the concrete panels that rotated and moved in CB2. Similar to the concrete crushing seen in the deconstructable composite beam tests, crushing at the top region of the panels was also observed in CB2. The authors concluded that the localized concrete failure mode between adjacent concrete planks led to the lower ultimate flexural strength of CB2 than CB1, as shown in Figure 5.46. However, this conclusion is not supported by the results presented in Table 5.12 which indicate that localized concrete crushing does not reduce the strength of the composite beams, particularly for Test 3-M20-3C-RL, the behavior of which is not governed by the shear connectors.

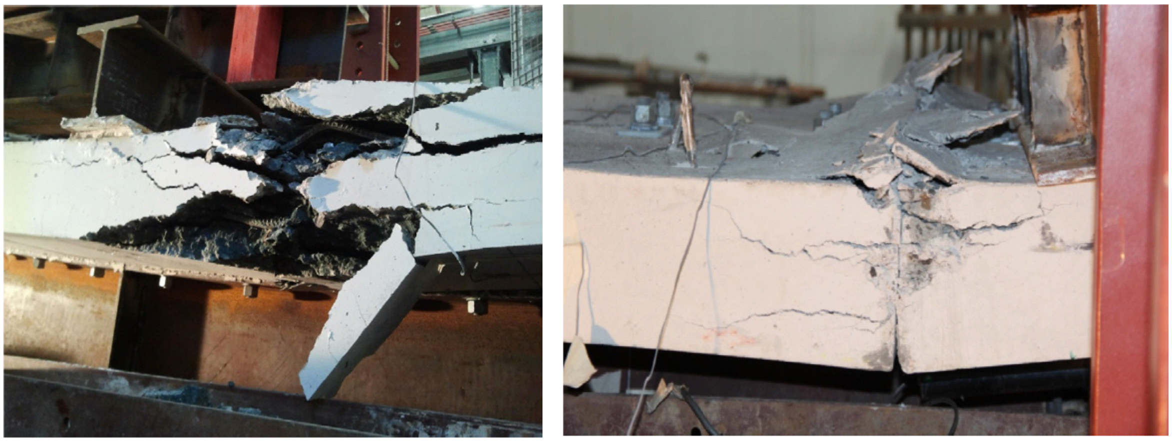

a) CB1 b) CB 2

Figure 5.46 Concrete crushing in different composite beam specimens [after (Ataei et al. 2016)]

5.6.2.7 *Ductility*

In conventional composite floor systems, the behavior of partially composite beams with low composite action was reported to be less ductile than that of fully composite beams or partially composite beams with high composite action. For example, Figure 5.47 illustrates the relationship between the normalized flexural strength and center deflection of the composite beams tested by Toprac (1965). Beams 11 through 15 had a percentage of composite action of 100%, 75.8%, 32.4%, 33.2%, 33.2%, and 18.9%, respectively. Shear stud fracture occurred in Beams 13 through 15. Although the flexural strengths of all the beams exceeded the strengths predicted by the AISC provisions, Beams 13 through 15 exhibited limited plastic deformation after reaching their ultimate flexural strengths.

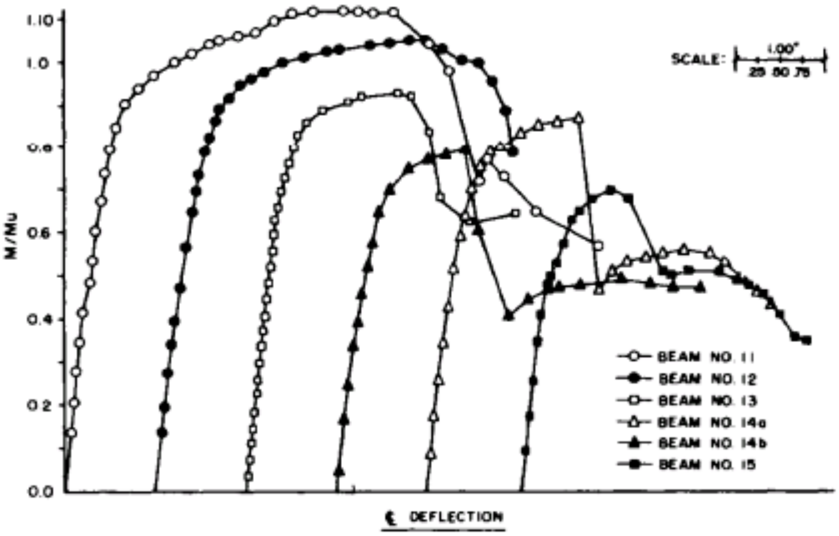

Note: M_u is the predicted ultimate flexural strength of the fully composite beam (i.e.,Beam 11).

Figure 5.47 M/M_u versus center deflection for composite beams [after (Toprac 1965)]

Although composite beams normally exhibit ductile behavior, there is no consensus on how to define ductility quantitatively. In the commentary for Appendix 1 in AISC 360-16 (2016), rotational ductility is defined for steel beams, as shown in Figure 5.48. However, this definition cannot be applied directly to composite beams, which possess little or no overstrength.

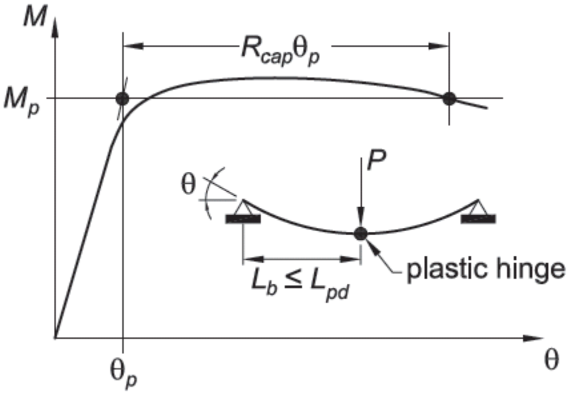

Note: θ_p is the elastic rotation at M_p, which is the nominal plastic strength of the steel beam.

Figure 5.48 Definition of rotation capacity [after (AISC 360-16)]

The ductility of composite beams could be defined in several ways. The load-deflection curve or moment-rotation curve of a composite beam can be idealized as an elastic-perfectly-plastic response, as shown in Figure 5.49. The slope of the elastic curve is taken as the stiffness of the composite beam which is calculated using a lower-bound moment of inertia. This results in a smaller and more conservative ductility index, compared to using the tested stiffness of the beam as the slope of the elastic curve. The plastic plateau may correspond to the peak strength predicted according to the AISC provisions, 80% of the predicted peak strength, or the tested peak strength of the composite beam. The deflection or rotation at the intersection of the elastic curve and the plastic plateau is defined as the yield deflection or rotation of the beam. The ultimate deflection or rotation uses the deflection or rotation at which the beam strength descends to 80% of the predicted strength. Otherwise, the deflection or rotation at which the test is terminated is employed as the ultimate deflection or rotation of the composite beam.

Since almost no strength reduction is exhibited, the maximum deflections and rotations are employed as the ultimate deflections or rotations of the specimens. Therefore, the ductility of the composite beam specimens is calculated as:

$$\mu = \Delta_u/\Delta_y \text{ or } \theta_u/\theta_y \tag{5.4}$$

Where Δ_y and θ_y are the yield deflection and yield rotation of the specimen, respectively; Δ_u and θ_u are the ultimate deflection and ultimate rotation of the specimen, respectively.

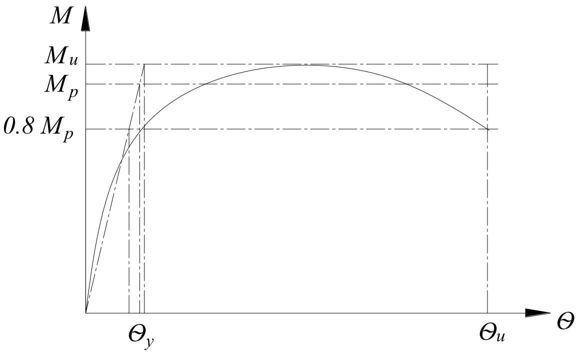

Figure 5.49 Yield deformation and ultimate deformation of a composite beam

The yield deflection or rotation, ultimate deflection or rotation, and ductility of the specimens are given in Table 5.13. It is shown that the ductility calculated based on the load-deflection curves is larger than that obtained from the moment-rotation curves. All the specimens have a ductility of at least 3, indicating that the beams would demonstrate significant plastic deformation at their ultimate strengths and sufficient warnings of imminent failure.

Key parameters, such as strength, stiffness and ductility, cannot fully represent the overall load-deflection behavior of composite beams. It is instrumental to address this in comparing the overall behavior of conventional composite beams using monolithic composite slabs and shear studs to that of deconstructable composite beams using precast concrete planks and clamps. A direct way is to plot different load-deflection curves together. However, the load-deflection curve of a composite beam is dependent on the test setup, such as the length of the beam, the moment of inertia of the beam section, and the loading pattern. In Figure 5.50, the load-deflection curves are modified to eliminate the influences of these parameters. For each curve, the load is normalized relative to the peak strength of the beam, and the deflection is multiplied by the stiffness of the beam which is calculated using a lower-bound moment of inertia. The specimens tested by Grant (1973) and Rambo-Rodenberry (2002) are employed as examples of conventional composite beams, as the lengths and sizes of these beams are similar to those tested in the beam tests. The test configurations for these two sets of experiments are given in Figure 5.51. Equations (5.5) through (5.16) show the stiffness of the beams used in the comparison.

As depicted in Figure 5.50a, the overall load-deflection behavior of the deconstructable composite beams is similar, even though Beam 1-M24-2C-RH appears to be more flexible than the others. In Figure 5.50b, the curves representing the tests performed by Rambo-Roddenberry (2002) are very close, since the specimens differ only in the percentage of composite action. The beams tested by Grant (1973) are different in several aspects, including length, degree of shear connection, concrete slab width and height, etc., which may result in the disparity among the curves. Figure 5.50c shows that the behavior of the deconstructable composite beams resembles that of the conventional composite beams.

Deconstructable composite beams:

Test 1
$$k = \frac{EI}{0.01575l^3} = 29800 \times 1188/(0.01575 \times 360^3) = 48.18\, kips/in. \tag{5.5}$$

Test 2
$$k = \frac{EI}{0.01575l^3} = 29800 \times 958/(0.01575 \times 360^3) = 38.85\, kips/in. \tag{5.6}$$

Test 3
$$k = \frac{EI}{0.01575l^3} = 30000 \times 853/(0.01575 \times 360^3) = 34.82\, kips/in. \tag{5.7}$$

Test 4
$$k = \frac{EI}{0.01575l^3} = 29500 \times 631/(0.01575 \times 360^3) = 25.33\, kips/in. \tag{5.8}$$

Conventional composite beams:

Grant (1973)

Beam 1c1
$$k = \frac{EI}{0.01537l^3} = 29400 \times 860/(0.01537 \times 288^3) = 68.86\, kips/in. \tag{5.9}$$

Beam 1c2a
$$k = \frac{EI}{0.0163l^3} = 30100 \times 863/(0.0163 \times 384^3) = 28.14\, kips/in. \tag{5.10}$$

Beam 1c2b
$$k = \frac{EI}{0.0163l^3} = 28900 \times 940/(0.0163 \times 384^3) = 29.43\,kips/in. \tag{5.11}$$

Beam 1c3
$$k = \frac{EI}{0.01537l^3} = 29400 \times 797/(0.01537 \times 288^3) = 63.82\,kips/in. \tag{5.12}$$

Beam 1c4
$$k = \frac{EI}{0.0163l^3} = 28900 \times 1081/(0.0163 \times 384^3) = 33.85\,kips/in. \tag{5.13}$$

Rambo-Roddenberry (2002)

Test 1
$$k = \frac{EI}{0.01418l^3} = 29000 \times 863/(0.01418 \times 360^3) = 37.83\,kips/in. \tag{5.14}$$

Test 2
$$k = \frac{EI}{0.01418l^3} = 29000 \times 797/(0.01418 \times 360^3) = 34.94\,kips/in. \tag{5.15}$$

Test 3
$$k = \frac{EI}{0.01418l^3} = 29000 \times 833/(0.01418 \times 360^3) = 36.52\,kips/in. \tag{5.16}$$

Table 5.13 Ductility of composite beam specimens

Specimen	Δ_y (in.)			θ_y (rad)			Δ_u (in.)	θ_u (rad)	Ductility					
									Deflection			Rotation		
	M_p	M_u	$0.8M_p$	M_p	M_u	$0.8M_p$			M_p	M_u	$0.8M_p$	M_p	M_u	$0.8M_p$
1-M24-2C-RH	2.54	2.57	2.03	0.023	0.023	0.018	13.6	0.082	5.35	5.29	6.70	3.57	3.53	4.46
2-M24-1C-RL	2.60	2.63	2.08	0.023	0.024	0.019	13.7	0.083	5.27	5.21	6.59	3.55	3.51	4.43
3-M20-3C-RL	2.44	2.36	1.95	0.021	0.020	0.017	16.0	0.082	6.56	6.78	8.21	3.88	4.00	4.84
3-M20-3C-RL	2.50	2.98	2.00	0.023	0.027	0.018	14.8	0.087	5.92	4.97	7.40	3.80	3.20	4.75

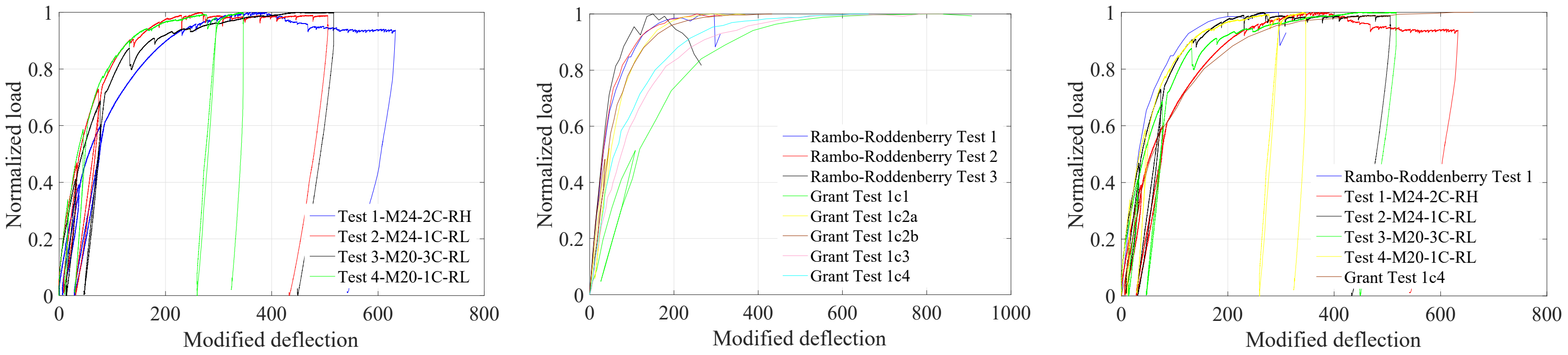

a) Deconstructable composite beams

b) Conventional composite beams

c) Deconstructable and conventional composite beams

Figure 5.50 Load-deflection curve comparison

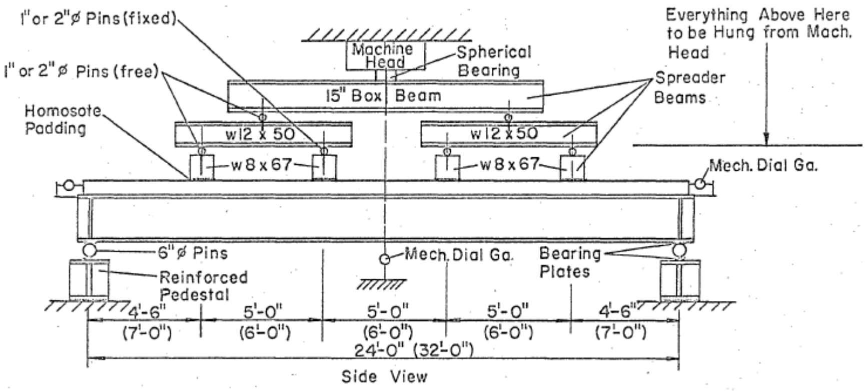
1" or 2"ø Pins (fixed)
1" or 2"ø Pins (free)
Homosote Padding
Machine Head
Spherical Bearing
15" Box Beam
w12 x 50
w12 x 50
w8 x 67
w8 x 67
Everything Above Here to be Hung from Mach. Head
Spreader Beams
Mech. Dial Ga.
6"ø Pins
Reinforced Pedestal
Mech. Dial Ga.
Bearing Plates
4'-6" (7'-0")
5'-0" (6'-0")
5'-0" (6'-0")
5'-0" (6'-0")
4'-6" (7'-0")
24'-0" (32'-0")
Side View

a) Grant (1973)

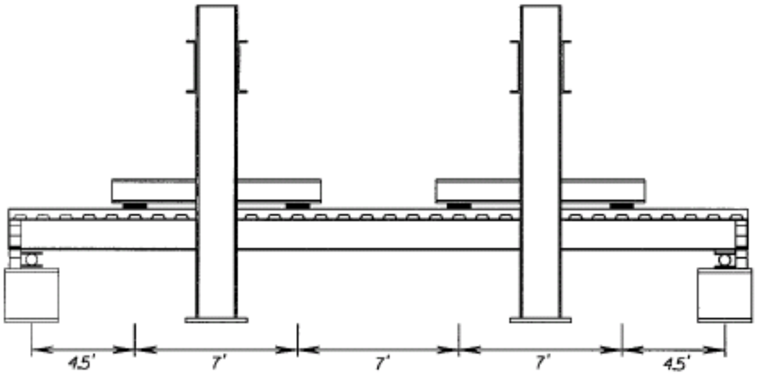

b) Rambo-Roddenberry (2002)

Figure 5.51 Composite beam test setups [after (Grant 1973) and (Rambo-Roddenberry 2002)]

In addition to evaluating ductility at a component level, ductility was also studied at a cross-section level. A ductile moment-curvature response is required for the plastic design of continuous beams. In plastic design, ductility allows moment redistribution to occur after the plastic strength of the weakest section in the system is reached. Ultimately, the system attains the maximum strength when all the plastic hinges form and the system becomes unstable. It is shown that negative moment hinges are “strain-hardening”, and moment redistribution occurs because of their ductile behavior. In contrast, depending on the material properties and geometries of the steel beam and concrete slab, positive moment hinges could exhibit either “strain-hardening” or “strain-softening” behavior. To ensure moment redistribution at positive moment hinges, the section has to meet certain ductility criteria (Rotter et al. 1978; Oehlers et al. 1995).

5.6.2.8 *Camber*

In conventional composite construction, steel beams are commonly cambered before pouring the concrete slab to counteract the deflection caused by a portion of the dead load, full dead load or full dead load plus a portion of the live load (Ricker 1989). Camber can be achieved by either force (cold bending) or heat (hot bending). The amount of camber should be carefully assessed. Insufficient camber makes more concrete accumulate at the center of the beam and results in a ponding effect. On the other hand, excessive camber leads to the exposure of the shear studs welded onto the steel beams or concrete slabs with excessive thickness. Two papers presented at the 1996 North American Steel Construction Conference advocated the use of 80% of the dead load for cambering, as the shear tab connections at the ends of composite beams provide some rotational resistance, restraining the deflection of the beams (Downey 2006).

The stress induced by camber is illustrated in Figure 5.52. During camber, the top flange of the steel beam is in tension, and the bottom flange is in compression. Despite the tensile and compressive stress, the cambered steel section is in equilibrium after the process is complete. When a steel beam is cambered, the material deforms into the inelastic region and plastic deformation occurs. Residual deformation exists after the process is finished. Since the steel beam specimens in the experimental program are not cambered, the influences of the camber stress are not accounted for in the load-deflection curves. The camber stress has no effect on the ultimate strengths of the beams, but the linear elastic behavior of the beams is affected since the sections yield earlier, which is similar to the effect of residual stress on the ultimate strengths and elastic behavior of steel beams.

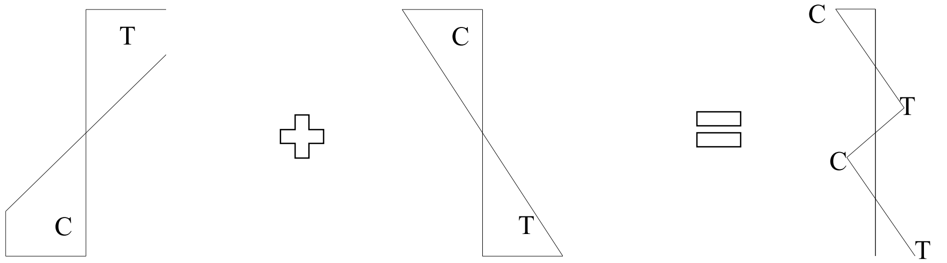

Loading Unloading Resultant stress

Figure 5.52 Camber stress in a symmetric steel section

5.6.2.9 *Effect of friction produced by actuator loading and self-weight of specimen*

In the composite beam specimens, the required shear flow between the steel beam and concrete planks is equilibrated by the shear resistance of the clamping connectors and the additional friction at the steel/concrete interface produced by the self-weight of the planks and the actuator loads. The beneficial effect of the additional friction is estimated by calculating the ratio of the friction induced due to the self-weight and actuator loading to the total shear resistance between the maximum moment section and the near support. The axial force at the steel/concrete interface is conservatively assumed to equal the actuator loading and self-weight of the planks, while the actual axial force distribution is governed by Equation (5.17) and illustrated in Figure 5.53. A value of 0.17, which is calculated in Table 4.11 in Chapter 4, is used as the frictional coefficient between the top flange of the steel beam and the cast surface of the concrete plank. The ratios given in Table 5.14 show that the contribution from the actuator loading and self-weight of the composite beam specimens to the total horizontal shear resistance of the specimens is very small. This may indicate that the behavior of the beam would not be strongly affected if the actuator loading is not applied on the concrete planks, but to the bottom flange of the steel beam.

$$q - r = \frac{dV_c}{dx} \tag{5.17}$$

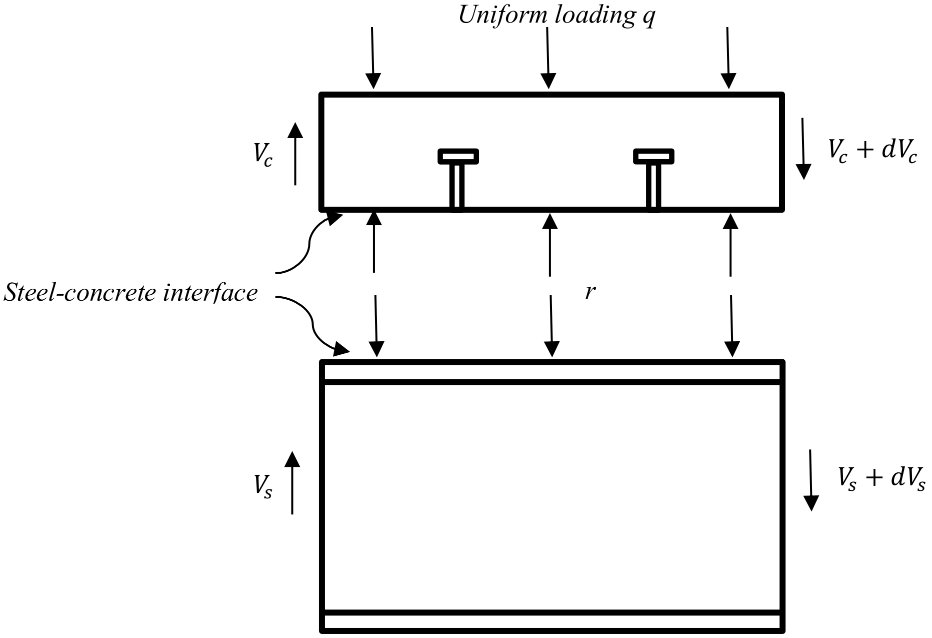

Figure 5.53 Axial interface force in a composite beam

Table 5.14 Effect of additional friction produced by self-weight and actuator loading

Specimen #	Clamps			Actuators and self-weight				Total resistance (kips)	Ratio
	n	Q_n (kips)	nQ_n (kips)	F_N (kips)		μ	μF_N (kips)		
1-M24-2C-RH	22	22.1	486.2	55.1	7.52	0.17	10.65	496.8	0.021
2-M24-1C-RL	12	22.1	265.2	47.4	7.52	0.17	9.34	274.5	0.034
3-M20-3C-RL	36	13.8	496.8	33.4	7.52	0.17	6.96	503.8	0.014
4-M20-1C-RL	12	13.8	165.6	37.4	7.52	0.17	7.64	173.2	0.044

5.6.3 Slip of clamps

In an idealized situation, due to the symmetry of the beam, the relative slip between the concrete and steel is zero at the center section in a simply supported composite beam under uniform loading, and the slip variation along the length of the beam can be calculated using Equation (5.18), and the parameters are shown in Figure 5.54. Based on this equation, the slip between the steel beam and concrete slab increases from zero at the center section to the maximum at the end of the beam.

$$s = u_c - u_s = \int_0^L \varepsilon_c \, dx - \int_0^L \varepsilon_s \, dx \tag{5.18}$$

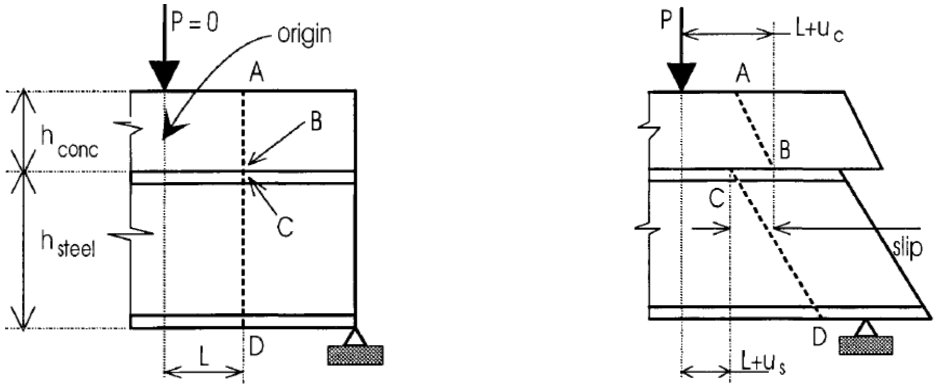

a) Undeformed configuration b) Deformed configuration

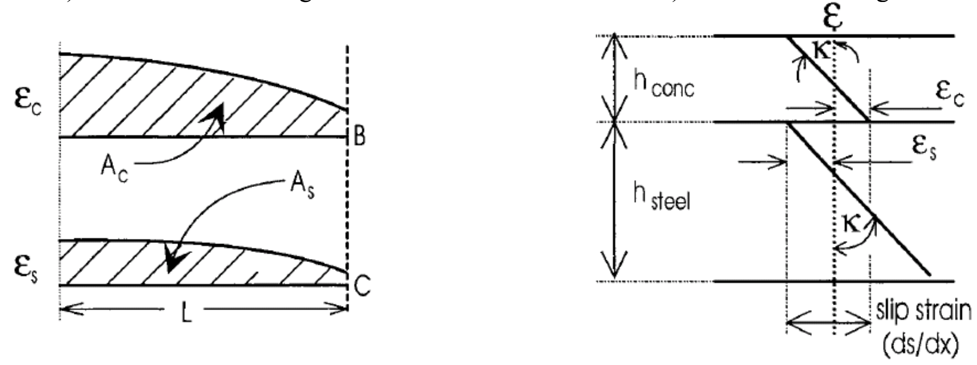

c) Strain distribution d) Slip strain

Figure 5.54 Slip in a composite beam [after (Oehlers et al. 1995)]

The applied load-slip response for all the beam specimens is plotted in Figure 5.55. As demonstrated in the pushout tests, the clamping connectors are very stiff before slip occurs. Likewise, the initial stiffness of the load-slip curves of the beam specimens is very large, but as the ultimate strength is approached, the curves become nearly horizontal.

The ultimate slip demand of the clamps in Specimens 2-M24-1C-RL and 4-M20-1C-RL is greater than the slip capacity of a 3/4 in. steel headed stud anchor embedded in a solid concrete slab, which is about 0.29 in. based on the equations proposed by Oehlers et al. (1986), but much smaller than the slip capacity of the clamps tested in the pushout tests (see Chapter 4). The AISC Specification (2016), for the first time, explicitly requires consideration of the ductility demand at the steel-concrete interface of composite beams to avoid premature shear connector failure. Given their excellent slip capacity, this check might be omitted for the clamping connectors.

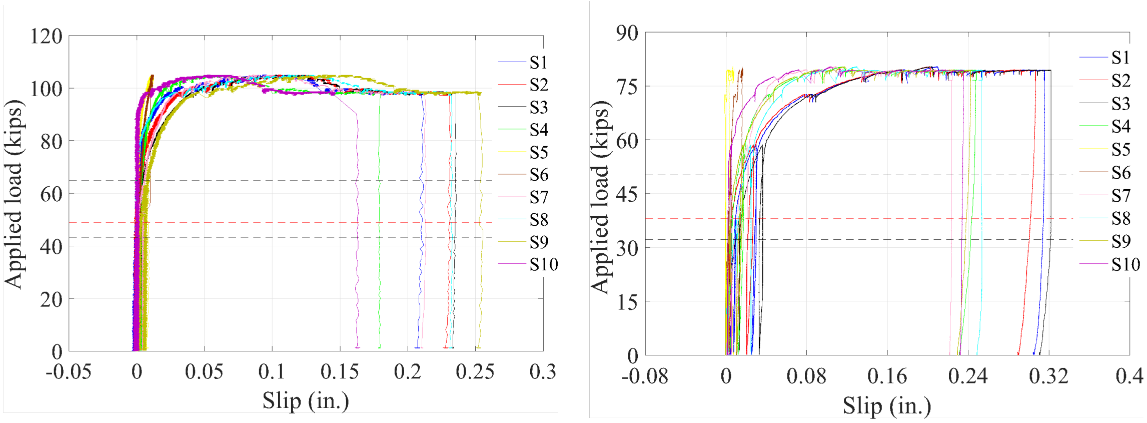

Test 1-M24-2C-RH Test 2-M24-1C-RL

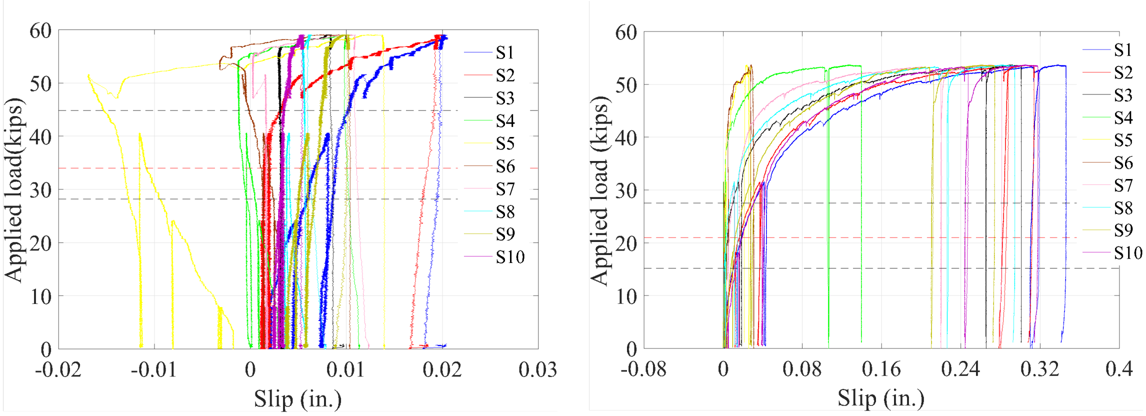

Test 3-M20-3C-RL Test 4-M20-1C-RL

Note: If the beam is strength-controlled and efficiently designed, the two black dashed lines illustrate the range of the full service loading, and the red dashed line indicates the full service loading when the dead load is 92.5 psf, as is used in the prototype structrues in Chapter 3.

Figure 5.55 Applied load-slip response of composite beam specimens

The black dashed lines in Figure 5.55 indicate the range of the full service loading of the beams. At serviceability, the slip experienced by the clamps is no more than 0.02 in. in Tests 2-M24-1C-RL and 4-M20-1C-RL, which is approximately 1/18 of the ultimate slip measured in the tests. Although the degree of shear connection of Beam 2-M24-1C-RL is much smaller than that of Beam 1-M24-2C-RH, the maximum measured slip in Beam 2 is not significantly larger than that in Beam 1. The slip is trivial in Specimen 3-M20-3C-RL, since the specimen is a fully composite beam and the percentage of composite action is very high. The comparison of the slip measurements between different tests further justifies that the degree of interaction is proportional to the degree of shear connection, while the amount of slip is inversely proportional to the degree of shear connection. Compared to the slips the clamps undergo in the pushout tests, the ultimate slips of the clamps in the composite beam specimens are much smaller. The slips at S5 and S6 are trivial in all the specimens, which is in agreement with the relatively constant moment and insignificant shear between the inner loading points.

In Test 2-M24-1C-RL, the clamps slipped during the loading/unloading cycles, while the clamps were not as responsive to these cycles in Test 1-M24-2C-RH which has a much higher percentage of composite action. This observation also applies to Tests 3-M20-3C-RL and 4-M20-1C-RL. In Tests 2-M24-1C-RL and 4-M20-1C-RL, the unrecoverable slip is shown in Figure 5.55 after the beams are unloaded. This is a source of the permanent deflection of these two beams during the loading/unloading cycles.

Depending on whether the beam is loaded or reloaded, the behavior of the clamps differs significantly. For example, the load-slip curve of Test 2-M24-1C-RL begins to soften before completing the 40% cycles. The softening behavior continues as the beam is loaded to the peak strength of the 60% cycle. The beam is then unloaded and reloaded, and very stiff behavior is exhibited by the clamps. The distinct behavior of the clamps at different stages partially explains why the initial stiffness of the load-deflection or moment-rotation curve is smaller than that of the reloading curves of the 60% cycle and 80% cycle.

As shown in Figure 5.56, the slip variation along the length of the beams is different from the idealized variation given in Figure 5.54, but the slip distribution appears to follow the same pattern as the load increases. The irregularity of the slip measurements in Test 3-M20-3C-RL may result from the insufficient resolution of the slip sensors for such small movement and the sensitivity of the actual slip to secondary effects, such as gaps between the concrete planks, nonlinearity of the beam, and crushing of the concrete planks. However, the slip measurements are adequate to show that Specimen 3 is a composite beam with almost full interaction at the steel/concrete interface. Some asymmetry is usually seen in the tests, with one end being more responsive to the loading and displaying larger slips than the other end.

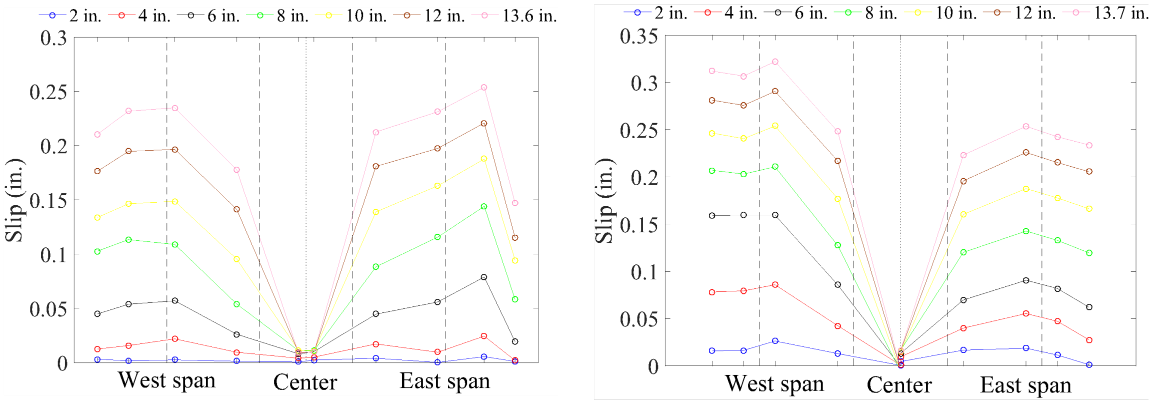

Test 1-M24-2C-RH

Test 2-M24-1C-RL

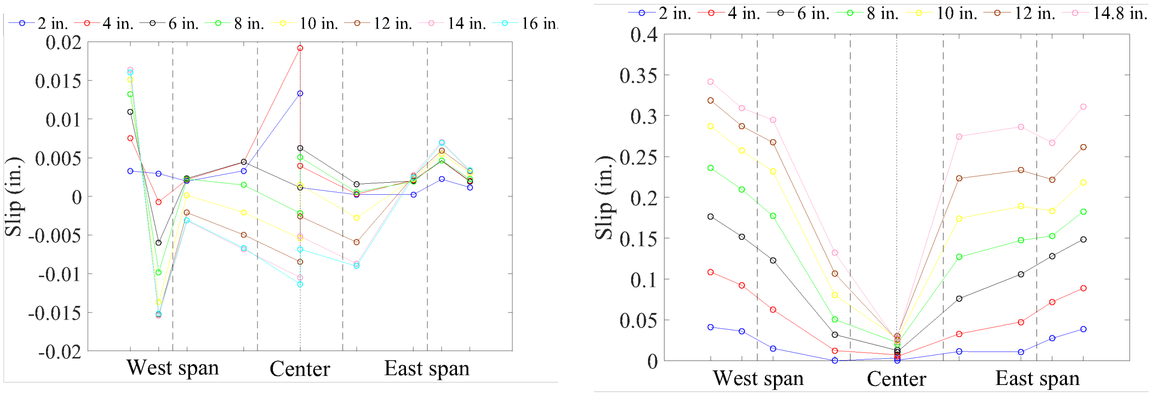

Test 3-M20-3C-RL

Test 4-M20-1C-RL

Note: The dashed lines show the positions of the applied loads. The dotted lines indicate the center sections of the beams.

Figure 5.56 Slip of clamping connectors along the beams at various load levels

5.6.4 Beam section strain

5.6.4.1 *Strain distribution along the depth of the section*

In a composite beam, as shown in Figure 5.57, the plastic neutral axis (PNA) locations vary depending on the strengths of the steel beam, concrete slab, and shear connectors. For a fully composite beam, only one PNA exists which develops in the concrete slab (or the steel section) if the strength of the steel section is smaller (or larger) than that of the concrete slab. The stress and strain distribution of case 3 in Figure 5.57 is typical of partially composite beams where the strength of the shear connectors governs. In order to maintain equilibrium, both the concrete slab and steel beam are partially in tension and partially in compression. Hence, one PNA lies in the concrete slab; the other one lies in the steel beam.

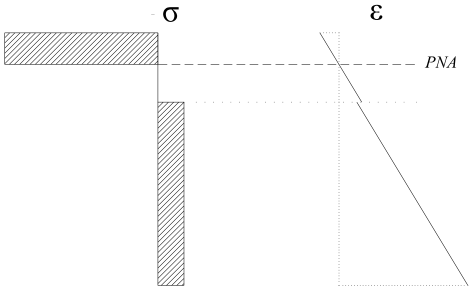

Case 1: full shear connection; $A_sF_y < 0.85f_c'A_c$ *and* $\sum Q_n$

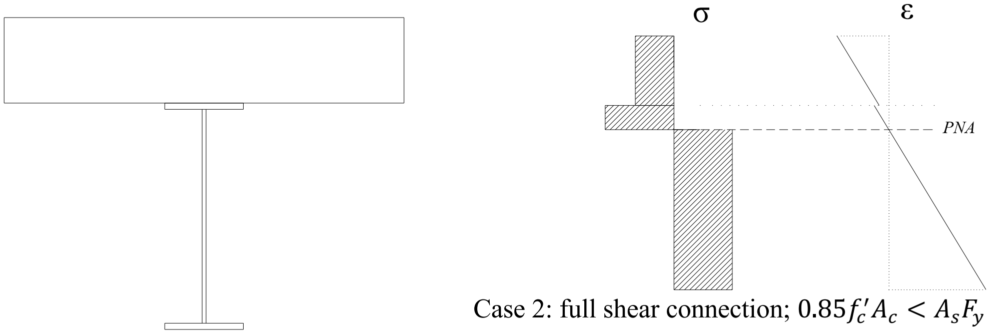

Case 2: full shear connection; $0.85f_c'A_c < A_sF_y$ *and* $\sum Q_n$

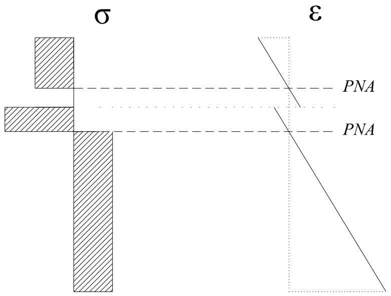

Case 3: partial shear connection; $\sum Q_n < A_sF_y$ *and* $0.85f_c'A_c$

Figure 5.57 Stress and strain diagrams for full and partial shear connection

Figure 5.58 illustrates the strain distribution along the depth of the instrumented composite beam sections in the specimens. The locations of the sections can be found in Figure 5.11 in Section 5.4. As shown in Figure 5.12, the arrangement of the strain gages is symmetric with respect to the weak axis of the steel section. The steel section strains use the average of the readings from the two gages at the same location. Except for the center section (section 3), the concrete strain at the top (or bottom) surface uses the average of the top (or bottom) strain measurements. At section 3, the concrete strains were measured across the width of the slab, but the strains were not uniform due to the shear lag effect (see Section 5.6.8). Because they are closer to the steel section, readings from NT3, M and ST3 are used for the top strain calculation, and readings from NB3 and

SB3 are used for the bottom strain calculation. Figure 5.12 illustrates the locations of these gages.

By comparing the curvature in the steel beam and the curvature in the concrete plank, the assumption that plane sections remain plane can be verified at various load levels. Shifting of the neutral axis (NA) locations is demonstrated in all the graphs. The NA in the steel sections are located above the mid-height of the steel sections, which implies that the clamping connectors enable the steel beams and concrete planks to behave compositely, shifting the NA towards the concrete planks. The tensile strains at the bottom flanges of the beams are also much greater than the compressive strains at the top flanges of the beams. The following conclusions can be drawn from Figure 5.58 for the instrumented sections in the beam specimens:

- Beam 1-M24-1C-RH: Although Beam 1-M24-1C-RH is a partially composite beam, the strain distribution of the sections is different from case 3 depicted in Figure 5.57. The NA is seen in the steel web at sections 1 and 5, but the concrete plank measurements imply the planks are in full compression. At sections 2 and 4, the NA in the steel web is higher than those at sections 1 and 5, and the concrete planks are again shown to be fully in compression. As the load increases, the bottom surface of the plank at section 3 is barely in tension, and the whole center steel section is also in tension. This strain distribution is somewhat similar to case 1 in Figure 5.57.

- Beam 2-M24-1C-RL and Beam 4-M20-1C-RL: The strain distribution of all the sections resembles case 3 described in Figure 5.57. Two NA are found at each section, with one existing in the concrete plank and the other one lying in the steel web. The NA in the steel beam migrates towards the top steel flange as the loading increases, but the rise is not as tremendous as that seen in Beams 1-M24-1C-RH and 3-M20-3C-RL. Compared to Beams 1-M24-1C-RH and 3-M20-3C-RL, the tensile strains measured at the bottom surfaces of the planks are normally much larger.

- Beam 3-M20-3C-RL: Beam 3-M20-3C-RL is a fully composite beam with high composite action, but a small amount of slip strain is still observed at all the sections in the beginning of the test. A NA lies in the steel web at sections 1 and 5. The concrete plank is fully in compression at section 5, but the plank at section 1 is partially in compression. Steel section 4 is in full tension at the ultimate state of the beam, but steel section 2 is partially in tension. At the ultimate state, the whole center steel section is in tension and the strain distribution becomes similar to case 1 depicted in Figure 5.57. Although the bending moment of section 3 is larger than that of section 2, the strain at the bottom flange of section 3 is occasionally less than of section 2.

Overall, at the ultimate state, with the exception of Beam 1-M24-1C-RH, the strain diaphragms at the center sections of the beams conform to the theoretical strain diagrams shown in Figure 5.57. For the partially composite beams (i.e., Beams 2-M24-1C-RL and 4-M20-1C-RL), two NA are seen at the center section, with one NA lying in the steel beam and the other one lying in the concrete slab. Slip strain is found at the steel/concrete interface. For the fully composite beam (i.e., Beam 3-M20-3C-RL), only one NA exists which lies in the concrete plank, and strain continuity is seen at the steel/concrete interface. Since the percentage of composite action of the partially composite beam 1-M24-1C-RH is as large as 82.7%, its behavior is somewhat similar to a fully composite beam.

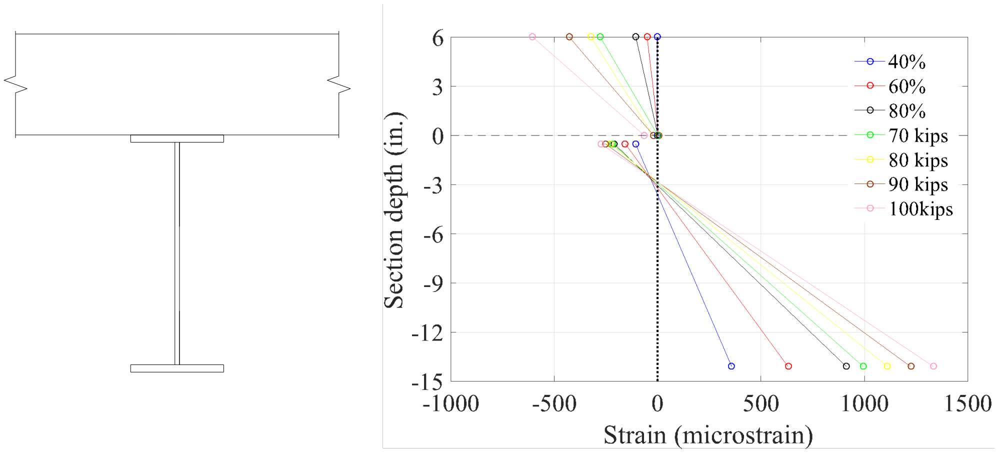

Section 1

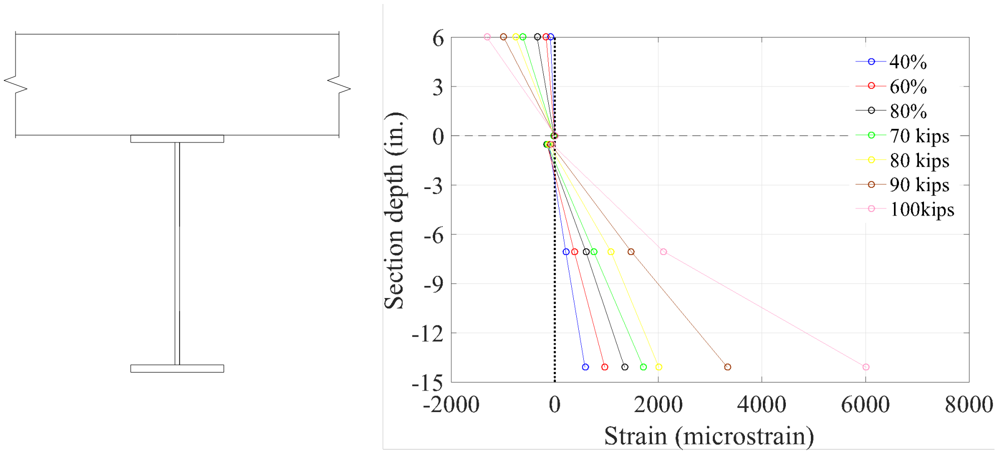

Section2

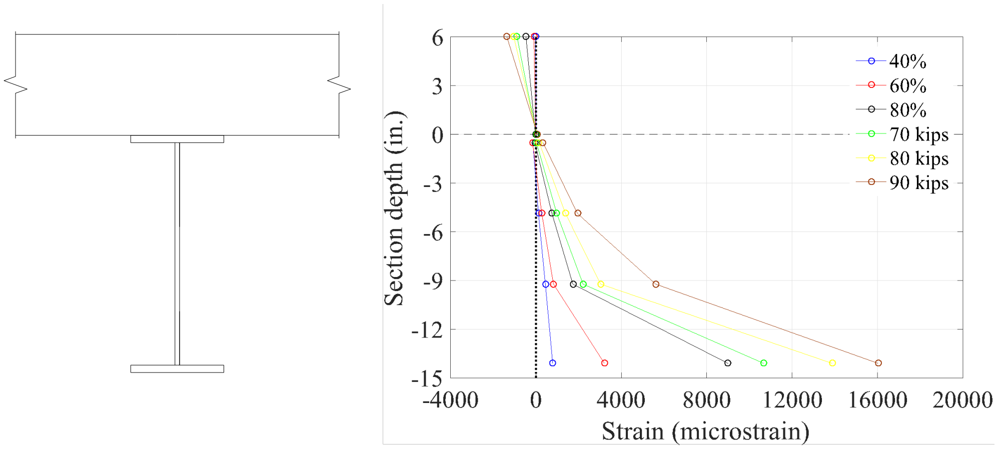

Section 3

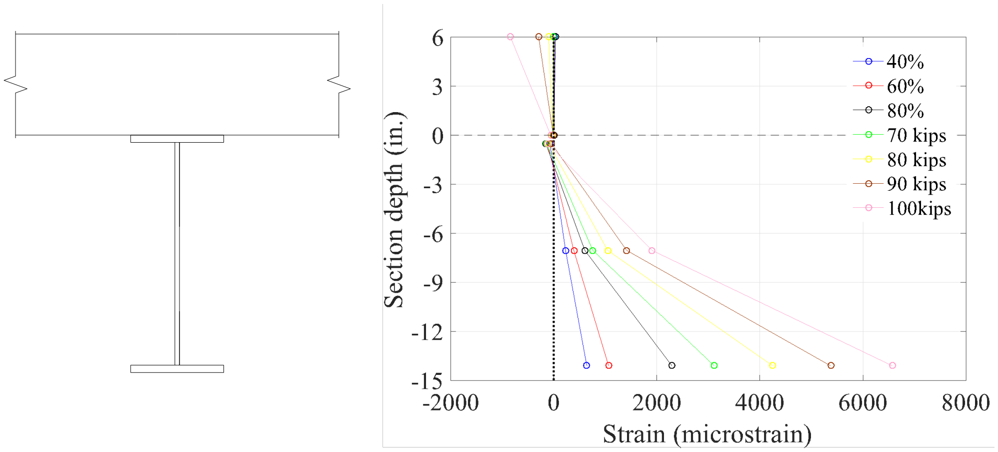

Section 4

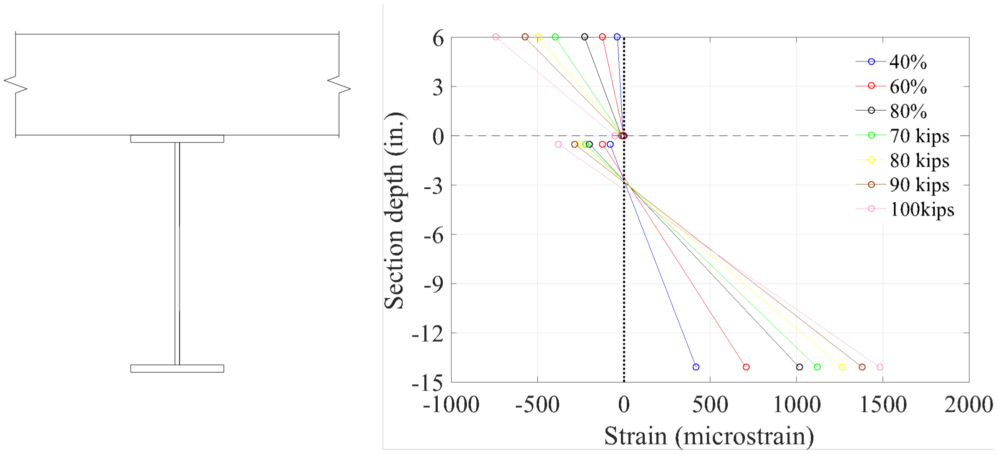

Section 5

Test 1-M24-2C-RH

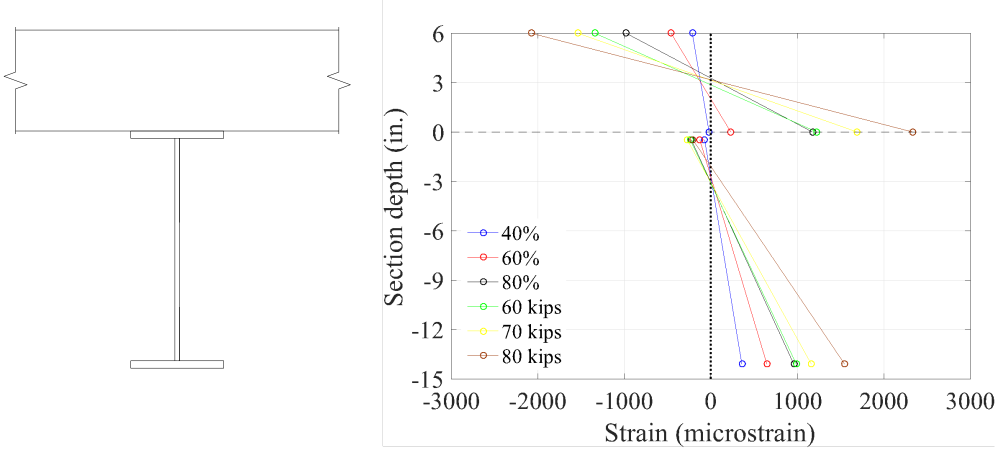

Section 1

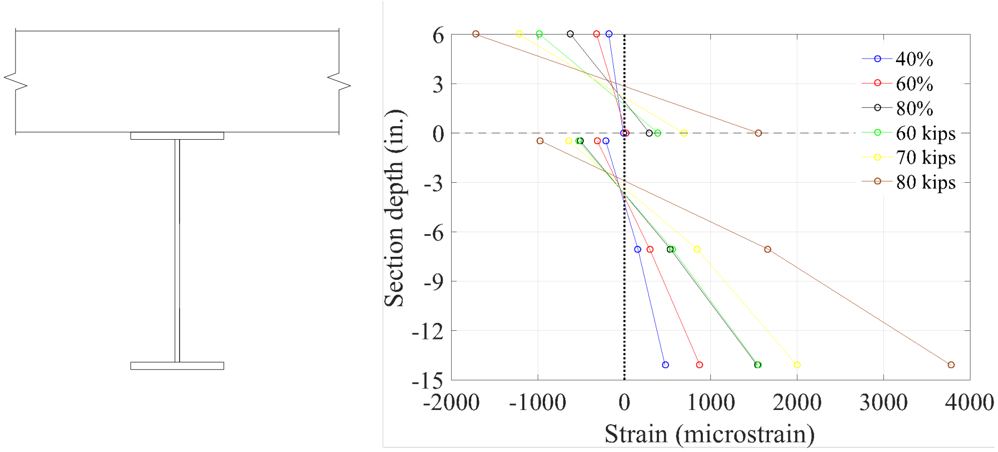

Section2

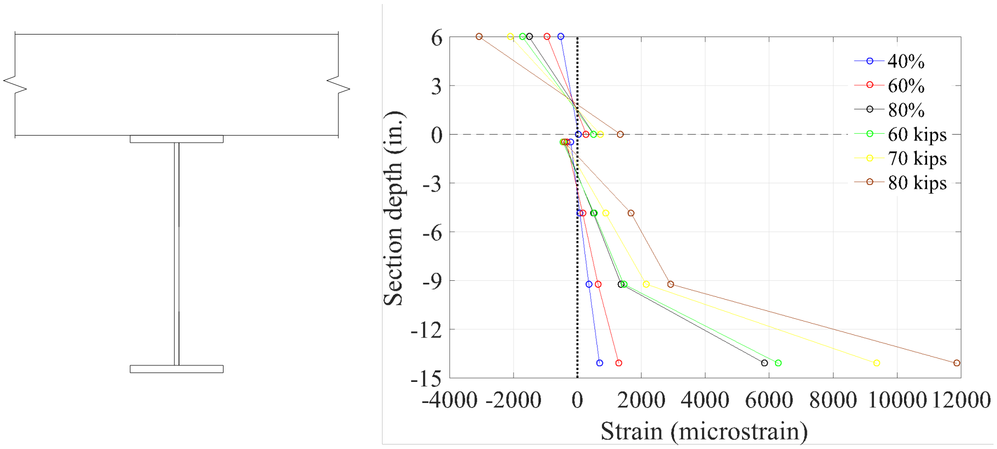

Section 3

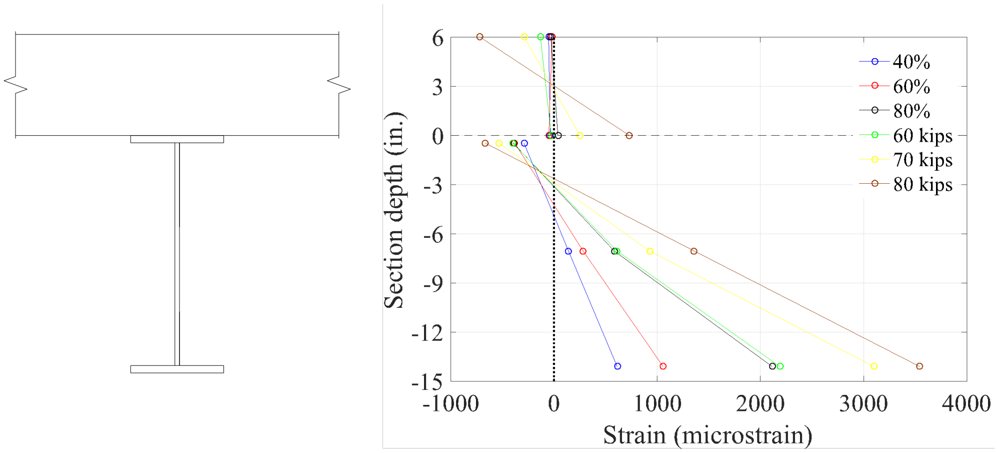

Section 4

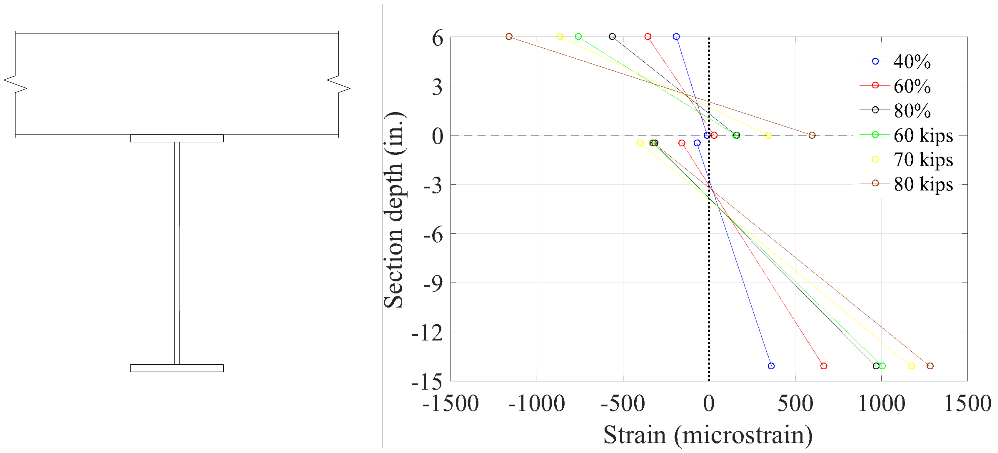

Section 5

Test 2-M24-1C-RL

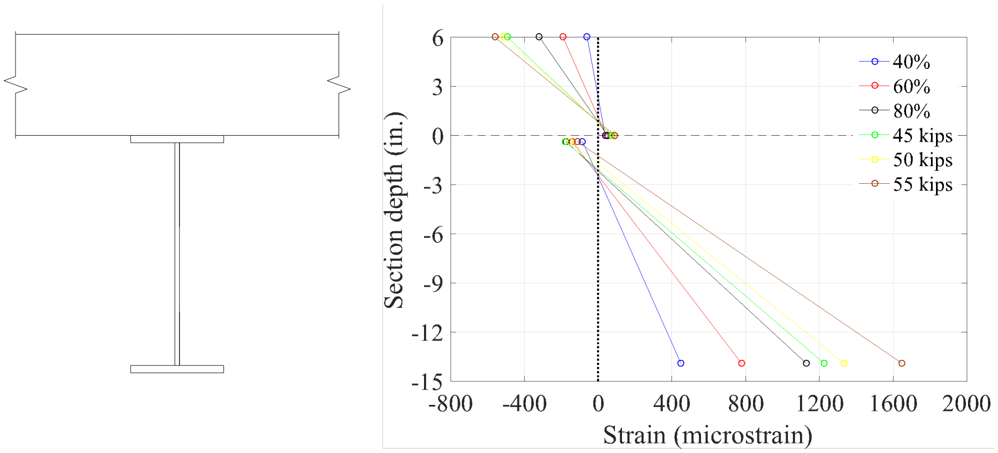

Section 1

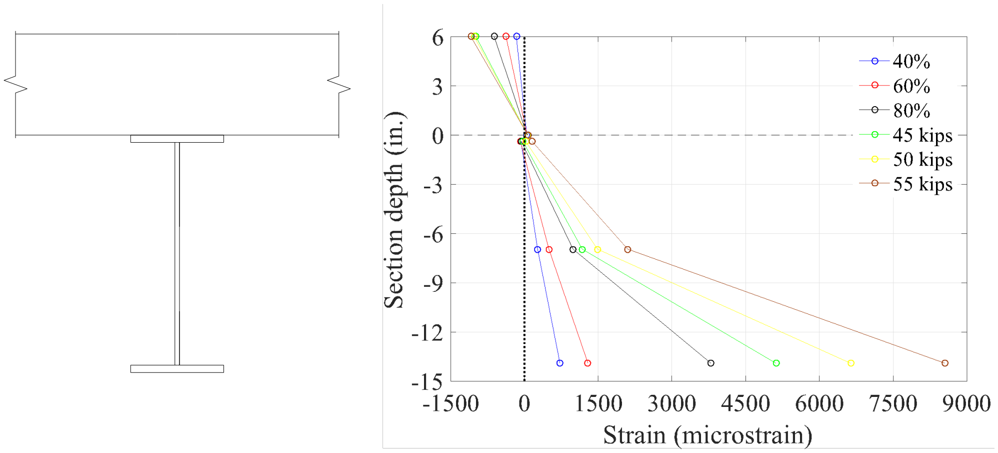

Section2

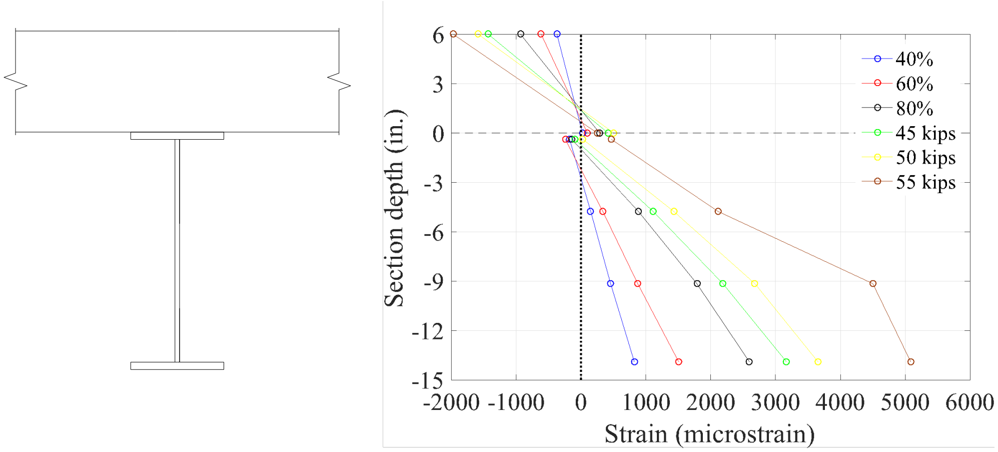

Section 3

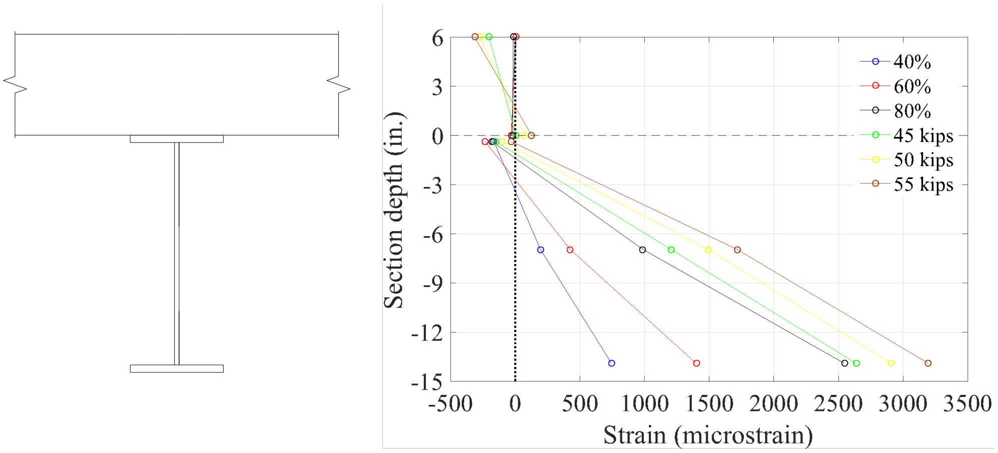

Section 4

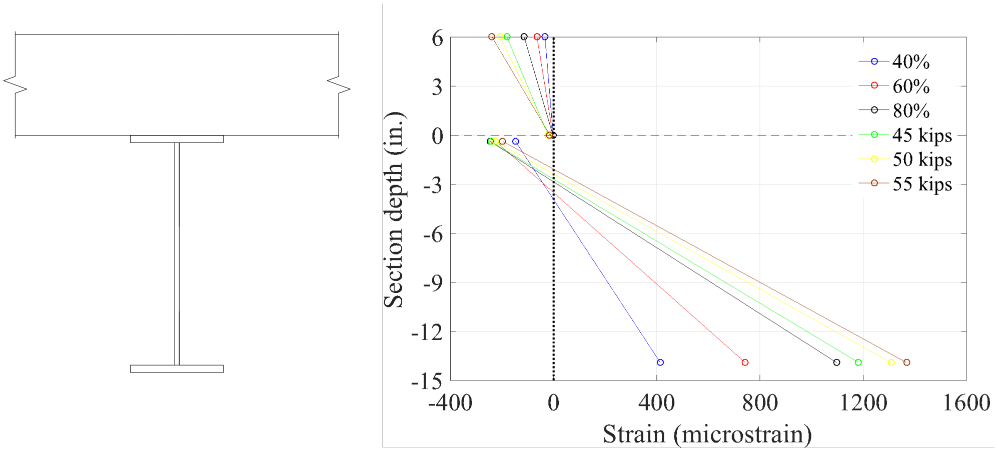

Section 5

Test 3-M20-3C-RL

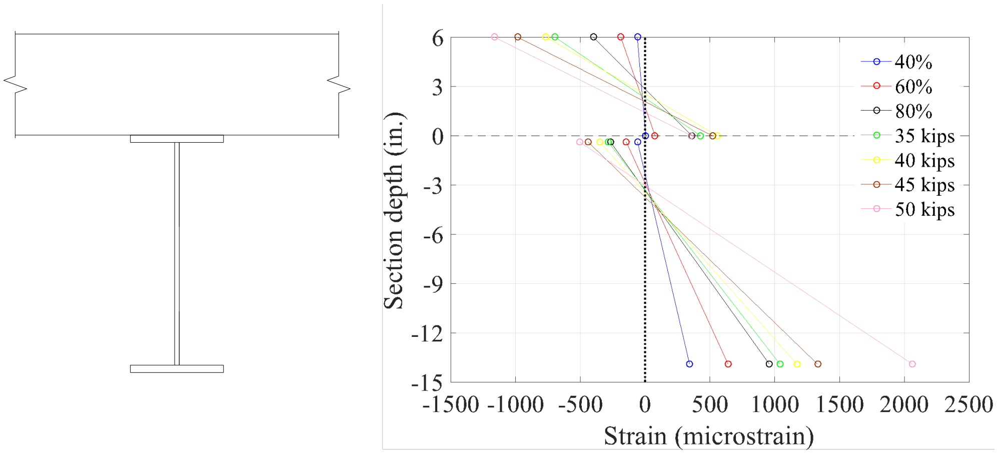

Section 1

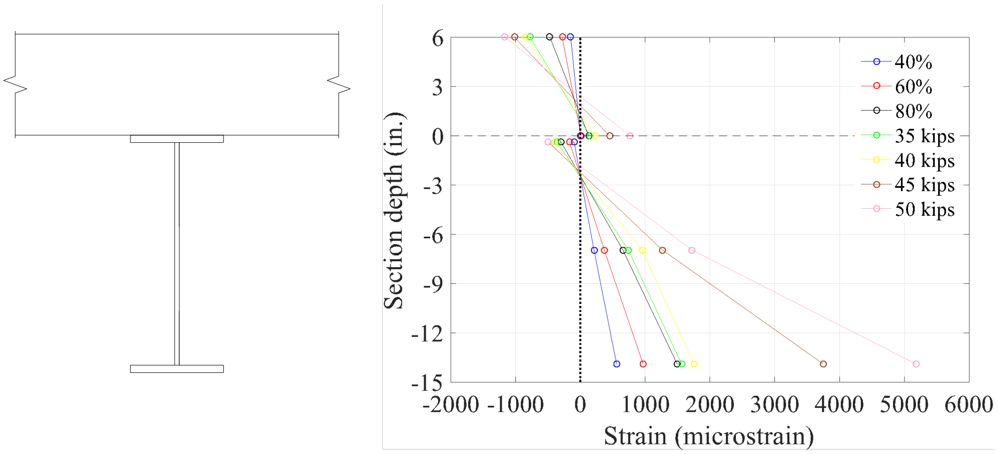

Section2

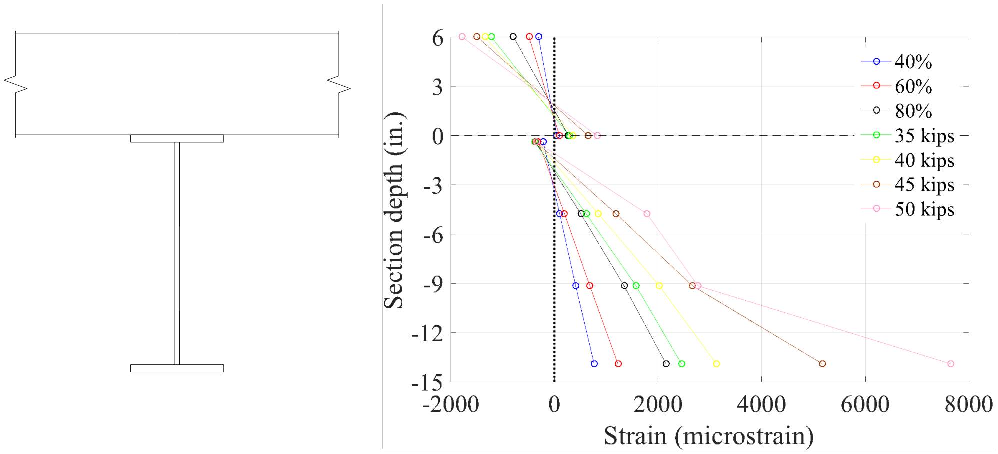

Section 3

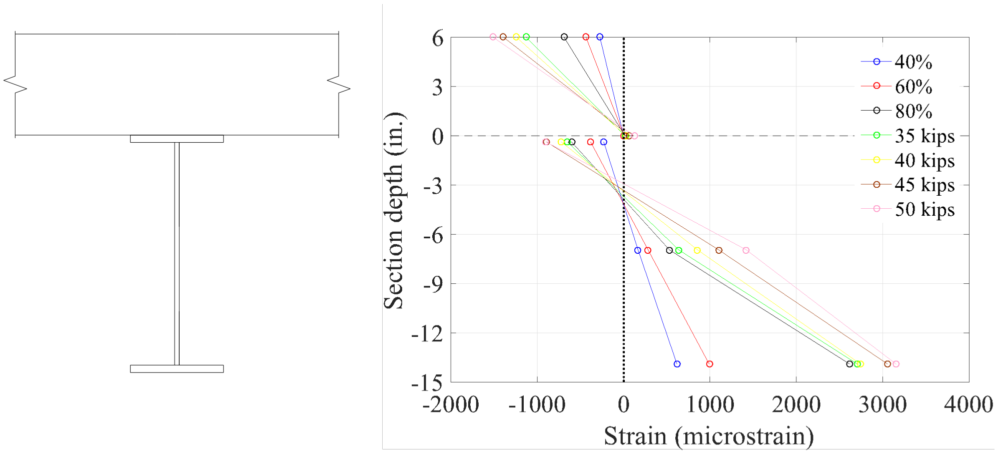

Section 4

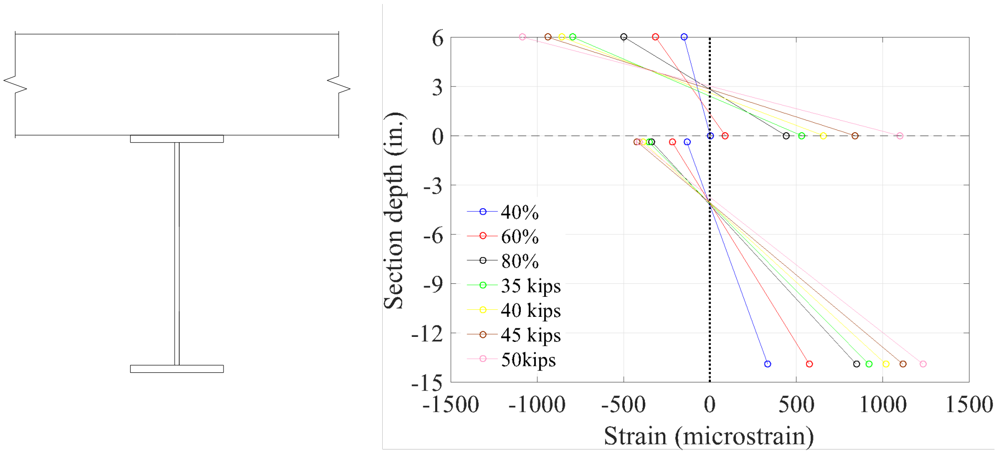

Section 5

Test 4-M20-1C-RL

Note: The dashed lines delineate the steel-concrete interface of the sections; the dotted lines depict the zero strain locations; the loading shown in the legends represents the applied actuator loading.

Figure 5.58 Strain distribution at instrumented sections

5.6.4.2 *Location of neutral axis in steel beam*

The NA in a steel section can be located by finding the zero strain position. The applied load versus NA location response is plotted in Figure 5.59 through Figure 5.62. In these plots, The NA location is measured from the bottom flange of the steel section. The NA of all the instrumented sections normally rise along with increasing loading or deflection. Distinct behavior is seen at the center sections in Beams 1-M24-2C-RH and 3-M20-3C-RL and Beams 2-M24-1C-RL and 4-M20-1C-RL. In Beams 1 and 3, the NA of section 3 ascend very quickly at the ultimate state of the beams. When the NA lie in the concrete planks, the steel sections are in full tension. It is unrealistic that the NA of section 3 are above the top surfaces of the concrete planks, which could be due to neglecting the slip existing at the steel/concrete interface. Concrete crushing occurring at the center plank of Beam 3 may cause the descending of the NA of section 3. The migration of the NA of section 3 in Beams 2 and 4 is not as significant as that in Beams 1 and 3.

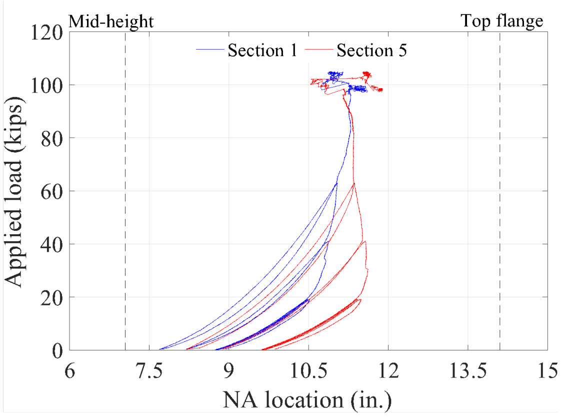

Sections 1 and 5

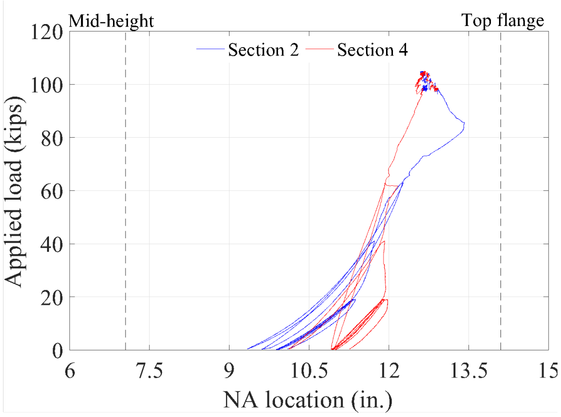

Sections 2 and 4

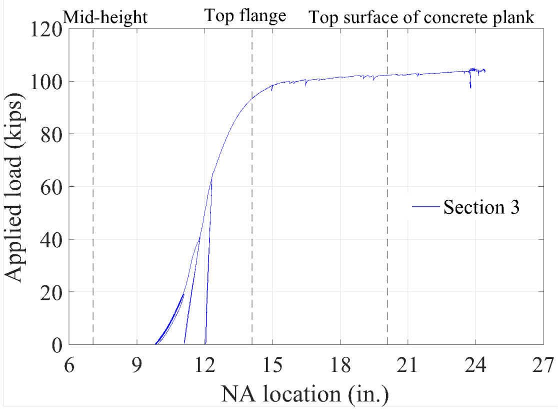

Section 3

Figure 5.59 Applied load versus neutral axis location in steel beam in Test 1-M24-2C-RH

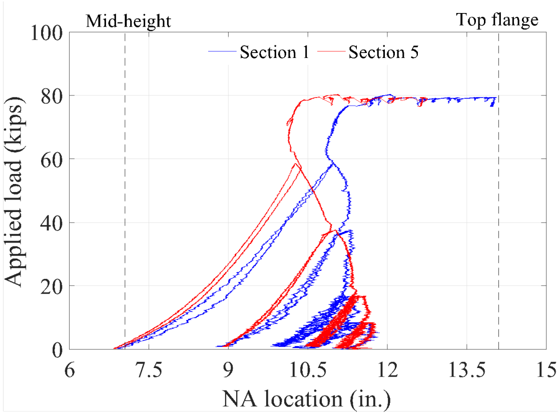

Sections 1 and 5

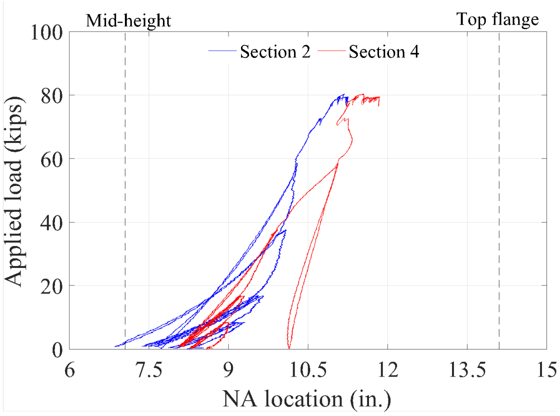

Sections 2 and 4

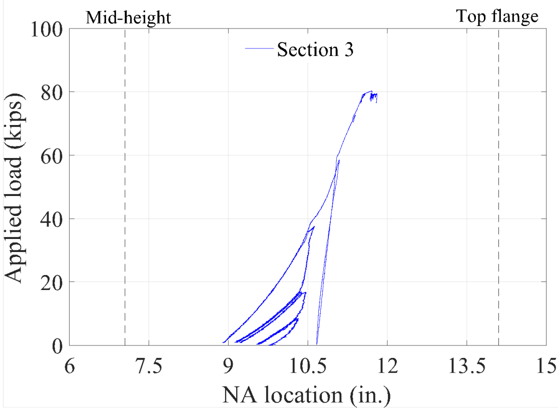

Section 3

Figure 5.60 Applied load versus neutral axis location in steel beam in Test 2-M24-1C-RL

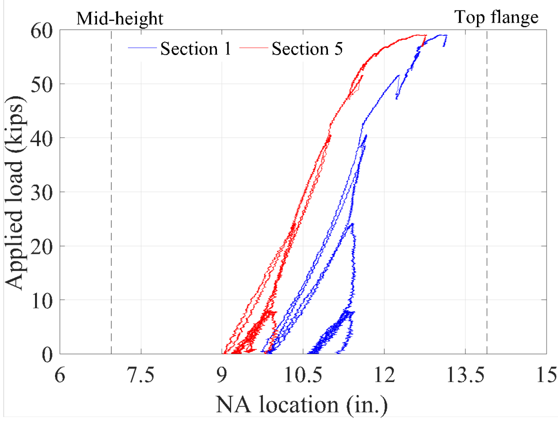

Sections 1 and 5

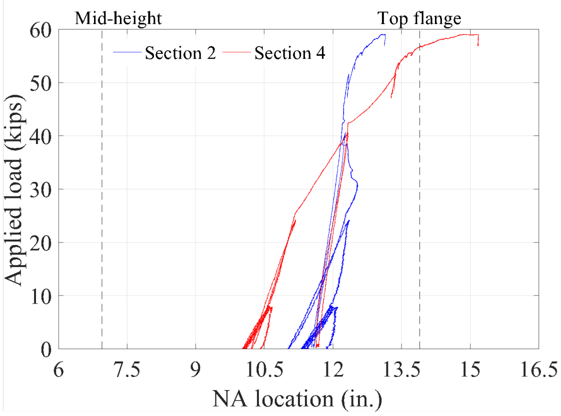

Sections 2 and 4

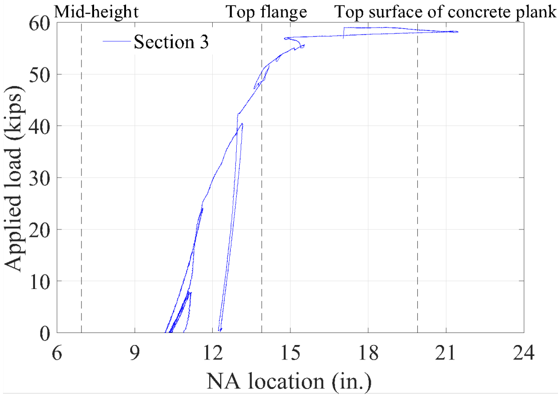

Section 3

Figure 5.61 Applied load versus neutral axis location in steel beam in Test 3-M20-3C-RL

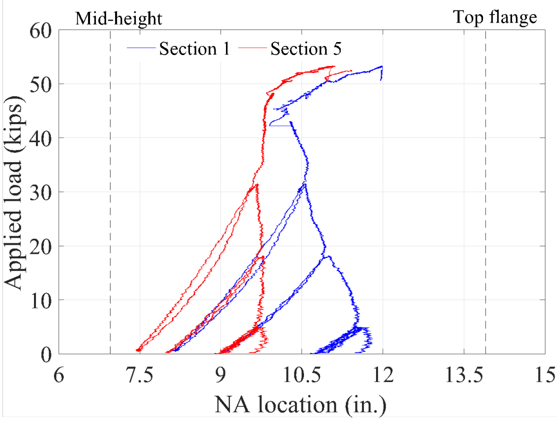

Sections 1 and 5

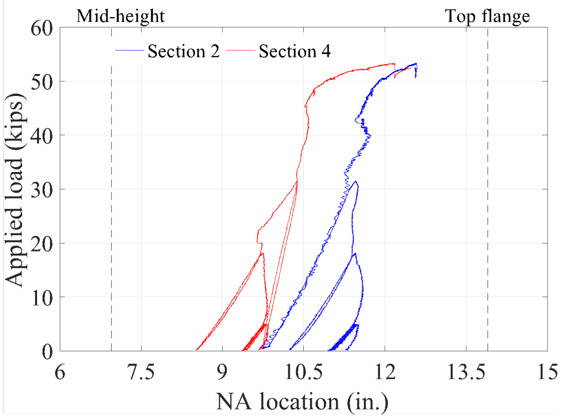

Sections 2 and 4

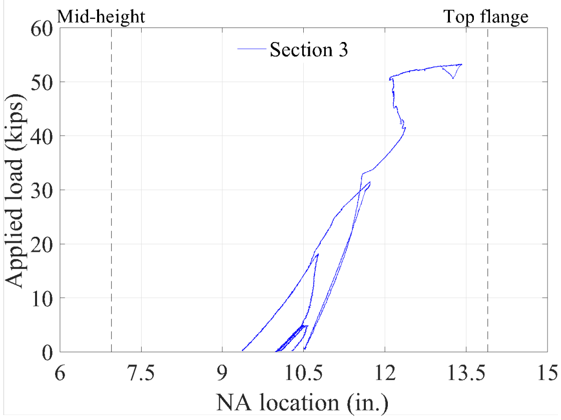

Section 3

Figure 5.62 Applied load versus neutral axis location in steel beam in Test 4-M20-1C-RL

5.6.4.3 *Load versus steel section strain*

The applied load versus steel section strain relationship is illustrated in Figure 5.63. The following can be observed:

- Beams 1: At sections 1 and 5, the compressive strains measured at the top flanges grow along with increasing load. Since the behavior of sections 1 and 5 is nearly elastic, the load versus bottom flange strain curves are almost linear throughout the test. The compressive strains at the top flanges of sections 2 and 4 first increase until the 80% cycle, then decrease, and eventually increase again. For section 3, the top flange strain first increases in compression until the 60% cycle, then decreases, and finally increases in tension, implying the NA has migrated above the bottom of the top flange. Because of the rapid increase in the readings of gages 4NBF, 3NBF, and 3SBF, curves 3BF and 4BF are different from the other curves. When the average bottom flange strain reaches 1063 με, the load versus 3BF curve exhibits a plateau. However, the load-center deflection curve does not exhibit clear nonlinearity at the same strain, which may imply that the yielding of the bottom flange is quite localized and has a minimal impact on the behavior of the beam.

- Beam 2: At sections 1 and 5, the compressive strains measured at the top flanges first increase and then decrease, while the strains of sections 2 and 4 increase throughout the test. The top flange strain of section 3 grows until 60 kips, and the subsequent variation is insignificant. The load versus 3BF curve is no longer linear when the average bottom flange strain exceeds 1020 με, but the load-center deflection curve still shows a linear relationship.

- Beam 3: For all the sections, the strains of the top flanges first increase in compression, and then decrease. At sections 1 and 5, the top flange strains remain compressive throughout the test, while tensile strains are eventually seen at the top flanges at the other sections, indicating the NA have risen above the bottom of the top flanges. For section 3, the curves for the other strains are similar, but the slopes are different since the strains increase at different rates. It is noticed that the bottom flange strain is occasionally smaller than the strains measured at the web.

- Beam 4: At all the sections, the compressive strains measured at the top flanges first increase and then decrease. At a strain of 1340 με at the bottom flange of the center section, the load versus 3BF curve is nonlinear. Meanwhile, the load-center deflection curve becomes nonlinear, which is probably initiated by yielding of the steel beam.

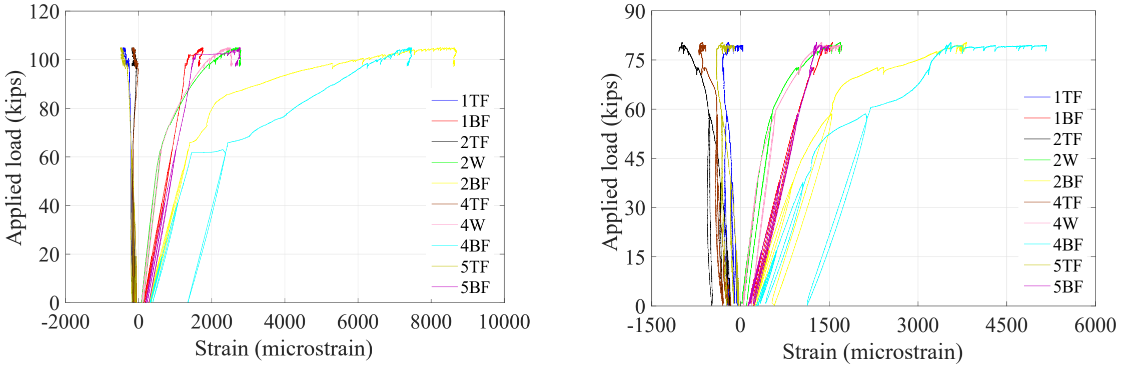

Sections 1, 2, 4, and 5

Sections 1, 2, 4, and 5

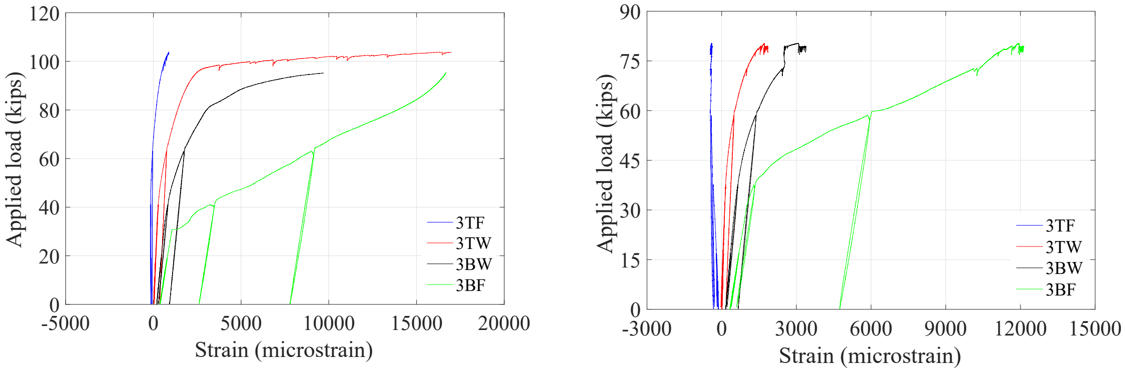

Section 3
Test 1-M24-2C-RH

Section 3
Test 2-M24-1C-RL

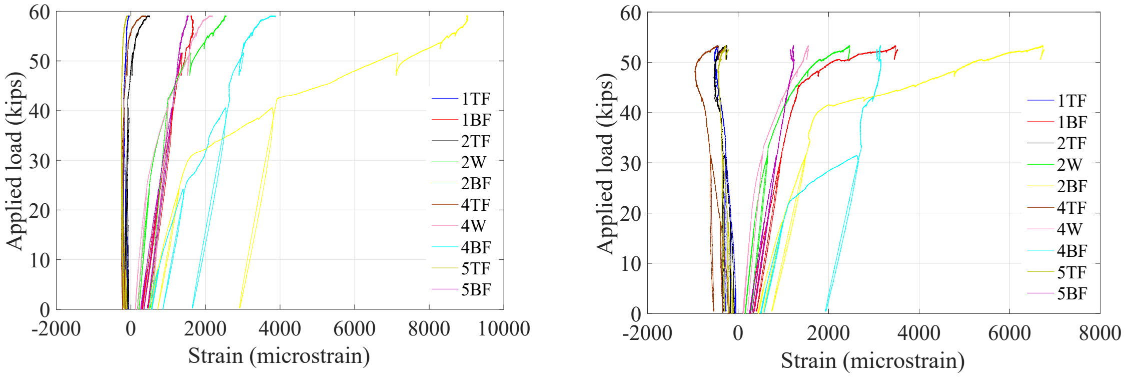

Sections 1, 2, 4, and 5

Sections 1, 2, 4, and 5

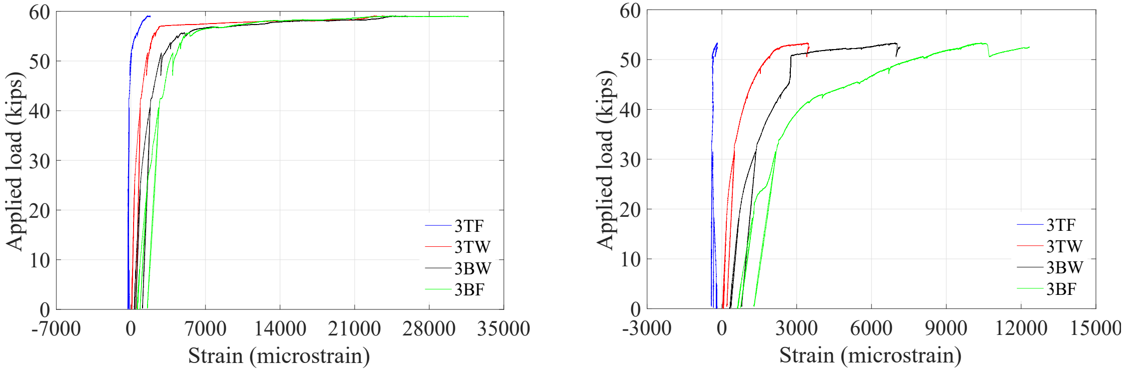

Section 3
Test 3-M20-3C-RL

Section 3
Test 4-M20-1C-RL

Figure 5.63 Applied load-steel section strain curves for beam specimens

5.6.4.4 *Verification of strain gage readings*

To estimate the internal forces of the composite beam sections, strain gages are attached along the depth of the steel sections. The strain gage readings can be verified by comparing the actual moment and the calculated moment at the gaged sections. The actual moment is the external moment produced by the actuator loading and solved by statics, and the calculated moment is the internal moment calculated using the axial strain measurements.

The internal axial force and bending moment of the beam sections attached with strain gages are determined as follows. The instrumented steel section was divided into a number of rectangular elements. Linear regression was performed using the strain measurements to find the best fitting line for the strain profile of the section. The strain at the centroid of a rectangular element was calculated from the linear equation, and the corresponding stress was found using the stress-strain curve established from material testing. Elastic unloading was presumed for any strain decrease. The internal axial force and bending moment at the steel section were derived by integrating the force and moment at each element. A different approach was adopted for calculating the internal axial force and bending moment in the concrete plank. Since force equilibrium was strictly satisfied at any cross section of the beam, the compressive force in the concrete plank was equal to the resultant tensile force in the steel beam. However, the location of the resultant compressive force in the concrete plank varied throughout the test and could not be readily determined. Therefore, as given in the parentheses in Figure 5.64 through Figure 5.67, the position of the compressive force was assumed, which contributes to the disparity between the calculated moment and actual moment in the plots. The inaccuracy in the assumed resultant force location only affects the calculated moment of the composite section, not the calculated axial force in the steel section. In addition, the measured strains from the gages were localized strains that may not approximate the strain distribution of the whole gaged section. Despite these limitations, the calculated moment (internal moment) matches the actual moment (external moment) well throughout the tests, particularly for small loading, validating the readings of the strain gages. More details can be found in Appendix F.2.6.

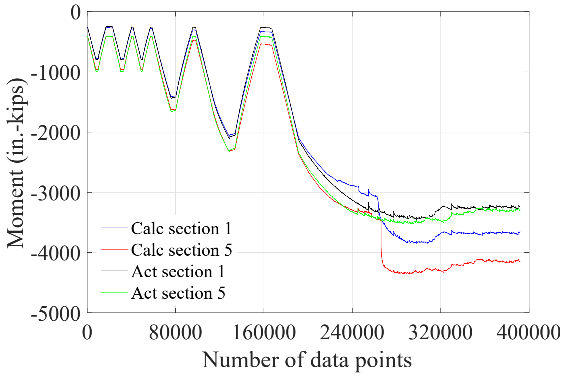

Sections 1 and 5 (mid-height)

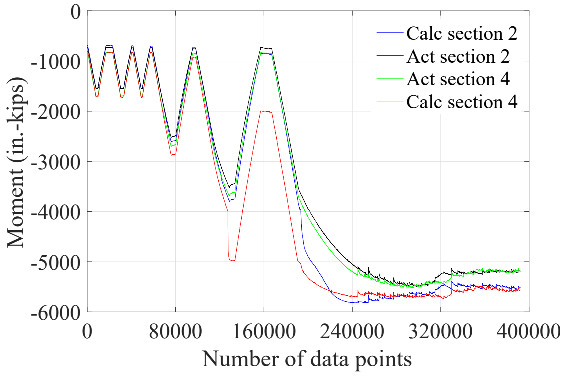

Sections 2 and 4 (top)

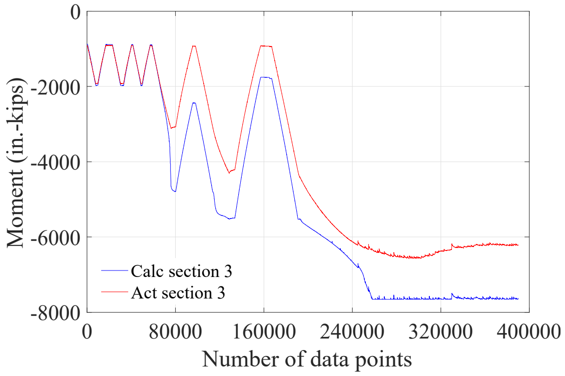

Section 3 (top)

Figure 5.64 Actual moment versus calculated moment in Test 1-M24-2C-RH

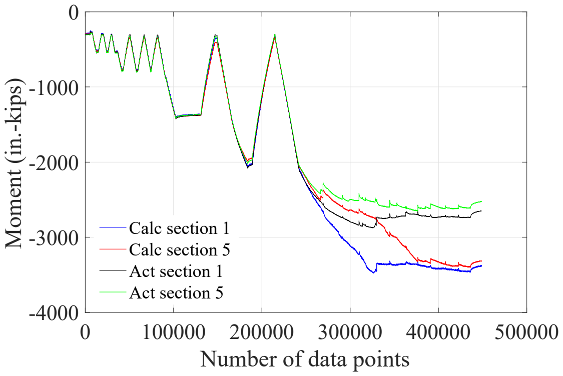

Sections 1 and 5 (mid-height)

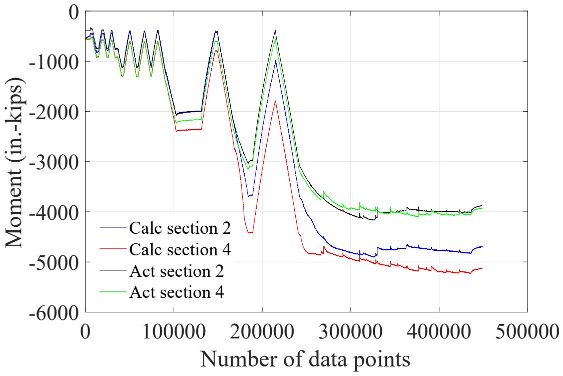

Sections 2 and 4 (top)

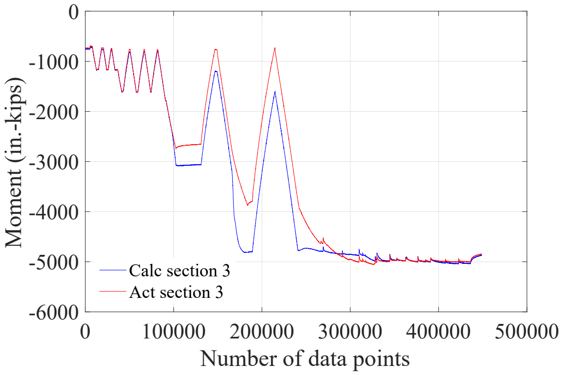

Section 3 (top)

Figure 5.65 Actual moment versus calculated moment in Test 2-M24-1C-RL

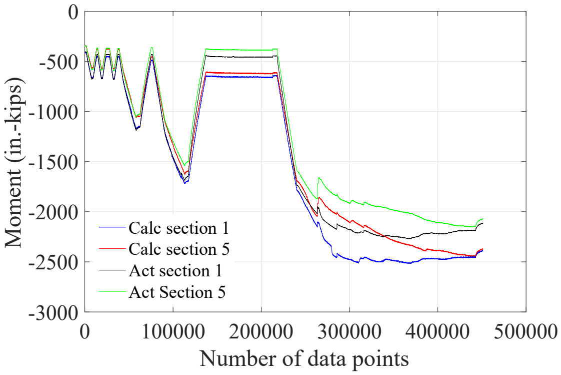

Sections 1 and 5 (mid-height)

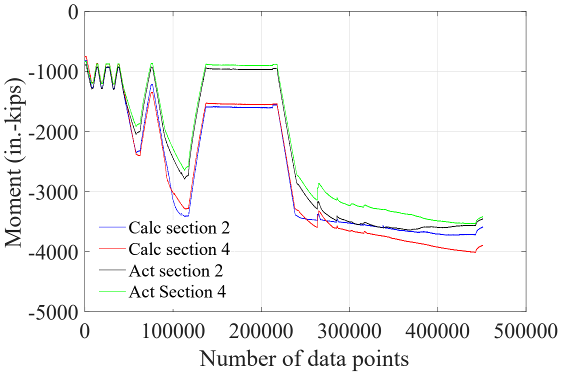

Sections 2 and 4 (top)

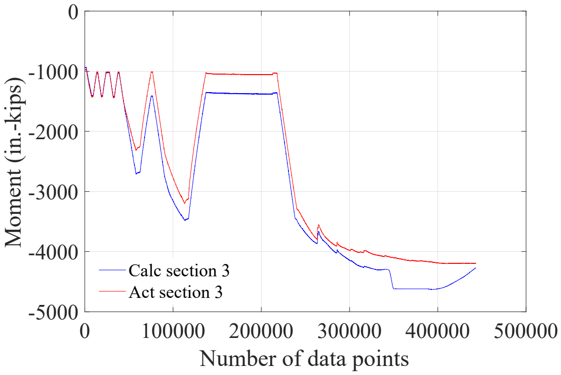

Section 3 (top)

Figure 5.66 Actual moment versus calculated moment in Test 3-M20-3C-RL

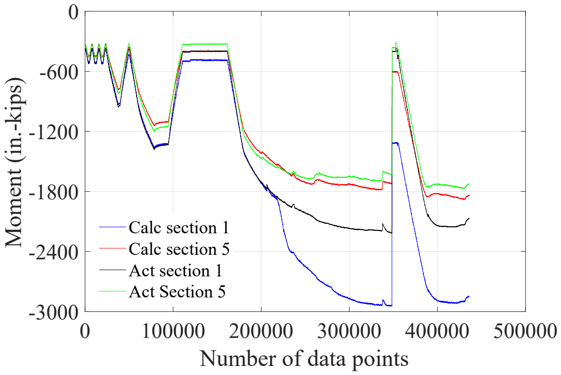

Section 1 (mid-height)

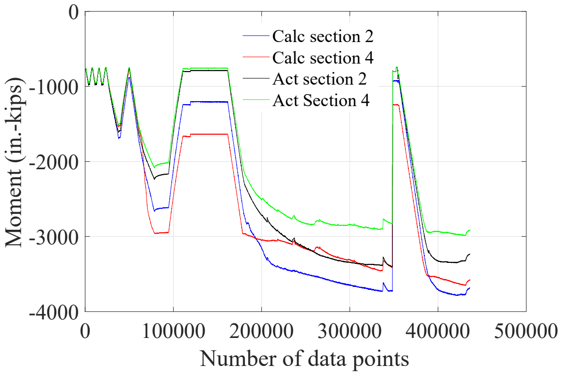

Section 2 (top)

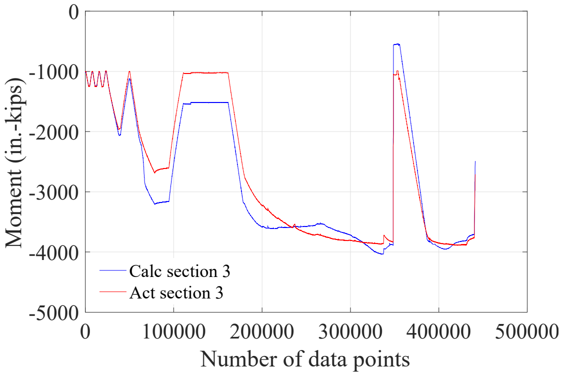

Section 3 (top)

Figure 5.67 Actual moment versus calculated moment in Test 4-M20-1C-RL

5.6.5 Bolt tension

In the pushout tests, it is shown that the bolt tension generally decreases as the slip between the steel beam and concrete plank increases. To demonstrate the behavior of the bolts in actual composite beams, uniaxial strain gages and rosette strain gages were attached on numerous bolts in each specimen. The results obtained in the beam tests are also used to verify the conclusions drawn from the pushout tests. Figure 5.68 shows the forces and resulting stresses the bolts are subjected to. The stress distribution is simplified and approximated using elastic theories, whereas the actual stress distribution is complex due to the inelastic behavior of the bolts. During bolt pretension, the applied torque generates both tension and torsion in the bolt shanks. The torsion depends on the tolerance and friction between the components (i.e., nut threads, bolt threads, washers, etc.). During the beam test, the bolts are under shear force transferred from the clamps, as illustrated in Figure 4.67 in Chapter 4. Hence, the forces the bolts are subjected to include axial tension, bending moment, shear and torsion. The bending moment is produced by the shear force as well as the torsion and asymmetric boundary conditions shown in Figure 4.53 in Chapter 4. Uniaxial strain gages measure the axial strain of the bolts due to the axial tension and bending moment, but the influences of the shear force and torsion are ignored. Rosette strain gages are thus utilized to account for the shear stresses. The comparison between the bolt axial stress results that account for the shear strain and the corresponding results that ignore the shear strain indicates that the calculated axial stress is usually a little smaller when considering the shear strain.

The applied load versus bolt tension response is shown in Figure 5.69 for the gaged bolts in the beam specimens. The load and bolt tension are also normalized relative to the peak strength of the specimen and the initial bolt tension, respectively. In Tests 1-M24-2C-RH and 2-M24-1C-RL, except for one bolt, the pretension force of all the bolts is above 46.1 kips (205 kN), which is the minimum bolt pretension for Group A M24 bolts in Table J3.1M in AISC 360-16. As discussed in Section 5.6.2.3, because of the deformation of the top steel flanges, the M20 bolts used with the planks from the third concrete pour could be inadequately elongated. As a result, the initial bolt pretension of several M20 bolts is below 31.9 kips (142 kN), which is the minimum bolt pretension for Group A M20 bolts in Table J3.1M in AISC 360-16 (2016). It is seen that the tension of all the bolts reduces along with increasing actuator loads. Compared to the bolts at the ends of the beams, the tension variation of the bolts close to the center of the beams is insignificant. The tiny slip of the middle clamps justifies the slight tension change of the center bolts. This conclusion is also substantiated by the negligible tension variation of all the bolts in Test 3-M20-3C-RL.

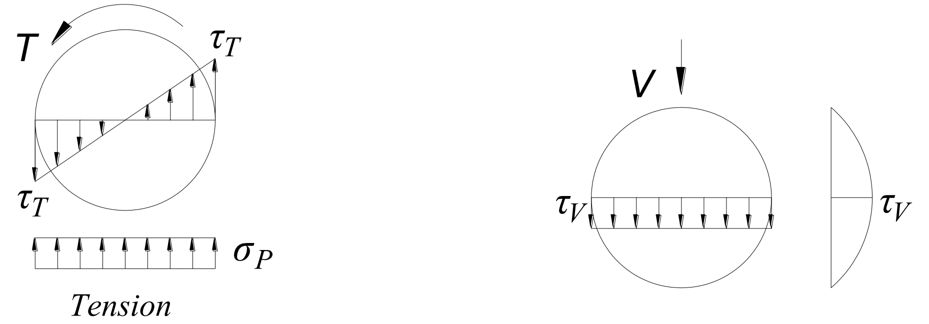
T
τT
τT
σP
Tension
V
τV
τV

Torsion due to bolt pretensioning

Shear force transferred from clamps

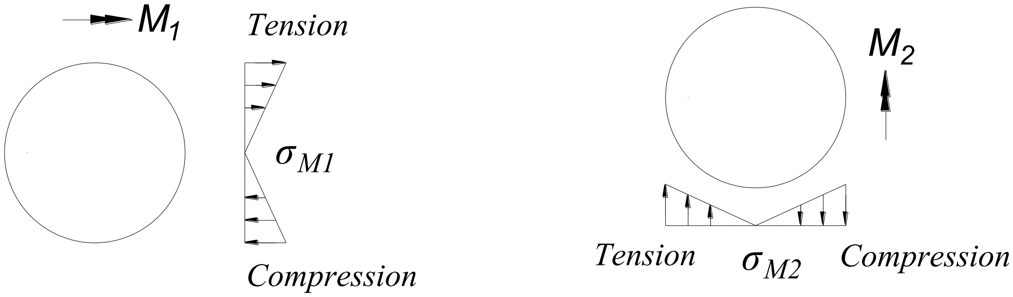
M1
Tension
σM1
Compression
M2
Tension
σM2
Compression

Bending moment due to shear force and asymmetric boundary condition

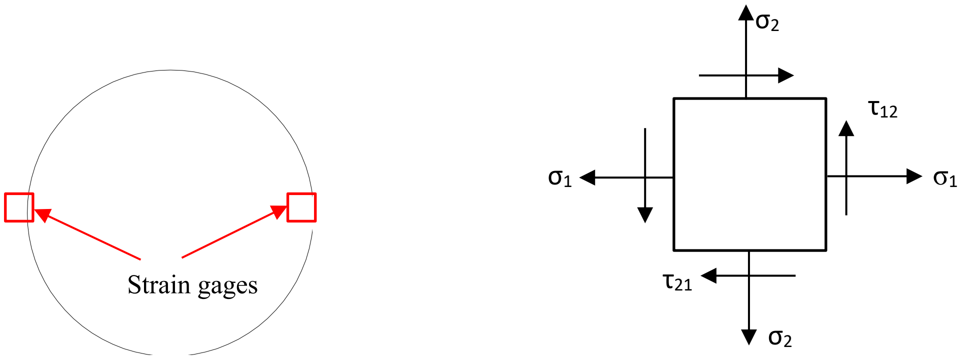
Strain gages
σ2
τ12
σ1
σ1
τ21
σ2

σ_2 could be generated by T, M_1 and M_2; τ_{12} could be generated by T and V;

Stress state of an infinitesimal element at the gaged locations

Figure 5.68 Force and stress distribution in bolt shank

Since the required flexural strength of a beam at full service loading is approximately 56% ~ 75% of the flexural capacity of the beam, the ratio of the bolt tension at serviceability to the initial bolt tension is larger than 0.9 for all the specimens, except for three bolts in Test 4-M20-1C-RL, as demonstrated in Figure 5.69. In all the graphs that designate service loading, the dashed lines do not correspond to 0.56 and 0.75, since the self-weight of the specimens is excluded from the applied actuator loading. In Test 4, as shown in Figure E.46 in Appendix E, one of the two gages attached on bolts 2TEN, 2TES and 2TWS debonded. For the two gages attached on the bolt, it is commonly seen that the reading from the gage close to the steel beam varies throughout the test, while the measurement from the gage away from the steel beam stays almost the same. Therefore, compared to using the average gage measurement as the bolt axial strain, the reduction of the bolt axial stress could be overestimated for bolts 2TEN, 2TES and 2TWS, since the functioning gages on these bolts are close to the steel beam and the axial strain readings of these gages decrease during the tests. Similar to the insignificant bolt tension reduction at small slips (around 0.02 in.) in the pushout tests, the tension of the bolts in the beam specimens reduces slightly at serviceability because the slip of the clamps is insignificant under unfactored loads.

In Test 1-M24-2C-RH, clear plateau regions are not seen in most of the curves illustrated in Figure 5.70. The slip at the instrumented bolts ranges from 0.15 in. to 0.22 in., and the bolt tension reduction varies from 15% to 30%. Several curves in Test 2-M24-1C-RL begin to level off. At a slip of 0.3 in., the pretension of some bolts decreases as little as 10%. Some curves plateau at slips much smaller than 0.3 in. In general, the pretension loss of the instrumented bolts is less than 25%. As would be expected in Test 3-M20-3C-RL, because the slip of the clamps is less than 0.02 in., the bolt tension reduction is around 5%. As for Test 4-M20-1C-RL, except for bolts 2TEN and 2TWS where only one of the two uniaxial strain gages displays proper readings, the pretension loss of the instrumented bolts is less than 25%. Figure 4.65 in Chapter 4 illustrates that when the frictional coefficient is 0.35, the bolt tension reduction has not plateaued at a slip of approximately 0.3 in., and the bolt tension is about 70% of the initial bolt pretension at this slip. These results from the FE analysis for the pushout tests are similar to the observations for the bolts in the beam tests.

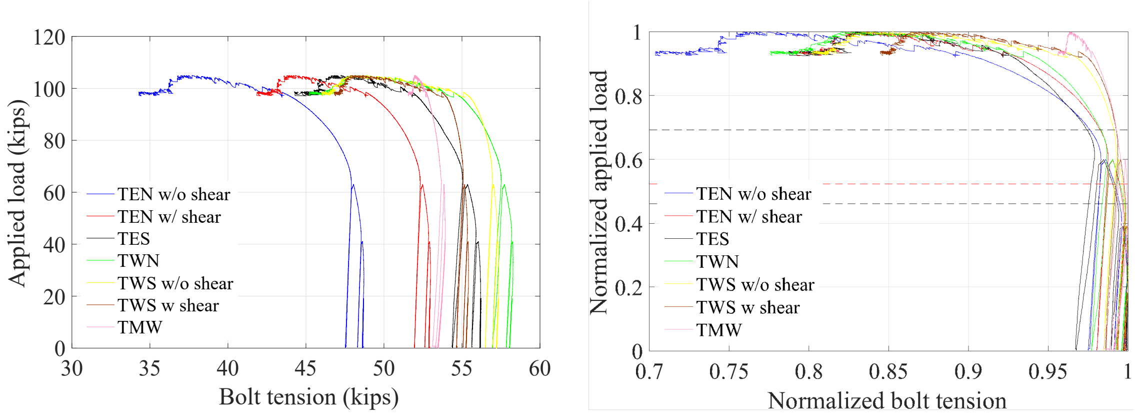

Test 1-M24-2C-RH

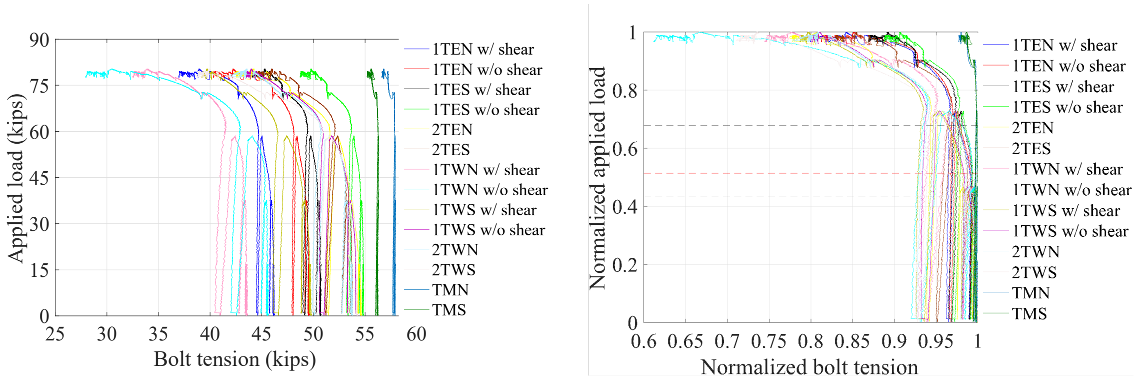

Test 2-M24-1C-RL

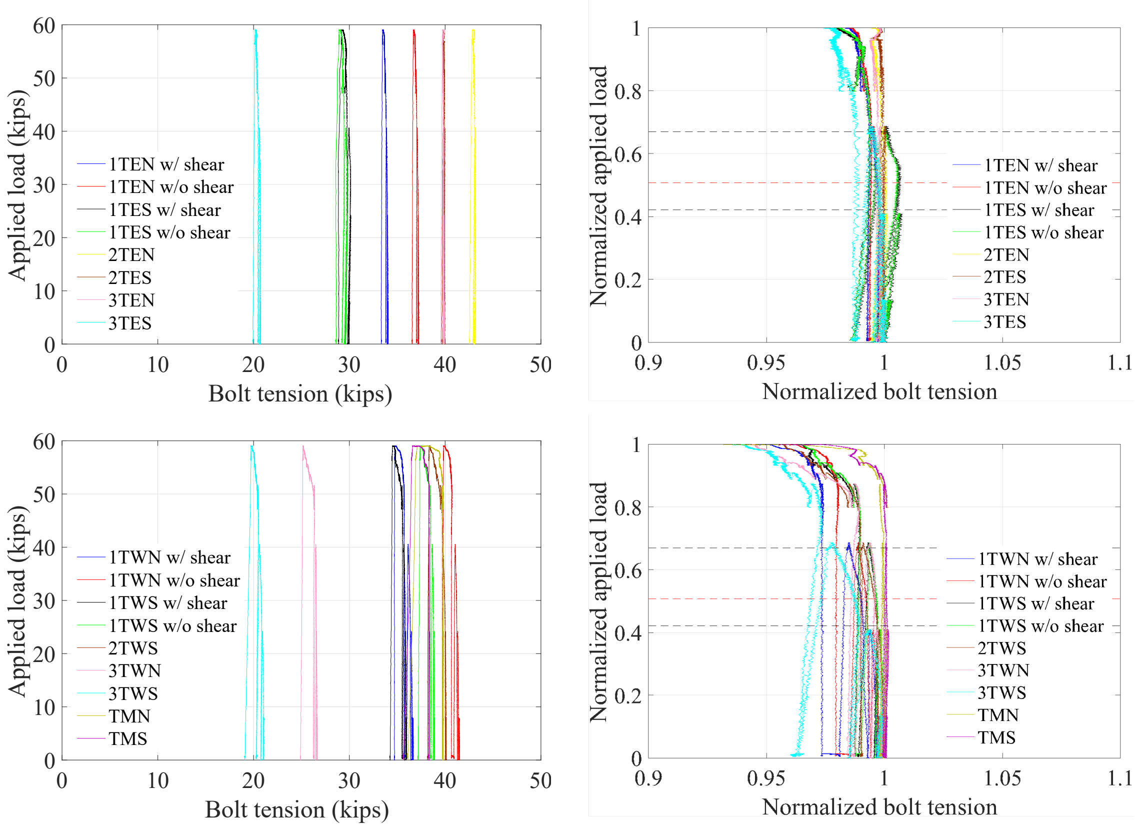

Test 3-M20-3C-RL

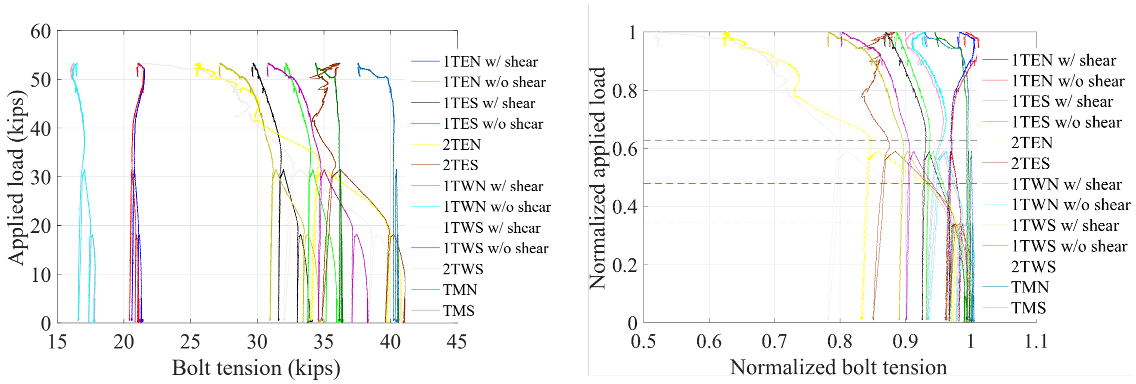

Test 4-M20-1C-RL

Note: If the beam is strength-controlled and efficiently designed, the two black dashed lines in the normalized applied load versus normalized bolt tension graphs illustrate the range of the full service loading, and the red dashed line indicates the full service loading when the dead load is 92.5 psf, as is used in the prototype structrues in Chapter 3.

Figure 5.69 Applied load versus bolt tension response for the beam specimens

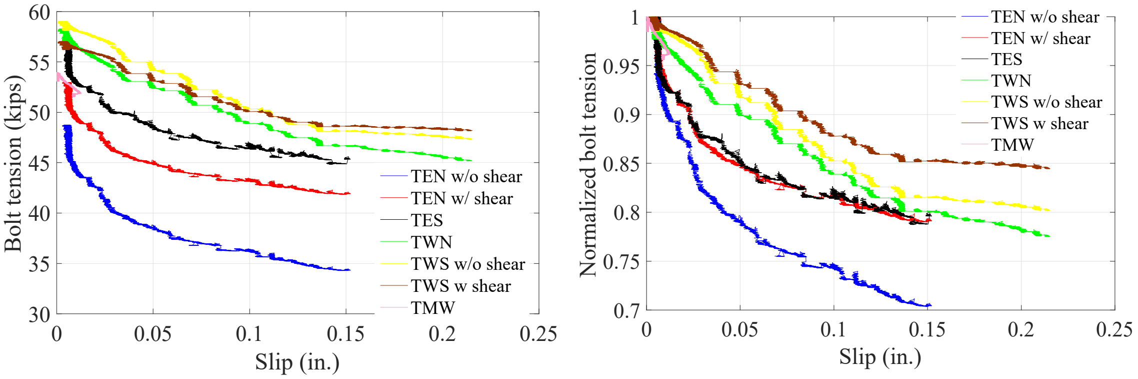

Test 1-M24-2C-RH

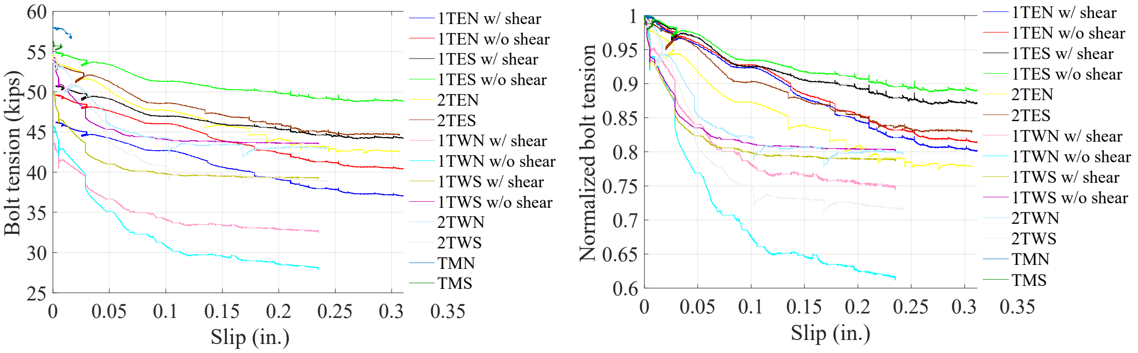

Test 2-M24-1C-RL

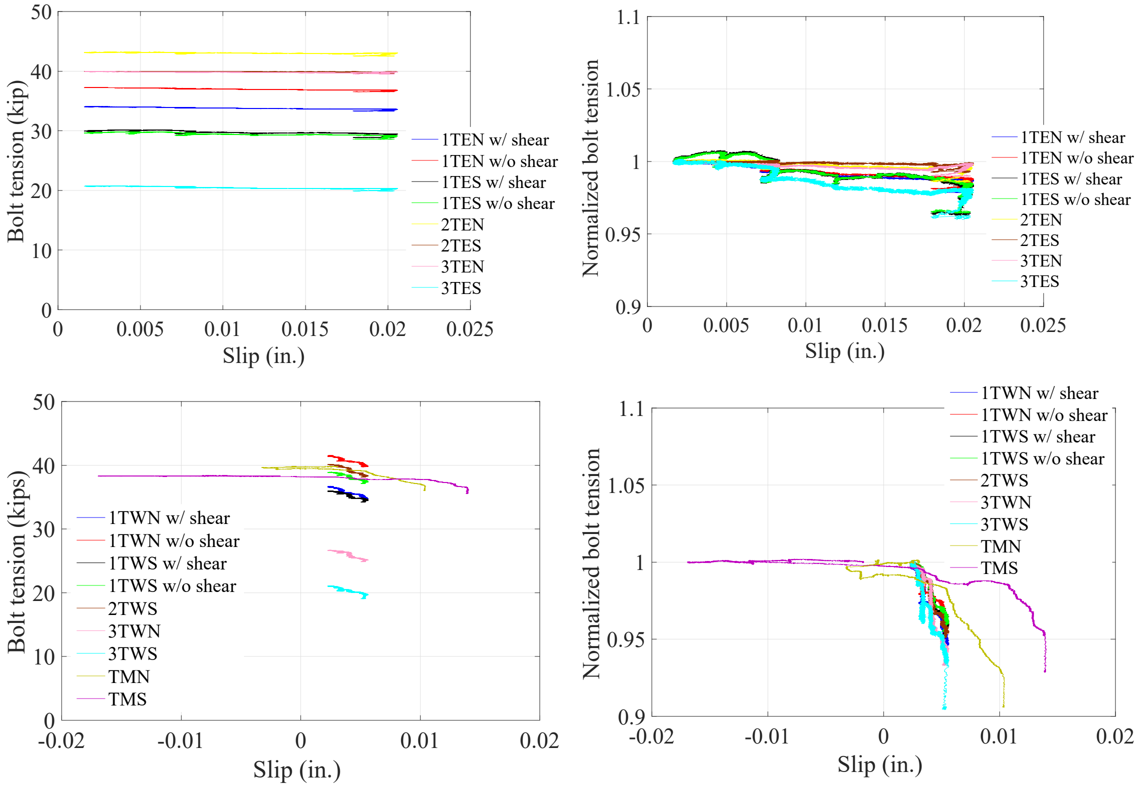

Test 3-M20-3C-RL

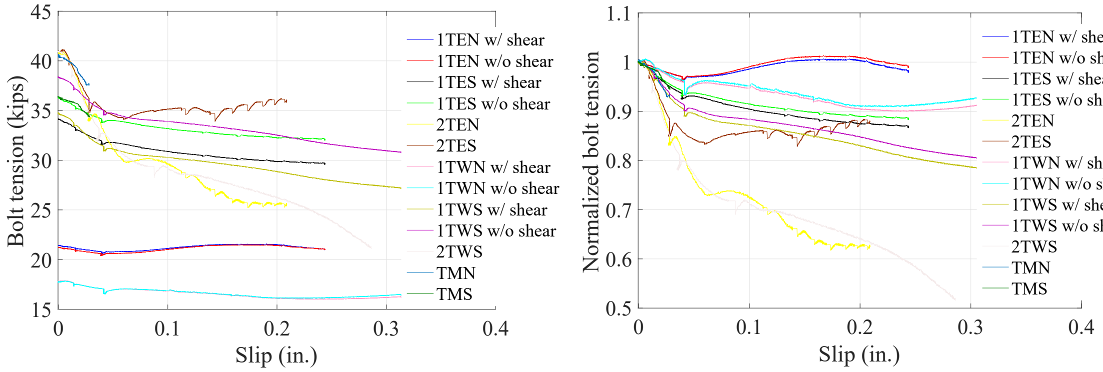

Test 4-M20-1C-RL

Figure 5.70 Bolt tension versus slip response for the beam specimens

5.6.6 Rod tension

The applied load versus rod tension relationship is depicted in Figure 5.71. In general, the tension of the rods decreased throughout the tests. For the rods connecting planks that did not exhibit crushing, minor tension reduction was seen, whereas the tension reduced more pronouncedly in the rods that connected heavily crushed concrete planks. As shown in Figure 5.17, the localized compressive stress between adjacent concrete specimens might have led to premature concrete crushing that was observed in the beam tests. Therefore, the rod tension reduction could be less if the planks had better quality control. Since the ASTM A36-14/A529-05 Grade 50 rods utilized in the beam specimens were yielded after pretensioning, any elongation has little effect on the tension variation of the rods, but a small amount of shortening during the test could decrease the axial force substantially. Hence, concrete crushing has a significant impact on the rod tension variation. Figure 5.72 shows the deformation of the rod spanning the west inner loading point section in Test 1-M24-2C-RH. The rod was bent to accommodate the rotation of the plastic hinge, which could release the axial deformation and reduce the tension.

According to the experimental results, the performance of the deconstructable composite beams was not affected by the behavior of the rods which were designed to resist diaphragm forces. The loss of rod tension under unfactored gravity loading (or service loading) may release the normal force between adjacent concrete planks and thus decrease the in-plane seismic resistance of the system. Nonetheless, because of the bending of the composite beams under gravity loading, additional compression is generated between the concrete planks, which could possibly compensate for the reduction of the capacity to resist diaphragm forces in the floor system.

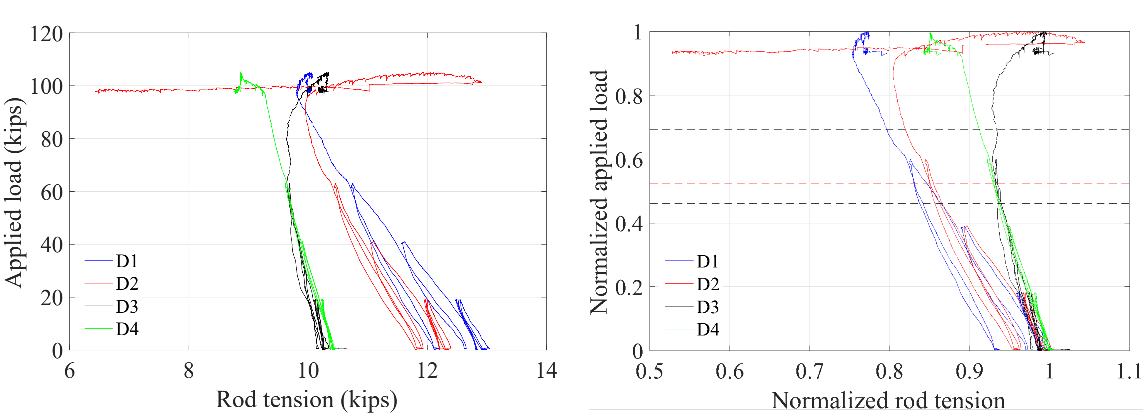

Test 1-M24-2C-RH

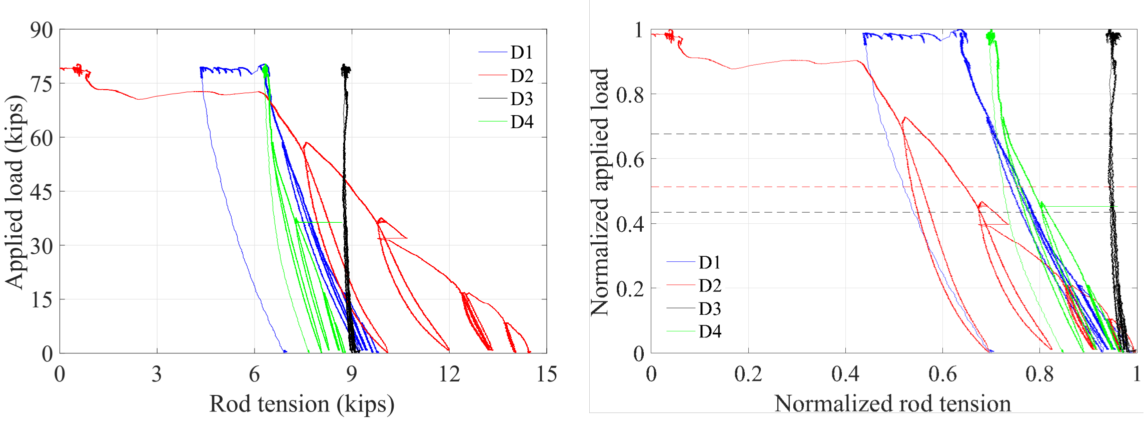

Test 2-M24-1C-RL

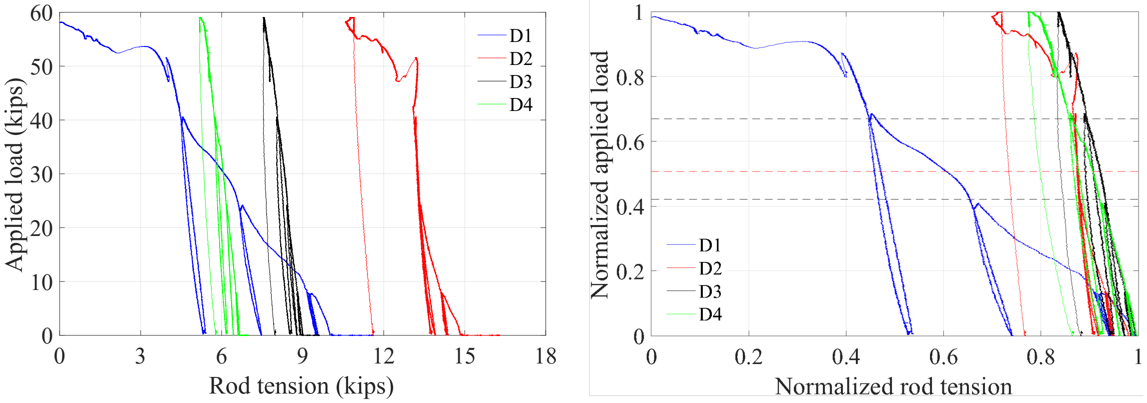

Test 3-M20-3C-RL

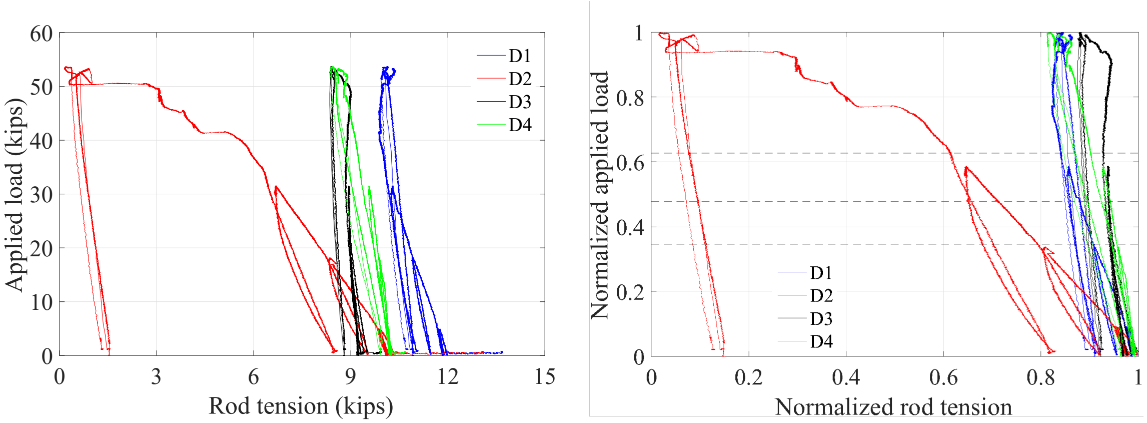

Test 4-M20-1C-RL

Note: If the beam is strength-controlled and efficiently designed, the two black dashed lines in the normalized applied load versus normalized bolt tension graphs illustrate the range of the full service loading, and the red dashed line indicates the full service loading when the dead load is 92.5 psf, as is used in the prototype structrues in Chapter 3.

Figure 5.71 Applied load versus rod tension

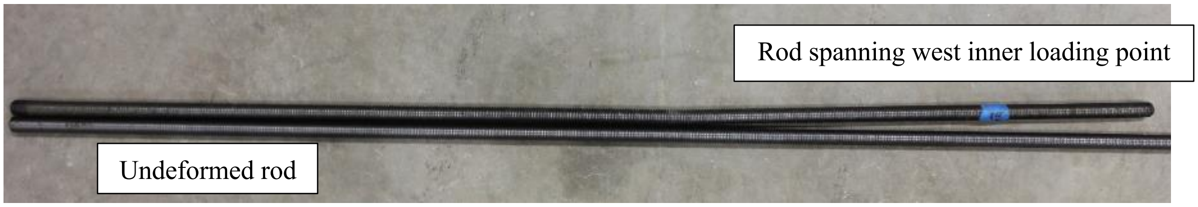

Figure 5.72 Deformation of fully threaded rod in Test 1-M24-2C-RH

5.6.7 Response of channel anchors and reinforcement

In Test 2-M24-1C-RL, several channel anchors were instrumented with rosette strain gages to estimate the tensile and shear forces acting on the anchors. By comparing Figure 4.48 and Figure 5.73, it is noted that the channels embedded in the beam specimens are different from those cast in the pushout specimens in terms of length and anchor layout. Appendix F.1.3 provides details on the calculation of the tensile and shear stresses, and the results are shown in Figure 5.74. The forces the anchors were subjected to can be calculated by multiplying the stresses with the cross-sectional area of the anchors, which equals to 0.372 in.^{2}. The anchors were mainly under tensile forces which generally did not vary much throughout the test. The shear forces transferred to the anchors were insignificant, which justifies the statement in the Eurocode 2 (CEN 2009) that the majority of the shear force acting on the anchor channels is transferred to concrete directly through channel bearing, and only a small fraction flows into the anchors via bending of the anchors. As expected, the normal force perpendicular to the anchor tension was negligible. In all the beam tests, anchor-related concrete failure modes did not occur.

As discussed in Section 4.5.9 in Chapter 4, a two–dimensional plane stress state, which is assumed for the channel anchors, may be invalidated because of the out-of-plane forces that generate bending of the anchors with respect to their weak axes. However, the variations of the measured anchor stresses throughout Test 2-M24-1C-RL appear to indicate that the anchors were indeed in a plane-stress state and the out-of-plane deformation of the channel anchors could be insignificant. In future investigation, two strain gages, which are attached on both sides of the channel anchors, could be used to rule out the influences of the out-of-plane deformation of the channel anchors.

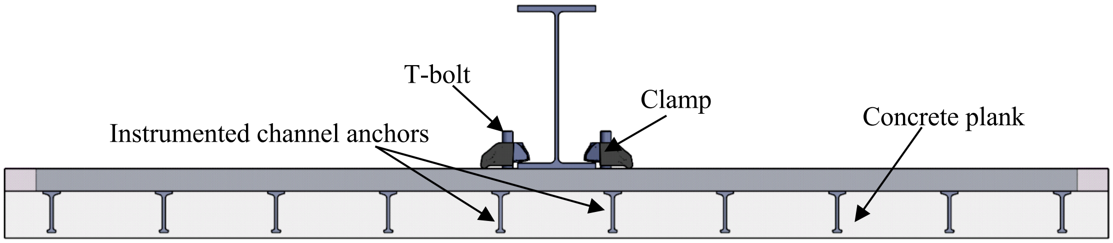

Figure 5.73 Channel anchor and bolt positions in a beam test specimen

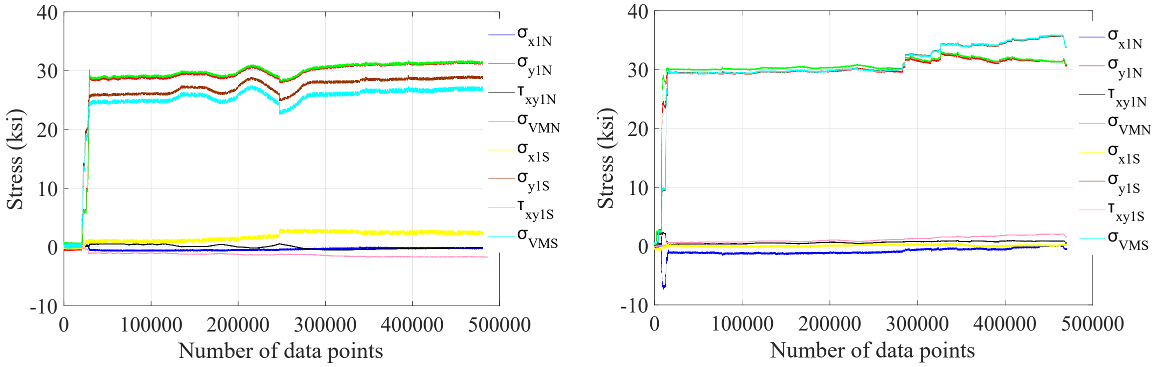

West end plank

Center plank

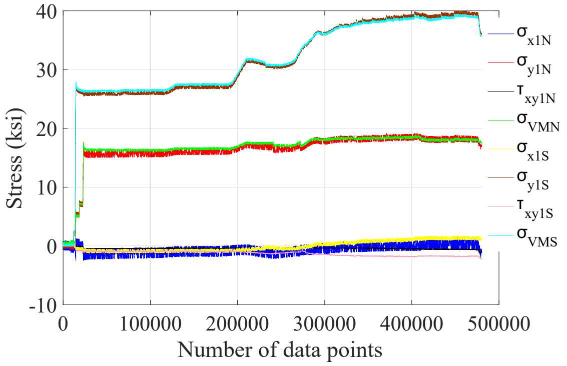

East end plank

Note: σ_y *describes the normal stress along the axial direction of the anchor;* σ_x *indicates the normal stress perpendicular to the axial direction of the anchor;* τ_{xy} *represents the shear stress acting on the anchor.*

Figure 5.74 Channel anchor stress in beam 2-M24-1C-RL

As shown in Figure E.49 in Appendix E, all the reinforcement is elastic throughout the tests. Using the measured transverse reinforcement strains, the curvature of the planks in the transverse direction can be determined. The strain profiles are then extrapolated to the top surfaces of the concrete planks and compared to the compressive strains measured at the center of the planks by linear potentiometers. Figure 5.75 illustrates the comparison of the concrete compressive strains determined using these two methods. The disparities may be attributed to the following: (1) the strain gages have a better resolution than the linear potentiometers for measuring very small deformation; (2) nominal transverse reinforcement locations were used in the calculations, while the actual positions of the bars may differ; (3) the plane section assumption used to extrapolate the strain profile is not entirely valid throughout the test; (4) the bond between the transverse reinforcement and the surrounding concrete may fail, underestimating the actual concrete strain. As a result, it is difficult to determine whether the strain gages give a better estimate at the beginning of the test, but the readings from the linear potentiometers may be more reliable at relatively large deformations.

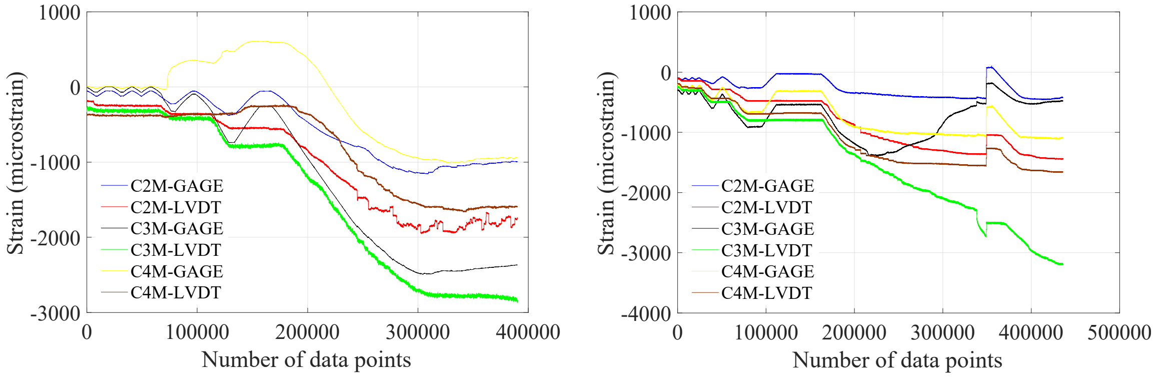

Test 1-M24-2C-RH Test 4-M20-1C-RL

Figure 5.75 Concrete compressive strain comparison

5.6.8 Effective width

When a composite beam is under flexure, the concrete slab is subjected to combined in-plane normal stress and shear stress. The existence of the shear stress and shear strain invalidates the plane section assumption, and the normal stress distribution along the width of the slab is no longer uniform. This phenomenon is called shear lag. The concept of effective width is thus utilized to account for shear lag and simplify beam design.

The effective width is commonly defined using Equation (5.19) and depicted in Figure 5.76. Because the effective width is dependent on the stress distribution along the width of the slab, it could change with the loading, especially after the beam deviates from being elastic.

$$b_{eff} = \frac{\int_{-b/2}^{b/2} \sigma dx}{\sigma_{max}} \tag{5.19}$$

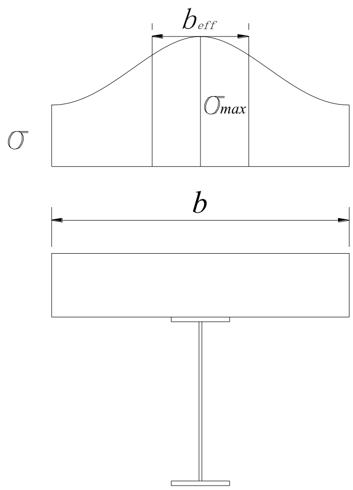

Figure 5.76 Effective width of a composite beam

Recent studies on conventional composite beams utilizing shear studs have demonstrated that the effective width of a composite beam is greater at the ultimate state than at the serviceability condition, and it can almost be taken as the whole slab width (Amadio et al. 2002, 2004). The effective width of a concrete slab for computing the nominal flexural strength of a composite beam is defined in the AISC Specification (AISC 2016a) as the sum of the effective widths for each side of the beam centerline. Each of the effective widths is the smallest of:

(1) 1/8 of the beam span
(2) 1/2 of the distance to the centerline of the adjacent beam
(3) the distance to the edge of the slab

As mentioned in Section 5.4, the concrete strains were measured with linear potentiometers rather than strain gages. The concrete strains were calculated by dividing the displacement measurements with the gage length (i.e., 8 in.). It should be noted that linear potentiometers are less accurate than strain gages at very small deformation, but strain gages could malfunction if concrete cracking or crushing occurs at the instrumented region. The longitudinal strain distribution along the width of the center concrete plank is depicted for each beam specimen in Figure 5.77. The strain distribution patterns are similar in all the graphs. The compressive strains in the middle of the planks are larger than those near the ends of the planks. It is also seen that the strain increase is faster in the middle than at the ends of the planks. At the last load level shown in the legends of the plots, the strain distribution is far from being uniform.

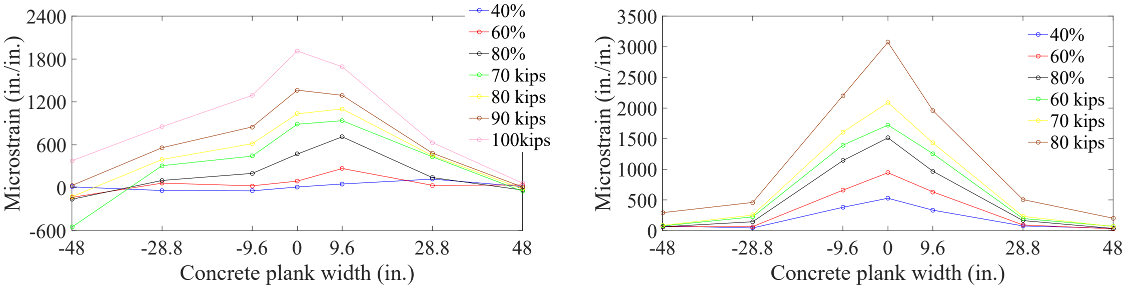

a) Test 1-M24-2C-RH b) Test 2-M24-1C-RL

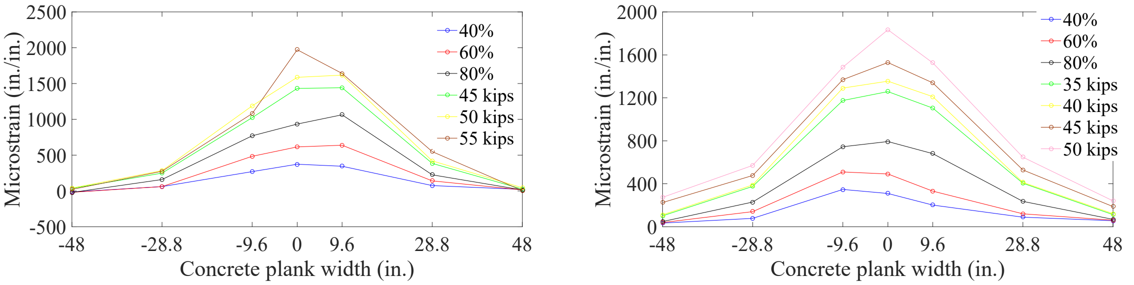

c) Test 3-M20-3C-RL d) Test 4-M20-1C-RL

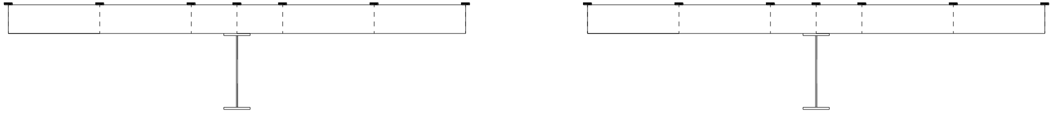

Note: The loading shown in the legends represents the applied actuator loading.

Figure 5.77 Longitudinal strain distribution on the top surfaces of center concrete planks

After the strain distribution along the width of the plank is known, the stress distribution can be calculated accordingly, and the effective width of the concrete plank can be evaluated with Equation (5.19). With the measurements from discrete locations, the effective width of the center concrete plank of the composite beams is calculated using Equation (5.20). More details can be found in Appendix F.2.4.

$$b_{eff} = \frac{(\sigma_{NT1} + \sigma_{ST1} + \sigma_M) \times 9.6 + (\sigma_{NT2} + \sigma_{ST2}) \times 19.2 + (\sigma_{NT3} + \sigma_{ST3}) \times 14.4}{\sigma_{max}} \quad (5.20)$$

The stress results show that the maximum compressive stress does not always occur in the middle of the slab. The stress distribution in Figure 5.76 is more likely to be achieved in a monolithic concrete slab. In the deconstructable composite beams in which precast concrete planks are used, the force flow and the stress distribution also depend on the contact between the planks. The applied load versus effective width relationship is provided in Figure 5.78. The following conclusions can be drawn:

(1) In the first two tests, during the loading/unloading cycles, the effective width decreases when the beam is loaded, and increases when the load is removed. When the cycles are completed and the beam is reloaded with increasing deflection, the effective width first reduces and then increases. The effective width of Beam 3-M20-3C-RL does not change much throughout the test. The result for Test 4-M20-1C-RL is unique among all the graphs in that the effective width increases as the beam is loaded, and stays the same when the beam is unloaded.

(2) At large deflections, the effective widths of all the beam specimens increase along with increasing deflections. As the gaps between adjacent concrete planks were closed when the beams deflected substantially, more concrete could be involved in resisting compression. Force redistribution, for example, due to concrete crushing, could also happen which distributes the compression in a concrete plank to a larger width.

(3) The effective widths of the beam specimens are smaller than the width given in the AISC Specification (AISC 2016a), which is 90 in., 1/4 of the beam span. This is because the compressive force between adjacent concrete planks cannot flow through gaps. As shown in Figure 5.19, gaps are common at the ends of a plank; consequently, the compression at the ends of the plank is nonexistent until the gaps are closed.

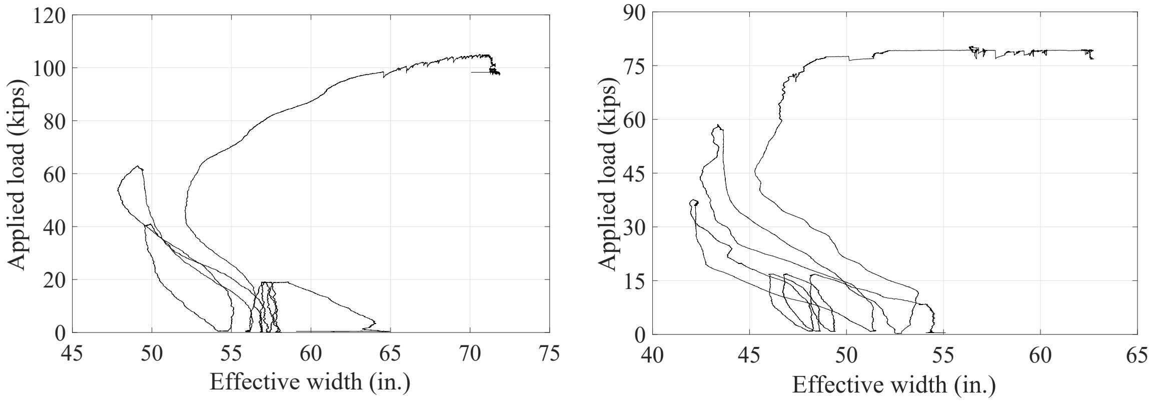

Test 1-M24-2C-RH

Test 2-M24-1C-RL

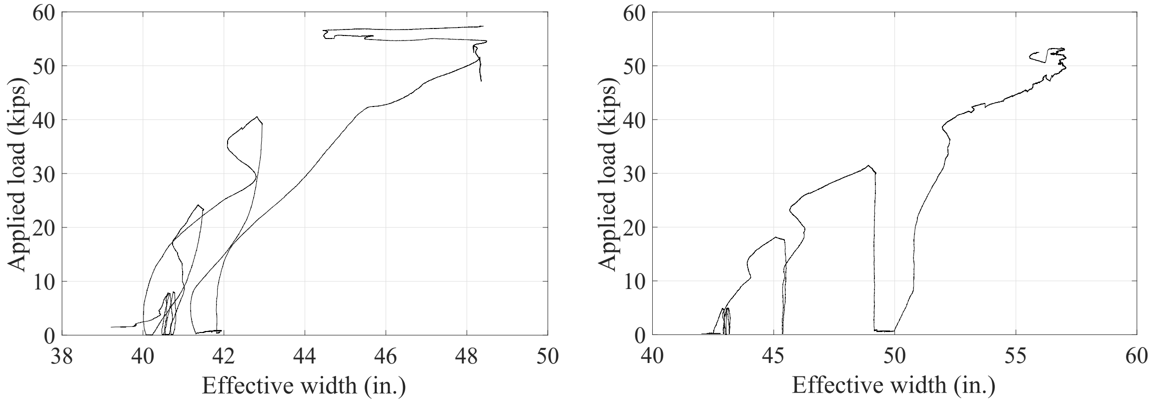

Test 3-M20-3C-RL

Test 4-M20-1C-RL

Figure 5.78 Applied load versus effective width for all the specimens

Conceptually, when determining the flexural strength of a composite beam, the selected effective width should be larger than that used for elastic stiffness calculation, since the former is determined for the ultimate state of the beam, and the latter is calculated while the beam behaves elastically. Using W14x38 and W14x26 as examples, the plots in Figure 5.79 indicate that assuming the beams are fully composite, when the effective width of the concrete slab is 96 in., the strength and stiffness are approximately 15% ~ 20% larger than those determined with 24 in. effective width, but the differences are around 5% when 48 in. is employed. The differences also reduce when the degree of composite action of the beam decreases. When the effective width is 24 in., the compressive strength of the slab is 612 kips ($0.85f'_c A_c$), which is 9.3% and 59.2% larger than the tensile strength of the W14x38 and W14x26 sections, respectively. Hence, if the compressive strength of the slab is significantly larger than the tensile strength of the steel beam and the shear strength of the shear connectors, different effective widths have minimal impacts on the calculated strength and stiffness of the beams, which may justify the use of the same effective width for both strength and stiffness calculations. In addition, it is illustrated that the ultimate flexural strengths of the composite beams are not very sensitive to the degree of shear connection. This explains why it is problematic to back-calculate the strength of shear connectors from the tested flexural strengths of composite beams. For simplicity, it could be suggested that the effective width calculation in AISC 360-16 (2016) be utilized for the deconstructable composite beam specimens, as using the AISC effective width provisions results in a good estimate of the ultimate flexural strengths of the beam specimens.

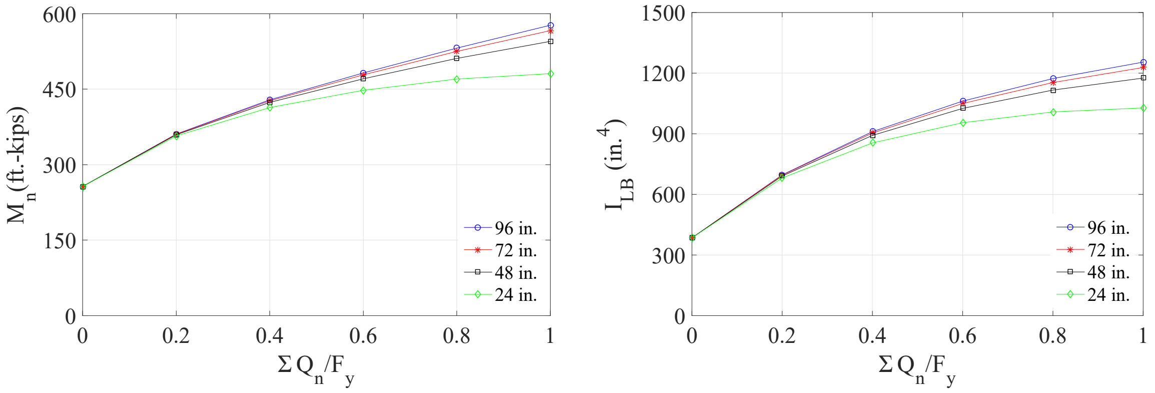

Strength Stiffness

W14x38

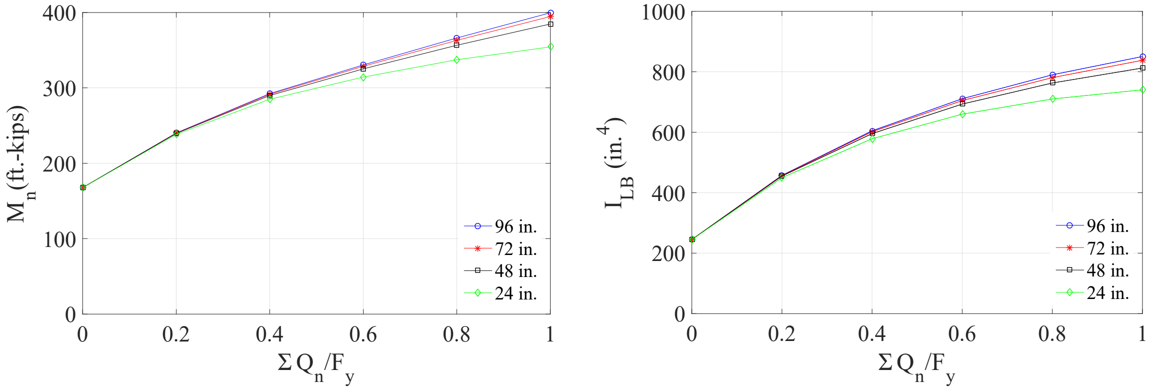

Strength Stiffness

W14x26

Note: f_y=50 ksi; f_c'=5 ksi; t=6 in.

Figure 5.79 Effects of slab width on the strength and stiffness of composite beams

Since the effective widths of the deconstructable composite beams are affected by the contact between the planks, construction tolerances play an important role in distributing the compression across the concrete planks. Future investigation necessitates use of planks with tongue-and-groove joints and with qualities comparable to those manufactured in a precast concrete plant.

5.6.9 Behavior of clamping connectors in pushout tests and beam tests

The performance of the shear connectors tested in the pushout tests and beam tests should be correlated so as to validate the effectiveness of using pushout tests to investigate the behavior of shear connectors. For the beam specimens, after the axial forces are calculated for the steel sections attached with strain gages, the resultant shear resistance of the clamps between two gaged steel sections is equal to the difference of the net tension at these two sections. Hence, the average clamp shear in this region, $\bar{Q}_i$, can be determined as the normal force difference, ΔF_i , divided by the number of shear connectors n_i. The average slip the clamp undergoes, Δ_i, is taken as the mean of the slip measurements in this region. Using Beam 1 as an example, the calculation of the average shear resistance and average slip is illustrated in Figure 5.80. However, this calculation is questionable for regions 3 and 4 in two aspects. First, it is assumed that zero slip occurs at the center of the beam, which is not entirely correct throughout the test. Usually, the maximum moment section, which is one of the two inner loading point sections, is regarded as a zero slip location, and the reversal of the slip direction occurs at this section. Second, the average slip calculation is also problematic for the two regions, since the measurements from S5 and S6 are much smaller than those from S4 and S7.

The applied load versus shear resistance per connection is shown in Figure 5.81. Regions 3 and 4 are not included in the graphs. In all the plots, the shear resistance of the clamps in regions 1 and 6 which are close to the end supports increases throughout the tests, while the resistance of those in regions 2 and 5 generally increases until the 80% cycle and then reduces, implying shear force redistribution from the inner clamps to the outer clamps.

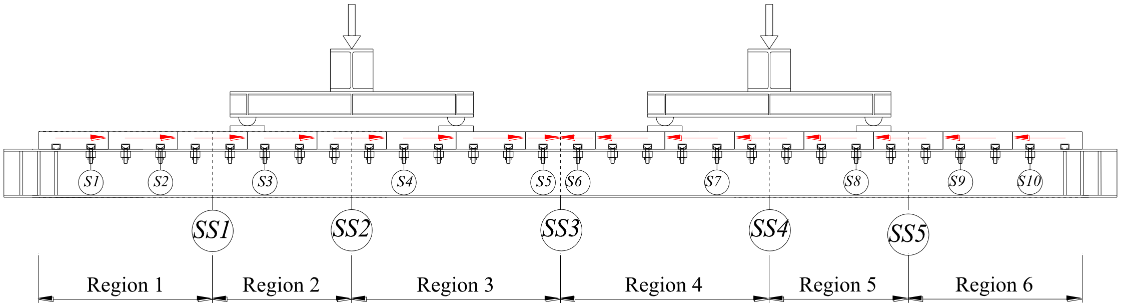
S1
S2
S3
S4
S5
S6
S7
S8
S9
S10
SS1
SS2
SS3
SS4
SS5
Region 1
Region 2
Region 3
Region 4
Region 5
Region 6

Regions 1 and 6: $\bar{Q}_1 = F_{ss1}/8$; $\Delta_1 = (S_1 + S_2)/2$; $\bar{Q}_6 = F_{ss5}/8$; $\Delta_6 = (S_9 + S_{10})/2$

Regions 2 and 5: $\bar{Q}_2 = (F_{ss2} - F_{ss1})/8$; $\Delta_2 = S_3$; $\bar{Q}_5 = (F_{ss4} - F_{ss5})/8$; $\Delta_5 = S_8$

Regions 3 and 4: $\bar{Q}_3 = (F_{ss3} - F_{ss2})/12$; $\Delta_3 = (S_4 + S_5)/2$; $\bar{Q}_4 = (F_{ss3} - F_{ss4})/12$; $\Delta_4 = (S_6 + S_7)/2$

Note: The red arrows indicate the assumed direction of the shear resistance from the clamps.

Figure 5.80 Average shear resistance and average slip calculation

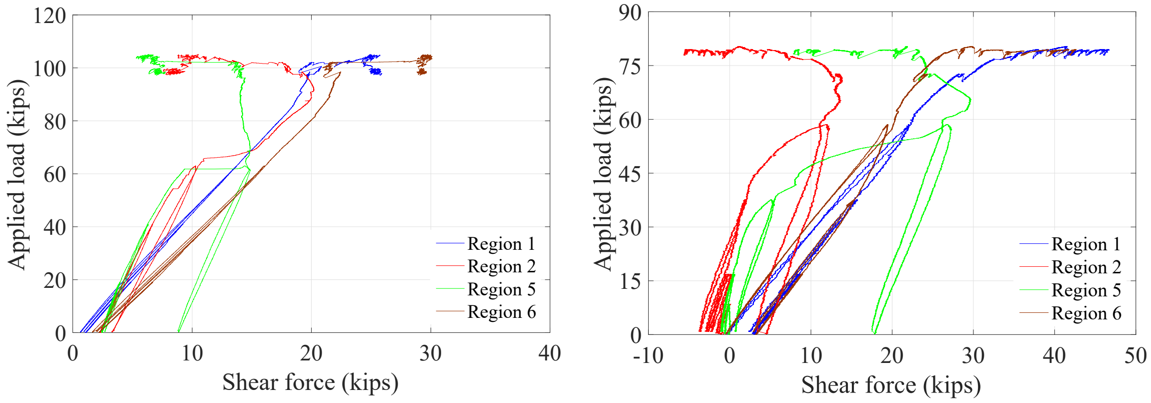

Test 1-M24-2C-RH

Test 2-M24-1C-RL

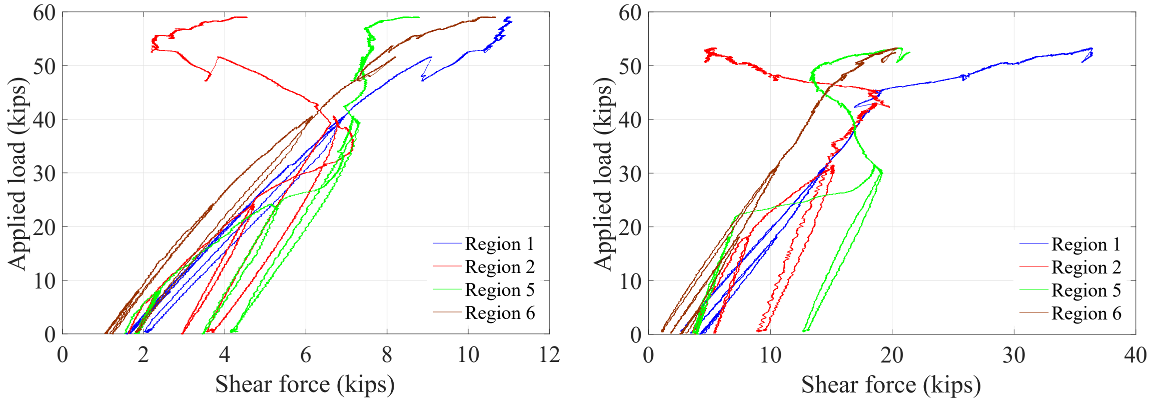

Test 3-M20-3C-RL

Test 4-M20-1C-RL

Figure 5.81 Applied load versus shear resistance per connector

Figure 5.82 illustrates the comparison of the load-slip relationships of the clamping connectors in the pushout tests and beam tests. The representative curves for the pushout tests are the load-slip responses from Test 2-M24-2C-RH-LM and Test 9-M20-2C-RH-LM in Table 4.1. Generally, the clamps in the beam tests have similar initial stiffness as those in the pushout tests. The strengths of all the clamps in Test 1-M24-2C-RH gradually plateau, but this is not seen in the other beams. In all the tests, the clamping connectors in regions 1 and 6 outperform those in the pushout tests in terms of strength. Errors may exist in the curves of Test 3-M20-3C-RL, since the tiny slip may not be measured accurately.

In the pushout tests, the clamps are under pure shear and resist the applied actuator forces evenly. The behavior of the clamps is not strongly affected by the steel beams and concrete planks that are nearly elastic throughout the tests. Nonetheless, the performance of the clamps in the composite beams is much more complicated. The shear resistance of the clamps is achieved through indirect shear loading produced by flexure of the beams. All the specimens are simply supported beams, and the bending moment at a cross section can be easily calculated if the applied loading is known. However, the internal force distribution is indeterminate and dependent upon the load-slip responses of the clamps and nonlinearity of the materials, both of which vary throughout the tests.

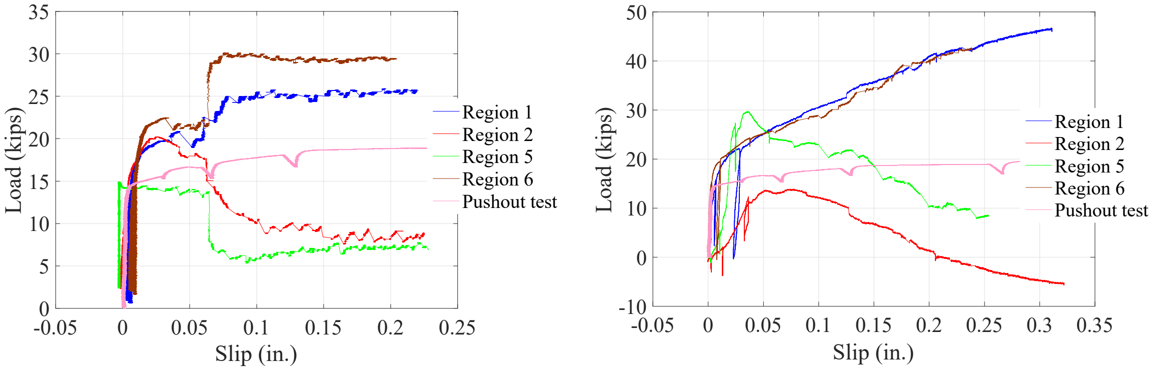

Test 1-M24-2C-RH

Test 2-M24-1C-RL

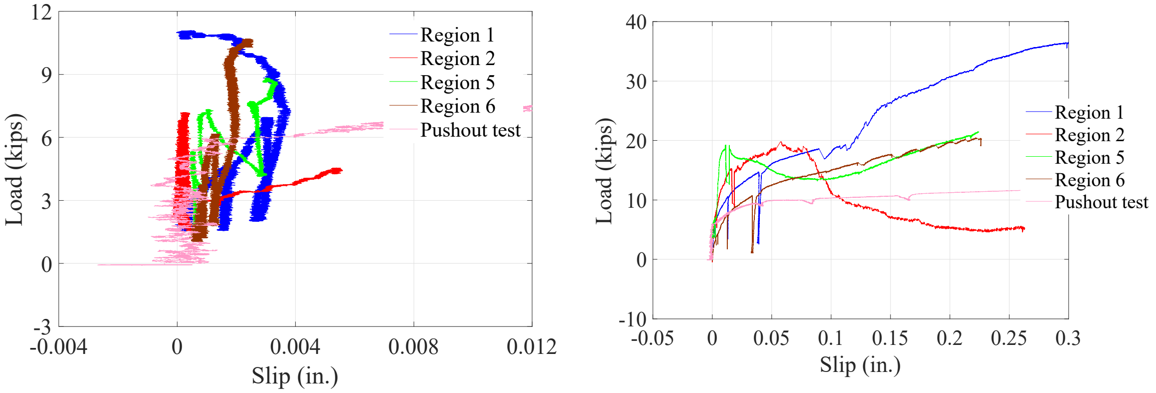

Test 3-M20-3C-RL

Test 4-M20-1C-RL

Figure 5.82 Load-slip curve comparison between pushout tests and beam tests

5.7 Finite element analysis

Finite element models were developed in ABAQUS/CAE for the composite beam test specimens and analyzed in ABAQUS/Explicit, which is effective for simulations containing material failure and contact. This procedure can be used for quasi-static problems if the loads are applied sufficiently slowly.

5.7.1 Finite element model and mesh

The finite element models adopted similar meshing strategies to the pushout test specimens. T-bolts were meshed with C3D8R and C3D6. Cast-in channels, threaded rods, steel beams and concrete planks were meshed with C3D8R only. Reinforcement was modelled using T3D2. Clamps were defined as rigid parts. A meshed beam specimen is shown in Figure 5.83.

5.7.2 Boundary conditions, load applications and contact

Roller supports were created in the finite element models. At one end, the roller was free to roll, while the roller on the other end was constrained from any movement. This boundary condition is the same as that used for the composite beam test specimens. During the tests, bending of the beams forced the actuator swivels to rotate, which should be accounted for as a boundary condition. However, the resistance from the actuator swivels is relatively small compared to the loading applied to the beams. Hence, this bound condition is neglected.

The loading process was divided into two steps. Bolt and rod pretension was first applied by assigning thermal expansion coefficients and temperature changes to the materials. The structure was then loaded in the Y direction to a midspan deflection of 15 in. using displacement control.

The spreader beams were connected using tie constraints, making all the active DOFs equal for the surface pair. The interactions between the concrete planks and the reinforcement and between the concrete planks and the channel anchors were simulated with an embedded constraint. Only the translational DOFs of the embedded components were constrained to those of the corresponding points in the plank. The contact behavior between surfaces was defined in the normal direction and the tangential direction. “Hard contact” was selected for the normal behavior. A penalty formulation was used to characterize the behavior along the interface. In this formulation, no limit is placed on the shear stress, and an elastic slip is used that generates a small amount of relative movement between the surfaces when they are still sticking. The frictional coefficient was taken as 0.35 for all the surfaces. This coefficient is the same as the one used in the simulation for the pushout specimens. General contact, rather than the contact pair algorithm, was selected to automatically select potential contact surfaces.

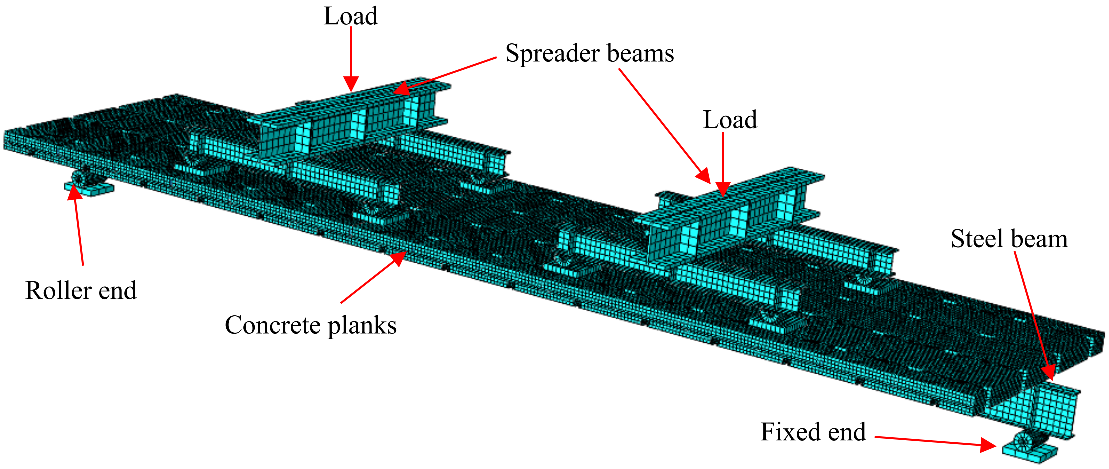

Figure 5.83 Finite element model of composite beam test specimen

5.7.3 Material model for concrete

The concrete damaged plasticity model in ABAQUS was used to model the concrete planks. The compressive stress-strain curve is linear until $0.4f_c'$ is reached, and the remaining part of the curve adopts the relationship proposed by Popovics (1973), see Equation (4.22). The elastic modulus was calculated using Equation (4.23). The Poisson's ratio was taken as 0.15. The default parameters specified in ABAQUS for the concrete damaged plasticity model were used to characterize the plastic behavior under general stress and stress state. The tensile stress-strain curve consists of two linear segments, with the first segment simulating the behavior of concrete up to crack initiation, and the second segment representing the dissipation of the tensile stress as the crack width increases. Mesh dependency, which means mesh refinement does not lead to a converged solution for the problems, exists for concrete with no or little reinforcement when concrete is under tension. To eliminate mesh dependency, a postfailure stress-strain relationship was defined which assumed the ultimate strain at nearly zero stress to be 10 times the cracking strain. Typical concrete compressive and tensile stress-strain curves are plotted in Figure 5.84.

Concrete damage variables characterize stiffness degradation when the specimen is unloaded from any point on the softening branch. The damage variables range from zero for an undamaged model to one, exhibiting complete loss of strength and stiffness. The derivation of the concrete compressive and tensile damage variables is given in Equations (4.24) and (4.25). Typical damage evolution of concrete under compression and tension is shown in Figure 5.85. The compressive and tensile strengths of the concrete planks are based on the tested compressive strength and splitting tensile strength of the concrete cylinders cast along with the planks, which are provided in Table 5.5.

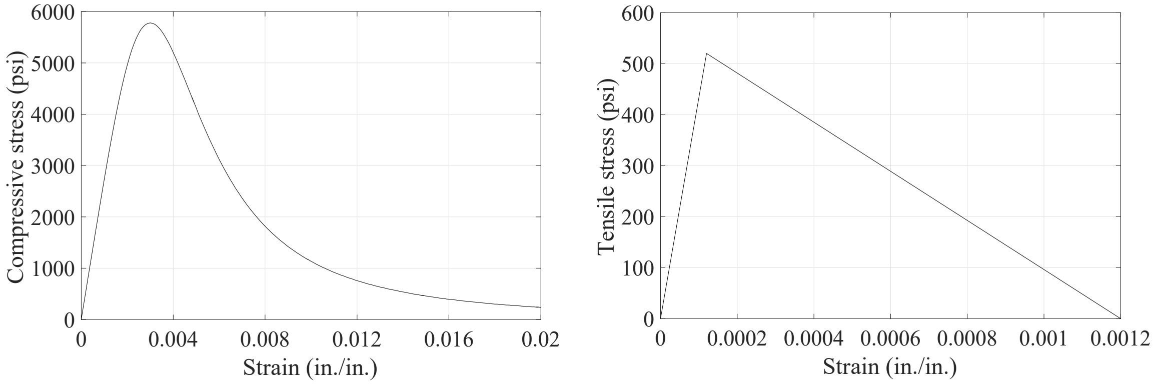

a) Compression (f_c'= 5780 psi) b) Tension (f_t= 520 psi)

Figure 5.84 Concrete stress-strain curves for beam 1

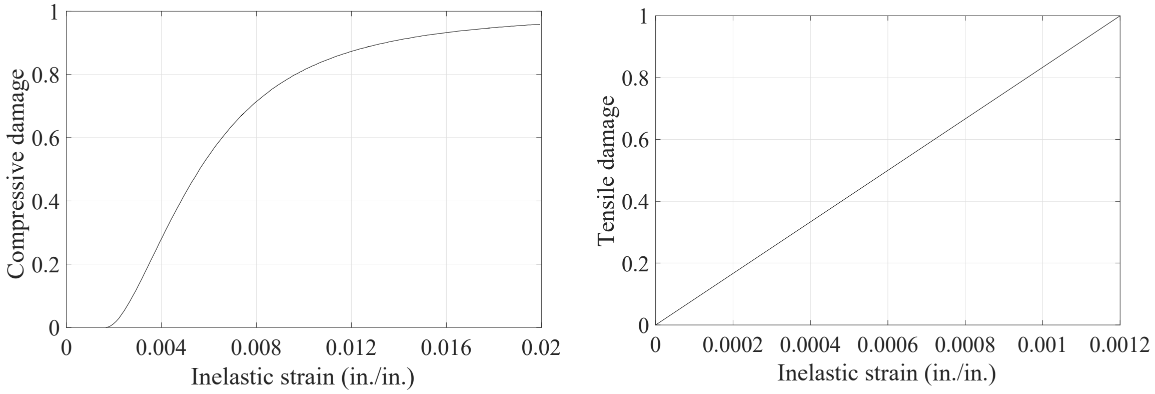

a) Compression b) Tension

Figure 5.85 Concrete damage variables

5.7.4 Material models for steel beam, reinforcement, channels and bolts

Steel beams, reinforcement, channels, rods and bolts were simulated using the metal model which uses the Von Mises yield function and associated flow rule. Trilinear stress-strain relationships were assumed for the steel beams and rods. An elastic-perfectly-plastic material was defined for the reinforcement, while a bilinear relationship was employed for the channels. Typical material constitutive models are illustrated in Figure

5.86. The mechanical behavior was assumed to be the same in both tension and compression. The bolt stress-strain curve used for the analysis is given in Figure F.27 in Appendix F. All the materials used measured material properties, which can be found in Table 5.3.

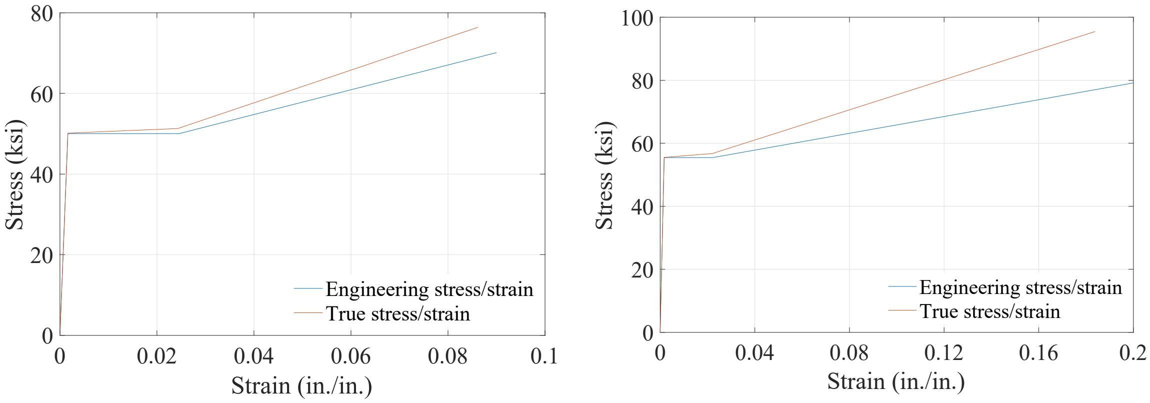

a) W14x38 flange b) 45 in. long rod

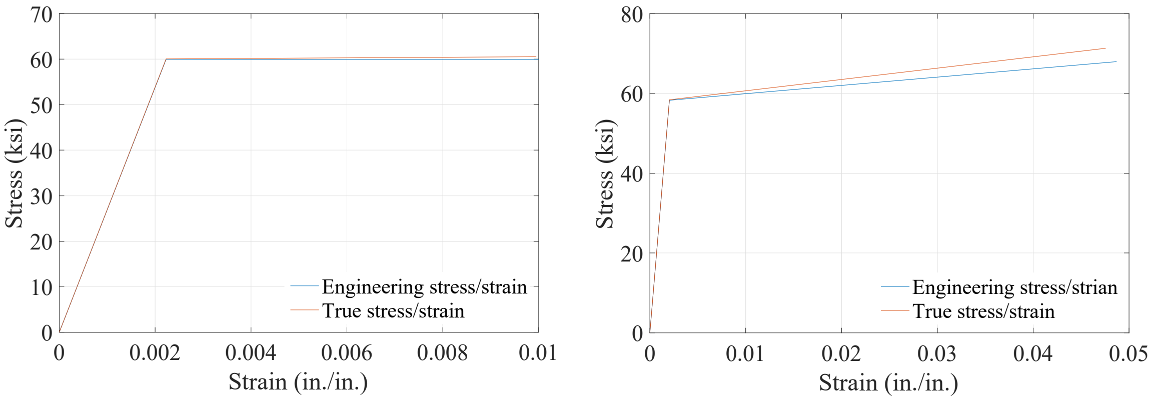

c) Longitudinal reinforcement d) Channel flange

Figure 5.86 Material stress-strain curves

5.7.5 Finite element analysis results

The computational load-deflection curves are compared to the experimental results in Figure 5.87. Major events are marked on the curves, including slip of the clamps, yielding of the steel beams and concrete crushing. Even though some events are not pinpointed from the simulation, the finite element models adequately predict the overall performance of the beam specimens, and the assumed frictional coefficient of 0.35 is also justified.

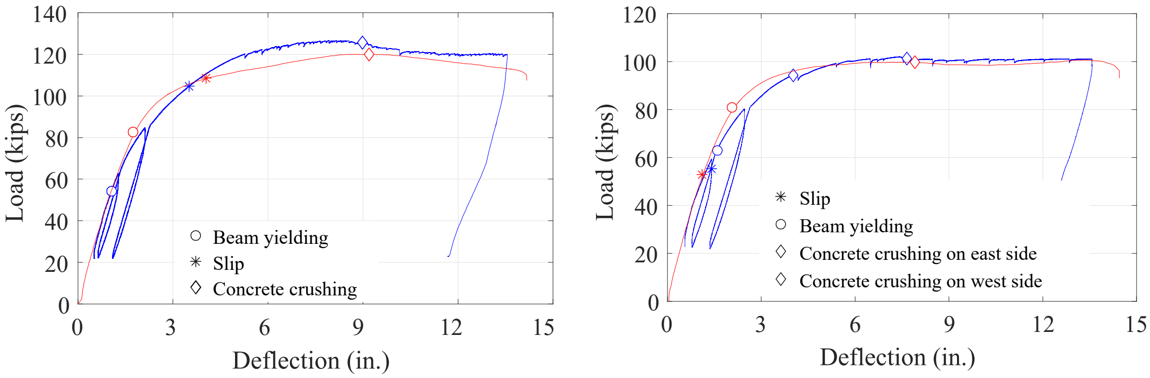

a) Test 1-M24-2C-RH b) Test 2-M24-1C-RL

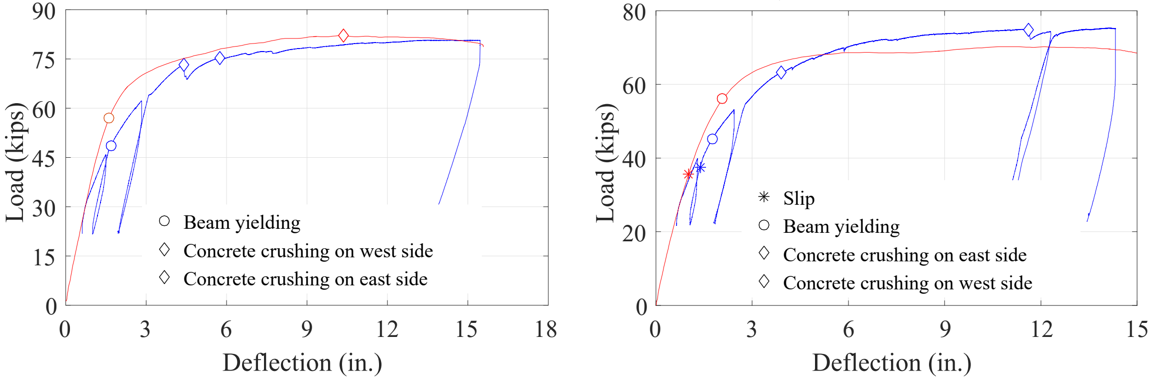

c) Test 3-M20-3C-RL d) Test 4-M20-1C-RL

Note: The test results are shown in blue; the finite element analysis results are shown in red.

Figure 5.87 Load-deflection curve comparison

As with the definition in Section 5.6.2, slip of the clamps is identified when the maximum slip between the steel beam and the concrete planks is greater than 0.02 in. The occurrence of this event is a little earlier in the tests than in the finite element analysis. The load-slip curves from the experiments and finite element simulation are compared in Figure 5.88. In the beam specimens, the clamps did not begin to slip until the frictional resistance at the contact surfaces was overcome. In contrast, the friction simulation in general contact in ABAQUS/Explicit allows a very small amount of slip while the contact surfaces are still sticking. As a result, the behavior of the clamps in the simulation is not as stiff as the physical behavior of the clamps in the tests. Figure 5.88 also shows that the slips are overestimated in the finite element analysis.

Prior to steel beam yielding, it is seen that the experimental load-deflection curves tend to be more flexible than the finite element analysis results. Because of the residual stresses in the steel beam specimens, yielding may first occur at the flange-to-web joints where tensile residual stresses exist, which reduces the overall stiffness of the beams. More importantly, the test results are affected by settling of the composite beams which is neglected in the simulation. It is shown that the initial stiffness of the computational curves is very close to that of the reloading curves of the 60% and 80% cycles. The more flexible behavior of the clamps in the simulation does not appear to affect the elastic stiffness of the composite beams because the elastic stiffness of the beams is influenced not only by the clamps but also by the beams and concrete planks.

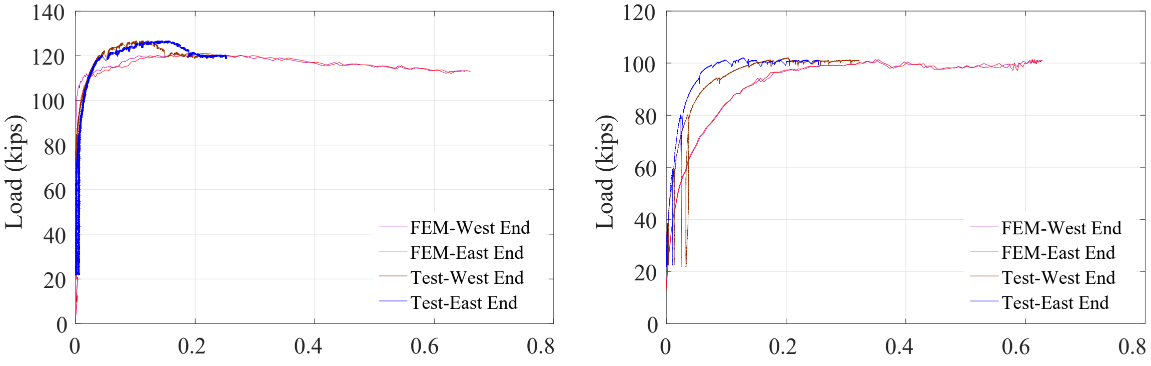

a) Test 1-M24-2C-RH b) Test 2-M24-1C-RL

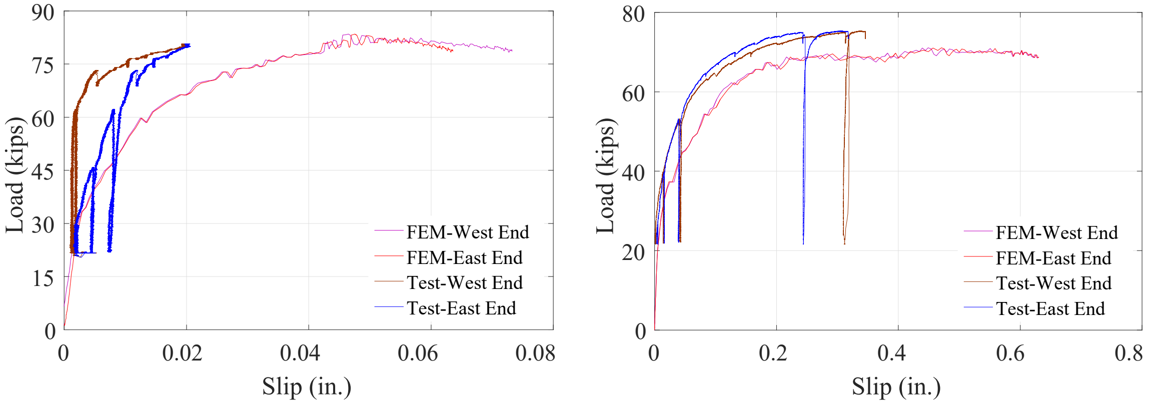

c) Test 3-M20-3C-RL d) Test 4-M20-1C-RL

Figure 5.88 Load-slip curve comparison

The finite element analysis results show that concrete crushing happens at the inner loading points in the first three specimens (see Figure 5.89), which is consistent with the observations in Tests 1 and 2. Nonetheless, concrete crushing in Test 3 occurred at the center section. Although the flexural strengths of the beam specimens were not affected, concrete crushing could happen prematurely in the tests because of the geometry of the planks illustrated in Figure 5.17 in Section 5.6. Therefore, it is reasonable that concrete crushing happens earlier in the test specimens than in the finite element analysis.

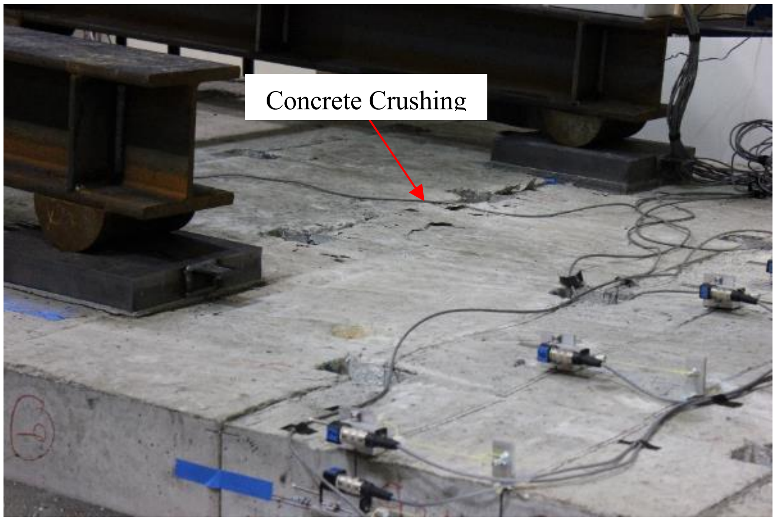
Concrete Crushing

a) Test

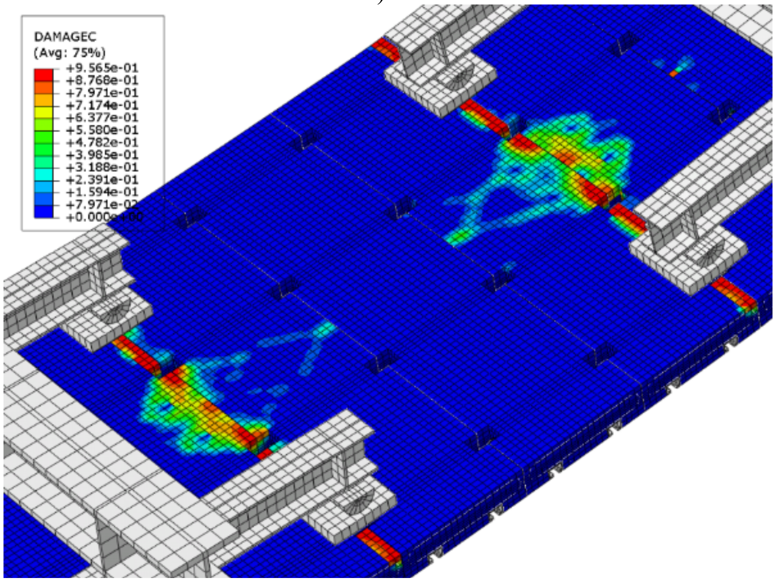
DAMAGEC
(Avg: 75%)
+9.565e-01
+8.768e-01
+7.971e-01
+7.174e-01
+6.377e-01
+5.580e-01
+4.782e-01
+3.985e-01
+3.188e-01
+2.391e-01
+1.594e-01
+7.971e-02
+0.000e+00

b) FE Simulation

Note: A larger damage index indicates more significant concrete compressive crushing.

Figure 5.89 Crushing between concrete planks at inner loading point sections at peak strength (Test 1-M24-2C-RH)

Table 5.15 summarizes the strength and stiffness comparison between the finite element analysis results, experimental results and AISC predictions.

Table 5.15 Composite beam strength and stiffness comparison

Test #	Strength (ft.-kips)					Stiffness (kips/in.)				
	M_{FEM}	M_e	M_t	M_{FEM}/M_e	M_{FEM}/M_t	k_{FEM}	k_e	k_t	k_{FEM}/k_e	k_{FEM}/k_t
1	545	571	565	0.95	0.96	50.0	52.8	49.5	0.95	1.01
2	457	469	464	0.97	0.98	46.5	44.3	38.9	1.05	1.20
3	376	364	376	1.03	1.00	40.0	36.9	34.2	1.08	1.17
4	320	351	296	0.91	1.08	35.0	34.7	25.3	1.01	1.38
Mean				0.968	1.007	Mean			1.022	1.190
Standard deviation				0.0436	0.0441	Standard deviation			0.0510	0.1325
COV				0.0450	0.0438	COV			0.0499	0.1114

Note:

M_{FEM} = *Flexural strength from FEM;* M_e = *Experimental flexural strength;* M_t = *Calculated flexural strength using tested steel and concrete strength as well as tested clamp strength;*

k_{FEM} = *Beam stiffness from FEM;*k_e = *Experimental beam stiffness;* k_t = *Calculated beam stiffness using tested steel and concrete strength as well as tested clamp strength.*

5.8 Design recommendations

Experimental results and computational results presented in this chapter indicate that the AISC design provisions (AISC 360-16) for conventional composite beams that utilize metal deck and steel headed stud anchors are applicable to deconstructable composite beams that utilize concrete planks and clamps. In AISC 360-16, the effective width of an interior composite beam is a function of the beam span and beam length. A lower-bound moment of inertia is recommended for stiffness calculation. A rigid-plastic method is used for computing the ultimate flexural strength of the beam so long as web buckling is not a controlling limit state. The results from this research show that these provisions could be used for the deconstructable composite beams without any modification.

- *Effective width*

The experimental results show that the effective widths of the deconstructable composite beam specimens are smaller than those calculated in accordance with AISC 360-16, as a result of the cutouts in the concrete planks and the gaps between adjacent concrete planks.

As shown in Figure 5.79, the effects of different effective widths on the ultimate flexural strength and elastic stiffness of composite beams are insignificant when the plastic strength of the concrete slab is much larger than the tensile strength of the steel beam and the shear strength of the shear connectors, as is the case for most interior beams and girders.

Hence, it is recommended that the effective width of deconstructable composite beams may be determined as per AISC 360-16 (2016), as using the AISC effective width provisions results in a good estimate of the ultimate flexural strengths of the beam specimens. Further investigation is needed to ascertain the influences of construction tolerances on effective widths.

- *Elastic stiffness*

Table 5.12 shows that the tested stiffness of the deconstructable composite beam specimens is underestimated by the stiffness calculated using a lower bound moment of inertia [I_{LB} from AISC (2016a)]. However, it is not clear whether the elastic stiffness of a deconstructable beam is strongly affected by the percentage of composite action. As shown in Table 5.12, the first two beam specimens have different percentages of composite action and stiffness, whereas the last two beams have different percentages of composite action, but similar stiffness.

It is recommended in design that the elastic stiffness of deconstructable composite beams be estimated with a lower bound moment of inertia.

- *Flexural strength*

In this research, only the positive flexural strength of deconstructable composite beams designed with compact steel sections is investigated. For three out of the four beam specimens, the AISC design equations (AISC 2016a) well predict their ultimate flexural strength. The strength of the fourth beam is also conservatively estimated by the AISC provisions (AISC 2016a).

Therefore, the plastic design method provided in AISC 360-16 is applicable to deconstructable composite beams. A resistance factor of 0.9 is recommended, according to the discussion in Chapter 6.

5.9 Conclusions

After completing the pushout tests, four full-scale composite beam specimens were designed and tested. Each specimen consisted of a 30-foot long beam attached with fifteen 2-ft.-wide planks using clamping connectors. The actuator loads were spread using spreader beams at four points along the length (six-point bending) to mimic a secondary beam under approximately uniform loading. The specimens were loaded to 40% of their expected flexural strength and then reloaded three times. Two more cycles were then undertaken, with one cycle at 60% and the other one at 80% of the estimated flexural strength. After completing the loading/unloading cycles, the beams were then loaded until the deflections were excessive.

All the beams demonstrated ductile behavior with little or no strength degradation, and the tests were terminated because of excessive deflection. The stiffness calculated using a lower bound moment of inertia [I_{LB} from AISC (2016a)] underestimates the tested stiffness of the deconstructable composite beam specimens. The ultimate flexural strengths of the beams are also predicted using AISC design equations (AISC 2016a), and the tested strengths are close to the predictions.

After completing the tests, the composite beams were disassembled. The beams are intact except for the impressions on the top flange under the clamp teeth. In typical applications where a beam would not be subjected to ultimate loads, it is anticipated the steel beam would be in its elastic state when deconstructed.

Based on the experimental and analysis results presented in this chapter, the following conclusions can be reached:

(1) To resist in-plane diaphragm forces during earthquakes, ASTM A36-14/A529-05 Grade 50, 5/8 in. diameter fully threaded rods were designed to connect adjacent concrete planks to ensure structural integrity. One turn after a snug-tight condition is decided for pretensioning the rods after performing pretension tests on two rods to determine the number of turns of the nut. At the ultimate state, the tensile deformation of the rods released, and both rods failed because of excessive torsional deformation.

(2) The load-beam center deflection curves indicate that the deconstructable composite beams using clamping connectors behaved in a ductile manner. At full service loading, the behavior of the beams was slightly nonlinear, likely due to slight separation of the planks due to flexure of the beam, slight yielding of the steel beams, or slight slip of the clamps. However, the steel beams and concrete planks in the deconstructable composite beams are believed to be reusable with minor or no concern about any possible yielding that might occur during their service life. All the beams deflected to approximately L/25, and the experiments were terminated due to the limitation of the test configuration. Along with excessive beam deflection, significant steel beam yielding and localized concrete crushing were seen, but very little or no strength degradation was observed from the load-deflection curves. The plastic hinges that formed in all the specimens indicate excellent rotational capacity of the beams.

(3) The load-displacement curves or moment-rotation curves of the beam specimens were idealized as elastic-perfectly-plastic responses. Yield deformation and ultimate deformation were defined, and the ductility of the specimens is shown to be larger than 3. The load-deflection behavior of the deconstructable composite beam specimens is similar to that of conventional composite beams.

(4) After undergoing three elastic cycles (i.e., 40% of the expected beam strength), all beams exhibited permanent deflection which mainly resulted from settling of the beams. Probably due to fit-up issues and a lack of continuity, such as gaps

between adjacent concrete planks, beam settling appears to be more significant in the deconstructable specimens than in conventional composite beams designed with monolithic concrete slabs.

(5) Compared to conventional composite beams utilizing shear studs and monolithic concrete slabs, the lack of continuity in the concrete plank system does not appear to affect the strength and stiffness of the deconstructable composite beams, as is demonstrated by the comparison between the test results and the predictions based on the design equations given in AISC 360-16.

(6) During the test, the slip of the clamps was measured at several locations along the length of the beam. The comparison of the slip measurements between different specimens verifies that the slip of the shear connectors in a composite beam is inversely proportional to the degree of shear connection. The percentage of composite action of Beam 3-M20-3C-RL is higher than 100%, and consequently the maximum slip of the clamps is only 0.02 in. Among all the specimens, the maximum slip is 0.35 in. in Test 4-M20-1C-RL which has a degree of shear connection of 43.8%.

(7) In the pushout tests, the M20 clamps did not behave as ductile as the M24 clamps. As the WT section moved, the clamps rotated and strength reduction initiated at a slip of 0.68 in. in the monotonic test. Two composite beams utilizing M20 clamps were tested, and the maximum slip of the clamps is 0.35 in., much smaller than 0.68 in. This may imply that strength degradation of the M20 clamps did not occur in the beam tests. However, testing of composite beams with much lower percentage of composite action (<25%) may reveal other findings.

(8) Based on the axial strain measurements, the neutral axes in the steel beams and concrete planks are located. Although Beam 1-M24-2C-RH is a partially composite beam, the strain distribution is distinct from those of Beams 2-M24-1C-RL and 4-M20-1C-RL. For each instrumented section in Beams 2 and 4, two

neutral axes are clearly seen in the steel beam and concrete plank. In Beam 1, as the loading increases, the neutral axis in the steel beam of the center section rises into the concrete plank, while a single neutral axis remains in the steel beam at the other sections. Similarly, the neutral axis in the steel beam of the center section of Beam 3-M20-3C-RL ascends quickly into the concrete plank.

(9) The same number of turns of the nut determined in the pushout test program was utilized for pretensioning the bolts used in the beam specimens. After pretensioning, the axial force of most gaged bolts exceeded the minimum pretension requirements for Group A bolts in Table J3.1M in AISC 360-16. Similar to the observations attained from the pushout tests, the pretension of the instrumented bolts decreased in the beam tests, and the reduction is strongly affected by the slip of the clamps. At serviceability, the slip of the clamps in the beams was minimal (<0.04 in.), and the tension reduction was normally less than 10%. In all the specimens, the slip of the middle clamps was trivial throughout the tests, and the tension of the middle bolts maintained. In Beam 3-M20-3C-RL, the maximum slip of the clamps is less than 0.02 in., and the tension reduction is negligible for the gaged bolts. According to the finite element analysis results of the pushout specimens, the axial force of the bolts decreases to 3/4 of their initial pretension at a slip of approximately 0.3 in. Similarly, the largest tension reduction of the bolts instrumented in the beam specimens is approximately 25%.

(10) The axial force of the fully threaded rods normally decreased in the tests. At serviceability, the tension of the rods decreased approximately 20%, and the reduction was more for the rods connecting planks that were crushed at the ultimate state of the beams. Because concrete crushing released the tensile strain of the rods spanning the crushed regions, the tension of these rods ultimately dissipated.

(11) Shear lag is exhibited by the strain distribution along the width of the center plank. It is shown that the strain close to the center of the plank is greater than that

near the ends of the plank. This pattern maintained throughout the test, since the gaps at the ends of the plank persisted and inhibited the force flow. Therefore, the effective widths of the deconstructable composite beam specimens are smaller than those calculated in accordance with AISC 360-16. Since the effective widths of the deconstructable composite beams are affected by the contact between the planks, use of planks with tongue-and-groove joints and with qualities comparable to those manufactured in a precast concrete plant may result in larger effective widths. The influence of the effective width on the strength and stiffness of a composite beam is also shown to be insignificant.

(12) The load-slip curves of the clamps in the beam specimens were correlated to those obtained from the pushout tests. In both tests, the initial stiffness of the load-slip curves is large, and the clamps begin to slip at approximately the same loading. In terms of strength, the clamps close to the ends of the beam specimens outperformed those in the pushout tests, since it is shown that shear redistribution occurred in the beams from the inner clamps to the outer clamps.

(13) Finite element models, which take into account material nonlinearity, geometric nonlinearity and contact between different components, were developed for the beam specimens. A frictional coefficient of 0.35 was assumed for all the contact surfaces. The overall behavior of the beam specimens is well predicted by the finite element models.

6. RELIABILITY ASSESSMENT OF COMPOSITE BEAMS

AISC 360-16 permits design of steel structures using either Load and Resistance Factor Design (LRFD) or Allowable Strength Design (ASD). The LRFD method (Ravindra and Galambos 1978) has as its design basis for each limit state the criteria as expressed in Equation (6.1).

$$\emptyset R_n \geq \sum \gamma_i Q_i \tag{6.1}$$

The left side of the equation represents the resistance, i.e., design strength, of the component, and the right side of the equation describes the loading effects, i.e., required strength, on the component. The LRFD load combinations should be selected accordingly, e.g., from ASCE 7-10 (ASCE 2010).

In Chapter 4, design equations are proposed to estimate the slip strength and peak strength of the clamps. As presented in Chapter 5, the AISC composite beam flexural strength model predicts the flexural strength well for the deconstructable beam specimens. Despite the limited number of tests conducted in this research, strength reduction factors are derived in this chapter for these design equations.

The design criteria expressed in Equation (6.1) includes the load effect, Q, and the resistance, R. The two random variables are assumed to be statistically independent. Since these two parameters are commonly the product of several other variables, they often follow a lognormal distribution. The probability of the limit state being exceeded can be defined as:

$$p_f = P(R - Q < 0) \tag{6.2}$$

An equivalent representation is given as:

$$p_f = P(\ln(R) - \ln(Q) < 0) = P(\ln{(R/Q)} < 0) \tag{6.3}$$

If a standard variate is introduced,

$$U = \frac{\ln\left(\frac{R}{Q}\right) - (\ln\left(\frac{R}{Q}\right))_m}{\sigma_{\ln(R/Q)}} \tag{6.4}$$

where $(\ln(R/Q))_m$ and $\sigma_{\ln(R/Q)}$ are the mean and standard deviation, respectively, of the variable $\ln(R/Q)$.

Combining Equations (6.3) and (6.4), the probability of the limit state being exceeded is calculated as

$$\begin{aligned} p_f &= P\left(\ln\left(\frac{R}{Q}\right) < 0\right) \\ &= P\left(U < -\frac{\left(\ln\left(\frac{R}{Q}\right)\right)_m}{\sigma_{\ln(R/Q)}}\right) = F_u(-\frac{\left(\ln\left(\frac{R}{Q}\right)\right)_m}{\sigma_{\ln(R/Q)}}) \end{aligned} \tag{6.5}$$

where F_u is the cumulative distribution function of the standard variate.

From Equation (6.5), the safety of the structure is determined by the quantity $\frac{\left(\ln\left(\frac{R}{Q}\right)\right)_m}{\sigma_{\ln(R/Q)}}$; this quantity, β, is a reliability index. However, the probability distribution of R/Q is commonly unknown, and β is often approximated using the first-order second moment probability theory:

$$\beta = -\frac{\left(\ln\left(\frac{R}{Q}\right)\right)_m}{\sigma_{\ln(R/Q)}} \approx \frac{\ln\left(\frac{R_m}{Q_m}\right)}{\sqrt{V_R^2 + V_Q^2}} \tag{6.6}$$

where R_m and Q_m are the mean of R and Q, respectively; V_R and V_Q are the corresponding coefficients of variation.

Lind (1971) proposed a linear approximation for the square root term using a separation coefficient α:

$$\sqrt{V_R^2 + V_Q^2} \approx \alpha(V_R + V_Q) \tag{6.7}$$

Combining Equations (6.6) and (6.7), the following expression is obtained:

$$R_m = Q_m e^{\alpha\beta(V_R + V_Q)} \tag{6.8}$$

Rewriting Equation (6.8):

$$\frac{e^{-\alpha\beta V_R}\, R_m}{R_n} R_n = \frac{Q_m e^{\alpha\beta V_Q}}{Q_n} Q_n \tag{6.9}$$

or

$$\emptyset R_n = \gamma Q_n \tag{6.10}$$

where $\emptyset$ and γ are the resistance factor and load factor, respectively.

According to Equations (6.9) and (6.10), in the LRFD method, the resistance factor and load factor are obtained after the reliability index, β, is selected for the structure. Therefore, the resistance factor is

$$\emptyset = e^{-\alpha\beta V_R} \frac{R_m}{R_n} \tag{6.11}$$

From Equation (6.11), it is seen that the resistance factor is affected by the separation coefficient, α, the reliability index, β, and the coefficient of variation of the structure's resistance, V_R.

V_R and V_Q need to be derived to compute the separation coefficient α, which is derived as:

$$\alpha = \frac{\sqrt{1 + (V_R/V_Q)^2}}{1 + (V_R/V_Q)} \tag{6.12}$$

Calculation of V_R

The actual resistance R of a structure usually takes the form:

$$R = R_n M F P \tag{6.13}$$

where R_n is the code-specified nominal resistance; M accounts for the variation in material strength or stiffness; F represents the uncertainties in specimen fabrication; P describes the uncertainties inherent in the design equation.

The coefficient of variation of the resistance is thus defined as

$$V_R = \sqrt{{V_M}^2 + {V_F}^2 + {V_P}^2 + {V_M}^2{V_F}^2 + {V_F}^2{V_P}^2 + {V_M}^2{V_P}^2 + {V_M}^2{V_F}^2{V_P}^2} \tag{6.14}$$

where V_M, V_F, and V_P are the coefficients of variation of M, F, and P, respectively.

V_M and V_F are conventionally taken as 0.10 and 0.05 (Galambos and Ravindra 1976; Galambos and Ravindra 1978), whereas V_P is the coefficient of variation of the test-to-predict ratios. Since V_M, V_F, and V_P are usually very small, the product terms in Equation (6.14) are usually higher order terms and omitted.

Statistical analysis on the yield stress of steel shapes was reported in Galambos and Ravindra (1978) and shown in Table 6.1. Without distinguishing flanges from webs, Hansell et al. (1978) recommended $(F_y)_m = 1.07F_y$ and $V_{F_y} = V_M = 0.10$. It should be noted that this statistical investigation was based on tensile testing data for A36 steel during the 1960s and 1970s. Since then, the rolling process has changed, the steel shape producers are different, and the ASTM specifications have also evolved. As such, numerous researchers have studied the material properties of recent steel shapes (Frank and Read 1993; Rex and Easterling 1999; Jaquess and Frank 1999; Brockenbrough 2000; Dexter et al. 2000; Bartlett et al. 2003). A992 Grade 50 steel, which is the most common material specification for W shapes, was only investigated in Dexter et al. (2000) and Bartlett et al. (2003). Since a much larger dataset was documented by Dexter et al. (2000), the reported statistical information, as given in Table 6.2, is used to calculate the resistance factor for the flexural strength of deconstructable composite beams. The mean yield strengths in Table 6.2 need to be reduced by 4.4 ksi to obtain the mean static yield strengths. Therefore, the mean static yield strengths of A992 steel flanges and webs are

51.4 ksi and 52.1ksi, respectively, and the corresponding coefficients of variation are 0.058 and 0.054. It is thus appropriate to assume that $(F_y)_m = 1.035F_y$ and $V_{F_y} = V_M = 0.056$.

Table 6.1 Material properties reported by Galambos and Ravindra (1978)

Material properties	Mean Value (ksi)	COV
Elastic modulus (tension)	29000	0.06
Elastic modulus (compression)	29000	0.06
Elastic modulus (shear)	11200	0.03
Possion’s ratio	0.30	0.03
Yield stress in flanges	1.05 F_y	0.10
Yield stress in webs	1.10 F_y	0.11
Yield stress in shear	0.64 F_y	0.10
Strain-hardening modulus	600	0.25

Table 6.2 Material properties reported by Dexter et al. (2000)

ASTM specification		A572 Gr. 50 (flange)	A992 (flange)	A992 (web)
Number of Data		1,052	20,295	4,925
Yield strength (ksi)	Mean	60.5	55.8	56.5
	COV	0.066	0.058	0.054
Tensile strength (ksi)	Mean	76.3	73.3	73.3
	COV	0.050	0.044	0.046
Yield/Tensile ratio	Mean	0.790	0.760	0.770
	COV	0.047	0.040	0.089

Calculation of V_Q

The load effect Q on a structure usually takes the form:

$$Q = E(c_D AD + c_L BL) \tag{6.15}$$

where D and L represent dead and live load intensities, respectively; c_D and c_L are deterministic factors that convert loading intensities into load effects; A and B account for the uncertainties in the transformation of loads into load effects; E reflects the uncertainties in the structural analysis.

The coefficient of variation of the load is thus defined as:

$$V_Q \approx \sqrt{{V_E}^2 + \frac{{c_D}^2{A_m}^2{D_m}^2({V_A}^2 + {V_D}^{\,2}) + {c_L}^2{B_m}^2{L_m}^2({V_B}^2 + {V_L}^2)}{(c_D A_m D_m + c_L B_m L_m)^2}} \tag{6.16}$$

where V_D, V_L, V_A, V_B, and V_E are the coefficients of variation of D, L, A, B, and E, respectively; D_m, L_m, A_m, B_m, and E_m are the mean of D, L, A, B, and E, respectively ; the mean value of E is assumed to be unity.

For a beam, c_D and c_L equal sl^2 in which s is the beam spacing and l is the beam span. The following values were suggested in Ravindra and Galambos (1978): $V_E = 0.05$; $A_m = 1.0$; $V_A = 0.04$; $B_m = 1.0$; $V_B = 0.2$; $D_m = D_c$; $V_D = 0.04$. D_c is the code-specified dead load.

The mean and standard deviation of L were given by McGuire and Cornell (1974).

$$L_m = 14.9 + 763/\sqrt{A_I} \tag{6.17}$$

$$\sigma_L = \sqrt{11.3 + \frac{15000}{A_I}} \tag{6.18}$$

$$V_L = L_m/\sigma_L \tag{6.19}$$

where A_I is the influence area which equals twice the tributary area for floor beams.

For a floor beam, if the influence area is known, L_m and V_L can be calculated with Equations (6.17) through (6.19). After knowing L_m, V_L, and D_c, V_Q is calculated using Equation (6.16). Given V_R and V_Q, the separation factor α is then obtained from Equation (6.12). According to Hansell et al. (1978), the separation coefficient α is instead taken as 0.55, thus indicating that V_L is not calculated for this work. The resistance factor is calculated as:

$$\emptyset = e^{-0.55\beta V_R} \frac{R_m}{R_n} \tag{6.20}$$

It was suggested in Ravindra and Galambos (1978) that $\beta = 3.0$ and $\beta = 4.5$ be selected for developing resistance factors for members and connections, respectively. However, the AISC Specification (2016a) chose 2.6 and 4.0 as reliability indexes for members and connections, respectively. In this study, $\beta = 4.0$ is used to calculate resistance factors for the shear strength design equations of clamps, while the resistance factor for the positive flexural strength design equation of deconstructable composite beams is calculated based on a reliability index of 3.0.

6.1 Shear strength of clamping connectors

Because the resistance and load factors are interdependent and the load factors are calibrated assuming a reliability index of 3.0 for the structure as a whole, an adjustment factor, C, should be applied to Equation (6.20) when the reliability index for a structural component is not equal to 3.0. The adjustment factor was derived in Fisher et al. (1978) as:

$$C = \frac{1.086(1.0933 + 1.3936L/D)}{e^{0.0275\beta}(1 + 0.03111\beta + (1 + 0.1313\beta)L/D)} \tag{6.21}$$

where L/D is the live load to dead load ratio.

The expression in Equation (6.21) can be fitted by a second-order polynomial using linear regression analysis. When L/D is equal to 3.0, Equation (6.21) is simplified as

$$C = 0.0093\beta^2 - 0.1658\beta + 1.4135 \tag{6.22}$$

If a reliability index of 4.0, which corresponds to a probability of failure of 3.17×10^{-5}, is assumed for the clamping connectors, the adjustment factor is calculated as 0.90.

To be consistent with the nomenclature and derivations given in the literature (Fisher et al. 1978; Grondin et al. 2007; Moore et al. 2008), some of the equations and parameters in this section are expressed slightly differently from those shown in the previous section.

Equation (6.20) is rewritten as:

$$\emptyset = C\rho_R e^{-0.55\beta V_R} \tag{6.23}$$

where ρ_R is the bias coefficient, which is the average value of the ratio of the tested strength to the nominal strength [same as R_m/R_n in Equation (6.20)].

Design equations are proposed in Section 4.7 to predict the slip strength and peak strength for clamps. These equations and the notations are repeated here.

$$Q_s = k_d \mu_s D_u T_b n_s \tag{6.24}$$

$$Q_p = k_d k_r \mu_p D_u T_b n_s \tag{6.25}$$

Where

k_d and k_r = coefficients accounting for the portion of bolt tension transferred to the clamp teeth and the bolt tension reduction at peak strength, which are 0.70 and 0.75, respectively

μ_s = mean slip coefficients, which is 0.17 in the pushout series

μ_p = idealized frictional coefficient at peak strength, which is 0.35in the pushout series.

D_u =1.13, a multiplier representing the ratio of the mean installed bolt pretension to the specified minimum bolt tension

T_b = minimum fastener tension given in Table J3.1M in AISC 360-16

n_s = number of slip planes, which is 2

To distinguish the probabilistic parameters from the deterministic parameters, Equations (6.24) and (6.25) can be simplified as:

$$Q = D_u \times \mu \times A_b \times 0.75 F_u \times (k_d \, k_r \, n_s) \tag{6.26}$$

where k_d, k_r, and n_s are deterministic variables; D_u is the ratio of the actual bolt tension to the minimum required bolt tension; μ is the frictional coefficient; A_b is the nominal cross-sectional area of the T-bolts; F_u is the ultimate tensile strength of the T-bolts. 0.75 is assumed to be the ratio of the effective tension area of the threaded portion of a T-bolt to the nominal cross-sectional area of the bolt.

The bias coefficient, ρ_R, and the coefficient of variation, V_R, are derived as:

$$\rho_R = \rho_T \rho_G \rho_M \rho_P \tag{6.27}$$

$$V_R = \sqrt{{V_T}^2 + {V_G}^2 + {V_M}^2 + {V_P}^2} \tag{6.28}$$

where $\rho_T, \rho_G, \rho_M,$ and ρ_P are bias coefficients for bolt pretension, cross-sectional geometry [same as F in Equation (6.13)], material strength [same as M in Equation (6.13)], and professional factor [same as P in Equation (6.13)], respectively; $V_T, V_G, V_M,$ and V_P represent the coefficients of variation for bolt pretension, cross-sectional geometry [same as V_F in Equation (6.14)], material strength [same as V_M in Equation (6.14)], and professional factor [same as V_P in Equation (6.14)], respectively.

The uncertainties of μ_s and μ_p are embedded in ρ_P and V_P, whereas the variability of D_u is included in ρ_T and V_T. ρ_P and V_P are calculated in Table 6.3. This table is different from Table 4.12 in Chapter 4, since the predicted strengths are calculated using the minimum bolt tension and actual bolt tension in Table 4.12 and Table 6.3, respectively. . Based on the pretension test results presented in Section 4.4.3, the actual bolt tension is approximately 1.3 times the minimum bolt tension.

The values of the other parameters in Equations (6.27) and (6.28) are given in Table 6.4. Given the lack of such statistical information for the T-bolts, the information collected for regular bolts are used in the calculations. In Table 6.4, ρ_T and V_T are based on the turn-of-nut method for bolt installation, and these values are different when the calibrated wrench method is used. ρ_G and V_G are based on the measurements of 285 A325 and A490 bolts with nominal diameters of 3/4 in., 7/8 in., and 1 in. ρ_M and V_M are reported for A325 bolts, which are equivalent to the Grade 8.8 T-bolts used with the clamps. This statistical information is different for A490 bolts.

Table 6.3 Tested-to-predicted strength ratio of monotonic pushout specimens

Specimen	Tested strength (kips)		Predicted strength (kips)		Ratio	
	Q_s	Q_p	Q_s	Q_p	Slip	Peak
2-M24-2C-RH-LM	60.8	88.5	57.1	88.1	1.07	1.01
4-M24-2C-RH-LM-S	56.5	87.9	57.1	88.1	0.99	1.00
7-M24-3C-RH-LM	87.0	130.1	85.6	132.2	1.02	0.98
9-M20-2C-RH-LM	36.5	55.3	39.5	61.0	0.92	0.90
				Mean	1.00	0.97
				SD	0.0532	0.0412
				COV	0.0532	0.0424

Table 6.4 Parameters for resistance factor calculation

Parameter	Value	Reference
ρ_T	1.22	Kulak et al. (1987)
V_T	0.05	
ρ_G	0.994	Stankevicius et al. (2007)
V_G	0.005	
ρ_m	1.20	Fisher et al. (1978)
V_m	0.07	

With the values known for all the parameters, ρ_R and V_R are calculated as:

$$\rho_{Rslip} = 1.22 \times 0.994 \times 1.20 \times 1.00 = 1.4552 \tag{6.29}$$

$$\rho_{Rpeak} = 1.22 \times 0.994 \times 1.20 \times 0.97 = 1.4116 \tag{6.30}$$

$$V_{Rslip} = \sqrt{0.05^2 + 0.005^2 + 0.07^2 + 0.0532^2} = 0.1013 \tag{6.31}$$

$$V_{Rpeak} = \sqrt{0.05^2 + 0.005^2 + 0.07^2 + 0.0424^2} = 0.0960 \tag{6.32}$$

Hence, if D_u is equal to 1.13, the resistance factors are calculated as:

$$\emptyset_{vslip} = 0.90 \times 1.4552 \times e^{-0.55\times4.0\times0.1013}/1.13 = 0.9275 \tag{6.33}$$

$$\emptyset_{vpeak} = 0.90 \times 1.4116 \times e^{-0.55\times4.0\times0.0960}/1.13 = 0.9102 \tag{6.34}$$

Therefore, a resistance factor of 0.9 may be recommended for the slip strength and peak strength design equations of the clamps investigated in this research.

6.2 Flexural strength of composite beams

For the flexural strength calculation of composite beams, β is taken as 3.0, which corresponds to a probability of failure of 1.3×10^{-3}. The resistance factor is calculated as:

$$\emptyset = e^{-0.55\times3.0V_R}\frac{R_m}{R_n} \tag{6.35}$$

$$\frac{R_m}{R_n} = \frac{(F_y)_m}{(F_y)_n}(\frac{Test}{Prediction})_m \tag{6.36}$$

where $\left(F_y\right)_m$ is the mean static yield stress of steel beams; $\left(F_y\right)_n$ is the nominal static yield stress of steel beams; $\left(F_y\right)_m/\left(F_y\right)_n$ is taken as 1.035, as discussed in prior sections.

In Equation (6.36), "Test" denotes the tested flexural strengths of the specimens, while "Prediction" refers to the predicted flexural strengths of the specimens using tested material properties. Depending on whether the clamp strengths use those obtained from the pushout tests or those predicted by the proposed design equations in Section 4.7, the predicted flexural strengths vary. The tested flexural strengths and predicted flexural strengths of the composite beam specimens are given in Table 6.5.

Table 6.5 Tested-to-predicted strength ratio of composite beam specimens

Test #	Strength (ft.-kips)				
	M_e	M_{t1}	M_{t2}	M_e/M_{t1}	M_e/M_{t2}
1-M24-2C-RH	571	565	538	1.01	1.06
2-M24-1C-RL	469	466	448	1.01	1.05
3-M20-3C-RL	364	376	376	0.97	0.97
4-M20-1C-RL	351	296	292	1.19	1.20
Mean				1.045	1.070
Standard deviation				0.0853	0.0843
COV				0.0816	0.0788

Note:

M_e = Experimental flexural strength; M_{t1} = Calculated flexural strength using tested steel and concrete strength as well as tested clamp strengths; M_{t2} = Calculated flexural strength using tested steel and concrete strength as well as predicted clamp strengths

The coefficient of variation of the resistance is calculated as:

$$V_{R1} = \sqrt{{V_M}^2 + {V_F}^2 + {V_{P1}}^2} = \sqrt{0.056^2 + 0.05^2 + 0.082^2} = 0.1112 \tag{6.37}$$

$$V_{R2} = \sqrt{{V_M}^2 + {V_F}^2 + {V_{P2}}^2} = \sqrt{0.056^2 + 0.05^2 + 0.079^2} = 0.1090 \tag{6.38}$$

In this equation, V_M uses 0.056, as discussed in prior sections, and V_F still uses 0.05 according to Galambos and Ravindra (1976). V_{R1} and V_{R2} represent the coefficients of variation of the resistance calculated using the tested strengths and predicted strengths as the clamp strengths, respectively.

Using Equations (6.35) and (6.36), the resistance factor is calculated as

$$\emptyset_{b1} = e^{-0.55\times3.0\times\sqrt{0.056^2+0.05^2+0.082^2}}(1.035 \times 1.045) = 0.900 \tag{6.39}$$

$$\emptyset_{b2} = e^{-0.55\times3.0\times\sqrt{0.056^2+0.05^2+0.079^2}}(1.035 \times 1.070) = 0.925 \tag{6.40}$$

$\emptyset_{b1}$ and $\emptyset_{b2}$ represent the resistance factors calculated using the tested strengths and predicted strengths as the clamp strengths, respectively.

It is also reasonable to argue that V_M and V_F are incorporated in V_P and to ignore the first two terms in Equations (6.39) and (6.40). In this case, the resistance factor is

$$\emptyset_{b1} = e^{-0.55\times3.0\times0.082}(1.035 \times 1.045) = 0.945 \tag{6.41}$$

$$\emptyset_{b2} = e^{-0.55\times3.0\times0.079}(1.035 \times 1.070) = 0.972 \tag{6.42}$$

In this derivation, the uncertainties of materials, fabrication, and flexural strength design equations are included, but the variation of the clamping connector strength is accounted for indirectly, which is similar to the approach taken by the AISC Specification (2016a) for composite beams. In AISC 360-16 (2016), for shear studs utilized in composite beams, if steel failure governs, the shear strength of a shear stud anchor embedded in a solid concrete slab is determined as: $Q_n = 0.75A_{sa}F_u$, where A_{sa} is the cross-sectional area (in.^{2}) and F_u is the specified minimum yield strength of a steel headed stud anchor (ksi). A resistance factor is not given for this equation, as the factor is included as part of the overall resistance factor for the flexural strength of composite beams. In contrast, when shear studs are employed in applications other than composite beams, such as steel reinforced concrete columns (SRCs), concrete filled tubes (CFTs), and steel-concrete (SC) composite walls, the shear strength of a shear stud anchor is calculated as: $Q_{nv} = A_{sa}F_u$. A resistance factor of 0.65 is used for this equation, and the resistance factor is derived based on a reliability index, β, of 4.0 (Pallarés et al. 2009). In Rambo-Rodenberry (2002), the other approach is shown which takes into consideration the variation of the shear stud strength explicitly. The resistance factor is found to be a function of d_1, d_2, d_3, and the percentage of composite action of the beam.

Parameters d_1, d_2, and d_3 are illustrated in Figure 5.44. It is shown that the resistance factor varies slightly if the variation of the shear stud strength is accounted for explicitly.

Base on the above discussions, the resistance factor for the positive flexural strength design equation of deconstructable composite beams may be taken as 0.9, which is consistent with the factor used for conventional composite beams utilizing metal deck and steel headed stud anchors.

7. CONCLUSIONS AND FUTURE WORK

A deconstructable composite floor system is proposed which consists of precast concrete planks and steel beams connected using clamping connectors. This system maintains the benefits of composite construction, such as enhanced flexural strength and stiffness, reduced steel beam size and weight, and ease of construction. In conventional composite floor systems, steel beams are commonly recycled, and concrete slabs are sent to landfill or downcycled for aggregate; however, sustainable design of composite beams and floors is achieved in the new system by enabling deconstruction and reuse of the structural components and reducing the energy consumption and material waste.

Prior to the experimental investigation, life cycle assessments were performed to quantify the environmental benefits of adopting DfD in the design of buildings by comparing the environmental impacts of prototype structures designed with the deconstructable composite floor systems to those of the buildings with the conventional composite floor systems, and the results are briefly presented in Chapter 3. From a dismantler's perspective, challenges and opportunities for dismantling current steel structures and the flow of the demolished materials are also identified in this chapter. The experimental program in this research mainly includes pushout tests that were conducted to quantify the strength and ductility of the deconstructable clamping connectors and composite beam tests that were performed to investigate the behavior of the clamping connectors in a realistic manner and study the strength, stiffness and ductility of deconstructable composite beams with different levels of composite action.

7.1 Summary of pushout tests

The behavior of shear connectors is normally studied in pushout tests in which the connectors are loaded in shear directly. Although pushout tests cannot precisely replicate the forces the shear connectors are subjected to in composite beams, if properly designed, they are proven to be adequate to quantify the strength, stiffness, and ductility of the shear connectors.

The pushout test program includes two series of tests. In the pretension tests, the number of turns of the nut was first determined to ensure that adequate and reliable axial force would be generated in the bolts. Pushout tests were then performed to study the strength and ductility of the clamping connectors and explore the influences of the testing parameters.

The clamping system uses T-bolts inserted into cast-in channels. Because the cast-in channels can deform when the bolts are pretensioned, more turns of the nut than in standard bolted connections are needed to enable the bolts to deform into the inelastic range and meet the minimum pretension requirements in the AISC Specification (2016a). Three M24 and M20 bolts were tested under torqued tension until fracture to develop the relationship between the number of turns of the nut and the bolt axial force. Except for one M24 bolt that fractured at the bolt heads, most bolts in the pretension tests ultimately fractured due to combined axial and torsional deformation. Two turns and 1.5 turns after a snug-tight condition were selected for pretensioning the M24 and M20 bolts, respectively. It is also noted that in the M24 bolt tests, moderate plastic deformation occurred in the channel lips, while the inelastic deformation of the channel lips was minor when the M20 bolts were pretensioned.

After the number of turns of the nut for the M24 and M20 bolts was selected, the pushout specimens were tested using a self-reacting frame. The specimens consisted of 4 ft. × 2 ft. × 6 in. precast concrete planks attached to WT5x30 or WT4x15.5 sections using the clamping connectors. WT5x30 and WT4x15.5 sections represent typical floor beams with different flange thicknesses, with the larger WT tested with the M24 clamps and the smaller WT tested with the M20 clamps. The WT4x15.5 sections were also used with the M24 clamps, requiring shims between the clamps and the WT flange since the flange was relatively thin. Parameters for the pushout tests include bolt diameter, number of channels, reinforcement configuration, loading protocol, and use of shims. In the lightly reinforced specimens, the reinforcement was designed only for gravity loading. Additional supplementary reinforcement was placed around the channel anchors to prevent anchor-related failures in the heavily reinforced specimens. The pushout tests were all displacement-controlled. The AISC loading protocol for beam-to-column moment connections was used as a guide for establishing a cyclic loading history for the clamped connections.

Based on the pushout test results and finite element analysis results, the following conclusions can be reached:

(1) The load-slip curve of Test 2-M24-2C-RH-LM, which is a baseline specimen, indicates that the behavior of the M24 clamps is ductile under monotonic loading. Compared to shear studs which normally fracture at a much smaller slip, the M24 clamping connectors can retain almost 80% of the peak strength even at 5 in. slip.

(2) Shims were used for specimens using M24 clamps and thin flange sections, and undesirable load oscillation was observed due to a stick-slip mechanism, although the peak strength was not affected. Usage of the selected shims between the clamp and the flange may be limited to applications where the slip of the clamps is small, such as in composite beams that are part of gravity systems. Different types of shims, such as brass shims, could be further investigated to eliminate load oscillation.

(3) Compared to the monotonic specimens, the peak strengths of the cyclic specimens are approximately 20% lower, which is comparable to the strength decrease seen in steel headed stud anchors when subjected to cyclic loading. After undergoing a couple of cycles, the strengths of the cyclic specimens begin to degrade, which could be attributed to the reduction of the bolt pretension and the lowering of frictional coefficient as a result of the abrasion between the clamp teeth and steel flange and between the concrete plank and steel beam. However, the load-slip behavior of the cyclically loaded pushout specimens is excellent within 1 in. slip which is conservatively assumed to be typical slip ranges for clamps used in composite diaphragms. The hysteresis load-slip loops show excellent energy dissipating capacity of the clamping connectors, and thus they may perform well

if used as connectors between composite diaphragms and steel collectors in lateral force-resisting systems.

(4) A considerable load drop was seen after 0.68 in. slip in the load-slip curve of the monotonic specimen using M20 bolts. Large rotation and complete disengagement of clamps were noted. If the M20 clamps are utilized in composite beams where the slip demand is normally much less than 0.68 in., the strength degradation is not a concern. If they are needed to withstand large slip, the performance of the M20 clamps could be improved by increasing the contact area between the clamp teeth and steel beam and between the clamp tail and concrete plank to delay rotation or developing an interlocking design where the channel lips fully restrain the rotation of the clamps. With the steel blocks inserted into the channels to support the clamp tails, the cyclically loaded specimen performed better than the corresponding monotonic specimen, even though all the clamps ultimately lost contact with the beam flanges.

(5) In terms of strength and state of cracks, the cyclic pushout specimen with light reinforcement did not perform worse than the specimen with heavy reinforcement. This implies that the additional reinforcement was not engaged which was designed to bridge potential cracking planes due to channel anchor forces. This is further proved by the low stress in the reinforcement. For the channel configuration investigated in this research, the bolt pretension force is primarily resisted by the reactions at the clamp tail and the steel beam flange, rather than transferring to the channel anchors. Therefore, the limit states for anchor channels in common applications, such as concrete cone failure under tension, are negligible, and the supplementary reinforcement has minimal effects on the behavior of the specimens.

(6) A strut-and-tie model is used to explain the formation of the cracks which were induced by the friction acting on the concrete surface, rather than concrete pryout failure. Since the frictional force at the steel-concrete interface distributes in a non-uniform manner, the damage concentrates on one side of the concrete plank

when it is loaded monotonically. These cracks may affect the reusability of the planks, but they do not affect the overall behavior of the clamping connectors.

(7) According to the bolt axial strains measured in the cyclic tests, the bolt tension gradually decreases. When the slip is small, the tension decrease is primarily attributed to the shear force acting on the bolt. At large slips, the damage to the steel flange and clamp teeth caused by abrasion could release the bolt tension. Soon after slip occurs (approximately 0.02 in.), the bolt tension reduces below the minimum bolt pretension for Group A bolts in Table J3.1M in AISC 360-16.

(8) Because of the ductile behavior of the clamps, the shear force applied to the steel beams is distributed among the clamps, demonstrating the potential of using clamps as shear connectors in composite beams. With the strain gages attached on the steel beams, the force distribution in the system is validated by the axial force plots that show the force variation at different sections along the beam length.

(9) The strength and stiffness of the clamping connectors are compared to those of steel headed stud anchors. A single M24 clamp has a similar shear capacity to a single conventional 3/4 in. diameter shear stud. Since friction is the mechanism of resisting the shear flow, the initial stiffness of the clamps is larger than that of shear studs. The ultimate slip of both M24 and M20 clamps is also greater than that of 3/4 in. diameter shear studs.

(10) Finite element models were developed which takes into account material nonlinearity, geometric nonlinearity and contact between different components. Assuming a frictional coefficient of 0.35, the finite element models predict the peak strength of the baseline test specimens well, although the slip at which the peak strength occurs is shifted because of the friction simulation in ABAQUS which assumes an elastic slip while the two contact surfaces are still sticking. A parametric study was performed to study the influences of different frictional coefficients. Based on the finite element models and test results, design equations, similar to those used for calculating the resistance of slip-critical bolted joints, are

recommended for estimating the slip strength and peak shear strength of the clamping connectors under monotonic loading. It is seen that the equations predict the slip strength and peak strength of the clamps very well. A coefficient of 0.8 could be used with the monotonic shear strength as the cyclic shear strength of the clamps.

7.2 Conclusions from composite beam tests

Since the forces the shear connectors are subjected to in pushout tests are not the same as those in composite beams, beams tests are essential to study the behavior of the shear connectors in a realistic manner and validate the findings from the pushout tests. Based on the beam test results, design methodologies for determining the flexural strength and stiffness of the composite beams are also determined.

Prior to testing the beam specimens, the number of turns of the nut was established for pretensioning the ASTM A36-14/A529-05 Grade 50, 5/8 in. diameter fully threaded rods which are utilized to connect adjacent concrete planks and resist in-plane diaphragm forces during earthquakes. One complete turn of the nut from a snug-tight position was determined after performing calibration tests where rods passing through two planks were torqued until fracture. The rods ultimately fractured because of excessive torsional deformation.

After determining the number of turns of the nut for pretensioning the bolts and rods, four full-scale deconstructable composite beams were designed and tested which are representative of the beams designed in the prototype structures in Chapter 3. Each beam specimen consisted of a 30-foot long beam attached with fifteen 2-ft.-wide planks using clamping connectors. Parameters explored in the beam tests include bolt diameter, percentage of composite action and reinforcement configuration. The actuator loading was spread using spreader beams at four points along the length (six-point bending) to mimic a secondary beam under approximately uniform loading. A pin support and a roller support were placed at the ends of the beams to permit horizontal movement as well as end rotation. The concrete planks were 8 ft. wide, which is sufficient to avoid any premature concrete failure in narrow slabs.

The specimens were loaded to 40% of their expected flexural strength and then reloaded three times. Two more cycles were then undertaken, with one cycle at 60% and the other one at 80% of the estimated flexural strength. These cycles are intended to mimic serviceability conditions. After completing the loading/unloading cycles, the beams were then loaded until the deflections were excessive.

Based on the beam test results and finite element analysis results, the following conclusions can be reached:

(1) To resist in-plane diaphragm forces during earthquakes, ASTM A36-14/A529-05 Grade 50, 5/8 in. diameter fully threaded rods were designed to connect adjacent concrete planks to ensure structural integrity. One turn after a snug-tight condition is decided for pretensioning the rods after performing pretension tests on two rods to determine the number of turns of the nut. At the ultimate state, the tensile deformation of the rods released, and both rods failed because of excessive torsional deformation.

(2) The load-beam center deflection curves indicate that the deconstructable composite beams using clamping connectors behaved in a ductile manner. At the full service loading, the behavior of the beams was slightly nonlinear, likely due to slight separation of the planks due to flexure of the beam, slight yielding of the steel beams, or slight slip of the clamps. However, the steel beams and concrete planks in the deconstructable composite beams are believed to be reusable with minor or no concern about any possible yielding that might occur during their service life. All the beams deflected to approximately L/25, and the experiments were terminated due to the limitation of the test configuration. Along with excessive beam deflection, significant steel beam yielding and localized concrete crushing were seen, but very little or no strength degradation was observed from

the load-deflection curves. The plastic hinges that formed in all the specimens indicate excellent rotational capacity of the beams.

(3) The load-displacement curves or moment-rotation curves of the beam specimens were idealized as elastic-perfectly-plastic responses. Yield deformation and ultimate deformation were defined, and the ductility of the specimens is shown to be larger than 3. The load-deflection behavior of the deconstructable composite beam specimens is similar to that of conventional composite beams.

(4) After undergoing three elastic cycles (i.e., 40% of the expected beam strength), all beams exhibited permanent deflection which mainly resulted from settling of the beams. Probably due to fit-up issues and a lack of continuity, such as gaps between adjacent concrete planks, beam settling appears to be more significant in the deconstructable specimens than in conventional composite beams designed with monolithic concrete slabs. Professional construction practices, use of tongue-and-groove joints between planks, and similar appropriate approaches would likely avoid much of the settling behavior.

(5) Compared to conventional composite beams utilizing shear studs and monolithic concrete slabs, the lack of continuity in the concrete plank system does not appear to affect the strength and stiffness of the deconstructable composite beams, as is demonstrated by the comparison between the test results and the predictions based on the design equations given in AISC 360-16.

(6) During the test, the slip of the clamps was measured at several locations along the length of the beam. The comparison of the slip measurements between different specimens verifies that the slip of the shear connectors in a composite beam is inversely proportional to the degree of shear connection. The percentage of composite action of Beam 3-M20-3C-RL is higher than 100%, and consequently the maximum slip of the clamps is only 0.02 in. Among all the specimens, the maximum slip is 0.35 in. in Test 4-M20-1C-RL which has a degree of shear connection of 43.8%.

(7) In the pushout tests, the M20 clamps did not behave as ductile as the M24 clamps. As the WT section moved, the clamps rotated and strength reduction initiated at a slip of 0.68 in. in the monotonic test. Two composite beams utilizing M20 clamps were tested, and the maximum slip of the clamps is 0.35 in., much smaller than 0.68 in. This may imply that strength degradation of the M20 clamps did not occur in the beam tests. However, testing of composite beams with much lower percentages of composite action (<25%) may reveal other findings.

(8) Based on the axial strain measurements, the neutral axes in the steel beams and concrete planks are located. At the ultimate state, the locations of the neutral axes and the strain diaphragms of the center sections conform to those determined from a plastic analysis. Although Beam 1-M24-2C-RH is a partially composite beam, the strain distribution is distinct from those of Beams 2-M24-1C-RL and 4-M20-1C-RL, which are partially composite beams with a percentage of composite action of approximately 40%. For each instrumented section in Beams 2 and 4, two neutral axes are clearly seen in the steel beam and concrete plank. In Beam 1, as the loading increases, the neutral axis in the steel beam of the center section rises into the concrete plank, while a single neutral axis remains in the steel beam at the other sections. Similarly, the neutral axis in the steel beam at the center section of Beam 3-M20-3C-RL, which is a fully composite beam, ascends quickly into the concrete plank.

(9) The same number of turns of the nut determined in the pushout test program was utilized for pretensioning the bolts used in the beam specimens. After pretensioning, the axial force of most gaged bolts exceeded the minimum pretension requirements for Group A bolts in Table J3.1M in AISC 360-16. Similar to the observations attained from the pushout tests, the pretension of the instrumented bolts decreased in the beam tests, and the reduction is strongly affected by the slip of the clamps. At serviceability, the slip of the clamps in the beams was minimal (<0.04 in.), and the tension reduction was normally less than

10%, indicating that the tension of most bolts remains above the minimum required pretension. In all the specimens, the slip of the middle clamps was trivial throughout the tests, and the tension of the middle bolts maintained. In Beam 3-M20-3C-RL, the maximum slip of the clamps is less than 0.02 in., and the tension reduction is negligible for the gaged bolts. According to the finite element analysis results of the pushout specimens, the axial force of the bolts decreases to 3/4 of their initial pretension at a slip of approximately 0.3 in. Similarly, the largest tension reduction of the bolts instrumented in the partially beam specimens (i.e., Beams 1-M24-2C-RH, 2-M24-1C-RL and 4-M20-1C-RL) is approximately 25%. Even though the bolt tension reduces as the slip of the clamps increases, the load-slip curves of the monotonic pushout specimens utilizing M24 clamps and the load-center deflection curves of the composite beams are ductile. This indicates that either the detrimental effects of bolt tension reduction are offset by the beneficial effects of frictional coefficient increase or the bolt tension reduction gradually stabilizes at large slips. Based on the pushout test and beam test results, bolt tension reduction does not affect the monotonic behavior of the M24 clamps or the flexural behavior of the composite beam specimens.

(10) The axial force of the fully threaded rods normally decreased in the tests. At serviceability, the tension of the rods decreased approximately 20%, and the reduction was more for the rods connecting planks that were crushed at the ultimate state of the beams. Because concrete crushing released the tensile strain of the rods spanning the crushed regions, the tension of these rods ultimately dissipated. If the planks were constructed with tongue-and-groove joints and tighter quality control, crushing of the concrete plank specimens could be deferred, mitigating the rod tension reduction. According to the beam test results, the performance of the deconstructable composite beams was not affected by the behavior of the rods which were designed to resist diaphragm forces. However, whether the rod tension decrease would affect the diaphragm resistance of the system should be investigated further.

(11) Shear lag is exhibited by the strain distribution along the width of the center plank. It is shown that the strain close to the center of the plank is greater than that near the ends of the plank. This pattern maintained throughout the test, since the gaps at the ends of the plank persisted and inhibited the force flow. Therefore, the effective widths of the deconstructable composite beam specimens are smaller than those calculated in accordance with AISC 360-16. Since the effective widths of the deconstructable composite beams are strongly affected by the contact between the planks, use of planks with tongue-and-groove joints and with qualities comparable to those manufactured in a precast concrete plant may result in larger effective widths. The influences of the effective width on the strength and stiffness of a composite beam are shown to be insignificant. Hence, it is recommended that the effective width of deconstructable composite beams may be determined as per AISC 360-16, as using the AISC effective width provisions results in a good estimate of the ultimate flexural strengths of the beam specimens.

(12) The load-slip curves of the clamps in the beam specimens were correlated to those obtained from the pushout tests. In both tests, the initial stiffness of the load-slip curves is very large, and the clamps begin to slip at approximately the same loading. In terms of strength, the clamps close to the ends of the beam specimens outperformed those in the pushout tests, since it is shown that shear redistribution occurred in the beams from the inner clamps to the outer clamps.

(13) Finite element models, which take into account material nonlinearity, geometric nonlinearity and contact between different components, were developed for the beam specimens. A frictional coefficient of 0.35 was assumed for all the contact surfaces. The overall behavior of the beam specimens is well predicted by the finite element models.

7.3 Recommendations

7.3.1 Design

7.3.1.1 *Clamping connectors*

Two design equations are developed to predict the slip strength and peak strength of the clamping connectors under monotonic loading. After pretensioning the bolt, the bolt tension distributes to the clamp teeth and clamp tail. Only the normal force at the clamp teeth contributes to the shear resistance of the system; therefore, a coefficient of 0.7 is used to account for the portion of bolt tension transferred to the clamp teeth. Free body diagrams show that the bolts in the clamping system are subjected to shear force transferred from the clamps. The shear force releases the axial elongation of the bolts, and as a result, the bolt tension gradually decreases, and the reduction is approximately 1/4 based on the finite element analysis results.

The proposed design equations are slightly conservative, since the factor of D_u, which represents the ratio of the mean installed bolt pretension to the specified minimum bolt tension, is conservatively taken as 1.13. Assuming a reliability index of 4.0 for the clamps, 0.9 is recommended as the reduction factor for the slip strength and peak strength design equations. A coefficient of 0.8 could be used with the monotonic shear strength as the cyclic shear strength of the clamps.

7.3.1.2 *Deconstructable composite beams*

The effective widths of the deconstructable composite beams may be determined as per AISC 360-16 (2016), and a lower-bound moment of inertia could be used to conservatively estimate the stiffness of the beams.

As the tested flexural strengths of the deconstructable beam specimens are very close to those predicted with the AISC provisions, the design methodology, given in the AISC Specification (AISC 2016a) for calculating the positive flexural strength of composite beams using monolithic concrete slabs and shear studs, can be applied to the deconstructable composite beams. A reliability analysis is performed for the beam specimens. A reliability index of 3.0 is presumed for the composite beams, and a reduction factor of 0.9 is derived.

7.3.2 Future research

The conclusions reached from this research project show that it is feasible to design composite beams with clamping connectors to enable disassembly of the structural components in the system. In the current system, the channel, T-bolt, and clamp are commercially available components. The components are not designed to work together in the proposed configuration, which resulted in certain behavior limitations that could be addressed by the development of modified components tailored to this particular application. Improvements of the current clamping system are recommended below.

(1) To reuse the concrete planks, the inelastic deformation of the channel lips generated due to bolt pretension should be minimized or eliminated. A simple solution is to roll channels with higher yield strength and thicker channel lips.

(2) Bolts with higher pretension force (higher bolt grade or larger diameter) may generate greater shear resistance than those investigated in the current test program, thereby reducing the number of bolts and clamps. As a result, the energy and material consumption for the fabrication of the clamps and bolts are decreased.

(3) The monotonic strength of the M20 clamps degrades at large slips. This could be addressed by increasing the contact area between the clamp teeth and the steel beam and between the clamp tail and the concrete plank to delay rotation or by designing the embedded channel to fully restrain the rotation of the clamp using an interlocking connection.

(4) The cyclic strengths of the pushout specimens decrease along with increasing slips. Because the strength reduction is mainly attributed to the abrasion between the steel flanges and the clamp teeth, the clamps could be redesigned such that the clamp teeth do not dig into the steel flanges. However, this redesign may adversely affect the strength of the clamps under monotonic loading, since the

strength increase from the slip load to the peak strength results from overcoming the digging effects.

Future research directions are given below:

(1) Slip tests, similar to that given in Appendix A in the RCSC Specification (RCSC 2014), could be designed and performed to quantify the frictional coefficients at the steel-concrete interface and the steel-clamp interface.

(2) Pushout specimens with different surface conditions could be tested. The effect of brass shims may be studied. Beam specimens with different lengths, steel sizes, frictional coefficients and percentages of composite action, and edge-of-slab or opening in the slab could be tested. The influences of the tongue-and-groove joints that are neglected in this research could be investigated. Since the shear strength of the M20 clamps may decline at large slips, composite beams with very low degree of shear connection are of particular interest. Based on the test results, the proposed design equations can be validated and the reduction factors can be updated.

(3) The diaphragm behavior of the deconstructable composite floor system could be investigated experimentally and computationally, including the progression of damage, the load-deformation response, force distribution between the steel chords and concrete planks, load transfer from the floor system to the collector beams and LFRS, etc.

REFERENCES

AASHTO (2003). *Guide specifications for design and construction of segmental concrete bridges:2003 interim revisions, 2nd Edition*. American Association of State Highway and Transportation Officials, Washington, DC.

ABAQUS 6.11 (2011). *Abaqus User Manual*, Dassault Systèmes Simulia Corp., Providence, Rhode Island.

ACI (2011). *Building code requirements for structural concrete (ACI 318-11) and commentary*, American Concrete Institute, Farmington Hills, Michigan.

AISC (2016). *Code of Standard Practice for Steel Buildings and Bridges (AISC 303-16)*, American Institute of Steel Construction, Chicago, Illinois.

AISC (2016a). *Specification for Structural Steel Buildings*, American Institute of Steel Construction, Chicago, Illinois.

AISC (2016b). *Seismic Provisions for Structural Steel Buildings*, American Institute of Steel Construction, Chicago, Illinois.

Amadio, C., Fedrigo, C., Fragiacomo, M., and Macorini, L. (2004). "Experimental evaluation of effective width in steel–concrete composite beams," *Journal of Constructional Steel Research*, Vol. 60, No. 2, pp.199-220.

Amadio, C., and Fragiacomo, M. (2002). “Effective width evaluation for steel–concrete composite beams," *Journal of Constructional Steel Research*, Vol. 58, No. 3, pp. 373-388.

Anderson, N. S., and Meinheit, D. F. (2005). "Pryout capacity of cast-in headed stud anchors". *PCI journal*, Vol. 50, No. 2, pp. 90-112.

Arıoglu, N., Girgin, Z. C., and Arıoglu, E. (2006). "Evaluation of ratio between splitting tensile strength and compressive strength for concretes up to 120 MPa and its application in strength criterion". *ACI Materials Journal*, Vol. 103, No. 1, pp. 18-24.

ASCE (2010). *Minimum Design Loads for Buildings and Other Structures*, American Society of Civil Engineers, Reston, Virginia

ASTM (2011). *Standard Test Methods for Splitting Tensile Strength of Cylindrical Concrete Specimens (C496/C496M-11)*, American Society for Testing and Materials, Philadelphia, Pennsylvania.

ASTM (2012). *Standard Practice for Making and Curing Concrete Test Specimens in the Field (C31/C31M-12)*, American Society for Testing and Materials, Philadelphia, Pennsylvania.

ASTM (2013). *Standard Test Methods for Tension Testing of Metallic Materials (E8/E8M-13a)*, American Society for Testing and Materials, Philadelphia, Pennsylvania.

ASTM (2014). *Standard Test Methods for Compressive Strength of Cylindrical Concrete Specimens (C39/C39M-14a)*, American Society for Testing and Materials, Philadelphia, Pennsylvania.

ASTM (2014). *Standard Test Methods for Determining the Mechanical Properties of Externally and Internally Threaded Fasteners, Washers, Direct Tension Indicators, and Rivets (F606/F606M-14a)*, American Society for Testing and Materials, Philadelphia, Pennsylvania.

ASTM (2014). *Standard Test Methods and Definitions for Mechanical Testing of Steel Products (A370-14)*, American Society for Testing and Materials, Philadelphia, Pennsylvania.

Ataei, A., Bradford, M. A., and Liu, X. (2016). "Experimental study of composite beams having a precast geopolymer concrete slab and deconstructable bolted shear connectors," *Engineering Structures*, Vol. 114, pp. 1-13.

Bazant, Z. P. (1984). "Size effect in blunt fracture: concrete, rock, metal," *Journal of Engineering Mechanics*, Vol. 110, No. 4, pp. 518-535.

Bartlett, F. M., Dexter, R. J., Graeser, M. D., Jelinek, J. J., Schmidt, B. J., and Galambos, T. V. (2003). "Updating standard shape material properties database for design and reliability," *Engineering Journal,* AISC, Vol. 40, No. 1, pp. 2-14.

British Standards Institute (2008). *BS 5975: 2008: Code of practice for temporary works procedures and the permissible stress design of falsework,* London, UK.

Brockenbrough, R. L. (2000). "MTR Survey of Plate Material Used in Structural Fabrication," Final Report to American Institute of Steel Construction, R. L. Brockenbrough & Associates, Inc., Pittsburgh, P A.

Brown, C., Hajjar, J. F., Eckelman, M., Wang, L., and Webster, M. D. (2014). "Life-Cycle Analysis of Deconstructable Composite Floor Systems". Report No. NEU-CEE-2014-01, Department of Civil and Environmental Engineering, Northeastern University, Boston, Massachusetts.

Burnet, M. J. and Oehlers, D. J. (2001), “Fracture of Mechanical Shear Connectors in Composite Beams,” *Mechanics of Structures and Machines*, Vol. 29, No. 1, pp.1–41.

Bursi, O. S., and Gramola, G. (1999). "Behaviour of headed stud shear connectors under lowcycle high amplitude displacements," *Materials and structures*, Vol. 3, No.4, pp. 290-297.

CEN (2004). *Eurocode 4: Design of Composite Steel and Concrete Structures, EN1994-1-1*, European Committee for Standardization, Brussels, Belgium.

CEN (2009). *Eurocode 2: Design of fastenings for use in concrete - Part 4-3: Anchor channels, EN1992-4-3*, European Committee for Standardization, Brussels, Belgium.

Chaboche, J. L. (1986). "Time-independent constitutive theories for cyclic plasticity," *International Journal of plasticity*, Vol. 2, No. 2, pp. 149-188.

Chinn, J. (1965). "Pushout Tests on Lightweight Composite Slabs," *AISC Engineering Journal*, Vol. 2, No. 4, pp. 129-134.

Civjan, S. A., and Singh, P. (2003). "Behavior of shear studs subjected to fully reversed cyclic loading," *Journal of Structural Engineering*, Vol. 129, No. 11, pp. 1466-1474.

Construction, M. H. (2011). Prefabrication and modularization: Increasing productivity in the construction industry, *Smart Market Report*.

Costello, D. (2014). Personal communication

Dexter, R.J., Graeser, M., Saari, W.K., Pascoe, C., Gardner, C.A., and Galambos, T.V. (2000). "Structural Shape Material Property Survey," Technical report for Structural Shape Producers Council, University of Minnesota, Minneapolis, MN.

Downey, E. W. (2006). Specifying camber. *Modern Steel Construction*, American Institute of Steel Construction, Chicago, Illinois.

Durmisevic, E., and Brouwer, J. (2002). "Design aspects of decomposable building structures," *Design for Deconstruction and Material Reuse. Proceedings of the CIB Task Group 39-Deconstruction Meeting, OMER S. DENIZ.*

Easterling, W. S., Gibbings, D. R., and Murray, T. M. (1993). "Strength of shear studs in steel deck on composite beams and joists," *Engineering Journal*, Vol. 30, No. 2, pp. 44-55.

Easterling, W. S., and Porter, M. L. (1994). "Steel-Deck-Reinforced Concrete Diaphragms. I," *Journal of Structural Engineering*, Vol. 120, No. 2, pp.560-576.

Energy Information Administration (2012). *Annual Energy Review*, U.S. Energy Information Administration, Washingtong, D.C.

Ernst, S. (2006). “Factors Affecting the Behavior of the Shear Connection of Steel-Concrete Composite Beams,” Ph.D. Dissertation, School of Engineering, University of Western Sydney, Sydney, Australia.

Fleischman, R. (2014). "Seismic Design Methodology Document for Precast Concrete Diaphragms," Final Report to the Charles Pankow Foundation, University of Arizona, Tucson, AZ.

Frank, K.H., and Read, D.R. (1993). "Statistical Analysis of Tensile Data for Wide-Flange Structural Shapes," Final Report to Structural Shape Producer's Council, University of Texas at Austin, Austin, TX.

Frank, K. H., and Yura, J. A. (1981). "An Experimental Study of Bolted Shear Connections," Report No. FHWA/RD-81/148, Federal Highway Administration, U.S. Department of Transportation, Washington, D.C., December.

Fisher, J. W., Ravindra, M. K., Kulak, G. L., and Galambos, T. V. (1978). "Load and resistance factor design criteria for connectors," *Journal of the Structural Division*, Vol. 104, No. 9, pp. 1427-1441.

Galambos, T. V., and Ravindra, M. K. (1976). "Load and Resistance Factor Design Criteria for Composite Beams," *Research Report No. 44*, Civil Engineering Department, Washington University, St. Louis, Missouri.

Galambos, T. V., and Ravindra, M. K. (1978). "Properties of Steel for Use in LRFD," *Journal of the Structural Division*, Vol. 104, No. 9, pp. 1459-1468.

Gattesco, N. (1999). "Analytical modeling of nonlinear behavior of composite beams with deformable connection," *Journal of Constructional Steel Research*, Vol. 52, No. 2, pp. 195-218.

Gattesco, N., and Giuriani, E. (1996). "Experimental study on stud shear connectors subjected to cyclic loading," *Journal of Constructional Steel Research*, Vol. 38, No. 1, pp.1-21.

Goble, G. G. (1968). "Shear strength of thin flange composite specimens," *Engineering Journal*, Vol. 5, No. 2, pp. 62-65.

Gorgolewski, M. (2008). "Designing with reused building components: some challenges," *Building Research and Information*, Vol. 36, No. 2, pp. 175-188.

Grant, J. A. (1973). "High strength steel composite beams with formed metal deck and low partial shear connections," MS thesis, Lehigh University.

Grant, J. A., Fisher, J. W., and Slutter, R. G. (1977). "Composite beams with formed steel deck," *Engineering Journal*, Vol. 14, No. 1, pp. 24-43.

Grigorian, C. E., and Popov, E. P. (1994). "Energy Dissipation with Slotted Bolted Connections". Report UCB/EERC-94/02. Earthquake Engineering Research Center, College of Engineering, University of California at Berkeley, Berkeley, California.

Grondin, G., Jin, M. and Josi, G. (2007). "Slip Critical Bolted Connections—A Reliability Analysis for the Design at the Ultimate Limit State," Structural

Engineering Report No. 270, Department of Civil and Environmental, Engineering, University of Alberta, Edmonton, Alberta.

Halfen (2011). *Halfen Anchoring Systems*, Halfen, Converse, Texas.

Halfen (2013). *Halfen Cast-In Channels: Technical Product Information*. Halfen, Langenfeld, Germany.

Hansell, W. C., Viest, I. M., Ravindra, M. K., and Galambos, T. V. (1978). "Composite beam criteria in LRFD," *Journal of the Structural Division*, Vol 104, NO. 9, pp. 1409-1426.

Hawkins, N. M., and Mitchell, D. (1984). "Seismic response of composite shear connections," *Journal of Structural Engineering*, Vol. 110, No. 9, pp. 2120-2136.

Hicks, S. (2007). "Strength and ductility of headed stud connectors welded in modern profiled sheeting," *Structural Engineer*, Vol. 85, No. 10, pp. 32-39.

Intelligent Engineering (2011). *SPS floors, Intelligent Engineering*, Ottawa, Ontario, Canada.

Jaquess, T.K., and Frank, K.H. (1999). *Characterization of the Material Properties of Rolled Sections*, Technical Report for SAC Joint Venture, University of Texas at Austin, Austin, Texas.

Jayas, B. S., and Hosain, M. U. (1988). "Behaviour of headed studs in composite beams: push-out tests," *Canadian Journal of Civil Engineering*, Vol. 15, No. 2, pp. 240-253.

Jayas, B. S., and Hosain, M. U. (1989). “Behaviour of headed studs in composite beams: full-size tests," *Canadian Journal of Civil Engineering*, Vol. 16, No. 5, pp. 712-724.

Johnson, R. P., and Yuan, H. (1998). "Models and design rules for stud shear connectors in troughs of profiled sheeting," *Proceedings of the Institution of Civil Engineers. Structures and buildings*, Vol.128, No.3, pp. 252-263.

Kibert, C. J. (2003). "Deconstruction: the start of a sustainable materials strategy for the built environment," *Industry and environment*, Vol. 26, No. 2-3, pp. 84-88.

Kulak, G. L., Fisher, J. W., and Struik, J. H. (1987). *A Guide to Design Criteria for Bolted and Riveted Joints*, Wiley, NY.

Lam, D. (2000). "New test for shear connectors in composite construction," *Composite Construction in Steel and Concrete IV*, American Society of Civil Engineers, May 2002, Alberta, Canada, pp. 404-414.

Lam, D., Dai, X., and Saveri, E. (2013). "Behavior of Demountable Shear Connectors in Steel-Concrete Composite Beams," *Composite Construction in Steel and Concrete VII*, American Society of Civil Engineers, July 2013, Queensland, Australia, pp. 618-631.

Lam, D., Dai, X., Ashour, A., and Rehman, N. (2017). "Recent research on composite beams with demountable shear connectors." *Steel Construction*, Vol. 10, No. 2, pp. 125-134.

Lee, J., and Fenves, G. L. (1998). "Plastic-damage model for cyclic loading of concrete structures," *Journal of engineering mechanics*, Vol. 124, No. 8, pp. 892-900.

Lee, S. S. M., and Bradford, M. A. (2013). "Sustainable composite beam behavior with deconstructable bolted shear connectors," *Composite Construction in Steel and Concrete VII*, American Society of Civil Engineers, July 2013, Queensland, Australia, pp. 445-455.

Leon, R.T. (1990), "Serviceability of Composite Floor," *Proceedings of the 1990 National Steel Construction Conference*, AISC, pp. 18:1–18:23.

Leon, R.T. and Alsamsam, I. (1993). "Performance and serviceability of composite floors." Structural Engineering in Natural Hazards Mitigation, *Proceedings of the ASCE Structures Congress*, ASCE, pp.1479-1484.

Lind, N. C. (1971). "Consistent partial safety factors," *Journal of the Structural Division*, Vol. 97, No. 6, pp. 1651-1669.

Lindapter (2011). *Steelwork Fixings Catalogue*, Lindapter, Bradford, U.K.

Lubliner, J., Oliver, J., Oller, S., and Onate, E. (1989). "A plastic-damage model for concrete," *International Journal of solids and structures*, Vol. 25, No. 3, pp. 299-326.

Luttrell, L. D. (2004). *Steel deck institute diaphragm design manual*. Steel Deck Institute.

Lyons, J. C., Easterling, W. S., and Murray, T. M. (1996), "Strength of Headed Shear Studs in Cold-formed Steel Deck," Thirteenth International Specialty Conference on Cold-Formed Steel Structures, St. Louis, Missouri U.S.A., October 17-18, 1996.

McGuire, R. K., and Cornell, C. A. (1974). "Live load effects in office buildings," *Journal of the Structural Division*, Vol 100, No. 7, pp. 1351-1366.

Moehle, Jack P., Hooper, John D., Kelly, Dominic J., and Meyer, Thomas R. (2010). "Seismic design of cast-in-place concrete diaphragms, chords, and collectors: a guide for practicing engineers," *NEHRP Seismic Design Technical Brief No. 3*, produced by the NEHRP Consultants Joint Venture, a partnership of the Applied Technology Council and the Consortium of Universities for Research in Earthquake Engineering, for the National Institute of Standards and Technology, Gaithersburg, MD, NIST GCR 10-917-4.

Moore, M. A., Rassati, G. A., and Swanson, J. A. (2008). "Evaluation of the current resistance factors for high-strength bolts," Final report submitted to the Research Council on Structural Connections, Department of Civil and Environmental Engineering, University of Cincinnati, Cincinnati, Ohio.

Moynihan, M. C., and Allwood, J. M. (2014). "Viability and performance of demountable composite connectors," *Journal of Constructional Steel Research*, Vol. 99, pp. 47-56.

Naraine, K. S. (1984). "Slip and uplift effects in composite beams." Master thesis, McMaster University.

Newmark, N. M., Siess, C. P., and Viest, I. (1951). "Tests and analysis of composite beams with incomplete interaction," *Proc. Soc. Exp. Stress Anal*, Vol. 9, No. 1, pp. 75-92.

O'Connor, J. (2004). "Survey on actual service lives for North American buildings," *Woodframe housing durability and disaster issues conference, Las Vegas*.

Oehlers, D. J., and Bradford, M. A. (1995). *Composite steel and concrete structural members: fundamental behaviour*, Oxford: Pergamon Press.

Oehlers, D. J., and Coughlan, C. G. (1986). "The shear stiffness of stud shear connections in composite beams," *Journal of Constructional Steel Research*, Vol. 6, No. 4, pp. 273-284.

Oehlers, D.J. and Johnson, R.P. (1987). "The strength of stud shear connections in composite beams", *The Structural Engineer*, Vol. 65, No.2, pp 44-48.

Oehlers, D. J., and Sved, G. (1995). "Composite beams with limited-slip-capacity shear connectors," *Journal of Structural Engineering*, Vol. 121, No. 6, pp. 932-938.

Ollgaard, J. G., Slutter, R. G., and Fisher, J. W. (1971). "Shear strength of stud connectors in lightweight and normal-weight concrete," *AISC Engineering Journal*, Vol. 8, No. 2, pp. 55-64.

Pallarés, L. and Hajjar, J. F. (2009). "Headed Steel Stud Anchors in Composite Structures: Part I. Shear," Report No. NSEL-013, Newmark Structural Laboratory Report Series (ISSN 1940-9826), Department of Civil and Environmental Engineering, University of Illinois at Urbana-Champaign, Urbana, Illinois, April.

Pathirana, S. W., Uy, B., Mirza, O., and Zhu, X. (2015). "Strengthening of existing composite steel-concrete beams utilising bolted shear connectors and welded studs," *Journal of Constructional Steel Research*, Vol.114, pp. 417-430.

PCI (2000). *Tolerances for Precast and Prestressed Concrete Construction (PCI MNL-135-00)*, Precast/Prestressed Concrete Institute, Chicago, Illinois.

PCI (2010). *PCI Design Handbook: Precast and Prestressed Concrete, 7th edition*, Precast/Prestressed Concrete Institute, Chicago, Illinois.

Prager, W. (1949). "Recent developments in the mathematical theory of plasticity," *Journal of Applied Physics*, Vol. 20, No. 3, pp. 235-241.

Popovics, S. (1973). "A numerical approach to the complete stress-strain curve of concrete," *Cement and concrete research*, Vol. 3, No. 5, pp. 583-599.

Qureshi, J., Lam, D., and Ye, J. (2011). "Effect of shear connector spacing and layout on the shear connector capacity in composite beams," *Journal of constructional steel research*, Vol. 67, No. 4, pp. 706-719.

Rambo-Roddenberry, M. D. (2002). "Behavior and strength of welded stud shear connectors." Doctoral dissertation, Virginia Polytechnic Institute and State University.

Ramesh, T., Prakash, R., and Shukla, K. K. (2010). "Life cycle energy analysis of buildings: An overview," *Energy and Buildings*, Vol. 42, No. 10, pp. 1592-1600.

Ranzi, G., Bradford, M. A., Ansourian, P., Filonov, A., Rasmussen, K. J. R., Hogan, T. J., and Uy, B. (2009). "Full-scale tests on composite steel–concrete beams with steel trapezoidal decking," *Journal of Constructional Steel Research*, Vol. 65, No. 7, pp. 1490-1506.

Ravindra, M. K., and Galambos, T. V. (1978). "Load and resistance factor design for steel," *Journal of the Structural Division*, ASCE, Vol. 104, No. ST 9, pp. 1337-1353.

RCSC (2014). *Specification for Structural Joints Using High-Strength Bolts*, Research Council on Structural Connections, Chicago, Illinois.

Rehman, N., Lam, D., Dai, X., and Ashour, A. (2016). "Experimental study on demountable shear connectors in composite slabs with profiled decking." *Journal of Constructional Steel Research*, Vol. 122, pp. 178-189.

Renz, B. (2005). Innovative Connections. *Modern Steel Construction*, American Institute of Steel Construction, Chicago, Illinois, August.

Rex, C. O., and Easterling, W. S. (1996). "Behavior and Modeling of Mild and Reinforcing Steel," *Research Report CE/VPI-ST 96/12*, Virginia Polytechnic Institute and State University, VA.

Ricker, D. T. (1989). "Cambering Steel Beams," *Engineering Journal*, AISC, Vol. 26, No. 4, 4th Quarter, pp.136-142.

Rotter, J. M., and Ansourian, P. (1978). "Cross-section behaviour and ductility in composite beams," *No. Research Rpt. 329 Monograph*, University of Sydney, School of Civil Engineering, Civil Engineering Laboratories.

Sabelli, Rafael, Sabol, Thomas A., and Easterling, Samuel W. (2011). "Seismic design of composite steel deck and concrete-filled diaphragms: A guide for practicing engineers," *NEHRP Seismic Design Technical Brief No. 5*, produced by the NEHRP Consultants Joint Venture, a partnership of the Applied Technology Council and the Consortium of Universities for Research in Earthquake Engineering, for the National Institute of Standards and Technology, Gaithersburg, MD, NIST GCR 11-917-10..

Saari, W. K., Hajjar, J. F., Schultz, A. E., and Shield, C. K. (2004). "Behavior of shear studs in steel frames with reinforced concrete infill walls," *Journal of Constructional Steel Research*, Vol. 60, No. 10, pp. 1453-1480.

SDI (2004). *Diaphragm design manual*, Third Edition (SDI DDMO3), Steel Deck Institute, Fox Grove, IL

Shen, C., P. Mamaghani, I. H., Mizuno, E., and Usami, T. (1995). "Cyclic behavior of structural steels. II: Theory," *Journal of Engineering Mechanics*, Vol. 121, No. 11, pp. 1165-1172.

Stankevicius, J., Georg, J., Grondin, G. Y., and Kulak, G. L. (2009). "Measurement of slip coefficient for grade ASTM A588 steel plates in slip-critical joints," Structural Engineering Report No. 268, Department of Civil and Environmental, Engineering, University of Alberta, Edmonton, Alberta.

Steel Construction (2012). *Recycling and Reuse,* http://www.steelconstruction.info/Recycling_and_reuse (accessed January 2014).

Teraszkiewicz, J.S. (1965). "Tests on stud shear connectors", *Road Research Laboratory Technical Note No. 36*, Crowthorne, U.K., December.

Toprac, A. A. (1965). “Strength of Three New Types of Composite Beams,” *Engineering Journal*, AISC, Vol. 2, No. 1, 1st Quarter, 21-30.

Towns, J., Cockerill, T., Dahan, M., Foster, I., Gaither, K., Grimshaw, A., Hazlewood, V., Lathrop, S., Lifka, D., Peterson, G.D., Roskies, R., Scott, J. R., and Wilkins-Diehr, D. (2014)." XSEDE: accelerating scientific discovery," *Computing in Science & Engineering*, Vol. 16, No. 5, pp. 62-74.

Turmo, J. O. S. E., Ramos, G., and Aparicio, A. C. (2006). "Shear strength of dry joints of concrete panels with and without steel fibres: Application to precast segmental bridges," *Engineering Structures*, Vol.28, No. 1, pp. 23-33.

U.S. Environmental Protection Agency (2008). *Municipal Solid Waste in the United States: 2007 Facts and Figures*, EPA 530-R-08-010, Washington, D.C., November.

U.S. Environmental Proteaction Agency (EPA) (2014). *US EPA,* http://www.epa.gov/climatechange/wycd/waste/downloads/concrete-chapter10-28-10.pdf.

Vulcraft (2001). *Steel and Joist Girders, Steel Roof and Floor Deck, Composite and Non Composite Floor Joists*, Vulcraft, Florence, South Carolina.

Wang, L., Webster, M. D., and Hajjar, J. F. (2015). "Diaphragm Behavior of Deconstructable Composite Floor Systems," *Proceedings of the 8th International Conference on Behavior of Steel Structures in Seismic Areas (STESSA 2015),*Shanghai, China, July 1-3, 2015, China Architecture & Building Press, Beijing, China.

Webster, M., Kestner, D., Parker, J., and Johnson, M. (2007). "Deconstructable and Reusable Composite Slab," Winners in the Building Category: Component – Professional Unbuilt, Lifecycle Building Challenge <http://www.lifecyclebuilding.org/2007.php>

Wight, J. K., and MacGregor, J. G. (2009). *Reinforced Concrete: Mechanics and Design*, *6th edition*, Pearson Education, Inc., New Jersey.

Ziemian, R.D. (ed.) (2010). *Guide to Stability Design Criteria for Metal Structures*, 6th Ed., John Wiley & Sons, Inc., Hoboken, NJ.

APPENDICES

Appendix A PROTOTYPE STRUCTURE DESIGN SUMMARY

This appendix summarizes the design of the lateral-force resistance systems and gravity columns of the steel prototype buildings, based on the design methodology summarized in Chapter 3.

Table A.1 summarizes the sizes of the beams and girders of the 8 prototype buildings using deconstructable floor systems. The required number of clamps per beam and girder is also given. Table A.2 summarize the required number of shear studs per beam and girder and the sizes of the beams and girders of the 8 prototype buildings using traditional composite floor systems.

Table A.3 summarizes the sizes of the beams, girders, braces, and columns that make up the lateral resistance systems for both traditional and deconstructable buildings. Gravity columns are those not involved in the lateral system. Table A.4 summarizes the sizes of the gravity columns for both building types.

The columns and lateral resistance systems are designed to be the same for both traditional and deconstructable floor systems, since the concrete slabs and planks are both solid. Thus, Table A.3 and Table A.4 may be used for both systems.

Table A.1 Member sizes for the deconstructable composite floor system

Name	Floor interior beam		Floor exterior beam		Floor interior girder		Floor exterior girder	
	Member size	Number of bolts	Member size	Number of bolts	Member size	Number of bolts	Member size	Number of bolts
30-3-8-gc	W18x35	60	W14x22	32	W30x90	40	W21x55	40
30-3-6-gc	W18x40	60	W14x26	32	W30x99	40	W21x55	40
20-3-8-gc	W10x19	40	W10x15	24	W18x35	40	W12x19	32
20-3-6-gc	W12x22	40	W10x15	24	W18x40	40	W14x26	24
30-9-8-gc	W16x31	32	W12x22	32	W21x62	40	W16x40	40
30-9-6-gc	W14x30	32	W12x19	32	W21x55	40	W18x35	40
20-9-8-gc	W12x19	24	W10x15	24	W14x30	24	W12x19	24
20-9-6-gc	W12x16	24	W10x15	24	W14x26	24	W12x16	24

Table A.2 Member sizes for the conventional composite floor system with solid slabs

Name	Floor interior beam		Floor exterior beam		Floor interior girder		Floor exterior girder	
	Member size	Number of Shear Studs	Member size	Number of Shear Studs	Member size	Number of Shear Studs	Member size	Number of Shear Studs
30-3-8-sc	W18x35	48	W14x22	24	W27x84	88	W21x44	68
30-3-6-sc	W18x40	48	W14x26	36	W27x84	88	W21x50	68
20-3-8-sc	W12x19	30	W10x15	12	W18x35	30	W12x19	30
20-3-6-sc	W12x22	20	W10x15	12	W18x35	48	W14x22	24
30-9-8-sc	W12x19	30	W10x15	12	W21x44	52	W16x26	36
30-9-6-sc	W12x19	30	W10x15	12	W21x44	52	W16x26	44
20-9-8-sc	W10x15	12	W10x15	12	W12x19	30	W10x15	12
20-9-6-sc	W10x15	12	W10x15	12	W12x19	30	W10x15	12

Table A.3 Member sizes of lateral-force resisting systems

Name	Floor Level	Seismic Design (Beams)			Seismic Design (Girders)		
		Braces	Beams	Columns	Braces	Girders	Columns
		Member size	Member Size	Member Size	Member size	Member Size	Member Size
30-3-8	Roof	HSS4X4X5/16	W30X108	W8X40	HSS4X4X5/16	W30X108	W8X40
	3	HSS7X7X1/2	W30X99	W12X96	HSS7X7X1/2	W30X99	W10X77
	2	HSS8X8X5/8	W33X130	W14X132	HSS8X8X5/8	W36X135	W12X96
30-3-6	Roof	HSS4X4X5/16	W30X108	W8X40	HSS4X4X5/16	W30X108	W8X40
	3	HSS7X7X1/2	W30X99	W12X96	HSS7X7X1/2	W30X99	W10X77
	2	HSS8X8X5/8	W33X130	W14X132	HSS8X8X5/8	W36X135	W12X96
20-3-8	Roof	HSS3-1/2X3-1/2X1/4	W24X76	W8X40	HSS3-1/2X3-1/2X1/4	W24X76	W8X40
	3	HSS5-1/2X5-1/2X3/8	W21X50	W10X68	HSS5-1/2X5-1/2X3/8	W24X68	W8X67
	2	HSS6X6X1/2	W24X84	W10X77	HSS6X6X1/2	W30X99	W10X68
20-3-6	Roof	HSS3-1/2X3-1/2X1/4	W24X76	W8X40	HSS3-1/2X3-1/2X1/4	W24X76	W8X40
	3	HSS5-1/2X5-1/2X3/8	W21X50	W10X68	HSS5-1/2X5-1/2X3/8	W24X68	W8X67
	2	HSS6X6X1/2	W24X84	W10X77	HSS6X6X1/2	W30X99	W10X68
30-9-8	Roof	HSS4-1/2X4-1/2X5/16	W30X116	W8X40	HSS4-1/2X4-1/2X5/16	W30X116	W8X40
	9	HSS7X7X5/8	W24X76	W12X96	HSS7X7X5/8	W27X94	W10X88
	8	HSS9X9X5/8	W30X116	W12X106	HSS9X9X5/8	W30X116	W12X96
	7	W10X88	W30X124	W14X283	W10X88	W30X124	W14X233
	6	W12X96	W24X68	W14X283	W12X96	W24X76	W14X233
	5	W12X96	W30X124	W14X455	W12X96	W30X124	W14X426
	4	W12X106	W27X84	W14X455	W12X106	W30X99	W14X426
	3	W12X106	W30X124	W14X665	W12X106	W30X124	W14X605
	2	W12X106	W18X40	W14X665	W12X106	W21X44	W14X605

Table A.3 Member sizes of lateral-force resisting systems (continued)

Name	Floor Level	Seismic Design (Beams)			Seismic Design (Girders)		
		Braces	Beams	Columns	Braces	Girders	Columns
		Member size	Member Size	Member Size	Member size	Member Size	Member Size
30-9-6	Roof	HSS4-1/2X4-1/2X5/16	W30X116	W8X40	HSS4-1/2X4-1/2X5/16	W30X116	W8X40
	9	HSS7X7X5/8	W24X76	W12X96	HSS7X7X5/8	W24X76	W10X88
	8	HSS9X9X5/8	W30X116	W12X106	HSS9X9X5/8	W30X116	W10X88
	7	W10X77	W30X124	W14X257	W10X77	W30X124	W14X233
	6	W10X88	W30X99	W14X257	W10X88	W30X99	W14X233
	5	W12X96	W30X124	W14X455	W12X96	W30X124	W14X398
	4	W12X96	W18X35	W14X455	W12X96	W21X44	W14X398
	3	W12X96	W30X124	W14X665	W12X96	W30X124	W14X550
	2	W12X96	W18X35	W14X665	W12X96	W18X40	W14X550
20-9-8	Roof	HSS3-1/2X3-1/2X1/4	W24X76	W8X40	HSS3-1/2X3-1/2X1/4	W24X76	W8X40
	9	HSS6X6X1/2	W16X40	W8X67	HSS6X6X1/2	W21X50	W8X67
	8	HSS7X7X1/2	W21X55	W10X68	HSS7X7X1/2	W24X62	W8X67
	7	HSS7X7X5/8	W18X55	W14X159	HSS7X7X5/8	W21X62	W14X145
	6	HSS8X8X5/8	W21X62	W14X159	HSS8X8X5/8	W24X68	W14X145
	5	HSS8X8X5/8	W21X68	W14X283	HSS8X8X5/8	W24X76	W14X283
	4	HSS9X9X5/8	W21X55	W14X283	HSS9X9X5/8	W24X68	W14X283
	3	HSS9X9X5/8	W21X62	W14X426	HSS9X9X5/8	W24X76	W14X426
	2	HSS9X9X5/8	W14X22	W14X426	HSS9X9X5/8	W18X35	W14X426

Table A.3 Member sizes of lateral-force resisting systems (continued)

Name	Floor Level	Seismic Design (Beams)			Seismic Design (Girders)		
		Braces	Beams	Columns	Braces	Girders	Columns
		Member size	Member Size	Member Size	Member size	Member Size	Member Size
20-9-6	Roof	HSS3-1/2X3-1/2X1/4	W24X76	W8X40	HSS3-1/2X3-1/2X1/4	W24X76	W8X40
	9	HSS5-1/2X5-1/2X3/8	W16X40	W8X67	HSS5-1/2X5-1/2X3/8	W18X46	W8X58
	8	HSS7X7X1/2	W30X99	W8X67	HSS7X7X1/2	W30X99	W8X58
	7	HSS7X7X1/2	W18X55	W14X159	HSS7X7X1/2	W21X62	W14X145
	6	HSS7X7X5/8	W24X62	W14X159	HSS7X7X5/8	W24X68	W14X145
	5	HSS7X7X5/8	W18X55	W14X283	HSS7X7X5/8	W21X62	W14X283
	4	HSS8X8X5/8	W21X55	W14X283	HSS8X8X5/8	W24X62	W14X283
	3	HSS8X8X5/8	W18X55	W14X398	HSS8X8X5/8	W21X62	W14X398
	2	HSS8X8X5/8	W12X19	W14X398	HSS8X8X5/8	W16X31	W14X398

Table A.4 Member sizes of gravity columns

Name	Floor Level	Edge Column	Corner Column
		Member size	Member size
30-3-8	Roof	W8X31	W8X31
	3	W8X35	W8X31
	2	W12X53	W8X31
30-3-6	Roof	W8X31	W8X31
	3	W10X33	W8X31
	2	W10X49	W8X31
20-3-8	Roof	W8X31	W8X31
	3	W8X31	W8X31
	2	W8X31	W8X31
20-3-6	Roof	W8X31	W8X31
	3	W8X31	W8X31
	2	W8X31	W8X31
30-9-8	Roof	W8X31	W8X31
	9	W8X31	W8X31
	8	W8X31	W8X31
	7	W8X40	W8X31
	6	W10X49	W8X31
	5	W12X58	W10X39
	4	W12X65	W10X45
	3	W12X72	W10X49
	2	W12X79	W12X53
30-9-6-gc	Roof	W8X31	W8X31
	9	W8X31	W8X31
	8	W8X31	W8X31
	7	W8X35	W8X31
	6	W8X48	W8X31
	5	W10X49	W8X35
	4	W12X58	W8X40
	3	W12X65	W8X48
	2	W12X72	W10X49

Table A.4 Member sizes of gravity columns (continued)

Name	Floor Level	Edge Column	Corner Column
		Member size	Member size
20-9-8	Roof	W8X31	W8X31
	9	W8X31	W8X31
	8	W8X31	W8X31
	7	W8X31	W8X31
	6	W8X31	W8X31
	5	W8X31	W8X31
	4	W10X39	W8X31
	3	W10X45	W8X31
	2	W10X49	W8X31
20-9-6	Roof	W8X31	W8X31
	9	W8X31	W8X31
	8	W8X31	W8X31
	7	W8X31	W8X31
	6	W8X31	W8X31
	5	W8X31	W8X31
	4	W8X35	W8X31
	3	W8X40	W8X31
	2	W10X45	W8X31

Appendix B PRECAST CONCRETE PLANK DESIGN

B.1 Flexural reinforcement and shear reinforcement design

This appendix shows the design of the precast concrete planks and cast-in-place concrete slabs used in the prototype structures that are designed in Chapter 3 and represent office building occupancy. As per ASCE 7-10 (2010), in addition to dead load, floors should be designed for uniformly distributed live load and concentrated live load. The magnitudes of the dead load and uniform live load the prototype structures are subjected to are provided in Chapter 3. According to Table 4.1 in ASCE 7-10 (2010), the concentrated live load is assumed to be 2,000 lbs uniformly distributed over an area of 2.5 ft. by 2.5 ft. When used in design load combinations, this load should be multiplied by corresponding factors. Floors should be designed for the greater loading effects produced by the uniform live load and concentrated live load.

The floor plan for the buildings designed with deconstructable composite floor systems is given in Figure 1.4. Assuming the tongue-and-groove joints illustrated in Figure 1.1 transfer shear only, a one-plank strip may behave like a continuous beam with hinges at its ends and along its sides. However, a staggered two-plank strip has the capacity of transferring moment across all joints due to force transfer between the staggered planks. Conservatively, the planks and the reinforcement could be designed using twice the moment and shear obtained from continuous beam analysis. Alternatively, the load transfer between adjacent concrete planks and the required strengths for the planks could be determined from finite element analysis.

Reinforcement is also designed for monolithic cast-in-place concrete slabs used in conventional composite floor systems. Solid concrete slabs, rather than composite slabs, are assumed. The design of solid concrete slabs is slightly different from the design of composite slabs. In composite slabs, metal deck serves as positive reinforcement, and welded wire fabric or reinforcing bars are placed above the deck as the temperature and shrinkage reinforcement. Under negative bending, the metal deck is not permitted to be designed as compressive reinforcing steel, and the temperature and shrinkage reinforcement are normally insufficient for the negative bending moment over the steel supports. As a result, the concrete slab in the negative bending moment region may be designed as a conventional reinforced concrete slab.

All designs use ACI 318-11.

Parameters:

Load:

Uniform dead load = 92.5 psf

Uniform live load = 80 psf

Concentrated live load = 2,000 lbs

Slab/Plank:

Span = 10 ft.

Depth = 6 in.

Width = 24 in.

Concrete:

$f_c' = 4000\, psi$

Reinforcement:

Longitudinal reinforcement: No.4

$A_s = 0.2\, in.^2$

$f_y = 60\, ksi$

Other reinforcement: No.3

$A_s = 0.11\, in.^2$

$f_y = 60\, ksi$

Cast-in channels:

$f_y = 235\, MPa \approx 36\, ksi$

Calculations:

1. Required flexural strength

- Uniform loading

Load combination (9-1) in ACI 318-11: $w_u = 1.4 \times 92.5 = 129.5\, psf$

Load combination (9-2) in ACI 318-11 : $w_u = 1.2 \times 92.5 + 1.6 \times 80 = 239 psf$

Design line load for a two-foot wide plank $= 239 \times 2 = 478\, plf$

ACI Coefficients

ACI 318-11 recommends coefficients for the calculation of moment and shear for a one-way slab in Section 8.3.3, provided the following requirements are satisfied.

1. There are two or more continuous spans.
2. The spans are approximately equal, with the longer of the two adjacent spans not more than 1.2 times the length of the shorter one.
3. The loads are uniformly distributed.
4. The unfactored live load does not exceed three times the unfactored dead load.
5. The members are prismatic.

The coefficients, calculated using an influence line theory, take into consideration the loading patterns that lead to the maximum moment and shear in the slab. When the concrete planks or slabs are subjected to the uniform dead load (92.5 psf) and live load (80 psf), all these requirements are met in the design, and these coefficients could thus be used for the moment and shear calculation.

Moment:

The maximum positive moment:

$$M_{upos} = C_m\left(w_u {l_n}^2\right) = \frac{1}{14} \times 478 \times \frac{10^2}{1000} = 3.41\, ft - kips$$

The maximum negative moment:

$$M_{uneg} = C_m\left(w_u {l_n}^2\right) = \frac{1}{10} \times 478 \times \frac{10^2}{1000} = 4.78\, ft - kips$$

Shear:

The maximum shear:

$$V_u = C_v(w_u l_n/2) = 1.15 \times 478 \times 10/2000 = 2.75\, kips$$

These required bending moment and shear force can be utilized for the design of a two-foot-wide concrete strip in the conventional composite floor system, whereas a two-foot-wide concrete plank in the deconstructable composite floor system could be conservatively designed using twice these required strengths. It should be noted that the center-to-center spacing between the steel supports is employed in the calculations. More accurate results could be obtained by using clear spans.

Finite Element Analysis

A three-dimensional shell model was developed in ABAQUS/CAE and analyzed in ABAQUS/Standard, as illustrated in Figure B.1. In this model, the concrete planks within a region of one bay (30 ft.) by three bays (90 ft.) of the prototype building were included. The shells were meshed with the linear, finite-membrane-strain, reduced-integration, quadrilateral shell elements (S4R). Since the girder planks are clamped to the steel girders along their lengths, all degrees of freedom of the girder planks were fully restrained in the FEM. The steel beam supports cannot fully restrain the rotation of the planks; therefore, all the steel beams were idealized as roller supports, with the exception of one edge beam that was treated as a pin support. Rigid-end zones were ignored in this analysis.

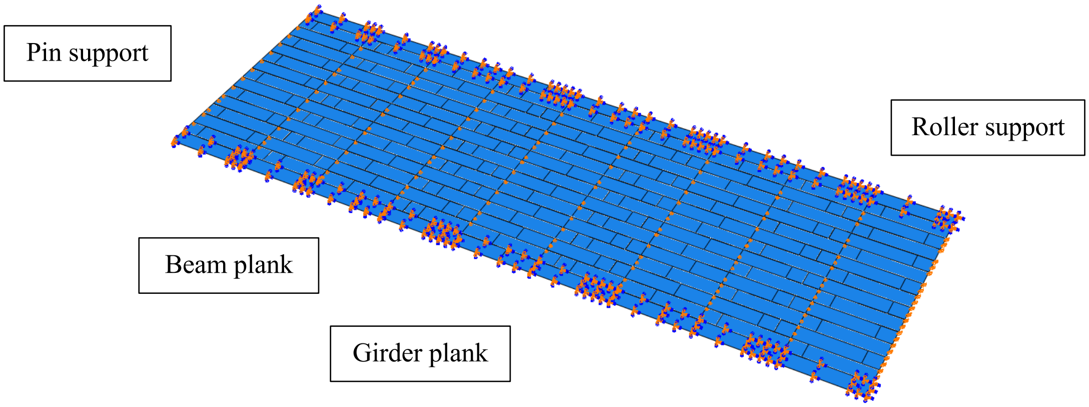

Figure B.1 Shell model of DfD floor system

The dead load was applied to the whole region, while the loading patterns of the live load were defined to produce the maximum loading effects, as given in Figure B.2. There should be some negative bending moments at the end supports of the floor system due to the rotational resistance of the spandrel beams. Consequently, a distributed moment of $w_u {l_n}^2/24$ was applied at the end supports of the model (Wight et al. 2009). In this linear analysis, the elastic modulus and Poisson's ratio of the concrete planks were defined as 4031 ksi and 0.15, respectively. Between adjacent concrete planks, tie constraints were utilized to allow shear force transfer, but the bending moment was released at the longitudinal and transverse joints.

- Concentrated loading

ASCE 7-10 (2010) requires that the concentrated load be distributed over an area of 2.5 ft. by 2.5 ft. Given that the width of the concrete planks is 2 ft., the distributed area of the concentrated force is simplified as a region of 2 ft. by 2 ft., which may result in a conservative design compared to the ASCE requirements. Figure B.3 illustrates the concentrated force locations where the maximum positive bending moment, maximum negative bending moment, and maximum shear were generated in the planks.

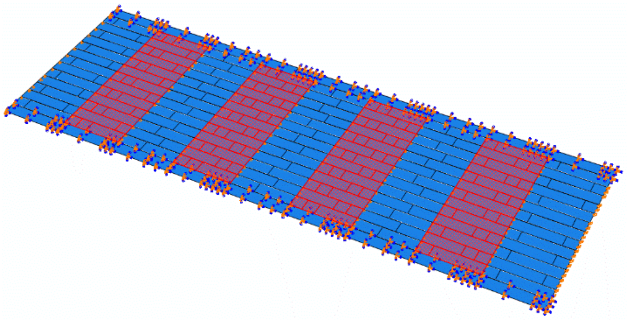

Case 1

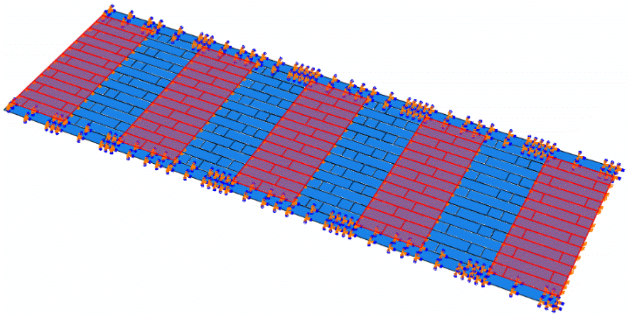

Case 2

a) Maximum positive bending moment at mid-span of plank

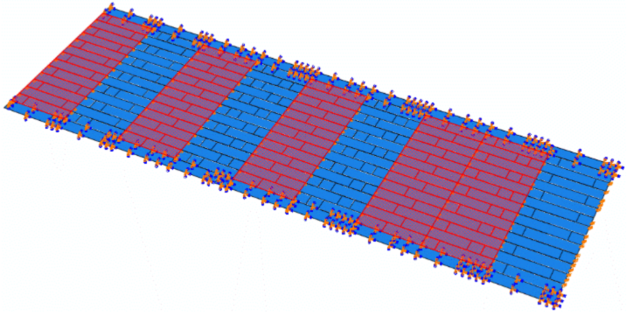

Case 3

b) Maximum negative bending moment and shear force at support

Note: The uniform live loading is applied at the shaded areas.

Figure B.2 Pattern uniform live loading for DfD floor system

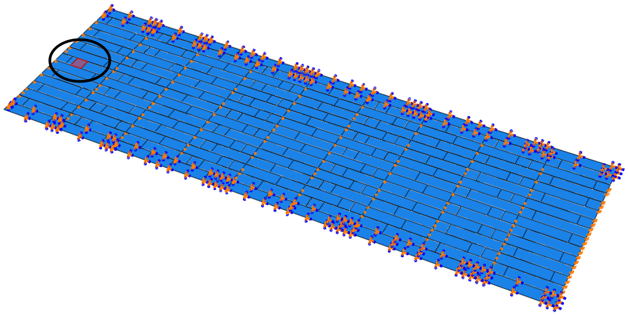

Case 1

a) Maximum positive bending moment at mid-span of plank

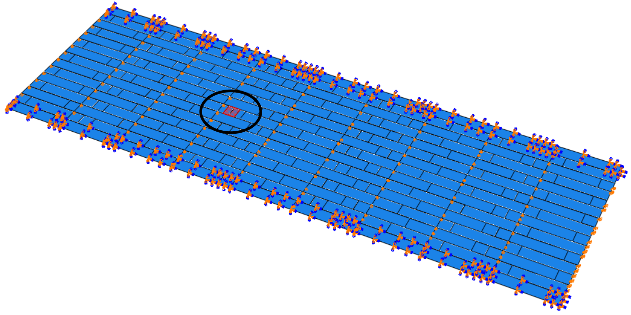

Case 2

b) Maximum negative bending moment at support

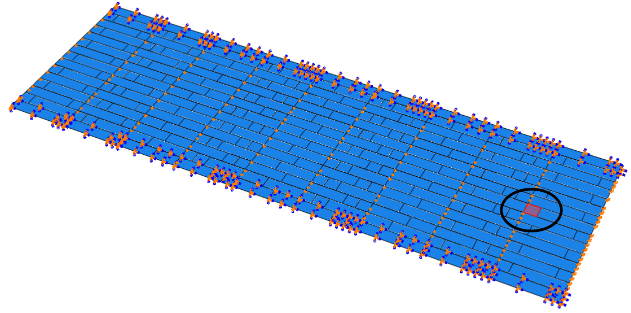

Case 3

c) Maximum shear force at support

Note: The concentrated live loading is applied at the shaded areas.

Figure B.3 Pattern concentrated live loading for DfD floor system

Table B.1 summarizes the design bending moment and shear force generated by the dead load and live load for the deconstructable concrete planks and conventional concrete slabs. The governing load combination is 1.2D + 1.6L. The strengths are given for a two-foot-wide plank or concrete strip. Under uniform loading, the required strengths for the planks in the DfD floor system, which are obtained from the finite element analysis, are close to those calculated using the ACI coefficients. In the DfD floor system, due to deformation compatibility, the loading effects are distributed over a larger region and resisted by numerous planks, even though the concentrated force is applied on a single plank. This conclusion could be validated by the strength comparisons shown in Figure B.4, which demonstrates the internal forces of the whole slab and of the plank subjected to the concentrated loading. The design of monolithic concrete slabs under concentrated loading could use a similar approach. According to Section 3.24.3.2 in AASHTO (2002), the distribution width, E, shall be (4 + 0.06S), but shall not exceed 7 ft. S is the span length given in Section 3.24.1. In this calculation, the distribution width is conservatively taken as 4.0 ft.

Table B.1 Required strengths for concrete slab and plank design

Loading type	Floor system	Moment (ft.-kips)			Shear (kips)
		Positive		Negative	
		Case 1	Case 2		
Uniform	DfD	2.74	3.74	4.30	2.63
	Conventional (ACI coefficients)	2.99 $(w_u l_n^2)/16$	3.41 $(w_u l_n^2)/14$	4.78 $(w_u l_n^2)/10$	2.75 $1.15(w_u l_n)/2$
Concentrated	DfD	3.11		2.81	2.89
	Conventional	3.78		3.37	2.64

In the finite element models, the stress outputs for the shell elements are bending stresses (S11 and S22) and in-plane shear stresses (S12). S11 and S22 represent bending stresses perpendicular to and parallel to the longitudinal direction of the planks, respectively. S11 are longitudinal bending stresses due to the one-way slab behavior of the floor system, while S22 are transverse bending stresses induced by the vertical shear transferred from adjacent planks. S11 and S22 are illustrated in Figure B.5 for different loading scenarios.

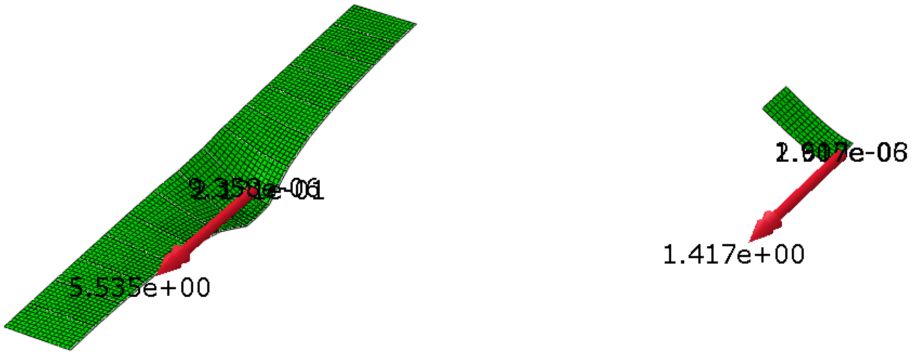
5.535e+00
1.417e+00

a) Maximum positive bending moment at mid-span of plank (units: ft.-kips)

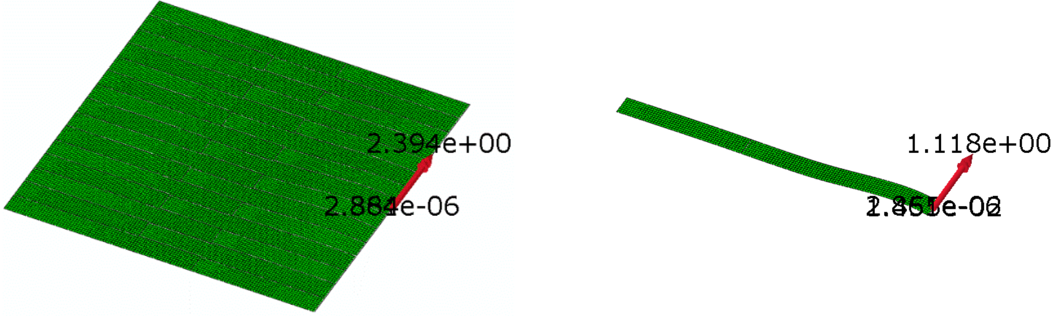
2.394e+00
2.884e-06
1.118e+00

b) Maximum negative bending moment at support (units: ft.-kips)

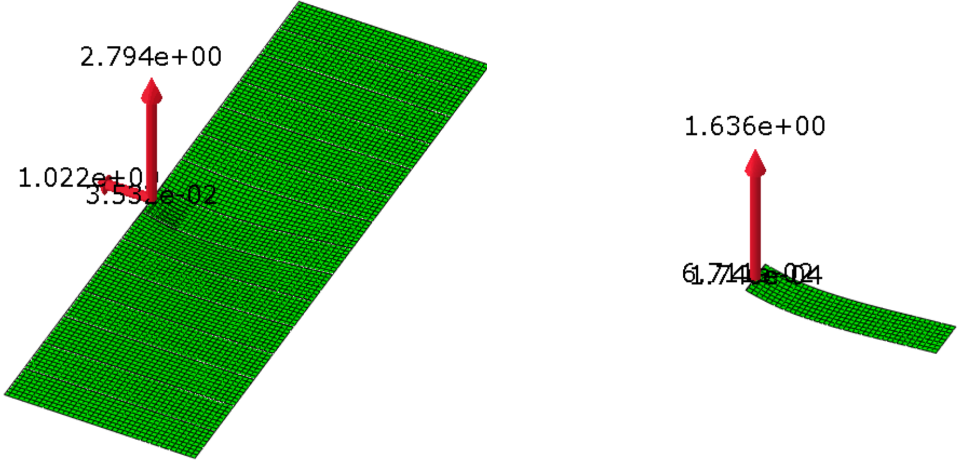
2.794e+00
1.022e+0
1.636e+00

c) Maximum shear force at support (units: kips)

Figure B.4 Required strengths of DfD planks under concentrated live loading

It is seen that S11 is greater than S22, indicating that transverse bending of the planks is not as significant as longitudinal bending. The maximum longitudinal bending stress is 52.44 kips/ ft.^{2} (0.364 ksi), and the maximum transverse bending stress is 12.12 kips/ ft.^{2} (0.084 ksi).

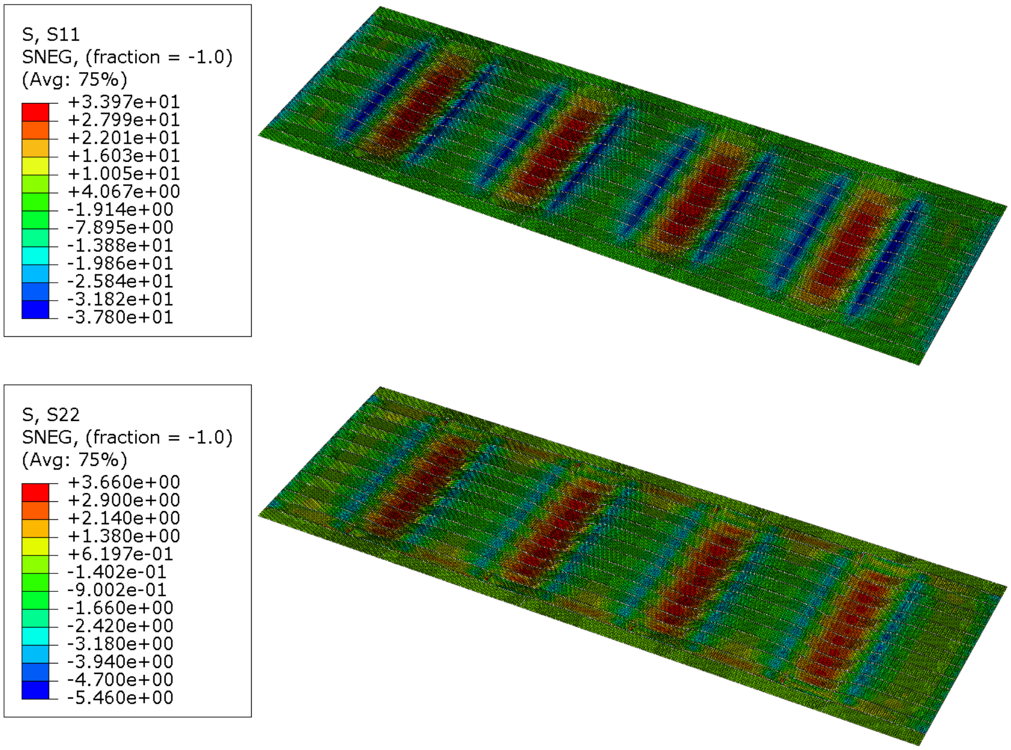
S, S11
SNEG, (fraction = -1.0)
(Avg: 75%)
+3.397e+01
+2.799e+01
+2.201e+01
+1.603e+01
+1.005e+01
+4.067e+00
-1.914e+00
-7.895e+00
-1.388e+01
-1.986e+01
-2.584e+01
-3.182e+01
-3.780e+01
S, S22
SNEG, (fraction = -1.0)
(Avg: 75%)
+3.660e+00
+2.900e+00
+2.140e+00
+1.380e+00
+6.197e-01
-1.402e-01
-9.002e-01
-1.660e+00
-2.420e+00
-3.180e+00
-3.940e+00
-4.700e+00
-5.460e+00

a) Uniform loading case 1

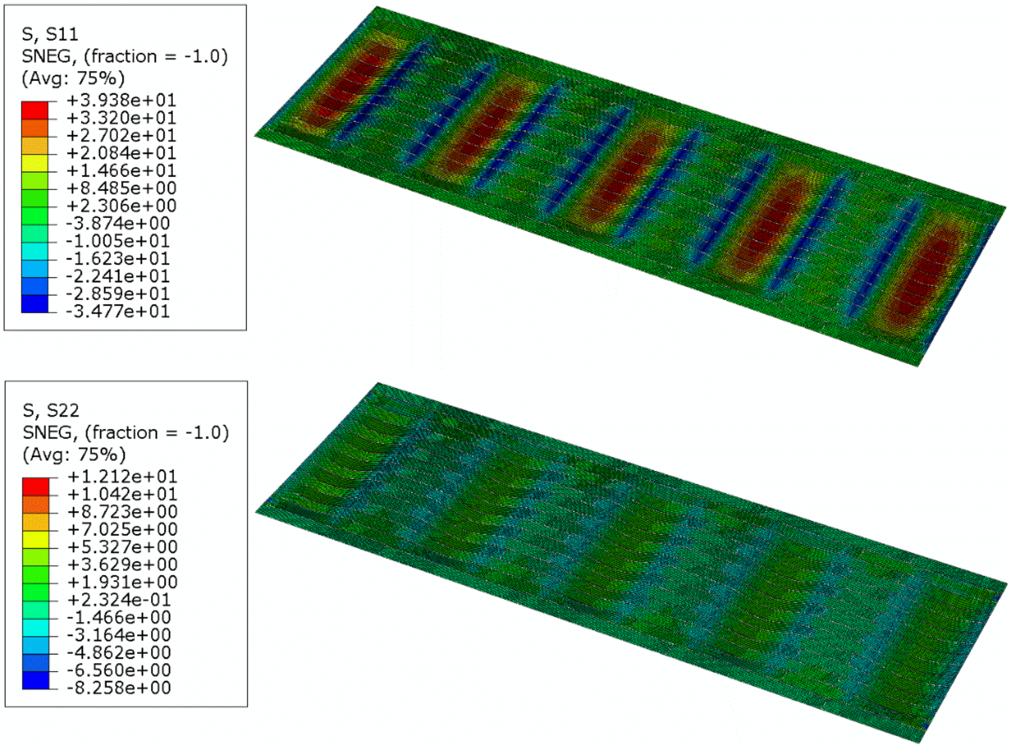
S, S11
SNEG, (fraction = -1.0)
(Avg: 75%)
+3.938e+01
+3.320e+01
+2.702e+01
+2.084e+01
+1.466e+01
+8.485e+00
+2.306e+00
-3.874e+00
-1.005e+01
-1.623e+01
-2.241e+01
-2.859e+01
-3.477e+01
S, S22
SNEG, (fraction = -1.0)
(Avg: 75%)
+1.212e+01
+1.042e+01
+8.723e+00
+7.025e+00
+5.327e+00
+3.629e+00
+1.931e+00
+2.324e-01
-1.466e+00
-3.164e+00
-4.862e+00
-6.560e+00
-8.258e+00

b) Uniform loading case 2

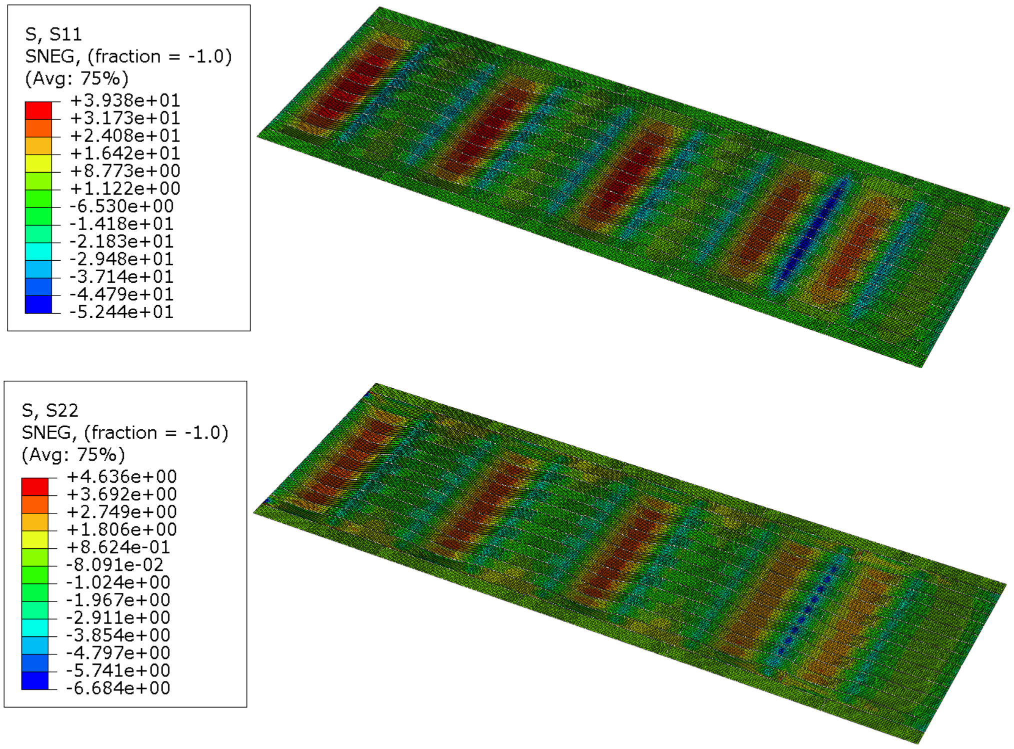

c) Uniform loading case 3

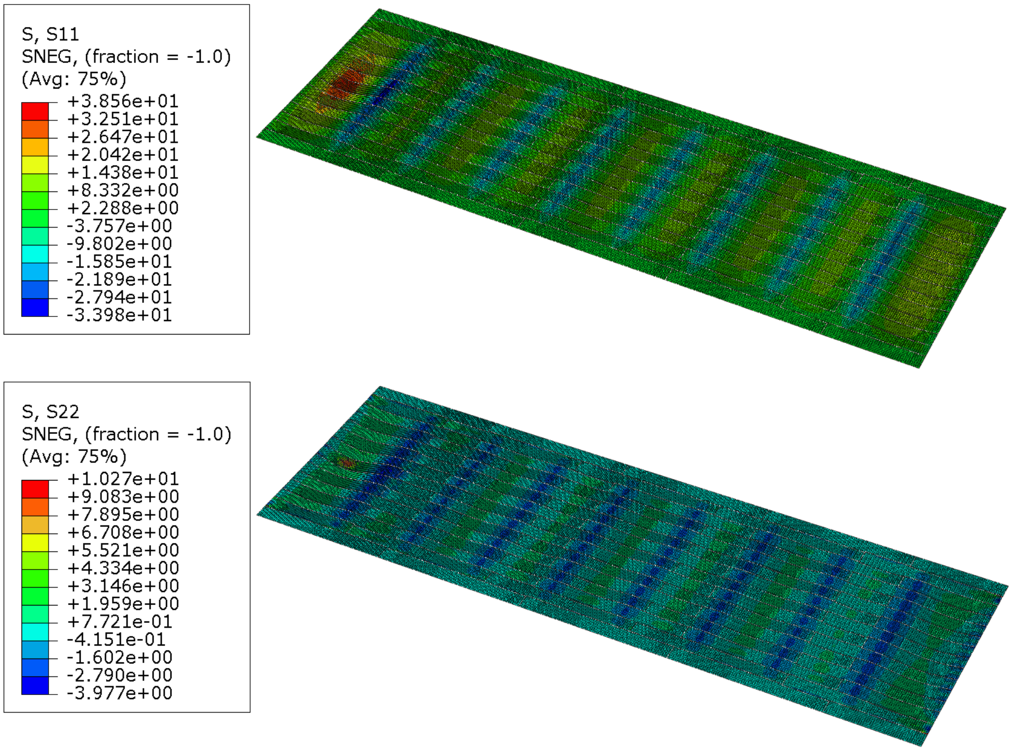

d) Concentrated loading case 1

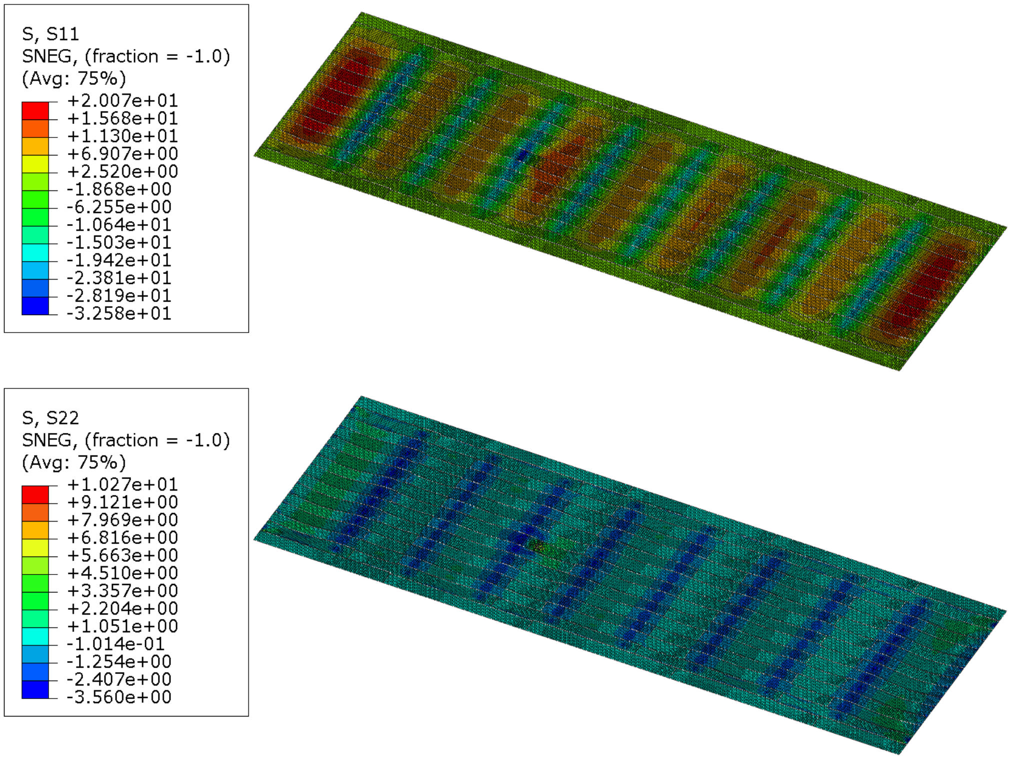
S, S11
SNEG, (fraction = -1.0)
(Avg: 75%)
+2.007e+01
+1.568e+01
+1.130e+01
+6.907e+00
+2.520e+00
-1.868e+00
-6.255e+00
-1.064e+01
-1.503e+01
-1.942e+01
-2.381e+01
-2.819e+01
-3.258e+01
S, S22
SNEG, (fraction = -1.0)
(Avg: 75%)
+1.027e+01
+9.121e+00
+7.969e+00
+6.816e+00
+5.663e+00
+4.510e+00
+3.357e+00
+2.204e+00
+1.051e+00
-1.014e-01
-1.254e+00
-2.407e+00
-3.560e+00

e) Concentrated loading case 2

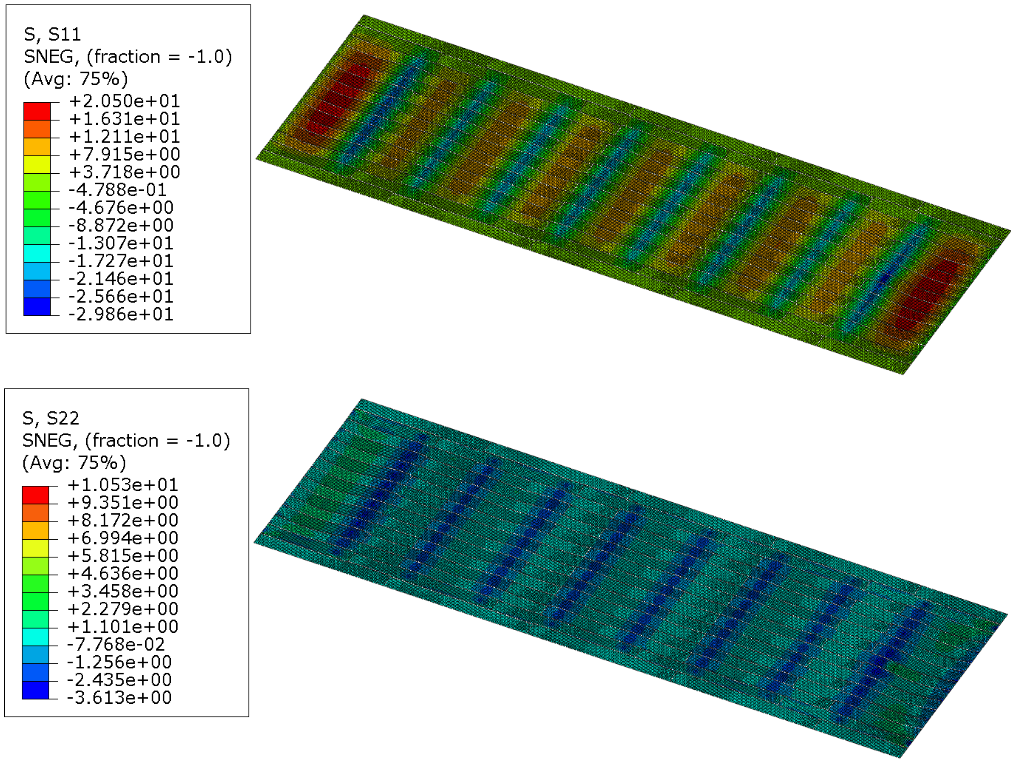
S, S11
SNEG, (fraction = -1.0)
(Avg: 75%)
+2.050e+01
+1.631e+01
+1.211e+01
+7.915e+00
+3.718e+00
-4.788e-01
-4.676e+00
-8.872e+00
-1.307e+01
-1.727e+01
-2.146e+01
-2.566e+01
-2.986e+01
S, S22
SNEG, (fraction = -1.0)
(Avg: 75%)
+1.053e+01
+9.351e+00
+8.172e+00
+6.994e+00
+5.815e+00
+4.636e+00
+3.458e+00
+2.279e+00
+1.101e+00
-7.768e-02
-1.256e+00
-2.435e+00
-3.613e+00

f) Concentrated loading case 3

Note: The bending stresses at the bottom surfaces of the planks are shown in this figure. Tensile stresses are positive, and compressive stresses are negative.

Figure B.5 Concrete plank bending stresses in different loading scenarios (units: kips/ft.^{2})

In addition to flexure, the concrete planks should be designed for torsion, which causes torsional shear stresses in the planks and might lead to torsional failure modes at the plank ends. Since the shell elements in the finite element models cannot output out-of-plane shear stresses, the torsional shear stresses in the planks are not readily available. The maximum torsion in a plank could be conservatively estimated as: $T = Pe = 1.6\,kips \times 0.5\,ft. = 0.8\,ft.-kips$. This calculation assumes that the concentrated live load is equally supported by two adjacent concrete planks, and that the generated torsion is resisted only at one end support of the plank. According to Section 11.5.1 in ACI 318-11, torsion effects could be ignored if the factored torsional moment is less than the following:

$$T_{th} = \phi\lambda\sqrt{f_c'}\left(\frac{A_{cp}^2}{p_{cp}}\right) = 0.75 \times 1 \times \sqrt{4000} \times \frac{(6 \times 24)^2}{2 \times (6 + 24)} = 1.37\,ft.-kips$$

It could be concluded that the torsion and resulting shear stresses induced by the concentrated live load can be neglected in the design of the planks.

2. Flexural and shear reinforcement design

Precast concrete plank

Two Grade 60 No.4 bars are designed for negative bending of the plank, while positive bending is resisted by the cast-in channels. The cross sectional area of the channels is 1.74 in.^{2}, and the centroid of the channel sections is 0.96 in. above the bottom surface of the concrete plank. The concrete cover for the negative reinforcement is taken as 3/4 in.

Positive moment capacity:

Assume the location of the neutral axis (NA) is 1.6 in. from the top surface of the plank. Consider strain compatibility in the cross section (see Figure B.6). When the outmost concrete fiber reaches a crushing strain of 0.003, the strain in the negative reinforcement:

$$\varepsilon_s' = \varepsilon_{cu}\frac{c - d'}{c} = 0.003 \times \frac{1.6 - 1.0}{1.6} = 0.001125$$

Tensile force in the cross section:

$$T_s = A_s f_y = 1.74 \times 2 \times 36 = 125.28\, kips$$

Compressive force in the cross section:

$$C_s' = A_s' f_y = 0.4 \times 0.001125 \times 29000 = 13.05\, kips$$

$$C_c = 0.85 f_c' ba = 0.85 \times 0.85 \times 4 \times 24 \times 1.6 = 110.976\, kips$$

$T_s \approx C_c + C_s'$, therefore, the assumed NA location is acceptable.

Nominal moment capacity:

$$M_n = T_s\left(d - \frac{a}{2}\right) - C_s'\left(d' - \frac{a}{2}\right)$$

$$= 125.28 \times \left(6 - 0.96 - \frac{0.85 \times 1.6}{2}\right) - 13.05 \times \left(1 - \frac{0.85 \times 1.6}{2}\right) = 45.17\, ft - kips$$

Strain in the positive reinforcement when concrete reaches the crushing strain:

$$\varepsilon_s = \varepsilon_{cu}\frac{d - c}{c} = 0.003 \times \frac{6 - 0.96 - 1.6}{1.6} = 0.00645 > 0.005$$

The section is tension-controlled; therefore, the strength reduction factor $\emptyset = 0.9$.
Available positive moment capacity:

$$\emptyset M_n = 0.9 \times 45.17 = 40.65 > 3.74\, ft - kips$$

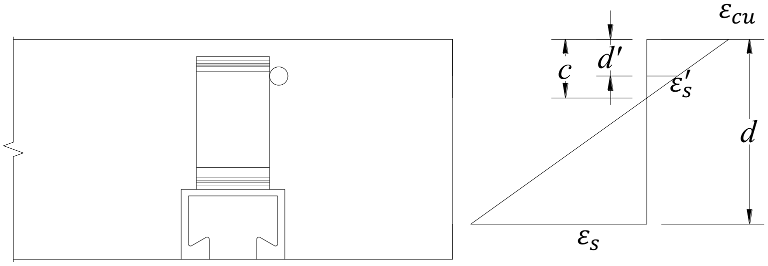

Figure B.6 Strain compatibility under positive bending

Negative moment capacity:

Assume the NA is 0.89 in. from the bottom surface of the plank.
Strain in the positive reinforcement:

$$\varepsilon_s' = \varepsilon_{cu}\frac{c-d'}{c} = 0.003 \times \frac{0.96-0.89}{0.89} = 0.000236$$

Tensile force in the cross section:

$$T_s = A_s f_y = 1.74 \times 2 \times 0.000236 \times 29000 = 23.81 kips$$

$$T_s' = A_s' f_y = 0.2 \times 2\ \times 60 = 24\ kips$$

Compressive force in the cross section:

$$C_c = 0.85 f_c' ba = 0.85 \times 0.85 \times 4 \times (24 - 2 \times 2.83) \times 0.89 = 47.17\ kips$$

$T_s' + T_s \approx C_c$, therefore, the assumed NA location is acceptable.

Nominal moment capacity:

$$M_n = 23.81 \times \left(0.96 - 0.89 \times \frac{0.85}{2}\right) + 24 \times \left(5 - 0.89 \times \frac{0.85}{2}\right) = 10.40\ ft - kips$$

Strain in the negative reinforcement when concrete reaches the crushing strain:

$$\varepsilon_s = \varepsilon_{cu}\frac{d-c}{c} = 0.003 \times \frac{5-0.89}{0.89} = 0.0139 > 0.005$$

The section is tension-controlled.
Available negative moment capacity:

$$\emptyset M_n = 0.9 \times 10.40\ = 9.36 > 4.30\ ft - kips$$

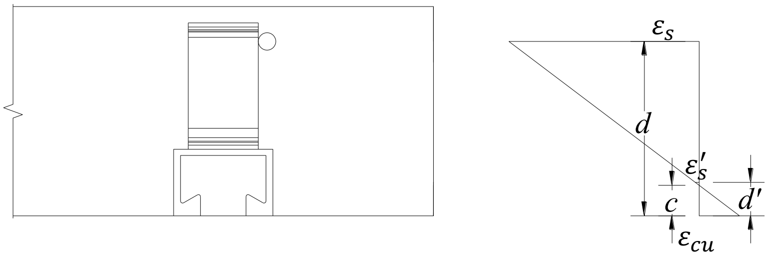

Figure B.7 Strain compatibility under negative bending

Cast-in-place concrete slab

Use two Grade 60 No.4 bars as negative reinforcement and two Grade 60 No.4 bars as positive reinforcement for a two-ft.-wide concrete slab strip. The concrete cover is taken as 3/4 in. for both reinforcement. It is clear that the negative moment capacity of the strip is the same as its positive moment capacity.

Positive moment capacity:

Assume the location of the neutral axis (NA) is 0.62 in. from the top surface of the plank. Consider strain compatibility in the cross section (see Figure B.6). When the outmost concrete fiber reaches a crushing strain of 0.003, the strain in the negative reinforcement:

$$\varepsilon_s' = \varepsilon_{cu}\frac{c-d'}{c} = 0.003 \times \frac{1.0-0.62}{0.62} = 0.0018$$

Tensile force in the cross section:

$$T_s = A_s f_y = 0.4 \times 60 = 24\ kips$$

$$T_s' = A_s' f_y = 0.4 \times 0.0018 \times 29000 = 21.33\ kips$$

Compressive force in the cross section:

$$C_c = 0.85 f_c' ba = 0.85 \times 0.85 \times 4 \times 24 \times 0.62 = 43.00\ kips$$

$T_s + T_s' \approx C_c$, therefore, the assumed NA location is acceptable.

Nominal moment capacity:

$$M_n = T_s'\left(d' - \frac{a}{2}\right) + T_s\left(d - \frac{a}{2}\right)$$

$$= 24 \times \left(6 - 1.0 - \frac{0.85 \times 0.62}{2}\right) + 21.33 \times \left(1 - \frac{0.85 \times 0.62}{2}\right) = 10.78\ ft - kips$$

Strain in the positive reinforcement when concrete reaches the crushing strain:

$$\varepsilon_s = \varepsilon_{cu}\frac{d-c}{c} = 0.003 \times \frac{6-1.0-0.62}{0.62} = 0.021 > 0.005$$

The section is tension-controlled; therefore, the strength reduction factor $\emptyset = 0.9$.

Available positive moment capacity:

$\emptyset M_n = 0.9 \times 10.78 = 9.70 > 4.78\, ft - kips$

Shear capacity:

Precast concrete plank

$\emptyset V_c = 0.75 \times 2\lambda\sqrt{f_c'}b_w d$

$= 0.75 \times 2 \times \sqrt{4000} \times (24 - 2 \times 2.83) \times (6 - 0.96)/1000 = 8.70 > 2.89\, kips$

Cast-in-place concrete slab

$\emptyset V_c = 0.75 \times 2\lambda\sqrt{f_c'}b_w d$

$= 0.75 \times 2 \times \sqrt{4000} \times 24 \times (6 - 1.0)/1000 = 11.38 > 2.75\, kips$

Based on Section 11.4.6.1 in ACI 318-11, no shear reinforcement is required for solid slabs when V_u is greater than 0.5 $\emptyset V_c$ and less than $\emptyset V_c$.

3. Deflection Check

Table 9.5(a) in ACI 318-11 provides the minimum thickness of one-way slabs unless deflections are calculated.

End bay:

Minimum plank thickness= $L/24 = 10 \times 12/24 = 5.00 < 6\, in.$

Interior bay:

Minimum plank thickness= $L/28 = 10 \times 12/28 = 4.29 < 6\, in.$

Deflection check is not needed here.

4. Detailing requirements

Minimum reinforcement ratio for bending:

$$A_{s,min} = \frac{3\sqrt{f_c'}}{f_y} b_w d \geq \frac{200}{f_y} b_w d$$

Precast concrete plank

For positive bending, $A_{s,min} = 200/36000 \times 5 \times (24 - 2 \times 2.83) = 0.51 < 3.48\ in^2$

For negative bending, $A_{s,min} = 200/60000 \times 5 \times (24 - 2 \times 2.83) = 0.31 < 0.4\ in^2$

The area of longitudinal reinforcement is adequate to prevent brittle failure due to cracking.

Cast-in-place concrete slab

For positive bending, $A_{s,min} = 200/60000 \times 5 \times 24 = 0.4\ in^2$

For negative bending, $A_{s,min} = 200/60000 \times 5 \times 24 = 0.4\ in^2$

The area of longitudinal reinforcement is adequate to prevent brittle failure due to cracking.

Maximum spacing:

The maximum spacing of bars used as primary flexural reinforcement in a one-way slab is three times the slab thickness or 18 in, whichever is smaller (Section 7.6.5 in ACI 318-11).The maximum bar spacing is also governed by crack-control provisions (Section 10.6.4 in ACI 318-11).

$$s = 15\left(\frac{40000}{f_s}\right) - 2.5c_c = 15\left(\frac{40000}{40000}\right) - 2.5 \times 0.75 = 13.1 > 12\left(\frac{40000}{f_s}\right) = 12\ in.$$

Where

f_s = the stress in the tension steel, which is taken as $2/3 f_y$ (psi)

c_c = the clear cover from the tension face of the slab to the surface of the reinforcement nearest to it (in.)

Therefore, use 12 in.as the maximum spacing for the flexural reinforcement.

Shrinkage and temperature reinforcement:

Precast concrete plank

Since the precast concrete planks are only 2 ft. wide and much of the shrinkage occurs before the planks are assembled into the structure, the shrinkage and temperature reinforcement in the direction normal to the flexural reinforcement is permitted to be waived, according to Section 16.4.1 in ACI 318-11. The flexural reinforcement crosses the potential cracks perpendicular to the span of the plank, limiting the widths of the cracks, but the minimum flexural reinforcement in the plank should be at least equal to the amount required in Section 7.12.2.1 in ACI 318-11 for shrinkage and temperature.

The minimum amount of shrinkage and temperature reinforcement is $A_s = 0.0018 \times 24 \times 6 = 0.26\, in^2$, which is smaller than the amount of positive and negative flexural reinforcement. Hence, the shrinkage and temperature reinforcement is not needed in the planks.

In reinforced concrete structures, bars are normally cut off where they are no longer required. In contrast, considering the reuse of deconstructed precast concrete planks in a new structure with a different layout, the potential maximum moment and shear force locations in the planks could change. As such, it may be assumed that any section of the precast concrete plank in the deconstructable floor system should be designed for the worst loading effects (i.e., maximum positive and negative bending moment and shear force). Consequently, the reinforcement may be placed through the length of the plank without cut-offs.

Cast-in-place concrete slab

The minimum amount of shrinkage and temperature reinforcement is $A_s = 0.0018 \times 24 \times 6 = 0.26\ in^2$. Provide No.4 bars at a spacing of 18 in., which is equivalent to a steel area of 0.27 in.^{2} in a two-ft.-wide concrete slab strip.

The reinforcement layout for the cast-in-place concrete slabs is illustrated in Figure B.8. According to Section 12.11.1 in ACI 318-11, the bottom bars are continued 6 in. into the beam supports. For the interior supports, the negative moment points of inflection are at $0.24l_n$ from the supports. It is required in Section 12.12.3 in ACI 318-11 to extend the negative bars beyond the inflection points at least d, $12d_b$ and $l_n/16$. Therefore, the negative reinforcement should be extended from the supports at least $0.24l_n + max(d, 12d_b, l_n/16) = 0.24 \times 120 + max\ (5, 12 \times 0.5, 120/16) = 36.3\ in.$ Because the steel beam sizes vary, the clear span is conservatively taken as the center-to-center spacing between the beams. In addition, Section 12.12.2 in ACI 318-11 requires that all the negative reinforcement must extend the development length, l_d, from the face of the support. The development length, l_d, is calculated as follows:

$$l_d = \frac{f_y \psi_t \psi_e}{25\lambda\sqrt{f_c^{'}}} d_b = \frac{60000 \times 1 \times 1}{25 \times \sqrt{4000}} d_b = 37.9 d_b = 19.0\ in.$$

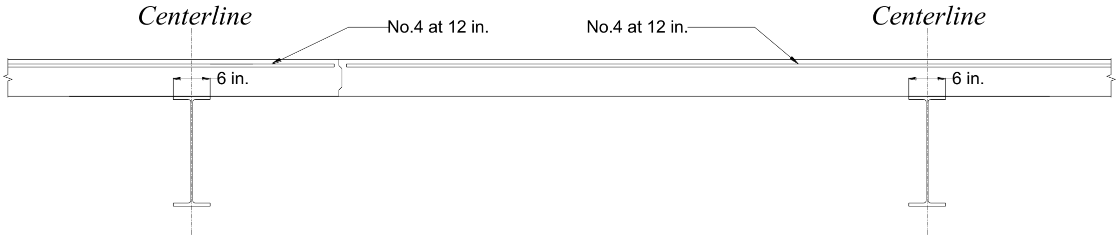
Centerline
No.4 at 12 in.
No.4 at 12 in.
Centerline
6 in.
6 in.

a) Precast concrete plank (cast-in channels used as positive reinforcement are not shown)

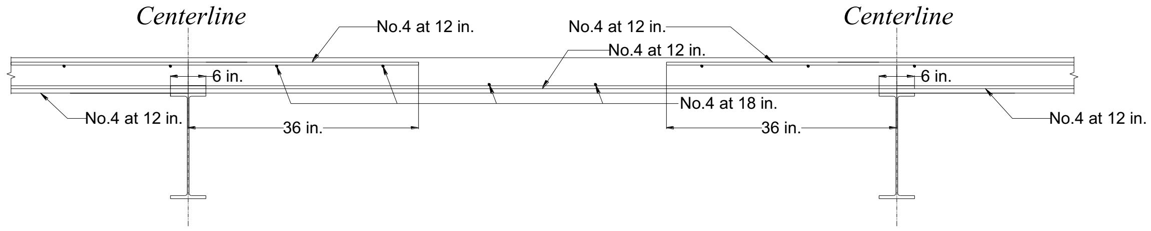
Centerline
No.4 at 12 in.
No.4 at 12 in.
No.4 at 12 in.
Centerline
6 in.
6 in.
No.4 at 18 in.
No.4 at 12 in.
36 in.
36 in.
No.4 at 12 in.

b) Cast-in-place concrete slab

Figure B.8 Reinforcement configurations

B.2 **Shear key design**

Tongue-and-groove joints are recommended for connecting adjacent concrete planks. The short end joints are more vulnerable than the long end joints, since they are required to transfer shear forces generated due to one-way slab behavior. In this section, the preliminary dimensions of the shear keys are given, and the shear strength of the keys is also calculated.

Multiple castellated shear keys are common in precast concrete segmental bridge constructions. Compared to epoxied joints, the construction of dry joints is not constrained by weather conditions and saves time. Two different mechanisms contribute to the shear strength of shear keys. The first mechanism is the frictional resistance when the contact surfaces attempt to move relative to each other. The second mechanism accounts for the support effects of the keys. Design equations, however, show significant variations in estimating the ultimate shear strength of shear keys. Research by Turmo et al. (2006) indicates that the AASHTO equation best predicts the strength. It is assumed in the AASHTO equation that no reinforcement is placed to reinforce the shear keys.

Figure B.9 illustrates the preliminary configuration of the shear keys in the precast concrete planks. The shear strength of the shear keys is calculated using the AASHTO equation, and the strength of the concrete plank is assumed to be 4 ksi.

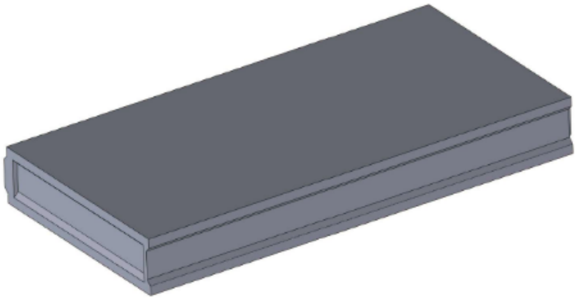

a) Proposed configuration

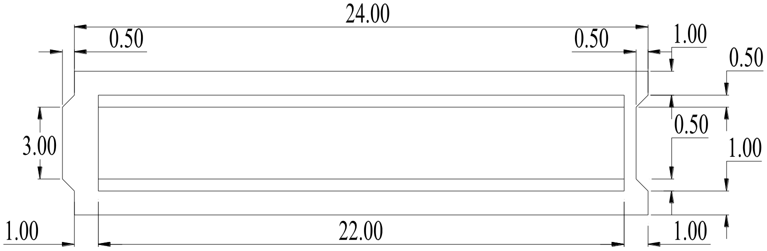

b) Shear key dimensions at short end joints (units: inches)

Figure B.9 Preliminary configuration of shear keys

In AASHTO, the nominal design shear strength of shear keys is given as:

$$V_u = A_k \cdot \sqrt{f_c'} \cdot (0.2048 \cdot \sigma_n + 0.9961) + 0.6 \cdot A_{sm} \cdot \sigma_n \tag{B.1}$$

Where

A_k = areas of all the keys of the failure plane (mm^2)

f_c' = concrete characteristic compressive strength (MPa)

σ_n = average compressive strength at the joint plane (MPa)

A_{sm} = contact area between flat surfaces of the failure plane (mm^2)

For the precast concrete planks, it is assumed that no normal force exists between the shear keys. With a strength reduction factor of 0.75 applied to Equation (B.1), the available shear strength of the shear keys is calculated as the smaller of the following two equations:

$$\begin{aligned} \emptyset V_u &= 0.75 \times 4 \times 22 \times \frac{25.4^{\,2}}{10^6} \times \sqrt{27.58} \times 0.9961 = 0.223\ MN \\ &= 50.13\ kips \end{aligned} \tag{B.2.1}$$

$$\emptyset V_u = 0.75 \times 1.5 \times 22 \times \frac{25.4^{\,2}}{10^6} \times \sqrt{27.58} \times 0.9961 = 0.0836\,MN \qquad \text{(B.3.2)}$$
$$= 18.80\,kips$$

The available shear strength of the cross-section of the concrete plank is determined as:

$$\emptyset V_c = 0.75 \times 2\lambda\sqrt{f_c'}b_w d = 0.75 \times 2 \times \sqrt{4000} \times 24 \times \frac{6 - 0.96}{1000} \qquad \text{(B.4)}$$
$$= 11.38\ \ kips$$

It is shown that the shear keys at the short ends of the planks are capable of resisting much larger shear force than the planks. Hence, under shear forces, the concrete planks are likely to fail prior to the shear keys.

Appendix C SPECIMEN DRAWINGS

This appendix contains the drawings of all the components in both the pushout tests and the beam tests, including shop drawings for the steel components, design drawings for the concrete specimens, details of the reinforcement, etc.

C.1 **Pushout tests**

C.1.1 Steel specimen shop drawings

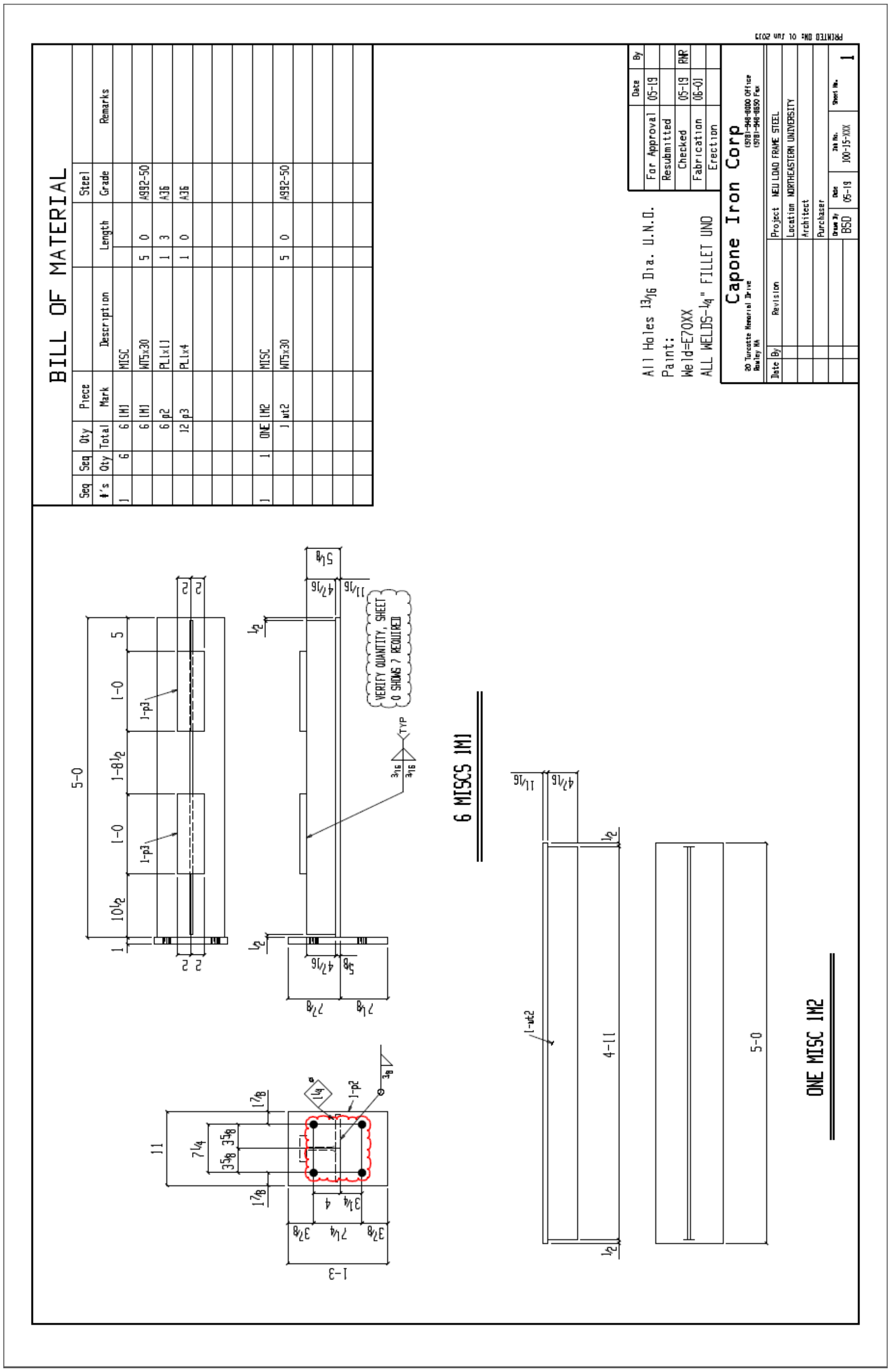
BILL OF MATERIAL
Seq #'s | Seq Qty | Qty Total | Piece Mark | Description | Length | Steel Grade | Remarks
1 | 6 | 6 | 1M1 | MISC
6 | 1M1 | WT5x30 | 5 0 | A992-50
6 | p2 | PL1x11 | 1 3 | A36
12 | p3 | PL1x4 | 1 0 | A36
1 | 1 | ONE | 1M2 | MISC
1 | wt2 | WT5x30 | 5 0 | A992-50
All Holes 13/16 Dia. U.N.O.
Paint:
Weld=E70XX
ALL WELDS-1/4" FILLET UNO
For Approval 05-19
Resubmitted
Checked 05-19 RNP
Fabrication 06-01
Erection
Date By
Capone Iron Corp
20 Turcotte Memorial Drive Rowley MA
(978)-948-8000 Office (978)-948-8650 Fax
Project NEW LOAD FRAME STEEL
Location NORTHEASTERN UNIVERSITY
Architect
Purchaser
Drawn By BSD
Date 05-19
Job No. 100-15-XXX
Sheet No. 1
Date By Revision
PRINTED ON: 01 Jun 2015
VERIFY QUANTITY, SHEET 0 SHOWS 7 REQUIRED
6 MISCS 1M1
ONE MISC 1M2
1-p3
1-p2
1-wt2
5-0
1-0
1-8 1/2
10 1/2
4-11
1-3
TYP
3/16
3/8
1/4
4 7/16
5/8
11/16
7 1/8
7 1/4
3 5/8
1 7/8
3 7/8
3 1/4
11
4
2
1/2

Figure C.1 Steel Section WT5x30

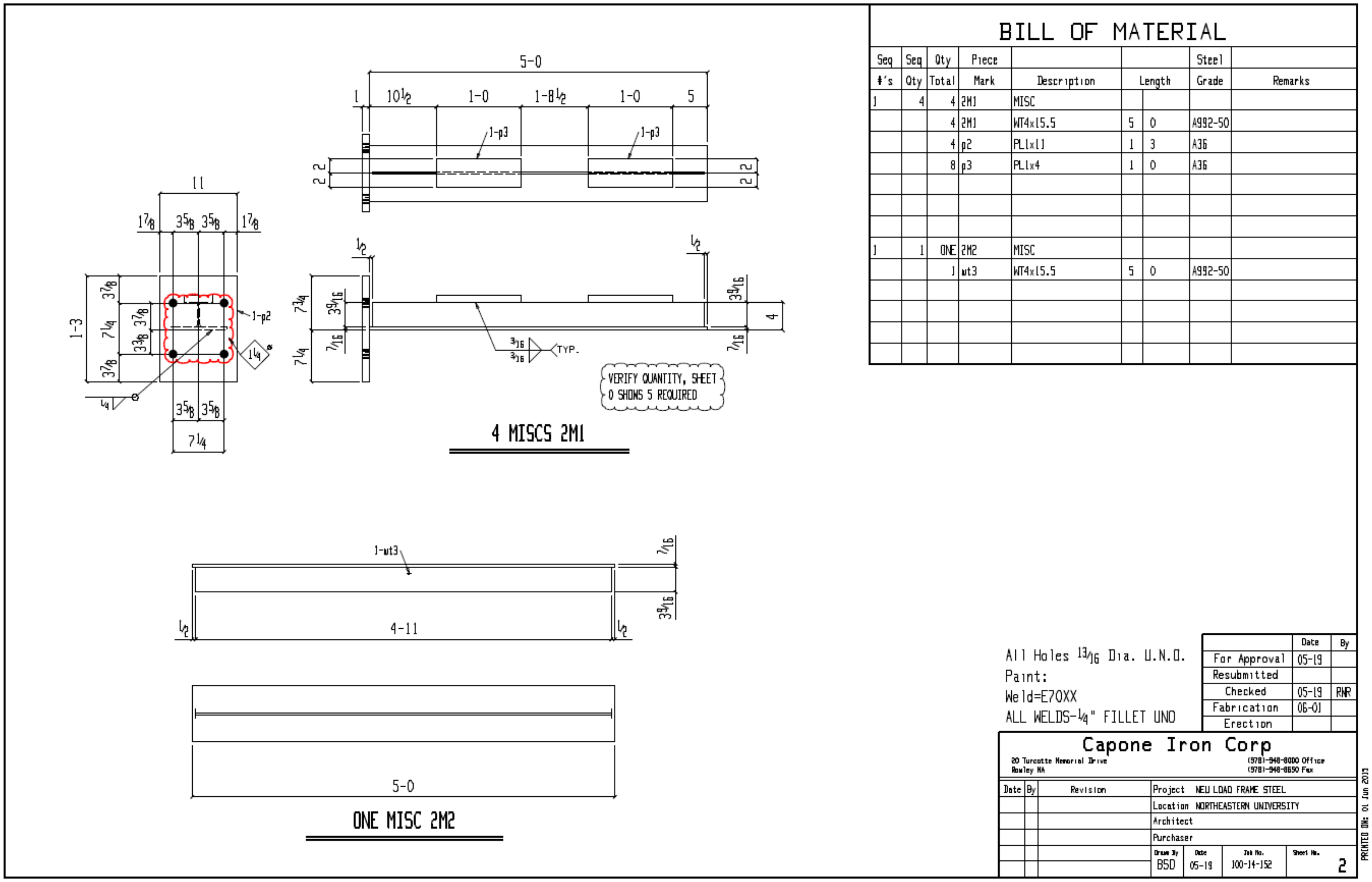
5-0
1
10½
1-0
1-8½
1-0
5
1-p3
1-p3
2 2
2 2
11
1⅞
3⅝ 3⅝
1⅞
3⅞
7¼
3⅞
3⅞ 3⅞
1-3
1-p2
¼
¼
3⅝ 3⅝
7¼
½
½
7¼
7¼
3$\frac{9}{16}$
$\frac{7}{16}$
3$\frac{9}{16}$
$\frac{7}{16}$
4
$\frac{3}{16}$
$\frac{3}{16}$
TYP.
VERIFY QUANTITY, SHEET 0 SHOWS 5 REQUIRED
4 MISCS 2M1
1-wt3
$\frac{7}{16}$
3$\frac{9}{16}$
½
4-11
½
5-0
ONE MISC 2M2
PRINTED ON: 01 Jun 2013

BILL OF MATERIAL

Seq	Seq	Qty	Piece				Steel	
#'s	Qty	Total	Mark	Description	Length		Grade	Remarks
1	4	4	2M1	MISC				
		4	2M1	WT4x15.5	5	0	A992-50	
		4	p2	PL1x11	1	3	A36	
		8	p3	PL1x4	1	0	A36	
1	1	ONE	2M2	MISC				
		1	wt3	WT4x15.5	5	0	A992-50	

All Holes $\frac{13}{16}$ Dia. U.N.O.
Paint:
Weld=E70XX
ALL WELDS-¼" FILLET UNO

	Date	By
For Approval	05-19	
Resubmitted		
Checked	05-19	RNR
Fabrication	06-01	
Erection		

Capone Iron Corp
20 Turcotte Memorial Drive
Rowley MA
(978)-948-8000 Office
(978)-948-8650 Fax

Date	By	Revision

Project NEU LOAD FRAME STEEL
Location NORTHEASTERN UNIVERSITY
Architect
Purchaser

Drawn By	Date	Job No.	Sheet No.
BSD	05-19	100-14-152	2

Figure C.2 Steel Section WT4x15.5

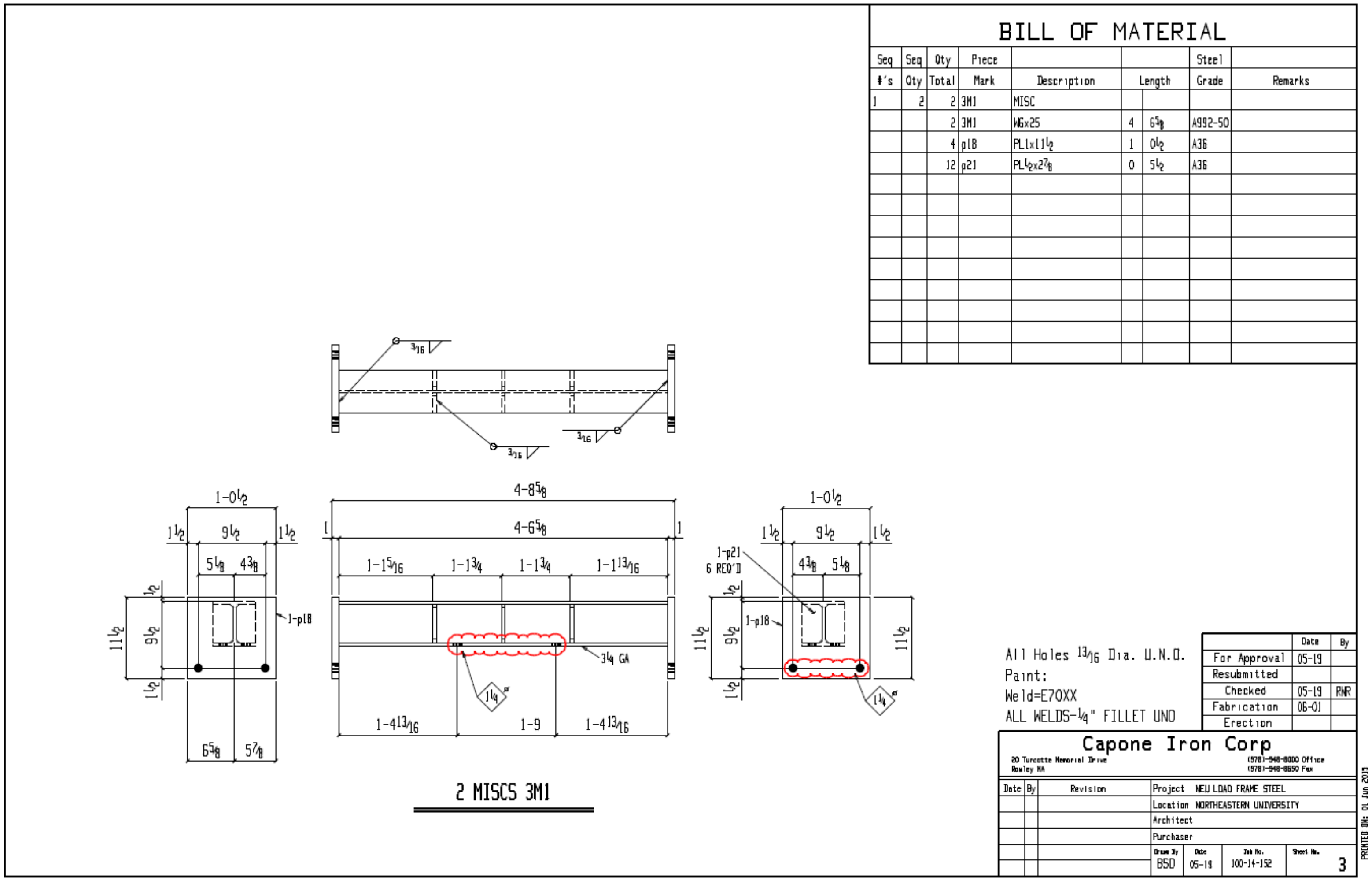

3/16
3/16
3/16
4-8⅝
4-6⅝
1
1
1-1 5/16
1-1¾
1-1¾
1-1 13/16
¾ GA
¼
1-4 13/16
1-9
1-4 13/16
1-0½
1½
9½
1½
5⅛
4⅜
½
9½
1½
11½
1-p18
6⅝
5⅞
1-p21
6 REQ'D
1-p18
1-0½
1½
9½
1½
4⅜
5⅛
½
9½
1½
11½
¼
2 MISCS 3M1

BILL OF MATERIAL

Seq	Seq	Qty	Piece				Steel	
#'s	Qty	Total	Mark	Description	Length		Grade	Remarks
1	2	2	3M1	MISC				
		2	3M1	W6x25	4	6⅝	A992-50	
		4	p18	PL1x11½	1	0½	A36	
		12	p21	PL½x2⅞	0	5½	A36	

All Holes 13/16 Dia. U.N.O.
Paint:
Weld=E70XX
ALL WELDS-¼" FILLET UNO

	Date	By
For Approval	05-19	
Resubmitted		
Checked	05-19	RNR
Fabrication	06-01	
Erection		

Capone Iron Corp
20 Turcotte Memorial Drive
Rowley MA
(978)-948-8000 Office
(978)-948-8650 Fax

Date	By	Revision

Project NEU LOAD FRAME STEEL
Location NORTHEASTERN UNIVERSITY
Architect
Purchaser

Drawn By	Date	Job No.	Sheet No.
BSD	05-19	100-14-152	3

PRINTED ON: 01 Jun 2013

Figure C.3 Stiffened W6x25 Beam Assembly

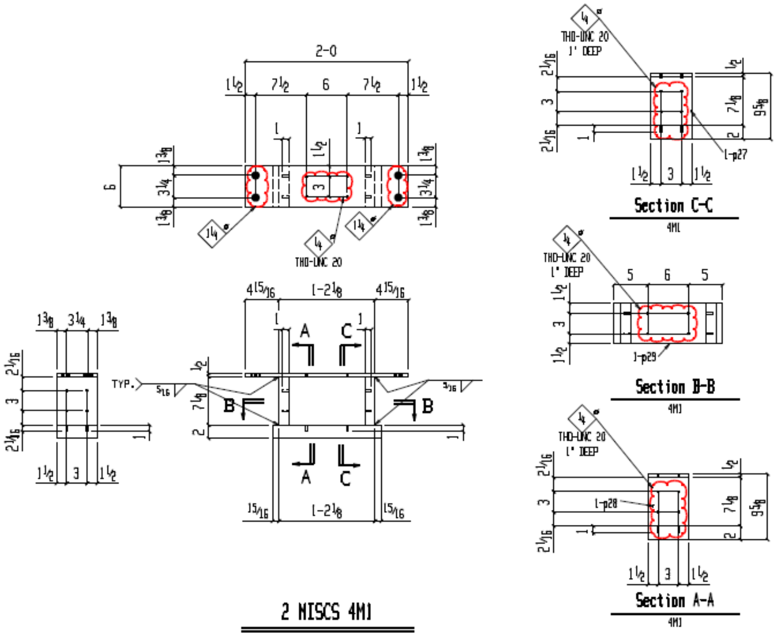
2-0
1½
7½
6
7½
1½
6
1⅜
3¼
1⅜
¼
THD-UNC 20
4 15/16
1-2⅛
A
C
B
TYP.
5/16
7⅛
2
1
15/16
2 1/16
3
1⅜
3¼
Section C-C
4M1
1-p27
9⅝
THD-UNC 20
1" DEEP
5
Section B-B
1-p29
Section A-A
1-p28
2 MISCS 4M1

BILL OF MATERIAL

Seq	Seq	Qty	Piece		Length		Steel	
#'s	Qty	Total	Mark	Description			Grade	Remarks
1	2	2	4M1	MISC				
		2	4M1	PL½x6	2	0	A36	
		2	p29	PL2x6	1	4	A36	
		2	p28	PL1½x6	0	7⅛	A36	
		2	p27	PL1½x6	0	7⅛	A36	

All Holes 13/16 Dia. U.N.O.
Paint:
Weld=E70XX
ALL WELDS-¼" FILLET UNO

	Date	By
For Approval	05-19	
Resubmitted		
Checked	05-19	RNR
Fabrication	06-01	
Erection		

Capone Iron Corp
20 Turcotte Memorial Drive
Rowley MA
(978)-948-8000 Office
(978)-948-8650 Fax

Date	By	Revision

Project NEU LOAD FRAME STEEL
Location NORTHEASTERN UNIVERSITY
Architect
Purchaser

Drawn By	Date	Job No.	Sheet No.
BSD	05-19	100-14-152	4

PRINTED ON: 01 Jun 2013

Figure C.4 Stability Frame for WT5x30

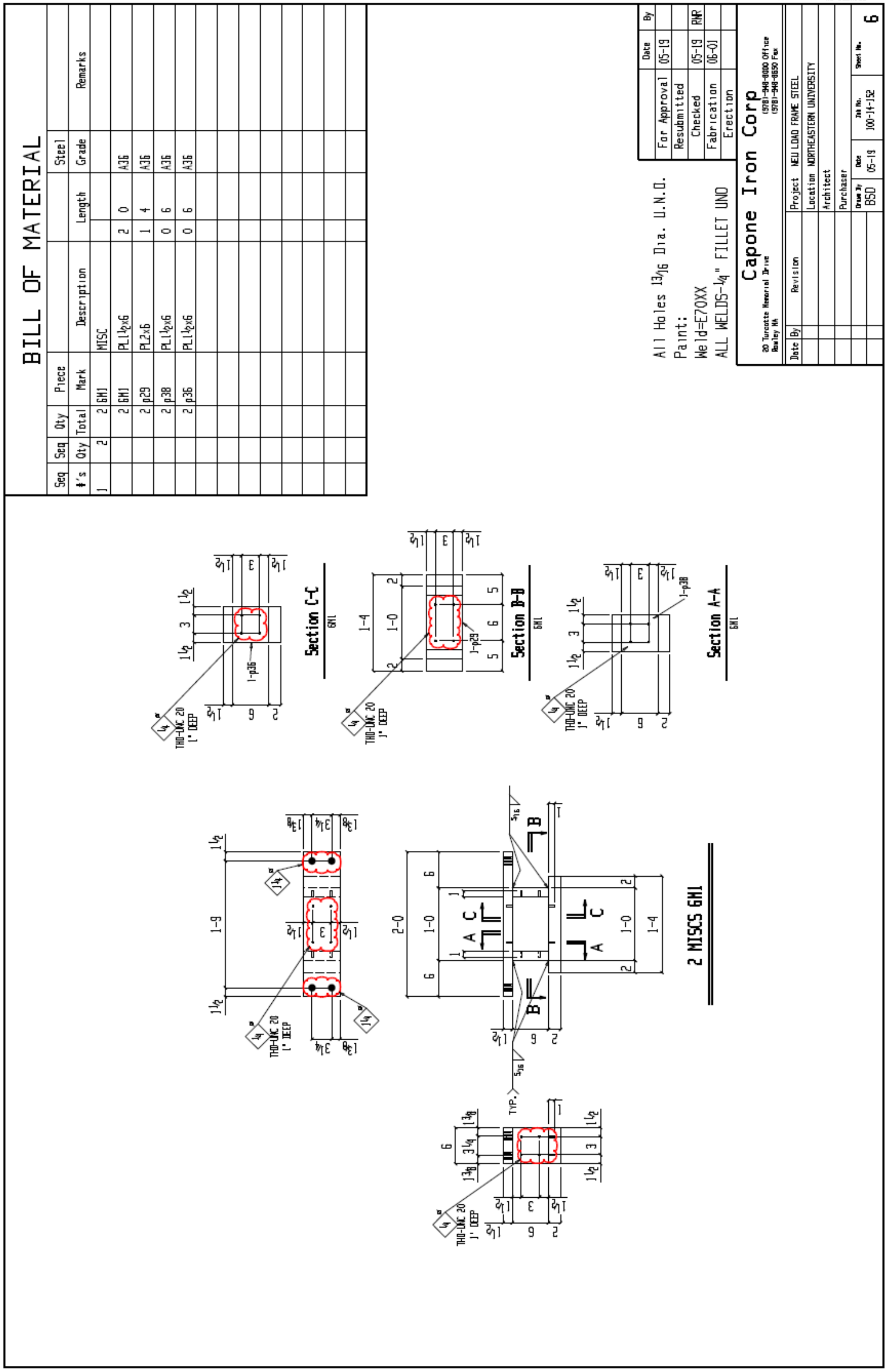

BILL OF MATERIAL

Seq #'s	Seq Qty	Qty Total	Piece Mark	Description	Length		Steel Grade	Remarks
1	2	2	GM1	MISC				
		2	GM1	PL1½x6	2	0	A36	
		2	p29	PL2x6	1	4	A36	
		2	p38	PL1½x6	0	6	A36	
		2	p36	PL1½x6	0	6	A36	

Section C-C
GM1
Section B-B
GM1
Section A-A
GM1
2 MISCS GM1
THD-UNC 20
1" DEEP
1-p36
1-p29
1-p38
TYP.
1-9
2-0
1-0
1-4
A
B
C
All Holes 13/16 Dia. U.N.O.
Paint:
Weld=E70XX
ALL WELDS-1/4" FILLET UNO
For Approval 05-19
Resubmitted
Checked 05-19 RNR
Fabrication 06-01
Erection
Capone Iron Corp
20 Turcotte Memorial Drive
Rowley MA
(978)-948-8000 Office
(978)-948-8650 Fax
Date
By
Revision
Project NEU LOAD FRAME STEEL
Location NORTHEASTERN UNIVERSITY
Architect
Purchaser
Drawn By BSD
Date 05-19
Job No. 100-14-152
Sheet No. 6
PRINTED ON: 01 Jun 2013

Figure C.5 Stability Frame for WT4x15.5

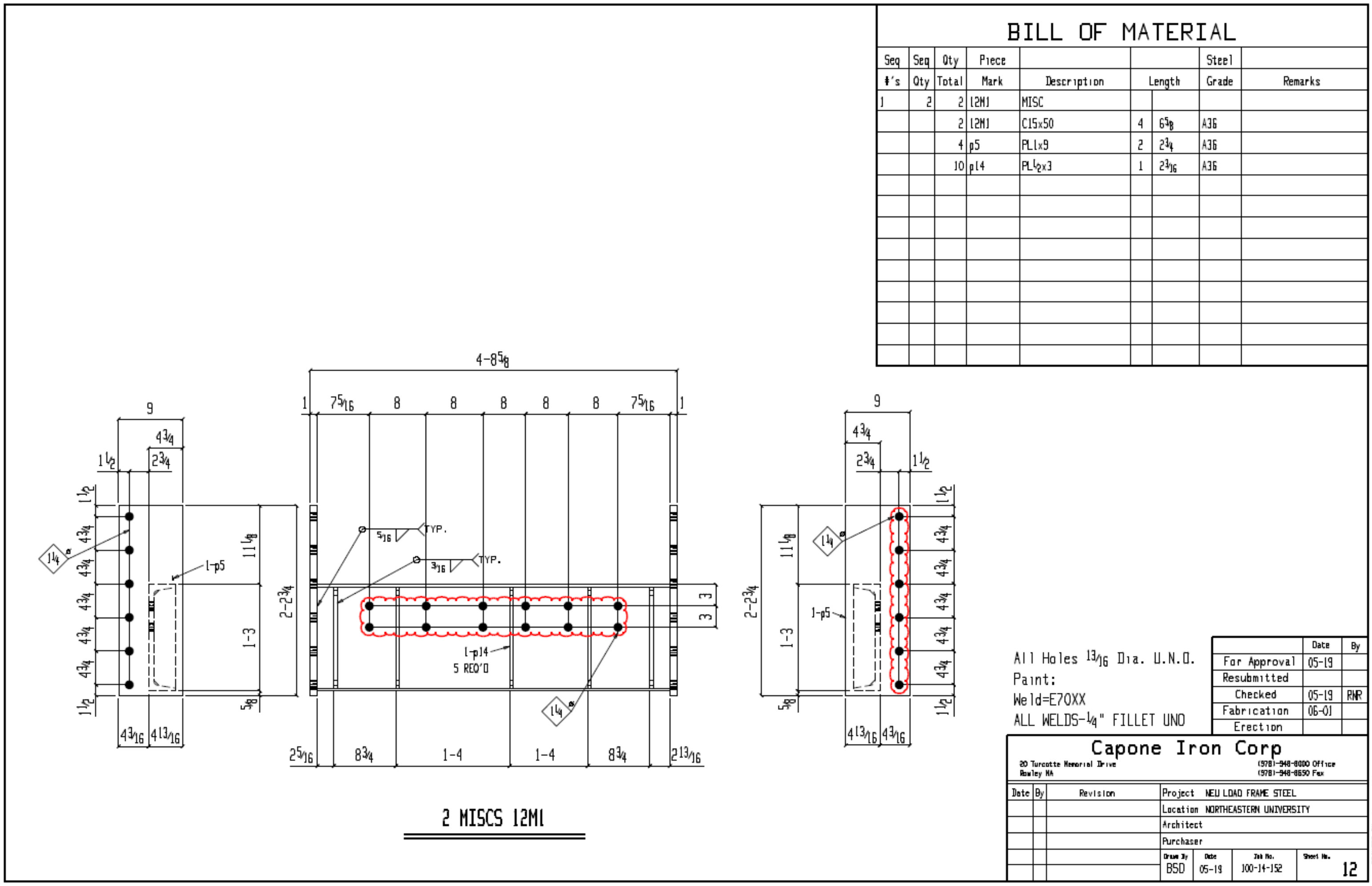
4-$5\frac{5}{8}$
9
$4\frac{3}{4}$
$2\frac{3}{4}$
$1\frac{1}{2}$
1
$7\frac{5}{16}$
8
8
8
8
8
$7\frac{5}{16}$
1
$1\frac{1}{4}$
1-p5
$11\frac{1}{8}$
1-3
2-$2\frac{3}{4}$
$\frac{5}{8}$
$4\frac{3}{16}$
$4\frac{13}{16}$
$\frac{5}{16}$ TYP.
$\frac{3}{16}$ TYP.
1-p14
5 REQ'D
3
3
$2\frac{5}{16}$
$8\frac{3}{4}$
1-4
1-4
$8\frac{3}{4}$
$2\frac{13}{16}$
2 MISCS 12M1

BILL OF MATERIAL

Seq	Seq	Qty	Piece				Steel	
#'s	Qty	Total	Mark	Description	Length		Grade	Remarks
1	2	2	12M1	MISC				
		2	12M1	C15x50	4	$6\frac{5}{8}$	A36	
		4	p5	PL1x9	2	$2\frac{3}{4}$	A36	
		10	p14	PL$\frac{1}{2}$x3	1	$2\frac{3}{16}$	A36	

All Holes $\frac{13}{16}$ Dia. U.N.O.
Paint:
Weld=E70XX
ALL WELDS-$\frac{1}{4}$" FILLET UNO

	Date	By
For Approval	05-19	
Resubmitted		
Checked	05-19	RNR
Fabrication	06-01	
Erection		

Capone Iron Corp
20 Turcotte Memorial Drive
Rowley MA
(978)-948-8000 Office
(978)-948-8650 Fax

Date	By	Revision	
			Project NEU LOAD FRAME STEEL
			Location NORTHEASTERN UNIVERSITY
			Architect
			Purchaser

Drawn By	Date	Job No.	Sheet No.
BSD	05-19	100-14-152	12

PRINTED ON: 01 Jun 2013

Figure C.6 Stiffened Channel C15x50

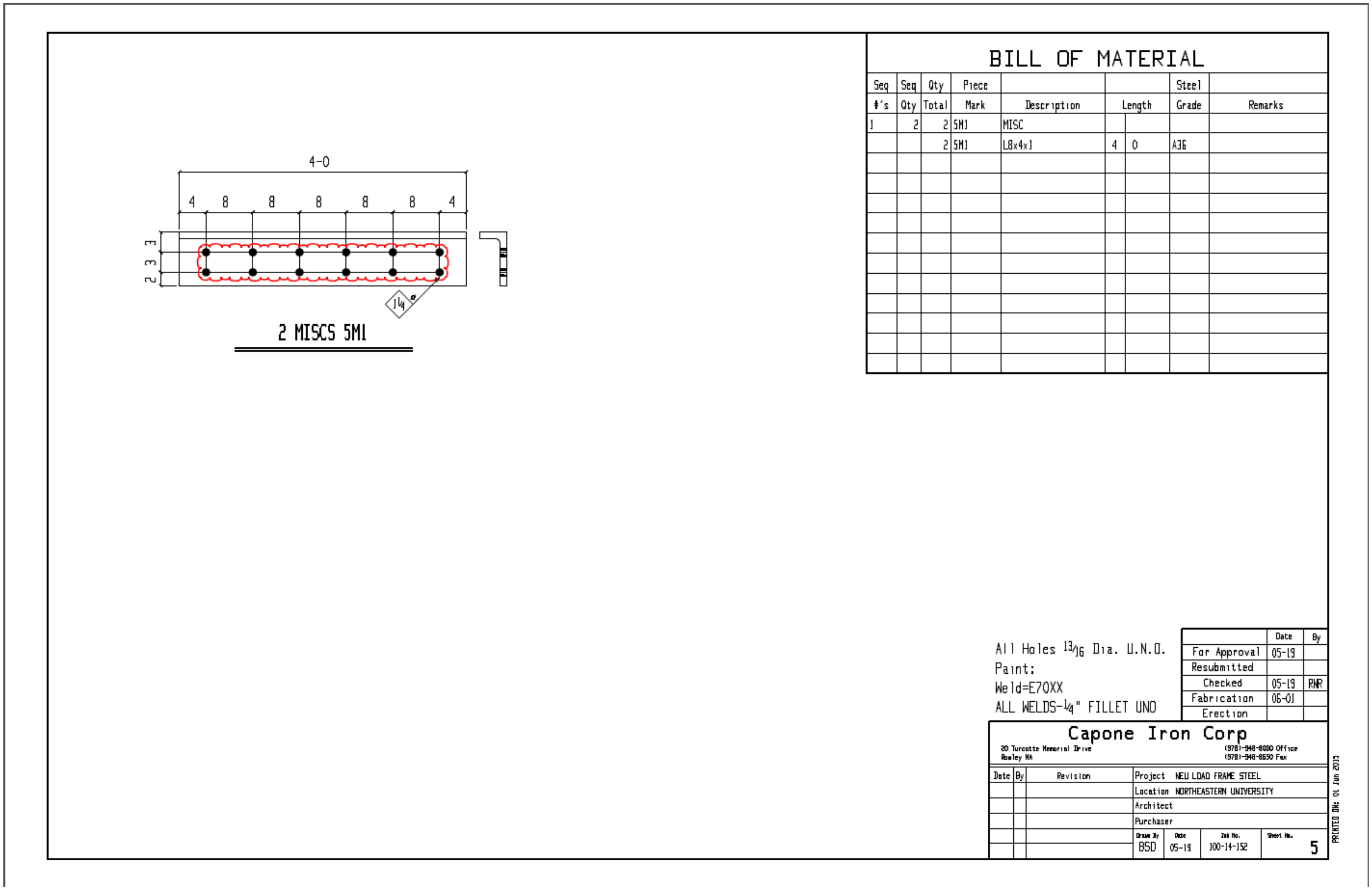

BILL OF MATERIAL

Seq	Seq	Qty	Piece				Steel	
#'s	Qty	Total	Mark	Description	Length		Grade	Remarks
1	2	2	5M1	MISC				
		2	5M1	L8x4x1	4	0	A36	

All Holes 13/16 Dia. U.N.O.
Paint:
Weld=E70XX
ALL WELDS-1/4" FILLET UNO

	Date	By
For Approval	05-19	
Resubmitted		
Checked	05-19	RNR
Fabrication	06-01	
Erection		

Capone Iron Corp
20 Turcotte Memorial Drive
Rowley MA
(978)-948-8000 Office
(978)-948-8650 Fax

Date	By	Revision

Project NEU LOAD FRAME STEEL
Location NORTHEASTERN UNIVERSITY
Architect
Purchaser

Drawn By	Date	Job No.	Sheet No.
BSD	05-19	100-14-152	5

PRINTED ON: 01 Jun 2013

Figure C.7 Reaction Angle

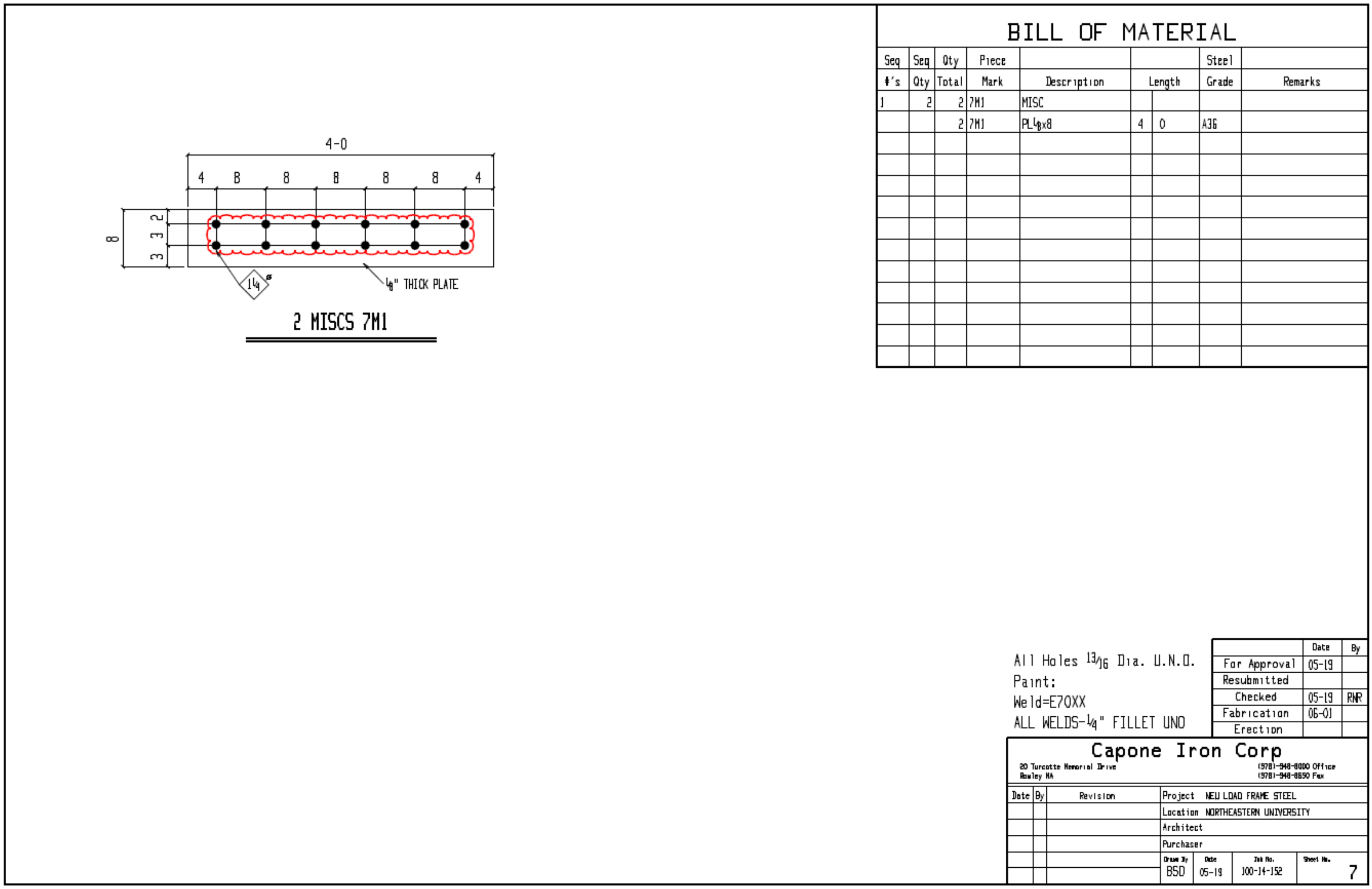

BILL OF MATERIAL

Seq	Seq	Qty	Piece				Steel	
#'s	Qty	Total	Mark	Description	Length		Grade	Remarks
1	2	2	7M1	MISC				
		2	7M1	PL1/8x8	4	0	A36	

All Holes 13/16 Dia. U.N.O.
Paint:
Weld=E70XX
ALL WELDS-1/4" FILLET UNO

	Date	By
For Approval	05-19	
Resubmitted		
Checked	05-19	RMR
Fabrication	06-01	
Erection		

Capone Iron Corp
20 Turcotte Memorial Drive
Rowley MA
(978)-948-8000 Office
(978)-948-8650 Fax

Date	By	Revision

Project NEU LOAD FRAME STEEL
Location NORTHEASTERN UNIVERSITY
Architect
Purchaser

Drawn By	Date	Job No.	Sheet No.
BSD	05-19	100-14-152	7

PRINTED ON: 01 Jun 2013

Figure C.8 Shim between Reaction Angle and Stiffened Channel for WT4x15.5

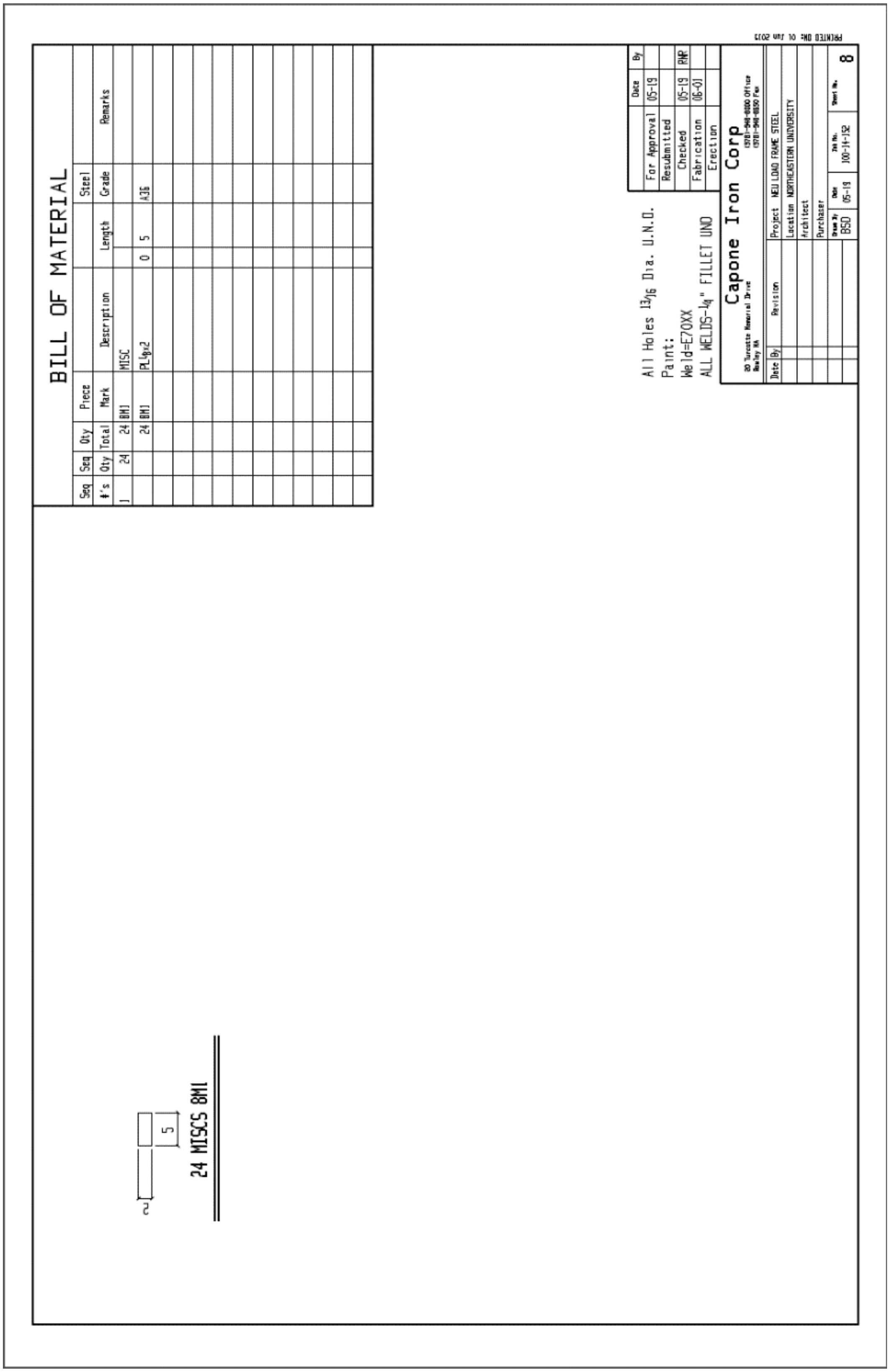

BILL OF MATERIAL

Seq	Seq	Qty	Piece			Steel	
#'s	Qty	Total	Mark	Description	Length	Grade	Remarks
1	24	24	8M1	MISC			
		24	8M1	PL$\frac{1}{8}$x2	0 5	A36	

All Holes 13/16 Dia. U.N.O.
Paint:
Weld=E70XX
ALL WELDS-1/4" FILLET UNO
For Approval 05-19
Resubmitted
Checked 05-19 RMR
Fabrication 06-01
Erection
Date
By
Capone Iron Corp
20 Turcotte Memorial Drive
Rowley MA
Date
By
Revision
Project NEW LOAD FRAME STEEL
Location NORTHEASTERN UNIVERSITY
Architect
Purchaser
Drawn By BSD
Date 05-19
Job No. 100-14-152
Sheet No. 8
PRINTED ON: 01 Jun 2015
2
5
24 MISCS 8M1

Figure C.9 Shim between WT4x15.5 and Clamp Tooth

C.1.2 Concrete specimen design drawings

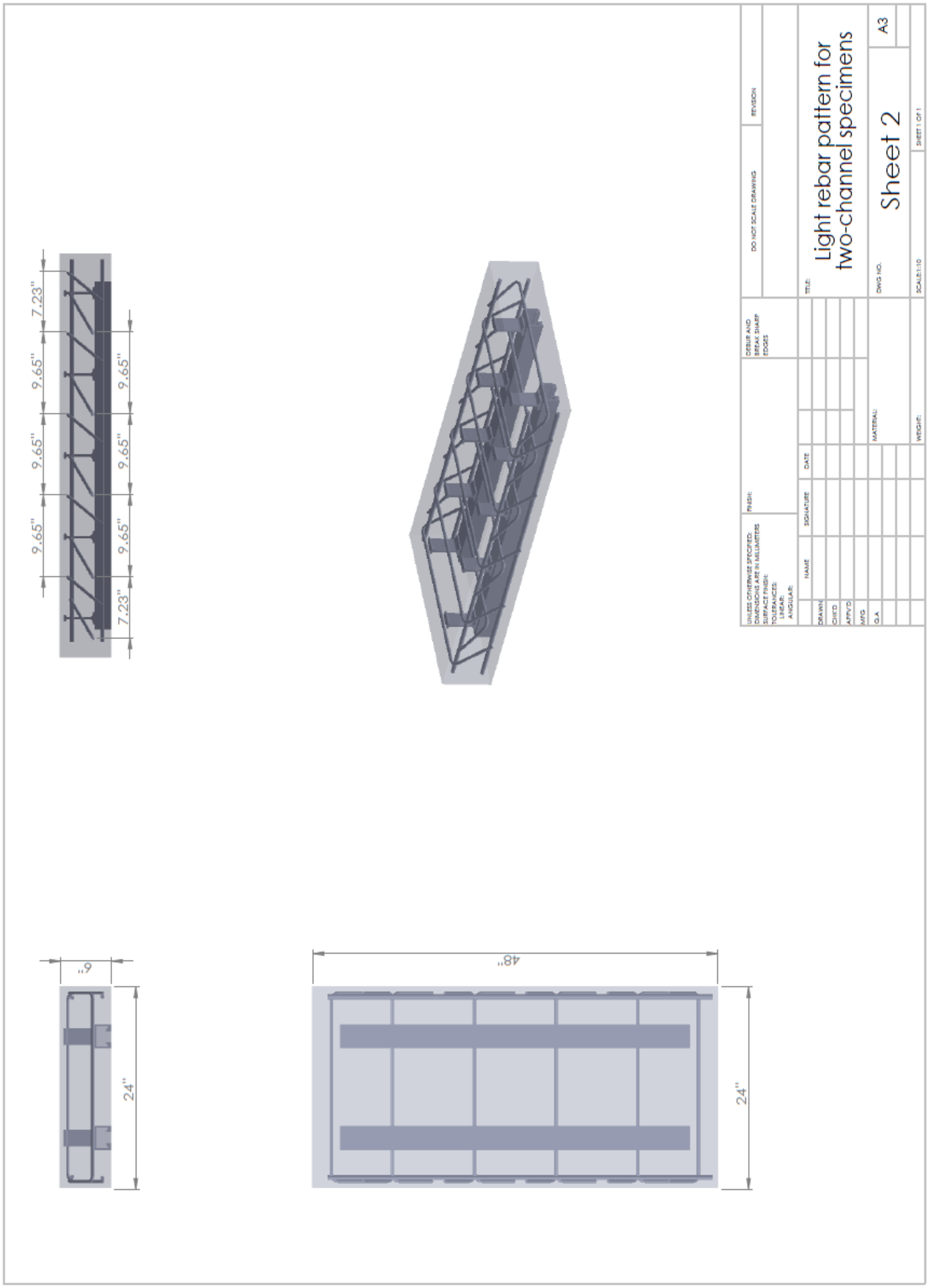
7.23"
9.65"
9.65"
9.65"
9.65"
9.65"
9.65"
7.23"
6"
24"
48"
24"
UNLESS OTHERWISE SPECIFIED:
DIMENSIONS ARE IN MILLIMETERS
SURFACE FINISH:
TOLERANCES:
LINEAR:
ANGULAR:
FINISH:
DEBUR AND BREAK SHARP EDGES
DO NOT SCALE DRAWING
REVISION
NAME
SIGNATURE
DATE
DRAWN
CHK'D
APPV'D
MFG
Q.A
TITLE:
Light rebar pattern for two-channel specimens
MATERIAL:
DWG NO.
Sheet 2
A3
WEIGHT:
SCALE:1:10
SHEET 1 OF 1

Figure C.10 Light Reinforcement Pattern

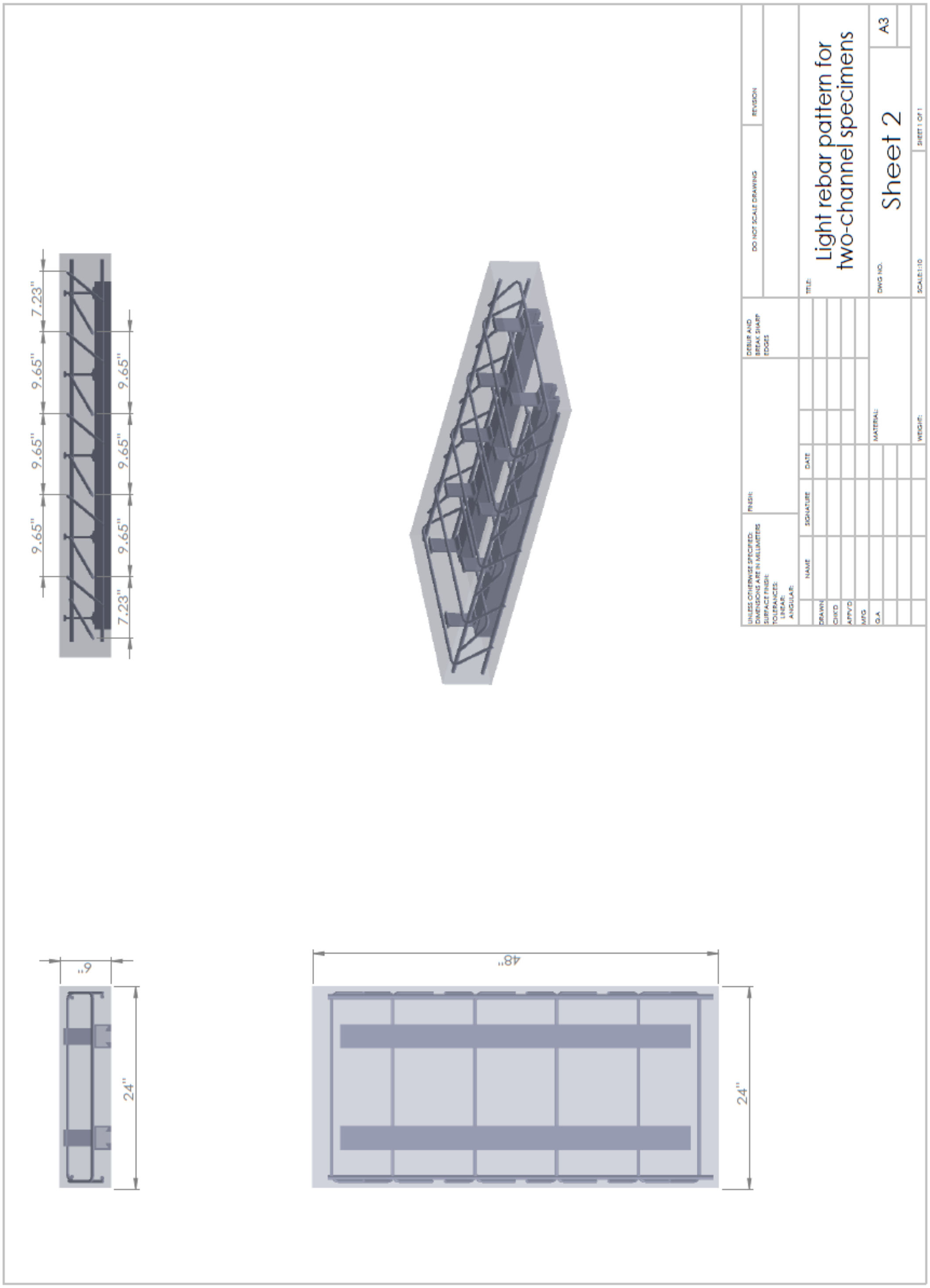
7.23"
9.65"
9.65"
9.65"
9.65"
9.65"
9.65"
7.23"
6"
24"
48"
24"
UNLESS OTHERWISE SPECIFIED:
DIMENSIONS ARE IN MILLIMETERS
SURFACE FINISH:
TOLERANCES:
LINEAR:
ANGULAR:
FINISH:
DEBUR AND BREAK SHARP EDGES
DO NOT SCALE DRAWING
REVISION
NAME
SIGNATURE
DATE
DRAWN
CHK'D
APPV'D
MFG
Q.A
TITLE:
Light rebar pattern for two-channel specimens
MATERIAL:
DWG NO.
Sheet 2
A3
WEIGHT:
SCALE:1:10
SHEET 1 OF 1

Figure C.11 Heavy Reinforcement Pattern for Two-Channel Specimens

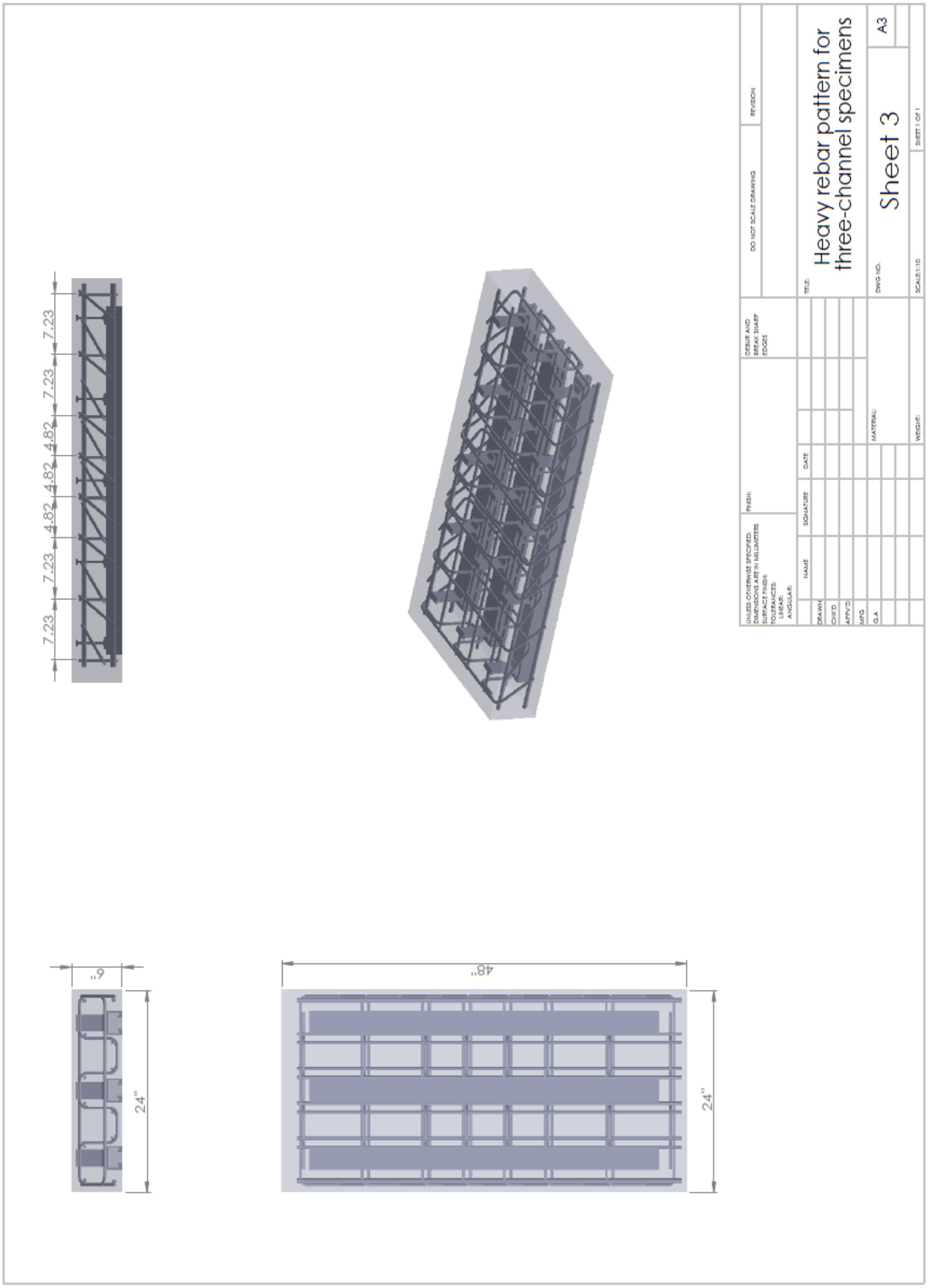
7.23
7.23
4.82
4.82
4.82
7.23
7.23
6"
24"
48"
24"
UNLESS OTHERWISE SPECIFIED:
DIMENSIONS ARE IN MILLIMETERS
SURFACE FINISH:
TOLERANCES:
LINEAR:
ANGULAR:
FINISH:
DEBUR AND BREAK SHARP EDGES
DO NOT SCALE DRAWING
REVISION
NAME
SIGNATURE
DATE
DRAWN
CHK'D
APPV'D
MFG
Q.A
MATERIAL:
WEIGHT:
TITLE:
Heavy rebar pattern for three-channel specimens
DWG NO.
Sheet 3
A3
SCALE:1:10
SHEET 1 OF 1

Figure C.12 Heavy Reinforcement Pattern for Three-Channel Specimens

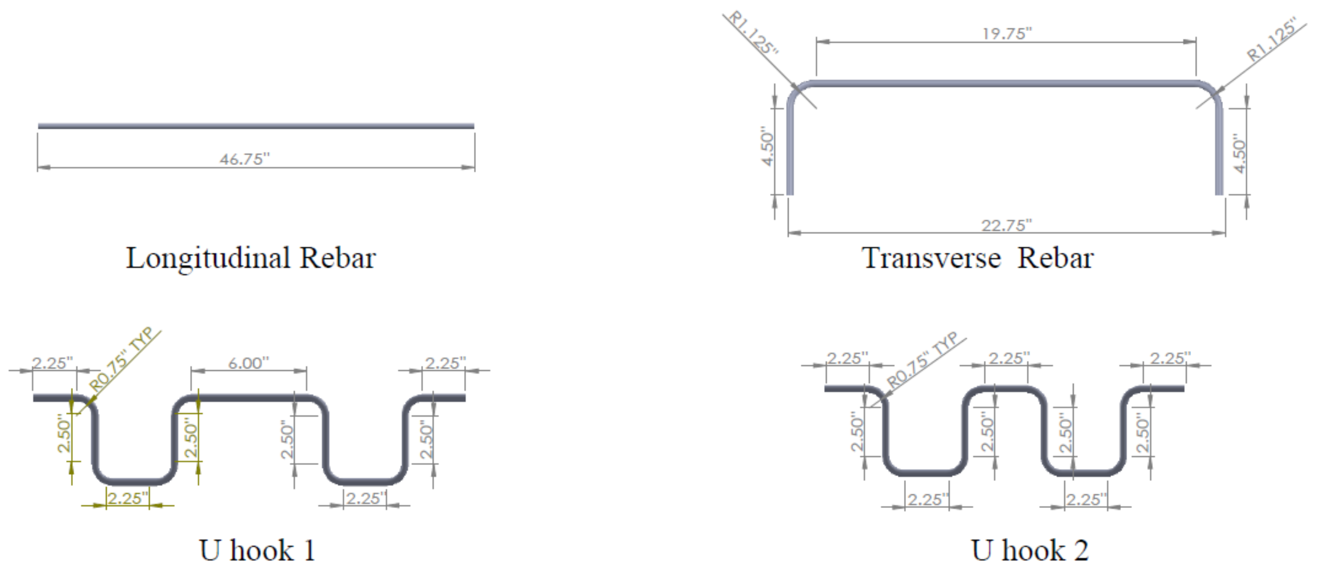
46.75"
Longitudinal Rebar
R1.125"
19.75"
R1.125"
4.50"
4.50"
22.75"
Transverse Rebar
2.25"
R0.75" TYP
6.00"
2.25"
2.50"
2.50"
2.50"
2.50"
2.25"
2.25"
U hook 1
2.25"
R0.75" TYP
2.25"
2.25"
2.50"
2.50"
2.50"
2.50"
2.25"
2.25"
U hook 2

Rebar quantity

	Number requested	Size	Length (in.)	Weight (lbs)
Longitudinal rebar	48	No.4	46.75	127
Longitudinal rebar	87	No.3	46.75	127
Transverse rebar	164	No.3	32.87	168
U hook 1	68	No.3	36.78	78
U hook 2	20	No.3	33.03	21
Total				521

Note:

1. Reinforcement shall be deformed reinforcement with a minimum yield strength of 60,000 psi.
2. A706 refinforcement is requested for weldability.
3. Material specification documentation is requested.

	NAME	SIGNATURE	DATE		
DRAWN					
CHK'D					
APPV'D					
MFG					
Q.A				MATERIAL:	
				WEIGHT:	

FINISH:
DEBUR AND BREAK SHARP EDGES
DO NOT SCALE DRAWING
REVISION
TITLE:
Rebar drawing
DWG NO.
A3
SCALE:1:5
SHEET 1 OF 1

Figure C.13 Reinforcement Details

C.1.3 Cast-in channel drawing

HALFEN CUSTOM ANCHOR CHANNEL ~ PART No. X12005-1

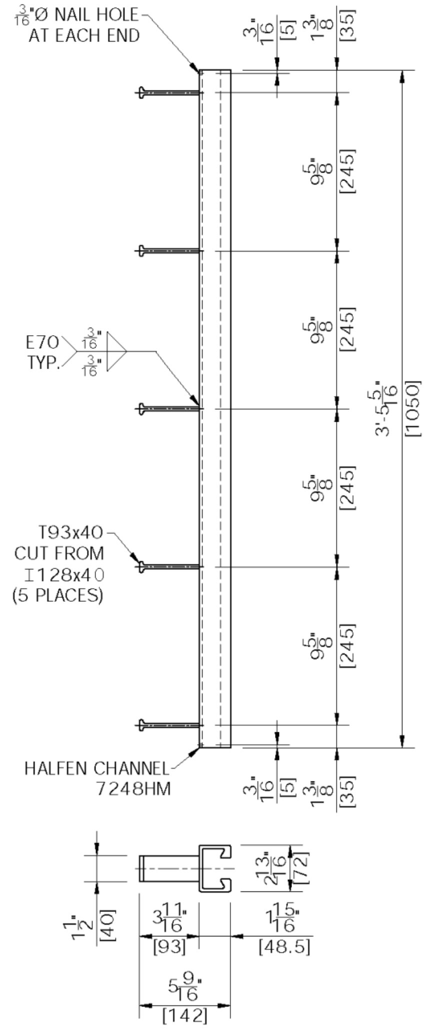
3/16"Ø NAIL HOLE AT EACH END
3/16" [5]
1 3/8" [35]
9 5/8" [245]
9 5/8" [245]
9 5/8" [245]
9 5/8" [245]
3'-5 5/16" [1050]
E70 3/16" 3/16" TYP.
T93x40 CUT FROM I128x40 (5 PLACES)
HALFEN CHANNEL 7248HM
3/16" [5]
1 3/8" [35]
2 13/16" [72]
1 1/2" [40]
3 11/16" [93]
1 15/16" [48.5]
5 9/16" [142]

HOT DIP GALVANIZE AFTER FABRICATION THEN FOAM FILL

Work Order:	Mark:	Qty:	Project No:	12005
HALFEN YOUR BEST CONNECTIONS	Project: -		Drawn by:	MRM
	Notice of Copyright © 2015 Halfen USA, Inc. All rights to this document and information contained herein are the exclusive property of Halfen USA, Inc. This drawings may not be copied or disclosed to others without the prior written consent of Halfen USA, Inc.	**Halfen USA, Inc.** PO Box 547 - 8521 FM 1976 Converse, TX 78109 PH: 800-423-9140 FAX: 888-277-1695	Drawing No:	1
			Date:	2.16.15
			Revision: △	-
Tolerances, bending radiuses, edge and surface finishes in accordance with Halfen-factory standards, unless otherwise noted.			Page 1	of 1

Figure C.14 Cast-in channel details

C.2 Beam tests

C.2.1 Steel specimen shop drawings

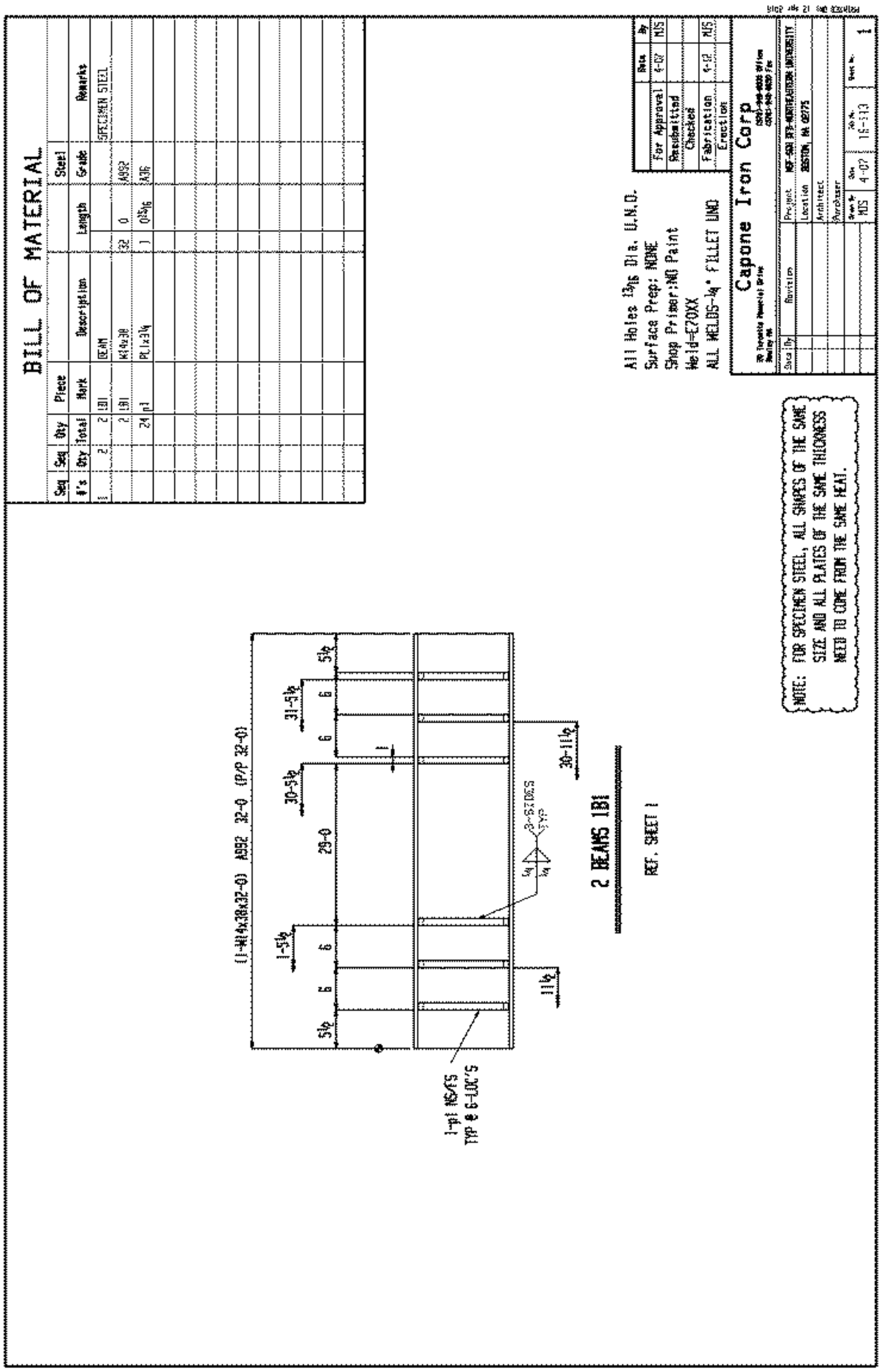

BILL OF MATERIAL

Seq #'s	Seq Qty	Qty Total	Piece Mark	Description	Length		Steel Grade	Remarks
1	2	2	1B1	BEAM				SPECIMEN STEEL
		2	1B1	W14x38	32	0	A992	
		24	p1	PL1x3¼	1	0 25/16	A36	

All Holes 13/16 Dia. U.N.O.
Surface Prep: NONE
Shop Primer: NO Paint
Weld=E70XX
ALL WELDS-¼" FILLET UNO

	Date	By
For Approval	4-07	MJS
Resubmitted		
Checked		
Fabrication	4-12	MJS
Erection		

Capone Iron Corp

Date	By	Revision		
			Project	NSF-NORTHEASTERN UNIVERSITY
			Location	BOSTON, MA 02775
			Architect	
			Purchaser	
			Drawn by MJS	Date 4-07
			Job No. 15-313	Sheet No. 1

NOTE: FOR SPECIMEN STEEL, ALL SHAPES OF THE SAME SIZE AND ALL PLATES OF THE SAME THICKNESS NEED TO COME FROM THE SAME HEAT.

(1-W14x38x32-0) A992 32-0 (P/P 32-0)
5½
6
6
31-5½
30-5½
29-0
1-5½
6
6
5½
1
30-11½
11½
¼
¼
3-SIDES TYP
2 BEAMS 1B1
REF. SHEET 1
1-p1 NS/FS
TYP @ 6-LOC'S

Figure C.15 Steel Section W14x38

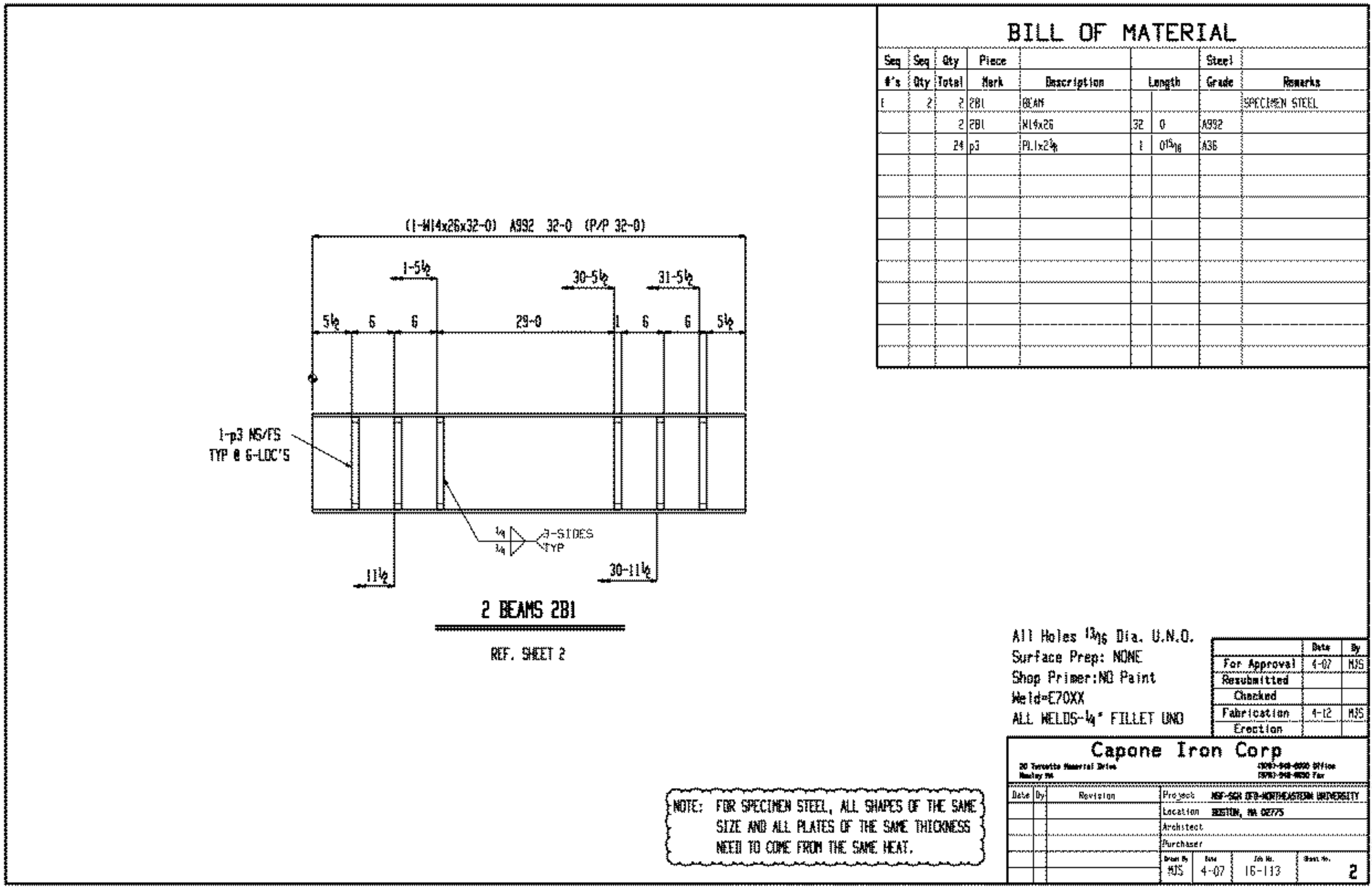
(1-W14x26x32-0) A992 32-0 (P/P 32-0)
1-5½
30-5½
31-5½
5½
6
6
29-0
1
6
6
5½
1-p3 NS/FS
TYP @ 6-LOC'S
¼
¼
3-SIDES
TYP
11½
30-11½
2 BEAMS 2B1
REF. SHEET 2

BILL OF MATERIAL

Seq	Seq	Qty	Piece				Steel	
#'s	Qty	Total	Mark	Description	Length		Grade	Remarks
1	2	2	2B1	BEAM				SPECIMEN STEEL
		2	2B1	W14x26	32	0	A992	
		24	p3	PL1x2¾	1	0$^{15}/_{16}$	A36	

All Holes $^{13}/_{16}$ Dia. U.N.O.
Surface Prep: NONE
Shop Primer:NO Paint
Weld=E70XX
ALL WELDS-¼" FILLET UNO

	Date	By
For Approval	4-07	MJS
Resubmitted		
Checked		
Fabrication	4-12	MJS
Erection		

Capone Iron Corp

Date	By	Revision	
			Project NSF-SGR IFB-NORTHEASTERN UNIVERSITY
			Location BOSTON, MA 02775
			Architect
			Purchaser

Drawn By	Date	Job No.	Sheet No.
MJS	4-07	16-113	2

NOTE: FOR SPECIMEN STEEL, ALL SHAPES OF THE SAME SIZE AND ALL PLATES OF THE SAME THICKNESS NEED TO COME FROM THE SAME HEAT.

Figure C.16 Steel Section W14x26

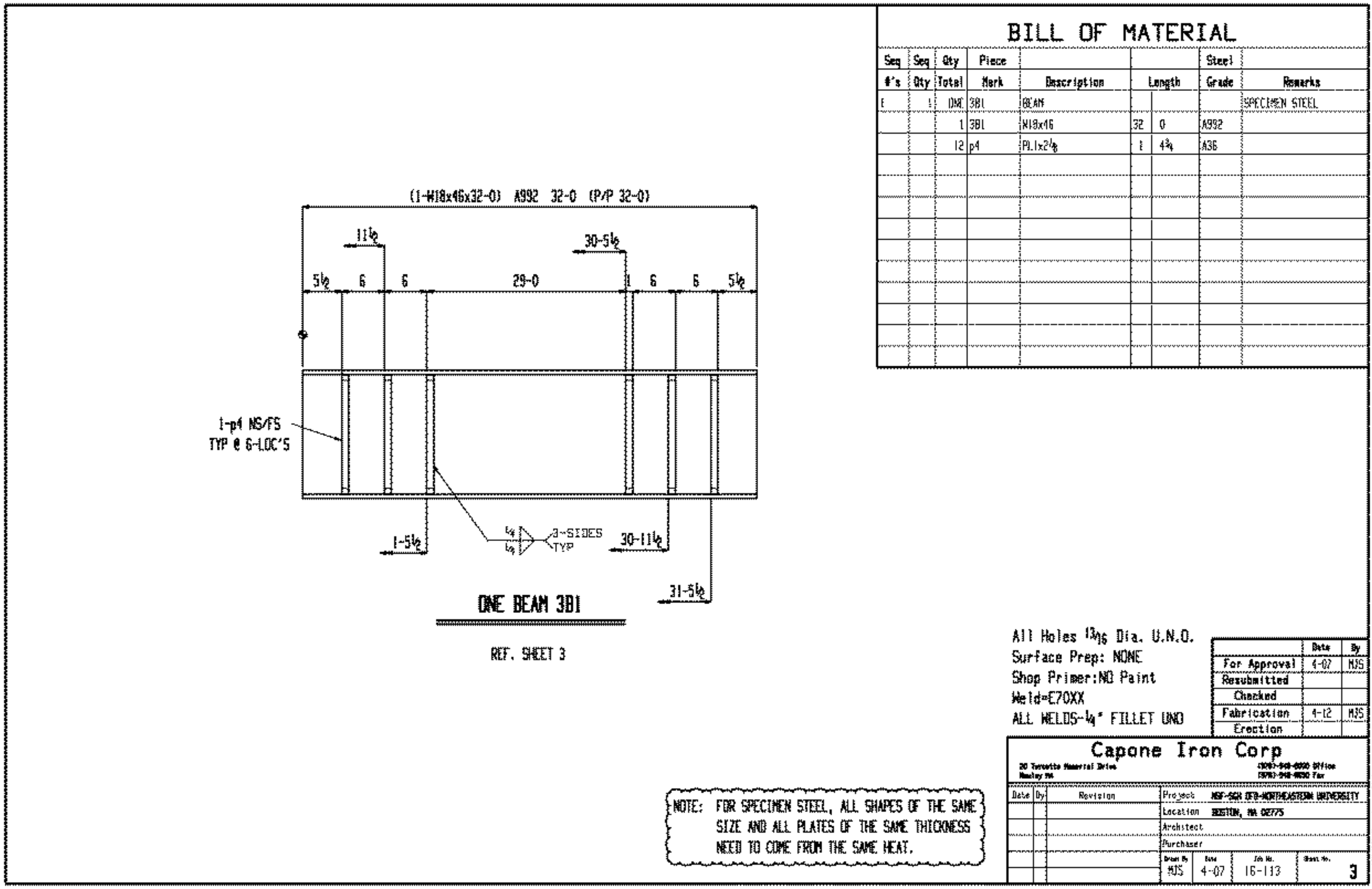
(1-W18x46x32-0) A992 32-0 (P/P 32-0)
11½
30-5½
5½
6
6
29-0
1
6
6
5½
1-p4 NS/FS
TYP @ 6-LOC'S
1-5½
¼
¼
3-SIDES
TYP
30-11½
31-5½

ONE BEAM 3B1

REF. SHEET 3

BILL OF MATERIAL

Seq	Seq	Qty	Piece				Steel	
#'s	Qty	Total	Mark	Description	Length		Grade	Remarks
E	1	ONE	3B1	BEAM				SPECIMEN STEEL
		1	3B1	W18x46	32	0	A992	
		12	p4	PL1x2⅛	1	4¾	A36	

All Holes ¹³⁄₁₆ Dia. U.N.O.
Surface Prep: NONE
Shop Primer:NO Paint
Weld=E70XX
ALL WELDS-¼" FILLET UNO

	Date	By
For Approval	4-07	MJS
Resubmitted		
Checked		
Fabrication	4-12	MJS
Erection		

Capone Iron Corp

Date	By	Revision

Project NSF-SGR [illegible]-NORTHEASTERN UNIVERSITY
Location BOSTON, MA 02775
Architect
Purchaser

Drawn By	Date	Job No.	Sheet No.
MJS	4-07	16-113	3

NOTE: FOR SPECIMEN STEEL, ALL SHAPES OF THE SAME SIZE AND ALL PLATES OF THE SAME THICKNESS NEED TO COME FROM THE SAME HEAT.

Figure C.17 Steel Section W18x46

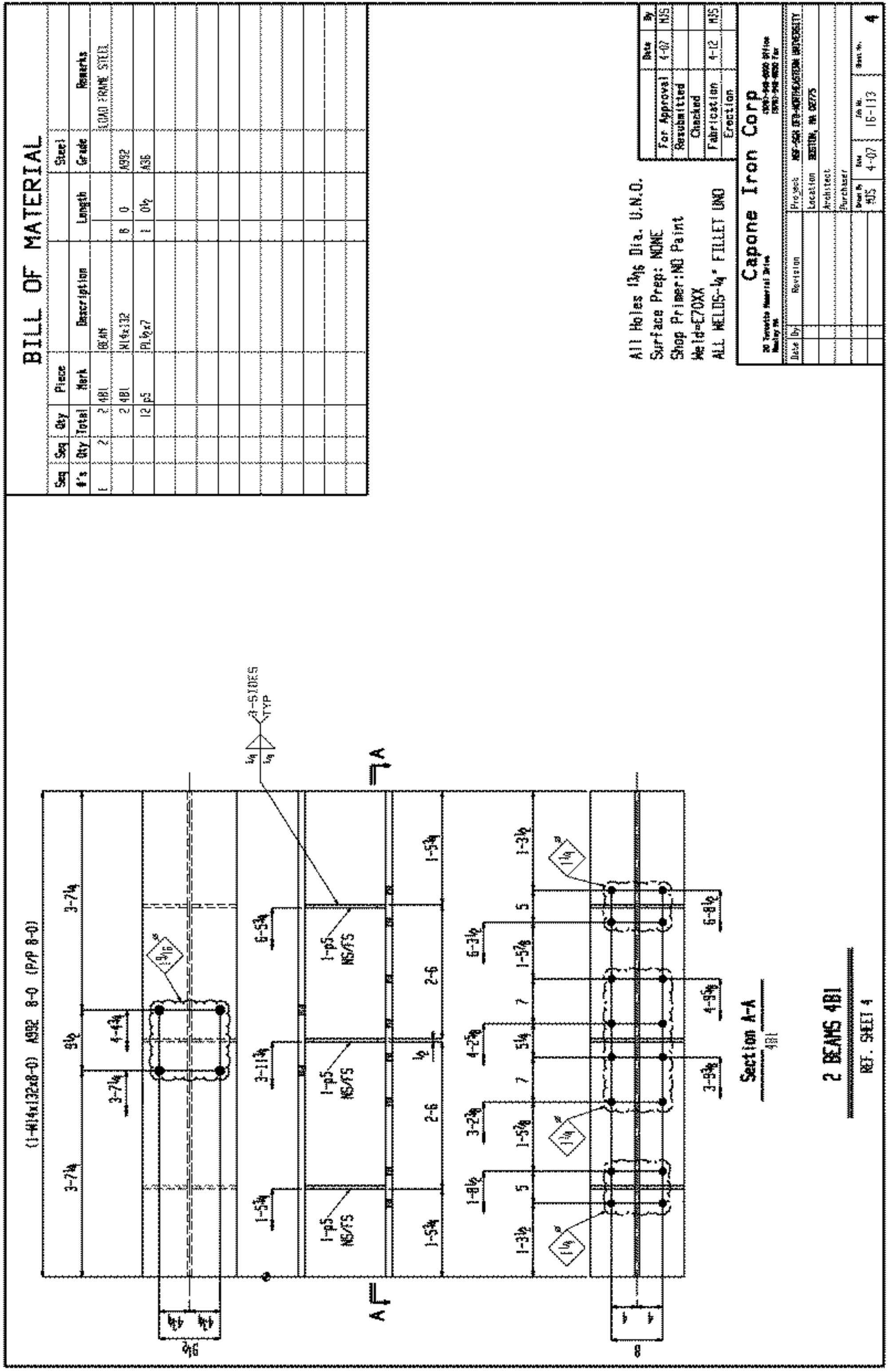
BILL OF MATERIAL
Seq #'s
Seq Qty
Qty Total
Piece Mark
Description
Length
Steel Grade
Remarks
1 2 2 4B1 BEAM LOAD FRAME STEEL
2 4B1 W14x132 8 0 A992
12 p5 PL½x7 1 0½ A36
All Holes 13/16 Dia. U.N.O.
Surface Prep: NONE
Shop Primer:NO Paint
Weld=E70XX
ALL WELDS-¼" FILLET UNO
For Approval 4-07 MJS
Resubmitted
Checked
Fabrication 4-12 MJS
Erection
Date By
Capone Iron Corp
Date By Revision
Project
Location BOSTON, MA 02775
Architect
Purchaser
Drawn By MJS
Date 4-07
Job No. 16-113
Sheet No. 4
(1-W14x132x8-0) A992 8-0 (P/P 8-0)
3-7¼
9½
3-7¼
4-4¼
1-p5 NS/FS
1-5¾
3-11¾
6-5¾
2-6
½
2-6
1-5¾
3-SIDES TYP
A
Section A-A
4B1
2 BEAMS 4B1
REF. SHEET 4
8

Figure C.18 Top Spreader Beam W14x132

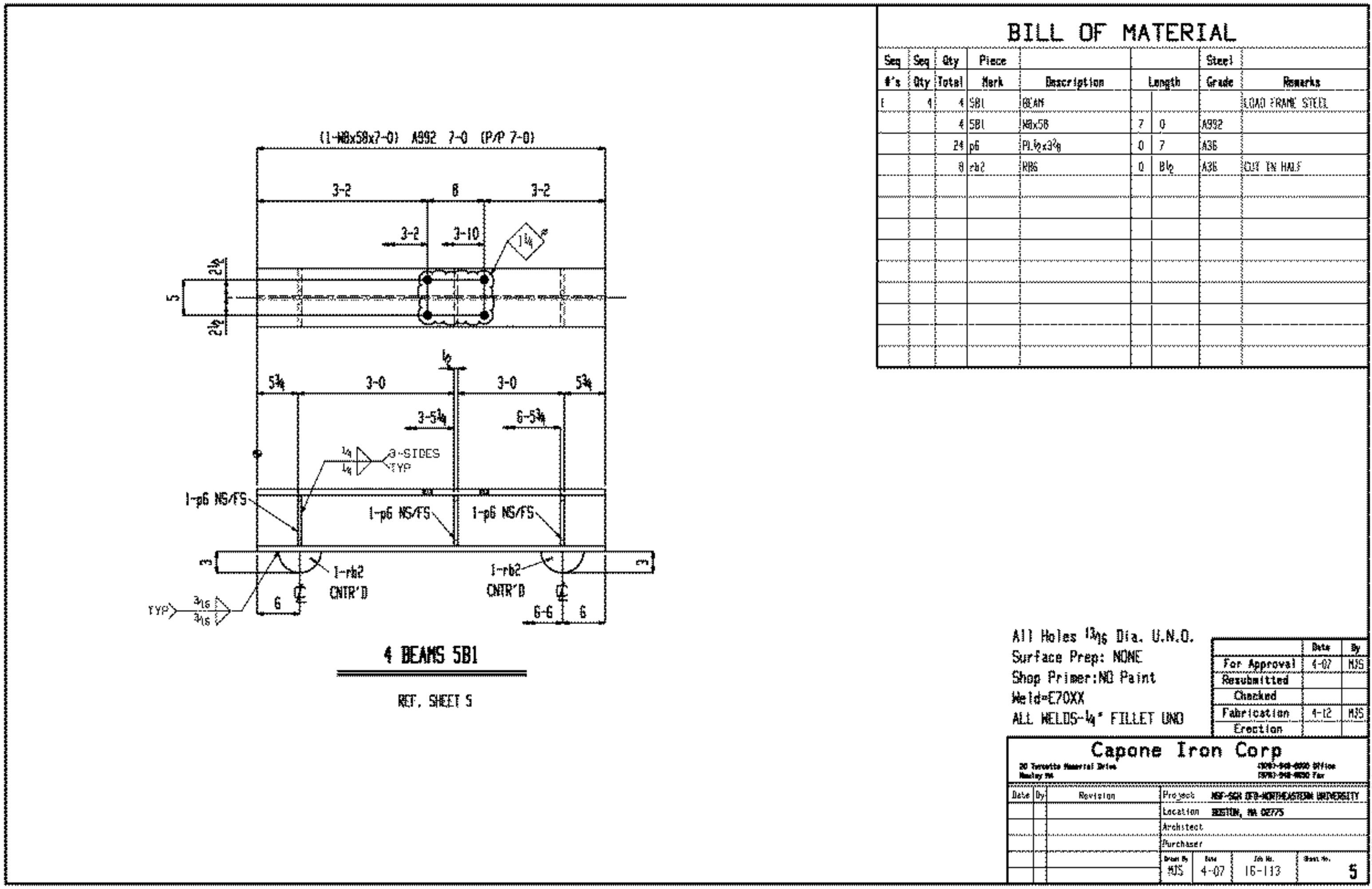
(1-W8x58x7-0) A992 7-0 (P/P 7-0)
3-2
8
3-2
3-2
3-10
1¾
2½
5
2½
½
5¾
3-0
3-0
5¾
3-5¾
6-5¾
¼
¼
3-SIDES TYP
1-p6 NS/FS
1-p6 NS/FS
1-p6 NS/FS
3
3
1-rb2 CNTR'D
1-rb2 CNTR'D
TYP
3/16
3/16
6
6-6
6
4 BEAMS 5B1
RET, SHEET 5

BILL OF MATERIAL

Seq	Seq	Qty	Piece		Length		Steel	
#'s	Qty	Total	Mark	Description			Grade	Remarks
E	4	4	5B1	BEAM				LOAD FRAME STEEL
		4	5B1	W8x58	7	0	A992	
		24	p6	PL½x3⅜	0	7	A36	
		8	rb2	RB6	0	8½	A36	CUT IN HALF

All Holes 13/16 Dia. U.N.O.
Surface Prep: NONE
Shop Primer:NO Paint
Weld=E70XX
ALL WELDS-¼" FILLET UNO

	Date	By
For Approval	4-07	MJS
Resubmitted		
Checked		
Fabrication	4-12	MJS
Erection		

Capone Iron Corp

Date	By	Revision		
			Project	NSF-SGR IFB-NORTHEASTERN UNIVERSITY
			Location	BOSTON, MA 02775
			Architect	
			Purchaser	

Drawn By	Date	Job No.	Sheet No.
MJS	4-07	16-113	5

Figure C.19 Bottom Spreader Beam W8x58

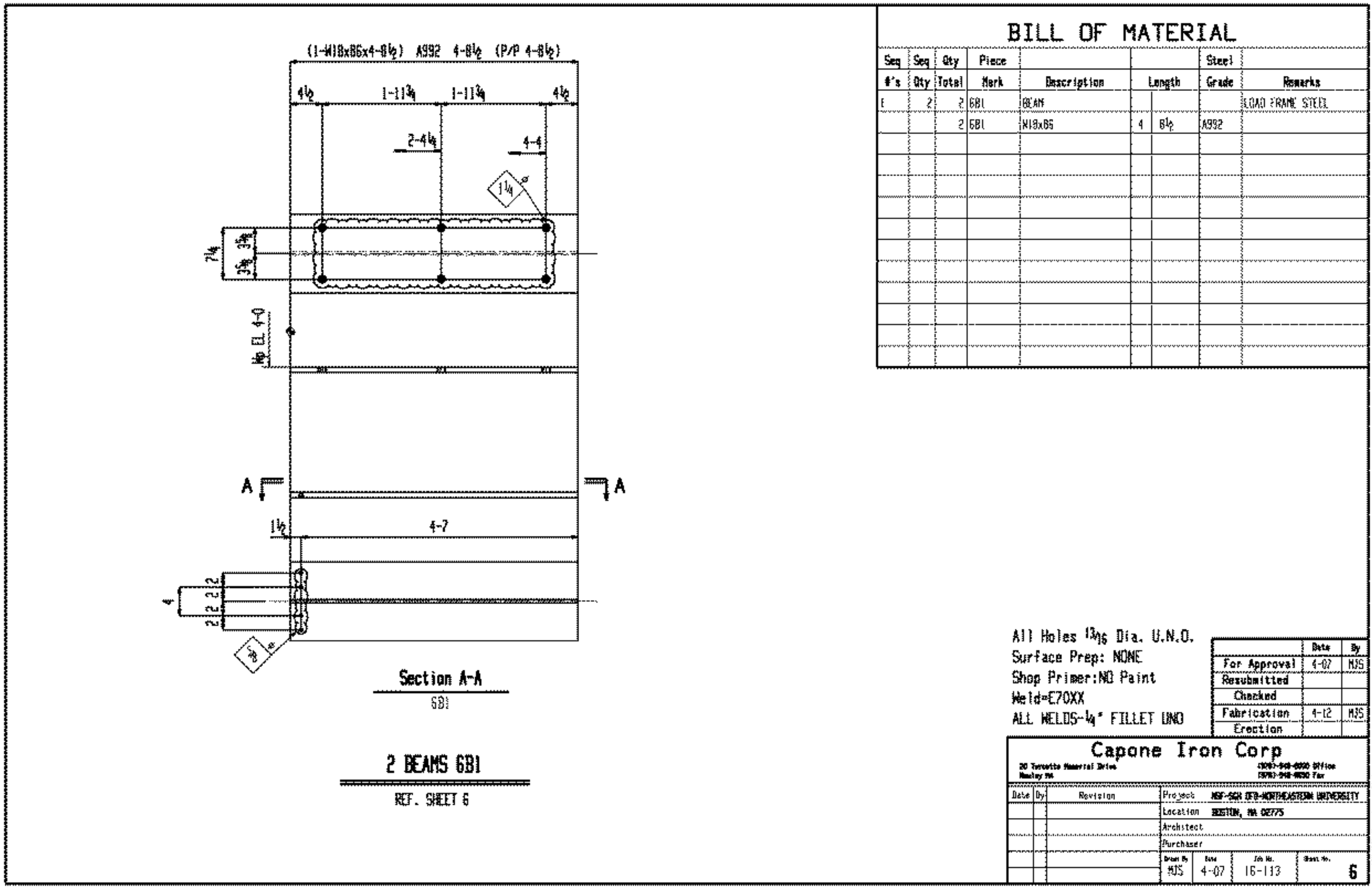
(1-W18x86x4-8½) A992 4-8½ (P/P 4-8½)
4½
1-11¾
1-11¾
4½
2-4¼
4-4
1¼
7¼
3⅝
3⅝
⅝ EL 4-0
A
A
1½
4-7
4
2
2
2
2
5/8
Section A-A
6B1
2 BEAMS 6B1
REF. SHEET 6

BILL OF MATERIAL

Seq #'s	Seq Qty	Qty Total	Piece Mark	Description	Length	Steel Grade	Remarks
E	2	2	6B1	BEAM			LOAD FRAME STEEL
		2	6B1	W18x86	4 8½	A992	

All Holes 13/16 Dia. U.N.O.
Surface Prep: NONE
Shop Primer:NO Paint
Weld=E70XX
ALL WELDS-¼" FILLET UNO

	Date	By
For Approval	4-07	MJS
Resubmitted		
Checked		
Fabrication	4-12	MJS
Erection		

Capone Iron Corp

Date	By	Revision

Project NSF-SGR IFB-NORTHEASTERN UNIVERSITY
Location BOSTON, MA 02775
Architect
Purchaser

Drawn By	Date	Job No.	Sheet No.
MJS	4-07	16-113	6

Figure C.20 Brace Section W18x86

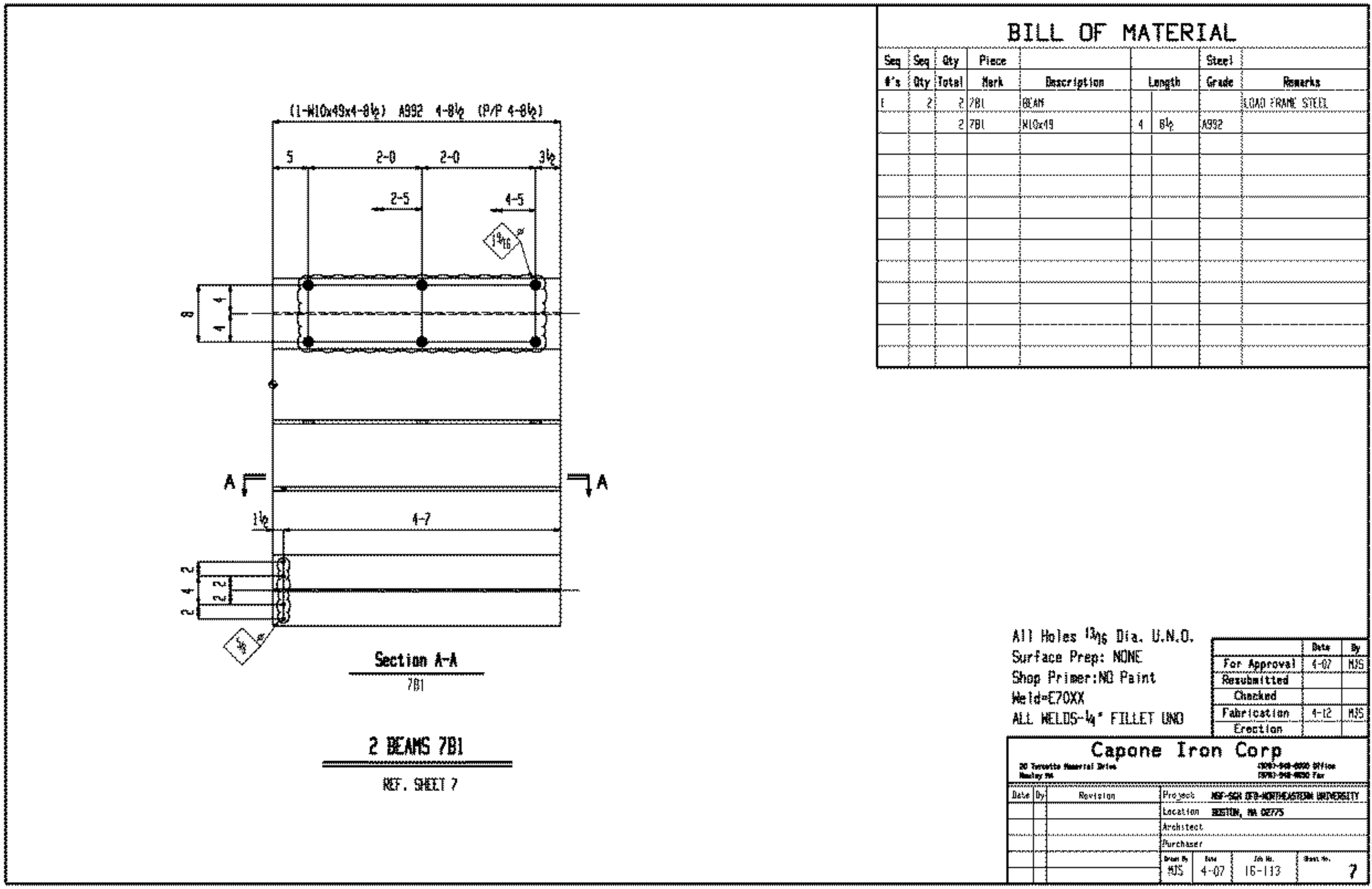
(1-W10x49x4-8½) A992 4-8½ (P/P 4-8½)
5
2-0
2-0
3½
2-5
4-5
1⁹⁄₁₆
8
4
4
A
A
1½
4-7
2
4
2
2
2
⅝
Section A-A
7B1
2 BEAMS 7B1
REF. SHEET 7
All Holes ¹³⁄₁₆ Dia. U.N.O.
Surface Prep: NONE
Shop Primer:NO Paint
Weld=E70XX
ALL WELDS-¼" FILLET UNO
Date
By
For Approval
4-07
MJS
Resubmitted
Checked
Fabrication
4-12
MJS
Erection
Capone Iron Corp
Date
By
Revision
Project
NORTHEASTERN UNIVERSITY
Location
BOSTON, MA
Architect
Purchaser
Drawn By
MJS
Date
4-07
Job No.
16-113
Sheet No.
7

BILL OF MATERIAL

Seq	Seq	Qty	Piece				Steel	
#'s	Qty	Total	Mark	Description	Length		Grade	Remarks
E	2	2	7B1	BEAM				LOAD FRAME STEEL
		2	7B1	W10x49	4	8½	A992	

Figure C.21 Brace Section W10x49

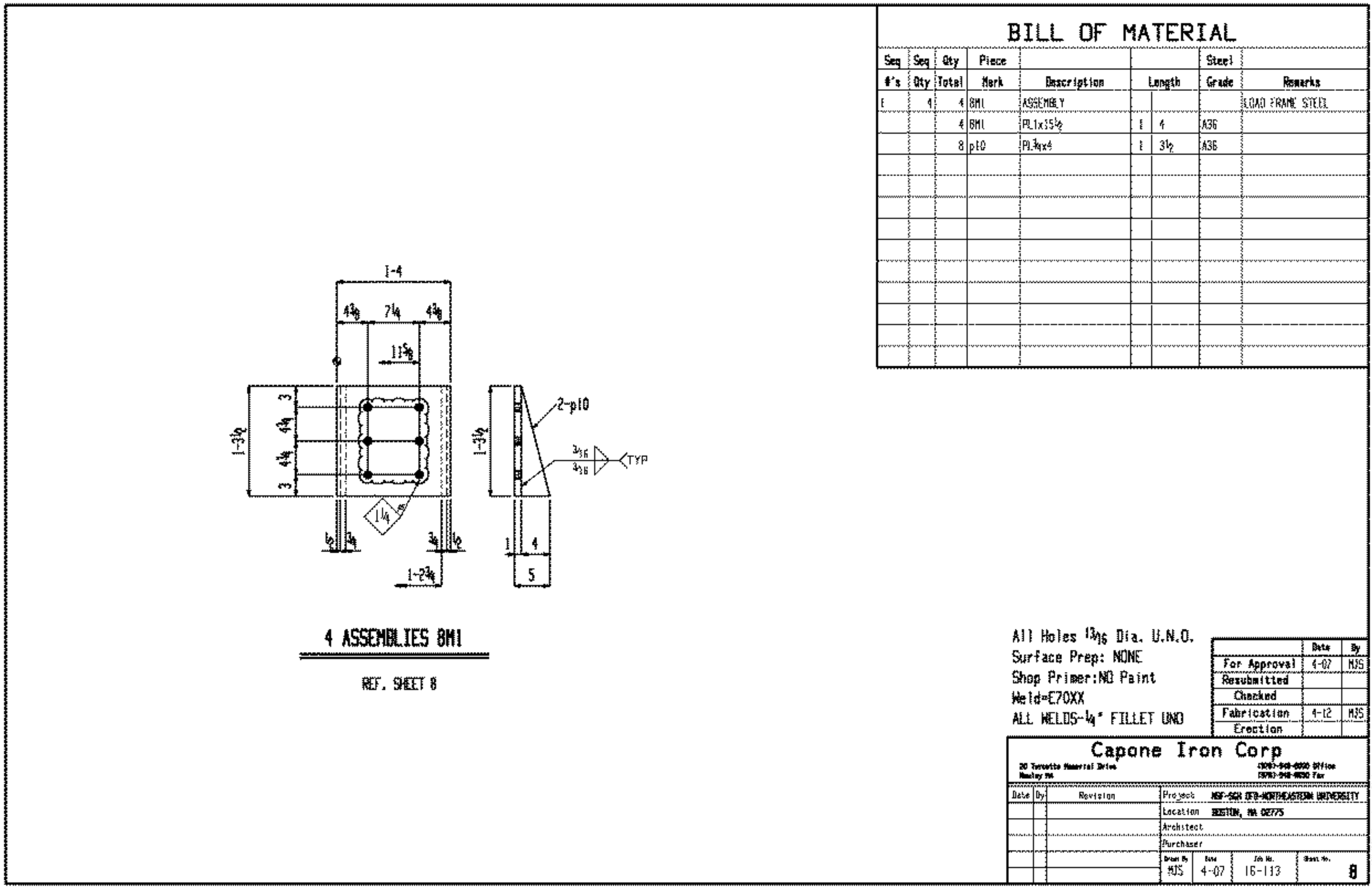
1-4
4 3/8
7 1/4
4 3/8
11 5/8
3
4 1/4
4 1/4
3
1-3 1/2
1 1/4
1/2
3/4
3/4
1/2
1-2 3/4
1-3 1/2
2-p10
3/16
3/16
TYP
1
4
5
4 ASSEMBLIES 8M1
REF. SHEET 8
Capone Iron Corp
Date
By
For Approval
4-07
MJS
Resubmitted
Checked
Fabrication
4-12
MJS
Erection
Date
By
Revision
Project
NSF-SGR IFB-NORTHEASTERN UNIVERSITY
Location
BOSTON, MA 02775
Architect
Purchaser
Drawn By
MJS
Date
4-07
Job No.
16-113
Sheet No.
8

BILL OF MATERIAL

Seq	Seq	Qty	Piece				Steel	
#'s	Qty	Total	Mark	Description	Length		Grade	Remarks
E	4	4	8M1	ASSEMBLY				LOAD FRAME STEEL
		4	8M1	PL1x15 1/2	I	4	A36	
		8	p10	PL3/4x4	I	3 1/2	A36	

All Holes 13/16 Dia. U.N.O.
Surface Prep: NONE
Shop Primer:NO Paint
Weld=E70XX
ALL WELDS-1/4" FILLET UNO

Figure C.22 Flange Tab for Column Base

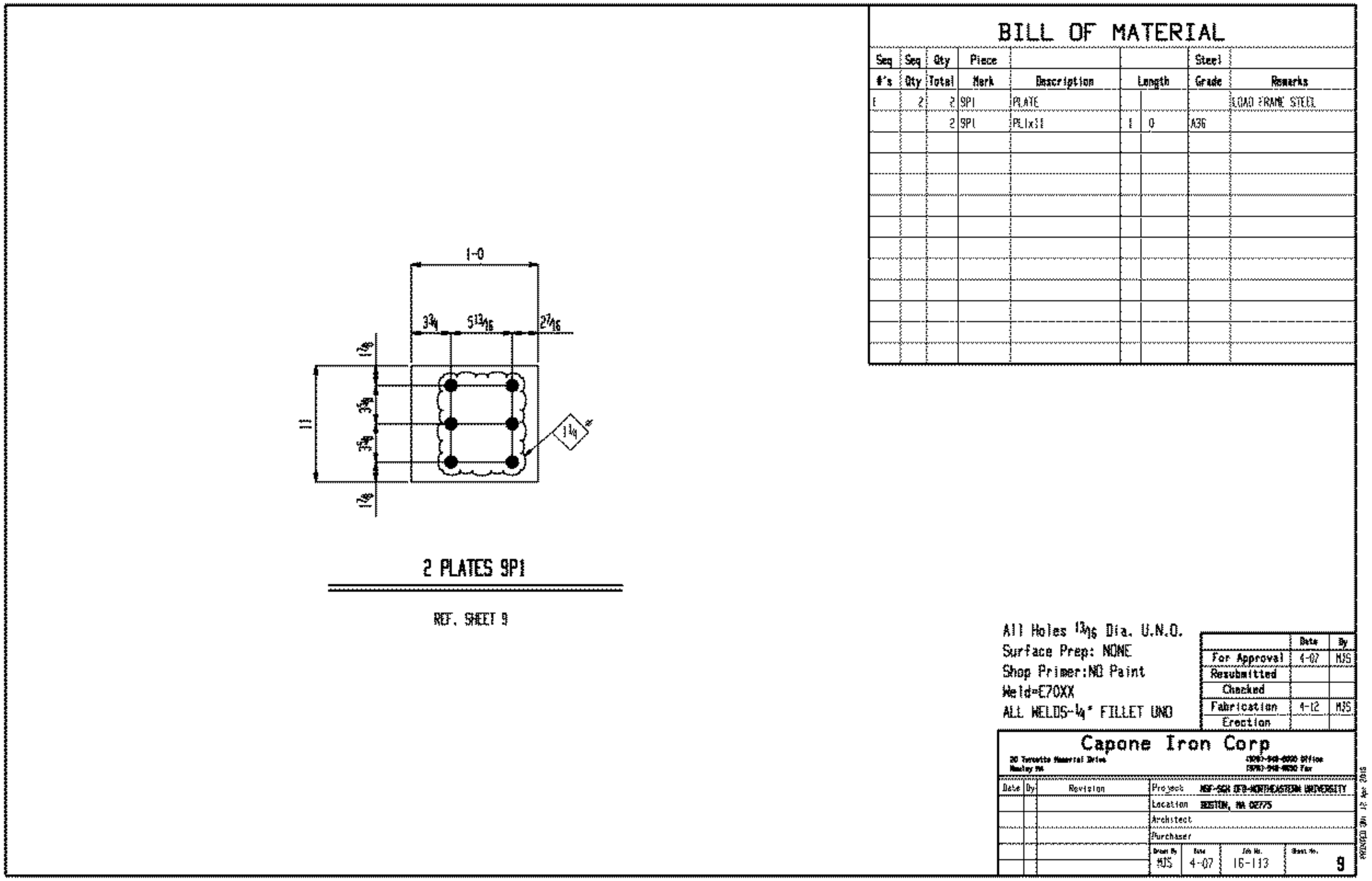

BILL OF MATERIAL

Seq #'s	Seq Qty	Qty Total	Piece Mark	Description	Length		Steel Grade	Remarks
1	2	2	9P1	PLATE				LOAD FRAME STEEL
		2	9P1	PL1x11	1	0	A36	

All Holes 13/16 Dia. U.N.O.
Surface Prep: NONE
Shop Primer:NO Paint
Weld=E70XX
ALL WELDS-¼" FILLET UNO

	Date	By
For Approval	4-07	MJS
Resubmitted		
Checked		
Fabrication	4-12	MJS
Erection		

Capone Iron Corp

Date	By	Revision		
			Project	NSF-SGR IFB-NORTHEASTERN UNIVERSITY
			Location	BOSTON, MA 02775
			Architect	
			Purchaser	

Drawn By	Date	Job No.	Sheet No.
MJS	4-07	16-113	9

Figure C.23 Web Tab for Column Base

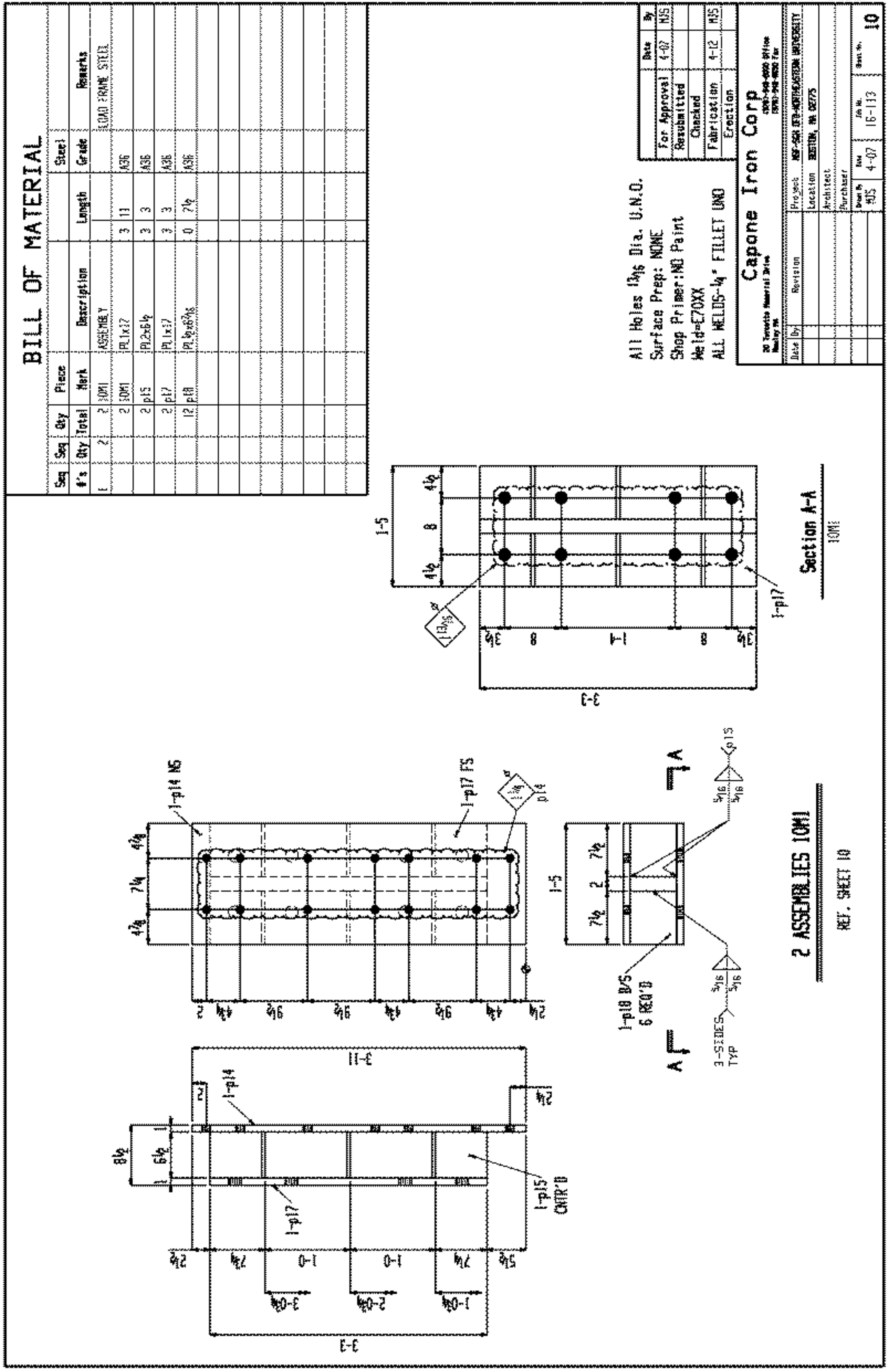

BILL OF MATERIAL

Seq	Seq	Qty	Piece				Steel	
#'s	Qty	Total	Mark	Description	Length		Grade	Remarks
1	2	2	10M1	ASSEMBLY				LOAD FRAME STEEL
		2	10M1	PL1x37	3	11	A36	
		2	p15	PL2x6½	3	3	A36	
		2	p17	PL1x37	3	3	A36	
		12	p18	PL½x6⁹⁄₁₆	0	7½	A36	

All Holes ¹³⁄₁₆ Dia. U.N.O.
Surface Prep: NONE
Shop Primer:NO Paint
Weld=E70XX
ALL WELDS-¼" FILLET UNO

Capone Iron Corp

Date	By	Revision

Project	NSF-GCR UTB-NORTHEASTERN UNIVERSITY
Location	BOSTON, MA 02775
Architect	
Purchaser	

Drawn By	Date	Job No.	Sheet No.
MJS	4-07	16-113	10

	Date	By
For Approval	4-07	MJS
Resubmitted		
Checked		
Fabrication	4-12	MJS
Erection		

Section A-A
10M1
1-5
4½
8
4½
3-3
3¼
8
1-4
8
3¼
¹³⁄₁₆
1-p17
2 ASSEMBLIES 10M1
REF. SHEET 10
1-p14 NS
1-p17 FS
p14
4½
7¼
4½
2
4¾
9½
9½
4¾
9½
4¾
2¼
1-5
7½
2
7½
1-p18 B/S
6 REQ'D
⁵⁄₁₆
p15
3-SIDES
TYP
A
A
3-11
8½
6½
1
1
1-p14
1-p17
1-p15
CNTR'D
2½
2¼
3½
7¼
1-0
1-0
7¼
3½
3-0¾
2-0¾
1-0¾
3-3

Figure C.24 Cross Beam Adapter

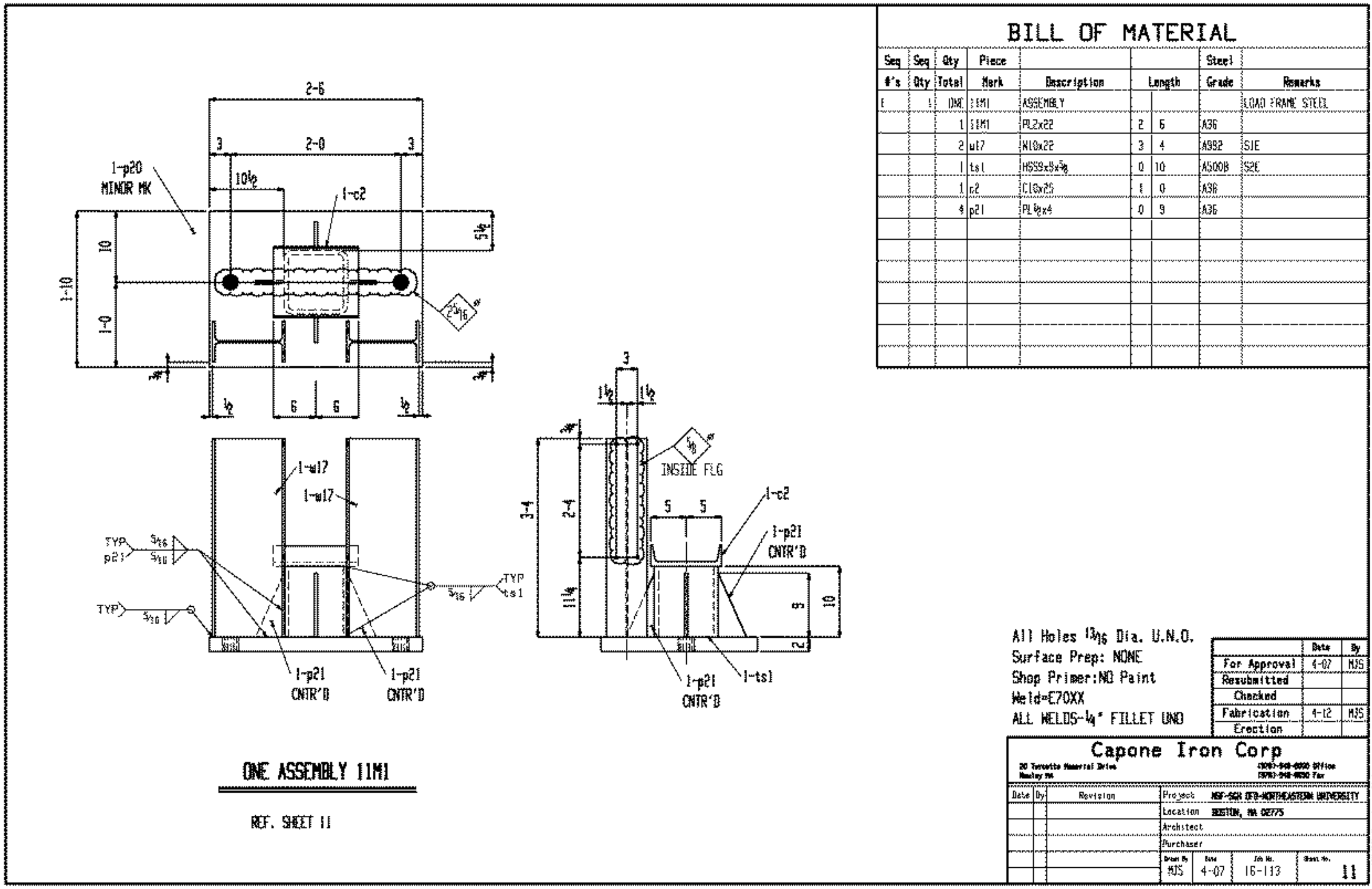
2-6
2-0
3
3
10½
1-p20
MINOR MK
1-c2
5½
10
1-0
1-10
2 5/16
½
6
6
½
1-w17
1-w17
TYP
p21
5/16
5/16
TYP
5/16
TYP
ts1
5/16
1-p21
CNTR'D
1-p21
CNTR'D
ONE ASSEMBLY 11M1
REF. SHEET 11
3
1½
1½
5/8
INSIDE FLG
3-4
2-4
11¼
5
5
1-c2
1-p21
CNTR'D
9
10
2
1-p21
CNTR'D
1-ts1

BILL OF MATERIAL

Seq	Seq	Qty	Piece				Steel	
#'s	Qty	Total	Mark	Description	Length		Grade	Remarks
E	1	ONE	11M1	ASSEMBLY				LOAD FRAME STEEL
		1	11M1	PL2x22	2	6	A36	
		2	w17	W10x22	3	4	A992	SIE
		1	ts1	HSS9x9x5/8	0	10	A500B	S2E
		1	c2	C10x25	1	0	A36	
		4	p21	PL5/8x4	0	9	A36	

All Holes 13/16 Dia. U.N.O.
Surface Prep: NONE
Shop Primer:NO Paint
Weld=E70XX
ALL WELDS-1/4" FILLET UNO

	Date	By
For Approval	4-07	MJS
Resubmitted		
Checked		
Fabrication	4-12	MJS
Erection		

Capone Iron Corp

Date	By	Revision	
			Project NSF-SGR IFB-NORTHEASTERN UNIVERSITY
			Location BOSTON, MA 02775
			Architect
			Purchaser
			Drawn By MJS · Date 4-07 · Job No. 16-113 · Sheet No. 11

Figure C.25 Beam Roller Support

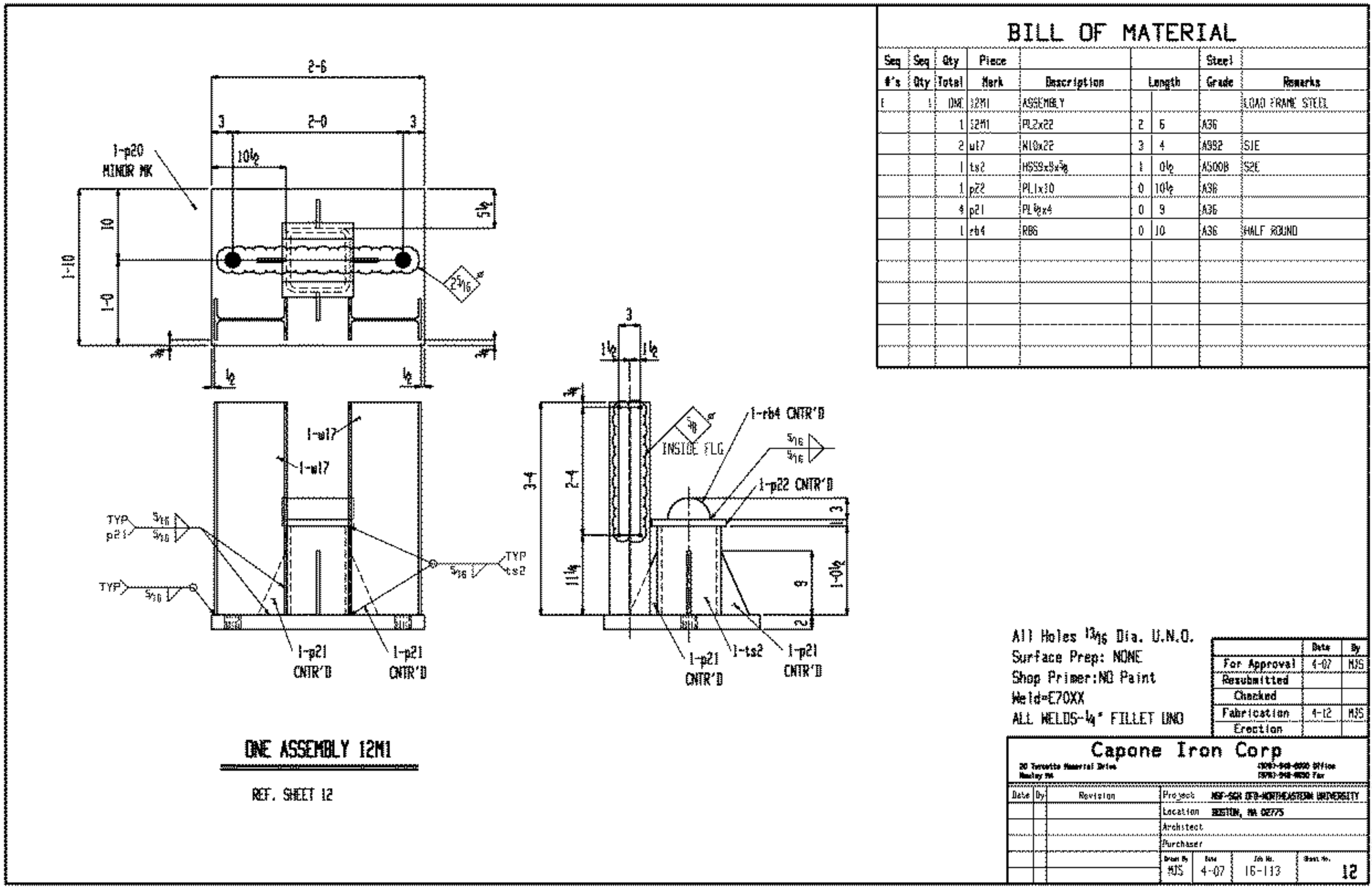
2-6
3
2-0
3
10½
1-p20
MINOR MK
10
1-0
1-10
5½
2 5/16
½
½
1-wl7
1-wl7
TYP
p21
5/16
5/16
TYP
5/16
TYP
ts2
5/16
1-p21
CNTR'D
1-p21
CNTR'D
ONE ASSEMBLY 12M1
REF. SHEET 12
3
1½
1½
5/8
INSIDE FLG
1-rb4 CNTR'D
5/16
5/16
1-p22 CNTR'D
3
3-4
2-4
11¼
9
1-0½
2
1-p21
CNTR'D
1-ts2
1-p21
CNTR'D
PRINTED ON 12 Apr 2016

BILL OF MATERIAL

Seq	Seq	Qty	Piece				Steel	
#'s	Qty	Total	Mark	Description	Length		Grade	Remarks
E	1	ONE	12M1	ASSEMBLY				LOAD FRAME STEEL
		1	12M1	PL2x22	2	6	A36	
		2	wl7	W10x22	3	4	A992	S1E
		1	ts2	HSS9x9x5/8	1	0½	A500B	S2E
		1	p22	PL1x10	0	10½	A36	
		4	p21	PL½x4	0	9	A36	
		1	rb4	RB6	0	10	A36	HALF ROUND

All Holes 13/16 Dia. U.N.O.
Surface Prep: NONE
Shop Primer:NO Paint
Weld=E70XX
ALL WELDS-¼" FILLET UNO

	Date	By
For Approval	4-07	MJS
Resubmitted		
Checked		
Fabrication	4-12	MJS
Erection		

Capone Iron Corp

Date	By	Revision		
			Project	NSF-SGR IFB-NORTHEASTERN UNIVERSITY
			Location	BOSTON, MA 02775
			Architect	
			Purchaser	

Drawn By	Date	Job No.	Sheet No.
MJS	4-07	16-113	12

Figure C.26 Beam Pin Support

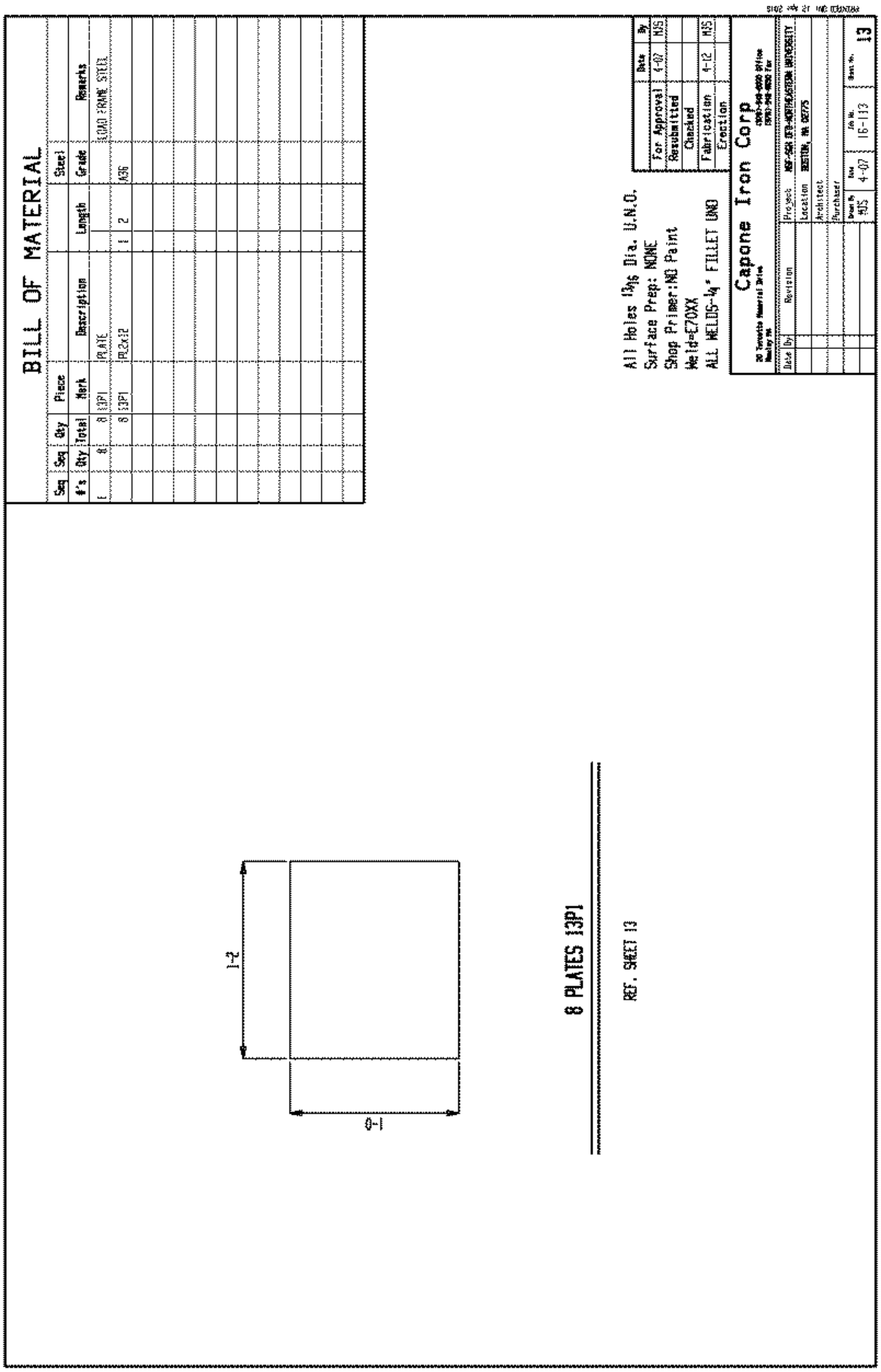
BILL OF MATERIAL
Seq #'s
Seq Qty
Qty Total
Piece Mark
Description
Length
Steel Grade
Remarks
1
8
8 13P1
PLATE
LOAD FRAME STEEL
8 13P1
PL2x12
1 2
A36
All Holes 13/16 Dia. U.N.O.
Surface Prep: NONE
Shop Primer:NO Paint
Weld=E70XX
ALL WELDS-1/4" FILLET UNO
For Approval 4-07 MJS
Resubmitted
Checked
Fabrication 4-12 MJS
Erection
Date
By
Capone Iron Corp
Date
By
Revision
Project
Location BOSTON, MA 02775
Architect
Purchaser
Drawn By MJS
Date 4-07
Job No. 16-113
Sheet No. 13
1-2
1-0
8 PLATES 13P1
REF. SHEET 13

Figure C.27 Plate under Bottom Spreader Beam

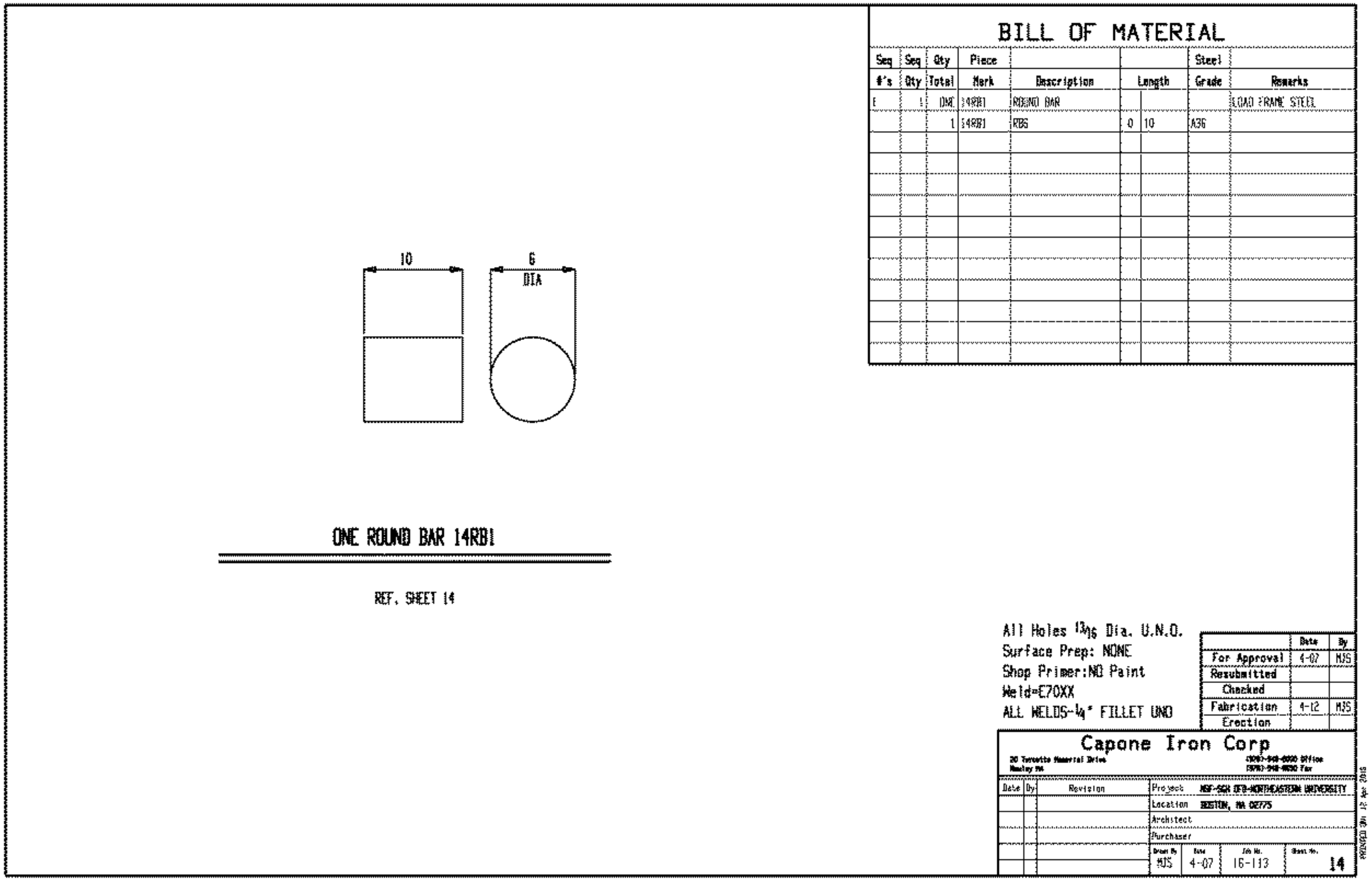
10
6
DIA
ONE ROUND BAR 14RB1
REF. SHEET 14
Capone Iron Corp
Project
Location
Architect
Purchaser
Drawn By
MJS
Date
4-07
Job No.
16-113
Sheet No.
14
Date
By
Revision

BILL OF MATERIAL

Seq	Seq	Qty	Piece				Steel	
#'s	Qty	Total	Mark	Description	Length		Grade	Remarks
E	1	ONE	14RB1	ROUND BAR				LOAD FRAME STEEL
		1	14RB1	RB6	0	10	A36	

All Holes 13/16 Dia. U.N.O.
Surface Prep: NONE
Shop Primer:NO Paint
Weld=E70XX
ALL WELDS-1/4" FILLET UNO

	Date	By
For Approval	4-07	MJS
Resubmitted		
Checked		
Fabrication	4-12	MJS
Erection		

Figure C.28 6'' Roller

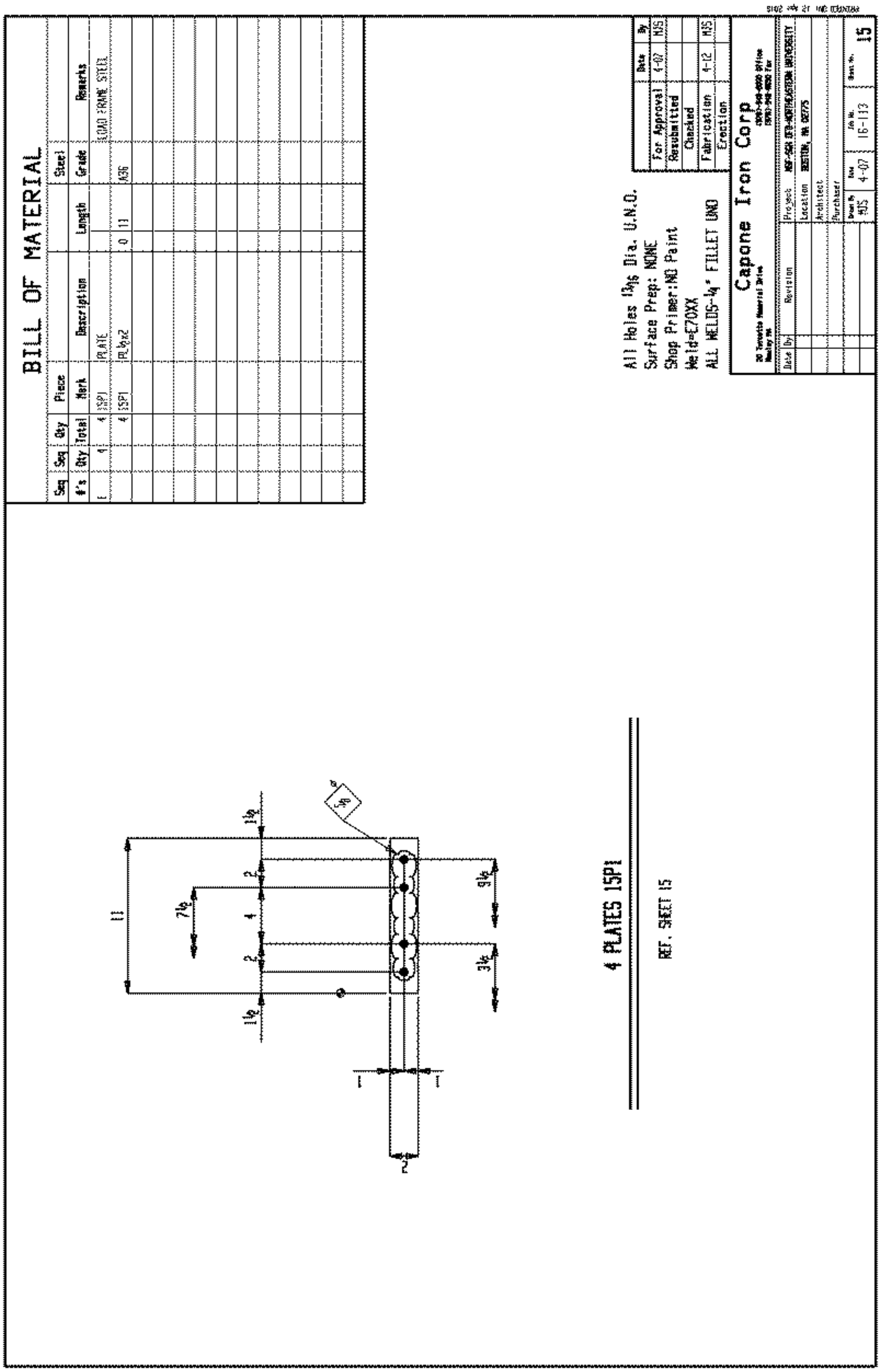

BILL OF MATERIAL

Seq	Seq	Qty	Piece				Steel	
#'s	Qty	Total	Mark	Description	Length		Grade	Remarks
E	4	4	15P1	PLATE				LOAD FRAME STEEL
		4	15P1	PL ½x2	0	11	A36	

All Holes 13/16 Dia. U.N.O.
Surface Prep: NONE
Shop Primer:NO Paint
Weld=E70XX
ALL WELDS-¼" FILLET UNO

	Date	By
For Approval	4-07	MJS
Resubmitted		
Checked		
Fabrication	4-12	MJS
Erection		

Capone Iron Corp

Date	By	Revision

Project [illegible] NORTHEASTERN UNIVERSITY
Location BOSTON, MA [illegible]
Architect
Purchaser

Drawn By	Date	Job No.	Sheet No.
MJS	4-07	16-113	15

Figure C.29 Clamp Plate for Braces

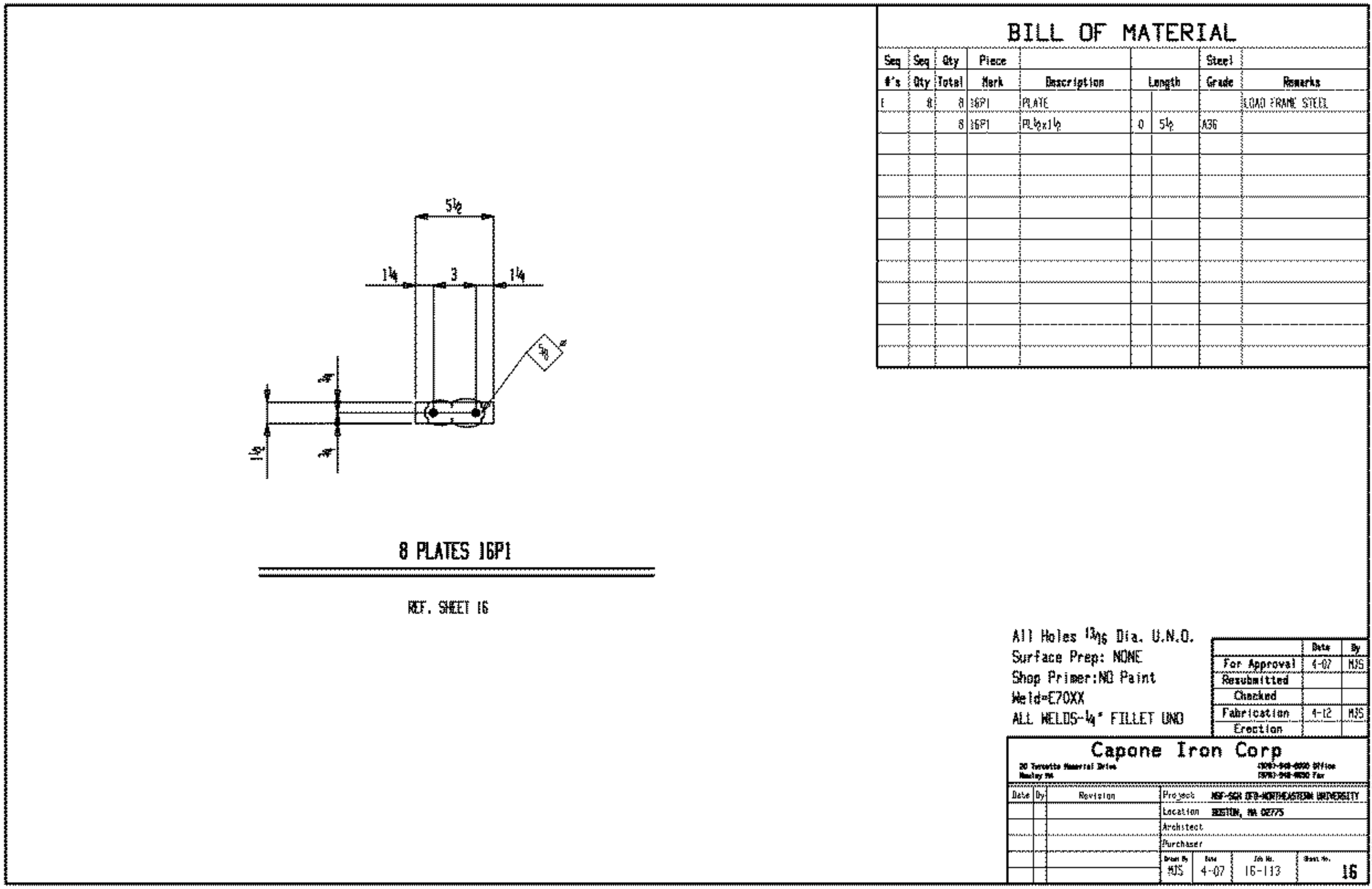

BILL OF MATERIAL

Seq	Seq	Qty	Piece				Steel	
#'s	Qty	Total	Mark	Description	Length		Grade	Remarks
E	8	8	16P1	PLATE				LOAD FRAME STEEL
		8	16P1	PL½x1½	0	5½	A36	

All Holes 13/16 Dia. U.N.O.
Surface Prep: NONE
Shop Primer:NO Paint
Weld=E70XX
ALL WELDS-¼" FILLET UNO

5½
1¼
3
1¼
5/8
¼
¼
1½
8 PLATES 16P1
REF. SHEET 16
Date
By
For Approval
4-07
MJS
Resubmitted
Checked
Fabrication
4-12
MJS
Erection
Capone Iron Corp
Date
By
Revision
Project
Location
Architect
Purchaser
Drawn By
MJS
Date
4-07
Job No.
16-113
Sheet No.
16

Figure C.30 Clamp Plate for Column Ends

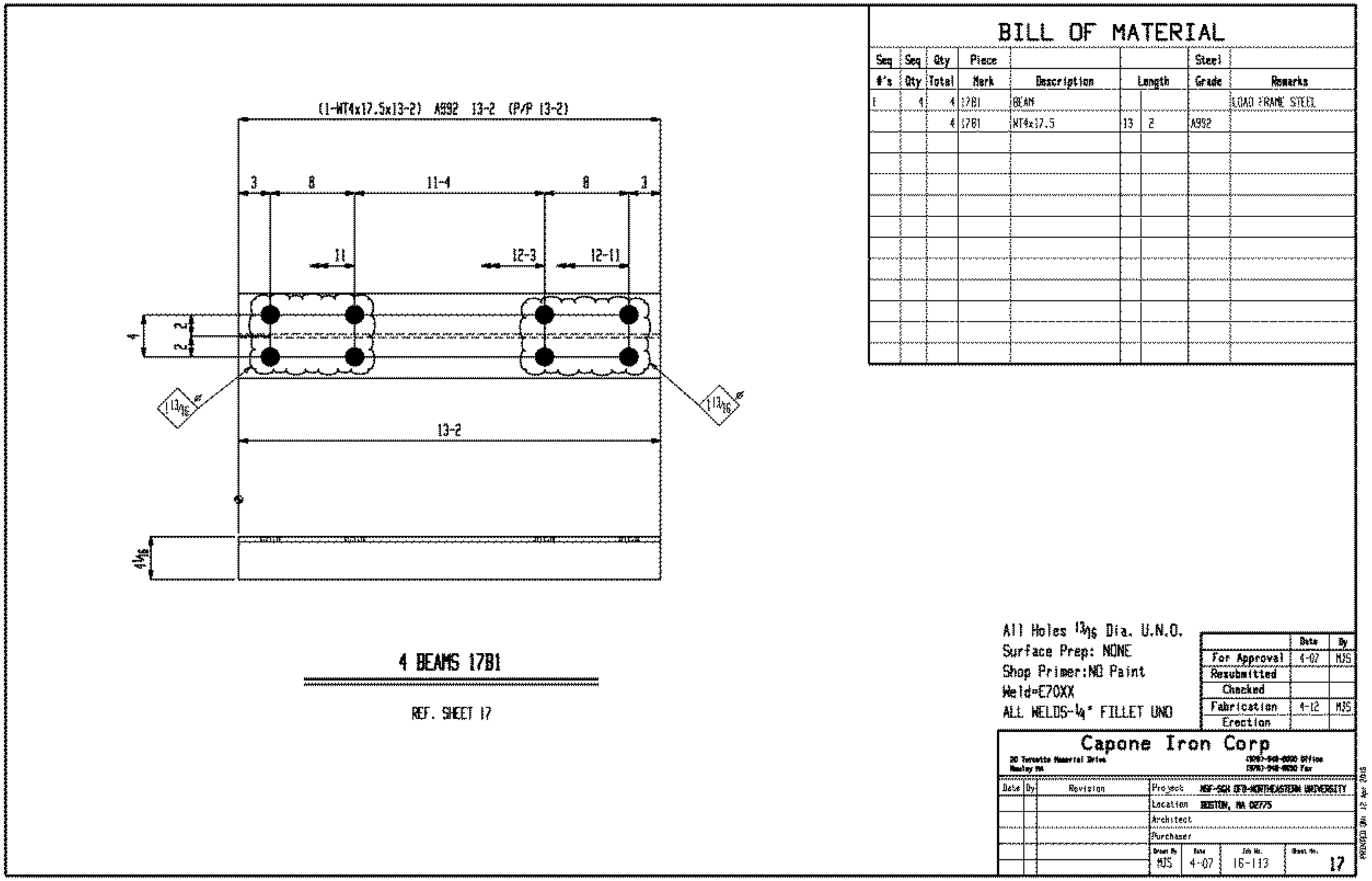
(1-WT4x17.5x13-2) A992 13-2 (P/P 13-2)
3
8
11-4
8
3
11
12-3
12-11
4
2
2
1 13/16
1 13/16
13-2
4 1/16
4 BEAMS 17B1
REF. SHEET 17
All Holes 13/16 Dia. U.N.O.
Surface Prep: NONE
Shop Primer:NO Paint
Weld=E70XX
ALL WELDS-1/4" FILLET UNO
Date
By
For Approval
4-07
MJS
Resubmitted
Checked
Fabrication
4-12
MJS
Erection
Capone Iron Corp
Date
By
Revision
Project
NSF-SGR IFD-NORTHEASTERN UNIVERSITY
Location
BOSTON, MA 02775
Architect
Purchaser
Drawn By
MJS
Date
4-07
Job No.
16-113
Sheet No.
17

BILL OF MATERIAL

Seq	Seq	Qty	Piece				Steel	
#'s	Qty	Total	Mark	Description	Length		Grade	Remarks
E	4	4	17B1	BEAM				LOAD FRAME STEEL
		4	17B1	WT4x17.5	13	2	A992	

Figure C.31 Brace Section WT4x17.5

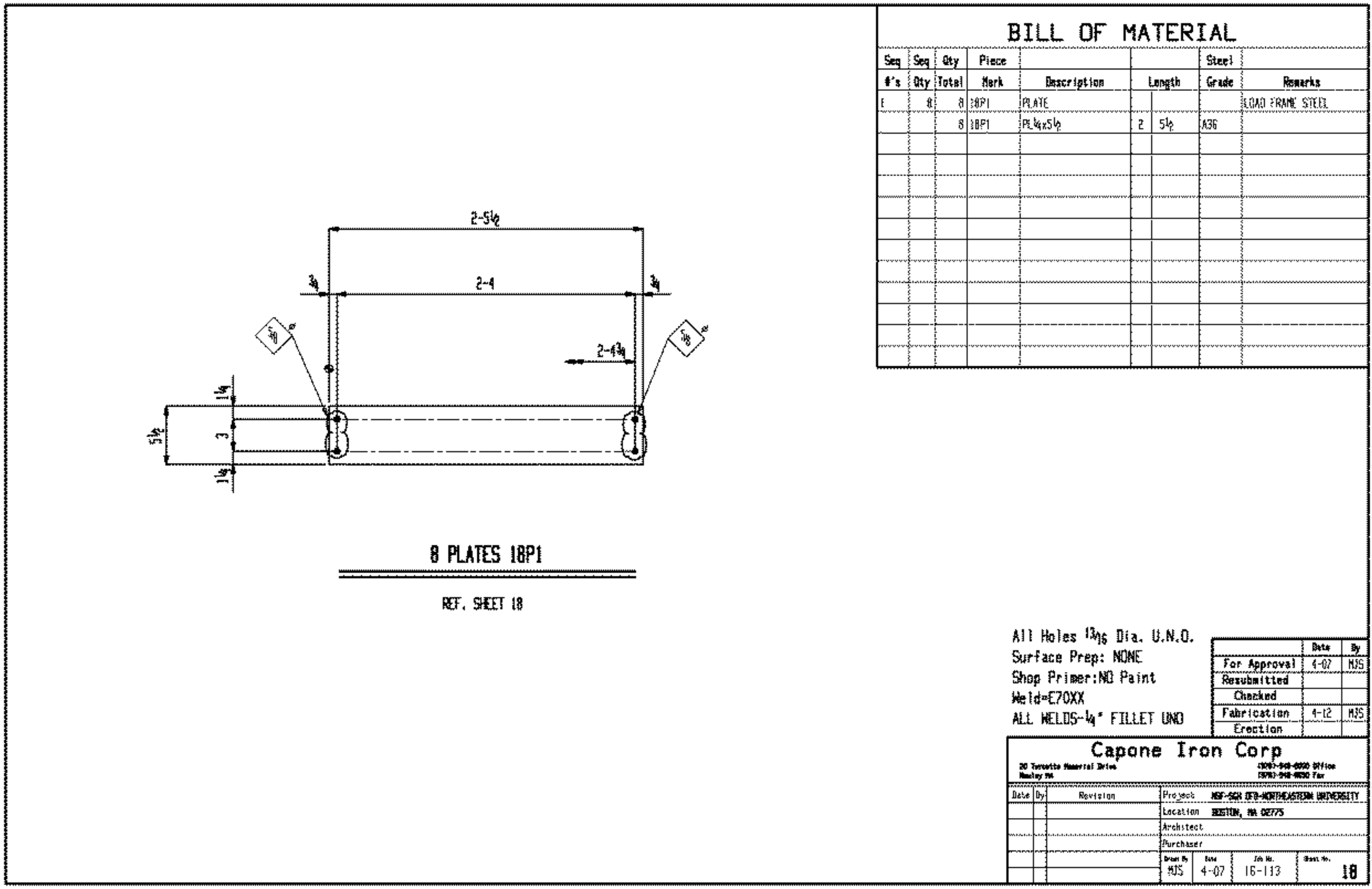

BILL OF MATERIAL

Seq	Seq	Qty	Piece				Steel	
#'s	Qty	Total	Mark	Description	Length		Grade	Remarks
E	8	8	18P1	PLATE				LOAD FRAME STEEL
		8	18P1	PL¼x5½	2	5½	A36	

All Holes 13/16 Dia. U.N.O.
Surface Prep: NONE
Shop Primer:NO Paint
Weld=E70XX
ALL WELDS-¼" FILLET UNO

	Date	By
For Approval	4-07	MJS
Resubmitted		
Checked		
Fabrication	4-12	MJS
Erection		

Capone Iron Corp

Date | By | Revision

Project NSF-SGR IFB-NORTHEASTERN UNIVERSITY
Location BOSTON, MA 02775
Architect
Purchaser

Drawn By	Date	Job No.	Sheet No.
MJS	4-07	16-113	18

Figure C.32 Clamp Plate for Braces

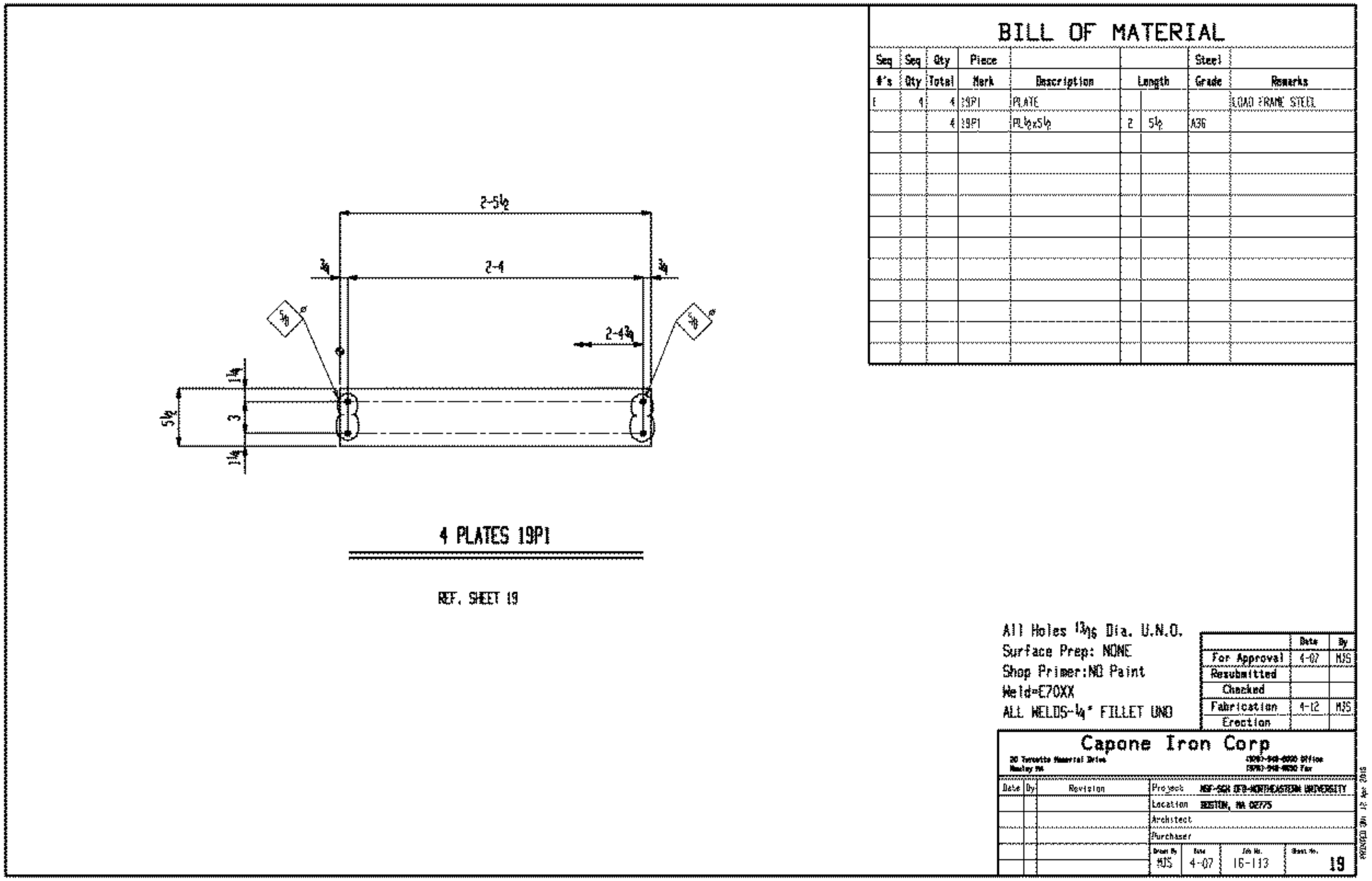
2-5½
2-4
¾
¾
2-4¾
5/8
5/8
5½
1¼
3
1¼
4 PLATES 19P1
REF. SHEET 19
Capone Iron Corp
Project NSF-SGR IFB-NORTHEASTERN UNIVERSITY
Location BOSTON, MA 02775
Architect
Purchaser
Drawn By MJS
Date 4-07
Job No. 16-113
Sheet No. 19
Date
By
Revision

BILL OF MATERIAL

Seq #'s	Seq Qty	Qty Total	Piece Mark	Description	Length		Steel Grade	Remarks
E	4	4	19P1	PLATE				LOAD FRAME STEEL
		4	19P1	PL½x5½	2	5½	A36	

All Holes 13/16 Dia. U.N.O.
Surface Prep: NONE
Shop Primer:NO Paint
Weld=E70XX
ALL WELDS-¼" FILLET UNO

	Date	By
For Approval	4-07	MJS
Resubmitted		
Checked		
Fabrication	4-12	MJS
Erection		

Figure C.33 Column End Shim 1

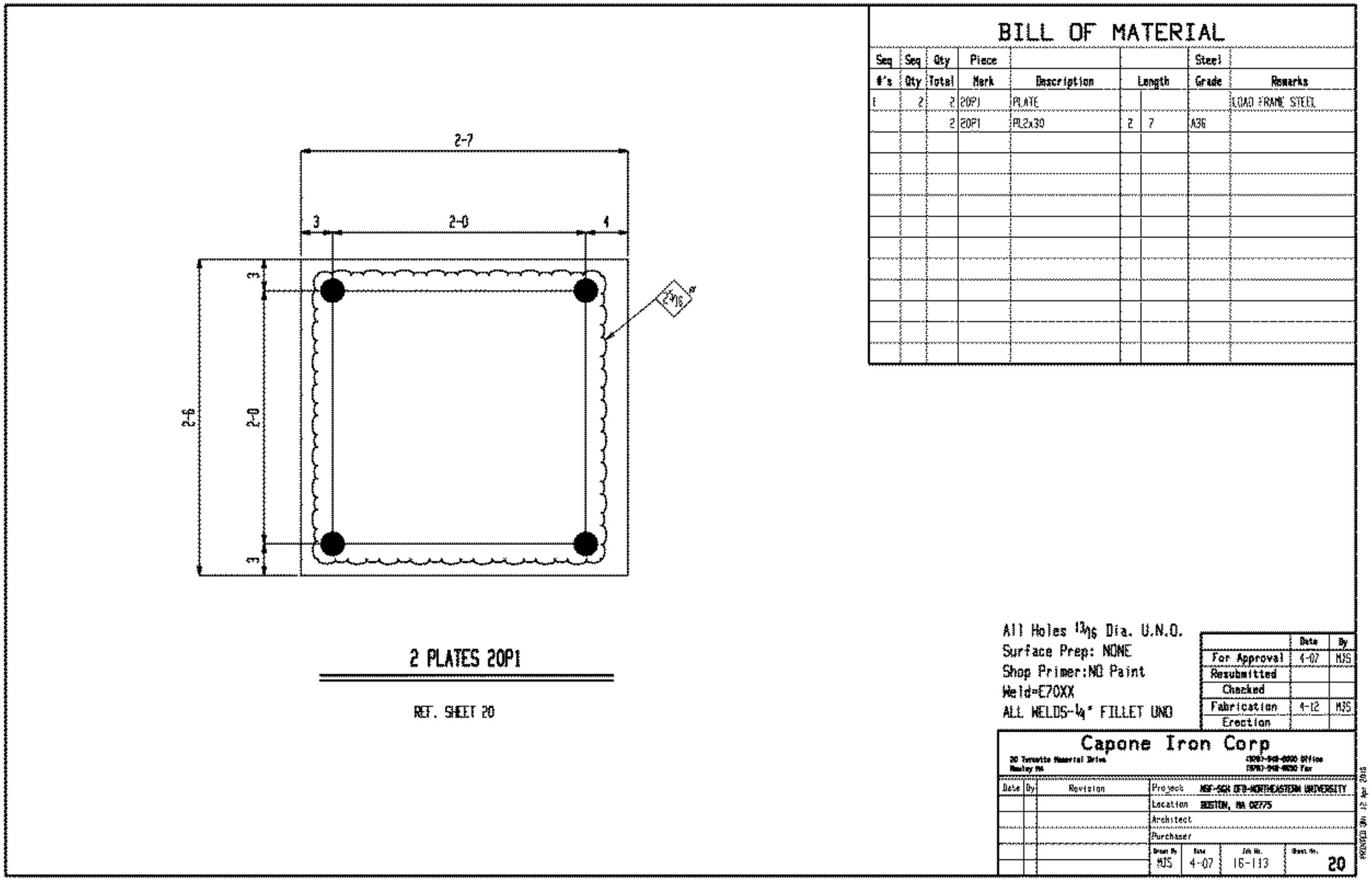
BILL OF MATERIAL
Seq #'s | Seq Qty | Qty Total | Piece Mark | Description | Length | Steel Grade | Remarks
E | 2 | 2 | 20P1 | PLATE | | | LOAD FRAME STEEL
| | 2 | 20P1 | PL2x30 | 2 7 | A36 |
2-7
3
2-0
4
2-6
2-0
3
3
3/16
2 PLATES 20P1
REF. SHEET 20
All Holes 13/16 Dia. U.N.O.
Surface Prep: NONE
Shop Primer:NO Paint
Weld=E70XX
ALL WELDS-1/4" FILLET UNO
Date | By
For Approval | 4-07 | MJS
Resubmitted
Checked
Fabrication | 4-12 | MJS
Erection
Capone Iron Corp
Date | By | Revision
Project NSF-SGR IFB-NORTHEASTERN UNIVERSITY
Location BOSTON, MA 02775
Architect
Purchaser
Drawn By MJS
Date 4-07
Job No. 16-113
Sheet No. 20
PRINTED ON 12 Apr 2016

Figure C.34 Column End Shim 2

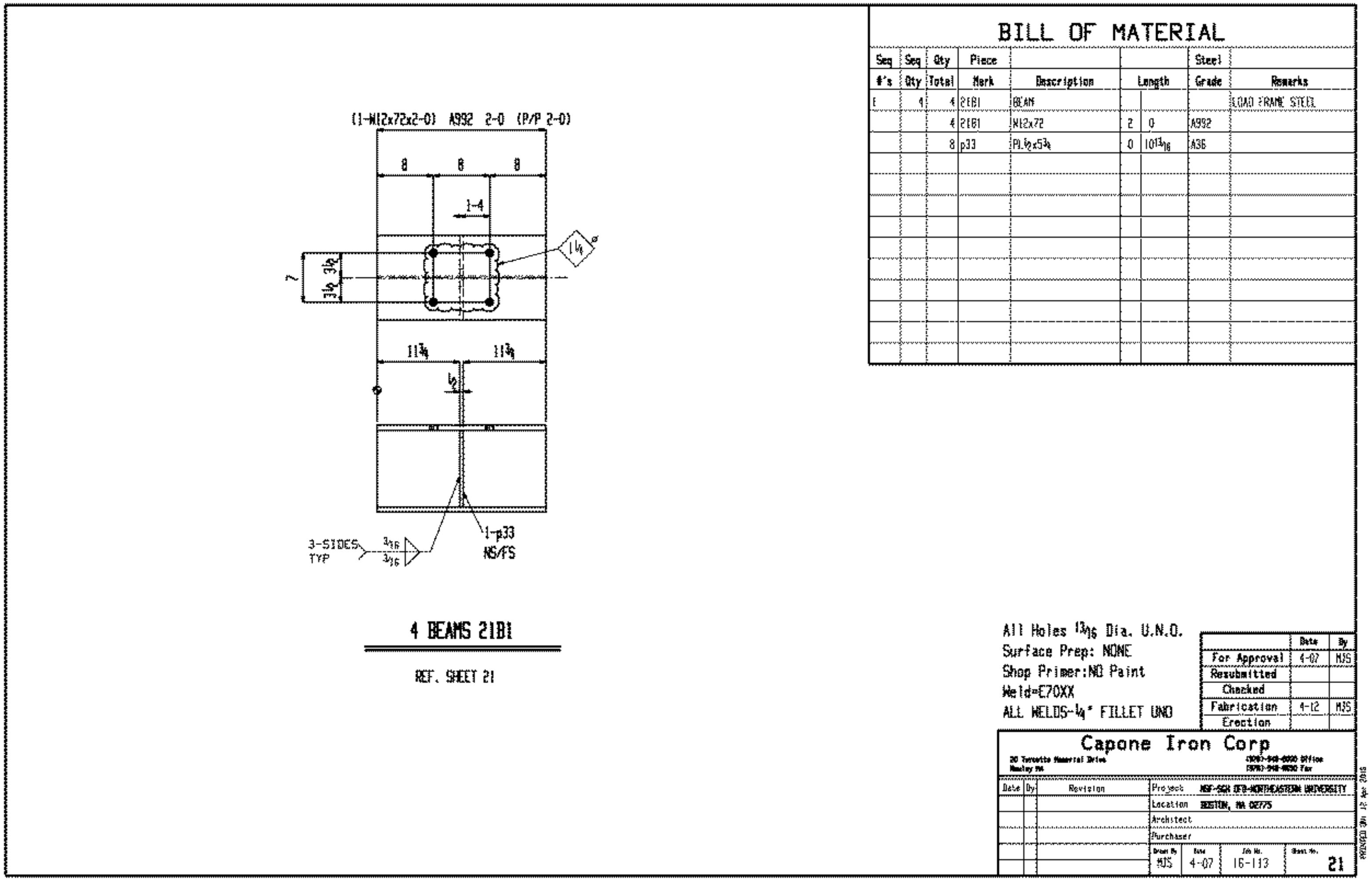
(1-W12x72x2-0) A992 2-0 (P/P 2-0)
8
8
8
1-4
1¼
7
3½
3½
11¾
11¾
½
3-SIDES TYP
3/16
3/16
1-p33 NS/FS
4 BEAMS 21B1
REF. SHEET 21

BILL OF MATERIAL

Seq #'s	Seq Qty	Qty Total	Piece Mark	Description	Length		Steel Grade	Remarks
E	4	4	21B1	BEAM				LOAD FRAME STEEL
		4	21B1	W12x72	2	0	A992	
		8	p33	PL½x5¾	0	10 13/16	A36	

All Holes 13/16 Dia. U.N.O.
Surface Prep: NONE
Shop Primer:NO Paint
Weld=E70XX
ALL WELDS-¼" FILLET UNO

	Date	By
For Approval	4-07	MJS
Resubmitted		
Checked		
Fabrication	4-12	MJS
Erection		

Capone Iron Corp

Date	By	Revision

Project NSF-SGR CFB-NORTHEASTERN UNIVERSITY
Location BOSTON, MA 02775
Architect
Purchaser

Drawn By	Date	Job No.	Sheet No.
MJS	4-07	16-113	21

Figure C.35 Stub Beam W12x72

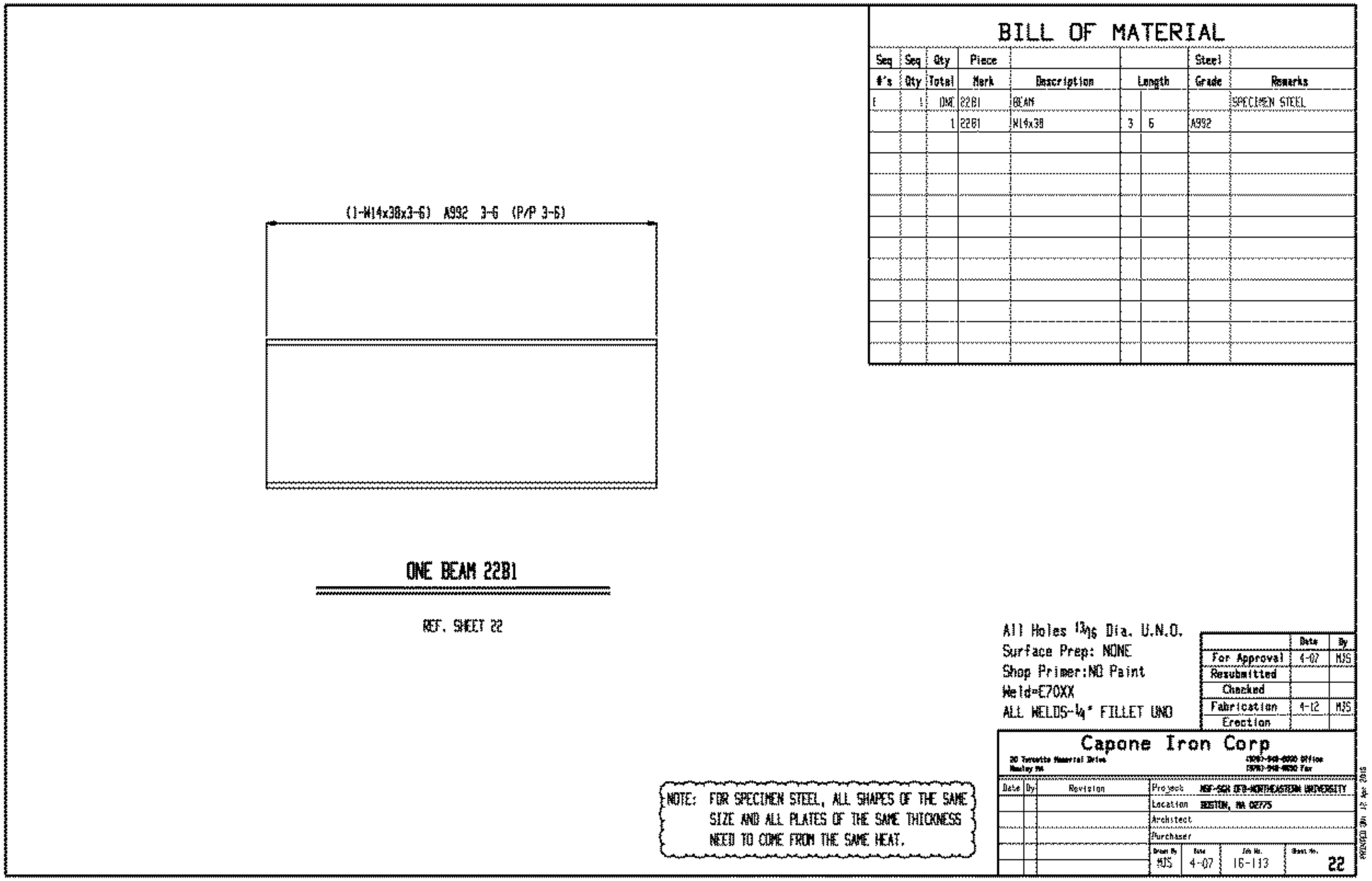
BILL OF MATERIAL
Seq #'s
Seq Qty
Qty Total
Piece Mark
Description
Length
Steel Grade
Remarks
E
1
ONE
22B1
BEAM
SPECIMEN STEEL
1
22B1
W14x38
3
6
A992
(1-W14x38x3-6) A992 3-6 (P/P 3-6)
ONE BEAM 22B1
REF. SHEET 22
All Holes 13/16 Dia. U.N.O.
Surface Prep: NONE
Shop Primer:NO Paint
Weld=E70XX
ALL WELDS-1/4" FILLET UNO
Date
By
For Approval
4-07
MJS
Resubmitted
Checked
Fabrication
4-12
MJS
Erection
Capone Iron Corp
Date
By
Revision
Project
NSF-SGR IFB-NORTHEASTERN UNIVERSITY
Location
BOSTON, MA 02775
Architect
Purchaser
Drawn By
MJS
Date
4-07
Job No.
16-113
Sheet No.
22
NOTE: FOR SPECIMEN STEEL, ALL SHAPES OF THE SAME SIZE AND ALL PLATES OF THE SAME THICKNESS NEED TO COME FROM THE SAME HEAT.

Figure C.36 Coupon Section W14x38

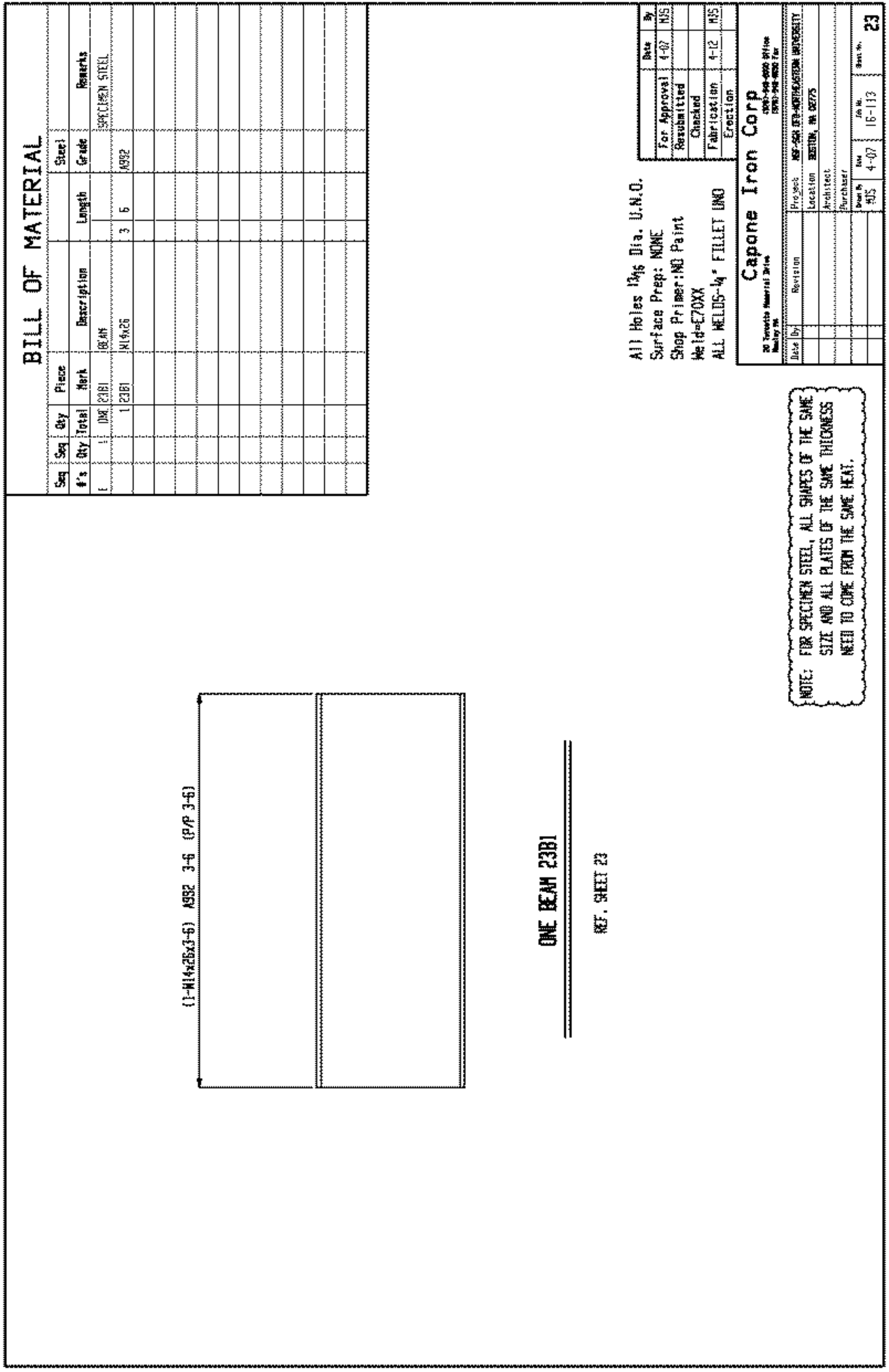
BILL OF MATERIAL
Seq
Seq
Qty
Piece
Steel
#'s
Qty
Total
Mark
Description
Length
Grade
Remarks
1
1
DR
23B1
BEAM
SPECIMEN STEEL
1
23B1
W14x26
3 6
A992
All Holes 13/16 Dia. U.N.O.
Surface Prep: NONE
Shop Primer:NO Paint
Weld=E70XX
ALL WELDS-1/4" FILLET UNO
For Approval
4-07
MJS
Resubmitted
Checked
Fabrication
4-12
MJS
Erection
Date
By
Capone Iron Corp
Date
By
Revision
Project
NSF-SGH DTB-NORTHEASTERN UNIVERSITY
Location
BOSTON, MA 02775
Architect
Purchaser
MJS
4-07
16-113
23
NOTE: FOR SPECIMEN STEEL, ALL SHAPES OF THE SAME SIZE AND ALL PLATES OF THE SAME THICKNESS NEED TO COME FROM THE SAME HEAT.
(1-W14x26x3-6) A992 3-6 (P/P 3-6)
ONE BEAM 23B1
REF. SHEET 23

Figure C.37 Coupon Section W18x46

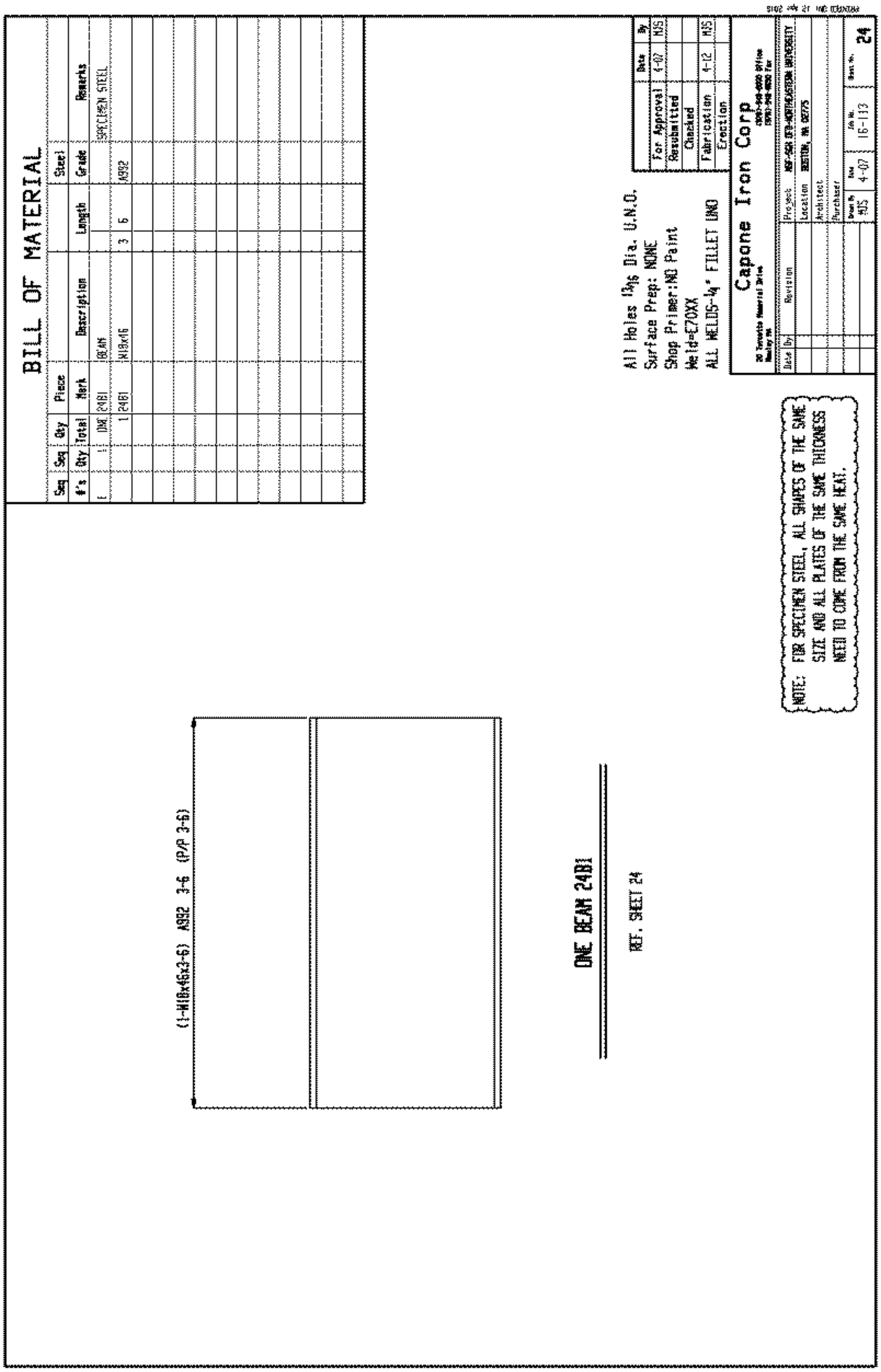
(1-W18x46x3-6) A992 3-6 (P/P 3-6)
ONE BEAM 24B1
REF. SHEET 24
All Holes 13/16 Dia. U.N.O.
Surface Prep: NONE
Shop Primer:NO Paint
Weld=E70XX
ALL WELDS-1/4" FILLET UNO
NOTE: FOR SPECIMEN STEEL, ALL SHAPES OF THE SAME SIZE AND ALL PLATES OF THE SAME THICKNESS NEED TO COME FROM THE SAME HEAT.
Capone Iron Corp
Project NSF-SGR DFB-NORTHEASTERN UNIVERSITY
Location BOSTON, MA 02775
Architect
Purchaser
Date
By
Revision
For Approval 4-07 MJS
Resubmitted
Checked
Fabrication 4-12 MJS
Erection
Drawn By MJS
Date 4-07
Job No. 16-113
Sheet No. 24
PRINTED 12 Apr 2016

BILL OF MATERIAL

Seq #'s	Seq Qty	Qty Total	Piece Mark	Description	Length		Steel Grade	Remarks
E	1	ONE	24B1	BEAM				SPECIMEN STEEL
		1	24B1	W18x46	3	6	A992	

Figure C.38 Coupon Section W14x38

C.2.2 Concrete specimen design drawings

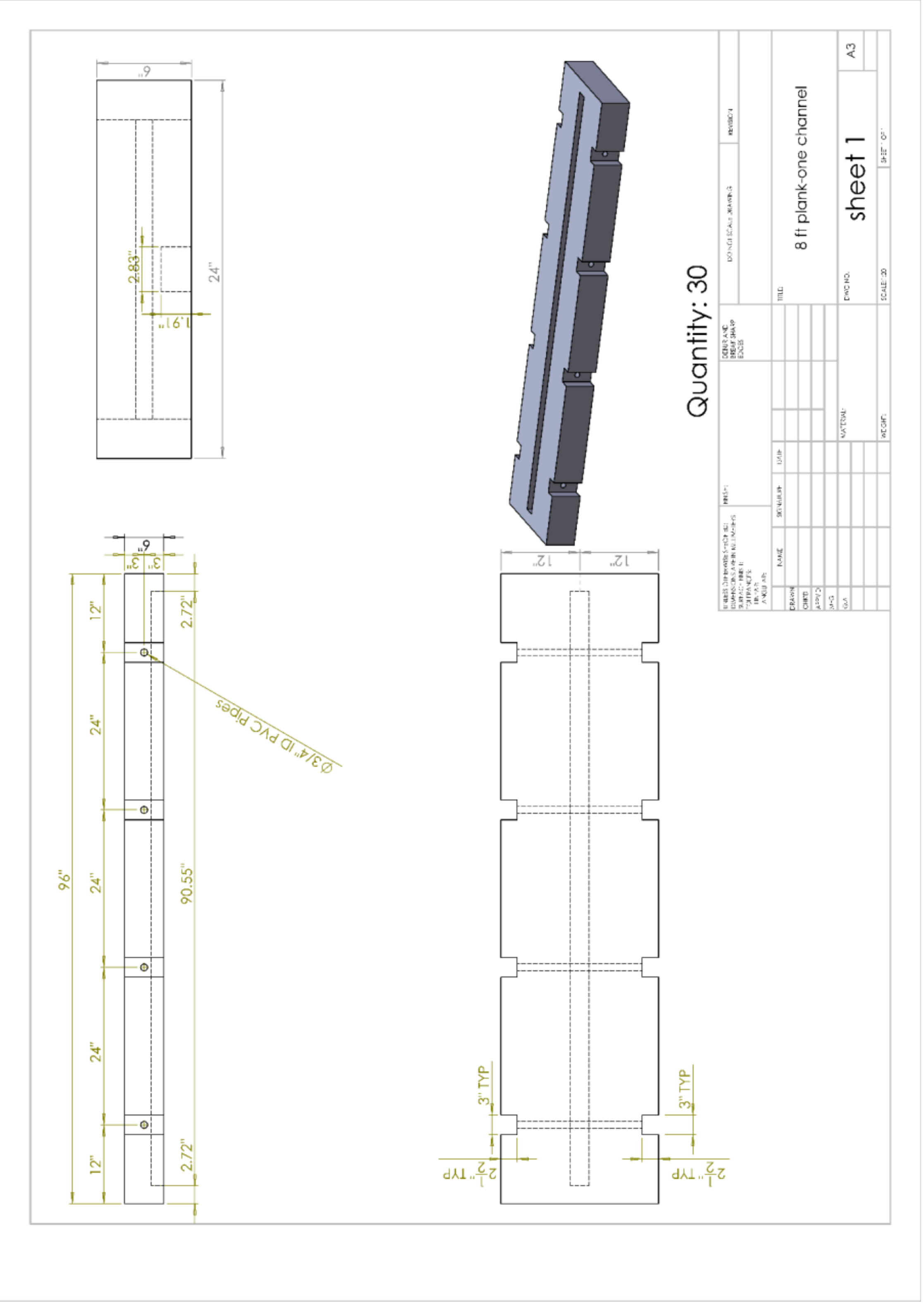
6"
24"
2.83"
1.91"
6"
3"
3"
12"
24"
24"
24"
12"
96"
2.72"
90.55"
2.72"
Ø3/4" ID PVC Pipes
12"
12"
3" TYP
3" TYP
2 1/2" TYP
2 1/2" TYP
Quantity: 30
8 ft plank-one channel
sheet 1
A3
TITLE:
DWG NO.
MATERIAL:
WEIGHT:
SCALE:1:20
SHEET 1 OF 1
REVISION
DO NOT SCALE DRAWING
FINISH:
DEBUR AND BREAK SHARP EDGES
NAME
SIGNATURE
DATE
DRAWN
CHK'D
APPV'D
MFG
Q.A

Figure C.39 One-Channel Specimen

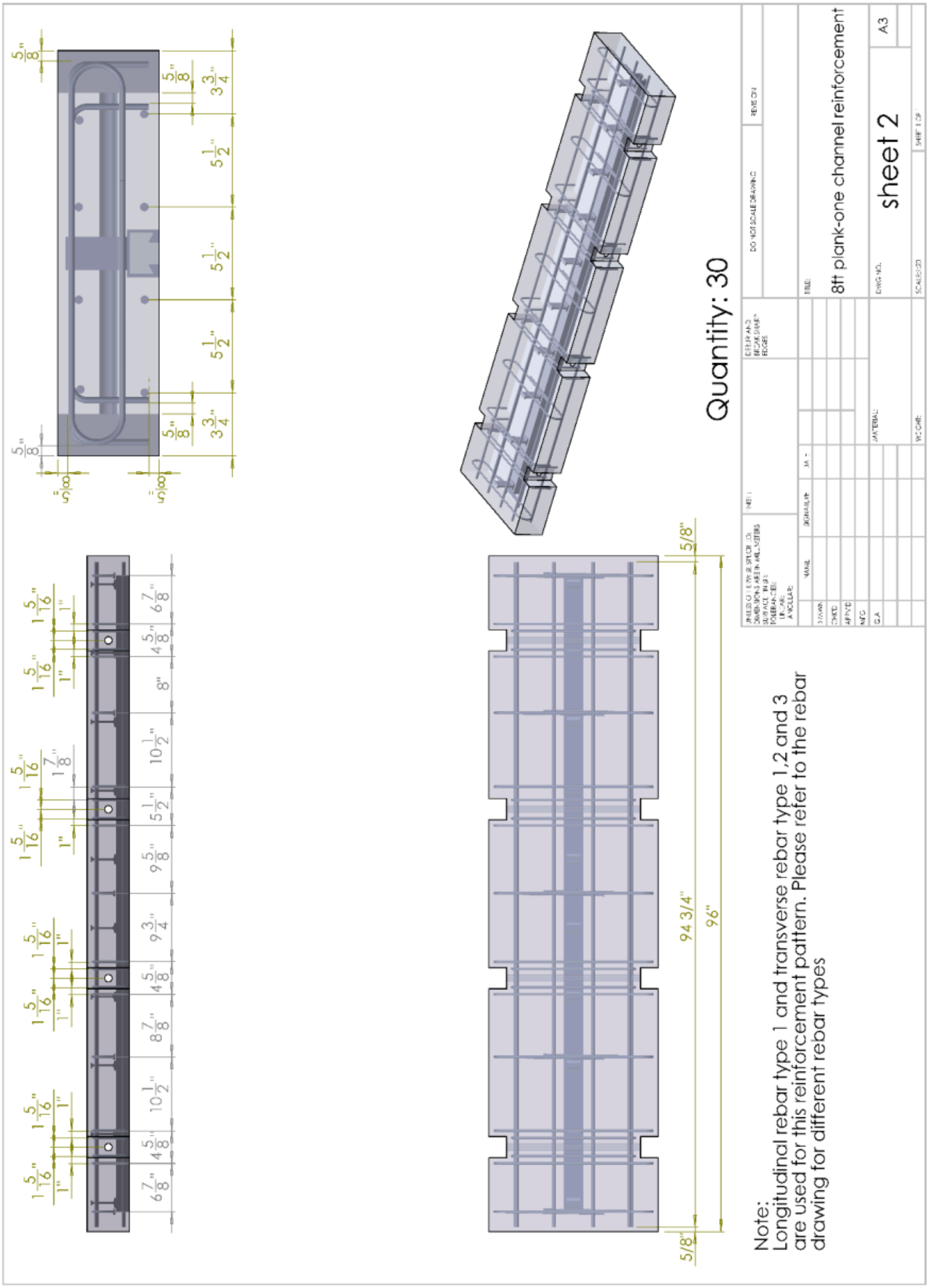
5/8"
5/8"
3 3/4"
5 1/2"
5 1/2"
5 1/2"
5/8"
3 3/4"
5/8"
1 5/16"
1"
7/8"
6 7/8"
4 5/8"
8"
10 1/2"
5 1/2"
9 5/8"
9 3/4"
4 5/8"
8 7/8"
10 1/2"
4 5/8"
6 7/8"
5/8"
94 3/4"
96"
5/8"
Quantity: 30
Note:
Longitudinal rebar type 1 and transverse rebar type 1,2 and 3 are used for this reinforcement pattern. Please refer to the rebar drawing for different rebar types
DO NOT SCALE DRAWING
REVISION
TITLE:
8ft plank-one channel reinforcement
DWG. NO.
sheet 2
A3
MATERIAL:
WEIGHT:
SCALE:1:23
SHEET 1 OF 1

Figure C.40 One-Channel Specimen Reinforcement

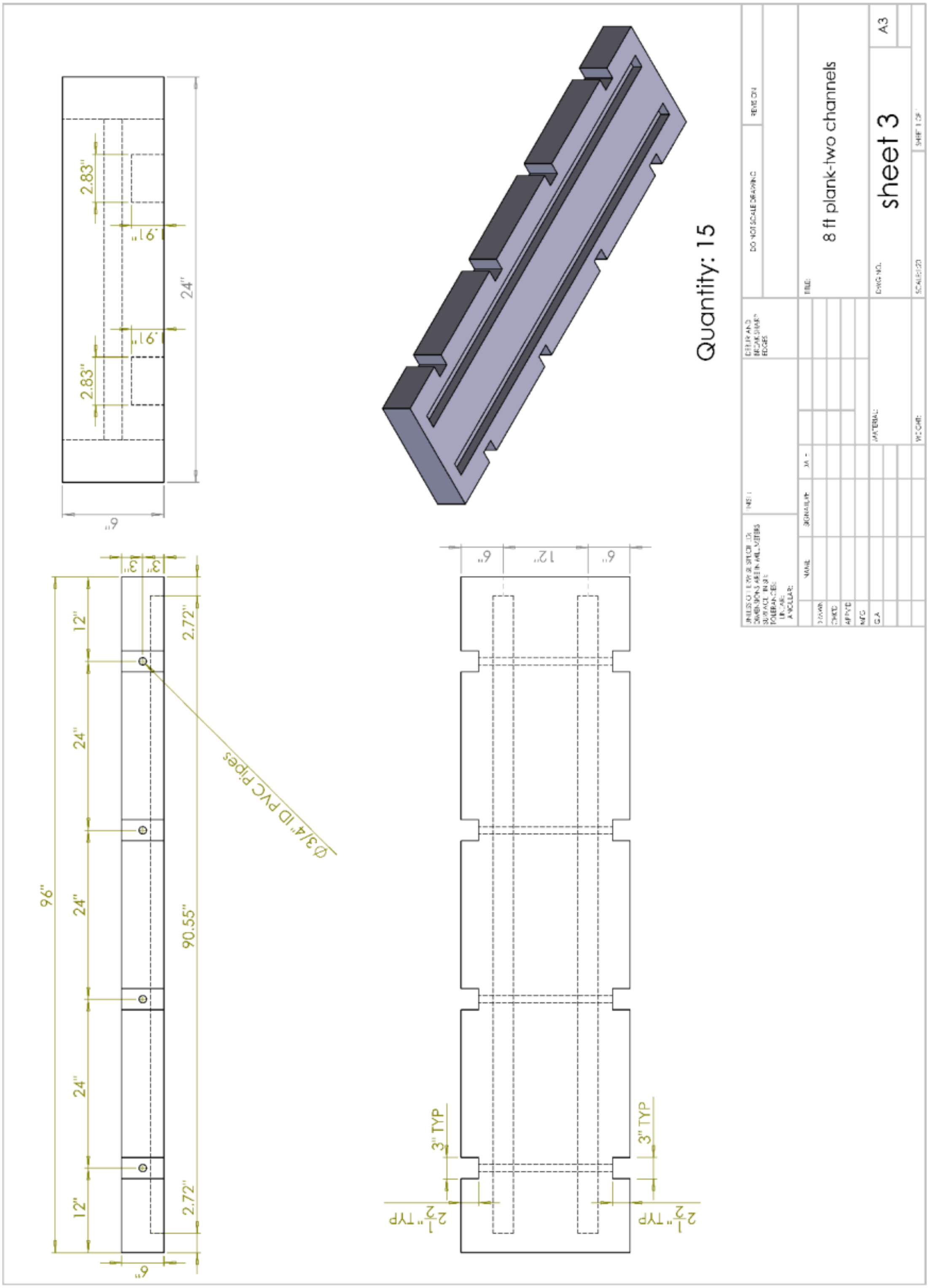
2.83"
.91"
2.83"
.91"
24"
6"
3"
3"
12"
24"
24"
24"
12"
96"
2.72"
90.55"
2.72"
6"
Ø3/4" ID PVC Pipes
6"
12"
6"
3" TYP
3" TYP
2 1/2" TYP
2 1/2" TYP
Quantity: 15
DO NOT SCALE DRAWING
REVISION
TITLE:
8 ft plank-two channels
DWG. NO.
sheet 3
A3
SCALE:1:20
SHEET 1 OF 1
WEIGHT:
MATERIAL:
DRAWN
CHK'D
APPV'D
MFG
Q.A
NAME
SIGNATURE
DATE
FINISH:
DEBUR AND BREAK SHARP EDGES

Figure C.41 Two-Channel Specimen

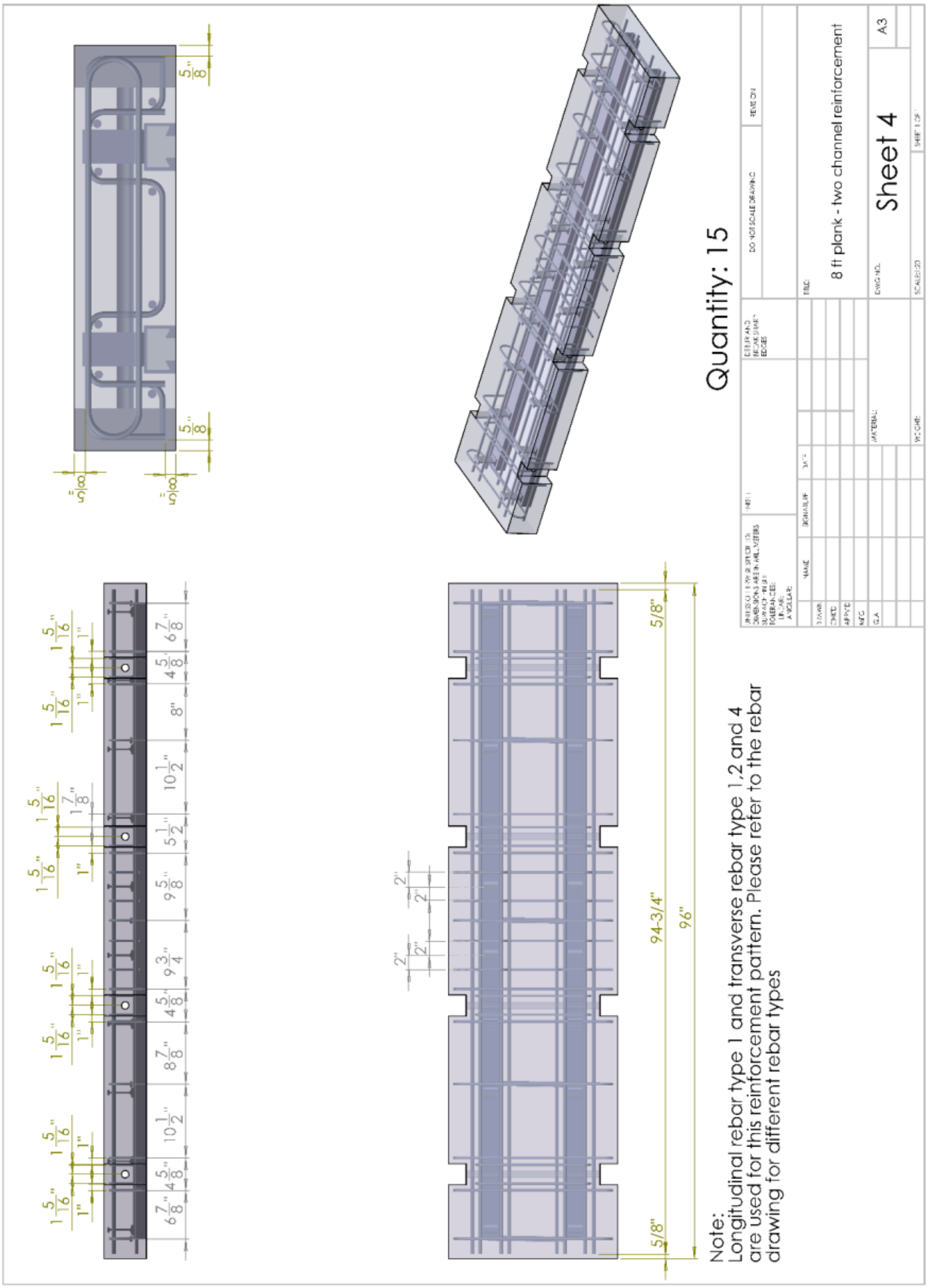
Quantity: 15
8 ft plank - two channel reinforcement
Sheet 4
A3
DO NOT SCALE DRAWING
5/8"
5/8"
94-3/4"
96"
2"
2"
2"
2"
1 5/16"
1"
6 7/8"
4 5/8"
8"
10 1/2"
5 1/2"
1 7/8"
9 5/8"
9 3/4"
8 7/8"

Note:
Longitudinal rebar type 1 and transverse rebar type 1,2 and 4 are used for this reinforcement pattern. Please refer to the rebar drawing for different rebar types

Figure C.42 Two-Channel Specimen Reinforcement

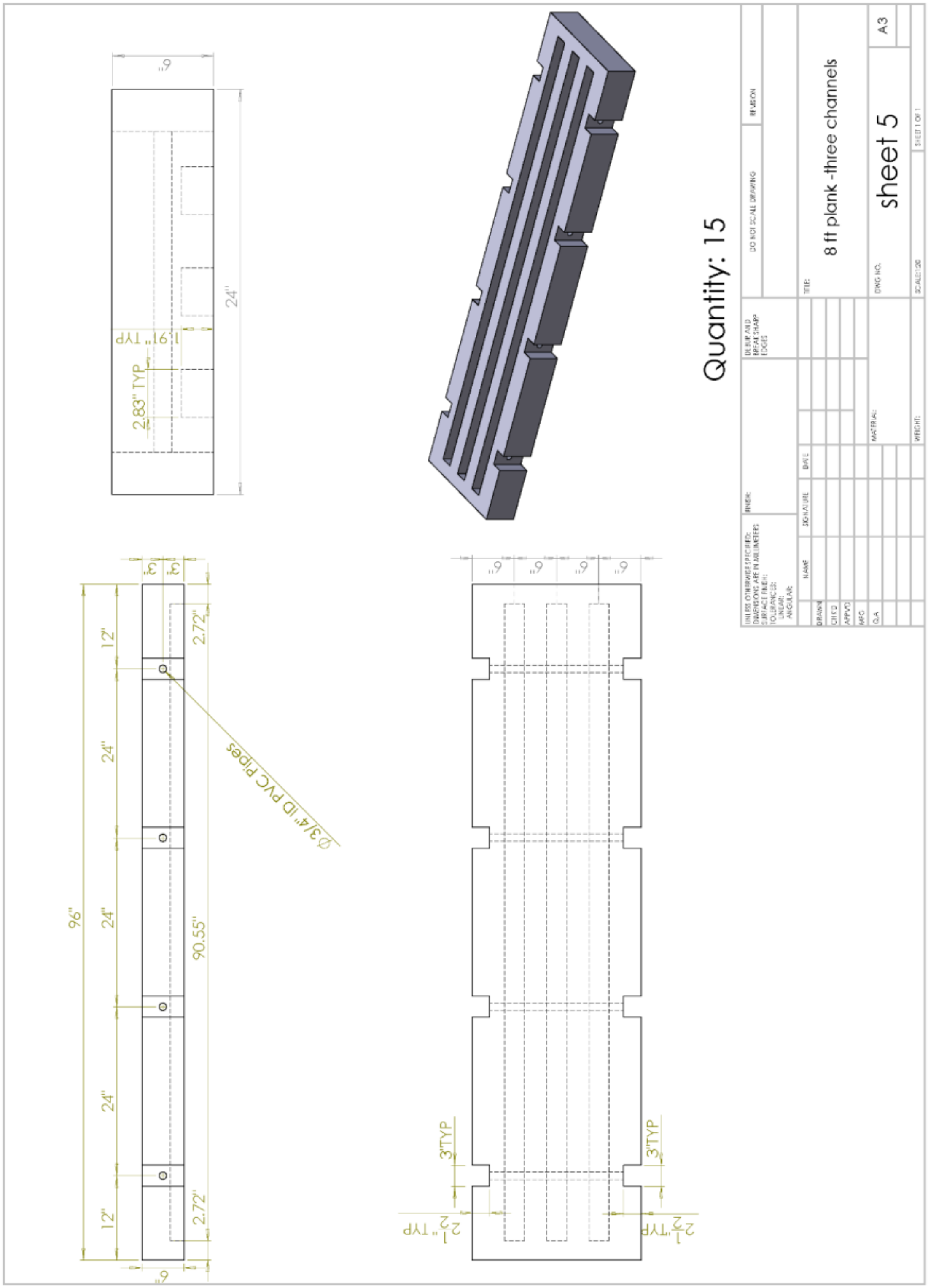
Quantity: 15
8 ft plank -three channels
sheet 5
A3
DO NOT SCALE DRAWING
REVISION
TITLE:
DWG NO.
SCALE:1:20
SHEET 1 OF 1
WEIGHT:
MATERIAL:
DEBUR AND BREAK SHARP EDGES
FINISH:
UNLESS OTHERWISE SPECIFIED: DIMENSIONS ARE IN MILLIMETERS SURFACE FINISH: TOLERANCES: LINEAR: ANGULAR:
NAME
SIGNATURE
DATE
DRAWN
CHK'D
APPV'D
MFG
Q.A
6"
24"
1.91" TYP
2.83" TYP
3"
12"
96"
90.55"
2.72"
Ø3/4" ID PVC Pipes
3"TYP
2 1/2" TYP

Figure C.43 Three-Channel Specimen

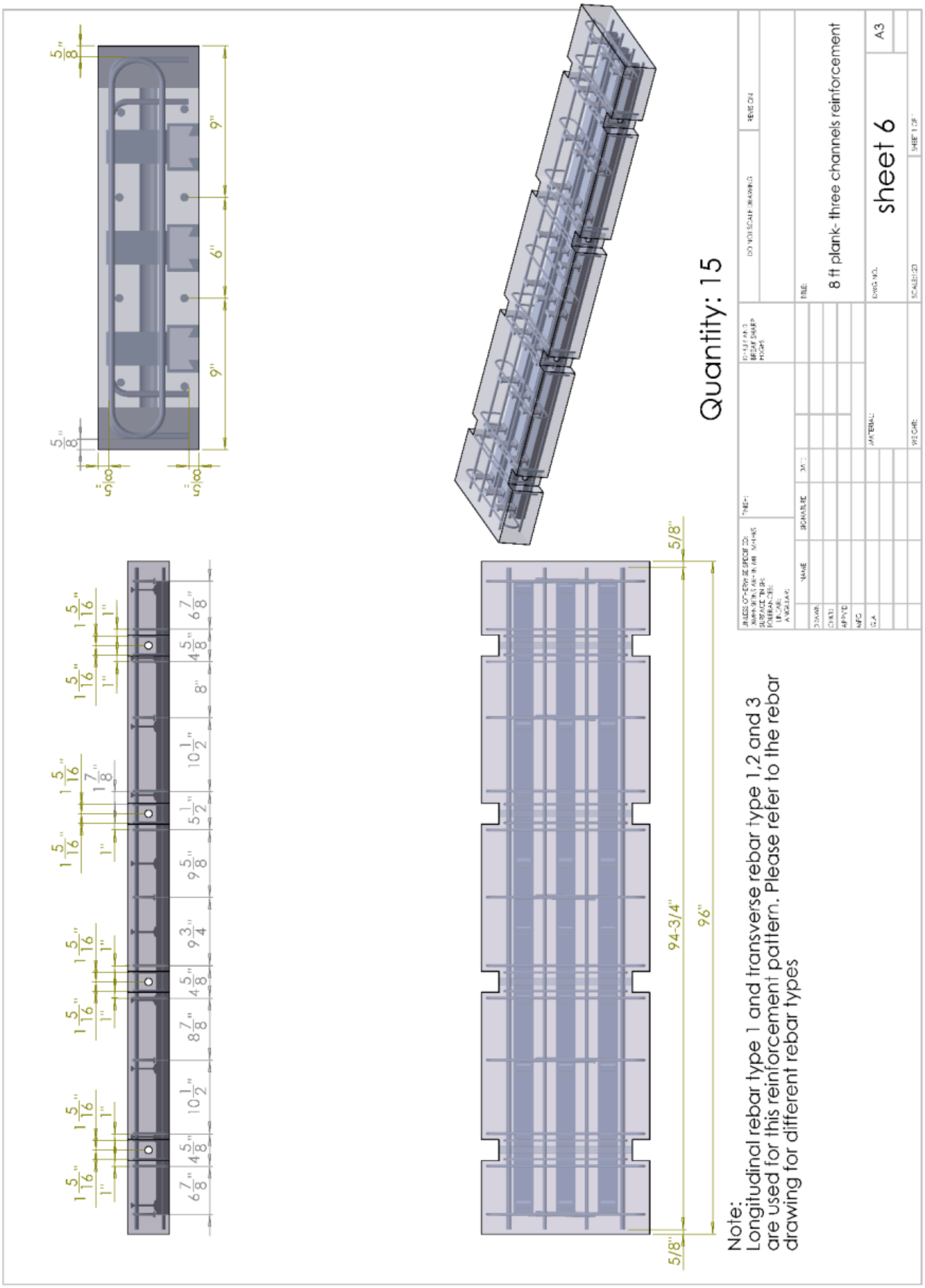
5/8"
9"
6"
9"
5/8"
5/8"
5/8"
1 5/16"
1"
7/8"
6 7/8"
4 5/8"
8"
10 1/2"
1 7/8"
5 1/2"
9 5/8"
9 3/4"
8 7/8"
94-3/4"
96"
Quantity: 15
Note:
Longitudinal rebar type 1 and transverse rebar type 1,2 and 3 are used for this reinforcement pattern. Please refer to the rebar drawing for different rebar types
8 ft plank- three channels reinforcement
sheet 6
A3
DO NOT SCALE DRAWING
REVISION
TITLE:
DWG NO.
SCALE:1:20
WEIGHT:
MATERIAL:
NAME
SIGNATURE
DATE
DRAWN
CHK'D
APPV'D
MFG
Q.A
FINISH:
SHEET 1 OF 1

Figure C.44 Three-Channel Specimen Reinforcement

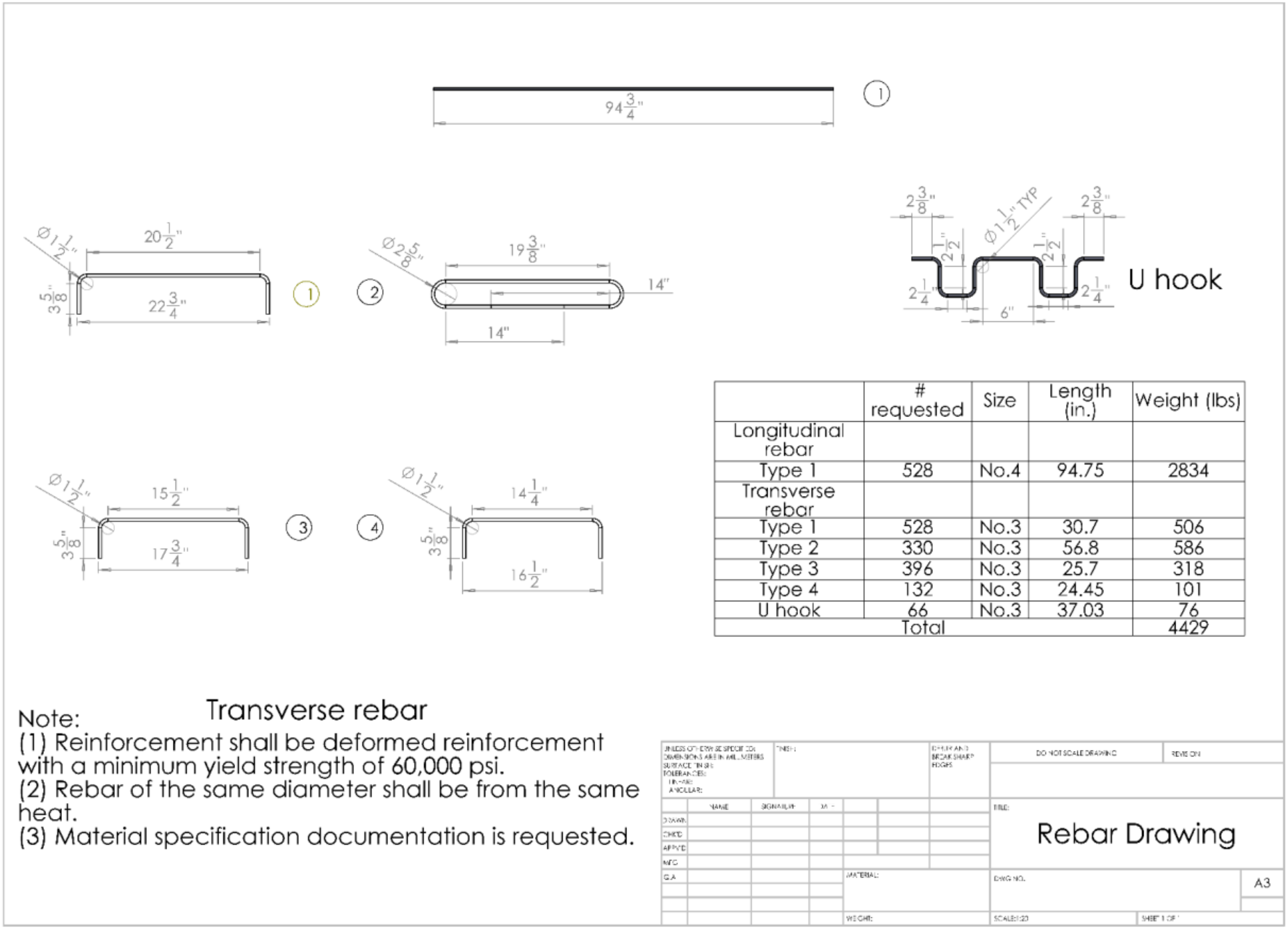
$94\frac{3}{4}$"
①
$\varnothing 1\frac{1}{2}$"
$20\frac{1}{2}$"
$3\frac{5}{8}$"
$22\frac{3}{4}$"
①
②
$\varnothing 2\frac{5}{8}$"
$19\frac{3}{8}$"
14"
14"
$2\frac{3}{8}$"
$\varnothing 1\frac{1}{2}$" TYP
$2\frac{3}{8}$"
$1\frac{1}{2}$"
$1\frac{1}{2}$"
$2\frac{1}{4}$"
6"
$2\frac{1}{4}$"
U hook
$\varnothing 1\frac{1}{2}$"
$15\frac{1}{2}$"
$3\frac{5}{8}$"
$17\frac{3}{4}$"
③
④
$\varnothing 1\frac{1}{2}$"
$14\frac{1}{4}$"
$3\frac{5}{8}$"
$16\frac{1}{2}$"
Transverse rebar
DO NOT SCALE DRAWING
REVISION
TITLE:
Rebar Drawing
DWG NO.
A3
MATERIAL:
WEIGHT:
SCALE:1:20
SHEET 1 OF 1
NAME
SIGNATURE
DRAWN
CHK'D
APPV'D
MFG
Q.A
FINISH:
DEBUR AND BREAK SHARP EDGES

	# requested	Size	Length (in.)	Weight (lbs)
Longitudinal rebar				
Type 1	528	No.4	94.75	2834
Transverse rebar				
Type 1	528	No.3	30.7	506
Type 2	330	No.3	56.8	586
Type 3	396	No.3	25.7	318
Type 4	132	No.3	24.45	101
U hook	66	No.3	37.03	76
Total				4429

Note:
(1) Reinforcement shall be deformed reinforcement with a minimum yield strength of 60,000 psi.
(2) Rebar of the same diameter shall be from the same heat.
(3) Material specification documentation is requested.

Figure C.45 Reinforcement Details

C.2.3 Cast-in channel drawing

HALFEN CUSTOM ANCHOR CHANNEL ~ PART No. X17056-2

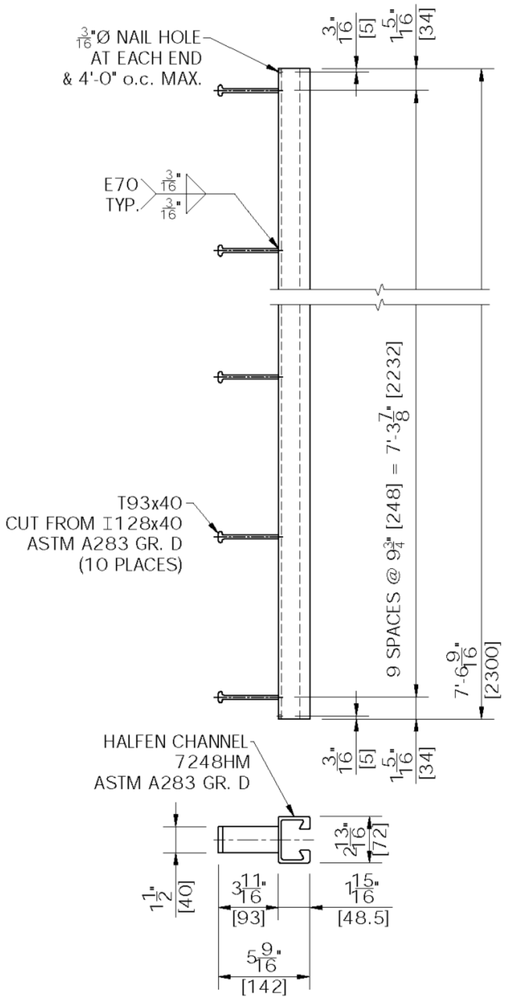
3/16"Ø NAIL HOLE
AT EACH END
& 4'-0" o.c. MAX.
3/16" [5]
1 5/16" [34]
E70 TYP. 3/16" 3/16"
9 SPACES @ 9 3/4" [248] = 7'-3 7/8" [2232]
7'-6 9/16" [2300]
T93x40
CUT FROM I128x40
ASTM A283 GR. D
(10 PLACES)
3/16" [5]
1 5/16" [34]
HALFEN CHANNEL
7248HM
ASTM A283 GR. D
2 13/16" [72]
1 1/2" [40]
3 11/16" [93]
1 15/16" [48.5]
5 9/16" [142]

MILL FINISH - FOAM FILL AFTER FABRICATION

NOTE:
1. THESE PHASE MUST BE FROM THE SAME HEAT NUMBER
2. 3.1 CERTIFICATE REQUIRED

Work Order:	Mark:	Qty:	Project No:	17056
Project: -			Drawn by:	MRM
Notice of Copyright © 2016 Halfen USA, Inc. All rights to this document and information contained herein are the exclusive property of Halfen USA, Inc. This drawings may not be copied or disclosed to others without the prior written consent of Halfen USA, Inc.	Halfen USA, Inc. PO Box 547 - 8521 FM 1976 Converse, TX 78109 PH: 800-423-9140 FAX: 888-277-1695		Drawing No:	2
			Date:	2.16.16
			Revision: △	-
Tolerances, bending radiuses, edge and surface finishes in accordance with Halfen-factory standards, unless otherwise noted.			Page 1	of 1

Figure C.46 Cast-in channel details

Appendix D MILL CERTIFICATIONS

This appendix contains the mill certifications for the specimen materials used in both the pushout tests and the beam tests.

D.1 **Pushout tests**

D.1.1 Steel frame

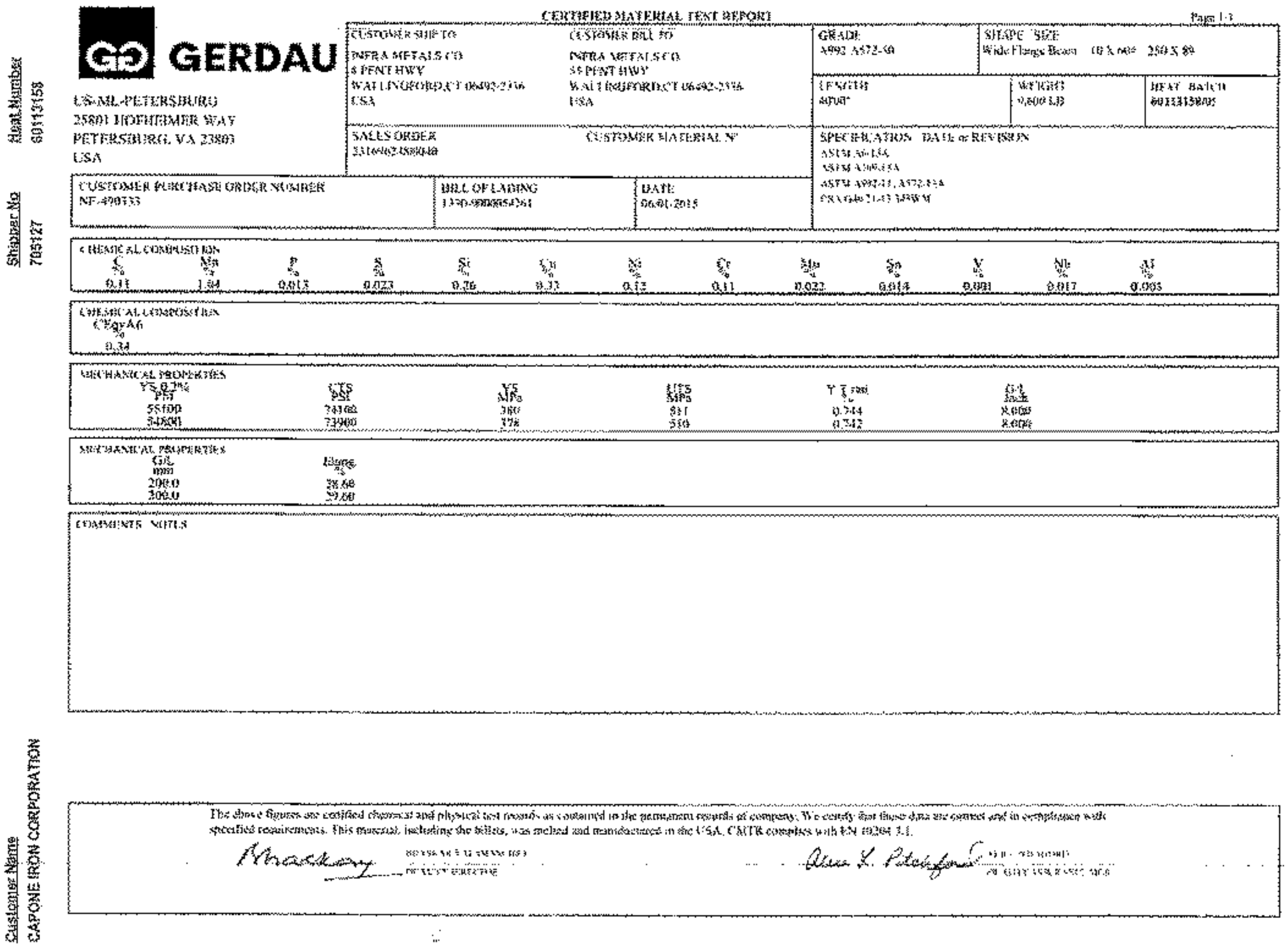

Heat Number
60113158

Shipper No
705127

Customer Name
CAPONE IRON CORPORATION

GERDAU

US-ML-PETERSBURG
25801 HOFHEIMER WAY
PETERSBURG, VA 23803
USA

CERTIFIED MATERIAL TEST REPORT

Page 1/3

CUSTOMER SHIP TO INFRA METALS CO 8 PENT HWY WALLINGFORD,CT 06492-2336 USA	CUSTOMER BILL TO INFRA METALS CO 58 PENT HWY WALLINGFORD,CT 06492-2336 USA	GRADE A992 A572-50	SHAPE / SIZE Wide Flange Beam / 10 X 60# / 250 X 89	
		LENGTH 40'00"	WEIGHT 9,600 LB	HEAT / BATCH 60113158/05
SALES ORDER 3316462/058040	CUSTOMER MATERIAL Nº	SPECIFICATION / DATE or REVISION ASTM A6-14A ASTM A709-13A ASTM A992-11, A572-13A CSA G40.21-13 345WM		
CUSTOMER PURCHASE ORDER NUMBER NF-490733	BILL OF LADING 1330-0000654051	DATE 06/01/2015		

CHEMICAL COMPOSITION

C %	Mn %	P %	S %	Si %	Cu %	Ni %	Cr %	Mo %	Sn %	V %	Nb %	Al %
0.11	1.04	0.013	0.023	0.26	0.33	0.13	0.11	0.022	0.014	0.001	0.017	0.003

CHEMICAL COMPOSITION

CEqyA6 %
0.34

MECHANICAL PROPERTIES

YS 0.2% PSI	UTS PSI	YS MPa	UTS MPa	Y/T ratio	G/L Inch
55100	74100	380	511	0.744	8.000
54800	73900	378	510	0.742	8.000

MECHANICAL PROPERTIES

G/L mm	Elong. %
200.0	28.60
200.0	29.60

COMMENTS / NOTES

The above figures are certified chemical and physical test records as contained in the permanent records of company. We certify that these data are correct and in compliance with specified requirements. This material, including the billets, was melted and manufactured in the USA. CMTR complies with EN 10204 3.1.

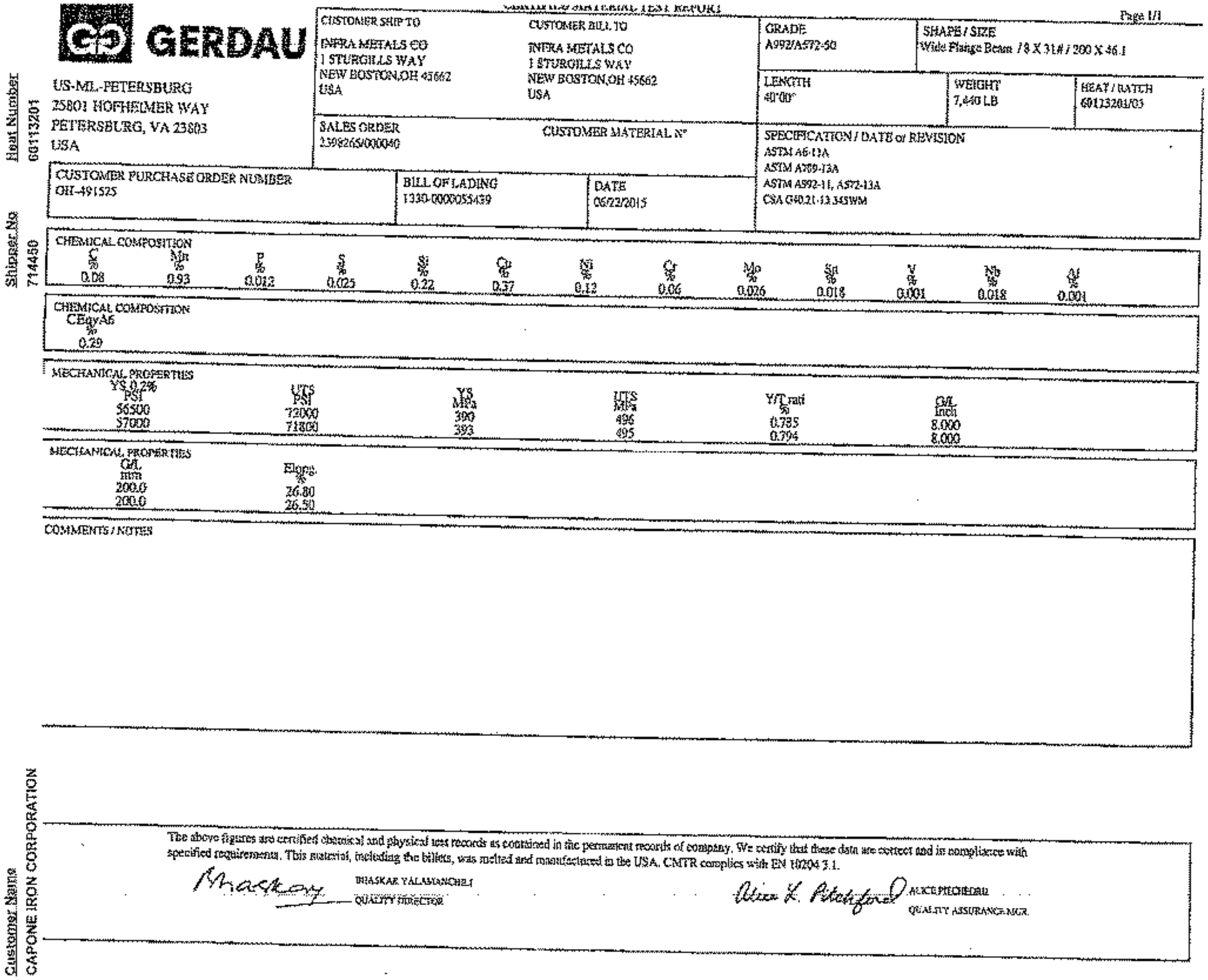

GERDAU

[illegible] MATERIAL TEST REPORT

Page 1/1

US-ML-PETERSBURG
25801 HOFHEIMER WAY
PETERSBURG, VA 23803
USA

Heat Number
60113201

Shipper No
714450

CUSTOMER SHIP TO INFRA METALS CO 1 STURGILLS WAY NEW BOSTON,OH 45662 USA	CUSTOMER BILL TO INFRA METALS CO 1 STURGILLS WAY NEW BOSTON,OH 45662 USA	GRADE A992/A572-50	SHAPE / SIZE Wide Flange Beam / 8 X 31# / 200 X 46.1	
		LENGTH 40'00"	WEIGHT 7,440 LB	HEAT / BATCH 60113201/03
SALES ORDER 2398265/000040	CUSTOMER MATERIAL N°	SPECIFICATION / DATE or REVISION ASTM A6-13A ASTM A709-13A ASTM A992-11, A572-13A CSA G40.21-13 345WM		

CUSTOMER PURCHASE ORDER NUMBER	BILL OF LADING	DATE
OH-491525	1330-0000055439	06/22/2015

CHEMICAL COMPOSITION

C %	Mn %	P %	S %	Si %	Cu %	Ni %	Cr %	Mo %	Sn %	V %	Nb %	Al %
0.08	0.93	0.012	0.025	0.22	0.37	0.12	0.06	0.026	0.018	0.001	0.018	0.001

CHEMICAL COMPOSITION

CEqyA6 %
0.29

MECHANICAL PROPERTIES

YS 0.2% PSI	UTS PSI	YS MPa	UTS MPa	Y/T rati %	G/L Inch
56500	72000	390	496	0.785	8.000
57000	71800	393	495	0.794	8.000

MECHANICAL PROPERTIES

G/L mm	Elong. %
200.0	26.80
200.0	26.50

COMMENTS / NOTES

Customer Name
CAPONE IRON CORPORATION

The above figures are certified chemical and physical test records as contained in the permanent records of company. We certify that these data are correct and in compliance with specified requirements. This material, including the billets, was melted and manufactured in the USA. CMTR complies with EN 10204 3.1.

BHASKAR YALAMANCHILI
QUALITY DIRECTOR

Alice K. Pitchford
ALICE PITCHFORD
QUALITY ASSURANCE MGR.

D.1.2 Halfen channels and bolts

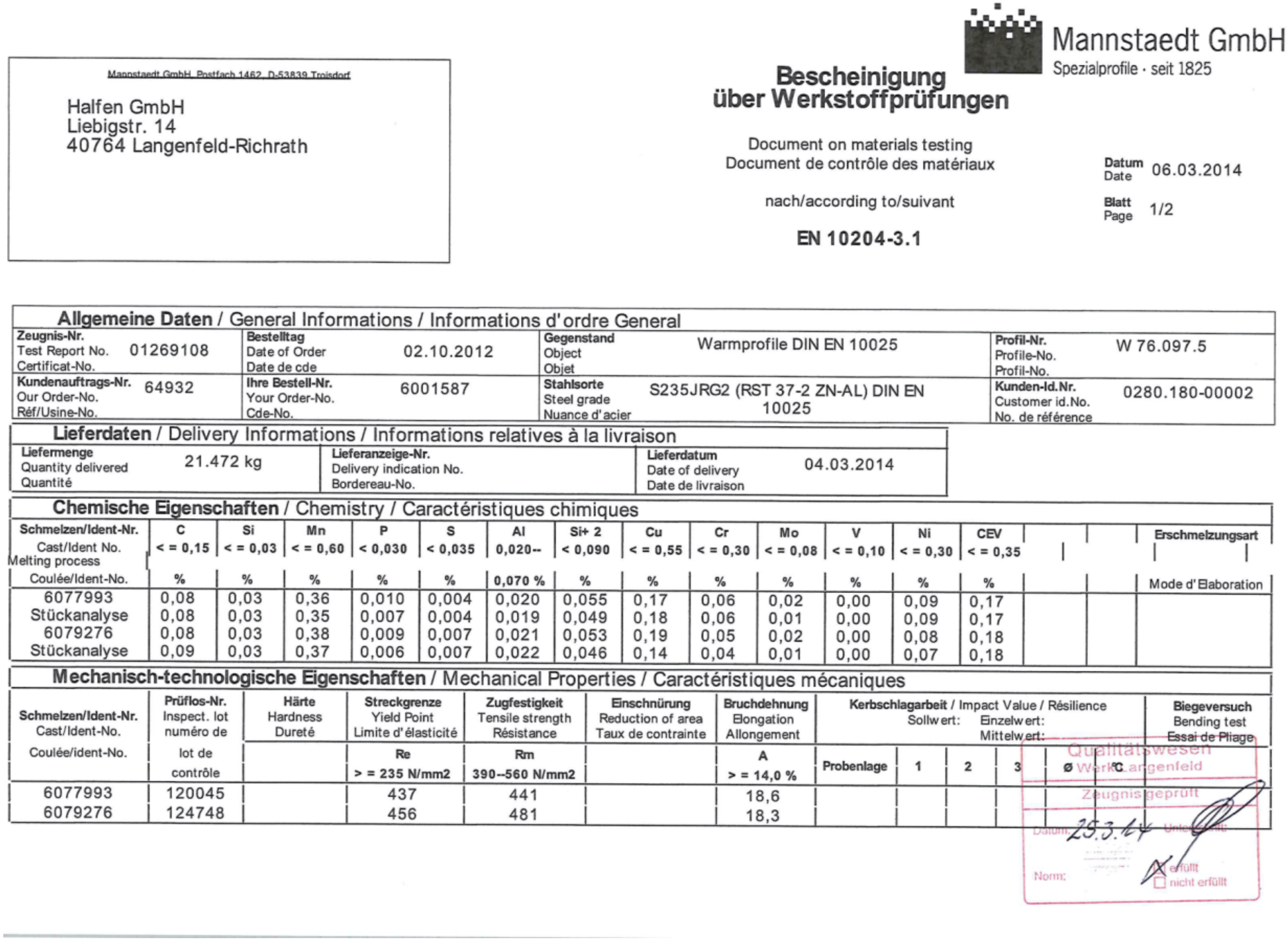

Mannstaedt GmbH
Spezialprofile · seit 1825

Bescheinigung über Werkstoffprüfungen

Document on materials testing
Document de contrôle des matériaux

nach/according to/suivant

EN 10204-3.1

Datum Date 06.03.2014
Blatt Page 1/2

Mannstaedt GmbH, Postfach 1462, D-53839 Troisdorf

Halfen GmbH
Liebigstr. 14
40764 Langenfeld-Richrath

Allgemeine Daten / General Informations / Informations d'ordre General

Zeugnis-Nr. Test Report No. Certificat-No.	01269108	**Bestelltag** Date of Order Date de cde	02.10.2012	**Gegenstand** Object Objet	Warmprofile DIN EN 10025	**Profil-Nr.** Profile-No. Profil-No.	W 76.097.5
Kundenauftrags-Nr. Our Order-No. Réf/Usine-No.	64932	**Ihre Bestell-Nr.** Your Order-No. Cde-No.	6001587	**Stahlsorte** Steel grade Nuance d'acier	S235JRG2 (RST 37-2 ZN-AL) DIN EN 10025	**Kunden-Id.Nr.** Customer id.No. No. de référence	0280.180-00002

Lieferdaten / Delivery Informations / Informations relatives à la livraison

Liefermenge Quantity delivered Quantité	21.472 kg	**Lieferanzeige-Nr.** Delivery indication No. Bordereau-No.		**Lieferdatum** Date of delivery Date de livraison	04.03.2014

Chemische Eigenschaften / Chemistry / Caractéristiques chimiques

Schmelzen/Ident-Nr. Cast/Ident No. Melting process	C	Si	Mn	P	S	Al	Si+ 2	Cu	Cr	Mo	V	Ni	CEV			**Erschmelzungsart**
	< = 0,15	< = 0,03	< = 0,60	< 0,030	< 0,035	0,020--	< 0,090	< = 0,55	< = 0,30	< = 0,08	< = 0,10	< = 0,30	< = 0,35			
Coulée/Ident-No.	%	%	%	%	%	0,070 %	%	%	%	%	%	%	%			Mode d'Elaboration
6077993	0,08	0,03	0,36	0,010	0,004	0,020	0,055	0,17	0,06	0,02	0,00	0,09	0,17			
Stückanalyse	0,08	0,03	0,35	0,007	0,004	0,019	0,049	0,18	0,06	0,01	0,00	0,09	0,17			
6079276	0,08	0,03	0,38	0,009	0,007	0,021	0,053	0,19	0,05	0,02	0,00	0,08	0,18			
Stückanalyse	0,09	0,03	0,37	0,006	0,007	0,022	0,046	0,14	0,04	0,01	0,00	0,07	0,18			

Mechanisch-technologische Eigenschaften / Mechanical Properties / Caractéristiques mécaniques

Schmelzen/Ident-Nr. Cast/Ident-No.	**Prüflos-Nr.** Inspect. lot numéro de	**Härte** Hardness Dureté	**Streckgrenze** Yield Point Limite d'élasticité	**Zugfestigkeit** Tensile strength Résistance	**Einschnürung** Reduction of area Taux de contrainte	**Bruchdehnung** Elongation Allongement	**Kerbschlagarbeit** / Impact Value / Résilience Sollwert: Einzelwert: Mittelwert:						**Biegeversuch** Bending test Essai de Pliage
Coulée/ident-No.	lot de contrôle		Re > = 235 N/mm2	Rm 390--560 N/mm2		A > = 14,0 %	Probenlage	1	2	3	ø	°C	
6077993	120045		437	441		18,6							
6079276	124748		456	481		18,3							

Qualitätswesen
Werk Langenfeld
Zeugnis geprüft
Datum: 25.3.14 Unterschrift:
Norm:
☒ erfüllt
☐ nicht erfüllt

Mannstaedt GmbH
Spezialprofile · seit 1825

Mannstaedt GmbH, Postfach 1462, D-53839 Troisdorf

Halfen GmbH
Liebigstr. 14
40764 Langenfeld-Richrath

Bescheinigung über Werkstoffprüfungen

Document on materials testing
Document de contrôle des matériaux

nach/according to/suivant

EN 10204-3.1

Datum Date 06.03.2014

Blatt Page 2/2

Allgemeine Daten / General Informations / Informations d'ordre General

Zeugnis-Nr. Test Report No. Certificat-No.	01269108	**Bestelltag** Date of Order Date de cde	02.10.2012	**Gegenstand** Object Objet	Warmprofile DIN EN 10025	**Profil-Nr.** Profile-No. Profil-No.	W 76.097.5
Kundenauftrags-Nr. Our Order-No. Réf/Usine-No.	64932	**Ihre Bestell-Nr.** Your Order-No. Cde-No.	6001587	**Stahlsorte** Steel grade Nuance d'acier	S235JRG2 (RST 37-2 ZN-AL) DIN EN 10025	**Kunden-Id.Nr.** Customer id.No. No. de référence	0280.180-00002

Zusatzinformationen / Additional Information / Informations complémentaires

120045	Kaltgerichtet
124748	Kaltgerichtet

Die gelieferten Produkte sind frei von ionisierender Strahlung, die über die natürliche Strahlung hinausgeht.
The delivered products are free of ionized emission, which is above the natural emission.
Les produits livrés n´ont pas été exposés à des rayons ionisants dépassant le rayonnement naturel.

Bei Rückfragen wenden Sie sich bitte an / If you have any queries please contact / Pour tout renseignement complémentaire veuillez vous adresser à:
Peter Leye (p.leye@mannstaedt.de; Tel.: + 49(0)2241/84-2327) oder / or / ou Marco Vostell (m.vostell@mannstaedt.de; Tel.: + 49(0)2241/84-2324)

Der Werkssachverständige / The Work's Inspector / L'expert d'usine: Joachim Braun

Maschinell erstellter Beleg, ohne Unterschrift gültig. / This document has been issued electronically and is valid without signature. / Document valable sans signature.

Qualitätswesen
Werk Langenfeld
Zeugnis geprüft
Datum: 25.03.14 Unterschrift:
Norm: ☒ erfüllt
☐ nicht erfüllt

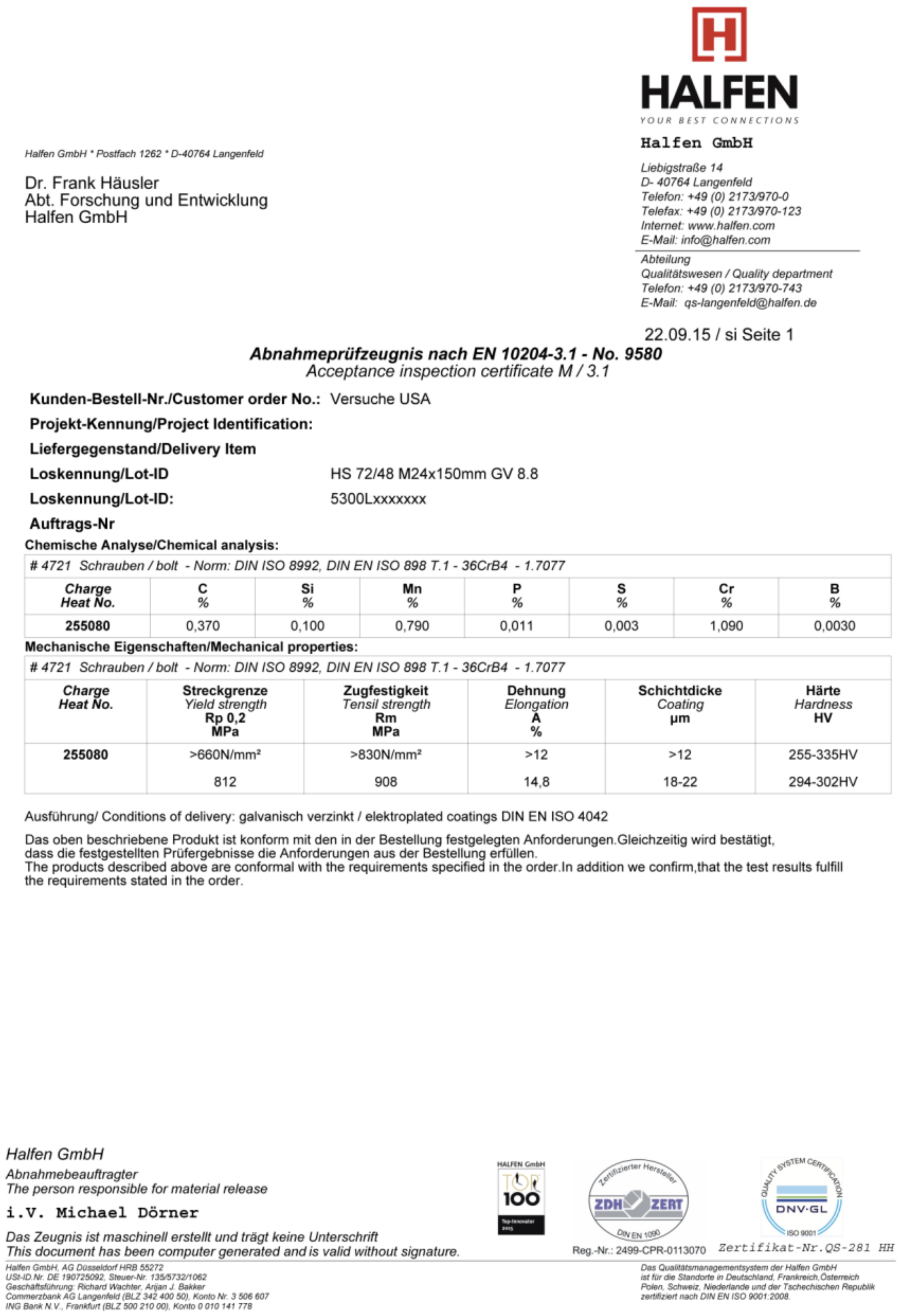

HALFEN
YOUR BEST CONNECTIONS

Halfen GmbH
Liebigstraße 14
D- 40764 Langenfeld
Telefon: +49 (0) 2173/970-0
Telefax: +49 (0) 2173/970-123
Internet: www.halfen.com
E-Mail: info@halfen.com

Abteilung
Qualitätswesen / Quality department
Telefon: +49 (0) 2173/970-743
E-Mail: qs-langenfeld@halfen.de

Halfen GmbH * Postfach 1262 * D-40764 Langenfeld

Dr. Frank Häusler
Abt. Forschung und Entwicklung
Halfen GmbH

22.09.15 / si Seite 1

Abnahmeprüfzeugnis nach EN 10204-3.1 - No. 9580

Acceptance inspection certificate M / 3.1

Kunden-Bestell-Nr./Customer order No.: Versuche USA

Projekt-Kennung/Project Identification:

Liefergegenstand/Delivery Item

Loskennung/Lot-ID HS 72/48 M24x150mm GV 8.8

Loskennung/Lot-ID: 5300Lxxxxxxx

Auftrags-Nr

Chemische Analyse/Chemical analysis:

# 4721 Schrauben / bolt - Norm: DIN ISO 8992, DIN EN ISO 898 T.1 - 36CrB4 - 1.7077

Charge* *Heat No.	**C** *%*	**Si** *%*	**Mn** *%*	**P** *%*	**S** *%*	**Cr** *%*	**B** *%*
255080	0,370	0,100	0,790	0,011	0,003	1,090	0,0030

Mechanische Eigenschaften/Mechanical properties:

# 4721 Schrauben / bolt - Norm: DIN ISO 8992, DIN EN ISO 898 T.1 - 36CrB4 - 1.7077

Charge* *Heat No.	**Streckgrenze** *Yield strength* **Rp 0,2 MPa**	**Zugfestigkeit** *Tensil strength* **Rm MPa**	**Dehnung** *Elongation* **A %**	**Schichtdicke** *Coating* **µm**	**Härte** *Hardness* **HV**
255080	>660N/mm²	>830N/mm²	>12	>12	255-335HV
	812	908	14,8	18-22	294-302HV

Ausführung/ Conditions of delivery: galvanisch verzinkt / elektroplated coatings DIN EN ISO 4042

Das oben beschriebene Produkt ist konform mit den in der Bestellung festgelegten Anforderungen.Gleichzeitig wird bestätigt, dass die festgestellten Prüfergebnisse die Anforderungen aus der Bestellung erfüllen.
The products described above are conformal with the requirements specified in the order.In addition we confirm,that the test results fulfill the requirements stated in the order.

Halfen GmbH
Abnahmebeauftragter
The person responsible for material release

i.V. Michael Dörner

Das Zeugnis ist maschinell erstellt und trägt keine Unterschrift
This document has been computer generated and is valid without signature.

HALFEN GmbH TOP 100 Top-Innovator 2015

Zertifizierter Hersteller ZDH ZERT DIN EN 1090
Reg.-Nr.: 2499-CPR-0113070

QUALITY SYSTEM CERTIFICATION DNV·GL ISO 9001
Zertifikat-Nr.QS-281 HH

Halfen GmbH, AG Düsseldorf HRB 55272
USt-ID.Nr. DE 190725092, Steuer-Nr. 135/5732/1062
Geschäftsführung: Richard Wachter, Arjan J. Bakker
Commerzbank AG Langenfeld (BLZ 342 400 50), Konto Nr. 3 506 607
ING Bank N.V., Frankfurt (BLZ 500 210 00), Konto 0 010 141 778

Das Qualitätsmanagementsystem der Halfen GmbH ist für die Standorte in Deutschland, Frankreich,Österreich Polen, Schweiz, Niederlande und der Tschechischen Republik zertifiziert nach DIN EN ISO 9001:2008.

HALFEN
YOUR BEST CONNECTIONS

HALFEN USA
PO Box 547, 8521 FM 1976
Converse, Texas 78109
USA
Phone: (800) 423 9140
Fax: (877) 874 7923
Internet: www.halfenusa.com
E-Mail: info@halfenusa.com

CONCRETE - Anchoring Systems
FACADE - Fixing Systems
FRAMING - Products and Systems

EMail: ahernandez@halfenusa.com

Northeastern University
2 Evans St.
APT R
Woburn, MA 01801 4804

February 24, 2016

Acceptance Inspection Certificate M / 3.1

Customer PO No: kyle 01-14-16
Delivery Item: Halfen HS 72/48 M20x100 GV-S (8.8) – Bolts and Nuts
Project Name: Northeastern University
Order: S023259

Chemical Analysis:

According to Standard: DIN ISO 8992, DIN EN ISO 898-1/-2

Charge Heat No:	C %	Si %	Mn %	P %	S %	Cr %	Mo %	B %	Ni %
245954	0.370	0.090	0.770	0.008	0.003	1.08	-	0.0026	-

Mechanical properties:

According to Standard: DIN ISO 8992, DIN EN ISO 898-1/-2

Charge Heat No.	Yield Point (Rp) MPa	Tensile strength (Rm) MPa	Elongation (A) %	Hardness HV	Coating µm
245954	818	905	15.6	289-302	18-22

The products described above are conformal with the requirements specified in the order. In addition we confirm that the test results fulfill the requirements specified in the order.

Halfen USA, Inc.
Alonso Hernandez- Operational Quality Manager

D.1.3 Lindapter clamps and washers

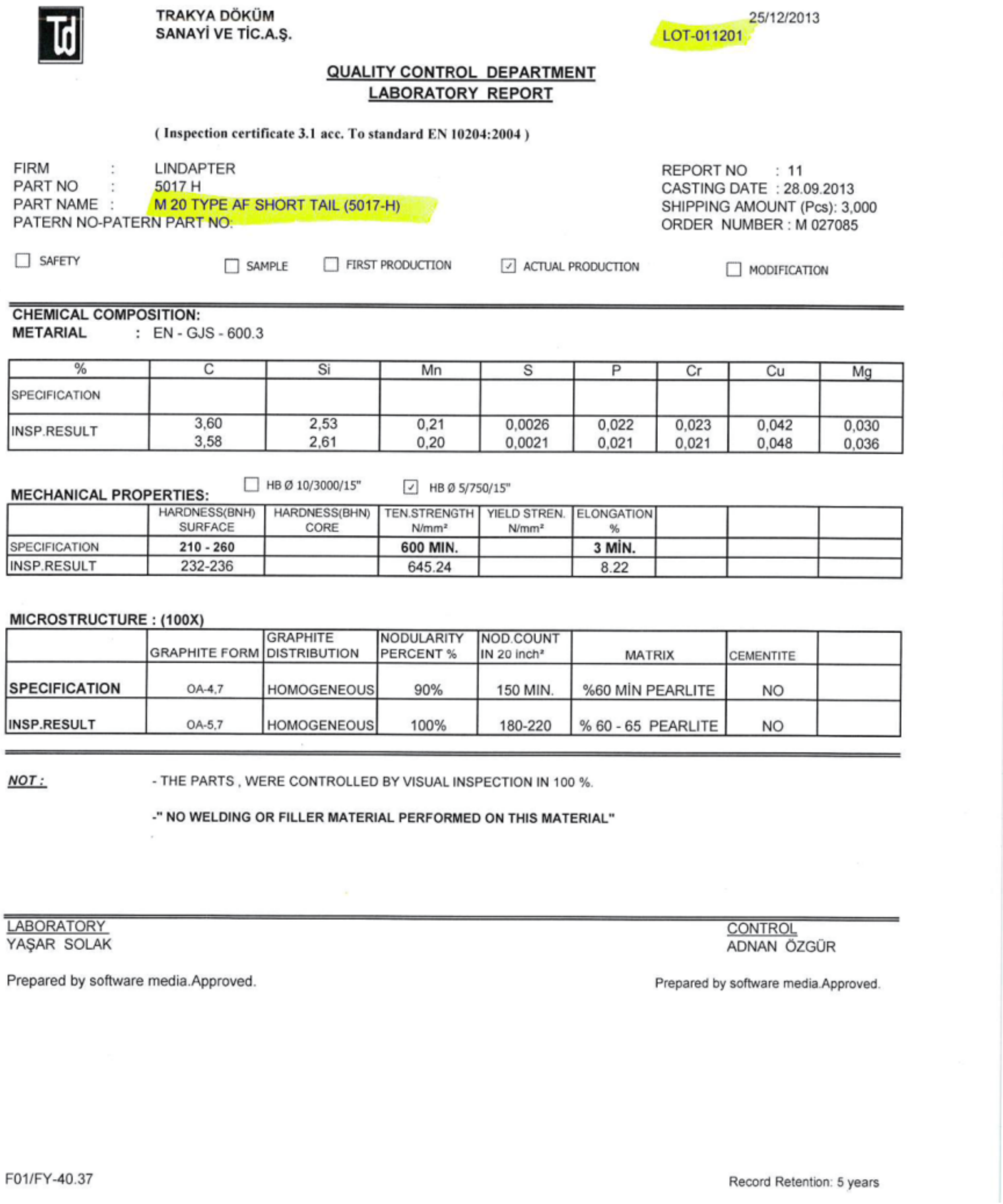

TRAKYA DÖKÜM
SANAYİ VE TİC.A.Ş.

LOT-011201 25/12/2013

QUALITY CONTROL DEPARTMENT
LABORATORY REPORT

(Inspection certificate 3.1 acc. To standard EN 10204:2004)

FIRM : LINDAPTER
PART NO : 5017 H
PART NAME : M 20 TYPE AF SHORT TAIL (5017-H)
PATERN NO-PATERN PART NO:

REPORT NO : 11
CASTING DATE : 28.09.2013
SHIPPING AMOUNT (Pcs): 3,000
ORDER NUMBER : M 027085

☐ SAFETY ☐ SAMPLE ☐ FIRST PRODUCTION ☑ ACTUAL PRODUCTION ☐ MODIFICATION

CHEMICAL COMPOSITION:
METARIAL : EN - GJS - 600.3

%	C	Si	Mn	S	P	Cr	Cu	Mg
SPECIFICATION								
INSP.RESULT	3,60 3,58	2,53 2,61	0,21 0,20	0,0026 0,0021	0,022 0,021	0,023 0,021	0,042 0,048	0,030 0,036

MECHANICAL PROPERTIES: ☐ HB Ø 10/3000/15" ☑ HB Ø 5/750/15"

	HARDNESS(BNH) SURFACE	HARDNESS(BHN) CORE	TEN.STRENGTH N/mm²	YIELD STREN. N/mm²	ELONGATION %			
SPECIFICATION	**210 - 260**		**600 MIN.**		**3 MİN.**			
INSP.RESULT	232-236		645.24		8.22			

MICROSTRUCTURE : (100X)

	GRAPHITE FORM	GRAPHITE DISTRIBUTION	NODULARITY PERCENT %	NOD.COUNT IN 20 inch²	MATRIX	CEMENTITE	
SPECIFICATION	OA-4,7	HOMOGENEOUS	90%	150 MIN.	%60 MİN PEARLITE	NO	
INSP.RESULT	OA-5,7	HOMOGENEOUS	100%	180-220	% 60 - 65 PEARLITE	NO	

NOT : - THE PARTS , WERE CONTROLLED BY VISUAL INSPECTION IN 100 %.

-" NO WELDING OR FILLER MATERIAL PERFORMED ON THIS MATERIAL"

LABORATORY
YAŞAR SOLAK

Prepared by software media.Approved.

CONTROL
ADNAN ÖZGÜR

Prepared by software media.Approved.

F01/FY-40.37

Record Retention: 5 years

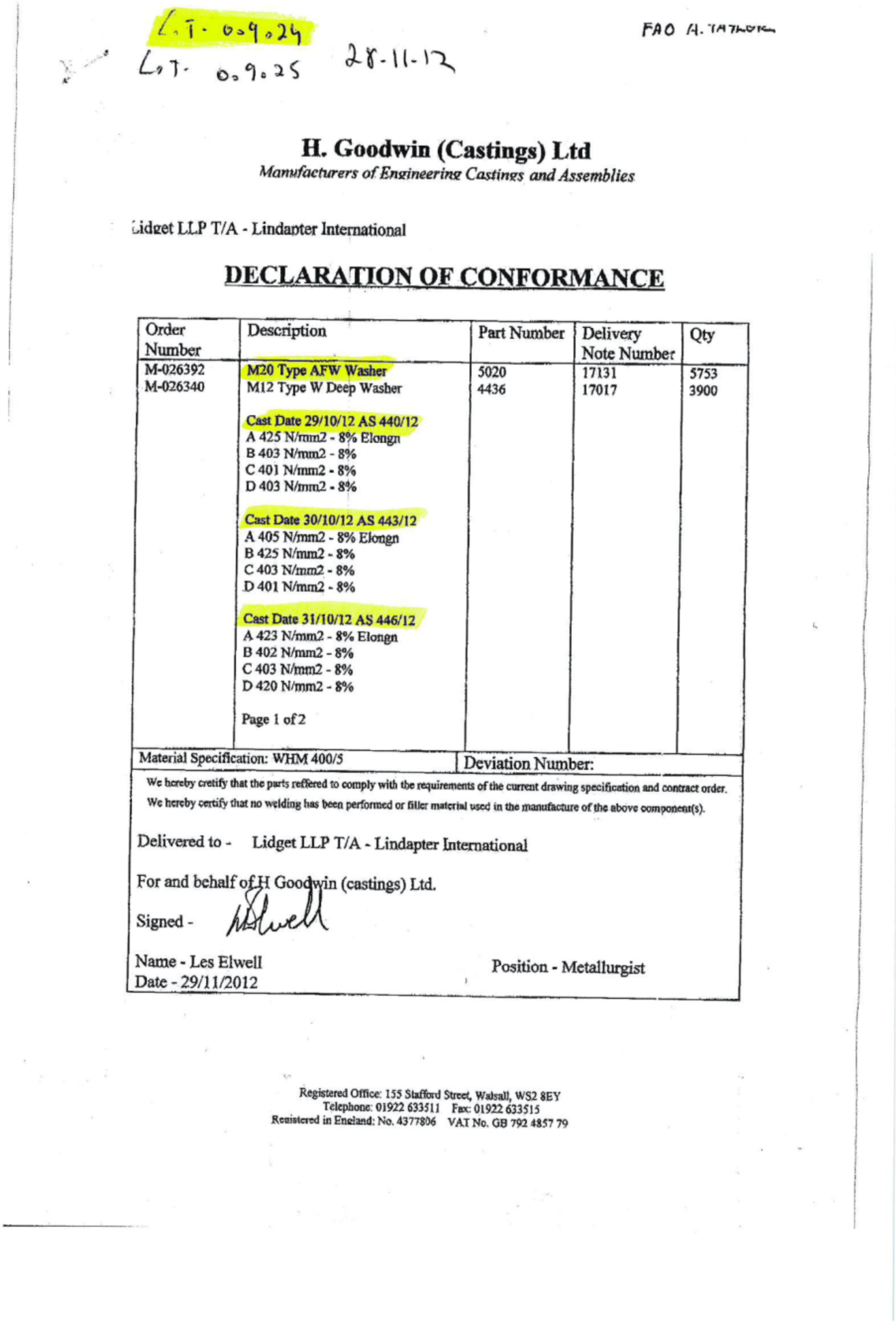

L.T. 09.024
L.T. 09.25 28-11-12

FAO A. TATLOW

H. Goodwin (Castings) Ltd

Manufacturers of Engineering Castings and Assemblies

Lidget LLP T/A - Lindapter International

DECLARATION OF CONFORMANCE

Order Number	Description	Part Number	Delivery Note Number	Qty
M-026392	M20 Type AFW Washer	5020	17131	5753
M-026340	M12 Type W Deep Washer	4436	17017	3900
	Cast Date 29/10/12 AS 440/12 A 425 N/mm2 - 8% Elongn B 403 N/mm2 - 8% C 401 N/mm2 - 8% D 403 N/mm2 - 8%			
	Cast Date 30/10/12 AS 443/12 A 405 N/mm2 - 8% Elongn B 425 N/mm2 - 8% C 403 N/mm2 - 8% D 401 N/mm2 - 8%			
	Cast Date 31/10/12 AS 446/12 A 423 N/mm2 - 8% Elongn B 402 N/mm2 - 8% C 403 N/mm2 - 8% D 420 N/mm2 - 8%			
	Page 1 of 2			

Material Specification: WHM 400/5

Deviation Number:

We hereby cretify that the parts reffered to comply with the requirements of the current drawing specification and contract order.

We hereby certify that no welding has been performed or filler material used in the manufacture of the above component(s).

Delivered to - Lidget LLP T/A - Lindapter International

For and behalf of H Goodwin (castings) Ltd.

Signed - LElwell

Name - Les Elwell
Date - 29/11/2012

Position - Metallurgist

Registered Office: 155 Stafford Street, Walsall, WS2 8EY
Telephone: 01922 633511 Fax: 01922 633515
Registered in England: No. 4377806 VAT No. GB 792 4857 79

FAO A.TAYLOR .

H GOODWIN CASTINGS LTD

DATE 29.10.12.

FURNACE 3

TIME	STD ID	C	SI	Mn	S	P
	6554	1·99	1·95	·449	·077	·188.
Correction factor		–·09	+·06	-·009	+·001	-·008

AS	440	12.

TIME	SAMPLE	Thermal Analysis			Spectro	Analysis	WHITEHEART BASE								ADDITIONS
	ID	CE	C	Si	C	SI	Mn	S	P	Cr	Ni	Al	B	Mn/S	
	B1	3·32	3·11	·82.	3·00	·68	·203	7192	·008	·018	·019	·006	·007	·53	·551
IDEAL	MIN	3.3	3.1	0.75	3.1	0.75	0.2	0.11	n/a	n/a	n/a	n/a	n/a	0.5	
RANGE	MAX	3.55	3.3	0.85	3.3	0.85	0.4	0.23	0.1	0.055	0.1	0.005	0.02	0.6	

LoT. 009024

LoT. 009025

FAO A-TAYLOR

H GOODWIN CASTINGS LTD

DATE 30·10·82.

FURNACE
3

TIME	STD ID	C	SI	Mn	S	P
	65514	1·97	1·95	·435	·082	·218.
Correction factor		-·07.	+·06.	+·005	-006	-038.

AS	443	12

TIME	SAMPLE	Thermal Analysis			Spectro	Analysis		WHITEHEART BASE							
	ID	CE	C	SI	C	SI	Mn	S	P	Cr	NI	Al	B	Mn/S	ADDITIONS
	B1		3·11	1·00	3·02	·66	·267	·189	· —	·015	·021	·005	·006	·72.	All Charge Back.
	B5	3·50	3·36	·59.	3·31	·51	·452	>·192	·018	·023	·031	·006	·007	·44.	1 Si ·25
	B5cl				3·25	·85	·471	>·192	·013	·025	·028	·006	·007	·43.	
IDEAL	MIN	3.3	3.1	0.75	3.1	0.75	0.2	0.11	n/a	n/a	n/a	n/a	n/a	0.5	
RANGE	MAX	3.55	3.3	0.85	3.3	0.85	0.4	0.23	0.1	0.056	0.1	0.005	0.02	0.6	

Co7 · 0·9·24
CoT – 0·9·25

FAO A. TAYLOR

H GOODWIN CASTINGS LTD

DATE 3\|10\|12

FURNACE 3

TIME	STD ID	C	SI	Mn	S	P
	65514	2.00	1.92	.469	.090	.196
Correction factor		-.00	+.09	-.029	-.014	-.016.

AS 446 12

TIME	SAMPLE	Thermal Analysis			Spectro	Analysis		WHITEHEART BASE							ADDITIONS
	ID	CE	C	Si	C	Si	Mn	S	P	Cr	Ni	Al	B	Mn/S	
6.57	B1	3.09	2.93	.80.	2.6	.55	.415	>.192	.002	.020	.022	.005	.007	.47.	1kg C 1.75 Si
	B1 L1				3.15	.86	.369	>.192	.019	.022	.022	.005	.007	.54.	
	B3	3.32	3.11	.85.	3.24	.77	.420	>.192	.016	.020	.017	.005	.008	.50	.3 Si
	B3 L1				3.00	.78	.456	>.192	.019	.020	.022	.005	.009	.50.	
IDEAL	MIN	3.3	3.1	0.75	3.1	0.75	0.2	0.11	n/a	n/a	n/a	n/a	n/a	0.5	
RANGE	MAX	3.55	3.3	0.85	3.3	0.85	0.4	0.23	0.1	0.055	0.1	0.005	0.02	0.6	

LOT. 009024
LOT -009025

TRAKYA DÖKÜM
SANAYİ VE TİC.A.Ş.

25/12/2013
LOT-011195

QUALITY CONTROL DEPARTMENT
LABORATORY REPORT

(Inspection certificate 3.1 acc. To standard EN 10204:2004)

FIRM : LINDAPTER
PART NO : 5077 H
PART NAME : M 24 TYPE AF SHORT TAIL (5077-H)
PATERN NO-PATERN PART NO:

REPORT NO : 09
CASTING DATE : 14.12.2013
SHIPPING AMOUNT (Pcs): 500
ORDER NUMBER : M 027113

☐ SAFETY ☐ SAMPLE ☐ FIRST PRODUCTION ☑ ACTUAL PRODUCTION ☐ MODIFICATION

CHEMICAL COMPOSITION:
METARIAL : EN - GJS - 600.3

%	C	Si	Mn	S	P	Cr	Cu	Mg
SPECIFICATION								
INSP.RESULT	3,59 3,59	2,53 2,59	0,22 0,22	0,0025 0,0025	0,032 0,033	0,022 0,021	0,082 0,075	0,030 0,036

MECHANICAL PROPERTIES: ☐ HB Ø 10/3000/15" ☑ HB Ø 5/750/15"

	HARDNESS(BNH) SURFACE	HARDNESS(BHN) CORE	TEN.STRENGTH N/mm^2	YIELD STREN. N/mm^2	ELONGATION %			
SPECIFICATION	**210 - 260**		**600 MIN.**		**3 MİN.**			
INSP.RESULT	236-239		634.56		8.2			

MICROSTRUCTURE : (100X)

	GRAPHITE FORM	GRAPHITE DISTRIBUTION	NODULARITY PERCENT %	NOD.COUNT IN 20 inch^2	MATRIX	CEMENTITE	
SPECIFICATION	OA-4,7	HOMOGENEOUS	90%	150 MIN.	%60 MİN PEARLITE	NO	
INSP.RESULT	OA-5,7	HOMOGENEOUS	100%	180-220	% 60 - 65 PEARLITE	NO	

NOT : - THE PARTS , WERE CONTROLLED BY VISUAL INSPECTION IN 100 %.

-" NO WELDING OR FILLER MATERIAL PERFORMED ON THIS MATERIAL"

LABORATORY
YAŞAR SOLAK

Prepared by software media.Approved.

CONTROL
ADNAN ÖZGÜR

Prepared by software media.Approved.

F01/FY-40.37

Record Retention: 5 years

TRAKYA DÖKÜM
SANAYİ VE TİC.A.Ş.

31/01/2014
LOT-011457

QUALITY CONTROL DEPARTMENT
LABORATORY REPORT

(Inspection certificate 3.1 acc. To standard EN 10204:2004)

FIRM : LINDAPTER
PART NO : 5077 H
PART NAME : M 24 TYPE AF SHORT TAIL (5077-H)
PATERN NO-PATERN PART NO:

REPORT NO : 01
CASTING DATE : 11.01.2014
SHIPPING AMOUNT (Pcs): 2,000
ORDER NUMBER : M 027121

☐ SAFETY ☐ SAMPLE ☐ FIRST PRODUCTION ☑ ACTUAL PRODUCTION ☐ MODIFICATION

CHEMICAL COMPOSITION:
METARIAL : EN - GJS - 600.3

%	C	Si	Mn	S	P	Cr	Cu	Mg
SPECIFICATION								
INSP.RESULT	3,60 3,62	2,54 2,57	0,25 0,28	0,0033 0,0026	0,038 0,041	0,017 0,017	0,022 0,023	0,029 0,031

MECHANICAL PROPERTIES: ☐ HB Ø 10/3000/15" ☑ HB Ø 5/750/15"

	HARDNESS(BNH) SURFACE	HARDNESS(BHN) CORE	TEN.STRENGTH N/mm²	YIELD STREN. N/mm²	ELONGATION %			
SPECIFICATION	**210 - 260**		**600 MIN.**		**3 MİN.**			
INSP.RESULT	223-227		632.46		10.92			

MICROSTRUCTURE : (100X)

	GRAPHITE FORM	GRAPHITE DISTRIBUTION	NODULARITY PERCENT %	NOD.COUNT IN 20 inch²	MATRIX	CEMENTITE	
SPECIFICATION	OA-4,7	HOMOGENEOUS	90%	150 MIN.	%60 MİN PEARLITE	NO	
INSP.RESULT	OA-5,7	HOMOGENEOUS	100%	180-220	% 60 - 65 PEARLITE	NO	

NOT : - THE PARTS , WERE CONTROLLED BY VISUAL INSPECTION IN 100 %.

-" NO WELDING OR FILLER MATERIAL PERFORMED ON THIS MATERIAL"

LABORATORY
YAŞAR SOLAK

CONTROL
ADNAN ÖZGÜR

Prepared by software media.Approved.

Prepared by software media.Approved.

F01/FY-40.37

Record Retention: 5 years

42596

Laminés Marchands Européens
BP1 - 59125 Trith-Saint-Léger France
Groupe Beltrame

CE
0398
Steel from Electric Arc Furnace

ABRAM PULMAN & SONS LTD
WALTON STREET

GB 0 HX6 1AN-SOWERBY BRIDGE

INSPECTION DOCUMENT N. 1108356
OFFICIAL REGULATION EN 10025-2

INSPECTION CERTIFICATE 3.1 - EN 10204
ENCLOSE CERTIFICATION CE

AGENT ORDER N.
CUSTOMER CODE 8056
CUSTOMER ORDER N. PO-042596
CONSIGNEE ABRAM PULMAN & SONS LTD
GRADE S275JR+AR

ADING NUMBER 2014 2309

LOADING DATE 6/02/2014

INTERNAL ORDER 2014 1294

IT.		CAST	SECTION	DIMENSIONS (mm)	CE	LENGTH	C	Si	Mn	P	S	Cu	Cr	Ni	V	Mo	N	Ti	Al	Nb	Ceq
1	LM	89351	FLAT	30X6	0398	6,00	0,08	0,19	0,57	0,021	0,034	0,36	0,08	0,11	0,001	0,03	0,0116	0,0008	0,002	0,001	0,23
2	LM	88123	FLAT	30X10	0398	6,00	0,08	0,18	0,53	0,033	0,035	0,34	0,11	0,16	0,001	0,03	0,0066	0,0009	0,002	0,001	0,23
3	LM	89024	FLAT	40X5	0398	6,00	0,08	0,20	0,60	0,025	0,034	0,34	0,08	0,17	0,002	0,03	0,0088	0,0008	0,002	0,001	0,24
3	LM	89337	FLAT	40X5	0398	6,00	0,08	0,18	0,62	0,030	0,032	0,39	0,09	0,15	0,001	0,03	0,0085	0,0009	0,002	0,001	0,24
5	LM	88525	FLAT	50X5	0398	6,00	0,08	0,19	0,62	0,018	0,026	0,39	0,07	0,17	0,002	0,03	0,0110	0,0001	0,002	0,002	0,24
6	LM	87802	FLAT	50X10	0398	6,00	0,10	0,21	0,62	0,032	0,034	0,41	0,10	0,18	0,002	0,03	0,0098	0,0005	0,001	0,001	0,27
7	LM	88803	SQUARE	20	0398	6,00	0,07	0,20	0,62	0,024	0,033	0,32	0,10	0,15	0,001	0,03	0,0088	0,0001	0,001	0,001	0,23
8	LM	89215	ROUND	20	0398	6,00	0,09	0,19	0,58	0,019	0,034	0,39	0,08	0,17	0,003	0,03	0,0089	0,0005	0,001	0,001	0,25

IT.		CAST	ORIGIN	PRODUCT REGULATION	TEST NUM	Bdls n.	WEIGHT kg	TENSILE TEST			IMPACT TEST KV (J)			GRAIN
								ReH/MPa	Rm/MPa	A5%	Individual values	Average	°C	
1	LM	89351	TRITH	EN 10058	489976	1	2355	294	429	33,4				
2	LM	88123	TRITH	EN 10058	446723	1	2331	298	426	33,0				
3	LM	89024	TRITH	EN 10058	478542	1	2307	300	436	34,0				
3	LM	89337	TRITH	EN 10058	489324	2	4736	304	439	34,0				
	LM	88525	TRITH	EN 10058	461699	2	4663	303	439	34,0				
5	LM	88525	TRITH	EN 10058	461700			305	441	33,8				
6	LM	87802	TRITH	EN 10058	466326	2	4864	306	436	32,2				
7	LM	88803	TRITH	EN 10059	472751	1	2165	298	429	33,6				
8	LM	89215	TRITH	EN 10060	484844	1	2172	298	429	32,5				

LT. 011629

INSPECTOR	FACTORY	DATE	QUALITY CONTROL DEPT	QUALITY ASSURANCE DEPT
	TRITH	6/02/2014	Florian Devisscher	Oriane Devallez

GRUPPO AFV BELTRAME

D.1.4 Reinforcement

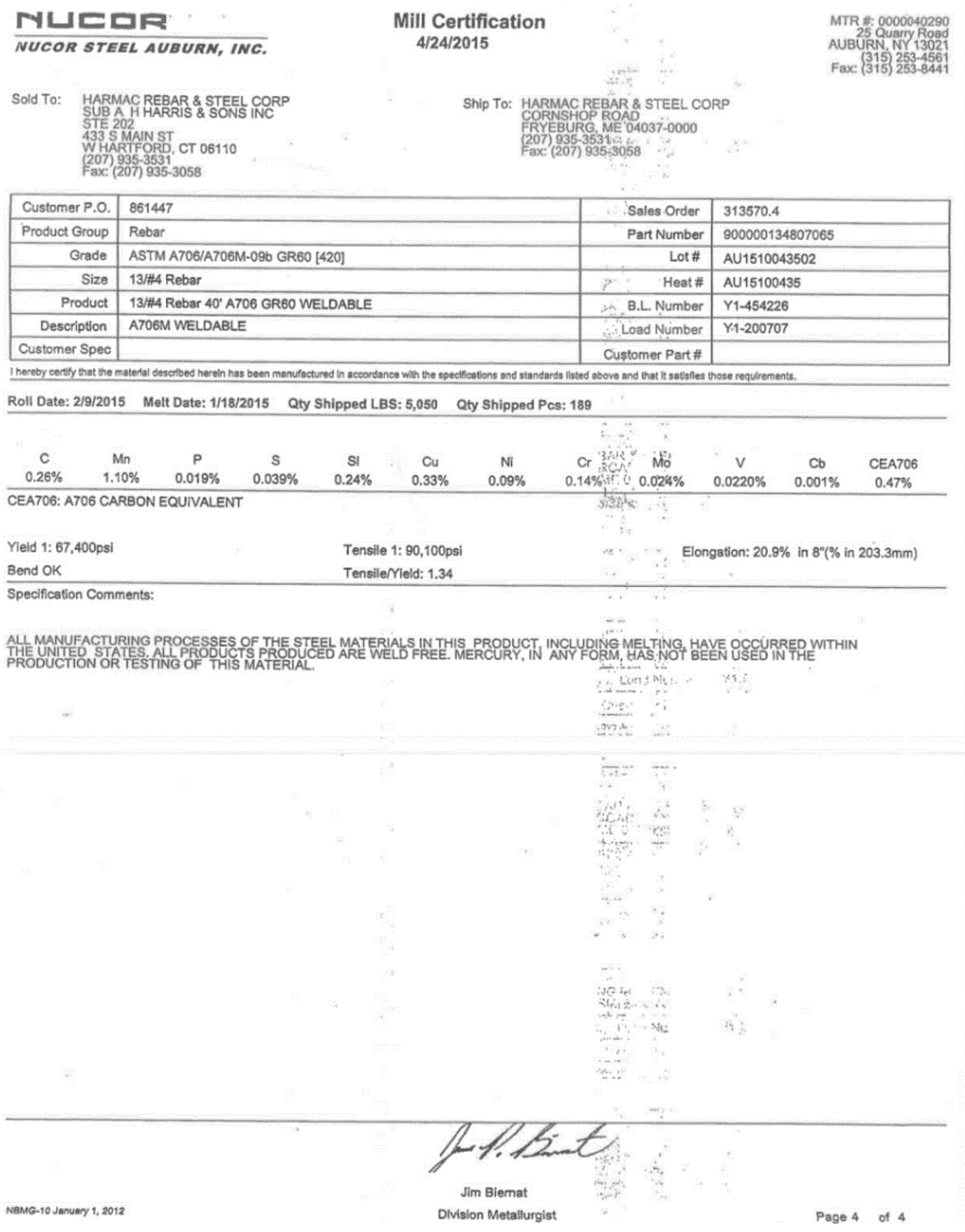

NUCOR
NUCOR STEEL AUBURN, INC.

Mill Certification
4/24/2015

MTR #: 0000040290
25 Quarry Road
AUBURN, NY 13021
(315) 253-4561
Fax: (315) 253-8441

Sold To:
HARMAC REBAR & STEEL CORP
SUB A H HARRIS & SONS INC
STE 202
433 S MAIN ST
W HARTFORD, CT 06110
(207) 935-3531
Fax: (207) 935-3058

Ship To:
HARMAC REBAR & STEEL CORP
CORNSHOP ROAD
FRYEBURG, ME 04037-0000
(207) 935-3531
Fax: (207) 935-3058

Customer P.O.	861447	Sales Order	313570.4
Product Group	Rebar	Part Number	900000134807065
Grade	ASTM A706/A706M-09b GR60 [420]	Lot #	AU1510043502
Size	13/#4 Rebar	Heat #	AU15100435
Product	13/#4 Rebar 40' A706 GR60 WELDABLE	B.L. Number	Y1-454226
Description	A706M WELDABLE	Load Number	Y1-200707
Customer Spec		Customer Part #	

I hereby certify that the material described herein has been manufactured in accordance with the specifications and standards listed above and that it satisfies those requirements.

Roll Date: 2/9/2015 Melt Date: 1/18/2015 Qty Shipped LBS: 5,050 Qty Shipped Pcs: 189

C	Mn	P	S	Si	Cu	Ni	Cr	Mo	V	Cb	CEA706
0.26%	1.10%	0.019%	0.039%	0.24%	0.33%	0.09%	0.14%	0.024%	0.0220%	0.001%	0.47%

CEA706: A706 CARBON EQUIVALENT

Yield 1: 67,400psi
Tensile 1: 90,100psi
Elongation: 20.9% in 8"(% in 203.3mm)
Bend OK
Tensile/Yield: 1.34

Specification Comments:

ALL MANUFACTURING PROCESSES OF THE STEEL MATERIALS IN THIS PRODUCT, INCLUDING MELTING, HAVE OCCURRED WITHIN THE UNITED STATES. ALL PRODUCTS PRODUCED ARE WELD FREE. MERCURY, IN ANY FORM, HAS NOT BEEN USED IN THE PRODUCTION OR TESTING OF THIS MATERIAL.

Jim Biernat
Division Metallurgist

NBMG-10 January 1, 2012

Page 4 of 4

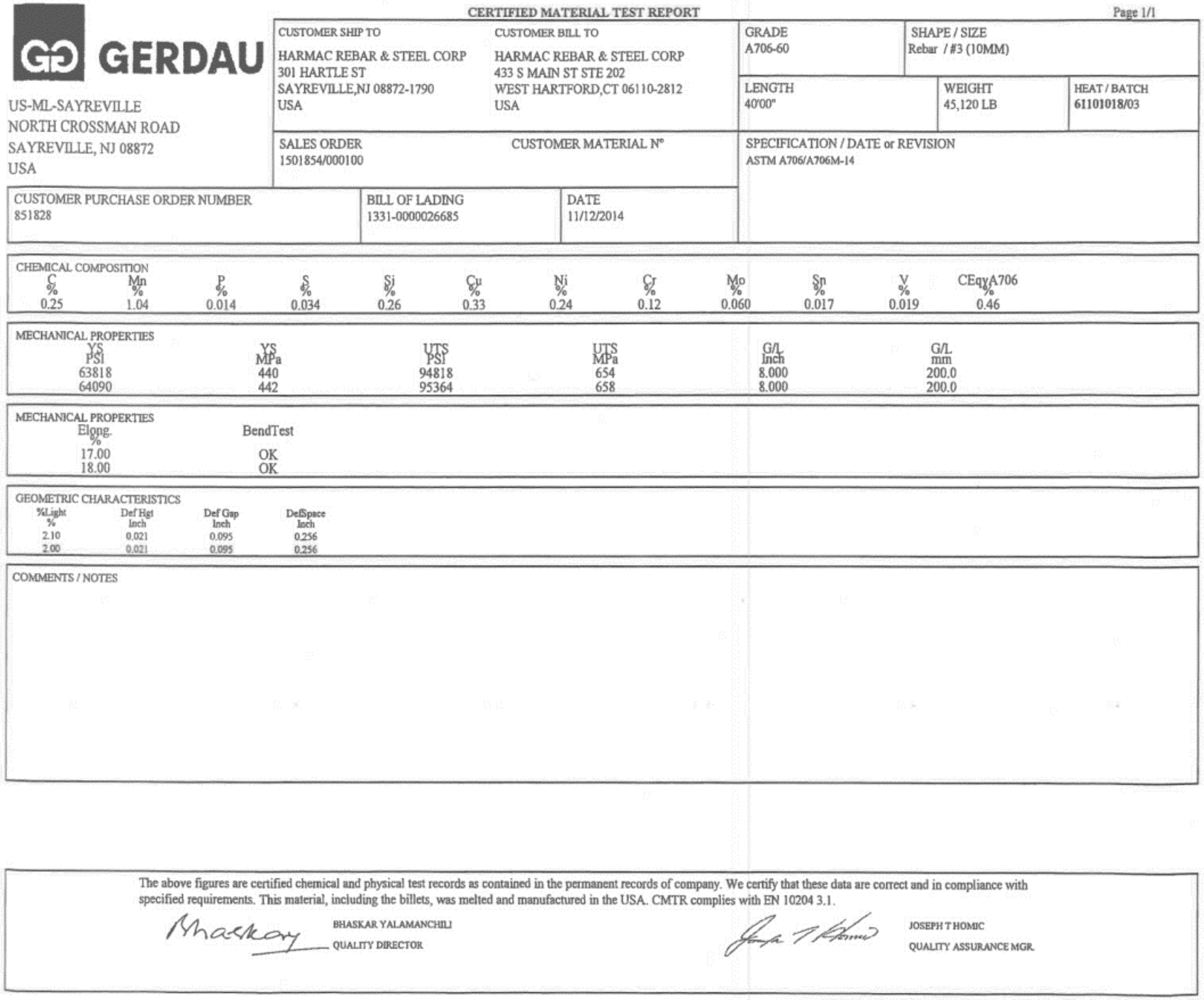

GERDAU

US-ML-SAYREVILLE
NORTH CROSSMAN ROAD
SAYREVILLE, NJ 08872
USA

CERTIFIED MATERIAL TEST REPORT

Page 1/1

CUSTOMER SHIP TO HARMAC REBAR & STEEL CORP 301 HARTLE ST SAYREVILLE,NJ 08872-1790 USA	CUSTOMER BILL TO HARMAC REBAR & STEEL CORP 433 S MAIN ST STE 202 WEST HARTFORD,CT 06110-2812 USA	GRADE A706-60	SHAPE / SIZE Rebar / #3 (10MM)	
		LENGTH 40'00"	WEIGHT 45,120 LB	HEAT / BATCH 61101018/03
SALES ORDER 1501854/000100	CUSTOMER MATERIAL Nº	SPECIFICATION / DATE or REVISION ASTM A706/A706M-14		

CUSTOMER PURCHASE ORDER NUMBER	BILL OF LADING	DATE
851828	1331-0000026685	11/12/2014

CHEMICAL COMPOSITION

C %	Mn %	P %	S %	Si %	Cu %	Ni %	Cr %	Mo %	Sn %	V %	CEqyA706 %
0.25	1.04	0.014	0.034	0.26	0.33	0.24	0.12	0.060	0.017	0.019	0.46

MECHANICAL PROPERTIES

YS PSI	YS MPa	UTS PSI	UTS MPa	G/L Inch	G/L mm
63818	440	94818	654	8.000	200.0
64090	442	95364	658	8.000	200.0

MECHANICAL PROPERTIES

Elong. %	BendTest
17.00	OK
18.00	OK

GEOMETRIC CHARACTERISTICS

%Light %	Def Hgt Inch	Def Gap Inch	DefSpace Inch
2.10	0.021	0.095	0.256
2.00	0.021	0.095	0.256

COMMENTS / NOTES

The above figures are certified chemical and physical test records as contained in the permanent records of company. We certify that these data are correct and in compliance with specified requirements. This material, including the billets, was melted and manufactured in the USA. CMTR complies with EN 10204 3.1.

BHASKAR YALAMANCHILI
QUALITY DIRECTOR

JOSEPH T HOMIC
QUALITY ASSURANCE MGR.

D.1.5 Concrete

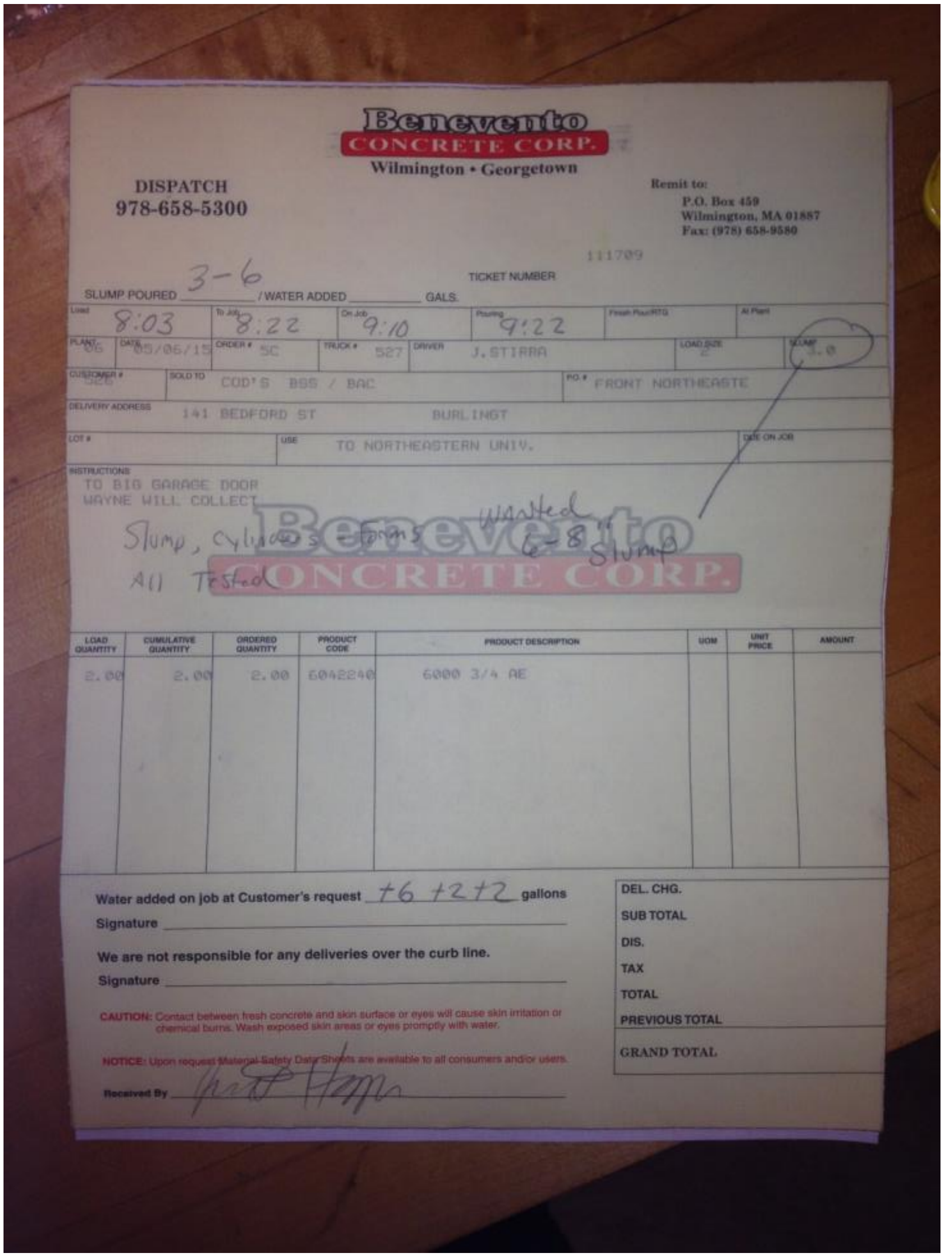

Benevento
CONCRETE CORP.
Wilmington • Georgetown

DISPATCH
978-658-5300

Remit to:
P.O. Box 459
Wilmington, MA 01887
Fax: (978) 658-9580

111709
TICKET NUMBER

SLUMP POURED 3-6 / WATER ADDED ______ GALS.

Load 8:03	To Job 8:22	On Job 9:10	Pouring 9:22	Finish Pour/RTG	At Plant	
PLANT 06	DATE 05/06/15	ORDER # 5C	TRUCK # 527	DRIVER J.STIRRA	LOAD SIZE 2	SLUMP 3.0

CUSTOMER # [illegible]
SOLD TO COD'S BSS / BAC
P.O. # FRONT NORTHEASTE
DELIVERY ADDRESS 141 BEDFORD ST BURLINGT
LOT #
USE TO NORTHEASTERN UNIV.
DUE ON JOB

INSTRUCTIONS
TO BIG GARAGE DOOR
WAYNE WILL COLLECT

Slump, cylinders + forms
All Tested

Wanted
6-8" Slump

LOAD QUANTITY	CUMULATIVE QUANTITY	ORDERED QUANTITY	PRODUCT CODE	PRODUCT DESCRIPTION	UOM	UNIT PRICE	AMOUNT
2.00	2.00	2.00	6042240	6000 3/4 AE			

Water added on job at Customer's request +6 +2+2 gallons
Signature ______

We are not responsible for any deliveries over the curb line.
Signature ______

CAUTION: Contact between fresh concrete and skin surface or eyes will cause skin irritation or chemical burns. Wash exposed skin areas or eyes promptly with water.

NOTICE: Upon request Material Safety Data Sheets are available to all consumers and/or users.

Received By ______

DEL. CHG.
SUB TOTAL
DIS.
TAX
TOTAL
PREVIOUS TOTAL
GRAND TOTAL

D.2 **Beam tests**

D.2.1 Steel frame

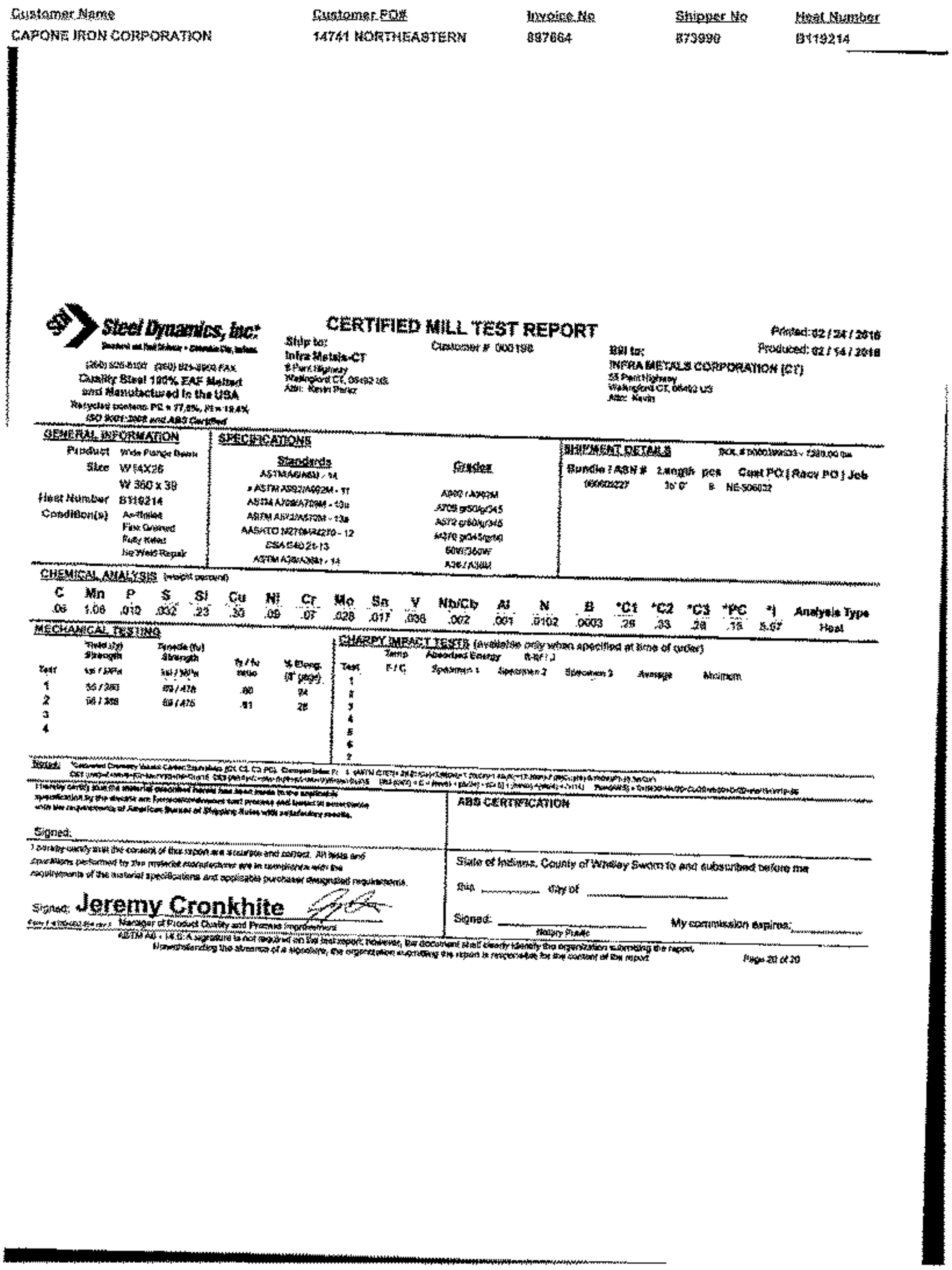

Customer Name	Customer PO#	Invoice No	Shipper No	Heat Number
CAPONE IRON CORPORATION	14741 NORTHEASTERN	897664	873990	B119214

Steel Dynamics, Inc.

(260) 625-8100 (260) 625-8950 FAX
Quality Steel 100% EAF Melted
and Manufactured in the USA
Recycled content: PC = 77.8%, PI = 18.4%
ISO 9001:2008 and ABS Certified

CERTIFIED MILL TEST REPORT

Printed: 02 / 24 / 2016
Produced: 02 / 14 / 2016

Ship to:
Infra Metals-CT
8 Park Highway
Wallingford CT, 06492 US
Attn: Kevin Parker

Customer # 000198

Bill to:
INFRA METALS CORPORATION (CT)
55 Park Highway
Wallingford CT, 06492 US
Attn: Kevin

GENERAL INFORMATION

Product: Wide Flange Beam
Size: W14X26
W 360 x 39
Heat Number: B119214
Condition(s): As-Rolled
Fine Grained
Fully Killed
No Weld Repair

SPECIFICATIONS

Standards	Grades
ASTM A6/A6M - 14	
ASTM A992/A992M - 11	A992 / A992M
ASTM A709/A709M - 13a	A709 gr50/gr345
ASTM A572/A572M - 13a	A572 gr50/gr345
AASHTO M270/M270 - 12	M270 gr345/gr50
CSA G40.21-13	50W/350WF
ASTM A36/A36M - 14	A36 / A36M

SHIPMENT DETAILS

Bundle / ASN #	Length	pcs	Cust PO / Recv PO / Job
1666602227	30' 0"	8	NE-506032

CHEMICAL ANALYSIS (weight percent)

C	Mn	P	S	Si	Cu	Ni	Cr	Mo	Sn	V	Nb/Cb	Al	N	B	*C1	*C2	*C3	*PC	*I	Analysis Type
.06	1.06	.010	.032	.23	.30	.09	.07	.028	.017	.036	.002	.001	.0102	.0003	.28	.33	.28	.15	5.67	Heat

MECHANICAL TESTING

Test	Yield (Fy) Strength ksi / MPa	Tensile (Fu) Strength ksi / MPa	Fy / Fu ratio	% Elong. (8" gage)
1	55 / 383	69 / 476	.80	24
2	56 / 388	69 / 475	.81	26
3				
4				

CHARPY IMPACT TESTS (available only when specified at time of order)

Test	Temp F / C	Absorbed Energy ft-lbf / J Specimen 1	Specimen 2	Specimen 3	Average	Minimum
1						
2						
3						
4						
5						
6						
7						

Notes: *Calculated Chemistry Values: Carbon Equivalents (C1, C2, C3, PC), Corrosion Index (I)

I hereby certify that the material described herein has been made to the applicable specification by the electric arc furnace/continuous cast process and tested in accordance with the requirements of American Bureau of Shipping Rules with satisfactory results.

Signed:

ABS CERTIFICATION

I hereby certify that the contents of this report are accurate and correct. All tests and operations performed by the material manufacturer are in compliance with the requirements of the material specifications and applicable purchaser designated requirements.

Signed: Jeremy Cronkhite
Manager of Product Quality and Process Improvement

State of Indiana, County of Whitley Sworn to and subscribed before me

this ________ day of ________________

Signed: ________________ My commission expires: ________
Notary Public

ASTM A6 - 14.5: A signature is not required on the test report; however, the document shall clearly identify the organization submitting the report. Notwithstanding the absence of a signature, the organization submitting the report is responsible for the content of the report.

Page 20 of 20

Customer Name	Customer PO#	Invoice No	Shipper No	Heat Number
CAPONE IRON CORPORATION	14741 NORTHEASTERN	897664	873990	1603346

```
NUCOR STEEL - BERKELEY                          CERTIFIED MILL TEST REPORT                              3/21/16  8:43:24
P.O. Box 2259                                                                 100% EAF MELTED AND MANUFACTURED IN THE USA
Mt. Pleasant, S.C.  29464                                                   All beams produced by Nucor-Berkeley are cast and
Phone: (843) 336-6000                                                       rolled to a fully killed and fine grain practice.
                                                          Mercury has not been used in the direct manufacturing of this material.

    Sold To: INFRA METALS CO VA                   Ship To: INFRA-METALS CO                       Customer #.:  1828 -   2
             580 MIDDLETOWN BLVD                           1900 BESSEMER ROAD                    Customer PO: VA-505875
                                                                                                 B.O.L. #...: 1190260
             LANGHORNE, PA   19047                         PETERSBURG, VA   23805                                  MOS: A

SPECIFICATIONS: Tested in accordance with ASTM specification A6/A6M-14 and A370. Quality Manual Rev 86 (12-8-15).
   AASHTO : M270-345M270-50-13
   ASME : SA-36  13
   ASTM : A992-11(15)/A36-14/A529-14-50/A572 50-15/A709-50 15
   CSA : G40.21-50W/G40.2150WM/G402150WMT
************************************************************ *****************************************************************
                  Heat#       Yield/  Yield Tensile        |   C    |   Mn   |   P    |   S    |   Si   |   Cu   |   Ni   |  CE1  |
Description      Grade(s)    Tensile  (PSI)  (PSI)   Elong |   Cr   |   Mo   |   Sn   |   B    |   V    |   Nb   | ****** |  CE2  |
Part #        Test/Heat JW   Ratio   (MPa)  (MPa)     %    | ****** |   Ti   | ****** | ****** |   N    | ****** |   Ct   |  Pcm  |
-------------------------------------------------------------------------------------------------------------------------------
W14X34           1603288       .80    56500  70300  25.93  |  .07   | 1.00   |  .007  |  .023  |  .24   |  .14   |  .04   |  .26  |
  035' 00.00"    A992-11(15                390    485      |  .03   |  .01   |  .0112 |  .0007 |  .005  |  .030  |        | .3049 |
 W360X51                       .81    57200  70800  25.01  |        |  .001  |        |        |  .0054 |        |  3.66  | .1426 |
  010.6680m                                394    488      5 Pc(s)   5,950 lbs                                    Inv#:      0

W14X34           1514967       .80    55500  69100  25.26  |  .07   | 1.06   |  .007  |  .023  |  .20   |  .09   |  .03   |  .26  |
  055' 00.00"    A992-11(15                383    476      |  .03   |  .01   |  .0049 |  .0004 |  .004  |  .032  |        | .3143 |
 W360X51                       .81    60100  74200  24.63  |        |  .001  |        |        |  .0031 |        |  2.51  | .1402 |
  016.7640m                                414    512      5 Pc(s)   9,350 lbs                                    Inv#:      0

W14X38           2600074       .82    57800  70700  22.96  |  .07   | 1.01   |  .009  |  .017  |  .24   |  .06   |  .03   |  .25  |
  030' 00.00"    A992 11(15                399    487      |  .02   |  .01   |  .0061 |  .0006 |  .004  |  .029  |        | .2933 |
 W360X57.8                     .80    55200  68700  26.05  |        |  .001  |        |        |  .0050 |        |  2.44  | .1357 |
  009.1440m                                381    474      5 Pc(s)   5,700 lbs                                    Inv#:      0

W14X38           1603346       .81    57900  71300  24.24  |  .07   | 1.01   |  .005  |  .018  |  .24   |  .07   |  .02   |  .25  |
  035' 00.00"    A992-11(15                399    492      |  .02   |  .00   |  .0069 |  .0007 |  .005  |  .031  |        | .2946 |
 W360X57.8                     .81    56900  70600  24.20  |        |  .001  |        |        |  .0042 |        |  2.28  | .1346 |
  010.6680m                                392    487      5 Pc(s)   6,650 lbs                                    Inv#:      0
************************************************************ *****************************************************************
Elongation based on 8" (20.32cm) gauge length. 'No Weld Repair' was performed.  Hg free and no contact with Hg during manufacture.
CI  = 26.01Cu+3.88Ni+1.20Cr+1.49Si+17.28P-(7.29Cu*Ni)-(9.10Ni*P)-33.39(Cu*Cu)   CE1= C+(Mn/6)+((Cr+Mo+V)/5)+((Ni+Cu)/15)
Pcm = C+(Si/30)+(Mn/20)+(Cu/20)+(Ni/60)+(Cr/20)+(Mo/15)+(V/10)+5B                CE2 = C+((Mn+Si)/6)+((Cr+Mo+V+Cb)/5)+((Ni+Cu)/15)

I hereby certify that the contents of this report are accurate and         Bruce A. Work
correct. All test results and operations performed by the material      ------------------
manufacturer are in compliance with material specifications, and          Metallurgist/
when designated by the Purchaser, meet applicable specifications.        Quality Control
```

D.2.2 Fully threaded rods

45 in. long fully threaded rods used in beam test 1

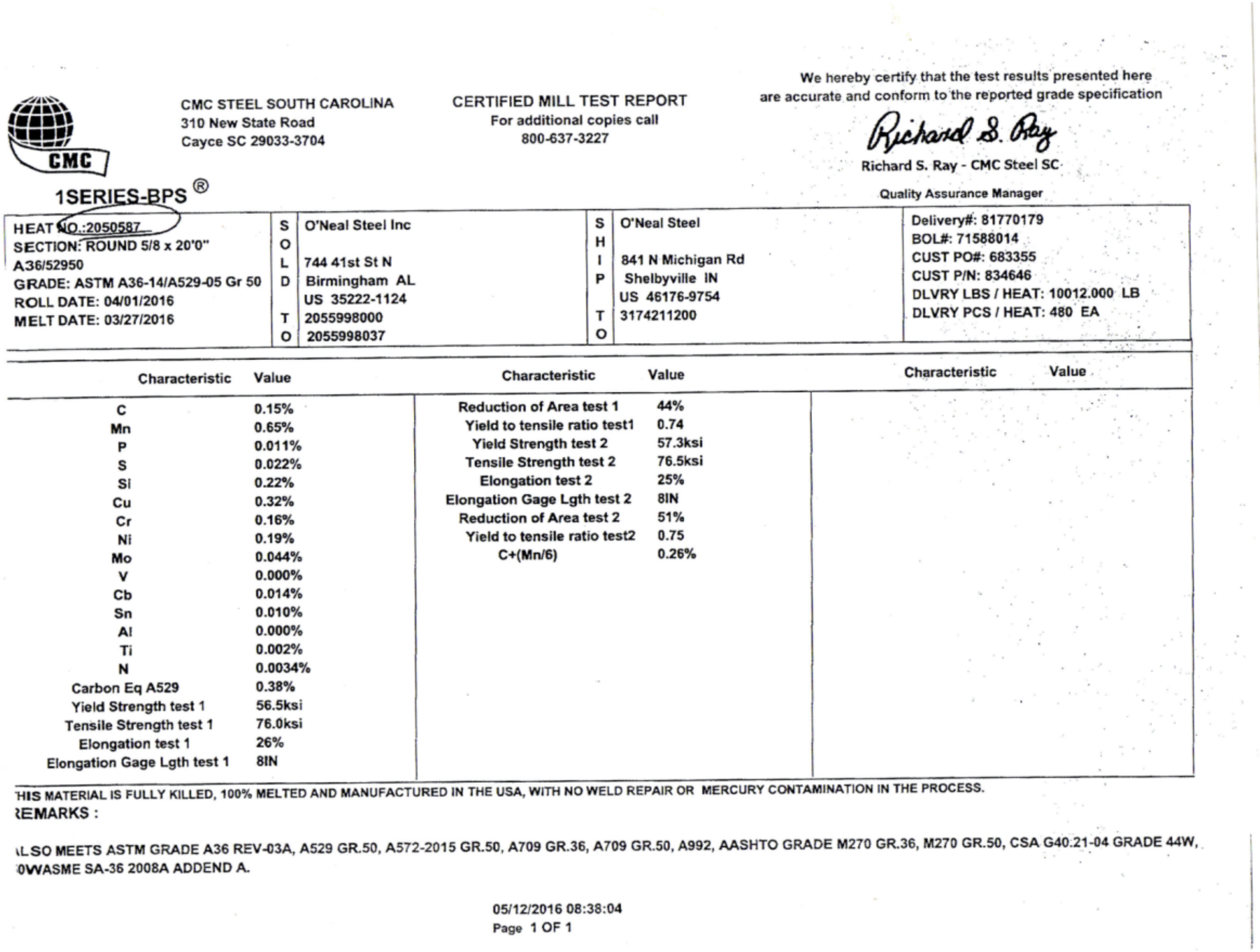

CMC STEEL SOUTH CAROLINA
310 New State Road
Cayce SC 29033-3704

CERTIFIED MILL TEST REPORT
For additional copies call
800-637-3227

We hereby certify that the test results presented here are accurate and conform to the reported grade specification

Richard S. Ray
Richard S. Ray - CMC Steel SC
Quality Assurance Manager

1SERIES-BPS ®

HEAT NO.:2050587
SECTION: ROUND 5/8 x 20'0"
A36/52950
GRADE: ASTM A36-14/A529-05 Gr 50
ROLL DATE: 04/01/2016
MELT DATE: 03/27/2016

SOLD TO
O'Neal Steel Inc
744 41st St N
Birmingham AL
US 35222-1124
2055998000
2055998037

SHIP TO
O'Neal Steel
841 N Michigan Rd
Shelbyville IN
US 46176-9754
3174211200

Delivery#: 81770179
BOL#: 71588014
CUST PO#: 683355
CUST P/N: 834646
DLVRY LBS / HEAT: 10012.000 LB
DLVRY PCS / HEAT: 480 EA

Characteristic	Value	Characteristic	Value	Characteristic	Value
C	0.15%	Reduction of Area test 1	44%		
Mn	0.65%	Yield to tensile ratio test1	0.74		
P	0.011%	Yield Strength test 2	57.3ksi		
S	0.022%	Tensile Strength test 2	76.5ksi		
Si	0.22%	Elongation test 2	25%		
Cu	0.32%	Elongation Gage Lgth test 2	8IN		
Cr	0.16%	Reduction of Area test 2	51%		
Ni	0.19%	Yield to tensile ratio test2	0.75		
Mo	0.044%	C+(Mn/6)	0.26%		
V	0.000%				
Cb	0.014%				
Sn	0.010%				
Al	0.000%				
Ti	0.002%				
N	0.0034%				
Carbon Eq A529	0.38%				
Yield Strength test 1	56.5ksi				
Tensile Strength test 1	76.0ksi				
Elongation test 1	26%				
Elongation Gage Lgth test 1	8IN				

HIS MATERIAL IS FULLY KILLED, 100% MELTED AND MANUFACTURED IN THE USA, WITH NO WELD REPAIR OR MERCURY CONTAMINATION IN THE PROCESS.

REMARKS :

LSO MEETS ASTM GRADE A36 REV-03A, A529 GR.50, A572-2015 GR.50, A709 GR.36, A709 GR.50, A992, AASHTO GRADE M270 GR.36, M270 GR.50, CSA G40.21-04 GRADE 44W, OWASME SA-36 2008A ADDEND A.

05/12/2016 08:38:04
Page 1 OF 1

46.5 in. long fully threaded rods used in beam test 1

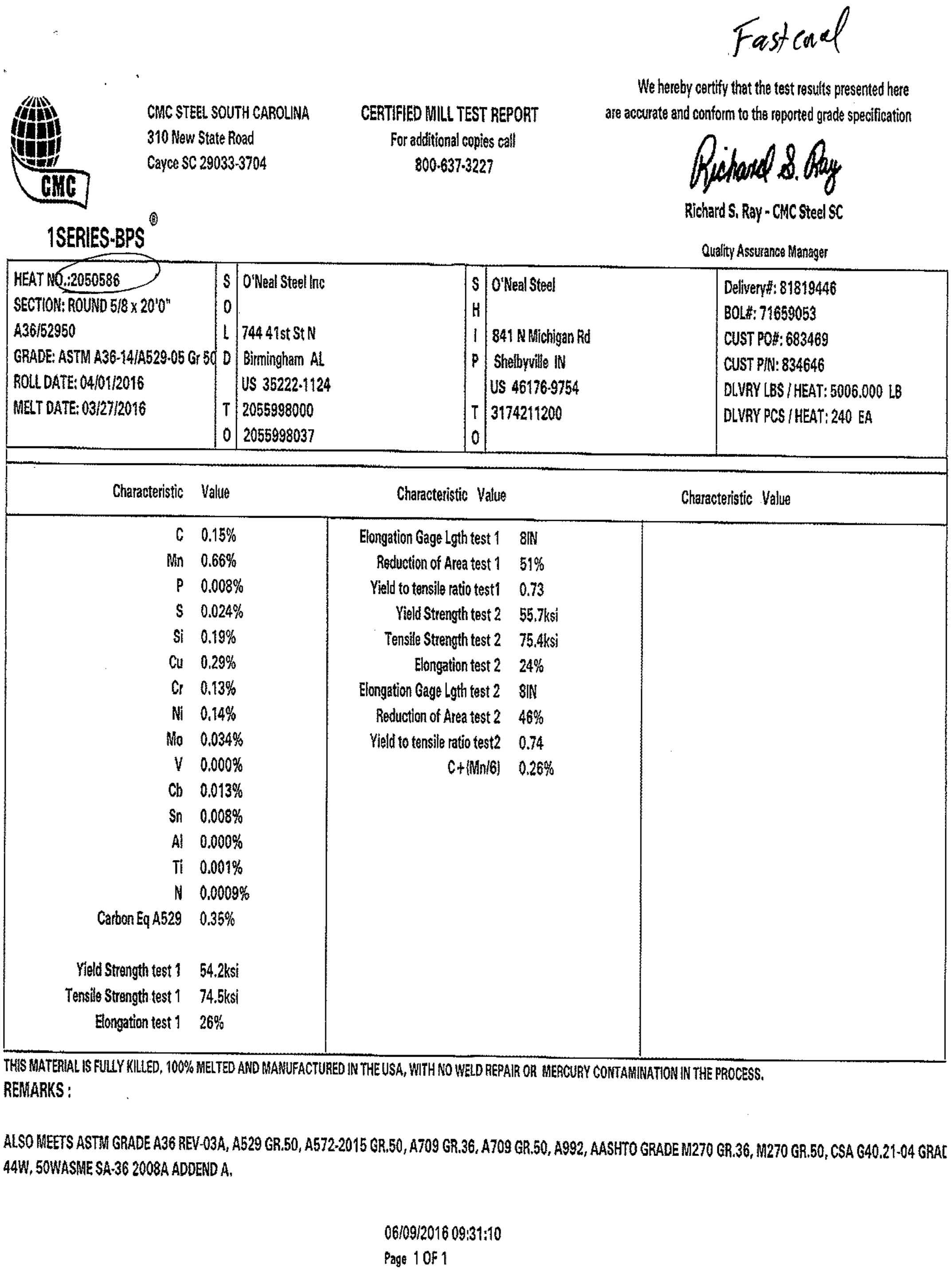

Fastcal

CMC

1SERIES-BPS®

CMC STEEL SOUTH CAROLINA
310 New State Road
Cayce SC 29033-3704

CERTIFIED MILL TEST REPORT
For additional copies call
800-637-3227

We hereby certify that the test results presented here are accurate and conform to the reported grade specification

Richard S. Ray
Richard S. Ray - CMC Steel SC
Quality Assurance Manager

HEAT NO.:2050586
SECTION: ROUND 5/8 x 20'0"
A36/52950
GRADE: ASTM A36-14/A529-05 Gr 50
ROLL DATE: 04/01/2016
MELT DATE: 03/27/2016

SOLD TO
O'Neal Steel Inc
744 41st St N
Birmingham AL
US 35222-1124
2055998000
2055998037

SHIP TO
O'Neal Steel
841 N Michigan Rd
Shelbyville IN
US 46176-9754
3174211200

Delivery#: 81819446
BOL#: 71659053
CUST PO#: 683469
CUST P/N: 834646
DLVRY LBS / HEAT: 5006.000 LB
DLVRY PCS / HEAT: 240 EA

Characteristic	Value	Characteristic	Value	Characteristic	Value
C	0.15%	Elongation Gage Lgth test 1	8IN		
Mn	0.66%	Reduction of Area test 1	51%		
P	0.008%	Yield to tensile ratio test1	0.73		
S	0.024%	Yield Strength test 2	55.7ksi		
Si	0.19%	Tensile Strength test 2	75.4ksi		
Cu	0.29%	Elongation test 2	24%		
Cr	0.13%	Elongation Gage Lgth test 2	8IN		
Ni	0.14%	Reduction of Area test 2	46%		
Mo	0.034%	Yield to tensile ratio test2	0.74		
V	0.000%	C+(Mn/6)	0.26%		
Cb	0.013%				
Sn	0.008%				
Al	0.000%				
Ti	0.001%				
N	0.0009%				
Carbon Eq A529	0.35%				
Yield Strength test 1	54.2ksi				
Tensile Strength test 1	74.5ksi				
Elongation test 1	26%				

THIS MATERIAL IS FULLY KILLED, 100% MELTED AND MANUFACTURED IN THE USA, WITH NO WELD REPAIR OR MERCURY CONTAMINATION IN THE PROCESS.

REMARKS :

ALSO MEETS ASTM GRADE A36 REV-03A, A529 GR.50, A572-2015 GR.50, A709 GR.36, A709 GR.50, A992, AASHTO GRADE M270 GR.36, M270 GR.50, CSA G40.21-04 GRAD
44W, 50WASME SA-36 2008A ADDEND A.

06/09/2016 09:31:10
Page 1 OF 1

46.5 in. long fully threaded rods used in other tests

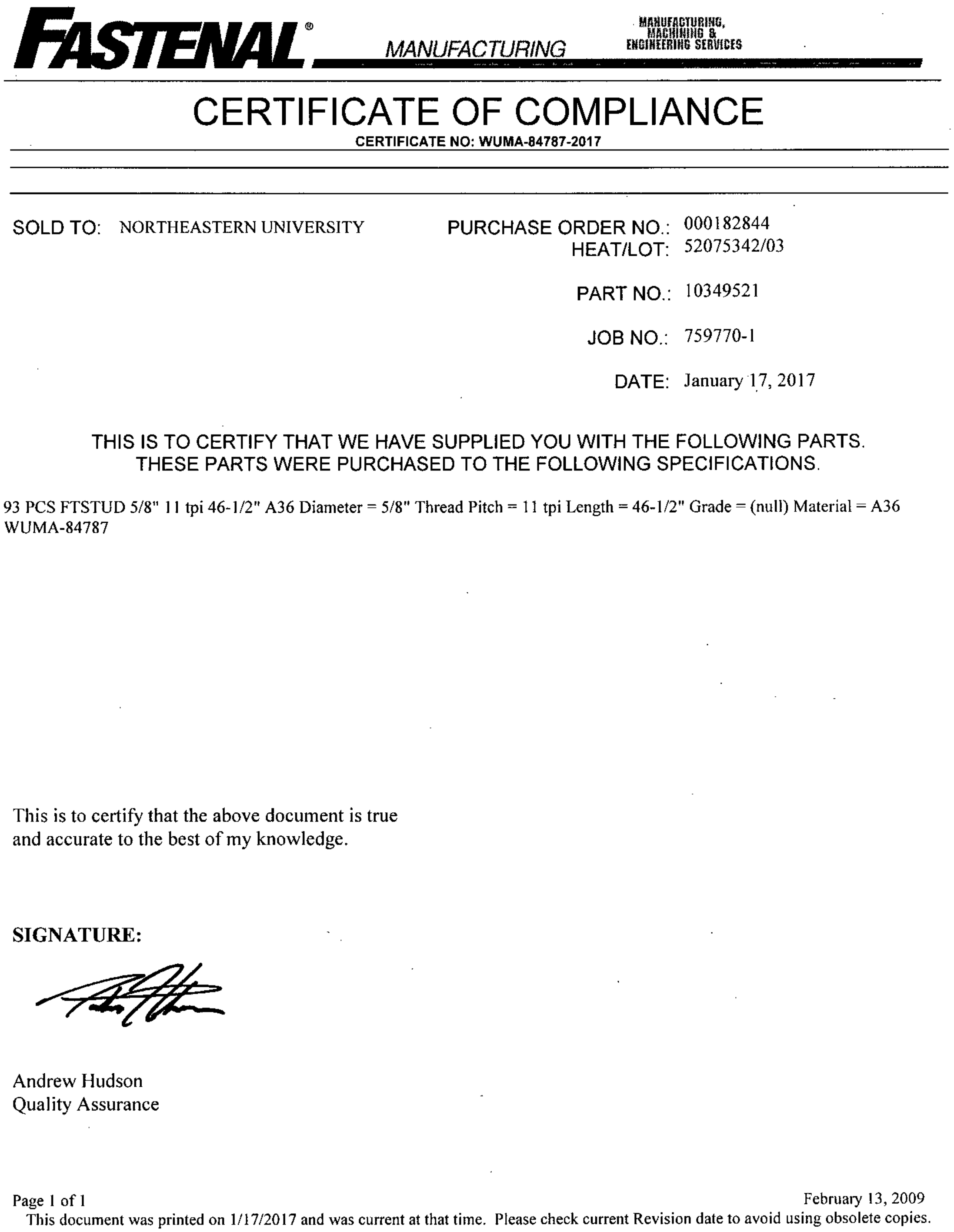

FASTENAL® MANUFACTURING

MANUFACTURING,
MACHINING &
ENGINEERING SERVICES

CERTIFICATE OF COMPLIANCE

CERTIFICATE NO: WUMA-84787-2017

SOLD TO: NORTHEASTERN UNIVERSITY

PURCHASE ORDER NO.: 000182844
HEAT/LOT: 52075342/03

PART NO.: 10349521

JOB NO.: 759770-1

DATE: January 17, 2017

THIS IS TO CERTIFY THAT WE HAVE SUPPLIED YOU WITH THE FOLLOWING PARTS.
THESE PARTS WERE PURCHASED TO THE FOLLOWING SPECIFICATIONS.

93 PCS FTSTUD 5/8" 11 tpi 46-1/2" A36 Diameter = 5/8" Thread Pitch = 11 tpi Length = 46-1/2" Grade = (null) Material = A36
WUMA-84787

This is to certify that the above document is true
and accurate to the best of my knowledge.

SIGNATURE:

Andrew Hudson
Quality Assurance

Page 1 of 1 February 13, 2009
This document was printed on 1/17/2017 and was current at that time. Please check current Revision date to avoid using obsolete copies.

```
                         .McNeilus Certification

 SOLD  0100325                              SHIPPED
   TO  FASTENAL GENERAL ACCOUNT                  TO Fastenal Company #1
       PO BOX 978                                   1801 Theuer Blvd
       WINONA, MN  55987-0978                       Winona, MN  55987



PART #                0902581                BOL:01988159-79817
SALES DESCRIPTION.............     GRADE  ITEM   ORDER  DATE SHIPPED  1/06/17
HR ROUND  9/16"          20'       A36    HR056 01987930 QTY SHIPPED    337.920
ASTM A36
CUSTOMER ORDER NO. 000182844                RELEASE                CONTRACT
VENDOR GERDAU AMERISTEEL US INC       MILL NO.              COUNTRY/ORIGIN CAN

HEAT NO. 52075342/03                   CHEMICAL ANALYSIS

C           MN          P           S           SI          CU          NI
   .1790       .7090       .0200      .0360       .1700       .3330      .0870

CR         MO          CB/NB       V           AL          N           TI
   .1330      .0330       .0000      .0003       .0000       .0000      .0000

                                 MECHANICAL / PHYSICAL PROPERTIES

ROCKWELL    TENSILE MN   YIELD MIN   ELONGATION  GRAIN SIZE  TENSILE     YIELD
  000             .000        .000         .00         .000  75.8040   53.6800

ELONGATION  GAUGE        TENSILE     ROCKWELL
 24.0000        .0000        .000         .000         .000  00000 000


>

WE CERTIFY THE ANALYSIS SHOWN ABOVE ARE TRUE AND EXACT AS CONTAINED
IN THE PERMANENT RECORDS OF    MCNEILUS STEEL, INC    .  THESE RECORDS MAY BE
EXAMINED BY YOUR PERSONNEL OR ANY AGENT AUTHORIZED BY YOU.
QUALITY MANAGER
TIM JOHNSTON

MCNEILUS STEEL, INC.
DODGE CENTER, MN
```

D.2.3 Halfen channels and bolts

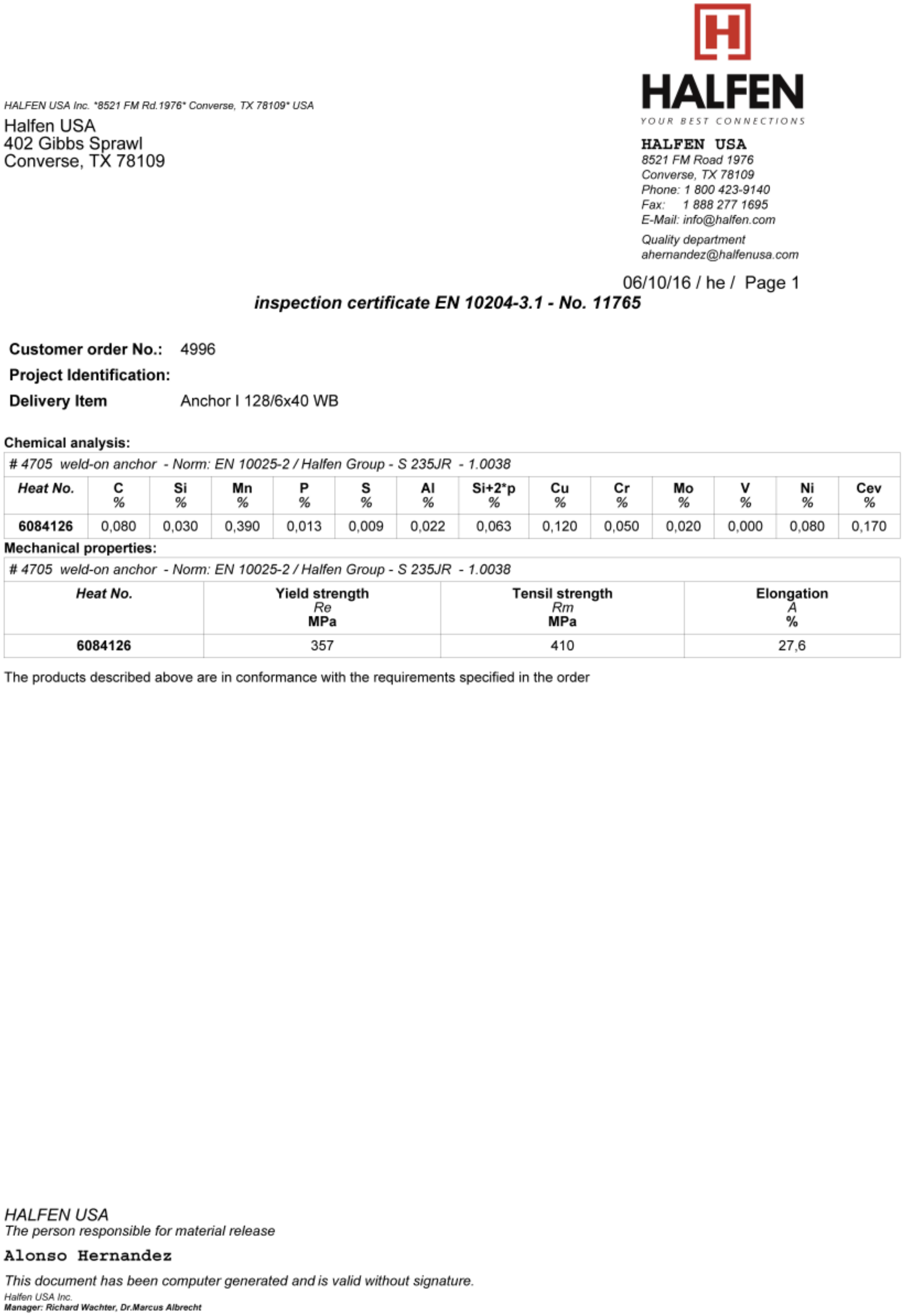

HALFEN USA Inc. *8521 FM Rd.1976* Converse, TX 78109* USA

Halfen USA
402 Gibbs Sprawl
Converse, TX 78109

HALFEN
YOUR BEST CONNECTIONS

HALFEN USA
8521 FM Road 1976
Converse, TX 78109
Phone: 1 800 423-9140
Fax: 1 888 277 1695
E-Mail: info@halfen.com

Quality department
ahernandez@halfenusa.com

06/10/16 / he / Page 1

inspection certificate EN 10204-3.1 - No. 11765

Customer order No.: 4996
Project Identification:
Delivery Item Anchor I 128/6x40 WB

Chemical analysis:

# 4705 weld-on anchor - Norm: EN 10025-2 / Halfen Group - S 235JR - 1.0038

Heat No.	**C** %	**Si** %	**Mn** %	**P** %	**S** %	**Al** %	**Si+2*p** %	**Cu** %	**Cr** %	**Mo** %	**V** %	**Ni** %	**Cev** %
6084126	0,080	0,030	0,390	0,013	0,009	0,022	0,063	0,120	0,050	0,020	0,000	0,080	0,170

Mechanical properties:

# 4705 weld-on anchor - Norm: EN 10025-2 / Halfen Group - S 235JR - 1.0038

Heat No.	**Yield strength** *Re* **MPa**	**Tensil strength** *Rm* **MPa**	**Elongation** *A* **%**
6084126	357	410	27,6

The products described above are in conformance with the requirements specified in the order

HALFEN USA
The person responsible for material release

Alonso Hernandez

This document has been computer generated and is valid without signature.
Halfen USA Inc.
Manager: Richard Wachter, Dr.Marcus Albrecht

HALFEN
YOUR BEST CONNECTIONS

Halfen GmbH

Liebigstraße 14
D- 40764 Langenfeld
Telefon: +49 (0) 2173/970-0
Telefax: +49 (0) 2173/970-123
Internet: www.halfen.com
E-Mail: info@halfen.com

Abteilung
Qualitätswesen / Quality department
Telefon: +49 (0) 2173/970-743
E-Mail: qs-langenfeld@halfen.de

Halfen GmbH * Postfach 1262 * D-40764 Langenfeld

Halfen USA
402 Gibbs Sprawl

78109 Converse, TX
UNITED STATES

04.01.16 / ba / Seite 1

Abnahmeprüfzeugnis nach EN 10204-3.1 - No. 10430
inspection certificate EN 10204-3.1

Kunden-Bestell-Nr./Customer order No.:	PO 047 P007700-1
Projekt-Kennung/Project Identification:	
Liefergegenstand/Delivery Item	HM 72/48-WB-6070
Loskennung/Lot-ID	5300L6965244
Loskennung/Lot-ID:	5300L6965245 Pos. 21
Auftrags-Nr	5300S253926

Chemische Analyse/Chemical analysis:

# 4840 Warm-Schienen/hot-rolled channel - Norm: EN 10025-2 / Halfen Group - S 235JR - 1.0038

Charge Heat No.	C %	Si %	Mn %	P %	S %	Al %	Si+2*p %	Cu %	Cr %	Mo %	V %	Ni %	Cev %
6090296	0,070	0,030	0,360	0,010	0,007	0,022	0,055	0,140	0,040	0,010	0,000	0,070	0,150

Mechanische Eigenschaften/Mechanical properties:

# 4840 Warm-Schienen/hot-rolled channel - Norm: EN 10025-2 / Halfen Group - S 235JR - 1.0038

Charge Heat No.	**Streckgrenze** *Yield strength* **Re MPa**	**Zugfestigkeit** *Tensil strength* **Rm MPa**	**Dehnung** *Elongation* **A %**
6090296	436	443	15,0

Das oben beschriebene Produkt ist konform mit den in der Bestellung festgelegten Anforderungen.
The products described above are conformal with the requirements specified in the order.

RECEIVED
FEB 08 2016
HALFEN USA

Halfen GmbH
Abnahmebeauftragter
inspection representative

i.V. Michael Dörner

Das Zeugnis ist maschinell erstellt und trägt keine Unterschrift
This document has been computer generated and is valid without signature.

Reg.-Nr.: 2499-CPR-0113070 Zertifikat-Nr.QS-281 HH

Halfen GmbH, AG Düsseldorf HRB 55272
USt-ID.Nr. DE 190725092, Steuer-Nr. 135/5732/1062
Geschäftsführung: Richard Wachter, Arjan J. Bakker
Commerzbank AG Langenfeld (BLZ 342 400 50), Konto Nr. 3 505 607
ING Bank N.V., Frankfurt (BLZ 500 210 00), Konto 0 010 141 778

Das Qualitätsmanagementsystem der Halfen GmbH ist für die Standorte in Deutschland, Frankreich, Österreich Polen, Schweiz, Niederlande und der Tschechischen Republik zertifiziert nach DIN EN ISO 9001:2008.

HALFEN
YOUR BEST CONNECTIONS

HALFEN USA
PO Box 547, 8521 FM 1976
Converse, Texas 78109
USA
Phone: (800) 423 9140
Fax: (877) 874 7923
Internet: www.halfenusa.com
E-Mail: info@halfenusa.com

CONCRETE - Anchoring Systems
FACADE - Fixing Systems
FRAMING - Products and Systems

EMail: ahernandez@halfenusa.com

Kostos Building/Northeastern
Univ.
141 S BEDFORD ST
BURLINGTON, MA 01803 5118

July 12, 2016

Acceptance Inspection Certificate M / 3.1

Customer PO No: Jerome 02-18-16
Delivery Item: Halfen HS 72/48 M20x100 GV-S (8.8) – Bolts and Nuts
Project Name: Northeastern University
Order: S023808

Chemical Analysis:

According to Standard: DIN ISO 8992, DIN EN ISO 898-1/-2

Charge Heat No:	C %	Si %	Mn %	P %	S %	Cr %	Mo %	B %	Ni %
153808	0.36	0.13	0.84	0.009	0.005	1.10	0.01	0.0018	0.05

Mechanical properties:

According to Standard: DIN ISO 8992, DIN EN ISO 898-1/-2

Charge Heat No.	Yield Point (Rp) MPa	Tensile strength (Rm) MPa	Elongation (A) %	Hardness HV	Coating µm
153808	824	910	14.9	292-302	18-22

The products described above are conformal with the requirements specified in the order. In addition we confirm that the test results fulfill the requirements specified in the order.

Halfen USA, Inc.
Alonso Hernandez- Operational Quality Manager

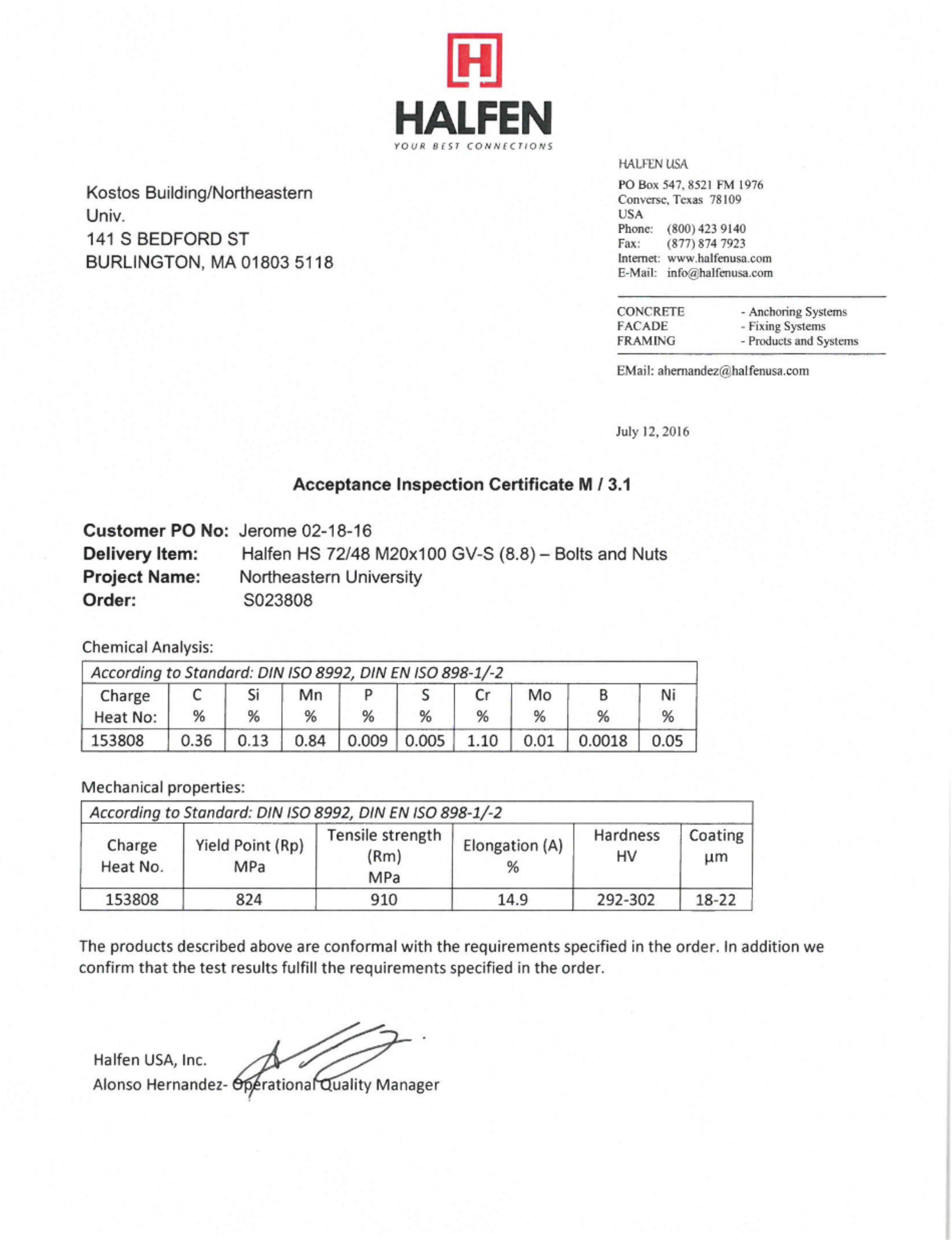

HALFEN
YOUR BEST CONNECTIONS

HALFEN USA
PO Box 547, 8521 FM 1976
Converse, Texas 78109
USA
Phone: (800) 423 9140
Fax: (877) 874 7923
Internet: www.halfenusa.com
E-Mail: info@halfenusa.com

CONCRETE	- Anchoring Systems
FACADE	- Fixing Systems
FRAMING	- Products and Systems

EMail: ahernandez@halfenusa.com

Kostos Building/Northeastern
Univ.
141 S BEDFORD ST
BURLINGTON, MA 01803 5118

July 12, 2016

Acceptance Inspection Certificate M / 3.1

Customer PO No: Jerome 02-18-16
Delivery Item: Halfen HS 72/48 M20x100 GV-S (8.8) – Bolts and Nuts
Project Name: Northeastern University
Order: S023808

Chemical Analysis:

According to Standard: DIN ISO 8992, DIN EN ISO 898-1/-2									
Charge Heat No:	C %	Si %	Mn %	P %	S %	Cr %	Mo %	B %	Ni %
153808	0.36	0.13	0.84	0.009	0.005	1.10	0.01	0.0018	0.05

Mechanical properties:

According to Standard: DIN ISO 8992, DIN EN ISO 898-1/-2					
Charge Heat No.	Yield Point (Rp) MPa	Tensile strength (Rm) MPa	Elongation (A) %	Hardness HV	Coating µm
153808	824	910	14.9	292-302	18-22

The products described above are conformal with the requirements specified in the order. In addition we confirm that the test results fulfill the requirements specified in the order.

Halfen USA, Inc.
Alonso Hernandez- Operational Quality Manager

D.2.4 Lindapter clamps and washers

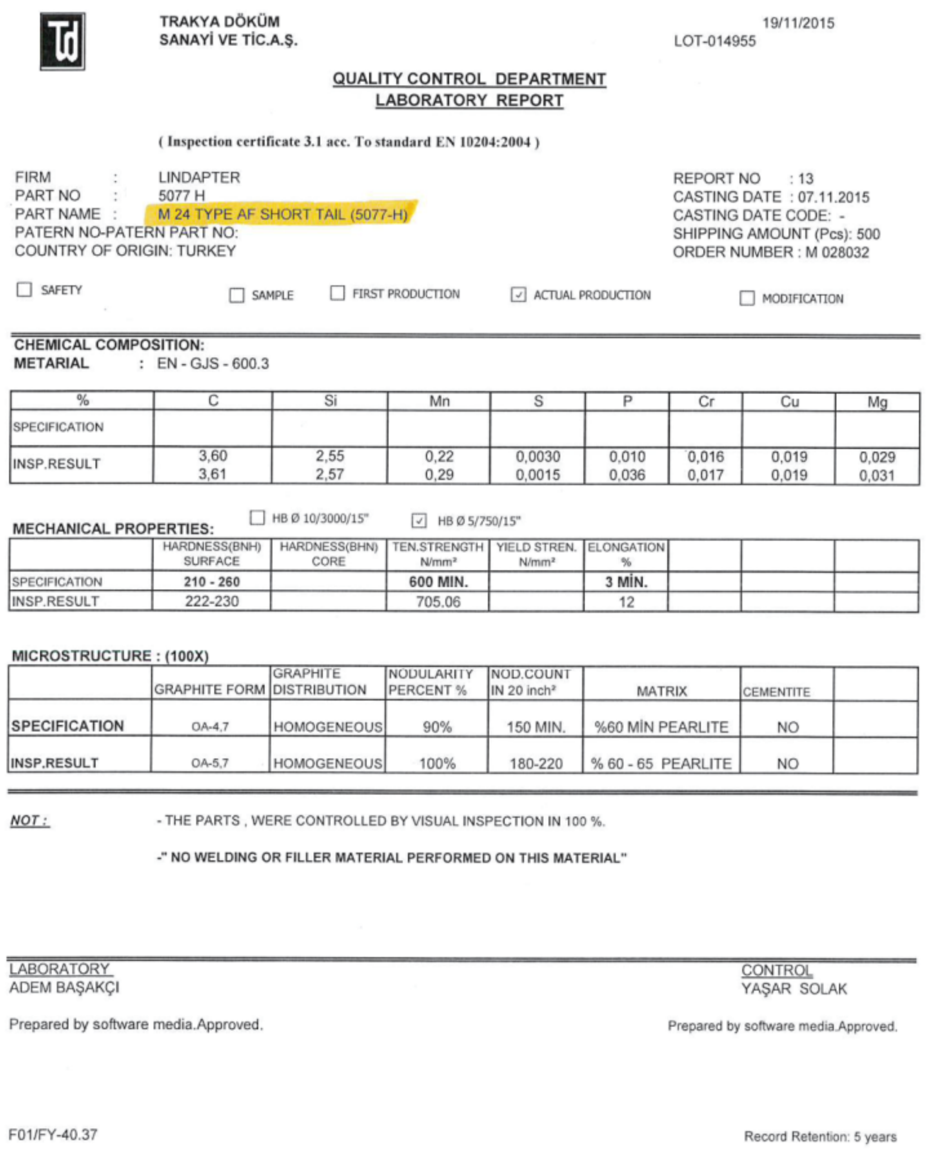

TRAKYA DÖKÜM
SANAYİ VE TİC.A.Ş.

19/11/2015
LOT-014955

QUALITY CONTROL DEPARTMENT
LABORATORY REPORT

(Inspection certificate 3.1 acc. To standard EN 10204:2004)

FIRM : LINDAPTER
PART NO : 5077 H
PART NAME : M 24 TYPE AF SHORT TAIL (5077-H)
PATERN NO-PATERN PART NO:
COUNTRY OF ORIGIN: TURKEY

REPORT NO : 13
CASTING DATE : 07.11.2015
CASTING DATE CODE: -
SHIPPING AMOUNT (Pcs): 500
ORDER NUMBER : M 028032

☐ SAFETY ☐ SAMPLE ☐ FIRST PRODUCTION ☑ ACTUAL PRODUCTION ☐ MODIFICATION

CHEMICAL COMPOSITION:
METARIAL : EN - GJS - 600.3

%	C	Si	Mn	S	P	Cr	Cu	Mg
SPECIFICATION								
INSP.RESULT	3,60 3,61	2,55 2,57	0,22 0,29	0,0030 0,0015	0,010 0,036	0,016 0,017	0,019 0,019	0,029 0,031

MECHANICAL PROPERTIES: ☐ HB Ø 10/3000/15" ☑ HB Ø 5/750/15"

	HARDNESS(BNH) SURFACE	HARDNESS(BHN) CORE	TEN.STRENGTH N/mm²	YIELD STREN. N/mm²	ELONGATION %			
SPECIFICATION	**210 - 260**		**600 MIN.**		**3 MİN.**			
INSP.RESULT	222-230		705.06		12			

MICROSTRUCTURE : (100X)

	GRAPHITE FORM	GRAPHITE DISTRIBUTION	NODULARITY PERCENT %	NOD.COUNT IN 20 inch²	MATRIX	CEMENTITE	
SPECIFICATION	OA-4,7	HOMOGENEOUS	90%	150 MIN.	%60 MİN PEARLITE	NO	
INSP.RESULT	OA-5,7	HOMOGENEOUS	100%	180-220	% 60 - 65 PEARLITE	NO	

NOT : - THE PARTS , WERE CONTROLLED BY VISUAL INSPECTION IN 100 %.

-" NO WELDING OR FILLER MATERIAL PERFORMED ON THIS MATERIAL"

LABORATORY
ADEM BAŞAKÇI

Prepared by software media.Approved.

CONTROL
YAŞAR SOLAK

Prepared by software media.Approved.

F01/FY-40.37

Record Retention: 5 years

TRAKYA DÖKÜM
SANAYİ VE TİC.A.Ş.

30/09/2015
LOT-014623

QUALITY CONTROL DEPARTMENT
LABORATORY REPORT

(Inspection certificate 3.1 acc. To standard EN 10204:2004)

FIRM : LINDAPTER
PART NO : 5077 H
PART NAME : M 24 TYPE AF SHORT TAIL (5077-H)
PATERN NO-PATERN PART NO:
COUNTRY OF ORIGIN: TURKEY

REPORT NO : 10
CASTING DATE : 05.09.2015
CASTING DATE CODE:
SHIPPING AMOUNT (Pcs): 500
ORDER NUMBER : M 027957

☐ SAFETY ☐ SAMPLE ☐ FIRST PRODUCTION ☑ ACTUAL PRODUCTION ☐ MODIFICATION

CHEMICAL COMPOSITION:
METARIAL : EN - GJS - 600.3

%	C	Si	Mn	S	P	Cr	Cu	Mg
SPECIFICATION								
INSP.RESULT	3,62	2,58	0,24	0,0028	0,031	0,016	0,046	0,028

MECHANICAL PROPERTIES: ☐ HB Ø 10/3000/15" ☑ HB Ø 5/750/15"

	HARDNESS(BNH) SURFACE	HARDNESS(BHN) CORE	TEN.STRENGTH N/mm²	YIELD STREN. N/mm²	ELONGATION %			
SPECIFICATION	**210 - 260**		**600 MIN.**		**3 MİN.**			
INSP.RESULT	223-229		705.06		12			

MICROSTRUCTURE : (100X)

	GRAPHITE FORM	GRAPHITE DISTRIBUTION	NODULARITY PERCENT %	NOD.COUNT IN 20 inch²	MATRIX	CEMENTITE	
SPECIFICATION	OA-4,7	HOMOGENEOUS	90%	150 MIN.	%60 MİN PEARLITE	NO	
INSP.RESULT	OA-5,7	HOMOGENEOUS	100%	180-220	% 60 - 65 PEARLITE	NO	

NOT : - THE PARTS , WERE CONTROLLED BY VISUAL INSPECTION IN 100 %.

-" NO WELDING OR FILLER MATERIAL PERFORMED ON THIS MATERIAL"

LABORATORY
ADEM BAŞAKÇI

Prepared by software media.Approved.

CONTROL
YAŞAR SOLAK

Prepared by software media.Approved.

F01/FY-40.37

Record Retention: 5 years

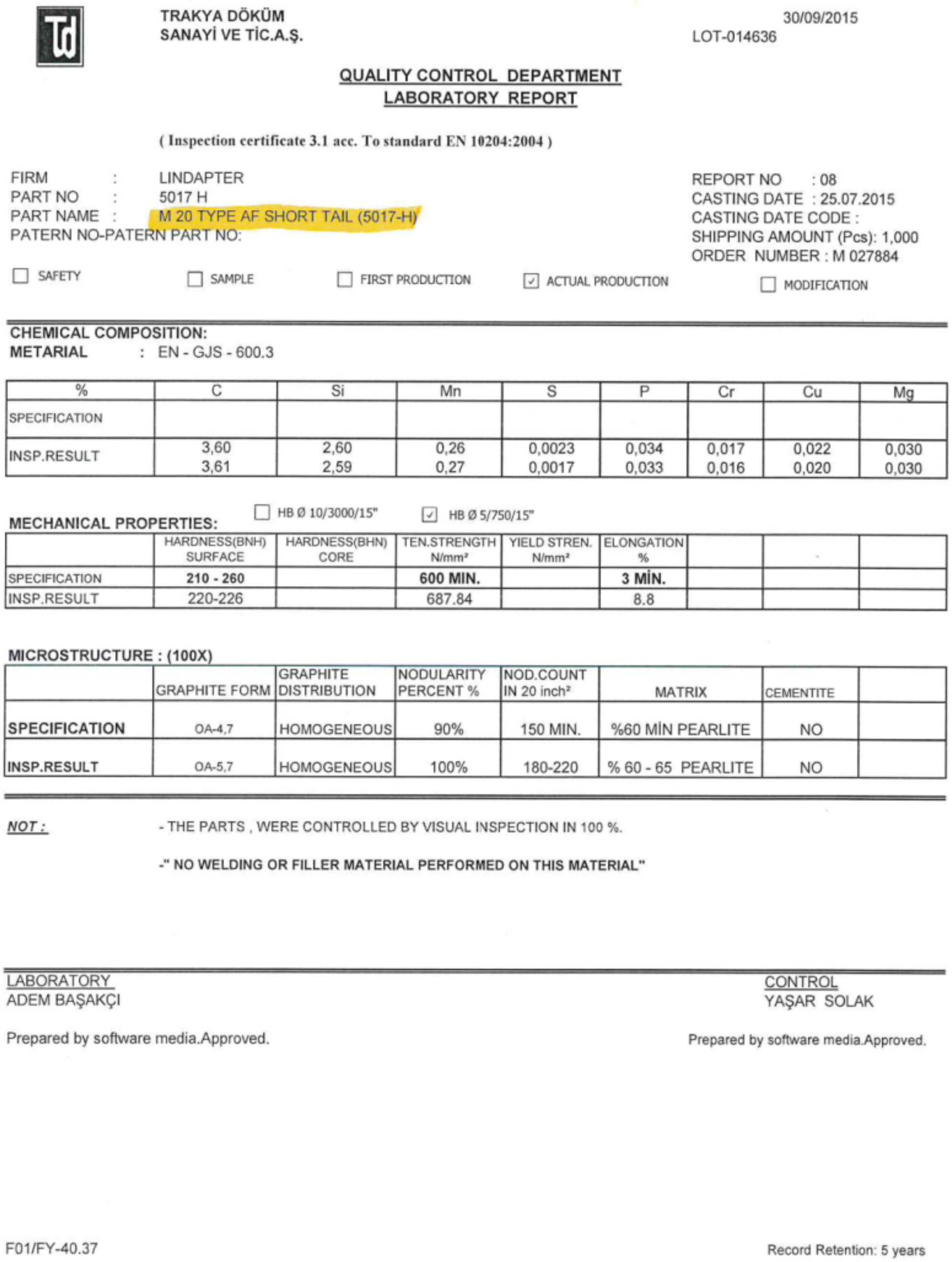

TRAKYA DÖKÜM
SANAYİ VE TİC.A.Ş.

30/09/2015
LOT-014636

QUALITY CONTROL DEPARTMENT
LABORATORY REPORT

(Inspection certificate 3.1 acc. To standard EN 10204:2004)

FIRM : LINDAPTER
PART NO : 5017 H
PART NAME : M 20 TYPE AF SHORT TAIL (5017-H)
PATERN NO-PATERN PART NO:

REPORT NO : 08
CASTING DATE : 25.07.2015
CASTING DATE CODE :
SHIPPING AMOUNT (Pcs): 1,000
ORDER NUMBER : M 027884

☐ SAFETY ☐ SAMPLE ☐ FIRST PRODUCTION ☑ ACTUAL PRODUCTION ☐ MODIFICATION

CHEMICAL COMPOSITION:
METARIAL : EN - GJS - 600.3

%	C	Si	Mn	S	P	Cr	Cu	Mg
SPECIFICATION								
INSP.RESULT	3,60 3,61	2,60 2,59	0,26 0,27	0,0023 0,0017	0,034 0,033	0,017 0,016	0,022 0,020	0,030 0,030

MECHANICAL PROPERTIES: ☐ HB Ø 10/3000/15" ☑ HB Ø 5/750/15"

	HARDNESS(BNH) SURFACE	HARDNESS(BHN) CORE	TEN.STRENGTH N/mm²	YIELD STREN. N/mm²	ELONGATION %			
SPECIFICATION	**210 - 260**		**600 MIN.**		**3 MİN.**			
INSP.RESULT	220-226		687.84		8.8			

MICROSTRUCTURE : (100X)

	GRAPHITE FORM	GRAPHITE DISTRIBUTION	NODULARITY PERCENT %	NOD.COUNT IN 20 inch²	MATRIX	CEMENTITE	
SPECIFICATION	OA-4,7	HOMOGENEOUS	90%	150 MIN.	%60 MİN PEARLITE	NO	
INSP.RESULT	OA-5,7	HOMOGENEOUS	100%	180-220	% 60 - 65 PEARLITE	NO	

NOT : - THE PARTS , WERE CONTROLLED BY VISUAL INSPECTION IN 100 %.

-" NO WELDING OR FILLER MATERIAL PERFORMED ON THIS MATERIAL"

LABORATORY
ADEM BAŞAKÇI

Prepared by software media.Approved.

CONTROL
YAŞAR SOLAK

Prepared by software media.Approved.

F01/FY-40.37

Record Retention: 5 years

Lot · 015128   B-027303   8·1·16

3.1 Material Test Certificate

Quality : S275JR , C,Pickled,MEDIUM/NORMAL OILING ,Skinpassed **Milden Steels Ltd**

Thickness:	6.00	**Net Weight:**	18.240	**Width:**	1253.0
Internal Diameter:	762	**Specification Name:**	BSEN10025-2:2004	**Specification Grade:**	S275JR+AR
Edge Condition:	MILL EDGE	**Branding:**	Yes	**Linear Meterage**	386

Mechanical Details

Rockwell B Result		Yield Stress	328
Tensile Stress	493	Elongation 80mm	27

Cast Analysis

C	0.1460	Si	0.0060	Mn	0.8550	P	0.0130	S	0.0100	Cr	0.0220	Mo	0.0010
Ni	0.0200	T.Al	0.0470	As	0.0010	B	0.0002	Co	0.0060	Cu	0.0210	N	0.0037
Nb	0.0010	Pb		Sn	0.0020	Ti	0.0010	V	0.0020	W		Zr	
Al Sol	0.0430	Cd		CaO		H		Fe		FeO		MnO	

AFW20 -GRN 27222

PAGE 1

WATERHOUSE PRESSINGS MANUFACTURING LTD WP21

L, I: 014827 13.11.18

Certificate of
Conformance

Precision Pressing for Industry
SNAYGILL IND ESTATE, SKIPTON, NORTH YORKSHIRE BD23 2QR
Telephone : Skipton (01756-794577/8) Fax : (01756-701481)

E-mail : paul@waterhousepressings.co.uk ------ WEBSITE : http://www.waterhousepressings.co.uk

CHARACTERISTIC	Upper tol	Lower tol	1st sample	2nd sample	3rd sample			High-Ok-Lo
Hole	26.00	minimum	26.49	26.48	26.50			OK
Thickness	10.50	10.00	10.10	10.10	10.12			OK
Stamp								
Visual Deep								OK
Burrs minimal								OK

Batch quantity	2,057	3 Samples		visual	1 stillage			Compiled by
								W.P.M Ltd

SPEC NO	10539	CUSTOMER	Lindapter International	
ORDER NOs	B-027445	CUSTOMER NO	N/A	
PART NUMBER	AFW24U	ISSUE LEVEL	2	
INSPECTION Lvl	ZERO DEFECT	DRAWING NUMBER	LSTD - 2791	

FAULTS FOUND	DEVIATIONS & REASON	AS DISCUSSED

CONCESSION NUMBER	GIVEN BY		
REF NUMBER			

INSPECTION CARRIED OUT BY : PAUL WATERHOUSE	
DATE: 13.11.15	APPROVED BY : PAUL WATERHOUSE

Made in UK________________________________

CELSA STEEL UK
OFFICES: Build. 58, Castle Works, East Moors Road
CF24 5NN Cardiff (United Kingdom)

CELSA GROUP CELSA MANUFACTURING UK

CARES QUALITY SYSTEMS ISO 9001 2008
UKAS 7100

CE

INSPECTION CERTIFICATE
BS-EN 10204-2004, Type 3.1

Standard
BS-EN 10025-2004

Customer

Destination:

Delivery number:25942570
Order number :15643932
Your order :001723

MATERIAL Hot rolled structural steel products	CAST	C %	MN %	SI %	S %	P %	Cr %	N %	NI %	Cu %	Mo %	V %	CE %	Reh MPA	Rm MPA	A 5.65 %	T °C	Rea1 J	Rea2 J	Rea3 J	Rea Av J
S 275 JR +AR 300X10 L.6.0m	CM094111	0.10	0.57	0.15	0.034	0.026	0.100	0.010	0.12	0.39	0.019	0.000	0.249	322	454	36.9					
S 275 JR +AR 50X10 6m	CM094194	0.12	0.53	0.15	0.029	0.023	0.099	0.011	0.16	0.43	0.025	0.000	0.271	343	486	42.7					
S 275 JR +AR 50X10 6m	CM094194	0.12	0.53	0.15	0.029	0.023	0.099	0.011	0.16	0.43	0.025	0.000	0.271	342	483	42.7					
S 275 JR -AR 50X10 6m	CM094194	0.12	0.53	0.15	0.029	0.023	0.099	0.011	0.16	0.43	0.025	0.000	0.271	342	478	42.1					
S 275 JR +AR 50X10 6m	CM094194	0.12	0.53	0.15	0.029	0.023	0.099	0.011	0.16	0.43	0.025	0.000	0.271	341	484	42.1					
S 275 JR -AR 50X12 6m	CM094195	0.09	0.51	0.16	0.028	0.020	0.096	0.011	0.16	0.44	0.022	0.000	0.239	335	462	40.7					
S 275 JR +AR 50X12 6m	CM094195	0.09	0.51	0.16	0.028	0.020	0.096	0.011	0.16	0.44	0.022	0.000	0.239	336	462	4070					

The materials has been evaluated and radiation is within national limits
Product suitable for galvanizing: 0.14<=Si<=0.25 & P<=0.035.

Steel making process -
Electric arc

Certified that the material detailed hereon meets the
requirements of the specified standard.
Cardiff, 17.09.2014

Stuart Thomas
Quality Manager

LOT: 014827

AFC0244

PAGE 2.

D.2.5 Reinforcement

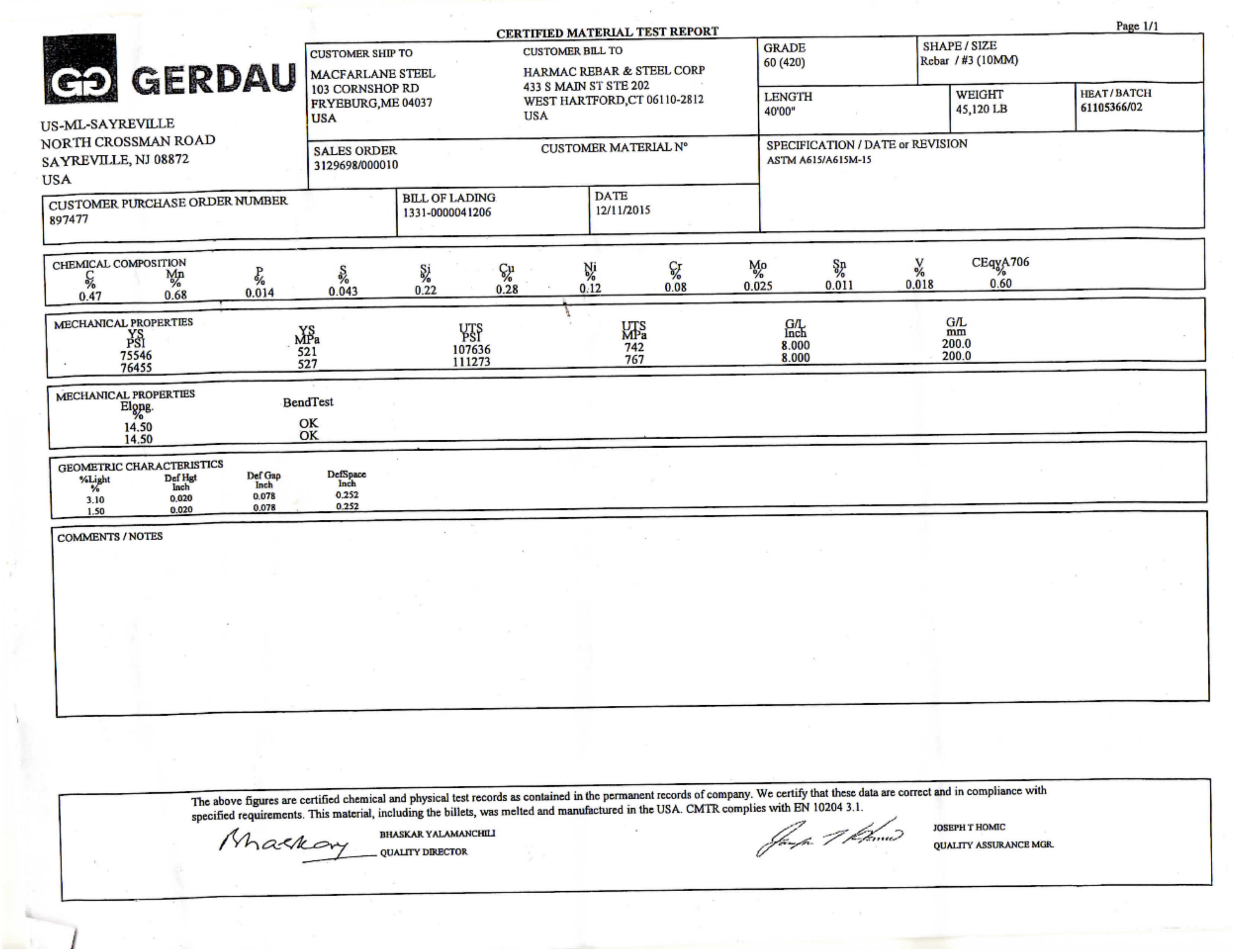

Page 1/1

CERTIFIED MATERIAL TEST REPORT

GERDAU

US-ML-SAYREVILLE
NORTH CROSSMAN ROAD
SAYREVILLE, NJ 08872
USA

CUSTOMER SHIP TO
MACFARLANE STEEL
103 CORNSHOP RD
FRYEBURG,ME 04037
USA

CUSTOMER BILL TO
HARMAC REBAR & STEEL CORP
433 S MAIN ST STE 202
WEST HARTFORD,CT 06110-2812
USA

GRADE 60 (420)	SHAPE / SIZE Rebar / #3 (10MM)	
LENGTH 40'00"	WEIGHT 45,120 LB	HEAT / BATCH 61105366/02

SALES ORDER
3129698/000010

CUSTOMER MATERIAL N°

SPECIFICATION / DATE or REVISION
ASTM A615/A615M-15

CUSTOMER PURCHASE ORDER NUMBER	BILL OF LADING	DATE
897477	1331-0000041206	12/11/2015

CHEMICAL COMPOSITION

C %	Mn %	P %	S %	Si %	Cu %	Ni %	Cr %	Mo %	Sn %	V %	CEqyA706 %
0.47	0.68	0.014	0.043	0.22	0.28	0.12	0.08	0.025	0.011	0.018	0.60

MECHANICAL PROPERTIES

YS PSI	YS MPa	UTS PSI	UTS MPa	G/L Inch	G/L mm
75546	521	107636	742	8.000	200.0
76455	527	111273	767	8.000	200.0

MECHANICAL PROPERTIES

Elong. %	BendTest
14.50	OK
14.50	OK

GEOMETRIC CHARACTERISTICS

%Light %	Def Hgt Inch	Def Gap Inch	DefSpace Inch
3.10	0.020	0.078	0.252
1.50	0.020	0.078	0.252

COMMENTS / NOTES

The above figures are certified chemical and physical test records as contained in the permanent records of company. We certify that these data are correct and in compliance with specified requirements. This material, including the billets, was melted and manufactured in the USA. CMTR complies with EN 10204 3.1.

BHASKAR YALAMANCHILI
QUALITY DIRECTOR

JOSEPH T HOMIC
QUALITY ASSURANCE MGR.

Welcome BROCKIE.GERRY@AHHARRIS.COM

03/15/16 Nucor Announces Guidance For Its First Quarter Earnings

Click here to complete Nucor's online credit application

HOME | SIGN OUT

NUCOR | PRODUCTS | MY ACCOUNT | REPORTS | ANNOUNCEMENTS | Safety First NO ONE GETS HURT ON OUR SHIFT TODAY.

MILL CERTIFICATION DETAILS

Cart: 1
CONTINUE SHOPPING

PDF VERSION | EMAIL REPORT

<< Return To Search

Request Original Mill Certificate

Purchase Order #:	901011	**Heat #:**	AU15106921
Customer:	HARMAC REBAR & STEEL CORP - OSSIPEE	**Customer Part #:**	
Bill of Lading :	468204	**.Length:**	40'0"
Certified By :	Jim Biernat	**Date:**	11/24/2015
Lot #:	AU1510692101	**Tag #:**	AU1511136961
Grade:	ASTM A615/A615M-14 GR 60[420] AASHTO M31-07	**Size :**	# 4(13) RS
Melt Date :	11/24/2015	**Divison :**	NSAU-Auburn, NY
Qty Shipped LBS:	59745	**Qty Shipped PCS :**	2236
Comments:		**Roll Date :**	11/25/2015

Chemical Properties -Wt.%

C	Mn	Si	S	P	Cu	Cr	Ni	Mo
0.39	1.02	0.22	0.066	0.026	0.36	0.22	0.15	0.039
V	Nb							
0.0020	0.001							

Physical Properties

	Imperial-psi
Tensile:	96800
Yield:	66500
Elongation (in 8 inches):	15.5
Elongation (in 2 inches):	
Bend Test:	OK

Carbon Equiv:

I hereby certify that the material described herein has been manufactured in accordance with the specification and standards listed above and that it satisfies those requirements. All melting and manufacturing process were performed in the United States of America unless otherwise noted on the mill test report.

Jim P. Biernat
Chief Metallurgist

HOME | LOCATIONS | PRIVACY POLICY | TERMS & CONDITIONS | CAREERS | FAQ | SIGN OUT

© 2014 Nucor Corporation

NUCOR
NUCOR STEEL CONNECTICUT, INC.

Mill Certification
4/4/2016

MTR #: W1-179556
35 Toelles Road
WALLINGFORD, CT 06492
(203) 265-0615
Fax: (203) 284-8125

Sold To: HARMAC REBAR & STEEL CORP
CORP CENTER W
433 S MAIN ST
STE 202
W HARTFORD, CT 06110
(207) 935-3531

Ship To: HARMAC REBAR-REBAR
CORNSHOP ROAD
FRYEBURG, ME 04037
(207) 935-3531

Customer P.O.	907606		
Product Group	Rebar	Sales Order	233429.2
Grade	ASTM A615-16 / A706-16 & AASHTO M 31-15 Gr 60	Part Number	95013276CT46000
Size	#4 Rebar (Coil)	Lot #	WL1690001840
Product	#4 Rebar A615/A706 GR60 625X420	Heat #	JK16100307
Description	A615/A706 GR60 (CT2)	B.L. Number	W1-477579
Customer Spec		Load Number	W1-179556
		Customer Part #	

I hereby certify that the material described herein has been manufactured in accordance with the specifications and standards listed above and that it satisfies those requirements.

Melt Date: 1/22/2016

C	Mn	P	S	Si	Cu	Ni	Cr	Mo	V	Cb	Sn
0.26% CEA706 0.47%	1.15%	0.030%	0.035%	0.24%	0.28%	0.09%	0.14%	0.020%	0.0420%	0.002%	0.012%

CEA706: A706 CARBON EQUIVALENT

Roll Date: 3/24/2016

Yield 1: 67,100psi
Bend OK

Tensile 1: 98,850psi
Tensile/Yield: 1.47

Elongation: 16.3% in 8"(% in 203.3mm)

Specification Comments:

1. Except where noted, all manufacturing processes including melting were performed in the USA.
2. No mercury, mercury compounds or mercury containing devices came into contact with this product.
3. Weld repair was not performed on this material.
4. Hexavalent Chromium, Radium or Alpha Source materials in in any form were not used in the production or testing of this material

Charlie Hyatt
Division Metallurgist

D.2.6 Concrete

Pour 1

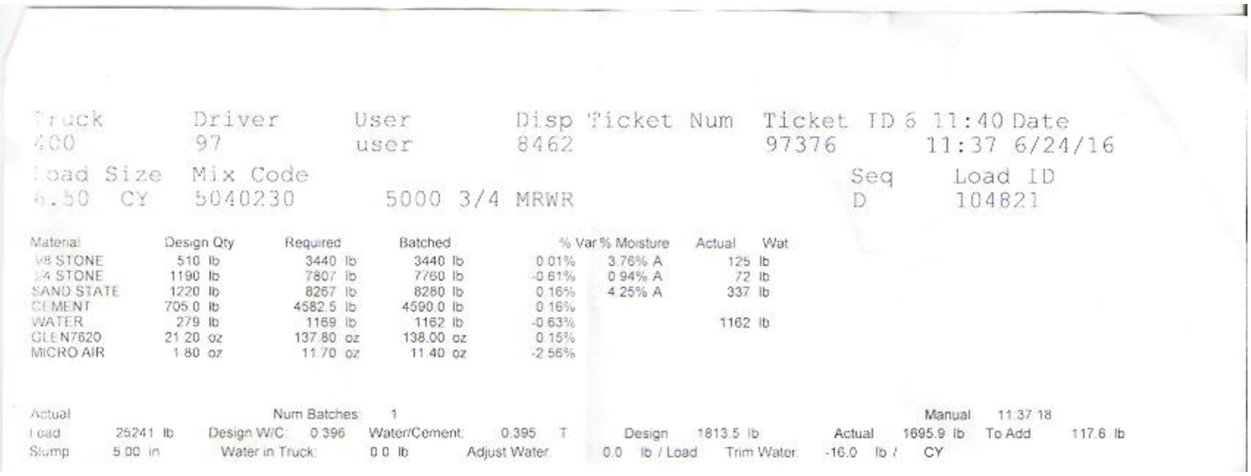

Truck	Driver	User	Disp Ticket Num	Ticket ID 6	11:40 Date
400	97	user	8462	97376	11:37 6/24/16

Load Size	Mix Code		Seq	Load ID
6.50 CY	5040230	5000 3/4 MRWR	D	104821

Material	Design Qty	Required	Batched	% Var	% Moisture	Actual Wat
3/8 STONE	510 lb	3440 lb	3440 lb	0.01%	3.76% A	125 lb
3/4 STONE	1190 lb	7807 lb	7760 lb	-0.61%	0.94% A	72 lb
SAND STATE	1220 lb	8267 lb	8280 lb	0.16%	4.25% A	337 lb
CEMENT	705.0 lb	4582.5 lb	4590.0 lb	0.16%		
WATER	279 lb	1169 lb	1162 lb	-0.63%		1162 lb
GLEN7620	21.20 oz	137.80 oz	138.00 oz	0.15%		
MICRO AIR	1.80 oz	11.70 oz	11.40 oz	-2.56%		

Actual Num Batches: 1 Manual 11:37:18

Load 25241 lb Design W/C: 0.396 Water/Cement: 0.395 T Design 1813.5 lb Actual 1695.9 lb To Add 117.6 lb

Slump 5.00 in Water in Truck: 0.0 lb Adjust Water: 0.0 lb / Load Trim Water: -16.0 lb / CY

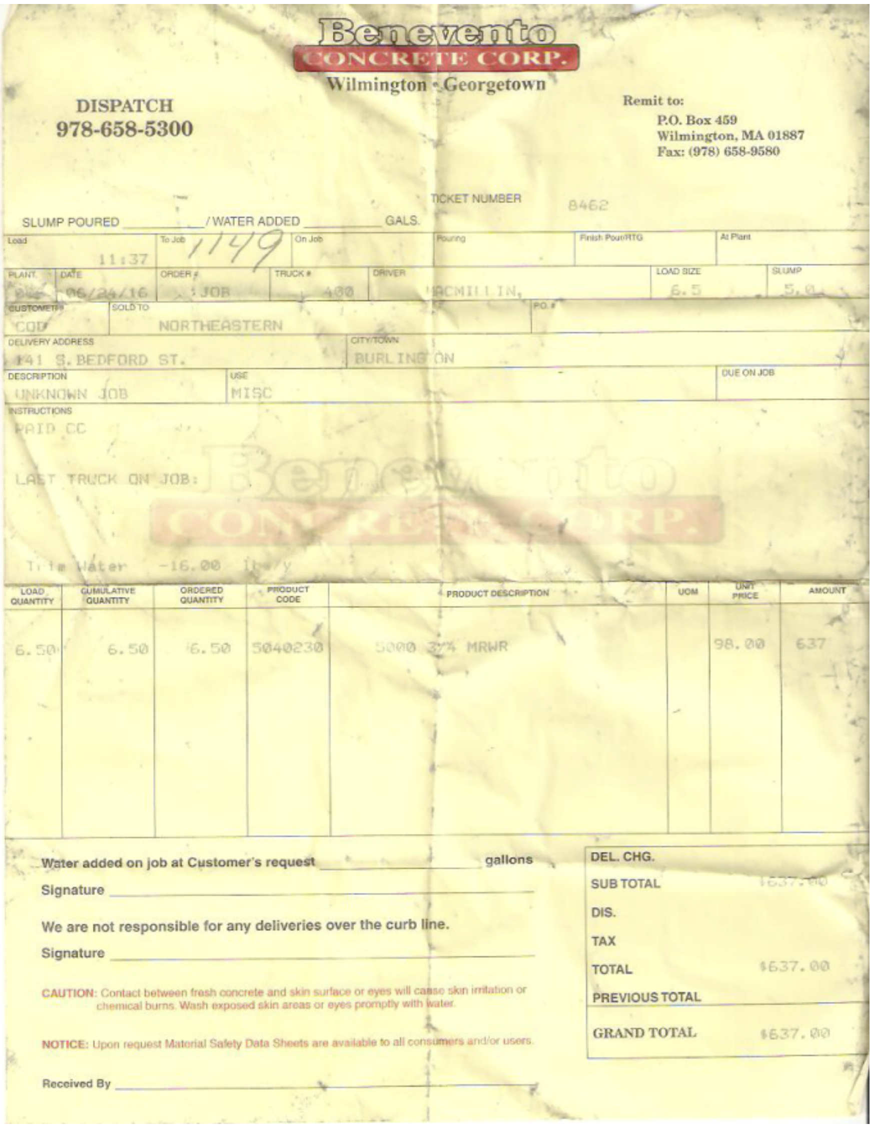

Benevento
CONCRETE CORP.
Wilmington • Georgetown

DISPATCH
978-658-5300

Remit to:
P.O. Box 459
Wilmington, MA 01887
Fax: (978) 658-9580

TICKET NUMBER 8462

SLUMP POURED ________/ WATER ADDED ________ GALS.

Load	To Job	On Job	Pouring	Finish Pour/RTG	At Plant
11:37	1149				

PLANT	DATE	ORDER #	TRUCK #	DRIVER	LOAD SIZE	SLUMP
04	06/24/16	JOB	400	MACMILLIN,	6.5	5.0

CUSTOMER #	SOLD TO	P.O. #
COD	NORTHEASTERN	

DELIVERY ADDRESS	CITY/TOWN
141 S.BEDFORD ST.	BURLINGTON

DESCRIPTION	USE	DUE ON JOB
UNKNOWN JOB	MISC	

INSTRUCTIONS
PAID CC

LAST TRUCK ON JOB:

Trim Water -16.00 lbs/y

LOAD QUANTITY	CUMULATIVE QUANTITY	ORDERED QUANTITY	PRODUCT CODE	PRODUCT DESCRIPTION	UOM	UNIT PRICE	AMOUNT
6.50	6.50	6.50	5040230	5000 3/4 MRWR		98.00	637

Water added on job at Customer's request ________ gallons

Signature ________

We are not responsible for any deliveries over the curb line.

Signature ________

CAUTION: Contact between fresh concrete and skin surface or eyes will cause skin irritation or chemical burns. Wash exposed skin areas or eyes promptly with water.

NOTICE: Upon request Material Safety Data Sheets are available to all consumers and/or users.

Received By ________

DEL. CHG.	
SUB TOTAL	$637.00
DIS.	
TAX	
TOTAL	$637.00
PREVIOUS TOTAL	
GRAND TOTAL	$637.00

a

Pour 2

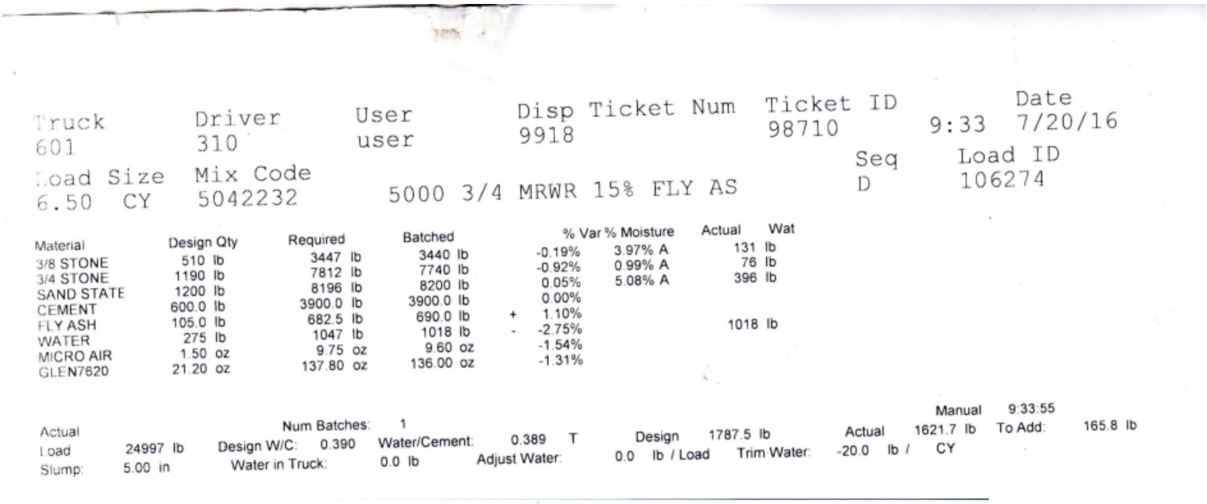

Truck	Driver	User	Disp Ticket Num	Ticket ID		Date
601	310	user	9918	98710	9:33	7/20/16

Load Size	Mix Code		Seq	Load ID
6.50 CY	5042232	5000 3/4 MRWR 15% FLY AS	D	106274

Material	Design Qty	Required	Batched		% Var	% Moisture	Actual Wat
3/8 STONE	510 lb	3447 lb	3440 lb		-0.19%	3.97% A	131 lb
3/4 STONE	1190 lb	7812 lb	7740 lb		-0.92%	0.99% A	76 lb
SAND STATE	1200 lb	8196 lb	8200 lb		0.05%	5.08% A	396 lb
CEMENT	600.0 lb	3900.0 lb	3900.0 lb		0.00%		
FLY ASH	105.0 lb	682.5 lb	690.0 lb	+	1.10%		
WATER	275 lb	1047 lb	1018 lb	-	-2.75%		1018 lb
MICRO AIR	1.50 oz	9.75 oz	9.60 oz		-1.54%		
GLEN7620	21.20 oz	137.80 oz	136.00 oz		-1.31%		

Manual 9:33:55

Actual Load 24997 lb

Slump: 5.00 in

Num Batches: 1

Design W/C: 0.390

Water in Truck: 0.0 lb

Water/Cement: 0.389 T

Adjust Water: 0.0 lb / Load

Design 1787.5 lb

Trim Water: -20.0 lb / CY

Actual 1621.7 lb

To Add: 165.8 lb

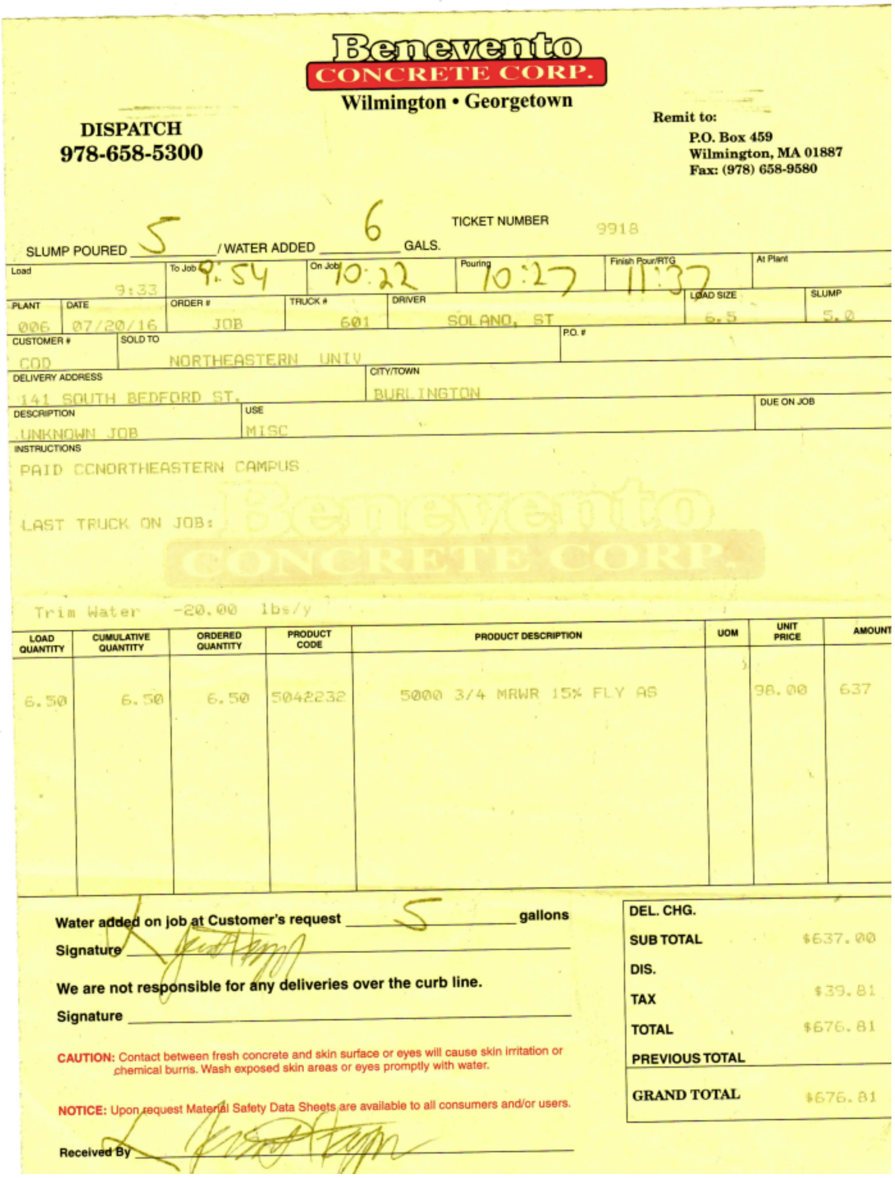

Benevento
CONCRETE CORP.
Wilmington • Georgetown

DISPATCH
978-658-5300

Remit to:
P.O. Box 459
Wilmington, MA 01887
Fax: (978) 658-9580

SLUMP POURED 5 / WATER ADDED 6 GALS.

TICKET NUMBER 9918

Load 9:33	To Job 9:54	On Job 10:22	Pouring 10:27	Finish Pour/RTG 11:37	At Plant

PLANT 006	DATE 07/20/16	ORDER # JOB	TRUCK # 601	DRIVER SOLANO, ST	LOAD SIZE 6.5	SLUMP 5.0

CUSTOMER # COD

SOLD TO NORTHEASTERN UNIV

P.O. #

DELIVERY ADDRESS 141 SOUTH BEDFORD ST.

CITY/TOWN BURLINGTON

DESCRIPTION UNKNOWN JOB

USE MISC

DUE ON JOB

INSTRUCTIONS

PAID CCNORTHEASTERN CAMPUS

LAST TRUCK ON JOB:

Trim Water -20.00 lbs/y

LOAD QUANTITY	CUMULATIVE QUANTITY	ORDERED QUANTITY	PRODUCT CODE	PRODUCT DESCRIPTION	UOM	UNIT PRICE	AMOUNT
6.50	6.50	6.50	5042232	5000 3/4 MRWR 15% FLY AS		98.00	637

Water added on job at Customer's request 5 gallons

Signature

We are not responsible for any deliveries over the curb line.

Signature

CAUTION: Contact between fresh concrete and skin surface or eyes will cause skin irritation or chemical burns. Wash exposed skin areas or eyes promptly with water.

NOTICE: Upon request Material Safety Data Sheets are available to all consumers and/or users.

Received By

DEL. CHG.	
SUB TOTAL	$637.00
DIS.	
TAX	$39.81
TOTAL	$676.81
PREVIOUS TOTAL	
GRAND TOTAL	$676.81

Pour 3

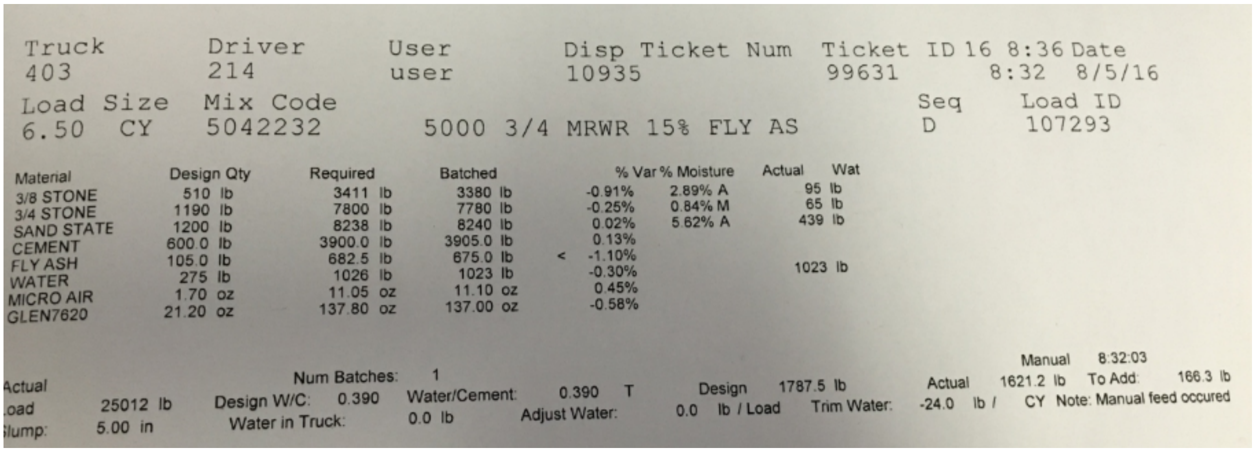

Truck	Driver	User	Disp Ticket Num	Ticket ID	16 8:36	Date
403	214	user	10935	99631	8:32	8/5/16

Load Size	Mix Code		Seq	Load ID
6.50 CY	5042232	5000 3/4 MRWR 15% FLY AS	D	107293

Material	Design Qty	Required	Batched		% Var	% Moisture	Actual Wat
3/8 STONE	510 lb	3411 lb	3380 lb		-0.91%	2.89% A	95 lb
3/4 STONE	1190 lb	7800 lb	7780 lb		-0.25%	0.84% M	65 lb
SAND STATE	1200 lb	8238 lb	8240 lb		0.02%	5.62% A	439 lb
CEMENT	600.0 lb	3900.0 lb	3905.0 lb		0.13%		
FLY ASH	105.0 lb	682.5 lb	675.0 lb	<	-1.10%		
WATER	275 lb	1026 lb	1023 lb		-0.30%		1023 lb
MICRO AIR	1.70 oz	11.05 oz	11.10 oz		0.45%		
GLEN7620	21.20 oz	137.80 oz	137.00 oz		-0.58%		

Manual 8:32:03

Actual Load 25012 lb

Slump: 5.00 in

Num Batches: 1

Design W/C: 0.390

Water in Truck: 0.0 lb

Water/Cement: 0.390 T

Adjust Water: 0.0 lb / Load

Design 1787.5 lb

Trim Water: -24.0 lb / CY

Actual 1621.2 lb

To Add: 166.3 lb

Note: Manual feed occured

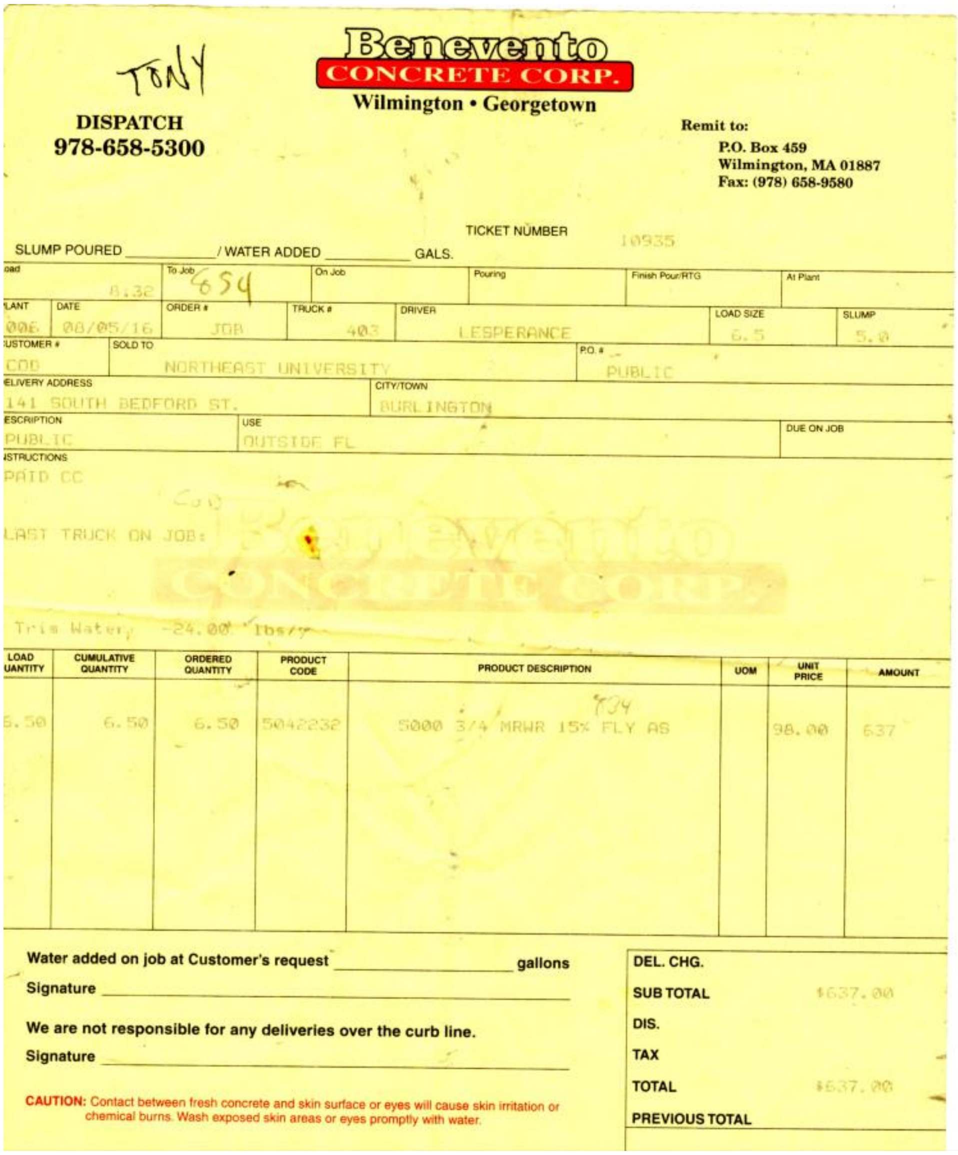

TONY

Benevento CONCRETE CORP.
Wilmington • Georgetown

DISPATCH
978-658-5300

Remit to:
P.O. Box 459
Wilmington, MA 01887
Fax: (978) 658-9580

TICKET NUMBER 10935

SLUMP POURED ____________ / WATER ADDED ____________ GALS.

oad 8:32	To Job 654	On Job	Pouring	Finish Pour/RTG	At Plant

LANT 006	DATE 08/05/16	ORDER # JOB	TRUCK # 403	DRIVER LESPERANCE	LOAD SIZE 6.5	SLUMP 5.0

USTOMER # COD	SOLD TO NORTHEAST UNIVERSITY	P.O. # PUBLIC

ELIVERY ADDRESS 141 SOUTH BEDFORD ST.	CITY/TOWN BURLINGTON

ESCRIPTION PUBLIC	USE OUTSIDE FL	DUE ON JOB

NSTRUCTIONS
PAID CC

LAST TRUCK ON JOB:

Trim Water: -24.00 lbs/y

LOAD UANTITY	CUMULATIVE QUANTITY	ORDERED QUANTITY	PRODUCT CODE	PRODUCT DESCRIPTION	UOM	UNIT PRICE	AMOUNT
6.50	6.50	6.50	5042232	934 5000 3/4 MRWR 15% FLY AS		98.00	637

Water added on job at Customer's request ________________ **gallons**

Signature ______________________________

We are not responsible for any deliveries over the curb line.

Signature ______________________________

CAUTION: Contact between fresh concrete and skin surface or eyes will cause skin irritation or chemical burns. Wash exposed skin areas or eyes promptly with water.

DEL. CHG.	
SUB TOTAL	$637.00
DIS.	
TAX	
TOTAL	$637.00
PREVIOUS TOTAL	

Appendix E EXPERIMENTAL RAW DATA

This appendix contains all the raw data from the experimental programs. All the data was automatically converted to and output in engineering units within the data acquisition system. The data was saved and is plotted with initial offsets subtracted out. Long pauses that exhibited little appreciable change in value of the raw data were removed for clarity.

E.1 **Pushout test specimens**

E.1.1 Pretension tests

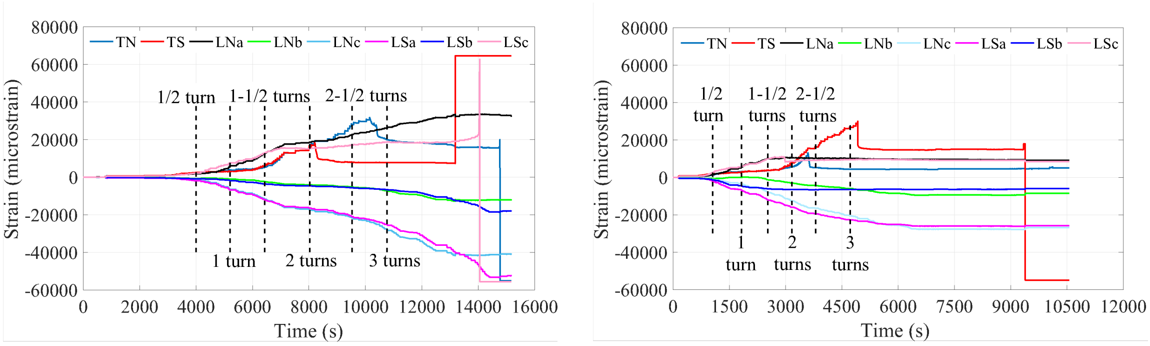

M24 bolt test 1 M24 bolt test 2

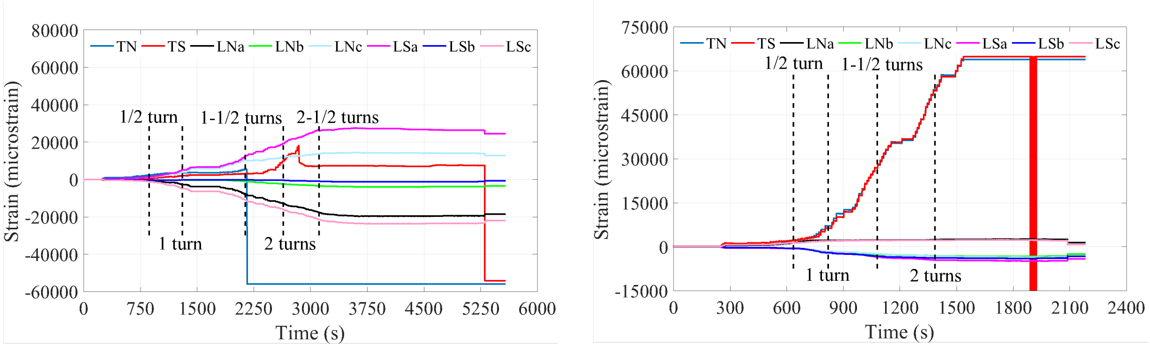

M24 bolt test 3 M20 bolt test 1

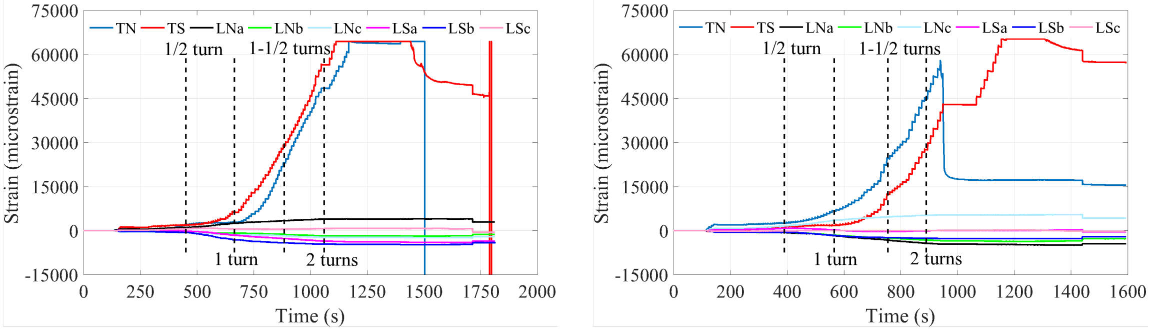

M20 bolt test 2 M20 bolt test 3

Figure E.1 Strain gage readings in bolt pretension tests

E.1.2 Pushout tests

E.1.2.1 Actuator forces, actuator displacements and slips

Two 110 kips actuators were used in the pushout tests. The plots titled “Actuator Force Variation” show the summation of the actuator forces, while the average of the actuator displacements is given in the figures titled “Actuator Displacement Variation”.

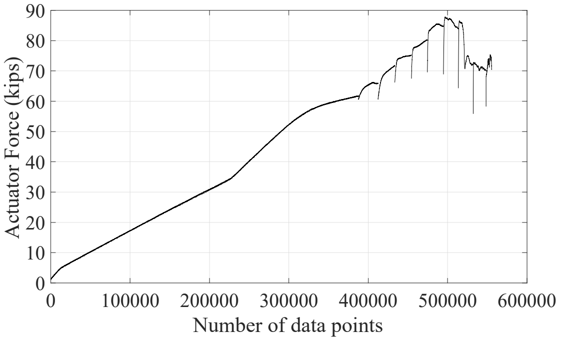

Actuator force variation

Actuator displacement variation

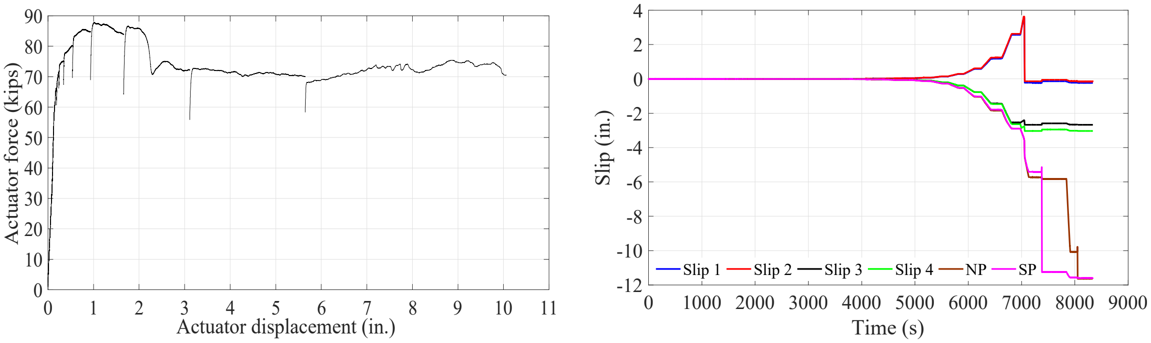

Actuator force versus Actuator displacement

Slip versus Time

Figure E.2 Actuator forces, actuator displacements and slips in Test 2-M24-2C-RH-LM

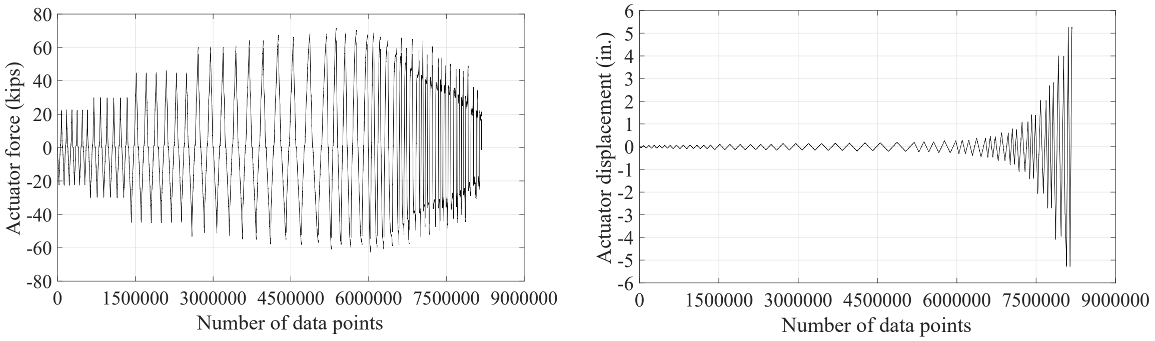

Actuator force variation

Actuator displacement variation

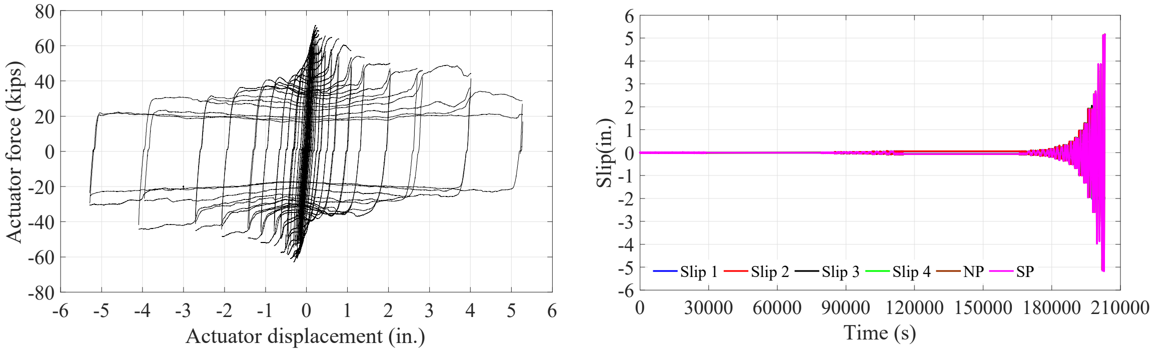

Actuator force versus Actuator displacement

Slip versus Time

Figure E.3 Actuator forces, actuator displacements and slips in Test 3-M24-2C-RL-LC

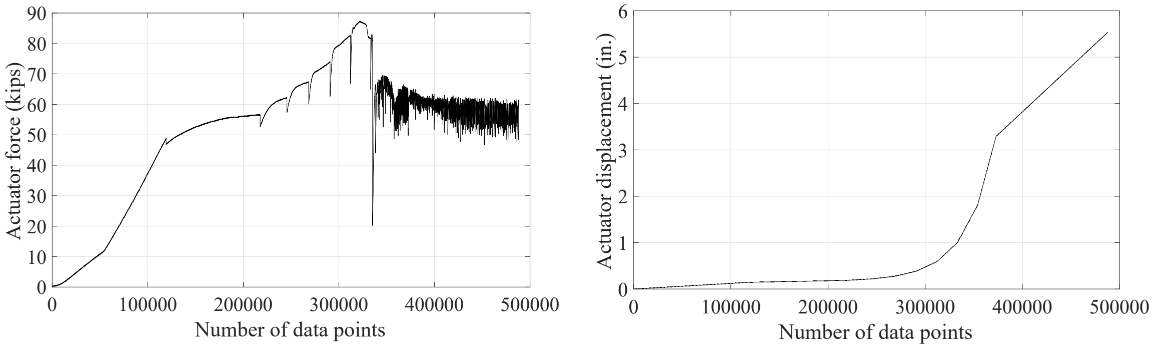

Actuator force variation

Actuator displacement variation

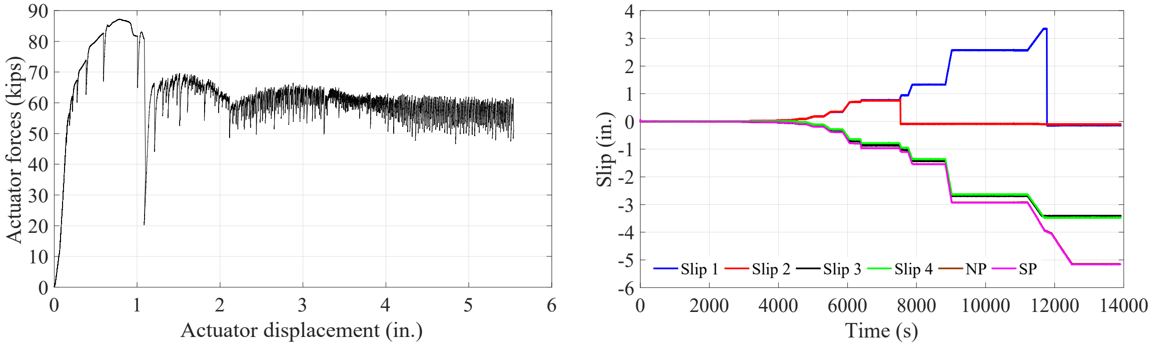

Actuator force versus Actuator displacement

Slip versus Time

Figure E.4 Actuator forces, actuator displacements and slips in Test 4-M24-2C-RH-LM-S

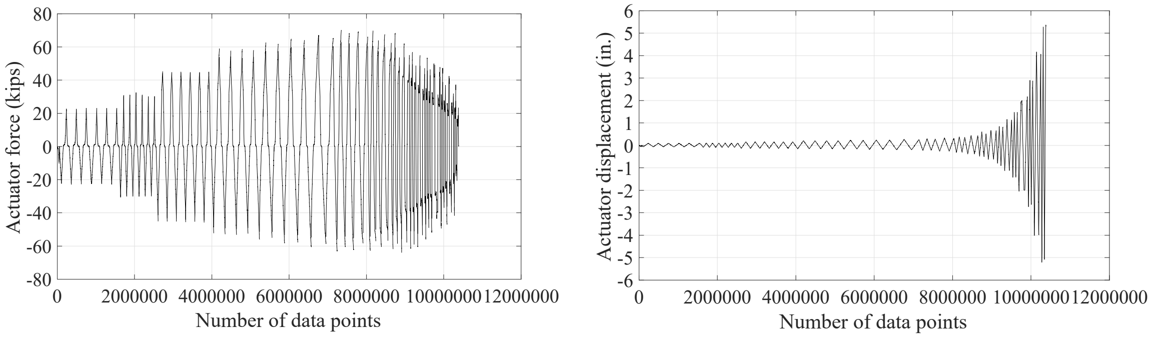

Actuator force variation

Actuator displacement variation

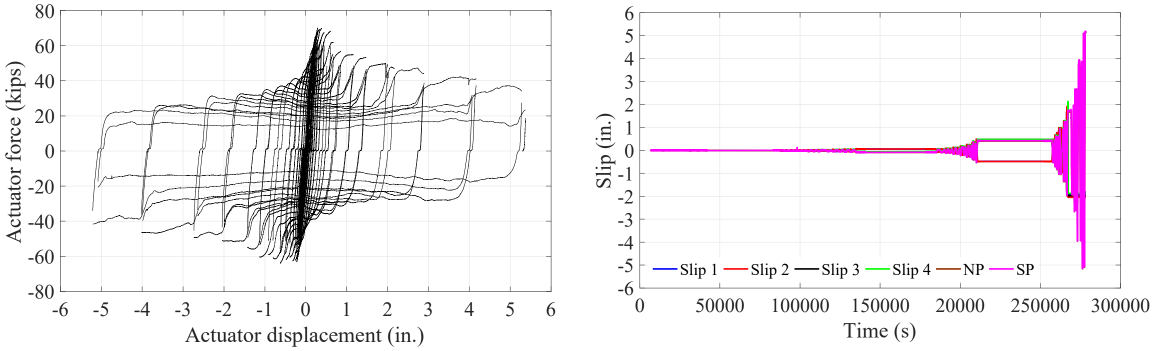

Actuator force versus Actuator displacement

Slip versus Time

Figure E.5 Actuator forces, actuator displacements and slips in Test 5-M24-2C-RH-LC

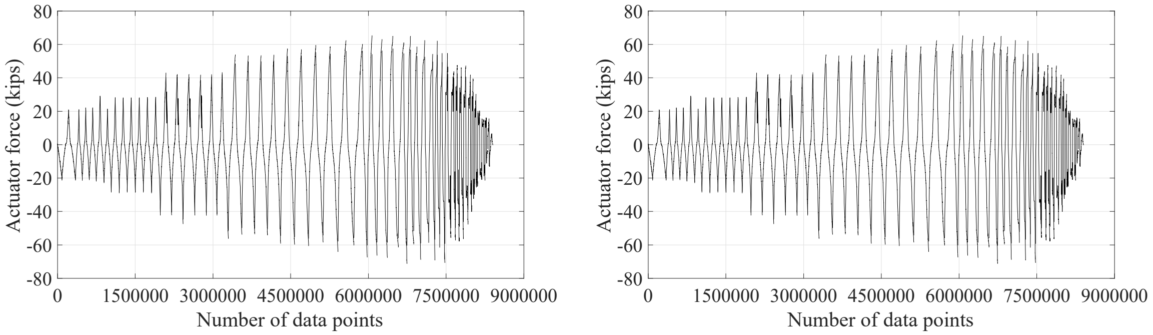

Actuator force variation

Actuator displacement variation

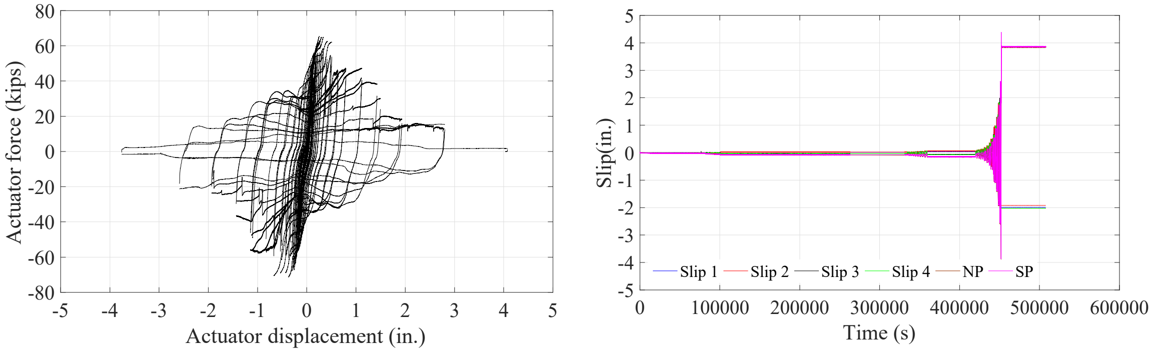

Actuator force versus Actuator displacement

Slip versus Time

Figure E.6 Actuator forces, actuator displacements and slips in Test 6-M24-2C-RH-LC-S

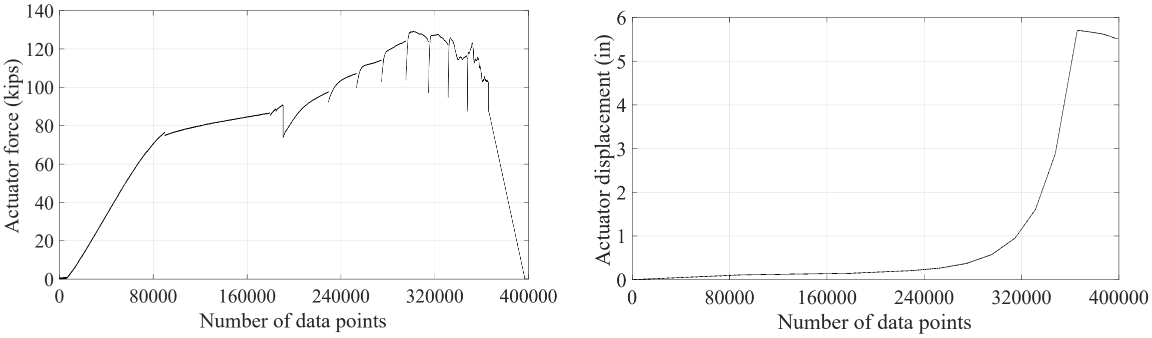

Actuator force variation Actuator displacement variation

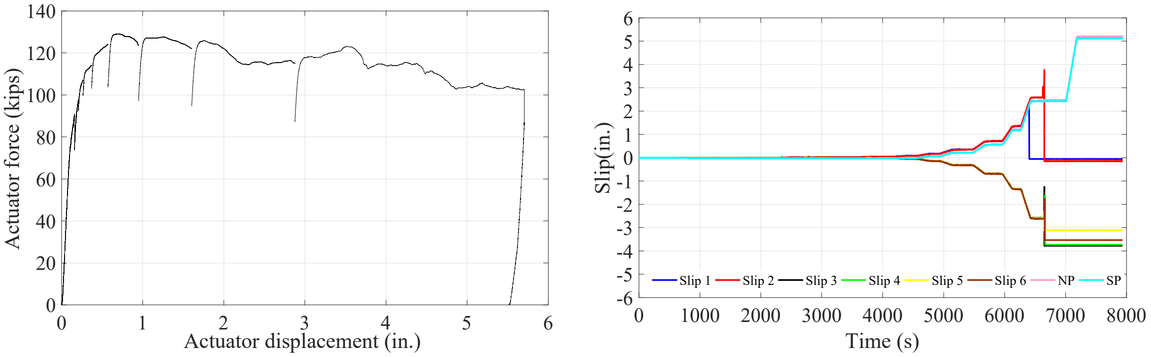

Actuator Force versus Actuator Displacement Slip versus Time

Figure E.7 Actuator forces, actuator displacements and slips in Test 7-M24-3C-RH-LM

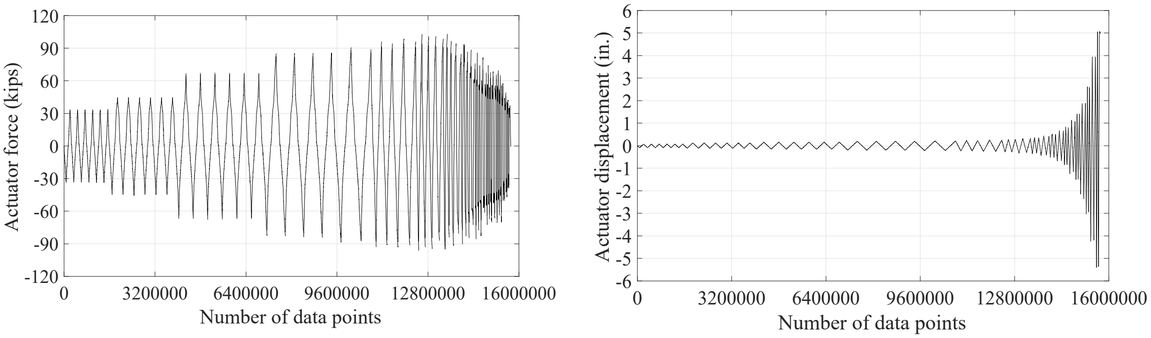

Actuator force variation Actuator displacement variation

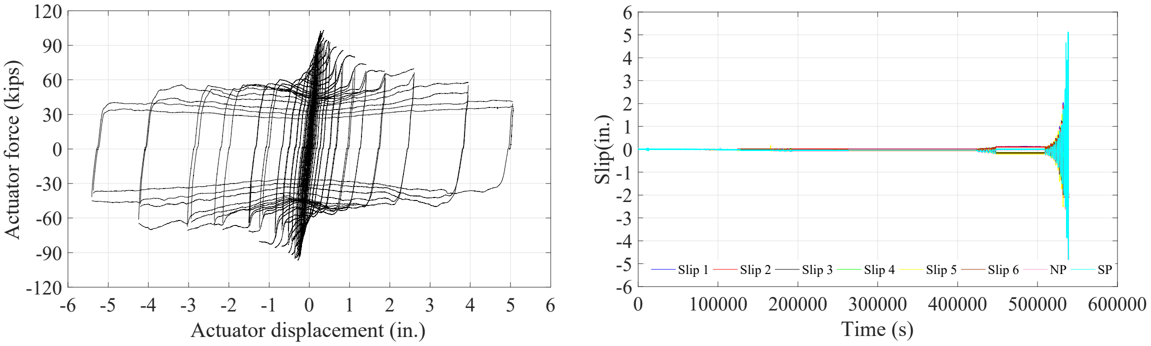

Actuator force versus Actuator displacement Slip versus Time

Figure E.8 Actuator forces, actuator displacements and slips in Test 8-M24-3C-RH-LC

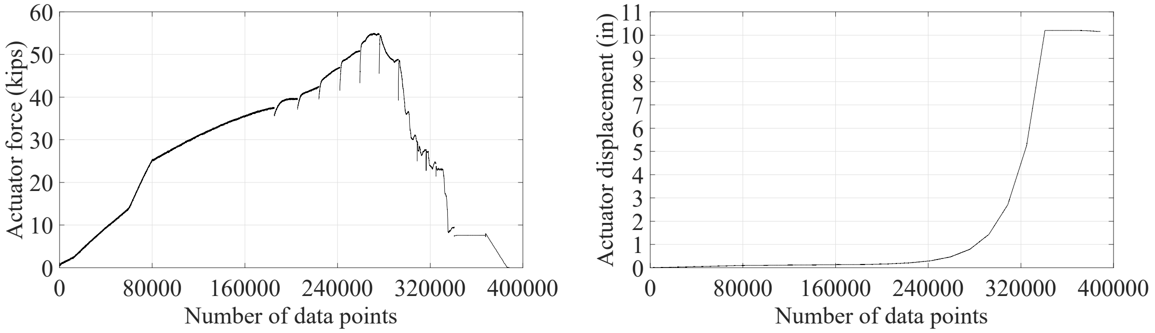

Actuator force variation

Actuator displacement variation

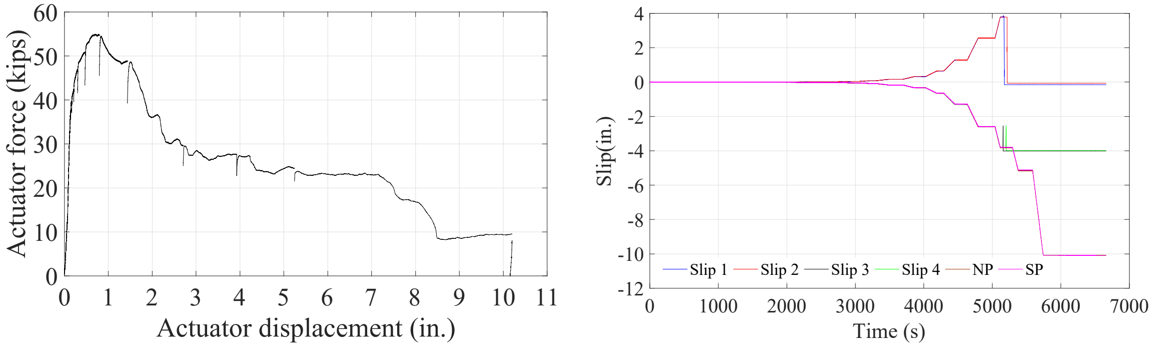

Actuator force versus Actuator displacement

Slip versus Time

Figure E.9 Actuator forces, actuator displacements and slips in Test 9-M20-2C-RH-LM

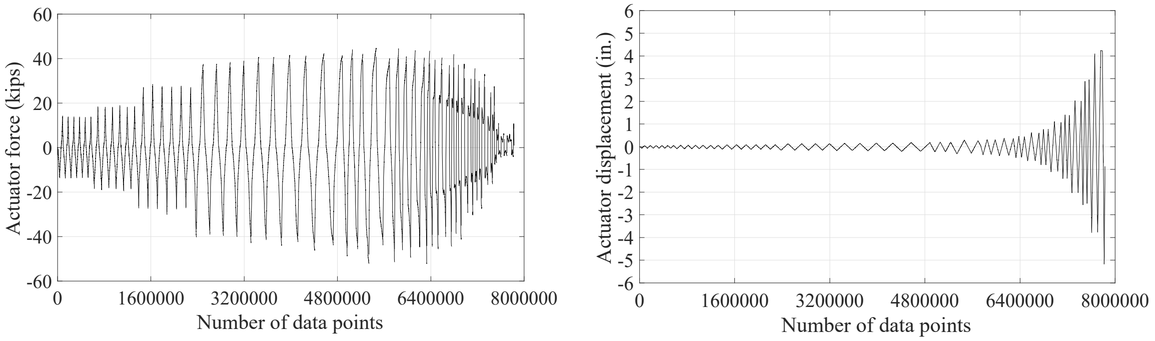

Actuator force variation

Actuator displacement variation

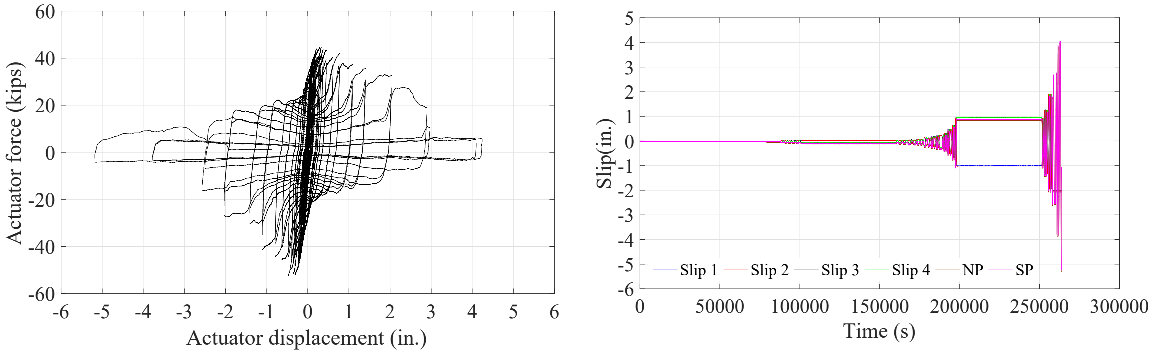

Actuator force versus Actuator displacement

Slip versus Time

Figure E.10 Actuator forces, actuator displacements and slips in Test 10-M20-2C-RH-LC

E.1.2.2 Beam strain gages

After pretensioning the bolts, the flange strains were generally larger than the web strains, and the outside strains on the flanges were larger than the inside strains, because those locations are closer to the clamps. The strains on the flanges were usually tensile (positive values). The readouts fluctuated while the cyclic shear force was applied. In Test 10-M20-2C-RH-LC, several gages behaved abnormally, as indicated by the drift of the readings while the test was paused.

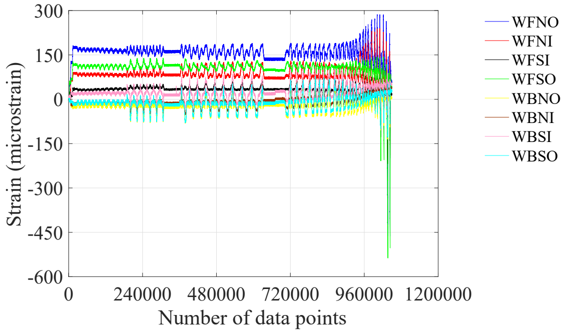

West section

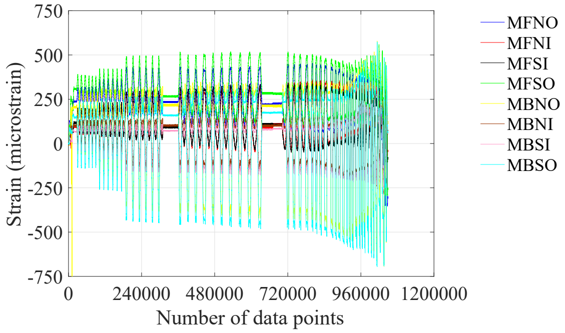

Middle section

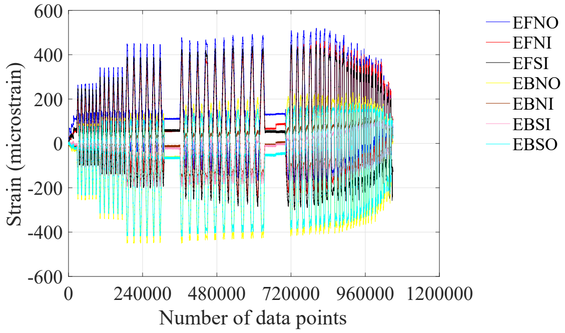

East section

Figure E.11 Beam strain gage readings in Test 3-M24-2C-RL-LC

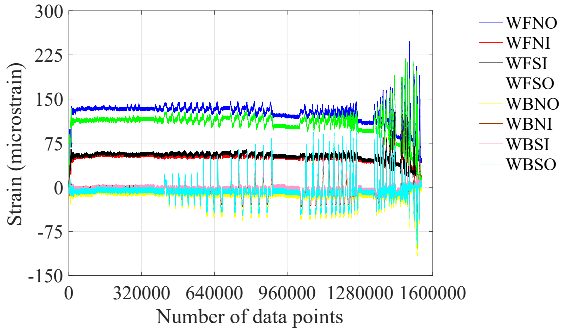

West section

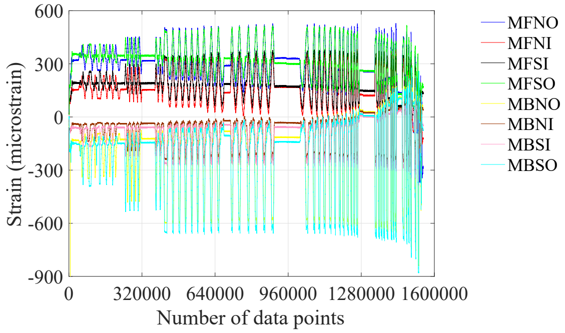

Middle section

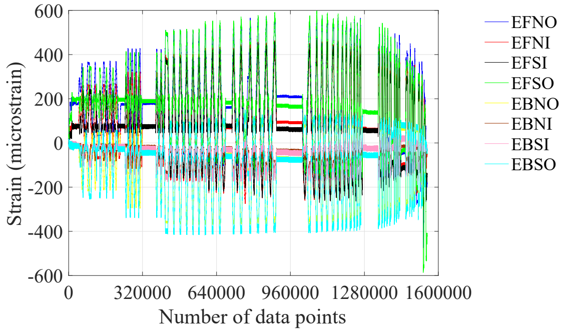

East section

Figure E.12 Beam strain gage readings in Test 5-M24-2C-RH-LC

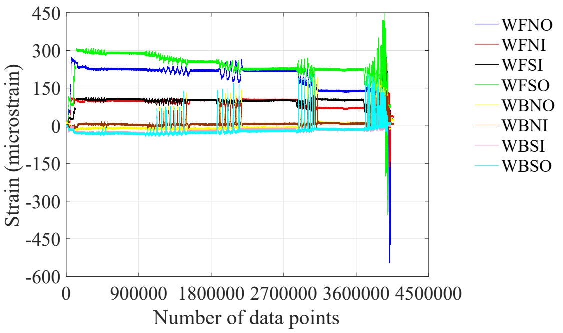

West section

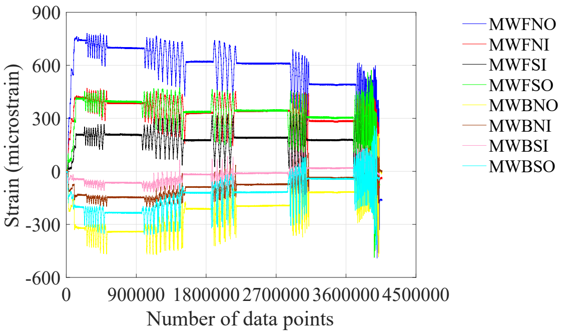

Middle west section

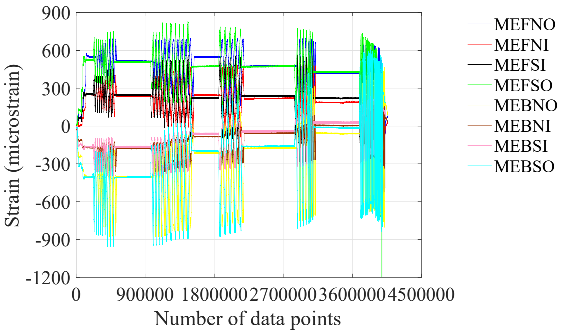

Middle east section

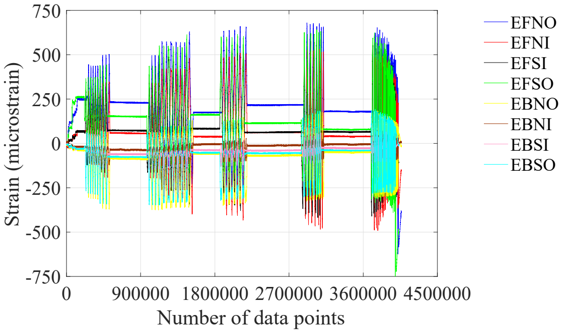

East section

Figure E.13 Beam strain gage readings in Test 8-M24-3C-RH-LC

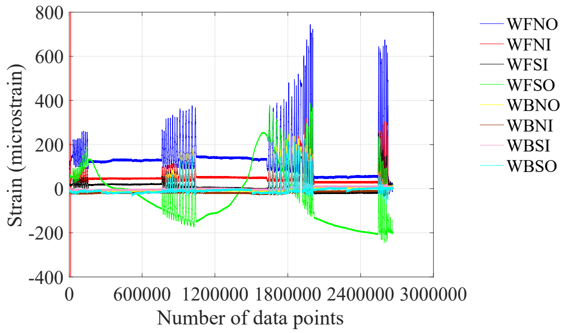

West section

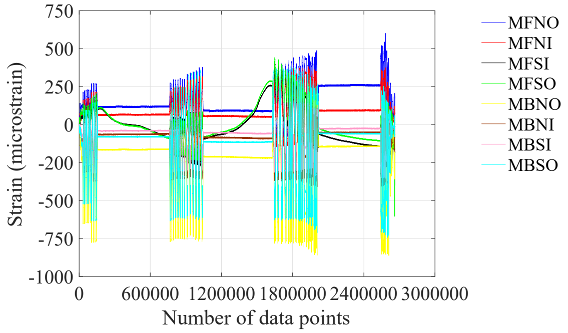

Middle section

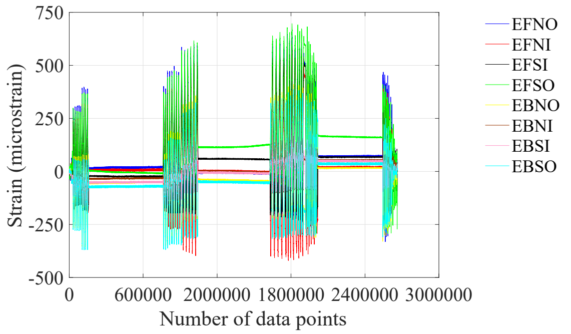

East section

Figure E.14 Beam strain gage readings in Test 10-M20-2C-RH-LC

E.1.2.3 Bolt strain gages

After pretensioning, the strain measurements from the gages away from the steel section were commonly smaller than those from the gages close to the section. During pretension, the substantial strain difference between the two gages attached on the same bolt came from the bending of the bolt. As the cyclic shear force was applied, fluctuation was observed in the strain measurements.

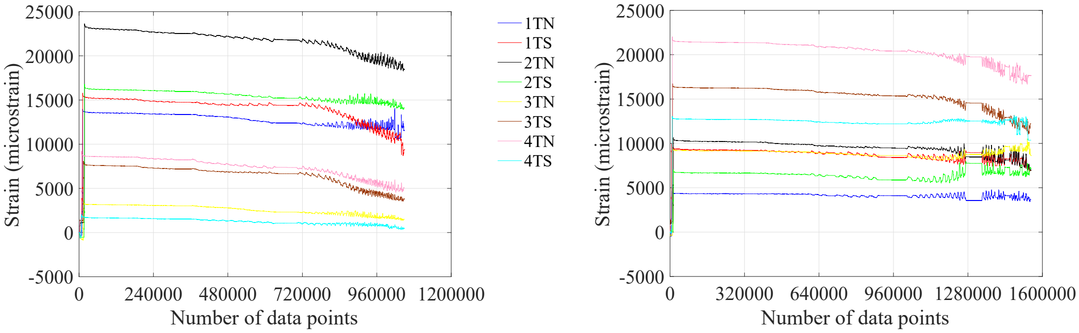

Test 3-M24-2C-RL-LC Test 5-M24-2C-RH-LC

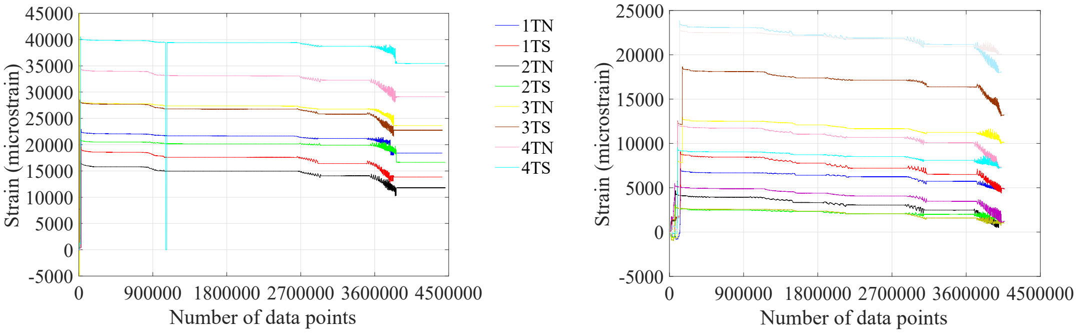

Test 6-M24-2C-RH-LC-S Test 8-M24-3C-RH-LC

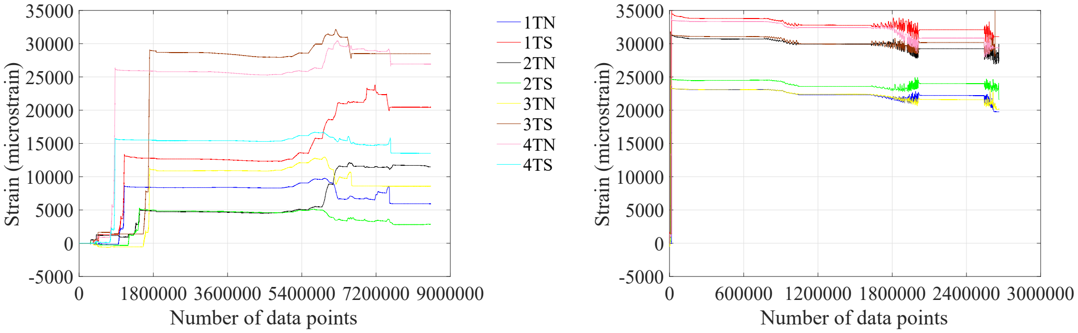

Test 9-M20-2C-RH-LM Test 10-M20-2C-RH-LC

Figure E.15 Bolt strain gage readings in pushout tests

E.1.2.4 Channel lip strain gages

The readings from the rosette strain gages displayed a similar pattern as that observed from the bolt strain gages. The strains measured by the legs closer to the steel section were usually negative (compressive), while positive (tensile) strains were measured by the legs away from the steel section. Since the pretension force for the M20 bolt is smaller than that of the M24 bolt, the channel lip strains were smaller in the tests using M20 bolts. Because of different scales of the graphs, the variation of the strains due to the applied shear force seems to be more appreciable in the M20 bolt tests than in the M24 bolt tests.

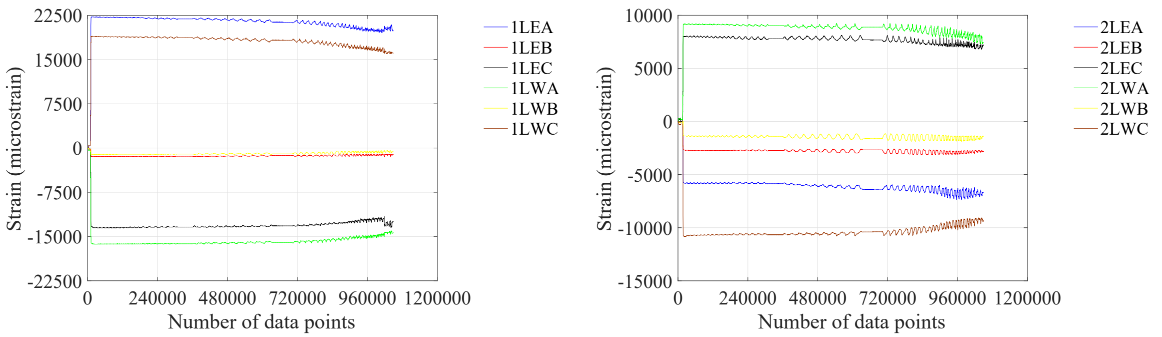

Channel 1 Channel 2

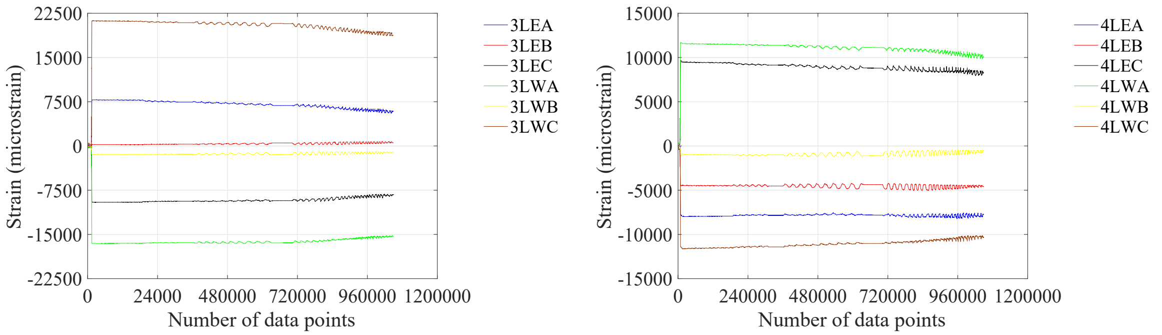

Channel 3 Channel 4

Figure E.16 Channel lip strain gage readings in Test 3-M24-2C-RL-LC

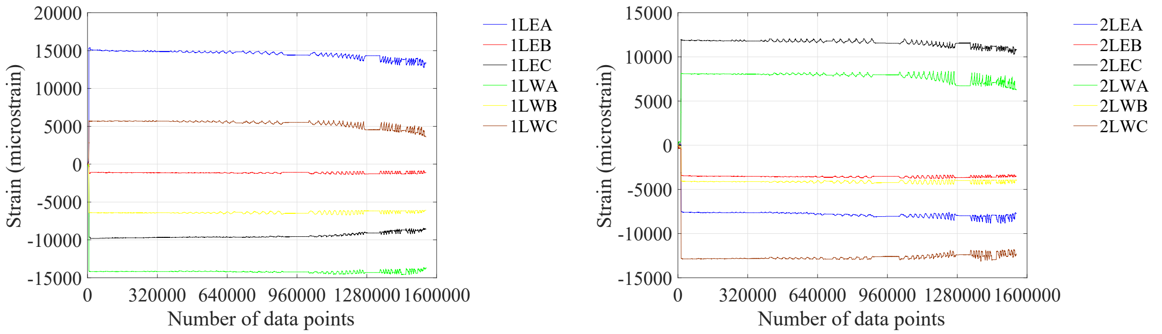

Channel 1 Channel 2

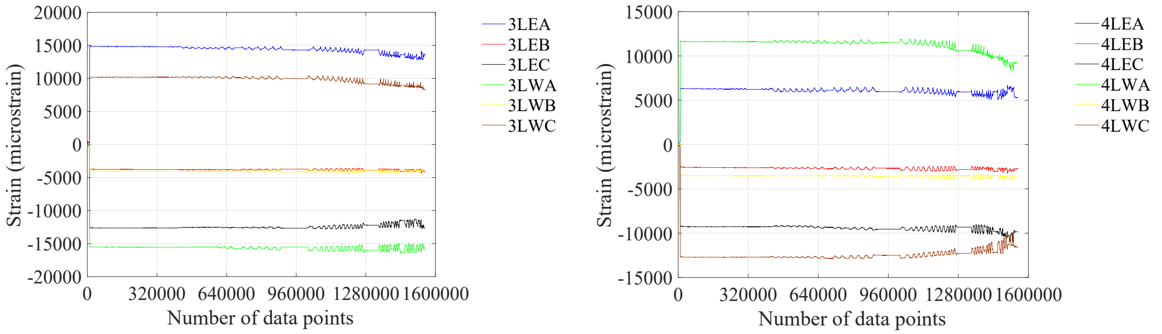

Channel 3 Channel 4

Figure E.17 Channel lip strain gage readings in Test 5-M24-2C-RH-LC

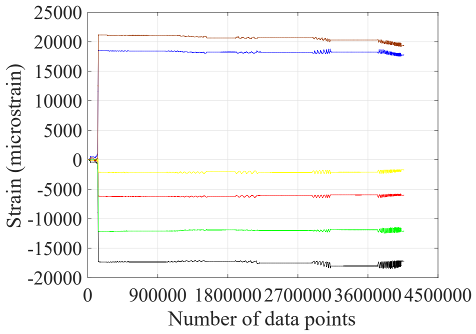

Channel 1

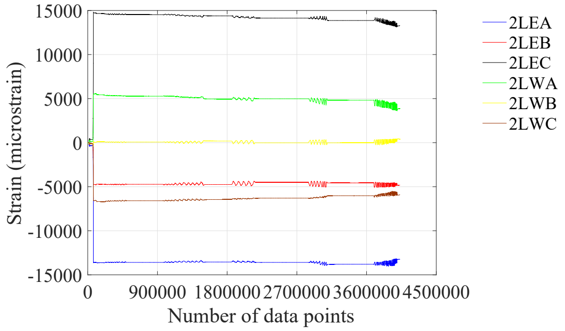

Channel 2

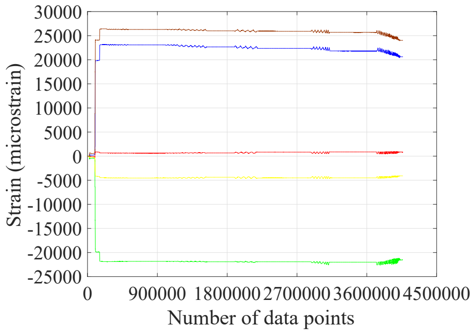

Channel 3

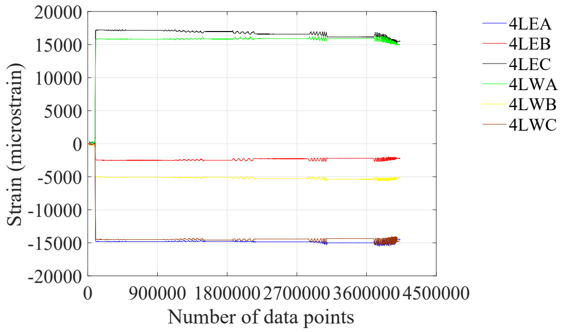

Channel 4

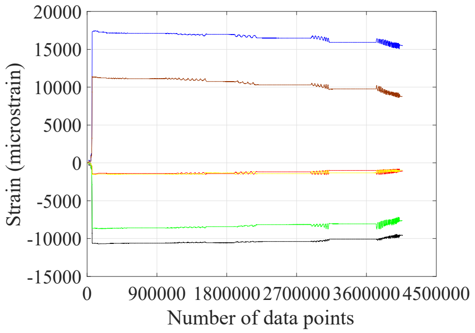

Channel 5

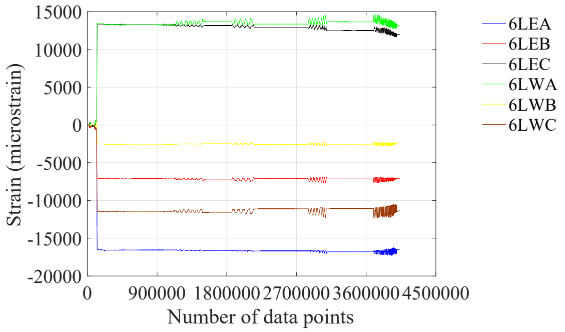

Channel 6

Figure E.18 Channel lip strain gage readings in Test 8-M24-3C-RH-LC

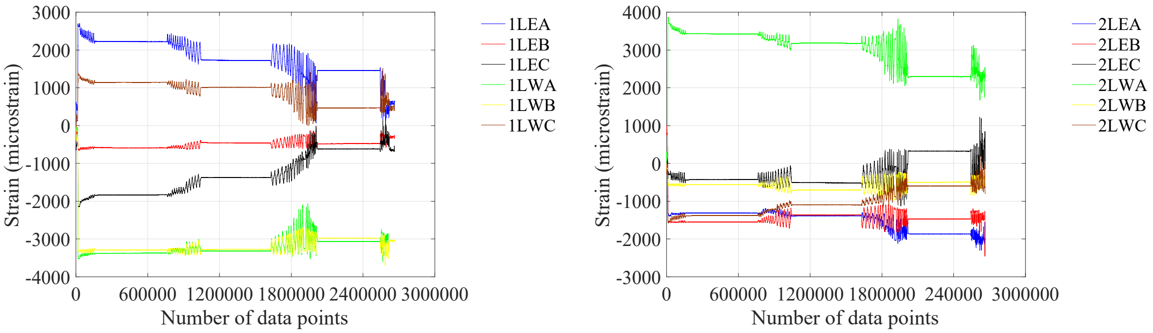

Channel 1 Channel 2

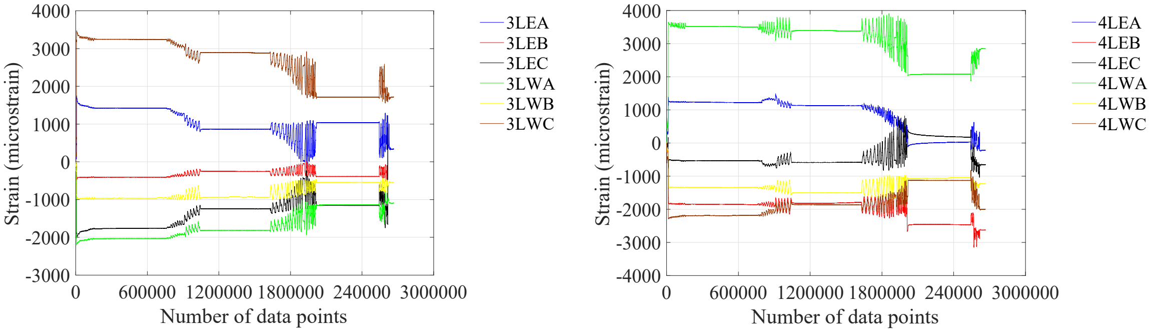

Channel 3 Channel 4

Figure E.19 Channel lip strain gage readings in Test 10-M20-2C-RH-LC

E.1.2.5 Channel anchor strain gages

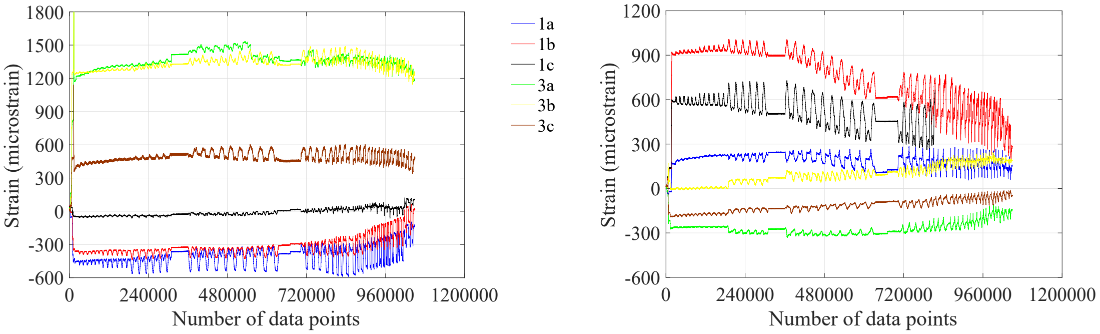

Channels 1 and 3 Channels 2 and 4

Figure E.20 Channel anchor strain gage readings in Test 3-M24-2C-RL-LC

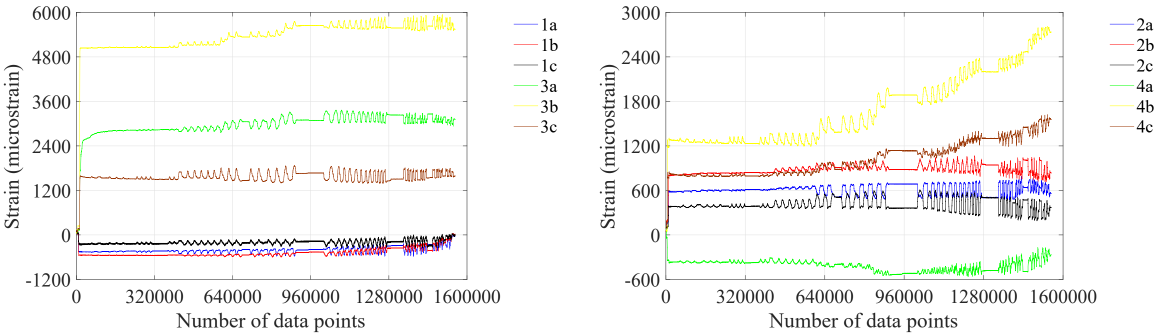

Channels 1 and 3 Channels 2 and 4

Figure E.21 Channel anchor strain gage readings in Test 5-M24-2C-RH-LC

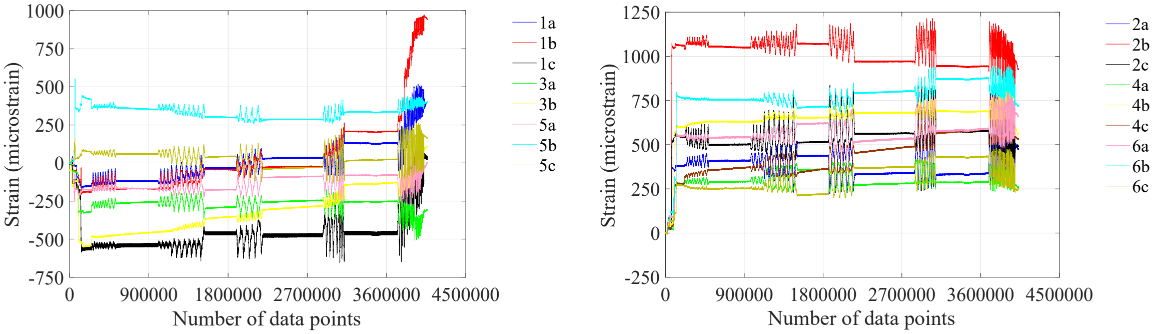

Channels 1,3 and 5 Channels 2,4 and 6

Figure E.22 Channel anchor strain gage readings in Test 8-M24-3C-RH-LC

E.1.2.6 Reinforcement strain gages

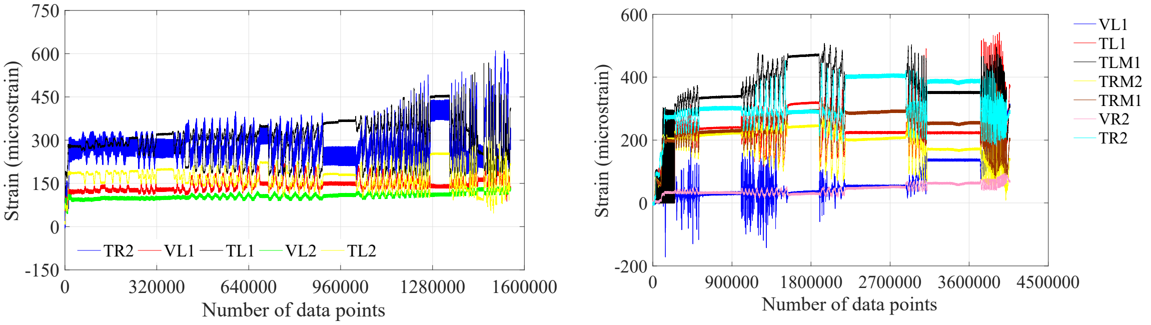

Test 5-M24-2C-RH-LC Test 8-M24-3C-RH-LC

Figure E.23 Reinforcement strain gage readings in pushout tests

E.2 **Beam test specimens**

In some figures, the variations of the parameters are omitted during the removal of the shoring; therefore, these plots may not start from the origin of the graphs.

E.2.1 Actuator forces and actuator displacements

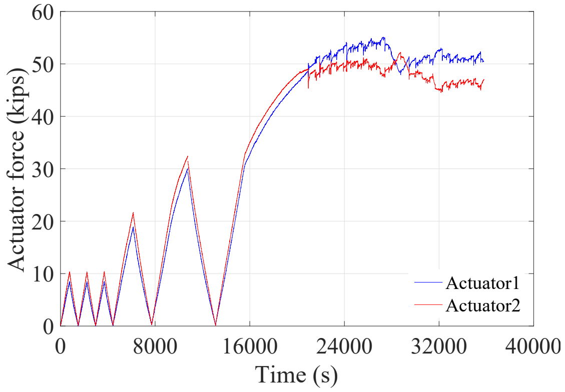

Actuator force

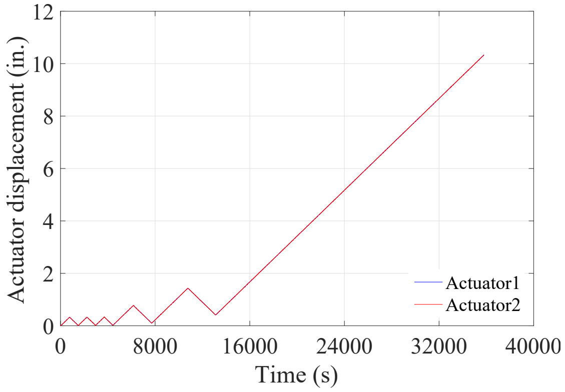

Actuator displacement

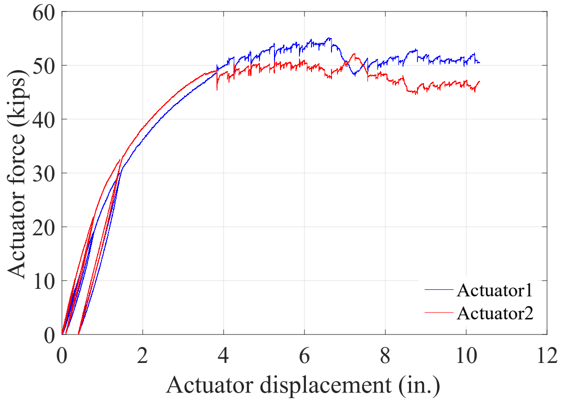

Actuator force versus actuator displacement

Figure E.24 Actuator forces and actuator displacements in Test 1-M24-2C-RH

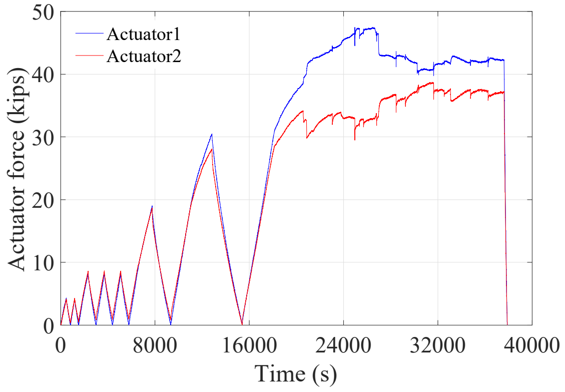

Actuator force

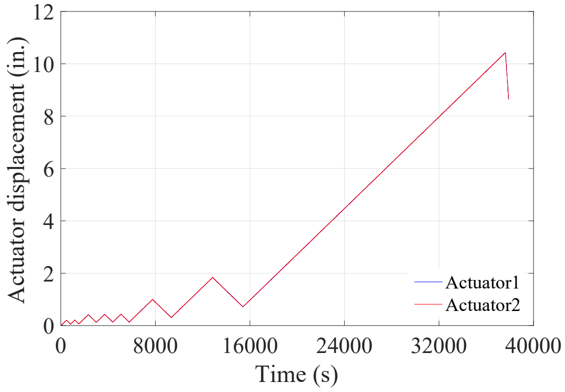

Actuator displacement

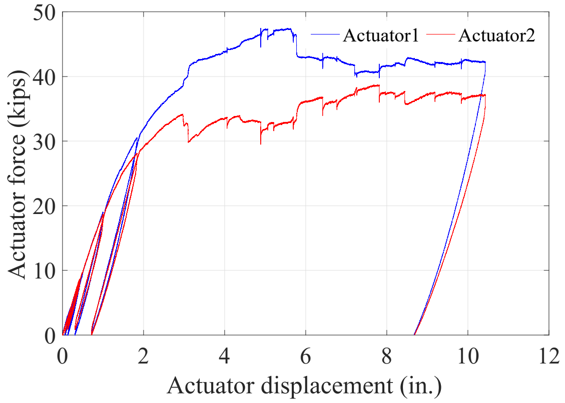

Actuator force versus actuator displacement

Figure E.25 Actuator forces and actuator displacements in Test 2-M24-1C-RL

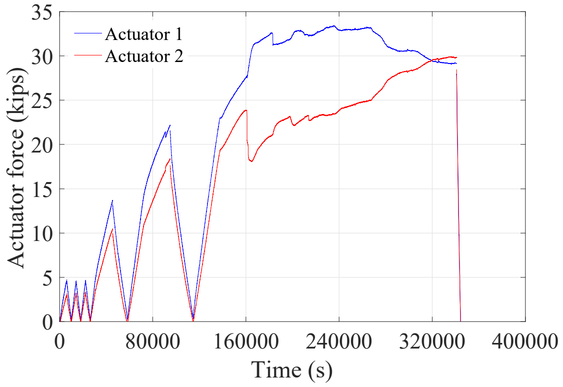

Actuator force

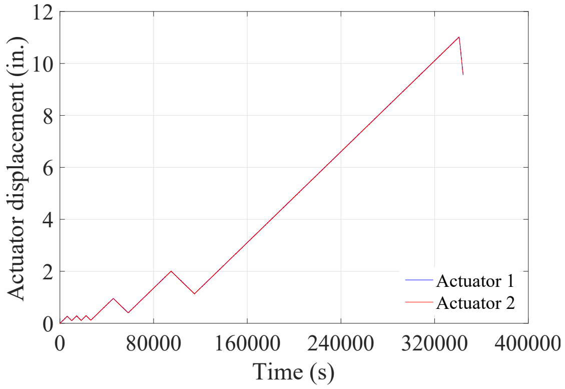

Actuator displacement

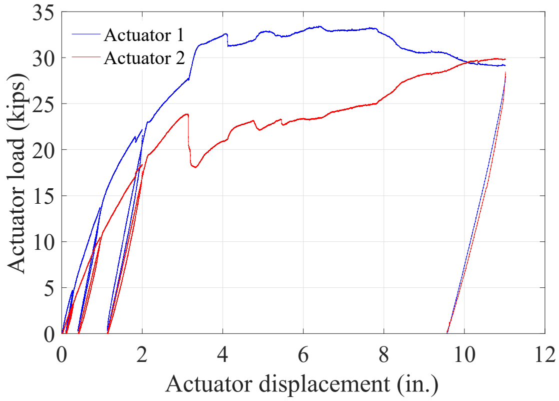

Actuator force versus actuator displacement

Figure E.26 Actuator forces and actuator displacements in Test 3-M20-3C-RL

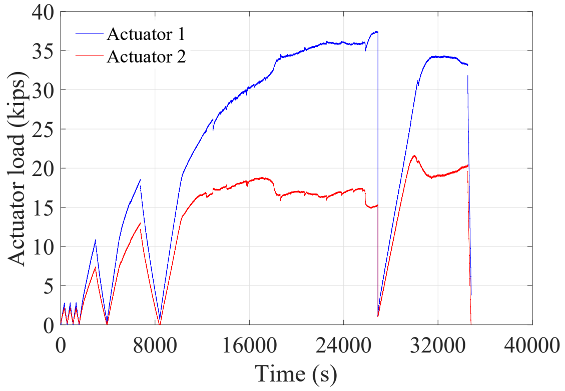

Actuator force

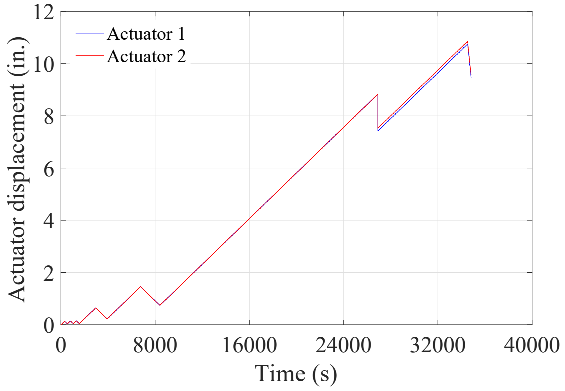

Actuator displacement

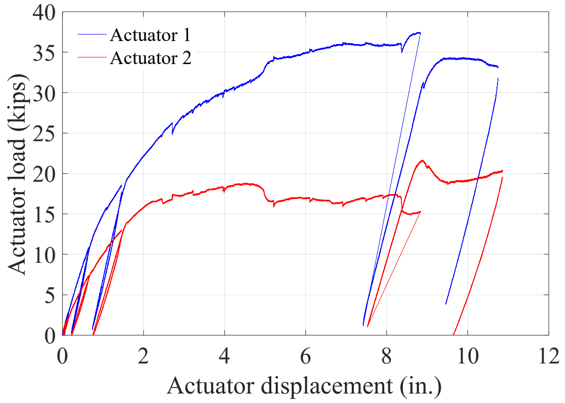

Actuator force versus actuator displacement

Figure E.27 Actuator forces and actuator displacements in Test 4-M20-1C-RL

E.2.2 Beam deformation

In all the plots shown in this section, downward vertical deflection is positive, and the horizontal movement is positive when the west (or east) end moves in the west (or east) direction.

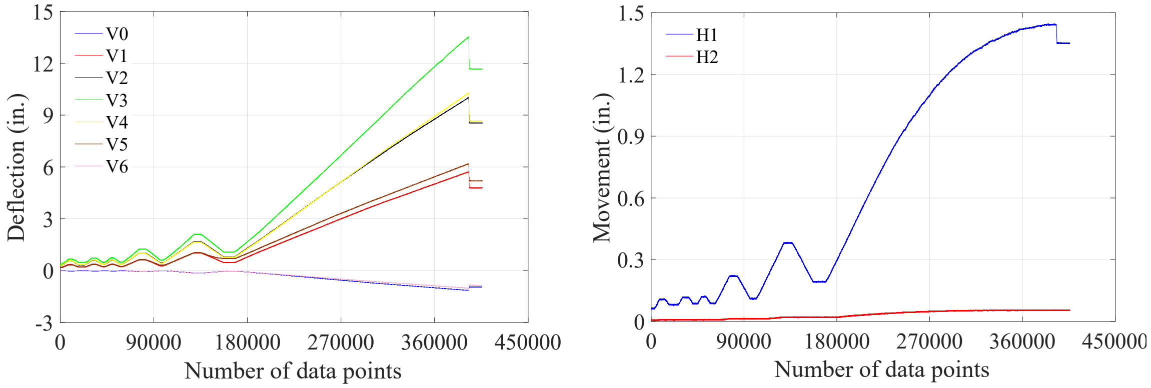

Vertical deflection Horizontal movement

Figure E.28 Beam deformation in Test 1-M24-2C-RH

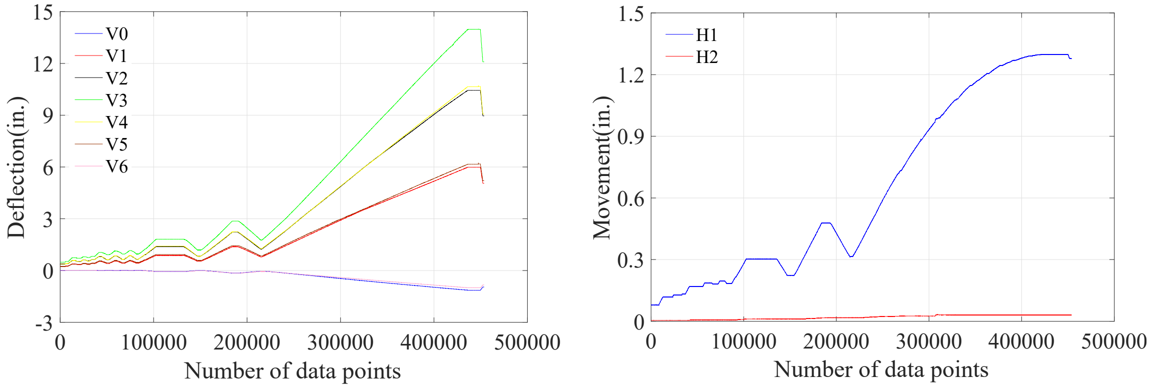

Vertical deflection Horizontal movement

Figure E.29 Beam deformation in Test 2-M24-1C-RL

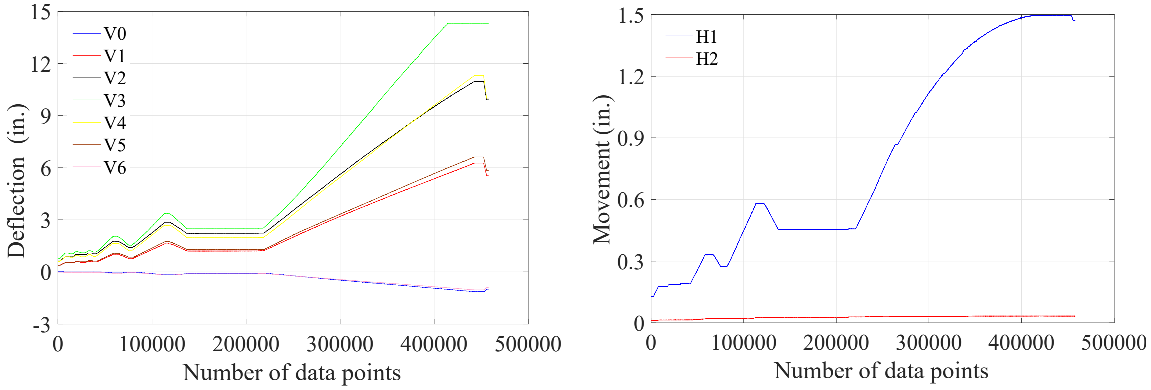

Vertical deflection Horizontal movement

Figure E.30 Beam deformation in Test 3-M20-3C-RL

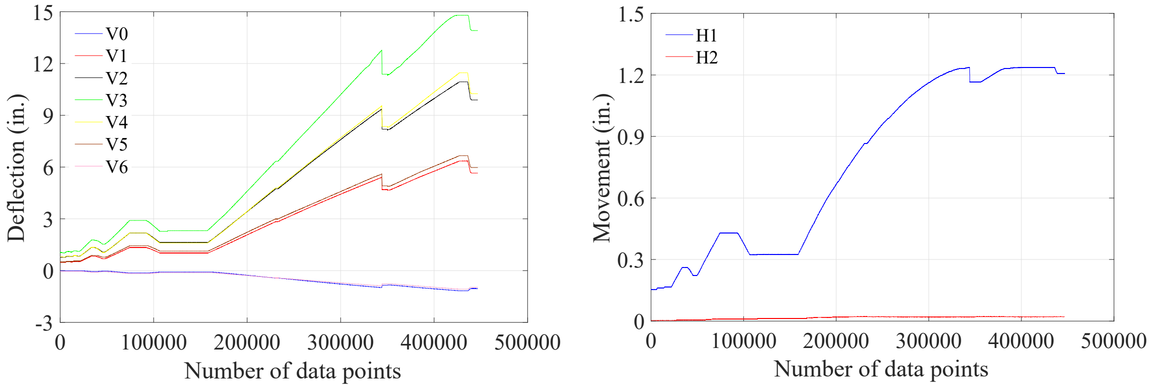

Vertical deflection Horizontal movement

Figure E.31 Beam deformation in Test 4-M20-1C-RL

E.2.3 Beam rotation

In all the tests, since the loading of the specimens was displacement-controlled, symmetry is seen in the rotation of the beams under flexure (i.e., IY1 and IY2). For Test 4-M20-1C-RL, more rotation is seen at the east side than the west side, which could relate to the significant plastification at the east inner loading point section. Since the lateral braces prevented excessive lateral deformation of the concrete slabs, titling of the system was restrained, which is evidenced by the almost constant rotation shown by IX1 and IX2.

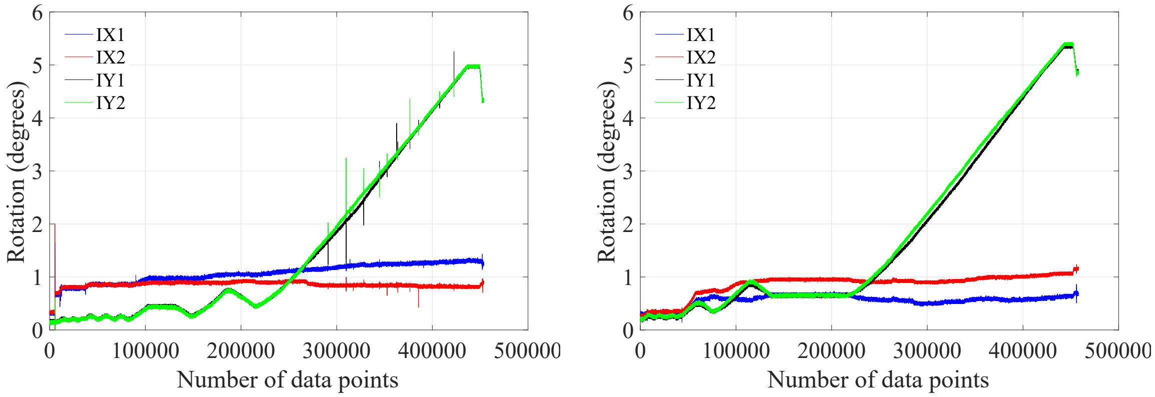

Test 2-M24-1C-RL

Test 3-M20-3C-RL

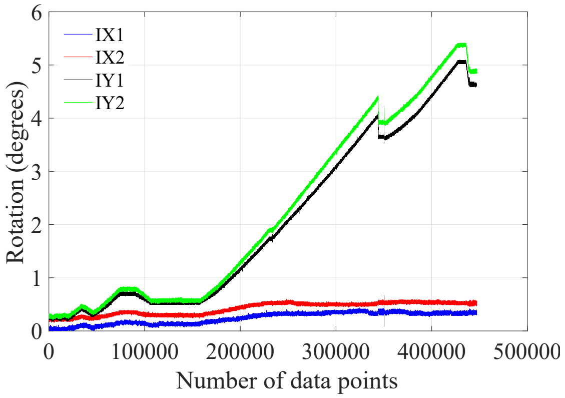

Test 4-M20-1C-RL

Note: IX indicates the tilting of the concrete slab; IY indicates the rotation of the beam under flexure. 1 and 2 refer to the west and east side of the beam, respectively.

Figure E.32 Loading structure rotation in beam tests

E.2.4 Slip of clamps

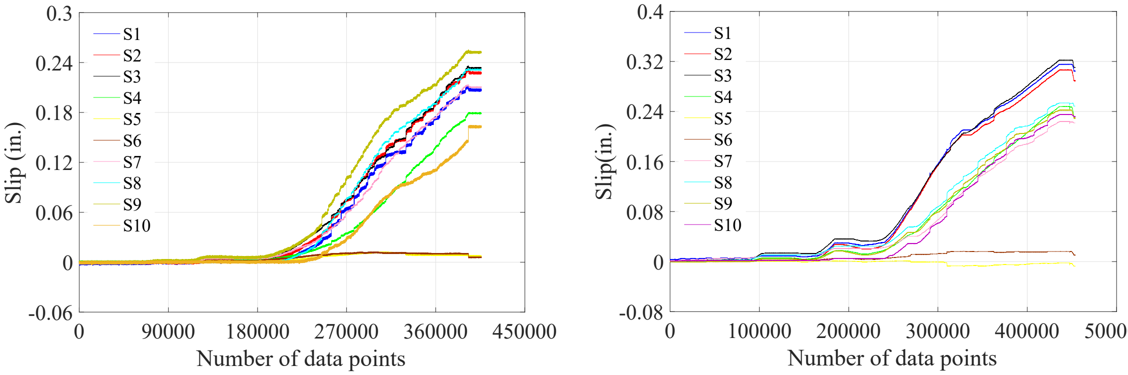

Test 1-M24-2C-RH

Test 2-M24-1C-RL

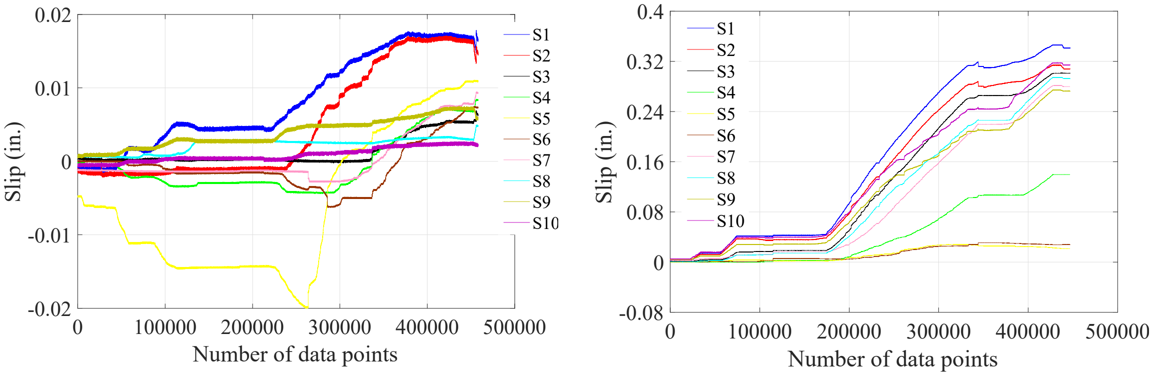

Test 3-M20-3C-RL

Test 4-M20-1C-RL

Figure E.33 Slip measurements in beam tests

E.2.5 Rod tension

In Figure E.34, the dashed lines divide each curve into two segments to distinguish the pretension phase from the beam test phase. During the pretension phase, if the tension variation of a rod was tracked, the DAQ would run until the process was complete. When the DAQ was switched on next time to measure the tension of a different bar, the currently recorded tension of the previously pretensioned bar was usually less than the previous tension measurement for the same bar (<15%). Restarting the DAQ is a cause of the offsets in the measurements. Meanwhile, the differences may reflect the actual rod tension change which could be induced by relaxation and the pretension of nearby bolts and rods. Therefore, the data is not post-processed to eliminate the offsets.

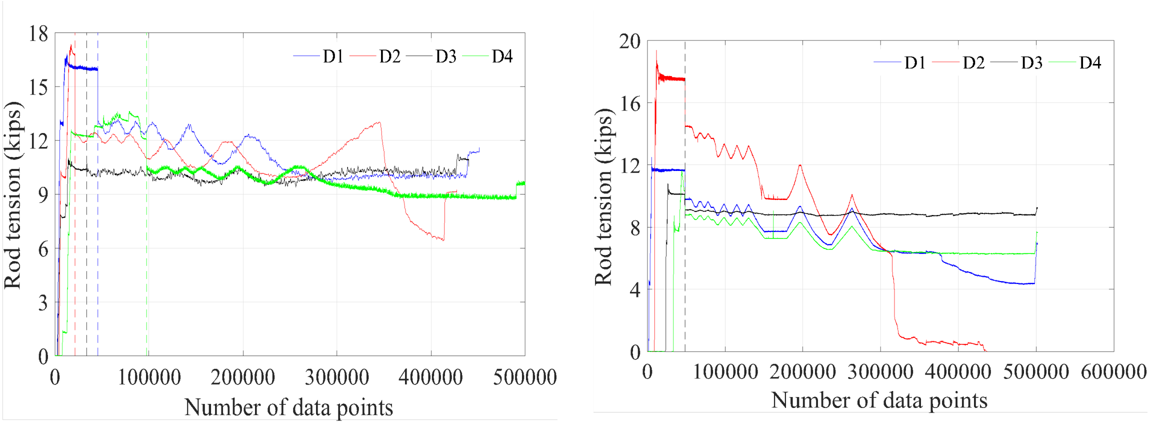

Test 1-M24-2C-RH

Test 2-M24-1C-RL

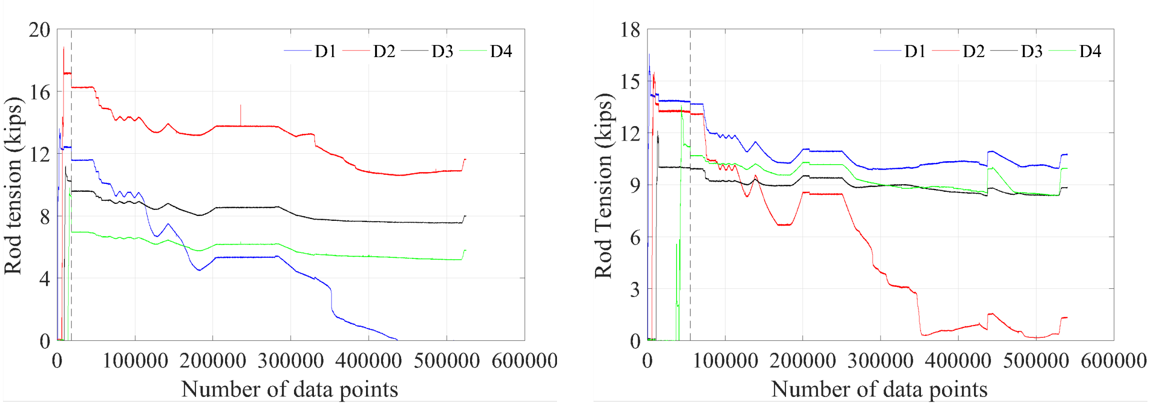

Test 3-M20-3C-RL

Test 4-M20-1C-RL

Figure E.34 Rod tension variation in beam tests

E.2.6 Steel section strain gages

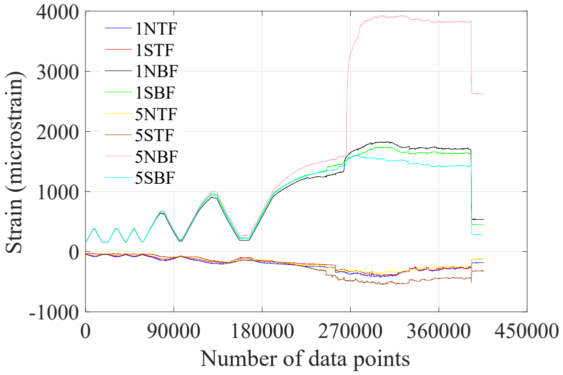

Sections 1 and 5

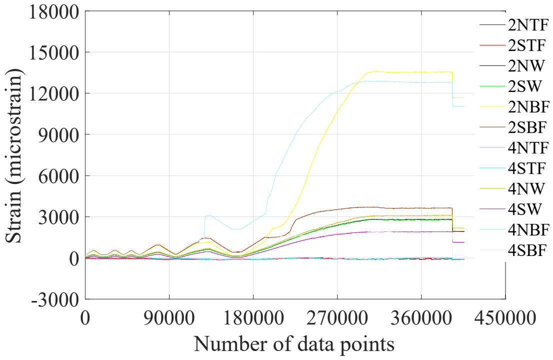

Sections 2 and 4

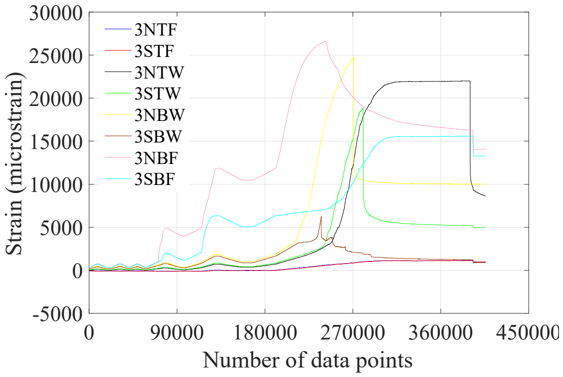

Section 3

Figure E.35 Steel beam strain readings in Test 1-M24-2C-RH

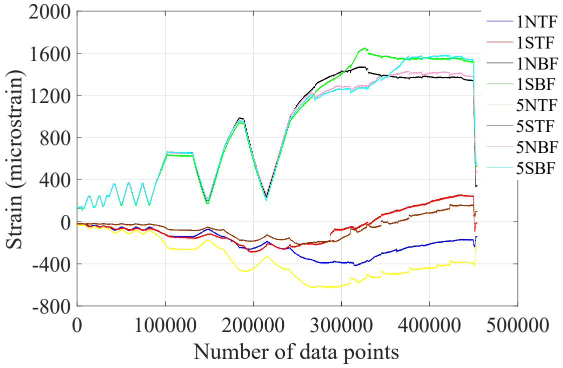

Sections 1 and 5

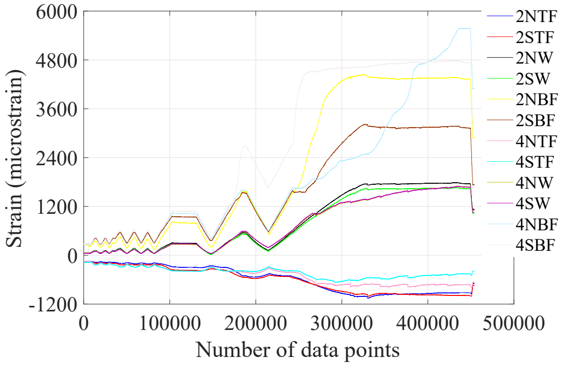

Sections 2 and 4

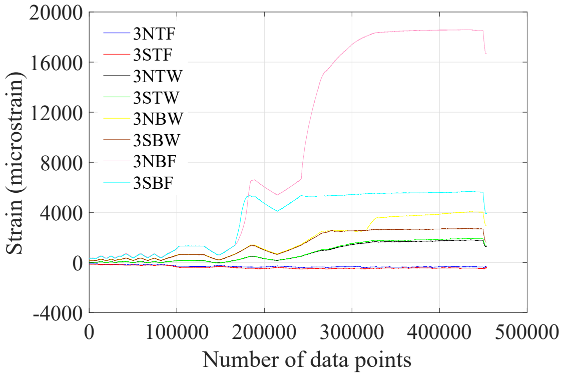

Section 3

Figure E.36 Steel beam strain readings in Test 2-M24-1C-RL

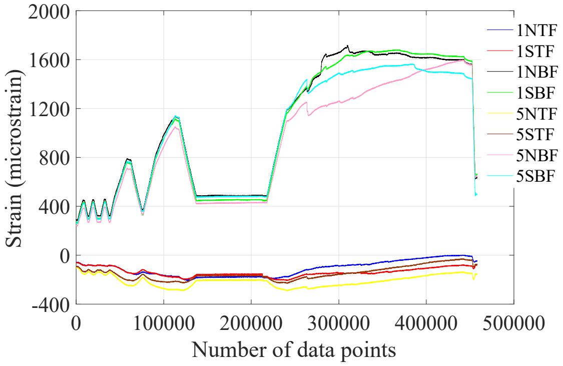

Sections 1 and 5

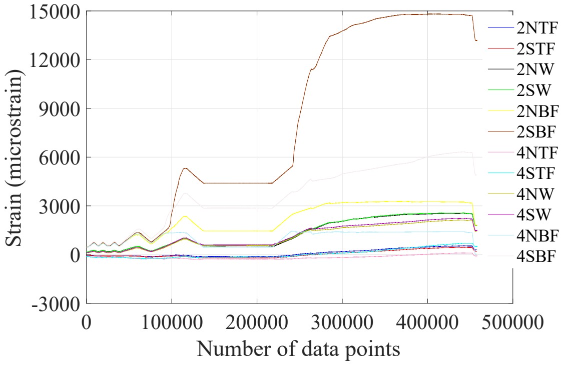

Sections 2 and 4

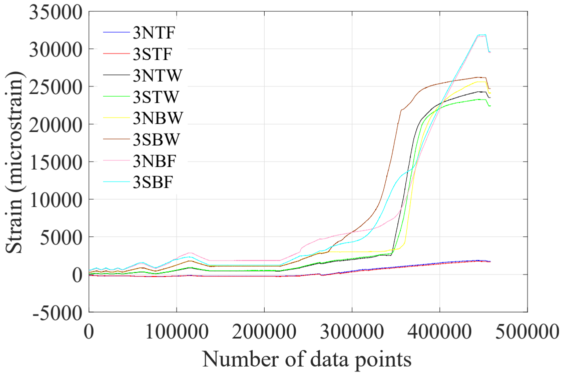

Section 3

Figure E.37 Steel beam strain readings in Test 3-M20-3C-RL

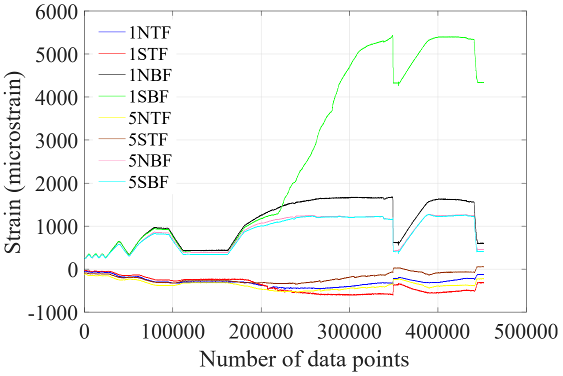

Sections 1 and 5

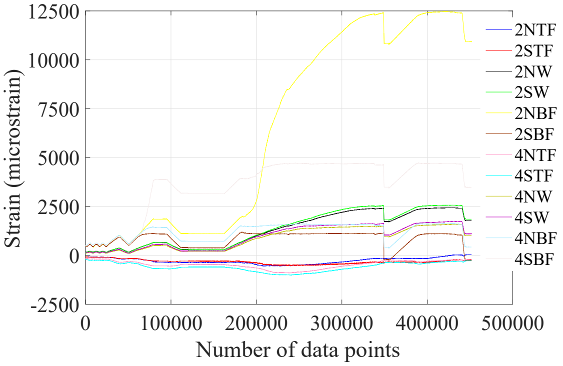

Sections 2 and 4

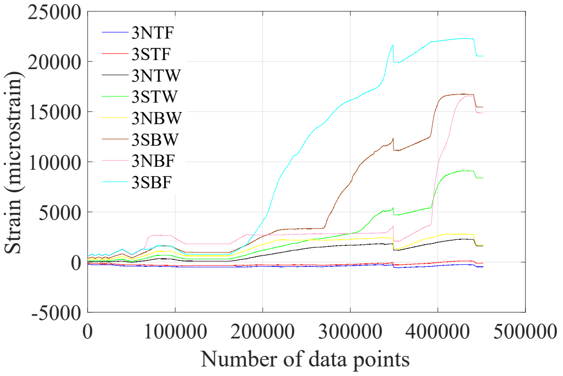

Section 3

Figure E.38 Steel beam strain readings in Test 4-M20-1C-RL

E.2.7 Concrete plank strain

At very small loading, the sensors were not very responsive. During the loading/unloading cycles, the measurements did not return to zero after removing the loads, which could relate to the settling of the beam. In all the tests, bangs, which result from the slip between the steel beam and the concrete planks, led to beam vibration and abrupt changes in the measurements.

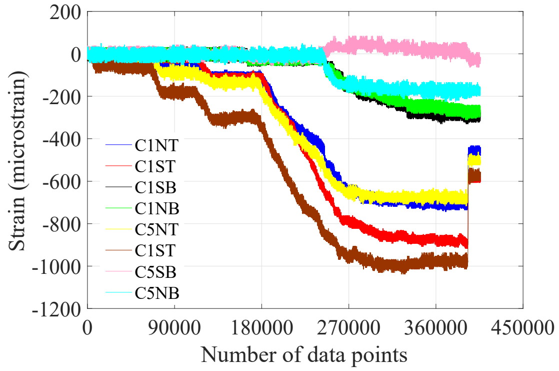

Sections 1 and 5

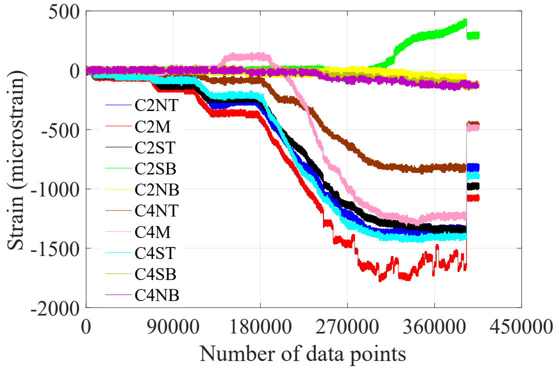

Sections 2 and 4

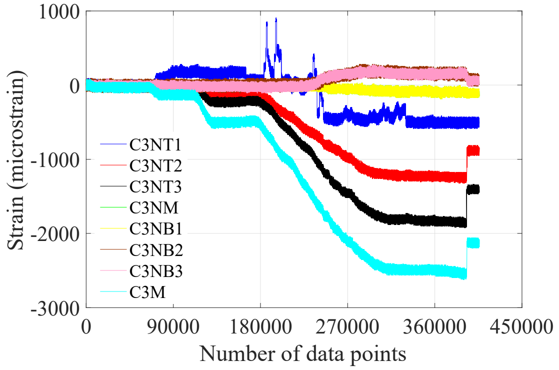

Section 3 (North)

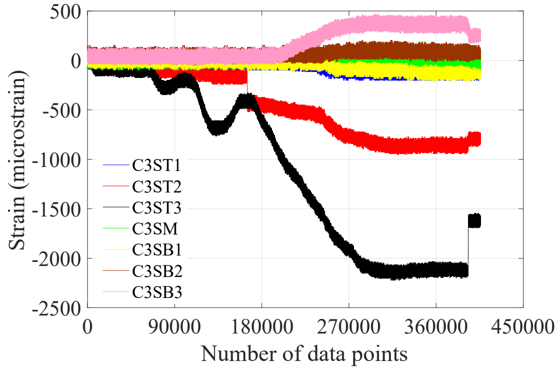

Section 3 (South)

Figure E.39 Concrete plank strain Test 1-M24-2C-RH

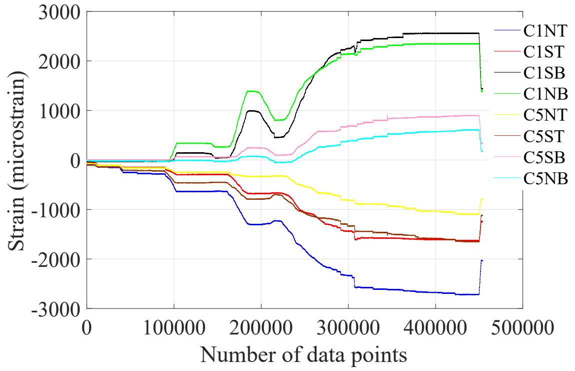

Sections 1 and 5

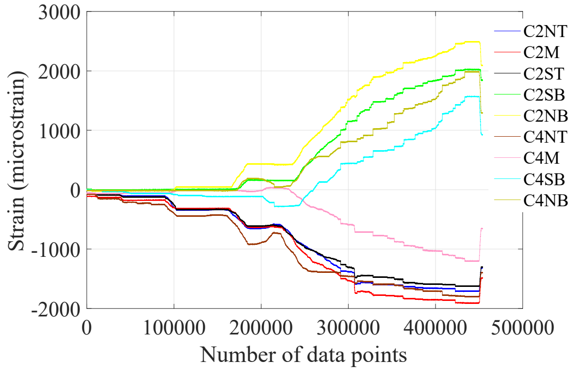

Sections 2 and 4

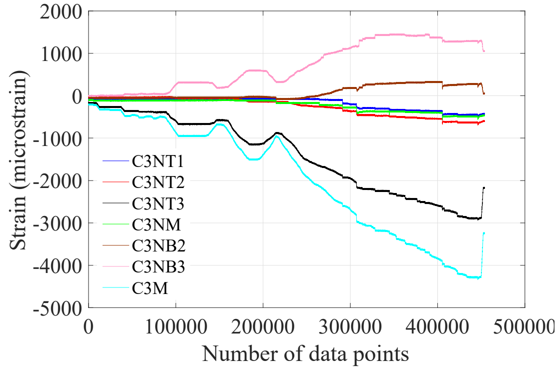

Section 3 (North)

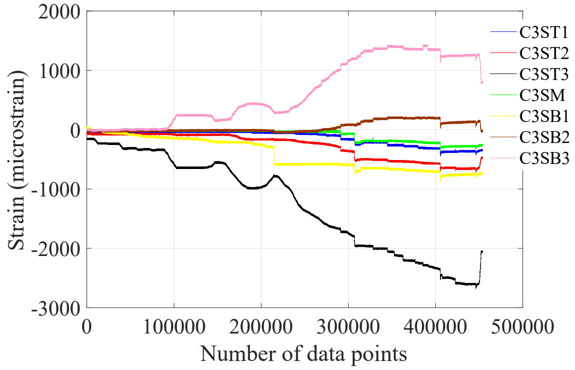

Section 3 (South)

Figure E.40 Concrete plank strain Test 2-M24-1C-RL

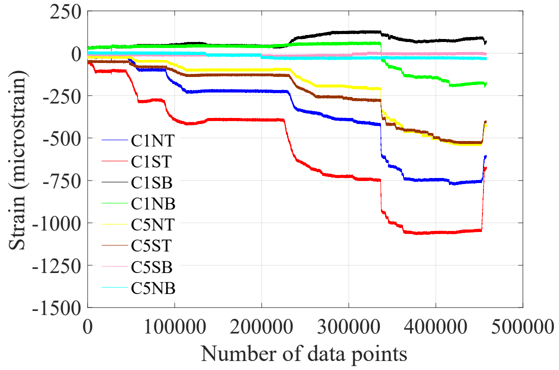

Sections 1 and 5

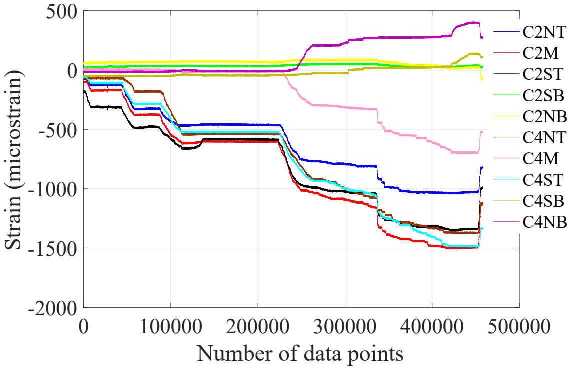

Sections 2 and 4

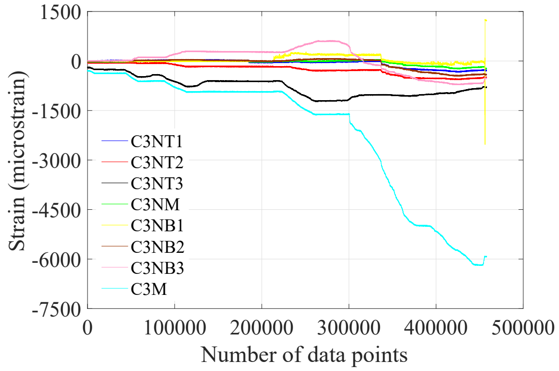

Section 3 (North)

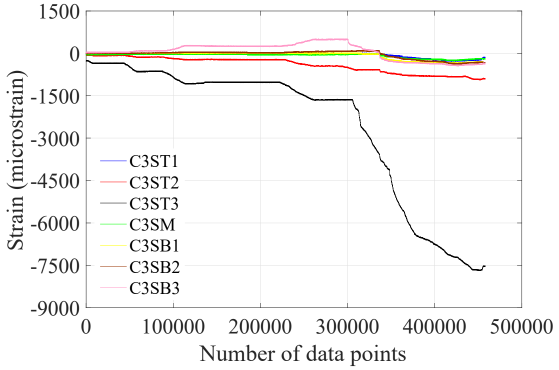

Section 3 (South)

Figure E.41 Concrete plank strain in Test 3-M20-3C-RL

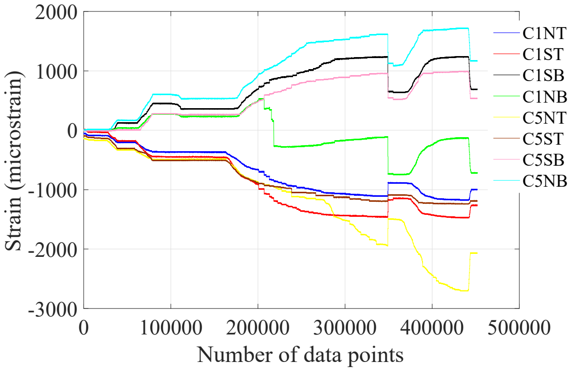

Sections 1 and 5

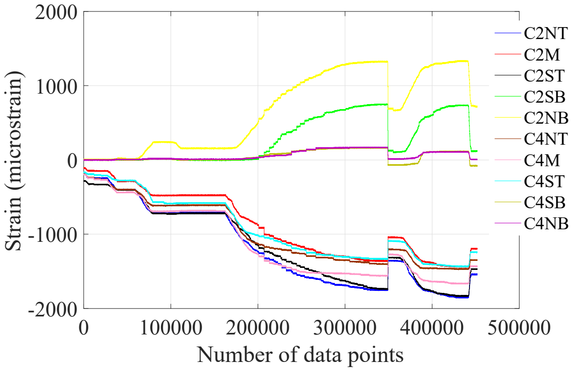

Sections 2 and 4

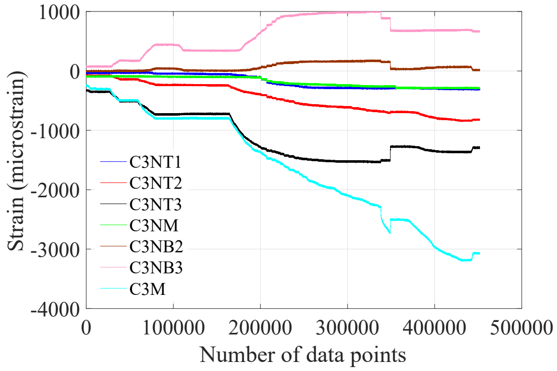

Section 3 (North)

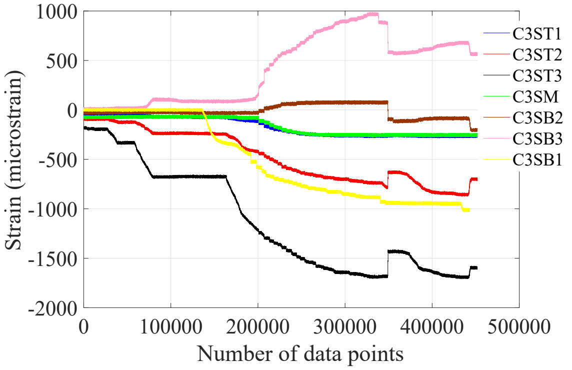

Section 3 (South)

Figure E.42 Concrete plank strain in Test 4-M20-1C-RL

E.2.8 Bolt strain gages

The pretension phase and beam test phase are separated by the dashed lines in the following figures. In Test 1, Test 3 and Test 4, while pretensioning the bolts, some strain gages attached on the bolt shanks were debonded, and the measurements from the debonded gages during the beam tests are thus not shown in the plots. In all the tests, between the two gages attached on the same bolt, the axial strain measurement from the gage close to the steel section was generally smaller than that from the gage away from the beam. The former varied throughout the experiments, while the latter almost maintained the same value. All the strain gage measurements in Test 3 showed tiny changes.

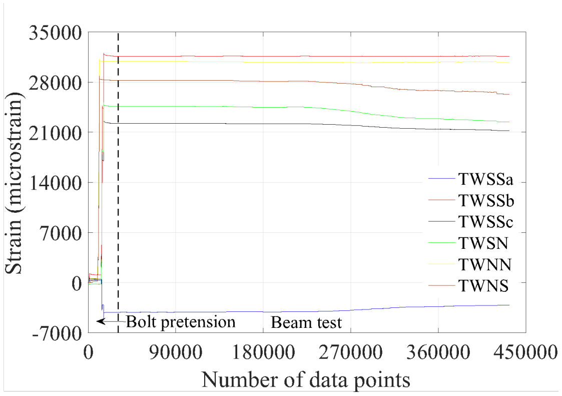

West bolts

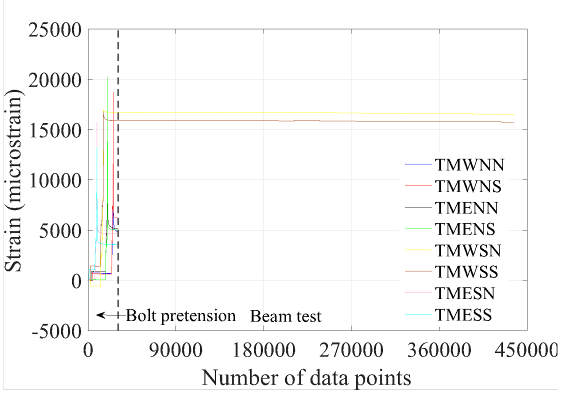

Center bolts

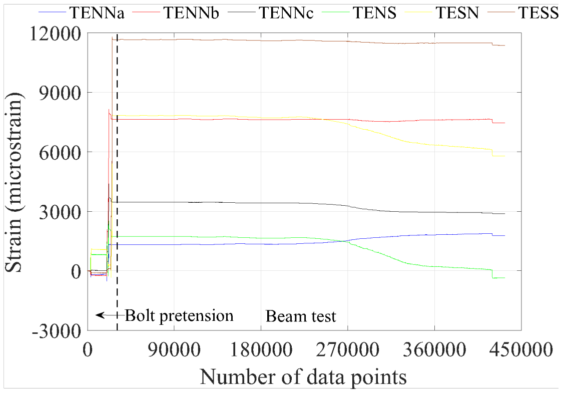

East bolts

Figure E.43 Bolt strain readings in Test 1-M24-2C-RH

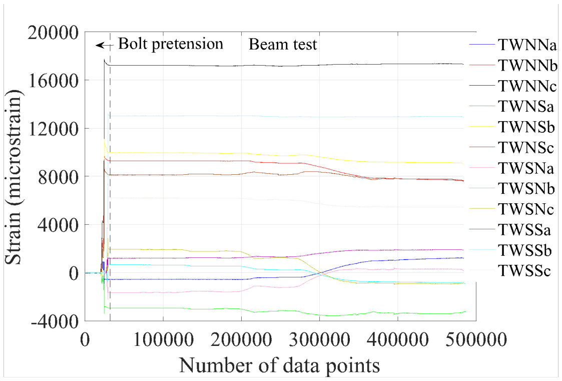

West bolts (bolts at plank 1)

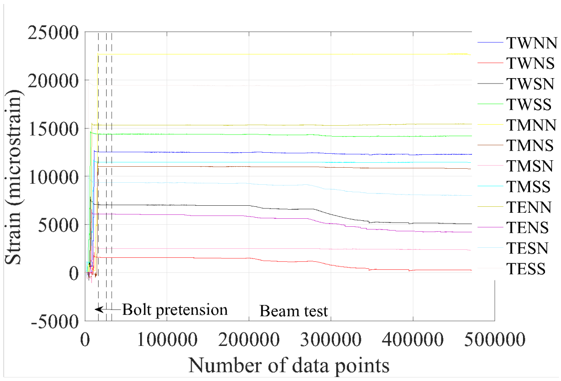

Center bolts and bolts at planks 2 and 14

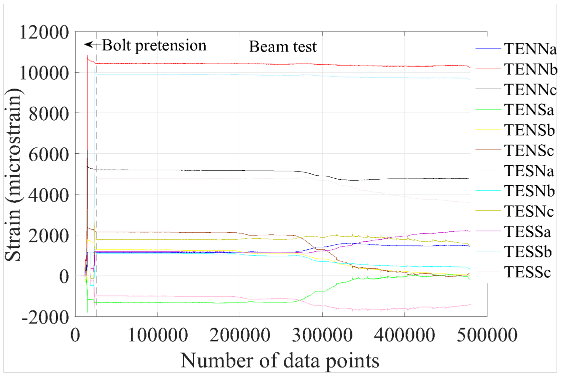

East bolts (bolts at plank 15)

Figure E.44 Bolt strain readings in Test 2-M24-1C-RL

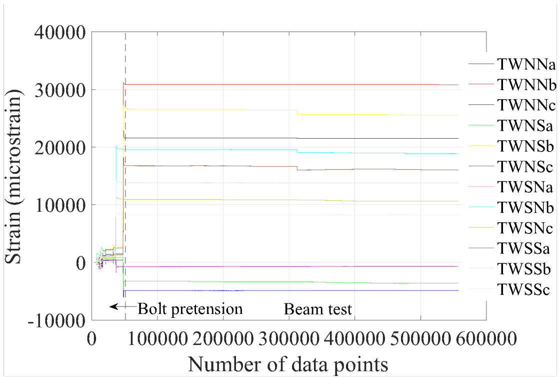

West bolts

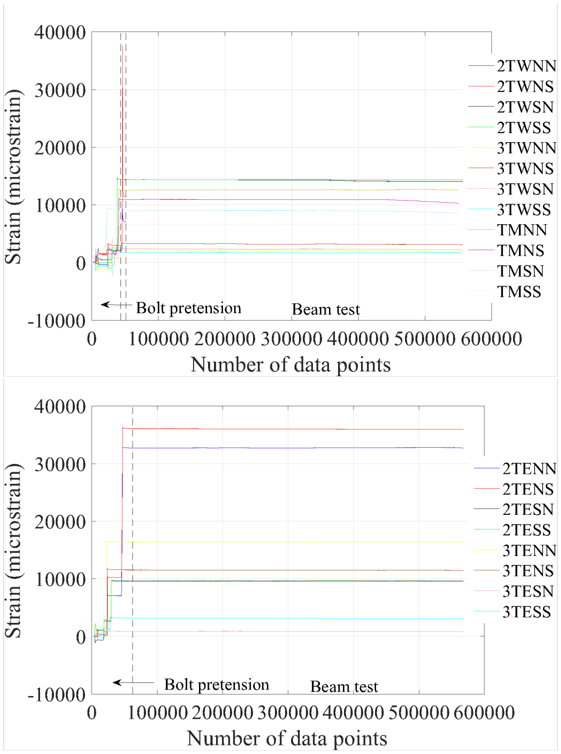

Other bolts

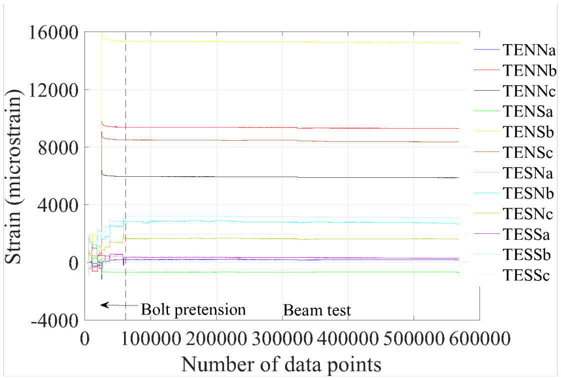

East bolts

Figure E.45 Bolt strain readings in Test 3-M20-3C-RL

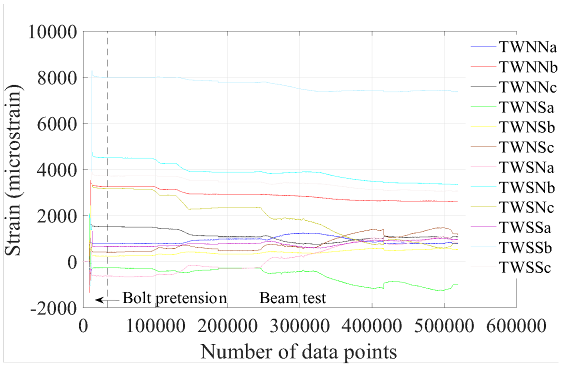

West bolts (bolts at plank 1)

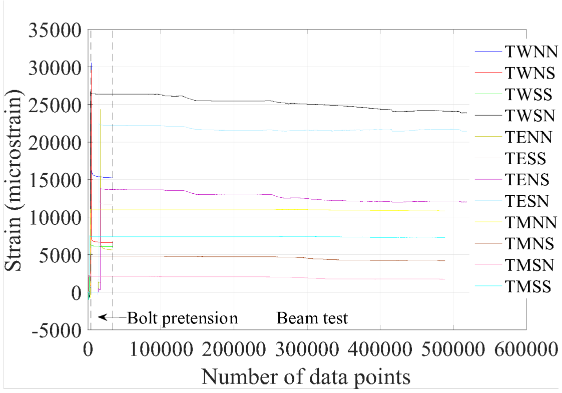

Center bolts and bolts at planks 2 and 14

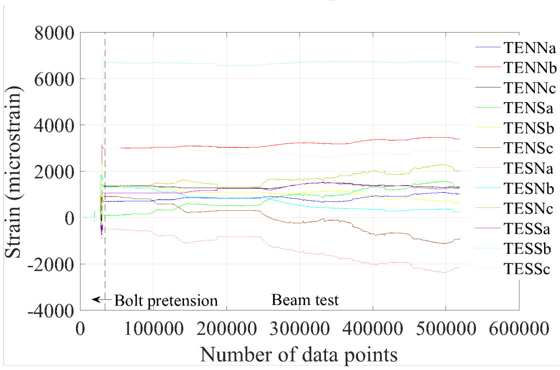

East bolts (bolts at plank 15)

Figure E.46 Bolt strain readings in Test 4-M20-1C-RL

E.2.9 Channel lip strain gages

The deformation of the channel lips was mainly generated while the bolts were pretensioned. During the beam tests, the lip strains appeared to vary concurrently with the bolt axial strains. Since the slip of the center bolts was trivial, the axial forces of the bolts held. Consequently, the changes of the lip strains were not considerable. At the beam ends, the axial strains of the bolts decreased at large slips, and the lip strains varied accordingly. Several gages opened up during the tests, and the readings from these gages are thus not plotted in the graphs.

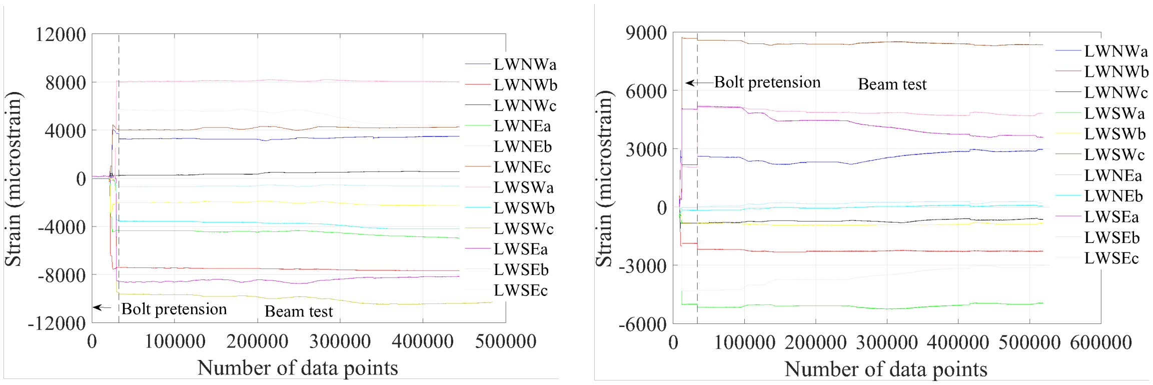

West plank West plank

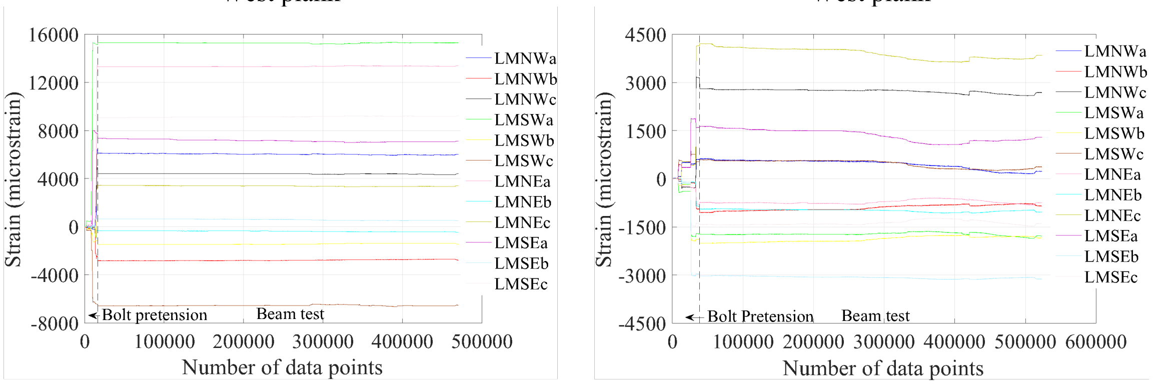

Middle plank Middle plank

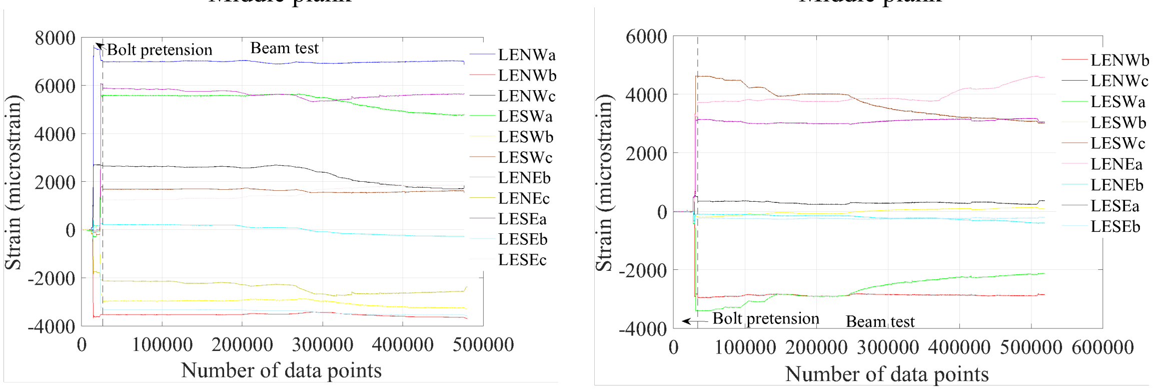

East plank East plank

Test 1-M24-2C-RH Test 4-M20-1C-RL

Figure E.47 Channel lip strain readings in beam tests

E.2.10 Channel anchor strain gages

The readings from the strain gages attached on the channel anchors indicate the deformation of the channel anchors. Throughout the tests, most of the strain measurements did not vary considerably.

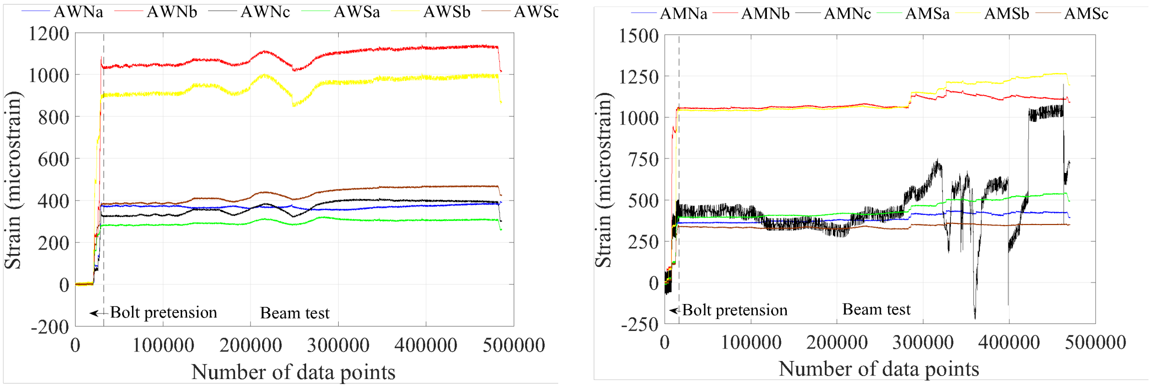

West end (plank 1) Middle (plank 8)

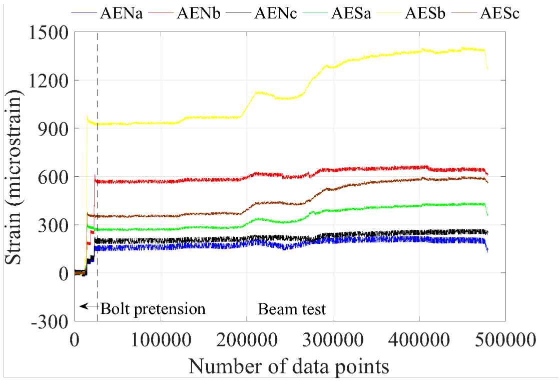

East end (plank 15)

Test 2-M24-1C-RL

Figure E.48 Channel anchor strain readings in beam tests

E.2.11 Reinforcement strain gages

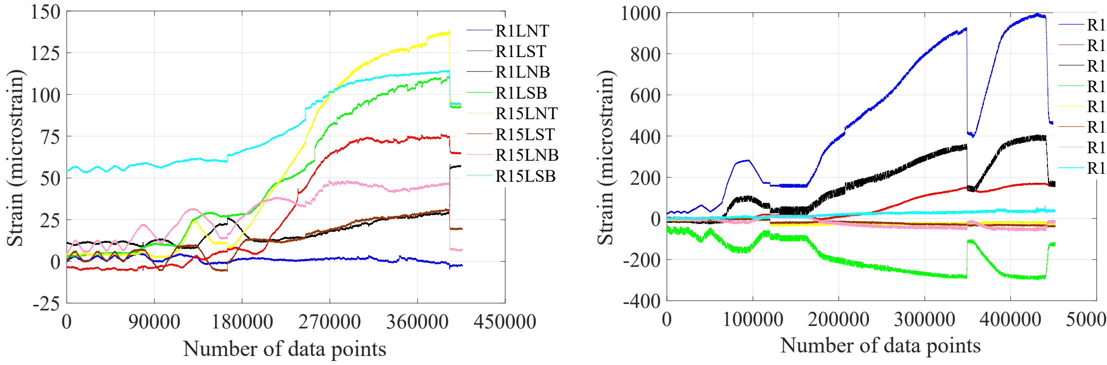

Planks 1 and 15 Planks 1 and 15

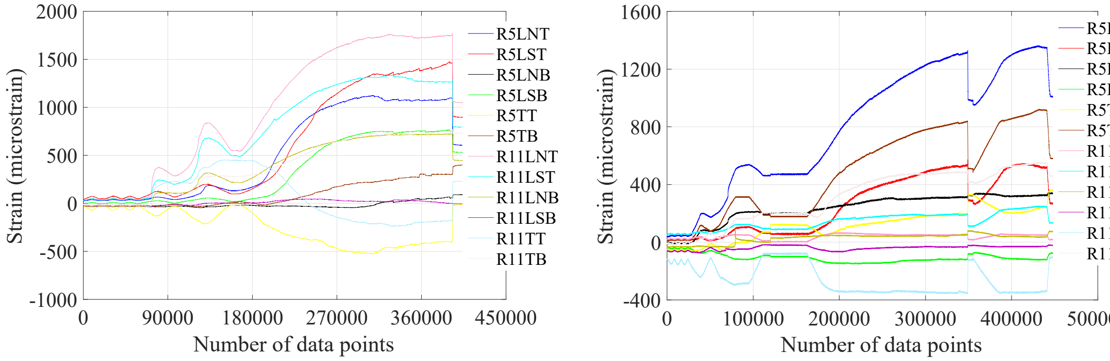

Planks 5 and 11 Planks 5 and 11

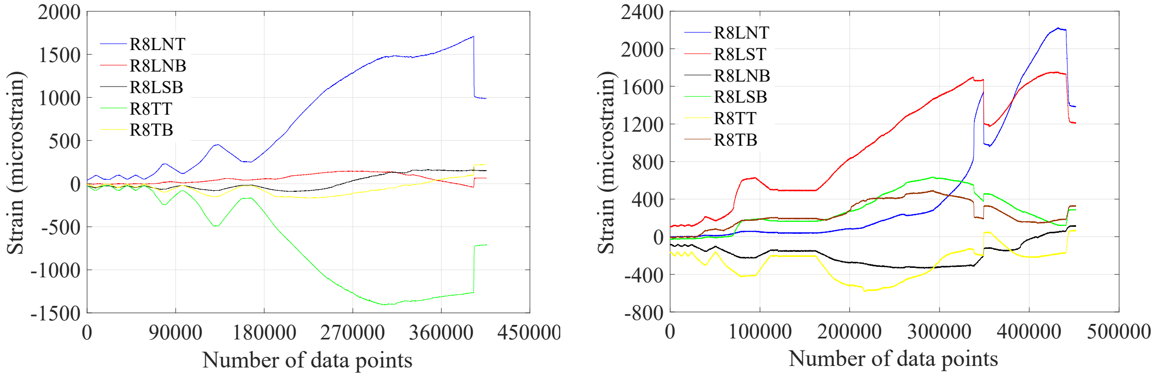

Plank 8 Plank 8

Test 1-M24-2C-RH Test 4-M20-1C-RL

Figure E.49 Reinforcement strain readings in beam tests

Appendix F DATA REDUCTION

Using procedures provided in this appendix, useful quantities are extracted from the raw data displayed in Appendix E.

F.1 Pushout tests

The strategies for handling abnormal strain gage data are as follows:

(1) Small drifts in strain values were commonly seen in the strain gage measurements in the cyclic tests that lasted for days, and they were eliminated for the subsequent data by subtracting the differences between the readings after pausing the test on the previous day and the readings before resuming the test on the next day.

(2) In Test 5-M24-2C-RH-LC, a tiny portion of the raw data was lost during the first loading cycle of the loading history due to crash of the DAQ system. After reviewing the existing data, it was believed that the offset in the gage readings before and after the crash was insignificant. Since the missing data belonged to one of the elastic cycles, the effect of those data on interpreting the results was less important, and therefore no change was made to the raw data.

(3) A few gages debonded or displayed erratic readings. These gages are not included in the plots in Appendix E. When these gages are essential for calculations, a substitute is found which potentially has the same measurement. For example, when gage EFSO was dead in Test 3-M24-2C-RL-LC, gage EFNO was utilized along with other gages on the south side to estimate the axial force at the east section. However, a reasonable substitute does not exist for gage 3c in Test 8-M24-3C-RH-LC. Quantities, such as tensile stress and shear stress, were not computed for this anchor.

(4) Spikes were occasionally seen in the strain gage measurements. The readings, however, became normal afterwards. For those gages, the raw data with spikes was used for calculations. As a result, the processed data also shows spikes which should be disregarded, such as the spike in channel anchor strain ε_{y3} and stress σ_{y3} due to the measurement from gage 3b in Test 3-M24-2C-RL-LC.

(5) After strain gage calibration, several gages still exhibited readings as large as 100 microstrains. The whole measurements from those gages were offset such that the readings started from zero. Subsequent strain measurements and data reduction were not affected.

(6) Erratic readings from bolt strain gages were minimally manipulated, because the calculated inelastic stress is dependent on the deformation history. The pretension of bolt 3 in Test 6-M24-2C-RH-LC-S was calculated using the south strain gage data only. The sharp drop shown in the south strain gage attached on bolt 4 was removed, since the measurement became normal afterwards. When estimating the tension of bolt 4 in Test 10-M20-2C-RH-LC, only the north strain gage data was used.

F.1.1 Load distribution among clamps

In the clamping system, the shear force distribution among the clamps can be indicated by the axial force variation along the length of the steel beam. Using the strain measurements from the gages attached on the steel beam, the axial force at different cross sections of different specimens is calculated in this section.

In order to calculate the axial force at the gaged beam sections, three assumptions are made: (1) plane sections remain plane; (2) the axial stress is uniform along the flange and web thickness; (3) since the axial force mainly flows through the flange, the contribution from the top plates welded on the web is neglected. The process is shown below:

Contribution from the web:

$$\Phi_N = \frac{3(\varepsilon_5 - \varepsilon_6)}{d - t_f} \tag{F.1}$$

$$\Phi_S = \frac{3(\varepsilon_7 - \varepsilon_8)}{d - t_f} \tag{F.2}$$

$$\varepsilon_{tN} = \varepsilon_5 + \Phi_N \frac{d - t_f}{3} \tag{F.3}$$

$$\varepsilon_{tS} = \varepsilon_7 + \Phi_S \frac{d - t_f}{3} \tag{F.4}$$

$$\varepsilon_{bN} = \varepsilon_6 - \Phi_N (t_f + \frac{d - t_f}{3}) \tag{F.5}$$

$$\varepsilon_{bS} = \varepsilon_8 - \Phi_S (t_f + \frac{d - t_f}{3}) \tag{F.6}$$

$$P_w = \frac{(\varepsilon_{tN} + \varepsilon_{tS} + \varepsilon_{bN} + \varepsilon_{bS})}{4} E d t_w \tag{F.7}$$

Contribution from the flange:

$$P_f = \frac{(\varepsilon_1 + \varepsilon_2 + \varepsilon_3 + \varepsilon_4)}{4} E (b_f - t_w) t_f \tag{F.8}$$

Figure F.1 shows the definition of the notation. The axial force variation at different cross sections for different specimens is plotted in Figure F.2 through Figure F.5. In these plots, positive values represent tensile forces, and negative values represent compressive forces.

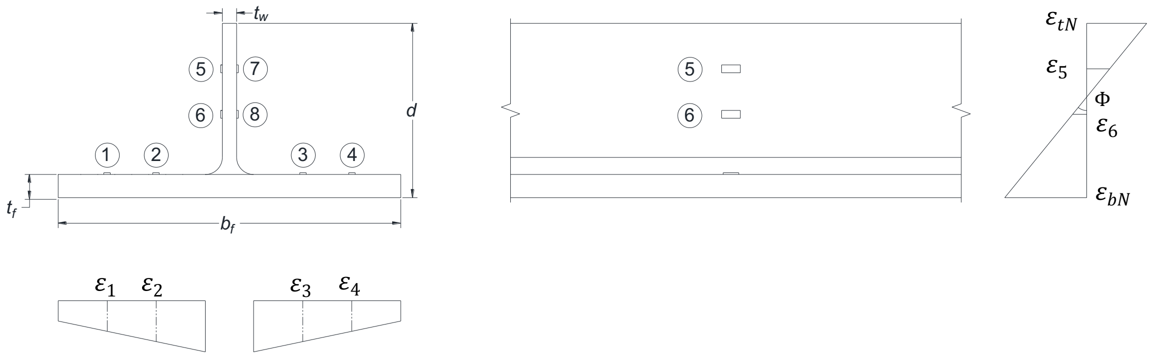

t_w
⑤
⑦
⑥
⑧
d
①
②
③
④
t_f
b_f
ε_1
ε_2
ε_3
ε_4
⑤
⑥
ε_{tN}
ε_5
Φ
ε_6
ε_{bN}

Figure F.1 Strain gage locations and numbering for WT sections

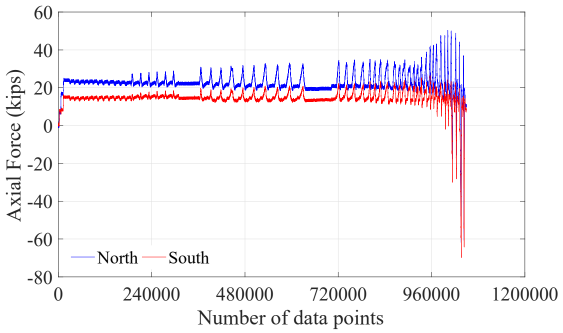

West section

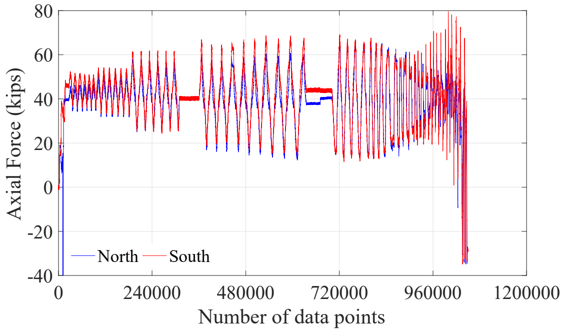

Middle section

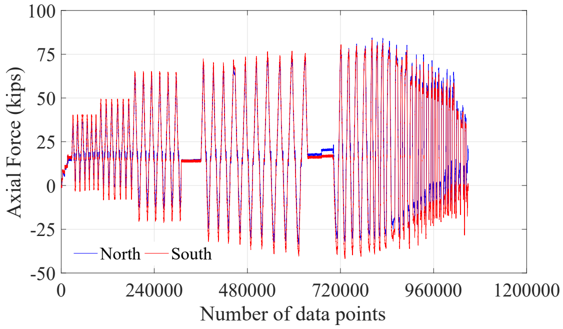

East section

Figure F.2 Axial force variation for cross sections in WT beam in Test 3-M24-2C-RL-LC

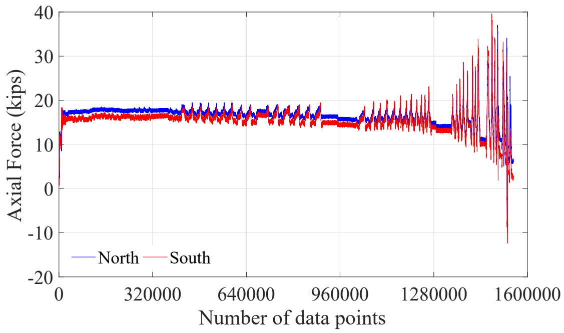

West section

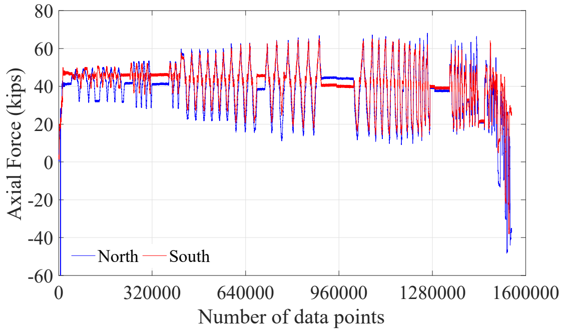

Middle section

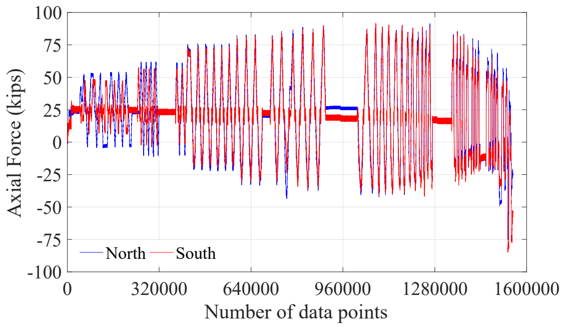

East section

Figure F.3 Axial force variation for cross sections in WT beam in Test 5-M24-2C-RH-LC

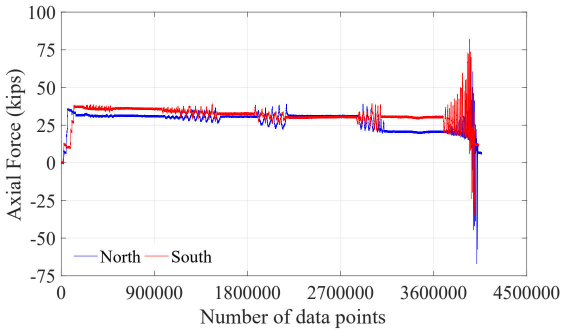

West section

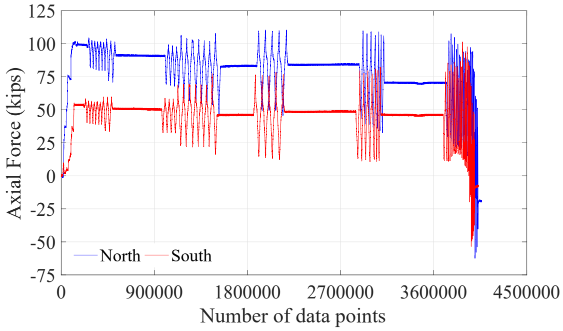

Middle west section

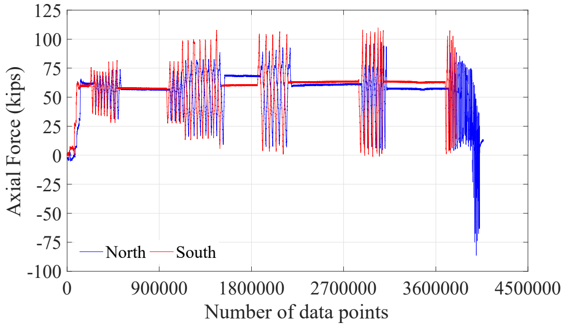

Middle east section

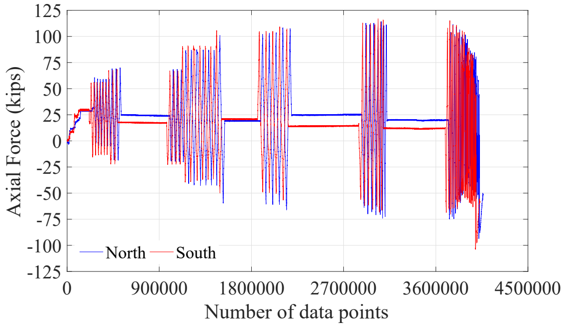

East section

Figure F.4 Axial force variation for cross sections in WT beam in Test 8-M24-3C-RH-LC

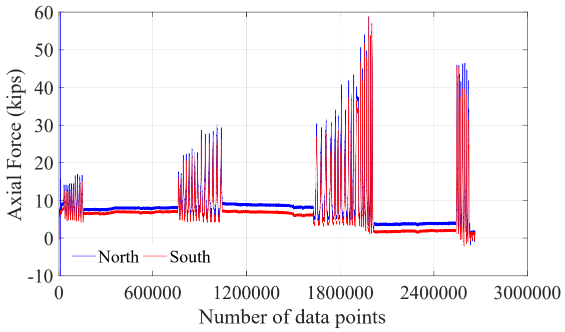

West section

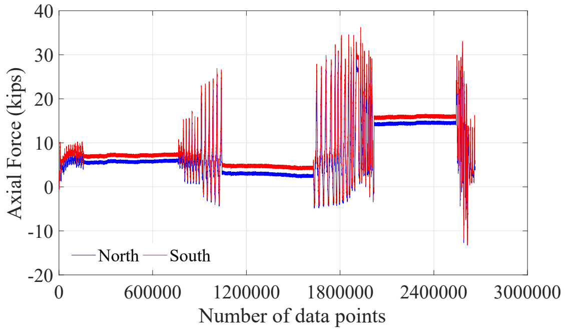

Middle section

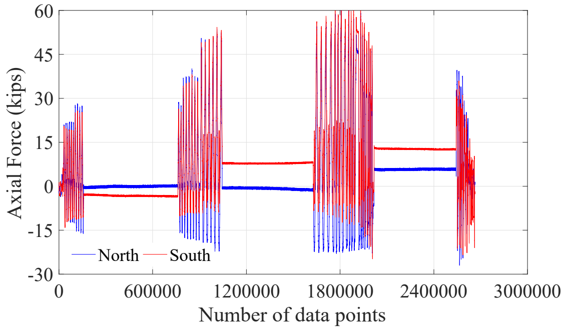

East section

Figure F.5 Axial force variation for cross sections in WT beam in Test 10-M20-2C-RH-LC

F.1.2 Bolt pretention force variation

Since the tension of the T-bolts directly affects the shear strength and behavior of the clamps, numerous bolts were instrumented with strain gages to track the bolt tension variation throughout the tests. Due to the nonlinear behavior of the bolts, the conversion from the measured inelastic strains to inelastic stresses with the Chaboche model is demonstrated in this section.

In the Chaboche model without isotropic hardening, the nonlinear kinematic strain hardening rule determines how the yield surface is translated in the stress space following the backstresses. The hardening law for each backstress is

$$d\boldsymbol{\alpha}_k = \frac{C_k}{\sigma^0}(\boldsymbol{\sigma} - \boldsymbol{\alpha}_k)d\varepsilon_{eq}^{pl} - \gamma_k \boldsymbol{\alpha}_k d\varepsilon_{eq}^{pl} \tag{F.9}$$

Where C_k is the initial kinematic hardening modulus; γ_k is the rate at which the kinematic hardening modulus decreases with increasing plastic strain. Both are independent parameters and can be calibrated with monotonic coupon testing data. σ^0 is the size of the yield surface; ε_{eq}^{pl} is the equivalent plastic strain. The overall backstress is calculated as:

$$\boldsymbol{\alpha} = \sum_{k=1}^{N} \boldsymbol{\alpha}_k \tag{F.10}$$

Where N is the number of backstresses.

The conversion from measured inelastic strains to inelastic stresses was conducted in ABAQUS/Standard with a single three-dimensional, linear, reduced integration solid element, as shown in Figure F.6. Material properties assigned to the element included elastic modulus and Possion's ratio, which were 30900 ksi and 0.3, respectively. The kinematic hardening behavior of the material was defined by specifying half-cycle data. In ABAQUS, the input stress and strain are true stress and true plastic strain. However, the stress and strain obtained from tensile coupon testing are nominal stress and nominal strain, which are calculated based on the undeformed configuration of the coupons. The relationship between the two types of strain and stress values is shown in Equations (F.11) and (F.12) (ABAQUS 2011).

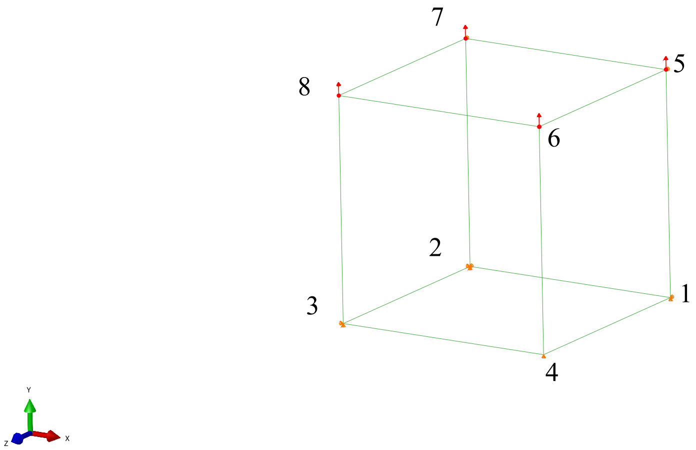

Figure F.6 Stress analysis model

$$\varepsilon_{true} = ln\,(1 + \varepsilon_{nom}) \tag{F.11}$$

$$\sigma_{true} = \sigma_{nom}(1 + \varepsilon_{nom}) \tag{F.12}$$

The true plastic strain is thus calculated as

$$\varepsilon_{true}^{pl} = \varepsilon_{true} - \sigma_{true}/E \tag{F.13}$$

The input yield stress and plastic strain values provided in Table F.1 were based on a stress-strain relationship that is the average of the four tested stress-strain curves, as shown in Figure F.7. Three backstresses were defined to adequately characterize the variation of the strain hardening modulus. In the finite element model, nodes 1, 2, 5, and 7 were restrained from moving in the Z direction, while the bottom nodes were fixed in the Y direction, and nodes 2 and 3 were prevented from translating in the X direction. The strain measurements were used as the displacement assigned to the top nodes.

Table F.1 Pushout test bolt stress and strain

Stress (ksi)		Strain	
Engineering	True	Engineering	True
105.900	106.27	0.0035	0.00000
113.475	113.93	0.0040	0.00031
118.525	119.24	0.0060	0.00212
121.475	122.69	0.010	0.00598
123.500	125.23	0.014	0.00985
125.200	127.45	0.018	0.01372
127.075	129.87	0.022	0.01756
127.825	130.89	0.024	0.01948
130.200	134.37	0.032	0.02715
130.850	135.30	0.034	0.02906
131.675	136.68	0.038	0.03287
132.350	137.91	0.042	0.03668
132.875	138.99	0.046	0.04048

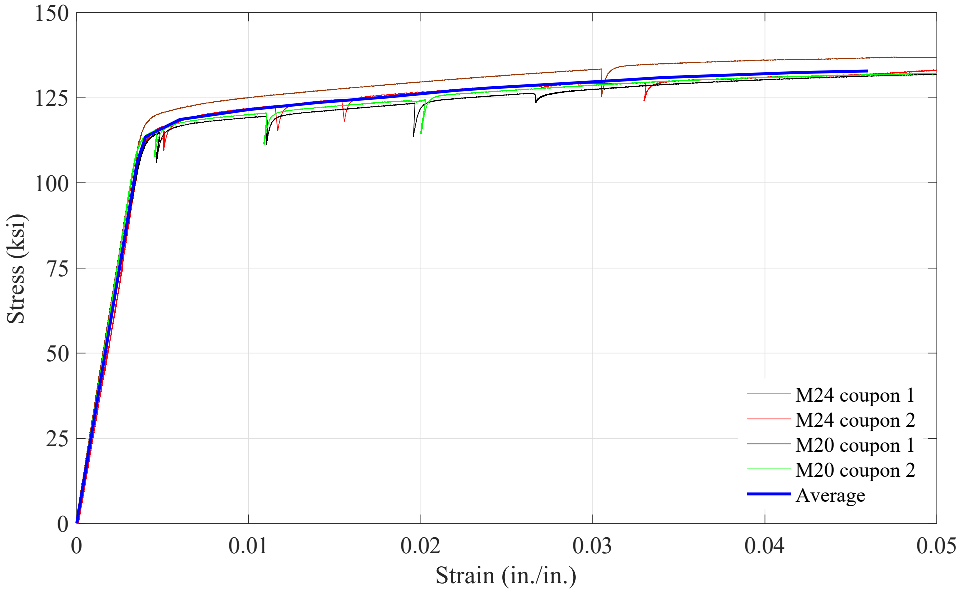

Figure F.7 Pushout test bolt stress-strain curves

F.1.2.1 Pretension test

Using measured bolt strains, the stress-strain relationships and the bolt stresses at different number of turns of the nut are illustrated in Figure F.8.

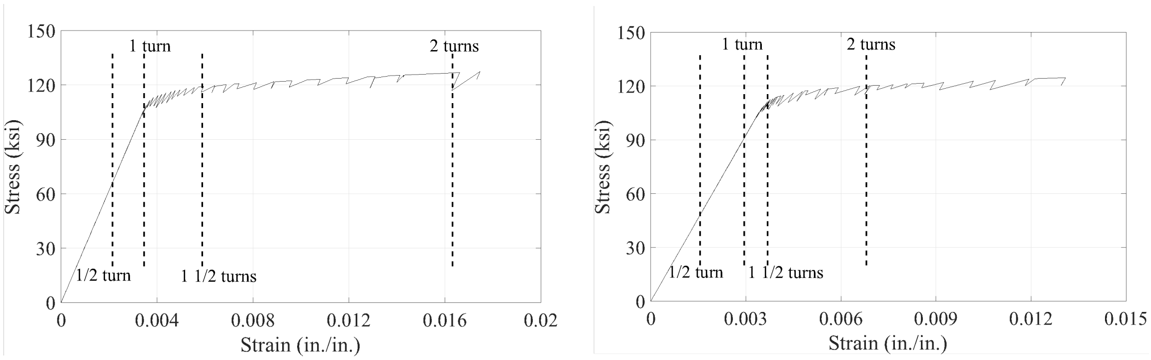

M24 bolt test 1 M24 bolt test 2

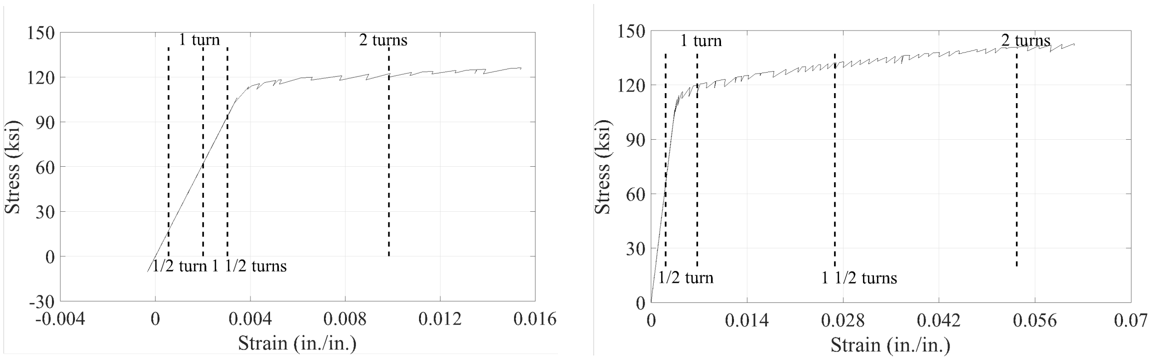

M24 bolt test 3 M20 bolt test 1

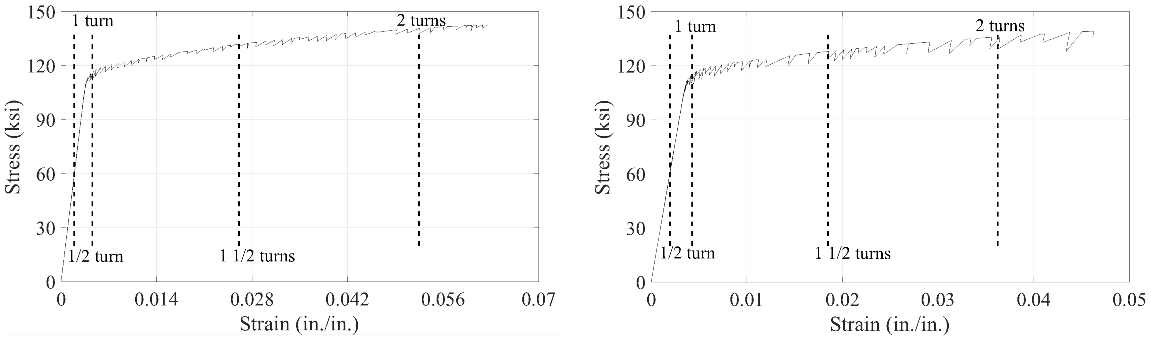

M20 bolt test 2 M20 bolt test 3

Figure F.8 Bolt material loading and unloading behavior in pretension tests

F.1.2.2 Pushout test

Using measured bolt strains, the tension variation of the instrumented bolts in several tests is illustrated in Figure F.9. The loading/unloading behavior of the bolt material during the tests is given in Figure F.10.

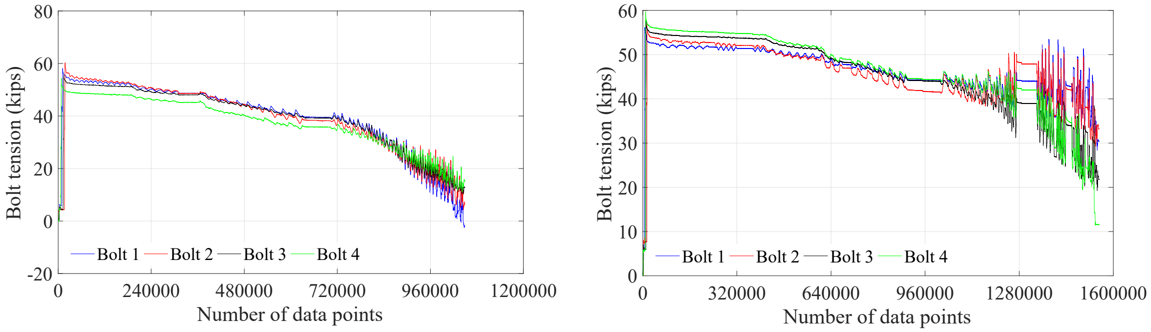

Test 3-M24-2C-RL-LC

Test 5-M24-2C-RH-LC

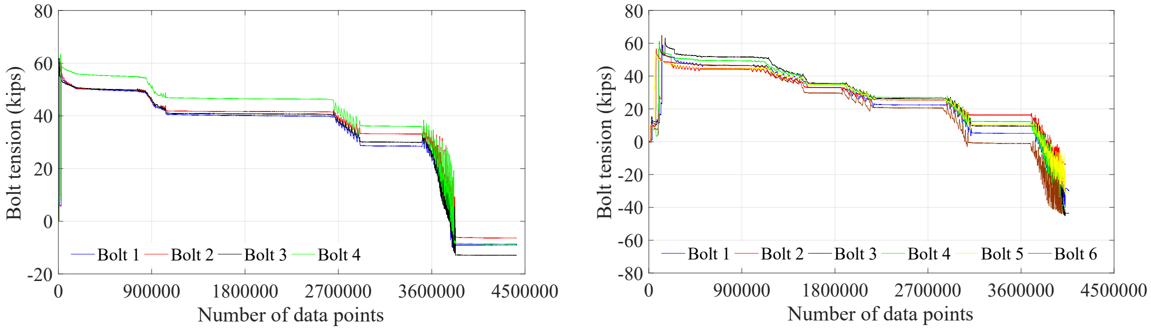

Test 6-M24-2C-RH-LC-S

Test 8-M24-3C-RH-LC

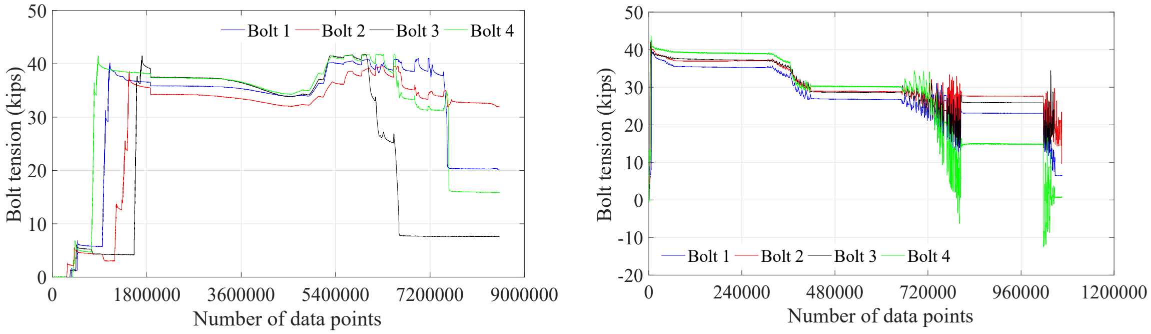

Test 9-M20-2C-RH-LM

Test 10-M20-2C-RH-LC

Figure F.9 Bolt axial force variation in pushout tests

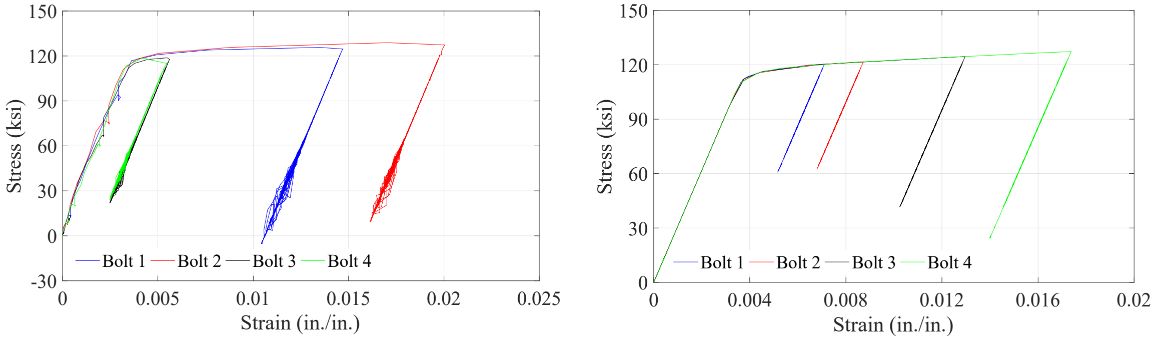

Test 3-M24-2C-RL-LC Test 5-M24-2C-RH-LC

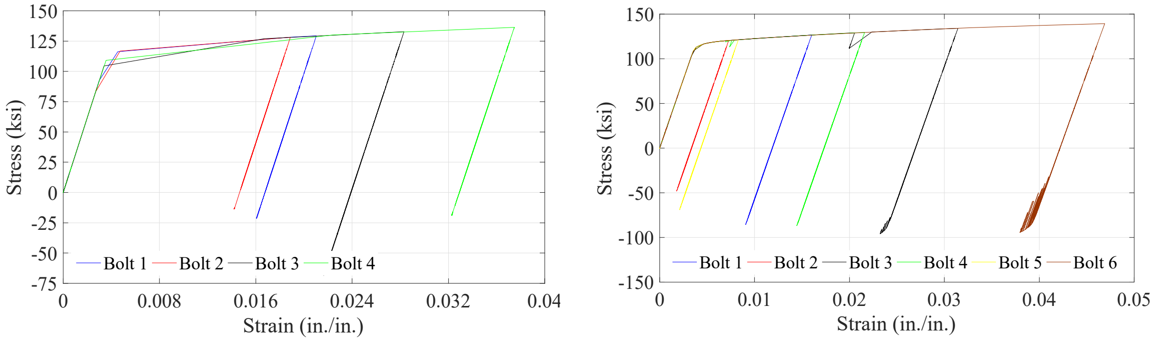

Test 6-M24-2C-RH-LC-S Test 8-M24-3C-RH-LC

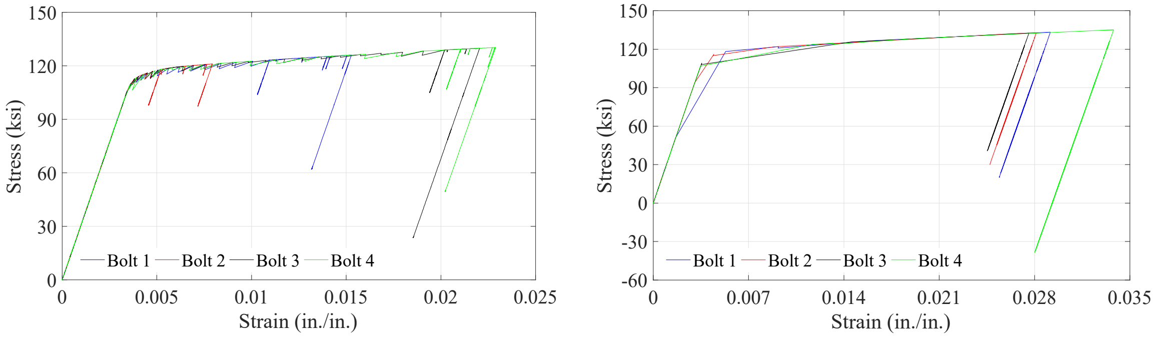

Test 9-M20-2C-RH-LM Test 10-M20-2C-RH-LC

Figure F.10 Bolt material loading and unloading behavior in pushout tests

F.1.3 Forces acting on channel anchors

Several channel anchors were instrumented with rosette strain gages to determine the tension and shear forces the anchors were subjected to throughout the pushout tests. The conversion from the measured anchor strains to the anchor stresses is demonstrated in this section.

Two-dimensional strain transformation is shown in Figure F.11. The orientation of the three legs in a rosette strain gage attached on a channel anchor is shown in Figure F.12. A coordinate system is also defined for the transformed strains. Given the three strain measurements from a rosette strain gage, the axial and shear strain can be calculated using the following equations.

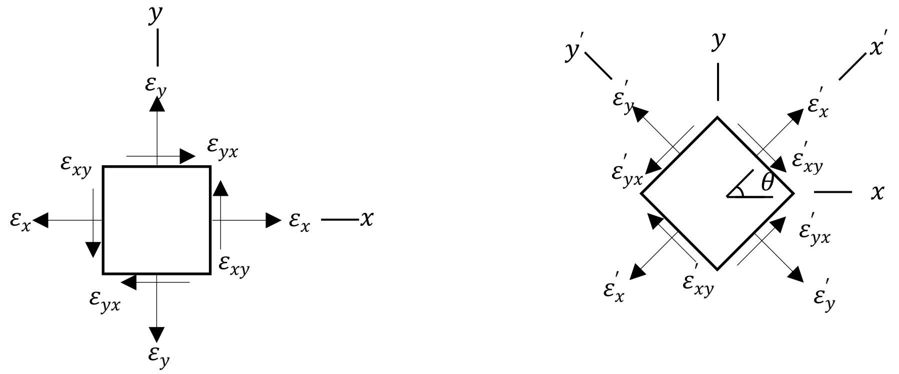
y
ε_y
ε_{yx}
ε_{xy}
ε_x
ε_x
x
ε_{xy}
ε_{yx}
ε_y
y'
y
x'
ε_y'
ε_x'
ε_{yx}'
ε_{xy}'
θ
x
ε_{yx}'
ε_x'
ε_{xy}'
ε_y'

Figure F.11 Strain transformation between different coordinates

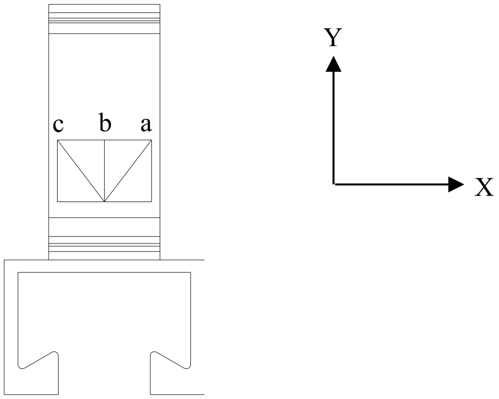

Figure F.12 Rosette strain gage orientation and defined coordinate system

$$\varepsilon_x' = \varepsilon_x cos^2\theta + \varepsilon_y sin^2\theta + \gamma_{xy} sin\theta cos\theta \qquad \text{(F.14)}$$

$$\varepsilon_a = \varepsilon_x cos^2\frac{\pi}{4} + \varepsilon_y sin^2\frac{\pi}{4} + \gamma_{xy} sin\frac{\pi}{4} cos\frac{\pi}{4} = \frac{1}{2}(\varepsilon_x + \varepsilon_y + \gamma_{xy}) \qquad \text{(F.15)}$$

$$\varepsilon_b = \varepsilon_x cos^2\frac{\pi}{2} + \varepsilon_y sin^2\frac{\pi}{2} + \gamma_{xy} sin\frac{\pi}{2} cos\frac{\pi}{2} = \varepsilon_y \qquad \text{(F.16)}$$

$$\varepsilon_c = \varepsilon_x cos^2\frac{3\pi}{4} + \varepsilon_y sin^2\frac{3\pi}{4} + \gamma_{xy} sin\frac{3\pi}{4} cos\frac{3\pi}{4} = \frac{1}{2}(\varepsilon_x + \varepsilon_y - \gamma_{xy}) \qquad \text{(F.17)}$$

$$\varepsilon_x = \varepsilon_a + \varepsilon_c - \varepsilon_b \qquad \text{(F.18)}$$

$$\varepsilon_y = \varepsilon_b \tag{F.19}$$

$$\gamma_{xy} = \varepsilon_a - \varepsilon_c \tag{F.20}$$

Where

$\varepsilon_a, \varepsilon_b, \varepsilon_c$ = strain measurements from the rosette strain gages

$\varepsilon_x, \varepsilon_y, \varepsilon_{xy}$ = strain components with respect to the defined coordinate system

The stress-strain relationship for elastic elements in a two-dimensional plane stress state is provided in Equations (F.21) through (F.24). The Von Mises yield criterion in Equation (F.25) is utilized to ascertain that the anchors are elastic.

$$\begin{pmatrix} \sigma_x \\ \sigma_y \\ \tau_{xy} \end{pmatrix} = \frac{E}{1-\nu^2} \begin{pmatrix} 1 & \nu & 0 \\ \nu & 1 & 0 \\ 0 & 0 & (1-\nu)/2 \end{pmatrix} \begin{pmatrix} \varepsilon_x \\ \varepsilon_y \\ \gamma_{xy} \end{pmatrix} \tag{F.21}$$

$$\sigma_x = \frac{E}{1-\nu^2}(\varepsilon_x + \nu\varepsilon_y) \tag{F.22}$$

$$\sigma_y = \frac{E}{1-\nu^2}(\varepsilon_y + \nu\varepsilon_x) \tag{F.23}$$

$$\tau_{xy} = G\gamma_{xy} \tag{F.24}$$

$$\sigma_{VM} = \sqrt{{\sigma_x}^2 + {\sigma_y}^2 - \sigma_x\sigma_y + 3{\tau_{xy}}^2} \tag{F.25}$$

Where

E = modulus of elasticity

G = shear modulus

ν = Possion’s ratio

When the anchor material was inelastic, the strains were converted into stresses using the single element model shown in Figure F.6. To prevent rigid body motion of the element, the same boundary conditions described in Section F.1.2 were defined. The transformed axial strain in the y direction (i.e., ε_y) was assigned to the top nodes, while the transformed axial strain in the x direction (i.e., ε_x) and shear strain (i.e., γ_{xy}) were applied to nodes 1 and 4 and nodes 7 and 8, respectively. The displacement of nodes 5 and 6 was the summation of ε_x and γ_{xy}. The material stress-strain relationship given in Table 4.10 in Chapter 4, which is obtained from tensile coupon testing, was employed for the anchors. The variation of the anchor strain and stress is plotted in Figure F.13 through Figure F.15.

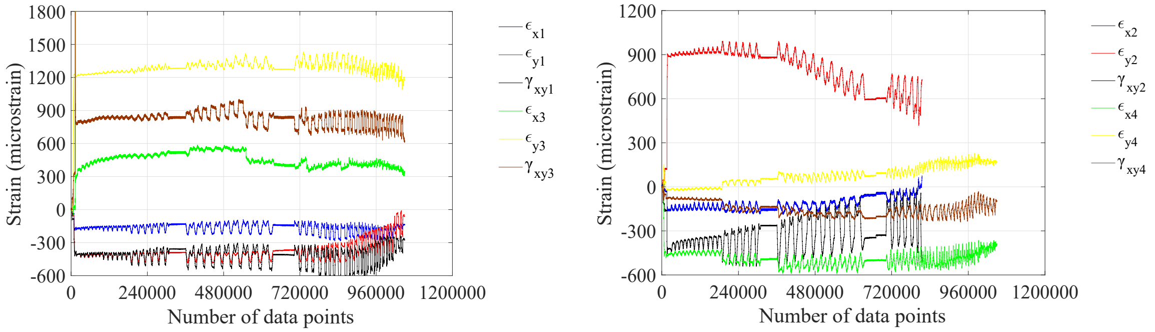

Anchors 1 and 3 Anchors 2 and 4

Strain components

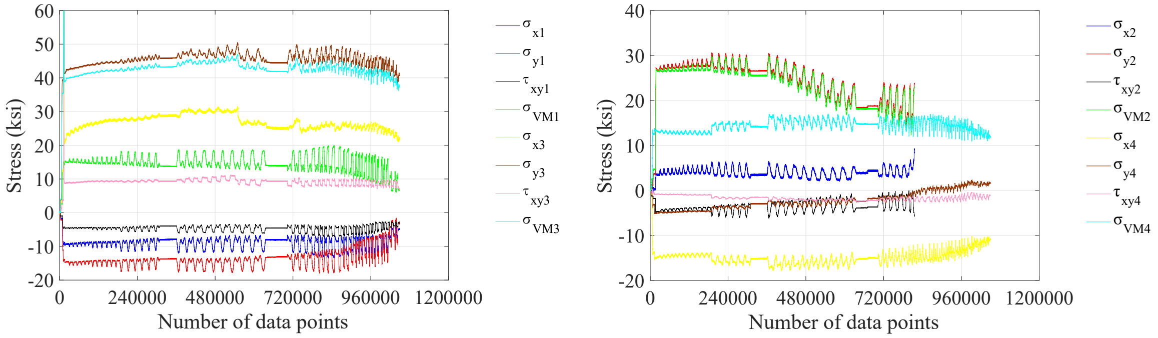

Anchors 1 and 3 Anchors 2 and 4

Stress components

Figure F.13 Anchor strain and stress variation in Test 3-M24-2C-RL-LC

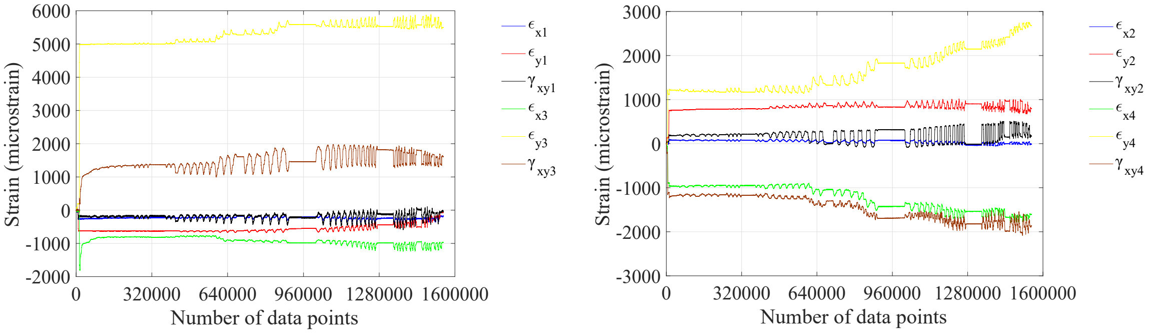

Anchors 1 and 3 Anchors 2 and 4

Strain components

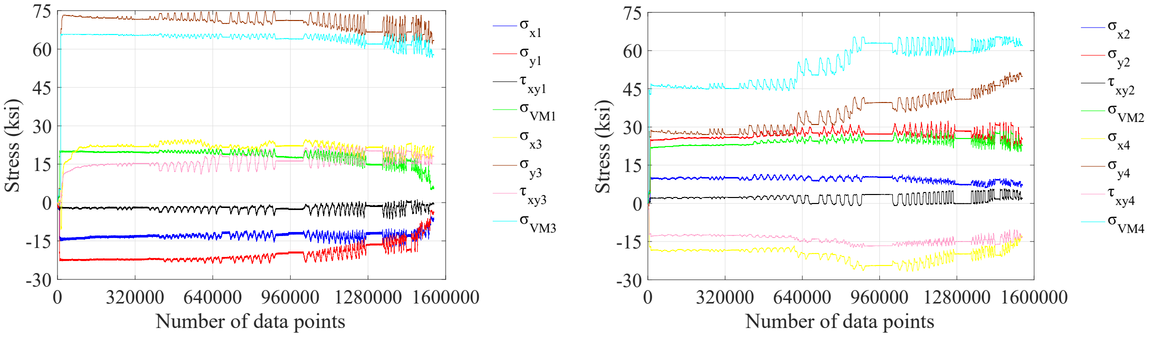

Anchors 1 and 3 Anchors 2 and 4

Stress components

Figure F.14 Anchor strain and stress variation in Test 5-M24-2C-RH-LC

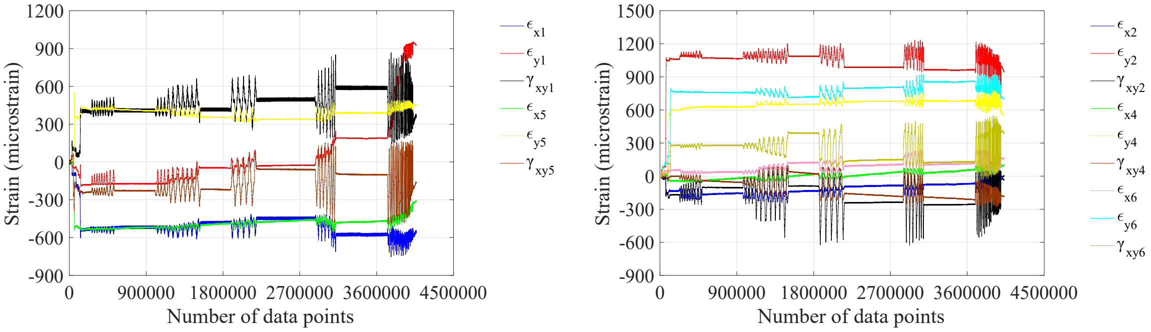

Anchors 1 and 5 Anchors 2, 4 and 6

Strain components

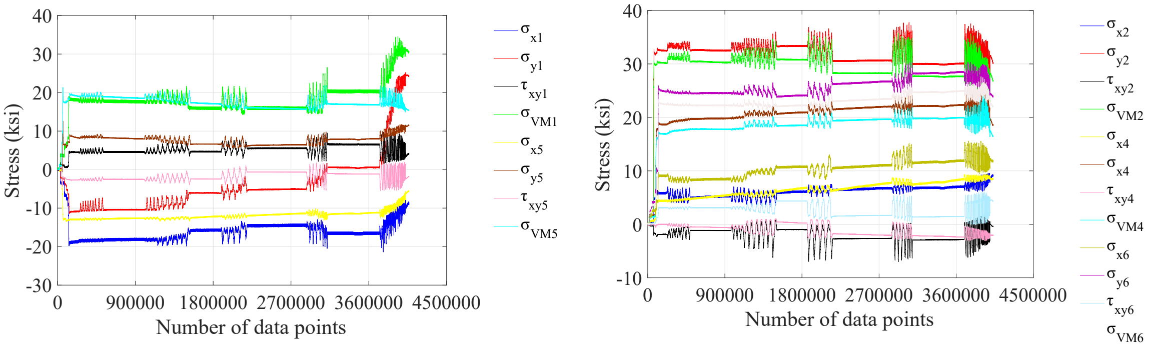

Anchors 1 and 5 Anchors 2, 4 and 6

Stress components

Figure F.15 Anchor strain and stress variation in Test 8-M24-3C-RH-LC

F.2 Beam tests

The strategies for handling abnormal linear potentiometer measurements and strain gage data are as follows:

(1) When the specimen was left unloaded overnight, small drifts were commonly seen in the strain gage measurements. These drifts were eliminated by subtracting the differences between the readings after pausing the test on the previous day and the readings before resuming the test on the next day.

(2) Although significant differences may exist in the strain measurements between the uniaxial gages attached on the north side of the steel web and those attached on the south side of the web, the average strain measurements were utilized for data reduction unless one of the two strain gages was debonded.

(3) If the concrete strain measurement was drifted significantly overnight or was distinctly different from all the other gages, it was disregarded, and a counterpart was used as a substitute. For example, in Test 1-M24-2C-RH, the reading from linear potentiometer C3ST2 continued increasing while the load was removed, and this measurement was replaced with that from C3NT2.

(4) A few gages displayed erratic readings. These gages are not included in the plots in Appendix E. When these gages are essential for data reduction, a substitute is found which potentially has the same measurement. For example, gage AMNc in Test 2-M24-1C-RL was discarded because of its erratic reading. Gage AMSc was thus utilized along with the other gages to estimate the forces the anchor was subjected to.

(5) Erratic readings from bolt strain gages were minimally manipulated, because the calculated inelastic stress is dependent on the deformation history.

F.2.1 Error in vertical and horizontal deflection measurements

When the beams deflected, the locations where the vertical and horizontal deflections were measured moved not only in the vertical direction but also in the horizontal direction. As a result, the error of the measurements has to be evaluated or corrected.

The measurements at the beam ends can be modified using Equations (F.26) and (F.27). A diagram is shown in Figure F.16a to illustrate the relationships between the parameters. The comparison between the measured end displacements and modified end displacements is plotted in Figure F.17.

$$(L_h - H_{modified})^2 + {V_{modified}}^2 = (L_h - H_{measurement})^2 \tag{F.26}$$

$$(L_v + V_{modified})^2 + {H_{modified}}^2 = (L_v + V_{measurement})^2 \tag{F.27}$$

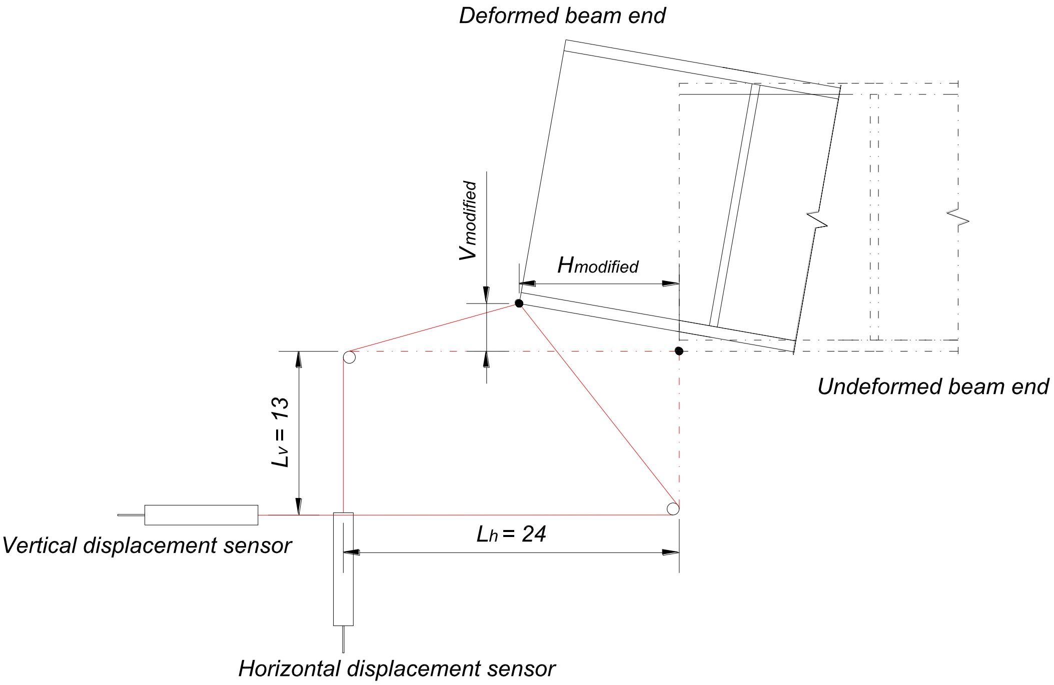
Deformed beam end
V modified
H modified
Undeformed beam end
Lv = 13
Lh = 24
Vertical displacement sensor
Horizontal displacement sensor

a) Displacement measurements at beam ends

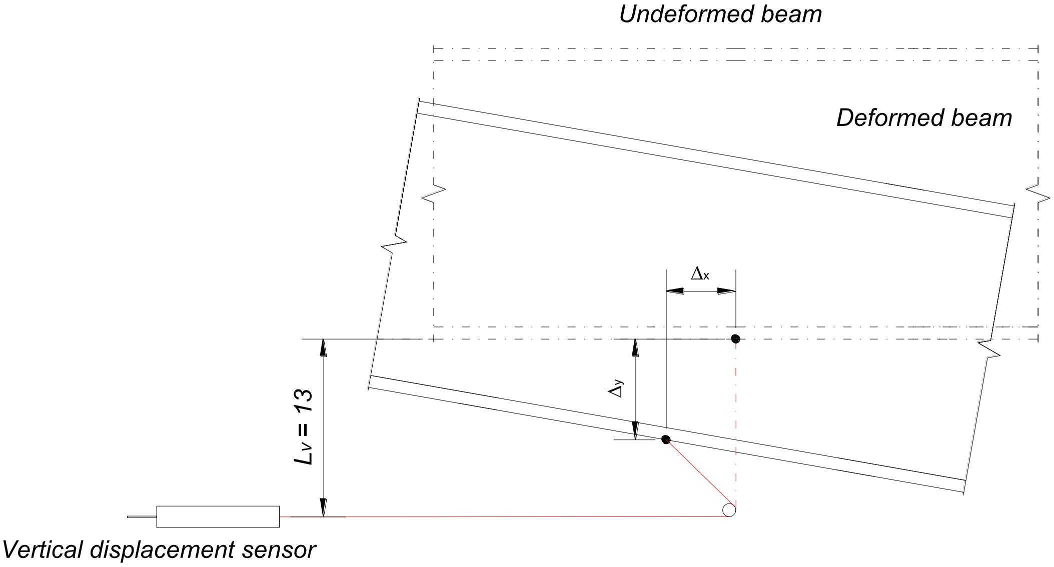
Undeformed beam
Deformed beam
Δx
Δy
Lv = 13
Vertical displacement sensor

b) Vertical displacement measurement along beam length

Note: Red lines are strings; solid black dots are magnetic hooks attached to steel beams and strings.

Figure F.16 Measurement error calculation

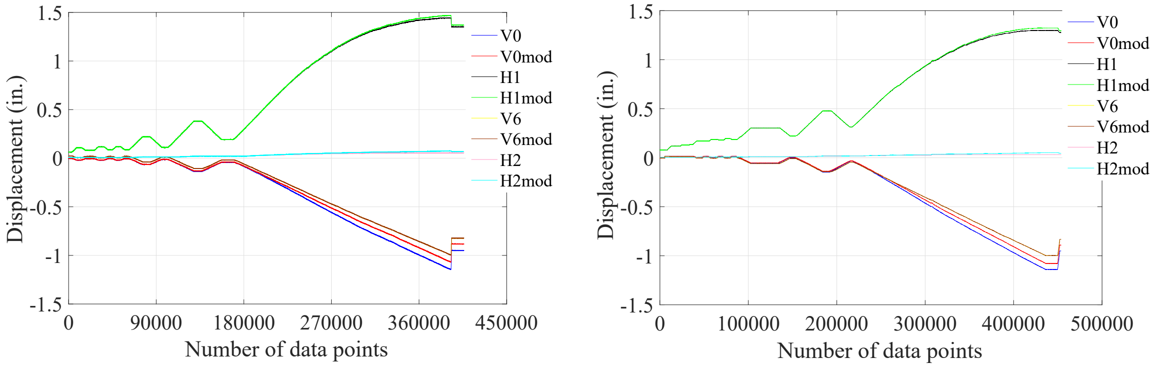

Specimen 1-M24-2C-RH Specimen 2-M24-1C-RL

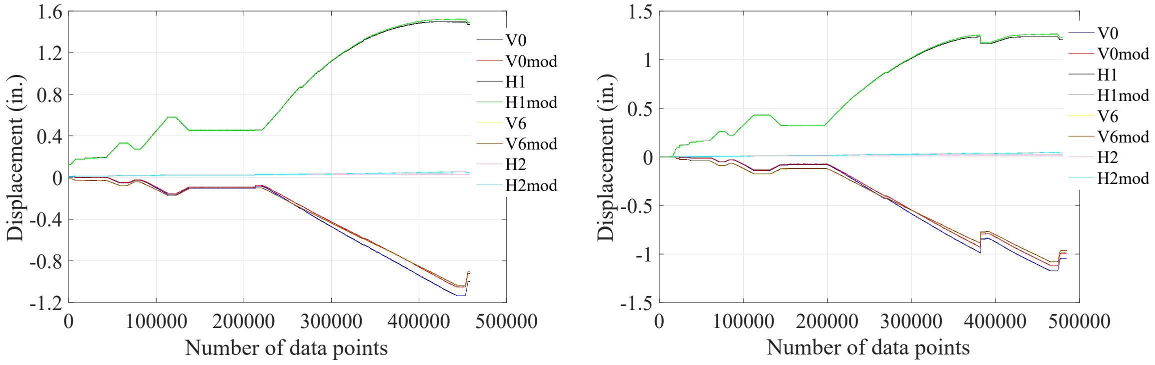

Specimen 3-M20-3C-RL Specimen 4-M20-1C-RL

Figure F.17 Measured displacements and modified displacements

During testing, it was observed that locations V0 through V3 moved westwards, while the other locations moved eastwards. The calculation of the vertical displacement measurement errors is given in the diagram in Figure F.16b and Equation (F.28). For locations V1 through V5, only the residual horizontal deformation was measured after terminating the test, as shown in Table F.2. It is assumed that the horizontal displacement varied linearly with the vertical displacement throughout the tests.

Table F.2 Residual horizontal movements at various locations of beam specimens (units: inches)

Specimen #	V1	V2	V3	V4	V5
1-M24-2C-RH	1.65	1.61	0.67	-0.39	-0.16
2-M24-1C-RL	1.60	1.60	0.89	-0.05	-0.17
3-M20-3C-RL	2.13	2.13	1.14	-0.19	-0.24
4-M20-1C-RL	2.28	2.00	1.18	-0.20	-0.12

Note: Errors may exist in the measurements at V4 and V5 sections. Positive values indicate westward movement, and negative values indicate eastward movement.

$$V_{error} = \frac{L_v - \sqrt{{\Delta_x}^2 + (L_v - \Delta_y)^2}}{\Delta_y} - 1 \tag{F.28}$$

The relative vertical displacement measurement error variation along with the beam deformation is shown in Figure F.18. From these figures, it is found that the errors increase with increasing vertical deflections, and the error increase is more quickly at the ultimate state of the beams. The maximum error is less than 7% in Specimen 3-M20-3C-RL, which is negligible. In addition, since the measurements of the ultimate deflections are less important than those for the serviceable deflections, the vertical displacement measurements of all the beam specimens are used without any modification.

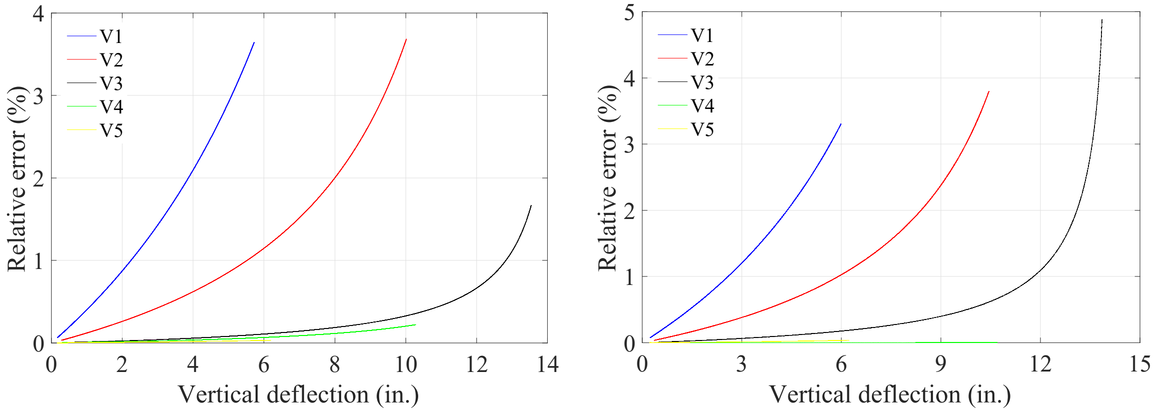

Specimen 1-M24-2C-RH

Specimen 2-M24-1C-RL

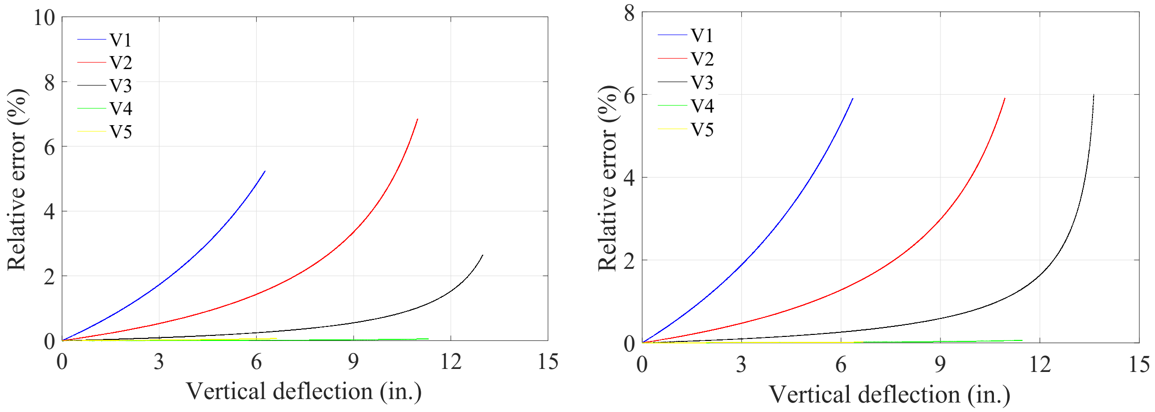

Specimen 3-M20-3C-RL

Specimen 4-M20-1C-RL

Figure F.18 Relative vertical deflection measurement errors

F.2.2 Beam end rotation calculation

The behavior of the beam specimens is demonstrated using load-center deflection curves as well as moment-end rotation curves. During the beam tests, the beam end rotations were not measured directly. Instead, they are calculated in this section using the vertical displacement measurements at the ends of the beams.

The deformation at the roller end of a composite beam specimen is illustrated in Figure F.19. The beam end extension is assumed to be rigid, and the beam end rotation is thus determined as:

$$\theta = \arctan\left(\frac{V_{modified}}{H_{modified} + 12}\right) \tag{F.29}$$

Although the horizontal movement at the pin end of the beam is minimal and $H_{modified}$ in Equation (F.29) could be omitted, Equation (F.29) is still used to calculate the rotation at the pin end of the beam.

$V_{modified}$ and $H_{modified}$ are calculated in Section F.2.1 and shown in Figure F.17. The variation of the end rotations of the beam specimens is plotted in Figure F.20. The average of the two rotations at the roller end and the pin end is used in the moment-end rotation curves.

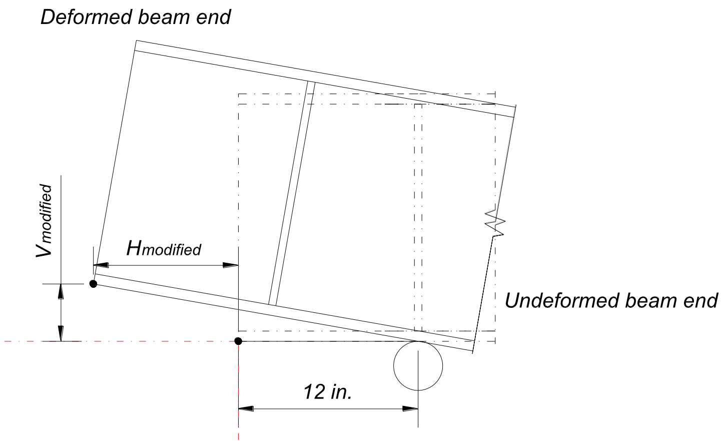

Figure F.19 Beam end rotation calculation

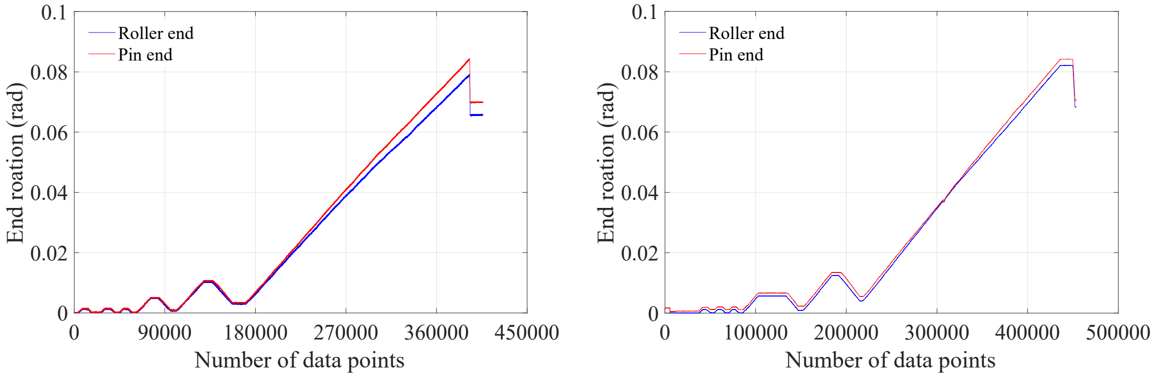

Specimen 1-M24-2C-RH

Specimen 2-M24-1C-RL

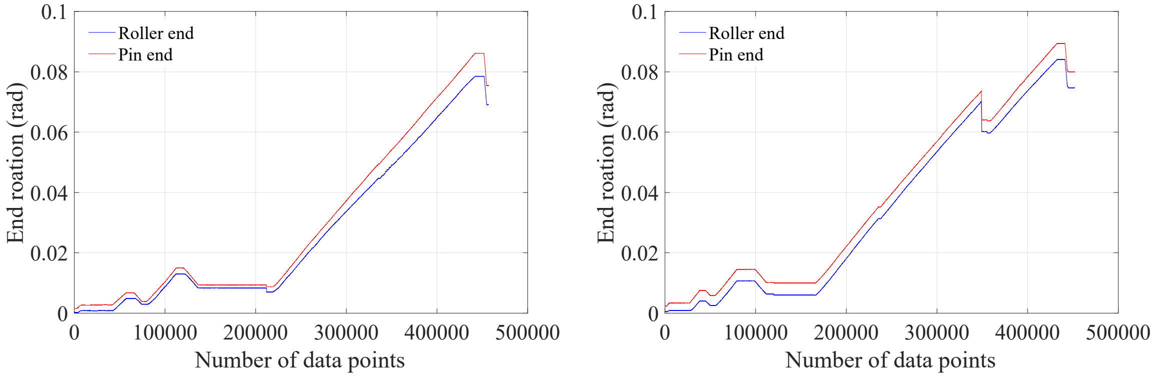

Specimen 3-M20-3C-RL

Specimen 4-M20-1C-RL

Figure F.20 End rotation variation of beam specimens

F.2.3 Beam 3 center deflection extrapolation

By the time the full stroke of the center string pot, which measures the center deflection of the beam, was reached, the load-deflection curve still ascended slowly. It was thus decided to continue deflecting the beam until the beam almost touched the concrete strong floor or the load plateaued. Although the center deflection was not measured after the center string pot was disabled, it is extrapolated in this section using the displacement measurements from the other sensors.

As plotted in Figure F.21, linear relationships can be assumed between the center deflection and the other vertical displacement measurements, particularly at large deflections. The midspan deflection is thus extrapolated using the other deflections, and the average of the extrapolated curves indirectly represents the center deflection of the beam after disabling the center string pot, as illustrated in Figure F.22. Hence, both the direct vertical deflection measurement from the center string pot and the indirect vertical deflection measurement extrapolated from the other sensors are used in the load-center deflection curve of this specimen.

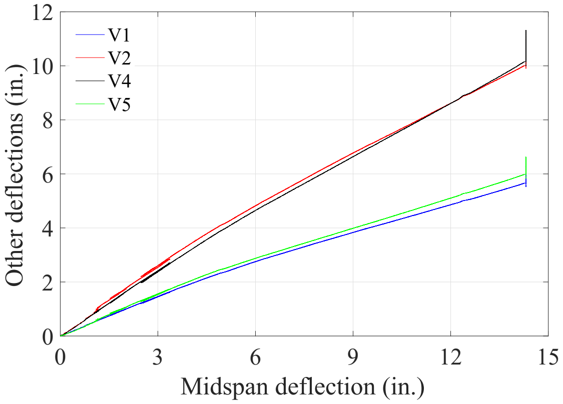

Figure F.21 Other vertical deflections versus center deflection

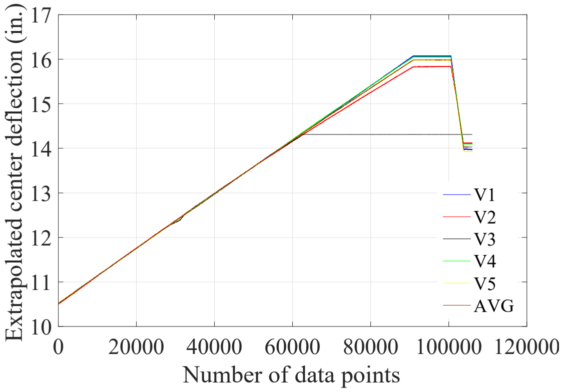

Figure F.22 Extrapolated center deflection

F.2.4 Effective width calculation

As discussed in Section 5.4, the compressive strains along the width of the center concrete plank were measured with displacement sensors. To calculate the effective width of the beam specimens, the compressive stress distribution needs to be calculated from the compressive strain distribution.

The stains were converted to stresses by implementing the concrete constitutive model proposed by Popovics (1973) and given in Equations (4.22) and (4.23) in Chapter 4. The strain corresponding to the peak compressive stress was defined as 0.003, and the crushing strain was set as 0.005. In Test 3-M20-3C-RL, concrete crushing happened at the center plank of the beam, and concrete spalling was seen at the top surface of the center plank where the displacement sensors were attached. As a result, the measured compressive strains were overestimated, and some strain measurements were as large as 0.0075. The data was processed until the measured strain reached 0.005. The compressive strain and stress variations at the center concrete plank are plotted for all the specimens in Figure F.23 through Figure F.26.

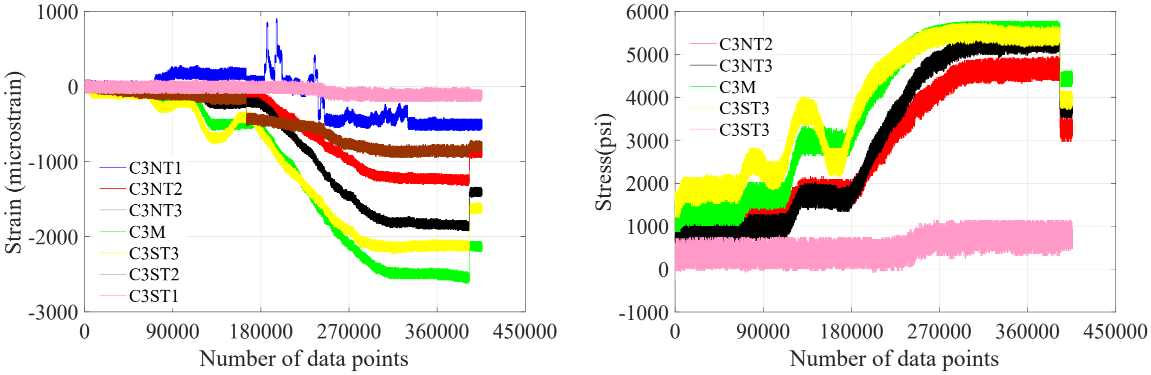

Strain variation Stress variation

Figure F.23 Center concrete plank compressive strain and stress variation in Test 1-M24-2C-RH

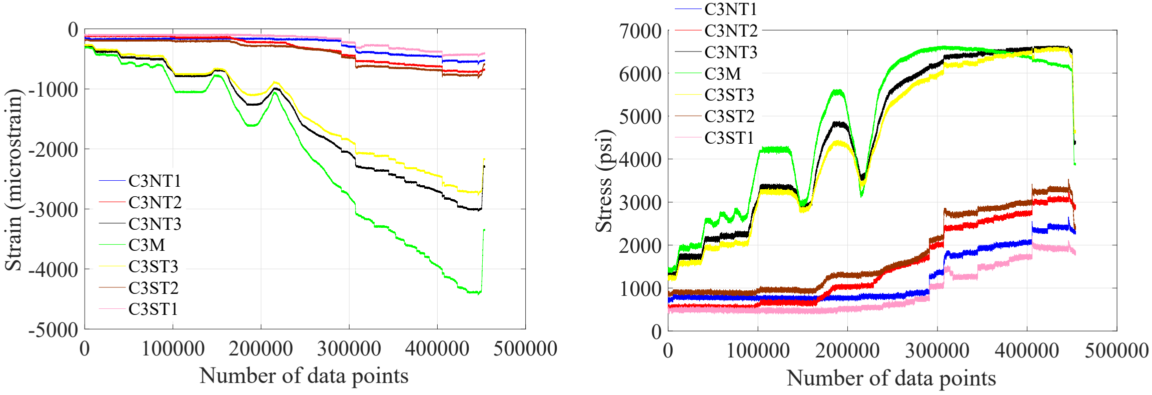

Strain variation Stress variation

Figure F.24 Center concrete plank compressive strain and stress variation in Test 2-M24-1C-RL

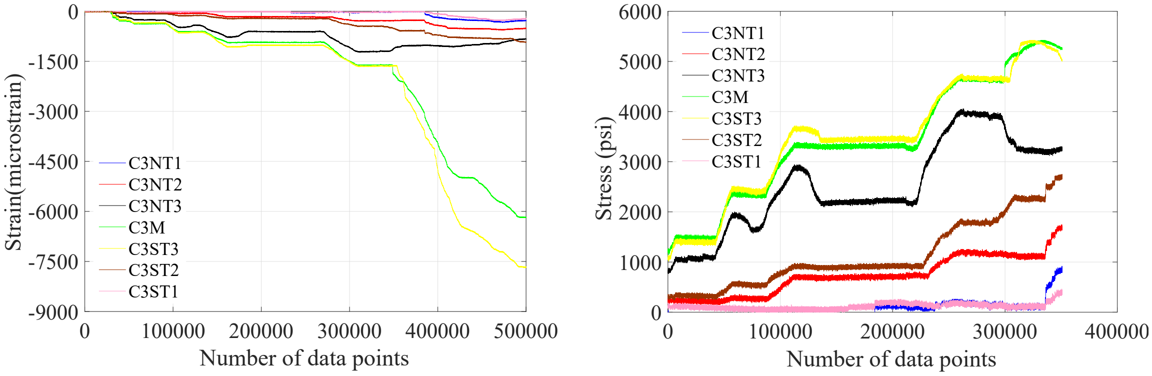

Strain variation Stress variation

Figure F.25 Center concrete plank compressive strain and stress variation in Test 3-M20-3C-RL

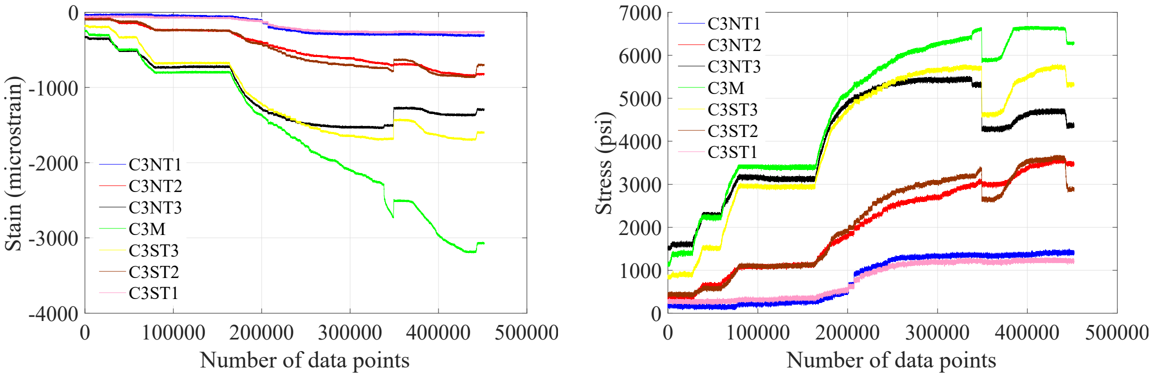

Strain variation Stress variation

Figure F.26 Center concrete plank compressive strain and stress variation in Test 4-M20-1C-RL

F.2.5 Bolt tension variation

Numerous bolts were instrumented with uniaxial strain gages and rosette strain gages to track the bolt tension variation throughout the beam tests. The measured inelastic strains are converted to inelastic stresses in this section.

The stress-strain curves for the M24 and M20 bolts used in the beam tests are illustrated in Figure F.27. A stress-strain curve is developed to represent the average stress-strain relationship of the six round coupons. The stress and strain values for the representative stress-strain curve are provided in Table F.3. The methods of converting the strain measurements to bolt axial stresses can be found in Sections F.1.2 and F.1.3.

The bolt tension variation is plotted in Figure F.28 for the bolts in all the beam specimens. Rosette strain gages were attached on the shanks of some bolts to ascertain the influences of the shear strain resulting from the torque during bolt pretension and the shear force while the beam was loaded. The comparison between the curves that account for the shear strain and the corresponding curves that ignore the shear strain indicates that the calculated axial stress is usually a little smaller when considering the shear strain. Figure F.29 shows the loading/unloading behavior of the bolt material. When the shear strain is considered, the axial stress versus axial strain relationship does not follow the uniaxial stress-strain curve.

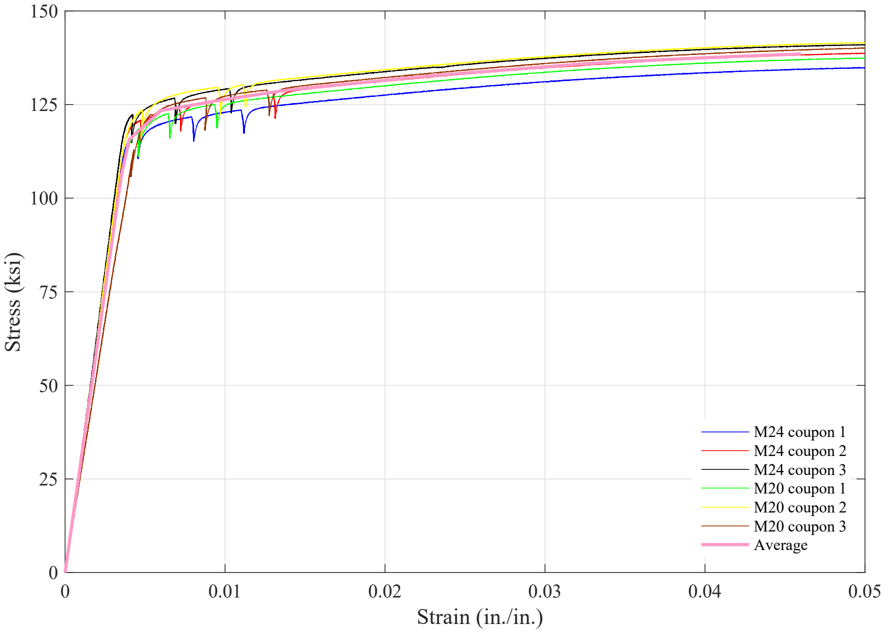

Figure F.27 Beam test bolt stress-strain curves

Table F.3 Beam test bolt stress and strain

Stress (ksi)		Strain	
Engineering	True	Engineering	True
105.900	106.271	0.0035	0.0000
115.600	116.062	0.004	0.00021
123.417	124.157	0.006	0.00194
126.400	127.664	0.010	0.00579
128.933	130.738	0.014	0.00964
130.683	133.036	0.018	0.01351
132.300	135.211	0.022	0.01736
133.067	136.260	0.024	0.01928
135.700	140.042	0.032	0.02694
136.233	140.865	0.034	0.02885
137.167	142.379	0.038	0.03266
137.900	143.692	0.042	0.03646
138.483	144.854	0.046	0.04026

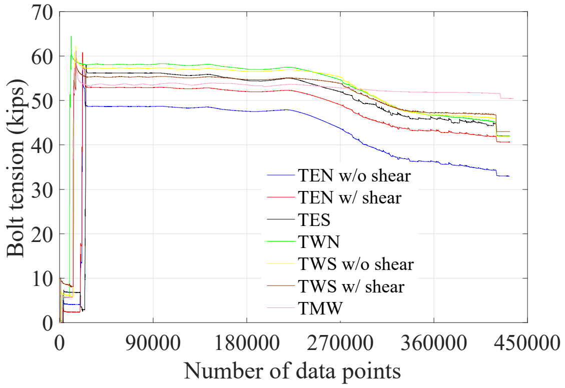

Test 1-M24-2C-RH

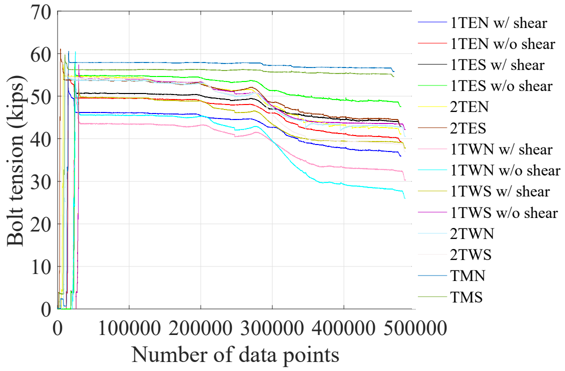

Test 2-M24-1C-RL

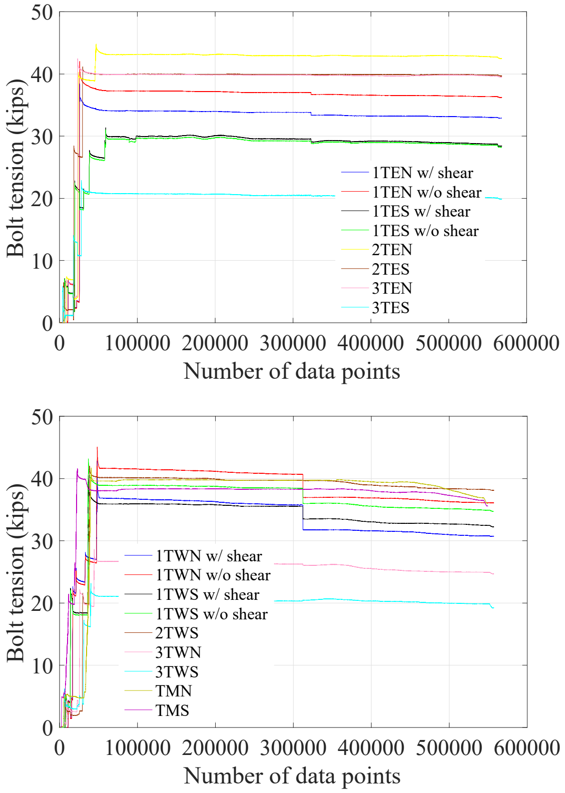

Test 3-M20-3C-RL

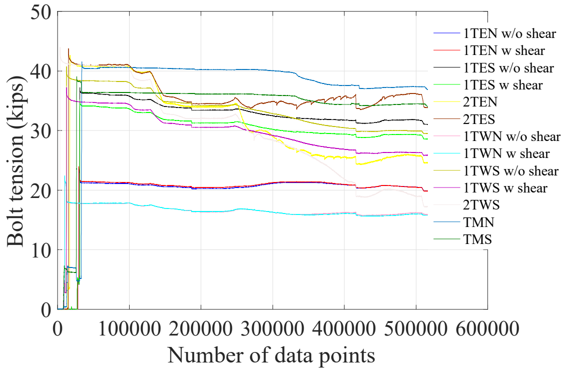

Test 4-M20-1C-RL

Figure F.28 Bolt tension variation in beam tests

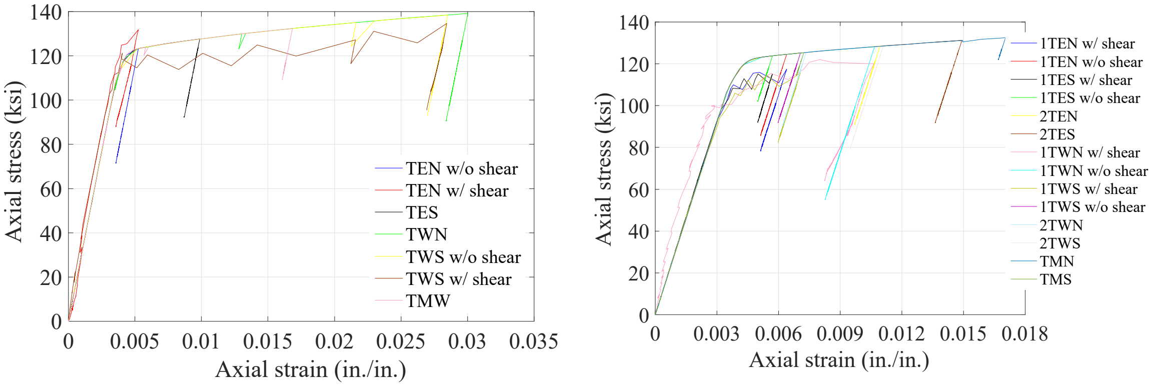

Test 1-M24-2C-RH

Test 2-M24-1C-RL

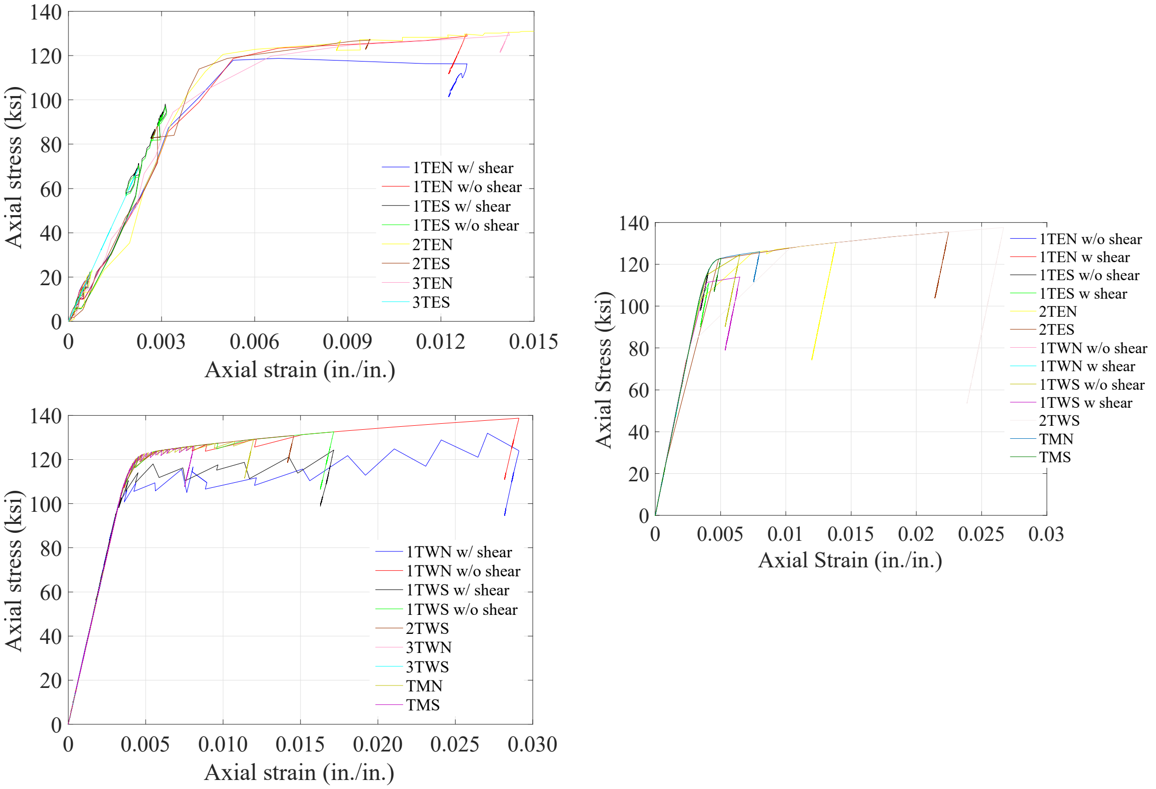

Test 3-M20-3C-RL

Test 4-M20-1C-RL

Figure F.29 Bolt material loading and unloading behavior in beam tests

F.2.6 Axial force and bending moment at a cross section

In this section, the actual moment at a section denotes the external moment which is produced by the self-weight of the specimen and the actuator forces and determined using moment equilibrium, while the calculated moment at a section describes the internal moment attained with strain measurements and moment integration. The comparison between the two moments is used to validate the readings from the strain gages.

At the instrumented sections, the internal forces can be calculated using either actuator forces or strain measurements. The calculation of the internal moment using the steel section strain measurements is illustrated in Figure F.30. The curvature of the steel section was deduced from the strain measurements along the depth of the section. Plane sections were assumed to remain plane, and the presumed strain distribution was linear. The slope k_0 and the y-intercept k_1 were thus obtained using linear regression, as given in Equations (F.30) and (F.31).

$$k_0 = \frac{(n\sum_{i=1}^{n} y_i\varepsilon_i) - (\sum_{i=1}^{n} y_i)(\sum_{i=1}^{n} \varepsilon_i)}{n\sum_{i=1}^{n} {y_i}^2 - (\sum_{i=1}^{n} y_i)^2} \tag{F.30}$$

$$k_1 = (\sum_{i=1}^{n} \varepsilon_i - k\sum_{i=1}^{n} y_i)/n \tag{F.31}$$

Where

n = number of strain gage measurements

ε_i = the ith strain measurement

y_i = the location of the ith strain measurement measured from the bottom surface of the steel section

Another two assumptions were made:

(1) During the unloading phase, the measured steel strains could decrease, and elastic unloading was assumed. The interaction among different stresses was disregarded. For example, the gaged steel sections were under combined flexure and shear, but the influence of the shear force on the axial strain measurements was ignored. From tensile coupon testing, the uniaxial constitutive models for the steel beams were obtained which consisted of three regions, namely, the elastic region, the plateau region, and the strain hardening region.

(2) The radii at the flange-to-web joints in a steel section were ignored. In other words, the section was simplified as three rectangles that represented the two

flanges and the web. The measured dimensions were used to calculate the axial force and bending moment at the cross section.

When calculating the axial force and moment, the steel section was divided into multiple small rectangles which were similar to the shaded region in Figure F.30. This region had a width of b_i and a height of h_i. The average strain of the region was obtained using the linear regression model. Based on the uniaxial stress-strain curves of the materials and the strain history, the stress was found which corresponded to the average strain. The axial force of the shaded region was thus calculated as the multiplication of the stress by the area of the region, and the moment was taken with respect to the bottom surface of the steel section. For the steel beam, the flanges and web were divided into 4 and 40 layers, respectively. The resultant compressive force in the concrete plank was calculated using force equilibrium, and the magnitude was equal to the resultant axial tension in the steel section. However, the position of the compression could not be readily determined and might vary throughout the test.

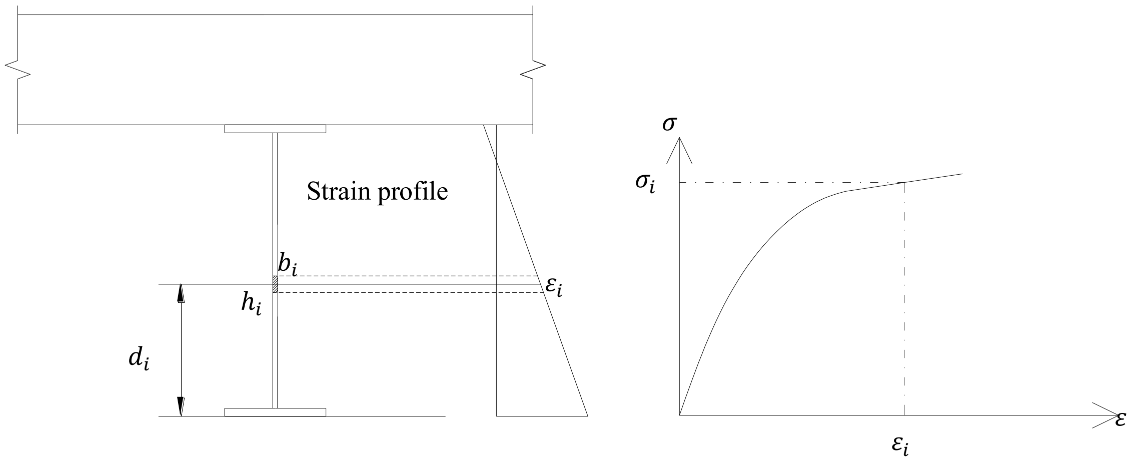

$$\varepsilon_i = k_0 d_i + k_1$$

$$F_s = \sum F_i = \sum \sigma_i b_i h_i$$

$$F_c = F_s$$

$$M = \sum M_i = \sum F_i d_i + F_c d_c$$

Figure F.30 Internal force calculation for a composite beam section

In the beam specimens, the resultant compression in the concrete planks is anticipated to rise as the beam deflects, because adjacent concrete planks gradually separate at the bottom and contact at the top edges. Therefore, if the compression in the plank is assumed to be stationary in the moment calculation, the calculated moment cannot match the actual moment throughout the whole test. Nonetheless, the axial tension of the steel section is not dependent on the location of the resultant compression. For all the gaged sections, a lower bound moment and an upper bound moment were calculated. When determining the lower bound moment, the resultant forces were located at the centroid of the planks. To obtain the upper bound moment, it was assumed that the resultant compression in the concrete planks acted at the top edges where concrete crushing usually occurred during the tests. The calculated moment and actual moment are compared for all the sections and illustrated in Figure F.31 through Figure F.34.

Before the actuator loading is applied, under self-weight, the actual moment is approximately 650 in.-kips at sections 1 and 5, 981 in.-kips at sections 2 and 4, and 1170 in.-kips at section 3. These moments are larger than the upper bound and lower bound moments calculated according to the strain gage measurements. It is possible that the beam was not completely shored during construction, and the self-weight was partially taken by the beam itself, which was not captured by the strain gages. In other words, under self-weight, the actual strains at the gaged locations could be underestimated by the strain gage measurement. In each graph in Figure F.31 through Figure F.34, the actual moment curve is drawn twice, one shown in green and the other one in black. They are offset such that the green curve and the black curve start from the same value as the lower bound moment curve and the upper bound moment curve, respectively.

It is observed from Figure F.31 through Figure F.34 that:

- Beam 1: At section 1, during the loading/unloading cycles, the lower bound moment is very close to the actual moment. The difference between the two moments grows until the measurement from gage 1NBF increases more quickly than the other gages, and the calculated lower bound moment finally exceeds the actual moment. For section 5, the lower bound moment matches the actual moment very well until the reading of gage 5NBF increases dramatically which may indicate localized deformation of the region where gage 5NBF is attached. The sharp strain increase starts at a strain of 1605 με, close to the yielding strain of 1647 με. At section 2, the upper bound moment is very close to the actual moment during the three 40% cycles. For the rest of the testing, the actual moment lies between the lower bound moment and the upper bound moment. Similarly, at section 4, minimal differences are seen between the upper bound moment and the actual moment during the three 40% cycles. At a strain of 1422 με, the reading from gage 4NBF increases abruptly, which results in the sudden change in the calculated moment. The localized deformation happens at a strain of 1422 με, smaller than the yielding strain of 1647 με. For the same reason, when the beam is unloaded, the calculated moment is much larger than the actual moment. The comparison at the ultimate state indicates the resultant compression is located between the centroid and the top edge of the plank, which may relate to the crushing between planks 10 and 11. When calculating the internal moment, the debonded gages on section 3 were excluded, and only gages 3NTF, 3STF, 3NTW, and 3SBF were utilized. It is shown that the actual moment is between the two extremes during the 40% cycles. Because of gage 3SBF, the calculated moment increases much faster than the actual moment at data point 7000. The moment comparison at the end of the test appears to imply the compression in the center plank is close to the mid-height of the plank, which contradicts the anticipation that the compressive force rises as the test proceeds.

- Beam 2: At sections 1 and 5, during the three 40% cycles, the actual moment lies between the lower bound moment and the upper bound moment. The differences between the lower bound moment and the calculated moment gradually vanish. In the end, both calculated moments are much larger than the actual moment, suggesting that the compression in the planks is below the centroid of the planks, which is counterintuitive. For section 2, the upper bound moment is close to the actual moment until the 80% cycle. Afterwards, the actual moment is slightly less than the lower bound moment. At section 4, the upper bound moment matches the actual moment during the 40% cycles. Since the 80% cycle, the actual moment of section 4 is smaller than the calculated moment. Around 1500 με (data point 171000), the reading of gage 4SBF grows faster than the other gages, and this may overestimate the calculated moment. Eventually, the lower bound moment is about 10% larger than the actual moment. At section 3, the actual moment is close to the upper bound moment during the 40% cycles and at the end of the test. Minor concrete crushing happened between planks 8 and 9 later in the test, but the resultant compression may still stay at the top edge of plank 8 (section 3). At a strain of 1391 με (data point 167000), measurements from both gages at the bottom flange increase more quickly than the other gages on the same section. When the load on the beam is removed, large differences are found between the actual moment and the calculated moment.

- Beam 3: At sections 1 and 5, during the loading/unloading cycles, when the beam is loaded, the error between the lower bound moment and the actual moment is around 5%, but the error is much larger when the load is removed. In the end, the lower bound moment is about 10% larger than the actual moment. For sections 2 and 4, the upper bound moment is close to the actual moment during the three 40% cycles. Afterwards, the actual moment is smaller than the calculated moment for both sections until the end of the test. At the end of the test, the upper bound moment at section 2 matches the actual moment, while the actual moment of section 4 is fairly close to the lower bound moment. Although minor concrete crushing occurred between planks 5 and 6 at a deflection of 11.5 in., the resultant compression may not descend. For section 3, the difference between the upper bound moment and the calculated moment is small during the 40% cycles. Eventually, the actual moment lies between the upper bound moment and lower bound moment, indicating the descending of the resultant compression in the plank, which could be related to the localized concrete crushing at the top edge of the center plank.

- Beam 4: At sections 1 and 5, the difference between the actual moment and the lower bound moment is relatively small throughout the test. The reading of gage 1SBF increases dramatically at a strain of 1311 με, smaller than the yield strain of 1630 με. As a result, the calculate moment is much greater. For section 2, the upper bound moment is closer to the actual moment during the 40% cycles. The difference between the lower bound moment and the actual moment gradually reduces, and the actual moment eventually falls between the lower bound moment and the upper bound moment. For section 4, the upper bound moment matches the actual moment during the 40% cycles and the 60% cycle. At 1120 με (data point 65300), the reading of 4SBF grows much more quickly than the other gages, and thus the calculated moment is overestimated. The lower bound moment is close to the actual moment at the end of the test, which may be due to the crushing between planks 10 and 11 at a deflection of 3.8 in. At section 3, the difference between the actual moment and the upper bound moment is minimal during the 40% cycles and the 60% cycle, while the actual moment is close to the lower bound moment at the 80% cycle. After the cycles are completed, the actual moment matches the upper bound moment.

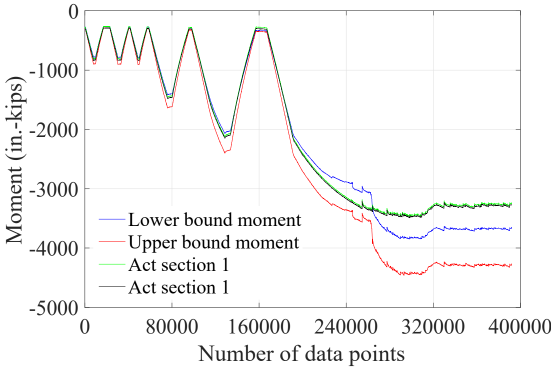

Section 1

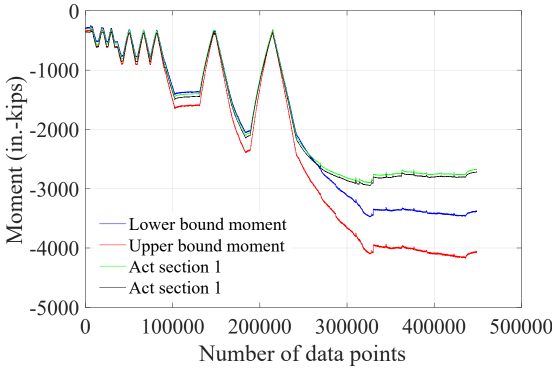

Section 1

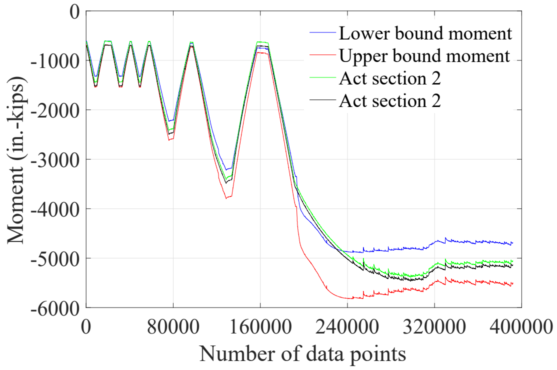

Section 2

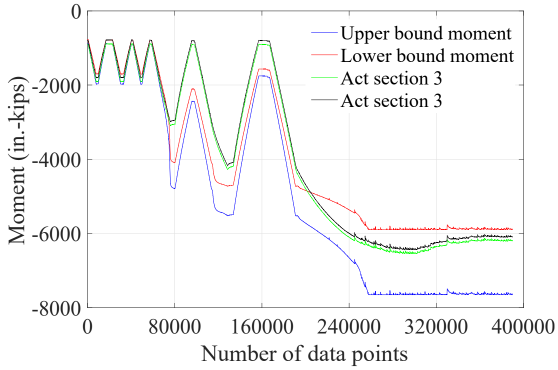

Section 3

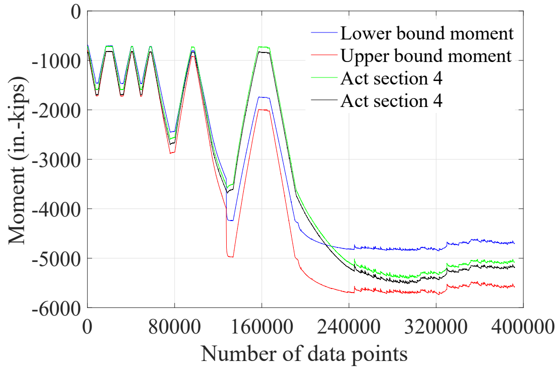

Section 4

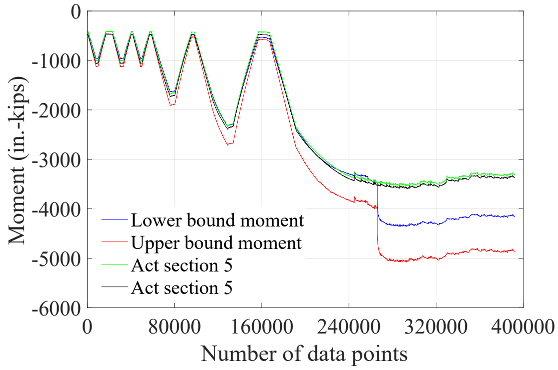

Section 5

Figure F.31 Actual moment versus calculated moment in Test 1-M24-2C-RH

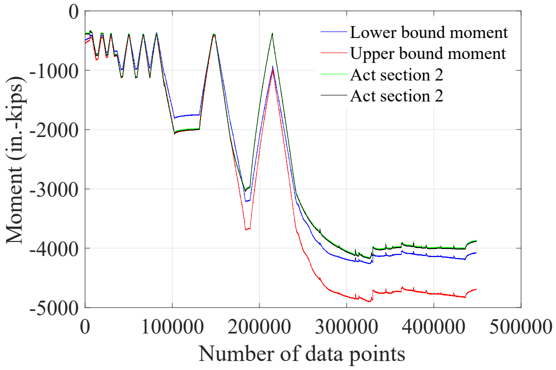

Section 2

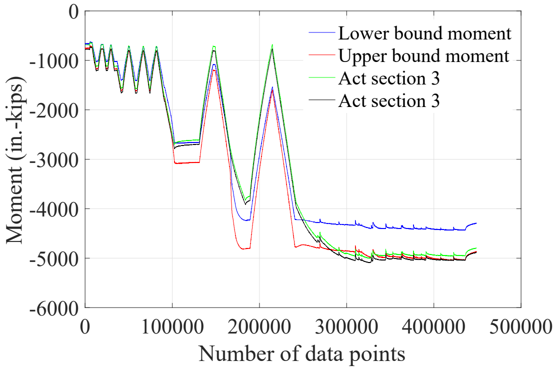

Section 3

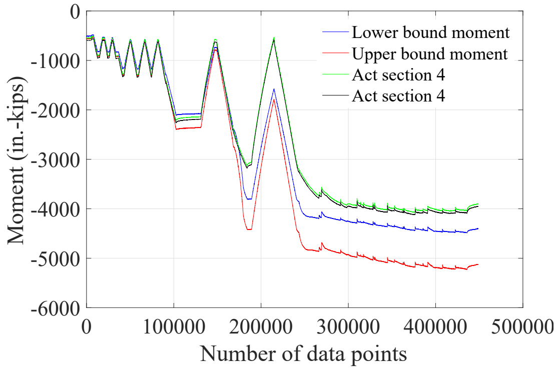

Section 4

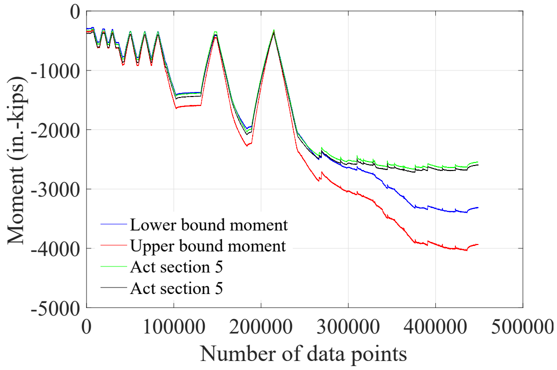

Section 5

Figure F.32 Actual moment versus calculated moment in Test 2-M24-1C-RL

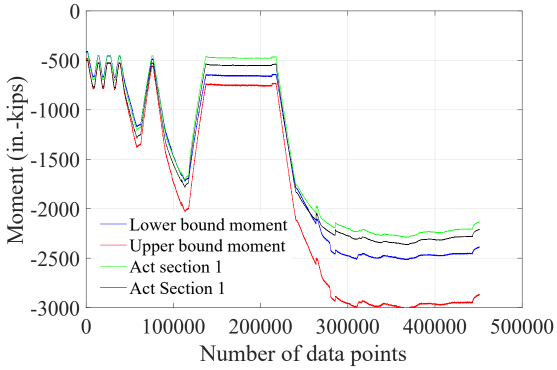

Section 1

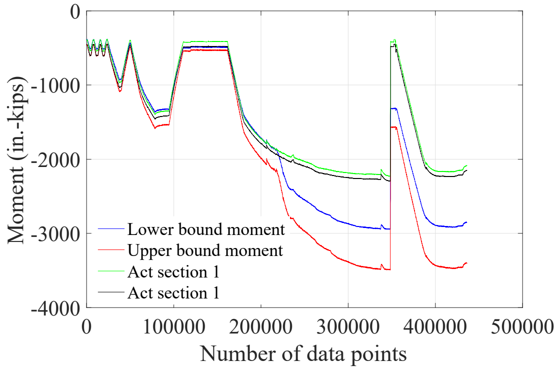

Section 1

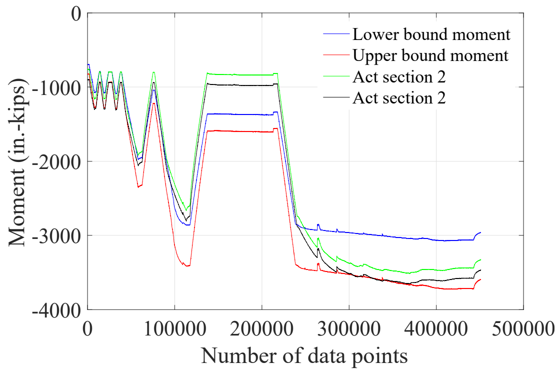

Section 2

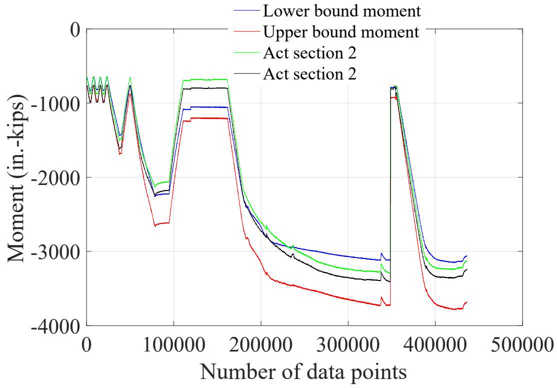

Section 2

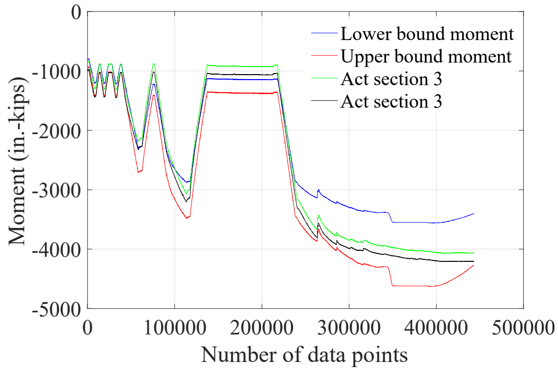

Section 3

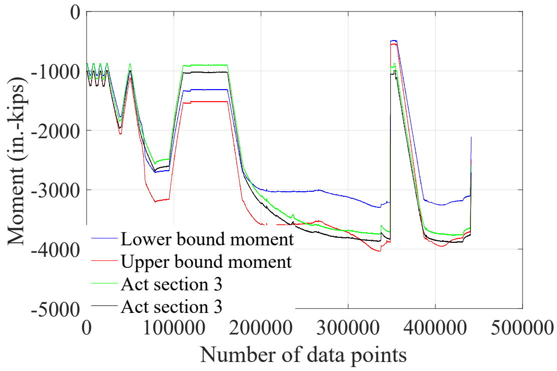

Section 3

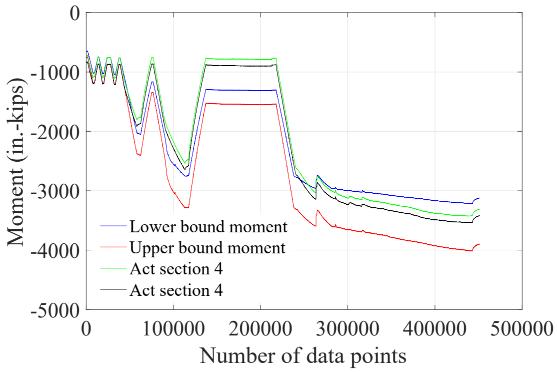

Section 4

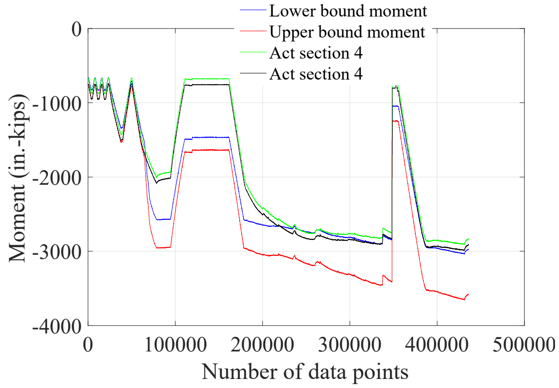

Section 4

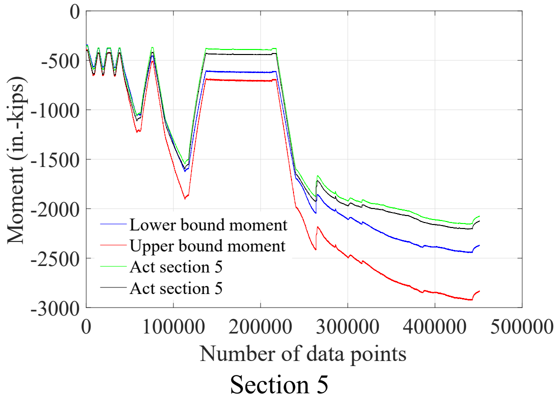

Figure F.33 Actual moment versus calculated moment in Test 3-M20-3C-RL

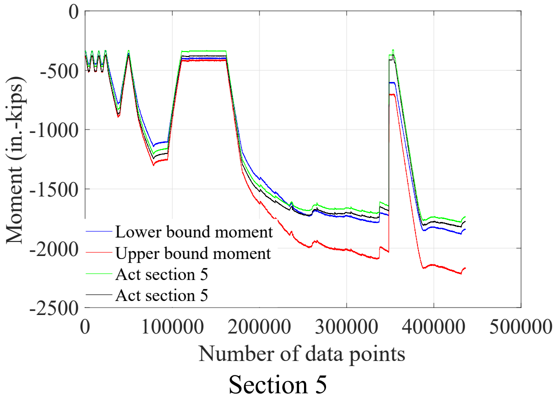

Figure F.34 Actual moment versus calculated moment in Test 4-M20-1C-RL

The axial force variation of the instrumented steel sections is provided in Figure F.35. As discussed in Section 5.6.9 in Chapter 5, based on force equilibrium, the net tension difference between two steel sections is equal to the resultant shear resistance of the clamps placed between these two sections. The variation of the average shear resistance of the clamps in each of the six regions illustrated in Figure 5.80 in Chapter 5 is plotted in Figure F.36.

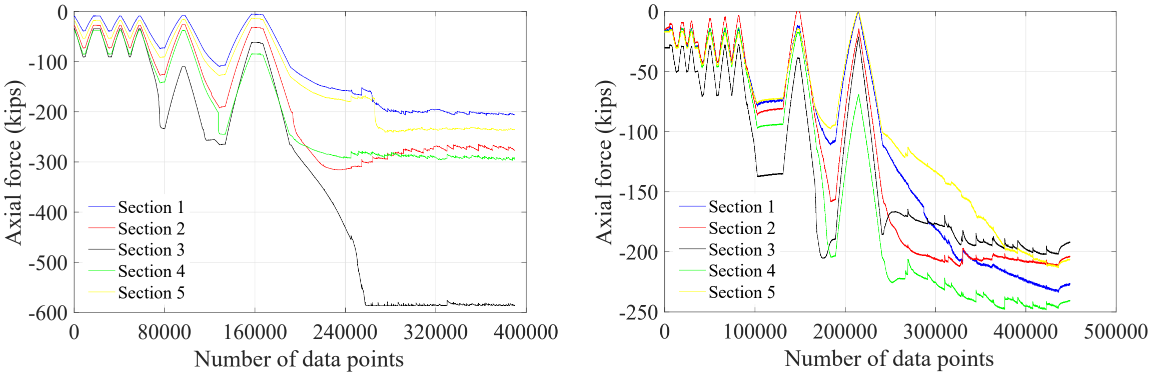

Test 1-M24-2C-RH Test 2-M24-1C-RL

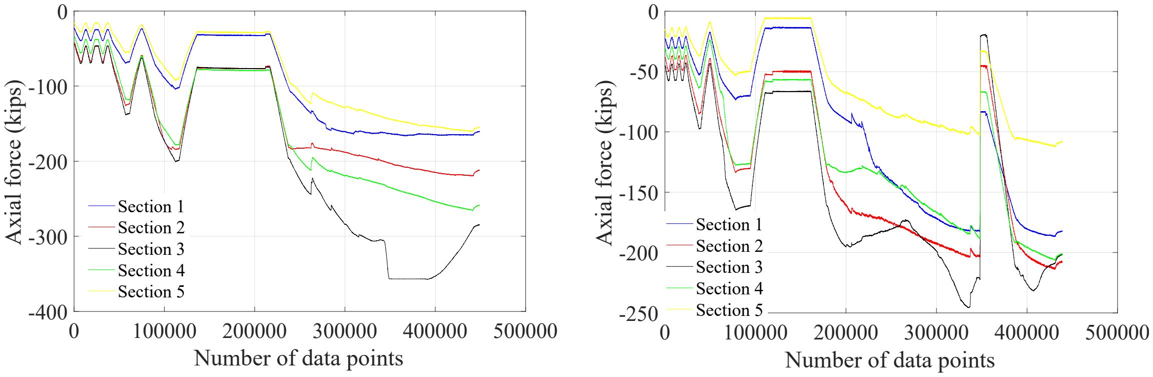

Test 3-M20-3C-RL Test 4-M20-1C-RL

Figure F.35 Calculated axial forces at the instrumented steel sections

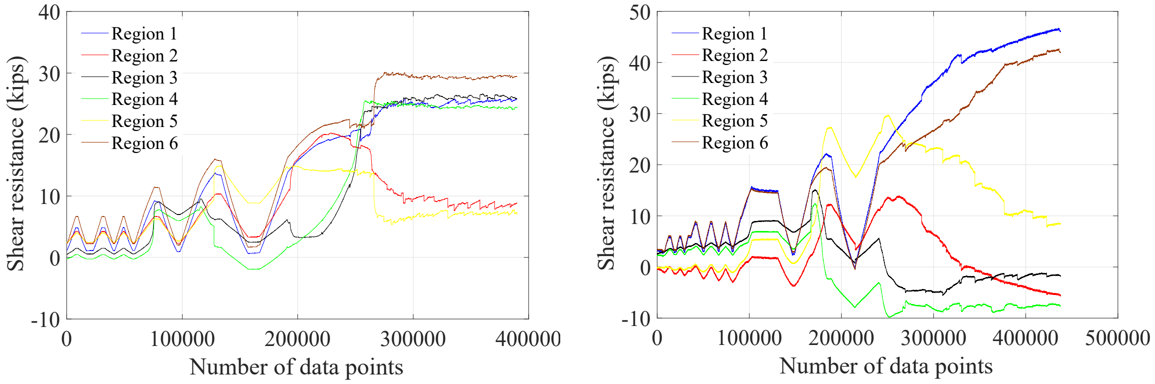

Test 1-M24-2C-RH Test 2-M24-1C-RL

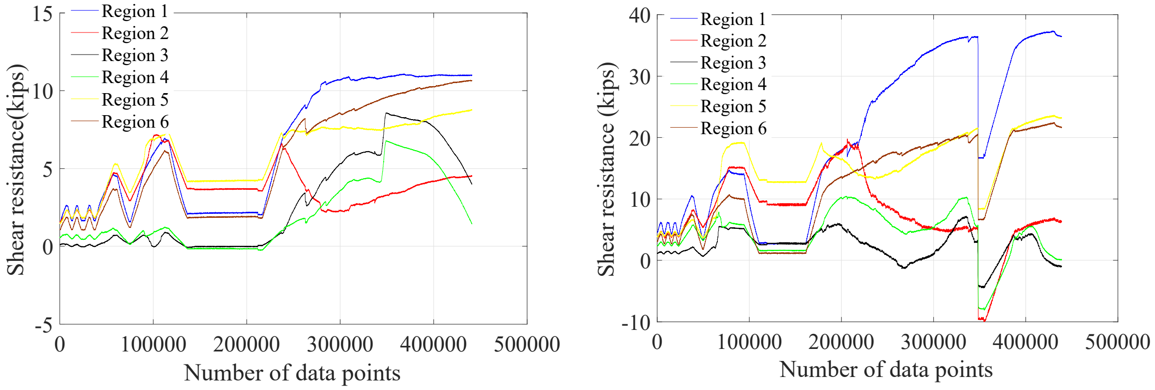

Test 3-M20-3C-RL Test 4-M20-1C-RL

Figure F.36 Shear resistance variation of clamp in different regions (per connector)

F.2.7 Location of neutral axis in steel beam

Since the axial strain at a neutral axis (NA) is zero, the NA in the steel section can be located using the strain measurements of the steel section. The position of the NA can be found using Equation (F.32) and Equations (F.30) and (F.31). The variation of the NA location, which is measured from the bottom flange of the steel section, is depicted in Figure F.37 through Figure F.40.

$$y_{NA} = -k_1/k_0 \tag{F.32}$$

In Tests 1-M24-2C-RH and 3-M20-3C-RL, the NA at section 3 gradually rises into the concrete plank. Extrapolated with the strains of the steel beam, the NA is eventually above the top surface of the concrete plank. The unrealistic shifting of the extrapolated NA could be due to neglecting the slip existing at the steel/concrete interface.

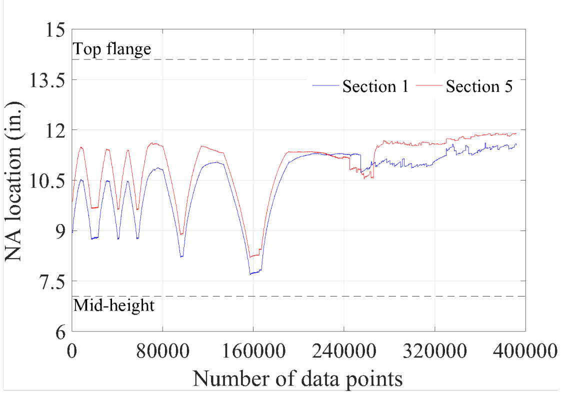

Sections 1 and 5

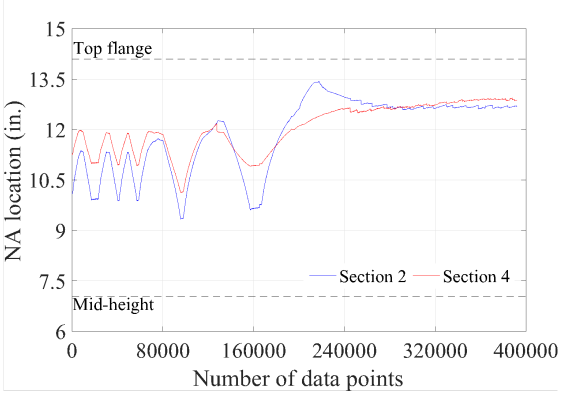

Sections 2 and 4

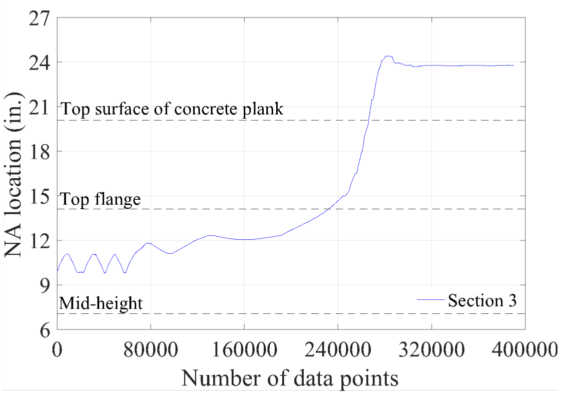

Section 3

Figure F.37 Locations of neutral axes in steel sections in Test 1-M24-2C-RH

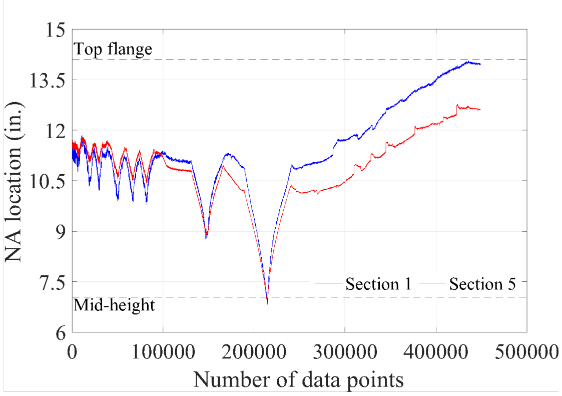

Sections 1 and 5

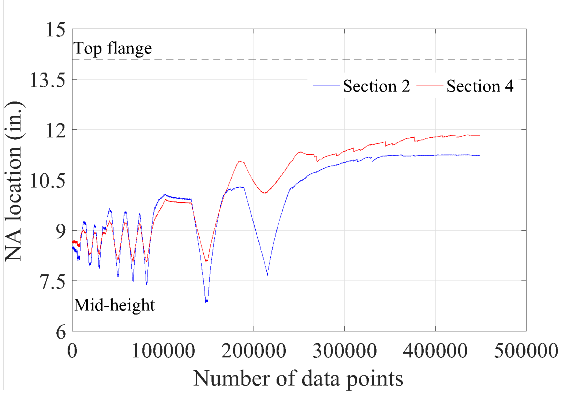

Sections 2 and 4

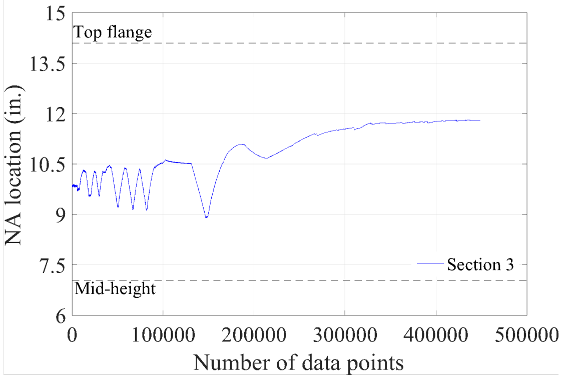

Section 3

Figure F.38 Locations of neutral axes in steel sections in Test 2-M24-1C-RL

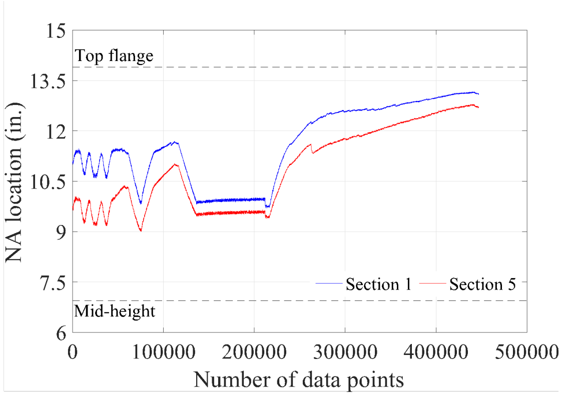

Sections 1 and 5

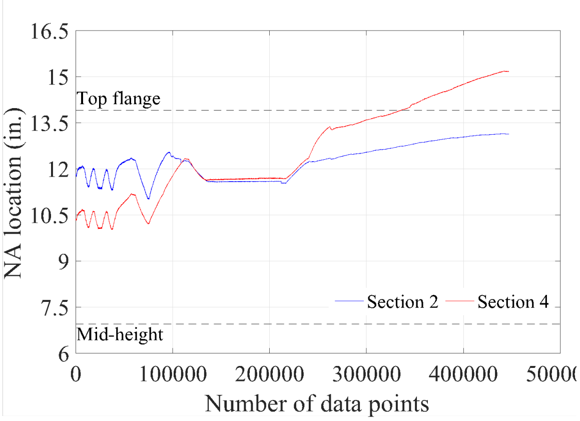

Sections 2 and 4

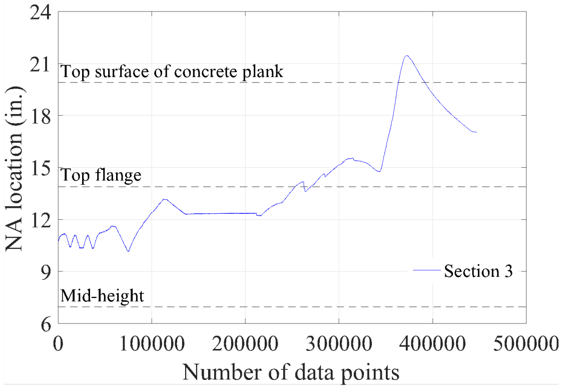

Section 3

Figure F.39 Locations of neutral axes in steel sections in Test 3-M20-3C-RL

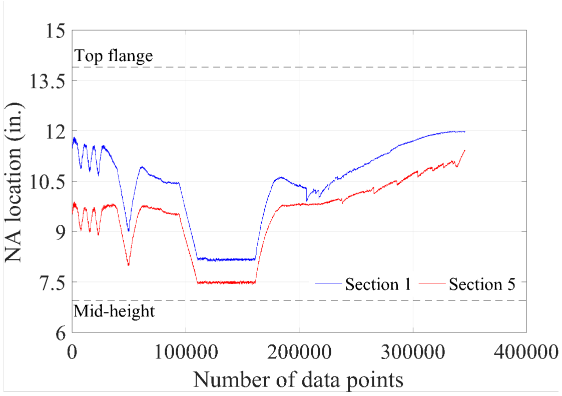

Sections 1 and 5

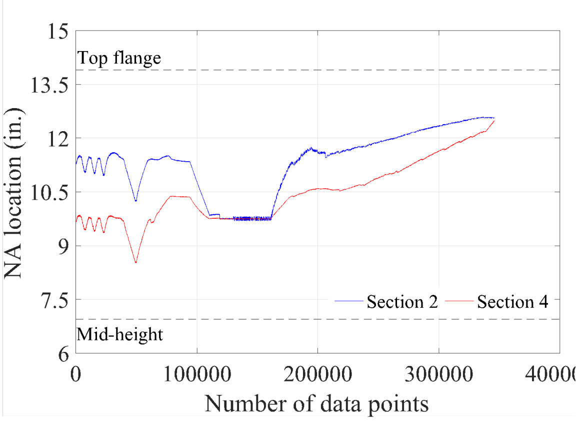

Sections 2 and 4

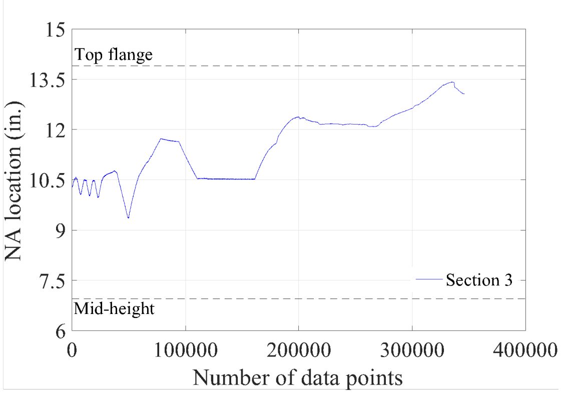

Section 3

Figure F.40 Locations of neutral axes in steel sections in Test 4-M20-1C-RL

F.2.8 Forces acting on channel anchors

In Test 2-M24-1C-RL, several channel anchors were instrumented with rosette strain gages to estimate the tensile and shear forces the anchors were subjected to. Section F.1.3

provides details on the calculation of the tensile and shear stresses. The calculated anchor strains and stresses are shown in Figure F.41.

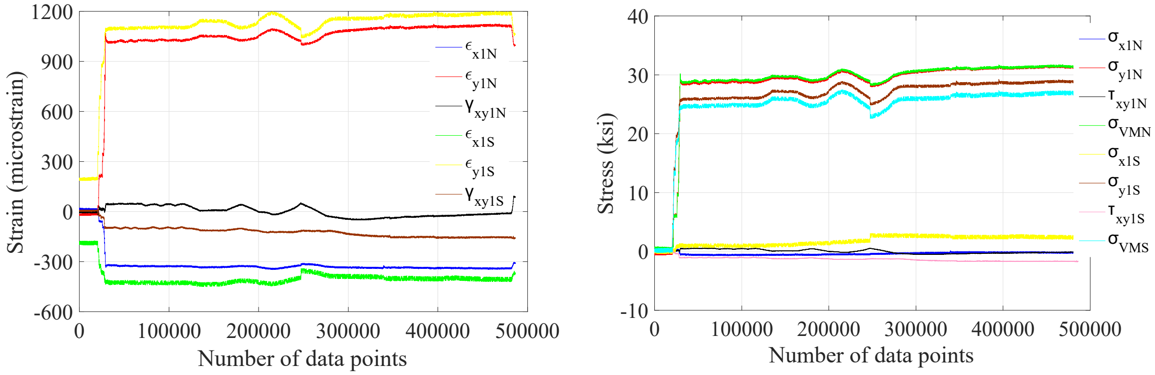

Strain components

Stress components

West end

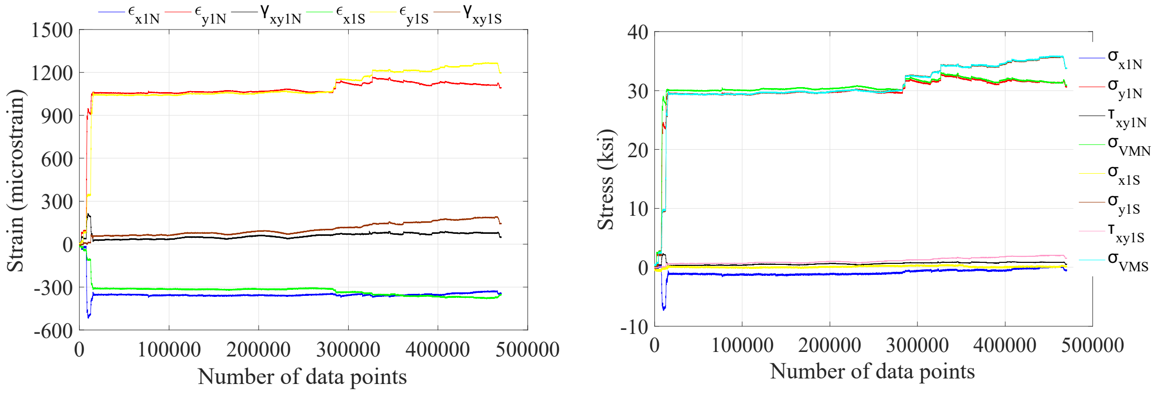

Strain components

Stress components

Middle

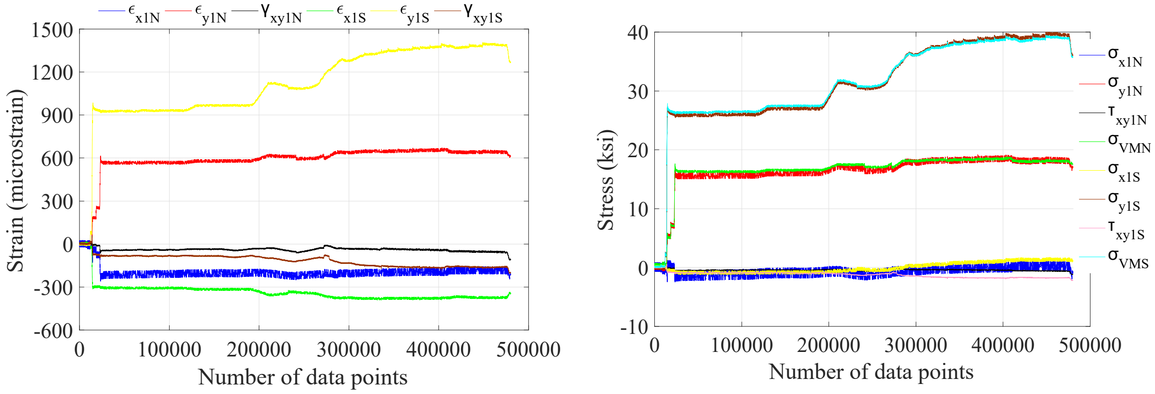

Strain components

Stress components

East end

Figure F.41 Anchor strain and stress variation in beam test

Appendix G SELECTION OF REACTION ANGLES IN PUSHOUT TESTS

In the pushout tests, the steel reaction angles are selected for the concrete plank specimen to simulate the support provided by adjacent concrete planks in a composite beam, which could vary considerably depending on the location of the concrete plank in the beam. Two scenarios in a 30 ft. long composite beam are illustrated Figure G.1. In the beam, the end plank bears against the rest of the planks on the left half of the beam, while the plank next to the middle plank is supported by half of the middle plank. Hence, for an intermediate plank, the bearing stiffness provided by adjacent planks is between these two extremes.

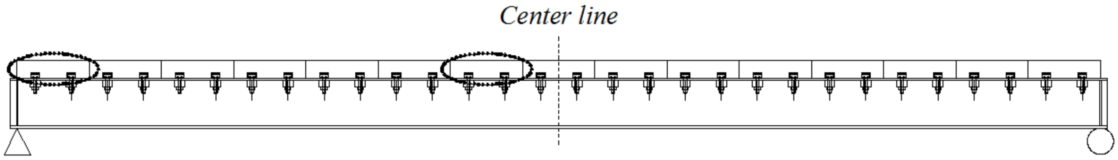

Figure G.1 Two scenarios in a composite beam

Shown in Figure G.2, three simplified elastic finite element models were developed to calculate the bearing stiffness for the concrete plank. The two scenarios illustrated in Figure G.1 were simulated in models a and b, with model a and b representing the plank next to the middle plank and the end plank, respectively. The bearing stiffness of the selected steel angle was calculated in model c. In models a and b, the thickness of the supporting plank was adjusted to 4 in., which is equal to the height of the angle leg. One surface of the supporting plank was restrained from moving in all directions, since this is the plane of symmetry in the composite beam. Unlike the other two models, the bottom surface of the reaction angle was restrained in model c, representing the testing condition. Surface tractions were applied on the concrete plank surface. The width of the loading region mimics the width of a steel beam. The elastic modulus and Poisson’s ratio for the concrete plank were taken as 3605 ksi and 0.15, while these two parameters were 29000 ksi and 0.3 for the angle section.

The calculated stiffness for the three models is 3385 kips/in, 658 kips/in and 2149 kips/in, respectively. Because the bearing stiffness of the steel reaction angle falls between the two extremes, the angle is an appropriate choice.

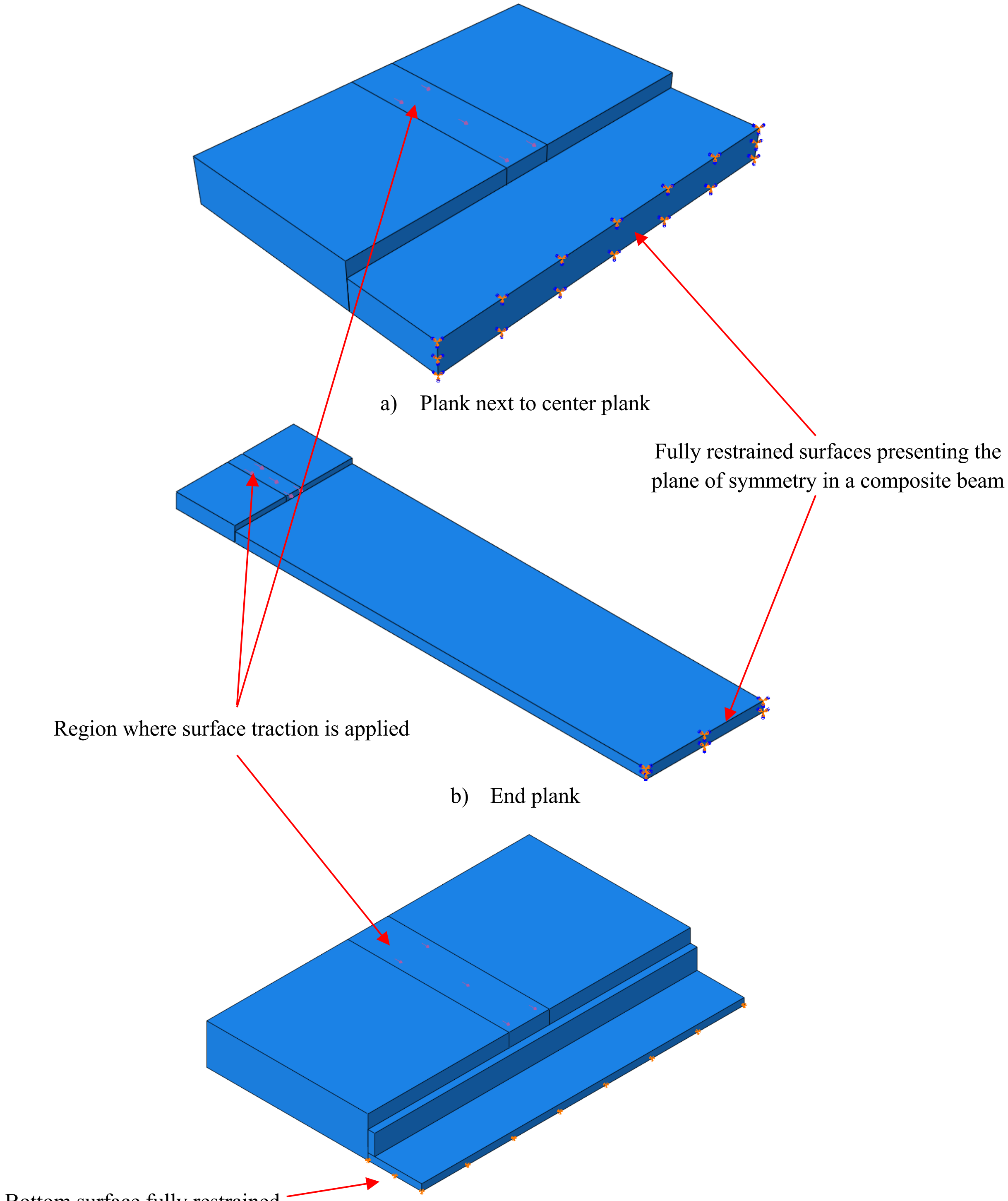
Fully restrained surfaces presenting the plane of symmetry in a composite beam
Region where surface traction is applied
Bottom surface fully restrained

a) Plank next to center plank

b) End plank

c) Steel reaction angle

Figure G.2 Finite element models developed for bearing stiffness comparison

Appendix H SHEAR FORCE TRANSFER FOR COMPOSITE DIAPHRAGMS, LIFTING INSERTS, AND FULLY THREADED RODS DESIGN

H.1 Shear force transfer for composite diaphragms

In the prototype structures outlined in Chapter 3, the clamps between the steel beams and concrete slabs are determined based on the design of the composite beams and girders under gravity loading. It is not clear whether the number of clamps is adequate to transfer the in-plane diaphragm forces to the lateral force-resisting systems (LFRS). Hence, the shear resistance of the clamps connecting the composite diaphragm and LFRS is compared to the inertia force generated in the diaphragm in this section. The 30-9-6 and 30-3-6 structures, which are presented in Chapter 3 and shown in Figure H.1, are used as examples.

The in-plane diaphragm forces for the prototype structures are calculated in accordance with ASCE 7-10. The basic information of the prototype structures is repeated here. Low gravity loading is employed to represent office occupancy, which is a uniform load of 92.5 psf dead load (32 psf for roof) and 80 psf live load. High gravity loading corresponds to storage warehouse, which is designed for a uniform load of 92.5 psf dead load (32 psf for roof) and 250 psf live load. The weights of the partitions and walls, which are 20 psf and 15 psf equivalent, respectively, are also taken into account for seismic force calculation. The building is presumed to be located in Los Angeles. The site is classified as site D. Special concentrically braced frames (SCBF) (AISC 2016b) are chosen as the lateral force-resisting systems.

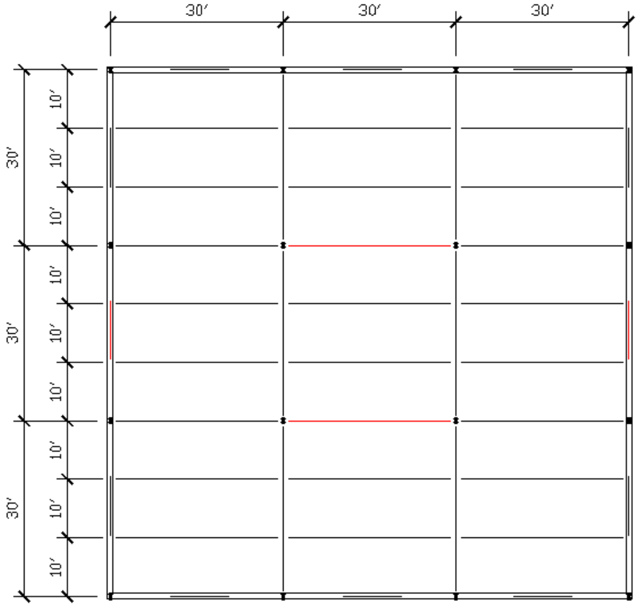

Note: The red lines show the lateral force-resisting systems.
Figure H.1 Prototype structure floor plan

Diagphragm force calculation as per ASCE 7-10

According to ASCE 7-10 Section 12.10.1.1, the diaphragm should be designed for inertial forces determined as the maximum of approaches (1) and (2), as outlined below:

(1) The design seismic force from the structural analysis of LFRS. This is commonly taken as the force from the Equivalent Lateral Force Procedure, where

$$F_x = C_{vx} W \tag{H.1}$$

$$C_{vx} = \frac{w_x h_x^k}{\sum_{i=1}^{n} w_i h_i^k} \tag{H.2}$$

(2) The diaphragm design force F_{px}, where

$$F_{px} = \frac{\sum_{i=x}^{n} F_i}{\sum_{i=x}^{n} w_i} w_{px} \tag{H.3}$$

but not less than

$$F_{px,min} = 0.2 S_{DS} I_e w_{px} \tag{H.4}$$

and not need exceed

$$F_{px,min} = 0.2 S_{DS} I_e w_{px} \tag{H.5}$$

Each diaphragm should be designed to resist the peak response at that floor level. However, it is conservative to design the LFRS using the sum of the peaks at all levels, as the peaks at different levels do not occur simultaneously due to higher modes. Thus, the lateral forces in Approach 1, which are determined from the analysis of the vertical elements in the LFRS, could underestimate the diaphragm forces.

Low gravity:

Diaphragm force obtained based on Approach 1:

According to Table 12.6-1 in ASCE 7-10, the Equivalent Lateral Force (ELF) procedure is permitted to be used for the building.

The period of the building is calculated as:

$$T_a = C_t h_n^x = 0.02 \times 117^{0.75} = 0.71\,s$$

The seismic response coefficient is determined as:

$$C_s = \frac{S_{DS}}{\left(\frac{R}{I_e}\right)} = \frac{2S_{MS}}{3\left(\frac{R}{I_e}\right)} = \frac{2F_aS_S}{3\left(\frac{R}{I_e}\right)} = \frac{2 \times 1.0 \times 2.0}{3 \times \frac{6}{1.0}} = 0.222$$

$$\leq \frac{S_{D1}}{T\left(\frac{R}{I_e}\right)} = \frac{2F_vS_1}{3T\left(\frac{R}{I_e}\right)} = \frac{2 \times 1.5 \times 0.75}{3 \times 0.71 \times \frac{6}{1.0}} = 0.176$$

$$C_s \geq 0.044 S_{DS} I_e = 0.044 \times 1.33 \times 1.0 = 0.059 \geq 0.01$$

$$C_s = 0.176$$

The weight of the building is:

$$W = 294 + 1032 \times 8 = 8550\ kips$$

The base shear is determined as:

$$F_x = C_{vx}V = 0.176 \times 8550 = 1505\ kips$$

Vertical force distribution:

Level	w_x (kips)	h_x(ft.)	h_x^k	$w_x h_x^k$	C_{vx}	F_x(kips)
Roof	294	117	188	55380	0.070	105.222
9	1032	104	165	170772	0.216	324.468
8	1032	91	143	147443	0.186	280.143
7	1032	78	121	124447	0.157	236.450
6	1032	65	99	101832	0.129	193.481
5	1032	52	77	79668	0.101	151.369
4	1032	39	56	58056	0.073	110.308
3	1032	26	36	37166	0.047	70.616
2	1032	13	17	17339	0.022	32.944
			Total	792103	1	1505

Diaphragm force obtained based on Approach 2:

Using Equation (H.3), the estimated maximum force induced at a diaphragm level is calculated as follows:

Level	w_x (kips)	$\sum_{i=x}^{n} w_i$(kips)	F_i(kips)	$\sum_{i=x}^{n} F_i$ (kips)	F_{px}(kips)
Roof	294	294	105.222	105.222	105.222
9	1032	1326	324.468	429.69	**334.419**
8	1032	2358	280.143	709.833	310.665
7	1032	3390	236.450	946.283	288.072
6	1032	4422	193.481	1139.764	265.996
5	1032	5454	151.369	1291.133	244.307
4	1032	6486	110.308	1401.441	222.986
3	1032	7518	70.616	1472.057	202.070
2	1032	8550	32.944	1505.001	181.656

Minimum diaphragm design force:

$$F_{px,min} = 0.2S_{DS}I_e w_{px} = 0.2 \times 1.33 \times 1.0 \times 1032 = 274.51\ kips$$

Maximum diaphragm design force:

$$F_{px,min} = 0.4S_{DS}I_e w_{px} = 0.4 \times 1.33 \times 1.0 \times 1032 = 549.02\ kips$$

The diaphragm design force is $334.42\ kips$ in both directions, which is between the minimum and maximum diaphragm design force. The equivalent uniform loading is $334.42\ kips/90\ ft. = 3.72\ kips/ft.$

High gravity:

Diaphragm force obtained based on Approach 1:

According to Table 12.6-1 in ASCE 7-10, the Equivalent Lateral Force (ELF) procedure is permitted to be used for the building.

Period of the building:

$$T_a = C_t h_n^x = 0.02 \times 39^{0.75} = 0.31\ s$$

Seismic response coefficient:

$$C_s = \frac{S_{DS}}{\left(\frac{R}{I_e}\right)} = \frac{2S_{MS}}{3\left(\frac{R}{I_e}\right)} = \frac{2F_a S_S}{3\left(\frac{R}{I_e}\right)} = \frac{2 \times 1.0 \times 2.0}{3 \times \frac{6}{1.0}} = 0.222$$

$$\leq \frac{S_{D1}}{T\left(\frac{R}{I_e}\right)} = \frac{2F_v S_1}{3T\left(\frac{R}{I_e}\right)} = \frac{2 \times 1.5 \times 0.75}{3 \times 0.31 \times \frac{6}{1.0}} = 0.403$$

$$C_s \geq 0.044S_{DS}I_e = 0.044 \times 1.33 \times 1.0 = 0.059 \geq 0.01$$

$$C_s = 0.222$$

Weight of the building:

$$W = 294 + 1488 \times 2 = 3270\ kips$$

Base shear:

$$F_x = C_{vx}V = 0.222 \times 3270 = 725.9\ kips$$

Vertical force distribution:

Level	w_x (kips)	h_x(ft.)	h_x^k	$w_x h_x^k$	C_{vx}	F_x(kips)
Roof	294	39	39.0	11466	0.161	119.761
3	1488	26	26.0	38688	0.559	404.092
2	1488	13	13.0	19344	0.280	202.046
			Total	69498	1.0	725.900

Diaphragm force obtained based on Approach 2:

Using Equation (H.3), the estimated maximum force induced at a diaphragm level is calculated as follows:

Level	w_x (kips)	$\sum_{i=x}^{n} w_i$(kips)	F_i(kips)	$\sum_{i=x}^{n} F_i$ (kips)	F_{px}(kips)
Roof	294	294	119.761	119.761	119.761
3	1488	1782	404.092	523.853	**437.426**
2	1488	3270	202.046	725.900	330.318

Minimum diaphragm design force:

$$F_{px,min} = 0.2 S_{DS} I_e w_{px} = 0.2 \times 1.33 \times 1.0 \times 1488 = 395.81\ kips$$

Maximum diaphragm design force:

$$F_{px,min} = 0.4 S_{DS} I_e w_{px} = 0.4 \times 1.33 \times 1.0 \times 1488 = 791.62\ kips$$

The diaphragm design force is $437.43\ kips$ in both directions, which is between the minimum and maximum diaphragm design force. The equivalent uniform loading is $4.86\ kips/ft$.

Figure H.2 shows the floor that has the largest diaphragm force in each structure. The steel sections are labelled which connect the diaphragms to the LFRS. For the 30-9-6 structure, the collector beams are W18x35 sections which have a percentage of composite action of 61.1%, while the girders that belong to the LFRS use W24x76 sections which are designed as non-composite sections. For the 30-3-6 structure, the collector beams are W21x55 sections which have a percentage of composite action of 38.9%, while the girders that belong to the LFRS use W30x99 sections which are designed as non-composite sections. All the girders that are a part of the LFRS have a minimum composite action of 25% (Sabelli et al. 2011).

In the 30-9-6 structure, the total shear resistance of the clamps that transfer the diaphragm force to the perimeter frame is calculated as:

$$\sum Q = (0.611 \times 50 \times 10.3 \times 4 + 0.25 \times 22.4 \times 50 \times 2) \times 0.8 = 1455\ kips$$
$$> 334\ kips$$

In the 30-3-6 structure, the total shear resistance of the clamps that transfer the diaphragm force to the perimeter frame is calculated as:

$$\sum Q = (0.389 \times 50 \times 16.2 \times 4 + 0.25 \times 29 \times 50 \times 2) \times 0.8 = 1588\ kips$$
$$> 437\ kips$$

Similar to the 25% strength reduction seen in steel headed stud anchors under cyclic loading (Pallarés et al 2009), a 20% strength reduction is proposed for the clamps (see Section 4.5.4.2 for further discussion). The comparison indicates that the clamps designed for gravity loading are adequate to transfer the diaphragm force. As the resistance of the clamps is much larger than the design diaphragm force, it could be inferred that the slip of the clamps is negligible under design earthquakes.

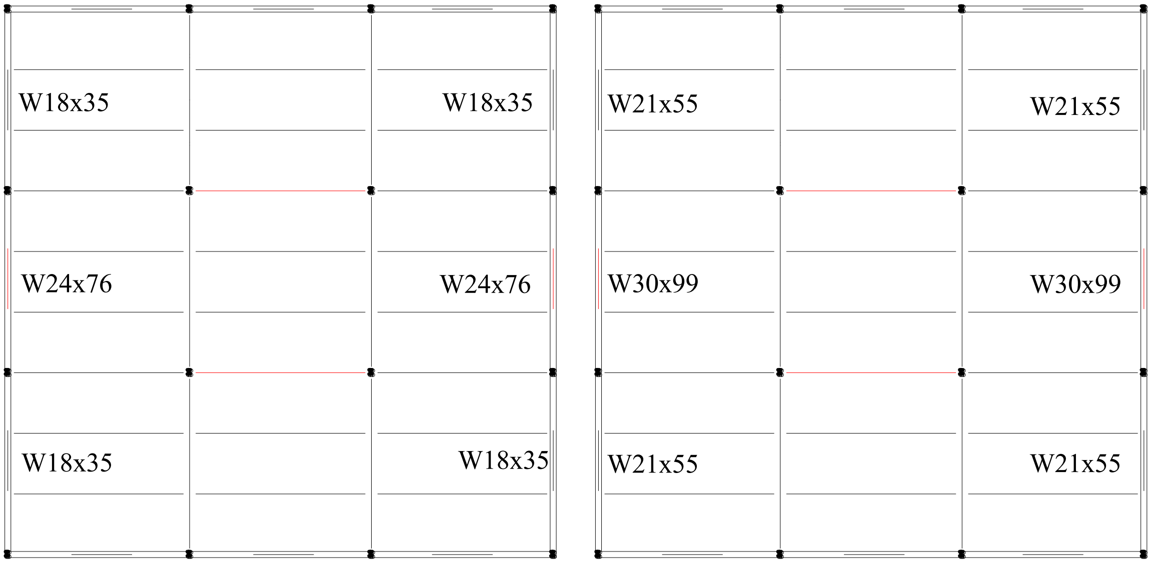

a) 9th floor in the 30-9-6 frame b) 3rd floor in the 30-3-6 frame

Figure H.2 Member sizes for the exterior girders and collector beams

H.2 Lifting points on concrete planks

In this work, it was necessary to use lifting hooks to transport the precast concrete planks in the beam specimens. When detailing these precast concrete components, calculations are thus required to ensure that the components have sufficient strength to resist temporary loading during form removal, transportation, erection, etc.

In this work, the lifting inserts are placed at the two outer fifth points of the planks to minimize the maximum bending moment induced by handling. It is expected that the most critical handling for these planks is to pull the specimens out of the formwork. Two sections are deemed to govern: (1) the section with the largest bending moment; (2) the section with the smallest moment of inertia, which is the section containing the cutouts and embedded PVC pipe. The maximum tensile stress in the concrete planks is conservatively calculated with the maximum bending moment and the section with the smallest moment of inertia.

The following calculations identify that the tensile stress in a concrete plank induced by its self-weight during lifting of the concrete plank is below the modulus of rupture of the concrete plank, which indicates that the selected lifting points are effective.

Parameters:

Concrete plank:

Plank length $l = 8\ ft.$

Plank depth $d = 6\ in. = 0.5\ ft.$

Plank width $b = 2\ ft.$

Density $\rho = 150\ lbs/ft^3$

Calculation:

Figure H.3 illustrates the moment diagram of a concrete plank under its self-weight. The maximum positive bending moment is generated at the center section of the plank, while the maximum negative bending moment occurs at the lifting points.

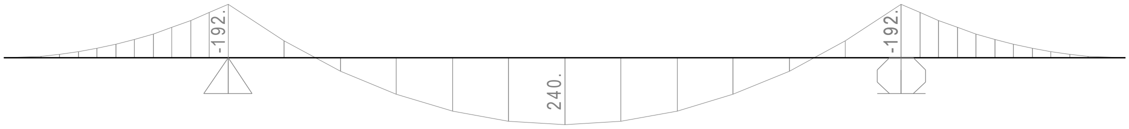

Figure H.3 Moment diagram of a concrete plank under gravity loading (units: lb-ft)

The maximum bending moment in the panel is:

$$M_{pos} = \frac{1}{40} q l^2 = \frac{1}{40} \rho b h l^2 = \frac{1}{40} \times 150 \times \frac{6}{12} \times 2\ \times 8^2 = 240\ lb - ft$$

Figure H.4 illustrates the section with the smallest moment of inertia.

The location of the elastic neutral axis (measured from the bottom of the section) in this section is:

$$y=\frac{19\times(6-1.05)\times3-2.81\times1.91\times2\times1.91/2}{19\times6-2.81\times1.91\times2-1.05\times19}=3.26\;in.$$

The sectional moment of inertia (without considering the cast-in channels) is:

$$\begin{aligned}I&=\frac{1}{12}\times19\times(6^3-1.05^3)+19\times(6-1.05)\times(3.26-3)^2\\&\quad-2\times\frac{1}{12}\times1.91^3\times2.81-2\times1.91\times2.81\times\left(3.26-\frac{1.91}{2}\right)^2\\&=286.2\;in^4\end{aligned}$$

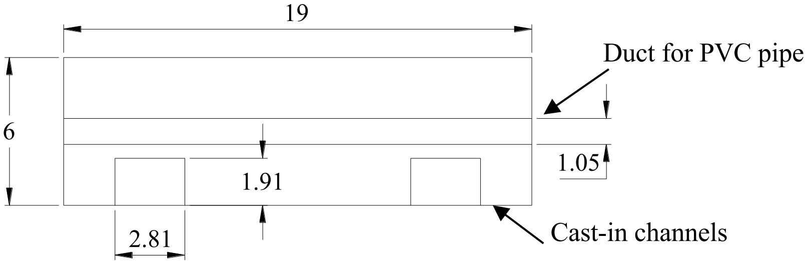

Figure H.4 Section with the smallest moment of inertia (units: inches)

The tensile stress in the panel is thus:

$$f_t=\frac{M_{pos}}{I}c=\frac{240\times12\times3.26}{286.2}=32.80\;psi$$

According to Table 5.5 in Chapter 5, the concrete planks reached a compressive strength of at least 3,500 psi by the time the specimens were lifted.

The modulus of rupture of the concrete planks may be taken as:

$$f_r=7.5\lambda\sqrt{f_c'}=7.5\times\sqrt{3500}=444\;psi$$

A multiplier is employed to account for formwork suction and impact. Conservatively, 1.7 is selected from Table 8.3.1 in PCI Design Handbook (2010). In addition, a safety factor of 1.5 is recommended in the handbook for the modulus of rupture.

With the multiplier, the maximum tensile stress $= 1.7 \times 32.80 = 56\, psi$

With the safety factor, the modulus of fracture of the planks $= 444/1.5 = 296 \gg 56\, psi$

The above calculation shows that the selected lifting points are effective.

H.3 Selection of fully threaded rods

The design of a composite diaphragm commonly assumes that bending of the diaphragm is resisted by the steel chords, and the diaphragm has to be designed for the shear force (Sabelli et al. 2011). In the deconstructable composite diaphragm, the shear force is resisted by the friction between adjacent planks, and then resisted by the steel rods provided that the friction is overcome and the steel rods start to bear against the concrete planks. The selection of the threaded rods is based on the in-plane diaphragm force calculated in Section H.1.

When the lateral force-resisting system is at the exterior of the structure, as shown in Figure H.1, the maximum shear demand occurs at the collectors. The largest required shear flow between the planks is $437.43\, kips/2/90\, ft. = 2430\, lbs/ft.$

The shear friction analogy can be adapted to select the threaded rods, and a shear friction coefficient of 0.6 given in Section 11.6.4.3 of ACI 318-11 may be valid. However, a frictional coefficient of 1.0 is assumed when choosing the threaded rods in the composite beam tests. The higher frictional coefficient leads to smaller rods with less pretensioning force, which makes the assembly of the test specimens easier. More importantly, in real practice, an interlocking mechanism can be achieved with intermittent tongue-and-groove joints, or the concrete surfaces can be purposely roughened. A higher coefficient of friction can thus be justified. In addition, the flexural behavior of the composite beam specimens under gravity loading is not believed to be strongly affected by the pretension force in the rods.

Based on the calculations in Section H.1, using dual-certified ASTM A36-14/A529-05 Grade 50 rods with a nominal yield strength and a nominal tensile strength of 50 ksi and 70 ksi, respectively, 5/8 in. fully threaded rods are selected. The normal force between the planks is taken as the lower value determined from the limit states of tensile yielding and tensile rupture.

The stress area of a 5/8 in. thread rod is:

$$= 0.785(D - \frac{0.9743}{n})^2 = 0.785 \times (0.625 - \frac{0.9743}{11})^2 = 0.226\, in.^2$$

Where

$D =$ nominal bolt diameter

$n =$ number of threads per inch

The limit state of tensile yielding:

$$\emptyset_t P_n = \emptyset_t F_y A_g = 0.9 \times 50 \times 0.226 \ = 10.17\, kips$$

The limit state of tensile rupture:

$$\emptyset_t P_n = \emptyset_t F_u A_e = 0.75 \times 70 \times 0.226 \ = 11.87\, kips$$

If the spacing between the rods is 4 ft., the available shear flow between the planks = $10170\, lbs/4\, ft. = 2543 > 2430\, lbs/ft.$

Appendix I MOMENT OF INERTIA OF A COMPOSITE BEAM SECTION

When the design of a composite beam is controlled by deflection, a reasonable evaluation of the moment of inertia of the composite section is necessary. In the AISC 360-16 commentary (2016), several types of moment of inertia are defined. When the composite beam behaves elastically, an equivalent moment of inertia, I_{equiv} , is used, which is the moment of inertia of the transformed section. If the beam is a partially composite beam, I_{equiv} is interpolated between the moment of inertia of the steel section and the equivalent moment of inertia of the fully composite section. However, Leon et al. (1993) indicates that the deflection of a composite beam under serviceability cannot be estimated accurately with I_{equiv}; therefore, an effective moment of inertia, I_{eff}, is recommended which is taken as $0.75\ I_{equiv}$. A lower bound moment of inertia, I_{LB} , is also suggested, which neglects the contribution of the concrete in the tensile zone to the overall stiffness of the beam. It is demonstrated that I_{LB} also gives a good estimate of the elastic stiffness of the composite beam (Leon et al. 1993). The values of these moment of inertia are calculated below.

- Equivalent moment of inertia

The location of the elastic neutral axis is measured from the bottom surface of the steel section and computed using Equation (I.1). The cast-in channels and supplementary reinforcement placed around the anchors are ignored in the calculation.

$$y_{ENA} = \frac{\frac{tb_{eff}}{n}\left(d+\frac{t}{2}\right) + A_s\frac{d}{2} + N_{tb}\frac{1}{4}\pi d_{tb}^2(d+D_{tb}) + N_{bb}\frac{1}{4}\pi d_{bb}^2(d+D_{bb})}{\frac{tb_{eff}}{n} + A_s + N_{tb}\frac{1}{4}\pi d_{tb}^2 + N_{bb}\frac{1}{4}\pi d_{bb}^2} \tag{I.1}$$

Where

b_{eff} = effective width of the concrete plank (in.)

d = nominal height of the steel section (in.)

d_{bb} = nominal bottom transverse bar diameter (in.) = 0.375 in.

d_{tb} = nominal top transverse bar diameter (in.) = 0.375 in.

f_c' = concrete compressive strength (psi)

n = modulus ratio = E_s/E_c

t = nominal thickness of the concrete plank (in.) = 6 in.

A_s = nominal area of the steel section (in^2.)

D_{bb} = nominal distance between the bottom bars and the top surface of the steel section (in.) = 2.19 in.

D_{tb} = nominal distance between the top bars and the top surface of the steel section (in.) = 5.19 in.

E_s = elastic modulus of the steel section (psi)

E_c = elastic modulus of the concrete plank (psi) = $57000\sqrt{f_c'}$

N_{bb} = number of bottom transverse bars = 5

N_{tb} = number of top transverse bars = 21

The transformed moment of inertia of a fully composite section is then given in Equation (I.2).

$$\begin{aligned} I_{tr} &= I_s + A_s\left(y_{ENA} - \frac{d}{2}\right)^2 + \frac{1}{12n} b_{eff} t^3 + \frac{t b_{eff}}{n}\left(d + \frac{t}{2} - y_{ENA}\right)^2 \\ &+ N_{tb}\frac{1}{4}\pi d_{tb}^2 (d + D_{tb} - y_{ENA})^2 + N_{bb}\frac{1}{4}\pi d_{bb}^2 (d + D_{bb} - y_{ENA})^2 \end{aligned} \tag{I.2}$$

Where

I_s = nominal moment of inertia for the structural steel section (in^4.)

When the section is partially composite, the equivalent moment of inertia could be approximated with Equation (C-I3-3) given in the AISC 360-16 commentary (2016).

$$I_{equiv} = I_s + \sqrt{\left(\frac{\sum Q_n}{C_f}\right)}(I_{tr} - I_s) \tag{I.3}$$

Where

$\sum Q_n$ = strength of steel anchors between the point of maximum positive moment and the point of zero moment to either side (kips)

C_f = compressive force in concrete slab for fully composite beam; smaller of A_sF_y and $0.85f_c'A_c$ (kips)

A_c = area of concrete slab within the effective width (in^2.)

- Lower bound moment of inertia

The equations for the elastic neutral axis and moment of inertia are given in Equations (C-I3-1) and (C-I3-2) in the AISC 360-16 commentary (2016).

$$Y_{ENA} = \frac{A_s d_3 + \frac{\sum Q_n}{F_y}(2d_3 + d_1)}{A_s + \frac{\sum Q_n}{F_y}} \tag{I.4}$$

$$I_{LB} = I_s + A_s(Y_{ENA} - d_3)^2 + \frac{\sum Q_n}{F_y}(2d_3 + d_1 - Y_{ENA})^2 \tag{I.5}$$

Where

d_1 = distance from the compressive force in the concrete to the top surface of the steel section (in.)

d_3 = distance from the resultant steel tensile force for full section tension yield to the top surface of the steel section (in.) = $d/2$

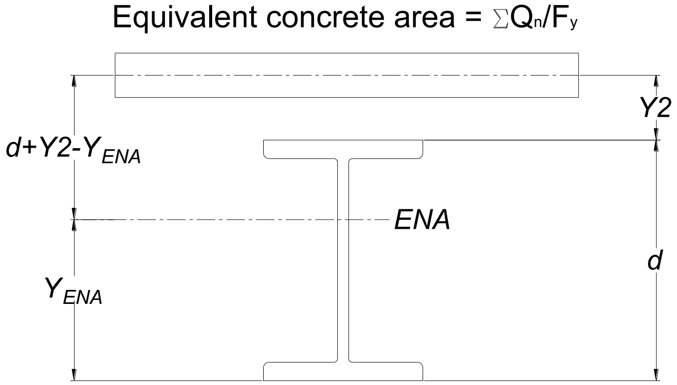

Figure I.1 Lower bound moment of inertia (reproduced from AISC 2016a)

The different values for moment of inertia are shown in Table I.1. In this table, the nominal clamp strengths employ the strengths predicted with Equation (4.27) in Chapter 4, and the tested clamp strengths use the strengths obtained from the pushout tests presented in Chapter 4. The predicted shear strengths of the M24 and M20 clamps are 19.15 kips and 13.25 kips, respectively, while the tested shear strengths of the M24 and M20 clamps are 22.13 kips and 13.83 kips, respectively. In Chapter 5, these values of I_{LB} are used to calculate the estimated elastic stiffness of the composite beams specimens, which are then compared to the measured elastic stiffness from the experiments. An effective width of 90 in. is used in the calculations in Table I.1; Chapter 5 has further discussion about appropriate effective widths to use for computing moment of inertia of these beams.

Table I.1 Moment of inertia calculation

Parameters	Nominal				Tested			
	Beam 1	Beam 2	Beam 3	Beam 4	Beam 1	Beam 2	Beam 3	Beam 4
f_c' (psi)	5,000	5,000	5,000	5,000	5,780	6,630	5,420	6,670
f_y (psi)	50,000	50,000	50,000	50,000	52,500	52,500	46,900	49,000
E_s (ksi)	29000	29000	29000	29000	29800	29800	30000	29500
E_c (ksi)	4030	4030	4030	4030	4333	4641	4196	4686
n	7.20	7.20	7.20	7.20	6.88	6.42	7.15	6.30
b_{eff} (in.)	90	90	90	90	90	90	90	90
A_s (in^2.)	11.2	11.2	7.69	7.69	11.2	11.2	7.69	7.69
d (in.)	14.1	14.1	13.9	13.9	14.1	14.1	13.9	13.9
y_{ENA} (in.)	15.89	15.89	16.06	16.06	15.93	16.00	16.07	16.15
Y_{ENA} (in.)	12.86	11.15	13.21	10.79	12.75	11.04	13.24	10.86
I_s (in^4.)	385	385	245	245	385	385	245	245
I_{tr} (in^4.)	1622	1622	1183	1183	1638	1661	1189	1222
S_{tr} (in^3.)	102.08	102.08	73.66	73.66	102.82	103.81	73.99	75.67
$\sum Q_n$ (kips)	421.3	229.8	477	159	486.2	265.2	496.8	165.6
C_f (kips)	560	560	384.5	384.5	588	588	360.3	377.7
A_c (in^2.)	540	540	540	540	540	540	540	540
I_{equiv}	1458	1178	1183	848	1524	1242	1184	892
S_s (in^3.)	54.6	54.6	35.3	35.3	54.6	54.6	35.3	35.3
S_{eff} (in^3.)	95.78	85.02	73.66	59.97	98.45	87.65	73.99	62.03
I_{LB}	1146	918	848	612	1188	958	853	631
I_{LB}/I_{equiv}	0.79	0.78	0.72	0.72	0.78	0.77	0.72	0.71

Appendix J COMPOSITE BEAM STRENGTH AND STIFFNESS CALCULATION

For assessing the performance of the composite beams in Chapter 5, calculations of the flexural strength and stiffness of these beams are needed. These calculations are demonstrated using Specimens 2-M24-1C-RL, 3-M20-3C-RL, and 4-M20-1C-RL as examples and outlined in this appendix. These three beams represent a partially composite beam with a neutral axis lying in the steel flange, a fully composite beam, and a partially composite beam with a neutral axis lying in the steel web, respectively. Tested material properties are used in the following calculations.

- Specimen 2-M24-1C-RL

Parameters:

Beam span:

Length = 30 ft.

Slab:

Slab depth = 6.0 in.

Slab width = 96 in.

Concrete:

$f_c' = 6632\ psi$

$E_c = 57000 \times \sqrt{6632} = 4641914\ psi$

Steel section: W14x38

$A_s = 11.2\ in.^2$

$d = 14.1\ in.$

$d_3 = d/2 = 14.1/2 = 7.05\ in.$

$t_f = 0.515\ in.$

$b_f = 6.77\ in.$

$t_w = 0.31\ in.$

$f_{yf} = 50.07\ ksi$

$f_{yw} = 56.63\ ksi$

$A_f = 2b_f t_f = 2 \times 6.77 \times 0.515 = 6.97\ in.^2$

$A_w = A_s - A_f = 11.2 - 6.97 = 4.23\ in.^2$

Clamps:

$Q_n = 22.1\ kips$

$n = 30$

Calculations:

1. Percentage of composite action

The percentage of composite action is calculated for the maximum moment section which is located at one of the two inner loading points.

The percentage of composite action of the beam is calculated as:

$$\sum Q_n / (A_f f_{yf} + A_w f_{yw}) = 12 \times 22.1 / \ (6.97 \times 50.07 + 4.23 \times 56.63) \ = 45.1\%$$

2. Experimental flexural strength of the beam

From the moment diagram illustrated in Figure J.1, it is seen that under the applied actuator loads the largest required flexural strength occurs at one of the two inner loading points of the beam. The variation of the bending moment at the center section and the two inner loading point sections is plotted in Figure J.2. In addition, the self-weight of the composite beam and loading structures also generates bending moment at these sections. The maximum bending moment at these sections is given in Table J.1.

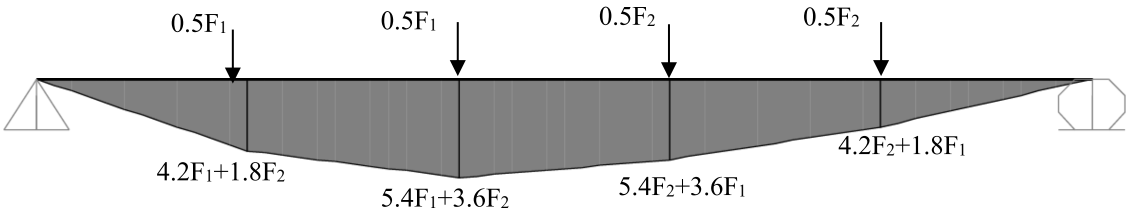

Figure J.1 Moment diagram for Beam 2

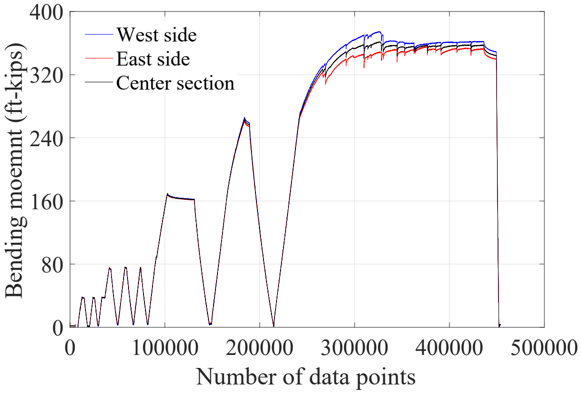

Figure J.2 Bending moment at center and inner loading point sections due to actuator loading

Table J.1 Breakdown of bending moment (units: ft.-kips)

Sections	Applied actuator loads	Weight of composite beam	Weight of loading structures	Total
West inner loading point	374.68	72	22.5	469.2
Center	361.71	75	22.5	459.2
East inner loading point	355.58	72	22.5	450.1

Therefore, the available flexural strength of the beam is 469.2 ft.-kips.

3. Predicted flexural strength of the beam

3.1 The strength of shear connectors placed between zero and maximum moment sections is equal to

$$\sum Q_n = 12 \times 22.1 = 265.2\ kips$$

3.2 Calculate the effective width of the concrete planks

$$b_e = \frac{1}{4} of\ beam\ span = \frac{1}{4} \times 360 = 90\ in. < 96\ in.$$

3.3 Calculate the compressive force, C, in the concrete plank at the ultimate state. This force is the smallest of

$$C_1 = P_y = A_s f_y = 6.97 \times 50.07 + 4.23 \times 56.63 = 588.5\ kips$$

$$C_2 = 0.85 A_c f_c' = 0.85 \times 90 \times 6 \times 6632/1000 = 3044\ kips$$

$$C_3 = \sum Q_n = 265.2\ kips$$

$$C = \min\left(A_s f_y, 0.85 A_c f_c', \sum Q_n\right) = 265.2\ kips$$

3.4 Calculate the depth of the equivalent rectangular concrete stress block

$$a = \frac{C}{0.85 b_e f_c'} = \frac{265.2}{0.85 \times 90 \times 6.632} = 0.523\ in.$$

$$d_1 = 6.0 - 0.523/2 = 5.74\ in.$$

3.5 Determine the location of the neutral axis in the steel beam

Because $C_1 - 2b_f t_f f_{yf} = 588.5 - 6.97 \times 50.07 = 239.5\ kips < 265.2\ kip$, the neutral axis lies in the top steel flange.

$$d_2 = \frac{1}{2} \frac{C_1 - C}{2b_f f_{yf}} = \frac{1}{2} \times \frac{588.5 - 265.2}{2 \times 6.77 \times 50.07} = 0.238\ in.$$

3.6 Calculate the flexural strength of the beam

$$M = C(d_1 + d_2) + P_y(d_3 - d_2)$$

$$= 265.2 \times (5.74 + 0.238) + 588.5 \times (7.05 - 0.238) = 466.2\ ft - kips$$

4. Predicted stiffness of the beam

The stiffness of the beam is estimated using the lower bound moment of inertia of the composite beam section, which is given in Table I.1 in Appendix I. For a beam under four concentrated forces applied at equal spacing, the stiffness can be calculated with the following equation.

$$k = \frac{EI}{0.01575 l^3} = \frac{29800 \times 958}{0.01575 \times 360^3} = 38.9\ kips/in.$$

- Specimen 3-M20-3C-RL

Parameters:

Beam span:

Length = 30 ft.

Slab:

Slab depth = 6.0 in.

Slab width = 96 in.

Concrete:

$f_c' = 5420\ psi$

$E_c = 57000 \times \sqrt{5420} = 4196377\ psi$

Steel section: W14x26

$A_s = 7.69\ in.^2$

$d = 13.9\ in.$

$d_3 = d/2 = 13.9/2 = 6.95\ in.$

$t_f = 0.42\ in.$

$b_f = 5.03\ in.$

$t_w = 0.255\ in.$

$f_{yf} = 45.57\ ksi$

$f_{yw} = 48.43\ ksi$

$A_f = 2b_f t_f = 2 \times 5.03 \times 0.42 = 4.23\ in.^2$

$A_w = A_s - A_f = 7.69 - 4.23 = 3.46\ in.^2$

Clamps:

$Q_n = 13.8\ kips$

$n = 90$

Calculations:

1. Percentage of composite action

The percentage of composite action is calculated for the maximum moment section which is located at one of the two inner loading points.

The percentage of composite action of the beam is calculated as:

$$\sum Q_n/(A_f f_{yf} + A_w f_{yw}) = 36 \times 13.8/\ (4.23 \times 45.57 + 3.46 \times 48.43)\ = 137.9\%$$

2. Experimental flexural strength of the beam

The variation of the bending moment at the center section and the two inner loading point sections under actuator loading is plotted in Figure J.3. The maximum bending moment at these sections is given in Table J.2.

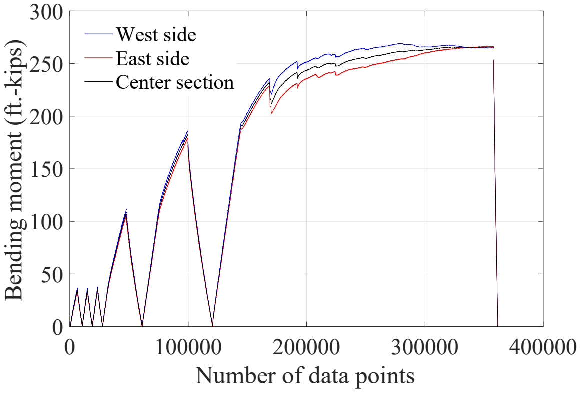

Figure J.3 Bending moment at center and inner loading point sections due to actuator loading

Table J.2 Breakdown of bending moment (units: ft.-kips)

Sections	Applied actuator loads	Weight of composite beam	Weight of loading structures	Total
West inner loading point	269.16	72	22.5	363.7
Center	266.30	75	22.5	363.8
East inner loading point	265.72	72	22.5	360.2

Therefore, the available flexural strength of the beam is 363.8 ft.-kips.

3. Predicted flexural strength of the beam

3.1 The strength of shear connectors placed between zero and maximum moment sections is equal to

$$\sum Q_n = 36 \times 13.8 = 496.8\ kips$$

3.2 Calculate the effective width of the concrete planks

$$b_e = \frac{1}{4} of\ beam\ span = \frac{1}{4} \times 360 = 90\ in. < 96\ in.$$

3.3 Calculate the compressive force, C, in the concrete plank at the ultimate state. This force is the smallest of

$$C_1 = P_y = A_s f_y = 4.23 \times 45.57 + 3.46 \times 48.43 = 360.3\ kips$$

$$C_2 = 0.85 A_c f_c' = 0.85 \times 90 \times 6 \times 5420/1000 = 2488\ kips$$

$$C_3 = \sum Q_n = 496.8\ kips$$

$$C = \min\left(A_s f_y, 0.85 A_c f_c', \sum Q_n\right) = 360.3\ kips$$

3.4 Calculate the depth of the equivalent rectangular concrete stress block

$$a = \frac{C}{0.85 b_e f_c'} = \frac{360.3}{0.85 \times 90 \times 5.42} = 0.869\ in.$$

$$d_1 = 6.0 - 0.869/2 = 5.566\ in.$$

3.5 Determine the location of the neutral axis in the steel beam

Since this specimen is a fully composite beam, only one neutral axis exists which lies in the concrete plank. Therefore, $d_2 = 0$.

3.6 Calculate the flexural strength of the beam

$$M = C(d_1 + d_2) + P_y(d_3 - d_2)$$
$$= 360.3 \times (5.566 + 0) + 360.3 \times (6.95 - 0) = 375.8\ \ ft - kips$$

4. Predicted stiffness of the beam

The stiffness of the beam is estimated using the lower bound moment of inertia of the composite beam section, which is given in Table I.1 in Appendix I. For a beam under four concentrated forces applied at equal spacing, the stiffness can be calculated with the following equation.

$$k = \frac{EI}{0.01575l^3} = \frac{30000 \times 853}{0.01575 \times 360^3} = 34.8\ kips/in.$$

- Specimen 4-M20-1C-RL

Parameters:

Beam span:

Length = 30 ft.

Slab:

Slab depth = 6.0 in.

Slab width = 96 in.

Concrete:

$f_c' = 6670\ psi$

$E_c = 57000 \times \sqrt{6670} = 4655194\ psi$

Steel section: W14x26

$A_s = 7.69\ in.^2$

$d = 13.9\ in.$

$d_3 = d/2 = 13.9/2 = 6.95\ in.$

$t_f = 0.42\ in.$

$b_f = 5.03\ in.$

$t_w = 0.255\ in.$

$f_{yf} = 48.37\ ksi$

$f_{yw} = 50.03\ ksi$

$A_f = 2b_f t_f = 2 \times 5.03 \times 0.42 = 4.23\ in.^2$

$A_w = A_s - A_f = 7.69 - 4.23 = 3.46\ in.^2$

Clamps:

$Q_n = 13.8\ kips$

$n = 30$

Calculations:

1. Percentage of composite action

The percentage of composite action is calculated for the maximum moment section which is located at one of the two inner loading points.

The percentage of composite action of the beam is calculated as:

$$\sum Q_n/(A_f f_{yf} + A_w f_{yw}) = 12 \times 13.8/\ (4.23 \times 48.37 + 3.46 \times 50.03)\ = 43.8\%$$

2. Experimental flexural strength of the beam

The variation of the bending moment at the center section and the two inner loading point sections under actuator loading is plotted in Figure J.4. The maximum bending moment at these sections is given in Table J.3.

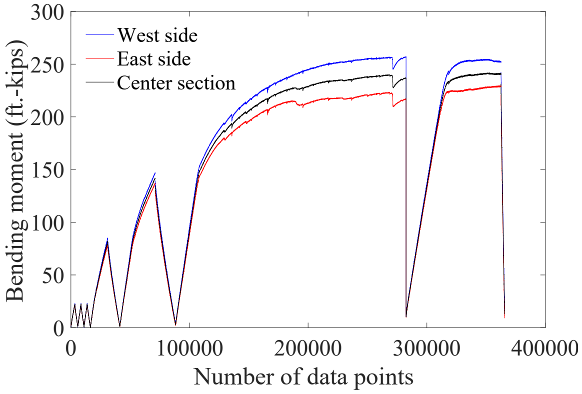

Figure J.4 Bending moment at center and inner loading point sections due to actuator loading

Table J.3 Breakdown of bending moment (units: ft.-kips)

Sections	Applied actuator loads	Weight of composite beam	Weight of loading structures	Total
West inner loading point	256.98	72	22.5	351.5
Center	241.66	75	22.5	339.2
East inner loading point	229.58	72	22.5	324.1

Therefore, the available flexural strength of the beam is 351.5 ft.-kips.

3. Predicted flexural strength of the beam

3.1 The strength of shear connectors placed between zero and maximum moment sections is equal to

$$\sum Q_n = 12 \times 13.8 = 165.6\ kips$$

3.2 Calculate the effective width of the concrete planks

$$b_e = \frac{1}{4} of\ beam\ span = \frac{1}{4} \times 360 = 90\ in. < 96\ in.$$

3.3 Calculate the compressive force, C, in the concrete plank at the ultimate state. This force is the smallest of

$$C_1 = P_y = A_s f_y = 4.23 \times 48.37 + 3.46 \times 50.03 = 377.7\ kips$$

$$C_2 = 0.85 A_c f_c' = 0.85 \times 90 \times 6 \times 6670/1000 = 3062\ kips$$

$$C_3 = \sum Q_n = 165.6\ kips$$

$$C = \min\left(A_s f_y, 0.85 A_c f_c', \sum Q_n\right) = 165.6\ kips$$

3.4 Calculate the depth of the equivalent rectangular concrete stress block

$$a = \frac{C}{0.85 b_e f_c'} = \frac{165.6}{0.85 \times 90 \times 6.67} = 0.324\ in.$$

$$d_1 = 6.0 - 0.324/2 = 5.838\ in.$$

3.5 Determine the location of the neutral axis in the steel beam

Because $C_1 - 2b_f t_f f_{yf} = 377.7 - 4.23 \times 48.37 = 173.1\ kips > 165.6\ kip$, the neutral axis lies in the steel web.

According to AISC 2016a, the steel section is idealized as the model illustrated in Figure J.5. This model assumes that

$$A_f = flange\ area = b_f t_f$$
$$A_w = web\ area = (d - 2k)t_w$$
$$K_{dep} = k - t_f$$
$$K_{area} = \left(A_s - 2A_f - A_w\right)/2$$

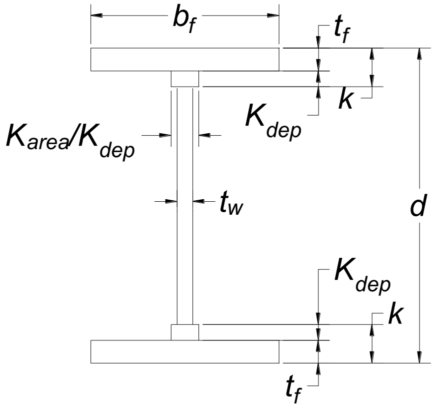

Figure J.5 Idealized W-shape steel section (reproduced from AISC 2016a)

Assume the neutral axis lies in K_{dep}. The location of the neutral axis is calculated as:

$$d_2 = t_f + \frac{C_1 - 2b_f t_f f_{yf} - \sum Q_n}{2f_{yf}\dfrac{K_{area}}{K_{dep}}}$$

$$= 0.42 + \frac{173.1 - 165.6}{2 \times 48.37 \times \dfrac{7.69 - 4.23 - (13.9 - 2 \times 0.82) \times 0.255}{2 \times (0.82 - 0.42)}} = 0.606$$

$$< 0.82\ in.$$

3.6 Calculate the flexural strength of the beam

Take moment with respect to the location of the resultant concrete plank compression. All the notations used in the following equation are illustrated in Figure J.6.

$$M = P_y\left(\frac{d_3}{2} + d_1\right) - 2b_f t_f f_{yf}\left(\frac{t_f}{2} + d_1\right) - (P_y - 2b_f t_f f_{yf} - \sum Q_n)(d_1 + \frac{d_2 + t_f}{2})$$

$$= 377.7 \times (6.95 + 5.84) - 204.61 \times (0.21 + 5.84) - 7.5 \times (5.84 + \frac{0.61 + 0.42}{2})$$

$$= 295.4\ ft - kips$$

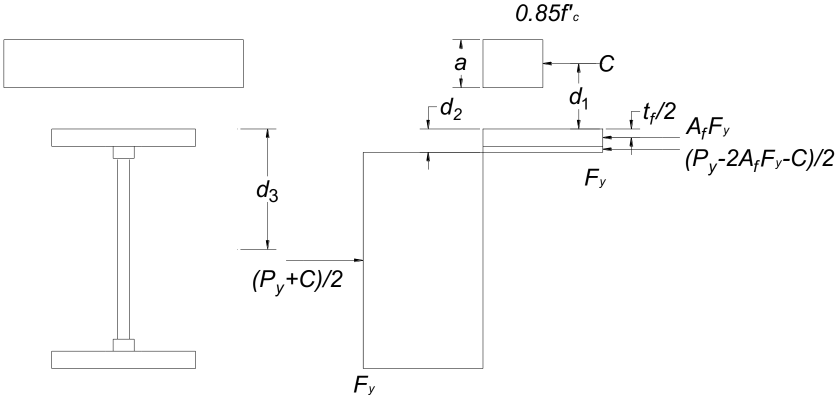

Figure J.6 Composite beam flexural strength calculation (Neutral axis in steel web)

4. Predicted stiffness of the beam

The stiffness of the beam is estimated using the lower bound moment of inertia of the composite beam section, which is given in Table I.1 in Appendix I. For a beam under four concentrated forces applied at equal spacing, the stiffness can be calculated with the following equation.

$$k = \frac{EI}{0.01575 l^3} = \frac{29500 \times 631}{0.01575 \times 360^3} = 25.3\ kips/in.$$

Appendix K DIAPHRAGM BEHAVIOR OF DECONSTRUCTABLE COMPOSITE FLOOR SYSTEMS

The material presented in this appendix is published in the following paper:

Wang, L., Webster, M. D., and Hajjar, J. F. (2015). "Diaphragm Behavior of Deconstructable Composite Floor Systems," *Proceedings of the 8th International Conference on Behavior of Steel Structures in Seismic Areas (STESSA 2015),* Shanghai, China, July 1-3, 2015, China Architecture & Building Press, Beijing, China.

A series of preliminary finite element analyses has been conducted to study the diaphragm behavior of the deconstructable composite floor system. All the finite element models were developed in ABAQUS/CAE and analyzed in ABAQUS/Explicit. The analyses presented here employed the explicit method to solve quasi-static problems by applying cyclic loads sufficiently slowly to render the dynamic response negligible.

K.1 Finite element model and mesh

The finite element model, illustrated in Figure K.1, represents half of a 30 ft. by 30 ft. diaphragm, which is composed of staggered precast concrete planks that are compressed together using threaded rods and then clamped to the steel beams. A similar test setup was utilized by Easterling and Porter (1994) to investigate composite diaphragms. Steel beams with sizes W14x30 and W12x19, acting as the chords in the diaphragm, were selected to represent potential beam sizes in a gravity system, and the shear connectors were designed accordingly. A W18x40 member was chosen as the steel girder that is part of the seismic force resisting system along the perimeter. The number of connectors between the steel girder and girder plank was varied to explore different failure modes. No reinforcement was used in the planks in these simulations.

Cast-in channels were meshed with both eight-node reduced integration brick elements (C3D8R) and six-node reduced integration triangular prism elements (C3D6R), while the steel beams and concrete planks were meshed with C3D8R only. The complex geometry of the clamps and the bolts, modelled in detail in this work, necessitated use of four-node tetrahedron elements (C3D4).

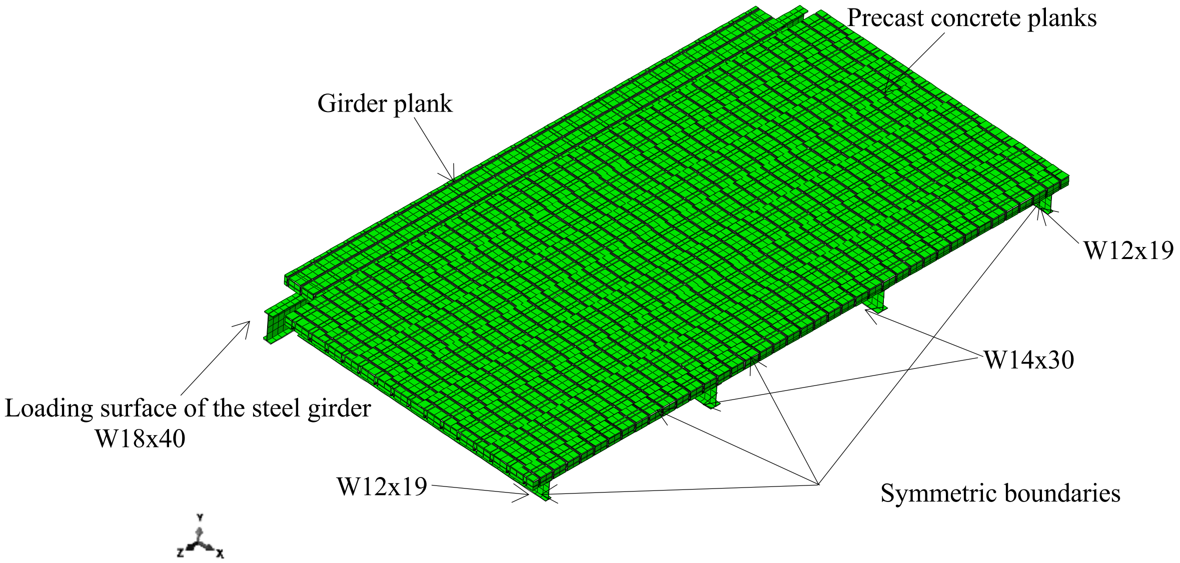

Figure K.1 Deconstructable composite diaphragm finite element model

K.1.1 Boundary conditions, load applications and contact

A symmetric boundary condition, as show in Figure K.1, was defined such that nodes on these surfaces were prevented from translating in the X direction and rotating in the Y and Z directions. The ends of the steel girder were restrained from moving vertically to avoid rigid body motion of the system.

The loading history in these analyses was divided into three steps. Compression between planks was simulated by applying pressure on all the side surfaces of the diaphragm slab except for the surface where the boundary condition was defined, which is acceptable unless the response in the vicinity of the rods is studied. Bolt pretension was then obtained by assigning a thermal expansion coefficient and temperature change to the bolts, creating thermal shrinkage and generating tensile forces in the shanks because of the constraints at the bolt ends. The steel girder was then subjected to cyclic loading using displacement control in the Z direction. The displacement history is provided in

Figure K.2. All the loadings were applied slowly and smoothly to minimize dynamic effects and obtain a quasit-static solution.

The contact behavior between surfaces was defined in the normal direction with “Hard contact” and in the tangential direction using a penalty formulation. The frictional coefficient was taken as 0.3 for all the surfaces. General contact was selected to automatically define potential contact surfaces.

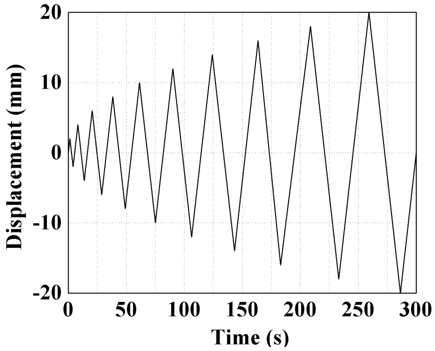

Figure K.2 Displacement loading history for computational models

K.1.2 Material models

- Material model for concrete

Concrete tensile cracking and compressive crushing were accounted for using the concrete damaged plasticity model provided in ABAQUS. The tensile stress-strain relationship is linear elastic until the cracking stress is reached, and a softening stress-strain curve follows representing the formation of cracking. The compressive stress-strain response is linear elastic until the initial yield stress. The subsequent response is characterized by strain hardening and strain softening beyond the ultimate stress. Under cyclic loading, this concrete model can capture opening and closing of cracks observed in tests by allowing for stiffness recovery when the load is reversed. The compressive stress-strain curve in BS EN 1992-1-1, provided in Equation (K.1), was employed for this analysis. The elastic modulus was calculated using Equation (K.2). The Poisson’s ratio was taken as 0.2.

$$\frac{\sigma_c}{f_{cm}} = \frac{k\eta - \eta^2}{1 + (k-2)\eta} \tag{K.1}$$

$$E_{cm} = 22(\frac{f_{cm}}{10})^{0.33} \tag{K.2}$$

Where,

f_{cm}= mean value of concrete cylinder compressive strength (MPa)

σ_c= concrete compressive stress (MPa)

$\eta = \frac{\varepsilon_c}{\varepsilon_{c1}}$

ε_c= concrete compressive strain

ε_{c1}= concrete compressive strain corresponding to peak stress f_{cm}

$\varepsilon_{c1} = 0.7 f_{cm}^{0.31} \leq 2.8$

$k = \frac{1.05 E_{cm} \times \varepsilon_{c1}}{f_{cm}}$

The default parameters specified in ABAQUS for the concrete damaged plasticity model were used to characterize the plastic behavior under general stress and stress state. The parameters include: dilation angle = 38°, eccentricity = 0.1. K_c, the ratio of the second invariant of the stress deviator on the tensile meridian to that on the compressive meridian at initial yield at a given first invariant of stress such that the maximum principal stress is negative, is equal to 0.67. The ratio of biaxial compressive yield stress to uniaxial compressive yield stress σ_{bo}/σ_{co} is taken as 1.16.

Concrete damage variables characterize stiffness degradation when the specimen is unloaded from any point on the softening branch. The damage variables range from zero for an undamaged model to one, exhibiting complete loss of strength and stiffness. Concrete tensile damage D_c and compressive damage D_t were derived using the following expressions:

$$D_c = 1 - \sigma_c / f_c \tag{K.3}$$

$$D_t = 1 - \sigma_t / f_t \tag{K.4}$$

Because mesh sensitivity exists for concrete with little or no reinforcement, tension stiffening is defined in terms of a stress-displacement curve rather than a stress-strain curve to eliminate localization issues.

- Material models for steel beams, channels and bolts

An elastic-perfectly-plastic material model is defined for the steel beams and channels. The nominal yield stress for the steel beams and channels is taken as 345 MPa. The elastic modulus is taken as 200 GPa for all of these components. The mechanical behavior is assumed to be the same in both tension and compression. A typical stress-strain curve for Grade 8.8 bolt material is provided in Kulak et al. (1987) and used for the analysis, as seen in Figure K.3.

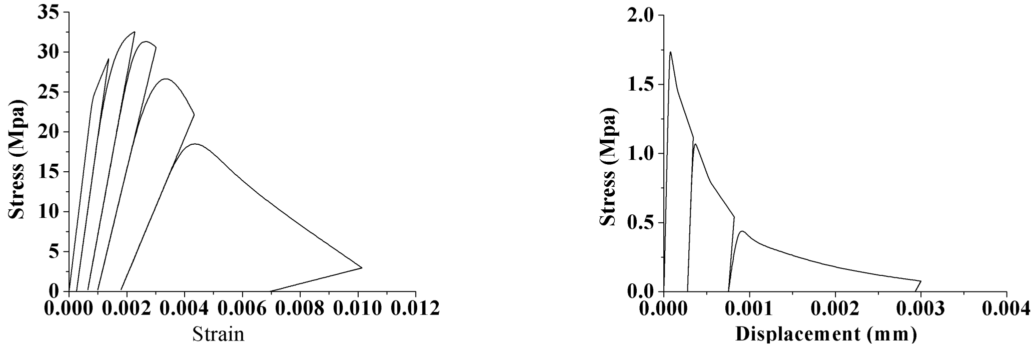

a) Concrete cyclic compressive behavior b) Concrete cyclic tensile behavior

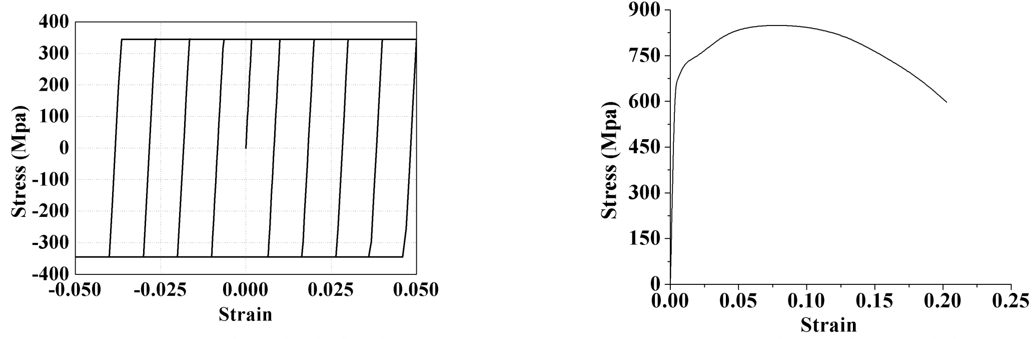

c) Steel cyclic behavior d) Bolt material

Figure K.3 Material stress-strain curves

K.2 Analysis results

The parameters of the computational models for the diaphragm system are listed in Table K.1, including the compressive stress between adjacent planks and the number of shear connectors between the steel girder and girder plank. The different compressive stresses in the table correspond to different spacing between the threaded rods. For example, when the threaded rods are placed at a distance of 4 ft., an equivalent compressive stress of 1.5 MPa is assumed. Although the steel girder is designed as a bare steel section, at least twenty shear connectors are needed to ensure a minimum of 25% composite action (AISC 2016a). The spacing of the clamps is reduced from 3 ft. to 2 ft. when 28 clamps are used for the steel girder.

Table K.1 Analytical model parameters

Model Number	Compressive stress (MPa)	Number of shear connectors
1	1.5	28
2	1.5	20
3	3.0	28
4	3.0	20
5	6.0	28
6	6.0	20

The cyclic load-displacement curves are plotted in Figure K.4. The limit state for the first four models is joint sliding due to diaphragm shear; therefore, the compression between adjacent planks is directly related to the ultimate strength. The hysteresis loops are almost identical for Model 1 and Model 2, even though the number of shear connectors varies. Small, but slightly different, slip between the steel girder and girder plank is found for Models 3 and 4, which could explain that the hysteresis curves for the two models are very much alike, but differences do exist. Because the clamping stress between the planks is doubled, the peak strength of Model 3 (Model 4) is twice that of Model 1 (Model 2). Distinct load-displacement curves are plotted for Model 5 and Model 6, as their limit state is slip of the clamps between the steel girder and girder plank. The number of shear connectors affects the ultimate strength of the diaphragms. After doubling the clamping stress, the strength increase of Model 3 is larger than Model 4, which is reasonable since Model 4 has fewer clamps and slip happens earlier than Model 3. All the diaphragms demonstrate ductile behavior with no strength and stiffness degradation. All the limit states observed from the simulations are shown in Figure K.5.

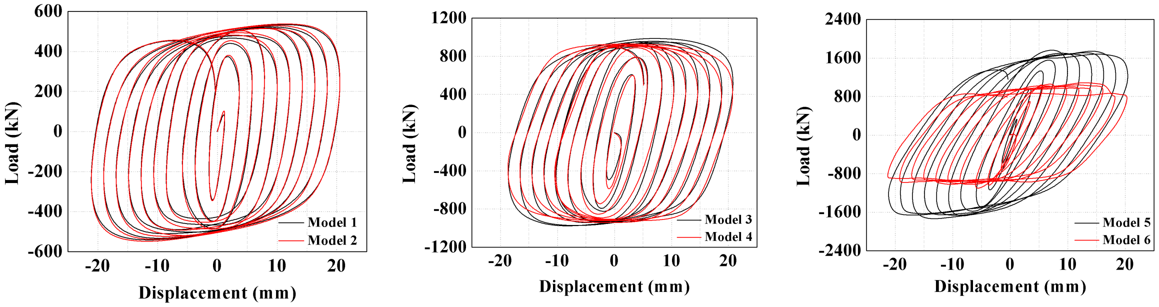

Figure K.4 Load-displacement curves

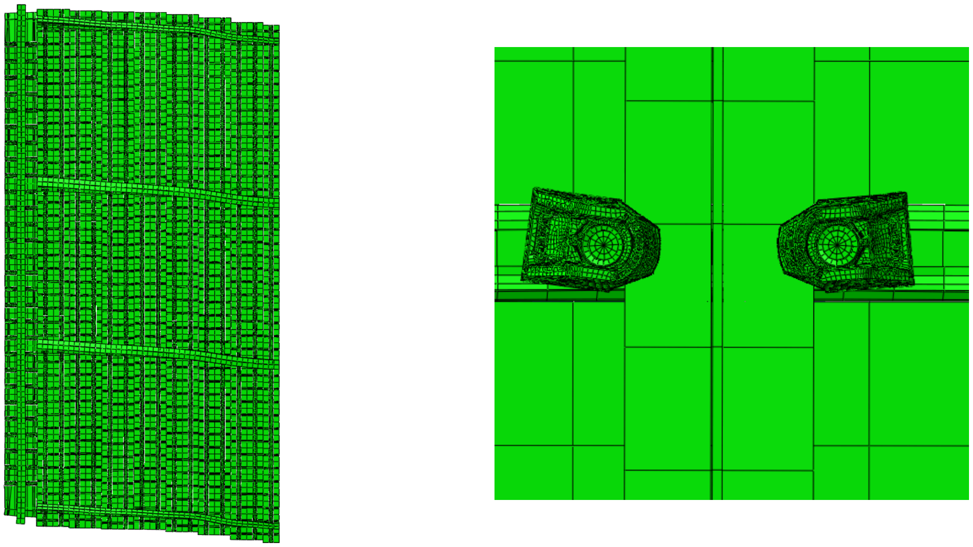

Joint sliding

Rotation of clamps

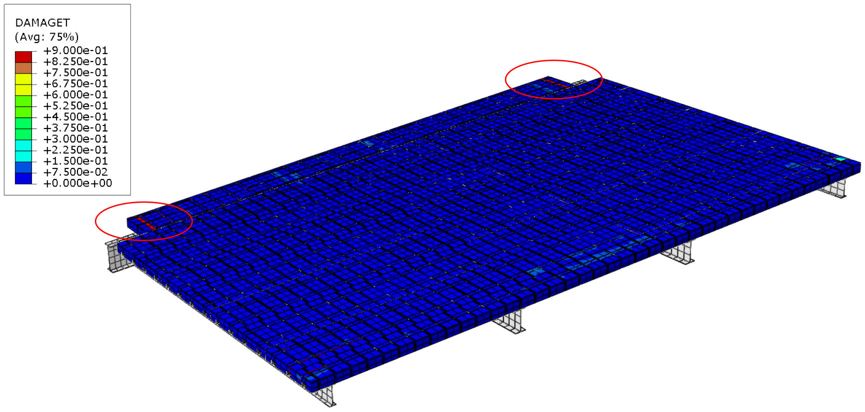
DAMAGET
(Avg: 75%)
+9.000e-01
+8.250e-01
+7.500e-01
+6.750e-01
+6.000e-01
+5.250e-01
+4.500e-01
+3.750e-01
+3.000e-01
+2.250e-01
+1.500e-01
+7.500e-02
+0.000e+00

Localized concrete tensile damage

Figure K.5 Limit states of deconstructable composite diaphragm models

In the diaphragm models, the moment at the symmetric boundaries is shared by the steel chords and the concrete slab in accordance with their relative stiffness. Figure K.6 shows the ratio of the moment distributed to steel to the moment resisted by concrete for all the models during the cyclic loading process. The ratios for Models 1 and 2 are almost the same, since they have the same limit state. More force flows into concrete in Models 3 and 5 than Models 4 and 6. As the compressive stress between the concrete planks increases, less force flows into the steel framing. It can be concluded that the majority of the external force follows the stiffer load path and flows into the concrete slab, and the rest goes through the steel chords that are bent about their weak axes.

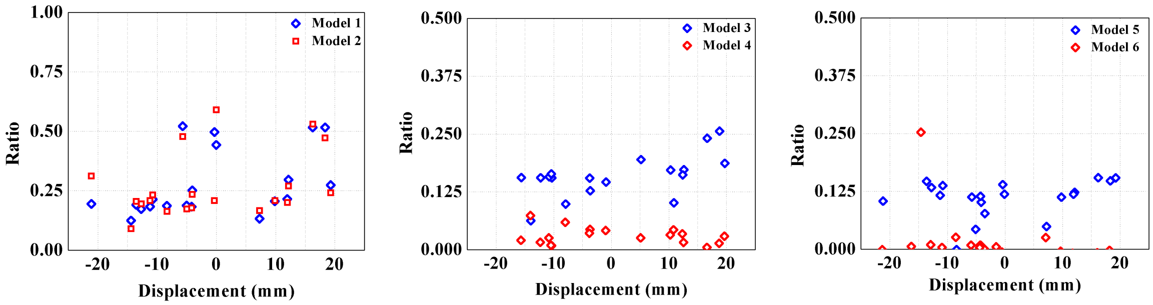

Figure K.6 Steel moment to concrete moment ratio

While diagonal cracking may be seen in monolithic concrete diaphragms, this failure mode is uncommon in precast concrete diaphragms, since the joint between the diaphragms provides a weak link in the system. This argument is validated by the minimal concrete tensile damage observed in the diaphragm models. Joint opening due to diaphragm bending, another potential limit state for a precast concrete diaphragm, did not occur for the models developed.